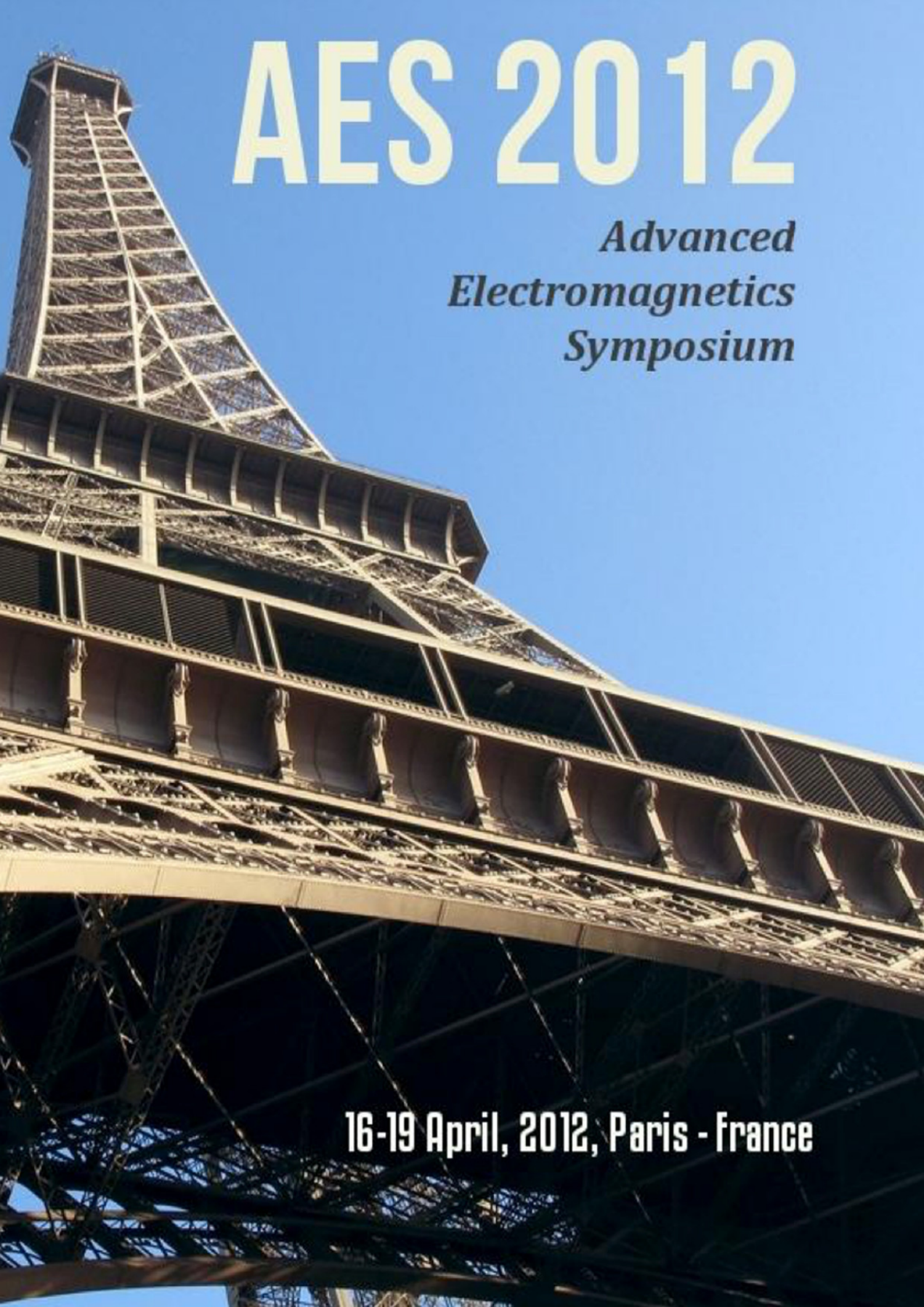


AES 2012

Advanced Electromagnetics Symposium

16-19 April, 2012, Paris - France

ISBN: 978-2-9545460-8-7

AES 2012, Paris – France

Advanced Electromagnetics Symposium

Edited by

Saïd Zouhdi | University Paris-Sud, France
&
Xavier Begaud | Telecom Paristech, France

Organizers

AES 2012 General Chair

Said Zouhdi, Paris Sud University, France

AES 2012 General co-Chairs

Xavier Begaud, Telecom Paristech, France
Alain Priou, Paris-Ouest University, France

Organizing Committee

L. Bernard, France
Y. Bernard, France
E. Berthelot, France
R. Corcolle, France
J. C. Cousin, France
L. Daniel, France
O. Dubrunfaut, France
A. C. Lepage, France
L. Santandrea, France
J. Sarrazin, France

International Advisory Committee

Y. Antar, Canada
P. Banerjee, India
A. Bossavit, France
M. Chandra, Germany
J. Chazelas, France
C. Christopoulos, UK
A. G. D'Assunção, Brazil
P. de Maagt, Netherlands
V. Fouad Hanna, France
A. Georgiadis, Spain
Y. Hao, UK
N. Ida, USA
K. Ito, Japan
A. Karwowski, Poland
A. Kladas, Greece
K. Langenberg, Germany
E. Li, China
L.-W. Li, China
K. M. Luk, Hong Kong
J. Mao, China
M. Ney, France
A. Razek, France
A. Sibille, France
A. Sihvola, Finland
P. Smith, Australia
G. Uhlmann, France
J. C. Vardaxoglou, UK

Technical Program Committee

A. Alu, USA
M. Ahachad, UAE
S. E. Barbin, Brazil
A. Boltasseva, USA
P. Coquet, France
C. Craeye, Belgium
T. J. Cui, China
R. Dkiouak, Morocco
J. Hu, China
B. Huyart, France
Y. Jaouen, France
A. Khenchaf, France
A. Kishk, Canada
K. Kitayama, Japan
J.-M. Lopez, France
H. Ouslimani, France
E. Pottier, France
C.-W. Qiu, Singapore
A. Raizer, Brazil
O. Ramahi, Canada
J.T. Sri Sumantyo, Japan
R. Staraj, France
Dr Goran M Stojanović, Serbia and Montenegro
H. Süß, Germany
N. Vallestero, USA
V. Y. Vu, Viet Nam
T.-L. Wu, Taiwan
W.-Y. YIN, China
A. I. Zaghloul, USA
J. Zhu, USA

Special Session Organizers

A. Sibille, France
J. Wiart, France
J.-C. Badot, France
O. Dubrunfaut, France
J. Hao, France
R. Mittra, USA
Y. Hao, UK
Y. Bernard, France
L. Daniel, France
B. Ravelo, France
A. Zhukov, Spain
L. Panina, Russia
J.-C. Levy, France
M. Krawczyk, Poland
K. Fukunaga, Japan
J. Wiart, France
S. Gonzalez Garcia, Spain
K. M. Luk, Hong Kong
K. Wa Leung, Hong Kong
K. Tong, UK
H. C. C. Fernandes, Brazil
Z. Hu, UK
H. Ouslimani, France
R. Staraj, France
J.-M. Ribero, France

Sponsors & Supporters

We wish to thank the following organizations for their contribution to the success of this conference:

Telecom Paristech, France
SUPELEC, France
GDR Ondes, France
IOP Publishing, UK
EPL, Uk
Hemera, France
CST, Germany
IEEE-APS, USA
URSI, Belgium

Contents

Design and analysis of optical and microwave antennas:
Is it simply a matter of scaling? 14
Raj Mittra

Tunable current-mode filter using DXCCII 18
Muhammed A. Ibrahim

The electrostatic model of gravity 22
Ioan Rusu

Pressure effect on properties of corona discharge in an
electrostatic precipitator 32
*Nouri Hamou, Mehdaoui Akila, Baali Aissa, Aissou Massinissa
and Zebboudj Youcef*

Comparison of transmission line and electromagnetic approaches to
modeling of buried horizontal wires of finite length 40
*B. Markovski, L. Grcev, V. Arnautovski-Toseva, K. Drissi, S. Grceva,
K. Kerroum and A. Kuhar*

Focusing of electromagnetic field by a 3-D cassegrain reflector
system coated with chiral medium 45
M. J. Mughal, A. R. Farooqi and M. M. Ali

Resonant frequency of a rectangular and an equitriangular
tunable microstrip antennas and comparison 50
L. Djouablia, C. Aissaoui and A. Benghalia

Effect of large transverse curvature in high-frequency diffraction 60
Ivan Andronov and Daniel Bouche

Analysis of electromagnetic scattering by a composite
cylinders using WCIP method 66
J. Selmi, R. Bedira, A. Gharsallah and H.Baudrand

Effects of quasi-static approximation of green's functions in the
model of a horizontal wire conductor in homogeneous soil 71
Vesna Arnautovski-Toseva, Khalil El Khamlichi Drissi and L. Grcev

An efficient computational technique for performance
prediction of inductors on flexible substrates 80
*Nikola Jeranče, Nataša Samardžić, Dragana Vasiljević
and Goran Stojanović*

The limitation of time-harmonic models of the superlens 87
Wolfgang J. R. Hoefer

An electric field volume integral equation approach to simulate surface plasmon polaritons 91
Rob Remis and Edoardo Charbon

Efficient compression of far field matrices in multipole algorithms based on spherical harmonics and radiating modes 101
Arne Schröder, Heinz-D. Brüns and Christian Schuster

A Bayesian approach to determine the electric field of broadcasting medium wave.....106
Juliana Monteiro, Jasmine Araújo, Josiane Rodrigues, Simone Fraiha, Hermínio Gomes, Renato Francês, Gervásio Cavalcante and Adaildo D'Assunção

Efficient computation of the magnetic field of low-frequency antenna.....109
Rania Oubaid, Yvan Lefevre and Jean Rene Poirier

Time-domain semiconductor structure simulation based on 2D/3D coupled electromagnetism/transport modeling.....116
C. Dalle

Curvilinear vector finite difference approach to the computation of waveguide modes 121
A. Fanti, G. Mazzarella and G. Montisci

Combined FVTD/PSTD schemes with enhanced spectral accuracy for the design of large-scale EMC applications 130
Nikolaos V. Kantartzis, Alexandros I. Dimitriadis and Theodoros D. Tsiboukis

Pulse dispersion in layered cylindrical dielectric waveguides.....140
Ioannis O. Vardiambasis, Theodoros N. Kapetanakis, Melina P. Ioannidou and Angela P. Moneda

Lumped balanced interconnect H-tree network modeling.....147
Blaise Ravelo and Thomas Eudes

Shorting via arrays for the suppression of simultaneous switching noise (SSN) in multilayer PCBs.....156
Jianjie Li, Junfa Mao and Siwei Ren

Fast and accurate modeling of PCB interconnection lines for high-rate signal integrity time-domain measurement 160
Thomas Eudes, Blaise Ravelo and Rabee Al Hayek

3D-modelling of an aperture illuminated by a HF electromagnetic source for EMC application 168
Zakia Abidi, Mohamed Djennah, Bernard Bandelier and Françoise Rioux-Damidau

Influence of the line configuration and the shielding wire on the over voltages induced on overhead power distribution lines caused by indirect lightning strokes 173
Nassima M'ziou, Ahmed Boubakeur and Mahdi Izadi

Electromagnetic simulation of a magnetically-coupled ZOR on YIG thin film 182
Aziza Zermane, Bruno Sauviac, Bernard Bayard and Abdelmadjid Benghalia

Electromagnetic compatibility in hospitals for electromedical equipment and personal communication systems 185
S. de Miguel, M.A. Martín, J. del Pozo, V. Febles, J. García, D. S. Suárez, J.C. Fernández de Aldecoa and V. Ramos

Design and calibration of a wideband TEM-cell for material Characterization 190
S. K. Yee, A Kazemipour, A. Sayeg and M. Z. Mohd Jenu

Transfer of orbital angular momentum on macroscopic object in the UHF band 194
Ronan Niemiec, Christian Brousseau, Olivier Emile and Kouroch Mahdjoubi

Fresnel field to far field transformation based on two-dimensional Fourier series expansion 200
Yury V. Krivosheev, Alexander V. Shishlov, Aleksey K. Tobolev and Irina L. Vilenko

Wideband calculable antenna for EMC measurements 208
Syarfa' Zahirah Sapuan, Alireza Kazemipour and Mohd Zarar Mohd Jenu

On the evaluation of the shielding effectiveness of electrically large enclosure 211
Angelo Gifuni, Antonio Sorrentino, Alessandro Fanti, Giuseppe Ferrara, Maurizio Migliaccio, Giuseppe Mazzarella, and Federico Corona

Diffraction by a lossy 90° dielectric wedge 217
Gianluca Gennarelli and Giovanni Riccio

MESUA: A model dedicated to radar detection in bistatic and/or monostatic mode 221
Ngoc Truong Minh Nguyen, David Lautru and Hélène Roussel

The reconstruction of objects buried in a stratified medium with rough interfaces 228
Ö. Özdemir and H. Haddar

Electromagnetic scattering by 3D dielectric objects buried under 2D rough surfaces 231
Yasemin Altuncu

A novel multiband fractal antenna 235
Crislane Silva, Lidiane Araujo, Antonio Belfort and Marcos de Melo

Band-notched small square monopole antenna surrounded by rotated C-shaped parasitic structure for UWB applications 239
Mohammad Ojaroudi, Nasser Ojaroudi and Shervin Amiri

Microstrip-fed slot antenna with band-notch performance for UWB wireless communications 243
Nasser Ojaroudi, Mohammad Ojaroudi and Shervin Amiri

Multipole theory for tight focusing of polarized light: Application to hemispherical solid immersion lens (SIL) for subsurface imaging 246
Thanh Xuan Hoang, Xudong Chen and Colin J.R. Sheppard

Space-efficient UWB tapered slot antenna 251
Anatoliy Boryssenko and Elen Boryssenko

Full and compact polarimetry modes using RADARSAT2 data 255
Boularbah Souissi, Mounira Ouarzeddine and Aichouche Belhadj-Aissa

Quad band CPW antenna for PCS, bluetooth, WiMAX and WLAN applications 265
Masoumeh Darvish and Hamid Reza Hassani

Multi band monopole antenna for MIMO systems 270
Masoumeh Darvish and Hamid Reza Hassani

Compact PCB-embedded GPS antenna loaded with lumped elements 274
Jungho Ahn, Junho Choi, Seunghwan Kim and Young-Sik Kim

A compact dual-band dual-port diversity antenna for LTE 277
Lila Mouffok, Anne Claire Lepage and Julien Sarrazin and Xavier Begaud

Ionospheric depletion detection for Indian SBAS, GAGAN 282
Prachi Joshi, P.R.Mahapatra, A.S. Ganeshan and S. Nirmala

Photonic band gaps in 2D photonic crystals composed of core-shell particles 286
Amel Labbani And Abdelmadjid Benghalia

High-voltage Tesla coil discharges guided and triggered by femtosecond laser filaments in air....290
Yohann Brelet, Aurélien Houard, Benjamin Forestier, Yi Liu, Bernard Prade, Jérôme Carbonnel, Yves-Bernard André and André Mysyrowicz

Femtosecond laser filament guided electric discharge as an RF plasma virtual antenna....295
Benjamin Forestier, Aurélien Houard, Yohann Brelet, Jérôme Carbonnel, Bernard Prade, Yves-Bernard André, Michel Pellet and André Mysyrowicz

VHDL-AMS modeling of VCSEL light transmission through the graded-index optical fiber....298
Fatima Zohra Baouche, Farida Hobar and Yannick Hervé

Simulation of the propagation of the solitons in presence of the Raman Effect and the third-order dispersion in the optical fiber links....301
Lyes Bahloul, L. Cherbi, W. Medellel and A.Bellil

Significance of quantum communication in LEO satellite transmission networks....307
Skander Aris, Abderraouf Messai, Hatem Mokhtari, Nadjim Merabtine, Mosleh M. Alharti and Malek Benslama

Exact solution of coupled differential equations of stimulated Brillouin scattering....312
J. Malekzadeh and F. M. Akbari

ANFIS-based estimation of auditory brainstem response changes in rabbits due to GSM-900 radiation exposure....315
Theodoros N. Kapetanakis, Ioannis O. Vardiambasis, Antigoni Kaprana and Melina P. Ioannidou

Measuring kinetics of enzymatic hydrolysis of acetylcholine in presence of high voltage pulses by dielectric characterization....319
C. Gilbert and O. Meyer

Glucose quantification in highly scattering media using diffuse reflectance polarimetry....323
E. T. Aksenov, G.A. Kafidova, D.V. Mokrova and V.M. Petrov

ELU-1: Emotions language unified is a BCI for communication support for patients with chronic motor disabilities....327
A. Fanti, M. Franceschelli, P.Maxia and D. Salpietro

3D Computer modeling of an MRI antenna steeped in a dielectric substrate....330
Zakia Abidi, Mohammed Djennah, Bernard Bandelier

and Françoise Rioux-Damidau

Retrieval of the relevant parameters of natural multilayer systems 335
Demetrio Macías, Ana Luna, Diana Skigin, Alexandre Vial and Marina Inchaussandague

Actin Filaments Can Serve as Nonlinear Electrical Network.....341
Dalibor L. Sekulic and Miljko V. Sataric

Effects of RF/ MW emitted from mobile-phone base-stations on plant growth using chlorophyll a fluorescence and vegetative growth 346
S. T. Kafi, A. M. Ahmed, Samah Osman, Ahmed Bakheit and A. K. Sabir Ali

Optical response of composite materials: comparison of different approaches 356
Guillermo Ortiz, Marina Inchaussandague, Diana Skigin, Ricardo Depine and Luis Mochán

Comprehensive study of compact LHM CSRR and CSSR-based design BPWG filter.....362
Ehab K. I. Hamad, Hany A. Atallah and Mohamed A. Hassanien

Virtual singular scattering of electromagnetic waves in transformation media concept 368
Yurii Barabanenkov, Mikhail Barabanenkov and Sergey Nikitov

Dual-band coherent perfect absorption/thermal emission from ultrathin bilayers.....376
Simin Feng

Cut wires grating - single longitudinal wire" planar metastructure to achieve microwave magnetic resonance in a single wire 382
Galina Kraftmakher and Valery Butylkin

Optimization for both the size and spacing between two antennas for a 2 * 2 MIMO system using MNG metamaterial.....389
Belgacem Aouadi, Mondher Labidi and Jamel Belhadj Tahar

Damping of the opaque band and layer-by-layer transmission through disordered two dimensional photonic crystals.....393
Yurii Barabanenkov, Mikhail Barabanenkov

On the dynamics of cutting arc plasmas: the role of the power supply ripple.....400
L. Prevosto, B. Mancinelli and H. Kelly

Magnetic shape memory alloys as smart materials for micro-positioning devices.....404

A. Hubert, N. Calchand, Y. Le Gorrec and J.-Y. Gauthier

Surface impedance of BaFe2-xNixAs2 in the radio frequency range.....414
A. Abbassi, M. Saint-Paul, R. Dkiouak, M. R. Britel, Zhao-Sheng Wan, Huinqian Luo, Xiagye Lu, Cong Ren and Hai-Hu Wen

An electromagnetic suspension platform for position and tracking control verification 417
Chin E. Lin and Wei-Cheng Huang

Investigation of ionized fields due to bipolar DC transmission lines 424
M. Aissou, A. K. Laifaoui, H. Aitsaid. H. Nouri and Y. Zebboudj

Analytical model for the TeraHertz noise in In0.53Ga0.47As n+nn+ diodes 428
Fatima Zohra Mahi, Luca Varani, Paval Shiktorov and Evgenij Starikov and Viktor Gruzhinskis

Pspice modeling of nonlinear transmission lines analog to digital conversion.....433
Hala J. El-Khozondara, Rifa J. El-Khozondar, Ibtesam Abu Ariban and B. Z. Essimbi

Compact active integrated antenna by using an interdigital coupling strip for WiMAX applications 439
Mohammad Ojaroudi, Jalil Mazloum, Ali Jalali and Nasser Ojaroudi

A 20 – 40 GHz Balun in 0.13 µm GaAs pHEMT Technology 442
Antoine Khy and Bernard Huyart

Microstrip low-pass filters by using novel defected ground structure slot with a pair of protruded T-shaped strips inside the slot 446
Mohammad Ojaroudi, Nasser Ojaroudi, Reza Habibi and Homauon Ebrahimian

Facet phase's influence on adiabatic chirp and transmission penalty for index-coupled distributed-feedback lasers.....450
Kechaou Khalil, Thedrez Bruno, Grillot Frédéric, Erasme Didier and Aubin Guy Kazmierski Christophe

Some features of magnetometric and sensor devices based on the field effect hall sensor.....455
M. L. Baranochnikov, A. V. Leonov, V. N. Mordkovich, D. M. Pazhin and M. M. Filatov

A simple ferromagnetic hysteresis model for current transformer simulation.....460
Tiago Staudt, Mauricio Rigoni, Walter P. Carpes Jr., Nelson Jhoe Batistela

Thermal reduction in portable systems using DVS technique diary 468
R. Sulaiman

Design, manufacturing and characterization of integrated inductors with magnetic layers for DC-DC converter.....472
Dagal Yaya, Désiré Allassem, Mahamoud Youssouf, Ali Siblini, Jean Pierre Chatelon and Jean Jacques Rousseau

Study and fabrication of a planar integrated magnetic transformer.....477
F. Kahlouche, Khamis Youssouf, Mahamoud Youssouf, A. Siblini, S. Capraro, J. P. Chatelon and J. J. Rousseau

New advances in monitoring the aging of electric cables in nuclear power plants 480
Maud Franchet, Nicolas Ravot, Nicolas Grégis, Josy Cohen and Odile Picon

A simple electromagnetic analysis of magnetic NDE using a double rectangular coil an a Hall Effect sensor.....485
Laroussi Bettaieb, Hamid Kokabi and Michel Poloujadoff

Reconsidering ampere's double layer representation for magnetic field evaluation in a NDE application 491
Michel Poloujadoff, Laroussi Bettaieb and Hamid Kokabi

Time- and frequency-domain evaluation of stochastic parameters on signal lines.....498
Paolo Manfredi, Igor S. Stievano, Flavio G. Canavero

Statistical uncertainty budget in a reverberation chamber.....507
Philippe Besnier, Christophe Lemoine and Abdou Khadir Fall

Sensitivity analysis to compute advanced stochastic problems in uncertain and complex electromagnetic environments 513
Sébastien Lalléchère, Basile Jannet, Pierre Bonnet, Sébastien Girard and Françoise Paladian

Study of a reverberation chamber shape inspired from chaotic cavities 522
K. Selemani, E. Richalot, O. Legrand and F. Mortessagne

Multivariate uncertainty analysis of scattered electric field from building facades in urban environment 527
Shermila Mostarshedi, Bruno Sudret, Elodie Richalot, Joe Wiart and Odile Picon

Statistical models for antennas.....532
A. Sibille, C. Roblin, M.A. Yousuf, M. Sacko, Z. Mhanna and E. De Mur

Dielectric relaxations due to electrons in oxides.....540

Jean-Claude Badot

Design and evaluation of two coaxial transmission lines to characterize electromagnetism properties of hard clays (non crushed) and concrete 546
T. Bore, D. Placko, D. Coelho, S. Delepine-Lesoille, C. Gatabin, P. Sabouroux, G. Six and F. Taillade

Multiscale electronic transport mechanism and true conductivities in amorphous carbon-LiFePO4 nanocomposites 556
K. A. Seid, B. Lestriez, J.-C. Badot, O. Dubrunfaut, D. Guyomard and S. Levasseur

Signs, curls, and time variations: learning to appreciate Faraday's law 562
A. Sihvola, J. Leppävirta and H. Kettunen

Difficulties in teaching electromagnetism: an eight-year experience at Pierre and Marie Curie University 567
H. Roussel and M. Hélier

Waves are not vectors, and fields are not waves either 571
Alain Bossavit

Fractional-order rectangular waveguides 576
R. Ismail and A. G. Radwan

Experimental demonstration of two kinds of carpet cloak 579
Di Bao, Khalid Z. Rajab and Yang Hao

Comparison of piezoelectric switching shunt circuits for vibration suppression 584
Yuan-Ping Liu, Dejan Vasic and François Costa

Electromagnetic controllable surfaces based on trapped-mode effect 594
V. Dmitriev, S. Prosvirnin, V. Tuz and M. N. Kawakatsu

Preliminary electrical characterization of piezoelectric transformer for plasma glow discharge generator 601
F. Pigache, C. Nadal and Y. Lefevre

Analysis of coupling between electric cables and multi-dimensional-dipoles near-field radiation 607
E. R. Rajkumar, M. Bensetti, B. Ravelo and M. Kadi

Near-field map radiated by structures disturbed by arbitrary transient signals 616
Yang Liu and Blaise Ravelo

On the time-domain near-field radiation with PWS method 625

Yang Liu, Blaise Ravelo and Jaleleddine Ben Hadj Slama

Experimental reconstructions of dielectric targets with metallic inclusions by microwave imaging 635
Ricardo Monleone, Andrea Randazzo, Matteo Pastorino and Andrea Salvadè

Experimental characterization of tuneable metamaterials based on ferromagnetic microwires.....642
J. Carbonell, H. García-Miquel and J. Sánchez-Dehesa

Equivalence between low field microwave absorption and giant magnetoimpedance through the poynting vector 644
Raúl Valenzuela

To the theory of nonreciprocal microwave transmission along a bianisotropic-dielectric-ferrite metasandwich 649
V.S. Butylkin, G.A. Kraftmakher, and V.P. Mal'tsev

Giant magnetoimpedance in thin wires: manipulation of magnetic anisotropy.....655
Valentina Zhukova, Mihail Ipatov and Arcady Zhukov

Magnons in samples with exchange and dipolar long ranged interactions: Spin wave resonance intensities and Brillouin spectral linewidths 661
Jean-Claude S. Levy

Application of electromagnetic waves for the degradation mechanisms of painted wooden cultural properties.....668
M.-J.Kim, Y.Kohdzuma, and K.Fukunaga

Feasibility of imaging technology using micro- and millimeter wave for nondestructive inspection of wooden buildings.....672
Yuko Fujiwara, Yoshihisa Fujii, Soichi Tanaka, Shogo Okumura Hiroyoshi Togo, Shoji Mochizuki, T. Kojima and NaoyaKukutsu

A framework to design temporal basis functions used in boundary element methods for transient electromagnetic scattering 675
Elwin van 't Wout, Duncan R. van der Heul, Harmen van der Ven and Cornelis Vuik

Accurate and efficient quadratures for transient electromagnetic potentials.....680
Anatoliy Boryssenko

A compact dual-band antenna for 2.4/5.2 GHz WLAN applications 685
Peng Zhang and Wen-Xun Zhang

Design of a 60 GHz metamaterial antenna for wireless BAN applications 688
Alessio Brizzi, Lianhong Zhang, Alice Pellegini and Yang Hao

Transverse transmission line method for spherical coordinates and antenna applications 692
H. C. C. Fernandes and A. S. Silva Neto

High-impedance surface absorbers: Theory and applications 697
F. Costa and A. Monorchio

Development of X Band metamaterial radar absorber 702
Mahmoud A. Abdalla, Zihrun. Hu

An analytical model for plasmonic radar absorbers 706
A. Noor and Z. Hu

Millimeter-wave elastomeric antennas 710
Sami Hage-Ali, Yovan Orlic, Nicolas Tiercelin, Ronan Sauleau, Philippe Pernod, Vladimir Preobrazhenski and Philippe Coquet

Design and Analysis of Optical and Microwave Antennas: Is it Simply a Matter of Scaling?

Raj Mittra

Electromagnetic Communication Laboratory, Penn State University, USA
*corresponding author, E-mail: rajmittra@ieee.org

Abstract

Recently, there has been a considerable interest in Nanoantennas, which find primary applications in the optical and terahertz frequency range. Some of these applications include optical sensing, serving as receptors of infrared energy in solar cells, lenses for terahertz radiation, and directed energy devices at infrared frequencies. Microwave antennas, on the other hand, have their own set of applications, both for communication and sensing. We all know, of course, that Maxwell's equations can be scaled with frequency. This prompts us to examine the question: "Is it possible to design optical antennas simply by scaling their microwave counterparts, or should we follow different strategies for the two frequency regimes?"

Keywords: Optical antennas, sensors, plasmonics, Dipole Moment (DM) method

HF, VHF, UHF and Microwave antennas have a long history, and they are recognized to be one of the key elements in enabling technologies, such as mobile communication, radio, television and sensing. In contrast to microwave and other low frequency antennas, optical antennas have received significant attention of researchers and engineers only relatively recently (see [1-32]) because of their potential applications in biological sensors, in photovoltaics (PVs), and in systems designed to focus and direct energy at infrared and terahertz frequencies by utilizing devices that are alternatives to conventional dielectric lenses. Intuitively, it would be natural for us to extend the design concepts of low frequency antennas by simply employing the principles of scaling, since it is a well known fact that Maxwell's equations do scale straightforwardly from one frequency to another, provided we also scale the material properties on an as- needed basis. We should realize, however, that the design goals for optical antennas (for examples, see Figs. 1 through 8) can be very different from those of their microwave counterparts. In the optical regime, we desire to enhance the absorption cross-section and the quantum yields in PVs, improve the efficiency levels of photochemical and photophysical detectors, boost the efficiencies of nanoscale light emitting devices, and increase the resolution of optical microscopes, etc. Since these objectives are typically very different from those for the microwave antennas, we may need to examine the design strategies very carefully to see if we can indeed leverage what we know about low frequency antennas to speed up the design of their optical versions.

We point out, as a starter, that although optical antennas, examples of which appear in Figs.1 through 8, often bear close resemblance to microwave antennas in their shape– though obviously not in size–they do possess an attribute that distinguishes them from their lower frequency counterparts; they exploit the unique properties of metal nanostructures that are plasmonic in nature only when the frequency is sufficiently high, for instance, in the optical frequency regime.

Another key problem that needs to be addressed in dealing with Nanoantennas pertains to their fabrication, which requires access to specialized technology, e.g., photolithographic techniques that can accurately handle dimensions on the order of 10 nm. In addition, the properties of materials we have available at our disposal at visible and near-visible wavelengths are often substantially different from those at microwave frequencies. For these reasons, simply attempting to scale a microwave radiator does not typically lead to an optical antenna with identical characteristics. Thus, development of new materials, such as metamaterials, as well as fabrication of practical devices utilizing these materials, which are typically both lossy and dispersive, pose significant challenges for us today.

The paper will describes a number of nanoscale devices suitable for optical frequencies that have been developed by taking a cue from their microwave counterparts and will point out both the potentials, as well as challenges that we face when we design them. We will also touch on a subject that is of considerable interest today, namely the feasibility of designing nanoantennas at lower frequencies, such as RF and microwaves, by using carbon nanotubes (CNTs) to realize antennas that are much smaller than those realized by using conventional materials. We will examine the question of whether such CNT-based Nanoantennas for RF and Microwaves are indeed the proverbial "holy grails," which have been highly sought after by engineers for decades, but have managed to elude us until now.

Finally, we will address a very important design issue, which also distinguishes the design of optical antennas from their microwave counterparts. What we are referring to here is the unique challenges we face when modeling Nanoantennas, stemming from the fact that almost all of the existing

commercial CEM (Computational EM) codes either break down or become highly inaccurate when dealing with nanoscale devices. This is because they often make simplifying approximations that are dubious at best and, consequently, lead to erroneous results. Fortunately, to mitigate the problem of simulating the performance of nanoscale devices, new modeling techniques, e.g., the DM (dipole moment) method [33-36], and efficient techniques for accurate modeling of artificial magnetic and dielectric materials are being actively developed by the author and will be discussed in the presentation.

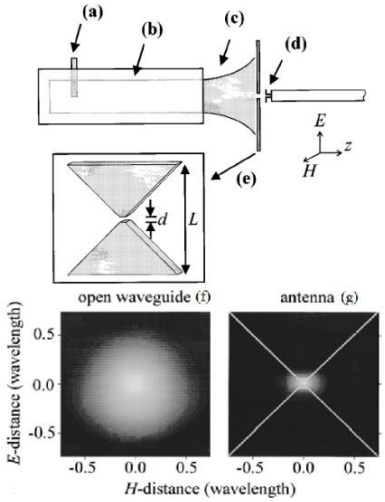


Fig.1. Microwave Antenna which is scaled down for optical frequency: (a) the microwave source; (b) the waveguide; (c) the illumination beam; (d) the dipole probe; (e) the antenna; (f) field intensity 2.5 cm in front of the open end of the rectangular waveguide; (g) field intensity measured 0.5 cm in front of the bow-tie antenna, which is positioned 2.5 cm in front of the open end of the waveguide.

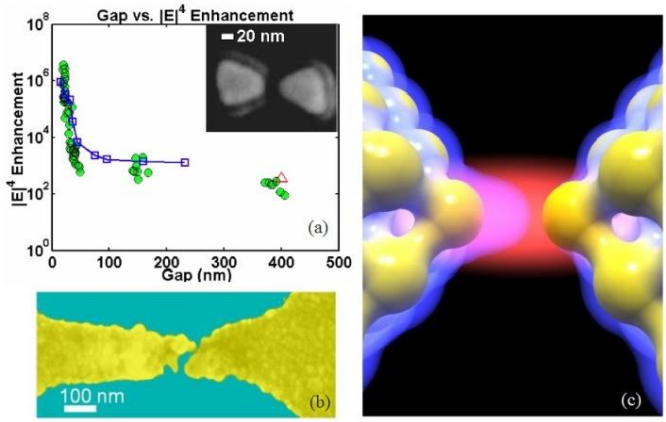


Fig.2. (a) Comparison of experimental (circles) and theoretical (open squares) values of the square of intensity enhancement for bowties.

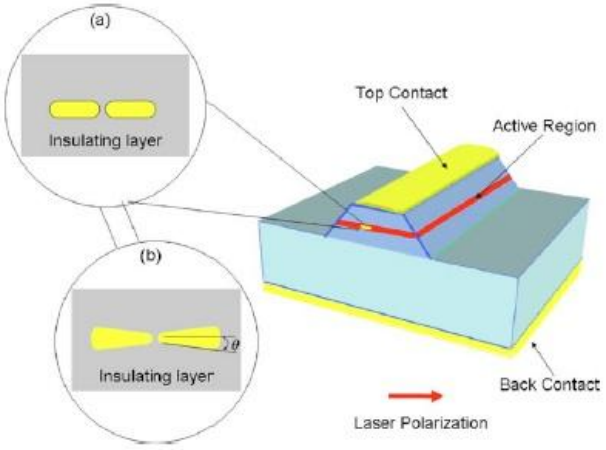


Fig.3. Plasmonic laser antenna: (a) nanorod design; (b) bow tie design.

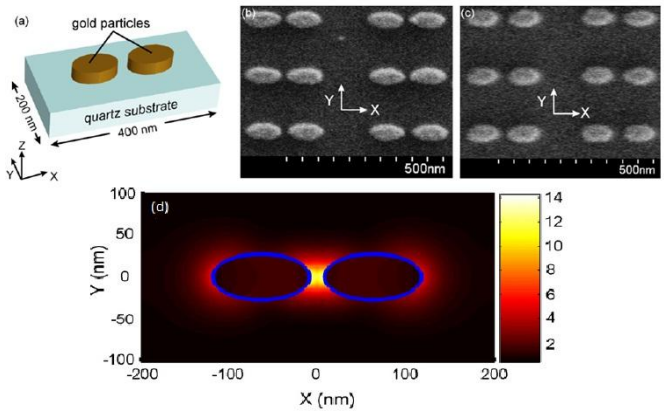


Fig.4. (a) The schematic of a unit cell; (b and c) FESEM images of samples A and B; (d) Normalized electric field map of a unit cell.

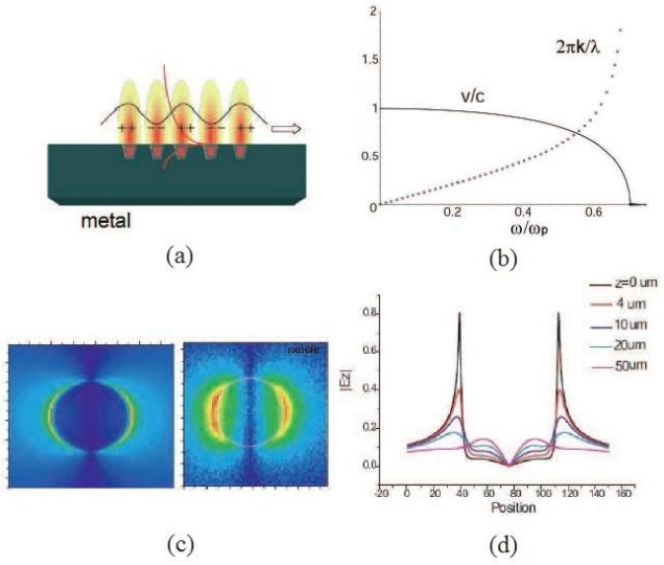


Fig.5. (a) Antenna based on surface plasmon polariton (SPP); (b) Dispersion relations; (c) Simulation and experimental results; (d) Electric field at various distances.

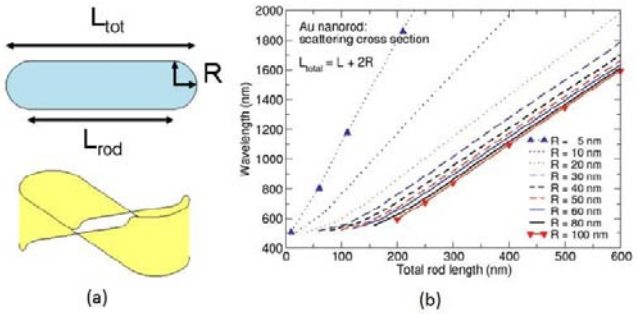


Fig.6. (a) Cylindrical nanorod with hemispherical caps and surface charge density typical for a dipolar resonance; (b) Dependence of dipole resonance wavelength on L_{total} for different R.

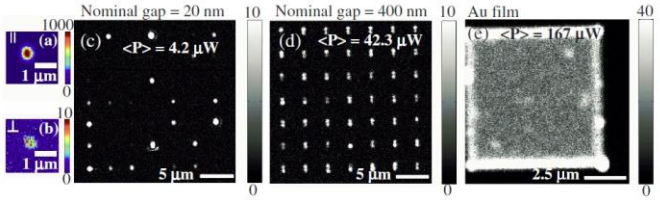


Fig.7. Visible luminescence images from bowtie arrays with nominal gap sizes of 20 nm (c) and 400 nm (d), as well from a smooth Au film (e), with 10 ms per pixel, 830 nm pump, and average incident powers (c) 4:2 W, (d) 42:3 W, (e) 167 W. Strong TPPL originates from the edges of the film in (e) due to increased surface roughness resulting from the lift-off procedure. Incident polarization dependence is shown in (a) and (b) for a 20 nm gap bowtie at high power (note different scales).

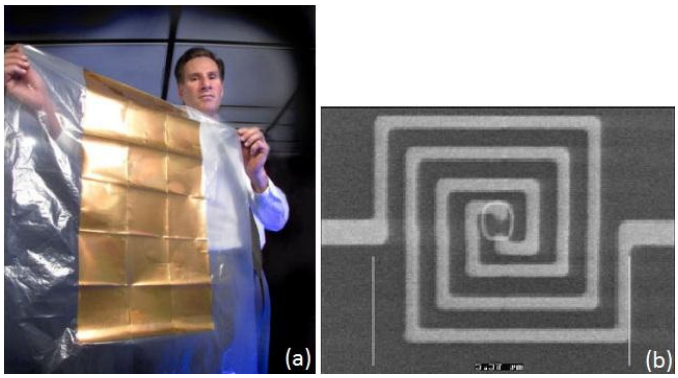


Fig.8. (a) Plastic sheet of nanoantenna arrays with roughly 260 million antennas in each square; (b) SEM image.

References

[1] Optical antenna: Towards a unity efficiency near-field optical probe, R. Grober, R. Schoellkopf, and D. Prober, Appl. Phys. Lett. 70, 1354 (1997).

[2] Plasmonic nanoantenna arrays for the visible, Liu Z, Boltasseva A, Pedersen R H, Bakker R M, Kildishev A V, Drachev V P and Shalaev V M 2008 Metamaterials 2 45

[3] Q. H. Park, "Optical antennas and plasmonics," Contemp. Phys. 50(2), 407–423 (2009).

[4] G. W. Bryant, F. J. García de Abajo, and J. Aizpurua, "Mapping the plasmon resonances of metallic nanoantennas," Nano Lett. 8(2), 631–636 (2008).

[5] Simplified model for periodic nanoantennae: linear model and inverse design Borneman J, Chen K-P, Kildishev A and Shalaev V 2009 Opt. Express 17 11607–17

[6] P. J. Schuck, D. P. Fromm, A. Sundaramurthy, G. S. Kino, and W. E. Moerner, "Improving the mismatch between light and nanoscale objects with gold bowtie nanoantennas," Phys. Rev. Lett. 94, 017402 (2005).

[7] A. Sundaramurthy, P. J. Schuck, N. R. Conley, D. P. Fromm, G. S. Kino, and W. E Moerner, "Toward nanometer-scale optical photolithography: utilizing the near-field of bowtie optical nanoantennas," Nano Lett. 6, 355-360 (2006).

[8] J. N. Farahani, H. J. Eisler, D. W. Pohl, M. Pavius, P. Fluckiger, P. Gasser, and B. Hecht, "Bow-tie optical antenna probes for single-emitter scanning near-field optical microscopy," Nanotechnology, 18, 125506 (2007).

[9] E. Cubukcu, E. A. Kort, K. B. Crozier, and F. Capasso, "Plasmonic laser antenna," Appl. Phys. Lett. 89, 093120 (2006).

[10] O. L. Muskens, J. G. Rivas, V. Giannini, and J. A. Sanchez-Gil, "Optical scattering resonances of single plasmonic nanoantennas," arXiv:cond-mat/0612689v3 (2006).

[11] Corkish, R., M. A. Green, and T. Puzzer.""Solar Energy Collection By Antennas." Elsevier Science Ltd. (2003): 1–7. ScienceDirect. Elsevier. 15 Feb. 2009.

[12] D.K. Kotter, S.D. Novack, W.D. Slafer, P. Pinhero. "Solar Nantenna Electromagnetic Collectors." INL/CON-08-13925. Idaho National Laboratory, Idaho Falls ID. August 2008.

[13] B. Berland, "Photovoltaic Technologies Beyond the Horizon: Optical Rectenna Solar Cell," NREL/SR-520-33263, National Renewable Energy Laboratory (NREL), 2003, <http://www.nrel.gov/docs/fy03osti/33263.pdf>.

[14] Electromagnetic wave energy converter, US Patent.

<http://patft.uspto.gov/netacgi/nph-Parser?Sect1=PTO1&Sect2=HITOFF&d=PALL&p=1&u=%2Fnetahtml%2FPTO%2Fsrchnum.htm&r=1&f=G&l=50&s1=3760257.PN.&OS=PN/3760257&RS=PN/3760257>.

[15] Device for conversion of light power to electric power, US Patent. <http://patft.uspto.gov/netacgi/nph-Parser?Sect1=PTO1&Sect2=HITOFF&d=PALL&p=1&u=%2Fnetahtml%2FPTO%2Fsrchnum.htm&r=1&f=G&l=50&s1=4445050.PN.&OS=PN/4445050&RS=PN/4445050>.

[16] Guang H. Lin, Reyimjan Abdu, and John O'M. Bockris. "Investigation of resonance light absorption and rectification by subnanostructures." Journal of Applied Physics 80.1 (1996): 565-568.

[17] Green, Hank. "Nano-Antennas for Solar, Lighting, and Climate Control," Ecogeek. 7 Feb. 2008. 15 Feb. 2009. Interview with Dr. Novack, <http://www.ecogeek.org/content/view/1357/>.

[18] "SERS detection of biomolecules using lithographed nanoparticles towards a reproducible SERS biosensor." Catalina David, Nicolas Guillot, Hong Shen, Timothée Toury and Marc Lamy de la Chapelle Nanotechnology, 21, 475501(2010).

[19] "Surface enhanced Raman scattering optimization of gold nanocylinder arrays: Influence of the localized surface plasmon resonance and excitation wavelength." N. Guillot, H. Shen, B. Frémaux, O. Péron, E. Rinnert, T. Toury, and M. Lamy de la Chapelle Applied Physics Letter, 97, 023113(2010).

[20] "Impedance Matching and Emission Properties of Nanoantennas in an Optical Nanocircuit." Huang, J.-S.; Feichtner, T.; Biagioni, P.; Hecht, B. *Nano Lett*. **2009**, *9*, 1897–1902.

[21] <http://nanoscience.bu.edu/nanophotonics05-files/papers/Pohl%20Optical%20Antennas.pdf>.

[22] <http://www.nano-optics.ch/research.html>.

[23] Optical antenna with a single carbon nanotube <http://www.nanowerk.com/spotlight/spotid=1442.php>.

[24] Researchers create novel nanoantennas <http://www.swinburne.edu.au/chancellery/mediacentre/media-centre/news/2011/05/researchers-create-novel-nanoantennas>.

[25] Rutherglen, Burke, et.al.. Nanoletters.7, 3005. (2007)

[26] Schumacher, T., Kratzer, K., Molnar, D., Hentschel, M., Glessen, H., & Lippitz, M. "Nanoantenna-enhanced ultrafast nonlinear spectroscopy of a single gold nanoparticle." *Nature Communications* 2.333, 1-5 (2011).

[27] Seok, T.J., Jamshidi, A., Kim, M., Dhuey, S., Lakhani, A., Choo, H., Schuck, P.J., Cabrini, S., Schwartzberg, A.M., Bokor, J., Yablonovitch, W., and Wu, M.C. "Radiation engineering of optical antennas for maximum field enhancement." *Nanoletters* 11, 2606-2610 (2011).

[28] Hanke, T., Cesar, J., Knittel, V., Trügler, A., Hohenester, U., Leitenstorfer, A., and Bratschitsch, R. "Tailoring spatiotemporal light confinement in single plasmonic nanoantennas." *Nanoletters* 12, 9920996 (2012).

[29] Suh, J.Y., Huntington, M.D., Kim, C.H., Zhou, W., Wasielewski, M.R., and Odom, T.W. "Extraoridinary nonlinear absorption in 3D bowtie nanoantennas." *Nanoantennas* 12, 269-274 (2012).

[30] Vesseur, E.J.R. and Polman, A. "Plasmonic whispering gallery cavities as optical nanoantennas." *Nanoletters* 11, 5524-5530 (2011).

[31] Dorfmüller, J., Dregely, D., Esslinger, M., Khunsin, W., Vogelgesang, R., Kern, K., and Giessen, H. "Near-field dynamics of optical yagi-uda nanoantennas." *Nanoantennas* 11, 2819-2824 (2011).

[32] Adato, R., Yanik, A.A., and Altug, H. "On chip plasmonic monopole nano-antennas and circuits." *Nanoantennas* 11, 5219-5226 (2011).

[33] B. T. Draine and P. J. Flatau, "Discrete-dipole approximation for scattering calculations," J. Opt. Soc. Am. A, vol. 11, pp. 1491-1499, April 1994.

[34] R. Mittra, C. Pelletti, K. Panayappan and A. Monorchio, "The Dipole Moment (DM) and Recursive Update in Frequency Domain (RUFD) Methods: Two Novel Techniques in Computational Electromagnetics," *The Radio Science Bulletin*, no. 338, pp. 7-24, September 2011.

[35] A. Rashidi, H. Mosallaei and R. Mittra, "Scattering analysis of plasmonic nanorod antennas: A novel numerically efficient computational scheme utilizing macro basis functions," *J. Appl. Phys*., vol. 109, pp. 123109-123120, June 2011.

[36] A. Rashidi, H. Mosallaei and R. Mittra, "Numerically efficient analysis of array of plasmonic nanorods illuminated by an obliquely incident plane wave using the characteristic basis function method," *J. Comput. Theor. Nanosci*ence (to appear)

Tunable Current-Mode Filter Using DXCCII

Muhammed A. Ibrahim

Engineering Department, Engineering College, Salahaddin University, Zanko Qr., Kerkuk Street, 44002, Erbil, Iraq
E-mail: mabdulbaki@hotmail.com

Abstract

A new current-mode biquad filter based on employing dual-X second generation current conveyors (DXCCIIs) is introduced. The filter circuit uses two grounded capacitors with two MOS transistors and realizes a lowpass and a bandpass responses. The proposed circuit is electronically tunable by adjusting the control voltage of the gate of the MOS transistors.

1. Introduction

In electrical engineering applications, it is well known that an analog filter is an important block that is widely used for continuous-time signal processing. It can be found in many fields for instance, communication, measurement and instrumentation, and control systems. One of the most popular analog filters is the universal biquadratic filter as it can provide several functions [1]. Recently the research activities have trended to the development of current-mode (CM) filters since they offer several potential advantages such as wider bandwidth, better linearity, wider dynamic range and simplicity of signal operation compared with their voltage-mode (VM) counterparts [2]. Therefore, a number of multifunction CM filters based on CM active elements have been presented [3-18]. Multifunction filters are able to achieve more than one basic filter function simultaneously with the same topology.

A biquadratic filter is a very useful second-order function block for realizing high-order circuit transfer functions. The biquadratic circuit, employing various types of the current conveyors has already been reported in the literature. Unfortunately, these reported circuits suffer from one or more of following weaknesses:

- Excessive use of the active and/or passive elements
- Requirement for changing circuit topologies to achieve several functions
- Lack of electronic adjustability (tunability)
- The pole frequency and quality factor cannot be tuned independently

Active filters with current or voltage controllable (tunable) frequency have a wide range of applications in the signal processing and instrumentation area. Therefore, new advantageous filter topologies can be realized by introducing dual-X current conveyors (DXCCIIs) in the filter design that leads to voltage controllability of the filters.

2. Circuit Description

A DXCCII is a five-terminal block, shown in Figure 1, that is characterized by [19]

$$I_Y=0,\ V_{Xp}=V_Y,\ V_{Xn}=-V_Y,\ I_{Zp}=I_{Xp},\ I_{Zn}=I_{Xn} \qquad (1)$$

The proposed new CM biquadratic filter using two DXCCIIs, two MOS transistors and two grounded capacitors is shown in Figure 2. The circuit can realize band-pass (BP) and low-pass (LP) functions simultaneously.



Figure 1: The electrical symbol of DXCCII

Thanks to the DXCCII, which supplies $V_{Xp}=V_Y$ and $V_{Xn}=-V_Y$, by which the drain-source voltage of the triode MOS is fully differential. This enhances the linearity of this tunable MOS resistor. This makes the proposed circuit be electronically tunable by adjusting the control voltage of the gate of the MOS transistors.

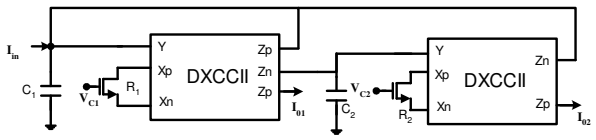


Figure 2: The proposed tunable CM LP and BP filter

Using the preceding equations, a routine analysis of the proposed filter circuit shown in Figure 2, yields the following transfer functions:

$$\frac{I_{BP}}{I_{in}} = \frac{I_{o1}}{I_{in}} = \frac{\frac{s}{R_1 C_1}}{s^2 + \frac{1}{R_1 C_1} s + \frac{1}{R_1 R_2 C_1 C_2}} \quad (2a)$$

$$\frac{I_{LP}}{I_{in}} = \frac{I_{o2}}{I_{in}} = -\frac{1}{s^2 + \frac{1}{R_1 C_1} s + \frac{1}{R_1 R_2 C_1 C_2}} \quad (2b)$$

Eqs. (2a) and (2b) represent the CM filter functions for BP and LP responses, respectively. The parameters ω_o and Q are given by:

$$\omega_o = \sqrt{\frac{1}{R_1 R_2 C_1 C_2}}, \quad Q = \sqrt{\frac{R_1 C_1}{R_2 C_2}} \quad (3)$$

The resistance value of the electronic resistors R_1 & R_2 constructed by MOS transistors working in teriod region is calculated from

$$R = \frac{1}{K_n (V_C - V_{th})} \quad (4)$$

where, V_{th} is the threshold voltage and K_n is the transconductance parameter of the MOS transistor and V_C is the control voltage applied to the gate of the transistor.

The circuit requires no component matching conditions for realizing the transfer functions listed above. Additionally, the circuit parameters Q and ω_0 can be tuned orthogonally by adjusting the bias voltages of the MOS transistors' gates and grounded capacitors.

Sensitivity analysis of the filter parameters shows that

$$S_{R_1}^{\omega_o} = S_{R_2}^{\omega_o} = S_{C_1}^{\omega_o} = S_{C_2}^{\omega_o} = \quad S_{R_2}^{Q} = \quad S_{C_2}^{Q} = S_{R_1}^{Q} = S_{C_1}^{Q} = -\frac{1}{2}$$

It is clear from sensitivity analysis that the biquadratic circuit has very low sensitivities with respect to the circuit components.

It is obvious that the biquadratic circuit configuration is very suitable for implementation CMOS VLSI technology.

3. Simulation Results

In order to confirm the theoretical validity of the proposed filter configuration given in Figure 2 it is simulated with SPICE simulation program. To implement the DXCCIIs the CMOS structure given in Figure 3 is used [19]. The aspect ratios of the MOS transistors are given in Table 1. The device model parameters TSMC 0.25µm CMOS process model parameters given in Table 2 are used for the SPICE simulations and the supply voltages of V_{DD}=-V_{SS}=1 V are selected. Note here that an additional current output terminal can be constructed easily just by adding two MOS transistors by connecting them in parallel with M13 and M15 of the CMOS structure given in Figure 3.

Simulated magnitude responses of the proposed filter circuit are given in Figure 4. For this purpose, equal equivalent resistances of 2.2 kΩ and the capacitance values of C_1 and C_2 are taken as C_1=2C_2=50 pF for a natural frequency of $f_o \approx$ 3.7 MHz and a quality factor of Q=0.707. The W/L ratio for the equal MOS resistors is chosen as 3/0.5.

To show the electronical tunability of the proposed filter, different values of V_{C1} and V_{C2} as 0.8 V, 0.9 V and 1 V are selected to obtain resonance frequencies of 3.7 MHz, 4.6 MHz, and 5.4 MHz, respectively. The results are shown, as an example, for the BP response in Figure 5.

It can be observed from Figures 4-5 that the simulation results agree well with the theoretical ones. However, the differences between ideal (theoretical) and simulated responses mainly stem from the parasitic effects and non-ideal current and voltage gains of the DXCCIIs.

Table 1: Transistor dimensions of the CMOS DXCCII [19]

Transistor	W (µm)	L (µm)
M1-M2, M4-M5	2	0.25
M3, M6-10, M15-M20	4	0.25
M11-M14	8	0.25

4. Conclusions

A new CM multifunction filter using only two DXCCIIs is proposed in this work. The validity of the proposed filter has been demonstrated through SPICE simulations. The proposed filter has the following advantages:

(i) The configuration of the filter is simple due to the use of only two DXCCIIs and minimum number of grounded capacitors with only two MOS transistors

(ii) Realization of the LP and BP filter responses from the same configuration simultaneously

(iii) Low sensitivities

(iv) Employing only grounded capacitors so it is easy to realize the proposed filter in IC process

(v) It is free from the critical active and passive component matching conditions and/or cancellation constraints

(vi) No need to employ inverting-type current input signal or double input current signal to realize the filter functions

(vii) Capability of electronically adjusting of the parameters ω_o and Q, through adjusting the bias voltage of MOS resistors

(ix) ω_o can be adjusted without disturbing Q (orthogonally controllable)

(iix) Suitable for implementation with CMOS technology

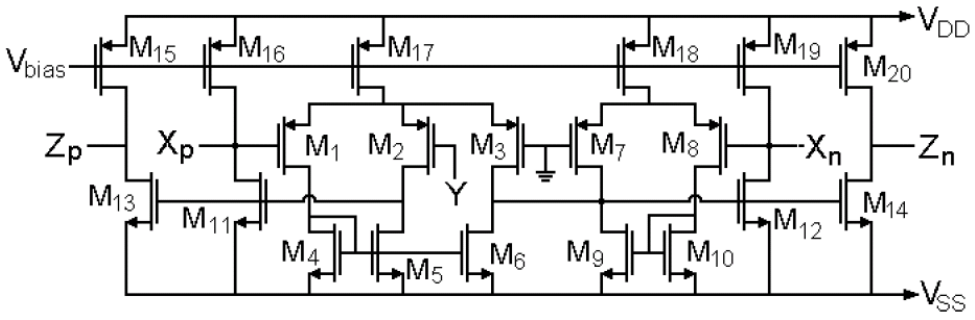


Figure 3: The CMOS realization of DXCCII used for the simulations derived from [19].

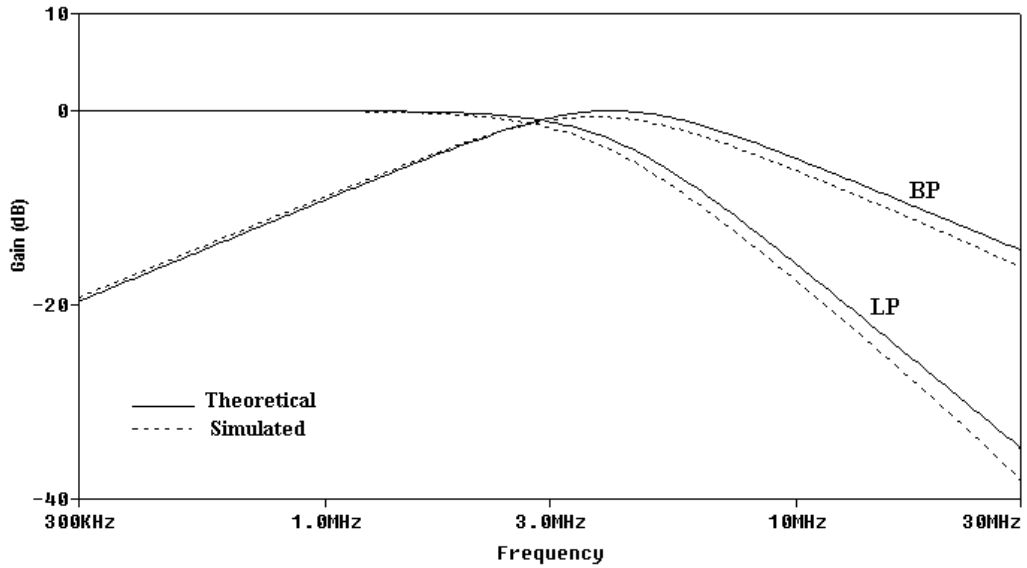


Figure 4: Magnitude responses of the proposed filter for BP and LP responses

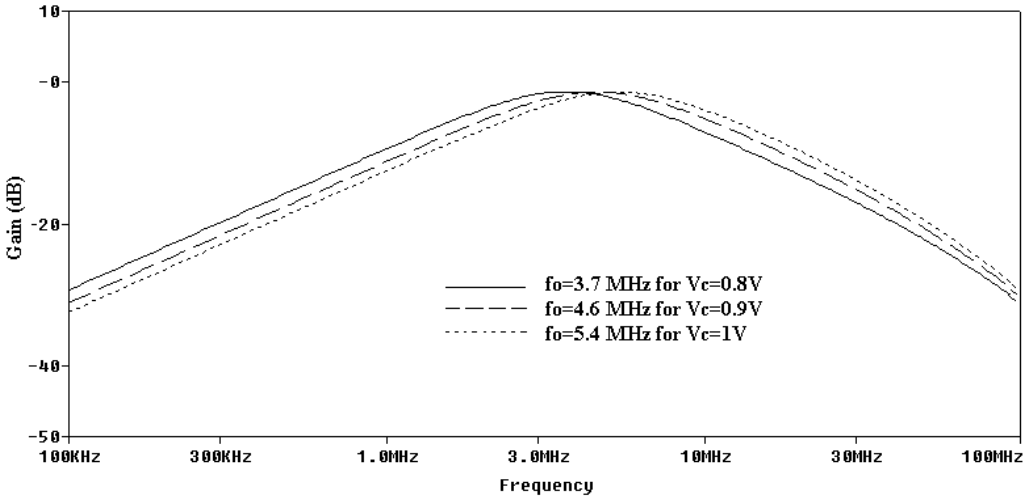


Figure 5: Magnitude of the BP response for different control voltages

Table 2: 0.25µm TSMC CMOS parameters

```
.MODEL NT NMOS (                    LEVEL  = 3
+ TOX    = 5.7E-9        NSUB   = 1E17        GAMMA  = 0.4317311
+ PHI    = 0.7           VTO    = 0.4238252   DELTA  = 0
+ UO     = 425.6466519   ETA    = 0           THETA  = 0.1754054
+ KP     = 2.501048E-4   VMAX= 8.287851E4   KAPPA  = 0.1686779
+ RSH    = 4.062439E-3   NFS    = 1E12        TPG    = 1
+ XJ     = 3E-7          LD     = 3.162278E-11  WD   = 1.232881E-8
+ CGDO   = 6.2E-10      CGSO   = 6.2E-10     CGBO   = 1E-10
+ CJ     = 1.81211E-3    PB     = 0.5         MJ     = 0.3282553
+ CJSW   = 5.341337E-10  MJSW   = 0.5         )

.MODEL PT PMOS (                    LEVEL  = 3
+ TOX    = 5.7E-9        NSUB   = 1E17        GAMMA  = 0.6348369
+ PHI    = 0.7           VTO    = -0.5536085  DELTA  = 0
+ UO     = 250           ETA    = 0           THETA  = 0.1573195
+ KP     = 5.194153E-5   VMAX = 2.295325E5  KAPPA  = 0.7448494
+ RSH    = 30.0776952    NFS    = 1E12        TPG    = -1
+ XJ     = 2E-7          LD     = 9.968346E-13  WD   = 5.475113E-9
+ CGDO   = 6.66E-10     CGSO   = 6.66E-10    CGBO   = 1E-10
+ CJ     = 1.893569E-3   PB     = 0.9906013   MJ     = 0.4664287
+ CJSW   = 3.625544E-10  MJSW   = 0.5         )
```

References

[1] M. Siripruchyanun and W. Jaikla, Current-mode biquadratic filter using DO-CCCDBAs, *International Journal of Circuit Theory and Applications*, 38: 321–330, 2010.

[2] W. Roberts and A.S. Sedra, All Current-Mode Frequency Selective Circuits, *Electronics Lett*., 25: 759-761, 1989.

[3] C.M. Chang, Universal Active Current Filter with Single Input and Three Outputs Using CCIIs, *Electronics Lett*., 29: 1932-1933, 1993.

[4] S. Özoguz and C. Acar, Universal Current-Mode Filter with Reduced Number of Active and Passive Components, *Electronics Lett*., 33: 948-949, 1997.

[5] S. Özoguz, A. Toker, and O. Çiçekoglu, New Current-Mode Universal Filters Using Only Four (CCII+)s, *Microelectronics J.*, 30: 255-258, 1999.

[6] R. Senani, A Simple Approach of Deriving Single-Input Multiple-Output Current-Mode Biquad Filters, *Frequenz*, 50: 124-127, 1996.

[7] H. Y. Wang, & C. T. Lee, Versatile insensitive currentmode universal biquad implementation using current conveyors, *IEEE Transactions on Circuits and Systems-II: Analog and Digital Signal Processing*, 48: 409–413, 2001.

[8] E. Yuce and S. Minaei, Signal Limitations of the Current-Mode Filters Employing Current Conveyors, *AEU Int. J. Electronics and Communications*, 62: 193-198, 2008.

[9] N.A. Shah, M. Quadr and S.Z. Iqbal, Current-mode multifunction filter using current differencing transconductance amplifier, *Indian Journal of Pure & Applied Physics*, 45: 767-769, 2007.

[10] W. Trangsirat, Novel current-mode and voltage-mode universal biquad filters using single CFTA, *Indian Journal of Engineering & Materials Sciences*, 17: 99-104, 2010.

[11] Fabre, O. Saaid, F. Wiest, and C. Boucheron, Current Controlled Bandpass Filter Based on Translinear Conveyors, *Electronics Lett*., 31:.1727-1728, 1995.

[12] E. Yuce, S. Tokat, S. Minaei and O. Cicekoglu, Stability problems in current-mode filters, *AEU Int. J. Electronics and Communications*, 61: 580-588, 2007.

[13] S. Minaei and S. Türköz, New Current-Mode Current-Controlled Universal Filter with Single Input and Three Outputs*, Int. J. Electronics*, 88: 333-337, 2001.

[14] S. Minaei and S. Türköz, Current-Mode Electronically Tunable Universal Filter Using Only Plus-Type Current Controlled Conveyors and Grounded Capacitors, *ETRI Journal*, 26: 292-296, 2004.

[15] H.P. Chen and P.L. Chu, Versatile universal electronically tunable current-mode filter using CCCIIs, *IEICE Electronics Express*, 6: 122-128, 2009.

[16] S. Minaei, Electronically Tunable Current-Mode Universal Biquad Filter Using Dual-X Current Conveyors, *Journal of Circuits, Systems, and Computers (JCSC)*, 18: 665-680, 2009.

[17] E. Yuce, and S. Minaei, ICCII-Based Universal Current-Mode Analog Filter Employing Only Grounded Passive Components, *Analog Integrated Circuits and Signal Processing*, 58: 161-169, 2009.

[18] A.M. Soliman, New Current-Mode Bandpass Filters Using Three Single-Output ICCIIs, *Active and Passive Electronic Components*, 2007: 1-5.

[19] A. Zeki and A. Toker, The dual-X current conveyor (DXCCII): A new active device for tunable continuous-time filters, *International Journal of Electronics*; 89: 913–923, 2002.

The Electrostatic Model of Gravity

Ioan Rusu

Electrica Serv Romania, SISE Muntenia Nord
*corresponding author, E-mail: ioandanrusu@yahoo.com

Abstract

Gravity discovered by Isaac Newton and defined as the phenomenon of mutual attraction of bodies, dependent of their mass and distance between them, does not have until now a scientifically sustained explanation regarding the generation of this force.
According to atomic and nuclear studies, the gravity is hypothetically attributed to a nuclear particle called graviton, particle that would generate the gravity forces but whose existence was not proved by laboratory tests.
From his studies and research compared to the existing theories carried out on the hydrogen atom, the author Ioan Rusu discovered that:
- The static spatial field of the proton generates strong attraction forces for other electrons in the vicinity of the atom
- By attracting the electrons of the atoms in the immediate vicinity the proton of the atom attracts in fact the electron - proton assemblies, namely the neighbouring atoms, and thus chemical bonds between atoms are created and molecules are formed.
- When the static field of a proton belonging to atom attracts distant electrons, meaning far located electron – proton assemblies, the force generated is the gravity force which is much smaller than the force of chemical bonds.

1. Introduction

From the classical theory for the simplest atom, the atom of hydrogen, consisting of one proton and one electron orbiting the proton, and considering that the proton imaginative dimension is the size of a stadium while the one of the electron is the size of a bead and the distance of the electron rotation against the proton is about 10 km, the following has been found:

- Both the proton of positive charge and the electron of negative charge exercise an electrostatic field
- The electron of negative charge is captured by the proton gravity field and is orbiting the proton according to Bohr's first postulate.
- Electrostatic force of attraction exerted by the proton is balanced by the centrifugal force of the electron

Studing the hydrogen atom, the author Ioan Rusu discovered that:

- The positive charge of the proton and the negative charge of the electron are cloud charges which decrease with the distance. The total compensation of the proton positive cloud charge by a negative charge would mean that around the proton, the negative charge would have the shape of a covering sphere.
- The hydrogen atom is in a balanced state with one proton and one electron in rotation, but the static spatial field of the proton is not completely annihilated by the static spatial field of the electron. The spatial field of the proton far exceeds the limits of the electron orbit.
- Also, the static negative field of the electron is spatial and occupies a circular arc on the orbit around the proton
- The static spatial field of the proton generates strong attraction forces for other electrons in the vicinity of the hydrogen atom
- By attracting the electrons of the atoms in the immediate vicinity the proton of the hydrogen atom attracts in fact the electron - proton assemblies, namely the neighbouring atoms, and thus chemical bonds between atoms are created and molecules are formed.
- When the static field of a proton belonging to a hydrogen atom attracts distant electrons, meaning far located electron – proton assemblies, the force generated is *the gravity force* which is much smaller than the atomic force or the force of chemical bonds.

In the particular case of the hydrogen mass, the gravity forces generated by protons for distant electron – proton assemblies, lead to the attraction of atoms to the central atom. In this case the shape of the gas mass will be finally a spherical one.

2. Atomic spatial forces

The physical dimension of a proton is about 10^{-15}m being infinitely greater than the dimension of an electron which is about 10^{-22}m, the electrostatic charges, positive for the proton Q_p and negative for the electron Q_e, are comparable in value and theoretically mathematical compensated.

$$Q_p - Q_e = 0 \quad (1)$$

Let us consider a stationary proton and an electron which is moving to the proton due to the electrostatic attraction forces

The equation (1) $Q_p - Q_e = 0$ is true both for the proton and for the electron for a stationary regime only. When the electron is entering the electrostatic field of the

proton, the two fields interfere and the electron is oriented due to its own speed to a certain orbit around the proton and it continues his movement.

According to Fig 2, the electron and the interfering electrostatic fields, rotate around the proton at a speed comparable to the light speed. From his visual area, an outside observer should see during a complete rotation of the electron, the negative electrostatic field of the electron, followed by the positive electrostatic field of the proton. As the electron rotation speed around the proton, is comparable to the speed of light, practically there is no technical possibility to measure either the proton or the electron electrostatic field when the electron is moving on its orbit. If for the proton-electron assembly we consider an analogical magnetic model, Fig 3 is showing the lines of the magnetic field. It can be seen that the attraction of the magnetic poles N-S doesn't totally collect the magnetic fields of the two poles. Both, North and South Poles, even being in direct interaction, are developing their own magnetic space fields in all directions, similarly to the case of protons and electrons in Fig.2.

3. Formation of molecules from free hydrogen atoms

To study the generation of the universal attraction, two isolated atoms of hydrogen are considered each being situated at a distance large enough not to form a molecule, within an ideal imponderability environment and in absence of any external forces including gravity and electromagnetic forces.

Protons reject each other. Electrons reject each other as they have the same type of charge. Protons and electrons attract each other as shown in Figure 4. Within the hydrogen atom, the electron is attracted by the proton by electrostatic force.

Within an atom, protons and electrons create a permanent electrostatic bond. If we had to exemplify by a similar experiment from magnetism, the resulting situation would be as shown by Figure 5.

Between the magnet 1 and the magnet 2, even separated by a certain distance, i.e. by a plastic separator, the magnitude of the attraction force depends on the distance between magnets and it remains constant.

To the two magnets assembly from Fig 5 another magnet is attached as shown in Fig 6, but the distance between magnet 2 and magnet 3 is much smaller. Due to this fact, the attraction force between magnet 2 and magnet 3 is much bigger than in case of attraction between magnet 1 and

If a mechanical tensile force F is applied to magnet 1 it can be seen that the magnet 2 and 3 are moving in the same direction.

Fig 7 presents the case of two hydrogen atoms with protons placed successively with electrons in line. Similarly to the magnets situation shown in Fig. 6 it results that the proton of the atom 2, interacts with the electron of the atom 1 .Due to the strong static bond between the proton and the electron of the same atom by the attraction of the proton of one atom and the electron of the other atom the two atoms 1 and 2 move one to another. As the electron rotates around the proton with the speed of light, there is a false theory that the electron charge annihilates the proton charge because the electrostatic field of the proton cannot be seen or measured from outside sequentially on the electron orbit.

The attraction force between the proton of the atom 2 and the electron-proton assembly of the atom 1 is practically defined as gravity force. The model in Fig 7 was called by the author Ioan Rusu, *The Electrostatic Gravity Model***.**

Due to the action of the attraction force between the two hydrogen atoms (see Fig 7) their approach is done until reaching an equilibrium distance, according to Fig 8, as following:

- The protons reach a minimal critical distance, when the repulsive action starts due to electrostatic forces
- The electrons of the two atoms, during their move, keep between them a permanent minimum critical distance due to the electrostatic rejecting forces

The attraction force between the protons of one atom and the electron of the other atom become stronger due to the decrease of the distance between the atoms and becomes the chemical bond between atoms within molecules

When a supplementary third atom occurs in the first two hydrogen atoms neighborhood (see Fig 9), the attraction forces between the proton of the first atom and the proton of the second atom to the electron of the third atom, in fact toward the electron-proton assembly of the third atom, which are gravity forces lead to the bonding of the third atom to the hydrogen molecule, already composed from two atoms, according to Fig. 10.

In the new molecule made up of three atoms, due to the electrostatic repulsive forces between protons, repulsive forces between electrons and attraction forces between protons-electrons (assembly electron-proton=atom) the protons and the electrons take a position of equal distance between them. The new formed bonds between the 3 hydrogen atoms in one new molecule are *chemical bonds*.

If an agglomeration of hydrogen atoms exists, due to the space electrostatic attraction forces between the proton and the electron (electrons-protons assembly = atoms), meaning to the gravitational forces, the hydrogen atoms move and bind to the new hydrogen molecule, by forming a gas agglomeration.

For the hydrogen agglomeration generated from molecules chemical bonded according to Fig 11, the protons by space electrostatic attraction with the electrons (electrons-protons assembly = atoms) create a variety of electrostatic forces vectors whose vector sum is oriented toward the center of the agglomeration of gas.

The proton of the central atom also attracts the electron of the distant atom, meaning the electron-proton assembly. This force is also considered as part of *gravitational force*.

According to Fig 11 it can be seen that electrons are spatially interposed between the proton of the central atom and protons of the neighboring atoms.

The spatial arrangement proton-electron-proton represents the spatial location of the electrostatic fields positive-negative-positive. The rejection proton-proton is shielded by the electron due to its location between the two protons. Thus, the possibility for the atoms to be brought close together, in fact for the protons to be closely located as the

mutual repulsive force is shielded by the electrons placed between them, can be explained by using the electrostatic model of gravity.

4. The electrostatic model of gravity applied for explaining the attraction of non-electrized bodies by positively or negatively electrized bodies

By rubbing an ebonite or plastic stick with fur, wool, etc, it can be seen that ebonite and plastic become statically electrized and attract pieces of paper or hairs, dust, etc.
It was demonstrated by experiments that some bodies become negatively charged, as ebonite, amber and the others become positively charged, as plastic and glass.
Practically by friction, the ebonite receives supplementary electrons becoming negatively electrized while the plastic releases electrons becoming positively electrized. Both bodies, even being differently electrized exert the same attraction forces on pieces of paper which are not electrized.
According to Fig 12, the protons of the paper pieces interact with the electrons of the ebonite which is negatively charged. The ebonite electrons being more numerous and being linked by atomic bonds create an important supplementary electrostatic attraction force with respect to the gravity force explicated in Fig 7. Due to the much bigger mass of the ebonite, the resultant forces of attractions lead to a move of the light pieces of paper to the ebonite.
According to Fig 13, the protons of positively charged plastic, without an important part of electrons enter in attraction with the paper electrons (in fact with the electron-proton assembly = paper atom). The plastic's protons being without electrons create an important supplementary electrostatic force, relative to *the gravity force* explained in Fig 7. As plastic has a much bigger mass, the resultant of the attraction forces leads to the move of light pieces of paper to the plastic stick.

5. The electrostatic gravity model applied to explain Coanda's effect

To study Coanda's effect, a solid body. is considered (i.e. a plastic stick which by rubbing with other materials releases electrons and becomes positively electrized), on which a liquid drop slides as shown in Fig 14.
Due to the action of the gravity force G, by Coanda's effect, the liquid drop moves by following the inclined surface of the solid. By using the electrostatic model of gravity, it results that between the plastic body and the liquid drop, attraction forces develop of gravity type similarly to the situation shown in Figure 6.
In case of the displacement a rubbing phenomenon of the drop against the plastic surface in zone A. is developing.
By rubbing, the plastic donates electrons to the drop and that one becomes negatively electrized. When the drop is entering the B area, it is already negatively charged and the protons of the plastic from that zone develop much bigger attraction forces for the supplementary drop's electrons, similarly to the attraction of paper to the plastic described in Fig 13.

6. The electrostatic gravity model applied to explain the thermonuclear reaction from the space hydrogen agglomerations, respectively from stars

From the results of physical research the thermonuclear reaction in stars, respectively from very large agglomerations of hydrogen is generated by gravity. In this sense, the scientific explanation is that due to the high pressure inside the stars, generated by gravity and of the high temperatures, the hydrogen atoms fuse to each other resulting in the helium atoms. From the hydrogen atoms containing one proton and one neutron helium atoms are formed which contain two electrons and nuclei consisting of two protons and two neutrons.
Using the electrostatic model of gravity, after explaining the gravitational forces in Fig7-11 the pressure increasing inside the hydrogen agglomeration, along with the increase of internal temperature and the start of thermonuclear reaction can be observed.

Steps for triggering the thermonuclear reaction:

1. When increasing the agglomeration of hydrogen, the gravitational force also increases with its vector resultant orientation to the central atom.
2. The gravitational force leads to atoms nearness according to the gravity static model.
3. The increase of gravity force due to gas agglomeration, leads to decrease of the distance between atoms
4. The distance between protons is reduced but due to their location in line proton - electron - proton as shown in Fig, 7, protons are not in a position to reject each other as between them an opposite charge electron is interposed.
5. The negatively charged electrons reject each other and due to the shrinking distance between protons, they are electrons, are forced by rejection to descend to lower orbits around the protons with release of energy. The mass of hydrogen begins to warm up.
6. The force of gravity increases while the distance between atoms still decreases, the electrons descend on even lower orbits releasing large amounts of energy. The gaseous mass continues to warm up.
7. When reaching a critical value of the forces of gravity and temperature, the distance between atoms is much smaller, the electrons are located on a lower energy orbit, the temperature of the hydrogen mass is very high, and because of the rejecting forces between electrons the central electron in Fig. 15, is forced to descend to the proton surface with the release of large quantities of energy. Thus the first neutron is formed.

Forces acting on the orbiting electron :

The electrostatic force of attraction to the proton Fp
The rotational centrifugal force on the orbit Fc
The rejection force with neighbouring electrons Fr
The vectorial resultant of the above mentioned forces pushes the electron located on the atom orbit to the proton surface while releasing a large amount of energy

$$FResultant=Fp+Fc+Fr \quad (2)$$

According to the electrostatic model of gravity, the electron and the proton are bonded and both particles keep their electric cloud charges, positive and negative respectively. The new assembly proton-electron = neutron of spin motion continues its spin movement.

8. By bonding the central electron to the proton rejecting pressure zone between the electrons from the layers 1, 2, etc ... is temporarily released.
9. The above phenomenon is repeated in the central area of the agglomeration of hydrogen to form neutrons
10. The new formed neutron, namely the proton-electron assembly bonded in spin movement, when aligned to a neighbouring atom, according to the electrostatic gravitational model bonds to the proton of the atom'

The new nucleic assembly i.e. proton- electron -proton- namely -proton neutron continues its spin movement. This explains the statements in physics asserting that "protons coexist with neutrons in nuclei" as shown in Fig. 18.

11. Formation of helium atom:

- At very high temperatures, atomic bonds between the orbiting electrons and nuclei are loosened. In the state of plasma, free electrons also occur.
- The avalanche production of neutrons, of neutron-proton pairs, of protons without electrons and free electrons leads to the formation in the center of the gas agglomeration of an area in which the energy barriers between protons and electrons are loosened and between neutrons and protons electrostatic combinations can occur, as shown in Fig. 18 as well as neutrons-neutrons as shown in Fig. 19, under pressure gravitational conditions.
- The formation of a helium atom is not chaotic. Under gravitational pressure conditions, by releasing electrons and sending them on protons through forces which reject the neighbouring electrons, the space forces of attraction and repulsion generated by neutrons (proton and electron bonded to proton) lead to the formation of spatial configuration of helium nucleus of 2 protons and 2 neutrons, which is a two-electrons balanced nucleus

The assembly in Fig. 20 represents the helium atom. The arrangement of the nucleus consisting of two protons and two neutrons, (two protons and two electrons) is spatial. Thus,

- the electrons screen the rejection electrostatic forces between protons
- the electrons between them, are screened by protons and do not reject each other
- the nucleus is formed as a stable whole and has its own spin movement.

12. Depending on the spatiality of electrostatic fields of neutrons namely a positive one given by the proton and a negative one given by the electron, protons bonding in stable combination is well determined and the number of neutrons is always at least equal to the number of protons. In the case of complex combinations, the spatial availability of protons ensures the bonding of additional protons neutrons, namely of the combination of electron-proton = neutron.
13. The new helium atoms formed in the center of the agglomeration of gas exert their electrostatic forces to the surrounding atoms, including gravitational forces and ensure the continuation of the thermonuclear reaction of the hydrogen atoms.

Following the steps for triggering the thermonuclear reaction, explained using the gravity electrostatic model, it results that the energy released is composed of:

o Radiations generated by electrons which descend on lower orbits because of the gravitational forces

o Radiations generated by the impact of electrons on the protons surface when forming neutrons. The impact force is given by the high speed of the electron, comparable to the speed of light and not by the mass of the electron which is very small as compared to the proton mass.

o Radiations generated by the impact of electrons from neutrons with the protons when helium nuclei are generates This impact, although it occurs at lower speeds, due to the large masses in motion, which in fact are the masses of two protons, is much higher than in electron-proton impact during the neutron formation .

7. Controlled and uncontrolled thermonuclear reaction using the electrostatic model of gravity

7.1 The hydrogen bomb

Artificially, uncontrolled thermonuclear reaction was performed to build the hydrogen bomb. The principles followed in its construction refer to the creation of conditions similar to those in the agglomerations of hydrogen, stars, outer space, namely: to very high temperatures in high pressure tight spaces which assimilate the phenomenon of gravity. Uncontrolled thermonuclear reaction in the hydrogen bomb is very easy to explain using the gravity electrostatic model, the phenomena being similar to those presented in Fig. 16 and Fig.18.

Since the electrons are deflected on the protons at lightning speed, the avalanche formation of neutrons and helium atoms with release of radiations is performed at the same speeds comparable to the speed of light; consequently the uncontrolled thermonuclear reaction on a fixed quantity of fuel is explosive.

7.2 Controlled thermonuclear reaction

According to the electrostatic model of gravity, the thermonuclear reaction involves:

1. Creating of strong gravitational forces conditions for the hydrogen mass subject to the thermonuclear reaction to ensure the deviation of the electrons from the atoms orbits to the protons in order to create neutrons.
2. Raising the temperature of the hydrogen mass thus reaching a temperature similar to that of stars to create free protons interacting with the newly formed neutrons ,by loosening the electrons energetic barrier,

Current research directions of the controlled thermonuclear reaction take into account specific solutions for:

- obtaining of plasma control in delimited spaces
- collisions between protons

- heating the mass of hydrogen by laser, etc...

According to the electrostatic model of gravity, getting of plasma in the laboratory without the possibility of its compression similarly to the gravitational compression in stars, does not ensure the development of the thermonuclear reaction by forming neutrons and protons and by their collision with protons due to electrostatic attraction proton-electron attached to proton = neutron with release of energy. Of course, research in the thermonuclear reaction field made substantial contributions in science.

From a technological perspective the artificial increase of gas mass pressure combined with the temperature increase at high values is very difficult to achieve.

Research solutions for the controlled thermonuclear reaction using the electrostatic model of gravity:

- studies and experiments on electrons infusion in plasma in order to force the electrons orbiting the hydrogen atoms to descend on protons with energy release and formation of neutrons which in turn combine with protons to form helium atoms,
- studies and experiments on electrons infusion in plasma to combine them with free protons, by the release of quanta of impact energy proton – electron = neutron proton attached to form helium atoms.
- *construction of mini-reactors of very low power with instantaneous and unique operation similar to the hydrogen bomb. The mini-reactors are placed inside heat capture enclosures of boiler type from thermo-power stations by means of which the heat released during the thermonuclear reaction is captured by the thermo-power plant. The solution of continuous operation is given by the successive time release of the mini-reactors .An example would be the development of mini-reactors where the reactive hydrogen mass, small as volume, is enclosed in a glass sphere, having the size of a tennis ball. Inside the sphere, triggering of the thermonuclear reaction will be achieved by increasing the volume of hydrogen pressure while increasing temperature by using lasers. The production of the thermonuclear explosion will lead to the sphere destruction with energy release in the enclosure to capture heat .The resistance of the enclosure at the thermonuclear mini-explosion must be ensured.*

8. Classification of interaction forces using electrostatic model of gravity

1. **Nuclear forces** - are the electrostatic forces of attraction from nuclei consisting of protons and neutrons, the forces of attraction between protons-and neutrons, namely between proton-electron-proton-. Due to addition of the electron to the proton (neutron), the distances between the positive and negative charges are zero and consequently the attraction forces are very high.

2. **Atomic forces** - are electrostatic forces between the nucleus (protons) and the electrons orbiting the atoms. The size of the attraction force is directly proportional to the distance between the nucleus and the electrons.

3. **Forces of chemical bonds** between atoms - are the forces of electrostatic attraction between the nucleus of an atom (protons) and the electrons of neighboring atoms. The attraction force size is smaller than the atomic force due to the longer distance between the nucleus and the electrons of neighboring atoms.

4. **Forces of gravity** - are the forces of electrostatic attraction between the nucleus of an atom (protons) and the electrons of distant atoms. The size of the attraction force is much smaller than the force of chemical bonds between atoms due to the very large distance between the nucleus and the electrons of the distant atoms

9. Conclusion

The electrostatic model of gravity is based on the study of the classical forces of electrostatic attraction and of the spatial disposition of positive and negative charges at the atomic level for the orbiting electron and proton. Ioan Rusu's researches on spatial arrangement and size of the electron and proton electrostatic fields, have demonstrated theoretically, using the magnetism analogy, that the negative charge of the electron and the positive charge of the proton, although mathematically can be considered equal in module ,physically they interfere partially but do not annul each other completely. By its electrostatic field the proton creates a bond with the orbiting electron but the spatial field of the proton also interferes to the electrons of the neighbouring or distant atoms. The rotation of the electron around the proton with the speed of light leads to the false theory that the electron charge annihilates the proton charge because the electrostatic field of the proton cannot be sequentially observed and measured on the electron rotation orbit from outside.

Using *the electrostatic model of gravity* new research directions opens up such as:

- In physics on the size and intensity of the spatial electrostatic fields for electrons, protons, neutrons, complex atomic nuclei
- In nuclear technology in the field of controlled thermonuclear reaction
- In mathematics by modeling the phenomenon of the gravity electrostatic model through equations

References

[1] N. Bohr, *Fizica atomică şi cunoaşterea umană*, Editura Stiintifica, Bucharest, 1969

[2] M. Born, *Fizica atomică*, Editura Ştiinţifică şi Enciclopedică, Bucharest, 1973

[3] A. Einstein, *Teoria relativitatii pe intelesul tuturor,* Editura Humanitas, Bucharest, 2005

[4] E. Luca, Gh. Zet, C. Ciubotariu, A. Paduraru, *Fizica Generala*, E.D.P., Bucharest, 1981

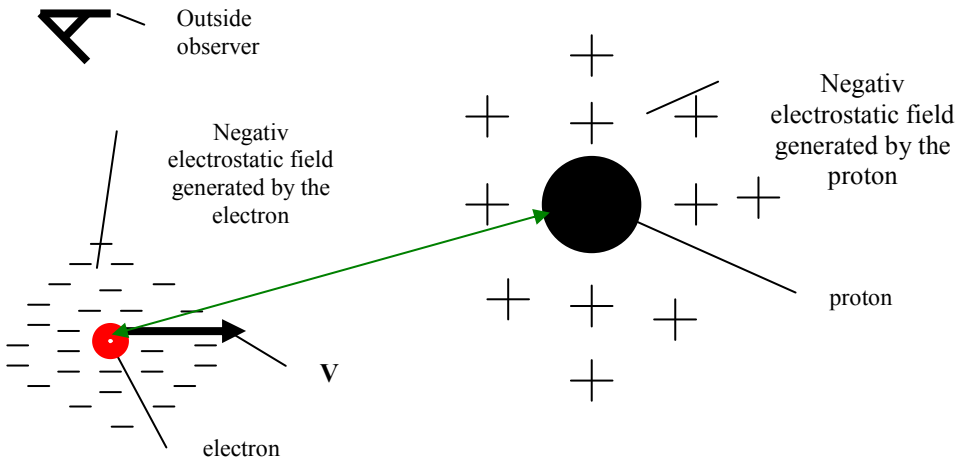


Figure 1

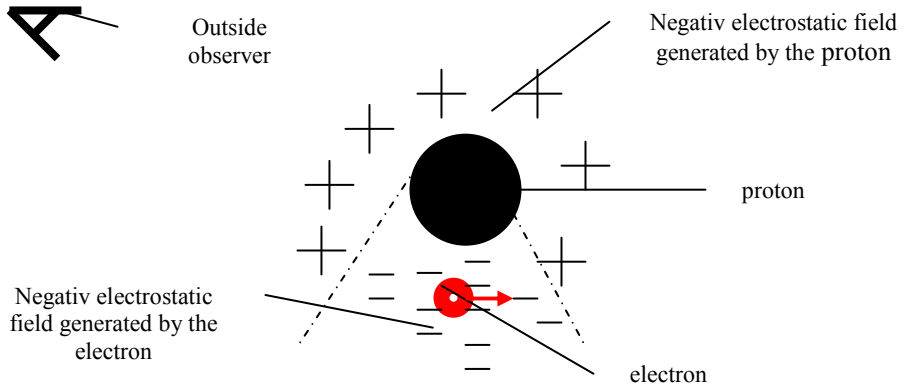


Figure 2

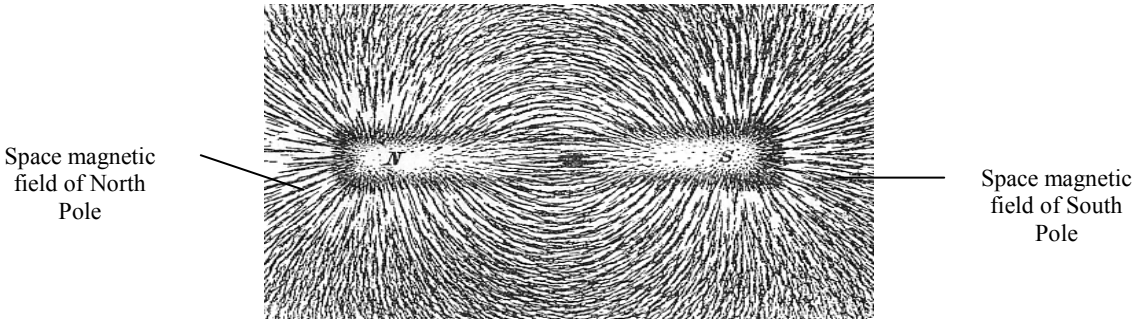


Figure 3

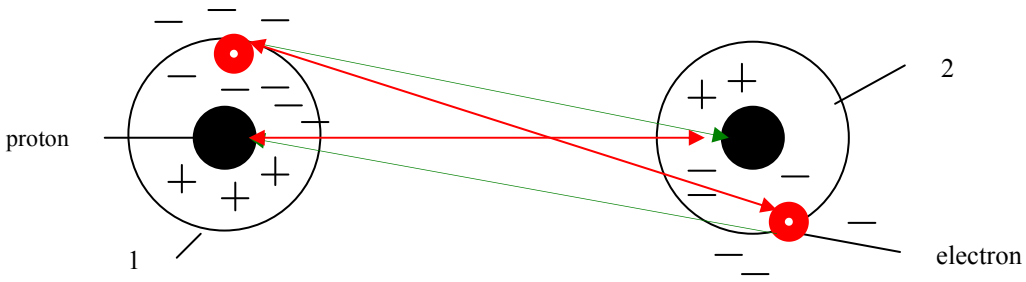


Figure 4

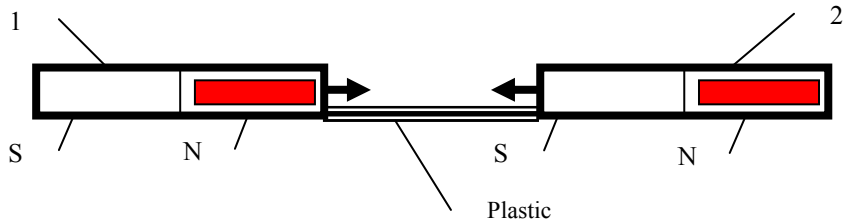


Figure 5

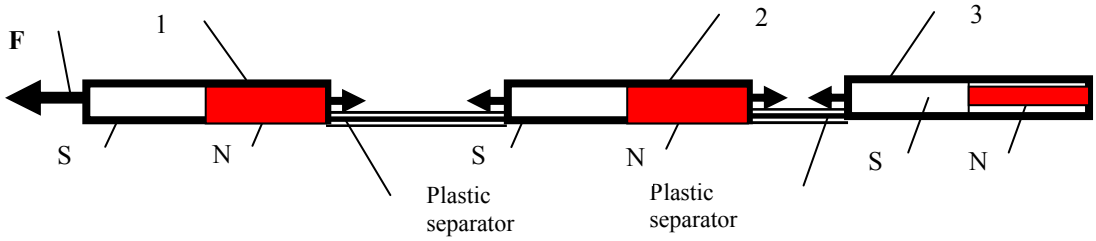


Figure 6

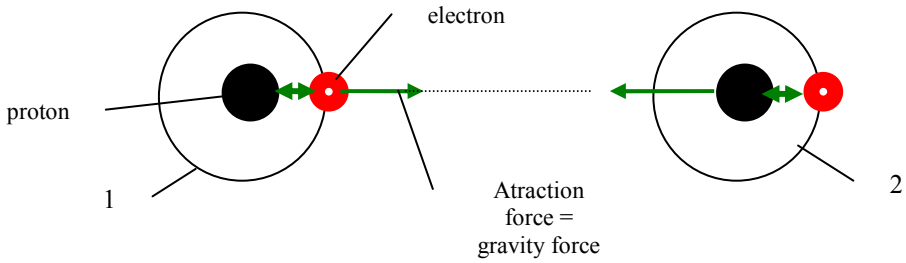


Figure 7

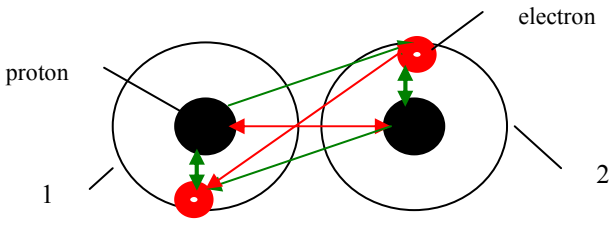


Figure 8

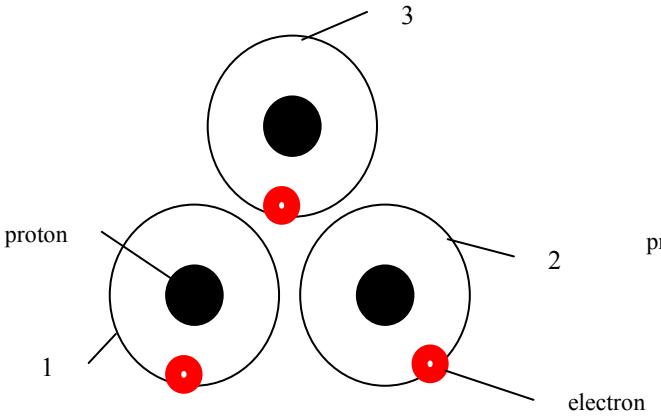


Figure 10

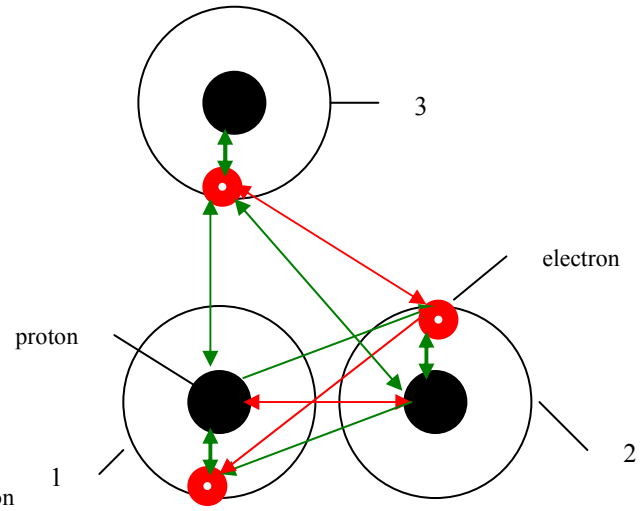


Figure 9

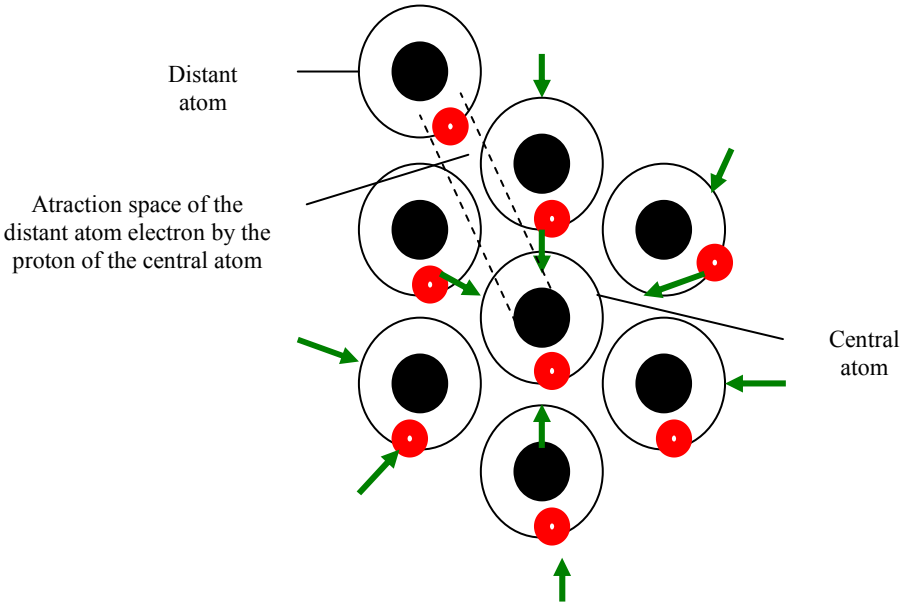


Figure 11

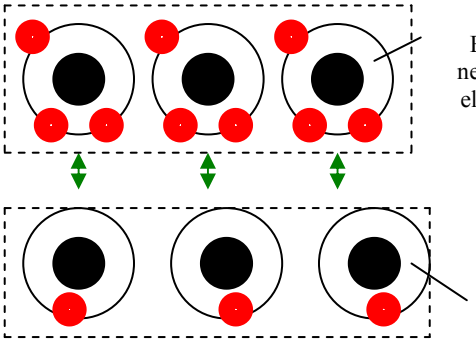


Figure 12

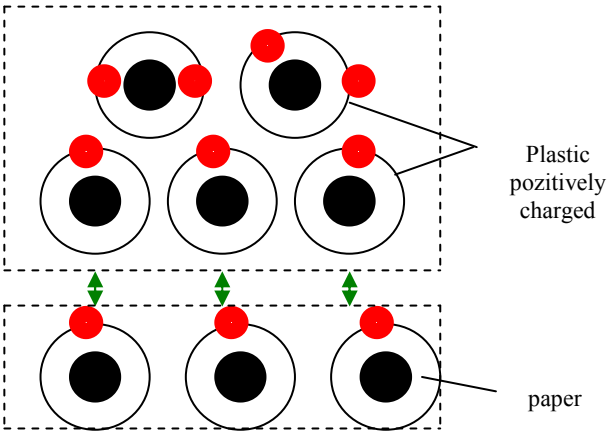


Figure 13

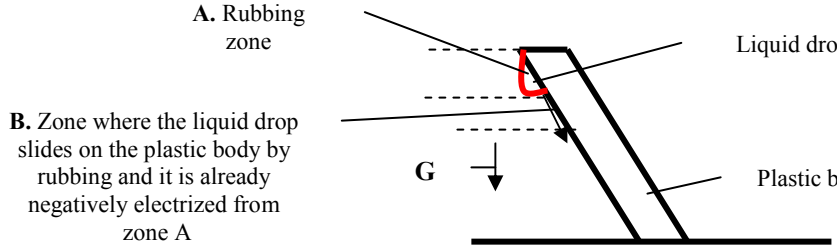


Figure 14

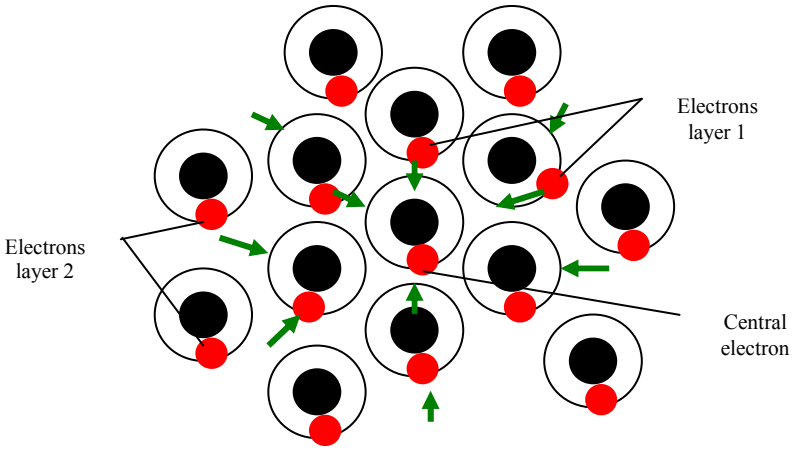


Figure 15

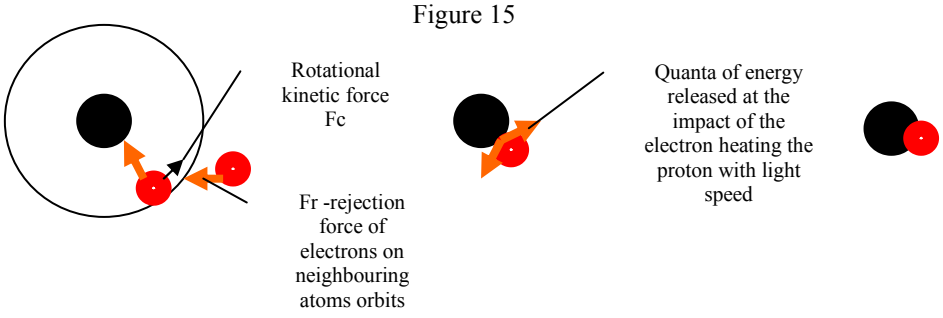


Figure 16

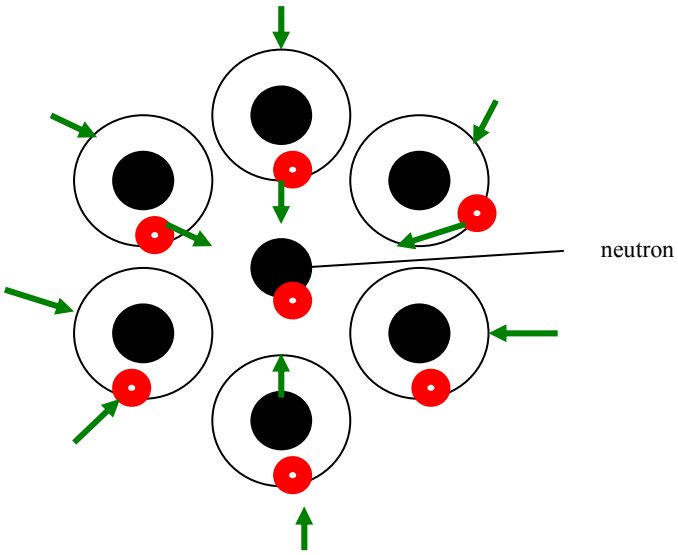


Figure 17

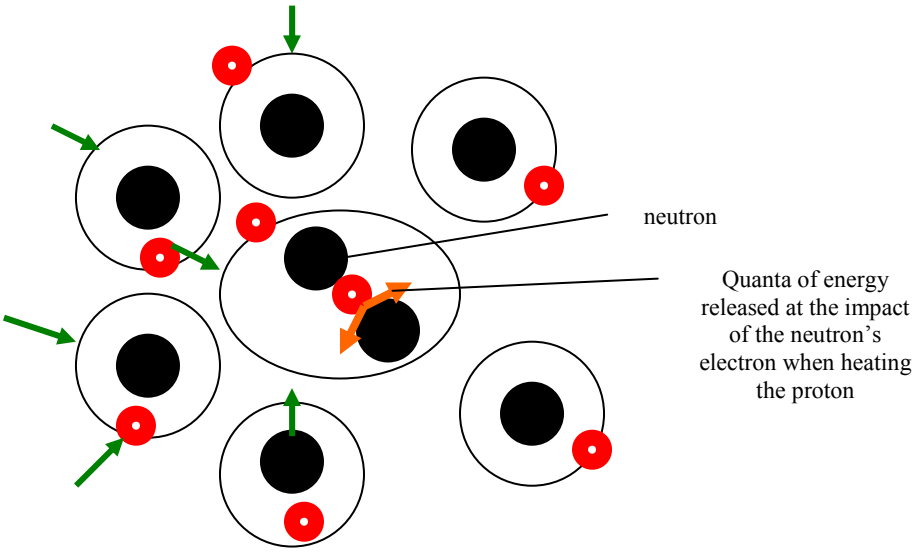


Figure 18

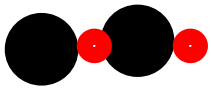


Figure 19

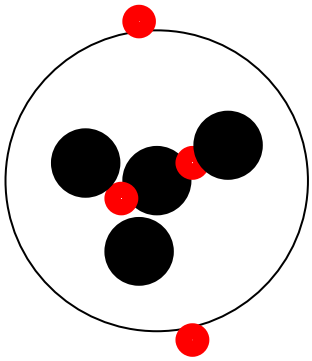


Figure 20

Pressure effect on properties of corona discharge in a electrostatic precipitator

Nouri Hamou [1,2*], Mehdaoui Akila[1], Baali Aissa[1], Aissou Massinissa[2]& Zebboudj Youcef[2]
[1]Department of Electrical Engineering, University of M'sila, 28000, Algeria
[2] Laboratoire de Génie Electrique de Bejaia (LGEB), University of Bejaia, 06000, Algeria
*corresponding author, E-mail: hm_nouri@yahoo.fr

Abstract

This paper aims at analysis of the corona discharge in wires - two planes configurations. The effect of the pressure in the electrostatic precipitators has been studied. Electrostatic precipitators have been used widely in industry, and play an important role in environmental protection. Electrostatic precipitation can be operated with high collection efficiency. Recently, ESP also has been used for cleaning indoor. Experimental results shows that discharged proprieties were strongly affected by the pressure for a given atmospheric condition. Changing the number of wires and values pressure not only changed the property of the gas but also affect the corona onset conditions and ion mobility. The apparent mobility has been identified by fitting the experimental data with an empirical current-voltage relationship.

Keywords: Corona discharge, Current-voltage characteristics, Current density, Onset voltage, Pressure.

Introduction

A corona is a process by which a current develops between two high- potential electrodes in a neutral fluid, usually air, by ionising that fluid so as to create plasma around one electrode, and by using the ions generated in plasma-processes as the charge carriers to the other electrode. In high-voltage, coronas may be positive or negative. This is determined by the polarity of the voltage using a highly-curved electrode.
DC has many advantages over conventional AC lines for long-distance power transmission. The economic feasibility of DC transmission has increased recently with development of high voltage terminal equipment. Corona discharge, as applied to Electrostatic Precipitators (ESP), is a gas discharge phenomenon associated with the ionization of gas molecules by high-energy electrons in a region of the strong electric field. Essentially, electrostatic precipitators remove dust by charging the constituent particles by means of the ions produced by the coronating electrodes. The electrically charged particles are then collected on the collecting plates toward which they are propelled via the electric field present in the interelectrode space, produced by the voltage applied to the emitter electrodes and the collector plates [1].
The process of corona generation in the air at atmospheric conditions requires a non uniform electrical field, which can be obtained by the use of a small diameter wire electrode and a plate or cylinder as the other electrode.
Industrial ESP are used with success to reduce the emissions of smoke, fumes and dust, playing an important role to maintain a clean environment and to achieve more healthy air quality [2]. They are able to remove more than 99 % of particulates from the flue gas [3]. In these systems, particles are charged by means of the ions produced by a dc corona discharge in the common cases. The particles migrate to the collecting plate due to the Coulomb forces, but they are also under the influence of the viscous forces due to the fluid flow and ionic wind [4-7].
In such systems, the knowledge of the pressure effect on DC corona discharge behavior is of crucial importance [8]. Some effect of pressure on DC corona are not well known and requires further investigations in order to achieve realistic and valid models, which are able to be integrated in a numerical simulation.
The main objective of this investigation is to study the effect of the pressure, varying from 0,1 bar up to saturated conditions (≈ 1 bar), on positive and negative corona discharge behavior in wire-to-plane electrostatic precipitator. Several design parameters were taken into consideration especially the number of active electrodes and their diameter. In particular, current-voltage curves, averaged power and onset voltage are analyzed and discussed.

2. Experimental setups

The schematic representations of the wire-to-plane ESP used in this investigation are shown in Fig. 1. The ESP, based on a DC corona, consisted of two parallel electrodes (stainless steel plates, 200-mm-length and 100-mm-width in x-direction and z-direction, respectively). Both parallel electrodes were grounded. The high voltage electrodes consisted of a stainless steel wires with 0.2 mm of diameter and parallel to z-axis midway between the grounded electrodes. The distance between both grounded plates is equal to 100 mm. In the first ESP (called 1W-ESP, Fig. 1a), only one wire was connected to the high voltage. However, the second configuration (called 3W-ESP, Fig. 1b) used 3 similar wires to create the corona discharges. The distance between two successive wires was set to 40 mm.

In this study the two DC high voltage polarities were used (positive and negative). The high voltage was applied by a DC power supply (SPELLMAN SL 150, ± 40 kV; ±3.75

mA) with an accuracy of 0.1 kV. The power supply was protected by a ballast resistor of 10kΩ. The time-averaged current was measured using a digital millimeter (METERMAN 37 XR, accuracy ≈1μA).

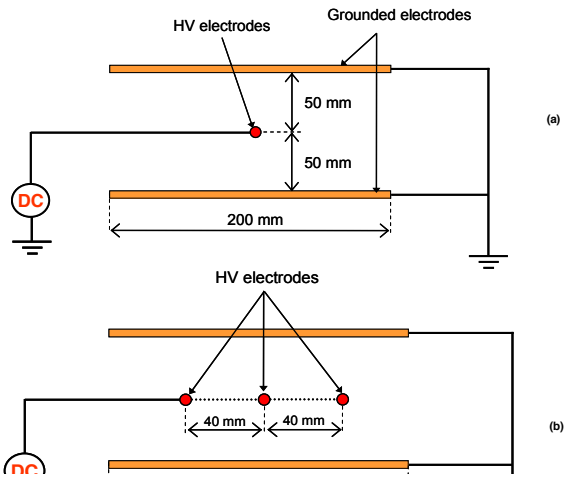


Figure 1: Electrostatic Precipitator configurations: (a) 1W-ESP, and (b) 3W-ESP

As shown in Fig. 2, the experiments were carried out inside a could cylindrical vessel (glass, 500 mm-high, and 250 mm-diameter) filed with clean air. This capsule with stand vacuum up 5 kPa. All the pressure, temperature and humidity sensors were securely placed within the chamber through completely sealed rubber plugs. The chamber pressure was decreased from 1 bar to 0,1 bar.

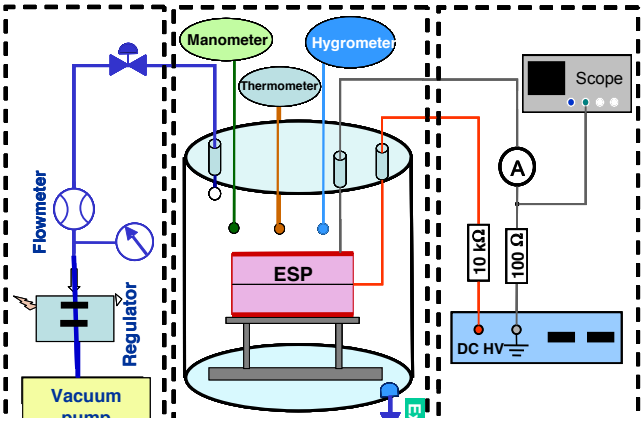


Figure 2: Experimental set up

Since the effect of temperature on the electrical behavior of a corona discharge has been examined extensively in the literature [9 - 13], the effect of pressure and the number of active electrodes were parameters taken into consideration in the present study. During each experiment, the temperature and relative humidity inside the test chamber are controlled.

Each current-voltage curves represents the average of five series of measurement. Between two of them, the gas is entirely renewed. Because the presence of corona can reduce the reliability of a system by degrading insulation. While corona is a low energy process, over long periods of time, it can substantially degrade insulators, causing a system to fail due to dielectric breakdown. The effects of corona are cumulative and permanent, and failure can occur without warning (Corona causes Ozone, Nitric and various other acids).

All measurements were made in an air-conditioned laboratory, where the temperature was maintained at 22°C and relative humidity was maintained at 50% (The physical parameters of air are regularly controlled).

2 Discussion

In this section, the effect of the ESP design and pressure on the current-voltage characteristics is discussed. Firstly, the optimum operating conditions for the ESP were determined by varying the design and operating parameters such as the wires number and the applied voltage. Before operating the ESP, corona current - voltage characteristics were measured in order to evaluate the electrical charge of particles. The current was measured at the collection plates.

3.1. Current-voltage characteristics

Figures 3a-3b show the current-voltage curves in the case of one wire- two plates electrostatic precipitator (1W-ESP) for both high voltage polarities.

The discharge current increases with the applied voltage however, when it exceeds the corona onset voltage (Vs) until gas breakdown occurs.

As expected, the corona discharge is ignited at lower voltage when the wire diameter decreases. The electric field E decries with the radii of wires (electrode). E is expressed in kilovolts per centimeter as [14,15]

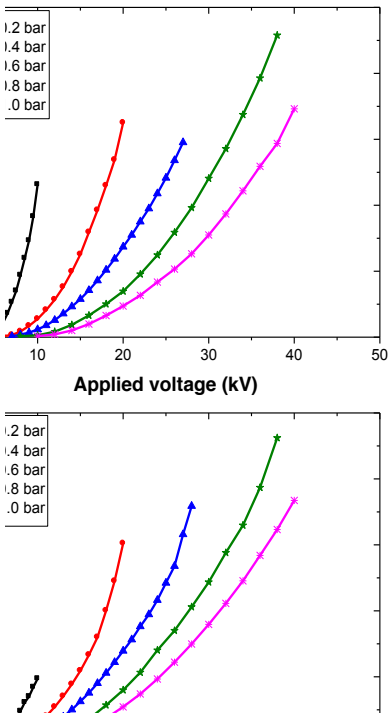
$$E = 30\eta[1 + (0.0906/r_0)^{1/2}], \qquad (1)$$

where r_0 is the conductor radius in centimeters and is the surface irregularity factor (1 for smooth conductors). Furthermore, one can also observe the effect of polarity on the current–voltage curves. Indeed, at a given voltage the discharge current is higher with the negative polarity, which could be explained by the difference between the apparent mobility of negative charge carriers compared to positive ones [16].

(a)

(b)

Figure 3: Current-voltage characteristic of 1W-ESP: (a) negative corona, (b) positive corona.



(a)

(b)

Figure 4: Current-voltage characteristic of 3W-ESP: (a) negative corona, (b) positive corona.

Similar discharge behavior was observed in the case of 3W-ESP, as shown in Figs. 4a-4b. Whatever the polarity, the discharge current increases with the high voltage electrode number. However, current magnitude using three wires is three times lower than the current magnitude with one wire ($I_{1wire} < I_{3wires} < 3\times I_{1wire}$). This is due to the electric field interaction between two successive high voltage wires. In fact, the distance between the wires is lower than the interelectrode gap.

The ionization process by a collision is the basis for gas multiplication. The number of electron-ion pairs created by a single electron drifting a unit distance in the field direction in a gas is denoted as the first Townsend coefficient of the gas. It depends principally upon the nature of the gas, the gas pressure, and the electric field intensity [17].

The pressure increase causes a variation of the ionization coefficient α, in the ionization region, and a variation of the ion mean free path length λ, in the drift region, for a fixed potential voltage value V between the electrodes.

The ionization and attachment coefficients can well be represented by the equations of the type [18, 19]:

$$\alpha/p = A\exp\left[-B\left(p/E\right)\right], \tag{2}$$

$$\eta/p = C + D\left(E/P\right)^2 + F\left(E/P\right), \tag{3}$$

where p is the atmospheric pressure in Pa and E the electric field in V.cm-1.

The constants A, B, C, D and F are determined by curve fitting the experimental results on ionization and attachment data [20]. Accordingly, for $0.19 < E/p < 0.45$, the values are $A = 4.778$; $B = 221$; $C = 0.01298$; $D = -541.10^{-6}$; $F = 0.87.10^{-5}$; and for $0.45 < E/p < 1.82$, the values are $A = 9.68$ and $B = 264$.

But for $E/p < 0.19$ and $E/p > 0.45$, the value of the attachment coefficient is not known. Ogasawara [21] has used a different equation to fit the experimental data of attachment valid over a wide range of E/p (0,08 to 3,8).

It is of the form

$$\eta/p = \frac{C\left(E/p\right)^2 - D\left(E/P\right) + F}{\left(E/P\right)^8 + G}, \tag{4}$$

where $C = 4.199.10^{10}$, $D = 2.623.10^{12}$, $F = 6.15.10^{13}$ and $G = 4.473.10^{15}$.

It is assumed that the transport properties of the air are determined by E/N, where E is the local electric field and N is the neutral gas density. For most real gases, P can be directly measured whereas N can not, we often quote the quality E/P in place of E/N (N is the number of molecules in unit volume).

As the pressure goes up, α decreases, thus producing a lower ionization rate close to the tip. As a consequence, the

current generated by the corona discharge decrease. The sequence of phenomena at 0,2 and 0,4 bar gas were essentially the same as at 1 bar, except that threshold potentials were correspondingly lower to Corona onset voltage.

3.2. Current density

The electric current density (Figs. 5 and 6) is defined as the electric current (an electric current is a displacement of a group electrical charges) per unit area (an area generally refers to the surface layer of an object).

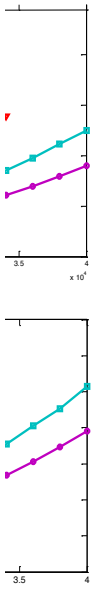


Figure 5: Variation of current density of 1W-ESP: (a) negative corona, (b) positive corona..

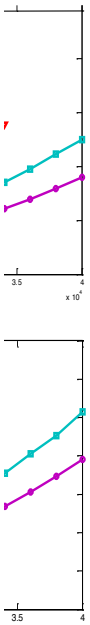


Figure 6: Variation of current density of 3W-ESP: (a) negative corona, (b) positive corona..

Mathematically, the current and current density are linked by the following relation [22]:

$$I = \iint_S J(x,y)dS \,, \tag{5}$$

I is the electric current in amperes A. $J(x,y)$ is the current density at the coordinates point (x,y) in A.m^{-2}. S is the area in m^2.

To calculate the distribution of current density in the plane (Figs. 7a – 7b), we use the expression given by Warburg [23- 25]:

$$J(\theta) = \begin{cases} J(0).\cos^m(\theta) \text{ Si } & \theta \le \dfrac{\pi}{3} \\ 0 \quad\quad\quad \text{Si } & \theta > \dfrac{\pi}{3} \end{cases}, \tag{6}$$

where $m = \begin{cases} 4.82 & \text{for positive corona discharge} \\ 4.65 & \text{for negative corona discharge} \end{cases}$

But many authors use a single value ($m = 5$) [26, 27].
For our case and for any triangle ABC (Fig. 7):

$$r = h.\tan g(\theta) \Rightarrow \cos(\theta) = \frac{h}{d}$$

$$d^2 = r^2 + h^2 - 2r.h\cos\hat{A} \Rightarrow d = \pm\sqrt{r^2 + h^2} \tag{7}$$

$$\Rightarrow \cos(\theta) = \frac{h}{\sqrt{r^2 + h^2}} = \frac{1}{\sqrt{1 + (r/h)^2}}\,;\ 0 \le \theta \le 60°.$$

Where r is a function of x and y in the plan:

$$r_i(x,y) = f(x,y) = \sqrt{x_i^2 + y_i^2} \tag{8}$$

x_i and y_i are the coordinates of any point in the plane grounded.

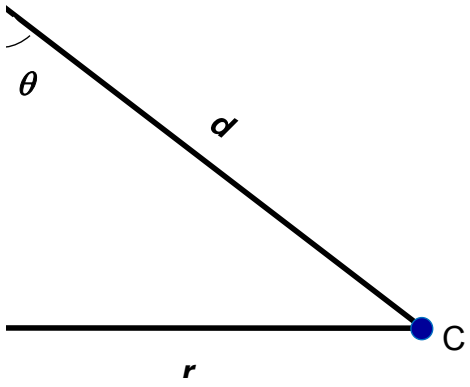


Figure 7: Triangle ABC.

We can write the distribution in terms of current density as a function only of the variables x and y:

$$J(x,y)=\frac{J_0}{\left[1+\left(\frac{x^2+y^2}{h^2}\right)\right]^{m-\frac{1}{2}}} \qquad (9)$$

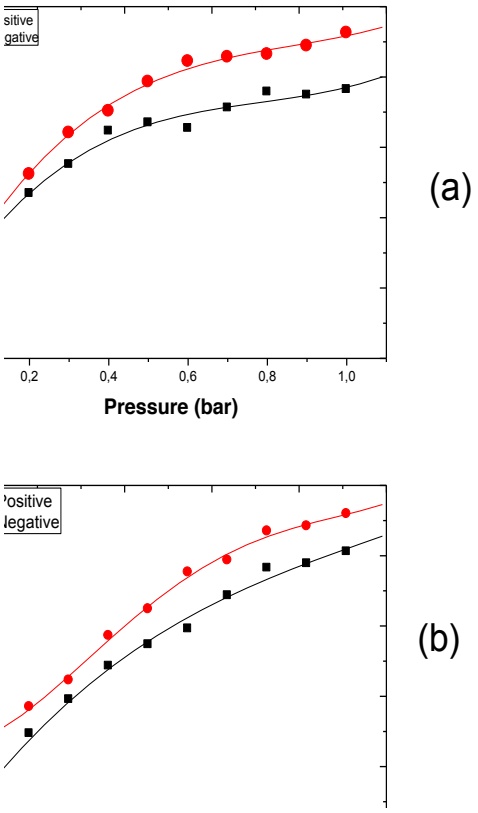


Figure 7: Current density Distribution at the plane.

Figure 8: Variation of corona onset voltage with pressure: (a) 1W-ESP, and (b) 3W-ESP.

3.3. Corona onset voltage

Figure 8 shows the evolution of V_s against the pressure for both high voltage polarities and the two ESP designs. Results are obtained from fitting the experimental data from the previous equation.

By applying correction factors, a discharge voltage measured in given test conditions, may be converted to the value that would have been obtained under the standard reference atmospheric conditions. Therefore we have:

$$V_{0p}=\delta.V_s, \qquad (10)$$

where δ is the air density correction factor. V_s is the onset voltage at standard reference atmosphere.

When the temperatures T and T_0 are expressed in degrees Celsius and the atmospheric pressures p and p_0 are expressed on the same units (kPa or mbar), the relative air density is:

$$\delta=\left(\frac{p}{p_0}\right)\left(\frac{273+T_0}{273+T}\right), \qquad (11)$$

The attempt to calculate the corona onset voltage is a reasonable first approximation since the surface field is the primary factor that influences corona for many electrode arrangements [20].

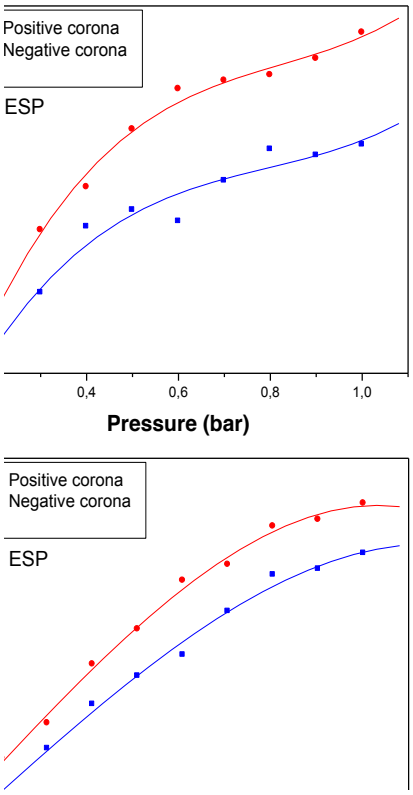
3.4. Corona onset field strength

Using the onset potential V_S we found by drawing the current–voltage $I = f(V)$ characteristic, E_0 can be calculated as follows [28]:

$$E_0=\frac{V_s}{H\ln(H/r_0)}, \qquad (12)$$

where r_0 is the conductor radius in centimetres and H is the distance between the wire and the collector plate.

Figures 9a-9b show the onset electric field curves in the case of one wire- two plates electrostatic precipitator for both high voltage polarities.



(a)

(b)

Figure 9: Variation of corona onset Field:
(a) 1W-ESP, and (b) 3W-ESP.

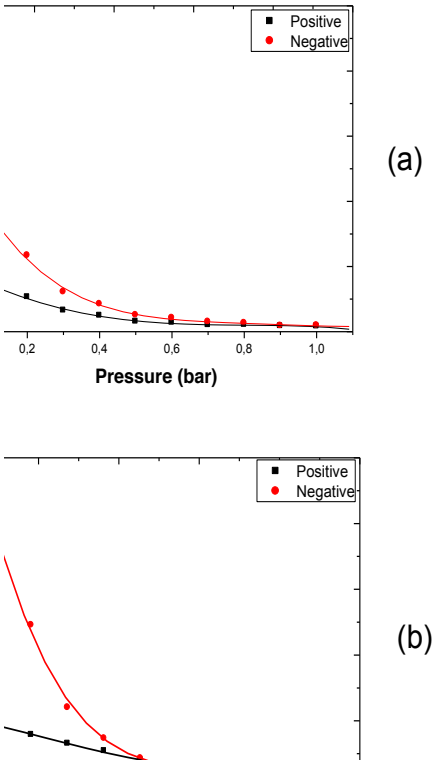
3.5. The mobility of the charge

The time-averaged discharge current, which crosses the inter electrode gap is a non-linear function of the applied voltage. Although the discharges include complex phenomena, a simple empirical relationship between current (I) and voltage (V) is generally used [29]. It is expressed by:

$$I = CV(V - V_s), \qquad (12)$$

Where V_s is the corona onset voltage and C is a constant that depends on the electrode configuration and the mobility of charge carriers.

The constant C, which is proportional to the apparent mobility of the charge carriers, is lower in the case of positive polarity. Figure 9 shows the evolution of C in different conditions of active electrode and gas properties.



(a)

(b)

Figure 9: Variation of C-constant with pressure:
(a) 1W-ESP, and (b) 3W-ESP.

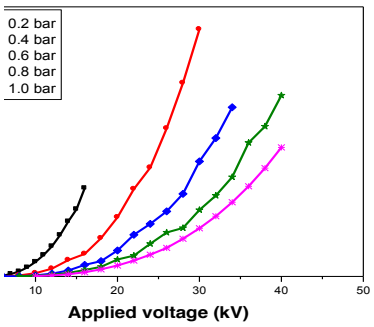
3.6. The power corona discharge

The average power consumption (P) of the discharge is calculated from the measurement of the current (I) and the voltage (V):

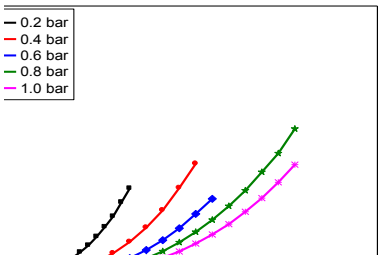
$$P = \frac{1}{N}\sum_{i=1}^{N} I(i).U(i), \qquad (13)$$

where N is the number of measurement series.

The effect of the pressure on the average power is shown in Figures 10 and 11. The discharge power is higher with the negative polarity and 3W- ESP, which could be explained by the difference between the apparent mobility and the electric field.

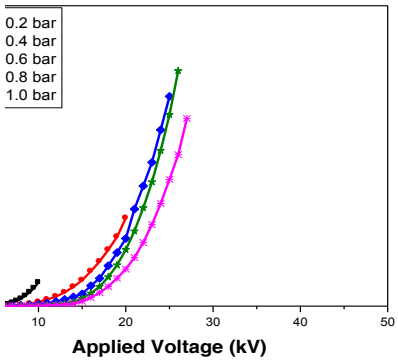


(a)

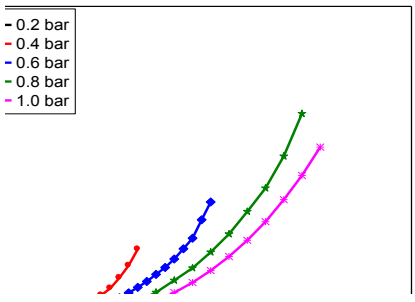


(b)

Figure 10: Corona power of 1W-ESP: (a) negative corona, (b) positive corona.



(a)



(b)

Figure 11: Corona power of 3W-ESP: (a) negative corona, (b) positive corona.

4. Conclusions

In this paper, the effect of pressure on a dc corona discharge behavior in wire-to-plane electrostatic precipitator has been investigated. Influence of numbers of active electrodes and their diameter were investigated.

In an electrostatic precipitator the voltage-current characteristics are important in diagnosing the electrical problems associated with it during its operation.

The apparent mobility, which is higher with three wires construction and thicker ones, decreases with increasing the pressure. The corona power in electrostatic precipitator depends upon atmospheric conditions and the applied voltage. The onset voltage and electric field are proportional to the increase of pressure. At low pressure, the number of Wires has no effect, but for high pressure onset voltage increase with the number of wires.

References

[1] J. Chen, Direct- Current corona on handed chemical reactions, PhD Thesis, University of Minnesota, USA. 2002.

[2] A. Mizuno, "Electrostatic precipitation", IEEE Trans. Dielectr. Electr. Insul., Vol. 7, pp. 615-624, 2000.

[3] J. S. Chang, "Next generation integrated electrostatic gas cleaning systems", J. Electrost., Vol. 57, pp. 273-291, 2003

[4] T.Yamamoto, H. R. Velkoff, "Electrohydrodynamics in an electrostatic precipitator", J. Fluid Mech., Vol. 108, pp. 1–18, 1981.

[5] P. Atten, F. M. J. Mccluskey, A. C. Lahjomri, "The electrohydrodynamic origin of turbulence in electrostatic precipitators", IEEE Trans. Ind. Appl., Vol. 23, pp. 705–711, 1987.

[6] J. Podliński, J. Dekowski, J. Mizeraczyk, D. Brocilo, J. S. Chang, "Electrohydrodynamic gas flow in a positive polarity wire-plate electrostatic precipitator and the related dust particle collection efficiency", J. Electrostat., Vol. 64, pp.259-262, 2006.

[7] N. Zouzou, B. Dramane, P. Braud, E. Moreau, G. Touchard, " EHD flow in DBD precipitator ", IJPEST, Vol.3, No. 3, pp.242-245, 2009.

[8] K. R. Parker, Applied Electrostatic Precipitation, Edition Kluwer Academic Publishers, London, 1997.

[9] H. Nouri , N. Zouzou, E. Moreau, L. Dascalescu, Y. Zebboudj, Effect of relative humidity on the collection efficiency of a wire-to-plane electrostatic precipitator,The IEEE Industry Applications Society Annual Meeting, Houston, Tx, ISSN: 0197-2618, Print ISBN: 978-1-4244-6393-0 3-7 October, 2010.

[10] H. Nouri and Y. Zebboudj (2010) Analysis of positive corona in wire-to-plate electrostatic precipitator. The European Physical Journal, Applied Physics 49, 11001.

[11] C. G. Noll, Temperature dependence of dc corona and charge-carrier entrainment in a gas flow channel. Journal of Electrostatics Vol.54, pp. 245–270, 2002.

[12] P. N. Mikropoulos, C. A. Stassinopoulos and B. C. Sarigiannidou, Positive Streamer Propagation and Breakdown in Air: the Influence of Humidity. IEEE Transactions on Dielectrics and Electrical Insulation Vol. 15, No. 2, pp. 416 – 425, 2008.

[13] R. Messaoudi, A. Younsi, F. Massines, B. Despax and C. Mayoux, Influence of Humidity on Current Waveform and Light Emission of a Low-frequency Discharge Controlled by a Dielectric Barrier. IEEE Transactions on Dielectrics and Electrical Insulation Vol. 3, No. 4, pp. 537 – 543, 1996.

[14] Z. M. Al-Hamouz, A Combined Algorithm Based on Finite Elements and a Modified Method of Characteristics for the Analysis of the Corona in Wire-Duct Electrostatic Precipitators. IEEE Transactions on industry applications, Vol. 38, NOo. 1, pp. 43 -49, 2002.

[15] F. W. Peek (1929) Dielectric phenomena in high voltage engineering. McGraw – Hill, New York, p.p. 52 – 80.

[16] G. P. Reichel, J. M. Mäkelä, R. Karch, J. Necid, "Bipolar charging of ultrafine particles in the size range below 10 nm", J. Aerosol Sci. Vol. 27, pp. 931–949, 1996.

[17] Z. Chuping, Bruyndonckx, M. Goldberg, S. A. Tavernier, Measurement of the First Townsend coefficient as a function of the Electric field for a TMAE-He Mixture. IEEE Trans. On Nuclear Science., Vol. 41, N°6, pp. 2671-2674,1994.

[18] R. Benocci, M. Urbano, L. Mauri "Study of a positive corona discharge in argon at different pressures", Eur. Phys. J. D , vol.37, pp.115-122, 2006.

[19] B. S. Rajanikanth and B. R. Prabhakar, Modeling of Prebreakdown VI Characteristics of a Wire-plate Electrostatic Precipitator Operating under Combined dc-pulse Energization. Vol. 1 No.6, pp. 1058 -1067, 1994.

[20] K.Yamazaki , R. G. Olsen, Application of a Corona Onset Criterion to Calculation of Corona Onset Voltage of Stranded Conductors. IEEE Transactions on Dielectrics and Electrical Insulation Vol. 11, No. 4, p.p. 674-680, 2004.

[21] M. Ogasawara, “Analysis of Formation Stage of Corona Discharge”, J. Phys. Soc. Japan, Vol. 21, No. 11, pp. 2360-2372, 1966.

[22] G. Goudet, Phénomènes électriques et magnétiques indépendants du temps. Traité d’électricité, Tome 1, Edition Masson, pp. 211 – 247, 1975.

[23] R. S. Sigmond, The unipolar corona space charge flow problem. Journal of electrostatics, 18, pp. 249 – 272, 1986.

[24] E. Warburg, Handbuch der physik, Vol. 14, Spinger, Berlin, pp. 154 – 155, 1927.

[25] J. H. Davidson, P. J. Mckinney, P. Linnebur, Three-Dimensional (3-D) model of electric field and space charge in the barbed plate-to plate precipitation, IEEE Trans. On ind. App. Vol. 32, No. 4, pp. 858-866, 1996.

[26] M. Goldman, A. Goldman, R. S. Sigmond, The corona discharge its properties and specifics uses,Pure & Appl. Chem., Vol. 57, No. 9, pp. 1353 – 1362, 1985.

[27] R. S. Sigmond, I. H. Lagstad, Mass and species transport in corona discharges, High Temp. Chem. Processes, Vol. 2, pp. 221 – 229, 1993.

[28] M.Abdel– Salam, Z. Al– Hamouz, Analysis of monopolar ionized field as influenced by ion diffusion, IEEE Trans. ,Ind. App, vol.31, pp.484- 493,1995.

[29] L. B. Loeb, Electric Coronas-Their Basic Physical Mechanisms, University of California Press, Berkeley and Los Angeles, 1965.

Comparison of Transmission Line and Electromagnetic Approaches to Modeling of Buried Horizontal Wires of Finite Length

B. Markovski[1], L. Grcev[1,2], V. Arnautovski-Toseva[3*], K. Drissi[3], S. Grceva[4], K. Kerroum[3], and A. Kuhar[1]

[1]Ss. Cyril and Methodius University, Skopje, Macedonia
[2]Macedonian Academy of Sciences and Arts, Skopje, Macedonia
[3]Blaise Pascal University, Institute Pascal, Clermont-Ferrand, France
[4]FON University, Skopje, Macedonia
*corresponding author, E-mail: Vesna.ARNAUTOVSKI@lasmea.univ-bpclermont.fr

Abstract

Transmission line approach is often applied for approximate modeling of buried horizontal wires in many electromagnetic compatibility applications. Although this approximation is usually related to long wires it is also applied for finite length wires. In this paper we analyze the validity domain of this approximation by comparison with a full wave electromagnetic method. We compare currents computed by the approximate and rigorous models in centrally fed wires for different wire lengths and earth characteristics, in wide frequency range.

1. Introduction

The electromagnetic analysis of buried wires is of interest in different research areas, such as: electromagnetic compatibility (EMC), lightning protection, communication, geophysics, power system and grounding studies [1]–[2]. The temptation to use transmission line (TL) formulation to buried horizontal wires is big due to the simplicity in implementation and possibility to use in existing software for high frequency and transient analysis, based on circuit approach. However, it is not a simple task to generally determine the validity domain of this approximate formulation since it often depends on the case considered and the computed quantities [3]. Another problem is the use of several different formulations for approximate evaluation of TL parameters. One approach to analyze the validity domain of different approximate approaches is to compare results with a full-wave rigorous method based on Maxwell's equations. This problem has recently attracted considerable attention [3]–[6].

In this paper we compare currents along horizontal buried wires computed by TL approach with currents computed by rigorous approach. We compare several TL formulations, three that are based on uniformly distributed RLC parameters [7], and additional three that are based on direct evaluation of the unit length impedance and admittance [8]. The rigorous formulation used as a reference is based on a method of moment solution of integral field equations in frequency domain, with exact Green functions for homogenous earth, implemented in the well known antenna computer code NEC4 [9].

2. System under analysis

Configuration of the analyzed system is illustrated in Fig. 1. Bare horizontal wire with radius a and length 2ℓ is buried in a homogeneous soil at depth d. The soil is characterized by its conductivity σ_g, permittivity $\varepsilon_g = \varepsilon_{rg}\varepsilon_0$, and permeability of vacuum μ_0.

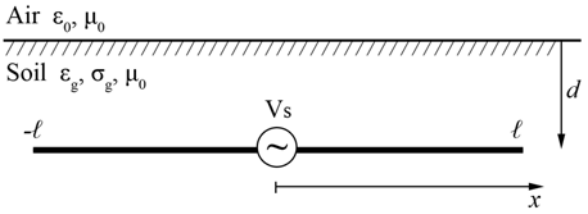


Figure 1: Configuration of the analyzed system.

Harmonic voltage source V_S is located at the middle point of the wire. The range of parameters considered in the analysis, is given in Table 1.

Table 1: Parameters of the analyzed system.

Parameter	Value	Unit
2ℓ	10, 100	m
a	0.007	m
d	1	M
ε_{rg}	10	
σ_g	0.1, 0.01, 0.001	S/m
V_s	1+j0	V
f	0.0001 – 10	MHz

3. Calculation of currents along the wire using TL approach

Buried wire in Fig. 1 is represented as a TL with open ends. The excitation is by a serial harmonic voltage source is in the middle point. The current distribution can be evaluated by a well known formula, for example from [10]:

$$I(x) = \frac{V_s}{2Z_{in}}\left[\cosh(\gamma x) - \frac{Z_{in}}{Z_0}\sinh(\gamma x)\right], \quad (1)$$

$$\gamma = \sqrt{ZY}, \quad (2)$$

$$Z_0 = \sqrt{\frac{Z}{Y}}, \quad (3)$$

$$Z_{in} = Z_0 \operatorname{ctanh}(\gamma \ell), \quad (4)$$

where x is distance along the wire from the source, γ is propagation constant, Z_0 is characteristic impedance and Z_{in} is input impedance of one half of the line (as seen by the source). The unit length impedance Z and admittance Y, are calculated using two different approaches, described in the following sections.

3.1. Uniformly distributed RLC parameters

A simple method to approximately estimate the required unit length parameters was suggested by Sunde [7, p. 256]. The leakage conductance, external inductance and capacitance of the finite length conductors were first derived from static (dc) conditions. Then, their values were divided by the conductor length, yielding the approximate unit length parameters:

$$G = \pi\sigma_g\left(\log\frac{2\ell}{\sqrt{2ad}} - 1\right)^{-1}, \quad (5)$$

$$L_1 = \frac{\mu_0}{2\pi}\left(\log\frac{2\ell}{a} - 1\right), \quad (6)$$

$$C = \varepsilon_g\pi\left(\log\frac{2\ell}{\sqrt{2ad}} - 1\right)^{-1}. \quad (7)$$

Effects of the earth surface are treated for the conductance and capacitance by applying the image theory, while they are neglected for the inductance, leading to expression equivalent to inductance of wire in homogeneous medium. This approximate method is still very popular and was recently compared with other methods for high-frequency and surge analysis of grounding electrodes [11]. However, there is no consensus in using an approximate expression for inductance and several formulas are often used in calculations. In addition to (6), here we also compare two additional approximate expressions for external inductance:

$$L_2 = \frac{\mu_0}{\pi}\left(\log\frac{2\ell}{\sqrt{2ad}} - 1\right), \quad (8)$$

$$L_3 = \frac{\mu_0}{2\pi}\left\{\ln\frac{2\ell}{a} + \frac{2d}{\ell}\left(\ln\frac{4d}{\ell} - 1\right) - \frac{1}{2}\left(\frac{2d}{\ell}\right)^2\right\}, \quad (9)$$

where (8) is derived from the image theory [11], and (9) is derived from an exact expression for the magnetic field due to a horizontal dc electric dipole in a lossy half-space [12].

The per unit length impedance and admittance are then calculated as

$$Z = j\omega L, \quad (10)$$

$$Y = G + j\omega C. \quad (11)$$

In the next text we will refer to the approaches in this section 3.1 as TL-RLC approaches.

3.2. Unit length impedance and admittance

Several expressions for the external impedance are available in the literature and their applicability in high-frequency analysis was recently investigated [8].

Here we compare the Sunde's expression for unit length impedance [7] and recently proposed simpler expression by Theethayi et al. [8]:

$$Z^{Sunde} = \frac{j\omega\mu_0}{2\pi}\left\{\begin{array}{l} 2\int_0^\infty \frac{e^{-2d\sqrt{\lambda^2+\gamma^2}}\cos(\lambda a)}{\lambda+\sqrt{\lambda^2+\gamma^2}}d\lambda \\ +K_0(\gamma a) \\ -K_0\left(\gamma\sqrt{a^2+4d^2}\right) \end{array}\right\}, \quad (12)$$

$$Z^{Theethayi} = \frac{j\omega\mu_0}{2\pi}\left\{\ln\left(\frac{1+\gamma a}{\gamma a}\right) + \frac{2e^{-2d|\gamma|}}{4+\gamma^2a^2}\right\}, \quad (13)$$

where K_0 is modified Bessel's function of second kind and zero order.

Unit length admittance is computed from (2), where the propagation constant is approximated by

$$\gamma = \sqrt{j\omega\mu_0\left(\sigma_g + j\omega\varepsilon_g\right)}. \quad (14)$$

The third compared formula is by Saad et al. [13]:

$$Z^{Saad} = \frac{j\omega\mu_0}{2\pi}\left\{K_0(\gamma a) + \frac{2e^{-2d\gamma}}{4+\gamma^2a^2}\right\}, \quad (15)$$

where low frequency approximation is used for the propagation constant

$$\gamma = \sqrt{j\omega\mu_0\sigma_g}. \quad (16)$$

In the next text we will refer to the approaches in this section 3.2 as TL-ZY approaches.

4. Numerical results

In this section we compare currents computed by different TL formulations with the currents computed by the antenna theory model for horizontal buried wires in frequency domain. We use the following scalar parameter, referred to as normalized RMS error [14]:

$$(\varepsilon_S)_{\mathrm{RMS}} = \left[\frac{\sum_{i=1}^{N} \left| \underline{I}_{Ei} - \underline{I}_{TLi} \right|^2}{\sum_{i=1}^{N} \left| \underline{I}_{Ei} \right|^2} \right]^{1/2} \cdot 100\% , \qquad (17)$$

where $\underline{I}_{Ei}$ and $\underline{I}_{TLi}$ are phasors of the current samples along the wire, computed by the rigorous and TL formulations, respectively, and N is number of samples.

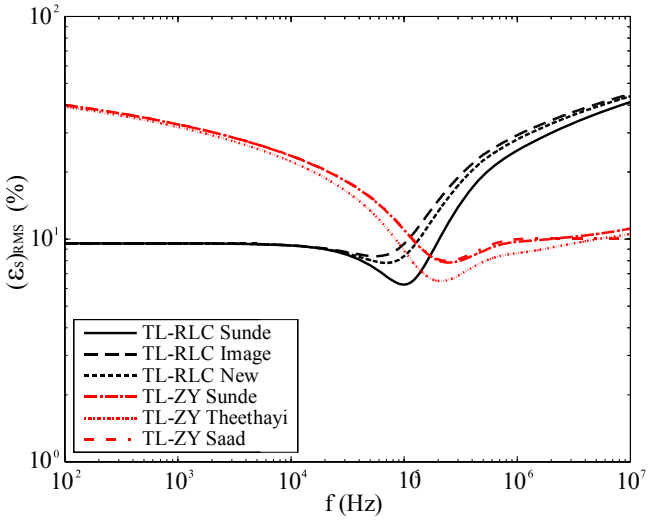
Figure 2 shows normalized RMS errors of computed currents for 10 m long wires and Fig. 3 for 100 m long wires, in soils with different conductivities.

One general conclusion, from the results in Fig. 2 for short wires (10 m long), is that there is a systematic difference between the different TL approaches and the antenna results, for all considered parameter values. This difference is always greater or equal to about 10%. Furthermore, results from the three TL-RLC approaches are somewhat grouped together, which is also the case for the results of the three TL-ZY approaches.

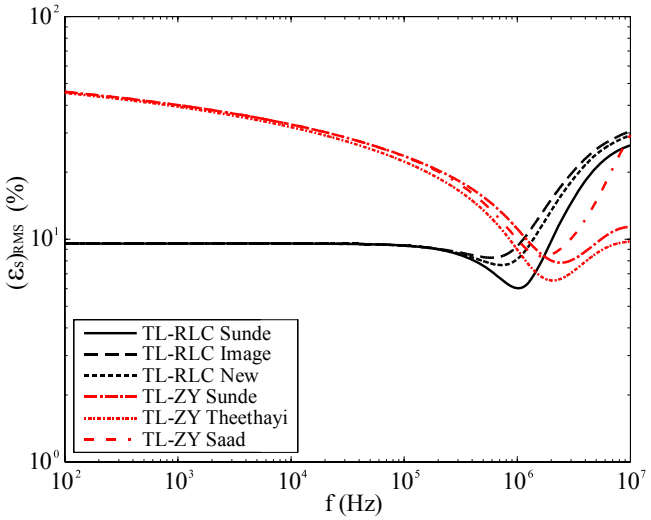
The differences between the TL-RLC and antenna approaches are constant (about 10%) at low frequencies and rise to few tens percents at high frequencies. Such increase starts at frequencies lower than about 100 kHz for highly conductive soil (σ = 0.1 S/m), Fig. 2a, and at frequencies higher that 500 kHz for less conductive soil (σ = 0.01 S/m), Fig. 2b. In cases in Figs. 2a and 2b, Sunde's formula for inductance (6) leads to smaller differences in high frequency ranges. For highly resistive soil (σ = 0.001 S/m) resonant behavior is visible in MHz range of frequencies, Fig. 2c. In this case, smaller differences with the antenna model are obtained using the formula (8).

The three TL-ZY approaches (12)–(16) lead to great differences with antenna model at low frequencies (more than about 40%). The difference is smaller with the rise of frequencies and become smaller than the TL-RLC at high frequency ranges for less resistive soil with σ = 0.1 S/m (Fig. 2a) and σ = 0.01 S/m (Fig. 2b). For highly resistive soil, with conductivity σ = 0.001 S/m (Fig. 2c) the differences with antenna model results are larger than for TL-RLC approaches in the whole considered frequency range. The Saad et al. formula (15) leads to larger differences at high frequencies.

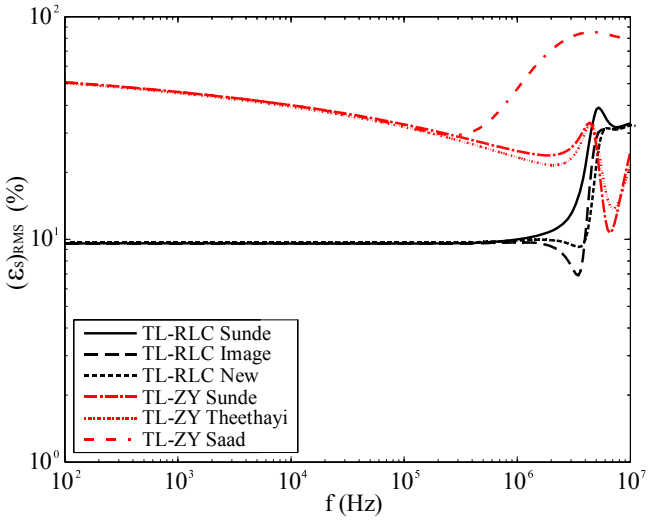
Results in Fig. 3 for longer wires (100 m long), also show systematic differences between TL and antenna results. The computed normalized RMS error is always larger or equal to about 10%. In the considered cases, TL-ZY approaches generally lead to smaller differences with the antenna model results than TL-RLC approaches, in nearly all considered ranges of parameters.



(a)

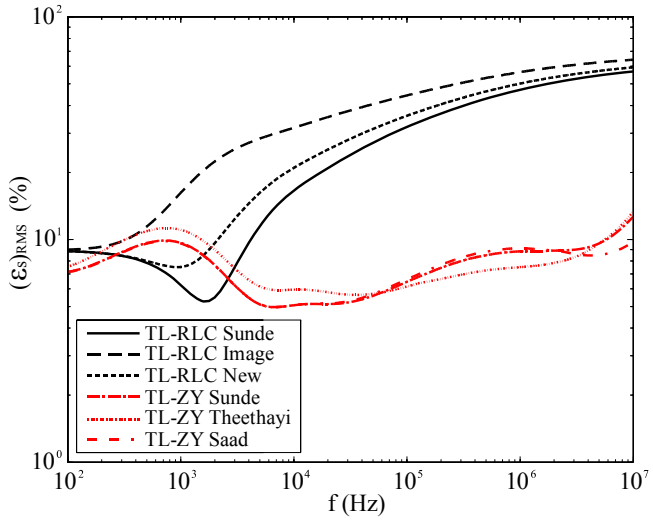


(b)

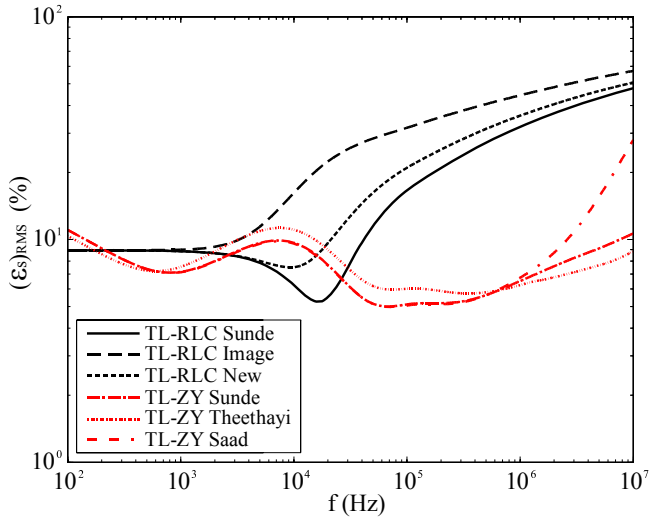


(c)

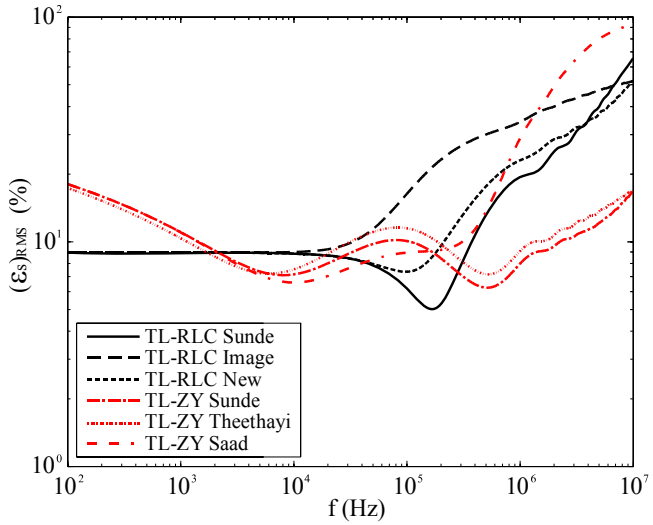
Figure 2: Normalized RMS error for currents in 10 m long buried wire (a) σ = 0.1 S/m, (b) σ = 0.01 S/m, (c) σ = 0.001 S/m



(a)



(b)



(c)

Figure 3: Normalized RMS error of currents in 100 m long buried wire (a) $\sigma = 0.1$ S/m, (b) $\sigma = 0.01$ S/m, (c) $\sigma = 0.001$ S/m

The computed error (17) between TL-RLC and antenna model is about 10% at 100 Hz and rises with frequencies up to about 50 %. Best results are obtained for Sunde's formula for inductance (6).

The TL-ZY approach leads to differences of about 10% in all cases, except Saad et al. formula (15) that leads to larger differences in high frequency ranges due to the low frequency approximation.

5. Conclusion

In this paper we compared currents computed by several TL formulations with currents computed by antenna model along buried horizontal wires that are fed at the center by harmonic series voltage source. We have computed normalized RMS error of the currents along the wire taking the antenna model results as reference. The following conclusions can be drawn from the present study:

- There is a systematic error (larger or equal to about 10%) between all TL approaches and antenna model for all values of parameters in considered ranges.
- TL formulations based on RLC parameters are more consistent with antenna model in the low frequency ranges and for smaller wire length, while after some switch frequency differences increase with frequency. Among considered three formulations, Sunde's formula for inductance (6) leads to smaller differences with antenna model.
- TL formulations based on unit length Z and Y lead to smaller differences with antenna model at high frequencies and for long wires. Among considered three formulations, Saad at al. formula (15) leads to largest differences with antenna model.

Acknowledgements

This work was supported in part by the FP7-PEOPLE-2009-IEF Project 253783, in part by the Republic of Macedonia Ministry of Education and Science, and in part by the Macedonian Academy of Sciences and Arts.

References

[1] Tesche, F. M., Ianoz, M. and Karlsson, T., *EMC Analysis Methods and Computational Models*, Wiley, New York, 1997.

[2] Vance, E. F., *Coupling to Shielded Cables*, Wiley-Interscience, New York, 1978.

[3] Grcev, L. and Grceva, S., "Comparison between exact and quasi-static methods for HF analysis of horizontal buried wires", IEEE Trans. Electromagn. Compat., Vol. 51, No. 4, 1051-1054, 2009.

[4] Theethayi, N., Baba, Y., Rachidi, F., Thottappillil, R., "On the choice between transmission line equations and full-wave Maxwell's equations for transient analysis of buried wires," IEEE Trans. Electromagn. Compat., Vol. 50, No. 2, 347-357, 2008.

[5] Poljak, D., Doric, V., Rachidi, F., Drissi, K., Kerroum, K., Tkachenko, S.V. and Sesnic, S., "Generalized form of telegrapher's equations for the electromagnetic field coupling to buried wires of finite length," IEEE Trans. Electromagn. Compat., Vol. 51, No. 2, 331-337, 2009.

[6] Grcev, L., "Modeling of grounding electrodes under lightning currents", IEEE Trans. Electromagn. Compat., Vol. 51, No. 3, 559-571, 2009.

[7] E. D. Sunde, *Earth Conduction Effects in Transmission Systems, 2nd ed*. Dover, New York, 1968.

[8] Theethayi, N., Thottappillil, R., Paolone, M., Nucci, C. A. and Rachidi, F., "External impedance and admittance of buried horizontal wires for transient studies using transmission line analysis," IEEE Trans. Dielectr. Electr. Insul., Vol. 14, No. 3, 751–761, 2007.

[9] Burke, G. J. and Miller, E. K., "Modeling antennas near to and penetrating a lossy interface," IEEE Trans. Antennas Propag., Vol. AP-32, No. 10, 1040–1049, 1984.

[10] A. A. Smith, Jr., *Coupling of External Electromagnetic Fields to Transmission Lines*. Wiley, New York, 1977.

[11] Grcev, L. and Grceva, S., "On HF circuit models of horizontal grounding electrodes", IEEE Trans. Electromagn. Compat., Vol. 51, No. 3, 873-875, 2009.

[12] Grcev, L., Markovski, B. and Grceva, S., "On inductance of buried horizontal bare conductors," IEEE Trans. Electromagn. Compat., vol. 53, no. 4, pp. 1083-1087, Nov. 2011.

[13] Saad, O., Gaba, G., Giroux, M., "A closed-form approximation for ground return impedance of underground cables", IEEE Trans. Power Delivery, vol. 11, no. 3, pp. 1536-1545, Jul 1996.

[14] Poggio, A., Bevensee, R., Miller, E. K., "Evaluation of some thin wire computer programs" in Proceedings of IEEE Antennas and Propagation Symposium, June 1974, Vol. 12, 181–184.

Focusing of Electromagnetic Field by a 3-D Cassegrain Reflector System Coated with Chiral Medium

M. J. Mughal, A. R. Farooqi* and M. M. Ali

Faculty of Electronic Engineering,
GIK Institute of Engineering Sciences and Technology, Topi (23640), Khyber Pakhtunkhwa, Pakistan.
*corresponding author, E-mail: abdulrazzaqf@gmail.com

Abstract

The electromagnetic field expressions for the focused field of a 3-D Cassegrain system with its paraboloidal reflector coated with chiral medium are analyzed. Maslov's method is used to find the field expressions at high frequencies. The dependency of focused field on the thickness of chiral coating, chirality parameter and relative permittivity is studied. It is concluded that the field strength at focal region increases by increasing the thickness of chiral layer, chirality parameter and relative permittivity of the chiral coating. Therefore, it is possible to maximize the focused field strength by adjusting these parameters.

1. Introduction

In focusing applications such as optical devices, laser cavities and solar energy collectors, different types of metallic and dielectric reflectors are used. The losses which occur due to these reflectors can be controlled by coating these reflectors with the layer of chiral medium as it has the property to minimize the losses by adjusting the parameter termed as chirality parameter [1, 2]. Such types of chiral coating may be useful for collection of data by remote sensing of different vegetation layers and also in biomedicine and biochemistry applications [3, 4].

In 19th century, the chiral medium was studied because of its optical rotation property. Later, it was theoretically and experimentally proved that left circularly polarized (LC) and right circularly polarized (RC) waves exist in the chiral medium. These waves have different phase velocities, it means that the chiral medium has two different refractive indices for LC and RC waves [5]. Also due to different circular polarizations, the waves have different modes of propagation [6]. Many scientists have explored the interaction and properties of electromagnetic waves with chiral slabs, reflection and transmission through chiral interfaces and characteristics of antennas embedded in the chiral medium [7-11].

To observe the field strength at focal region, Maslov's method is used as an alternative because Geometrical Optics (GO) is an approximate method and fails at focal points [12-19]. The physical explanation of Maslov's method and its comparison to different asymptotic ray theory (ART) techniques have been given by Ziolkowski et al. [12]. Analysis of focal region fields of chiral coated 2-D Cassegrain and Gregorian reflector systems has been done by [20, 21]. In this paper, focused field of a 3-D Cassegrain reflector is analyzed when its main paraboloidal reflector has a coating of chiral medium.

The present study is divided into five sections. Section 2 describes the relation of incident and reflected field amplitudes from perfect electric conductor (PEC) plane coated with a layer of chiral medium. In section 3, GO fields expressions for 3-D Cassegrain reflector system are presented. The simulation results and the conclusions are presented in section 4 and 5, respectively.

2. Relation of Incident and Reflected Fields by PEC Plane Coated with Chiral Medium

To observe the focal region fields of a 3-D Cassegrain system when its paraboloidal reflector has a coating of chiral material, the reflection phenomenon is considered from the PEC plane which is coated with a chiral layer as in [1, 2]. The region $z \leq 0$ is occupied with free space i.e., with parameters $(\varepsilon_0,\ \mu_0)$ while the region $0 \leq z \leq d$ consists of

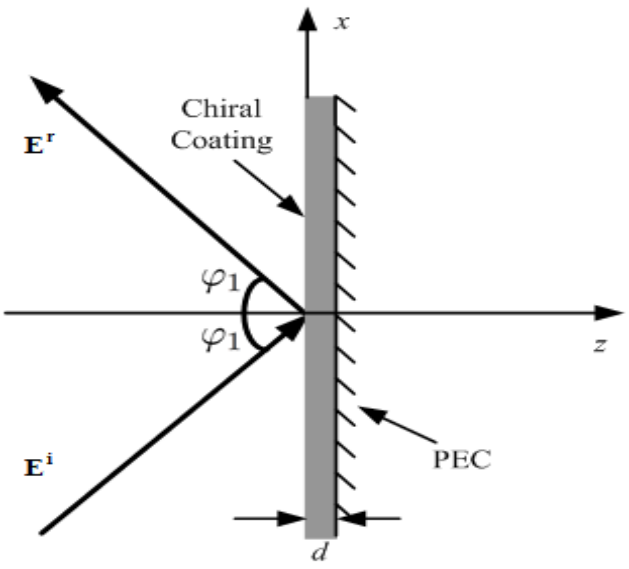


Figure 1: Reflection from the PEC plane coated with chiral medium

chiral layer i.e., ($\varepsilon,\ \mu$,β) which is actually the coating at PEC plane as shown in Figure 1. At interfaces $z = 0$ and $z = d$, the application of boundary conditions yields following equation [1],

$$\begin{bmatrix} B_\perp \\ B_\parallel \end{bmatrix} = \Big([r] + [T]\left([\Delta]\,[R_2]\,[\Delta] - [R]\right)^{-1}[t]\Big) \times \begin{bmatrix} A_\perp \\ A_\parallel \end{bmatrix} \tag{1}$$

where $A_\perp$, $B_\perp$ and $A_\parallel$, $B_\parallel$ are the amplitudes of perpendicular and parallel components of incident and reflected fields, respectively. In Equation (1), the matrices $[r]$, $[R]$, $[t]$, $[T]$, $[\Delta]$ and $[R_2]$ are of 2×2 order, defined in terms of Fresnel coefficients as given in [1]. By using this relation, the amplitudes of reflected waves from chiral coated 3-D Cassegrain reflector system are obtained in the next section.

3. Geometrical Optics Field for 3-D Cassegrain Reflector System Coated with Chiral Medium

Cassegrain reflector system consists of a paraboloidal and the hyperboloid reflector. The geometry equations of paraboloidal and the hyperboloid reflector of a 3-D Cassegrain system can be formulated as [13],

$$\zeta_1 = g - f + \frac{\sigma_1^2}{4f},\ \zeta_2 = \frac{d}{e}\sqrt{\sigma_2^2 + e^2},\ g^2 = d^2 + e^2 \tag{2}$$

where,

$$\sigma_1 = \xi_1^2 + \eta_1^2,\ \sigma_2 = \xi_2^2 + \eta_2^2,\ dH_2 = g\zeta_2 - d^2 \tag{3}$$

and (ξ_1, η_1, ζ_1) and (ξ_2, η_2, ζ_2) are the points in cartesian coordinate system which lie at the paraboloidal reflector and hyperboloid sub-reflector, respectively. Let the incident electromagnetic wave is traveling along the z-direction as shown in Figure 2. The Incident wave equation can be written as,

$$\mathbf{E}^i = \mathbf{a}_x \exp(-jk_o z) \tag{4}$$

Unit vectors $\mathbf{a}_{n1}$ and $\mathbf{a}_{n2}$ normal to the paraboloidal and hyperboloid surfaces are given as,

$$\mathbf{a}_{n1} = \sin\varphi_1\cos\varphi_2\mathbf{a}_x + \sin\varphi_1\sin\varphi_2\mathbf{a}_y - \cos\varphi_1\mathbf{a}_z \tag{5}$$

where,

$$\sin\varphi_1 = \frac{\sigma_1}{\sqrt{\sigma_1^2 + 4f^2}},\ \cos\varphi_1 = \frac{2f}{\sqrt{\sigma_1^2 + 4f^2}},\quad \tan\varphi_2 = \frac{\eta_1}{\xi_1} \tag{6}$$

and

$$\mathbf{a}_{n2} = -\sin\varphi_3\cos\varphi_2\mathbf{a}_x - \sin\varphi_3\sin\varphi_2\mathbf{a}_y + \cos\varphi_3\mathbf{a}_z \tag{7}$$

where,

$$\sin\varphi_3 = \frac{a\sigma_2}{b\sqrt{H_1H_2}},\ \cos\varphi_3 = \frac{b\zeta_2}{a\sqrt{H_1H_2}},\quad \tan\varphi_2 = \frac{\eta_2}{\xi_2} \tag{8}$$

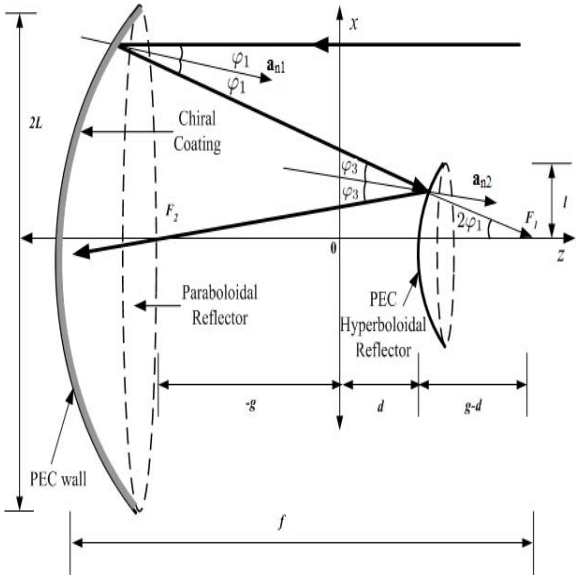


Figure 2: 3-D Cassegrain System

Here H_1 is the distance from point (ξ_2, η_2, ζ_2) to the focal point $z = -g$ and H_2 is the distance from the same point to the focal point $z = g$. The reflected wave from the paraboloidal surface will behave as incident wave for the hyperboloid reflector is given by,

$$\mathbf{E}_2^i = \mathbf{E}\exp\{jk_o(x\sin 2\varphi_1\cos\varphi_3 + y\sin 2\varphi_1\sin\varphi_3 - z\cos 2\varphi_1)\} \tag{9}$$

The rectangular components of the field reflected from paraboloidal reflector are given as [2],

$$E_x = B_\perp\sin^2\varphi_2 - B_\parallel\cos^2\varphi_2\cos 2\varphi_1 \tag{10}$$
$$E_y = -\cos\varphi_2\sin\varphi_2(B_\parallel\cos 2\varphi_1 + B_\perp) \tag{11}$$
$$E_z = -B_\parallel\sin 2\varphi_1\cos\varphi_2 \tag{12}$$

The initial value of the reflected wave from the surface of hyperboloid reflector can be obtained using snell's law as,

$$\mathbf{E}_2^r = -\mathbf{E}_2^i + 2(\mathbf{E}_2^i.\mathbf{a}_{n2})\mathbf{a}_{n2} \tag{13}$$

The rectangular components of reflected wave from the hyperboloid reflector are,

$$E_{2x}^r = -B_\perp\sin^2\varphi_2 + B_\parallel\cos^2\varphi_2\cos 2\varphi_1 - 2G\sin\varphi_3\cos\varphi_2 \tag{14}$$
$$E_{2y}^r = \cos\varphi_2\sin\varphi_2(B_\parallel\cos 2\varphi_1 + B_\perp) - 2G\sin\varphi_3\sin\varphi_2 \tag{15}$$
$$E_{2z}^r = -B_\parallel\sin 2\varphi_1\cos\varphi_2 + 2G\cos\varphi_3 \tag{16}$$

where,

$$G = -\sin\varphi_3\cos\varphi_2(B_\perp\sin^2\varphi_2 - B_\parallel\cos^2\varphi_2\cos 2\varphi_1) + \cos\varphi_2\sin^2\varphi_2\cos\varphi_3(B_\parallel\cos 2\varphi_1 + B_\perp) - B_\parallel\sin 2\varphi_1\cos\varphi_2\cos\varphi_3$$

The expression for the focal region field is calculated by using Maslov's method, given as [13],

$$\begin{aligned}\mathbf{E}(r) &= \frac{jk}{2\pi}\left[\int_{W_1}^{W_2}+\int_{-W_2}^{-W_1}\right]\int_0^{2\pi}\mathbf{E}_2^r\frac{H_2^3\cos^3\varphi_1\sin 2\varphi_1}{f^2}\\ &\times\sqrt{\frac{\cos(2\varphi_1-\varphi_3)}{2\cos\varphi_3}C\Lambda_\xi\Lambda_\eta\Lambda_\zeta}\\ &\times\exp[-jk_o\{C_o+\tau_1+C_{ex1}\\ &-r\sin\varphi\sin(2\varphi_1-2\varphi_3)\cos(\varphi_2-\phi)]d\varphi_1 d\varphi_2\end{aligned} \tag{17}$$

where,

$$\begin{aligned}\Lambda_\xi &= \frac{1+\tan 2\varphi_1\tan\varphi_1\cos^2\varphi_2}{1+\tan 2\varphi_1\tan\varphi_3\cos^2\varphi_2}\\ \Lambda_\eta &= \frac{1+\tan 2\varphi_1\tan\varphi_1\sin^2\varphi_2}{1+\tan 2\varphi_1\tan\varphi_3\sin^2\varphi_2}\\ \Lambda_\zeta &= 1-\frac{2ac}{H_1(H_2+a)}[\Lambda_\xi\cos^2\varphi_2+\Lambda_\eta\sin^2\varphi_2]\\ C &= \sin(2\varphi_1-2\varphi_3)\end{aligned}$$

The rectangular components of field are given as,

$$\begin{aligned}E_{2x}^r &= \frac{jk}{2\pi}\left[\int_{W_1}^{W_2}+\int_{-W_2}^{-W_1}\right]\int_0^{2\pi}\big(-B_\perp\sin^2\varphi_2\\ &+B_\parallel\cos^2\varphi_2\cos 2\varphi_1-2G\sin\varphi_3\cos\varphi_2\big)\\ &\times\frac{H_2^3\cos^3\varphi_1\sin 2\varphi_1}{f^2}\sqrt{\frac{\cos(2\varphi_1-\varphi_3)}{2\cos\varphi_3}C\Lambda_\xi\Lambda_\eta\Lambda_\zeta}\\ &\times\exp[-jk_o\{C_o+\tau_1+C_{ex1}\\ &-r\sin\theta\sin(2\varphi_1-2\varphi_3)\cos(\varphi_2-\phi)]d\varphi_1 d\varphi_2\end{aligned} \tag{18}$$

$$\begin{aligned}E_{2y}^r &= -\frac{jk}{2\pi}\left[\int_{W_1}^{W_2}+\int_{-W_2}^{-W_1}\right]\int_0^{2\pi}\{-2G\sin\varphi_3\sin\varphi_2\\ &+\cos\varphi_2\sin\varphi_2(B_\parallel\cos 2\varphi_1+B_\perp)\}\\ &\times\frac{H_2^3\cos^3\varphi_1\sin 2\varphi_1}{f^2}\sqrt{\frac{\cos(2\varphi_1-\varphi_3)}{2\cos\varphi_3}C\Lambda_\xi\Lambda_\eta\Lambda_\zeta}\\ &\times\exp[-jk_o\{C_o+\tau_1+C_{ex1}\\ &-r\sin\theta\sin(2\varphi_1-2\varphi_3)\cos(\varphi_2-\phi)]d\varphi_1 d\varphi_2\end{aligned} \tag{19}$$

$$\begin{aligned}E_{2z}^r &= \frac{jk}{2\pi}\left[\int_{W_1}^{W_2}+\int_{-W_2}^{-W_1}\right]\int_0^{2\pi}(2G\cos\varphi_3\\ &-B_\parallel\sin 2\varphi_1\cos\varphi_2\big)\\ &\times\frac{H_2^3\cos^3\varphi_1\sin 2\varphi_1}{f^2}\sqrt{\frac{\cos(2\varphi_1-\varphi_3)}{2\cos\varphi_3}C\Lambda_\xi\Lambda_\eta\Lambda_\zeta}\\ &\times\exp[-jk_o\{C_o+\tau_1+C_{ex1}\\ &-r\sin\theta\sin(2\varphi_1-2\varphi_3)\cos(\varphi_2-\phi)]d\varphi_1 d\varphi_2\end{aligned} \tag{20}$$

where the terms in phase function are given as,

$$\begin{aligned}C_o &= \frac{2f\cos 2\varphi_1}{1+\cos 2\varphi_1}-c\\ \tau_1 &= \sqrt{(\xi_2-\xi_1)^2+(\eta_2-\eta_1)^2+(\zeta_2-\zeta_1)^2}\\ C_{ex1} &= \frac{a^2\cos\varphi_3\cos(2\varphi_1-2\varphi_3)}{\sqrt{a^2\cos^2\varphi_3-b^2\sin^2\varphi_3}}\\ &+\frac{b^2\sin\varphi_3\sin(2\varphi_1-2\varphi_3)}{\sqrt{a^2\cos^2\varphi_3-b^2\sin^2\varphi_3}}\\ &-r\cos(2\varphi_1-2\varphi_3)\cos\theta\end{aligned}$$

and the limits of integration are chosen using relations,

$$\begin{aligned}W_1 &= 2\tan^{-1}\left(\frac{L}{2f}\right)\\ W_2 &= \tan^{-1}\left(\frac{l}{2c}\right)\end{aligned}$$

4. Results and Discussion

In this section, Equation (17) is solved numerically for $L = 16$, $l = 4$, $a = 5$, $b = 6$ and $kf = 20$. The limits of integration are taken using the formulas for W_1 and W_2. The effects of chiral layer thickness (d), chirality parameter (β) and relative permittivity (ε) on the focal region of a 3-D Cassegrain reflector system are investigated and analyzed.

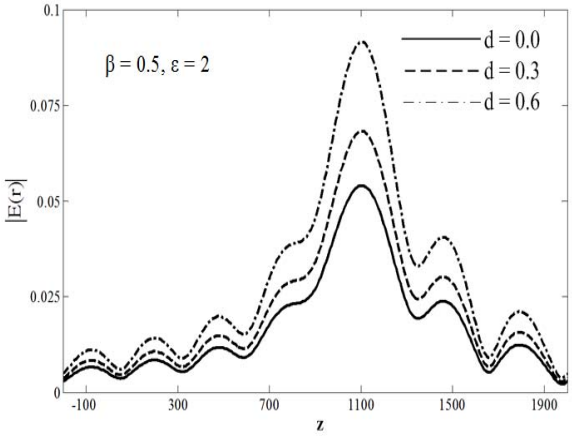


Figure 3: Chiral thickness effect in 3-D Cassegrain system

Figure 3 shows the dependence of chiral thickness (d) on the strength of focal region field. It is clear that by increasing the thickness, focal region field strength increases because of increase in the number of chiral medium molecules, here β and ε are kept constant i.e., $\beta = 0.5$ and $\varepsilon = 2$. Figure 4 indicates that by increasing the chirality parameter β keeping $\varepsilon = 2$ and $d = 0.1$, the focused field strength increases, the reason is the increased concentration of chiral medium molecules.

Figure 5 shows the effect of change in relative permittivity ε when $\beta = 0.5$ and $d = 0.1$. It is observed that grad-

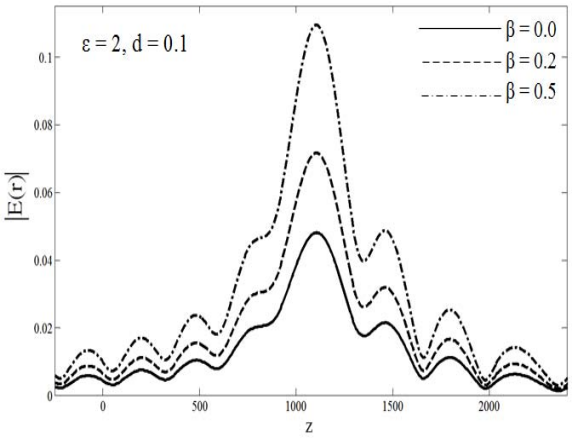


Figure 4: Chirality parameter effect in 3-D Cassegrain system

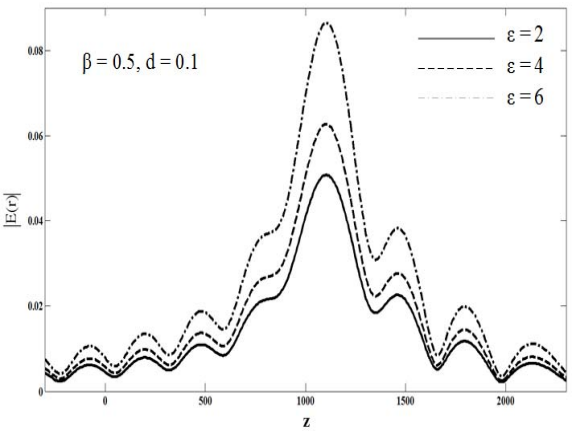


Figure 5: Relative permittivity effect in 3-D Cassegrain system

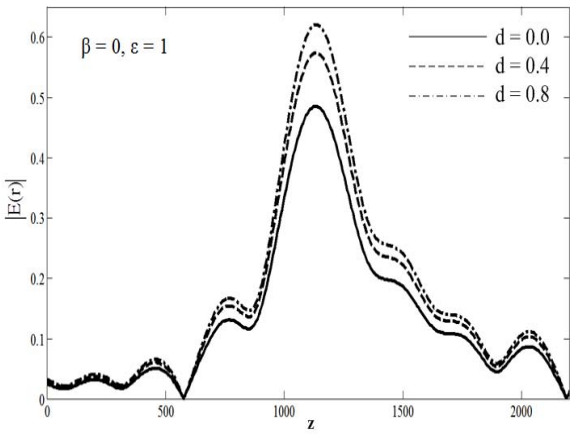


Figure 6: Dielectric thickness effect in 3-D Cassegrain system

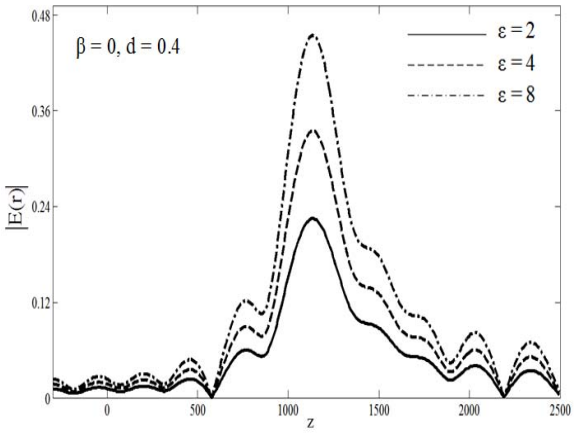


Figure 7: Dielectric relative permittivity effect in 3-D Cassegrain system

ual increase in the value of ε increases the strength of focal region field. The reason is, the chiral material impedance is inversely proportional to $\sqrt{\varepsilon}$. When ε is increased, there is decrease in η and ultimately the focal region field strength is increased.

Finally, the chirality parameter is fixed i.e., $\beta = 0$ and the dependency of dielectric thickness on focal region field is observed. Figure 6 shows the increased focal region field strength when d is increased keeping $\beta = 0$ and $\varepsilon = 2$. The effect of dielectric relative permittivity on focal region field is shown in Figure 7, with $\beta = 0$ and $d = 0.4$. The focal region field strength increases as value of relative permittivity is increased.

5. Conclusions

The focal region fields of a 3-D Cassegrain reflector system are observed with its paraboloidal reflector coated with chiral layer. It is concluded that by increasing the chiral coating thickness (d), chirality parameter (β) and relative permittivity (ε) of chiral coating, the strength of focal region field is increased. Also the dielectric layer coating effect is analyzed by putting the chirality parameter equal to zero. It is concluded that the focused field strength can be increased by increasing the relative permittivity ε and thickness d of the dielectric coating. Thus, present study is useful for the optimization in different focusing applications.

References

[1] M. Faryad and Q. A Naqvi, "High frequency expression for the field in the caustic region of a parabolic reflector coated with isotropic chiral medium," *J. of Electromagn. Waves and Appl*, Vol. 22, 965–986, 2008.

[2] T. Rahim, M. J. Mughal, Q. A. Naqvi and M. Faryad, "Focal region field of a paraboloidal reflector coated with isotropic chiral medium," *Progress In Electromagnetics Research*, Vol. 94, 351–366, 2009.

[3] E. Bahar, "Muller matrices for waves reflected and transmitted through chiral materials: waveguide modal solutions and applications," *J. Opt. Soc. Am. B*, Vol. 24, 1610–1619, 2007.

[4] H. Cory and I. Rosenhouse, "Electromgnetic wave reflection and transmission at a chiral-dielectric interface," *Journal of Modern Optics*, Vol. 38, 1229–1241, 1991.

[5] J. A. Kong, *Electromagnetic Wave Theory*, Wiley, New York, 1986.

[6] A. Lakhtakia, *Beltrami fields in chiral media*, Contemporary Chemical Physics, World Scientific Series, 1994.

[7] S. Bassiri, C. H. Papas and N. Engheta, "Electromagnetic wave propagation through a dielectric-chiral interface and through a chiral slab," *J. Opt. Soc. Am. A*, Vol. 5, 1450–1459, 1988.

[8] M. Q. Mehmood, and M. J. Mughal, "Analysis of focal region fields of PEMC gregorian system embedded in homogenous chiral medium," *Progress In Electromagnetics Research Letters*, Vol. 18, 155–163, 2010.

[9] M. Q. Mehmood, M. J. Mughal and T. Rahim, "Focal region fields of gregorian system placed in homogenous chiral medium," *Progress In Electromagnetics Research M* Vol. 11, 241–256, 2010.

[10] M. Q. Mehmood, M. J. Mughal and T. Rahim, "Focal region fields of cassegrain system placed in homogenous chiral medium," *Progress In Electromagnetics Research B*, Vol. 21, 329–346, 2010.

[11] I. V. Lindell, A. H. Sihvola, S. A. Tretyakov, A. J. Viitanen, *Electromagnetic Waves in Chiral and Bi-Isotropic Media*, Artech House, MA, 1994.

[12] R. W. Ziolkowski and G. A. Deschamps, "Asymptotic evaluation of high frequency field near a caustic: An introduction to Maslov's method," *Radio Sci.*, Vol. 19, 1001, 1984.

[13] A. Ghaffar, Q. A. Naqvi and K. Hongo,"Analysis of the fields in three dimensional cassegrain system," *Progress In Electromagnetics Research*, Vol. 72, 215–240, 2007.

[14] K. Hongo, Yu Ji and E. Nakajima, "High frequency expression for the field in the caustic region of a reflector using Maslov's method," *Radio Sci.*, Vol. 21, 911–919, 1986.

[15] K. Hongo and Yu Ji, "High frequency expression for the field in the caustic region of a cylindrical reflector using Maslov's method," *Radio Sci.*, Vol. 22, 357–366, 1987.

[16] A. Ghaffar, A. Hussain, Q. A. Naqvi and K. Hongo, "Radiation characteristics of an inhomogeneous slab using Maslov's method," *J. of Electromagn. Waves and Appl*, Vol. 22, 301–312, 2008.

[17] A. Aziz, A. Ghaffar, Q. A. Naqvi and K. Hongo, "Analysis of the fields in two dimensional Gregorian system," *J. of Electromagn. Waves and Appl*, Vol. 22, 85–97, 2008.

[18] A. Ghaffar, A. Rizvi, and Q. A. Naqvi, "Field in the focal space of symmetrical hyperboloidal focusing lens," *Progress In Electromagnetics Research*, Vol. 89, 255–273, 2009.

[19] T. M. Kayani, M. Q. Mehmood, M. J. Mughal, and T. Rahim, "Analysis of the field focused by hyperbolic lens embedded in chiral medium," *Progress In Electromagnetics Research M*, Vol. 20, 43–56, 2011.

[20] T. Rahim, M. J. Mughal and M. Hussnain, "Focal region field of a two dimensional gregorian system coated with isotropic chiral medium," *J. Electromagnetic Analysis and Applications*, Vol. 34, No. 10, 488–494, 2010.

[21] M. J. Mughal, T. Rahim, M. Hussnain and M. Q. Mehmood, "Caustic region fields of a two dimensional cassegrain system coated with isotropic chiral medium," *Proceedings of IEEE 19th Signal Processing and Communications Applications Conference (SIU 2011)*, Antalya, Turkey, April 2011, 279-282.

Resonant Frequency of a Rectangular and an Equitriangular Tunable Microstrip Antennas and Comparison

L.Djouablia, C.Aissaoui, and A.Benghalia

Laboratory of ultra high frequencies and semi conductor, Department of Electronics,
Engineering sciences Faculty. Mentouri University,of Constantine.
Route d'Ain El Bey 25000, Constantine, Algérie.
Fax: 0021331819010
ln_djouablia@live.fr

Abstract−Both rectangular and equilateral triangular microstrip patches antennas with and without an adjustable air gap of an isotropic substrate are investigated in this paper and compared. An applicable and efficient method based on an analytical process is proposed to calculate the value of the resonant frequency for different cases. The structure is analysed in spectral domain using the moment method and an electric field integral equation based on Galerkin's procedure. The electric field due to the basis current on the rectangular and triangular patch is described for each form and Green's function corresponding to each layer is determined.

1. INTRODUCTION:

Having relatively the same radiation properties as the rectangular microstrip antenna, the equilateral triangular patch finds an extensive application such as radars and satellite communication. However, the analysis and design of the rectangular microstrip antennas mounted on different structures have been extensively reviewed [1]-[4], but few studies have been performed for the determination of the resonant frequencies of the equilateral triangular microstrip structure [1], [5]-[9].

A rectangular and an equilateral triangular patch having the same surface area mounted on two different forms of substrate are investigated and compared. In the first instance, we compare the values of the resonant frequency for each patch implemented on single layer of an isotropic dielectric substrate. Secondly the same geometries are mounted on tow-layer structure in order to study the air-gap tuning effect on the resonant frequencies. The structures are modelled and analysed with spectral-domain method of moments [10], [11]. The resonant frequency is calculated for different values of the antenna's structural parameters.

In order to validate the proposed study, our results are compared with the data reported in the open literature for both rectangular and triangular microstrip antennas.

2. ANALYSIS FORMULATIONS:

The analysis of the proposed structures is leaded by the Galerkin's moment method (MoM) in the spectral domain using boundary conditions as an element to solve the problem. For this case we have developed the exact calculus of the dyadic Green's functions.

It is preferable to express the unknown patch current in terms of an appropriate basis functions formed by a set of transverse magnetic modes of the rectangular and triangular cavities with magnetic side walls and electric top and bottom walls. However, an appropriate basis current system is chosen from [3] for the rectangular patch, and from [6] for the triangular one. We have calculated analytically the Fourier Transform of the current components by applied a mathematical method [12], because of the complexity of the

triangular geometry. In this letter we are concerned only with the resonant frequency of the structure without considering the feed. It is assumed that the dielectric layers are an infinite isotropic dielectric. The metallic slabs (ground plane and patches) are perfect conductors having negligibly thin.

Starting by the Maxwell's equations, and assuming that the propagation is in the Z direction, for each layer *i* the wave equation in the spectral domain with free source is defined by the following equation:

$$\frac{\partial^2 \widetilde{E}_i}{\partial z^2} + K_{zi}^2 \widetilde{E}_i = 0 \tag{1}$$

E_i is the tangential components of incident electric field.

Where: $K_{zi}^2 = K_i^{\,2} - (K_x^2 + K_y^2)$ and $K_i^2 = \omega^2 \mu_i \varepsilon_i$

$K_{zi}, K_i, K_x and K_y$ are the propagation constants for each considering layer; ε_i and μ_i are respectively permittivity and permeability.

In spectral domain representation's (TM-TE) the electric field is represented on matrix form and in terms of longitudinal components as [13]:

$$\overline{E}(K_s, z) = \begin{bmatrix} \widetilde{E}^e(K_s, z) \\ \widetilde{E}^h(K_s, z) \end{bmatrix} = \overline{g}_i(K_s) \begin{bmatrix} \frac{j}{K_s} \frac{\partial \widetilde{E}_z(K_s, z)}{\partial z} \\ \frac{\omega \mu_0}{K_s} \widetilde{H}_z(K_s, z) \end{bmatrix} \tag{2}$$

Note that '– 'is used for vectorial quantities and '~ 'for spectral quantities.

$\widetilde{E}_Z$ and $\widetilde{H}_Z$ are respectively the electric and magnetic fields in the direction Z.

The solution of the wave equation is:

$$\overline{E}(K_Z, Z) = \overline{A} e^{-jK_Z Z} + \overline{B} e^{+jK_Z Z} \tag{3}$$

And

$$\overline{H}_Z(K_Z, Z) = \overline{g}(K_S)[\overline{A} e^{-jK_Z Z} - \overline{B} e^{+jK_Z Z}] \tag{4}$$

Where:

$$\overline{g}(K_S) = \begin{bmatrix} \frac{\omega \varepsilon_i}{K_Z} & 0 \\ 0 & \frac{K_Z}{\omega \mu_i} \end{bmatrix} \tag{5}$$

$\overline{A}$ and $\overline{B}$ are found when assuming the boundary conditions.

Now for each case we must evaluate the dyadic Green's function and the appropriate basis functions corresponding to the distribution's current on each patch.

However, to solve rigorously the problem, we consider at first the wave propagating media as a single layer limited between tow levels (Z_{i-1} and Z_i) as showing in Figure 1.

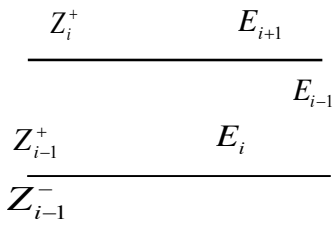


Figure 1: Model of theoretical wave propagating media

The problem will be solved when substituting the unknown coefficients $\overline{A}$ and $\overline{B}$ as:

$$\begin{cases} A(K_s) = (E^- + \overline{g}_i(K_s)^{-1} H^-) \dfrac{e^{-j\overline{K}_z Z_{i-1}^+}}{2} \\ B(K_s) = (E^- - \overline{g}_i(K_s)^{-1} H^-) \dfrac{e^{+j\overline{K}_z Z_{i-1}^+}}{2} \end{cases} \tag{6}$$

The electric and magnetic fields can be written now as:

$$\begin{cases} E^+ = E^- \cos(K_Z d_i) - jg^{-1} H^- \sin(K_Z d_i) \\ H^+ = H^- \cos(K_Z d_i) - jgE^- \sin(K_Z d_i) \end{cases} \tag{7}$$

The matrix form of the system (7) is represented as following:

$$\begin{bmatrix} E_i(K_S, Z_i^+) \\ H_i(K_S, Z_i^+) \end{bmatrix} = \overline{F}_i \begin{bmatrix} E_i(K_S, Z_i^-) \\ H_i(K_S, Z_i^-) \end{bmatrix} \tag{8}$$

$\overline{F}_i$ is the Green's matrix of the i^{th} layer (i=1,2,3) in the (TE, TM) representation.
The exact diagonal matrix Green's function is obtained by cascading the matrices $\overline{F}_i$ by simple multiplication yields

$$G = \begin{bmatrix} G_{11} & G_{12} \\ G_{12} & G_{22} \end{bmatrix} \tag{9}$$

Where:

$$G_{11} = \frac{K_x^2}{K_x^2 + K_y^2} \frac{D_m}{T_m} + \frac{K_y^2 K_0^2}{K_x^2 + K_y^2} \frac{D_e}{T_e} \tag{10}$$

$$G_{22} = \frac{K_y^2}{K_x^2 + K_y^2} \frac{D_m}{T_m} + \frac{K_x^2 K_0^2}{K_x^2 + K_y^2} \frac{D_e}{T_e} \tag{11}$$

$$G_{12} = \frac{K_x K_y}{K_x^2 + K_y^2} \frac{D_m}{T_m} - \frac{K_x K_y}{K_x^2 + K_y^2} \frac{D_e}{T_e} \tag{12}$$

D_m, D_e, T_m, T_e are terms evaluated and given for each case as:

2.1. Formulation for single layer:

The structure configuring a rectangular (or an equilateral triangular) patch antenna implemented on single dielectric layer is illustrated in Figure 2.

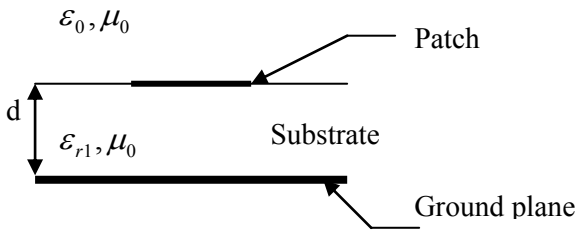


Figure 2: Cross section of the structure with one layer of substrate

$$D_m = \frac{-j}{\omega\varepsilon_0} K_{z0} K_{z1} \sin(K_{z1} d) \tag{13}$$

$$T_m = \varepsilon_{r1} K_{z0} \cos(K_{z1} d) + jK_{z1} \sin(K_{z1} d) \tag{14}$$

$$D_e = \frac{-j}{\omega\varepsilon_0} K_0^2 \sin(K_{z1} d) \tag{15}$$

$$T_e = K_{z1} \cos(K_{z1} d) + jK_{z0} \sin(K_{z0} d) \tag{16}$$

2.2. Formulation for two layers:

The Figure 3 illustrate a single patch on two layers, the upper layer is an isotropic dielectric substrate and the under one is air.

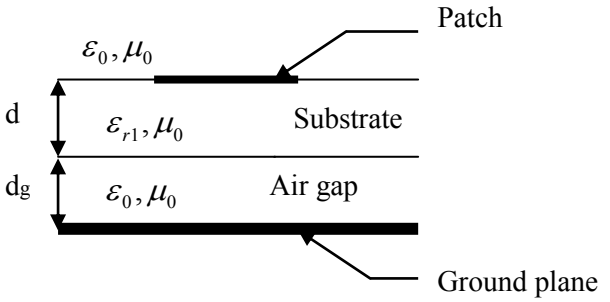


Figure 3: Cross section of a structure with two layers

$$D_m = K_{z0} K_{z1} \varepsilon_{r1} \sin(K_{z0} d_g) \cos(K_{z1} d_1) + K_{z0} K_{z1} \varepsilon_0 \cos(K_{z0} d_g) \sin(K_{z1} d) \tag{17}$$

$$\begin{aligned} T_m = {} & j\omega\varepsilon_0^2 \cos(K_{z0} d_g)(\varepsilon_{r1} K_{z0} \cos(K_{z1} d) + jK_{z1} \sin(K_{z1} d)) - \\ & \omega\varepsilon_{r1}\varepsilon_0 K_{z0} \cos(K_{z0} d_g)(\cos(K_{z1} d) + j\varepsilon_{r1} \frac{K_{z0}}{K_{z1}} \sin(K_{z1} d)) \end{aligned} \tag{18}$$

$$D_e = K_0^2 K_{z0} \sin(K_{z0} d_g) \cos(K_{z1} d) + K_0^2 K_{z1} \sin(K_{z1} d) \cos(K_{z0} d_g) \tag{19}$$

$$T_e = j\omega\varepsilon_0 K_{z0}\cos(K_{z0}d_g)(K_{z1}\cos(K_{z1}d) + jK_{z0}\sin(K_{z1}d)) - \omega\varepsilon_0 K_{z1}\sin(K_{z0}d_g)(K_{z0}\cos(K_{z1}d) + jK_{z1}\sin(K_{z1}d)) \quad (20)$$

Where: $j = \sqrt{-1}$, $K_{z1} = \sqrt{\varepsilon_{r1}K_0^2 - K_s^2}$, $K_{z0} = \sqrt{\varepsilon_g K_0^2 - K_s^2}$, $K_z = \sqrt{K_0^2 - K_s^2}$, $K_0 = \omega\sqrt{\varepsilon_0\mu_0}$

2.3. Choice of basis functions:

When applying Galerkin's method to solve the integral equation, it is preferable to express the unknown patch current in terms of an appropriate basis functions formed by a set of transverse magnetic modes of rectangular (or triangular) cavity.

For the rectangular patch illustrated in the Figure 5, the proposed basis functions from the reference [3, Eqs. (7a) and (7b)] are:

$$J_{xn} = \sin[\frac{n_1\pi}{a}(x + \frac{a}{2})]\cos[\frac{n_2\pi}{b}(y + \frac{b}{2}] \quad (21)$$

$$J_{ym} = \sin[\frac{m_2\pi}{b}(y + \frac{b}{2})]\cos[\frac{m_1\pi}{a}(x + \frac{a}{2})] \quad (22)$$

The Fourier transform of these functions were calculated and obtained in closed form by [15, Eqs. (27) and (31)].

The basis functions selected for the equilateral triangular patch shown in figure 4, are proposed by W. Chen, k. F. Lee and J. S. Dahele [6]:

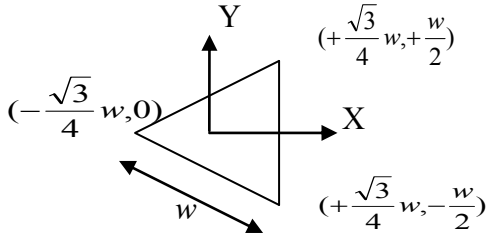


Figure 4: The proposed equilateral triangular patch

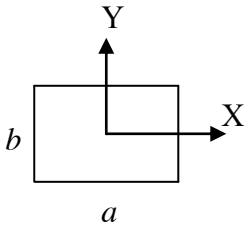


Figure 5: The rectangular patch

We have developed analytically the Fourier transform of these functions. The calculus requires the use of a mathematical approach reported in [12]. The obtained results were reported on the reference [16, Eqs. (4) and (5)]:

$$J_x(m,n) = \sqrt{3}[l\sin(\frac{2\pi lx}{\sqrt{3}w})\cos(\frac{2\pi(m-n)y}{3w}) + m\sin(\frac{2\pi mx}{\sqrt{3}w})\cos(\frac{2\pi(n-l)y}{3w}) + n\sin(\frac{2\pi nx}{\sqrt{3}w})\cos(\frac{2\pi(l-m)y}{3w})] \quad (23)$$

$$J_y(m,n) = (m-n)\cos(\frac{2\pi lx}{\sqrt{3}w})\sin(\frac{2\pi(m-n)y}{3w})$$
$$+(n-l)\cos(\frac{2\pi mx}{\sqrt{3}w})\sin(\frac{2\pi(n-l)y}{3w}) \quad (24)$$
$$+(l-m)\cos(\frac{2\pi nx}{\sqrt{3}w})\sin(\frac{2\pi(l-m)y}{3w})$$

The electric field integral equation is deduced by applying the boundary conditions requiring that the current distribution vanish on the rectangular (or the triangular) patch yields ($\widetilde{E}_{surface} = \widetilde{G}.\widetilde{J} = 0$) [17]; cascading the matrices by simple multiplication yields, the following matrix form is obtained for each case of the proposed structures.

$$\overline{B} = \begin{bmatrix} \overline{B}_1 & \overline{B}_2 \\ \overline{B}_3 & \overline{B}_4 \end{bmatrix} \begin{bmatrix} \overline{C} \\ \overline{D} \end{bmatrix} = 0 \quad (25)$$

Finally the complex resonant frequency $f = f_r + jf_i$ result from the resolution of the equation

$$\det(\overline{B}_{ij}) = 0 \quad (26)$$

3. NUMERICAL RESULTS AND DISCUSSIONS:

The proposed method can supply results for several considerations and different modes. Only analysis for the fundamental mode TM_{10} concerning the resonant frequency are presented in this paper. The rectangular patch surface's "*S*" is always taken similar as the triangular one. We have also taken account different substrate's thicknesses and effective dielectric constants for the two proposed structures. Numerical results vested from the processing of structures for the rectangular and the triangular patches are compared with them for each case with and without air gap.

3.1. Results and comparison for single layer's structure:

In this section several cases are taken account; the first table summarizes different values of the resonant frequency for both square and triangular patches having relatively the same surface $S = 1.32cm^2$ (a=b=1.15cm, and w=1.75cm), for substrate's permittivity of $\varepsilon_{r1} = 7.25$ and several thicknesses.

d(cm)	f_r (GHz) square patch [3]	f_r (GHz) square patch [our results]	f_r (GHz) triangular patch [our results]
0.10	4.734	4.830	4.7308
0.15	4.640	4.738	4.6585
0.20	4.541	4.632	4.6380
0.225	4.496	4.577	4.6341
0.25	4.457	4.520	4.6318

Table 1: Variation of the resonant frequency versus thickness of substrate (Single layer and square patch) for: $\varepsilon_{r1} = 7.25 and S = 1.32cm^2$

To compare a rectangular patch antenna with b=1.9cm and a=2.29cm and triangular patch antenna with w=3.17cm ($S = 4.35cm^2$), a typical plot representing variation of the resonant frequency (real part) versus the substrate's thicknesses for different effective dielectric constants is set on the figure 6.

We can see on table 1, that our results and those of the references [3] are closer for the square patch and slightly lower from the results of the triangular one. Generally for both square (rectangular) and equilateral triangular patch, the resonant frequency decrease when increasing the width of the substrate and its permittivity. Thus, from the figure 6 we can observe that the rectangular patch frequency's values are relatively lower than the triangular ones, the difference is more important for thin substrates, especially for $\varepsilon_{r1} = 2.32$.

When considering patches having the same surfaces and taking a=w and $b = a\dfrac{\sqrt{3}}{4}$;

the figure 7 represent variation of the resonant frequency versus patches dimensions. We can notice that the two curves have the same behaviour; the frequency of resonance decreases when dimensions of the patches increase. However, the triangular patch's frequencies are more important than that of the rectangular patch.

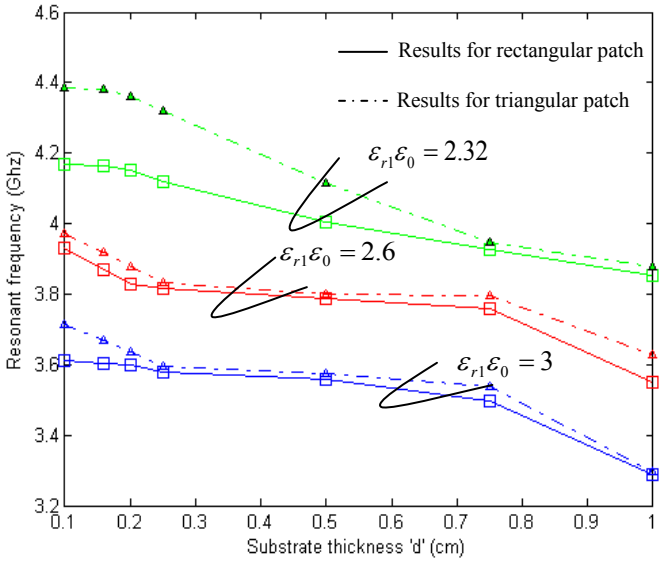


Figure 6: Variation of the resonant frequency versus Substrate's for TM10 mode, b=1.9cm, a=2.29cm, w=3.17cm and $\varepsilon_{r1} = 2.32$ (Duroid), 2.6 (Plexyglass), 3 (Mylar).

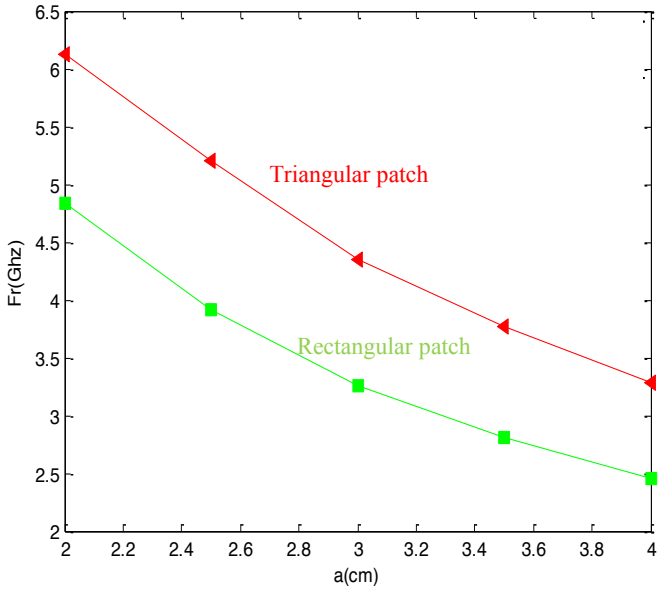


Figure 7: Variation of the resonant frequency versus patches dimensions (a=w and $b = a\frac{\sqrt{3}}{4}$) for TM10 mode, d=0.159cm, $\varepsilon_{r1} = 2.32$.

3.2. Results and comparison for the two layer's structure:

To study the air gap tuning effect on both rectangular and triangular patches (b=1.5cm, a=1cm, w=1.86cm, $S = 1.5cm^2$) and comparing the results, the resonant frequencies corresponding to different gap are presented in table 2 for d=0.5mm, $\varepsilon_{r1} = 3, 2.6 and 2.32$.

ε_{r1}	d_g (mm)	Equivalent permittivity ε_{equi}	f_r (Ghz) for rectangular patch [Our results]	f_r (GHz) for triangular patch [our results]
3	0.2	1.909	7.257	7.866
2.6	1	1.258	8.918	9.503
2.32	1.6	1.156	9.330	10.127

Table 2: Variation of the resonant frequency versus air gap's thickness (two layers) for: $\varepsilon_{r1} = 2.32, 2.6 and 3$, $d = 0.5mm$ and $S = 1.5cm^2$

Shape of patch	f_r (GHz) without air gap d_g=0mm	f_r (GHz) with air gap thick d_g=0.5mm	f_r (GHz) with air gap thick d_g=1mm
Rectangular [our results] (MoM)	0.989	1.134	1.216
Triangular [our results] (MoM)	1.305	1.522	1.628
Triangular[8] (cavity model)	1.278	1.436	1.509

Table 3: Variation of the resonant frequency versus air gap's thickness (two layers) for: $\varepsilon_{r1} = 2.32$, $d = 1.59mm$ and $S = 40.33cm^2$

The change of "*d*" and "*S*" has also a significant effect on frequency, for example for d=1.59mm, $\varepsilon_{r1} = 2.32$ and $S = 40.33cm^2$ ($w = 10cm, b = 4.33cm, a = 10cm$). Table 3 summarizes some values for several air gap widths.

Generally it can be seen that the behaviour of the frequency's variation versus the gap's width is the same for both rectangular and triangular patch; the resonant frequency increase when increasing the thick of the gap and the permittivity of the dielectric, but thus decreasing the equivalent permittivity. From the table 3, we observe that the values of the frequency decreases substantially when increasing the surface's patch and the substrate's thick simultaneously. This result is logical because in this case some electromagnetic interference can appear [17]. For the triangular patch, it must be mentioned that our results using moment method are relatively close from that of the reference [8] using cavity model method.
The noteworthy observation here is that the resonant frequencies values of the rectangular patch are relatively lower from that of the triangular ones unlike to the first case when the substrate is without air gap.

4. CONCLUSION:

We have carried out an investigation and comparison between two microstrip antenna's structures for two shapes of patch in each case. We have used new and rigorous approach based on an analytical calculation combined with the moment method in spectral domain. The study summarizes a characterization of both rectangular and an equilateral triangular microstrip antenna having the same surface, with and without an adjustable air gap. Generally it is observed from the obtained results that the resonant frequency of rectangular patch is relatively lower than the triangular one in all cases. However, the introduction of an adjustable air gap has a more pronounced effect on the resonant frequency for the proposed antenna's patches.

5. REFERENCES:

[1] Bahl. I.J , Bhartia. P, "Microstrip Antennas", Artech House, pp 31-177, 1982.
[2] Wong. K.L, Row. J.S, Kiu. C.W and Huang. KC, "Resonance of a rectangular microstrip patch on uniaxial substrate", *IEEE Trans micro theory tech*., vol. 41, 698-701, 1993.
[3] Chew. W.C and Liu. Q, "Resonance frequency of a rectangular microstrip patch", *IEEE* Trans. *Antennas Propagat*.,vol. AP-36,pp.1054-1056, Aug 1988

[4] Bahl. I.J, Bhartia.P and Stuchly.S.S, “design of microstrip antennas covered with a dielectric layer”, *IEEE Trans*. *Antennas Propagat*.,vol. AP-30,pp.314-318, Mar 1982
[5] Dahele. J.S and Lee. K.F, “On the resonant frequency of the triangular patch antenna”, *IEEE Trans Antennas Propagat*.,vol. AP-35,pp.100-101, Jan 1987.
[6] Wei Chen, Kai Fong Lee, and Dahele. S, “Theoretical and experimental studies of the resonant frequencies of the equilateral triangular microstrip antenna”, *IEEE*, *Trans on Antennas and propagat*, Vol 40, NO 10, PP 1253-1256, oct 1992.
[7] Garg. R and Long.S.A, “An improved formula for the triangular microstrip patch antenna”, *IEEE Trans Antennas Propagat*, vol.AP-36, p.570, Apr 1988.
[8] Cigdem Sekin Gurel, Erdem Yazgan, “New computation of the resonant frequency of a tunable equilateral triangular microstrip patch”, *IEEE*, *Trans on microwave theory and techniques*, Vol48, NO3, pp334-338, Mar 2000.
[9] Heelzajin. J and James. D.S, “Planar triangular resonators with magnetic walls”, *IEEE Trans micro theory tech*, vol. MTT-26, pp95-10, Feb 1978.
[10] Mirshekar-Syahkal.D, “Spectral domain method for microwave integrated circuits”, Research studies press LTD, John Willey and sons INC, 1989.
[11] Itho. T and Menzel. W, “A full wave analysis method for open microstrip structures”, *IEEE Trans*.*Antennas propagate*., vol. AP-29, pp63-67, Jan 1981.
[12] Jacque Douchet et Bruno Zwhalen, Calcul différentiel et intégral, fonctions réelles de plusieurs variables réelles (2eme édition), p.140-142.
[13] Fortaki. T and Benghalia. A, “Rigorous full-wave analysis of rectangular microstrip patches over ground planes with rectangular apertures in multilayered substrates that contain isotropic and uniaxial anisotropic materials”, Micro and opt tech lett, Vol 46, No 6, pp 496-500, Jun 2004.
[14] Dreher. A, “A new approach to dyadic Green’s function in spectral domain”, *IEEE Trans micro theory tech*., vol. 43, NO 11, Nov 1995.
[15] Newman. E.H and Forrai. D, “Scattering from a microstrip patch”, *IEEE Trans*. *Antennas propagate*., vol. AP-35, pp245-251, 1987.
[16] Djouablia. L and Benghalia. A, “Etude d’une antenne de forme triangle équilateral piégée en utilisant la methode spectrale et la methode de l’element de reference », Proceeding of JCMM’s conference, p. 29-31, France, Mars 2006.
[17] Mosig. J.R and Gardiol. F, "Techniques analytiques et numériques dans l’analyse des antennes microruban", annt.Telecommun, 40, N° 7-8,pp 411-437, 1985.

Effect of large transverse curvature in high-frequency diffraction

Ivan Andronov[1*], **Daniel Bouche**[2]

[1]University of St.Petersburg, Russia
[2]CEA/DAM, France
*corresponding author, E-mail: ivandronov@gmail.com

Abstract

High-frequency plane wave diffraction by strongly elongated bodies is considered. As well known at very high frequencies the field on the surface is given by Fock asymptotics. A similar approximation is derived for less high frequencies when the effect of large transverse curvature is essential. Both in the case of positive and in the case of negative transverse curvatures the attenuation of diffracted electromagnetic field in penumbra becomes smaller.

1. Introduction

Some problems of high-frequency diffraction remain difficult for numerical computation and the use of asymptotic methods is still actual. One of such problems is diffraction by strongly elongated bodies. It was noted that for on-axial incidence the field in the penumbra attenuates less quickly than described by V.A.Fock asymptotics [1]. In [2, 3] it was shown that, the reason for that less quick attenuation is in the large transverse curvature of the surface which influences the diffraction process via the parameter

$$\chi = k\rho_t^{3/2}\rho^{-1/2}, \tag{1}$$

where k is the wave number, ρ is the radius of curvature in longitudinal direction and ρ_t is the radius of transverse curvature. In the case of spheroid the parameter χ is constant and can be expressed via the semi-axes: small – a and large – b as

$$\chi = \frac{ka^2}{b}. \tag{2}$$

The asymptotic procedure developed in [3] in the supposition $k\rho \gg 1$, $\chi = O(1)$ results in the following leading order approximation for the induced current on spheroidal surface

$$J = e^{ikz} A\left(\frac{z}{b}, \chi\right) \sin\varphi, \tag{3}$$

where special function $A(\eta,\chi)$ is given by the integral

$$A(\eta,\chi) = \frac{2e^{-i\pi/4}}{\pi} \frac{e^{-i\chi\eta/2}}{\sqrt{\chi}\sqrt{1-\eta^2}} \int\limits_{-i\infty}^{+i\infty} \left(\frac{1-\eta}{1+\eta}\right)^{\mu} \times$$
$$\times \frac{\Gamma(1/2+\mu)\, W_{\mu,1}(-i\chi)}{W_{\mu,0}(-i\chi)\dot{W}_{\mu,1}(-i\chi) + \dot{W}_{\mu,0}(-i\chi)W_{\mu,1}(-i\chi)} d\mu \tag{4}$$

involving Whittaker functions $W_{\mu,\ell}$.

As shown in [4] for $\chi \to \infty$ formula (3) reduces to V.A.Fock asymptotics and in this sense is uniform with respect to transverse curvature.

The correctness of the asymptotics (3) is also check by comparison with test results computed by finite elements method by M.Duruflé (University of Bordeaux) [5].

2. The case of negative transverse curvature

In this paper in a similar manner we derive the asymptotic formula for the field excited by an incident plane wave on the surface which is convex in the direction of the incident wave and is concave in the transverse cross-section. We assume that the body possesses the symmetry of revolution and the incident wave runs along its axis (see fig. 1). In a vicinity of light-shadow boundary the surface can be approximated by one-sheeted hyperboloid and its deviation from that hyperboloid can be accounted for with the next order terms of the asymptotics, which however we do not derive in this paper.

The surface of hyperboloid is infinite, however we consider it only locally and exclude effects of multiple reflections.

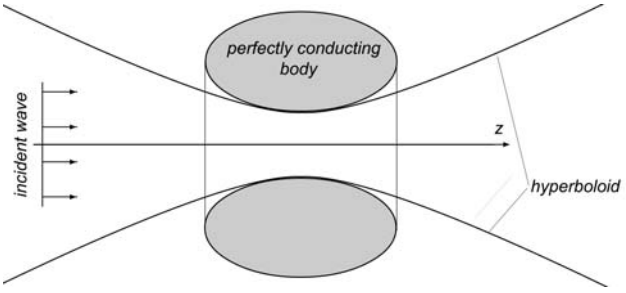


Figure 1: diffraction by a body with negative transverse curvature.

2.1. Coordinate system

Let us introduce the one-sheeted hyperboloid, which has the same radii of curvature at the light-shadow boundary as the surface under consideration. The semiaxes (small a and large b) of that hyperboloid are defined by the formulae

$$\rho = \frac{b^2}{a}, \qquad \rho_t = a. \tag{5}$$

Here ρ is the radius of curvature of the body in longitudinal cross-section on the light-shadow boundary and ρ_t is its radius of curvature in transverse cross-section.

We introduce hyperboloidal coordinates (ξ, η, φ)

$$z = p\xi\eta, \quad r = p\sqrt{1-\xi^2}\sqrt{1+\eta^2}, \quad p = \sqrt{b^2-a^2}, \tag{6}$$

where (r, φ, z) are cylindrical coordinates with the z axis coincident with the axis of the hyperboloid, and $z = 0$ on the light-shadow boundary. Coordinate ξ takes values $\xi \leq 1$, coordinate η varies from minus infinity to plus infinity.

The surface of the hyperboloid is given by the formula

$$\xi = const = \xi_0. \tag{7}$$

Taking into account that $a \ll b$, we get in the leading order

$$p = \frac{\rho}{m}\sqrt{\frac{\kappa}{2}}, \qquad \xi_0 = 1 - \frac{\kappa}{4m^2}, \tag{8}$$

where m is the usual asymptotic parameter [1]

$$m = \left(\frac{k\rho}{2}\right)^{1/3} \tag{9}$$

and

$$\kappa = 2m^2\frac{\rho_t}{\rho}. \tag{10}$$

We shall characterize the rate of elongation by the parameter $\chi \equiv \kappa^{3/2}2^{-1/2}$.

2.2. Maxwell equations

Maxwell equations

$$\begin{cases} \text{rot } \mathbf{E} = ik\mathbf{H}, \\ \text{rot } \mathbf{H} = -ik\mathbf{E} \end{cases} \tag{11}$$

in hyperboloidal coordinates take the form

$$\frac{\partial}{\partial\xi}h_\varphi E_\varphi - \frac{\partial}{\partial\varphi}h_\xi E_\xi = -ikh_\xi h_\varphi H_\eta, \tag{12}$$

$$\frac{\partial}{\partial\varphi}h_\eta E_\eta - \frac{\partial}{\partial\eta}h_\varphi E_\varphi = -ikh_\varphi h_\eta H_\xi, \tag{13}$$

$$\frac{\partial}{\partial\eta}h_\xi E_\xi - \frac{\partial}{\partial\xi}h_\eta E_\eta = -ikh_\eta h_\xi H_\varphi, \tag{14}$$

$$\frac{\partial}{\partial\xi}h_\varphi H_\varphi - \frac{\partial}{\partial\varphi}h_\xi H_\xi = ikh_\xi h_\varphi E_\eta, \tag{15}$$

$$\frac{\partial}{\partial\varphi}h_\eta H_\eta - \frac{\partial}{\partial\eta}h_\varphi H_\varphi = ikh_\varphi h_\eta E_\xi, \tag{16}$$

$$\frac{\partial}{\partial\eta}h_\xi H_\xi - \frac{\partial}{\partial\xi}h_\eta H_\eta = ikh_\eta h_\xi E_\varphi, \tag{17}$$

where h_ξ, h_η and h_φ are metric coefficients given by the formulae [6]

$$h_\xi = p\sqrt{\frac{\xi^2+\eta^2}{1-\xi^2}}, \quad h_\eta = p\sqrt{\frac{\xi^2+\eta^2}{1+\eta^2}}, \quad h_\varphi = p\sqrt{1-\xi^2}\sqrt{1+\eta^2}. \tag{18}$$

Assuming that the field dependence on the angle φ is given by the multiplier $e^{i\ell\varphi}$, from equations (12), (13), (15) and (16) we express E_ξ, E_η, H_ξ and H_η via E_φ and H_φ. Substituting these expressions into equations (14) and (17) yields the system of differential equations for E_φ and H_φ. We exploit now the symmetry of these two equations. By setting

$$E_\varphi = \widehat{P} + \widehat{Q}, \qquad H\varphi = -i\widehat{P} + i\widehat{Q}, \tag{19}$$

this system is reduced to two independent equations. We do not present here these very cumbersome equations.

2.3. Stretched coordinate and variables separation

Further we perform scaling of coordinate ξ and introduce new normal coordinate ν by the formula

$$\xi = 1 - \frac{\kappa}{4m^2}\nu. \tag{20}$$

Note that on the surface $\nu = 1$ and on the axis of hyperboloid $\nu = 0$.

Following the usual asymptotic procedure of Parabolic equation method [1] we extract the quick oscillating factor

$$\hat{P} = \exp(ikp\eta)P(\eta,\nu), \quad \hat{Q} = \exp(ikp\eta)Q(\eta,\nu) \tag{21}$$

and represent functions P and Q in the form of the series

$$P = \sum_{j=0} P_j m^{-j}, \qquad Q = \sum_{j=0} Q_j m^{-j}. \tag{22}$$

Sorting the terms in the equations for P and Q by the powers of the large parameter m, we get a recurrent system of equations for P_j and Q_j. In the leading order the equations are

$$\mathcal{L}_{1-\ell}\, P_0 = 0, \qquad \mathcal{L}_{1+\ell}\, Q_0 = 0, \tag{23}$$

where

$$\mathcal{L}_n = \nu\frac{\partial^2}{\partial\nu^2} + \frac{\partial}{\partial\nu} + \frac{i}{2}\chi(\eta^2+1)\frac{\partial}{\partial\eta} + \left(\frac{i}{4}\chi\eta - \frac{\chi^2\nu}{4} - \frac{n^2}{4\nu}\right). \tag{24}$$

Equations (23) allow variables separation. A particular solution of equation $\mathcal{L}_n U_n = 0$ can be written in the form of an integral by variables separation parameter μ in the form

$$U_n = U_n(\Omega, F) = \frac{1}{\sqrt{\chi\nu}\sqrt{1+\eta^2}}\times \times \int \Omega(\mu)e^{2\mu\,\arctan(\eta)}F_{i\mu,\,n/2}(\chi\nu)d\mu, \tag{25}$$

where Ω is arbitrary function and $F_{m,\,n/2}(x)$ is a solution of Whittaker equation [7]

$$\frac{d^2F}{dx^2} + \left(-\frac{1}{4} + \frac{m}{x} + \frac{1-n^2}{4x^2}\right)F = 0. \tag{26}$$

We shall choose appropriate solutions among Whittaker functions $M_{m,n/2}(x)$, $W_{m,n/2}(x)$, $M_{-m,n/2}(-x)$ and $W_{-m,n/2}(-x)$.

Electromagnetic field in the problem can be represented as the sum of the incident wave and some wave reflected from the surface. In the representation (25) for the incident wave which is regular at the axis of revolution, we can choose functions $M_{i\mu,n/2}(\chi\nu)$ or $M_{-i\mu,n/2}(-\chi\nu)$ which are regular at $\nu = 0$. The reflected wave is subject to radiation condition. So, when writing the representation (25) for the reflected wave we need to choose such solution of Whittaker equation which corresponds to waves propagating away from the surface. This wave is incoming in terms of coordinate ν. The domain of large ν is behind the boundary of hyperboloid, however the type of wave does not depend on the presence of the boundary, and we analyze it at $\nu >> 1$ with the use of the asymptotics [8]

$$W_{\beta,m}(x) \sim x^{\beta} e^{-x/2}, \qquad |x| \to \infty. \tag{27}$$

This chooses the solution $W_{-i\mu,\, n/2}\,(-\alpha\nu)$.

2.4. Incident and reflected fields

Let us find the representation (25) for the incident wave. We assume that locally it is a plane wave

$$\mathbf{E}^{(i)} = e^{ikz}\mathbf{e}_x, \qquad \mathbf{H}^{(i)} = e^{ikz}\mathbf{e}_y, \tag{28}$$

where $\mathbf{e}_x$ are $\mathbf{e}_y$ are unit vectors in Descartes coordinate system. In the hyperboloidal coordinate system this wave has the components

$$E_{\varphi}^{(i)} = e^{ikp\xi\eta}\cos\varphi, \qquad H_{\varphi}^{(i)} = e^{ikp\xi\eta}\sin\varphi \tag{29}$$

and for functions P, Q we get

$$P_0^{(i)} = \frac{1}{2}\exp\left(i\varphi - \frac{i}{2}\chi\nu\eta\right), \tag{30}$$

$$Q_0^{(i)} = \frac{1}{2}\exp\left(-i\varphi - \frac{i}{2}\chi\nu\eta\right). \tag{31}$$

Function $P_0^{(i)}$ satisfies the first parabolic equation in (23) with $\ell = 1$ and $Q_0^{(i)}$ satisfies the second parabolic equation with $\ell = -1$. The representations for both $P_0^{(i)}$ and $Q_0^{(i)}$ follow from the identity

$$\frac{\exp\left(\frac{i}{2}x\eta\right)}{\sqrt{x}\sqrt{1+\eta^2}} \int\limits_{-\infty}^{+\infty} e^{2\mu\arctan(\eta)} \frac{M_{-i\mu,0}(-x)}{\cosh(\pi\mu)} d\mu \equiv i \tag{32}$$

derived in [9]. We get

$$\begin{array}{l} P_0^{(i)} = e^{i\varphi} U_0(\Omega, M_{-i\mu,0}(-\chi\nu)), \\ Q_0^{(i)} = e^{-i\varphi} U_0(\Omega, M_{-i\mu,0}(-\chi\nu)) \end{array} \tag{33}$$

with

$$\Omega^{(i)} = \frac{-i}{\sqrt{\alpha}\cosh(\pi\mu)}. \tag{34}$$

Formulae (33) allows the total field of diffraction to be written in the form

$$E_{\varphi} = \frac{-ie^{ikp\eta}\cos(\varphi)}{\sqrt{\chi\nu}\sqrt{1+\eta^2}} \int\limits_{-\infty}^{+\infty} \frac{e^{2\mu\arctan(\eta)}}{\cosh(\pi\mu)} \Big(M_{-i\mu,0}(-\chi\nu) + \omega_0(\mu) W_{-i\mu,0}(-\chi\nu) + \omega_1(\mu) W_{-i\mu,1}(-\chi\nu) \Big) d\mu, \tag{35}$$

$$H_{\varphi} = \frac{-ie^{ikp\eta}\sin(\varphi)}{\sqrt{\chi\nu}\sqrt{1+\eta^2}} \int\limits_{-\infty}^{+\infty} \frac{e^{2\mu\arctan(\eta)}}{\cosh(\pi\mu)} \Big(M_{-i\mu,0}(-\chi\nu) + \omega_0(\mu) W_{-i\mu,0}(-\chi\nu) - \omega_1(\mu) W_{-i\mu,1}(-\chi\nu) \Big) d\mu. \tag{36}$$

Here we have taken into account the made above choice of particular solution $W_{-i\mu,n/2}(-\chi\nu)$ of Whittaker equation which corresponds to waves going away from the surface. Functions ω_0 and ω_1 should be taken such that the field satisfies the boundary conditions on the surface.

A special question is in the appropriate choice of the integration path. Namely, when using the representation for the incident plane wave, the path of integration can be deformed in the finite domain almost arbitrarily. The only restriction is that when performing such a deformation we can not cross the poles at semi-integer imaginary points. As it will be seen below the functions ω_0 and ω_1 have poles. This gives some additional restrictions on the possible deformations of the integration path. That is dependently on the deformation of the integration path in the representation of the incident wave we shall include or exclude contributions of poles presented in functions ω_0 and ω_1. We shall examine that poles below and choose the integration path. At this section we only fix the ends of the contour that starts from $-\infty$ and ends at $+\infty$.

2.5. Boundary conditions

The boundary conditions on a perfectly conducting surface of hyperboloid have the form

$$E_{\varphi}(\eta, 1) = 0 \tag{37}$$

and

$$E_{\eta}(\eta, 1) = 0. \tag{38}$$

With the help of the formula expressing E_{η} via E_{φ} and H_{φ} and accounting for (37) the second condition yields

$$2\frac{\partial H_{\varphi}(\eta, 1)}{\partial \nu} + H_{\varphi}(\eta, 1) = 0. \tag{39}$$

Substituting representations (35) and (36) into the conditions (37) and (39) we get the system of algebraic equations for the amplitude functions ω_0 and ω_1

$$\left\{ \begin{array}{l} \omega_0 W_{-i\mu,0}(-\chi) + \omega_1 W_{-i\mu,1}(-\chi) = -M_{-i\mu,0}(-\chi), \\ \omega_0 \dot{W}_{-i\mu,0}(-\chi) - \omega_1 \dot{W}_{-i\mu,1}(-\chi) = -\dot{M}_{-i\mu,0}(-\chi). \end{array} \right. \tag{40}$$

Here and below, dot denotes derivative of a function.

Table 1: Zeros of the denominator.

χ	μ_0	μ_1	μ_2	μ_3	μ_4
0.1	1.550622 + 0.393790 i	-0.000895 + 0.511917 i	-0.062846 + 1.356437 i	-0.074132 + 1.632544 i	-0.154036 + 2.295688 i
0.5	0.129071 - 0.056480 i	-0.186936 + 0.594482 i	-0.381803 + 1.154738 i	-0.461135 + 1.647171 i	-0.599989 + 2.148862 i
1.0	-0.120641 - 0.180254 i	-0.390031 + 0.517184 i	-0.616925 + 1.030631 i	-0.731991 + 1.547721 i	-0.897053 + 2.042077 i
2.0	-0.333362 - 0.373716 i	-0.643920 + 0.311608 i	-0.925053 + 0.814817 i	-1.096494 + 1.338831 i	-1.296782 + 1.835297 i
3.0	-0.448176 - 0.568983 i	-0.825406 + 0.098262 i	-1.148691 + 0.604578 i	-1.366097 + 1.130667 i	-1.595123 + 1.628809 i
5.0	-0.582388 - 0.984233 i	-1.095406 - 0.328612 i	-1.486433 + 0.184338 i	-1.777583 + 0.714907 i	-2.056523 + 1.215151 i

Solving this system we find

$$\omega_0 = -\frac{1}{Z}\Big(M_{-i\mu,0}(-\chi)\dot{W}_{-i\mu,1}(-\chi) + \dot{M}_{-i\mu,0}(-\chi)W_{-i\mu,1}(-\chi)\Big), \quad (41)$$

$$\omega_1 = \frac{1}{Z}\Big(\dot{M}_{-i\mu,0}(-\chi)W_{-i\mu,0}(-\chi) - M_{-i\mu,0}(-\chi)\dot{W}_{-i\mu,0}(-\chi)\Big), \quad (42)$$

where

$$Z = W_{-i\mu,0}(-\chi)\dot{W}_{-i\mu,1}(-\chi) + \dot{W}_{-i\mu,0}(-\chi)W_{-i\mu,1}(-\chi). \quad (43)$$

2.6. Induced current

Substituting these expressions into representation (36) and setting $\nu = 1$, we can find the current on the surface. To simplify the formula we use the expression for the Wronskian

$$\dot{M}_{\beta,0}(z)W_{\beta,0}(z) - M_{\beta,0}(z)\dot{W}_{\beta,0}(z) = \frac{1}{\Gamma(1/2-\beta)}, \quad (44)$$

which follows from formulae *13.1.22, 13.1.32* and *13.1.33* of [7], and exploit the symmetry property of Gamma function. The final formula for the induced current can be written as

$$J = e^{ikz}B\left(\frac{z}{b},\chi\right)\sin\varphi, \quad (45)$$

where

$$B(\eta,\chi) = \frac{2i}{\pi}\frac{e^{i\chi\eta/2}}{\sqrt{\chi}\sqrt{1+\eta^2}}\int\limits_{-\infty}^{+\infty} e^{2\mu\,\mathrm{arctan}(\eta)}\times \times \frac{W_{-i\mu,1}(-\chi)}{Z}\Gamma\left(\frac{1}{2}+i\mu\right)d\mu. \quad (46)$$

It is worth discussing the choice of the path of integration in (46). The subintegral expression has poles and values of the integral computed along different paths may differ in the contributions of the residues in that poles. Each of such residues corresponds to a creeping wave that propagates along the surface, and the only rigorous way to find out which waves should be included in the diffraction field is to match the asymptotics of the special function B for large negative η with the incident field. However this is not an easy question because on one hand letting $\eta \to -\infty$ yields no significant simplifications in the integral representation and we use numerical matching. On the other hand, the one-sheeted hyperboloid presents a kind of wave-guide with slowly varying cross-section and the incident field can be represented as a sum of modes or as a complicated combination of ray contributions undergoing multiple reflections from the walls. However we want to exclude these multiple reflections and expect the absolute value of the induced current to be close to 2 in the illuminated region.

There are also some non-rigorous speculations giving a hint on the choice of the integration path. The path of integration should not depend on frequency. While the elongation parameter χ depends on frequency, and the poles as shown below depend on χ, the path of integration should be chosen such that the poles do not cross it when χ varies from very small to very large values (almost from zero to infinity). One set of poles is associated with the gamma function. These poles are at points $\mu = i\left(\frac{1}{2}+n\right)$, $n = 0, 1, 2, \ldots$ The other poles are at zeros of the denominator Z, and need to be examined. For every fixed value of elongation parameter χ there is an infinite series of zeros μ_s, $s = 0, 1, 2, \ldots$ (see table 1, where we present 5 zeros with the minimal imaginary parts for different values of the elongation parameter). All zeros except μ_0 have negative real part for any value of the elongation parameter χ. When χ tends to zero, that is when the surface becomes extremely elongated these zeros approach the poles of the Gamma function in semi-integer points on the imaginary axis of μ. The zero μ_0 with the smallest imaginary part behaves as a function of χ in a different way. When χ is greater than $\chi_0 \approx 0.700777$ its real part is negative, but for more elongated surfaces this poles shifts to the right half-plane of μ and its real part grows to infinity when $\chi \to 0$. The residues in all the poles $\mu_1, \mu_2, \ldots$represent functions which decrease with $\eta \to +\infty$. The residue in the pole μ_0 decreases with η only if $\chi < \chi_0$. When the body is more elongated, $\chi > \chi_0$, the contribution of the residue in μ_0 grows with η, however remains bounded.

Basing on numerical experiments (see the next section, where we check that $|B| \to 2$ when $\eta \to -\infty$) we choose the path of integration in (46) such that it avoids zeros of the denominator from below.

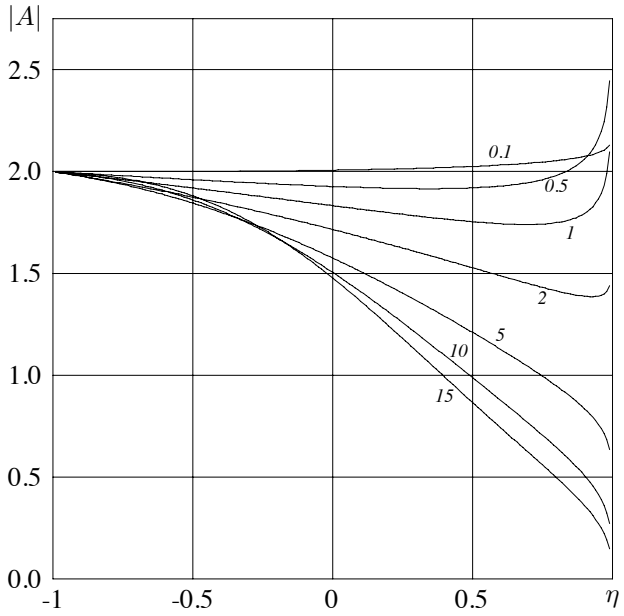


Figure 2: Amplitudes of induced currents on spheroids with $\chi = 0.1, 0.5, 1, 2, 5, 10$ and 15.

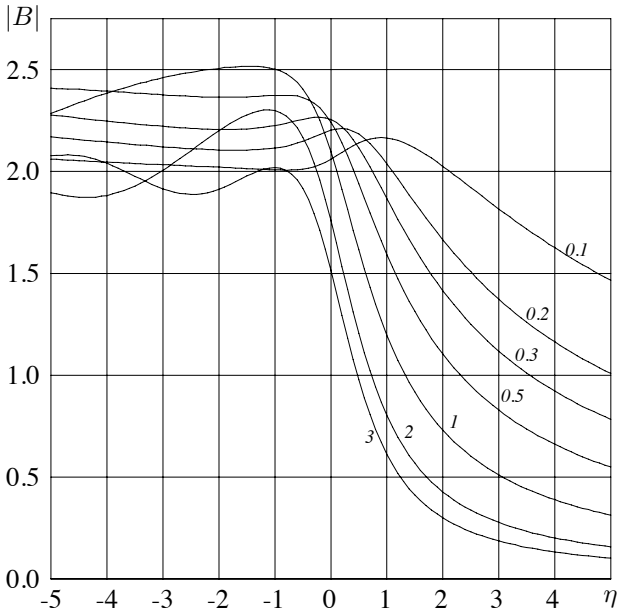


Figure 3: Amplitudes of induced currents on hyperboloids with $\chi = 0.1, 0.2, 0.3, 0.5, 1, 2$ and 3.

3. Numerical results

We present results of computations of functions A from (3) and B from (45). The integrals in (4) and (46) rapidly converge and the only difficulty is in the computation of Whittaker functions. This is done with the help of the code developed in [10] for the computation of Coulomb wave functions. Using the relations between Whittaker and Coulomb wave functions one can rewrite the integral representations (4) and (46) as

$$A(\eta,\chi) = \frac{4}{\sqrt{\pi}} \frac{e^{-i\chi\eta/2}}{\sqrt{\chi}\sqrt{1-\eta^2}} \int_{-\infty}^{+\infty} \left(\frac{1+\eta}{1-\eta}\right)^{i\mu} \times$$
$$\times H^+_{1/2}\left(\mu,\tfrac{\chi}{2}\right) \left\{ H^+_{1/2}\left(\mu,\tfrac{\chi}{2}\right) \dot{H}^+_{-1/2}\left(\mu,\tfrac{\chi}{2}\right) \right.$$
$$\left. + \dot{H}^+_{1/2}\left(\mu,\tfrac{\chi}{2}\right) H^+_{-1/2}\left(\mu,\tfrac{\chi}{2}\right) \right\}^{-1} \frac{e^{\pi\mu/2}}{\sqrt{\cosh(\pi\mu)}} d\mu \quad (47)$$

and

$$B(\eta,\chi) = \frac{4e^{i\pi/4}}{\sqrt{\pi}} \frac{e^{i\chi\eta/2}}{\sqrt{\chi}\sqrt{1+\eta^2}} \int_{-\infty}^{+\infty} e^{2\mu \arctan(\eta)} \times$$
$$\times H^-_{1/2}\left(-\mu, i\tfrac{\chi}{2}\right) \left\{ H^-_{1/2}\left(-\mu, i\tfrac{\chi}{2}\right) \dot{H}^-_{-1/2}\left(-\mu, i\tfrac{\chi}{2}\right) \right.$$
$$\left. + \dot{H}^-_{1/2}\left(-\mu, i\tfrac{\chi}{2}\right) H^-_{-1/2}\left(-\mu, i\tfrac{\chi}{2}\right) \right\}^{-1} \times$$
$$\times \frac{e^{-\pi\mu/2}}{\sqrt{\cosh(\pi\mu)}}\, d\mu. \quad (48)$$

Absolute values of special functions A and B from the asymptotics (3) and (45) are presented on figs. 2 and 3.

These figures show that the induced currents both on spheroids and on hyperboloids decrease along the surface less quicker the smaller the elongation parameter χ. The growth of current amplitude shown on fig. 2 in a vicinity of shadowed end of spheroids for $\chi \geq 2$ can be explained by the effect of focusing. However the asymptotic expansion (3) does treat this effect in a proper way. So, this effect may be artificially introduced by neglecting smaller order terms in the asymptotics.

Figure 3 shows that the induced currents have a maximum near the light-shadow boundary. When the body is not too strongly elongated this maximum is in the illuminated domain. However when the elongation increases (parameter χ decreases) the maximum shifts to the domain of geometrical shadow.

To justify the choice of the integration path we present on fig. 4 the absolute value of the function B with excluded contribution of the residue in the pole μ_0. We see that for negative η the absolute values of function B vary and do not approach to the expected value of 2 (compare with much better matching on fig. 3).

4. Conclusion

We have considered problems of diffraction by strongly elongated spheroid-like bodies and by strongly elongated hyperboloid-like bodies. In both cases the ratio of curvatures of the surface in longitudinal and in transverse cross-section was assumed asymptotically large. In the case of a spheroid-like body the transverse curvature is positive and in the case of a hyperboloid-like body it is negative. The asymptotic formula that describes induced currents on large strongly elongated spheroid was derived in previous papers and was shown to give very accurate approximation. In this paper we have presented asymptotic formula for the induced currents on large strongly elongated hyperboloid-

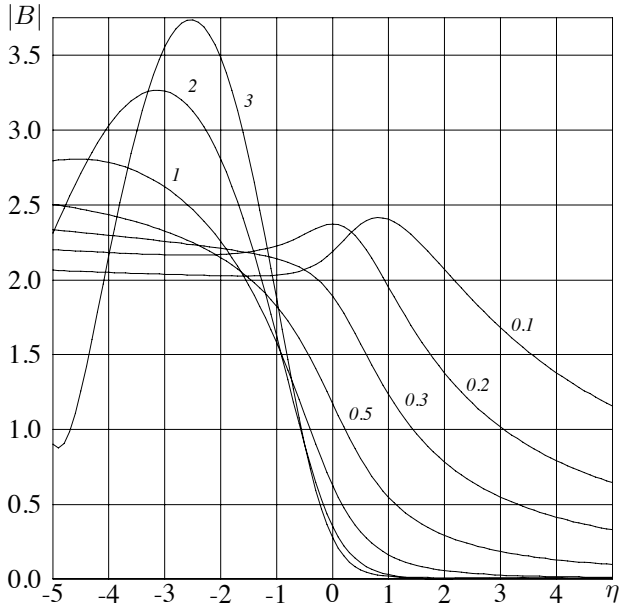


Figure 4: Induced current with excluded contribution of the creeping wave corresponding to the pole μ_0.

like surface. Computations according to that formulae show that both in the cases of positive and negative transverse curvatures attenuation becomes smaller when the surface becomes more elongated.

In the case of hyperboloid-like surface we have excluded contributions of multiply reflected rays. However these rays are never tangent to the surface of one-sheeted hyperboloid and therefore their field can be well described by ray method asymptotics.

Acknowledgement

The research of the first author is supported by CEA/DAM contract.

References

[1] V.A. Fock, Diffraction of radio-waves around the Earth's surface, *Journ. of Phys. of the U.S.S.R* 9: 255, 1945.

[2] I.V. Andronov, High-frequency asymptotics for diffraction by a strongly elongated body", *IEEE Antennas Wireless Propag. Lett.* 8: 872, 2009.

[3] I.V. Andronov, High frequency asymptotics of electromagnetic field on a strongly elongated spheroid, *PIERS Online* 5: 536–540, 2009.

[4] I.V. Andronov, Diffraction of a high-frequency electromagnetic wave by an elongated body of revolution, *J. of Communications Technology and Electronics* 56: 1317–1323, 2011.

[5] I.V. Andronov, D. Bouche, Forward and backward waves in high-frequency diffraction by an elongated spheroid, *Progress in Electromagnetics Research B* 29: 209–231. 2011.

[6] G.A. Korn, T.M. Korn, *Mathematical handbook for scientists and engineers,* McGraw-Hill, New York Toronto London, 1961.

[7] M.Abramowitz, I.Stegun, *Handbook of mathematical functions*, National Bureau of Standards, New York, 1964.

[8] I.S. Gradshtein, I.M. Ryzhik, *Table of Integrals, Series and Products,* Academic, New York, 1980.

[9] I.V. Andronov, Calculation of Diffraction by Strongly Elongated Bodies of Revolution, *Acoustical Physics* 58: 22–29, 2012.

[10] I.J. Thompson, A.R. Barnett, COULCC: A continued-fraction algorithm for Coulomb functions of complex order with complex arguments, *Comput. Phys. Commun.* 36: 363–372, 1985.

Analysis of Electromagnetic Scattering by a Composite Cylinders using WCIP Method

J. Selmi [1*], R. Bedira [1], A.Gharsallah[1] and H.Baudrand[2]

[1] Laboratoire de physique de la Matière Molle et Modélisation Electromagnétique, Faculté des Sciences de Tunis, 2092 ElManar, Tunisia

[2] Laboratoire LAPLACE, 2 Rue Camichel 31071 Toulouse France

Abstract

In this work, the Wave Concept Iterative Process (WCIP) has been applied to analyse the electromagnetic scattering problems conductor bodies and covered metallic arbitrary shapes, showing its accuracy and fast convergence. Numerical results illustrate the scattering current density and Radar Cross Section (RCS) for different structures.

1. Introduction

The electromagnetic scattering problems by metallic and covered objects of arbitrary shape placed in free space are of great scientific interest in the engineering applications, in telecommunications and others. In this work, a method called Wave Concept Iterative Process (WCIP) combined with a coordinate transformation has been extended to analyse electromagnetic scattering problems by arbitrary metallic shapes and composite bodies. The Wave Concept Iterative method was firstly presented and applied to analyse microwaves circuits [1].Then, it was successfully applied to reach various diffraction and scattering problems by conductor bodies [2]. Later the WCIP has been carried out to resolve the electromagnetic scattering by a conducting object coated by a thin dielectric layer [3.4].

This paper presents the Wave Concept Iterative method in order to analyse the electromagnetic scattering by a target covered by a dielectric material.

The Radar Cross Section (RCS) is reached for composite body and compared with metallic ones. To resolve this type of problem, surfaces can be divided in the small cells, theses cells can be placed on fictitious circular cylinder, so the electromagnetic problem in the cylindrical coordinates system can be resolved.

The covered metallic arbitrary shapes are used to approximately model several real structures, such as aircraft, fuse large and other cylindrical bodies [5-7]. This kind of structures has been analyzed widely with many numerical methods such as the Moment Method (MOM) [8] and the Finite Element Method (FEM) [9].

2. The Wave Concept Iterative Process (WCIP)

2.1 Concept of Waves

Consider an arbitrary shaped object bounded by surface S, and let $\vec{\mathbf{n}}$ denote the normal vector to the surface in each point as presented in Figure1.

The principle of the WCIP is the expressions of boundary and closing conditions in terms of waves, incident $\vec{\mathbf{A}}$ and reflected $\vec{\mathbf{B}}$, a system of equations relates both the incident and reflected waves is deduced from these conditions. This system is resolved by an iterative process. The resolution is achieved when a good precision is reached on the required value.

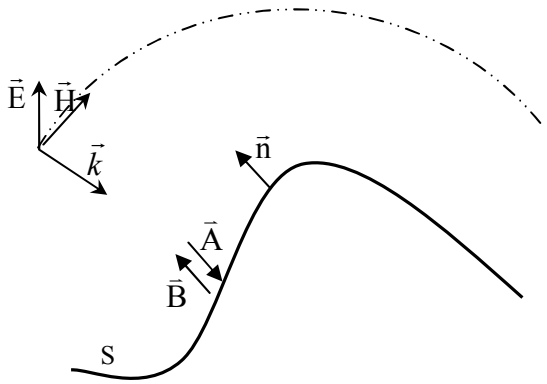


Figure 1: The scattering surface

$$\vec{\mathbf{A}} = \frac{1}{2\sqrt{\mathbf{Z_0}}}\left(\vec{\mathbf{E}} + \mathbf{Z_0}\left(\vec{\mathbf{H}} \wedge \vec{\mathbf{n}}\right)\right) \quad (1a)$$

$$\vec{B} = \frac{1}{2\sqrt{Z_0}}\left(\vec{E} - Z_0\left(\vec{H} \wedge \vec{n}\right)\right) \quad (1b)$$

with $\mathbf{Z_0}$ is an arbitrary impedance parameter, chosen as the free space impedance.

$$Z_0 = \sqrt{\frac{\mu_0}{\varepsilon_0}} = 120\pi\Omega \qquad (2)$$

$\vec{E}$ and $\vec{H}$ are the tangential components of electric and magnetic fields, respectively, where $\vec{n}$ denoted the normal vector to the surface S defined in each cells.

2.2. The Iterative process

The primary electromagnetic fields $(\vec{E}_0, \vec{H}_0)$ are introduced in the spatial domain with the adjunction of $\vec{A}_0$, the relationship between the incident and reflected fields is expressed by the following equations:

$$\vec{A} = \hat{\Gamma}\vec{B} \qquad (3)$$

$$\vec{B} = R\vec{A} + \vec{B}_0 \qquad (4)$$

where:

- $\hat{\Gamma}$ Designates the scattering operator described in the spectral domain, associated to the geometry of the target and represents the media interaction on the waves [10].
- R is a reflected coefficient defined on the surface in the special domain. Its value is R=-1 in the surface metallic case.

The Fourier Transform (TF) and its inverse (TF^{-1}) insure the links between the two domains, figure 2 [11]

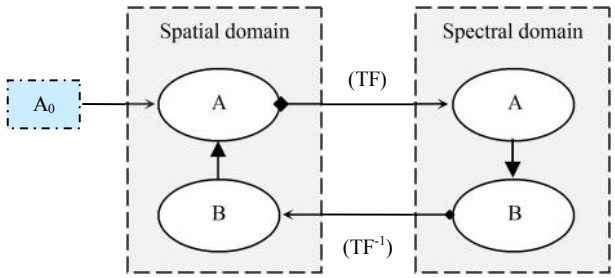


Figure 2: the iterative scheme

2.3. Scattering by a composite body

Let us consider a metallic surface Σ_2 coated by a thin dielectric material Σ_1 characterised by the relative permittivity $\varepsilon_r \neq 1$ figures 3.

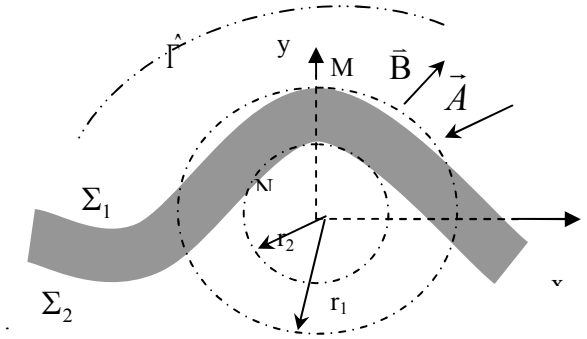


Figure.3: Dielectric layer coated metallic object

According to the interface conditions, the incident wave $\vec{A}$ is refracted by the first interface Σ_1 so the transmitted term $(T.\vec{A})$ reaches the second interface Σ_2 with a coefficient of attenuation e^{-jk_2h} and is reflected. Then, this wave returned on Σ_1 with the same term of the attenuation and after that it is refracted for the second time referring to this theory the iterative process explained in different media figure 4, and can be summarized by the following equations:

$$\begin{pmatrix} B_1 \\ B_2 \end{pmatrix}^{(P)} = \begin{pmatrix} R & T' \\ T & R' \end{pmatrix} \begin{pmatrix} \hat{\Gamma} & 0 \\ 0 & \Gamma_m \exp(-2jk_2h) \end{pmatrix} \times$$

$$\begin{pmatrix} B_1 \\ B_2 \end{pmatrix}^{(P-1)} + \begin{pmatrix} R & R \\ T & T \end{pmatrix} \begin{pmatrix} A_0 \\ B_0 \end{pmatrix} \qquad (5)$$

$\hat{\Gamma}$ and Γ_m are the scattering operator and the reflected coefficient defined on the metallic surface, respectively.

$$R = \frac{Z_2 - Z_1}{Z_2 + Z_1} \qquad (6)$$

$$R' = \frac{Z_1 - Z_2}{Z_2 + Z_1} \qquad (7)$$

$$T = \frac{2Z_2}{Z_2 + Z_1} \qquad (8)$$

$$T' = \frac{2Z_1}{Z_2 + Z_1} \qquad (9)$$

where Z_1 and Z_2 are the intrinsic impedances of the free space and the dielectric layer, respectively. Referring to equations (5), the concept of waves can be applied on the treated objects.

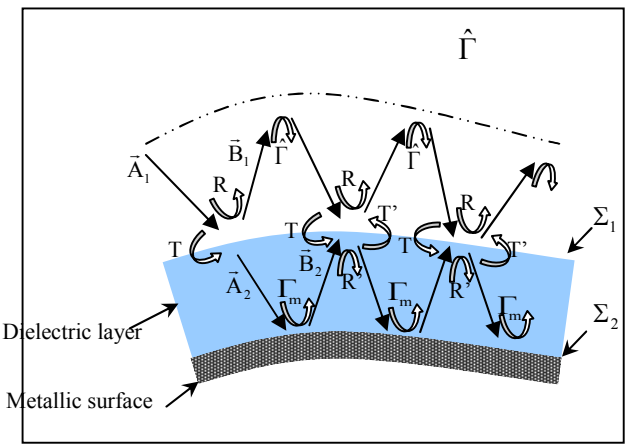


Figure 4: Iterative process on the dielectric layer

3. NUMERICAL RESULTS AND ILLUSTRATION

3.1. Square cylinder coated by dielectric mater

The geometry of the coated square conducting cylinder is shown in figure 5.

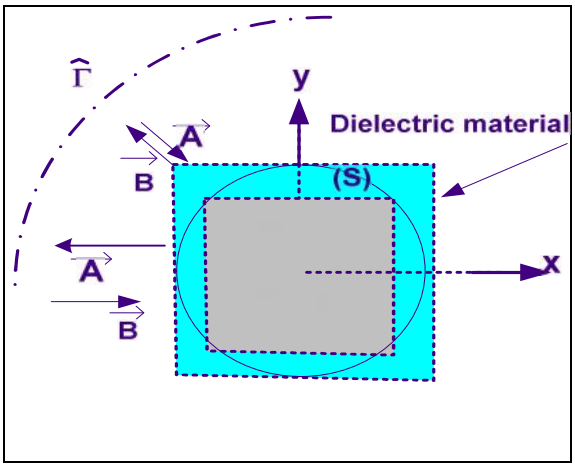


Figure 5: Square cylinder coated by dielectric materials

The Radar Cross Section (RCS) is calculated using the far-field transformation, defined by equation (10)[12]:

$$RCS = \lim_{\rho \to \infty} \left(2\pi\rho \frac{\left|E^{s}\right|^{2}}{\left|E^{i}\right|^{2}} \right) \quad (10)$$

Where the distance from the target to observation point is ρ, E^s and E^i are the scattering and the incident electric fields, respectively.

The following figure shows the evolution of the Radar Cross Section for a metallic square cylinder and coated one with dielectric layer.

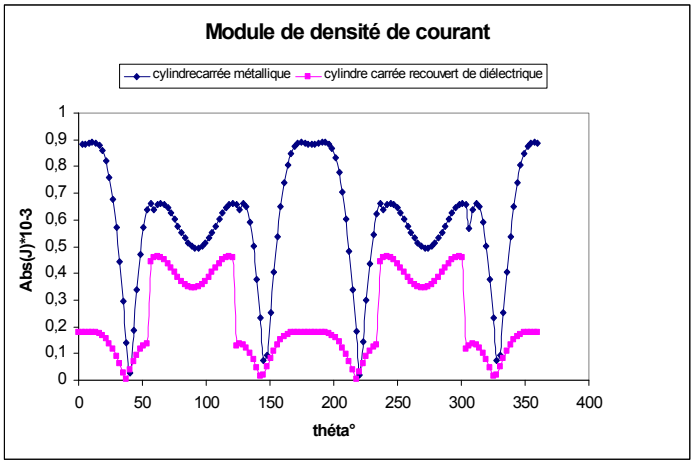


Figure6: The normalized current density of a metallic square cylinder and coated one.

When the cylinder is coated with dielectric material the density of radar cross section (RCS) is reduced, which improves the coating objects efficacy.

3.2. Super ellipsoid cylinder coated by dielectric materials

The structure is illustrated in the following figures. The super ellipsoid can be approximated by a rectangle cylinder [13]. In this case, the previous coordinate transformation and the iterative method are combined and applied to analyse scattering by surface treated targets [14].

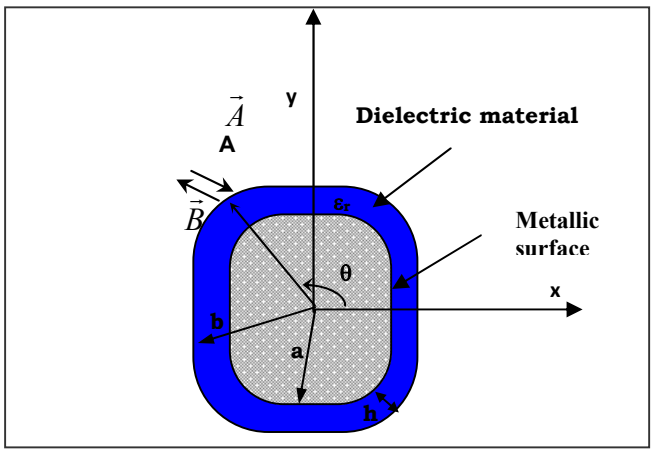


Figure 7: Super ellipsoid cylinder coated by dielectric materials

The following figure shows the evolution of the Radar Cross Section for a metallic super ellipsoid and coated one with dielectric layer.

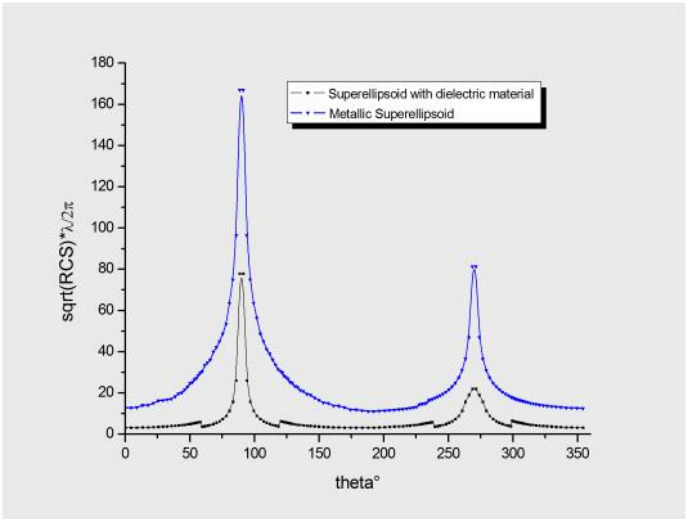


Figure.8: The evolution of RCS of a metallic super ellipsoid and a coated one.

The effect of dielectric materials coating super ellipsoid cylinder is shown in attenuation of the Radar Cross Section.

3.3. Metallic elliptic cylinder coated with dielectric materials

Let us assume an elliptic cylinder made of two layers, the inner one is bounded by the metallic cylinder Σ_2, while the external layer is formed by dielectric materials which permittivity is $\varepsilon = 2.8\varepsilon_0$ and permeability is $\mu = \mu_0$. The semi major and the semi minor axes of the metallic cylinder denoted by a and b, whereas the semi major and the semi minor axes of the external one are designated a_1 and b_1, figure9. The thickness of the dielectric layer is homogenous and denoting h, with, $a_1 = a + h$, $b_1 = b + h$ and $h = \frac{a}{100}$.

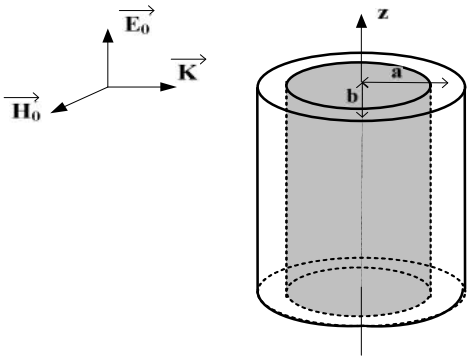


Figure 9: Elliptic section coated with dielectric materials

The WCIP leads to the scattering electric field and the current density at the surface in the side of the out space. The results are reported in figure 10, the Radar Cross Section of the elliptic cylinder coated with dielectric materials is represented and compared with metallic elliptic cylinder, and the effect of dielectric materials is shown in attenuation of the Radar Cross Section.

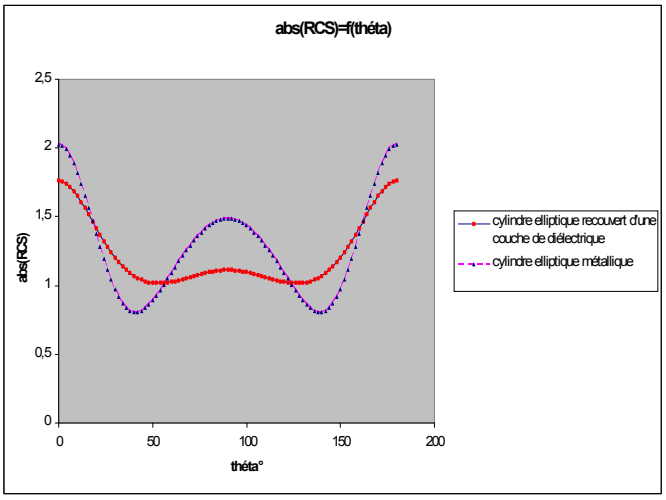


Figure10: The evolution of Radar Cross Section for a=2λ , b=0,5a a_1=a+h, b_1=b+h and h=a/100

The scattering structures are supposed invariants along the axial direction of the cylinders, as showing in figure9. The semi major axis of the ellipses remains constant $a = 2\lambda$, with λ is the wave length , and the semi minor axis is variable. Its value grows to reach the major one.

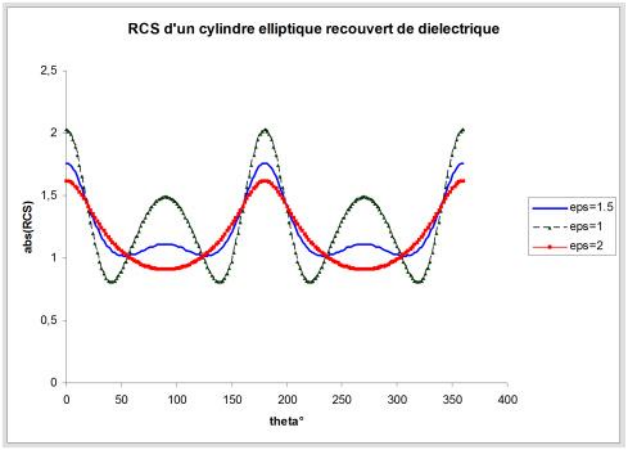


Figure11: The evolution of Radar Cross Section for different permittivity

The RCS by the ellipses, the situation is similar but there intensity increases when the value of the minor axis increases.

4. Conclusions

In the present work, the Wave Concept Iterative Process combined with geometry transformation has been extended to resolve the electromagnetic wave scattering problems by coated arbitrary shape cylinders with thin dielectric layer. The numerical results obtained here show the effect of size and the dielectric layer on the intensity of the Radar Cross Section RCS.

References

[1] R.S. N'Gongo and H. Baudrand, "Application of Wave Concept Iterative Procedure in Planar Circuits", Recent Res. Devel. Microwave Theory and Technique, vol.1, pp. 185-197, 1999.

[2] M.Azizi, H.Aubert and H.Baudrand, "A new Iterative Method for scattering problems", Proc of the Euro Microwave Conf, Bologna 1995, Vol.1, pp. 255-258.

[3] Mami, A. R. Bedira, A. Gharsallah, A. Gharbi and H. Baudrand, "Iterative Solution of Scattering by Surface-Treated Targets", Int. J RF and Microwave CAE, vol. 13, N°3, pp. 206-214, 2003.

[4] Bedira. R., A.Gharsallah, L.Desclos, AGharbi and H. Baudrand, "the Wave Concept Iterative Process: Scattering of a Conducting Target Coated by ThinDielectric Layer", IEEE Antennas and Propagation Society International Symposium, IEEE, vol. 2, pp. 98-101, 2002.

[5] A.-K. Hamid and F.R. Cooray, "Scattering by a Perfect

Electromagnetic Conducting Elliptic Cylinder", Progress in Electromagnetics Research Letters, vol.10, pp. 59-67, 2009.
[6] R. Ruppin, "Scattering of electromagnetic Radiation by a Perfect Electromagnetic conductor cylinder", Journal of Electromagnetic Waves and Applications, vol. 20, N° 13, pp.1853-1860, 2006.
[7] Xiang An and Zhi-Qing Lü, "A.Fast Algorithm Based on Practical Basic SolutionVectors Domain Decomposition Methode for Scattering Analysis of Electriclly Large Cylinders", Journal of Computational Physics, 219, pp. 930-942, 2006.
[8] RF.Harrington, "Field computation by moment methods" Mac.Millar. New York1968
[9] PP Silester and RL Ferrari. "Finite elements for energineering;" Combridge university press Cambridge U.K.1990.
[10] R.F. Harrington. "Time–harmonic electromagnetic fields". Mc Graw-Hill. New York. 1961.
[11] M. Yeddes, A. Gharsallah, A.Gharbi and H.Baudrand, "Characterization of Microstrip Ring with a Narrow Gap by an Iterative Method", International Journal of Microwave Science and Technology, 2008.
[12] C.A .Balanis, Advanced Engineering Electromagnetics, Wiley 1989.
[13] http://www.mathopenref.com/ellipse.html
[14] Selmi,J.R.Bedira, A.Ghasallah, A.Gharbi and H.Baudrand "Iterative Solution of electromagnetic scattering by arbitrary shaped cylinders" The Applied Computational Electromagnetic Society ACES, Vol 25, Number 7, 2010.

Effects of Quasi-Static Approximation of Green's Functions in the Model of a Horizontal Wire Conductor in Homogeneous Soil

Vesna Arnautovski-Toseva[1], Khalil El Khamlichi Drissi[1] and L. Grcev[2]

[1]Institute Pascal, Blaise Pascal University, Clermont Ferrand, France
[2]Faculty of Electrical Engineering and IT, Ss Cyril and Methodius University, Skopje, Macedonia
E-mail: Vesna.ARNAUTOVSKI@lasmea.univ-bpclermont.fr

Abstract

The paper presents two approximate quasi-static models of horizontal wire conductor buried in homogeneous lossy soil. The main objective is to analyze the approximation effects of image theory and complex image theory applied to simplify the Green's functions that arise in the rigorous electromagnetic (EM) model. A detailed study of the accuracy of the proposed two approximate models is given looking for possibilities to improve their consistency with respect to rigorous EM model.

1. Introduction

The electromagnetic analysis of horizontal wire-conductors buried in finitely conductive earth is often part of complex electromagnetic compatibility studies. Different strategies for modeling have been developed, ranging from transmission line theory to exact approach based on electromagnetic theory [1]. The last one is based on the electromagnetic theory and uses rigorous Sommerfeld formulation for the electric field due to elementary Hertz dipoles sources and thus represents the most accurate solution of the problem. This model involves numerical integration of appropriate Green's functions that take into account the influence of the air/soil half-spaces by rigorous Sommerfeld formulation [2]. However, such rigorous treatment in the electromagnetic model is very demanding in terms of both computer memory and time. For that reason approximate formulations have been intensively studied [3]–[7].

In this paper the authors investigate the effects of the proposed quasi-static approximations of the Green's functions related to the given problem. This study is based on the comparison of the current distribution along a center fed wire conductor buried in homogeneous lossy soil. The calculations are done in wide frequency range from 0.001 to 10 MHz. A detailed parametric analysis clearly illustrates the validity domain of the proposed approximations with respect to their practical applications.

2. Mathematical model

Consider x–directed horizontal conductor of radius a and length L placed at depth d in homogeneous lossy soil, as shown in Fig. 1. The central fed energization is assumed by a harmonic voltage generator V_S in frequency range from 1 kHz to 10 MHz, the time variation $e^{j\omega t}$ is assumed and suppressed. The air (medium "0") occupies the upper half-space ($z > 0$), whereas the soil (medium "1") occupies the lower half-space ($z < 0$). Both mediums are characterized by corresponding values of permeability μ_0 and permittivity ε_0 and $\varepsilon_1 = \varepsilon_0\varepsilon_r$ respectively. The conductivity of the soil is σ.

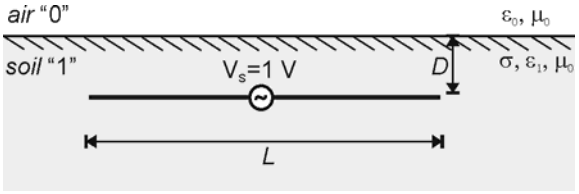


Figure 1: A center fed horizontal wire conductor in homogeneous lossy soil.

The rigorous EM model for a given problem is based on the Electric Field Mixed Potential Integral Equation (EF-MPIE) that is solved by the Method of Moments (MoM) using Galerkin formulation [8]. In due course, thin-wire conductor is divided into N+1 fictitious sections, as shown in Fig. 2.

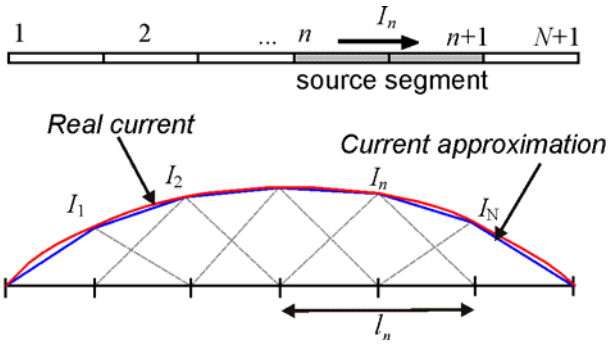


Figure 2: Approximation of the current with roof-top basis functions over two neighbor segments.

Next, the unknown current I is approximated by a sequence of expansion functions I_n ($n = 1, \ldots, N$) over two-neighbor sections thus forming a segment of length l_n. Here, we use roof-top expansion functions which results in a piecewise linear approximation of the current.

The boundary conditions regarding the tangential component of the electric field at the wire surface are satisfied approximately in an average (weighted) way. We choose the weighting functions to be the same roof-top functions. The current distribution is obtained by solving the well known matrix equation [9]

$$[Z]\cdot[I]=[V], \tag{1}$$

where the column matrix $[I]$ represents the unknown current samples, $[Z]$ is the generalized impedance matrix related to mutual impedances between segments, $[V]$ is the excitation matrix.

The elements of the impedance matrix denoted by z_{mn} represent self or mutual impedances between a pair of observation (m) and source (n) segment.

$$z_{mn}=\frac{V_{mn}}{I_n}=\frac{-1}{I_n}\int_{l_m} E_{nx}dl_m, \tag{2}$$

where E_{nx} is x–directed component of the electric field vector tangential to the surface of the observation segment m with length l_m due to filaments of current I_n and charge q_n along the axis of the source segment n. Here we use the following EF-MPIE [10, 11]

$$E_{nx}=-j\omega A_{nx}-\nabla V_n, \tag{3}$$

$$\begin{aligned} A_{nx}&=\int_{l_n} G_A^{xx} I_n dl_n \\ V_n&=\int_{l_n} G_V q_n dl_n \end{aligned}. \tag{4}$$

2.1. Exact formulation of the Green's functions

The rigorous EM model involves exact formulations for the Green's functions of the vector and scalar potentials. Here, G_A^{xx} is the x-component of the dyadic Green's function for the magnetic vector potential due to x-directed horizontal electric dipole HED in conductive half space. Respectively, G_V is the scalar potential Green's function due to one charge q associated to the HED.

The Green's functions G_A^{xx} and G_V are obtained firstly in the transformed Fourier domain by solving the corresponding wave equations with respect to the boundary conditions at the air-soil interface. Next, the spatial domain Green's functions are obtained by solving the following Sommerfeld-type integral

$$G_{A,V}=S_0\left\{\tilde{G}_{A,V}\right\}=\frac{1}{2\pi}\int_0^\infty \tilde{G}_{A,V}(\lambda)J_0(\lambda\rho)\lambda d\lambda. \tag{5}$$

The expressions for the vector and scalar Green's functions relative to this problem may be found in [12, 13].

$$\begin{aligned} G_A^{xx}&=\frac{\mu_0}{2}\left[G_{dir}+S_0\left\{R_{TE10}\frac{e^{-u_1|z+z'|}}{u_1}\right\}\right] \\ &=\frac{\mu_0}{2}\left[G_{dir}-G_{img}+S_0\left\{\frac{2e^{-u_1|z+z'|}}{u_1+u_0}\right\}\right] \end{aligned} \tag{6}$$

$$\begin{aligned} G_V&=\frac{1}{2\underline{\varepsilon}_1}\left[G_{dir}+S_0\left\{\frac{-u_1^2R_{TM10}+k_1^2R_{TE10}}{\lambda^2}\frac{e^{-u_1|z+z'|}}{u_1}\right\}\right] \\ &=\frac{1}{2\underline{\varepsilon}_1}\Big[G_{dir}+K_{10}G_{img}+ \\ &+S_0\left\{\frac{2k_1^2e^{-u_1|z+z'|}}{k_1^2u_0+k_0^2u_1}-\frac{2k_1^2e^{-u_1|z+z'|}}{u_1(k_1^2+k_0^2)}\right\}\Big] \end{aligned} \tag{7}$$

where R_{TE} and R_{TM} are Fresnel reflection coefficients [14]

$$R_{TE10}=\frac{u_1-u_0}{u_1+u_0}\qquad R_{TM10}=\frac{k_0^2u_1-k_1^2u_0}{k_0^2u_1+k_1^2u_0}, \tag{8}$$

and K_{10} is quasi-static reflection coefficient

$$K_{10}=\frac{k_1^2-k_0^2}{k_1^2+k_0^2}, \tag{9}$$

$$\begin{aligned} &u_i=\sqrt{\lambda^2-k_i^2};\quad i=0,1 \\ &k_0^2=\omega^2\mu_0\varepsilon_0;\quad k_1^2=\underline{\varepsilon}_r k_0^2 \\ &\underline{\varepsilon}_r=\varepsilon_r-j\sigma(\omega\varepsilon_0)^{-1}\quad \underline{\varepsilon}_1=\varepsilon_0\underline{\varepsilon}_r \end{aligned}. \tag{10}$$

The first term in Equations (6) and (7) corresponds to the direct term

$$G_{dir}=\frac{e^{-jk_1\sqrt{\rho^2+|z-z'|^2}}}{\sqrt{\rho^2+|z-z'|^2}}=\frac{e^{-jk_1R_{dir}}}{R_{dir}}, \tag{11}$$

where R_{dir} is the distance between the dipole and the observation point.

Respectively the term G_{img} corresponds to the image term

$$G_{img}=\frac{e^{-jk_1\sqrt{\rho^2+|z+z'|^2}}}{\sqrt{\rho^2+|z+z'|^2}}=\frac{e^{-jk_1R_{img}}}{R_{img}}, \tag{12}$$

where R_{img} is the distance between the image of the dipole located at $-z'$ and the observation point.

G_{dir} and G_{img} are obtained from the Sommerfeld identity

$$S_0\{\frac{e^{-u_1h}}{u_1}\}=\frac{1}{2\pi}\int_0^\infty\frac{e^{-u_1h}}{u_1}J_0(\lambda\rho)\lambda d\lambda=\frac{e^{-jk_1\sqrt{\rho^2+h^2}}}{\sqrt{\rho^2+h^2}} \tag{13}$$

where $h = |z \pm z'|$, and represents a spherical wave radiated by a Hertz dipole placed in infinite homogeneous medium "1", *i.e.* with propagation constant k_1.

The terms $S_0\{\cdot\}$ have no analytical solution. We determine their spatial domain solution by direct numerical integration in a similar way to the approach used by Burke et al. [15].

2.2. Quasi-static approximation of the Green's functions

The quasi-static approximations of the Green's functions G_A^{xx} and G_V are based on the exponential approximation of the spectral expressions that arise in $S_0\{\cdot\}$ when frequency tends to zero. The spatial domain Green's functions are later obtained in closed form in terms of Sommerfeld identity. In comparison to the classical quasi-static approach, this image representation involves the propagation effect [6, 7].

As $\omega \to 0$, and $k_0^2 \to 0$ the most simple approximation in spectral domain is based on $u_1 \sim u_0$ since $\lambda^2 >> k_n^2$ for $n = 0, 1$. By substitution in (8), we come to the following low-frequency approximation of the Fresnel reflection coefficients

$$R_{TE}^{10} \to 0 \qquad R_{TM}^{10} = \frac{k_0^2 - k_1^2}{k_0^2 + k_1^2} = -K_{10}, \tag{14}$$

This leads to the following approximation of (6) and (7)

$$G_A^{xx} \to \frac{\mu_0}{2} G_{dir} = \frac{\mu_0}{4\pi} \frac{e^{-ikR_{dir}}}{R_{dir}} \tag{15}$$

$$\begin{aligned} G_V &\to \frac{1}{2\underline{\varepsilon}_1}\left[G_{dir} + S_0\left\{ K_{10} \frac{e^{-u_1|z+z'|}}{u_1} \right\}\right] \\ &= \frac{1}{2\underline{\varepsilon}_1}\left[G_{dir} + K_{10} G_{img} \right] \end{aligned}. \tag{16}$$

The second approximation [7] is based on the assumption $u_0 \sim \lambda$, $u_1 \neq u_0$ and Wait-Spies [16] and Bannister's air-earth complex image theory [17]

$$\frac{2\lambda}{u_1 + \lambda} \approx 1 - e^{-\lambda d}, \tag{17}$$

$$e^{-u_1|z+z'|} = e^{-jk_1|z+z'|a} e^{-\lambda|z+z'|b} \tag{18}$$

where $d = 2/\gamma_1 = 2/\sqrt{j\omega\mu_0(\sigma + j\omega\varepsilon)}$ denotes complex depth and δ is skin depth. The constants a and b get values of 0.4 and 0.96 (valid when $R_2/\delta < 1$), or 0.96 and 0.4 (valid when $R_2/\delta > 1$) [3].

By using (17) and (18) we obtain the following approximate formulations of (6) and (7)

$$\begin{aligned} G_A^{xx} = \frac{\mu_0}{2}\Big[& G_{dir} + (K_{10} - 2) G_{img} \\ & + S_0\left\{ e^{-jk_1 a|z+z'|} e^{-\lambda b|z+z'|} \frac{1 - e^{-\lambda d}}{\lambda} \right\}\Big], \end{aligned} \tag{19}$$

$$\begin{aligned} G_V = \frac{1}{2\underline{\varepsilon}_1}\Big[& G_{dir} + (K_{10} - 2) G_{img} \\ & + S_0\left\{ e^{-jk_1 a|z+z'|} \frac{2e^{-\lambda b|z+z'|}}{\lambda} \right\}\Big] \end{aligned}. \tag{20}$$

Equations (19) and (20) may be readily evaluated by using the following analytic solutions

$$\begin{aligned} S_0\left\{ \frac{e^{-\lambda b|z+z'|}}{\lambda} \right\} &= \int_0^\infty e^{-\lambda(d+b|z+z'|)} J_0(\lambda\rho) d\lambda \\ &= \frac{1}{\sqrt{\rho^2 + (b|z+z'|)^2}} \end{aligned}, \tag{21}$$

$$\begin{aligned} S_0\left\{ \frac{e^{-\lambda(d+b|z+z'|)}}{\lambda} \right\} &= \int_0^\infty e^{-\lambda(d+b|z+z'|)} J_0(\lambda\rho) d\lambda \\ &= \frac{1}{\sqrt{\rho^2 + (d + b|z+z'|)^2}} \end{aligned}, \tag{22}$$

that leads to the following approximations of (6) and (7)

$$\begin{aligned} G_A^{xx} \to \frac{\mu_0}{4\pi}\Bigg[& G_{dir} + (K_{10} - 2) G_{img} + \frac{e^{-jk_1 a|z+z'|}}{\sqrt{\rho^2 + (b|z+z'|)^2}} \\ & - \frac{e^{-jk_1 a|z+z'|}}{\sqrt{\rho^2 + (d + b|z+z'|)^2}} \Bigg] \end{aligned} \tag{23}$$

$$G_V \to \frac{1}{4\pi\underline{\varepsilon}_1}\left[G_{dir} + (K_{10} - 2) G_{img} + \frac{2e^{-jk_1 a|z+z'|}}{\sqrt{\rho^2 + (b|z+z'|)^2}} \right] \tag{24}$$

3. Numerical results

To determine the domain of applicability of proposed approximate quasi-static expressions we compare the current along a horizontal conductor in homogeneous lossy soil in wide frequency range.

Firstly, we investigate the influence of the current components that arise respectively due to the two terms in the expression of the electric field (3) in the rigorous EM model. The first component of the current $\underline{I}_A$ is related to the magnetic vector potential A, whereas the second current component $\underline{I}_V$ is related to the electric scalar potential V. Thus, we define the phasor of the total current $\underline{I}$ as a sum of two components

$$\underline{I} = \underline{I}_A + \underline{I}_V. \tag{25}$$

Next, we investigate the accuracy of each of the proposed approximations: (15) and (23) for G_A^{xx}, and (16) and (24) for G_V. The objective of this analysis is to determine the error that arises when calculating the current $\underline{I}$ due to approximation of only one of the corresponding Green's functions G_A^{xx} and G_V.

Further, we develop two approximate models on the basis of the two sets of approximate Green's functions:

- Model A - based on the approximations (15) and (16);
- Model B – based on the approximations (23) and (24).

We compare the accuracy of the above models by comparing the current along the conductor with respect to rigorous EM solution on the basis of a rms error [18]

$$\varepsilon_{\text{rms}} = \left[\frac{\sum_{i=1}^{N} \left| \underline{I}_{EMi} - \underline{I}_{approxi} \right|^2}{\sum_{i=1}^{N} \left| \underline{I}_{EMi} \right|^2} \right]^{1/2}, \qquad (26)$$

where $\underline{I}_{EMi}$ and $\underline{I}_{approxi}$ are phasors of the current samples along the wire computed by the EM model and by using the approximate models A and B, and N is number of samples.

Here also, we compare the currents calculated by using the Numerical Electromagnetic Code (NEC) reflection coefficient approximation [19].

The studied cases are: L = 10-m (short conductor) and L = 100-m (long conductor), with radius a = 0.007 m positioned at depth D: 0.5 m, 1 m and 1.5 m. Three values for the soil conductivity σ are assumed: 0.001 S/m, 0.01 S/m and 0.1 S/m. The relative permittivity of the soil is fixed at ε_r = 10. The excitation is central feed by a harmonic voltage source of 1 V in frequency range from 1 kHz to 10 MHz.

3.1. Short 10-m conductor

We start our study by analyzing the effects of the two current components as given by (25). Fig. 3 shows the magnitudes of the total current $\underline{I}$ and its components $\underline{I}_A$ and $\underline{I}_V$ along a short 10-m conductor placed at depth of 1 m in lossy soil with conductivity of 0.01 S/m. The results correspond to frequencies of 0.1MHz, 1 MHz and 10 MHz.

As may be observed, in the lower frequency range (up to 0.1 MHz) the total current $\underline{I}$ is practically based on the $\underline{I}_V$ component, while $\underline{I}_A$ is negligible. At higher frequencies the magnitudes of $\underline{I}_A$ and $\underline{I}_V$ become of the same rang and much larger than the magnitude of the total current $\underline{I}$. This shows that the approximation of G_V is important in the lower frequency range whereas good approximation of both G_A^{xx} and G_V is very important at higher frequencies.

Fig. 4 shows the ε_{rms} error that arises due to each of the approximate expressions: (15) and (23) for G_A^{xx}, and (16) and (24) for G_V respectively. For that purpose we use the following expression

$$\begin{aligned} \underline{I}_{approx} &= \underline{I}_{approxA(15 or 23)} + \underline{I}_V \\ \underline{I}_{approx} &= \underline{I}_A + \underline{I}_{approxV(16 or 24)} \end{aligned}, \qquad (27)$$

where the approximate current $\underline{I}_{approx}$ is calculated in a way that only one of its components is calculated by using one of the corresponding approximate expressions, whereas the other current component is calculated by using the exact expression for the corresponding Green's function.

As may be observed, the expression (24) represents better approximation of G_V than the expression (16) in the intermediate frequency range, but it introduces some small error in the low frequency range. The expression (23) shows better agreement than (15) practically in all studied frequency range except at very high frequencies.

Next, we compare the accuracy of the approximate models A and B. Fig. 5 to Fig. 7 show respectively the current magnitude and phase calculated by using the EM model, the two approximate models A and B.

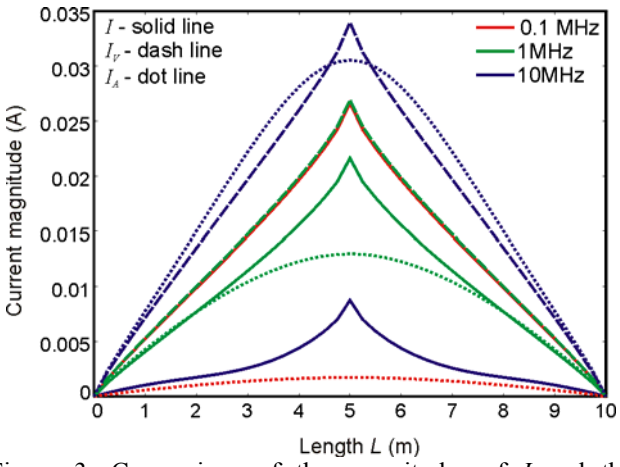


Figure 3: Comparison of the magnitudes of $\underline{I}$ and the corresponding components $\underline{I}_A$ and $\underline{I}_V$ at 0.1, 1 and 10 MHz (L = 10-m, D = 1 m, σ = 0.01 S/m).

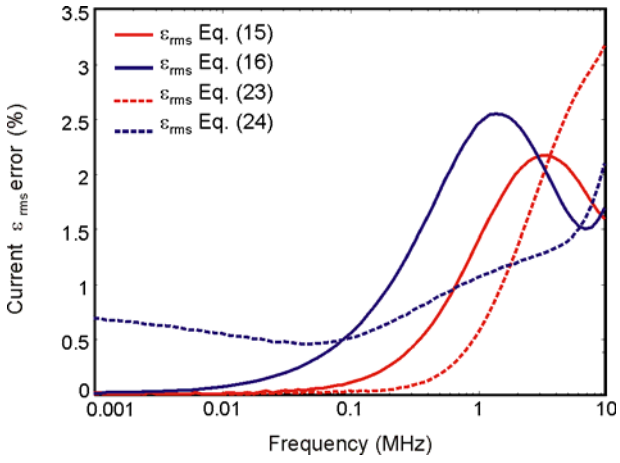


Figure 4: Current ε_{rms} error due to each of the approximations (15), (16), (23) and (24) (L = 10-m, D = 1 m, σ = 0.01 S/m).

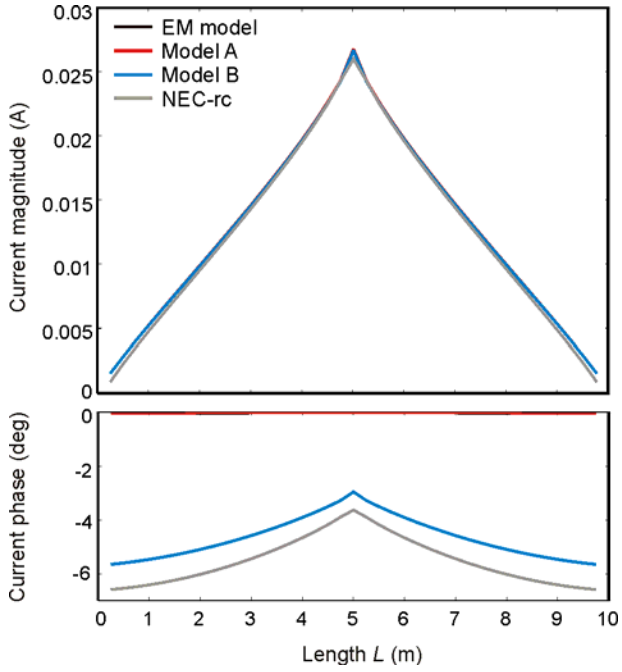


Figure 5: Current magnitude and phase at 0.1 MHz obtained by different models (L = 10-m, D = 1 m, σ = 0.01 S/m).

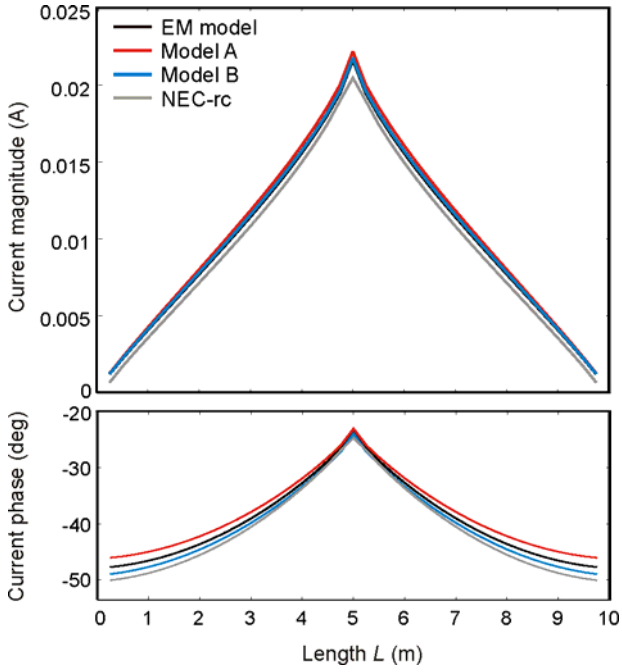


Figure 6: Current magnitude and phase at 1 MHz obtained by different models (L = 10-m, D = 1 m, σ = 0.01 S/m).

Here also, we represent the currents obtained by using NEC refection coefficient method (denoted by NEC-rc). For all three studied frequencies: 0.1 MHz; 1 MHz; and 10 MHz the results show generally very good agreement of the approximate currents with respect to the results obtained by using the EM model.

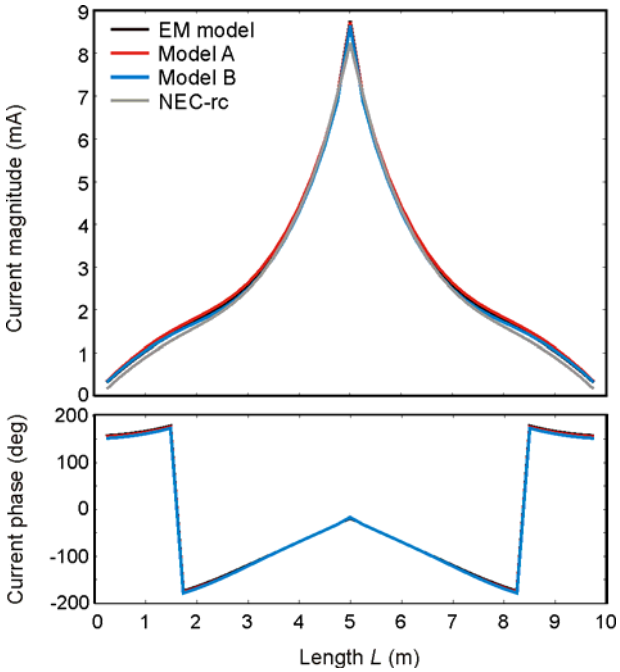


Figure 7: Current magnitude and phase at 10 MHz obtained by different models (L = 10-m, D = 1 m, σ = 0.01 S/m).

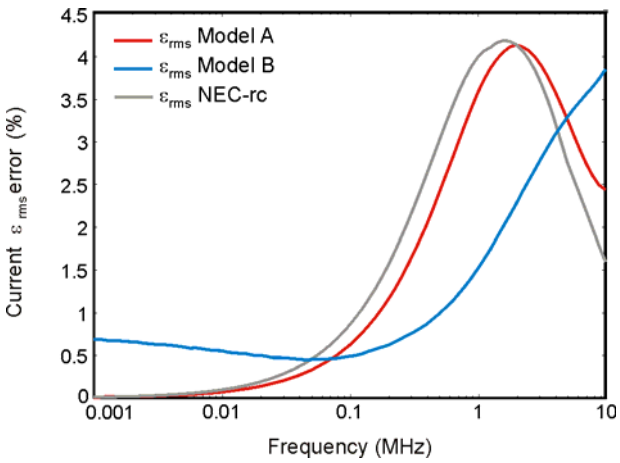


Figure 8: Current ε_{rms} error when using approximate models A, B and NEC-rc (L = 10-m, D = 1 m, σ = 0.01 S/m).

The ε_{rms} error (26) given in Fig. 8 shows that the accuracy of all models is within 5%. However, we my observe that Model A and NEC-rc show more significant dependence on the resonant frequency not observed in Model B. On the other hand, Model B introduces some small error at low frequencies, however not exceeding 1%.

Next, we study the influence of the soil conductivity on the accuracy of the proposed approximate models. The results are obtained for a short 10-m conductor placed at depth of 1 m in lossy soil with conductivity σ = 0.001 S/m (solid line) and σ = 0.1 S/m (dash line) respectively. As shown in Fig. 9, the ε_{rms} error has tendency to increase significantly when decreasing the soil conductivity. Again, the best agreement is obtained by using the Model B,

especially in case of high conductive soil. The accuracy of all models decreases significantly when the soil conductivity is low.

Finally, in Fig. 10 it may be observed the influence of the conductor depth D on the accuracy of the approximate models. The results are obtained for a short 10-m conductor placed at depth D of 0.5 m (solid line) and 1.5 m (dash line) respectively in lossy soil with $\sigma = 0.01$ S/m. The best accuracy is obtained by using Model B with about 5% ε_{rms} error. The other models show more significant dependence on the conductor depth.

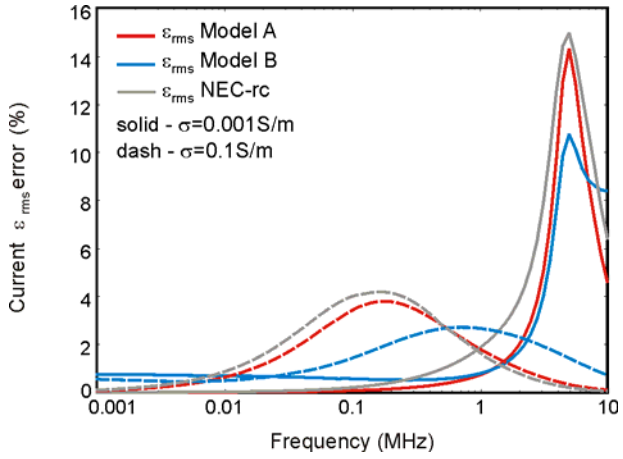


Figure 9: Influence of the soil conductivity on the current ε_{rms} error (L = 10-m, D = 1 m).

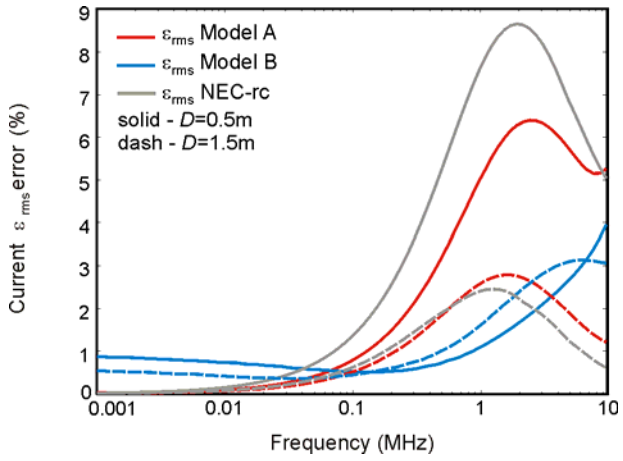


Figure 10: Influence of the conductor depth on the current ε_{rms} error (L = 10-m, $\sigma = 0.01$ S/m).

3.2. Long 100-m conductor

Firstly we study the total current $\underline{I}$ and its two components $\underline{I}_A$ and $\underline{I}_V$ along a 100-m long conductor at –1 m in lossy soil with conductivity of 0.01 S/m. The results given in Fig. 11 correspond to frequencies of 0.1 MHz, 1 MHz and 10 MHz. The results show that the currents $\underline{I}_A$ and $\underline{I}_V$ are of the same range even at lower frequencies. They tend to cancel each other resulting in much lower magnitude of the total current $\underline{I}$. This leads to the conclusion that the approximation of both Green's functions G_A^{xx} and G_V plays an important role in all studied frequency range.

Similarly as in previous section, Fig. 12 shows the ε_{rms} error that arises due to each of the approximate expressions: (15) and (23) for G_A^{xx}; and (16) and (24) for G_V. Again, the results show that the second set, i.e. expressions (23) and (24) represent better approximation of G_A^{xx} and G_V.

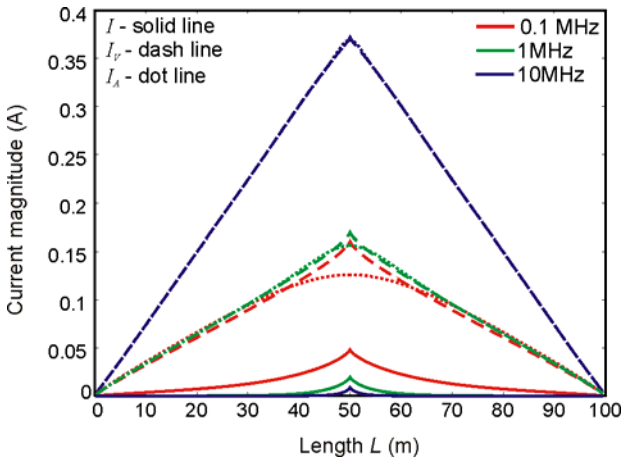


Figure 11: Comparison of the magnitudes of $\underline{I}$ and the corresponding components $\underline{I}_A$ and $\underline{I}_V$ at 0.1, 1 and 10 MHz (L = 100-m, D = 1 m, $\sigma = 0.01$ S/m).

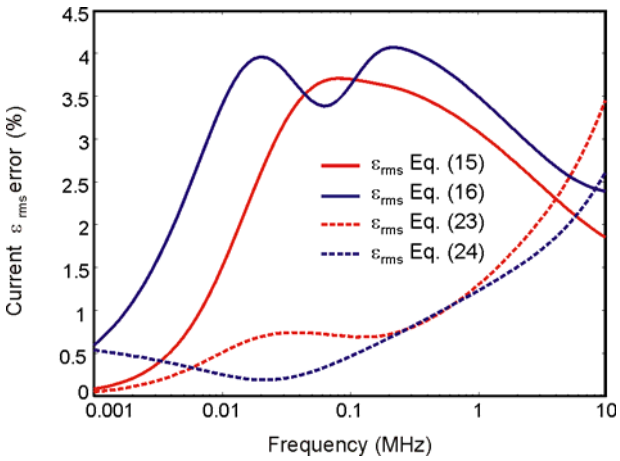


Figure 12: Current ε_{rms} error due to each of the approximations (15), (16), (23) and (24) (L = 100-m, D = 1 m, $\sigma = 0.01$ S/m).

We continue our analysis by comparing the currents calculated by using models A, B and NEC-rc. Fig. 13 to Fig. 15 show respectively the magnitude and phase of the current along a 100-m conductor placed at –1 m in homogeneous lossy soil with conductivity of 0.01 S/m calculated at 0.1 Hz, 1 MHz and 10 MHz.

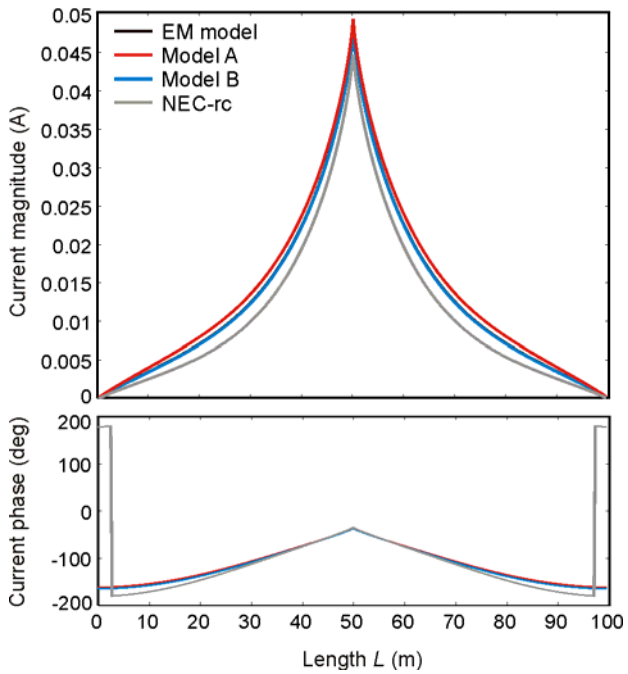


Figure 13: Current magnitude and phase at 0.1 MHz obtained by different models (L = 100-m, D = 1 m, σ = 0.01 S/m).

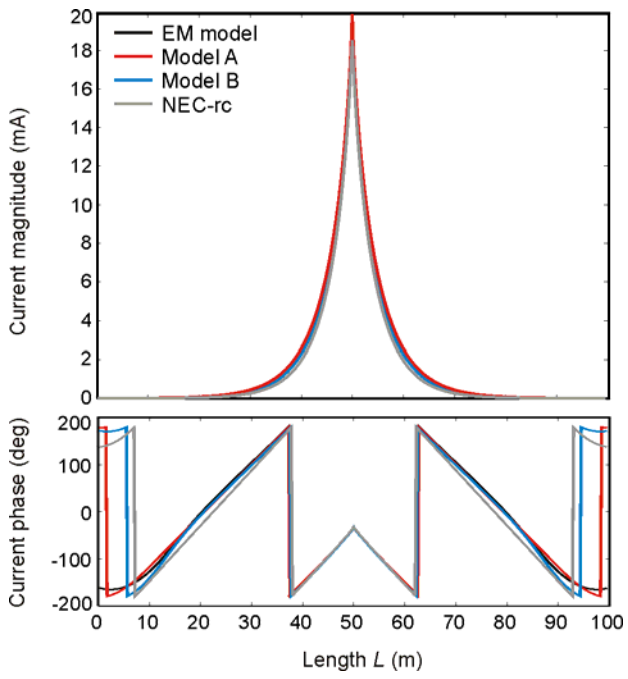


Figure 14: Current magnitude and phase at 1 MHz obtained by different models (L = 100-m, D = 1 m, σ = 0.01 S/m).

The corresponding ε_{rms} error (26) may be observed in Fig. 16. The best accuracy (max 2% ε_{rms} error) is obtained by using the model B. The results obtained by using Model A and NEC-rc show much higher ε_{rms} error around the resonant frequency.

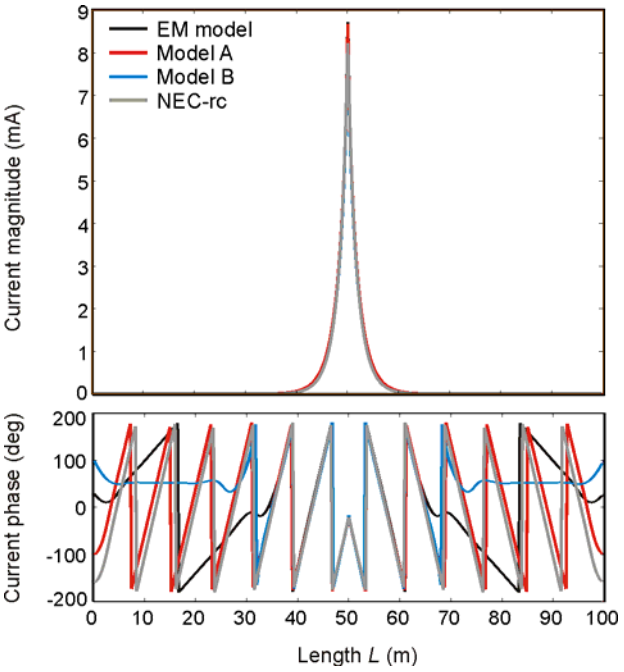


Figure 15: Current magnitude and phase at 1 MHz obtained by different models (L = 100-m, D = 1 m, σ = 0.01 S/m).

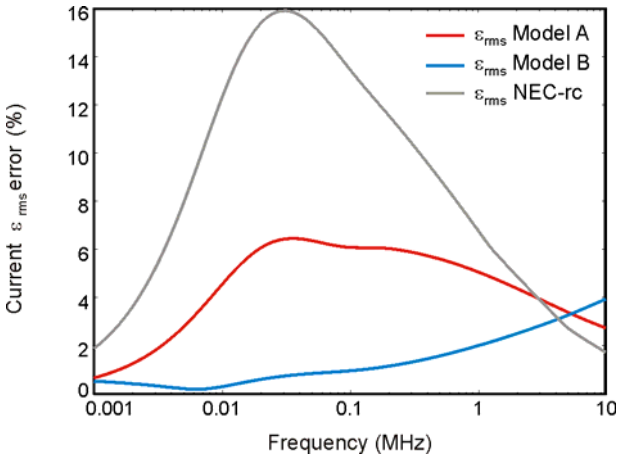


Figure 16: Current ε_{rms} error due to each of the approximations (15), (16), (23) and (24) (L = 100-m, D = 1 m, σ = 0.01 S/m).

Fig. 17 shows the accuracy of the approximate models regarding the soil conductivity. As may be observed, when the soil conductivity is low the ε_{rms} error tends to increase significantly, particularly at higher frequencies above 1 MHz. In case of very large value of the soil conductivity the accuracy of all models is much better.

In Fig. 18 it may be observed the variations of the ε_{rms} error with respect to the conductor depth D: 0.5 m (solid line) and 1.5 m (dash line). As may be observed, Model B results in max 5% ε_{rms} error, whereas the other models introduce higher ε_{rms} errors especially when the conductor is close to the soil surface.

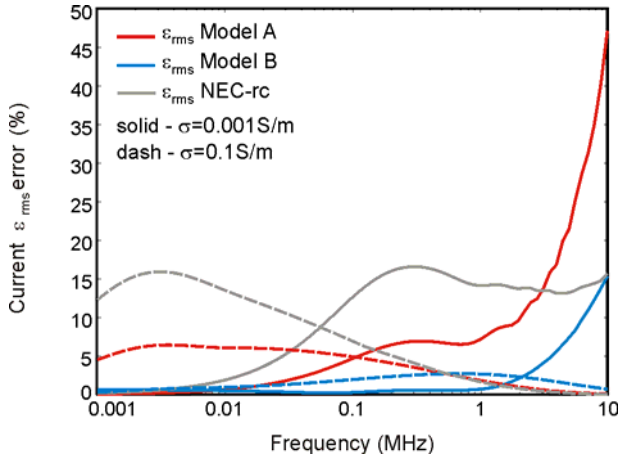


Figure 17: Influence of the soil conductivity on the current ε_{rms} error (L = 100-m, D = 1 m).

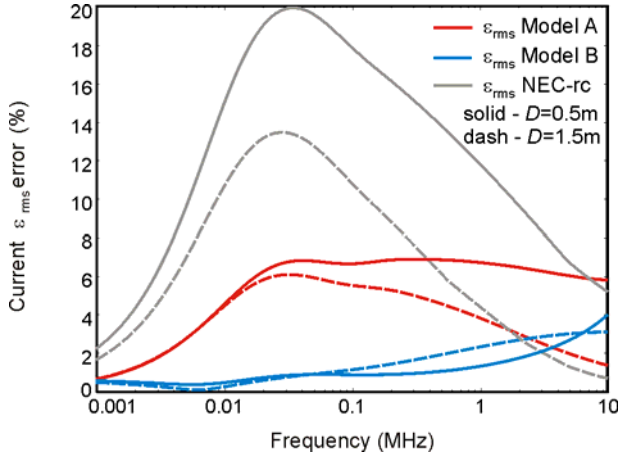


Figure 18. Influence of the conductor depth on the current ε_{rms} error (L = 100-m, σ = 0.01 S/m).

4. Conclusions

In the paper, the authors derive two approximate models of a horizontal wire conductor buried in homogeneous lossy soil. The two models are based on quasi-static image and complex image theory applied to the Green's functions related to this problem. The results of a detailed wide frequency range numerical analysis of a 10-m (short) and a 100-m (long) wire by using various soil parameters may be summarized in:

- The model A, based on the quasi-static image theory represents generally good approximation with respect to the rigorous EM model in all studied frequency range. However, this model shows limitations due to higher ε_{rms} error when in cases of low conductivity of the soil and when the conductor is located close to the soil surface. Similarly as NEC reflection coefficient model, the accuracy of this model shows significant dependence on the resonant frequency.
- The model B, based on the quasi-static complex image theory represents very good approximation with respect to the rigorous EM model in wide frequency range. The high accuracy of this model with max 5% ε_{rms} error is confirmed for all studied cases. The only exception concerns the case of low conductive soil (here σ = 0.001 S/m) when the ε_{rms} error exceeds 5% at very high frequencies, above few MHz.

Acknowledgements

This work has been realized within the FP7-PEOPLE-2009-IEF Project 253783.

References

[1] F.-M. Tesche, M. Ianoz, T. Karlsson, *EMC Analysis methods and computational models*, John Wiley and Sons, New York, 1997.

[2] A. Banos, *Dipole radiation in the presence of a conducting half-space*, Pergamon Press, Oxford, 1966.

[3] P. Bannister, Applications of complex image theory, *Radio Science* 4: 605–616, 1986.

[4] T. Takashima, T. Nakae, R. Ishibashi, Calculation of complex fields in conducting media, *IEEE Transactions on Electrical Insulation* 1: 1–7, 1980.

[5] J.-J. Yang, Y.-L. Chow, D.-G.Fang, "Discrete complex images of a three-dimensional dipole above and within a lossy ground", *IEE Proceedings H Microwaves, Antennas and Propagation*, pp. 319–326, 1991.

[6] V. Arnautovski-Toseva, K. El Khamlichi Drissi, K. Kerroum, *HF comparison of image and TL models of a horizontal thin-wire conductor in finitely conductive earth*, *Proc. SoftCOM 2011*, Split, Croatia, pp. 1–5, 2011.

[7] V. Arnautovski-Toseva, Approximate closed-form solution of the electric field due to HED within finitely conductive earth, *Proc. ICEAA 2011*, Turin, Italy, pp. 670 – 673, 2011.

[8] L. Grcev, F. Dawalibi, An electromagnetic model for transients in grounding systems, *IEEE Transactions on Power Delivery* 4: 1773–1781, 1990.

[9] R.-F. Harrington, *Field computation by moment method*, IEEE Press, New York, 1993.

[10] J.-R. Mosig, F.-E. Gardiol, A dynamic radiation model for microstrip structures, in *Advances in Electronics and Electron Physics*, P. W. Hawkes, Ed. New York: Academic pp. 139–237, 1982.

[11] K.-A. Michalski, The mixed-potential electric field integral equation for objects in layered media, *Archiv fuer Elektronik und Uebertragungstechnik* 5: 317–322, 1985.

[12] K.-A. Michalski, "On the scalar potential of a point charge associated with time-harmonic dipole in a layered medium", *IEEE Transactions on Antennas and Propagation* 35: 1299–1301, 1987.

[13] G. Dural, M. Aksun, Closed-form Green's functions for general sources and stratified media", *IEEE Transactions on Antennas and Propagation* 7: 1545–1552, 1995.

[14] W.-C. Chew, *Waves and Fields in Inhomogeneous Media*, Wiley–IEEE, New York, 1995.

[15] G.-J. Burke, E.-K. Miller, Modeling antennas near to and penetrat-ing a lossy interface", *IEEE Transactions on Antennas and Propagation* 10: 1040–1049, 1984.

[16] J.-R. Wait, K.-P. Spies, On the image representation of the quasi-static fields of a line current source above the ground, *Canadian Journal of Physics* 47: 2731–2733, 1969.

[17] P. Bannister, R. Dube, Simple expressions for horizontal electric dipole quasi-static range subsurface-to subsurface and subsurface-to-air propagation, *Radio Science* 3: 501–507, 1978.

[18] A. Poggio, R. Bevensee, E.-K. Miller, *Evaluation of some thin wire computer programs Proc. IEEE Antennas and Propagation Symposium*, 12: 181–184, 1974.

[19] NEC - Numerical Electromagnics Code (Method of Moments). [Online]. http://www.nec2.org/

An efficient computational technique for performance prediction of inductors on flexible substrates

Nikola Jeranče, Nataša Samardžić, Dragana Vasiljević, Goran Stojanović*

Faculty of Technical Sciences, University of Novi Sad, Serbia
*corresponding author, E-mail: sgoran@uns.ac.rs

Abstract

A computer program for modeling inductors on flexible substrates has been created and tested. Self and mutual inductances are obtained by integrating vector potential. The results are validated by comparison with analytical expressions and some measurement results. The program includes geometrical transformations for twisting conductive segments printed on flexible surface and for displacements.

1. Introduction

Electronics on flexible substrates is rapidly developing, promising new applications and low-cost components and circuits [1]. In this paper, we describe a computer program written in C++ designed for accurate modeling of inductors printed on flexible substrate. This program has two purposes: to help the design of inductors in various electronic circuits and to provide fast and reliable simulation tool for inductive position sensors. Therefore, it should take into account both twisting the surfaces on which the inductors are printed and relative displacements of inductors. The approach used for inductance calculation will be explained first. The modeling of inductors' geometry and displacements is detailed in the next section. After that, several examples of self- and mutual inductance calculation are provided and convergence of the method is investigated. Finally, a conclusion with discussion of results and possible improvements is given.

2. Inductance calculation by integration

A classical approach for modeling inductors of arbitrary shapes is using the finite element software, describing them as three-dimensional (3D) magnetostatic problem. However, the absence of ferromagnetic materials in modeled circuits has allowed us to simplify the inductance calculation by integrating vector potentials in the circuit due to the currents. By doing so, we no longer need time and memory consuming 3D finite element computation, and we also avoid the problem of domain truncation which can affect finite element results.

In order to perform the numerical integration, each inductor is divided into small volume elements.

The inductance is calculated by integrating over the elements using the formula [2]:

$$L = \frac{1}{I^2}\int \vec{J}\vec{A}dv \tag{1}$$

where: J – current density vector in the element; A – vector potential at the center of element; dv – volume of the element. The vector potential at a point is computed by integration through all the other elements in the problem, using the following expression [2]:

$$\vec{A} = \frac{\mu}{4\pi}\int \frac{\vec{J}}{R}dv \tag{2}$$

where: R – distance between elements; μ – magnetic permeability (of vacuum, in our case).

The integrals in (1) and (2) are calculated as sums over all the elements in the problem, excluding the elements where R=0. Some parameters from expression (2) have been illustrated in Figure 1. The vector potential of the element 1 is obtained by taking into account current density and distance of all the other elements with respect to the center of the element 1. For example, in Figure 1 the element 2, its current density and its distance R from the element 1 are shown.

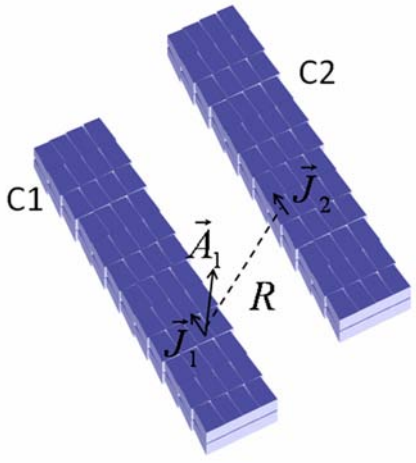


Figure 1: Elements on conductors C1 and C2

Obviously, it is not possible to take into account the current density of the element where the vector potential is calculated because in that case $R = 0$, and (2) is undefined.

In order to increase the accuracy for a given number of elements, the self-inductance of each element, considered as straight line segment with rectangular cross-sections is added in (1).

All results obtained by the program are saved in a log file. It is possible to see mutual inductances between all segments, which can be useful in verification of obtained results and in design of inductive components.

A significant advantage of this method is that only current carrying conductors are represented in the model, there is no need for meshing the empty space. Compared to the finite element method, this leads to several advantages: smaller number of elements, problems with badly shaped elements are avoided and the infinite domain is automatically taken into account.

3. Modeling the geometry of printed conductors

The geometry of printed conductors is described in three stages corresponding to printing, 3D geometry forming and displacement of inductors printed on flexible substrates.

The initial geometry of printed components is defined by the printed pattern. In the program, this pattern is described as sets of straight segments connected in series which are printed in plane - on a flat flexible substrate.

A flexible substrate can be deformed in many ways. This deformation is taken into account when three-dimensional coordinates of each element are calculated.

If there is more than one flexible inductor, their mutual inductance will vary with their relative position. The displacements of inductors are defined by transformation of three-dimensional coordinates for each of these inductors.

3.1. Initial printed geometry

The inkjet printing technology can be used to make thin layers of conducting material on a flexible substrate. In this way, it is possible to fabricate inductors on a flat substrate which can be twisted afterwards.

In the presented program, the conductors are described as set of straight conductive segments connected in series.

The coordinates of linear segments are entered in u-v plane, as a set of points which are connected with straight conductors. Each segment is assigned a division in the elements – a number of elements by length, by width and by thickness. A uniform current density is supposed for all segments, with total current equal to 1, in order to simplify calculation of integrals in (1) and (2).



Figure 2: A meander inductor printed using silver ink on a Kapton substrate

An example of the printed inductor is given in Figure 2. It was printed with silver ink on a Kapton flexible substrate using Dimatix ink-jet printer DMP-3000 [3]. In Figure 3, a representation of this inductor in our program is illustrated with uniform current density corresponding to each straight segment.



Figure 3: A meander inductor and its current density as they are represented in the program

It should be noted that this representation of the current density is only an approximation of real lines of current which depend on each conductor's geometry. It will be demonstrated that this approximation can give very accurate results in a large number of practical cases.

3.2. Modeling the final shape of flexible substrates

The u-v coordinates of elements obtained by the initial geometry input are transformed by the program into x-y-z coordinate system. The deformation of flexible substrate is defined by using by using appropriate mathematical expressions. In this manner, drawing complicated geometries in three dimensions is avoided and the structure is described in the same way as it is fabricated afterwards.

There are currently two modes of expressing three-dimensional coordinates in the program. The first one is defined by a set of coefficients c_{x0}, c_{y0}, c_{z0} … c_{x7}, c_{y7}, c_{z7} the meaning of which is given by:

$$\begin{aligned} x &= c_{x0} + c_{x1}u + c_{x2}v + c_{x3}\cos(c_{x7}u) + c_{x4}\sin(c_{x7}u) + c_{x5}u^2 + c_{x6}v^2 \\ y &= c_{y0} + c_{y1}u + c_{y2}v + c_{y3}\cos(c_{y7}u) + c_{y4}\sin(c_{y7}u) + c_{y5}u^2 + c_{y6}v^2 \\ z &= c_{z0} + c_{z1}u + c_{z2}v + c_{z3}\cos(c_{z7}u) + c_{z4}\sin(c_{z7}u) + c_{z5}u^2 + c_{z6}v^2 \end{aligned} \quad (3)$$

This mode is sufficient for describing some frequently used shapes, like planes and circular surfaces. However, the applications with spirally wound conductors have been investigated and are very promising [4]. For this reason, a second mode of expressing three-dimensional coordinates has been added, for this special case. Polar coordinates r and θ are used for this mode:

$$\begin{aligned} x &= c_{x0} + r\cos(\theta) \\ y &= c_{y0} + r\sin(\theta) \\ z &= c_{z0} + c_{z1}v \end{aligned} \quad (4)$$

Auxiliary variables r and θ are calculated from u which is equal to the total arc length of the spiral. It can be written:

$$du = rd\theta \quad (5)$$

$$r = r_0 + a\theta \quad (6)$$

where a is the pitch from one turn to the next divided by 2π.

From (5) and (6) and by fixing $\theta(0) = 0$, the final expressions for θ is obtained:

$$\theta = -\frac{r_0}{a} + \frac{\sqrt{r_0^2 + 2au}}{a} \qquad (7)$$

The x-y-z coordinates are obtained from u-v coordinates in the printing plane. The thickness of printed conductors is usually very small, but it can be divided into elements, which are then considered to be aligned on the normal of the surface.

3.3. Modeling the displacements of inductors

A matrix and a vector representing the displacement in three-dimensional space are used for each inductor separately. The displacement is described by following expression:

$$\begin{bmatrix} x' \\ y' \\ z' \end{bmatrix} = T \begin{bmatrix} x \\ y \\ z \end{bmatrix} + d \qquad (8)$$

where x, y and z are initial three-dimensional coordinates of the element in the inductor; x', y' and z' are three-dimensional coordinates of the element after the displacement; $\boldsymbol{T}$ is 3 by 3 matrix and $\boldsymbol{d}$ is vector with 3 elements.
The initial values for T and d are unit matrix and zero vector respectively.
The expression (8) is applied for each element in order to calculate the distance needed in (2) correctly.

4. Examples of inductance calculations

The aim of this work is to provide an efficient tool for calculating inductances of conductors with different geometry (shapes), which are likely to be used in various practical applications. In this section, self-inductances for three such shapes are calculated and compared with results obtained from analytical expressions and tables: straight line segments (no twisting), circular conductors and spirally rolled conductors.

4.1. Straight line segments

First step in validation is calculating the inductances of straight printed conductive segments having 31.4 mm length (l), 5 μm thickness and three different widths (w) equal to 1, 0.5 and 0.2 mm. A straight segment is shown in Figure 4.

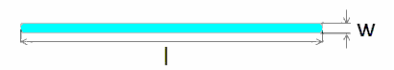


Figure 4: Straight line segment

These inductances (for different conductor widths) can be calculated using the following analytical expression [5]:

$$L = 0.002l\left(\ln\left(\frac{2l}{w+t}\right) + 0.5 + \frac{w+t}{3l}\right) \qquad (9)$$

where L is the inductance in nH, w is width, t is thickness, and l is length of conductive segment in centimeters. The inductances (practically just self-inductances) obtained by in-house developed software tool are given in Table 1, as well as those obtained from analytical expression (9).

Table 1: Calculated inductances (L) for straight conductors

w [mm]	L analytical [nH]	L our program [nH]
1	29.18	29.01
0.5	33.47	33.43
0.2	39.11	40.16

4.2. Circular conductors

We can apply the expressions (3), adjusting the coefficients c_{x0}, c_{y0}, c_{z0} … c_{x7}, c_{y7}, c_{z7} in order to obtain circular segments having same width and thickness and radius r (see Figure 5) such that l = 2πr.

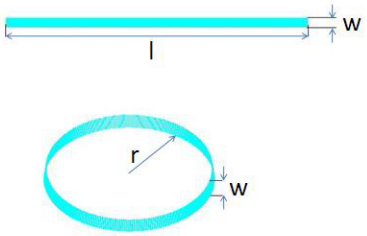


Figure 5: Straight line segment (up) and the corresponding circular segment (down) after rolling the straight segment.

Weinstein's formula for calculating the inductance of a circular segment has been used [6] for comparison with our program:

$$L = 4\pi r n^2(\mu + \lambda) \qquad (10)$$

where n is the number of turns in the coil (1 in our case) and

$$\lambda = \log(8\frac{r}{t}) + \frac{1}{12} - \pi\frac{x}{3} - \frac{1}{2}\log(1+x^2) + \frac{1}{12x^2}\log(1+x^2) + \frac{x^2}{12}\log(1+x^2) + \frac{2}{3}(x - \frac{1}{x})r\tan^{-1}(x) \qquad (11)$$

$$\mu = \frac{t^2}{96r^2}\left(\begin{array}{l} \left(\log(\frac{8r}{t}) - \frac{1}{2}\log(1+x^2)\right)(1+3x^2) + 3.45x^2 \\ + \frac{221}{60} - 1.6\pi x^3 + 3.2x^3\tan^{-1}(x) \\ - \frac{1}{10}\frac{1}{x^2}\log(1+x^2) + \frac{1}{2}x^4\log(1+\frac{1}{x^2}) \end{array}\right) \qquad (12)$$

where $x = w/t$, (w and t correspond to conductor's width and thickness, respectively).

The comparison of inductances obtained by expression (10) and by our program is given in Table 2.

Table 2: Calculated inductances (L) for circular conductors

w [mm]	L analytical [nH]	L our program [nH]
1	20.02	19.84
0.5	24.33	24.38
0.2	29.99	31.03

We can observe a very good agreement of results calculated by our program and by the analytical expression (10).

4.3. Spirally rolled conductors

A spiral conductor is defined by its width w, thickness t, inner radius r_0, the pitch D measured from one turn to the next and the number of turns N, as can be seen in Figure 6.

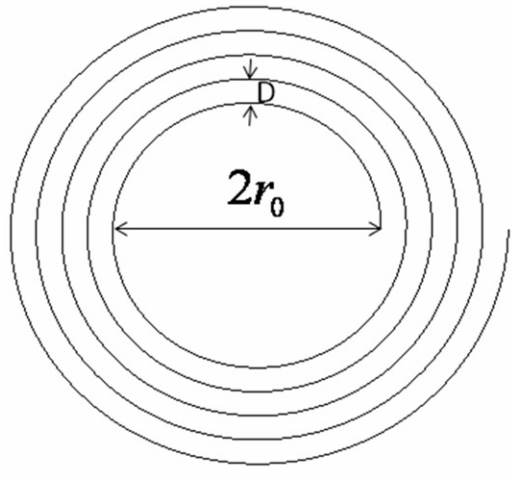


Figure 6: Spiral conductor

In reference [7], a self-inductance of a spiral conductor is calculated by an analytical expression which includes data from tables presented in [7] for this purpose.
In the presented program, a spiral conductor is obtained by entering a straight segment along the u axis and introducing spirally rolled plane, according to (7).
An example given in [7] considers a spiral conductor with following parameters: N = 38, r0 = 51.5 mm, w = 9.525 mm, t = 0.79 mm, D = 4 mm.
The inductance value obtained by the analytical expressions from [7] was 322.8 μH and the measured value acknowledged in [7] was 323.5 μH. The inductance value obtained by our program for the same geometrical parameters is 324.2 μH, which is very close to the reference values.

4.4. Conductors consisting of several straight segments

4.4.1. Square planar coil

The inductance of a square planar coil, shown in Figure 7, has been considered in reference [5].

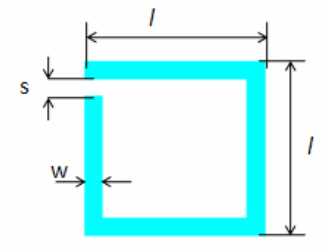


Figure 7: Square planar coil

The parameters of the coil in [5] were: l = 1 mm, w=0.1 mm, s = 0.1 mm.
The inductance obtained by our program is 1.994 nH which matches closely the value 1.9573 nH given in [5] as the most accurate one, obtained by expanded Grover formula.

4.4.2. Printed meander inductor

The inductance of printed meander inductor shown in Figure 2, having straight segments 10 mm long and 2 mm wide has been measured by impedance analyzer (HP-4194A). The inductance obtained by the program is 202 nH, while the measured value was 190 nH.

4.5. Mutual inductances

The mutual inductances of conductors depend on their relative position. The program takes into account the displacement given by (8) when mutual inductance is calculated. The aim is to provide a tool for calculation of mutual inductances of moving parts, for example in position sensors.
Let us consider two coaxial circular conductors having rectangular cross section with 1 mm width and 5 μm thickness. The first conductor has 5 mm radius and the second one 8 mm. The distance between their centers varies from 3 to 7 mm. These conductors are drawn in Figure 8.

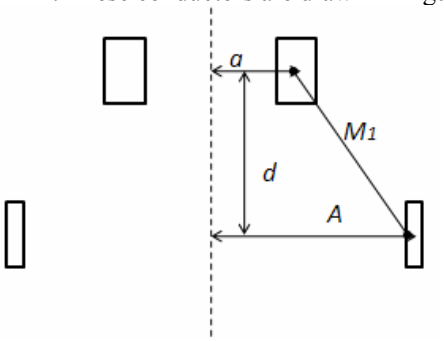


Figure 8: Two circular conductors with rectangular cross-section

It is possible to calculate the mutual inductance of these two conductors using the Rayleigh's formula [6]:

$$M = \frac{1}{6}(M_1 + M_2 + M_3 + M_4 + M_5 + M_6 + M_7 + M_8 - 2M_0) \quad (13)$$

where M_0 is mutual inductance of circles going through the centers of the coils, and M_1, M_2, … are mutual inductances of circles going through center of one coil and the middle of a boundary of the cross-section of the other coil.

The mutual inductances of the circles can be calculated using the Weinstein's formula [6]:

$$M_i = 4\pi\sqrt{Aa}\left(\left(1+\frac{3}{4}k'^2+\frac{33}{64}k'^4+\frac{107}{256}k'^6+\frac{5913}{16384}k'^8\right)\left(\log\left(\frac{4}{k'}\right)-1\right)\right.$$
$$\left.-\left(1+\frac{15}{128}k'^4+\frac{185}{1536}k'^6+\frac{7465}{65536}k'^8\right)\right) \tag{14}$$

where

$$k' = \sqrt{1-k^2}\,,\quad k = \frac{2\sqrt{aA}}{\sqrt{(a+A)^2+d^2}}\,, \tag{15}$$

A and a being the radii of two circles and d distance between their planes.

The mutual inductance of two coaxial circular coils, obtained by analytical expressions and by the program are compared in Table 3.

Table 3: Calculated mutual inductances (M) for two circular conductors

d [mm]	M analytical [nH]	M our program [nH]
3	5.21	5.21
4	4.30	4.30
5	3.52	3.51
6	2.88	2.87
7	2.35	2.35

Excellent agreement is observed between the values obtained by the program and those obtained by the analytical expression.

Another important feature of the program is the calculation of mutual inductances of conductors whose relative angle changes.

This feature is validated by the example of mutual inductance of inclined solenoids, found in the literature [8].

First solenoid has a radius 6 cm, length 12 cm and it is wound with 10 turns per centimeter. Second solenoid has a radius 5 cm, length 4 cm and it is wound with 15 turns per centimeter. The center of the second solenoid is always on the axis of the first solenoid, while the angle between their axes and the distance between their centers vary.

Their mutual inductances between these solenoids are calculated for the cases when their axes are inclined at an angle α, whose cosine is equal to 1, 0.9, 0.8, 0.7, 0.6, 0.5, 0.4, 0.3, 0.2, 0.1 and 0.

The data in reference [8] was compared with the data from another reference in the literature [9]. In [8] mutual inductances were obtained from thin filamentary coils, starting from the formula given by Grover [10]. In [9], mutual inductances were obtained as infinite series using Legendre polynomials.

The shapes and positions of the specified solenoids are easily entered in the program, however, it takes into account only one turn per solenoid (corresponding to one printed conductor). Therefore, the data given in [8] is adjusted by dividing it by *n1·n2*, *n1* and *n2* being the number of turns of first and second solenoid respectively (120 and 60).

We can now present the tables 4, 5, 6 and 7 with the results, given for four different distances *d*, between the center of the second solenoid from the middle plane of the first solenoid, equal to 0, 3 cm, 6 cm and 12 cm respectively. In the tables, M1 analytical is the mutual inductance from reference [8] divided by *n1·n2*, M2 analytical is the mutual inductance from reference [9] divided by *n1·n2*, and M program is the mutual inductance obtained by the program.

Table 4: Calculated mutual inductances (M) for two inclined solenoids, d = 0

Cos(α)	M1 ref [8] analytical [nH]	M2 ref [9] analytical [nH]	M our program [nH]
1	61.08	61.08	61.08
0.9	53.75	53.75	53.75
0.8	46.78	46.78	46.78
0.7	40.16	40.16	40.16
0.6	33.83	33.88	33.83
0.5	27.77	27.81	27.77
0.4	21.94	21.96	21.88
0.3	16.29	16.30	16.33
0.2	10.78	10.77	10.78
0.1	5.37	5.34	5.39
0	0	0	0.00

Table 5: Calculated mutual inductances (M) for two inclined solenoids, d = 3 cm

Cos(α)	M1 ref [8] analytical [nH]	M2 ref [9] analytical [nH]	M our program [nH]
1	55.91	55.91	55.91
0.9	48.79	48.79	48.78
0.8	42.26	42.26	42.26
0.7	36.16	36.16	36.17
0.6	30.42	30.42	30.42
0.5	24.97	24.97	24.97
0.4	19.74	19.74	19.69
0.3	14.68	14.68	14.72
0.2	9.72	9.72	9.72
0.1	4.84	4.84	4.86
0	0	0	0.00

Table 6: Calculated mutual inductances (M) for two inclined solenoids, d = 6 cm

Cos(α)	M1 ref [8] analytical [nH]	M2 ref [9] analytical [nH]	M our program [nH]
1	37.07	37.07	37.07
0.9	33.25	33.25	33.24
0.8	29.45	29.45	29.45
0.7	25.69	25.69	25.70
0.6	21.96	21.96	21.96
0.5	18.26	18.26	18.26
0.4	14.58	14.58	14.55
0.3	10.92	10.92	10.94
0.2	7.27	7.27	7.27
0.1	3.63	3.63	3.64
0	0.00	0.00	0.00

Table 7: Calculated mutual inductances (M) for two inclined solenoids, d = 12 cm

Cos(α)	M1 ref [8] analytical [nH]	M2 ref [9] analytical [nH]	M our program [nH]
1	8.55	8.55	8.55
0.9	8.27	8.27	8.27
0.8	7.83	7.83	7.83
0.7	7.22	7.22	7.22
0.6	6.42	6.46	6.46
0.5	5.59	5.59	5.59
0.4	4.60	4.60	4.60
0.3	3.53	3.53	3.53
0.2	2.39	2.39	2.39
0.1	1.21	1.21	1.21
0	0.00	0.00	0.00

In all considered cases, an excellent agreement of results obtained by the program and by two analytical methods is achieved.

5. Additional considerations

The presented in-house developed software tool is aimed at every-day use for engineering problems, thus some additional questions can be considered, for example, the acceptable number of elements needed to achieve the desired accuracy. Another practical question, related to the previous one, is the time needed for an accurate computation. At first, some modifications of the algorithm described in the section 2 will be explained. After that, some examples of inductance calculations with different number of elements will be given.

5.1. Program adjustments

Considering the expression (2), one can remark that the elements which are close to the point where vector potential is calculated are more significant for the final result. Therefore, we expect that influence of the currents at larger distances can be taken into account with smaller number of elements, thus increasing the speed of calculation without significant impact on the accuracy. In the presented program, the number of elements by length and by width is divided by two if a mutual inductance of two different segments is calculated.

The second solution to speed up the calculation is the use of parallel programming [11]. It is possible because the vector potentials can be calculated separately for each element.

5.2. Computational time and accuracy

The calculations which have already been detailed in Tables 1 and 2 (paragraphs 4.1 and 4.2) are now done with different number of elements in order to illustrate its impact at the computational time and accuracy. The times given in this section are obtained with intel i3 processor at 3.07 GHz using two threads (out of four). In Tables 8 and 9 the division is given by number of elements by length (N_l) and number of elements by width (N_w), there was always one element in thickness.

Table 8: Calculated inductances (L) from Table 1 for straight conductors with different divisions into elements

w [mm]	L analytical [nH]	L our program [nH]	Division N_l x N_w	Time [s]
1	29.18	31.81	100×30	2
1	29.18	30.27	150×30	3
1	29.18	29.57	300×50	37
1	29.18	29.01	500×36	54
1	29.18	29.1	600×50	149
0.5	33.47	39.51	100×30	2
0.5	33.47	36.37	150×30	3
0.5	33.47	34.68	300×50	37
0.5	33.47	33.48	500×36	55
0.5	33.47	33.59	600×50	150
0.2	39.11	58.41	100×30	2
0.2	39.11	49.76	150×30	3
0.2	39.11	40.89	300×50	37
0.2	39.11	40.49	500×36	52
0.2	39.11	38.94	600×50	148

Table 9: Calculated inductances (L) from Table 2 for circular conductors with different divisions into elements

w [mm]	L analytical [nH]	L program [nH]	Division N_l x N_w	Time [s]
1	20.02	22.65	100×30	2
1	20.02	21.11	150×30	5
1	20.02	20.42	300×50	63
1	20.02	19.86	500×36	94
1	20.02	19.95	600×50	264
0.5	24.33	30.35	100×30	3
0.5	24.33	27.23	150×30	6
0.5	24.33	25.54	300×50	64
0.5	24.33	24.34	500×36	94
0.5	24.33	24.45	600×50	253
0.2	29.99	49.26	100×30	3
0.2	29.99	40.62	150×30	5
0.2	29.99	31.76	300×50	67
0.2	29.99	31.36	500×36	93
0.2	29.99	29.81	600×50	251

The results converge towards the reference values of inductance as the number of elements increases. A very good performance is achieved for a number of elements which is acceptable for today's computers – reasonable computational times are obtained. For example, for 0.2 mm width the relative difference is changed from 64 % for 100×30 division up to -0.6 % for 600×50 division (Table 9).

6. Conclusion

A program for inductance calculation using integration of vector potential has been presented. Its main application is calculation self- and mutual inductances of printed conductors on a flexible substrate which can be twisted after the printing. The calculation of self-inductances of straight, circular, square and spiral conductors has been validated through comparison with analytical expressions. The calculated inductance of printed meander inductor has been compared with the measured value. Mutual inductance of circular conductors taking into account linear displacement and rotation has been compared with analytical expressions and very good agreement has been found. The convergence of results with variation of number of elements per segment has been successfully examined. Further developments could include calculation of current density, which would be useful for some conductor geometries, the dependence on frequency could also be added, etc.

Acknowledgements

Research presented in this paper was partly supported within the national project TR32016 and the equipment was provided within FP7 project APOSTILLE, no. 256615. The authors express their gratitude for the received support.

References

[1] W. S. Wong and A. Salleo, *Flexible Electronics: Materials and applications*, Springer Scence+Business Media, New York, 2009.

[2] W. R. Smythe, *Static and dynamic electricity*, McGraw-Hill Book Company Inc., New York, 1950.

[3] www.dimatix.com

[4] N. Jeranče, D. Vasiljević, N. Samardžić, G. Stojanović, *A Compact Inductive Position Sensor Made by Inkjet Printing Technology on a Flexible Substrate*, Sensors 2012, *12*, 1288-1298.

[5] H. Greenhouse, *Design of planar rectangular microelectronic inductors*, IEEE Trans. Parts Hybrids, vol. PHP-10, pp. 101-9, 1974.

[6] E. B. Rosa, F. W. Grover, *Formulas and tables for calculation of mutual and self-inductance*, Bulletin of the Bureau of Standards, vol. 8, 1-287, 1912.

[7] F. W. Grover, *Tables for the calculation of the inductance of circular coils of rectangular cross section*, Scientific Papers of the Bureau of Standards, no. 455 (vol.18), 1922.

[8] S. I. Babic, C. Akyel, *Calculating Mutual Inductance Between Circular Coils With Inclined Axes in Air*, IEEE Transactions on Magnetics, vol. 44, no. 7, pp. 1743-1750, 2008.

[9] C. Snow, *Formulas for Computing Capacitance and Inductance*, Washington, DC: National Bureau of Standards, Dec.1954.

[10] F. W. Grover, *Inductance Calculations*, New York: Dover, 1964.

[11] www.openmp.org

The Limitation of Time-Harmonic Models of the Superlens

Wolfgang J. R. Hoefer

Institute of High Performance Computing, A-Star
1 Fusionopolis Way, # 16-16 Connexis North, Singapore 138632
E-mail: hoeferwjr@ihpc.a-star.edu.sg

Abstract

Several generations of scientists and engineers have successfully solved electromagnetic problems using the frequency domain or time-harmonic approach. It is indeed very elegant and suitable for almost any practical applications. However, there are situations where the time-harmonic model is no longer practical and even leads to physically wrong conclusions, such as in highly nonlinear scenarios or in cases where the steady state is actually never reached. The time domain approach must be used in such cases to preserve causality and to avoid drawing conclusions that conflict with the laws of Physics.

1. Introduction

The introduction of the time-harmonic formalism into Maxwell's theory of electromagnetic fields, as we know it today, is due to Heaviside. It not only reduces the number of dimensions by one (since the time dimension can be omitted in all expressions), but the complex notation reduces differentiation and integration with respect to time to multiplication and division by $j\omega$, and allows both the active/passive and reactive properties of materials, structures and circuits to be described by a single complex number or function. However, this does not limit its application to processes with sinusoidal time dependence, since solutions of general time-dependence can be obtained through the Fourier or Laplace transform, as long as all properties are linear, and spectral data are known for a sufficiently large frequency range to yield a causal time response. One might thus think that time domain approaches are not really needed to solve transient, or at least, wideband electromagnetic problems.

One essential condition that is often neglected when using the time-harmonic form of Maxwell's equations, is that the fields must have actually reached a steady or stationary state. It is thus important to verify that this is indeed the case. If it is not, the time-harmonic solution can lead to confusion and to erroneous conclusions, as the well-publicized controversy over the "Perfect Lens" by Veselago/Pendry [1]-[3] has vividly demonstrated.

A classical case in point is the behavior of waveguides at or slightly below cutoff. The time-harmonic expression for the TE-mode input impedance of a semi-infinite waveguide below cutoff is given by the following expression:

$$Z_{in} = \frac{\omega\mu}{\beta} = \frac{\omega\mu}{-j\sqrt{k_c^2 - k_0^2}}, \qquad (1)$$

where k_c and k_0 are the cutoff and free-space numbers, respectively. Since this impedance is purely inductive and very large for values of k_0 close to k_c, one might tend to expect the average power flow into the waveguide to be zero. However this is not true since it will take a very long time to fill the waveguide with resonant energy, resulting in an extended net flow of the Poynting Vector into the guide. A transient time domain simulation of such a scenario will show this very clearly, but since it is not predicted by the time-harmonic expression (1) one might erroneously conclude that time domain methods do not work well at cutoff.

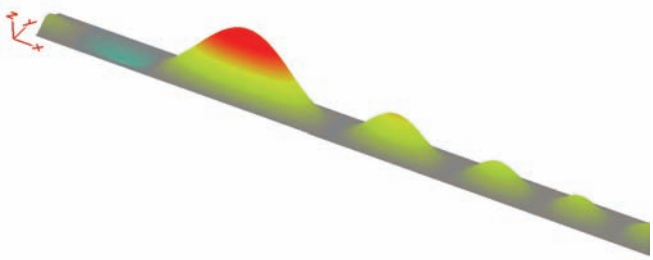


Fig. 1 Poynting Vector in x-direction at cutoff *(TE_{10}-mode, a=11 mm, f=13.62693 GH, shown at time t=1 ns).*

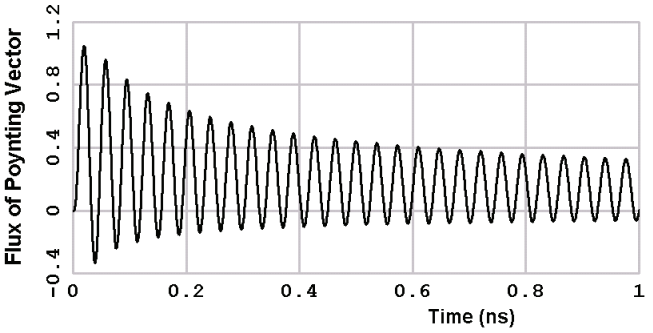


Fig. 2 Time-dependent flux of the Poynting vector through the input port of a semi-infinite TE_{10} rectangular waveguide at the cutoff frequency of *13.627 GHz (a=11 mm).*

2. The Veselago/Pendry Superlens

The Veselago/Pendry Superlens [1], [2] consists of an infinite slab of double-negative metamaterial with negative refractive index. This is a most unusual and controversial device that has challenged conventional ideas and has triggered a heated debate, in which some skeptics claimed that it is incompatible with the laws of physics, in particular that it violates causality and Einstein's postulate that the velocity of light is the same in all frames of reference [3]. Pendry has shown analytically [2] that as long as the object plane and the image plane are separated by twice the thickness of the lens, all spatial Fourier components of an object field will be perfectly transferred by the lens to the image plane and hence, the total image field will exactly replicate the object field.

2.1. Transient Response of the Superlens

The evanescent Fourier components of the image excite resonant modes of the electromagnetic surface polaritons of the superlens which decay exponentially away from the faces of the superlens. They have first been studied by Ruppin [4] and Haldane [5]. When excited by an electric field polarized parallel to the superlens, it can support the two weakly coupled resonant plasmonic surface modes shown in Fig. 3. The superlens behaves thus exactly like two weakly coupled resonators. When one of these resonators is excited by the evanescent field produced by sub-wavelength objects nearby, energy is progressively transferred to the second resonator over many cycles of oscillation. Both the event and the odd resonance are excited in the process, and the field distribution eventually converges to the steady state. The weaker the coupling between the two surface resonances, the longer it takes for the field to reach that steady state [3], [6]. This is obvious in Figs. 4 (a) to (c) where the settling of the image amplitude is shown for three spatial harmonics corresponding to transverse wavelengths $\lambda_t = \lambda_0/4, \lambda_0/8,$ *and* $\lambda_0/12$, respectively.

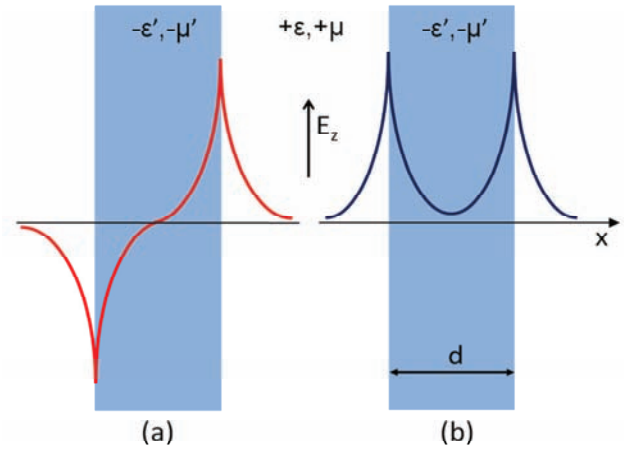


Fig. 3 Odd (a) and even (b) surface polaritons of a thin superlens excited by an evanescent field. The field E_z varies sinusoidally in y-direction (normal to the page). (From [6]).

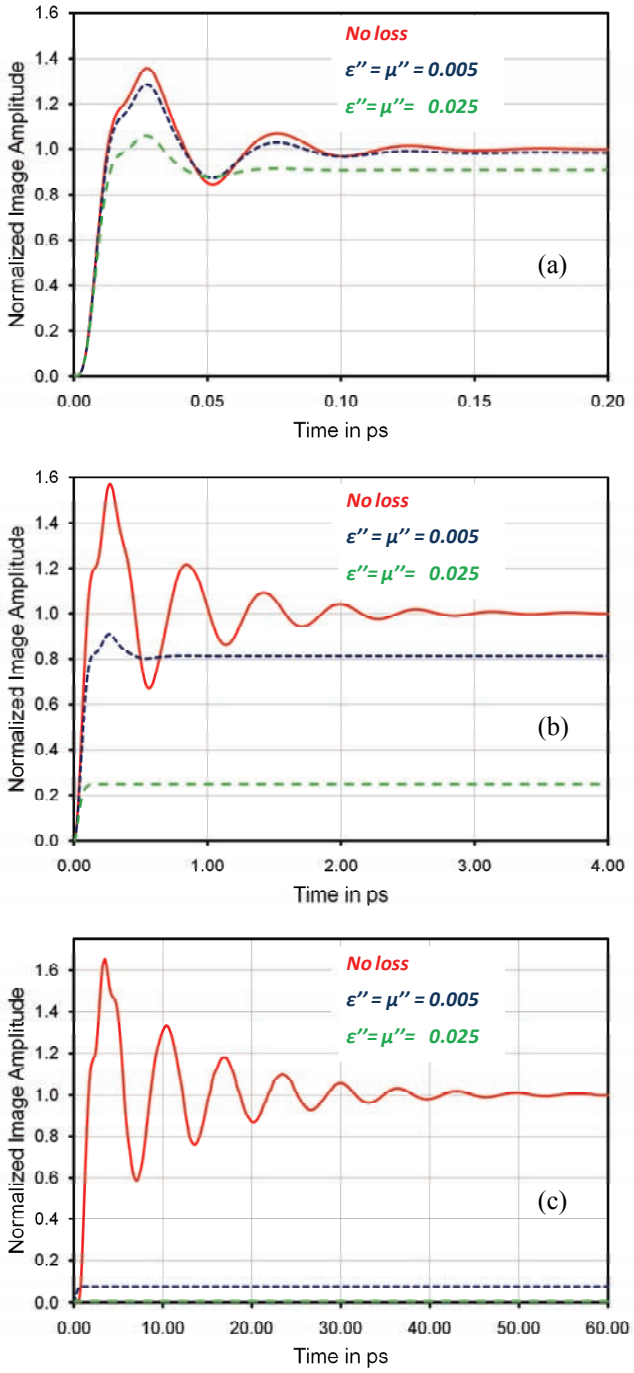


Fig. 4 Transient envelope of the image field transmitted by a superlens without and with losses, for three spatial harmonics: (a) $\lambda_t = \lambda_0/4$, (b) $\lambda_t = \lambda_0/8$, and (c) $\lambda_t = \lambda_0/12$. The other parameters are: *d=38 nm, ε'=1, μ'=1,* λ_0*=400 nm* (From [7]).

If one defines the settling time as the time at which the image field settles within ±1 percent of its steady-state amplitude, the settling time of the evanescent special harmonics increases exponentially with the spectral index p which we define by $\lambda_t = \lambda_0/(4p)$. These harmonics can also be considered as evanescent terms of a spatial Fourier series produced by a periodic array of line sources separated by $\lambda_0/4$. Fig. 5 shows this settling time as a function of the

spectral index p for a lossless superlens. This figure shows that the *5th* spatial harmonic will take about $3x10^{-8}$ *s* to settle, and the *10th* spatial harmonic almost *0.1 s*. This means that the image resolution will never reach perfection, since the finer detail of the image will take an ever longer time to emerge, exceeding two centuries for the *20th* term. Hence, the lens will never reach the steady state condition in the absence of losses. In conclusion the steady state condition is never fulfilled in the lossless superlens.

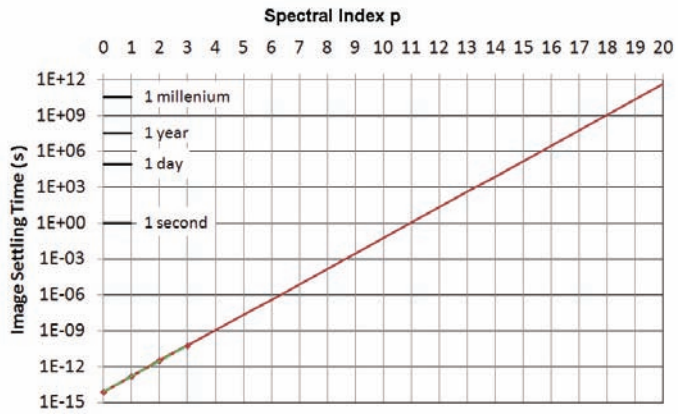


Fig. 5 Typical settling time for higher order terms of the spatial spectrum transmitted by an ideal superlens of *38 nm* thickness at *0.75 PHz* (λ_0*=400 nm).* (From [8]).

If the lens metamaterial is lossy, the settling time is greatly reduced, but so is the transmitted amplitude. The impact of loss on the transmitted image becomes more dramatic as the spectral index increases, and loss is thus, at present, the dominant factor that limits the resolution of the lens. One might think that settling time of the higher spatial terms is not an issue in time-harmonic analysis, and that frequency-domain computational models would thus, in the absence of losses, be able to reach a spatial resolution limited only by the space discretization. However, there is another factor that limits the resolution of time-harmonic computational models. Since higher spectral terms are associated with ever steeper exponential increases of the fields inside the lens, the ratio of fields at the two faces of the lens will at some point exceed the dynamic range of the computer. This is illustrated in Fig. 6. It shows the values of the function $e^{k_x d}$ which characterizes the dynamic range required to process a particular spectral term. k_x is the decay factor of the evanescent term in x-direction. For example, to process the term $p=6$ having a transverse wavelength $\lambda_t = \lambda_0/(6x4) = \lambda_0/24$, a dynamic range of *124.3 dB* is required, which is close to the typical range of a single-precision computer. Hence, only the first six evanescent terms of the spatial spectrum will reach the image plane, even in the lossless time-harmonic superlens models. This dynamic range limitation has indeed been observed in superlens simulations with time-harmonic electromagnetic simulators [6], [8] revealing the limiting effect of dynamic range on superresolution.

Table 1: Dynamic Range required to process the spectral terms inside the superlens.

Spectral term	Dynamic Range ~ $e^{k_x d}$	in dB
1	10.093	20.1
2	114.179	41.2
3	1258.804	62.0
4	13790.982	82.8
5	150711.121	103.6
6	1644951.778	124.3
7	17941204.287	145.1
8	195594550.066	165.8
9	2131734568.742	186.6
10	23228404962.587	207.3
11	253069685308.405	228.1
12	2756841042855.030	248.8
13	30029322551528.000	269.6
14	327076734616112.000	290.3
15	3562296147386820.000	311.0
16	38796370036411100.000	331.8
17	422509301701740000.000	352.5
18	4601169316011820000.000	373.3
19	50105915909485400000.000	394.0
20	545632609920803000000.000	414.7

3. Discussion

In a lossless Veselago/Pendry superlens consisting of double-negative metamaterial the steady-state cannot be reached in finite time. Conclusions based on a lossless time-harmonic model of the superlens must thus be considered with caution. In fact, only a time-domain analysis employing a dynamic model of the lens metamaterial will yield results that are always causal. When losses are present, frequency-domain analysis will give physical results, and the resolution will be reduced due to progressively greater attenuation of the higher spatial frequencies. However, even if one could compensate losses in the material, one would face other limiting factors, such as long settling times of the higher Fourier terms and finite dynamic range of the computer.

4. Conclusions

In this paper the importance of considering the dynamic time response of the superlens was discussed, and two phenomena that limit the achievable resolution were addressed in detail; these are the increasingly large settling times of the higher Fourier terms of the spatial spectrum, and the dynamic range of the computing system. While even small losses tend to overshadow these two issues, the latter become dominant in lossless numerical models of the superlens. Finally, their existence indicates that it is not possible to achieve very high superresolution by simply reducing or compensating losses.

Acknowledgements

The author gratefully acknowledges the support of the Science and Engineering Research Council of Singapore, the A-Star Agency and its Institute of High Performance Computing.

References

[1] Veselago, V. G. "The electrodynamics of substances with simultaneously negative values of ε and μ," *Sov. Phys. Usp.,* vol. 10, no. 4, 509–514, 1967.

[2] Pendry, J. B. "Negative refraction makes a perfect lens," *Phys. Rev. Lett.,* vol. 85, 3966-3969, 2000.

[3] Gomez-Santos, G. "Universal feature of the time evolution modes in the left-handed perfect lens," *Phys. Rev. Lett.,* vol. 90, no. 7, 2003.

[4] Ruppin, R. "Surface polariton of the left-handed medium," *Phys. Lett. A*, vol. 277, 61-64, 2000.

[5] Haldane, F. D. M. "Electromagnetic surface modes at interface with negative refractive index make a 'not-quite-perfect' lens," *Cond. Matt*., 0206420, 2002.

[6] Hor, Y. L., Hegde, R. S., Li, E. P., Hoefer, W. J. R. Transient Study of the Dynamic Response of the Veselago-Pendry Superlens" *in 2011 IEEE MTT-S Intl. Microw. Symp. Dig*., Baltimore, Jun. 5-10, 2011.

[7] Hegde, R., Y. L. Hor, Zs. Szabó, E. P. Li, W. J. R. Hoefer, "Veselago-Pendry Superlens Imaging Modeled with a Spectral Waveguide Approach", *in XXX URSI General Assembly & Scientific Symposium Dig*., paper #DB1.1, Istanbul, Turkey, Aug. 13-20, 2011.

[8] Hegde, R. S., Zs. Szabó, Y. Kiasat, Y. L. Hor, E. P. Li and W. J. R. Hoefer, "The Dynamics of Nanoscale Superresolution Imaging with the Superlens" *IEEE Trans. Microwave Theory Tech., Special Issue on Radio-Frequency Nanoelectronics,* vol. MTT-59, no. 10, pp. 2612-2623, Oct. 2011.

An Electric Field Volume Integral Equation Approach to Simulate Surface Plasmon Polaritons

Rob Remis*, Edoardo Charbon

Circuits and Systems Group
Faculty of Electrical Engineering, Mathematics and Computer Science
Delft University of Technology
Mekelweg 4, 2628 CD Delft
The Netherlands
*corresponding author, E-mail: r.f.remis@tudelft.nl

Abstract

In this paper we present an electric field volume integral equation approach to simulate surface plasmon propagation along metal/dielectric interfaces. Metallic objects embedded in homogeneous dielectric media are considered. Starting point is a so-called weak-form of the electric field integral equation. This form is discretized on a uniform tensor-product grid resulting in a system matrix whose action on a vector can be computed via the fast Fourier transform. The GMRES iterative solver is used to solve the discretized set of equations and numerical examples, illustrating the surface plasmon propagation, are presented. The convergence rate of GMRES is discussed in terms of the spectrum of the system matrix and through numerical experiments we show how the eigenvalues of the discretized volume scattering operator are related to plasmon propagation and the medium parameters of a metallic object.

1. Introduction

While photons and phonons are quanta of energy for light and mechanical vibrations, plasmons result from the quantization of plasma oscillations in a conductor. Plasmons are not elementary particles, like photons, but quasiparticles, like phonons; nonetheless, they can be used to transfer energy and information, when coupled to a photon to create a polariton [1, 2]. Surface plasmon polaritons (SPPs) occur usually at the interface between a dielectric and a conductor [3, 4].

In this paper SPPs are studied, in particular how they form, propagate, and dissipate in a variety of solid-state configurations mimicking the surface of a conventional CMOS structure. The paper outlines how the equations governing SPPs can be derived from Maxwell's equations and it describes the engine simulating SPP transients in details. The goal is to achieve the equivalent of a device simulator for SPPs for guiding researchers in the design process of data processing systems based on SPPs.

It is well known that SPPs can be excited by electromagnetic fields in three dimensions and by H-polarized fields in two dimensions (magnetic field strength parallel to the invariance direction) [4, 5]. Local and global solution methods are available to simulate these SPPs along a variety of metallic objects. In a local method, Maxwell's equations are discretized directly (as in the well known Finite-Difference Time-Domain method), whereas in a global method an integral form of these equations is solved. In this paper we use a global volume integral approach, since we are interested in electromagnetic fields operating in steady-state and electromagnetic field strength unknowns are defined on the scattering domain only. In addition, outward radiation is automatically taken into account via the Green's tensor of the background medium and there is no need to implement any absorbing boundary conditions as is the case in a local method. A global integral equation approach also allows us to analyze plasmon propagation in terms of the spectrum of the volume integral operator.

For three-dimensional electromagnetic fields and for H-polarized fields in two dimensions, the electric field strength satisfies a vectorial volume integral equation containing a gradient-divergence term that takes the effects of induced charges into account. It is well known that this term must be handled with care when discretizing the integral equation [4, 6]. In this paper, we follow the approach proposed, for example, in [6] and approximate the gradient-divergence term by second-order centered finite-differences. Furthermore, the singular Green's function is weakened in a manner that is consistent with the finite-difference approximation error and we make use of the Kronecker product to show that the discretized set of equations has a similar structure as the continuous volume integral operator. Details of the discretization procedure are provided, but to keep the bookkeeping to a minimum, we restrict ourselves to two-dimensional configurations only. Three-dimensional problems can be handled in a similar manner.

This paper is organized as follows. In Section 2, we briefly review the basic integral representation for the scattered electric field strength and formulate an integral equation for the total electric field strength inside the object of interest. This integral equation is discretized in Section 3 and a detailed description of the discretization procedure and the structure of the discretized set of equations is provided. In Section 4 we illustrate the performance of our integral equation solver through a number of numerical ex-

periments in which we simulate surface plasmon propagation along a golden strip and a silver plasmonic waveguide. The discretized set of equations is solved using the Generalized Minimum Residuals (GMRES) iterative solver [7] and a numerical analysis of its convergence rate for plasmonic configurations is presented as well.

2. Basic equations

We consider steady-state H-polarized fields in a two-dimensional configuration that is invariant in the z-direction. A (metallic) object occupies a bounded domain $\mathbb{D}^{\text{obj}}$ in the transverse xy-plane (see Figure 1) and is characterized by a position dependent admittance per unit length $\eta^{\text{s}}(\mathbf{x}) = \sigma^{\text{s}}(\mathbf{x}) + \text{j}\omega\varepsilon^{\text{s}}(\mathbf{x})$ and constant impedance per unit length $\zeta = \text{j}\omega\mu_0$. In these expressions, $\sigma^{\text{s}}(\mathbf{x})$ and $\varepsilon^{\text{s}}(\mathbf{x})$ are the conductivity and the permittivity of the object, respectively, and μ_0 is the permeability of vacuum.

The object is embedded in a homogeneous background medium that is characterized by a constant conductivity σ, permittivity ε, and permeability μ_0. We write the corresponding admittance and impedance per unit length as $\eta = \sigma + \text{j}\omega\varepsilon$ and $\zeta = \text{j}\omega\mu_0$, respectively. Furthermore, the wave number of the background medium is introduced as

$$k_{\text{b}} = (-\eta\zeta)^{1/2} \tag{1}$$

with $\text{Im}(k_{\text{b}}) \leq 0$.

Now let the external sources occupy a bounded domain $\mathbb{D}^{\text{src}}$ with $\mathbb{D}^{\text{src}} \cap \mathbb{D}^{\text{obj}} = \emptyset$ (see Figure 1). To find the electric field strength in and around the object, we make use of the linearity of Maxwell's equations and set up a scattering formalism. Specifically, we first introduce the incident electric field as the field that would be present in our domain of interest if the object was absent. We denote this field by $\mathbf{E}^{\text{inc}}$ and assume that it is known. Second, we take the presence of the object into account by introducing the scattered electric field as $\mathbf{E}^{\text{sc}} = \mathbf{E} - \mathbf{E}^{\text{inc}}$, where $\mathbf{E}$ is the total electric field strength. The scatterer acts as a source for the scattered electric field and it is well known that this field can be found at any point in the transverse plane from the integral representation [8]

$$\mathbf{E}^{\text{sc}}(\mathbf{x}) = (k_{\text{b}}^2 + \boldsymbol{\nabla}\boldsymbol{\nabla}\cdot) \int_{\mathbf{x}' \in \mathbb{D}^{\text{obj}}} G(\mathbf{x} - \mathbf{x}')\chi(\mathbf{x}')\mathbf{E}(\mathbf{x}')\,\text{d}A. \tag{2}$$

In the above equation, G is the Green's function of the homogeneous background medium and is given by

$$G(\mathbf{x}) = -\frac{\text{j}}{4} H_0^{(2)}(k_{\text{b}}|\mathbf{x}|), \tag{3}$$

where $H_0^{(2)}$ is the Hankel function of the second kind and order zero. This function has a logarithmic singularity at the origin [9]. Furthermore,

$$\chi(\mathbf{x}) = \frac{\eta^{\text{s}}(\mathbf{x})}{\eta} - 1, \tag{4}$$

is the contrast function of the object and it obviously vanishes if $\eta^{\text{s}} = \eta$, that is, if there is no object present.

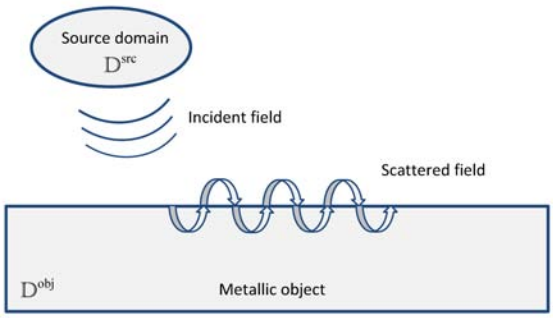


Figure 1: A metallic object illuminated by electromagnetic waves. The object occupies the object domain $\mathbb{D}^{\text{obj}}$. The sources are located in the source domain $\mathbb{D}^{\text{src}}$.

From the integral representation (2) it is clear that the scattered electric field strength is known as soon as the total electric field strength inside the object has been found. To find this total field, we restrict the observation vector $\mathbf{x}$ to the object domain $\mathbb{D}^{\text{obj}}$ and use the definition of the scattered electric field strength to obtain

$$\mathbf{E}(\mathbf{x}) - (k_{\text{b}}^2 + \boldsymbol{\nabla}\boldsymbol{\nabla}\cdot)\mathbf{A}(\mathbf{x}) = \mathbf{E}^{\text{inc}}(\mathbf{x}), \quad \mathbf{x} \in \mathbb{D}^{\text{obj}}, \tag{5}$$

where we have introduced the vector potential $\mathbf{A}$ as

$$\mathbf{A}(\mathbf{x}) = \int_{\mathbf{x}' \in \mathbb{D}^{\text{obj}}} G(\mathbf{x} - \mathbf{x}')\chi(\mathbf{x}')\mathbf{E}(\mathbf{x}')\,\text{d}A. \tag{6}$$

Equation (5) is an integral equation for the total electric field strength inside the scattering object. Written out in components, this equation becomes

$$E_x(\mathbf{x}) - k_{\text{b}}^2 A_x(\mathbf{x}) - \partial_x\partial_y A_y(\mathbf{x}) - \partial_x^2 A_x(\mathbf{x}) = E_x^{\text{inc}}(\mathbf{x}), \tag{7}$$

and

$$E_y(\mathbf{x}) - k_{\text{b}}^2 A_y(\mathbf{x}) - \partial_y\partial_x A_x(\mathbf{x}) - \partial_y^2 A_y(\mathbf{x}) = E_y^{\text{inc}}(\mathbf{x}), \tag{8}$$

with $\mathbf{x} \in \mathbb{D}^{\text{obj}}$. As mentioned above, by solving the above integral equation for the electric field strength, we have essentially solved the complete scattering problem, since the scattered field at any point in the transverse plane can then be found using the integral representation of Eq. (2).

2.1. The contrast function for metallic objects

For metallic objects, it is customary to use the relative complex permittivity ε_{r} as a constitutive parameter. Writing this parameter in terms of its real and imaginary part as

$$\hat{\varepsilon}_{\text{r}} = \varepsilon_1 - \text{j}\varepsilon_2, \tag{9}$$

where ε_1 and ε_2 are real-valued, we have

$$\sigma^{\text{s}} = \omega\varepsilon_0\varepsilon_2, \quad \varepsilon^{\text{s}} = \varepsilon_0\varepsilon_1, \quad \text{and} \quad \eta^{\text{s}} = \omega\varepsilon_0(\varepsilon_2 + \text{j}\varepsilon_1). \tag{10}$$

Now if the background medium is vacuum, we have $\eta = \mathrm{j}\omega\varepsilon_0$ and the contrast function becomes

$$\chi = \varepsilon_1 - 1 - \mathrm{j}\varepsilon_2, \tag{11}$$

showing that the contrast is simply a shifted version of the relative permittivity of the metal.

3. Discretizing the Integral Equation

Let the object occupy a rectangular domain with side length $\ell_x > 0$ in the x-direction and a side length $\ell_y > 0$ in the y-direction. Furthermore, let the origin $\mathcal{O}$ of our reference frame coincide with the upper left corner of our scattering domain. We introduce the grid coordinates

$$x_m = \frac{\delta x}{2} + m\delta x \quad \text{for } m = 0, 1, ..., M+1, \tag{12}$$

with $\delta x = \ell_x/(M+2)$, and

$$y_n = \frac{\delta y}{2} + n\delta y \quad \text{for } n = 0, 1, ..., N+1, \tag{13}$$

with $\delta y = \ell_y/(N+2)$. Notice that $x_0 = \delta x/2$, $x_{M+1} = \ell_x - \delta x/2$, $y_0 = \delta y/2$, and $y_{N+1} = \ell_y - \delta y/2$.

The scattering domain is divided into nonoverlapping discretization cells

$$\mathbb{S}_{i,j} = \{i\delta x < x < (i+1)\delta x, j\delta y < y < (j+1)\delta y\}, \tag{14}$$

for $i = 0, 1, ..., M+1$ and $j = 0, 1, ..., N+1$. Obviously, the total number of discretization cells is $(M+2)(N+2)$. The position vector of the midpoint of cell $\mathbb{S}_{i,j}$ is denoted by

$$\mathbf{x}_{i,j} = x_i\mathbf{i}_x + y_j\mathbf{i}_y,$$

for $i = 0, 1, ..., M+1$ and $j = 0, 1, ..., N+1$.

As a first step in the discretization procedure, we require that Eqs. (7) and (8) hold for all grid points within the scattering domain with position vectors $\mathbf{x}_{m,n}$, where $m = 1, 2, ..., M$ and $n = 1, 2, ..., N$. Consequently, we have

$$E_x(\mathbf{x}_{m,n}) - k_\mathrm{b}^2 A_x(\mathbf{x}_{m,n}) - \partial_x\partial_y A_y \,|_{\mathbf{x}=\mathbf{x}_{m,n}} - \partial_x^2 A_x \,|_{\mathbf{x}=\mathbf{x}_{m,n}} = E_x^{\mathrm{inc}}(\mathbf{x}_{m,n}), \tag{15}$$

and

$$E_y(\mathbf{x}_{m,n}) - k_\mathrm{b}^2 A_y(\mathbf{x}_{m,n}) - \partial_y\partial_x A_x \,|_{\mathbf{x}=\mathbf{x}_{m,n}} - \partial_y^2 A_y \,|_{\mathbf{x}=\mathbf{x}_{m,n}} = E_y^{\mathrm{inc}}(\mathbf{x}_{m,n}), \tag{16}$$

for $m = 1, 2, ..., M$ and $n = 1, 2, ..., N$. Notice that the discretization cells located at the outer boundary are not included. These cells are used as dummy cells to properly handle the discretization of the gradient-divergence term (see Subsection 3.1).

As a second step, we approximate the spatial derivatives in Eqs. (15) and (16) by second-order centered finite-differences. For example, the mixed derivative term $\partial_x\partial_y A_y \,|_{\mathbf{x}=\mathbf{x}_{m,n}}$ is approximated as

$$\partial_x\partial_y A_y \,|_{\mathbf{x}=\mathbf{x}_{m,n}} \approx \frac{A_y(\mathbf{x}_{m+1,n+1}) - A_y(\mathbf{x}_{m+1,n-1})}{4\delta x\delta y} - \frac{A_y(\mathbf{x}_{m-1,n+1}) - A_y(\mathbf{x}_{m-1,n-1})}{4\delta x\delta y} \tag{17}$$

and for the double derivative term (one-dimensional Laplacian) in the x-direction, we have

$$\partial_x^2 A_x \,|_{\mathbf{x}=\mathbf{x}_{m,n}} \approx \frac{A_x(\mathbf{x}_{m-1,n}) - 2A_x(\mathbf{x}_{m,n}) + A_x(\mathbf{x}_{m+1,n})}{\delta x^2}. \tag{18}$$

Similar finite-difference expressions are used for $\partial_y\partial_x A_x$ and $\partial_y^2 A_y$ at $\mathbf{x} = \mathbf{x}_{m,n}$.

All these local finite-difference approximations can be written in a more compact global form by introducing a number of field and differentiation matrices. Specifically, let us introduce the $(M+2)$-by-$(N+2)$ electric field matrices E_x and E_y with elements

$$(\mathsf{E}_x)_{m,n} = E_x(\mathbf{x}_{m-1,n-1}) \tag{19}$$

and

$$(\mathsf{E}_y)_{m,n} = E_y(\mathbf{x}_{m-1,n-1}) \tag{20}$$

for $m = 1, 2, ..., M+2$ and $n = 1, 2, ..., N+2$. Incident electric field matrices $\mathsf{E}_x^{\mathrm{inc}}$ and $\mathsf{E}_y^{\mathrm{inc}}$ are defined similarly. In addition, we introduce the vector potential matrices A_x and A_y with elements

$$(\mathsf{A}_x)_{m,n} = A_x(\mathbf{x}_{m-1,n-1}) \tag{21}$$

and

$$(\mathsf{A}_y)_{m,n} = A_y(\mathbf{x}_{m-1,n-1}) \tag{22}$$

for $m = 1, 2, ..., M+2$ and $n = 1, 2, ..., N+2$.

Differentiation in the x-direction is carried out by the M-by-$(M+2)$ differentiation matrices

$$\mathsf{X} = \frac{1}{2\delta x}\mathrm{tridiag}(-1, 0, 1)$$

and

$$\mathsf{L}_x = \frac{1}{\delta x^2}\mathrm{tridiag}(1, -2, 1)$$

while the N-by-$(N+2)$ matrices

$$\mathsf{Y} = \frac{1}{2\delta y}\mathrm{tridiag}(-1, 0, 1)$$

and

$$\mathsf{L}_y = \frac{1}{\delta y^2}\mathrm{tridiag}(1, -2, 1)$$

take care of differentiation in the y-direction. The first entry between the brackets in the above equations corresponds to a diagonal element.

Finally, we introduce the N-by-$(N+2)$ restriction matrix

$$\mathsf{R}_N = \begin{pmatrix} 0 & \mathsf{I}_N & 0 \end{pmatrix},$$

where I_N is the identity matrix of order N.

With the introduction of all these matrices, we can write the finite-difference approximation of Eqs. (15) and (16) in global form as

$$\mathsf{R}_M \mathsf{E}_x \mathsf{R}_N^T - k_\mathrm{b}^2 \mathsf{R}_M \mathsf{A}_x \mathsf{R}_N^T - \mathsf{X} \mathsf{A}_y \mathsf{Y}^T - \mathsf{L}_x \mathsf{A}_x \mathsf{R}_N^T = \mathsf{E}_x^{\mathrm{inc}} \tag{23}$$

and

$$\mathsf{R}_M \mathsf{E}_y \mathsf{R}_N^T - k_\mathrm{b}^2 \mathsf{R}_M \mathsf{A}_y \mathsf{R}_N^T - \mathsf{X} \mathsf{A}_x \mathsf{Y}^T - \mathsf{R}_M \mathsf{A}_y \mathsf{L}_y^T = \mathsf{E}_y^{\mathrm{inc}}, \tag{24}$$

respectively.

As a final step, we turn these equations into matrix-vector form by applying the vec-operation to both equations. Recall that for a given matrix A, $\mathrm{vec}(\mathsf{A})$ stacks the columns of matrix A from left to right into a single column vector [10]. Using this operation, we first introduce the vectors

$$\mathsf{e}_x = \mathrm{vec}(\mathsf{E}_x), \qquad \mathsf{e}_y = \mathrm{vec}(\mathsf{E}_y), \tag{25}$$

$$\mathsf{e}_x^{\mathrm{inc}} = \mathrm{vec}(\mathsf{E}_x^{\mathrm{inc}}), \quad \mathsf{e}_y^{\mathrm{inc}} = \mathrm{vec}(\mathsf{E}_y^{\mathrm{inc}}), \tag{26}$$

and

$$\mathsf{a}_x = \mathrm{vec}(\mathsf{A}_x) \quad \text{and} \quad \mathsf{a}_y = \mathrm{vec}(\mathsf{A}_y). \tag{27}$$

Applying now the vec-operation to Eqs. (23) and (24) separately, using the linearity of this operator, and the property [10]

$$\mathrm{vec}(\mathsf{A}\mathsf{X}\mathsf{B}^T) = (\mathsf{B} \otimes \mathsf{A})\mathrm{vec}(\mathsf{X}),$$

where $\otimes$ denotes the Kronecker (tensor) product, we arrive at

$$\mathsf{R}\mathsf{e}_x - k_\mathrm{b}^2 \mathsf{R}\mathsf{a}_x - (\mathsf{Y} \otimes \mathsf{X})\mathsf{a}_y - (\mathsf{R}_N \otimes \mathsf{L}_x)\mathsf{a}_x = \mathsf{e}_x^{\mathrm{inc}}, \tag{28}$$

and

$$\mathsf{R}\mathsf{e}_y - k_\mathrm{b}^2 \mathsf{R}\mathsf{a}_y - (\mathsf{Y} \otimes \mathsf{X})\mathsf{a}_x - (\mathsf{L}_y \otimes \mathsf{R}_N)\mathsf{a}_y = \mathsf{e}_y^{\mathrm{inc}}, \tag{29}$$

where $\mathsf{R} = \mathsf{R}_N \otimes \mathsf{R}_M$. The only thing left to do now, is to relate the vector potentials a_x and a_y to the electric field strengths e_x and e_y using the definition of the vector potential.

3.1. Weak form of the vector potential and its discretization

With $\mathbf{x} \in \mathbb{D}^{\mathrm{obj}}$, the expression for the vector potential cannot be discretized using standard Newton-Cotes quadrature formulas, because of the logarithmic singularity of the Green's function. Our approach is, therefore, to first weaken the Green's function such that this weakening is consistent with the second-order finite-difference discretization procedure discussed above [6]. In particular, we introduce the weakened Green's function G^{w} that satisfies

$$(\partial_x^2 + \partial_y^2 + k_\mathrm{b}^2) G^{\mathrm{w}} = -f(\mathbf{x}), \tag{30}$$

and the radiation condition at infinity. The right-hand side $f(\mathbf{x})$ is given by

$$f(\mathbf{x}) = \begin{cases} \dfrac{1}{\pi a^2} & \text{if } \mathbf{x} \in \mathbb{D}^{\mathrm{circ}}, \\ 0 & \text{if } \mathbf{x} \notin \mathbb{D}^{\mathrm{circ}}, \end{cases}$$

where $\mathbb{D}^{\mathrm{circ}}$ is a circular disk with radius $a = \frac{1}{2}\min\{\delta x, \delta y\}$ and centered at the origin. Clearly, f satisfies

$$\int_{\mathbf{x} \in \mathbb{R}^2} f(\mathbf{x})\, \mathrm{d}A = \frac{1}{\pi a^2} \int_{\mathbf{x} \in \mathbb{D}^{\mathrm{circ}}} \mathrm{d}A = 1,$$

and G^{w} approaches the original Green's function G as $a \downarrow 0$.

Replacing now the original Green's function by its weakened counterpart, we have

$$\mathbf{A}(\mathbf{x}) \approx \int_{\mathbf{x}' \in \mathbb{D}^{\mathrm{obj}}} G^{\mathrm{w}}(\mathbf{x} - \mathbf{x}') \chi(\mathbf{x}') \mathbf{E}(\mathbf{x}')\, \mathrm{d}A \tag{31}$$

and the expression on the right-hand side of the above equation is used to approximate the vector potential at the grid nodes with position vectors $\mathbf{x} = \mathbf{x}_{m,n}$.

To this end, we consider

$$\mathbf{A}(\mathbf{x}_{m,n}) \approx \int_{\mathbf{x}' \in \mathbb{D}^{\mathrm{obj}}} G^{\mathrm{w}}(\mathbf{x}_{m,n} - \mathbf{x}') \chi(\mathbf{x}') \mathbf{E}(\mathbf{x}')\, \mathrm{d}A, \tag{32}$$

for $m = 0, 1, ..., M+1$ and $n = 0, 1, ..., N+1$. Subsequently, we restrict ourselves to piecewise constant contrast functions for which χ is constant within each discretization cell. Writing

$$\chi(\mathbf{x}) = \chi_{i,j} \quad \text{if } \mathbf{x} \in \mathbb{S}_{i,j}, \tag{33}$$

where $\chi_{i,j}$ is position independent, we obtain

$$\mathbf{A}(\mathbf{x}_{m,n}) \approx \sum_{i=0}^{M+1} \sum_{j=0}^{N+1} \chi_{i,j} \int_{\mathbf{x}' \in \mathbb{S}_{i,j}} G^{\mathrm{w}}(\mathbf{x}_{m,n} - \mathbf{x}') \mathbf{E}(\mathbf{x}')\, \mathrm{d}A, \tag{34}$$

for $m = 0, 1, ..., M+1$ and $n = 0, 1, ..., N+1$. Finally, we approximate the remaining integral over the discretization cell using the midpoint rule and arrive at

$$\mathbf{A}(\mathbf{x}_{m,n}) \approx \delta x \delta y \sum_{i=0}^{M+1} \sum_{j=0}^{N+1} G^{\mathrm{w}}(\mathbf{x}_{m,n} - \mathbf{x}_{i,j}) \chi_{i,j} \mathbf{E}(\mathbf{x}_{i,j}), \tag{35}$$

for $m = 0, 1, ..., M+1$ and $n = 0, 1, ..., N+1$. Notice that the vector potential approximations are required at grid nodes with indices running from $m = 0$ to $m = M+1$ and $n = 0$ to $n = N+1$. The summations in Eq. (35) run from $i = 0$ to $M+1$ and from $j = 0$ to $j = N+$

1 as well. The electric field strength unknowns $\mathbf{E}(\mathbf{x}_{m,n})$, however, are defined at grid node coordinates $\mathbf{x} = \mathbf{x}_{m,n}$ with $m = 1, 2, ..., M$ and $n = 1, 2, ..., N$. To relate the vector potential to these electric field strength unknowns only, we always set the contrast to zero at the outer cells of the computational domain, that is, we set

$$\chi_{0,n} = 0 \quad \text{and} \quad \chi_{M+1,n} = 0 \tag{36}$$

for $n = 0, 1, ..., N + 1$, and

$$\chi_{m,0} = 0 \quad \text{and} \quad \chi_{m,N+1} = 0 \tag{37}$$

for $m = 1, ..., M$. Equation (35) can then equivalently be written as

$$\mathbf{A}(\mathbf{x}_{m,n}) \approx \delta x \delta y \sum_{i=1}^{M} \sum_{j=1}^{N} G^{\mathrm{w}}(\mathbf{x}_{m,n} - \mathbf{x}_{i,j}) \chi_{i,j} \mathbf{E}(\mathbf{x}_{i,j}), \tag{38}$$

for $m = 0, 1, ..., M + 1$ and $n = 0, 1, ..., N + 1$. However, to evaluate the vector potential values at the grid nodes we do not use Eq. (38), but follow an embedding procedure and implement Eq. (35) with the contrast at the boundaries set to zero. The electric field strength quantities at the outer cells then become redundant dummy variables, but the advantage of keeping these extra variables is that all approximate vector potential values can be computed very efficiently by evaluating Eq. (35) via two-dimensional FFTs. This is not possible if we use Eq. (38) to evaluate the vector potential at the required grid nodes.

From Eq. (35), we observe that the weakened Green's function is required at grid nodes outside the circular disk $\mathbb{D}^{\mathrm{circ}}$ and at the origin. To find these function values, we return to Eq. (30). The solution of this equation is given by

$$\begin{aligned} G^{\mathrm{w}}(\mathbf{x}) &= \frac{1}{\pi a^2} \int_{\mathbf{x}' \in \mathbb{D}^{\mathrm{circ}}} G(\mathbf{x} - \mathbf{x}') \, \mathrm{d}A \\ &= -\frac{\mathrm{j}}{4\pi a^2} \int_{\mathbf{x}' \in \mathbb{D}^{\mathrm{circ}}} H_0^{(2)}(k_{\mathrm{b}} |\mathbf{x} - \mathbf{x}'|) \, \mathrm{d}A \end{aligned} \tag{39}$$

and evaluating the integral for $\mathbf{x} \notin \mathbb{D}^{\mathrm{circ}}$, we find (see Appendix A)

$$G^{\mathrm{w}}(\mathbf{x}) = -\frac{\mathrm{j}}{2k_{\mathrm{b}}a} J_1(k_{\mathrm{b}}a) H_0^{(2)}(k_{\mathrm{b}}|\mathbf{x}|), \tag{40}$$

where J_1 is the first-order Bessel function of the first kind. Notice that the above expression for the weakened Green's function is just a scaled version of the original Green's function. To show that this scaling is consistent with the second-order finite-difference approximations of Eqs. (17) and (18), we use the series expansion of $J_1(k_{\mathrm{b}}a)$ around zero [9] and obtain

$$\begin{aligned} &G^{\mathrm{w}}(\mathbf{x}) = \\ &-\frac{\mathrm{j}}{2k_{\mathrm{b}}a} \left[\frac{k_{\mathrm{b}}a}{2} - \frac{(k_{\mathrm{b}}a)^3}{16} + \frac{(k_{\mathrm{b}}a)^5}{384} - ... \right] H_0^{(2)}(k_{\mathrm{b}}|\mathbf{x}|) = \\ &-\frac{\mathrm{j}}{4} H_0^{(2)}(k_{\mathrm{b}}|\mathbf{x}|) \left\{ 1 + O[(k_{\mathrm{b}}a)^2] \right\} \quad \text{as } k_{\mathrm{b}}a \downarrow 0, \end{aligned}$$

showing that the weakening procedure is indeed consistent with the second-order finite-difference discretization procedure.

Finally, at the origin the integral evaluates to (see Appendix A)

$$G^{\mathrm{w}}(\mathbf{0}) = -\frac{\mathrm{j}}{2k_{\mathrm{b}}a} \left[H_1^{(2)}(k_{\mathrm{b}}a) - \frac{2\mathrm{j}}{\pi k_{\mathrm{b}}a} \right] \tag{41}$$

and we call this weakened Green's function value the self patch element.

With this result, we have completely determined the discretized vector potential operator of Eq. (35). To write this operator in matrix-vector notation, we introduce the contrast vector c and contrast matrix C as

$$\mathsf{c} = \mathrm{vec}(\chi_{i,j}) \quad \text{and} \quad \mathsf{C} = \mathrm{diag}(\mathsf{c}). \tag{42}$$

In addition, we introduce the matrices $\tilde{\mathsf{G}}_{j,n}$, $j, n = 0, 1, ..., N + 1$, of order $M + 2$ with elements

$$\left(\tilde{\mathsf{G}}_{j,n} \right)_{i,m} = \delta x \delta y \, G^{\mathrm{w}}(\mathbf{x}_{m,n} - \mathbf{x}_{i,j}), \tag{43}$$

for $i, m = 0, 1, ..., M + 1$. With the introduction of these matrices, we can write

$$\mathsf{a}_x = \mathsf{G}\mathsf{C}\mathsf{e}_x \quad \text{and} \quad \mathsf{a}_y = \mathsf{G}\mathsf{C}\mathsf{e}_y, \tag{44}$$

where matrix G is given by

$$\mathsf{G} = \begin{pmatrix} \tilde{\mathsf{G}}_{0,0} & \tilde{\mathsf{G}}_{0,1} & ... & \tilde{\mathsf{G}}_{0,N+1} \\ \tilde{\mathsf{G}}_{1,0} & \tilde{\mathsf{G}}_{1,1} & ... & \tilde{\mathsf{G}}_{1,N+1} \\ \vdots & \vdots & & \vdots \\ \tilde{\mathsf{G}}_{N+1,0} & \tilde{\mathsf{G}}_{N+1,1} & ... & \tilde{\mathsf{G}}_{N+1,N+1} \end{pmatrix}. \tag{45}$$

Using Eq. (43), it is easily verified that matrix G is block Toeplitz and each block is Toeplitz as well (matrix G is a so-called Block-Toeplitz Toeplitz-Block or BTTB matrix). This implies that its action on a vector can be computed via two-dimensional FFTs. Furthermore, matrix G is symmetric (but not Hermitian) and all self patch elements are located on the diagonal.

Substituting Eq. (44) in Eqs. (28) and (29), we arrive at the system of equations

$$\mathsf{K}\mathsf{u} = \mathsf{u}^{\mathrm{inc}}, \tag{46}$$

where the system matrix is given by

$$\begin{aligned} \mathsf{K} = &\begin{pmatrix} \mathsf{R}(\mathsf{I} - k_{\mathrm{b}}^2 \mathsf{G}\mathsf{C}) & \mathsf{0} \\ \mathsf{0} & \mathsf{R}(\mathsf{I} - k_{\mathrm{b}}^2 \mathsf{G}\mathsf{C}) \end{pmatrix} \\ &- \begin{pmatrix} \mathsf{R}_N \otimes \mathsf{L}_x & \mathsf{Y} \otimes \mathsf{X} \\ \mathsf{Y} \otimes \mathsf{X} & \mathsf{L}_y \otimes \mathsf{R}_M \end{pmatrix} \begin{pmatrix} \mathsf{G}\mathsf{C} & \mathsf{0} \\ \mathsf{0} & \mathsf{G}\mathsf{C} \end{pmatrix} \end{aligned} \tag{47}$$

and the field vectors are given by

$$\mathsf{u} = \begin{pmatrix} \mathsf{e}_x \\ \mathsf{e}_y \end{pmatrix} \quad \text{and} \quad \mathsf{u}^{\mathrm{inc}} = \begin{pmatrix} \mathsf{e}_x^{\mathrm{inc}} \\ \mathsf{e}_y^{\mathrm{inc}} \end{pmatrix}. \tag{48}$$

Since the action of matrix K on a vector can be computed efficiently via FFTs, we solve Eq. (46) using an iterative method such as GMRES or BiCGStab [7].



Figure 2: Line source located next to a golden strip.

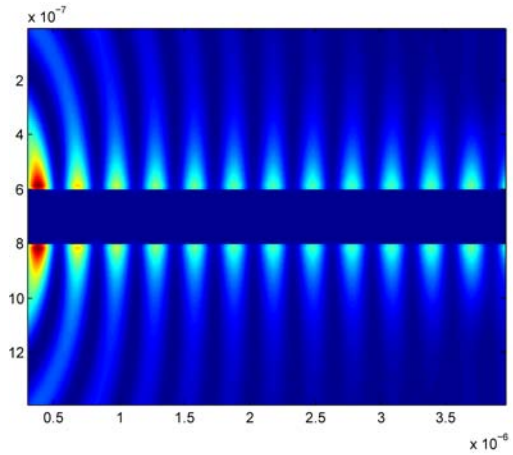


Figure 3: Snapshot of the instantaneous magnitude of the electric field strength in and around the golden strip.

4. Simulations

To illustrate the performance of our integral equation approach, we present two numerical experiments in which we simulate surface plasmon propagation. In both examples, the electromagnetic field is computed by iteratively solving Eq. (46) using the GMRES algorithm [7]. This algorithm takes an initial guess u_0 as input and generates field approximations u_1, u_2, ..., such that the Euclidean norm of the corresponding residual

$$\mathsf{r}_n = \mathsf{u}^{\text{inc}} - \mathsf{K}\mathsf{u}_n, \quad n = 1, 2, ..., \tag{49}$$

is minimized at every iteration. In our numerical experiments, we take $\mathsf{u}_0 = 0$ as an initial guess leading to an initial residual $\mathsf{r}_0 = \mathsf{u}^{\text{inc}}$. Iterations are terminated as soon as the normalized Euclidean norm of the residual $\|\mathsf{r}_n\|/\|\mathsf{r}_0\|$ falls below a user specified tolerance.

As a first example, we compute the electromagnetic field in and around a golden strip (see Figure 2). The strip is illuminated from the left by electromagnetic waves that are generated by a line source operating in steady-state at a frequency of $4.73 \cdot 10^{14}$ Hz ($\lambda = 633$ nm). The complex relative permittivity of gold is $\varepsilon_{\text{r}} = -11.6 - 1.2\text{j}$ at this frequency and the iteration process is terminated as soon as the normalized residual falls below 10^{-6}. A snapshot of the instantaneous magnitude of the electric field strength is shown in Figure 3 and the convergence history of GMRES is shown in Figure 4. We observe that initially there is a fairly sharp drop in the norm of the residual, but convergence slows down to a steady rate of decrease as GMRES

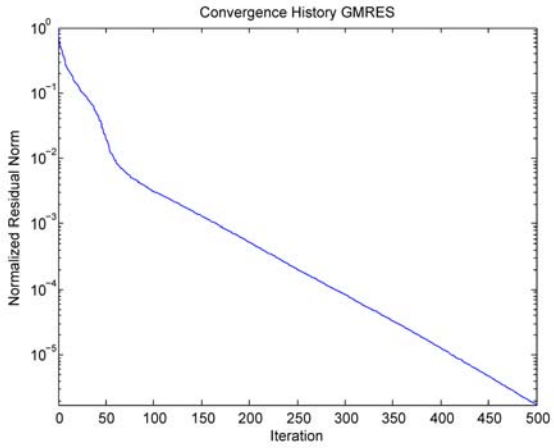


Figure 4: Convergence history of GMRES for the golden strip problem.

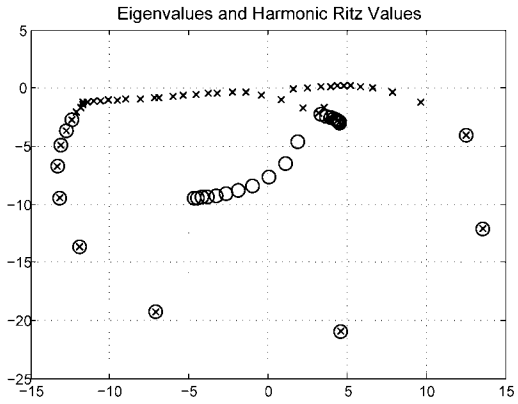


Figure 5: The first 30 eigenvalues of the system matrix with the smallest imaginary part (circles) and the first 50 harmonic Ritz values (crosses) for the golden strip problem.

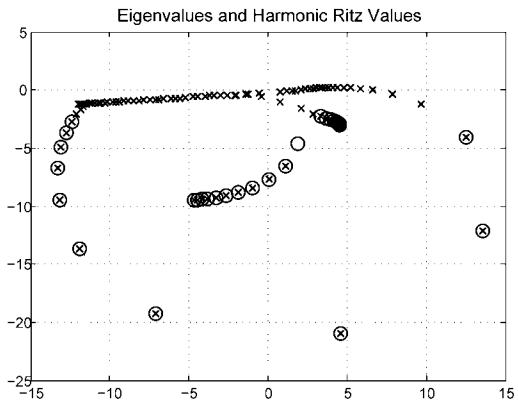


Figure 6: The first 30 eigenvalues of the system matrix with the smallest imaginary part (circles) and the first 100 harmonic Ritz values (crosses) for the golden strip problem.

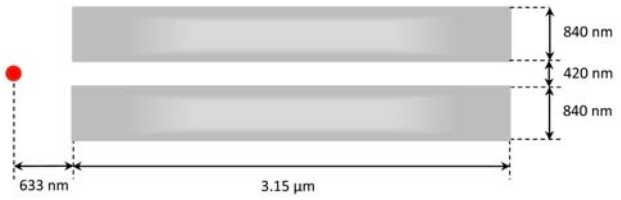


Figure 7: Line source located next to a plasmonic waveguide consisting of two silver strips.

proceeds (after about 50 iterations in the above example). To study this effect, we first recall that GMRES constructs field approximations u_k such that [7]

$$\|\mathsf{r}_k\| = \min_{p_k \in \mathcal{P}_k; p_k(0)=1} \|p_k(\mathsf{K})\mathsf{r}_0\|, \tag{50}$$

where $\mathcal{P}_k$ is the set of polynomials of degree $\leq k$. In other words, of all polynomials p_k belonging to $\mathcal{P}_k$ and normalized such that $p_k(0) = 1$, GMRES constructs the polynomial for which $\|p_k(\mathsf{K})\mathsf{r}_0\|$ is minimum. The roots of this optimal polynomial are called harmonic Ritz values [11] and approximate the eigenvalues of the system matrix K. We have computed these eigenvalue estimates after 50 and 100 iterations of the GMRES algorithm. We also computed the first 30 eigenvalues of the system matrix with the smallest imaginary part. These eigenvalues are shown as circles in Figures 5 and 6. In Figure 5, the crosses show the first 50 harmonic Ritz values obtained after 50 GMRES iterations, while the first 100 harmonic Ritz values are shown as crosses in Figure 6. From these figures, we observe that the harmonic Ritz values cluster along curves in the complex plane. Eigenvalues of banded Toeplitz matrices are known to have this property [11], but here we have a full BTTB-type matrix. Also note that the leftmost point of the upperleft spectral line corresponds to the complex relative permittivity $\varepsilon_{\mathrm{r}} = -11.6 - 1.2\mathrm{j}$ of the golden strip (see Figures 5 and 6). Finally, we observe that GMRES quickly approximates the eigenvalues located at the outer boundary of the spectrum as is typical for Krylov subspace methods [11]. The inner eigenvalues are approximated as GMRES proceeds and the harmonic Ritz values start to cluster along curves in the complex plane. Convergence slows down to a steady rate of decrease as soon as GMRES starts "filling" these curves.

In our second set of experiments, we consider a plasmonic waveguide consisting of two silver strips and an air gap (see Figure 7). The same source as in the previous example is placed to the left of the waveguide and it again operates at a wavelength of 633 nm. The complex relative permittivity of silver at this frequency is $\varepsilon_{\mathrm{r}} = -18.2 - 0.5\mathrm{j}$ [4]. Since the total waveguiding structure consists of air and silver and since the contrast function of silver has a larger absolute real part and a smaller absolute imaginary part (smaller losses) compared with gold, we expect that our solver converges at a slower rate than in the previous example. Figure 8 shows that this is indeed the case. After 750

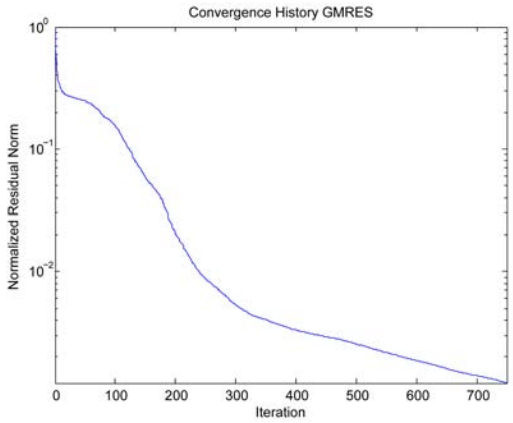


Figure 8: Convergence history of GMRES for the plasmonic waveguide problem.

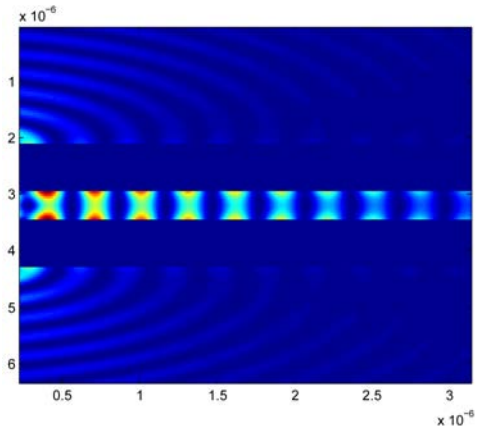


Figure 9: Snapshot of the instantaneous magnitude of the electric field strength in and around the plasmonic waveguide after 100 GMRES iterations.

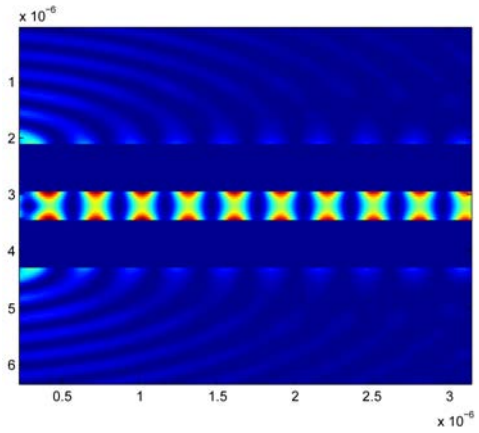


Figure 10: Snapshot of the instantaneous magnitude of the electric field strength in and around the plasmonic waveguide after 500 GMRES iterations.

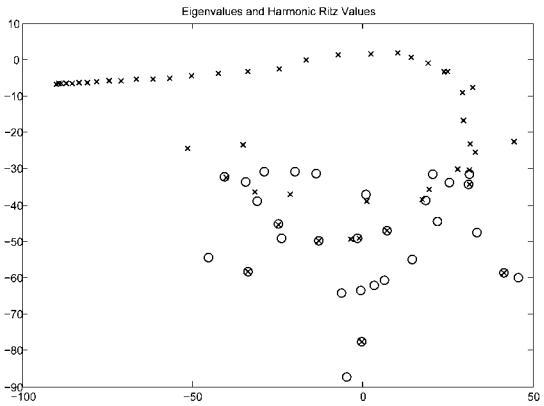


Figure 11: The first 30 eigenvalues of the system matrix with the smallest imaginary part (circles) and the first 50 harmonic Ritz values (crosses) for the plasmonic waveguide problem.

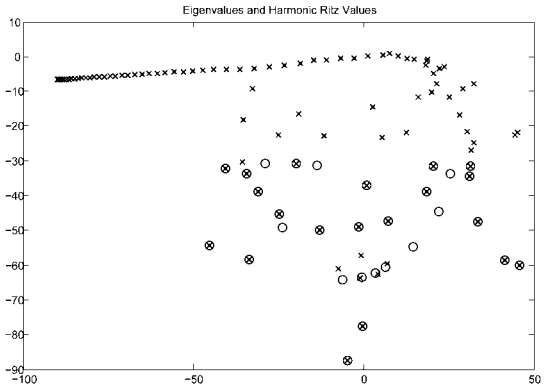


Figure 12: The first 30 eigenvalues of the system matrix with the smallest imaginary part (circles) and the first 100 harmonic Ritz values (crosses) for the plasmonic waveguide problem.

GMRES iterations, the normalized residual has dropped to $1.73 \cdot 10^{-3}$, while for the golden strip problem 500 iterations are sufficient to obtain a normalized residual that falls below 10^{-6}.

To illustrate how the field approximations improve as iteration proceeds, we show in Figures 9 and 10 snapshots of the magnitude of the electric field strength in and around the waveguide. Figure 9 shows the approximate electric field strength obtained after 100 iterations, while Figure 10 shows the approximate field obtained after 500 iterations. Comparing both figures, we observe that as the number of iterations increases, improvements go from left to right, that is, from the source (left-hand side of Figures 9 and 10) to the far end of the waveguide (right-hand side of Figures 9 and 10). The plasmonic wave is built up along the waveguide as iteration proceeds.

The first 30 eigenvalues of the system matrix with the smallest imaginary part have also been computed for this waveguide problem (circles in Figures 11 and 12) along with the harmonic Ritz values obtained after 50 and 100 iterations of GMRES (crosses in Figures 11 and 12, respectively). Again, we observe that eigenvalues at the outer boundary of the spectrum are approximated first, although after 50 iterations GMRES misses an extremal eigenvalue (see Figure 11). Furthermore, the harmonic Ritz values again cluster along curves in the complex plane. As opposed to the previous example, it is now difficult to recognize any material parameter values from the spectral curves in the complex plane, since the total scattering object is now inhomogeneous. The spectral analyses of this section do seem to indicate, however, that the clustering of harmonic Ritz values along curves may provide a spectral explanation of how a plasmonic wave along a metal/dielectric interface is approximated by an iterative solver such as GMRES.

5. Conclusions

In this paper, we have discussed a volume integral equation method to simulate propagation of surface plasmon polaritons in media that mimic the silicon-to-silicon dioxide interface on standard CMOS integrated circuits. We started from Maxwell's equations and formulated an integral equation for the electric field strength which contains a gradient-divergence term that takes the induces charges into account. The discretization of the integral equation was discussed in detail and by formulating the discretized set of equations in terms of Kronecker products, it was shown that the discretized system matrix has a similar structure as the continuous volume scattering operator. Moreover, the action of the system matrix on a vector can be computed via FFTs and we therefore used GMRES to iteratively solve the discretized integral equation. The convergence rate of the algorithm was discussed in detail, while numerical examples illustrated surface plasmon generation, propagation, and decay in different media.

Even though the simulator efficiently solves practical surface plasmon problems, we can still further improve its performance by preconditioning the discretized integral equation. Future work will focus on the development of an effective preconditioner. This may be beneficial in particular for surface plasmon simulations in electrically large geometries (geometries with a spatial extent in the order of, say, a hundred wavelengths). The eigenvalue analysis presented in this paper may then be helpful, since knowledge about the spectrum or pseudospectrum of the system matrix may provide us a means to construct an effective preconditioner [11].

We believe that the simulator presented in this paper is a practical and efficient tool to simulate surface plasmons and is especially useful to guide optimization of CMOS processes and geometries for plasmonics based data and energy transfer and miniaturization.

A. Explicit expression for the weak Green's function

To evaluate the integral in Eq. (39), we make use of the addition theorem for the Hankel function $H_0^{(2)}$ (see, for example [9]):

$$H_0^{(2)}(k_\mathrm{b}|\mathbf{x}-\mathbf{x}'|) = \begin{cases} \sum_{k=-\infty}^{\infty} J_k(k_\mathrm{b}|\mathbf{x}|)H_k^{(2)}(k_\mathrm{b}|\mathbf{x}'|)\exp(\mathrm{j}k\varphi), & |\mathbf{x}'| \geq |\mathbf{x}|, \\ \sum_{k=-\infty}^{\infty} J_k(k_\mathrm{b}|\mathbf{x}'|)H_k^{(2)}(k_\mathrm{b}|\mathbf{x}|)\exp(\mathrm{j}k\varphi), & |\mathbf{x}'| \leq |\mathbf{x}|, \end{cases} \tag{51}$$

where J_k is the kth order Bessel function of the first kind, $H_k^{(2)}$ is the kth order Hankel function of the second kind, and φ is the angle between $\mathbf{x}$ and $-\mathbf{x}'$.

Let us first evaluate the integral for observation points outside the circular disk $\mathbb{D}^{\mathrm{circ}}$. In this case, we have $|\mathbf{x}| > |\mathbf{x}'|$ and substituting the second line of Eq. (51) in Eq. (39), we obtain

$$G^{\mathrm{w}}(\mathbf{x}) = -\frac{\mathrm{j}}{4\pi a^2}\times \sum_{k=-\infty}^{\infty} H_k^{(2)}(k_\mathrm{b}|\mathbf{x}|)\int_{r=0}^{a} J_k(k_\mathrm{b}r)r\,\mathrm{d}r\int_{\varphi=0}^{2\pi}\exp(\mathrm{j}k\varphi)\,\mathrm{d}\varphi\,\mathrm{d}r, \tag{52}$$

where we have introduced polar coordinates as well. Now since

$$\int_{\varphi=0}^{2\pi}\exp(\mathrm{j}k\varphi)\,\mathrm{d}\varphi = \begin{cases} 2\pi & \text{if } k=0, \\ 0 & \text{if } k\neq 0, \end{cases} \tag{53}$$

the above simplifies to

$$G^{\mathrm{w}}(\mathbf{x}) = -\frac{\mathrm{j}}{2a^2}H_0^{(2)}(k_\mathrm{b}|\mathbf{x}|)\int_{r=0}^{a} J_0(k_\mathrm{b}r)r\,\mathrm{d}r \tag{54}$$

and using the differentiation property [9]

$$\frac{\mathrm{d}}{\mathrm{d}z}\left[zJ_1(z)\right] = zJ_0(z), \tag{55}$$

the integral can be evaluated as

$$\int_{r=0}^{a} J_0(k_\mathrm{b}r)r\,\mathrm{d}r = \frac{a}{k_\mathrm{b}}J_1(k_\mathrm{b}a). \tag{56}$$

Substitution then gives

$$G^{\mathrm{w}}(\mathbf{x}) = -\frac{\mathrm{j}}{2k_\mathrm{b}a}J_1(k_\mathrm{b}a)H_0^{(2)}(k_\mathrm{b}|\mathbf{x}|) \tag{57}$$

for $\mathbf{x}\notin\mathbb{D}^{\mathrm{circ}}$.

To evaluate $G^{\mathrm{w}}(\mathbf{0})$, we take $\mathbf{x}\in\mathbb{D}^{\mathrm{circ}}$ with $|\mathbf{x}| = \epsilon < a$ and subsequently take the limit $\epsilon\downarrow 0$. Integration over $\mathbb{D}^{\mathrm{circ}}$ is split in two parts: in one part we integrate from $|\mathbf{x}'| = \epsilon$ to $|\mathbf{x}'| = a$ (domain $\mathbb{D}_{1;\epsilon}$), while in the second part we integrate over a disk centered at the origin and having a radius ϵ (domain $\mathbb{D}_{2;\epsilon}$). Notice that when integrating over $\mathbb{D}_{1;\epsilon}$, we have $|\mathbf{x}'| > |\mathbf{x}| = \epsilon$, while if we integrate over $\mathbb{D}_{2;\epsilon}$, we have $|\mathbf{x}'| < |\mathbf{x}| = \epsilon$. To summarize, we have

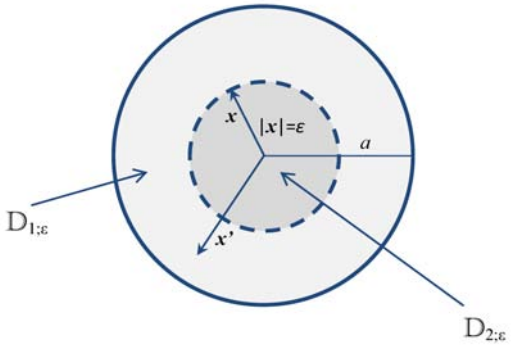


Figure 13: Integration over the domain $\mathbb{D}_{1;\epsilon}$.

$$G^{\mathrm{w}}(\mathbf{0}) = -\frac{\mathrm{j}}{4\pi a^2}\times \lim_{\epsilon\downarrow 0}\left[\int_{\mathbf{x}'\in\mathbb{D}_{1;\epsilon};|\mathbf{x}|=\epsilon} H_0^{(2)}(k_\mathrm{b}|\mathbf{x}-\mathbf{x}'|)\,\mathrm{d}A + \int_{\mathbf{x}'\in\mathbb{D}_{2;\epsilon};|\mathbf{x}|=\epsilon} H_0^{(2)}(k_\mathrm{b}|\mathbf{x}-\mathbf{x}'|)\,\mathrm{d}A\right]. \tag{58}$$

Let us start with the integral over $\mathbb{D}_{1;\epsilon}$ (see Figure 13). Since $|\mathbf{x}'| > |\mathbf{x}|$ in this case, we substitute the first line of Eq. (51) in the integrand and follow similar steps as above to obtain

$$\int_{\mathbf{x}'\in\mathbb{D}_{1;\epsilon};|\mathbf{x}|=\epsilon} H_0^{(2)}(k_\mathrm{b}|\mathbf{x}-\mathbf{x}'|)\,\mathrm{d}A = 2\pi J_0(k_\mathrm{b}\epsilon)\int_{r=\epsilon}^{a} H_0^{(2)}(k_\mathrm{b}r)r\,\mathrm{d}r. \tag{59}$$

Since the Hankel function satisfies Eq. (55) with J_0 and J_1 replaced by $H_0^{(2)}$ and $H_1^{(2)}$, respectively, the integral on the right-hand side in the above equation can be evaluated explicitly and we arrive at

$$\int_{\mathbf{x}'\in\mathbb{D}_{1;\epsilon};|\mathbf{x}|=\epsilon} H_0^{(2)}(k_\mathrm{b}|\mathbf{x}-\mathbf{x}'|)\,\mathrm{d}A = \frac{2\pi}{k_\mathrm{b}}J_0(k_\mathrm{b}\epsilon)\left[aH_1^{(2)}(k_\mathrm{b}a) - \epsilon H_1^{(2)}(k_\mathrm{b}\epsilon)\right]. \tag{60}$$

Using now the power series expansions of $J_0(x)$ and $H_1^{(2)}(x)$ around $x=0$, namely,

$$J_0(x) \approx 1 - \frac{x^2}{4}, \tag{61}$$

and

$$H_1^{(2)}(x) \approx \frac{2}{\pi}\frac{\mathrm{j}}{x} - \frac{\mathrm{j}x[2\ln(x)+\alpha]}{2\pi} \tag{62}$$

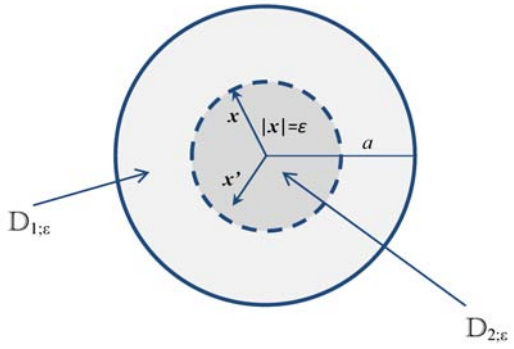


Figure 14: Integration over the domain $\mathbb{D}_{2;\epsilon}$.

where α is a constant (its particular value can be found in [9], but it is not relevant to us), we find

$$\lim_{\epsilon\downarrow 0}\frac{2\pi}{k_\mathrm{b}}J_0(k_\mathrm{b}\epsilon)aH_1^{(2)}(k_\mathrm{b}a)=\frac{2\pi}{k_\mathrm{b}}aH_1^{(2)}(k_\mathrm{b}a) \tag{63}$$

and

$$\lim_{\epsilon\downarrow 0}\frac{2\pi}{k_\mathrm{b}}J_0(k_\mathrm{b}\epsilon)\epsilon H_1^{(2)}(k_\mathrm{b}\epsilon)=\frac{4}{k_\mathrm{b}^2}\mathrm{j}. \tag{64}$$

Combining all results, we have

$$-\frac{\mathrm{j}}{4\pi a^2}\lim_{\epsilon\downarrow 0}\int_{\mathbf{x}'\in\mathbb{D}_{1;\epsilon};|\mathbf{x}|=\epsilon}H_0^{(2)}(k_\mathrm{b}|\mathbf{x}-\mathbf{x}'|)\,\mathrm{d}A=\frac{-\mathrm{j}}{2k_\mathrm{b}a}\left[H_1^{(2)}(k_\mathrm{b}a)-\frac{2\mathrm{j}}{\pi k_\mathrm{b}a}\right]. \tag{65}$$

Finally, we need to evaluate the integral over $\mathbb{D}_{2;\epsilon}$ (see Figure 14). We now have $|\mathbf{x}'|<|\mathbf{x}|=\epsilon$ and substituting the second line of Eq. (51) in the integrand leads to

$$\int_{\mathbf{x}'\in\mathbb{D}_{2;\epsilon};|\mathbf{x}|=\epsilon}H_0^{(2)}(k_\mathrm{b}|\mathbf{x}-\mathbf{x}'|)\,\mathrm{d}A=2\pi H_0^{(2)}(k_\mathrm{b}\epsilon)\int_{r=0}^{\epsilon}J_0(k_\mathrm{b}r)r\,\mathrm{d}r. \tag{66}$$

Since

$$\int_{r=0}^{\epsilon}J_0(k_\mathrm{b}r)r\,\mathrm{d}r=\frac{\epsilon}{k_\mathrm{b}}J_1(k_\mathrm{b}\epsilon), \tag{67}$$

we find

$$\int_{\mathbf{x}'\in\mathbb{D}_{2;\epsilon}}H_0^{(2)}(k_\mathrm{b}|\mathbf{x}-\mathbf{x}'|)\,\mathrm{d}A=\frac{2\pi\epsilon}{k_\mathrm{b}}H_0^{(2)}(k_\mathrm{b}\epsilon)J_1(k_\mathrm{b}\epsilon) \tag{68}$$

and upon taking the limit $\epsilon\downarrow 0$, we obtain

$$\lim_{\epsilon\downarrow 0}\int_{\mathbf{x}'\in\mathbb{D}_{2;\epsilon};|\mathbf{x}|=\epsilon}H_0^{(2)}(k_\mathrm{b}|\mathbf{x}-\mathbf{x}'|)\,\mathrm{d}A=0. \tag{69}$$

Finally, putting Eqs. (65) and (69) together, we arrive at

$$G^\mathrm{w}(\mathbf{0})=-\frac{\mathrm{j}}{2k_\mathrm{b}a}\left[H_1^{(2)}(k_\mathrm{b}a)-\frac{2\mathrm{j}}{\pi k_\mathrm{b}a}\right]. \tag{70}$$

References

[1] W. L. Barnes, A. Dereux, T. W. Ebbesen, Surface plasmon subwavelength optics, *Nature*, Vol. 424, pp. 824 – 830, 2003.

[2] E. Ozbay, Plasmonics: merging photonics and electronics at nanoscale dimensions, *Science*, Vol. 311, No. 5758, pp. 189 – 193, 2006.

[3] E. N. Economou, Surface plasmons in thin films, *Phys. Rev.*, Vol. 182, No. 2, pp. 539 – 554, 1969.

[4] L. Novotny, B. Hecht, *Principles of Nano-Optics*, Cambridge University Press, Cambridge, 2006.

[5] S. A. Maier, *Plasmonics: Fundamentals and Applications*, Springer, New York, 2007.

[6] A. Abubakar, P. M. van den Berg, Iterative forward and inverse algorithms based on domain integral equations for three-dimensional electric and magnetic objects, *J. Comput. Phys.*, Vol. 195, No. 1, pp. 236 – 262, 2004.

[7] Y. Saad, *Iterative Methods for Sparse Linear Systems*, Society for Industrial and Applied Mathematics, Philadelphia, 2003.

[8] W. C. Chew, *Waves and Fields in Inhomogeneous Media*, Wiley-IEEE Press, New York, 1999.

[9] M. Abramowitz, I. A. Stegun, *Handbook of Mathematical Functions*, Dover, New York, 1965.

[10] R. A. Horn, C. R. Johnson, *Matrix Analysis*, Cambridge University Press, Cambridge, 1990.

[11] L. N. Trefethen, M. Embree, *Spectra and Pseudospectra – The Behavior of Nonnormal Matrices and Operators*, Princeton University Press, Princeton, 2005.

Efficient Compression of Far Field Matrices in Multipole Algorithms based on Spherical Harmonics and Radiating Modes

Arne Schröder, Heinz-D. Brüns, Christian Schuster

Institut für Theoretische Elektrotechnik,
Technische Universität Hamburg-Harburg, Hamburg, Germany
E-mail: arne.schroeder@tu-harburg.de

Abstract

This paper proposes a novel compression of far field matrices in the fast multipole method and its multilevel extension for electromagnetic problems. The compression is based on a spherical harmonic representation of radiation patterns in conjunction with a radiating mode expression of the surface current. The method is applied to study near field effects and the far field of an antenna placed on a ship surface. Furthermore, the electromagnetic scattering of an electrically large plate is investigated. It is demonstrated, that the proposed technique leads to a significant memory saving, making multipole algorithms even more efficient without compromising the accuracy.

1. Introduction

The method of moments (MoM) [1] is well established for solving surface integral equations (SIEs) in the range of electromagnetic compatibility. Acceleration techniques like the fast multipole method (FMM) or the multilevel fast multipole algorithm (MLFMA) are often applied when analyzing electrically large objects to reduce both computation time and memory [2]. In order to gain a time- and memory-efficient FMM implementation, various measures have been introduced in the past [3]. This contribution proposes a compression of the far field matrices combining a spherical harmonic representation of the radiation pattern [4] with a radiating mode expression of the currents in a FMM group [5].

The paper is organized as follows: In Section 2 the fundamentals of MoM and FMM are briefly outlined. Section 3 describes the theoretical background of the proposed compression technique and in Section 4 two numerical examples are considered to investigate the impact of the developed approach on the required memory and the accuracy.

2. Formulation of MoM and FMM

The MoM can be applied to solve various types of SIEs. In this paper, it is focussed on the electric field integral equation (EFIE) for perfect electric conducting (PEC) bodies. Discretizing the EFIE with MoM leads to a system of linear equations

$$\mathbf{Z} \cdot \mathbf{I} = \mathbf{V} \,. \tag{1}$$

Here, $\mathbf{Z} \in \mathbb{C}^{N\times N}$ is the dense system matrix, $\mathbf{I} \in \mathbb{C}^{N\times 1}$ includes the unknown current amplitudes and $\mathbf{V} \in \mathbb{C}^{N\times 1}$ represents the excitation of the system. N is the number of unknowns. Applying FMM to MoM results in a blockwise approximated system matrix. The matrix block $\mathbf{Z}_{r,s}$ couples a group s of basis functions and a group r of test functions. It is approximated as [5]

$$\mathbf{Z}_{r,s} \approx \mathbf{R}_r^{\theta} \cdot \boldsymbol{\alpha}_{r,s} \cdot \mathbf{F}_s^{\theta} + \mathbf{R}_r^{\phi} \cdot \boldsymbol{\alpha}_{r,s} \cdot \mathbf{F}_s^{\phi} \,, \tag{2}$$

with $\boldsymbol{\alpha}_{r,s}$ and $\mathbf{R}_r^{\theta,\phi}$ being the translation matrix and the disaggregation matrices, respectively. The columns of the aggregation matrices

$$\mathbf{F}_s^{\theta,\phi} = \left[\mathbf{f}_{s1}(\mathbf{k}), \mathbf{f}_{s2}(\mathbf{k}), ..., \mathbf{f}_{sN_s}(\mathbf{k})\right]^{\theta,\phi} \tag{3}$$

are radiation patterns of the N_s basis functions in group s evaluated at K discrete points $\mathbf{k}_k$ on the unit sphere (k-space representation). For the i-th basis function of group s the radiation pattern is given by

$$\mathbf{f}_{si}(\mathbf{k}) = \int_S \left(\bar{\bar{\mathbf{I}}} - \hat{\mathbf{k}}\hat{\mathbf{k}}\right) \cdot \mathbf{b}_i(\mathbf{r}') e^{j\mathbf{k}\cdot\mathbf{d}_i} \, dS' \,, \tag{4}$$

where $\mathbf{d}_i$ is the distance between source point $\mathbf{r}'$ and the center of group s. $\bar{\bar{\mathbf{I}}}$ denotes the unit dyadic and $\hat{\mathbf{k}}$ is the normalized k-vector, pointing in radial direction on the unit sphere [2].

3. Compression of Far Field Matrices

In the following a compression technique for the aggregation matrices is described, which consist of two parts: The radiation pattern given by Equation (4) is represented by spherical harmonics and only radiating current modes are considered for the aggregation matrices given by Equation (3).

3.1. Spherical Harmonic Representation of the Aggregation Matrices

The number K is determined by the spectral content of the translation operator and the radiation patterns [2]. This leads to an oversampling of radiation patterns in the k-space formulation [4]. Thus, a more appropriate basis for the representation of $\mathbf{f}_{si}(\mathbf{k})$ should be applied. Since each radiation pattern is quasi-bandlimited (bandwidth P) [2], it can

be expressed by spherical harmonics Y_l^m as

$$\mathbf{f}_{si}(\mathbf{k}) \approx \sum_{l=0}^{P} \sum_{m=-l}^{m=l} \mathbf{c}_{si}^{l,m} Y_l^m(\mathbf{k}) \,, \tag{5}$$

where $\mathbf{c}_{si}^{l,m} \in \mathbb{C}^{3\times 1}$ are weighting coefficients for the x-, y- and z-component of $\mathbf{f}_{si}(\mathbf{k})$. Following Eq. (5), the aggregation matrices of group s read

$$\mathbf{F}_s^{x,y,z} \approx \mathbf{Y} \cdot \mathbf{C}_s^{x,y,z} \,. \tag{6}$$

Note that $\mathbf{F}_s^{x,y,z}$ are expressed in Cartesian coordinates to avoid Gibb's phenomenon caused by discontinuities at the poles of $\mathbf{F}_s^{\theta,\phi}$ in spherical coordinates. The discretized spherical harmonics are globally stored in $\mathbf{Y} \in \mathbb{C}^{K\times M_{sph}}$. The number of spherical harmonics is $M_{sph} = (P+1)^2$ according to Eq. (5). This representation leads to a memory reduction, since only coefficients $\mathbf{c}_{si}^{l,m}$ have to be stored instead of an explicit k-space pattern [4].

In [4] a radiation pattern is computed in k-space and then transferred to spherical harmonics. Instead of doing that, we propose to determine the coefficients $\mathbf{c}_{si}^{l,m}$ directly from a spherical wave expansion for plane waves [6]

$$e^{j\mathbf{k}\cdot\mathbf{d}_i} \approx 4\pi \sum_{l=0}^{P} \sum_{m=-l}^{m=l} j^l j_l\big(k|\mathbf{d}_i|\big) Y_l^m(\mathbf{k}) \bar{Y}_l^m(\mathbf{d}_i) \,, \tag{7}$$

where j_l is the spherical Bessel function of order l and $\bar{Y}$ denotes the conjugate of Y. Substituting Eq. (7) into Eq. (4) leads to the spherical harmonic representation of Eq. (5). Hence, the corresponding weighting coefficients $\mathbf{c}_{si}^{l,m}$ can be computed via

$$\mathbf{c}_{si}^{l,m} = 4\pi j^l \int_S \mathbf{b}_i(\mathbf{r}') j_l\big(k|\mathbf{d}_i|\big) \bar{Y}_l^m(\mathbf{d}_i) \, dS' \,. \tag{8}$$

In the implementation, this integral is numerically evaluated by a quadrature rule.

3.2. Radiating Current Modes

To further reduce memory it is exploited that only a few current modes contribute to the radiation pattern of a group [5]. These modes are determined by using a truncated singular value decomposition (TSVD) [7] of $\mathbf{C}_s \approx \mathbf{A}_s \cdot \mathbf{B}_s$, with $\mathbf{A}_s \in \mathbb{C}^{M_{sph}\times q_s}$ and $\mathbf{B}_s \in \mathbb{C}^{q_s\times N_s}$. Here, only q_s singular values larger than a predefined threshold ϵ are considered. The singular values for the matrices $\mathbf{C}_s^x$, $\mathbf{C}_s^y$ and $\mathbf{C}_s^z$ of an example structure are given in Fig. 1. Applying TSVD to the matrices $\mathbf{C}_s^{x,y,z}$ leads to the aggregation matrices

$$\mathbf{F}_s^{x,y,z} \approx \mathbf{Y} \cdot \mathbf{A}_s^{x,y,z} \cdot \mathbf{B}_s^{x,y,z} \,. \tag{9}$$

These matrices can be interpreted as follows: $\mathbf{B}$ transfers the considered basis functions into q_s radiating modes and $\mathbf{A}$ contains the weighting coefficients for the spherical harmonics of the far field pattern associated with these radiating modes. Figure 2 illustrates the radiating current modes corresponding to the three largest singular values of matrix $\mathbf{C}_1^x$. These modes are defined by the first three rows of $\mathbf{B}_1^x$.

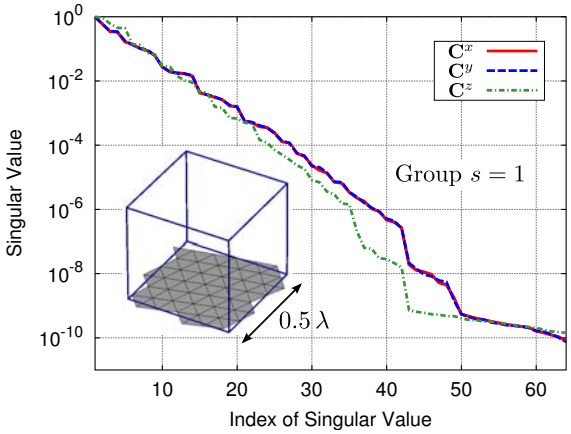


Figure 1: Singular values of the coeffcient matrices $\mathbf{C}_1^x$, $\mathbf{C}_1^y$ and $\mathbf{C}_1^z$ for an example structure inside a group with edge-length 0.5 λ.

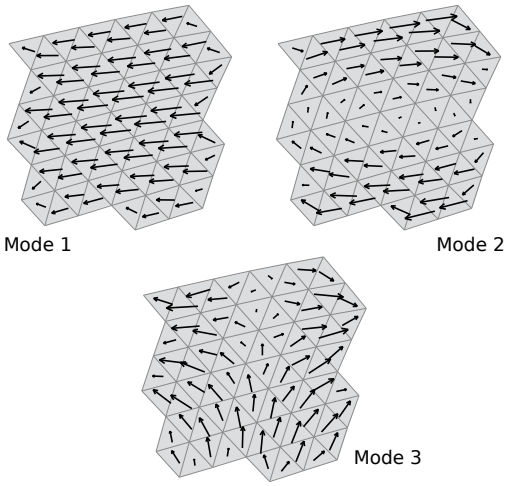


Figure 2: Current pattern in a group corresponding to the first, second and third singular value of matrix $\mathbf{C}_1^x$ for the example structure given in Fig 1.

3.3. Memory Complexity

The number of elements needed to be stored for the aggregation matrices of one group with N_s basis functions is shown in Table 1. Note that the memory required to hold $\mathbf{Y}$ is neglected, because it does not depend on the total number of unknowns. The factor 2 takes into account that θ- and ϕ-components have to be stored in the conventional approach and the compression with TSVD. The factor 3 takes into account the use of Cartesian components for the other techniques. As indicated in Table 1, the proposed method is superior to a pure spherical harmonic representation if the condition

$$q_s < \frac{M_{sph} N_s}{\big(M_{sph} + N_s\big)} \tag{10}$$

is fulfilled. Table 2 illustrates the resulting elements, needed to be stored for the considered example structure.

Table 1: Number of elements for one aggregation matrices with different compression methods.

Method	Elements
Conventional	$2KN_s$
TSVD [5]	$2q_s\left(K+N_s\right)$
Spherical Harmonics [4]	$3M_{sph}N_s$
Proposed Method	$3q_s\left(M_{sph}+N_s\right)$

In this example a threshold $\epsilon = 0.001$ is applied, which leads to $q_s = 20$. This factor is usually different for each matrix $\mathbf{C}_x, \mathbf{C}_y$ and $\mathbf{C}_z$ as shown in Fig. 1. For the sake of simplicity it is assumed to be the same for all matrices. Furthermore the value $P = 7$ leads to $M_{sph} = 64$. The group under consideration includes $N_s = 95$ basis functions and the number of points for discretizing the unit sphere is $K = 338$.

Table 2: Number of elements for the aggregation matrices associated with the example structure in Fig. 1.

Method	Elements	Factor
Conventional	64 220	-
TSVD of [5]	17 320	3.70
Spherical Harmonics [4]	18 240	3.52
Proposed Method	9 540	6.7

4. Numerical Results

Results of the proposed compression technique are presented in the following. This technique was applied to a MoM Code [8] with FMM and MLFMA acceleration, respectively. All computations have been performed in double precision on a PC with a 2.6 GHz AMD 6140 Opteron Processor. TFQMR [9] was used to solve the equation system iteratively. The first example to be considered is a ship model with a total length of 120 m as depicted in Fig. 3 and Fig. 4. The discretized surface involves 126 962 Rao-Wilton-Glisson (RWG) basis functions [10]. The ship is excited by a monopole antenna at a frequency of 72 MHz. The compression was carried out using the techniques described by [4], [5] and the proposed method for different parameters P and ϵ (a detailed accuracy analysis related to the value P can be found in [2]). These techniques have been applied to the FMM with a box size of $0.5\,\lambda$ and MLFMA with a box size of $0.25\,\lambda$ on the finest level. In all cases a Galerkin approach with $\mathbf{R} = \mathbf{F}^H$ was used. Table 3 illustrates the memory reduction for the aggregation matrices. The proposed technique has a better performance than the techniques suggested in [4] and [5] because it combines both aspects, i. e. spherical harmonics and radiating modes. It has to be emphasized, that the approach under consideration requires slightly more memory than the spherical harmonic representation, choosing $P = 4$ and $\epsilon = 0.001$. This is because the requirement of Eq. (10) has been violated

Table 3: Memory for the aggregation matrices with the proposed technique using FMM (box size: $0.5\,\lambda$) and MLFMA (box size: $0.25\,\lambda$). Example: ship surface with 126 962 unknowns.

FMM ($0.5\,\lambda$)	Memory (MB)	Factor
Conventional	1 310	-
$P = 8, \epsilon = 10^{-3}$	250.0	5.24
$P = 5, \epsilon = 10^{-2}$	123.4	10.6
[4] ($P = 5$)	209.3	6.26
[5] ($\epsilon = 10^{-2}$)	292.4	4.48

MLFMA ($0.25\,\lambda$)	Memory (MB)	Factor
Conventional	627.7	-
$P = 4, \epsilon = 10^{-3}$	148.0	4.24
$P = 4, \epsilon = 10^{-2}$	104.1	6.03
[4] ($P = 4$)	145.4	4.32
[5] ($\epsilon = 10^{-2}$)	289.5	2.17

for some groups of basis functions. In this first example the total memory for all required FMM matrices is reduced by 27% from 4.24 GB to 3.09 GB. The total memory for MLFMA is decreased from 1.30 GB to 0.82 GB, which corresponds to a 37% reduction. Fig. 3 shows the electric field along an observation path 1 m above the deck. Only small deviations are caused by the proposed technique. Furthermore the radiation pattern of the antenna is given in Fig. 4, where the deviation to a conventional approach is hardly noticeable. The time for compressing the far field matrices

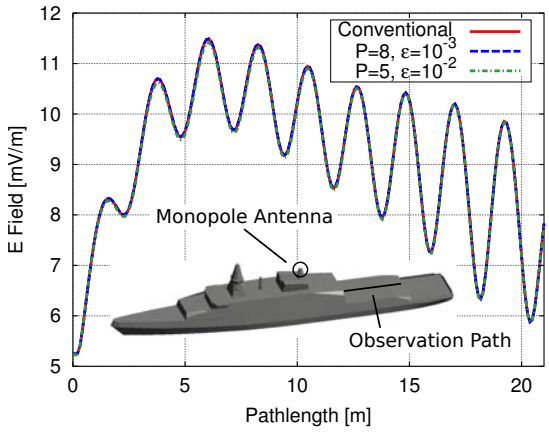


Figure 3: Max. magnitude of E field along the indicated observation path (length 21 m), computed with a conventional FMM approach and the proposed compression for aggregation matrices. P: Maximum order of spherical harmonics. ϵ: Accuracy of compression with TSVD.

was 46 s ($P = 8$) and 25 s ($P = 5$) for FMM as well as 10 s for MLFMA. These values are negligible compared to the total solution time for this problem with FMM (61 min) and MLFMA (22 min), respectively.

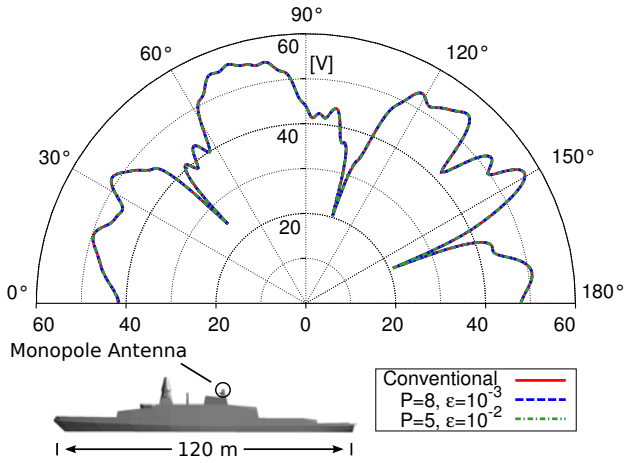


Figure 4: Radiation pattern in the upper hemisphere due to an monopole antenna placed on the ship surface. Comparison of proposed approach with conventional method. P: Maximum order of spherical harmonics. ϵ: Accuracy of compression with TSVD

The second example is an electrically large PEC plate excited by a linearly polarized plane wave as illustrated in Fig. 5. Two different cases are investigated: The square plate with an edge length of $a = 32\,\lambda$ and $a = 64\,\lambda$, respectively. In both cases it is discretized with 1 085 544 basis functions. Computational results for a conventional

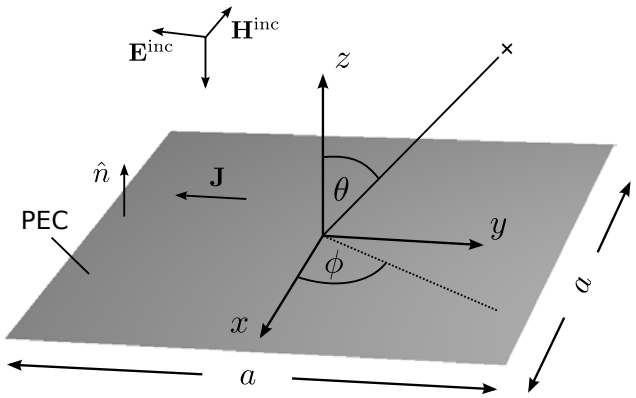


Figure 5: Considered PEC Plate in Cartesian coordinate system. Excitation with plane wave, incident angle is $\theta = 0$.

approach, the proposed technique with $P = 4$ and $\epsilon = 0.01$ as well as a pure spherical harmonic representation with $P = 4$ are given in Table 4. The memory required for the aggregation matrices with the introduced technique is 0.63 GB in case of $a = 32\,\lambda$ and 1.07 GB in case of $a = 64\,\lambda$ compared to 5.24 GB with a conventional approach. For $a = 64\,\lambda$, the total memory of all MLFMA matrices is decreased from 7.89 GB to 3.72 GB, which relates to 53%. Solving this problem with a residual tolerance $\epsilon_{\text{res}} = 3 \cdot 10^{-3}$ took 6.9 h on a single CPU. As illustrated by Table 4, the compression rate of the proposed technique

Table 4: Memory for the aggregation matrices with different compression techniques using MLFMA (box size: 0.25 λ). Example: square plate with 1 085 544 unknowns for the edge lengths $a = 32\,\lambda$ and $a = 64\,\lambda$

	MLFMA (0.25 λ)	Mem. (GB)	Factor
$32\,\lambda$	Conventional	5.24	-
	$P = 4, \epsilon = 10^{-2}$	0.63	8.32
	[4] ($P = 4$)	1.21	4.32
$64\,\lambda$	Conventional	5.24	-
	$P = 4, \epsilon = 10^{-2}$	1.07	4.93
	[4] ($P = 4$)	1.21	4.32

grows with the number of basis functions inside a group on the finest MLFMA level. For $a = 32\,\lambda$ the average number of basis functions in one group was 66.3, for $a = 64\,\lambda$ the average was 16.6 basis functions per group. To validate the accuracy of our approach, MLFMA is compared to an analytical estimation for the plate with $a = 64\,\lambda$. Based on assumptions known from physical optics, the surface current density is approximated by $\mathbf{J} \approx 2 \cdot \hat{n} \times \mathbf{H}_{\text{inc}}$. From this the bistatic radar cross section (RCS) is analytically computed using Green's function for the far field [11]. Since the plate is large in terms of wavelength, accurate results are expected for the reflected wave around $\theta = 0°$. Fig. 6 compares MLFMA with the analytical estimation. Here, the bistatic radar cross section for $\theta = 0° \ldots 90°$ and $\phi = 90°$ is given. A very good agreement can be observed in the range between $\theta = 0°$ and $\theta = 10°$. With increasing angle the deviations become more pronounced due to the optical approximation for the analytical computation.

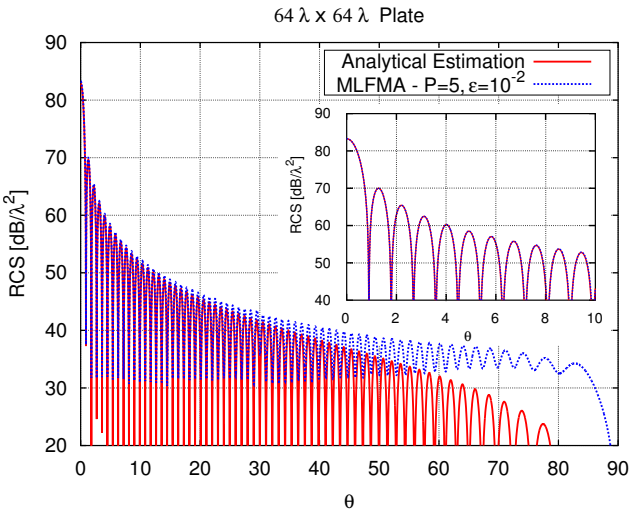


Figure 6: Bistatic RCS of a square PEC plate ($a = 64\,\lambda$) with 1 085 544 unknowns, computed with the proposed technique and an analytical estimation. P: Maximum order of spherical harmonics. ϵ: Accuracy of compression with TSVD

5. Conclusions

An efficient compression of far field matrices in multipole methods is proposed. The compression technique has been applied to the conventional FMM and its multilevel extension MLFMA, leading to a significant memory reduction up to 53%. It turns out that the developed method is superior to techniques known from literature. In addition to this the proposed approach is shown to be very accurate.

Acknowledgement

The work described in this paper and the research leading to these results has received funding from the European Community's Seventh Framework Programme FP7/2007-2013, under grant agreement no 205294, HIRF SE project.

References

[1] R. F. Harrington, "Matrix methods for field problems," *Proceedings of the IEEE*, vol. 55, no. 2, pp. 136–149, 1967.

[2] W. C. Chew, J.-M. Jin, E. Michielssen, and J. Song, *Fast and Efficient Algorithms in Computational Electromagnetics*. Artech House, 2001.

[3] S. Velamparambil, W. C. Chew, and J. Song, "10 million unknowns: is it that big?" *IEEE Antennas and Propagation Magazine*, vol. 45, no. 2, pp. 43 –58, 2003.

[4] T. F. Eibert, "A diagonalized multilevel fast multipole method with spherical harmonics expansion of the k-space integrals," *IEEE Transactions on Antennas and Propagation*, vol. 53, no. 2, pp. 814 – 817, 2005.

[5] J. L. Rodriguez, J. M. Taboada, M. G. Araujo, F. Obelleiro Basteiro, L. Landesa, and I. Garcia-Tunon, "On the use of the singular value decomposition in the fast multipole method," *IEEE Transactions on Antennas and Propagation*, vol. 56, no. 8, pp. 2325 –2334, 2008.

[6] J. D. Jackson, *Classical Electrodynamics Second Edition*. Wiley, 1975.

[7] P. C. Hansen, *Rank-Deficient and Discrete Ill-Posed Problems*. Philadelphia, USA: SIAM, 1997.

[8] Technische Universität Hamburg-Harburg. CONCEPT-II. [Online]. Available: http://www.tet.tu-harburg.de/concept

[9] R. W. Freund, "A transpose-free quasi-minimal residual algorithm for non-hermitian linear systems," *SIAM J. Sci. Comput.*, vol. 14, no. 2, pp. 470–482, 1993.

[10] S. M. Rao, D. R. Wilton, and A. W. Glisson, "Electromagnetic scattering by surfaces of arbitrary shape," *IEEE Transactions on Antennas and Propagation*, vol. 30, no. 3, pp. 409–418, 1982.

[11] C. A. Balanis, *Advanced engineering electromagnetics*. Wiley, 1989.

A Bayesian Approach to Determine the Electric Field of Broadcasting Medium Wave

Juliana Monteiro[1], Jasmine Araújo[1], Josiane Rodrigues[1,2,3], Simone Fraiha[1], Hermínio Gomes[1], Renato Francês[1], Gervásio Cavalcante[1], Adaildo D'Assunção[4]

[1]Federal University of Pará, Brazil
[2]Institute of Higher Studies of Amazon, Brazil
[3]Ipiranga Faculty, Brazil
[4]Federal University of Rio Grande do Norte, Brazil
*corresponding author, E-mail: jusantmont@ufpa.br

Abstract

This paper proposes a methodology based in computational intelligence to determine the electric field of broadcasting medium wave. A Bayesian network was generated using data collected from a measurement campaign carried out in Brasília city and it shows the correlation between Altitude and Electric field measured. Conditional probabilities values were used to generate probabilities values of the behavior of the electric field versus terrain´s altitude. Thus, in similar places this methodology can be applied without additional computational efforts.

1. Introduction

In Brazil, the medium wave digital broadcasting service is in a process of evaluation in order to define the standard to be adopted. It is important for the planning and management of the system to know the real amount of signal being propagated in determined condition, aiming it is also important to delimit the covering area of the signal. Thus, prediction models are used to delimit the theoretical value of the covering area [1]. In this work, the measured values of the E-field have been compared with the values obtained from computational intelligence simulation, inside the coverage area of the broadcasters in test. These simulations have been performed using the probability conditional tables generated by a Bayesian Network tool [2]. Thus, we provide a methodology for determining the correlation between altitude and electric field through the use of measuring technique and computational intelligence.

The paper is organized as follows: Section 2 presents the measurement campaigns where the measurements were conducted, Section 3 describes the computational intelligence model used and Section 4 describes the methodology employed, data processing used at the values collected at the measurement campaigns and the results, Section 5 concludes the paper.

2. Measurement Campaign

A measurement campaign was carried out in the heartland of the country and it aimed to collect electric field values at fixed and mobile (allowing the characterization of the channel and analysis of its coverage area by means of the parameters used in prediction models in use) over six radial routes (about 25.000 samples were collected), evenly distributed, with a radius of 120Km each. In this paper are being analyzed data from Routes 2 and 3. The medium wave signals collected in the measures were irradiated from the broadcast center of the Brazilian communications S/A – Radiobrás. The equipment used are also from Radiobrás and Anatel, the telecommunications regulatory agency in Brazil.

3. Computational Intelligence Model

The main objective of bayesian networks is to find valid and potentially useful patterns from the data. The extraction of knowledge from data can be seen as a process with, at least, the following steps: understanding of the application domain, selection and preparation of the data, data mining, evaluation of the extracted knowledge and consolidation and the use of the extracted knowledge. In this work, the computational intelligence algorithm used for data mining was based on Bayesian networks.

A Bayesian network is composed of several nodes, where each node of the network represents a variable, that is, an attribute of the database; directed arcs connecting them implies in the relation of dependency that the variable can possess over the others; and finally probability tables for each node. The Bayesian networks can be seen as encoding models of the probabilistic relationships between the variables that represent a given domain. These models possess as components a qualitative representation of the dependencies between the nodes and a quantitative (conditional probability tables of these nodes) structure, that can evaluate, in probabilistic terms, these dependencies. These components together provide an efficient

representation of the joint probability distribution of the variables of a given domain.

One of the major advantages of the Bayesian networks is their semantics, which facilitates, given the inherent causal representation of these networks, the understanding and the decision making process for the users of these models. Basically, due to the fact that the relations between the variables of the domain can be visualized graphically, besides providing an inference mechanism that allows quantifying, in probabilistic terms, the effect of these relations [3].

The Bayesian network type chosen to be used in this work was the Naive Bayesian Network, because it stands out among the many existing classification methods as one of the simplest and computationally more efficient; being also robust against noises in the data and irrelevant attributes, in such a way that they would not influence in the probabilities of the other attributes [3].

4. Methodology and Results

After a data cleaner, the altitude and electric field were used to generate a Naive Bayesian Network. The correlation between altitude and electric field for Route 2 and Route 3 are shown in Fig. 1 and Fig. 2.

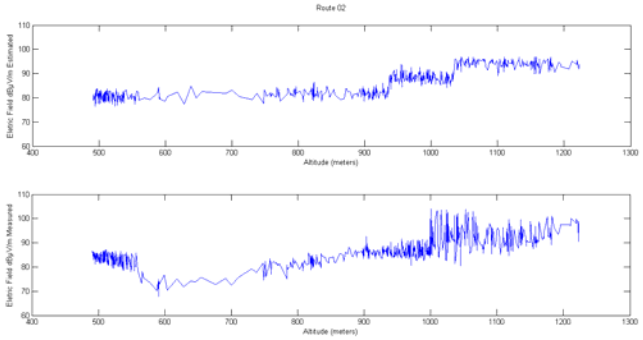


Figure 1. E- Field Estimated versus E- Field Measured for Route 2

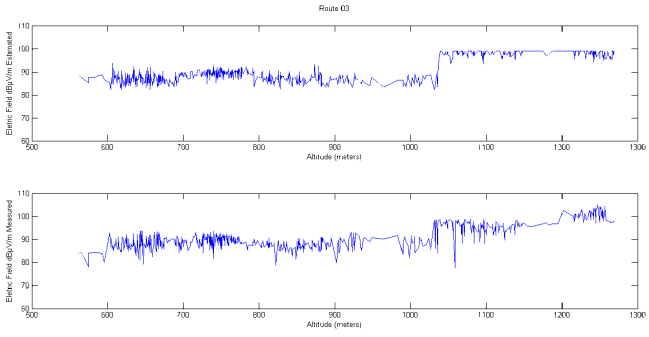


Figure 2. E-Field Estimated versus E- Field Measured for Route 3

In table I is one example of Conditional Probability Table obtained for Route 2 generated through the Naive Bayesian Network. In table II is showed the MSE and correlation indicators calculated for Routes 2 and 3.

Table I-Conditional Probabilities Values obtained from Bayesian Network

Conditional Probability Table	**Eletric Field**			
Altitude	*[67.83 83.40]*	*[83.4085.70]*	*[85.70 89.76]*	*[89.76104.01]*
[491.0 604.0]	0.534	0.285	0.180	0.000
[604.0 936.0]	0.412	0.282	0.300	0.006
[936.0 1033.0]	0.046	0.396	0.305	0.253
[1033.0 1223.0]	0.012	0.035	0.215	0.738

Table II – Calculated Data for Routes 2 and 3

	Route 2	**Route 3**
Mean Square Error (MSE) – Db	4,74	3,56
Correlation Measured Field x Altitude	0,8319	0,7523
Correlation Measured Field x Estimated Field	0,6658	0,7413

In Fig. 1 and Fig. 2 is showed the Electric Field estimated through the use of probabilities generated from the Bayesian network comparing with the electric field measured. According with table II, to Route 2 MSE is 4,74dB and for Route 3 is 3,56dB. The correlation between Measured Field and Altitude was 0,8319 for Route 2 and 0,7523 for Route 3. The correlation between Measured Field and Estimated Field for Route 2 was 0,6658 and 0,7413 for Route 3. This similarity is shown in Fig. 3 and Fig. 4, which shows respectively the electric field estimated by the program and the electric field measured.

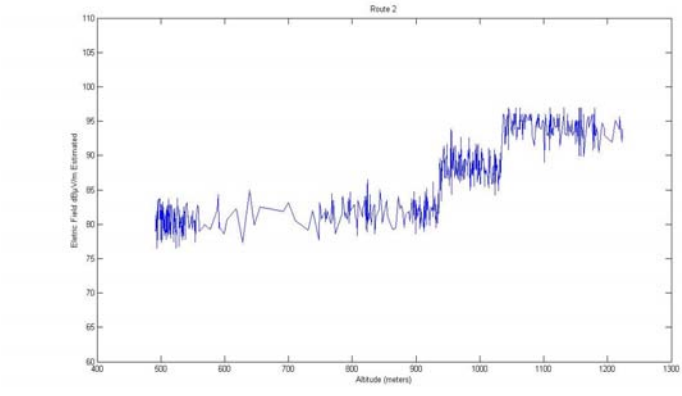


Figure 3. Electric Field Estimated for Route 2.

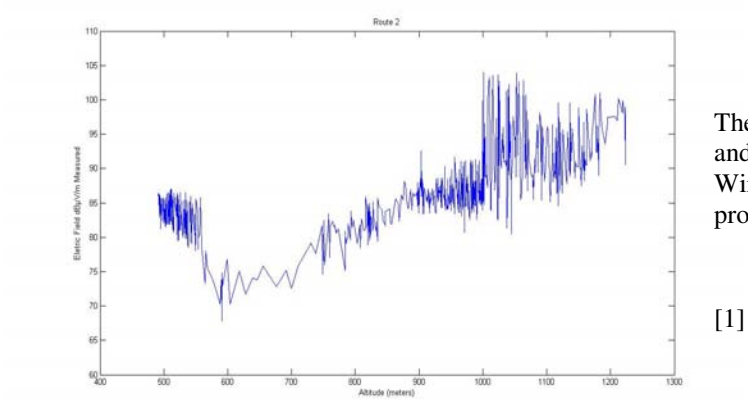


Figure 4. Electric Field Measured for Route 2.

For Route 3 the correlation between Measured Field and Estimated Field was 0,7413. The Fig. 5 and Fig. 6 shows the similarity for Route 3.

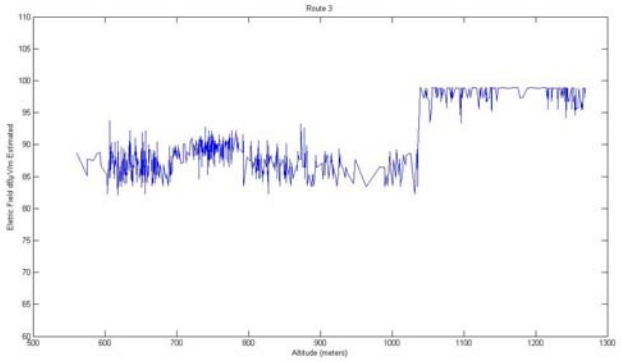


Figure 5. Electric Field Estimated for Route 3

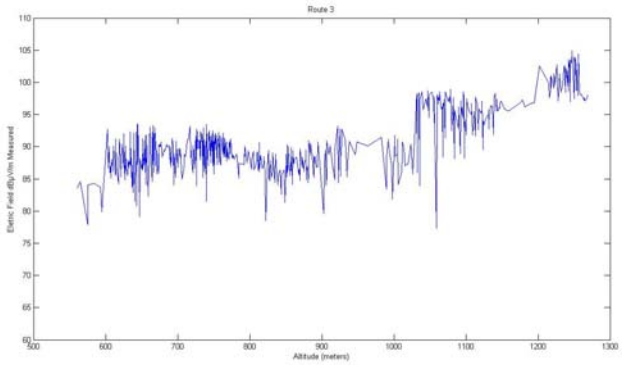


Figure 6. Electric Field Measured for Route 3

5. Conclusions

The coherent indicators evaluated by the study and the methodology proposed showed that the results are feasible to be used in similar terrains to predict the electric field without the use of measurement campaign.

Acknowledgements

The authors would like to thank to UFPA, CNPq and National Institute of Science and Technology - Wireless Communication (INCT-CSF) for the support provided for the research described in this paper.

References

[1] B. Monteiro, G.P.S. Cavalcante, H. S. Gomes, D. M. Rosário, F.F. Lima, H.A. Junior, "Evaluation of Radio Propagation Parameters for Field Strength Prediction Using Neural Network", Microwave and Optoelectronics International Conference, pp. 888 – 892, October 2007.

[2] Bayesware Discoverer, Copyright© 2000, Bayesware Limited. http://www.bayesware.com/ accessed in 01/10/11.

[3] A. L. S. et al. Strategies for improving the modeling and interpretability of bayesian networks. Data knowl. Eng., 63(1):91-107, November 2006.Lastname, F. M., Book Title, Wiley-Interscience, New York, 1986.

Efficient Computation of the Magnetic Field of Low-Frequency Antenna

Rania Oubaid, Yvan Lefevre*, and Jean Rene Poirier

[1]Université de Toulouse: INPT, UPS and CNRS; Laboratoire Plasma et Conversion d'Energie (LAPLACE);
Ecole Nationale Supérieure d´Electrotechnique, d´Electronique, d´Informatique, d´Hydraulique
et des Télécommunications (ENSEEIHT), F-31071 Toulouse cedex 7, France,
*Corresponding author, E-mail: Yvan.Lefevre@laplace.univ-tlse.fr

Abstract

The 3D magnetostatic moments method (MoM) is applied to a low frequency antenna for the fast computation of the magnetic field at short and large distance. The errors from 3D finite element results are very acceptable. The results are validated by finite element analysis and measurements.

1. Introduction

Low frequency magnetic communications are more and more applied in radio frequency identification (RFID). In tire pressure monitoring systems, a RFID is used to wake-up the pressure sensors and temperature sensors. In this wireless communication, the main component of the transmitter is a low frequency antenna operating at 125 kHz. This antenna is generally made of multi-turns coil wound around a ferrite core. One of the main challenge of manufacturers is to obtain very low power TPMS. One of the key to reach this challenge is to have a model that can quickly predict the magnetic field characteristics of low frequency antennas [1][2]. In this paper, we present a first step towards this goal: an efficient and simple tool to predict quickly the effect of the coil and core parameters on the magnetic field around the antenna is developed.

To calculate the magnetic field of this device a 3D finite-element or finite difference method can be used. But to calculate the magnetic field at large distance from the device, a huge amount of elements would be needed. [3] describes a model for a cylindrical ferrite rod core antenna. Using the axial symmetry, a 2D semi-numerical procedure, based on a vector potential formulation, is developed in order to calculate magnetic field at short and large distance. In our device, there is no axial symmetry so a 3D approach is needed. To calculate the static magnetic field, [4] presents a model based on magnetic moment method where the magnetized core is replaced by a distribution of induced magnetization. Assuming that magnetization is parallel to the axis of the cylindrical rod and uniform along its section, the rod is reduced to a line.

We will show that in our problem the magnetization cannot be assumed parallel to an axis nor uniform in a section of the core. Our tool is based on a 3D magnetostatic moment method (MoM) as presented in [5] and applied to ferrite core low-frequency RFID antennas with no axial symmetry. In this method, the magnetic field at any distance is calculated by a Volume Integral Equations Method (IEM) and only the core region and not the surrounding air region is meshed [6].

The article is organized as follows. In the next section, the calculation of the induced magnetization **M** in the core as done in [5] will be presented. The computation of elementary matrices is developed. The method to obtain a very fast and efficient method to calculate these elementary matrices is explained in section three. In section four, this method is applied to a low frequency antenna in order to develop a very efficient and simple specific tool for this kind of device. The results are compared to results obtained from a 3D finite element code (FEM). In section five, the influence of the mesh of the core and the influence of the value of the core permeability on the results are studied. The last section gives some concluding remarks.

2. Matrix formulation of Moment Method

A low frequency antenna is made of a ferrite core around which a coil is wounded as shown schematically on Fig. 1.

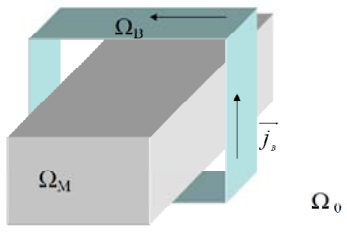


Figure 1: Theoretical configuration of the studied ferrite core and its coil

The flux density $\vec{B}(P)$ at any point P is given by the following expressions:

$$\vec{B}(P) = \overrightarrow{B_s}(P) + \overrightarrow{B_m}(P) \quad (1)$$

The first term of this expression is the flux density $\overrightarrow{B_S}(P)$ due to the coil Ω_B and which is expressed by means of the Biot and Savart law. The second term is the flux density due to the induced magnetization $\vec{M}(N)$in the core Ω_M and can

be expressed with the gradient of the magnetic scalar potential [5]:

$$\varphi_m(P) = \frac{1}{4\pi}\iiint_{\Omega_M} \frac{\overrightarrow{M(N)}\overrightarrow{r_{PN}}}{r_{PN}^3} d\Omega \quad (2)$$

where $\overrightarrow{r_{PN}}$ is the vector joining the interior point N to the point P. We have:

$$\overrightarrow{B_m}(P) = -\frac{\mu_0}{4\pi}\vec{\nabla}\{\varphi_m(P)\} \quad (3)$$

In order to compute $\overrightarrow{B_m}(P)$ at any point P, the induced magnetization $\vec{M}(N)$ must be known on each point N of the core Ω_M. Assuming that the core is not saturated, the relation between the magnetization and the flux density at any point Q in the core can be written as follows:

$$\mu\vec{M}(Q) = (\mu_r - 1)\vec{B}(Q) \quad (4)$$

where μ is the permeability and μ_r the relative permeability of the core.

2.1. Subdivision of the core

In order to establish the matrix formulation, the core volume is subdivided in N blocks. It is assumed that the magnetization is uniform in each block. In the block number I, V_I, the magnetization at each point Q of the block is given by:

$$\vec{M}(Q) = \overrightarrow{M_I} \quad (5)$$

An example of subdivision made with 4 blocks is shown on Fig. 2.

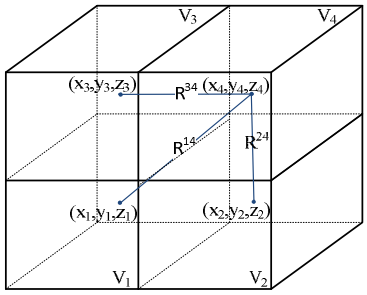


Figure 2: The division of the magnetized volume into 4 blocks. The magnetization in each block is uniform.

2.2. Induced flux density at the center of a block

In the following, the induced flux density at the center of a block, V_I, due to the magnetization $\overrightarrow{M^J}$ of a block, V_J, is noted $\overrightarrow{B_m^{IJ}}$. $\overrightarrow{R^{IJ}}$ is the vector joining a point N of the block V_J to the center of the block V_I. From(2) and (3), we have:

$$\overrightarrow{B_m^{IJ}} = -\frac{\mu_0}{4\pi}\iiint_{V_J}\left\{\vec{\nabla}\left(\frac{\overrightarrow{M^J}.\overrightarrow{R^{IJ}}}{(R^{IJ})^3}\right)\right\}dV \quad (6)$$

As $\overrightarrow{M^J}$ is uniform inside the block V_J, it can be shown that the volume integral (6) can be transformed to a surface integral on the external surface S_J of V_J (Fig. 3)

$$\overrightarrow{B_m^{IJ}} = \frac{\mu_0}{4\pi}\iint_{S_J}\frac{(\overrightarrow{M^J}.\vec{n})}{(R^{IJ})^3}\overrightarrow{R^{IJ}}\,dS \quad (7)$$

If $I \neq J$, the induced flux density $\overrightarrow{B_m^{IJ}}$, according to equation (6), can be expressed as:

$$\overrightarrow{B_m^{IJ}} = \frac{\mu_0}{4\pi}\iiint_{V_J}\left\{3\frac{(\overrightarrow{R^{IJ}}.\overrightarrow{M^J})}{(R^{IJ})^5}\overrightarrow{R^{IJ}} - \frac{\overrightarrow{M^J}}{(R^{IJ})^3}\right\}dV \quad (8)$$

If I=J, to avoid singularities due to the fact that R^{II} is null, expression (7) is used instead of expression (8). The induced flux density $\overrightarrow{B_m^I}$ at the center of a given block V_I, is the sum of the flux density $\overrightarrow{B_m^{II}}$ due to its own magnetization $\overrightarrow{M^I}$ and the flux density $\overrightarrow{B_m^{IJ}}$ due to the magnetization $\overrightarrow{M^J}$ of each of the remaining blocks V_J :

$$\overrightarrow{B_m^I} = \overrightarrow{B_m^{II}} + \sum_{\substack{J=1 \\ J\neq I}}^{N}\overrightarrow{B_m^{IJ}} \quad (9)$$

2.3. Decomposition on natural basis

Using an orthonormal basis $(\overrightarrow{e_1},\overrightarrow{e_2},\overrightarrow{e_3})$, the magnetization and the vector position can be decomposed into their components in this basis:

$$\begin{cases}\overrightarrow{M^J} = \sum_{k=1}^{3} M_k^J\overrightarrow{e_k} \\ \overrightarrow{R^{IJ}} = \sum_{k=1}^{3} R_k^{IJ}\overrightarrow{e_k}\end{cases} \quad (10)$$

and the induced flux density as well:

$$\overrightarrow{B_m^I} = \sum_{k=1}^{3} B_{mk}^I\overrightarrow{e_k} \quad (11)$$

According to (9), we have:

$$B_{mk}^I = B_{mk}^{II} + \sum_{\substack{J=1 \\ J\neq I}}^{N} B_{mk}^{IJ} \quad (12)$$

2.4. Putting volume integrals in a matrix form

In relation (12), B_{mk}^{IJ} is the kth component of vector $\overrightarrow{B_m^{IJ}}$. From (8), we can write:

$$B_{mk}^{IJ} = \frac{\mu_0}{4\pi}\iiint_{V_J}\left\{3\frac{(\overrightarrow{R^{IJ}}.\overrightarrow{M^J})}{(R^{IJ})^5}R_k^{IJ} - \frac{M_k^J}{(R^{IJ})^3}\right\}dV \quad (13)$$

Developing equation (13) leads to a matrix form:

$$\begin{Bmatrix}B_{m1}^{IJ}\\ B_{m2}^{IJ}\\ B_{m3}^{IJ}\end{Bmatrix} = \begin{bmatrix}F_{11}^{IJ} & F_{12}^{IJ} & F_{13}^{IJ}\\ F_{21}^{IJ} & F_{22}^{IJ} & F_{23}^{IJ}\\ F_{31}^{IJ} & F_{32}^{IJ} & F_{33}^{IJ}\end{bmatrix}\begin{Bmatrix}M_1^J\\ M_2^J\\ M_3^J\end{Bmatrix} \quad (14)$$

For $k \neq l$, F_{kl}^{IJ} is given by the integral:

$$F_{kl}^{IJ} = \frac{\mu_0}{4\pi}\iiint_{V_J} 3\frac{R_k^{IJ}.R_l^{IJ}}{(R^{IJ})^5}dV \quad (15)$$

and the diagonal components are given:

$$F_{kk}^{IJ} = \frac{\mu_0}{4\pi}\iiint_{V_J}\left[3\frac{(R_k^{IJ})^2}{(R^{IJ})^5} - \frac{1}{(R^{IJ})^3}\right]dV \quad (16)$$

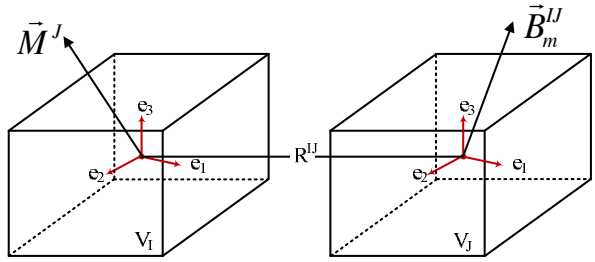


Figure 3: The induced flux density $\overrightarrow{B_m^{IJ}}$ on element I due to the magnetization $\overrightarrow{M^J}$ on element J.

2.5. Putting surface integral in a matrix form

In relation (12), B_{mk}^{II} is the kth component of vector $\overrightarrow{B_m^{II}}$. From (7), we can write:

$$\overrightarrow{B_m^{II}} = \frac{\mu_0}{4\pi}\iint_{S_I}\left[\frac{(\overrightarrow{M^I}.\vec{n})}{(R^{IQ})^3}\overrightarrow{R^{IQ}}\right]dS \quad (17)$$

$\overrightarrow{R^{IQ}}$ is the vector joining a point Q of surface S_I and the center of block V_I. The surface S_I can be decomposed in six surfaces such as (Fig. 4):

$$S_I = \bigcup_{k=-3}^{3} S_{Ik}$$

If k >0, then the normal vector to S_{Ik} is $\overrightarrow{e_k}$ and:

$$\overrightarrow{M^I}.\vec{n} = M_k^I$$

If k<0 the normal vector is $-\overrightarrow{e_k}$ and:

$$\overrightarrow{M^I}.\vec{n} = -M_k^I$$

Thus, integral (17) can be written in the form:

$$\overrightarrow{B_m^{II}} = \frac{\mu_0}{4\pi}\sum_{k=1}^{3}\left[\iint_{S_{Ik}}\frac{M_k^I}{(R^{IQ})^3}\overrightarrow{R^{IQ}}dS - \iint_{S_{I(-k)}}\frac{M_k^I}{(R^{IQ})^3}\overrightarrow{R^{IQ}}dS\right] \quad (18)$$

Knowing that:

$$\overrightarrow{R^{IQ}} = \sum_{l=1}^{3} R_l^{IQ}\,\overrightarrow{e_l} \quad (19)$$

and:

$$\overrightarrow{B_m^{II}} = \sum_{i=1}^{3} B_{mi}^{II}\overrightarrow{e_i} \quad (20)$$

the development of equation (18) leads to a matrix form:

$$\begin{Bmatrix} B_{m1}^{II} \\ B_{m2}^{II} \\ B_{m3}^{II} \end{Bmatrix} = \begin{bmatrix} F_{11}^{II} & F_{12}^{II} & F_{13}^{II} \\ F_{21}^{II} & F_{22}^{II} & F_{23}^{II} \\ F_{31}^{II} & F_{32}^{II} & F_{33}^{II} \end{bmatrix} \begin{Bmatrix} M_1^I \\ M_2^I \\ M_3^I \end{Bmatrix} \quad (21)$$

where (Fig. 4):

$$F_{ij}^{II} = \frac{\mu_0}{4\pi}\left[\iint_{S_{Ij}}\frac{R_i^{IQ}}{(R^{IQ})^3}dS - \iint_{S_{I(-j)}}\frac{R_i^{IQ}}{(R^{IQ})^3}dS\right] \quad (22)$$

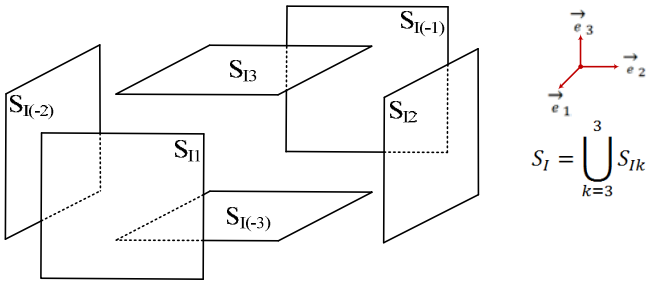


Figure 4: Surface of integration S_{Ik} to calculate the induced the flux density at the center of elementary volume I due to its own magnetization.

2.6. General matrix form

From (12), (14) and (21) the i^{th} component of the induced flux density on the center of block I can be written as follows:

$$B_{mi}^I = \sum_{J=1}^{N}\left(\sum_{j=1}^{3} F_{ij}^{IJ}.M_j^J\right) \quad (23)$$

This can be put in a general matrix form:

$$\{\beta^m\} = [\omega]\{\theta\} \quad (24)$$

where $\{\beta^m\}$ and $\{\theta\}$ are 3Nx1 column matrices containing respectively all the components of the induced flux density in each blocks and all the components of the magnetization vector in each block. Their components can be defined by:

$$\begin{cases} \beta_{3*(I-1)+i}^m = B_{mi}^I \\ \theta_{3*(I-1)+j} = M_j^I \end{cases} \quad (25)$$

$[\omega]$ is a 3Nx3N matrix that can be linked to the elementary matrices $[F^{IJ}]$ by the following relations:

$$\omega_{3*(I-1)+i,3*(J-1)+j} = F_{ij}^{IJ} \quad (26)$$

It is also possible to put equation (1) and (4) in a matrix form:

$$\begin{cases} \{\beta\} = \{\beta^S\} + \{\beta^m\} \\ \{\theta\} = \frac{\mu_r - 1}{\mu}\{\beta\} \end{cases} \quad (27)$$

where $\{\beta\}$ is a 3Nx1 column matrix containing the flux density components in each block and $\{\beta^S\}$ the column matrix with all the components of the flux density calculated by the Biot & Savart Law. From equations (24) and (27), we can write:

$$\left([I] - \frac{\mu_r - 1}{\mu}[\omega]\right)\{\theta\} = \frac{\mu_r - 1}{\mu}\{\beta^S\} \quad (28)$$

Solving equation (28) gives $\{\theta\}$ i.e. the components of the vector magnetization in each block. In the following, the matrix $[F^{IJ}]$ is called elementary interaction matrix and $[\omega]$ global interaction matrix

2.7. Computation of the magnetic flux density

Relation (27) allows to obtain the value of the flux density at the center of blocks inside the core.

At a point P, outside the core, knowing the magnetization $\overrightarrow{M^I}$ inside each block the flux density can be computed from equation (1) where:

$$\overrightarrow{B_S(P)} = \frac{\mu_0}{4\pi}\iiint_{\Omega_B}\frac{\overrightarrow{J(N)}\wedge\overrightarrow{r_{PN}}}{r_{PN}^3}dV \quad (29)$$

and:

$$\overrightarrow{B_m(P)} = \sum_{I=1}^{N}\frac{\mu_0}{4\pi}\iiint_{V_{IM}}\left\{3\frac{(\overrightarrow{M^I}\overrightarrow{r_{PN}})}{r_{PN}^5}\overrightarrow{r_{PN}} - \frac{\overrightarrow{M^I}}{r_{PN}^3}\right\}dV \quad (30)$$

3. Fast computation of interaction matrix

The main difficulty in the method of moment is the computation of elementary coefficient $[F^{IJ}]$ by means of the volume integrals (15) and (16) when I is different from J and by means of the surface integrals (22) when I equal J.

In low frequency antennas the ferrite core has generally a very regular geometric configuration, it is easy to divide them in blocks of the same size.

The surface integrations in (22) are done by the use of Gauss method. A relatively high number of integration points (ng=16) is taken. This number is necessary to ensure a relative error less than 0.5% with respect to the analytical solution [7]. To save computation time, as the blocks are of the same size, the surface integrations (22) are done only once. Thus, this relatively high number of integration points does not affect the total computation time.

The same number of integration points can be taken to compute the coefficients F_{kl}^{IJ} in (15) and (16). But, this number leads to a very high computation time. In fact, for the same number of integration points the precision of the computation of these coefficients depends on the mean distance between the center of elementary volume V_J and the integration points in the elementary volume V_I. If the center of the volume of integration is near the center of block V_J, a high number of integration points must be used and if it is far enough, the magnetic flux density is almost uniform inside the block, thus a lower number of integration points is sufficient to guarantee appropriate accuracy. Thus,

the number integration points must be adapted in function of the distance between the centers of blocks V_I and V_J. The variation of errors in function of distance between blocks and in function of the number of integration points have been studied (Fig. 5)

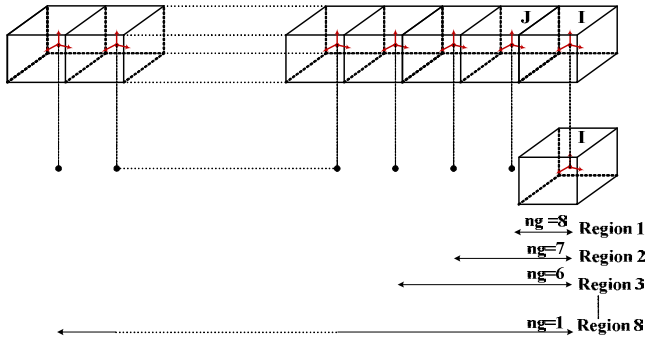


Figure 5: Illustration of the adaptation of the number of integration points in function of the distance between the centers of two blocks for a given desired relative errors.

For a given error relatively to results obtained from a supposed very high numbers of integration points (ng=20), the number of integration points in function of distance can be calculated. Figure 6 gives the results for relative errors of (erel=10^{-8}) and (erel=10^{-2}).

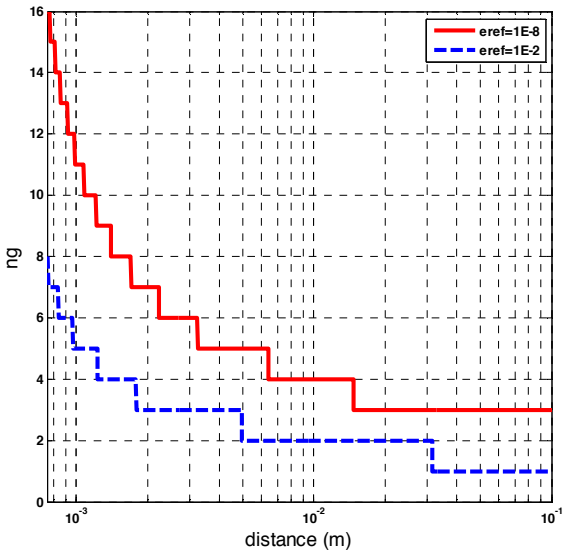


Figure 6: The value of adaptive ng in function of the distance between the centers of two blocks for two relative errors (eref=10^{-8} and eref=10^{-2}).

4. Application to a low frequency antenna

The formulations presented in the second section was numerically implemented and used to compute the magnetic flux density produced by low frequency antenna (LFA). Figure 1 shows the theoretical configuration of the studied low frequency ferrite core antenna. It is composed only of a coil (Ω_B) of N_w turns carrying a current I_s, and the ferromagnetic material (Ω_M) of relative magnetic permeability μ_r greater than unity. The geometry of the coil surrounding the ferrite core looks like a racetrack (Fig. 7). The size of the core and the coil are reported on Table I .

Table I: Size of the coil and the core of the antenna

Parameter	Symbol	Value	Unit
Number of turns	N_w	61	
Height of the coil (along Oz)	H_w	0.079	m
Thickness of the coil	E_w	0.0004	m
Height of core (along Oz)	H_c	0.085	m
Width of the core (along Oy)	W_c	0.008	m
Length of the core (along Ox)	L_c	0.003	m
Gap between coil and core	g_{wc}	0.0005	m

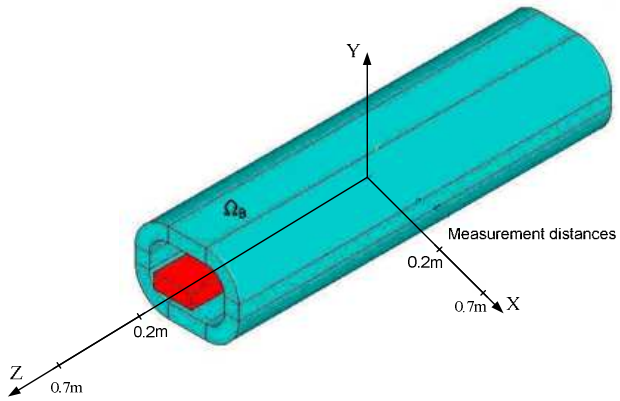


Figure 7: Geometries of the ferrite core and the racetrack coil

4.1. Computation of the flux density due to the coil

The first step of our study is the modeling of the flux density created by the racetrack coil. It can be easily computed by means of the Biot and Savart's law (29). The racetrack coil is crossed by a current density $\overrightarrow{J_S}$. Figure 8 shows the current density crossing the straight parts and the curved parts of the coil. The module of the current density is linked to the number of turns N_s and the actual value of current I_s in the coil by the relation:

$$S_B.J_S = N_W.I_S \qquad (31)$$

where S_B is the section of the coil perpendicular to the current density (Fig. 8).

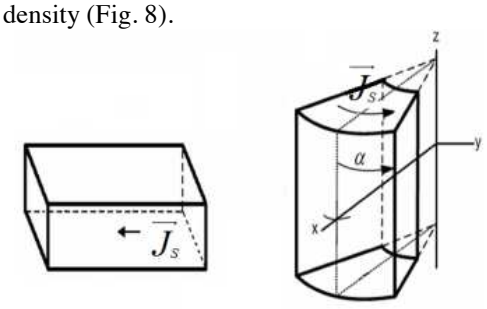


Figure 8: The geometries of the straight part and the curved part of the racetrack coil and direction of the current density

To compute the flux density $\overrightarrow{B_S}$ due to the coil, the straight parts and the curved parts are subdivided in straight or curved blocks. By means of Biot and Savart law, the flux density due to each block is computed and sum up in order

to get the source flux density $\overrightarrow{B_S}$ due to the whole coil. Table II shows the results obtained at different distance from the center of the coil along the Oz direction for a current density J_s of 1A.mm^{-2}. In order to calculate the magnetization by the developed method of moment, a very good accuracy is needed to calculate the flux density due to the coil.

Table II: Distribution along Oz, inside the upper half of the core, of the flux density due to the coil for different number of blocks (Nbloc) for a current density of Js=1.A.mm^{-2}: Values of Bz are in (mT)

Nbloc	Distance from the center of the core(m)				
	0.0085	0.017	0.0255	0,034	0.0425
72000	0.5008	049935	0.49470	0.46451	0.081676
36800	0.50105	0.49964	0.49499	0.46479	0.081718
7488	0.50025	5.0023	0.49695	0.46721	8.0756

Table II shows that 7488 blocks is sufficient to obtain a very good accuracy for the computation of the flux density inside the core. The detailed subdivision of the coil, for 7488 blocks, is given in table III: a curved part are divide in (nr.na.nz) blocks and, a straight part, in (nr.nw.nz) blocks.

Table III: Subdivision of racetrack coil

Direction	symbol	value
thickness	nr	4
angular	na	8
width	nw	5
height	nz	36

4.2. Finite Element Analysis (FEA)

In order to make a first validation, the results obtained by the developed method of moment are compared to numerical model obtained by the software package ANSYS/EMAG. Figure 9 shows the study domain considered for FEA.

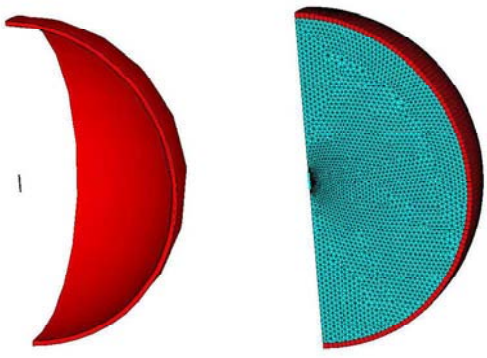


Figure 9: Left: study domain with in red a zone for a layer of infinite element, Right: the mesh of the study domain with in red infinite elements.

The study domain is a fourth part of the whole domain in order to save time and memory. The red zone is meshed of a layer of infinite element. In ANSYS/EMAG the reduced scalar magnetic potential formulation is used. The study domain has been meshed by 245000 elements and 48030 nodes. Figure 10 shows the finite element mesh around the core and its coil.

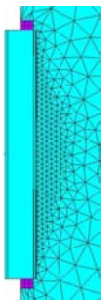


Figure 10: Finite element mesh around the LFA

4.3. Measurement set-up

Figure 11 shows the actual LFA with its stranded coil made with 61 turns.

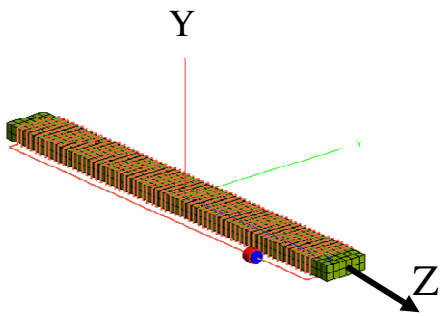


Figure 11: The actual low frequency antenna

The flux density due to the LFA has been measured along direction OX and OZ and at distance already specified on figure 7. The measurement set up is shown on figure 12.

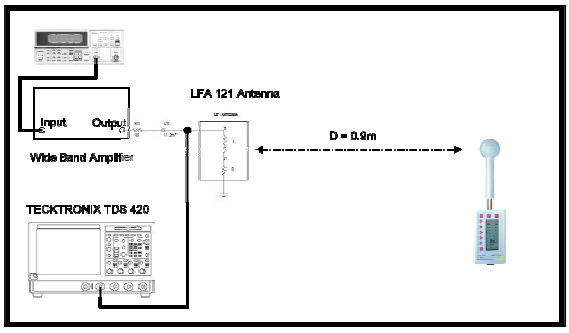


Figure 12: The measurement set up

The measurements has been made using AC supply at a frequency of 125kHz. As the conductors are very thin there is a very little difference from a DC situation. The main difference is due to the hysteresis phenomena in the ferrite core. It was experimentally verified that hysteresis

phenomena have a very little effect by measuring the inductance of the coil at different frequency around 125kHz.

4.4. Simulations results and measurements

The distributions of the magnetic flux density along the coil axis (Oz) and along (Ox) perpendicular to the coil axis shown on figure 7 have been calculated by the developed method moments and 3D finite element method (FEM). The results are compared to the values of the components of the flux density measured on a test bench (Fig. 12), the distribution of the flux density along (Oz) and (Ox) are shown on Fig. 13 and Fig. 14 respectively. The value of the measured current Is in the coil is 0.63A.

For the method of moment and finite element analysis the relative permeability of the core is taken equal to 3000 which is the value given by the data sheet of the employed ferrite material. The core is meshed with the same number of blocks (MoM) or elements (FEA) equal to (NVE=3528). The study gives very similar results. In fact, theoretically, to use FEA, the mesh of the surrounding space should extend off to infinity for an exact solution. Of course this is impossible, so it is necessary to arbitrarily decide how far the mesh should extend away from the model to get an acceptable solution. This can be a major problem. Make the exterior region too small, the solution may never be accurate enough. On the other hand, make it larger and the number of unknowns, hence, the solution time increases. We observe that the FEA needs very large number of elements in the material and in the surrounding space. In contrast, MoM requires few subdivisions. To obtain the accuracy of the results in Fig . 13 and Fig .14 only the core is subdivided. The CPU time required to compute the external flux density of an antenna in our approach is smaller than the one required for FEA. For example, the external flux density of low frequency antenna can be obtained with a precision better than 9% in less than 2 seconds, while it would take a few minutes with a FEM code on a same processor.

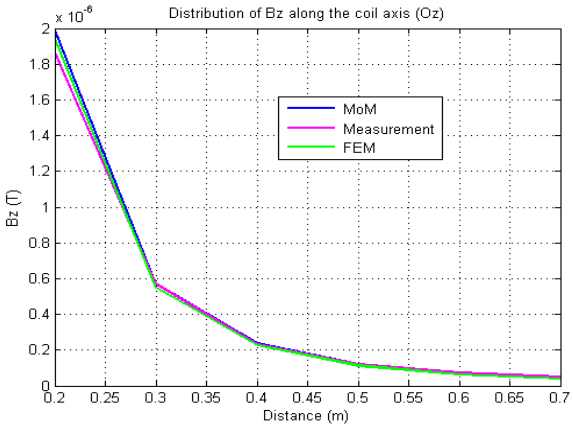


Figure 13: Distribution of magnetic field density computed by MoM and FEM and measured along the LFA axis (Oz)

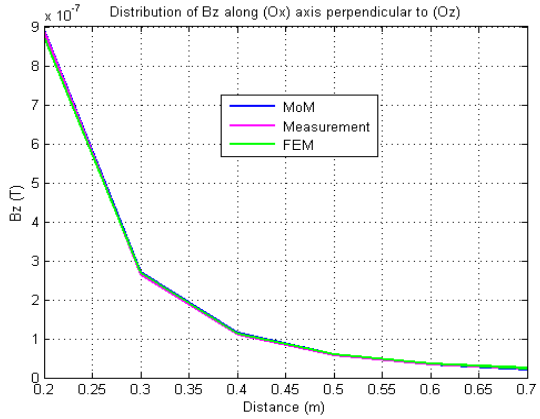


Figure 14: Distribution of magnetic field density computed by MoM and FEM and measured along (Ox) perpendicular to the LFA axis

5. Study of parameters variation

In order to assess, the results obtained by method of moments it is interesting to study how these results change with the variation of some parameters. In this last section, the influence of the number of subdivisions of the core and the permeability of the core are studied.

5.1. Influence of the subdivisions of the core

Several simulations with different subdivisions have been performed with the method of moment. Figure 15 shows the distribution of the component Bz of the flux density along the Ox direction for a current density of 1A.mm^{-2}. The precision of the field integral computation depends only on the number of subdivisions of the core region, but not on the mesh of an arbitrary exterior region, and boundary conditions applied at infinity as is the case with FEM codes. The results on Fig. 15 shows that the results quickly with the number of subdivisions. The relative quadratic error between the results obtain with the highest number of subdivisions and the lowest number of subdivisions is less than 5%.

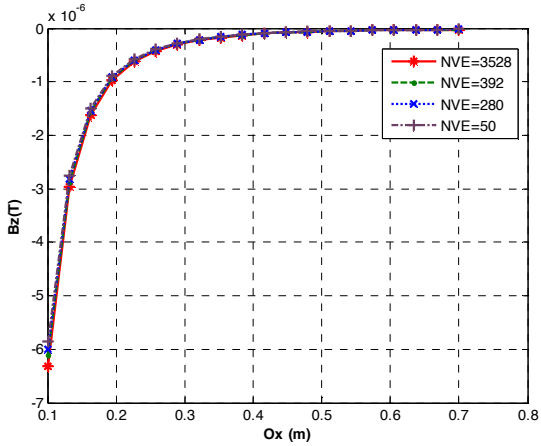


Figure 15: Distribution of the component Bz of the magnetic flux density along Ox computed by MoM for different number of subdivisions (NVE).

Table IV details the values of Bz along Ox for the distance [0.5:0.8] m for a value of the current density equal to 1.Amm^{-2}.

Table IV: Values of Bz (nT) computed along Ox

NVE	0.5	0.55	0.6	0.65	0.7	0.75
3528	56.0	46.8	39.5	33.7	28.9	25.0
392	54.1	45.3	38.2	32.6	28.0	24.2
280	53.2	44.4	37.5	32.0	27.5	23.8
50	51.9	43.4	36.6	31.2	26.8	23.2

5.2. Permeability variation

For the study of the permeability variation, the reference results are those obtained with the number of subdivisions equal to (NVE=3528) in the core region.

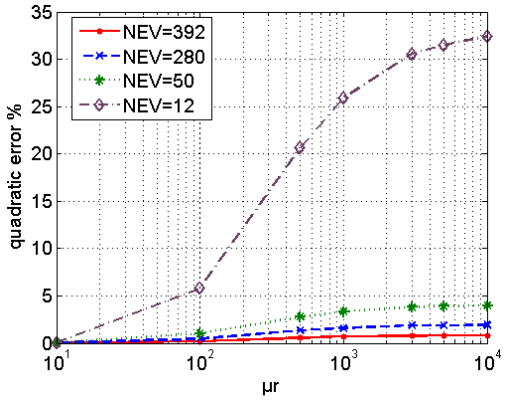


Figure 16: Influence of the variation of the permeability

The values of the relative quadratic error for μr=100, 500, 1000 with respect to the reference results are shown clearly in Table V and Fig. 16.

The method of moments leads to inaccuracies when the relative permeability is high, more than 100, and the number of subdivisions is low, less than 12. It leads to acceptable results (the quadratic error is less than 6%), for μr less than 100. Nevertheless, for a number of subdivisions equal to 50, the errors does not exceed 5% for any value of the permeability, which can be very satisfactory in compensation for a really fast and easy computation.

Table V: The percentage of the quadratic error for different number of subdivisions (NVE) and different values of the relative permeability with respect to reference results

NVE	Relative Permeability		
	100	500	1000
392	0.2026	0.5743	0.6878
280	0.4632	1.3438	1.5960
50	1.0356	2.7789	3.3299
12	5.8258	20.6059	25.8915

6. Conclusions

This paper has presented a new application of the method of moment. For this application the method of moment is more efficient than 3D FEA to calculate the magnetic fields at large distance from a low frequency antenna. With respect to FEM, the matrix system is smaller: a number of subdivisions of the core equal to 50 is sufficient to have a very good accuracy. Only few seconds is needed to solve the problem with MoM and the results are in a good agreement (less than 8%) with numerical results and measurements**.** In FEA we use a mesh of about 245000 elements and 48030 elements. This huge number of elements is needed to take into account the air region around the antenna.

References

[1]M. Albach, A. Stadler, and M. Spang, "The Influence of Ferrite Characteristics on the Inductance of Coils With Rod Cores", *Magnetics, IEEE Transactions on*, vol. 43, no. 6, pp. 2618-2620, 2007.

[2] A. Tran, M. Bolic, and M. C. E. Yagoub, "Magnetic-field coupling characteristics of ferrite-coil antennas for low-frequency RFID applications", *International Journal of Computer Science Issues IJCSI*, vol. 7, no. 4, p. 5, July 2010.

[3] A. Stadler, "Radiated magnetic field of a low-frequency ferrite rod antenna," in *Compatibility and Power Electronics (CPE), 2011 7th International Conference-Workshop*, 2011, pp. 283-288.

[4]Olivier Chadebec, Laure-Line Rouve, and Jean-Louis Coulomb, "New Methods for a Fast and Easy Computation of Stray Fields Created by Wound Rods", *IEEE TRANSACTIONS ON MAGNETICS*, vol. 38, MARCH 2002.

[5] O. Chadebec, J. L. Coulomb, and F. Janet, "A Review of Magnetostatic Moment Method", *IEEE Trans. Magn*, vol. 42, no. 4, pp. 515-520, April. 2006.

[6] A. Morandi, M. Fabbri, and P. L. Ribani, "A Modified Formulation of the Volume Integral Equations Method for 3-D Magnetostatics", *Magnetics, IEEE Transactions on*, vol. 46, no. 11, pp. 3848-3859, 2010.

.

Time-domain semiconductor structure simulation based on 2D/3D Coupled Electromagnetism/Transport Modeling

C. Dalle

Institut d'Electronique, de Microélectronique et de Nanotechnologies, UMR CNRS 8520

Département Hyperfréquences et Semiconducteurs, groupe Silphyde,

Cité Scientifique, Avenue Poincaré, B.P. 60069, 59652 Villeneuve d'Ascq Cédex, France
*corresponding author, E-mail: christophe.dalle@iemn.univ-lille1.fr

Abstract

In order to investigate the semiconductor device high frequency operation, we are developing a 2D/3D time-domain electromagnetic physical simulator. It is based on a self-consistent solution of both the Maxwell equations and the free carrier macroscopic conservation equation sets issued from the Boltzmann general transport equation. Its large potential application field presently concerns the THz distributed Transferred Electron Device (TED) but also the investigation of the heating process inside a semiconductor powder under the action of a high power microwave signal.

1. Introduction

The description of the influence of the free electric charges is still today a challenge in the semiconductor device electromagnetic modeling. In this context, we are presently developing a 2D/3D time-domain electromagnetic physical simulator including the free carrier transport phenomena description following the macroscopic approach. It has been originally devoted to the mm-wave distributed IMPATT diode modeling [1]. It is now used in the modeling of THz distributed Transferred Electron Devices (TED's). Because of its large potential application field, it is for example also used in the study of the transport physical phenomena involved in the electromagnetic heating of semiconductor powder grains.

2. The Electromagnetic simulator

The laboratory-made simulator is fundamentally split in two main entities (figure 1). The first one is devoted to the numerical solution of the Maxwell equations in the whole considered physical volume. This solution must be associated with the solution of the electrostatic Poisson/Ampere equation solution in order to account for the initial net electric charge distribution and the possible semiconductor device DC bias conditions. Thus, the electric field is split in DC and RF component $(\vec{E} = \vec{E}_{DC} + \vec{E}_{RF})$.

The transport model for the perfect or more realistic metal is directly implemented in the Maxwell model. Mur's absorbing boundary conditions are presently considered [2]. The calculated electromagnetic field $(\vec{E}, \vec{H})$ is the input quantity for the second entity which is devoted to the free carrier transport modeling. It relies on the macroscopic conservation equation set issued from the Boltzmann general transport equation namely any one of the drift-diffusion, energy and energy-momentum approaches. The conduction current density $\vec{J}_c$ is the quantity required by the Maxwell model.

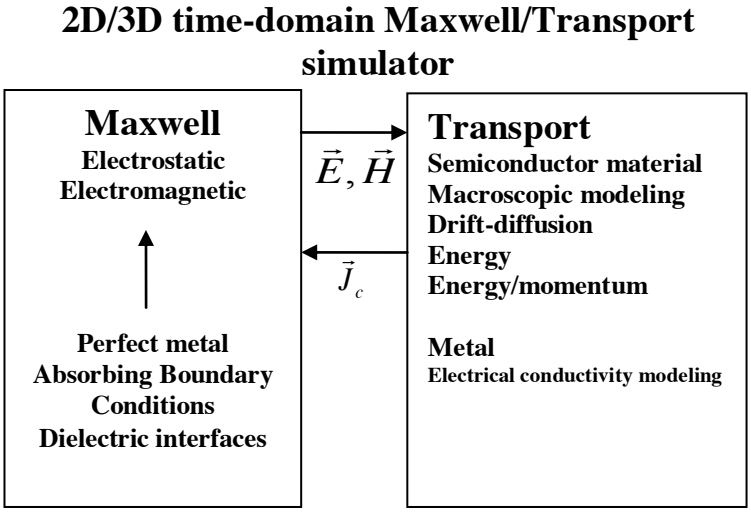


Figure 1

The numerical method of solution is the FDTD method. The spatial mesh is variable and the position of both the scalar and vector physical quantities is defined following the Yee's topology. The Alternating Direction Implicit method (ADI) is systematically used for the approximation of the partial differential Maxwell and carrier transport equations [3]. It leads to the efficient numerical solution of simple tridiagonal matrix/vector equations. Moreover, the implicit

method allows the use of time increment values close to those imposed by the macroscopic transport models.

3. THz distributed TED

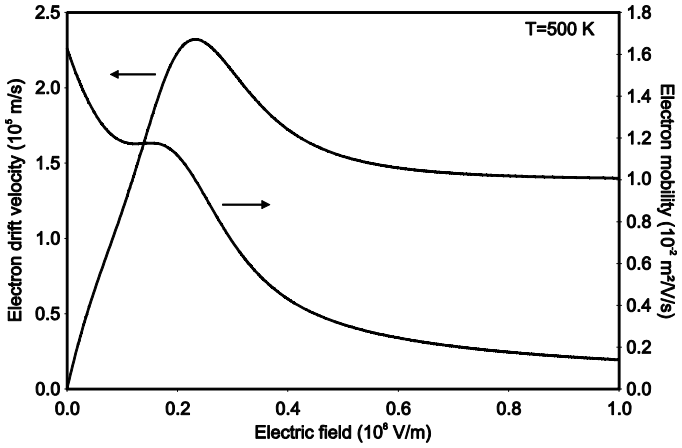


Figure 2: GaN velocity/field characteristic

A study is presently devoted to the InP and GaN N^+NN^+ distributed TED's at THz operating frequencies. The TED's RF operation fundamentally relies on the semiconductor material physical properties namely the existence of a negative differential mobility zone in the electron velocity/field characteristic as shown for GaN in figure 2. From an EM point of view, the structure, when simulated in two dimensions (2D), is similar to that of an active multilayered parallel plate waveguide (figure 2). In three dimensions (3D), the distributed TED's is nearly similar to an active microstrip line. The device RF operation is based on the interaction of a transversal EM wave, propagating in a parallel to the device N^+NN^+ epitaxial layers, and electrons mainly drifting perpendicular to the epitaxial layers. The EM wave amplification results from the transverse modulation of the electron motion under the action of the EM field in the device N active zone which consequently acts as a negative RF resistance medium.

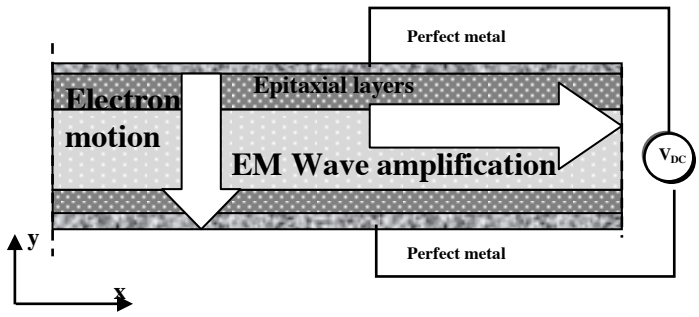


Figure 3: Distributed TED's basic structure

3.1. Mesa GaN TED's RF operation

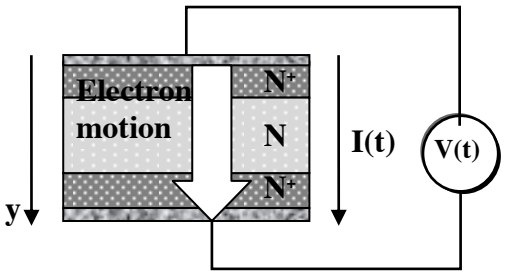


Figure 4: Mesa GaN TED's modeling

In a first approach, it is necessary to independently investigate the RF operation of the vertical (or mesa) N^+NN^+ doped TED structure. This study is performed by means of a classical one dimensional (1D) time domain quasi-electrostatic energy-momentum modeling. The electron unipolar transport model is based on a non-stationary macroscopic approach derived from the general Boltzmann transport equation and includes the free electron continuity, total energy and momentum equations [4]. It allows to account for the electron inertia effects at high operating frequencies such as THz ones by means of the relaxation time approximation. Note that the 1D model is also used to obtain the DC initial solution for 2D simulations. Thus, the geometrical and technological parameters of the device active zone are optimized under CW pure sine operating mode ($V(t)=V_{DC}+V_{RF}\sin\omega t$) (figure 4). The TED's non linear RF operation is an electronic longitudinal wave propagating through the device N active zone namely in the present case the electron accumulation layer and transit mode. Fourier analysis of both the bias voltage and current waveforms allows to calculate the device impedance (more especially the negative resistance level), RF emitted performance and conversion efficiency (figure 5). At one THz, the N active zone thickness is 0.22 µm. The doping level is 4. $10^{23}m^{-3}$. This value is related to the DC current density which is close to 2.4 10^{10} A/m^2. Indeed, a so high DC current density is necessary to maintain the device negative resistance level to a high enough value namely one ohm for a device area of 10^{-10} m^2. Note that the DC bias voltage is here as high as 12V to the detriment of the Joule dissipated power. Indeed, the internal electric field in the N active zone must overcome the semiconductor material threshold electric field (around 2.2 10^7 V/m in GaN) to yield the electronic transfer phenomenon and the formation of the electron accumulation layer.

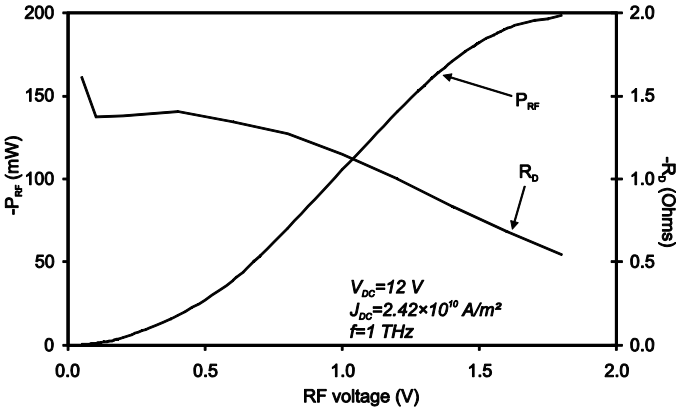


Figure 5: Evolutions of the RF emitted power P_{RF} and negative resistance level R_d as a function of the RF voltage for the optimum DC bias point.

3.2. THz GaN TED's 2D modeling

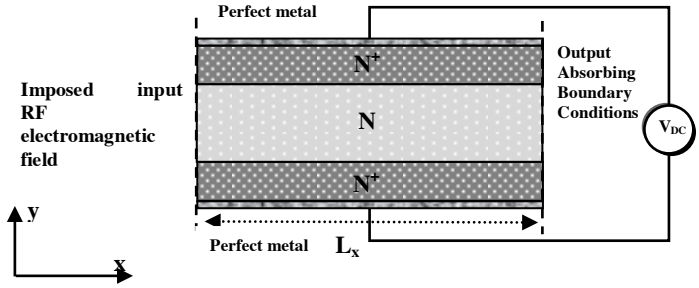


Figure 6: 2D distributed GaN TED's modeling

The 2D EM/energy-momentum model is used to investigate the interaction between the EM wave propagating along the epitaxial layers in the X direction and the electrons mainly moving transversally in the Y direction (figure 5). Mur first order boundary conditions are applied in the device output plan. This allows to study the propagation of a progressive wave through the structure. Thus, in amplification mode, the spatial electromagnetic field is imposed in the input plan (TM_{10} input propagating mode).

In CW oscillation operating mode, the device is "short-circuited" in the input plan and the RF component of the electromagnetic field is considered as zero (figure 6). The intrinsic performance of the structure as well as the Lx optimum device length can be evaluated. Figure 7 shows the instantaneous evolution of the Y direction transverse RF voltage V_{RFy} along the propagation X direction. This quantity is calculated from the circulation of the Y direction RF electric field component E_y along the Y direction. This result clearly illustrates how the EM field amplitude increases along the structure.

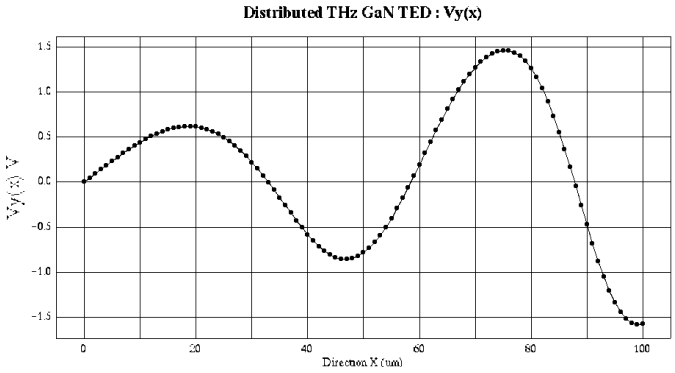


Figure 7 : Instantaneous Y direction RF voltage component V_{RFy} along the propagation direction under free running oscillation operating mode.

3.3. CW THz GaN TED's oscillator modeling

A best understanding of the RF operation and performance evaluation of the CW Thz GaN TED's oscillator requires a modeling including the whole circuit namely describing the active device/passive circuit interaction. A first improvement consist in taking into account the input and output matching circuit by means of external lumped elements in the 2D EM/transport model [5]. By other way, we have developed a full 3D EM/transport modeling. The model has been validated by means of the simulation of small size structures. However, the modeling of whole structure requires the implementation of the software on a more powerful computer such as a parallel one.

4. Semiconductor Powder Heating by EM waves

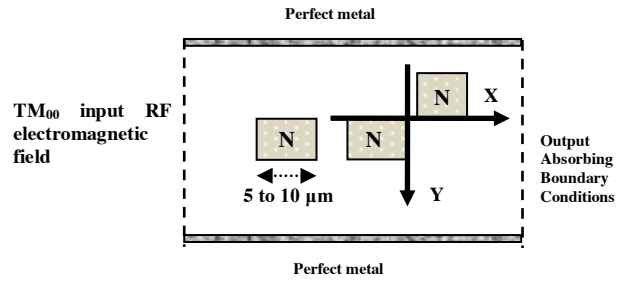
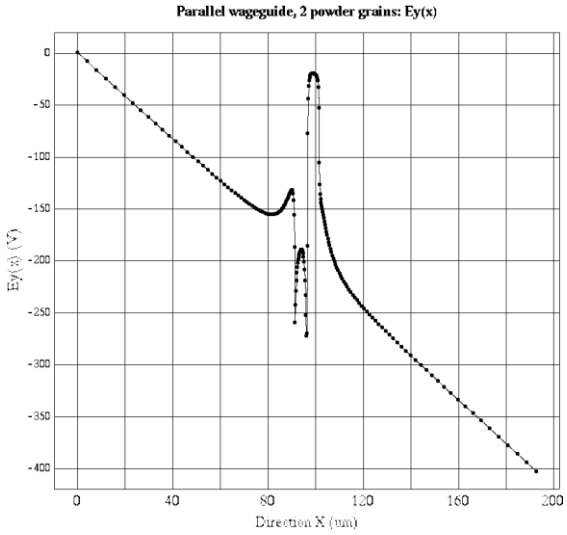
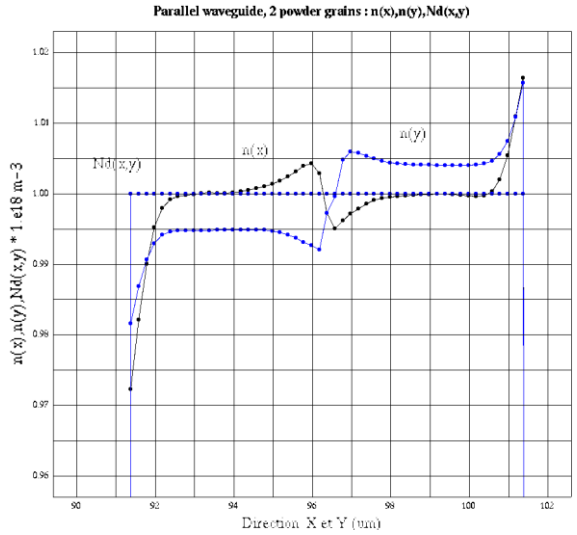


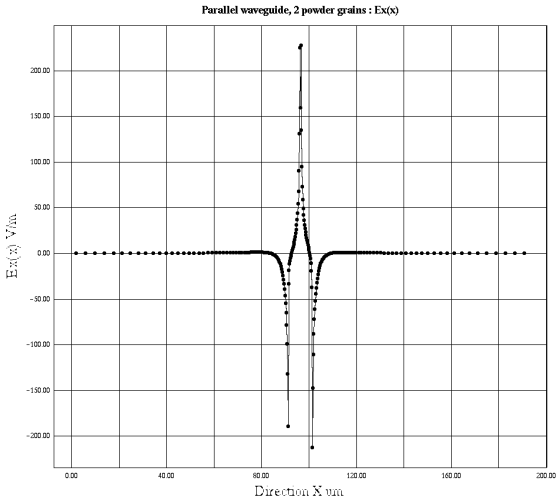
Figure 8

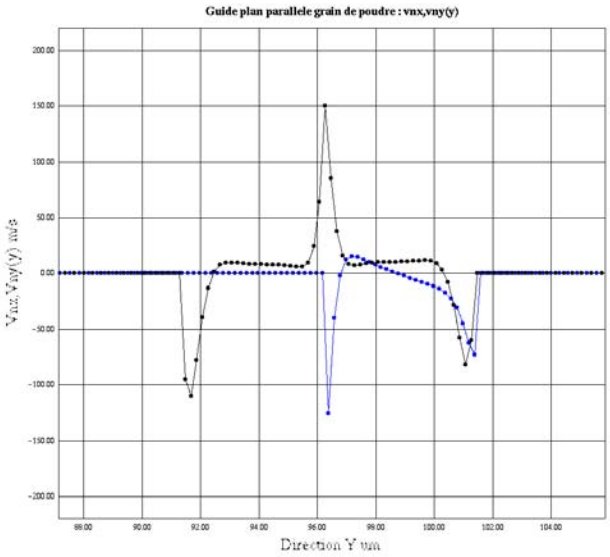
Because of its large potential application field, the simulator can be used to study the action of a high power microwave signal on a semiconductor powder namely SiC. Because of the frequency of interest (around 2 GHz), a drift-diffusion approach of the carrier transport is satisfactory. The goal is to investigate the internal motion of the free carriers inside the grains and to evaluate the induced heating process. Because of the computer time consumption, a 2D simulation is presently performed. Thus, in a first step, a single square grain is placed inside a parallel plate waveguide in which a TM_{00} EM wave is propagating (figure 8). Pure dielectric,

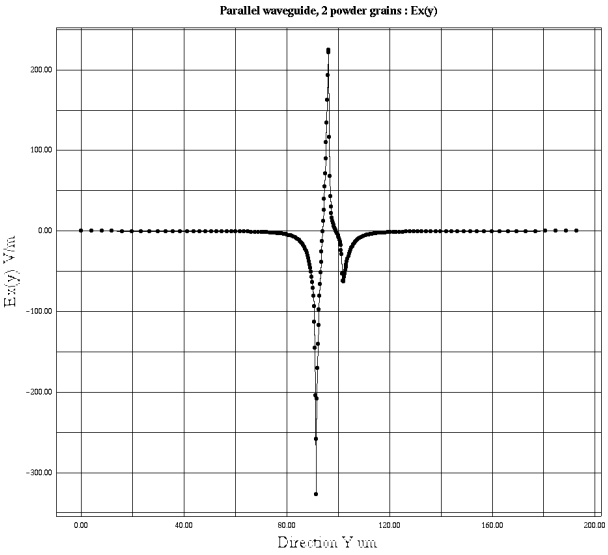
metal and semiconductor grains have been successively considered. Inside the semiconductor grain, the carriers are initially at thermal equilibrium and their motion is observed under the action of the external electric field leading to the appearance of accumulation and depletion layers at the grain surface. If a second grain in electric contact is added, a continuous carrier interchange is pointed out. As an illustration, figure 9 shows instantaneous evolutions of the electron and donor densities, velocity and X and Y direction electric field components along the two grains X and Y direction interfaces (see figure 8). The electric field evolutions show how the semiconductor grains disturb the EM wave propagation. The spatial distribution of the electric field inside the grains allows to calculate the absorbed RF power. The simulation of a larger number of grains would allow a better understanding of the macroscopic properties of the powder and a comparison with experimental data.











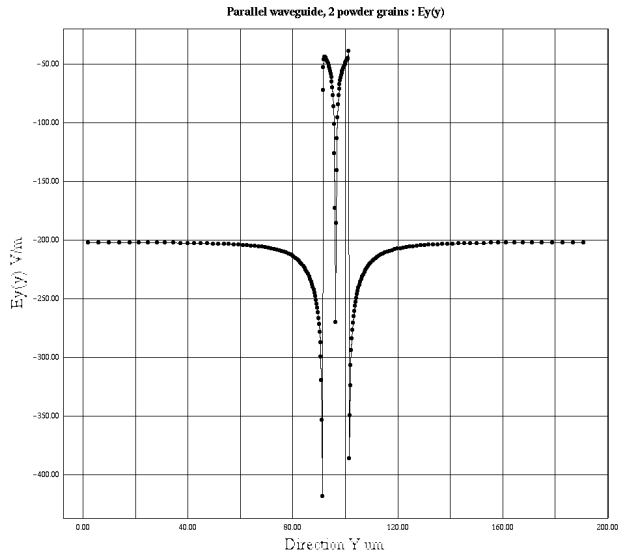


FIGURE 9

The simulation must be still improved. Indeed, dielectric losses and the effects occurring at the grain surface such as the carrier depletion must be taken into account. Moreover, the addition of the self consistent heat diffusion equation solution must be added in order to simulate both the RF and thermal transient operation.

5. Conclusions

A 2D/3D time-domain electromagnetic physical simulator has been presented. It is based on a self-consistent solution of both the Maxwell equations and the free carrier macroscopic conservation equation sets issued from the Boltzmann general transport equation. It is well suited to the modeling of non linear RF operation. Its large potential application field has been illustrated by means of two examples. The first one concerns the THz distributed Transferred Electron Device (TED). The second one concerns the investigation of the heating process inside semiconductor powder grains under the action of a high power microwave signal.

REFERENCES

[1] A. El Moussati, C. Dalle, “2D time-domain electromagnetic macroscopic numerical modelling on parallel computer: application to the mm-wave silicon DIMPATT diode”, Journal of Computer Electronics, Vol. 7, pp. 34-42, 2008.

[2] G. Mur, “Total-field absorbing boundary conditions for the time-domain electromagnetic field equations”, IEEE trans. Microwave Theory and Techniques, Vol. 40, N° 2, pp. 100-102, May 1998.

[3] T. Namiki, "3-D-ADI-FDTD method – Unconditionally stable time-domain algorithm for solving full vector Maxwell’s equations", IEEE Trans. Microwave Theory and Techniques, Vol. 48, N°10, pp. 1743–1748, October 2000.

[4] R. K. Mains, G. I. Haddad, P. A. Blakey, ’Simulation of GaAs IMPATT diodes including energy and velocity transport equations’, *IEEE Trans. Electron Devices*, Vol. 30, n°10, pp. 1327-1338, October 1983.

[5] M. Piket-May, A. Taflove and J. Baron "FD-TD modeling of digital signal propagation in 3-D circuits with passive and active loads", IEEE Trans. Microwave Theory and Techniques, Vol. 42, N° 8, pp.1514-1523, august 1994.

CURVILINEAR VECTOR FINITE DIFFERENCE APPROACH TO THE COMPUTATION OF WAVEGUIDE MODES

A. Fanti*, G. Mazzarella, and G. Montisci

Department of Electrical and Electronic Engineering,
University of Cagliari, 09123, Piazza d'Armi, Cagliari, Italy
*corresponding author, E-mail: alessandro.fanti@diee.unica.it

Abstract

We describe here a Vector Finite Difference approach to the evaluation of waveguide eigenvalues and modes for rectangular, circular and elliptical waveguides. The FD is applied using a 2D cartesian, polar and elliptical grid in the waveguide section. A suitable Taylor expansion of the vector mode function allows to take exactly into account the boundary condition. To prevent the raising of spurious modes, our FD approximation results in a constrained eigenvalue problem, that we solve using a decomposition method. This approach has been evaluated comparing our results to the analytical modes of rectangular and circular waveguide, and to known data for the elliptic case.

1. Introduction

In many applications, such as the analysis of waveguide junctions using mode matching [1], the knowledge of both eigenvalues and field distributions of waveguides modes [2] is required. The same type of information is also required in the analysis, using the method of moments (MoM), of thick-walled apertures [3]. Indeed, these apertures can be considered as stub waveguides, and the modes of these guides are the natural basis functions for the MoM [4].

Apart from some simple geometries, mode computation cannot be done in closed form, so that suitable numerical techniques must be used. Until now, many different numerical techniques have been proposed. The most popular [5] are the Finite Difference (FD) Method and scalar and vector Finite Element Method (FEM). FD techniques, despite of their long history, are still very popular because of their simplicity and computational effectiveness. However, they compute the Hertz potential eigenfunctions, so that, since the basis functions of the MoM are the vector eigenfunctions, a numerical derivative is required, which can results in a reduced accuracy.

Aim of this work is to present the direct computation of mode vectors in a waveguide, using a finite difference (FD) approximation of the vector Helmholtz equation on a suitable discretization grid. Since we are mainly interested in using those modes in the MoM, the entire development will be expressed in term of equivalent magnetic surface currents. For each grid point, suitable second–order Taylor approximations allow to replace the continuous eigenfunction problem with a discrete one. This leads to a matrix eigenvector problem, when suitable conditions are added. These come out from the boundary conditions (which are included directly in the problem matrix), and the solenoidal or irrotational condition on mode vectors. This constrained eigenvalue problem can then be solved using linear algebra techniques [6].

We consider here rectangular, circular and elliptic [7] waveguides. In order to improve both the accuracy and the computational effectiveness, a discretization grid fitting exactly the waveguide boundary is chosen. Therefore, our FD approach has been implemented using cartesian, polar and elliptic frameworks.

2. Description of the Technique

Let use consider a waveguide. The TE mode vectors $\overrightarrow{e}$ are the eigenfunctions of the Helmholtz equation :

$$\begin{cases} \nabla_t^2 \overrightarrow{e} + k_t^2 \overrightarrow{e} = 0 \\ \nabla_t \cdot \overrightarrow{e} = 0 \\ \overrightarrow{e} \times \overrightarrow{i_n}\Big|_C = 0 \end{cases} \tag{1}$$

where C is the contour of the waveguide section. If we introduce the (two-dimensional) magnetic current $\overrightarrow{M}$ equivalent to the transverse field $\overrightarrow{e} = \overrightarrow{i_z} \times \overrightarrow{M}$ we get from (1)

$$\nabla_t^2 \overrightarrow{e} = -\nabla_t \times \nabla_t \times \overrightarrow{e} = -\nabla_t \times \left[\overrightarrow{i_z} \nabla_t \cdot \overrightarrow{M}\right] = \left[-\nabla_t \times \nabla_t \times \overrightarrow{M} + \nabla_t^2 \overrightarrow{M}\right] \times \overrightarrow{i_z} \tag{2}$$

$$\nabla_t \cdot \overrightarrow{e} = \nabla_t \cdot \left[\overrightarrow{i_z} \times \overrightarrow{M}\right] = -\overrightarrow{i_z} \cdot \left[\nabla_t \times \overrightarrow{M}\right] = 0 \tag{3}$$

From (3), it follows that $\nabla_t \times \overrightarrow{M} = 0$. When substituted in (1) , after replacing and collecting terms we get:

$$\begin{aligned} &\nabla_t^2 \overrightarrow{e} + k_t^2 \overrightarrow{e} = \\ &\left[-\nabla_t \times \nabla_t \times \overrightarrow{M} + \nabla_t^2 \overrightarrow{M}\right] \times \overrightarrow{i_z} + k_t^2 \left(\overrightarrow{i_z} \times \overrightarrow{M}\right) = \\ &= \overrightarrow{i_z} \times \left[-\left(\nabla_t^2 \overrightarrow{M} + k_t^2 \overrightarrow{M}\right)\right] \end{aligned} \tag{4}$$

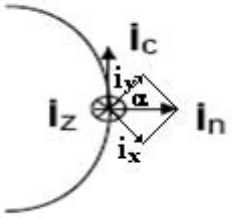


Figure 1: Vectors geometry with respect to the contour of the conductor.

The TE eigenvalue problem can therefore be rewritten, taking into account the contour geometry as in Fig.1, as:

$$\begin{cases} \nabla_t^2 \overrightarrow{M} + k_t^2 \overrightarrow{M} = 0 \\ \nabla_t \times \overrightarrow{M} = \dfrac{\partial M_y}{\partial x} - \dfrac{\partial M_x}{\partial y} = 0 \\ \overrightarrow{M} \cdot \overrightarrow{i_n}\Big|_C = M_x \cos(\alpha) + M_y \sin(\alpha) = 0 \end{cases} \tag{5}$$

In order to solve problem (5) with FD, both the unknown $\overrightarrow{M}$ and the equations of (5) are discretized, i.e., evaluated only on the points of a suitable grid. In this way, for each discretization point, we have a difference equation, corresponding the first of (5), expressed in terms of the samples of $\overrightarrow{M}$. This equation takes into account also the boundary condition on the waveguide contour. On the other hand, the requirement $\nabla_t \times \overrightarrow{M} = 0$, suitably discretized, must be imposed separately. As a consequence, (5) becomes a constrained matrix eigenvalue problem. It is worth noting that the latter requirement could be incorporated into the eigenvalue equations. In this way a standard matrix eigenvalue problems follows, but it can contain spurious solutions, which are not present in our formulation.

3. Rectangular waveguides

Let us consider first a rectangular waveguide, whose discretization grid is shown in Fig.2. Since this is the simpler structure, we discuss in detail, for this case, the passage from (5) to the discretized form.

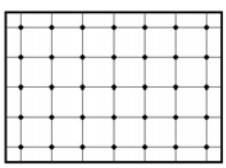


Figure 2: TE grid for the rectangular case.

The discretization of the first of (5) depends on the grid point that we consider. For an internal point P, as in Fig. 3, we can use a second-order Taylor expansion as:

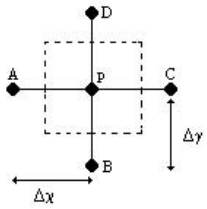


Figure 3: Internal Point of TE grid.

$$\begin{aligned} &\overrightarrow{M}_B = \\ &\overrightarrow{M}_P + \left.\frac{\partial \overrightarrow{M}}{\partial y}\right|_P \cdot (-\Delta y) + \frac{1}{2}\left.\frac{\partial^2 \overrightarrow{M}}{\partial y^2}\right|_P \cdot (-\Delta y)^2 \\ &\overrightarrow{M}_D = \\ &\overrightarrow{M}_P + \left.\frac{\partial \overrightarrow{M}}{\partial y}\right|_P \cdot (+\Delta y) + \frac{1}{2}\left.\frac{\partial^2 \overrightarrow{M}}{\partial y^2}\right|_P \cdot (+\Delta y)^2 \end{aligned} \tag{6}$$

Adding these equation we find:

$$\left.\frac{\partial^2 \overrightarrow{M}}{\partial y^2}\right|_P = \frac{1}{\Delta y^2} \cdot \left(\overrightarrow{M}_B + \overrightarrow{M}_D - 2\overrightarrow{M}_P\right) \tag{7}$$

Likely in the x direction:

$$\left.\frac{\partial^2 \overrightarrow{M}}{\partial x^2}\right|_P = \frac{1}{\Delta x^2} \cdot \left(\overrightarrow{M}_A + \overrightarrow{M}_C - 2\overrightarrow{M}_P\right) \tag{8}$$

Summing (7) and (8) we obtain :

$$\begin{aligned} \nabla_t^2 \overrightarrow{M}_P = &\frac{\overrightarrow{M}_A}{\Delta x^2} + \frac{\overrightarrow{M}_C}{\Delta x^2} + \frac{\overrightarrow{M}_B}{\Delta y^2} + \frac{\overrightarrow{M}_D}{\Delta y^2} + \\ &- \left(\frac{2}{\Delta x^2} + \frac{2}{\Delta y^2}\right) \overrightarrow{M}_P \end{aligned} \tag{9}$$

We need also to discretize the second of (5). Using a first–order Taylor expansion (compare (6)) we easily get:

$$\begin{aligned} &\left(\frac{\partial M_y}{\partial x} - \frac{\partial M_x}{\partial y}\right) = \\ &\frac{M_{C,y}}{2\Delta x} - \frac{M_{A,y}}{2\Delta x} - \frac{M_{D,x}}{2\Delta y} + \frac{M_{B,x}}{2\Delta y} = 0 \end{aligned} \tag{10}$$

For a boundary point P, as in Fig.4, we need a different approach, since D is not a sampling point for the current. We force in D the boundary condition $M_{D,y} = 0$, and incorporate it into the FD matrix. Now $M_{D,y}$ can be obtained as a Taylor expansion

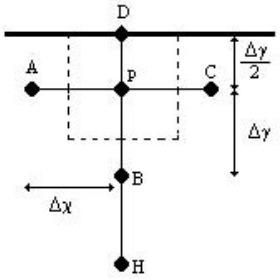


Figure 4: Boundary point.

$$M_{D,y} = M_{P,y} + \left.\frac{\partial M_y}{\partial y}\right|_P \cdot \left(+\frac{\Delta y}{2}\right) + \frac{1}{2}\left.\frac{\partial^2 M_y}{\partial y^2}\right|_P \cdot \left(+\frac{\Delta y}{2}\right)^2 \quad (11)$$

which can be added to $\frac{1}{2}M_{B,y}$ given by (6), to get:

$$\left.\frac{\partial^2 M_x}{\partial y^2}\right|_P = \frac{1}{\Delta y^2}\cdot(M_{H,x} - 2M_{B,x} + M_{P,x}) \quad (12)$$

and so for a boundary point P

$$\nabla_t^2 M_{P,y} = \frac{M_{A,y}}{\Delta x^2} + \frac{M_{C,y}}{\Delta x^2} + \frac{3M_{B,y}}{4\Delta y^2} + - \left(\frac{2}{\Delta x^2} + \frac{4}{\Delta y^2}\right) M_{P,y} \quad (13)$$

For the x–component $\nabla_t^2 M_{P,x}$ we need another grid point H (see Fig. 4), in which

$$M_{H,x} = M_{P,x} + \left.\frac{\partial M_x}{\partial y}\right|_P \cdot (2\Delta y) + \frac{1}{2}\left.\frac{\partial^2 M_x}{\partial y^2}\right|_P \cdot (2\Delta y)^2 \quad (14)$$

From (14) and $M_{B,x}$ given by (6) we get:

$$\left.\frac{\partial^2 M_x}{\partial y^2}\right|_P = \frac{1}{\Delta y^2}\cdot(M_{H,x} - 2M_{B,x} + M_{P,x}) \quad (15)$$

and the x–component of (9) is replaced by:

$$\nabla_t^2 M_{P,x} = \frac{M_{A,x}}{\Delta x^2} + \frac{M_{C,x}}{\Delta x^2} + \frac{M_{H,x}}{\Delta y^2} - 2\frac{M_{B,x}}{\Delta y^2} + - \left(\frac{2}{\Delta x^2} + \frac{1}{\Delta y^2}\right) M_{P,x} \quad (16)$$

In the same way, the condition (10) becomes:

$$\frac{M_{C,y}}{2\Delta x} - \frac{M_{A,y}}{2\Delta x} - \frac{M_{H,x}}{2\Delta y} + 4\frac{M_{B,x}}{2\Delta y} - 3\frac{M_{P,x}}{2\Delta y} = 0 \quad (17)$$

The FD matrix equivalent of (5) is then given by (9) (or (15) and (16) for a boundary point) with the constraint (10) or (17).

It is worth noting that the appproach described in this section can be used on more general waveguides, i.e., on all waveguides whose boundary is made of segments parallel to the cartesian axes.

4. Extension to the Circular and Elliptic waveguide

4.1. Circular waveguides

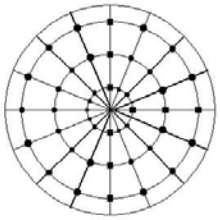


Figure 5: TE grid for a circular waveguide.

Let us consider now the discretization of (15) for a circular waveguide. In order to mantain the correct boundary condition, we use a polar discretization grid, as in Fig.5, with spacing $\Delta r, \Delta\vartheta$.

We start from the expansion of the vector Laplace operator in polar coordinates:

$$(\nabla_t^2 \overrightarrow{M})_r = \frac{\partial^2 M_r}{\partial r^2} + \frac{1}{r}\cdot\frac{\partial M_r}{\partial r} - \frac{M_r}{r^2} + \frac{1}{r^2}\cdot\frac{\partial^2 M_r}{\partial \vartheta^2} - \frac{2}{r^2}\cdot\frac{\partial M_\vartheta}{\partial \vartheta}$$
$$(\nabla_t^2 \overrightarrow{M})_\vartheta = \frac{\partial^2 M_\vartheta}{\partial r^2} + \frac{1}{r}\cdot\frac{\partial M_\vartheta}{\partial r} - \frac{M_\vartheta}{r^2} + \frac{1}{r^2}\cdot\frac{\partial^2 M_\vartheta}{\partial \vartheta^2} + \frac{2}{r^2}\cdot\frac{\partial M_r}{\partial \vartheta} \quad (18)$$

For each internal point (whose geometry is quite similiar to the one of Fig.3), using suitable Taylor approximations, as in the rectangular case, the derivatives in (18), in the sample point P, can be expresssed as:

$$\frac{\partial^2 M_\vartheta}{\partial \vartheta^2} = \frac{M_{A,\vartheta} + M_{C,\vartheta} - 2M_{P,\vartheta}}{\Delta\vartheta^2}$$
$$\frac{\partial M_\vartheta}{\partial \vartheta} = \frac{M_{C,\vartheta} - M_{A,\vartheta}}{2\Delta\vartheta}$$
$$\frac{\partial^2 M_\vartheta}{\partial r^2} = \frac{M_{B,\vartheta} + M_{D,\vartheta} - 2M_{P,\vartheta}}{\Delta r^2}$$
$$\frac{\partial M_\vartheta}{\partial r} = \frac{M_{D,\vartheta} - M_{B,\vartheta}}{2\Delta r}$$

$$\frac{\partial^2 M_r}{\partial r^2} = \frac{M_{B,r} + M_{D,r} - 2M_{P,r}}{\Delta r^2}$$
$$\frac{\partial M_r}{\partial r} = \frac{M_{D,r} - M_{B,r}}{2\Delta r}$$
$$\frac{\partial^2 M_r}{\partial \vartheta^2} = \frac{M_{A,r} + M_{C,r} - 2M_{P,r}}{\Delta \vartheta^2}$$
$$\frac{\partial M_r}{\partial \vartheta} = \frac{M_{C,r} - M_{A,r}}{2\Delta \vartheta}$$

When substituted in (18) we get:

$$\begin{aligned}(\nabla_t^2 \overrightarrow{M}_P)_r = \\ M_{B,r}K_1 + M_{D,r}K_2 + M_{A,r}K_3 + M_{C,r}K_3 \\ -M_{P,r}K_4 + M_{A,\vartheta}K_5 - M_{C,\vartheta}K_5 \\ (\nabla_t^2 \overrightarrow{M}_P)_\vartheta = \\ M_{B,\vartheta}K_1 + M_{D,\vartheta}K_2 + M_{A,\vartheta}K_3 + M_{C,\vartheta}K_3 \\ -M_{P,\vartheta}K_4 - M_{A,r}K_5 + M_{C,r}K_5\end{aligned} \tag{19}$$

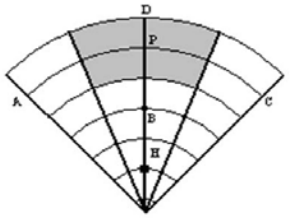


Figure 6: Boundary point of polar framework.

For a boundary point, such as P in Fig.6, the boundary condition is $M_{D,r} = 0$ and this condition can be incorporated into the FD matrix, much in the same way as in rectangular case. The result is that (19) is then replaced by:

$$\begin{aligned}(\nabla_t^2 \overrightarrow{M}_P)_r = \\ M_{B,r}H_1 + M_{A,r}K_3 + M_{C,r}K_3 \\ -M_{P,r}H_4 + M_{A,\vartheta}K_5 - M_{C,\vartheta}K_5 \\ (\nabla_t^2 \overrightarrow{M}_P)_\vartheta = \\ M_{H,\vartheta}K_1 - M_{B,\vartheta}H_2 + M_{A,\vartheta}K_3 + M_{C,\vartheta}K_3 \\ -M_{P,\vartheta}H_5 - M_{A,r}K_5 + M_{C,r}K_5\end{aligned} \tag{20}$$

The constants of (19) and (20) are

$$\begin{aligned} K_1 &= \tfrac{1}{\Delta r^2} - \tfrac{1}{2r_p\Delta r} & H_1 &= \tfrac{4}{3\Delta r^2} - \tfrac{1}{3r_p\Delta r} \\ K_2 &= \tfrac{1}{\Delta r^2} + \tfrac{1}{2r_p\Delta r} & H_2 &= \tfrac{2}{\Delta r^2} + \tfrac{4}{2r_p\Delta r} \\ K_3 &= \tfrac{1}{r_p^2\Delta\vartheta^2} & H_3 &= \tfrac{1}{r_p\Delta r} + \tfrac{2}{r_p\Delta\vartheta^2} \\ K_4 &= K_1 + K_2 + 2K_3 + \tfrac{1}{r_p^2} & H_4 &= 3H_1 + H_3 + 2K_3 \\ K_5 &= \tfrac{1}{2r_p^2\Delta\vartheta} & H_5 &= \tfrac{1}{r_p\Delta r} + \tfrac{3}{2r_p\Delta r} \\ & & & \quad -\tfrac{1}{r_p^2} - 2K_3 \end{aligned}$$

The constraint

$$\begin{aligned}\nabla \times \overrightarrow{M} &= \frac{1}{r}\cdot\frac{\partial\left(r\cdot M_\vartheta\right)}{\partial r} - \frac{1}{r}\cdot\frac{\partial M_r}{\partial\vartheta} \\ &= \frac{1}{r}\cdot M_\vartheta + \frac{\partial M_\vartheta}{\partial r} - \frac{1}{r}\cdot\frac{\partial M_r}{\partial\vartheta} = 0\end{aligned} \tag{21}$$

can be discretized in an internal point using a first–order Taylor expansion as:

$$\frac{M_{P,\vartheta}}{r_p} + \frac{M_{D,\vartheta} - M_{B,\vartheta}}{2\Delta r} - \frac{M_{C,r} - M_{A,r}}{2r_p\,\Delta\vartheta} = 0 \tag{22}$$

which becomes, in a boundary point:

$$\left(\frac{1}{r_p} + \frac{3}{2\Delta r}\right) M_{P,\vartheta} + \frac{M_{H,\vartheta}}{2\Delta r} - \frac{4M_{B,\vartheta}}{2\Delta r} - \frac{M_{C,r} - M_{A,r}}{2\Delta r_p\,\vartheta} = 0 \tag{23}$$

It remains to consider the circle center. In this point it is not possible to use a Taylor expansion since it is a singular point for the polar framework. Therefore, we integrate the first of (5) on a circle S with radius $\Delta r/2$

$$\int_S \nabla_t^2 \overrightarrow{M}\cdot dS = -k_t^2 \int_S \overrightarrow{M}\cdot dS \tag{24}$$

Because of (18), the Laplace operator becomes :

$$\nabla_t^2 \overrightarrow{M} = \nabla_t\left(\nabla_t\cdot\overrightarrow{M}\right) - \nabla_t\times\nabla_t\times\overrightarrow{M} = \nabla_t\left(\nabla_t\cdot\overrightarrow{M}\right)$$

and substituting in (24):

$$\int_S \nabla_t\left(\nabla_t\cdot\overrightarrow{M}\right)\cdot dS = -k_t^2\int_S \overrightarrow{M} dS \tag{25}$$

We apply the theorem of the gradient [8] to the l.h.s of (25)

$$\begin{aligned}\int_S \nabla_t\left(\nabla_t\cdot\overrightarrow{M}\right) dS = \int_C (\nabla_t\cdot\overrightarrow{M})\overrightarrow{i_n}\,dl = \\ \int_C (\nabla_t\cdot\overrightarrow{M})\,\overrightarrow{i_n}\frac{\Delta r}{2}d\vartheta\end{aligned} \tag{26}$$

From the divergence of $\overrightarrow{M}$ in polar coordinates we get, for the r.h.s of (26):

$$\int_C \frac{\partial\left(r\,M_r\right)}{\partial r}\,\overrightarrow{i_n}\frac{\Delta r}{2}\,d\vartheta + \int_C \frac{\partial M_\vartheta}{\partial\vartheta}\,\overrightarrow{i_n}d\vartheta \tag{27}$$

Since $\overrightarrow{i_n} = \overrightarrow{i_x}\cos(\vartheta) + \overrightarrow{i_y}\sin(\vartheta)$, we can decompose (26) in a x–component:

$$\begin{aligned}\int_C \frac{\partial\left(r\,M_r\right)}{\partial r}\,\overrightarrow{i_x}\cos(\vartheta)\,\frac{\Delta r}{2}d\vartheta + \\ \int_C \frac{\partial M_\vartheta}{\partial\vartheta}\,\overrightarrow{i_x}\cos(\vartheta)\,d\vartheta\end{aligned} \tag{28}$$

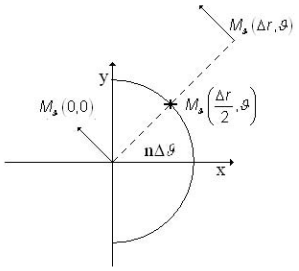


Figure 7: component of between center and next point.

and a y–component:

$$\int_C \frac{\partial\left(r\,M_r\right)}{\partial r}\,\overrightarrow{i_y}\sin\left(\vartheta\right)\frac{\Delta r}{2}d\vartheta+ \int_C \frac{\partial M_\vartheta}{\partial\vartheta}\,\overrightarrow{i_y}\sin\left(\vartheta\right)d\vartheta \tag{29}$$

The second integral of (28) and (29) can be evaluated by parts as

$$\begin{aligned}&\int_C \frac{\partial M_\vartheta}{\partial\vartheta}\cdot\overrightarrow{i_x}\cos\left(\vartheta\right)\cdot d\vartheta = \\ &= \left|M_\vartheta\cos\left(\vartheta\right)\right|_{-\pi}^{+\pi} - \int_{-\pi}^{+\pi} -M_\vartheta\sin\left(\vartheta\right)\cdot d\vartheta = \\ &= \int_{-\pi}^{+\pi} M_\vartheta\sin\left(\vartheta\right)\cdot d\vartheta\end{aligned} \tag{30}$$

$$\int_C \frac{\partial M_\vartheta}{\partial\vartheta}\cdot\overrightarrow{i_y}\sin\left(\vartheta\right)\cdot d\vartheta = -\int_{-\pi}^{+\pi} M_\vartheta\cos\left(\vartheta\right)\cdot d\vartheta \tag{31}$$

As a consequence, (25) becomes:

$$\begin{aligned}&\left[\int_C \frac{\partial\left(r\,M_r\right)}{\partial r}\cos\left(\vartheta\right)\frac{\Delta r}{2}d\vartheta + \int_{-\pi}^{+\pi} M_\vartheta\sin\left(\vartheta\right)d\vartheta\right]\overrightarrow{i_x} \\ &+\left[\int_C \frac{\partial\left(r\,M_r\right)}{\partial r}\sin\left(\vartheta\right)\frac{\Delta r}{2}d\vartheta + \int_{-\pi}^{+\pi} M_\vartheta\cos\left(\vartheta\right)d\vartheta\right]\overrightarrow{i_y} \\ &= -k_t^2\int_S \overrightarrow{M}_0\,dS\end{aligned} \tag{32}$$

wherein $\overrightarrow{M}_0$ is the value at the circle center, which must be expresssed in Cartesian coordinates: $\overrightarrow{M_0} = M_{0x}\overrightarrow{i_x} + M_{0y}\overrightarrow{i_y}$

To evaluate (32) we need $M_\vartheta\left(\frac{\Delta r}{2},\vartheta\right)$, $\left.\frac{\partial(r\cdot M_r)}{\partial r}\right|_{r=\frac{\Delta r}{2},\vartheta}$ along C, and therefore outside the discretization grid. In order to include (32) into the FD matrix, we must express both in terms of $\overrightarrow{M}$ at the discretization points, one as an average, and the other as a finite difference. Since $\overrightarrow{M_0}$ does not have polar components, $M_\vartheta\left(\frac{\Delta r}{2},\vartheta\right)$, $\left.\frac{\partial(r\cdot M_r)}{\partial r}\right|_{r=\frac{\Delta r}{2},\vartheta}$ must be computed as (compare Fig.7)

$$\begin{aligned}&M_\vartheta\left(\frac{\Delta r}{2},\vartheta\right) = \frac{1}{2}\left[M_\vartheta\left(\Delta r,\vartheta\right) + \lim_{\varepsilon\to 0} M_\vartheta\left(\varepsilon,\vartheta\right)\right] \\ &= \frac{1}{2}\left[M_\vartheta\left(\Delta r,\vartheta\right) + \left(M_{0,y}\cos\left(\vartheta\right) - M_{0,x}\sin\left(\vartheta\right)\right)\right]\end{aligned}$$

$$\begin{aligned}&\left.\frac{\partial\left(r\,M_r\right)}{\partial r}\right|_{\frac{\Delta r}{2},\vartheta} = \left[\frac{\left(r\,M_r\right)|_{\Delta r} - \lim_{\varepsilon\to 0}\left(r\,M_r\right)|_\varepsilon}{\Delta r}\right] = \\ &= \left[\frac{\Delta r\,M_r\left(\Delta r,\vartheta\right) - 0}{\Delta r}\right] = M_r\left(\Delta r,\vartheta\right)\end{aligned} \tag{33}$$

Therefore

$$\int_C \left.\frac{\partial\left(r\,M_r\right)}{\partial r}\right|_{\frac{\Delta r}{2},\vartheta}\cos\left(\vartheta\right)\frac{\Delta r}{2}\cdot d\vartheta = \sum_{q=1}^{N} M_{r,q}\cos\left(\vartheta_q\right)\Delta\vartheta \tag{34}$$

$$\int_C \left.\frac{\partial\left(r\,M_r\right)}{\partial r}\right|_{\frac{\Delta r}{2},\vartheta}\sin\left(\vartheta\right)\frac{\Delta r}{2}\cdot d\vartheta = \sum_{q=1}^{N} M_{r,q}\sin\left(\vartheta_q\right)\Delta\vartheta \tag{35}$$

where $M_{r,q} = M_r\left(\Delta r, q\Delta\vartheta\right)$, and

$$\begin{aligned}&\int_{-\pi}^{+\pi} M_\vartheta\sin\left(\vartheta\right)d\vartheta = \\ &= \frac{\Delta\vartheta}{2}\sum_{q=1}^{N}\left[M_{\vartheta,q} + M_{0,y}\cos\vartheta_q - M_{0,x}\sin\vartheta_q\right]\sin\vartheta_q\end{aligned} \tag{36}$$

$$\begin{aligned}&\int_{-\pi}^{+\pi} M_\vartheta\cos\left(\vartheta\right)d\vartheta = \\ &= \frac{\Delta\vartheta}{2}\sum_{q=1}^{N}\left[M_{\vartheta,q} + M_{0,y}\cos\vartheta_q - M_{0,x}\sin\vartheta_q\right]\cos\vartheta_q\end{aligned} \tag{37}$$

where $M_{\vartheta,q} = M_\vartheta\left(\Delta r, q\Delta\vartheta\right)$. Summing (35) and (37) we get, for the x–component of the l.h.s. of (32):

$$\begin{aligned}&\frac{\Delta\vartheta}{2}\sum_{q=1}^{N}\left[2M_{r,q}\cos\vartheta_q + M_{\vartheta,q}\sin\vartheta_q\right. \\ &\left.+M_{0,y}^q\sin\vartheta_q\cos\vartheta_q - M_{0,x}^q\sin^2\vartheta_q\right]\end{aligned} \tag{38}$$

In the same way, summing (34) and (36) we get, for the y–component of the l.h.s. of (32):

$$\frac{\Delta\vartheta}{2}\sum_{q=1}^{N}\left[2M_{r,q}\sin\vartheta_q - M_{\vartheta,q}\cos\vartheta_q - M^q_{0,y}\sin\vartheta_q\cos\vartheta_q + M^q_{0,x}\cos^2\vartheta_q\right] \tag{39}$$

4.2. Elliptic waveguides

In the same way as the circular case, in an elliptic waveguide, $\overrightarrow{M}$ is evaluated only on the points of a elliptic grid (see Fig.8) with spacing Δu, Δv.

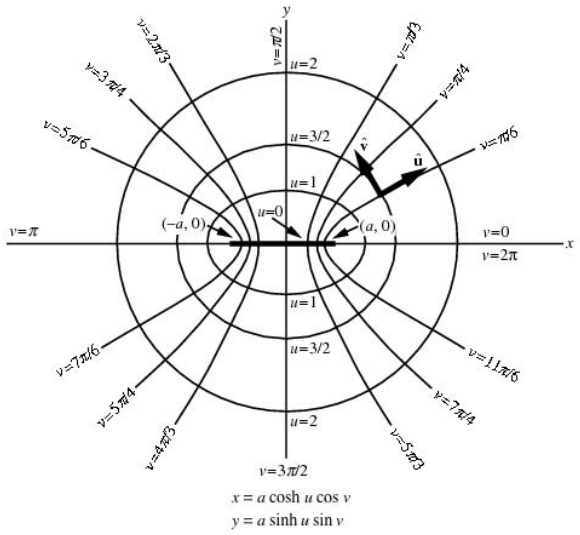


Figure 8: Geometry of the elliptic cylindrical coordinates.

The expression of the Laplace vector operator in elliptic coordinates can be simplified if we let $\overrightarrow{A} = h\,\overrightarrow{M}$, where

$$h = \frac{1}{a_f\sqrt{\sinh^2 u + \sin^2 v}}$$

is the common value of the scale factor, $2a_f$ being the inter–focal distance. The u component of $\nabla_t^2\overrightarrow{M}$ is

$$\begin{aligned}&-\frac{1}{h^5}\cdot\frac{\partial h^2}{\partial u}\cdot\frac{\partial A_u}{\partial u}+\frac{1}{h^3}\frac{\partial^2 A_u}{\partial u^2}-\\&\frac{1}{h^5}\cdot\frac{\partial h^2}{\partial u}\cdot\frac{\partial A_v}{\partial v}-\frac{\partial h}{\partial v}\cdot\frac{1}{h^3}\cdot\frac{\partial\left(A_v\right)}{\partial u}+\\&\frac{\partial h}{\partial v}\cdot\frac{1}{h^3}\cdot\frac{\partial A_u}{\partial v}+\frac{1}{h^5}\cdot\frac{\partial h^2}{\partial v}\cdot\frac{\partial A_v}{\partial u}-\\&\frac{1}{h^5}\cdot\frac{\partial h^2}{\partial v}\cdot\frac{\partial A_u}{\partial v}+\frac{1}{h^3}\cdot\frac{\partial^2\left(A_u\right)}{\partial v^2}\end{aligned} \tag{40}$$

and the v components is:

$$\begin{aligned}&-\frac{1}{h^5}\cdot\frac{\partial h^2}{\partial v}\cdot\frac{\partial A_u}{\partial u}-\\&\frac{1}{h^5}\cdot\frac{\partial h^2}{\partial v}\cdot\frac{\partial A_v}{\partial v}+\frac{1}{h^3}\frac{\partial^2 A_v}{\partial v^2}+\\&\frac{1}{h^3}\cdot\frac{\partial^2\left(A_v\right)}{\partial u^2}-\frac{1}{h^5}\cdot\frac{\partial h^2}{\partial u}\cdot\frac{\partial\left(A_v\right)}{\partial u}+\\&\frac{1}{h^5}\cdot\frac{\partial h^2}{\partial u}\cdot\frac{\partial A_u}{\partial v}\end{aligned} \tag{41}$$

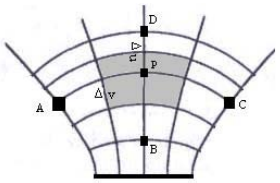


Figure 9: Internal point of the elliptic cylindrical coordinates grid TE.

For each internal grid point, as in Fig.9, a second order Taylor approximation allows to discretize the Laplace operator (40,41) in terms of the current samples at the neighboring points. The resulting derivatives are as follows:

$$\begin{aligned}\frac{\partial A_u}{\partial u}&=\frac{A_{D,u}-A_{B,u}}{2\Delta u}\\\frac{\partial A_v}{\partial u}&=\frac{A_{D,v}-A_{B,v}}{2\Delta u}\\\frac{\partial A_u}{\partial v}&=\frac{A_{C,u}-A_{A,u}}{2\Delta v}\\\frac{\partial A_v}{\partial v}&=\frac{A_{C,u}-A_{A,u}}{2\Delta v}\\\frac{\partial^2 A_u}{\partial u^2}&=\frac{1}{(\Delta u)^2}\left(A_{D,u}+A_{B,u}-2A_{P,u}\right)\\\frac{\partial^2 A_v}{\partial v^2}&=\frac{1}{(\Delta v)^2}\cdot\left(A_{C,v}+A_{A,v}-2A_{P,v}\right)\end{aligned} \tag{42}$$

The same simplification is obtained for the second equation (5) for elliptic case, since letting $\overrightarrow{A} = h\,\overrightarrow{M}$ makes this equation almost identical to the rectangular case:

$$\begin{aligned}&\frac{1}{h^2}\cdot\left(\frac{\partial A_v}{\partial u}-\frac{\partial A_u}{\partial v}\right)=\\&\frac{1}{h^2}\cdot\left(\frac{A_{C,u}-A_{A,u}}{2\Delta u}-\frac{A_{D,v}-A_{B,v}}{2\Delta v}\right)=0\end{aligned} \tag{43}$$

The singular points of the elliptical framework, either the foci, or the points on the inter–focal segment, require a different treatment. For a focus of the ellipse, Fig.10, as in the circular case we use the integral form of the eigenvalue equation, as in (25–27). The central term of (26) becomes

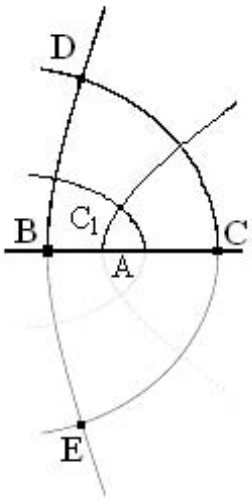


Figure 10: Focus A of the ellipse.

$$\int_C \nabla_t \overrightarrow{M} \cdot \overrightarrow{i_n} \cdot dl = \int_C \frac{1}{h^2} \cdot \frac{\partial M_u}{\partial u} \cdot \overrightarrow{i_n} dl + \int_C \frac{1}{h^2} \cdot \frac{\partial M_v}{\partial v} \cdot \overrightarrow{i_n} dl \tag{44}$$

The integrals are divided in 4 parts. We describe here in details only the evaluation of the part over C_1. Letting $Q = \left(a, \frac{\Delta v}{2}\right)$ and $R = \left(\frac{\Delta u}{2}, 0\right)$, we have

$$\begin{aligned} &\int_{C_1} \frac{1}{h^2} \cdot \frac{\partial M_u}{\partial u} \cdot \overrightarrow{i_n} \cdot dl = \int_o^{\frac{\Delta u}{2}} \frac{1}{h^2} \cdot \frac{\partial M_u}{\partial u} \cdot \overrightarrow{i_n} \cdot h \cdot du = \\ &\frac{1}{h} \cdot \overrightarrow{i_n}\Big|_{x_p} \cdot \int_o^{\frac{\Delta u}{2}} \frac{\partial M_u}{\partial u} \cdot du = \\ &\frac{-\overrightarrow{i_x}}{h\,(Q)} \left[\frac{M_u(A) + M_u(B) + M_u(C) + M_u(D)}{4} \right. \\ &\qquad \left. - \frac{M_u(A) + M_u(B)}{2} \right] \end{aligned} \tag{45}$$

and

$$\begin{aligned} &\int_{C_1} \frac{1}{h^2} \frac{\partial M_v}{\partial v} \overrightarrow{i_n} dl = \frac{1}{h} \overrightarrow{i_n} \frac{\partial M_v}{\partial v}\Big|_Q \int_0^{\frac{\Delta u}{2}} du = \\ &\frac{1}{h\,(Q)} \left(-\overrightarrow{i_x}\right) \left(\frac{M_v(B) - M_v(A)}{\Delta v} \right) \frac{\Delta u}{2} \end{aligned} \tag{46}$$

The same approach can be used for points on the inter–focal segment, such as the one in Fig.11

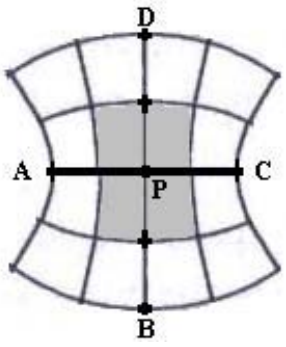


Figure 11: Point between foci.

5. Numerical Solution and Results

In all cases considered, we get a constrained eigenvalue problem as:

$$\begin{cases} \mathbf{A}\mathbf{x} = \lambda \mathbf{x} \\ \mathbf{C}^T \mathbf{x} = 0 \end{cases} \tag{47}$$

where $\mathbf{A}$ is a (2n,2n) matrix, and $\mathbf{C}$ is (2n,m) with $n > m$ and $\lambda = -k_t^2$. Of course, $\mathbf{A}$ is the discrete laplace operator, including the boundary condition, and $\mathbf{C}$ is the discrete form of the constrain $\nabla_t \times \overrightarrow{M} = 0$.

We can solve [9] (47) using the *QR* factorization: $\mathbf{C} = \mathbf{Q} \cdot \mathbf{R}$ where $\mathbf{Q}$ is an orthogonal (2n,2n) matrix $\left(\mathbf{Q}^{-1} = \mathbf{Q}^T\right)$ and $\mathbf{R}$ is a upper triangular matrix (2n,m). Substituting in second equation of (47) we get:

$$\begin{aligned} &\mathbf{C}^T \cdot \mathbf{x} = (\mathbf{Q} \cdot \mathbf{R})^T \cdot \mathbf{x} = \\ &\mathbf{R}^T \cdot \mathbf{Q}^T \cdot \mathbf{x} = \mathbf{R}^T \cdot \left(\mathbf{Q}^T \cdot \mathbf{x}\right) = 0 \end{aligned} \tag{48}$$

which suggest to change the unknown as:

$$\mathbf{y} = \mathbf{Q}^T \cdot \mathbf{x} \Rightarrow \mathbf{x} = \mathbf{Q} \cdot \mathbf{y} \tag{49}$$

so as (48) becomes:

$$\mathbf{C}^T \cdot \mathbf{x} = \mathbf{R}^T \cdot \mathbf{y} = 0 \tag{50}$$

Replacing $\mathbf{x} = \mathbf{Q} \cdot \mathbf{y}$ in the first of (47) and multiplying all members by $\mathbf{Q}^T$ we obtain:

$$\begin{aligned} &A \cdot Q \cdot y = \lambda \cdot Q \cdot y \Rightarrow Q^T \cdot A \cdot Q \cdot y = \\ &Q^T \cdot \lambda \cdot Q \cdot y \Rightarrow By = \lambda y \end{aligned} \tag{51}$$

where $\mathbf{B} = \mathbf{Q}^T \cdot \mathbf{A} \cdot \mathbf{Q}$ is a (2n,2n) matrix. The unknown can be partitioned in two vector $\mathbf{y} = \begin{vmatrix} \mathbf{u} \\ \mathbf{v} \end{vmatrix}$, where $\mathbf{u}$ and $\mathbf{v}$ are (n,1) vector. Then equations (50), (51) are rewritten in partitioned form as:

$$\begin{cases} \mathbf{B} \cdot \mathbf{y} = \lambda\, t\mathbf{y} \quad \Rightarrow \begin{vmatrix} \mathbf{B}_{11} & \mathbf{B}_{12} \\ \mathbf{B}_{21} & \mathbf{B}_{22} \end{vmatrix} \cdot \begin{vmatrix} \mathbf{u} \\ \mathbf{v} \end{vmatrix} = \lambda \begin{vmatrix} \mathbf{u} \\ \mathbf{v} \end{vmatrix} \\ \mathbf{R}^T \cdot \mathbf{y} = 0 \quad \Rightarrow \begin{vmatrix} \mathbf{T}_1 & \mathbf{0} \end{vmatrix} \cdot \begin{vmatrix} \mathbf{u} \\ \mathbf{v} \end{vmatrix} = 0 \end{cases} \tag{52}$$

where $\mathbf{B}_{ij}$ are (n,n) matrices, and $\mathbf{T}_1$, is an (invertible) triangular matrix . The second equation of (52) becomes:

$$\mathbf{T}_1 \cdot \mathbf{u} = 0 \quad \rightarrow \mathbf{u} = 0 \tag{53}$$

Therefore the first of (53) becomes:

$$\mathbf{B}_{22} \cdot \mathbf{v} = \lambda \mathbf{v} \tag{54}$$

and we need to extract the eigenvalues and eigenvectors of $\mathbf{B}_{22}$.

This discretized eigenvalues problem must be solved by numerical routine and the full matrix routines of Matlab have been used. The waveguide modes can then be obtained, from the eigenvalues $\mathbf{v}$ of $\mathbf{B}_{22}$, as

$$\mathbf{x} = \mathbf{Q} \cdot \begin{vmatrix} \mathbf{0} \\ \mathbf{v} \end{vmatrix} \tag{55}$$

Using *MATLAB* routines, we have performed an extensive validation of the approach presented. Some results are shown in the following, while a wider collection of data can be found in [10].

Table 1 shows the validation test for a rectangular waveguide, whose size (in normalized units) is 3.35×1.65, discretized in 134×66 square discretization cells. Our data have been compared with the known analytical results [2], both for the eigenvalues and the mode vectors. The same comparison has been made in Table 2 for a circular waveguide, with a radius equal to 4 (in normalized units), and using discretization steps of $\Delta r = 0.0396$, $\Delta \vartheta = 1^o$. In both tables k_{ta} and k_{tpv} are the eigenvalues computed analytically [2] and using our approach, $e_{\%}$ is the percentage error between them, and the last column shows the RMS difference between analytical mode vectors, and those compured using (55).

From these data, it appears that our technique is able to give all mode data with a very small error, both on eigenvalues and on eigenvectors. The error on the formes is no larger than $0.3\,\%$ for the rectangular guide and significantly smaller than this for the circular case. The RMS error on normalized modes is even smaller, being less than $5 \cdot 10^{-8}$ in both cases

Table 3 shows the validation test for an elliptic waveguide, with a length of the minor axis (in normalized units) equal to 4, and different eccentricities e_{cx}, discretized with $\Delta v = 1^o$, and a different number N_u of discretization ellipses. Though an analytical solution is available for elliptic waveguides [7], it effectiveness is very poor, and many numerical techniques has been proposed in the literature. As in many of those papers, we use, for our comparison, the eigenvalues k_{ta} obtained from the cut-off wavelength data reported in [11].

From the data in Table 3, it is clear that, for all cases shown, the eigenvalues k_{tpv} computed from our techniques are very accurate.

Table 1: Validation test for a rectangular waveguide.

n,m	k_{ta}	k_{tpv}	$e_{\%}$	RMS error $\cdot 10^{-6}$
10	0.93779	0.93777	0.002	0.000
20	1.87558	1.87541	0.017	0.001
01	1.90400	1.90382	0.017	0.001
11	2.12242	2.12225	0.017	0.014
21	2.67264	2.67238	0.026	0.002
30	2.81337	2.81280	0.057	0.002
31	3.39709	3.39650	0.059	0.031
40	3.75116	3.74981	0.134	0.005
02	3.80799	3.80662	0.137	0.005
12	3.92177	3.92041	0.135	0.036
41	4.20670	4.20540	0.131	0.056
22	4.24483	4.24347	0.136	0.058
50	4.68894	4.68632	0.262	0.010
32	4.73454	4.73300	0.153	0.054
51	5.06077	5.05823	0.254	0.081
42	5.34527	5.34322	0.206	0.017

Table 2: Validation test for a circular waveguide.

n,m	k_{ta}	k_{tpv}	$e_{\%}$	RMS error $\cdot 10^{-6}$
11	0.46030	0.46029	0.001	0.000
21	0.76356	0.76353	0.004	0.001
01	0.95793	0.95770	0.024	0.001
31	1.05030	1.05020	0.009	0.001
41	1.32939	1.32917	0.016	0.001
12	1.33286	1.33247	0.029	0.017
51	1.60390	1.60348	0.026	0.002
22	1.67653	1.67595	0.035	0.068
02	1.75390	1.75249	0.080	0.001
61	1.87532	1.87459	0.039	0.002
32	2.00381	2.00297	0.042	0.119
13	2.13408	2.13217	0.089	0.130
71	2.14446	2.14331	0.054	0.002
42	2.32060	2.31942	0.051	0.173
81	2.41186	2.41015	0.071	0.002
23	2.49237	2.48991	0.099	0.491

6. Conclusions

A Vector Finite Difference tecnique has been proposed for the computation of the modes and eigenvalues of rectangular, circular and elliptical waveguides. A suitable choice of the discretization grid, which exacly fits the waveguide boundary, allows to obtain a very effective and accurate procedure. The presented approach has been assessed against analytical modes of rectangular and circular waveguides, and data available in the open literature for elliptical waveguides. The agreement is excellent in all the cases.

References

[1] A. Wexler, Solution of waveguide discontinuities by modal analysis, *IEEE Trans. Microwave Theory and*

Table 3: Validation test for an elliptic waveguide.

			$N_u = 100$		$N_u = 200$		$N_u = 400$	
	e_{cx}	k_{ta} from [11]	k_{tpv} from [11]	$e_{\%}$	k_{tpv} from [11]	$e_{\%}$	k_{tpv} from [11]	$e_{\%}$
TEc_{11}	0.1	0.45818	0.45823	0.010	0.45812	0.013	0.45810	0.019
	0.5	0.40075	0.46047	0.006	0.46044	0.001	0.46043	0.001
	0.9	0.20450	0.46672	0.018	0.46676	0.009	0.46679	0.003
TEs_{11}	0.1	0.46021	0.46035	0.030	0.46024	0.007	0.46022	0.002
	0.5	0.45734	0.52547	0.004	0.52546	0.001	0.52545	0.000
	0.9	0.43752	0.99869	0.003	0.99871	0.001	0.99871	0.000
TEc_{21}	0.1	0.76163	0.76187	0.031	0.76169	0.007	0.76164	0.001
	0.5	0.69773	0.80168	0.005	0.80164	0.000	0.80163	0.001
	0.9	0.37441	0.85446	0.025	0.85456	0.013	0.85462	0.006
TEs_{21}	0.1	0.76166	0.76189	0.031	0.76171	0.007	0.76166	0.001
	0.5	0.71299	0.81922	0.005	0.81918	0.001	0.81917	0.001
	0.9	0.55702	1.27146	0.003	1.27148	0.001	1.27148	0.001
TEc_{01}	0.1	0.95556	0.95514	0.043	0.95545	0.011	0.95552	0.003
	0.5	0.90727	1.04224	0.014	1.04234	0.004	1.04237	0.001
	0.9	0.83739	1.91121	0.015	1.91141	0.004	1.91146	0.001
TEc_{31}	0.1	1.04767	1.04799	0.031	1.04773	0.006	1.04767	0.000
	0.5	0.96977	1.11424	0.004	1.11418	0.001	1.11417	0.002
	0.9	0.54108	1.23473	0.031	1.23491	0.017	1.23501	0.009

Techniques, vol. MTT-15, pp. 508-517, September 1967. 123-127, February 1998. December 2001.

[2] R. E. Collin, *Field Theory of Guided Waves*, Wiley-IEEE Press, 2001.

[3] G. Mazzarella, G. Montisci, Accurate Characterization of the Interaction between Coupling Slots and Waveguide Bends in Waveguide slot Arrays, *IEEE Trans. Microwave Theory and Techniques*, vol.48, issue(7), pp 1154-1157, July 2000.

[4] G. Mazzarella, G. Montisci, A Rigorous Analysis of Dielectric-Covered Narrow Longitudinal Shunt Slots with Finite Wall Thickness, *Journal of Electromagnetics Waves and Applications*, vol. 19, pp. 407-418, Oct.1999.

[5] T. Itoh, *Numerical Techniques for Microwave and Millimeter-wave Passive Structures*, Wiley, NY, 1989.

[6] W. Gander, G. H. Golub, U. Von Matt, A constrained eigenvalue problem, *Linear Algebra and its Applications*, vol.114-115, pp 815-839 , March-April 1989.

[7] L. J. Chu, "Electromagnetic waves in elliptic hollow pipes of metal," *J.Appl. Phys.*, vol. 9, pp. 583-591, September 1938.

[8] J. Van Bladel, *Electromagnetic Fields*, A SUMMA Book, New York, ,1985

[9] G. H. Golub, C. F. Van Loan, *Matrix Computations,* 3^{rd} *ed.*, The Johns Hopkins University Press, Baltimore, 1996.

[10] A.Fanti, *A Generalized finite difference aprroach to the computation of modes* , PhD Thesis, University of Cagliari 2012

[11] Sh. Zhang, Y. Chen, Eigenmodes Sequence for an Elliptical Waveguides with Arbitrary Ellipticity, *IEEE Trans. Microwave Theory and Techniques*, vol.43, issue(1), pp. 227-230, Jan. 1995.

Combined FVTD/PSTD Schemes with Enhanced Spectral Accuracy for the Design of Large-Scale EMC Applications

Nikolaos V. Kantartzis, Alexandros I. Dimitriadis, and Theodoros D. Tsiboukis

Department of Electrical and Computer Engineering,
Aristotle University of Thessaloniki, Thessaloniki GR-54124, Greece
*corresponding author, E-mail: tsibukis@auth.gr

Abstract

A generalized conformal time-domain method with adjustable spectral accuracy is introduced in this paper for the consistent analysis of large-scale electromagnetic compatibility problems. The novel 3-D hybrid schemes blend a stencil-optimized finite-volume time-domain and a multimodal Fourier-Chebyshev pseudo-spectral time-domain algorithm that split the overall space into smaller and flexible areas. A key asset is that both techniques are updated independently and interconnected by robust boundary conditions. Also, combining a family of spatial derivative approximators with controllable precision in general curvilinear coordinates, the proposed method launches a conformal field flux formulation to derive electromagnetic quantities in regions with fine details. For advanced grid reliability at dissimilar media interfaces, dispersion-reduced adaptive operators, which assign the proper weights to each spatial increment, are developed. So, the resulting discretization yields highly rigorous and computationally affordable simulations, devoid of lattice errors. Numerical results, addressing detailed comparisons of various realistic applications with reference or measurement data verify our methodology and reveal its significant applicability.

1. Introduction

The development of powerful time-domain solvers for contemporary electromagnetic compatibility (EMC) applications is solidly related to the correct representation of their size by the suitable spatial sampling rates [1–9]. Considering that their overall size should be frequently reconfigured to comply with modern standards or several prototypes prior to the selection of the final design parameters must be devised, the use of rigorous discrete models seems a very attractive means to restrict high fabrication costs. Such a task, though, is often rather difficult, as most devices comprise electrically-large homogeneous areas and fine details that require excessive overheads. To alleviate this hindrance, the finite-volume time-domain (FVTD) [10–14] and pseudospectral time-domain (PSTD) [15–17] techniques can be proven quite beneficial. However, the broadband operation of the preceding structures along with the usual frequency-dependence of their media properties, entail very large resolutions which are still expensive as well as potentially error prone. This is chiefly regular when variable-cell complexes are utilized near different material interfaces, as occurs in many EMC problems. Consequently, grid reflection arises, even if these interfaces are located in free-space regions. The strength of such undesired phenomena depends on the magnitude and abruptness of the grid wave mode velocity distribution and may be crucial in diverse large-scale applications. Pursuing the constant improvement of these important drawbacks, an assortment of proficient algorithms has been hitherto presented [18–25].

In this paper, a hybrid FVTD/PSTD method in general curvilinear coordinates with enhanced spectral precision for the consistent design and modeling of large-scale 3-D EMC structures is introduced. Established on a robust decomposition concept, the novel multimodal formulation launches a family of finite-volume operators for abrupt field variation and a Fourier-Chebyshev interpolation for periodic details. To this aim, spatial derivatives are evaluated via advanced operators of adjustable accuracy order to establish a conformal flux framework for all electromagnetic quantities under study. Both time-domain processes are separately updated, while robust continuity conditions guarantee their smooth boundary interconnection. Moreover, a stencil management technique sets the optimal lattice density and diminishes dispersion errors, while to retain consistency at media interfaces, adaptive nodal patterns are developed. In particular, by inserting auxiliary nodes at the interface, spatial increments can be computed through the convex combination of several possible candidates. Therefore, and unlike the unduly needs of existing approaches, discretization artifacts receive a notable reduction and total accuracy overwhelms typical thresholds. The proposed schemes, except their theoretical verification, are successfully applied to complex arrangements like large-scale planar microwave devices, antennas, waveguide structures, and anechoic/reverberation test facilities.

2. The hybrid 3-D time-domain method

A critical issue in large-scale EMC problems are the fine, regarding the minimum wavelength, geometric details with irregularly curved cross-sections [26]. Despite their limited appearance compared to homogeneous areas, they create non-separable wavefronts which demand high mesh densities.

2.1. Explicit multimodal formulation

To alleviate this serious defect in subwavelength regions, our

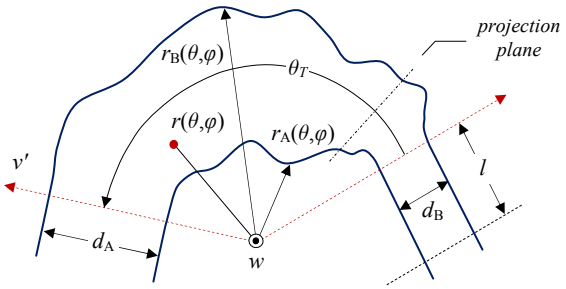


Figure 1: Transverse-plane view of a general discontinuity with constantly changing geometric features.

hybrid algorithm launches an efficient multimodal concept with controllable resolution. Let us consider the discontinuity of Fig. 1, spanning over an angle θ_T, with inner and outer mean radii $r_A(\theta, \varphi)$ and $r_B(\theta, \varphi)$. The basic point is the efficient separation of all propagating modes at κ preselected transverse planes, which fulfills the pertinent physical conditions. Thus, each component G can be expressed via infinite series as

$$G(r,\theta,\varphi)=\sum\nolimits_{\kappa}\xi_{\kappa}(r,\theta,\varphi)g_{\kappa}(r,\theta,\varphi)\,, \qquad (1)$$

with $$\xi_{\kappa}(r,\theta,\varphi)=N_{\kappa}\cos\left[\kappa\pi\left(\frac{r-r_A(\theta,\varphi)}{r_M(\theta,\varphi)}\right)\right], \qquad (2)$$

$$N_{\kappa}=\sqrt{\frac{4-3\delta_{\kappa 0}}{r_M(\theta,\varphi)}} \quad \text{for} \quad \delta_{\kappa\rho}=\int_{r_A}^{r_A+d_A}\xi_{\kappa}(r,\theta,\varphi)\xi_{\rho}(r,\theta,\varphi)dr \qquad (3)$$

$r_M(\theta, \varphi) = r_B(\theta, \varphi) - r_A(\theta, \varphi)$, ξ_κ the respective eigenfunctions and G_κ amplitude coefficients. An important asset of (1)-(3) is their conformal profile which enables the accurate modeling of the above details through the selection of r_A and r_B. Two adequately smooth functions that satisfy this aim, with $c_{\theta,\varphi} = (\theta - \varphi)/\theta_T$, $d = d_B - d_A$, $d_B = 1.35d_A$ and $\tau = \omega/c$, are

$$r_A(\theta,\varphi)=3d(c_{\theta,\varphi}-1.35)+0.6d_A-0.25d_B\,, \qquad (4)$$

$$r_B(\theta,\varphi)=-2d(c_{\theta,\varphi}-1.45)+0.1d_A+0.15d_B\,. \qquad (5)$$

Having attained the required decoupling of the complicated modes, the parametric method projects Maxwell's laws on the prefixed κ planes. Hence, a system of differential equations is derived, whose solutions act as transverse intermediate excitation surfaces in the discontinuity. Such an idea is proven promising and the most significant; it retains lattice duality even near the geometric oddity, in contrast to typical algorithms, which can not provide adequate treatment. Using the matrix notation, Ampere's and Faraday's laws become

$$\frac{\partial(\varepsilon\mathbf{E})}{\partial t}=\frac{1}{\tau}\left(\mathbf{\Lambda}^{\mathrm{A}}+\mathbf{\Lambda}^{\mathrm{B}}\mathbf{\Lambda}^{\mathrm{C}}\right)\nabla\times\mathbf{H}-\mathbf{\Lambda}^{\mathrm{D}}\mathbf{E}\,, \qquad (6)$$

$$\frac{\partial(\mu\mathbf{H})}{\partial t}=-\tau\mathbf{\Lambda}^{\mathrm{C}}\nabla\times\mathbf{E}+\left(\mathbf{\Lambda}^{\mathrm{E}}-\mathbf{\Lambda}^{\mathrm{D}}\right)\mathbf{H}\,, \qquad (7)$$

where **E** and **H** are the electric and magnetic field intensities, defined at the general coordinates (u,v,w). The elements of $\mathbf{\Lambda}^i$ (i = A,…,E) impedance matrices provide the main details of the structure, under investigation, and are obtained by means of all field continuity boundary constraints, as

$$\Lambda^{\mathrm{A}}_{\kappa\rho}=(-2)^{\kappa+\rho}\kappa^2/(3\kappa^2+\rho^2)\,, \qquad \Lambda^{\mathrm{B}}_{\kappa\rho}=(4\tau^2-5)\delta_{\kappa\rho}\,, \quad (8)$$

$$\Lambda^{\mathrm{C}}_{\kappa\rho}=2r_A(\theta,\varphi)+1.5d\,, \qquad \Lambda^{\mathrm{B}}_{\kappa\rho}=5r_M(\theta,\varphi)\delta_{\kappa\rho}-d/3\,, \quad (9)$$

$$\Lambda^{\mathrm{E}}_{\kappa\rho}=(-1)^{\kappa+\rho}N_{\kappa}N_{\rho}r_B(\theta,\varphi)/(5\kappa^2+7\rho^2)\,. \qquad (10)$$

2.2. Enhanced spectrally-accurate FVTD/PSTD schemes

The principal part of the proposed methodology lies on the hybridization of generalized FVTD and PSTD schemes. Starting from the former, we establish a curvilinear dual-cell grid, where a new class of derivative approximators of adjustable spectral accuracy is developed. Concerning temporal integration, the process uses a stable integration as the one of the finite-difference time-domain (FDTD) approach [27]. To increase its applicability, the 3-D algorithm involves cells with the four corners of their faces not necessarily lying on the same plane. Thus, the suitable unit vector direction cosines are employed to transform Maxwell's equations in the form of

$$\varepsilon\frac{\partial\mathbf{E}}{\partial t}-\mathcal{D}[\mathbf{H}]+\sigma\mathbf{E}=-\mathbf{J}_s \quad \text{and} \quad \mu\frac{\partial\mathbf{H}}{\partial t}+\mathcal{D}[\mathbf{E}]=\mathbf{0}\,, \quad (11)$$

which may be regarded analogous to the main conservation-law formulation. In (11), $\mathbf{J}_s$ is the source vector that gathers all possible external excitations imposed to our problem. Moreover, the parametric operator $\mathcal{D}[.]$ is denoted as

$$\mathcal{D}[\mathbf{G}]=\begin{bmatrix}S^K_v G_w-S^K_w G_v\\ S^K_w G_u-S^K_u G_w\\ S^K_u G_v-S^K_v G_u\end{bmatrix}+\sum_{l=1}^{K}\left(a_1S^l_u+a_2S^l_v+a_3S^l_w\right)\mathbf{G}\,, \quad (12)$$

where $\mathbf{G} = [\mathbf{E}, \mathbf{H}]^T$ with the second term defining the novel Kth-order approximation forms that correct existing stencils around curved interfaces or small geometric details. Note that parameters a_i (i = 1,2,3) assure the stability of the schemes and subdue late-time exponential oscillations [28]. Also, spatial derivatives in (12) are acquired via enhanced operators, whose spectral resolution is of order K. Therefore, we define

$$S^K_{\eta}\left[G|^t_{u,v,w}\right]=\frac{e^{K\Delta\eta/6}}{2\Delta\eta}M^L_{\eta,P}\left[G|^t_{u,v,w}\right]+\sum_{s=1}^{3}\left(3+\frac{\Delta\eta}{4s}\right)G|^t_{\eta\pm s\Delta\eta}\,, \quad (13)$$

with $\eta\in(u,v,w)$, $\Delta\eta\in(\Delta u,\Delta v,\Delta w)$ is the spatial increment and $M_{\eta,P}[.]$ allowing the fine regulation of spectral precision by diverse stencils and smoothness summation limit P. Particularly, considering the system metrics,

$$M^K_{\eta,P}\left[G|^t_{u,v,w}\right]=\sum_{s=1}^{K}T^{\eta}_s\left\{\sum_{p=1}^{P}R^{\eta}_{s,p}\,G|^t_{u,v,w}\right\}\,. \qquad (14)$$

Structural parameters T_s and $R_{s,p}$ increase algorithmic consistency in the case of complex discontinuities, frequently encountered in realistic EMC devices.

Bearing in mind the above analysis of spatial derivative calculation, Maxwell's equations can, now, be expressed as

$$\frac{\partial\mathbf{G}}{\partial t}+\mathbf{b}^{-1}\mathbf{Q}\mathbf{G}=\mathbf{b}^{-1}(\mathbf{L}+\mathbf{R}\mathbf{G})\,, \qquad (15)$$

for $$\mathbf{Q}\mathbf{G}=\begin{bmatrix}-\nabla\times\mathbf{H}\\ \nabla\times\mathbf{E}\end{bmatrix}, \quad \mathbf{L}=\begin{bmatrix}-\mathbf{J}_s\\ \mathbf{0}\end{bmatrix}, \quad \mathbf{R}=\begin{bmatrix}-\sigma\mathbf{I} & \mathbf{0}\\ \mathbf{0} & \mathbf{0}\end{bmatrix},$$

$\mathbf{b} = diag\{\varepsilon\mathbf{I}, \mu\mathbf{I}\}$, and $\mathbf{I}$ the identity matrix. If our computational domain Ω is divided into a prefixed number of cells Ω_i of boundary $\partial\Omega_i$, then (15) can be integrated over each Ω_i and

$$\iiint_{V_i}\partial_t\mathbf{G}dV+\iint_{\partial\Omega_i}\mathbf{b}^{-1}\Xi[\mathbf{n}_0]\mathbf{G}d\mathbf{s}=\iiint_{V_i}\mathbf{b}^{-1}\mathbf{L}d\mathbf{r}+\iiint_{V_i}\mathbf{b}^{-1}\mathbf{R}\mathbf{G}d\mathbf{r}\,, \qquad (16)$$

with $\boldsymbol{\Xi}[\mathbf{n}_0] = \begin{bmatrix} \mathbf{0} & -\boldsymbol{\mathcal{D}}[\mathbf{n}_0] \\ \boldsymbol{\mathcal{D}}[\mathbf{n}_0] & \mathbf{0} \end{bmatrix}$,

V_i the volume of Ω_i, and $\mathbf{n}_0$ the outward unit vector perpendicular to surface $\partial\Omega_i$. Observe that $\boldsymbol{\Xi}[\mathbf{n}_0]\mathbf{G}$ represents the flux through $\partial\Omega_i$. To exploit all fluxes through the cell faces, the concept of the cell average – i.e. the average of $\mathbf{G}$ placed at the barycenter of every cell [29] – is described by

$$G_i = V_i^{-1} \iiint_{V_i} \mathbf{G}(\mathbf{r}) dV \,, \tag{17}$$

where $\mathbf{r}$ is the position vector. For the required flux splitting, based on our FVTD formulation, matrix $\mathbf{F}[\mathbf{n}_0] = \mathbf{b}^{-1}\boldsymbol{\Xi}[\mathbf{n}_0]$, which can be decomposed to a sum of matrices with positive and negative eigenvalues, is also used. So, and recalling that the eigenvalues of $\mathbf{F}[\mathbf{n}_0]$ are given by $diag\{0,0,\upsilon,\upsilon,-\upsilon,-\upsilon\}$ for $\upsilon = (\mu\varepsilon)^{-1/2}$ and $\boldsymbol{\mathcal{K}} = \boldsymbol{\mathcal{D}}[\mathbf{n}_0]$, one arrives at

$$\mathbf{F}[\mathbf{n}_0] = \frac{1}{2}\begin{bmatrix} -\upsilon\boldsymbol{\mathcal{K}}^2 & -\varepsilon^{-1}\boldsymbol{\mathcal{K}} \\ \mu^{-1}\boldsymbol{\mathcal{K}} & -\upsilon\boldsymbol{\mathcal{K}}^2 \end{bmatrix} + \frac{1}{2}\begin{bmatrix} \upsilon\boldsymbol{\mathcal{K}}^2 & -\varepsilon^{-1}\boldsymbol{\mathcal{K}} \\ \mu^{-1}\boldsymbol{\mathcal{K}} & \upsilon\boldsymbol{\mathcal{K}}^2 \end{bmatrix}. \tag{18}$$

The surface integral on the left-hand side of (16) can be evaluated if flux $\mathbf{F}[\mathbf{n}_0]\mathbf{G}$ is already known on all faces of $\partial\Omega_i$. So, two subvectors of $\mathbf{G}$ are considered; one on the internal and the other on the external side of each face. Both terms are acquired through an interpolation process centered on the respective face side. Replacing (16)-(18) into (15), we derive

$$\frac{\partial \mathbf{G}}{\partial t} + \mathbf{Z}\mathbf{G} = \mathbf{Y} \,, \tag{19}$$

for $\mathbf{Z}$ a bloc-diagonal matrix with all media features and $\mathbf{Y}$ containing the source contributions of every grid cell. It is mentioned that $\mathbf{Z}$ is inverted only once at the beginning of our computations [6]. To complete the proposed FVTD procedure, time derivatives in (19) are approximated by the simple and stable leapfrog-like predictor-corrector scheme of

$$\mathbf{F}^{n+1/2} = \mathbf{F}^{n} - 0.5\Delta t \mathbf{A}\mathbf{F}^{n} \,, \tag{20a}$$

$$\mathbf{F}^{n+1} = \mathbf{F}^{n} - 0.5\Delta t \mathbf{A}\mathbf{F}^{n+1/2} \,, \tag{20b}$$

in which $\mathbf{A}$ is the conventional update matrix for vector $\mathbf{G}$.

Focusing on the second part of the hybridization, a curvilinear Fourier-Chebyshev PSTD interpolation is developed for sections of homogeneous media and periodical features. Since they are the majority in Ω, their analysis via a pseudo-spectral approach is anticipated to accelerate the total simulation. This is attained by evaluating spatial derivatives in terms of

$$\left.\frac{\partial G}{\partial \eta}\right|_{\Gamma}^{n} = \frac{2\pi}{L_\eta \Delta\eta} \mathcal{FFT}^{-1}\left\{ jk_\eta \mathcal{FFT}\left\{ G\big|_{i,j,k}^{n} \right\} \right\}, \tag{21}$$

with $\mathcal{FFT}$ and $\mathcal{FFT}^{-1}$ the Fourier and inverse Fourier transform, L_η the node number towards η-axis, and k_η the transformed wavevector component. Additionally, Γ describes all η coordinates along a straight-line cut through the transverse plane of the other two coordinates. In fact, (21) implies differentiation by the trigonometric Chebyshev-type polynomial

$$\left.\frac{\partial G}{\partial \eta}\right|_{\Gamma}^{n} = \frac{1}{L_\eta} \sum_{m=-L_\eta/2}^{m=L_\eta/2-1} j\frac{2\pi m}{L_\eta} \bar{G}(m)\big|_{\Gamma}^{n} e^{j2\pi m\Gamma/L_\eta} \,, \tag{22}$$

with $j^2 = -1$ and the barred $G(m)$ being the Fourier series of G and. Note that field values are located at specific non uniform mesh points $\psi_i = \pi i/L_\eta$, $i = 0,1,\ldots,2L_\eta - 1$. This permits space partition into collocated elements that conform to the boundaries of media distributions. Next, and in terms of a curvilinear coordinate transformation, each element is mapped into a cube, while all field quantities adjacent to internal interfaces are corrected to resolve the physical jump conditions.

Regarding temporal update, all temporal derivatives appearing in the PSTD forms are computed through a similar leapfrog notion, as in (20) for the FVTD forms, given by

$$\left.\frac{\partial G}{\partial t}\right|_{l}^{n} = \frac{15}{19\Delta t}\left(G\big|_{l}^{n+1/2} - G\big|_{l}^{n-1/2} \right) + O(\Delta t^2) \,, \tag{23}$$

thus facilitating the fully stable, non-oscillatory, and uniform time-advancement for the entire FVTD/PSTD method.

A closer inspection of (11)-(19) and (21), shows their ability to treat frequency-dependent setups owing to the direct tensor-oriented classification of constitutive parameters. So, dispersion errors are greatly minimized and broadband studies are easy to conduct. Finally, it should be emphasized that, except some limited storage needs, the proposed method does not increase the total CPU and memory burden.

3. Treatment of complex media interfaces

In the case of arbitrarily-curved interfaces formed by materials with considerably different constitutive parameters and losses, special attention must be drawn in order to circumvent severe instabilities and lattice discretization errors. Returning to (6), (7) or (15) and re-expressing cell average in (17) as

$$\mathcal{G}_{i,j,k}(t) = V_i^{-1} \iiint_{V_i} G(\mathbf{r},t) m_c(\varepsilon,\mu) dV \,, \tag{24}$$

with respect to an $(i\Delta u, j\Delta v, k\Delta w)$ mesh, where $V_i = \Delta u\Delta v\Delta w$ is the volume of the $p_{i,j,k}$ cell and m_c are functions of ε, μ constitutive parameters. The integral of (24) is calculated by a Gaussian quadrature along the edges and over the faces of $p_{i,j,k}$. Hence, for a general cell extending in the region of

$$p_{i,j,k} = [u_{i-1/2}, u_{i+1/2}] \times [v_{j-1/2}, v_{j+1/2}] \times [w_{k-1/2}, w_{k+1/2}] \,, \tag{25}$$

the cell average at the $(i, j+1/2, k)$ face is obtained via

$$\mathcal{G}_{i,j+1/2,k}(t) = \frac{1}{\Delta u\Delta w} \sum_{s=1}^{N}\sum_{q=1}^{N} f\left(\mathbf{r}(u_s, v_{j+1/2}, w_q)\right) V_q V_s \,, \tag{26}$$

for s, q referring to the N extra integration points u_s, w_q and structural coefficients V_s, V_q. So, all spatial derivatives in (15) are effectively approximated through

$$\frac{\partial G(\mathbf{r},t)}{\partial \eta} = P_\eta(\mathbf{r},t) + O[(\Delta\eta)^{M+1}] \,, \quad \text{for} \quad \eta \in (u,v,w) \tag{27}$$

and the piecewise polynomials $P_\eta(\mathbf{r},t)$. Next, we introduce a weighted convex combination S_r of all stencils related to the $p_{i,j,k}$ cell to reconstruct $P_\eta(\mathbf{r},t)$. As a matter of fact, the novel $(2M\text{-}1)$th-order schemes assign an optimal weight to each stencil in the vicinity of the interface, thus offering increased accuracy and reduced anisotropy and dissipation errors. Taking into account that v is the direction of interest, the proposed stencil classification is denoted as

$$\{S_r\}_{v}^{M-1} = \left\{ G\big|_{i,j-r+M/2,k}^{n}, G\big|_{i,j-r+3M/2,k}^{n}, \ldots, G\big|_{i,j+r-M/2,k}^{n} \right\}, \tag{28}$$

for $r = 0,1,\ldots,M\text{-}1$. Thus, a set of M interpolating polynomials, $Y_{M,v}(\mathbf{r},t)$, is recursively associated with these stencils, i.e.

$$Y_{M-1,v}^{2M-1}\left(\mathcal{G}\big|_{i,j-r+1/2,k}^{n},\ldots,\mathcal{G}\big|_{i,j+r-1/2,k}^{n}\right)$$
$$=b_M\sum_{\xi=0}^{M-1}\tau_{\xi,v}^{M}Y_{\xi,v}^{M}\left(\mathcal{G}\big|_{i,j-r+1/2,k}^{n},\ldots,\mathcal{G}\big|_{i,j+r-1/2,k}^{n}\right),\quad(29)$$

at time-step $n\Delta t$, while a similar process holds for directions u and v. Coefficients b_M, $\tau_{\xi,v}$ are computed by

$$b_M=\frac{1}{2\Delta v}\left|\mathbf{r}(u,v,w)-\mathbf{r}(u,v-M\Delta v/2,w)\right|,\qquad\sum_{\xi=0}^{M-1}\tau_{\xi,v}^{M}=1,$$

In (28), spatial increments are formed by the initial G quantities in contrast to (29) where cell averages are employed. For example, for $M=3$, the first member of $Y_{\xi,v}(\mathbf{r},t)$ is

$$Y_{1,v}^{3}(\mathbf{r},t)=\frac{b_3}{2}\left[\mathcal{G}\big|_{i,j,k}^{n}-\mathcal{G}\big|_{i,j-2,k}^{n}+b_3\left(\mathcal{G}\big|_{i,j-1,k}^{n}-\mathcal{G}\big|_{i,j-2,k}^{n}\right)\right].\quad(30)$$

Therefore, $P_v(\mathbf{r},t)$ are extracted by the summation of

$$Y_v(\mathbf{r},t)=\sum_{l=0}^{M-1}\frac{\chi_l^v}{\sum_{\xi=0}^{M-1}\chi_\xi^v}Y_{l,v}(\mathbf{r},t),\quad(31)$$

with
$$c_l^v=\frac{\chi_l^v}{(\kappa_e+\Theta_v)^M},\quad(32)$$

for a κ_e below 10^{-5} to evade inconsistencies. Parameters ρ_l typify every material in the structure [28], while Θ_v reads

$$\Theta_v=\sum_{s=1}^{M-1}\left\{\sum_{r=1}^{M-3}\left(\Delta^{M-s}\left[\mathcal{G}\big|_{i,j-M+r,k}^{n}\right]\right)^2\right\},\quad(33)$$

where $\Delta^{\gamma}[.]$ is a 3-D operator quantified by means of

$$\Delta^{1}\left[\mathcal{G}\big|_{i,j,k}^{n}\right]=\mathcal{G}\big|_{i,j+1,k}^{n}-\mathcal{G}\big|_{i,j,k}^{n},\quad(34a)$$

$$\Delta^{\gamma}\left[\mathcal{G}\big|_{i,j,k}^{n}\right]=\Delta^{\gamma-1}\left[\mathcal{G}\big|_{i,j+1,k+1}^{n}\right]-\Delta^{\gamma-1}\left[\mathcal{G}\big|_{i,j,k}^{n}\right].\quad(34b)$$

In this way, the hybrid method achieves fast and very accurate outcomes with prominent savings prior to actual implementation, since it can decrease large-scale EMC problems to much smaller interface sections unlike traditional schemes.

4. Performance and implementation aspects

A major aspect in the analysis of EMC structures with symmetries or periodicities is the separation of the domain into smaller regions, where a numerical scheme can be economically applied. Herein, to evade unnecessary discretizations of identical geometric areas, a domain decomposition algorithm is utilized. Our computational space is divided into N non-overlapping subdomains. Specifically, for planar symmetries or periodicities, these regions include one unit cell. For instance, when two subdomains ($i=1,2$) are considered, at their interface $\mathbf{E}_1$ and $\mathbf{H}_2$ (dually $\mathbf{E}_2$ and $\mathbf{H}_1$) vectors are related by

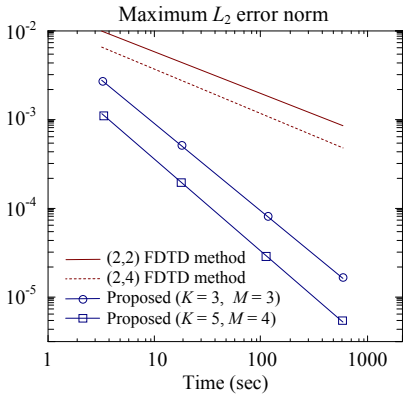
$$\hat{\mathbf{n}}_1\times\mu_{r,1r,1}^{-1}\nabla\times\mathbf{E}_1=-\mu_0\hat{\mathbf{n}}_2\times\partial_t\mathbf{H}_2,\quad(35a)$$

$$\hat{\mathbf{n}}_2\times\varepsilon_{r,2r,2}^{-1}\nabla\times\mathbf{H}_2=\varepsilon_0\hat{\mathbf{n}}_1\times\partial_t\mathbf{E}_1.\quad(35b)$$

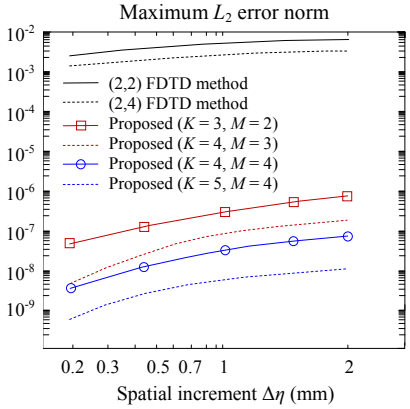
Also, for the artificial boundary oscillations, an equivalent surface current is employed, i.e.

$$\mathbf{J}_{s,i}=\hat{\mathbf{n}}_i\times\mu_{r,1}^{-1}\nabla\times\mathbf{E}_i\qquad\text{for}\quad i=1,2,\quad(36)$$

and $\mathbf{n}_i$ outward normal unit vectors. The proposed method along with (24)-(34) is proven stable for all types of numerical



(a)



(b)

Figure 2: Variation of the maximum L_2 error norm (a) versus time in sec and (b) spatial increment in mm.

simulations. Indeed, von Neumann's analysis shows that

$$\upsilon\Delta t\le(2K+M)\sin^{-1}(0.74)\left(\sum_{l=u}^{w}\sum_{m=u}^{w}\frac{g^h(u,v,w)}{\Delta l\Delta m}\right)^{-1/2},\quad(37)$$

with the summations denoting a consecutive cyclic permutation of (u,v,w) and $g^h(u,v,w)$ the system metrics. Note the less strict character of (37) than the FDTD Courant condition [27], due to the dependence on orders K and M. This implies that time-steps can be chosen quite larger, without arising any oscillatory exponential modes. Alternatively, stability can be certified via the energy inequality method [6], which gives

$$\left\|\mathbf{G}^{n+1}(t)\right\|\le\left\|\mathbf{G}^{n}(t)\right\|+\sum_{\tau=0}^{n}a\left\|\mathbf{G}^{\tau+1}\right\|,\quad(38)$$

where a is a growth factor. Inequality (38) guarantees that $\mathbf{G}(t)$ does not surpass a certain limit namely the system's energy is conserved. Also the dispersion relation of the hybrid method is greatly improved due to the parameterized adjustment of its spectral resolution, as compared to the one, $\mathcal{W}_{\text{FDTD}}$, of the usual FDTD approach. Therefore, we derive

$$\sin^2\left(\frac{\omega\Delta t}{2}\right)=\frac{11(\Delta t)^{3/7}}{6^{K+2M}\upsilon}\mathcal{W}_{\text{FDTD}}.\quad(39)$$

To substantiate these merits, we present the maximum values of the L_2 error norm versus time in Fig. 2a and versus spatial increment in Fig. 2b for different K and M orders. Obviously, the hybrid schemes exhibit a promising performance, as compared to two popular FDTD implementations.

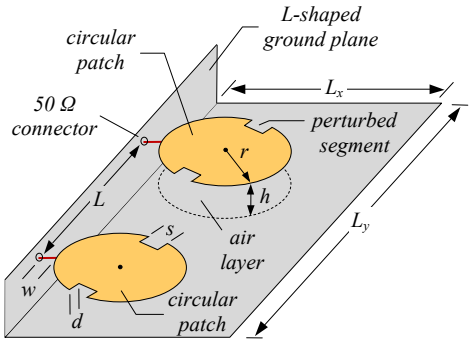


Figure 3: A circularly-polarized wideband 2×1 patch array.

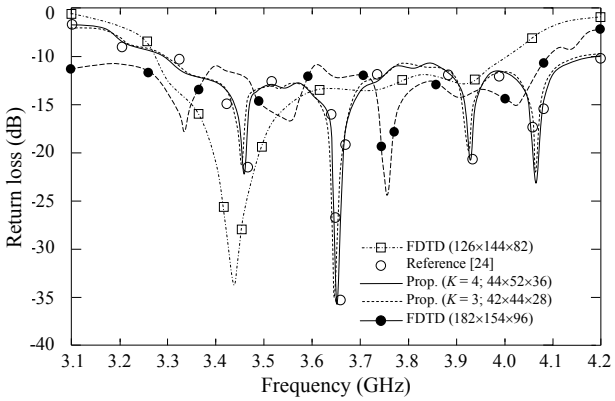


Figure 4: Return loss of the wideband 2×1 patch array.

5. Numerical results

The new methodology is verified by means of several real-world large-scale EMC applications, whose unbounded domain is truncated by a suitably adjusted 8-cell perfectly matched layer (PML) [30, 21] with complex frequency shifting attributes. Their selection has been mainly based on the dissimilarity of the involved media, fine details, electrical size and modeling difficulty. In fact, such issues cannot be adequately manipulated by the usual elongated steady-state simulations. Also, and wherever feasible, our results are compared with measurements or reference data from the literature.

The first structure is the 2×1 patch array of Fig. 3, whose cross-polarized profile is obtained by two perturbed segments (0.65% of the patch). Owing to its frequent use in many systems, the optimal design of this antenna needs a trustworthy simulation tool. Its dimensions are: L_x = 120 mm, L_y = 352 mm, r = 18 mm, L = 26 mm, h = 0.19 mm, w = 3.1 mm, d = 2.8 mm and s = 6.2 mm. The grid comprises 72×120×28 cells (for K = 3, M = 3), unlike the significantly (around 85%) larger regular FDTD grid. To certify the enhanced accuracy and economical profile of the new algorithm, Fig. 4 gives the return loss of the array. As detected, the computational burden remains quite small, compared to both FDTD simulations, considering the complexity of the problem, while the results of the hybrid schemes are in very good agreement with the reference data, even for the demanding resonant frequencies.

Next, we proceed to the coaxial waveguide of Fig. 5, which involves a set of microelectromechanical (MEMS) actuators for selective mode propagation. Its inner slab is based on a dielectric medium with ε_r = 5.2 and the basic dimensions are: L = 9.8 mm, a = 1.4 mm, and b = 5.6 mm. The selection of this problem is primarily attributed to the increasing use of complicated MEMS in several high-end arrangements. To this aim, the variation of the S_{21}-parameter magnitude versus the number of actuators is illustrated in Fig. 6. Additionally, Table 1 summarizes the resonance frequencies for three cases (with K = 4, M = 3 as our approximation orders) and several implementation details. It appears that, the proposed technique is very precise and cost-effective, attaining seriously minimized dispersion errors (up to 10 orders of magnitude) and satisfactorily reduced simulation times. It should be stressed that the contribution of the stencil-optimized concept of Section 3 in the modeling of the complicated interfaces between the actuators and the slab, is deemed critical.

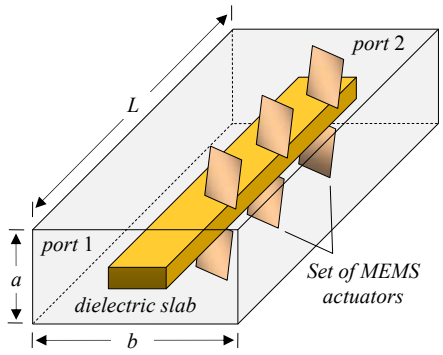


Figure 5: A two-port coaxial waveguide with a dielectric slab and several pairs of MEMS actuators.

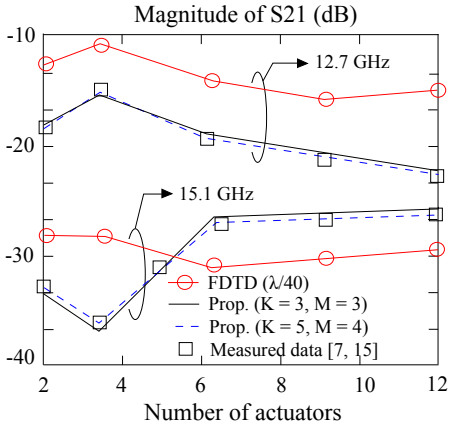


Figure 6: Magnitude of the S_{21} parameter versus actuators.

Table 1: Resonant frequencies of the coaxial waveguide

Ref. [7] [GHz]	Method	Comp. [GHz]	Error [%]	CPU Time	Maximum Dispersion
4 Actuators 10.571	FDTD	9.548	9.67	13.5 h	1.92×10^{-1}
	Proposed	10.570	0.01	6.8 h	2.87×10^{-11}
5 Actuators 15.892	FDTD	14.052	11.58	17.5 h	4.06
	Proposed	15.887	0.03	8.7 h	6.53×10^{-10}
6 Actuators 18.306	FDTD	15.573	14.93	20.2 h	7.39
	Proposed	18.297	0.05	10.4 h	4.01×10^{-10}

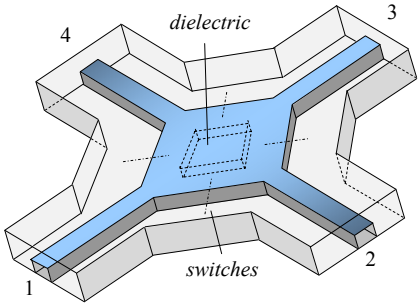


Figure 7: A four-port microwave splitter with a dielectric-based core and a diverse number of switches.

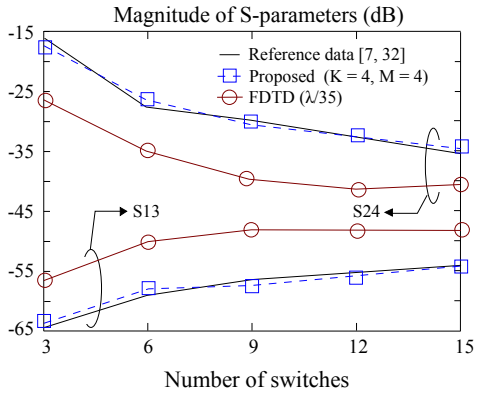


Figure 8: Magnitude of different *S*-parameters as a function of the switches number.

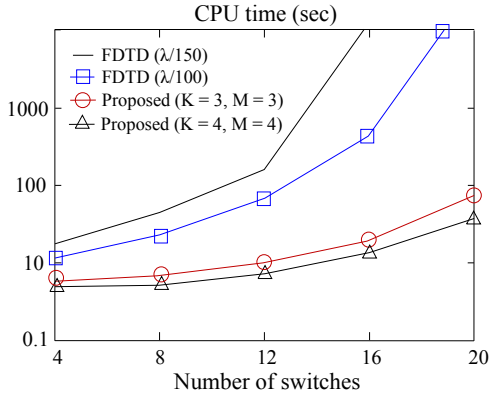


Figure 9: CPU-time required for the simulation of several splitter configuration as a function of the switches number.

Remaining in the area of electrically-large microwave devices, our analysis moves to the coaxial four-port microwave splitter with a 2.6×0.7×0.5 mm dielectric (ε_r = 8.2) region, depicted in Fig. 7. The outer conductor's cross-section is 6.1×5.3 mm and the inner's 1.4×0.8 mm. Figure 8 displays the behavior of S_{13} and S_{24} parameters with respect to the number of the involved switches. As observed, the FVTD/PSTD algorithm outperforms the traditional FDTD method, since it manages to efficiently associate the areas of abrupt and smooth field variation of the problem with its two techniques. Also, the required CPU time as the number of switches increases is, again, very small, as indicated in Fig. 15d.

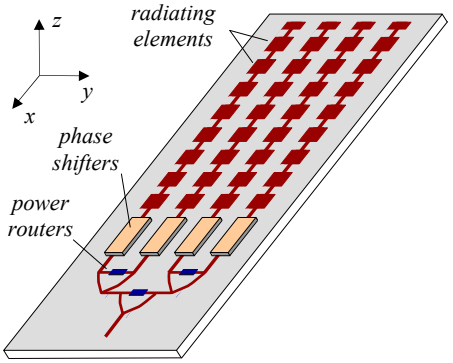


Figure 10: A reconfigurable MEMS-controlled antenna on a double-negative metamaterial substrate.

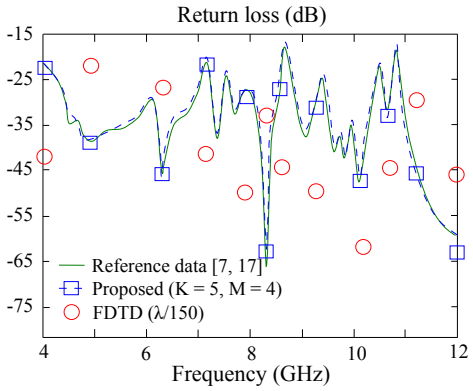


Figure 11: Return loss of the reconfigurable antenna.

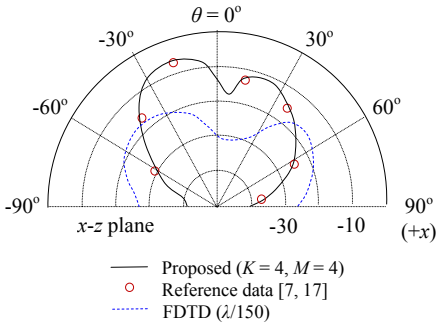


Figure 12: Radiation pattern of the reconfigurable antenna.

Let us, now, investigate the 12×14 monolithic antenna on a metamaterial substrate shown in Fig. 10. The directivity and main lobe of the structure are controlled by a set of MEMS power routers and phase shifters to obtain the necessary gain and radiation characteristics at a preselected frequency spectrum. For its discretization, the PSTD method is used for the MEMS elements (lattice: 32×36×24 cells), while the FVTD algorithm is applied in the rest of the domain (lattice: 68×84 ×46 cells). Particular attention is drawn on the interfaces between the MEMS and the substrate, where (24)-(34) are applied. In this context, Fig. 11 gives the return loss of the antenna and Fig. 12 its radiation pattern for different *K* and *M* orders. Again, the FDTD method – requiring a rather large resolution – does not cope with the problem. In contrast, the hybrid method is very precise for an 80% coarser grid.

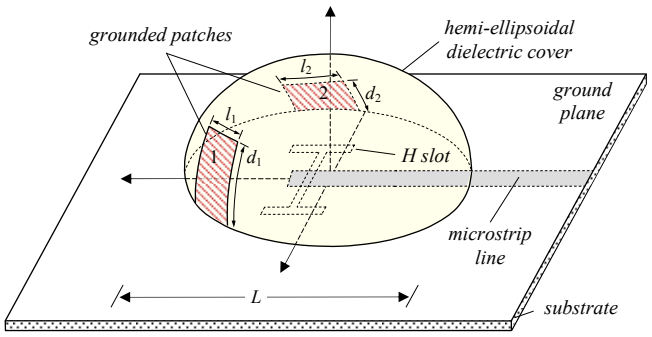


Figure 13: A hemi-ellipsoidal *H*-slot dielectric-loaded antenna with two patches.

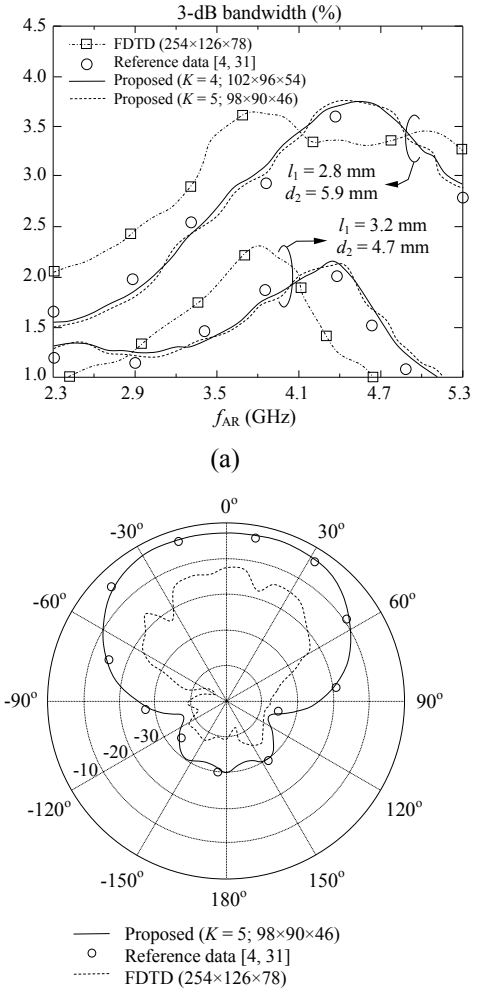


Figure 14: (a) 3-dB bandwidth versus axial ratio frequency and (b) radiation pattern for the hemi-ellipsoidal antenna.

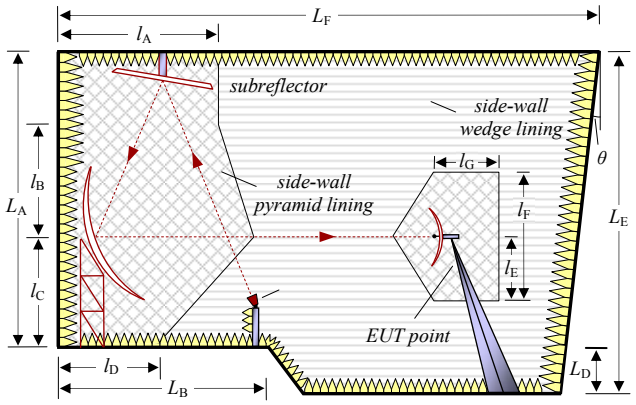


Figure 15: Geometry of an inclined-wall dual reflector compact range anechoic chamber.

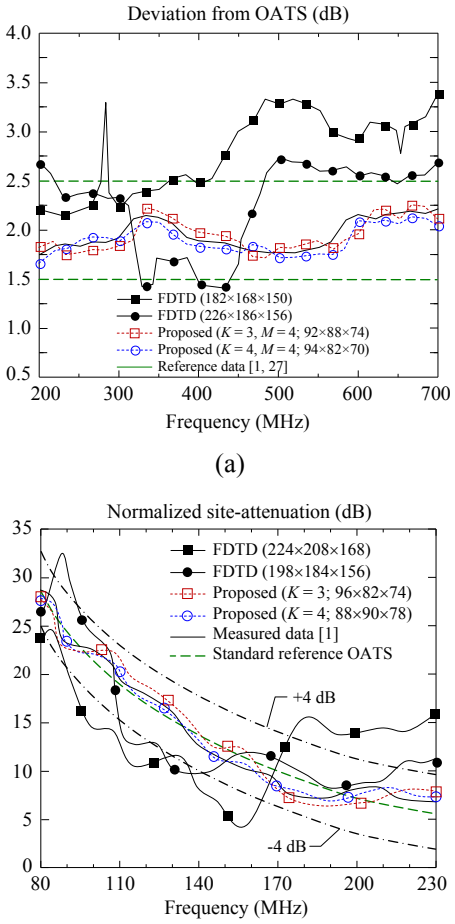


Figure 16: (a) Deviation from the OATS and (b) normalized site-attenuation for the inclined-wall compact ranger chamber.

Another electrically-large structure is the hemi-ellipsoidal *H*-slot antenna with a 1.34 mm thick dielectric ($\varepsilon_r = 4.4$) substrate and two patches for extra axial ratio (AR) and gain control (Fig. 13). The relative permittivity of the cover is $\varepsilon_{rc} = 6.2$, while $L = 28.3$ mm, $l_2 = 5.1$ mm, and $d_1 = 7.2$ mm. Figure 14a presents the 3-dB bandwidth versus AR frequency (f_{AR}) for two l_1, d_2 sets and the radiation pattern. As discerned, our technique is found to be very accurate even with a far more coarser grid, thus overwhelming the typical FDTD approach, which leads to rather misleading results.

Apart from the above applications, our investigation will, also, focus on several large-scale EMC test facilities, whose construction is very costly and thus any reliable simulation model is indeed necessary. The first structure is the inclined-wall dual reflector compact range anechoic chamber of Fig. 15, with a width of 7.6 m, $L_A = 6.4$ m, $L_B = 4.2$ m, $L_C = 5.2$ m,

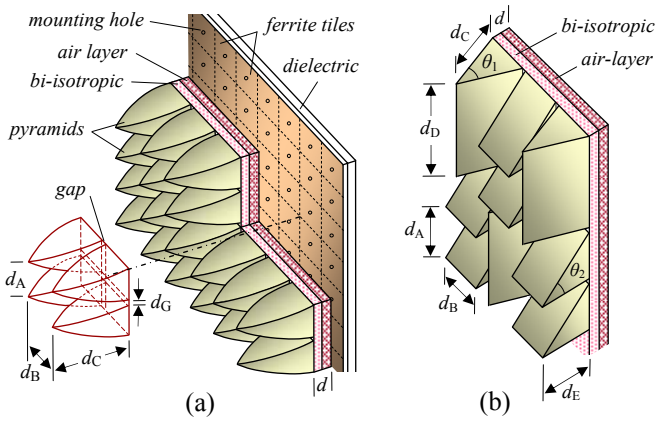


Figure 17: General structure of two absorber setups. (a) A pyramidal lining and (b) a set of alternating wedges.

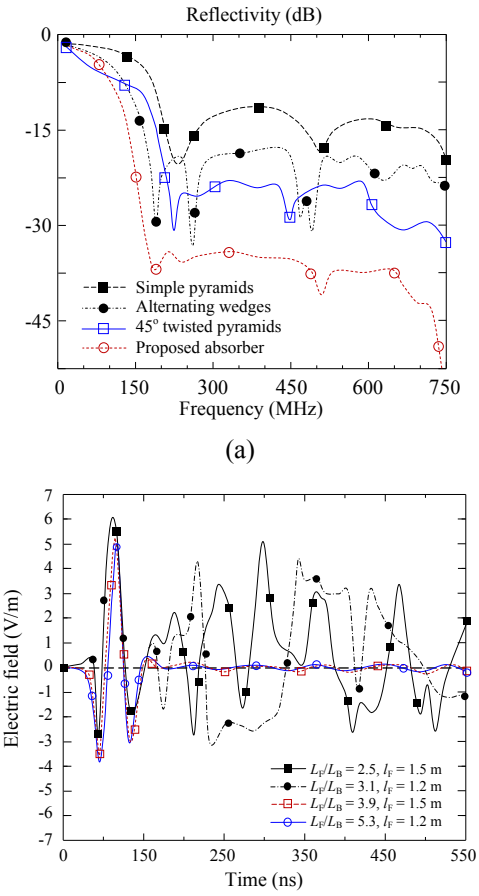


Figure 18: (a) Reflectivity comparison between existing absorbers and the proposed one and (b) electric field variation in the dual reflector chamber for different dimension ratios, sizes and heights of the quiet zone.

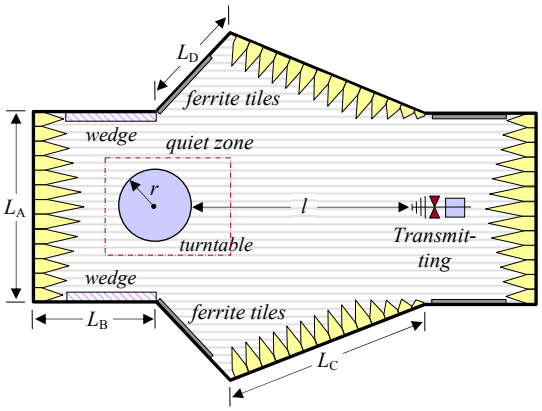


Figure 19: A double-horn semi-anechoic chamber with pyramidal absorbers and wedge linings.

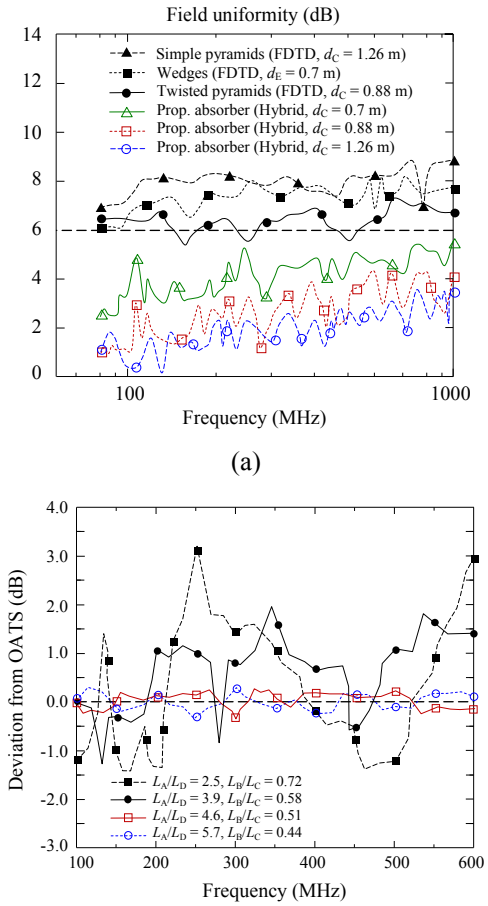


Figure 20: (a) Field uniformity and (b) efficiency optimization of the double horn semi-anechoic chamber.

L_D = 1.8 m, L_E = 7.6 m, and L_F = 11.2 m. The diameters of the sub- and main reflector are 2.85 m and 4.1 m, respectively. Additional dimensions are: θ = 6.5°, l_A = 3.0 m, l_B = 2.2 m, l_C = 1.9 m, l_D = 1.8 m, l_E = 1.1 m, l_F = 2.5 m, and l_G = 1.0 m. The chamber is lined with 20% carbon urethane pyramids and alternating wedges. Figure 16a shows the deviation from open area test site (OATS) and Figure 16b the normalized site-attenuation (NSA) of the facility's semi-anechoic version. Results indicate that despite its very fine lattice, the FDTD approach lacks to ensure measurement suitability in contrast to the novel algorithm which attains an 80% memory reduction. In this manner, we are able to correctly validate the chamber – i.e. full competence of performing reliable EMC or EMI measurements – prior to any construction attempt.

To improve the absorption performance of the compact range chamber, we introduce the generalized absorber lining of Fig. 17, which as observed consists of many dissimilar material interfaces. Hence, the use of the proposed methodology seems very appropriate. For our analysis, we use K = 4 and M = 3, while the lattice contains 104×129×142 cells, almost 85% coarser than the corresponding FDTD discretization for a resolution of $\lambda/20$. Figure 18a shows the reflectivity of several absorbers and Fig. 18b the electric field behavior in the quite zone for diverse chamber design parameters. The superior behavior of our absorber along with the accuracy of the hybrid technique is clearly visible.

Another type of EMC semi-anechoic chamber with an interesting low-frequency performance is the double-horn semi-anechoic chamber of Fig. 19. The structure has a height of 6.8 m and L_A = 6 m, L_B = 3.8 m, L_C = 7.3 m, L_D = 3.4 m, l = 7.2 m, while its lining combines pyramids with alternating wedge arrays (d_A = 0.24 m, d_E = 0.68 m in Fig. 17b). Note that the size of the pyramids behind the quiet zone follows a curved Chebyshev regime. To characterize this facility, field uniformity is depicted in Fig. 20b, which reveals the capability of the structure to perform measurements, unlike the FDTD method. Similar deductions are drawn from Fig. 20b, where the effects of the dimensions are thoroughly explored.

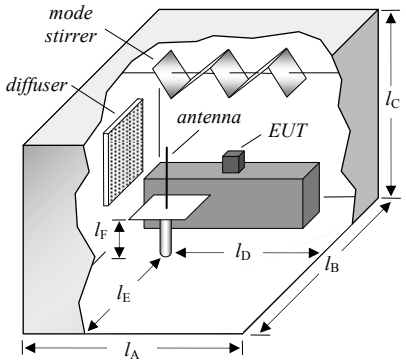


Figure 21: A general mode-stirred reverberation chamber.

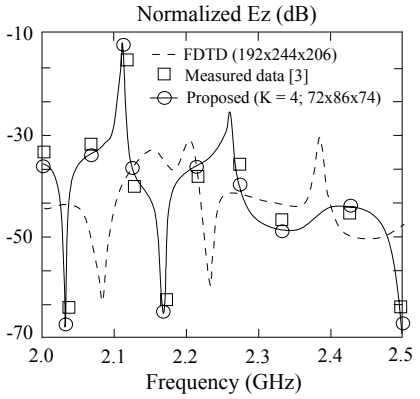


Figure 22: Amplitude of the normalized E_z component versus frequency in the interior of the reverberation chamber.

Finally, the hard-to-model reverberation chamber of Fig. 21, equipped with quadratic diffusers, i.e. gratings that diffract incident waves, is studied. Usual dimensions are: l_A = 3.22 m, l_B = 4.48 m, l_C = 3.64 m, l_D = 1.4 m, l_E = 1.9 m and l_F = 0.8 m. A point where existing schemes fail is the stirrer's treatment (θ_T = 34°). Herein, its movements are modeled with an interval of 22° and a 60 temporal sampling rate. Figure 22 illustrates the normalized E_z variation, while Fig. 23 provides the shielding effectiveness of a 1.5 mm thick fiber-glass-fiber plate. As detected, the FVTD/PSTD approach overwhelms all FDTD implementations in a fairly wideband sense.

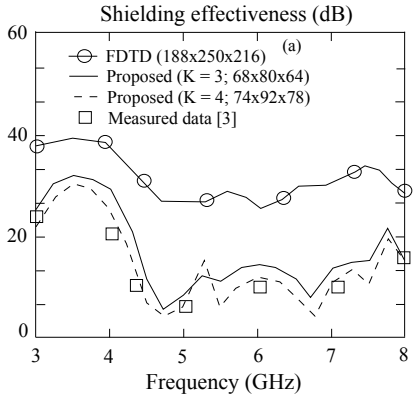


Figure 23: Shielding effectiveness by the mode-stirred reverberation facility for a 1.5 mm thick fiber-glass-fiber plate.

6. Conclusions

A hybrid time-domain methodology, based on advanced FVTD and PSTD schemes, has been proposed in this paper for the precise design and modeling large-scale 3-D EMC structures. Established through a low-complexity generalized rationale, the parametric technique introduces new operators with optimal nodal density and media-sensitive interface conditions. In essence, the FVTD approach uses a leap-frog integration scheme – conditionally stable and non-dissipative – that conserves the total charge in a global and local sense. Thus, canonical staggered-meshed formalisms (as in the FDTD algorithm) are efficiently circumvented with the computational overhead limited in reasonable levels. On the other hand, the PSTD concept uses Chebyshev polynomials, through a fast Fourier transform (FFT), instead of the customary finite-difference approximators, to evaluate spatial derivatives in areas of abrupt field variation. Due to its enhanced spectral accuracy, the PSTD technique entails only two cells per wavelength according to the Nyquist sampling theorem and, therefore, can deal with more challenging scenarios. Hence, and as realistic numerical evidence determines, artificial reflection errors are greatly suppressed and very rigorous as well as inexpensive solutions are acquired.

Acknowledgements

This research has been supported by the Aristotle University of Thessaloniki under grant 87908.

References

[1] C. Holloway, P. McKenna, R. Dalke, R. Perala, C. Devor, Time-domain modeling, characterization, and measurements of anechoic and semi-anechoic electro-

magnetic test chambers, *IEEE Trans. Electromagn. Compat.* 44: 102−118, 2002.

[2] C. Buccella, M. Feliziani, F. Maradei, G. Manzi, Magnetic field computation in a physically large domain with thin metallic shields, *IEEE Trans. Magn.* 41: 1708−1711, 2005.

[3] C. Bruns, R. Vahldieck, A closer look at reverberation chambers – simulation and experimental verification," *IEEE Trans. Electromagn. Compat.* 47: 612−626, 2005.

[4] S. Lee, M. Vouvakis, J.-F. Lee, "A non-overlapping domain decomposition method with non matching grids for modeling large finite arrays, *J. Comp. Phys.* 203: 1–21, 2005.

[5] M. Sarto, A. Tamburrano, Innovative test method for the shielding effectiveness measurement of thin films in wide frequency range, *IEEE Trans. Electromagn. Compat.* 48: 331−341, 2006.

[6] N. Kantartzis, T. Tsiboukis, *Modern EMC Analysis Techniques: Time-Domain Computational Schemes*, Morgan & Claypool Publishers, San Rafael, CA, 2008.

[7] B. Lakshminarayanan, D. Mercier, G. Rebeiz, High-reliability miniature RF-MEMS switched capacitors, *IEEE Trans. Microw. Theory Tech.* 56: 971–981, 2008.

[8] A. Duffy, A. Orlandi, H. Sasse, "Offset difference measure enhancement for the feature-selective validation method, *IEEE Trans. Electromagn. Compat.* 50: 413 −415, 2008.

[9] Y. Li, J. Zhu, Q. Yang, Z. Wei, Y. Guo, Y. Wang, Measurement of soft magnetic composite material using an improved 3-D tester with novel sensing coils, *IEEE Trans. Magn.* 46: 1971–1974, 2010.

[10] D. Baumann, C. Fumeuax, R. Vahldieck, Field-based scattering matrix extraction scheme for the FVTD method exploiting a flux-splitting algorithm, *IEEE Trans. Microw. Theory Tech.* 53: 3595–3605, 2005.

[11] D. Firsov, J. LoVetri, O. Jeffrey, V. Okhmatovski, C. Gilmore, W. Chamma, High-order FVTD on unstructured grids using an object-oriented computational engine, *ACES J.* 22: 71−82, 2007.

[12] C. Bommaraju, W. Ackermann, and T. Weiland, Convergence of error in FVTD methods on tetrahedral meshed in 3D, *Proc. Applied Electromagn. Conf. (AEMC)*, pp. 1–4, 2009.

[13] G. Bozza, D. Caviglia, L. Ghelardoni, and M. Pastorino, Cell-centered finite-volume time-domain method, *IEEE Microw. Wireless Compon. Lett.* 20: 477–479, 2010.

[14] I. Jeffrey, J. LoVetri, Interfacting thin-wire and circuit subcell models in unstructured time-domain field solvers, *IEEE Trans. Antennas Propag.* 60: 1−9, 2012.

[15] Q. Liu, G. Zhao, Review of PSTD methods for transient electromagnetics, *Int. J. Numer. Model.* 22: 299−323, 2004.

[16] X. Gao, M.S. Mirotznik, D.W. Prather, A method for introducing soft sources in the PSTD algorithm, *IEEE Trans. Antennas Propag.* 52: 1665−1671, 2004.

[17] Y.J. Fan, B.L. Ooi, M.S. Leong, Fast multipole accelerated Chebyshev pseudospectral time domain algorithm, *IET Microw., Antennas & Propag*. 1: 763−769, 2007.

[18] D. Vande Ginste, E. Michielssen, F. Olyslager, D. De Zutter, An efficient PML based on multilevel fast multipole algorithm for large microwave structures, *IEEE Trans. Antennas Propag.* 54: 1538−1548, 2006.

[19] Y. Song, N. Nikolova, M. Bakr, Efficient time-domain sensitivity analysis using coarse grids, *ACES J.* 23: 5−15, 2008.

[20] T. Ohtani, K. Taguchi, T. Kashiwa, Y. Kanai, J. Cole, Scattering analysis of large-scale coated cavity using the nonstandard FDTD method, *IEEE Trans. Magn.* 45: 1296 –1299, 2009.

[21] I. Ahmed, E.-H. Khoo, Erping Li, Development of the CPML for the three-dimensional stable LOD-FDTD method, *IEEE Trans. Antennas Propag.* 58: 832−837, 2010.

[22] R.S. Hedge, Z. Szabo, Y. Hor, Y. Kiasat, Erping Li, W.J.R. Hoefer, The dynamics of nanoscale super-resolution imaging with the superlens, *IEEE Trans. Microw. Theory, Tech.* 59: 2612−2623, 2011.

[23] B. Zhu, J. Lu, Erping Li, Electromagnetic compatibility benchmark-modeling for a dual-die CPU, *IEEE Trans. Electromagn. Compat.* 53: 91−98, 2011.

[24] H. Attia, L. Yousefi, O.M. Ramahi, "Analytical model for calculating the radiation field of microstrip antennas with artificial magnetic superstrates: Theory and experiment," *IEEE Trans. Antennas Propag.* 59: 1438–1445, 2011.

[25] P.-P. Ding, C.-W. Qiu, S. Zouhdi, Rigorous derivation and fast solution of spatial-domain Green's functions for uniaxial anisotropic multilayers using modified fast Hankel transform method, *IEEE Trans. Microw. Theory, Tech.* 60: 205−217, 2012.

[26] R. Nilavalan, I. Craddock, C. Railton, Quantifying numerical dispersion in non-orthogonal FDTD meshes, *IEE Proc. Microw. Antennas Propag.* 149: 23−27, 2002.

[27] A. Taflove, S. Hagness, *Computational Electrodynamics: The Finite-Difference Time-Domain Method*, Artech House, Norwood, MA, 2005.

[28] N. Kantartzis, T. Tsiboukis, and E. Kriezis, An explicit weighted essentially non-oscillatory time-domain algorithm for the 3-D EMC applications with arbitrary media," *IEEE Trans. Magn.* 42, 803−806, 2006.

[29] S. Noelle, W. Rosenbaum, M. Rumpf, 3D adaptive central schemes: Part I. Algorithms for assembling the dual mesh, *Appl. Numer. Math.* 56: 778–799, 2006.

[30] J.-P. Berenger, An optimized CFS-PML for wave-structure interaction problems, *IEEE Trans. Electromagn. Compat.* 54: 1−8, 2012.

[31] D. Pozar, *Microwave Engineering*, John Wiley & Sons, New York, NJ, 2005.

[32] J. van Bladel, *Electromagnetic Fields*, IEEE Press, New York, NJ, 2007.

Pulse Dispersion in Layered Cylindrical Dielectric Waveguides

Ioannis O. Vardiambasis[1*], Theodoros N. Kapetanakis[1], Melina P. Ioannidou[2], and Angela P. Moneda[2]

[1] Department of Electronics, Chania Branch, Technological Educational Institute (TEI) of Crete, Greece
[2] Department of Electronics, Alexander Technological Educational Institute of Thessaloniki, Greece
* ivardia@chania.teicrete.gr

Abstract

The distortion of a pulse or signal, caused by dispersion, as it propagates along a layered, cylindrical, dielectric waveguide is investigated. The cylindrical waveguide dispersion theory is combined with numerical techniques in order to study the distorted, due to dispersion, shape of dc and RF pulses propagating along the waveguide axis. Fourier transforms are used to analyze the pulses, interpreting the dispersion characteristics from the real frequency spectrum point of view. Numerical results, revealing the variable amount of pulse distortion, are presented for several values of both the cylindrical structure and the pulse parameters.

1. Introduction

The widespread use of optical communications may be attributed to the development of fiber optics cables, which are dielectric waveguides, usually of circular cross section. A dielectric waveguide is an open structure guiding the electromagnetic waves in discrete modes through internal reflections. The confinement of the energy within the dielectric structure is described analytically by Maxwell's equations and the boundary conditions at dielectric-dielectric boundaries [1]-[3].

Therefore, since TEM mode propagation is not supported, the phase constant of all propagating modes is not a linear function of frequency, resulting in dispersion. Due to the latter, electrical pulses and signals travelling along the dielectric waveguide become distorted, since the higher harmonics of the signal travel at a slower velocity than its lower harmonics.

Studying distortion due to dispersion is essential for the design of integrated circuits operating at high frequencies or switching speeds, because the form of the propagating signal is remarkably altered. The distortion characteristics of signals in dispersive materials [4], metallic waveguides [5], single microstrip lines [6]-[9], coupled microstrips [10]-[11], multiple strips [12], coplanar waveguides [13], and optical fibers [14]-[18] have been examined extensively using several techniques. On the other hand, the distortion of dc pulses and pulse-modulated RF waves, in layered cylindrical dielectric waveguides has in general received less attention [19].

In this paper, we study the distorted, due to dispersion, shape of dc and RF pulses propagating along layered cylindrical dielectric rods. We combine the cylindrical waveguide dispersion theory with numerical techniques, in order to examine the propagation constant variations as a function of frequency. The effect of these variations on pulse dispersion is studied using Fourier transforms to analyze the signals and interpret the dispersion characteristics.

Numerical results, revealing the variable amount of pulse distortion, are presented for several values of both the cylindrical structure parameters (radii and dielectric constants of the cylindrical layers) and the pulse parameters (type, shape, and width of the pulse).

2. Distortion of signals

In the frequency domain, a signal propagating along the z-axis of the waveguide can be written at a distance $z=L$ from a reference point ($z=0$), as in [7]:

$$S(\omega, L) = S(\omega, 0)\, \mathrm{e}^{-\gamma(\omega) \mathrm{L}}, \qquad (1)$$

where $S(\omega,0)$ is the Fourier transform of the signal (or pulse) and $\gamma(\omega)=\alpha(\omega)+j\beta(\omega)$ is the frequency-dependent complex propagation constant. In order to study distortion due to dispersion, we consider lossless waveguides with negligible attenuation constant $\alpha(\omega)$ and frequency dependent phase constant $\beta(\omega)$.

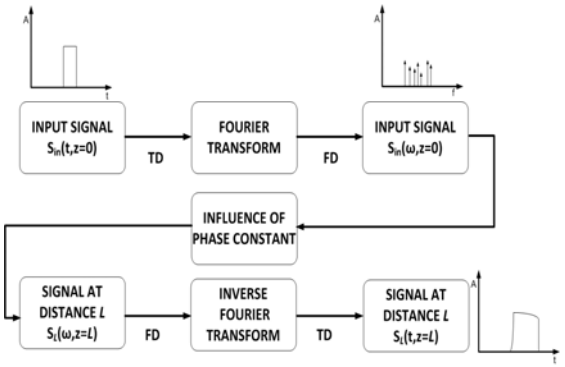


Figure 1: The methodology adopted to calculate the effect of distortion on propagating signals (where TD = time-domain, and FD = frequency-domain).

Taking the inverse Fourier transform of (1) leads to the following time-domain representation of the signal at $z=L$

$$s(t,L)=\frac{1}{2\pi}\int_{-\infty}^{\infty}\mathrm{S}(\omega,0)\,\mathrm{e}^{\mathrm{j}[\omega t-\beta(\omega)L]}\,\mathrm{d}\omega\,. \qquad (2)$$

This methodology, described thoroughly in [7], is also presented in Fig. 1. Since the Fourier transform of the transient signal $s(t,0)$ is easily obtained for many common pulses (i.e. triangular, square and Gaussian), and also for any RF wave modulated by these pulses [7], we just need to determine $\beta(\omega)$ of the "carrier" propagating mode for the cylindrical waveguide.

The frequency-dependent phase constant $\beta(\omega)$ results from the solution of a complex transcendental equation. Thus (2) cannot be expressed in closed form. Numerical integration is used with satisfactory accuracy for usual computer resources.

3. Dispersion of waveguide modes

In this paper we consider a layered dielectric circular cylindrical waveguide (Fig. 2); it consists of m concentric cylindrical dielectric (in general lossy) layers (regions 1,2,3,...,m). Each layer is identified through the corresponding dielectric permittivity ε_s, magnetic permeability μ_s, electric conductivity σ_s, and radius α_s (s=1,2,3,...,m). The structure is embedded in the unbounded dielectric space (region 0; ε_0, μ_0).

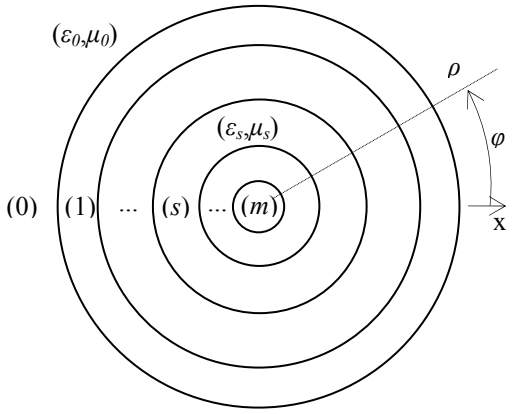


Figure 2: Geometry of an m-layered cylindrical dielectric waveguide.

Assuming the $\exp(+j\omega t)$ time-dependence suppressed throughout the analysis, let $[\bar{E}(\bar{\rho}),\bar{H}(\bar{\rho})]e^{-j\beta z}$ denote the field of a mode propagating in the structure of Fig. 2. Using the notation $J_n(.)$ and $H_n(.)$ to denote the Bessel and the second-kind Hankel functions of order n, we apply the separation of variables method and obtain the corresponding electromagnetic field z-components in all regions of space

$$\begin{bmatrix}E_z^0(\bar{\rho})\\ H_z^0(\bar{\rho})\end{bmatrix}=\sum_{n=-n_{\max}}^{n_{\max}}e^{jn\varphi}\,H_n(k_{c0}\rho)\begin{bmatrix}c_n^1\\ d_n^1\end{bmatrix} \qquad (3a)$$

$$\begin{bmatrix}E_z^s(\bar{\rho})\\ H_z^s(\bar{\rho})\end{bmatrix}=\sum_{n=-n_{\max}}^{n_{\max}}e^{jn\varphi}\left(J_n(k_{cs}\rho)\begin{bmatrix}a_n^s\\ b_n^s\end{bmatrix}+H_n(k_{cs}\rho)\begin{bmatrix}c_n^{s+1}\\ d_n^{s+1}\end{bmatrix}\right) \qquad (3b)$$

$$\begin{bmatrix}E_z^m(\bar{\rho})\\ H_z^m(\bar{\rho})\end{bmatrix}=\sum_{n=-n_{\max}}^{n_{\max}}e^{jn\varphi}\,J_n(k_{cm}\rho)\begin{bmatrix}a_n^m\\ b_n^m\end{bmatrix}, \qquad (3c)$$

where $n_{\max}\to\infty$, $(a_n^q,\,b_n^q,\,c_n^q,\,d_n^q)$ are the unknown expansion coefficients, the superscripts q (q=0,s) and s are used to identify the region of space, $k_{cq}^2=k_q^2-\beta^2$, $k_q^2=\omega\mu_q(\omega\varepsilon_q-j\sigma_q)$, and (ρ,φ) are the polar coordinates of $\bar{\rho}$ in the coordinate system associated with the cylindrical structure. The φ-components of the field may be found via

$$\begin{bmatrix}E_\varphi^q(\bar{\rho})\\ H_\varphi^q(\bar{\rho})\end{bmatrix}=\frac{j}{k_{cq}^2}\begin{bmatrix}-\dfrac{\beta}{\rho}\dfrac{\partial}{\partial\varphi} & \omega\mu_q\dfrac{\partial}{\partial\rho}\\ (-\omega\varepsilon_q+j\sigma_q)\dfrac{\partial}{\partial\rho} & -\dfrac{\beta}{\rho}\dfrac{\partial}{\partial\varphi}\end{bmatrix}\begin{bmatrix}E_z^q(\bar{\rho})\\ H_z^q(\bar{\rho})\end{bmatrix}. \qquad (4)$$

Then, application of the continuity conditions for the tangential components of $\bar{E}$ and $\bar{H}$ over all cylindrical boundaries, yields an infinite, homogeneous, linear set of ($4m\ n_{max}$) algebraic equations:

$$\left[\begin{array}{c|c}-\mathrm{J_n}(k_{cs}\alpha_s)\,\bar{\bar{I}} & \bar{\bar{H}}_n^{1-\delta_{1s}}(k_{c(s-1)}\alpha_s)\,\bar{\bar{I}}\\ \hline -\bar{\bar{P}}_n^s(\alpha_s) & \bar{\bar{Q}}_n^{s-1}(\alpha_s)\end{array}\right]_{4\times4}\cdot\left[\begin{array}{c}\begin{pmatrix}a_n^s\\ b_n^s\end{pmatrix}\\ \hline \begin{pmatrix}c_n^s\\ d_n^s\end{pmatrix}\end{array}\right]_{4\times1}+$$

$$+(1-\delta_{1s})\left[\frac{\mathrm{J_n}(k_{c(s-1)}\,\alpha_s)\,\bar{\bar{I}}}{\bar{\bar{P}}_n^{s-1}(\alpha_s)}\right]_{4\times2}\cdot\begin{pmatrix}a_n^{s-1}\\ b_n^{s-1}\end{pmatrix}_{2\times1}+$$

$$+(1-\delta_{ms})\left[\frac{-\mathrm{H_n}(k_{cs}\,\alpha_s)\,\bar{\bar{I}}}{-\bar{\bar{Q}}_n^s(\alpha_s)}\right]_{4\times2}\cdot\begin{pmatrix}c_n^{s+1}\\ d_n^{s+1}\end{pmatrix}_{2\times1}=\begin{bmatrix}\bar{\bar{0}}\\ \bar{\bar{0}}\end{bmatrix}, \qquad (5)$$

where $n=0,\pm1,\pm2,...,\pm n_{\max}$, δ_{1s} is the Kronecker delta, α_s denotes the radius of the sth cylindrical layer, $\bar{\bar{I}}$ is the unit matrix, and the 2x2 matrices $\bar{\bar{P}}_n^s(\rho)$ and $\bar{\bar{Q}}_n^s(\rho)$ are given by the expressions

$$\bar{\bar{P}}_n^s(\rho)=\begin{bmatrix}\dfrac{n\beta}{k_{cs}^2\rho}J_n(k_{cs}\rho) & \dfrac{j\omega\mu_s}{k_{cs}}J_n'(k_{cs}\rho)\\ \dfrac{-j\omega\varepsilon_s-\sigma_s}{k_{cs}}J_n'(k_{cs}\rho) & \dfrac{n\beta}{k_{cs}^2\rho}J_n(k_{cs}\rho)\end{bmatrix}, \qquad (6a)$$

$$\bar{\bar{Q}}_n^s(\rho)=\begin{bmatrix}\dfrac{n\beta}{k_{cs}^2\rho}H_n(k_{cs}\rho) & \dfrac{j\omega\mu_s}{k_{cs}}H_n'(k_{cs}\rho)\\ \dfrac{-j\omega\varepsilon_s-\sigma_s}{k_{cs}}H_n'(k_{cs}\rho) & \dfrac{n\beta}{k_{cs}^2\rho}H_n(k_{cs}\rho)\end{bmatrix}. \qquad (6b)$$

In order to obtain a nontrivial solution, we vanish the determinant of the homogeneous system (5) and we obtain the dispersion equation of the structure. This characteristic equation is treated numerically after truncating the size of the matrix to a finite value, i.e., by considering finite values

of n_{max} in (3a)-(3c). The solution results in the dispersion diagrams of the propagating modes supported by the cylindrical dielectric waveguide. Typical results are shown in Figs. 3 and 4, where the effective dielectric constant $(\beta/k_0)^2$ of the first five modes is presented versus the normalized frequency α_1/λ_0, for a dielectric rod and a cladded fiber, respectively.

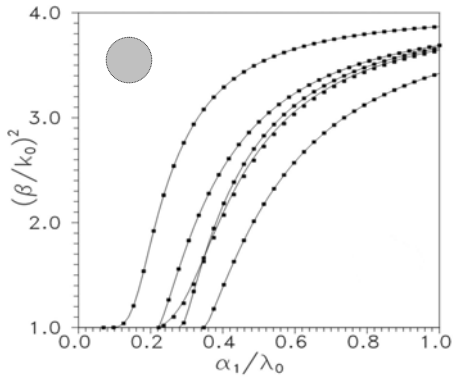


Figure 3: Dispersion diagrams for the first five modes propagating along a dielectric rod (structure of Fig. 2, with m=1, ε_1=4ε_0).

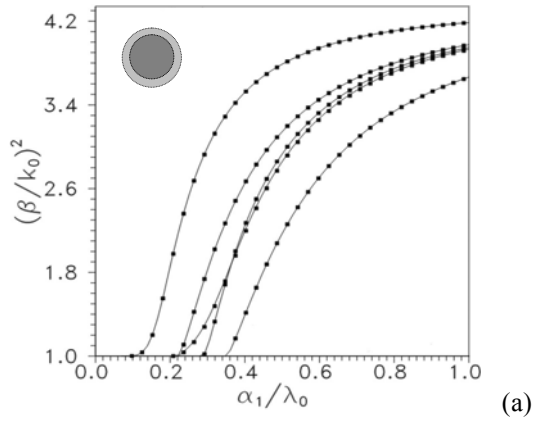


Figure 4: Dispersion diagrams for the first five modes, propagating along a cladded fiber (structure of Fig. 2, with m=2, ε_1=2.32ε_0, ε_2=4.34ε_0; (a) α_2=0.9α_1, and (b) α_2=0.4α_1).

Such structures can support an infinite number of modes, as in more complex geometries [20]-[22]. Considering that all dielectrics are perfect, for any given set of layer physical characteristics (radii, permittivities and permeabilities), only a finite number of unattenuated propagating waveguide modes exist with their fields localized in the dielectric core [1]-[3]. These modes are in general hybrid HE_{mn} and EH_{mn}, or pure TE_{0n} and TM_{0n} only, when the field configurations are symmetrical [1], [23]. All modes, except the dominant HE_{11}, exhibit cutoff frequencies, below which they cannot propagate unattenuated.

4. Numerical results

We consider Gaussian or square dc pulses (with 3dB-pulsewidth τ) propagating along the structure of Fig. 2, as signals supported by its dominant HE_{11} mode, whose dispersion diagram $\varepsilon_{r,eff}(\omega)$ has been determined in Section 3. Evaluation of the integral in (2) leads to the waveforms of the distorted Gaussian and square dc pulses shown in Figs. 5-15, along with the undistorted pulses included for reference. Figs. 5-9 refer to dielectric rod structures, while Figs. 10-15 refer to optical fiber structures.

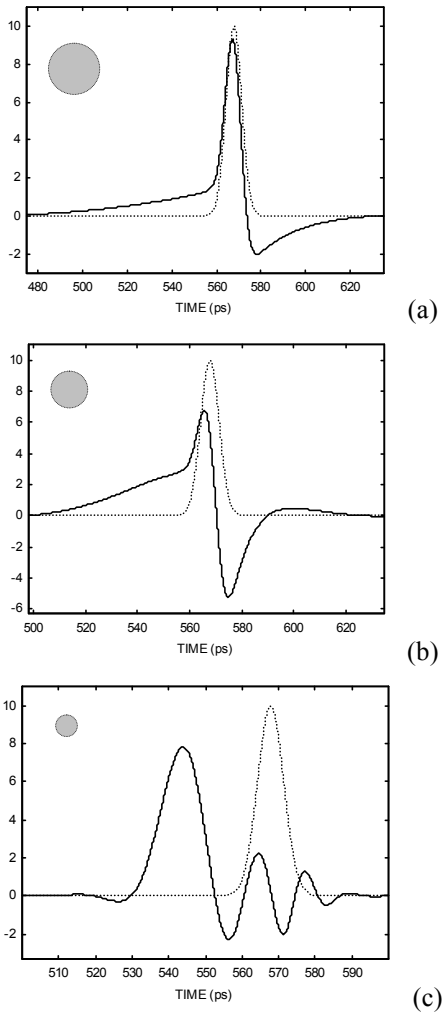
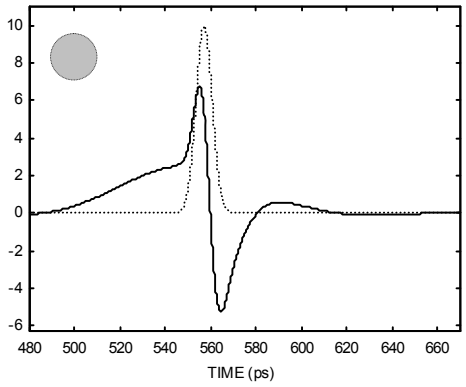
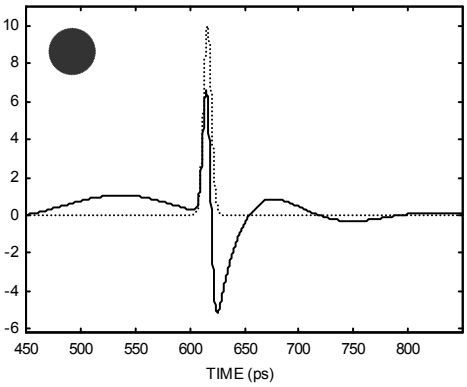


Figure 5: Distortion of a Gaussian dc pulse with τ=10ps, at a distance L=13cm along a dielectric rod (structure of Fig. 2, with m=1, ε_1=2.56ε_0; (a) α_1=10 mm, (b) α_1=5 mm, and (c) α_1=1 mm).

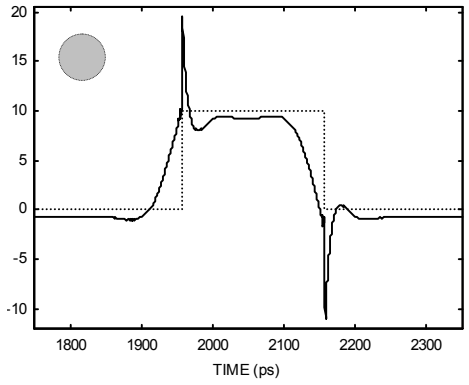


(a)

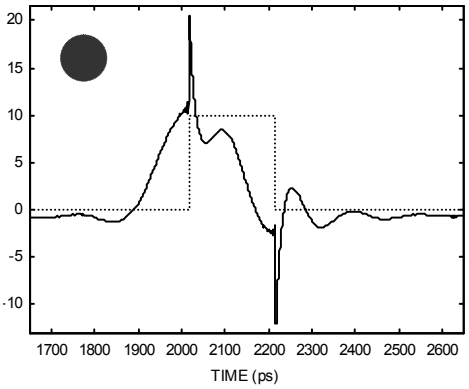


(b)

Figure 6: Distortion of a Gaussian dc pulse (τ=10ps) at a distance L=9cm along a dielectric rod (structure of Fig. 2, with m=1, α_1=4 mm; (a) ε_1=3.6ε_0, and (b) ε_1=15ε_0).

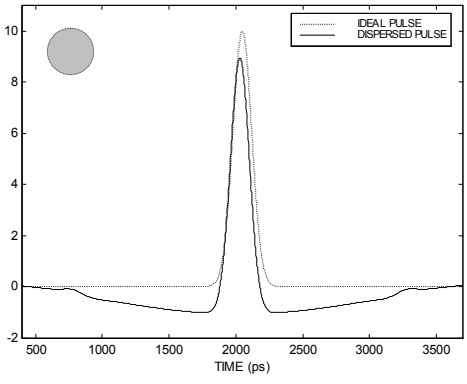


(a)

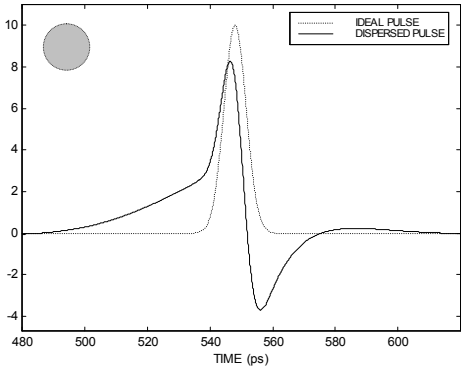


(b)

Figure 8: Distortion of a square dc pulse with τ=200ps at a distance L=9cm along a dielectric rod (structure of Fig. 2, with m=1, α_1=4 mm; (a) ε_1=3.6ε_0, and (b) ε_1=15ε_0).

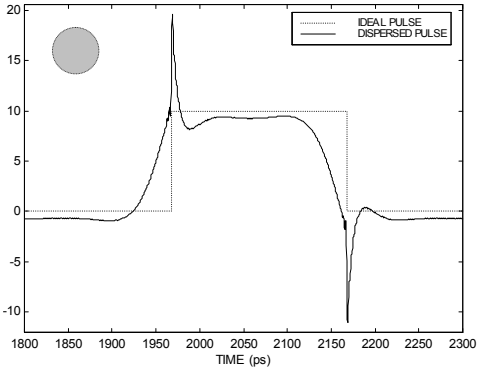


(a)

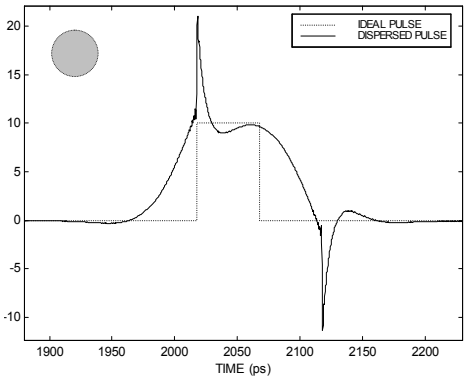


(b)

Figure 7: Distortion of a Gaussian dc pulse (with 3dB-pulsewidth τ) at a distance L=9mm along a dielectric rod (structure of Fig. 2, with m=1, α_1=5mm, and ε_1=2.56ε_0), when (a) τ=200ps, and (b) τ=10ps.

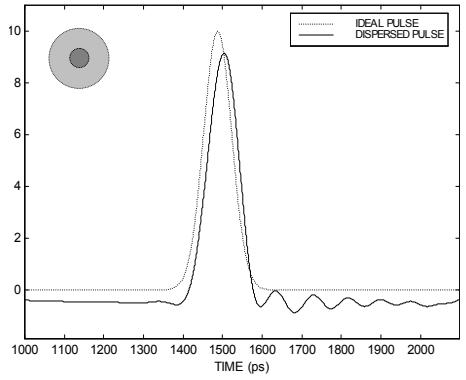


(a)

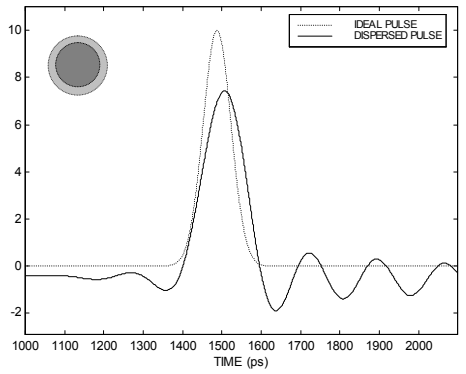


(b)

Figure 9: Distortion of a square dc pulse (with 3dB-pulsewidth τ) at a distance L=9mm along a dielectric rod (structure of Fig. 2, with m=1, α_1=5mm, and ε_1=2.56ε_0) when (a) τ=200ps, and (b) τ=100ps.

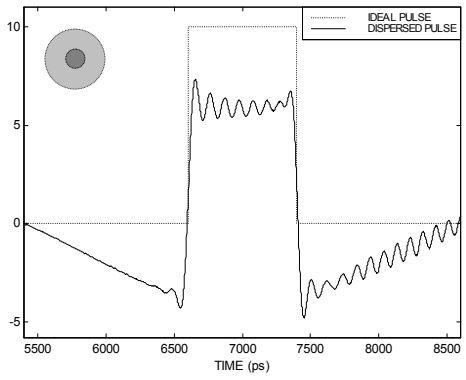


(a)

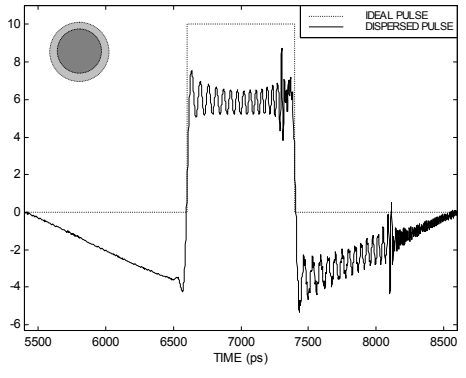


(b)

Figure 10: Distortion of a Gaussian dc pulse (τ=100ps) at a distance L=30cm along a two-layered fiber (structure of Fig. 2, with m=2, ε_1=2.32ε_0, ε_2=10ε_0, α_1=5mm; (a) α_2=0.1α_1, and (b) α_2=0.9α_1).

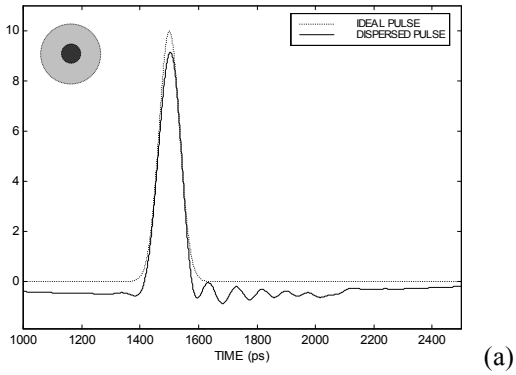


(a)

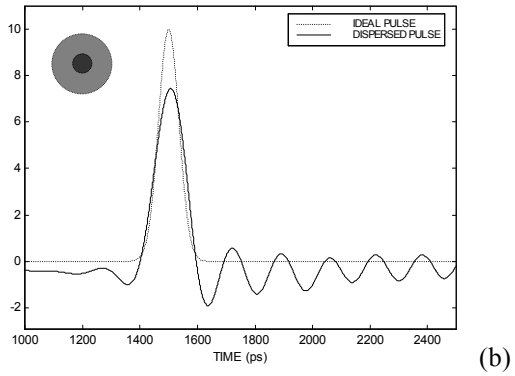


(b)

Figure 11: Distortion of a square dc pulse (τ=800ps) at a distance L=30cm along a two-layered fiber (structure of Fig. 2, with m=2, ε_1=2.32ε_0, ε_2=10ε_0, α_1=3mm; (a) α_2=0.1α_1, and (b) α_2=0.9α_1).

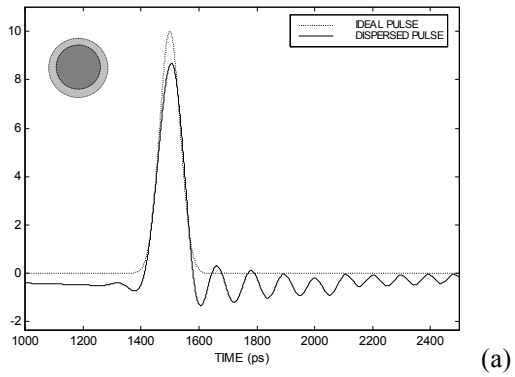


(a)

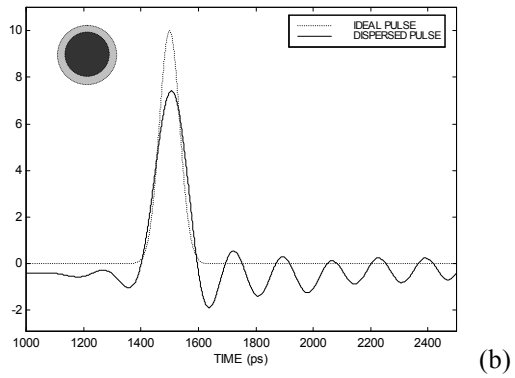


(b)

Figure 12: Distortion of a Gaussian dc pulse (τ=100ps) at a distance L=30cm along a two-layered fiber (structure of Fig. 2, with m=2, ε_2=10ε_0, α_1=5mm, α_2=0.1α_1; (a) ε_1=2.32ε_0, and (b) ε_1=8ε_0).

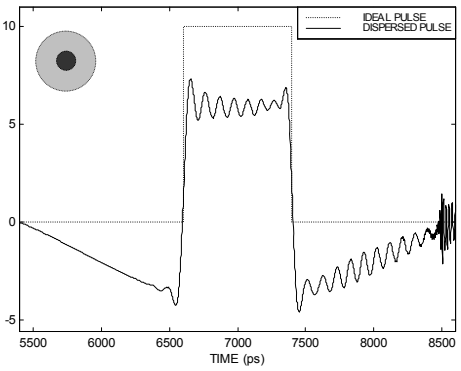


(a)

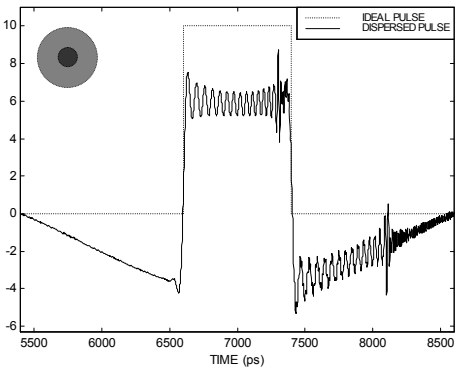


(b)

Figure 13: Distortion of a Gaussian dc pulse (τ=100ps) at a distance L=30cm along a two-layered fiber (structure of Fig. 2, with m=2, ε_1=2.32ε_0, α_1=5mm, α_2=0.9α_1; (a) ε_2=6ε_0, and (b) ε_2=10ε_0).

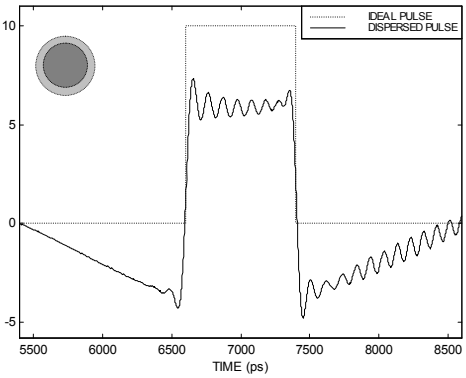


(a)

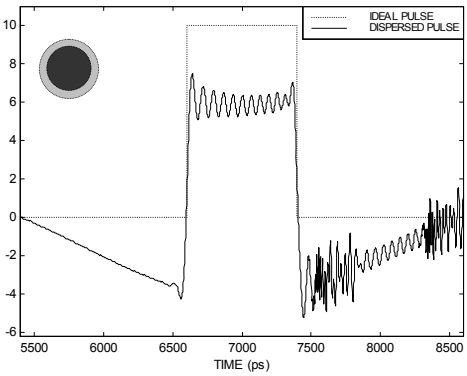


(b)

Figure 14: Distortion of a square dc pulse (τ=800ps) at a distance L=30cm along a two-layered fiber (structure of Fig. 2, with m=2, ε_2=10ε_0, α_1=3mm, α_2=0.1α_1; (a) ε_1=2.32ε_0, and (b) ε_1=8ε_0).



(a)



(b)

Figure 15: Distortion of a square dc pulse (τ=800ps) at a distance L=30cm along a two-layered fiber (structure of Fig. 2, with m=2, ε_1=2.32ε_0, α_1=3mm, α_2=0.9α_1; (a) ε_2=6ε_0, and (b) ε_2=10ε_0).

Figs. 5-15 indicate that pulses propagating along cylindrical dielectric waveguides can be significantly distorted, for several geometrical and operational characteristics of the structure, such as the radii of the circular cylinders, the dielectric constants of the cylindrical layers, the pulse width, and the pulse rise time. The waveforms of these distorted pulses are evaluated from (2) using numerical integration, while the waveforms of the original undistorted pulses are also drawn for comparison. In each Figure the undistorted pulse is placed according to its propagation velocity, which is related to the propagation constant of the dominant mode of the cylindrical waveguide at zero frequency [7].

Fig. 5 reveals the strong effect of the waveguide radius on the distortion of a Gaussian dc pulse, that has travelled distance L=13cm along a dielectric rod. For decreasing values of the rod's radius, the peak amplitude attenuates considerably, the pulse is increasingly displaced getting significantly wider, and the ringing becomes more and more intense.

Figs. 6 and 8 show the effect of the waveguide's dielectric material on the distortion of a pulse (Gaussian and square dc, respectively), that has travelled distance L=9cm along a dielectric rod. When the dielectric constant of the rod increases, then the amplitude, the displacement, the pulsewidth, and the ringing of the dispersed pulses differ slightly in the case of Fig. 6, and substantially in the case of Fig. 8. This contradictory behavior is reasonable for pulses with narrow and wide spectral content, as the Gaussian and the square pulse, respectively.

Figs. 7 and 9 depict the presumable effect of pulsewidth on the distortion of a pulse (Gaussian and square dc, respectively), that has travelled distance L=9cm along a dielectric rod. When the 3dB width of the input pulse decreases, then the amplitude attenuates, the distorted pulse is shifted and broadened, and the ringing appears. Especially, Fig. 9b exhibits the enhanced spectral needs of a square pulse (even for τ as high as 100ps), against the pure spectral needs of the Gaussian pulse shown in Fig. 7b (even for τ as low as 10ps).

The major distortion peaks along the leading and trailing edges of the pulses shown in Figs. 8 and 9, are justified in [7] because of the separation of the high and low spectral components of the square pulse.

Figs. 10 and 11 indicate the influence of the waveguide core radius on the distortion of a pulse (Gaussian and square pulse, respectively), that has travelled distance L=30cm along a two-layered fiber. When the radius of the fiber core increases, then the ringing rises definitely stronger and more intense, while the amplitude attenuates and the pulse broadens only in the case of an input Gaussian pulse (Fig. 10b).

Finally, Figs. 12-13 and 14-15 demonstrate the effect of the waveguide's electrical characteristics on the distortion of pulses (Gaussian and square dc, respectively), that have travelled distance L=30cm along a two-layered fiber. When the dielectric constant of the fiber core (Figs. 13 and 15) or cladding (Figs. 12 and 14) increases, then the displacement and pulsewidth barely change, while the amplitude

attenuates and the ringing rises stronger.

5. Conclusions

The propagation of dc pulses as they travel along a layered cylindrical dielectric waveguide has been investigated. The cylindrical waveguide dispersion theory was combined with analytical and numerical techniques, in order to obtain the appropriate phase constant dispersion and then study the distorted, due to this dispersion, shape of dc pulses propagating along the waveguide axis. Fourier transforms were used to analyze the pulses, interpreting the dispersion characteristics from the real frequency spectrum point of view. Numerical results, presented for several values of the structure and pulse parameters, revealed strong effects on pulse distortion.

Acknowledgement

This work was funded by the Research Committee of Alexander Technological Educational Institute of Thessaloniki, Greece.

References

[1] C.A. Balanis, *Advanced Engineering Electromagnetics*, John Willey & Sons, New York, 1989, pp. 506-535.

[2] E.E. Kriezis, D.P. Chrissoulidis, and A.G. Papagiannakis, *Electromagnetics and Optics*, World Scientific Pub Co, 1992, pp. 163-201.

[3] C. Yeh and F.I. Shimabukuro, *The Essence of Dielectric Waveguides*. Springer, 2008, pp. 137-160.

[4] C.M. Knop, "Pulsed electromagnetic wave propagation in dispersive media", *IEEE Trans. Antennas Propagat.*, vol. 12, pp. 494-496, July 1964.

[5] R.S. Elliott, "Pulse waveform degradation due to dispersion in waveguide", *IRE Trans. Microwave Theory Tech.*, vol. 5, no. 10, pp. 254-257, Oct. 1957.

[6] K.K. Li, G. Arjavalingam, A. Dienes, and J.R. Whinnery, "Propagation of picosecond pulses on microwave striplines", IEEE *Trans. Microwave Theory Tech.*, vol. 30, no. 12, pp. 1270-1273, Aug. 1982.

[7] R.L. Veghte and C.A. Balanis, "Dispersion of transient signals in microstrip transmission lines", *IEEE Trans. Microwave Theory Tech.*, vol. 34, no. 12, pp. 1427-1436, Dec. 1986.

[8] J.F. Whitaker, T.B. Norris, G. Mourou, and T.Y. Hsiang, "Pulse dispersion and shaping in microstrip lines", *IEEE Trans. Microwave Theory Tech.*, vol. 35, pp. 41-47, Jan. 1987.

[9] T. Leung and C.A. Balanis, "Attenuation distortion of transient signals in microstrip", *IEEE Trans. Microwave Theory Tech.*, vol. 36, no. 4, pp. 765-768, Apr. 1988.

[10] J.P. Gilb and C.A. Balanis, "Pulse distortion on multilayer coupled microstrip lines", *IEEE Trans. Microwave Theory Tech.*, vol. 37, no. 10, pp. 1620-1628, Oct. 1989.

[11] J.P. Gilb and C.A. Balanis, "Transient analysis of distortion and coupling in lossy coupled microstrips", *IEEE Trans. Microwave Theory Tech.*, vol. 38 (12), pp. 1894-1899, Dec. 1990.

[12] A.R. Djordjevic, T.K. Sarkar, and R.F. Harrington, "Time-domain response of multiconductor transmission lines", *Proc. IEEE*, vol. 75, pp. 743-764, June 1987.

[13] G. Hasnain, A. Deines, and J.R. Whinnery, "Dispersion of picosecond pulses in coplanar transmission lines", *IEEE Trans. Microwave Theory Tech.*, vol. 34, pp. 738-741, June 1986.

[14] X.Y. Zou, M. Imran, and S.M. Hayee, "Limitations in 10 Gb/s WDM optical-fiber transmission when using a variety of fiber types to manage dispersion and nonlinearities", *Journal of Lightwave Technology,* vol. 14, pp. 1144-1152, 1996.

[15] A.K. Shahi, V. Singh, and S.P. Ojha, "Dispersion characteristics of electromagnetic waves in circularly cored highly birefringent waveguide having elliptical cladding", *Progress In Electromagnetics Research*, vol. 75, pp. 51-62, 2007.

[16] J. Hult and S. Watt, "Dispersion measurement in optical fibers using supercontinuum pulses", *Journal of Lightwave Technology*, vol. 25, pp. 820-824, 2007.

[17] J. Sun and Le-Wei Li, "Dispersion of waves over a PEC cylinder coated with two-layer lossy dielectric materials", *IEEE Trans. on Antennas and Propagation*, vol. 55, pp. 877-881, 2007.

[18] A. Andalib, A. Rostami, and N. Granpayeh, "Analytical investigation and evaluation of pulse broadening factor propagating through nonlinear optical fibers (traditional and optimum dispersion compensated fibers)", *Progress In Electromagnetics Research*, vol. 79, pp. 119-139, 2008.

[19] M. Legenkiy and A. Butrym, "Pulse signals in open circular dielectric waveguide", *Progress In Electromagnetics Research Letters*, vol. 22, pp. 9-17, 2011.

[20] I.O. Vardiambasis, J.L. Tsalamengas, and J.G. Fikioris, "Hybrid wave propagation in generalized Goubau-type striplines", *IEE Proceedings- Microwaves, Antennas and Propagation*, vol. 144, no. 3, pp. 167-171, June 1997.

[21] I.O. Vardiambasis, J.L. Tsalamengas, and K. Kostogiannis, "Propagation of EM waves in composite bianisotropic cylindrical structures", *IEEE Transactions on Microwave Theory and Techniques*, vol. 51, no. 3, pp. 761-766, March 2003.

[22] I.O. Vardiambasis, "Propagation in cylindrical inset dielectric guide structures", pp. 415-420, chap. 40, part VI, vol. 2, *Proceedings of the European Computing Conference (ECC'07)*, Athens, Greece, 25-27 Sep 2007.

[23] C. Yeh, "Guided-wave modes in cylindrical optical fibers", *IEEE Trans. Education*, vol. 30, no. 1, pp. 43-51, Feb. 1987.

Lumped Balanced Interconnect H-Tree Network Modeling

Blaise Ravelo* and Thomas Eudes

IRSEEM (Institut de Recherche en Systèmes Electroniques Embarqués), EA 4353,
At the graduate school of engineering ESIGELEC,
Avenue Galilée, 76801 Saint Etienne du Rouvray, France.
*corresponding author, E-mail: blaise.ravelo@yahoo.fr / ravelo@esigelec.fr

Abstract

This paper is concerned with a practical modeling method of balanced clock H-tree for the signal integrity (SI) forecasting in microelectronic applications. The reduced model enables the determination of analytical expressions of the output voltages and the current trough the branches of the tree. Then, the global transfer function of the whole tree network is established. Analyses of the possibility to evaluate the partial and global transfer functions are also proposed. As application, a balanced H-tree composed of n = {3, 4, 5} levels RC-network is simulated. To demonstrate the relevance of the proposed theoretical concept, comparisons of frequency- and time-domain results were made. As result, predictions of propagation delays induced by the tree network understudy are performed. Very good agreements between the models extracted and simulations are found both in frequency- and time-domains. In the continuation to this work, extension of the global model for the unbalanced H-tree clock interconnects based on distributed elements is in progress.

1. Introduction

Since the invention of the first single chip processor Intel 4004 by Intel in 1970s [1-3], the mankind way of life is increasingly conditioned by the evolution of electronic systems toward the use of personal computers (PCs) and multifunction electronic mobile gadgets. This industrial revolution manifests with the need for communication anywhere around the world at any time and the increase of the operating frequencies and the microelectronic system integration density according to the Moore's law [2][4]. To meet this industrial need, ultra-high speed wired and wireless communicating system technology operating up to currently tens of GHz were deployed [5]. Due to the steady increase of electronic system integration density and operating frequency, the modern high-speed electronic equipment knows different technological bottlenecks as signal degradation due to unpredicted interconnect network influences [7-13]. In addition to the apparition of electromagnetic interferences (EMIs), many works demonstrated especially their influences on the power loss and their contribution to the interconnect delays, for example, in the RF/digital devices [5-7][14].
In order to deal with this unintentional technological limitation, intensive research works have been conducted particularly for enhancements of on-chip interconnects [14-21]. So, signal path algorithms and classical models permitting to minimize and somehow to cancel out these undesired degradation effects were proposed. Moreover, an equalization technique enabling to realize a signal recovery is introduced more recently [22-25]. Nowadays, several topologies of clock-trees, link bus models and optimized computation techniques have been introduced for MOS distribution networks [16-18].
In this scope, the most popular method used in microelectronics design industries were based on the first order RC-model which was introduced by Elmore in 1948 [26-40]. By denoting s the Laplace variable, by assuming the linear transfer function expressed as:

$$H(s) = \frac{\sum_{i=0}^{m} a_i s^i}{\sum_{j=0}^{n} b_j s^j}, \qquad (1)$$

with a_i and b_j real coefficients, and the integer orders $n > m$, the Elmore propagation delay is merely defined as [26]:

$$\tau_{Elmore} = \frac{b_1}{b_0} - \frac{a_1}{a_0}. \qquad (2)$$

As illustrated by this formula, the propagation delay expression was established from the first order coefficient of the transfer function. The advantage of this model lies on its simplicity and its possibility for estimating the propagation delay rapidly when considering sophisticated signal paths in the complex systems. Its main drawback is its drastic inaccuracy compared to the high order delay models. It was reported that usually, the Elmore model presents relative errors more than 30 %. For this reason, more accurate approximated second order RLC model for

calculating the propagation-, rise-/fall- and settling- time delays were developed in [41-42]. Furthermore, the unit step response of lumped RLC tree networks via the second moments of polynomial transfer function has been determined by the authors. Then, they deduce the basic characteristics of transient responses (over- or under-damped responses) and propose also the specific expression of the second order propagation delay. The main advantage of the former delay model is the fact that it enables to investigate the signal delay with good accuracy, particularly, for non-monotone time-domain responses. Furthermore, compared to the numerical methods as SPICE-computation, this model guarantees frequently relative error lower than 5 %. So far, the existing employed algorithms and methods for calculating the signal delays induced by n-levels of RC-tree mesh networks, of course, composed of cascaded R_kC_k-cells ($k = \{1 \ldots n\}$) is realized by the sum of the estimated propagation delays detected at between the branch of different nodes:

$$\tau_{Elmore} = \sum_{k=1}^{n} R_k C_k \ . \qquad (3)$$

The errors induced by this expression cannot be neglected when the level of interconnect tree network is higher (more than three). To improve the expression of this signal delay, an analytical method for extracting the global transfer function of n-levels of symmetrical H-tree-networks is developed in this paper.

To facilitate the understandability, the paper is structured in three different sections. In section 2, theoretical analysis for modeling of the symmetric clock tree networks consisted of L-cells is investigated. By using the transfer matrix theory, an analytic expression of the whole network transfer function is developed. The relation established will be exploited in section 3 for characterizing the high level clock RC-tree networks. Then, expressions of the whole signal delay models will be developed. For checking the effectiveness of established formulas, comparisons of the results from the models developed and SPICE-computation will be made in section 4. Then, comments and discussions on the effectiveness of models developed are proposed. Then, concluding remarks are offered in the last section.

2. Analytical modeling method of symmetrical lumped tree network

Over the last three decades, a tremendous progress was made concerning the design methodology and the fabrication of analog- and digital- microelectronic circuits. To ensure the synchronization of the data in the high speed numerical systems, the clock signal distribution plays important roles. Then, various clock tree network topologies were proposed for perfectly balanced signal in different points across the die area. Because of its ability to maintain the distributed interconnects and its flexibility for improving the network performance by concentrating on parameter variables, the symmetrical or balanced H-clock tree distribution is the one mostly used for insuring the signal synchronization according to fixed given instant time reference. This reason captures our motivation to conduct more and more deep investigation of clock tree network as proposed in this section. Before the examination of most important part of this work which is consecrated to the tree network modeling, we will start with a preliminary brief recall on the L-cell circuit theory.

2.1. Recall on the L-cell circuit theory

To generalize the functioning of the L-cell unit element, let us consider the circuit composed by Z_s series impedance and Y_p parallel admittance represented in Figure 1. By assuming that this is excited by the input voltage, v_i at node, N_i and exhibits the output voltage, v_o at the node, N_o.

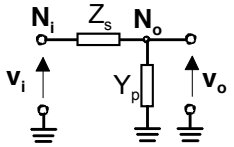


Figure 1: L-cell formed by Z_s series impedance and Y_p parallel admittance.

According to the classical electric circuit and system theory, it is well-known that the transfer matrix of the L-cell depicted in Figure 1 is written as:

$$[T] = \begin{bmatrix} 1 + Z_s Y_p & Z_s \\ Y_p & 1 \end{bmatrix}. \qquad (4)$$

By denoting s the Laplace variable, this matrix permits to determine the expression of the equivalent transfer function, $H(s)$ and the input impedance, $Z_{in}(s)$ formulated as:

$$H(s) = \frac{V_o(s)}{V_i(s)} = \frac{1}{T_{11}} = \frac{1}{1 + Z_s Y_p} \ . \qquad (5)$$

$$Z_{in}(s) = \frac{T_{11}}{T_{12}} = Z_s + \frac{1}{Y_p} \ . \qquad (6)$$

By the mathematical analogy, these elementary relations will serve us for extracting the basic characteristic of high level global tree network in the remainder of this paper.

2.2. Global analysis of L-cell tree network

Toward the basic transform of electric equivalence, the study of H-tree network can be relatively reduced to that of T-tree network. So, along this paper, the n level of L-tree distribution understudy is limited to the global topology depicted in Figure 2. At each node N_k ($k = \{1 \ldots n\text{-}1\}$), two L-cells are connected in parallel. It means that the input equivalent impedance at this node is the half the input impedance of one the downstream branch.

This finding explains the chain of electrical equivalent circuit of the branch indicated in red path of Figure 2 as presented in Figure 3. As highlighted in Figure 4, we can see that between the consecutive plans (P_k) and (P_{k+1}), the (N_kN_{k+1}) network is formed by $Z_s / 2^k$ -series impedance and $2^k Y_p$ -parallel admittance.

For the sake of the mathematical simplification, the output current flowing through the branch $N_k\,N_{k+1}$ and the input impedance seen at the plan (P_k) are respectively denoted by I_k and Z_k. Emphatically, through the simple equivalent impedance calculation, we can determine the input impedance, Z_k seen at the node, N_k in function of Z_{k+1} which is expressed as:

$$Z_k = \begin{cases} 2^{1-k} Z_s + \dfrac{Z_{k+1}}{1 + 2^{k-1} Y_p Z_{k+1}}, & if \quad k \le n-1 \\ \dfrac{1}{2^n Y_p}, & if \quad k = n \end{cases} . \qquad (7)$$

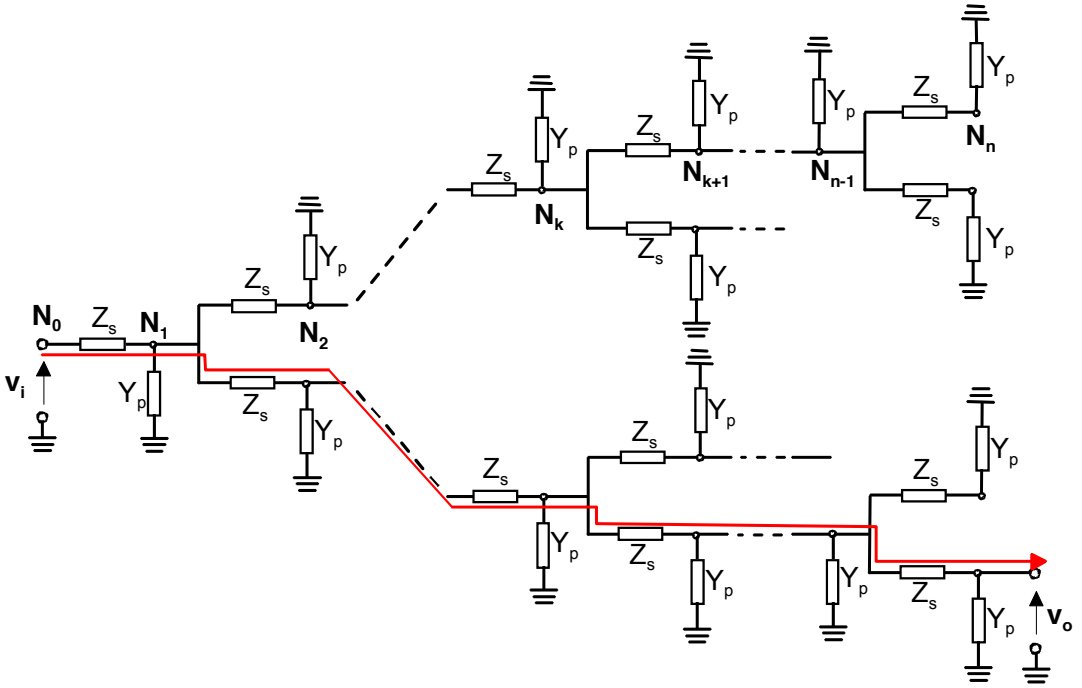


Figure 2: L-tree network composed of Z_s-series impedance and Y_p-parallel admittances.

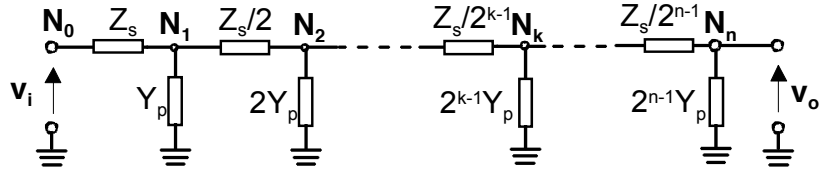


Figure 3: Electrical equivalent network of the red path of tree circuit shown in Figure 2.

The electrical analysis of the circuit proposed in Figure 4 enables to write expression of current, I_k flowing through electrical branch $N_k\,N_{k+1}$ given by:

$$I_{k+1} = \begin{cases} \dfrac{V_i}{Z_s + Z_1}, & if \quad k = 0 \\ \dfrac{I_k}{1 + 2^{k-1} Y_p Z_{k+1}}, & if \quad k \ge 1 \end{cases} . \qquad (8)$$

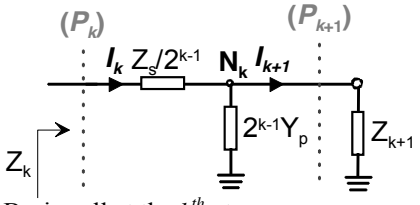


Figure 4: Basic cell at the k^{th}-stage.

Most importantly, by denoting $[T_{k-1}]$ the elementary transfer matrix of the (k-1)-th cell in the branch $N_{k-1}N_k$, similarly to the matrix expressed in (4), we can deduce the following expression:

$$[T_{k-1}] = \begin{bmatrix} 1 + Z_s Y_p & \dfrac{Z_s}{2^{k-1}} \\ \dfrac{1}{2^{k-1} Y_p} & 1 \end{bmatrix} . \qquad (9)$$

Subsequently, the association of n-cells cascaded presented in Figure 3 should have an equivalent whole chain matrix equal to the product of $[T_{k-1}]$ when k belongs to $\{1 \ldots n\}$. Meanwhile, the whole chain matrix, $[T_{1,n}]$ of the network stated in Figure 3 can be written as:

$$[T_{1,n}] = \prod_{k=1}^{k=n} \begin{bmatrix} 1 + Z_s Y_p & \dfrac{Z_s}{2^{k-1}} \\ \dfrac{1}{2^{k-1} Y_p} & 1 \end{bmatrix} . \qquad (10)$$

This expression explains that the transfer function denoted $H_n(s)$ associating this matrix can be determined recursively from the last elementary matrix, $[T_n]$. Though, the later can be calculated progressively through the following matrix recursive relation:

$$[T_{1,k-1}] = [T_{1,k}] \times [T_{k-1}]. \quad (11)$$

For the sake of analytic expressions simplification, in the remainder of this paper, we suppose that $[T_{1,k}]$ will be concatenated as follows:

$$[T_{1,k}] = \begin{bmatrix} T_{11}(k) & T_{12}(k) \\ T_{21}(k) & T_{22}(k) \end{bmatrix}. \quad (12)$$

By combining former equations (11) and (12), obviously for k belongs to {0… n-1}, toward a mathematical identification, after recursive relations between the elements of $[T_{1,k-1}]$ and $[T_{1,k}]$, we can establish that:

$$T_{11}(k-1) = (1 + Z_s Y_p) T_{11}(k) + 2^{-k+1} Z_s T_{21}(k), \quad (13)$$

$$T_{21}(k-1) = 2^{k-1} Y_p T_{11}(k) + T_{21}(k), \quad (14)$$

and

$$T_{11}(n) = 1 + Y_p Z_s, \quad (15)$$

$$T_{21}(n) = 2^{n-1} Y_p. \quad (16)$$

Accordingly, with the successive analysis from the ending termination of network presented in Figure 3, one gets the partial transfer function:

$$H_{n-k}(s) = \frac{V[N(n)]}{V[N(k)]} = \frac{1}{T_{11}(k)}. \quad (17)$$

Table 1: Transfer functions of L-cell tree networks formed by Z_s series impedance and Y_p parallel admittance for the level n = {1…6}.

n	Transfer function, $H_n(s)$
1	$H_1(s) = \frac{1}{1 + Z_s Y_p}$
2	$H_2(s) = \frac{1}{1 + 4Z_s Y_p + Z_s^2 Y_p^2}$
3	$H_3(s) = \frac{1}{1 + 11Z_s Y_p + 7Z_s^2 Y_p^2 + Z_s^3 Y_p^3}$
4	$H_4(s) = \frac{1}{1 + 26Z_s Y_p + 30Z_s^2 Y_p^2 + 10Z_s^3 Y_p^3 + Z_s^4 Y_p^4}$
5	$H_5(s) = \frac{1}{1 + 57Z_s Y_p + 102Z_s^2 Y_p^2 + 58Z_s^3 Y_p^3 + 13Z_s^4 Y_p^4 + Z_s^5 Y_p^5}$
6	$H_6(s) = \frac{1}{1 + 120Z_s Y_p + 303Z_s^2 Y_p^2 + 256Z_s^3 Y_p^3 + 95Z_s^4 Y_p^4 + 16Z_s^5 Y_p^5 + Z_s^6 Y_p^6}$

It is noteworthy that the partial transfer function $H_{n-k}(s)$ is also equal to the whole transfer function of k-level tree distribution, $H_k(s)$. In addition, knowing the transfer matrix $[T_{1,n}]$, it should be possible to formulate the global transfer function thanks to the following relation:

$$H(s) = \frac{V[N(n)]}{V[N(0)]} = \frac{1}{T_{11}(n)}. \quad (18)$$

Using this expression, the analytical calculation was established for the five transfer functions for n = {1…5}. Table 1 below summarizes the calculated results.

For the verification of the proposed theory efficiency, investigation of more concrete circuit formed by RC-cell will be performed in the next section.

3. RC-tree modeling

By taking $Z_s = R$ and $Y_p = Cs$, we can transpose the analysis of the previous section to the modeling of the classical RC-tree distribution. Figure 5 represents the simplified equivalent circuit of n-level of the RC-tree distribution depicted in Figure 3.

In this case, the elements of transfer matrix should be determined from aforementioned expressions (13), (14), (15) and (16), with the recursive relations:

$$T_{11}(n-k) = 1 + \sum_{l=1}^{n-k} a_{n-k}(l)(RCs)^l, \quad (19)$$

$$T_{21}(n-k) = 2^{k-1} Cs \left[\sum_{l=1}^{n-k} b_{n-k}(l)(RCs)^{l-1} \right]. \quad (20)$$

and

$$T_{11}(n) = 1 + RCs, \quad (21)$$

$$T_{21}(n) = 2^{n-1} Cs. \quad (22)$$

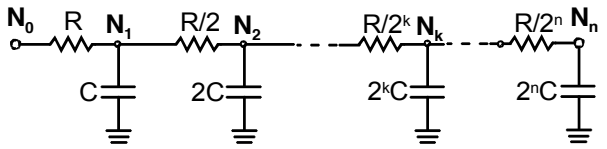


Figure 5: Equivalent circuit for the case of *n*-level of RC-tree network.

By identification and turning over the *k*-integer values, it can be demonstrated that the iterative relations for the determination of two first coefficients, a_{n-k} and b_{n-k} can be written as:

$$a_{n-k}(1)=\begin{cases}1 \quad if \quad k=0\\ 1+a_{n-k+1}(1)+4b_{n-k+1}(1) \quad if \quad k\geq 1\end{cases}, \tag{23}$$

$$a_{n-k}(2)=\begin{cases}0 \quad if \quad k=0\\ a_{n-k+1}(1)+a_{n-k+1}(2)+4b_{n-k+1}(2) \quad if \quad k\geq 1\end{cases}, \tag{24}$$

and

$$b_{n-k}(1)=\begin{cases}1/2 \quad if \quad k=0\\ 1/2+2b_{n-k+1}(1) \quad if \quad k\geq 1\end{cases}, \tag{25}$$

$$b_{n-k}(2)=\begin{cases}0 \quad if \quad k=0\\ \dfrac{a_{n-k+1}(1)}{2}+2b_{n-k+1}(2) \quad if \quad k\geq 1\end{cases}. \tag{26}$$

Because of the rise time value t_r and the misbehavior linked to the imperfection of digital device input impedance, the bandwidth of the numerical signal operating is practically limited. For the digital devices having input impedances analog to RC-circuit model, the frequency bandwidth of operated digital signal is defined as [10]:

$$f_{\max}=\frac{0.35}{t_r}. \tag{27}$$

This statement explains the possibility of the reduction or simplification of the transfer function, $H_n(s)$ denominator by proceeding with polynomial limited expansion. For the case of *n*-level tree network, one establishes that the second order approximated transfer function of the whole circuit represented in Figure 2 of section 2 can be formulated as follows:

$$H_n(s)=\frac{1}{1+\sum_{l=1}^{n-k}a_1(l)(RCs)^l}\approx\frac{1}{1+a_1(1)RCs+a_1(2)(RCs)^2+\ldots}, \tag{28}$$

For checking the validation of these theoretical concepts in more concrete context, application results from with symmetrical RC-tree networks are explored in the next section.

4. Validation results

It should be pointed out that the results proposed in this paper were obtained in the schematic environment of the electrical and electronic circuit SPICE-simulator run in the commercial Advanced Design System (ADS) software provided by Agilent™.

As schematized in Figure 6, a five-level clock tree distribution comprised of RC-network was first, designed and numerically analyzed. For illustrating the influence of tree network level number, the analysis was also extended to network circuitries containing n = {3, 4, 5}-levels. It is worth noted that each branch of the network understudy is consisted of identical pieces of RC-line with per unit resistance, R_u = 50 Ω/mm and capacitance, C_u = 2 pF/mm and length, d = 0.5 mm [33]. Meanwhile, the equivalent lumped parameters are equal to $R = R_u$ x d and $C = C_u$ x d.

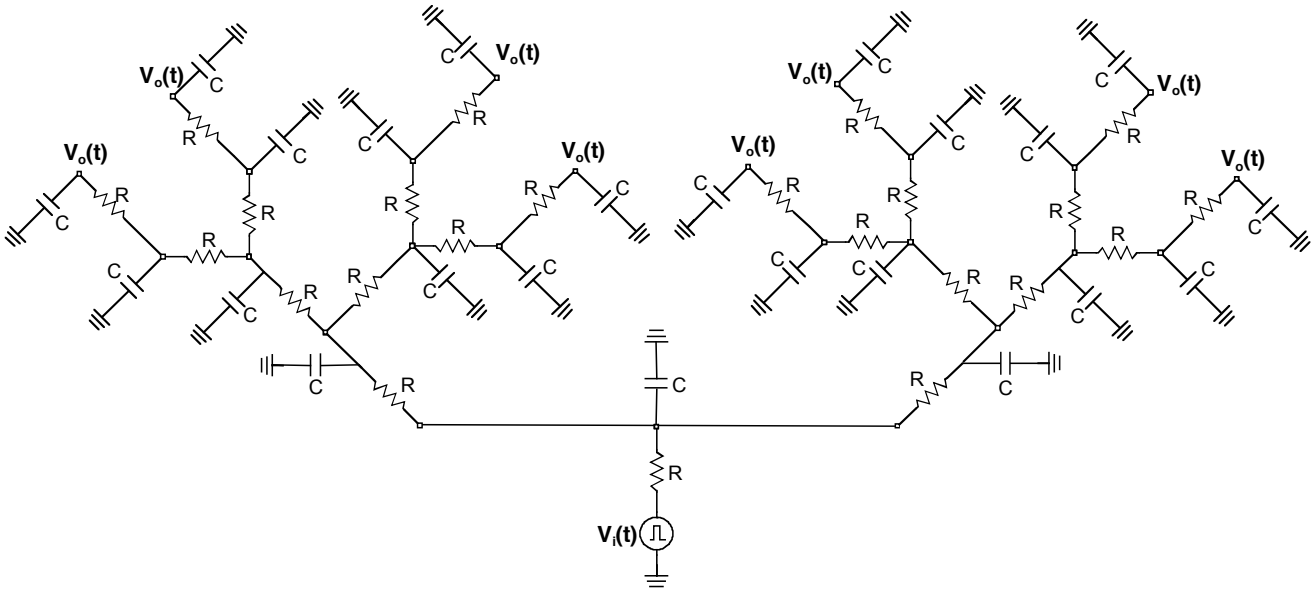


Figure 6: Circuit diagram of the simulated RC-tree network (R = 25 Ω, C = 1 pF and n = 5).

4.1. Frequency-domain validation

Afterwards, simulations run both in frequency- and time-domains, the results pictured in Figures 7 and Figure 8 are obtained. For the time domain analysis, the networks understudy were excited by a periodical trapezoidal transient source with amplitude, V_{max} = 1V, pulse width, T_w = 2 ns and with time duration, $T = 5T_w$ = 10 ns. Figures 7 view the frequency responses of the simulated RC-tree networks as shown in Figure 6 from DC to 5 GHz.

At noted that as forecasted theoretically, by the reason of symmetry, the voltages, $v_o(t)$ detected at the output terminals of the computed trees are the same as the output of the equivalent 1D network for $n = \{3, 4, 5\}$.

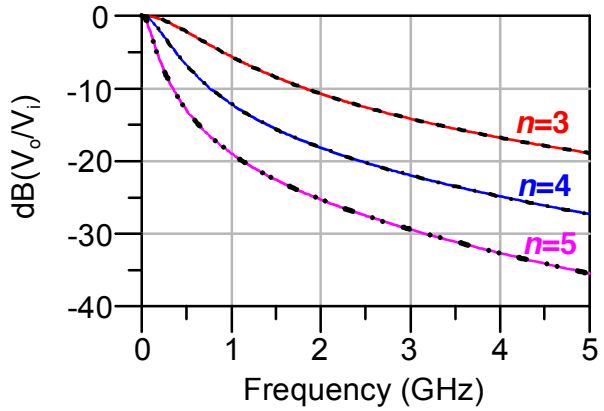


Figure 7(a): Comparisons of the transfer function magnitude from proposed model and the direct computed versus RC-tree level.

Moreover, one finds also that the results from the analytical models (plotted in thick dashed curves) are in very good agreement with ADS reference responses (plotted in thin colored curves, **red** for ***n* = 3**, **blue** for ***n* = 4** and **pink** for ***n* = 5**). As can be seen in Figure 7(a) and 7(b), the attenuation and phase values are obviously, more significantly considerable when n is greater.

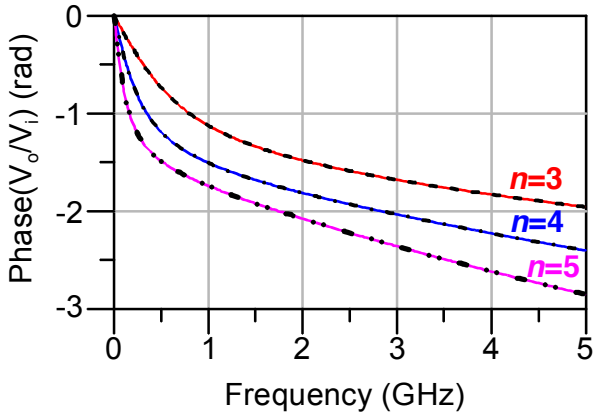


Figure 7(b): Comparisons of the transmission phase responses from proposed model and the direct computed versus RC-tree level.

4.2. Time-domain validations

In addition, time-domain simulations of the RC-circuit understudy for 10 ns-time duration generate the transient results displayed in Figs. 8. Once again, the calculated analytical results here plotted in thick dashed curves coincide very well with ADS reference responses here plotted in thin color curves.

As predicted in theory, one observes that the output tree signals are more degraded when n is higher. By using expressions (29) and (34), one estimates respectively the Elmore and Ismail-Friedman propagation delays induced by the tree distribution network understudy.

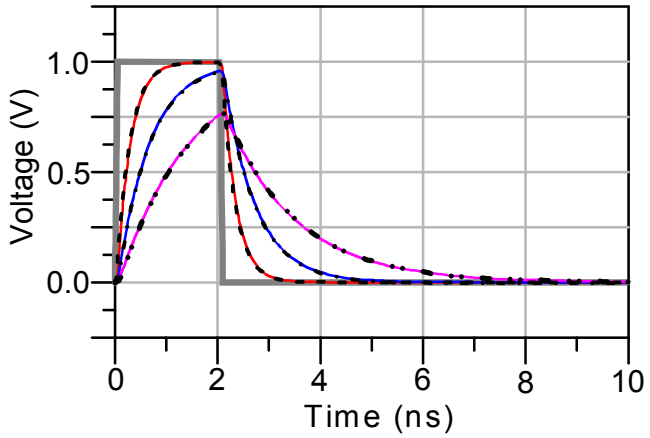


Figure 8: Comparisons between the time-domain results of the simulated circuit shown in Figure 6 from the proposed model and the direct computation.

Consequently, the comparison results between the simulated and assumed as the exact propagation delay and the approximated propagation delays stated in Table 3 are realized. Clearly, as forecasted, the delays increase with *n*-values.

Table 3: Comparison between the exact, Elmore and Ismail-Friedman (IF) delays versus *n*.

	Propagation delay, τ		
n	Exact	Elmore model	Ismail-Friedman model
3	0.20 ns	0.27 ns	0.20 ns
4	0.47 ns	0.65 ns	0.48 ns
5	1.02 ns	1.42 ns	1.05 ns

By using equation (30), we can assess also the computed network voltage attenuations, $v(T)/V_0$. For checking the relevance of this formula, further comparison with ADS results was also made and the numerical results are represented in Table IV. Clearly, it can be seen that the predicted analytical results fit very well with the SPICE-Ads computation.

Table 4: Comparison between the exact and the modeled voltage attenuation at $t = T$ versus *n*.

	$v(T)/V_0$	
n	Exact	Proposed model
3	1.000	0.999
4	0.956	0.954
5	0.750	0.754

Expression (35) enables to estimate the attenuations and the delays in function of level numbers which can be in order of hundreds. Moreover as evidenced in Tables 1 and 2, the proposed model can be adapted to other types of the clock sharing as the tree networks comprised of distributed elements. Finally, the computation time with hundred levels of tree network is in order of some ms that is very interesting compared to the classical slew metric computation. To sum up all the above theoretical and application analysis concluding remarks are provided in the following section.

5. Conclusions

A global modeling method of the symmetrical clock H-tree distribution constituted by L-cell lumped networks is successfully developed in this paper.
The equivalent circuit of the tree network under consideration is established whatever its level. The extraction of the exact expression of the tree network transfer function according to different levels is developed in detail, thanks to the transfer matrix exploitation. More importantly, the mathematical recursive relation for the determination of tree characteristic equation coefficients is also presented. In addition, it was demonstrated the possibility to determine parameters of tree network transient responses as attenuation, under-/over-shoots and propagation delays according to existing well-known models [26].

Compared to the methods published in [36-40] which are based on the moment calculation of linear transfer function, the proposed method is more efficient in terms of precision and computation time consuming, particularly, if the tree level is higher than tree. Moreover, by using the SPSICE simulation, very good agreements between the simulations and the results from the proposed models are observed. The obtained results confirm the relevance of the transfer function model of global multi-level tree network established. Thus, it was demonstrated also that the established model combined with the Elmore and Ismail-Friedman propagation delay expressions permits an easy and more accurately estimation of signal delays, distortions and losses caused by the clock tree distribution network.

For more concrete application environment, further investigation focused on the unbalanced clock tree distribution networks is in progress. Finally, as the future works, we planned also to use the tree network model developed in this paper for investigating the clock tree distribution network influence in the packaging system and also the interconnection of RF/analogue circuits as the on-chip SiP, PiP, SoC, PCB.

Acknowledgements

Acknowledgement is made to European Union (EU) and Upper Normandy region (FRANCE) for the support of this research through the European Interreg IVA project No 4081 entitled "Time-Domain Electromagnetic Characterization and Simulation (TECS)".

References

[1] G. E. Moore, "Cramming More components onto integrated circuits", *Electronics Magazine*, Vol. 38, No. 8, pp. 114-117, Apr. 1965.

[2] G. E. Moore, "Progress in digital integrated electronics," *in Proc. of the IEEE International Electron Devices Meeting*, pp. 11-13, Dec. 1975.

[3] J. S. Kilby, "Invention of the integrated circuits," *IEEE Transaction on Electron Devices*, Vol. 23, p. 648, July 1976.

[4] Moore's Law. [Online]. Available: http://www.intel.com/museum/archives/historydocs/mooreslaw.htm

[5] International Technology Roadmap for Semiconductors Update Overview, 2011. [Online]. Available: http://www.itrs.net/.

[6] M-E. Hwang, S-O. Jung and K. Roy, "Slope Interconnect Effort: Gate-Interconnect Interdependent Delay Modeling for Early CMOS Circuit Simulation", *IEEE Transaction CAS I*, Vol. 56, No. 7, pp. 1428-1441, Jul. 2009.

[7] M. Ghoneima, Y. Ismail and M. M. Khellah, J. Tschanz and V. De, "Serial-Link Bus: A Low-Power On-Chip Bus Architecture", *IEEE Transaction CAS I*, Vol. 56, No. 9, pp. 2020 - 2032, Sep. 2009.

[8] D. K. Sharma, B. K. Kaushik and R. K. Sharma, "VLSI interconnects and their testing: prospects and challenges ahead", *Journal of Engineering, Design and Technology*, Vol. 9, No. 1, pp. 63 – 84, 2011.

[9] N. Magen, A. Kolodny, U. Weiser and N. Shamir, "Interconnect-power dissipation in a microprocessor", *in Proc. of the ACM International Workshop on System Level Interconnect Prediction*, pp. 7-13, Feb. 2004.

[10] B. Ravelo and T. Eudes, "Fast estimation of RL-loaded microelectronic interconnections delay for the signal integrity prediction", *International Journal of Numerical Modelling: Electronic Networks, Devices and Fields* (Int. J. Numer. Model). DOI: 10.1002/jnm.838, 2012.

[11] B. Ravelo, "Microelectronic interconnect modeling with periodical lumped RLC-network", *To be published in Turkish Journal of Electrical Engineering & Computer Sciences* (*TJCEES*), 2012.

[12] B. Ravelo, "Delay modelling of high-speed distributed interconnect for the signal integrity prediction", *Eur. Phys. J. Appl. Phys.* (*EPJAP*), DOI: 10.1051/epjap/20121103742012, 2012.

[13] T. Eudes, B. Ravelo, and A. Louis, "Experimental Validations of a Simple PCB Interconnect Model for High-Rate Signal Integrity", *IEEE Transaction Electromagnetic Compatibility (EMC)*, DOI: 10.1109/TEMC.2011.2165216, 2012.

[14] B. Yun and S. S. Wong, "Optimization of Driver Preemphasis for On-Chip Interconnects," *IEEE Transaction CAS I*, Vol. 56, No. 9, pp. 2033-2041, Sep. 2009.

[15] J. Cong, L. He, C. K. Koh and P. H. Madden, "Performance Optimization of VLSI Interconnect Layout", *Integration VLSI Journal*, Vol. 21, No. 1-2, pp. 1-94, Nov. 1996.

[16] L. Xiao-Chun, M. Jun-Fa and T. Min, "High-speed Clock Tree Simulation Method Based on Moment Matching", *in Proc. of Progress In Electromagnetics Research Symposium* (*PIERS*), Hangzhou (China), Vol. 1, No. 2, pp. 142-146, 2005.

[17] L. Hungwen, S. Chauchin and L. J. Chien-Nan, "A Tree-Topology Multiplexer for Multiphase Clock System," *IEEE Transaction Circuits And Systems I*, Vol. 56, No. 1, pp. 124-131, Feb. 2009.

[18] N. Rakuljic and I. Galton, "Tree-Structured DEM DACs with Arbitrary Numbers of Levels", *IEEE Transaction Circuits And Systems I*, Vol. 52, No. 2, pp. 313 – 322, Feb. 2010.

[19] G. F. Bo and P. Ampadu, "On Hamming Product Codes With Type-II Hybrid ARQ for On-Chip Interconnects", *IEEE Transaction Circuits And Systems I*, Vol. 56, No. 9, pp. 2042-2054, Sep. 2009.

[20] M. Voutilainen, M. Rouvala, P. Kotiranta and T. Rauner, "Multi-Gigabit Serial Link Emissions and Mobile Terminal Antenna Interference", *in Proc. of 13th IEEE Workshop on Signal and Propagation Interconnects* (*SPI*), Strasbourg, France, May 2009.

[21] A. Deutsch, "High-Speed Signal Propagation on Lossy Transmission Lines," *IBM J. Res. Develop.*, Vol. 34, No. 4, pp. 601-615, Jul. 1990.

[22] B. Ravelo, A. Pérennec and M. Le Roy, "Equalization of Interconnect Propagation Delay with Negative Group Delay Active Circuits", *in Proc. of 11th IEEE Workshop on Signal and Propagation Interconnects* (*SPI*), Genova, Italy, pp. 15-18, May 2007.

[23] B. Ravelo, A. Pérennec and M. Le Roy, "Application of Negative Group Delay Active Circuits to Reduce the 50% Propagation Delay of RC-Line Model", *in Proc. of 12th IEEE Workshop on Signal and Propagation Interconnects* (*SPI*), Avignon, France, May 2008.

[24] B. Ravelo, A. Pérennec and M. Le Roy, "Experimental Validation of the RC-Interconnect Effect Equalization with Negative Group Delay Active Circuit in Planar Hybrid Technology", *in Proc. of 13th IEEE Workshop on Signal and Propagation Interconnects* (*SPI*), Strasbourg, France, May 2009.

[25] B. Ravelo, A. Perennec and M. Le Roy, "New Technique of Inter-Chip Interconnect Effects Equalization with Negative Group Delay Active Circuits", *VLSI, Chap. 20*, INTECH Book, Ed. by Pr. Z. Wang, pp. 409-434, Feb. 2010.

[26] W. C. Elmore, "The transient response of damped linear networks", *J. Appl. Phys.*, Vol. 19, pp. 55-63, Jan. 1948.

[27] L. Wyatt, *Circuit Analysis, Simulation and Design. North-Holland*, The Netherlands: Elsiever Science, 1978.

[28] Jr. P. Penfield and J. Rubinstein, "Signal delay in RC tree networks", *in Proc. of Caltech Conf. on VLSI*, pp. 269–283, 1981.

[29] J. Rubinstein, Jr. P. Penfield and M. A. Horowitz, "Signal delay in RC tree networks", *IEEE Transaction CAD*, Vol. 2, No. 3, pp. 202-211, Jul. 1983.

[30] C. A. Zukowski, "Relaxing bounds for linear RC mesh circuits," *IEEE Transaction CAD*, Vol. 5, pp. 305-312, 1986.

[31] P. K. Chan and M. D. F. Schlag, "Bounds on Signal Delay in RC Mesh Networks", *IEEE Transaction CAD*, Vol. 8, pp. 581-589, 1989.

[32] M. A. Horowitz, "Timing Models for MOS Pass Networks," *in Proc of IEEE ISCAS*, pp. 198-201, 1983.

[33] Jr. J. L. Wyatt, "Waveform Bounding for Fast Timing Analysis of MOS VLSI Circuits", *in Proc. of IEEE ISCAS*, pp. 760-761, 1983.

[34] Jr. J. L. Wyatt, "Signal Propagation Delay in RC Models for Interconnect", *Circuit Analysis, Simulation and Design, Part II: VLSI Circuit Analysis and Simulation*, A. Ruchli, ed., Vol. 3 in the series Advances in CAD for VLSI, North-Holland, 1987.

[35] D. Standley and Jr. J. L. Wyatt, "Improved Signal Delay Bounds for RC Tree Networks", *VLSI Memo*, No. 86-317, MIT, Cambridge, MAS (USA), May 1986.

[36] N. K. Jain, V. C. Prasad and A. B. Bhattacharyyaa, "Delay-Time Sensitivity in Linear RC Tree", IEEE Transaction CAS, Vol. 34, No. 4, pp. 443-445, 1987.

[37] L. Vandenberghe, S. Boyd and A. El Gamal, "Optimizing Dominant Time Constant in RC Circuits", *IEEE Transaction CAD*, Vol. 17, No. 2, pp. 110-125, Feb. 1998.

[38] C. A. Marinov and A. Rubio, "The Energy Bounds in RC Circuits", *IEEE Transaction Circuits And Systems I*, Vol. 46, No. 7, pp. 869-871, Jul. 1999.

[39] A. C. Deng and Y. C. Shiau, "Generic Linear RC Delay Modeling for Digital CMOS Circuits", *IEEE Transaction CAD*, Vol. 9, No. 4, pp. 367-376, Apr. 1990.

[40] R. Gupta, B. Tutuianu and L. T. Pileggi, "The Elmore delay as a bound for RC trees with generalized input signals", *IEEE Transaction CAD*, Vol. 16, No. 1, pp. 95-104, 1997.

[41] A. B. Kahng, and S. Muddu, "An Analytical Delay model of RLC interconnects", *IEEE Transaction CAD*, Vol. 16, pp. 1507-1514. , Dec. 1997

[42] A. Ligocka and W. Bandurski, "Effect of Inductance on Interconnect Propagation Delay in VLSI Circuits", *in Proc. of 8th Workshop on Signal and Propagation Interconnects* (*SPI*), pp. 121-124, 9-12 May 2004.

Shorting Via Arrays for the Suppression of Simultaneous Switching Noise (SSN) in Multilayer PCBs

Jianjie Li[1], Junfa Mao[1], Siwei Ren[1],

[1]Key Laboratory of Ministry of Education of China for Research of Design and Electromagnetic Compatibility of High speed Electronic Systems, Shanghai Jiao Tong University, Shanghai 200240, China
*corresponding author, E-mail: mj.li@yahoo.com.cn

Abstract

The low-frequency characteristic of shorting via arrays for the suppression of simultaneous switching noise (SSN) in multilayer printed circuit boards (PCBs) is investigated firstly. It is found that two plane pairs connected by shorting via arrays have the same transmission coefficients in low-frequency range. Based on this low-frequency characteristic, shorting via arrays and embedded capacitance are combined together for the SSN suppression in multiple plane pairs in multilayer PCBs. The -40dB SSN suppression bandwidth of the fabricated board starts from near DC to several Giga Hz. Good agreement between simulated and measured results is observed.

1. Introduction

With the increase of clock speed and decrease of supply voltage, simultaneous switching noise (SSN) has become one of the major problems in high-speed printed circuit boards (PCBs) [1]. Multiple resonance modes between the power/ground planes excited by SSN can cause serious signal integrity (SI), power integrity (PI) and electromagnetic interference (EMI) problems for high-speed circuits [2, 3].

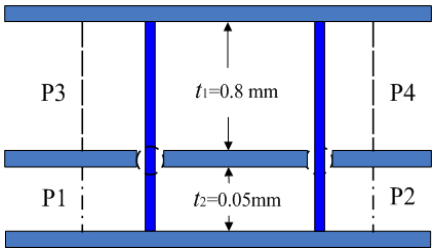
Many approaches have been taken to mitigate the SSN. Adding discrete decoupling capacitors between the power/ground planes is a common method to suppress the SSN [4]. However, this approach has a limitation of frequency bandwidth (usually less than a few hundred MHz) due to the self-resonance effect associated with the effective series inductance of the surface-mounted capacitors. In the past ten years, electromagnetic bandgap (EBG) structures have been proposed for minimizing the SSN coupling between power/ground planes. Mushroom-type EBG (MEBG) and planar EBG (PEBG) are two widely studied categories. MEBG consists of three layers where periodic metallic patches are inserted between the power/ground planes and connected to one of the planes through the vias [5, 6]. In order to reduce fabrication cost, PEBG have been introduced by designing the periodic patterns directly on the power or ground metal planes [7]. However, the metal layer etched slots may cause potential SI and power handling problems. One of common drawbacks of MEBG and PEBG is that the lower cutoff frequency cannot be reduced significantly and will deteriorate the noise suppression characteristic in low-frequency range [8, 9]. Shorting via arrays applied on power distribution network (PDN) is another possible solution for the suppression of SSN [10, 11]. In the multilayer PCBs, two solid planes with same dc voltage potential are connected by the shorting vias. Since the continuity of the solid planes is not broken, shorting via arrays would have good low-frequency noise suppression characteristics and is a promising solution that can overcome the drawbacks of the above mentioned two techniques for the suppression of SSN.

Ref. [11] revealed the high-frequency characteristic of short via arrays, while the low-frequency performance was not studied. In this paper, the low-frequency performance of multilayer PCBs with shorting via arrays is investigated firstly. In low-frequency range, same transmission coefficients are observed in two plane pairs connected by shorting vias. Based on this low-frequency performance, shorting via arrays and embedded capacitance are combined together to achieve excellent noise suppression in multiple plane pairs simultaneously. Both simulation and measurement are presented to validate our ideas.

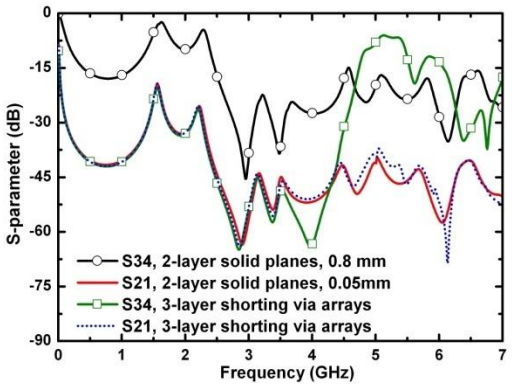
2. Low frequency performance of multilayer PCBs with shorting via arrays

The stack-up of a simulated 3-layer board with shorting via arrays is shown in Fig. 1(a). The dimension of the board is 45 mm × 45 mm, t1=0.8mm, t2=0.05mm, the diameter of via is 0.4mm, and spacing between shorting vias is 8 mm. Periodic anti-pads are etched on the center layer. The dielectric is FR4 with a dielectric constant of 4.4 and a loss tangent of 0.02. Two ports are located at (6.5 mm, 6.5 mm) and (30.5 mm, 38.5 mm). Both the 2-port transmission coefficients when two ports are located at top and bottom plane pairs are simulated, respectively. Schematic of port placement is illustrated in Fig. 1(a). To simplify the illustration, port 1 and port 2 are depicted with port 3 and port 4 in the same figure.

Fig. 1 (b) shows the simulated results. Transmission coefficients of two traditional 2-layer solid planes with dielectric thickness of 0.8 mm and 0.05 mm respectively are also given in Fig. 1(b) for comparison. The dimension, port position and dielectric constant of 2-layer solid planes are



(a)



(b)

Figure 1: (a) Side view of 3-layer PCB with shorting via arrays. (b) Simulated transmission coefficients.

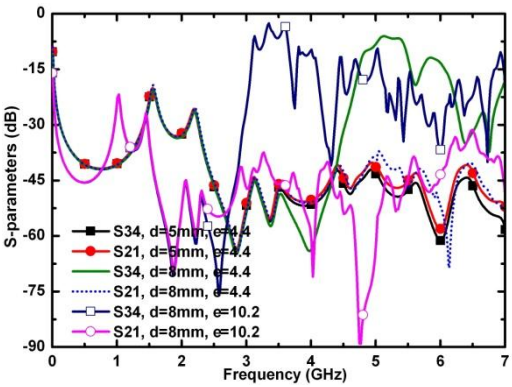
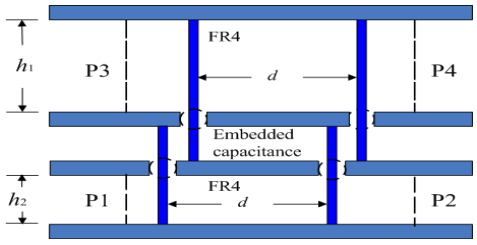


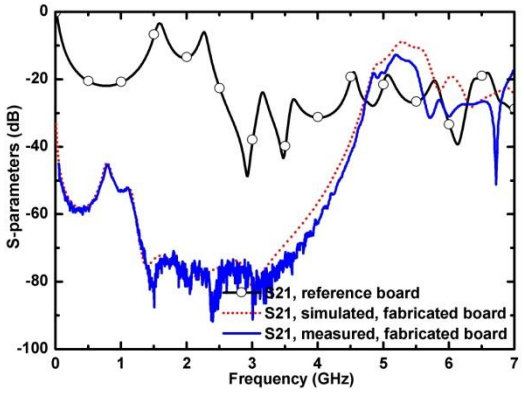
Figure 2: The effect of via spacing and dielectric constant on the transmission coefficients.

the same as that of 3-layer board. Due to thin dielectric substrate is used, the noise suppression characteristic of 0.05 mm thick 2-layer board is better than that of 0.8 mm thick 2-layer board. It can also be observed that S_{21} and S_{34} of the 3-layer board with shorting via arrays are almost the same below 3 GHz. The noise of quarter wavelength smaller than the spacing of the shorting vias cannot be suppressed and an upper cutoff frequency of S_{34} is observed [11].

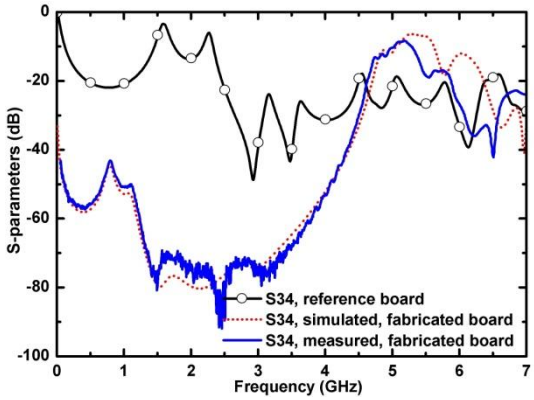
The maximal frequency of keeping same transmission coefficients (MFSTC) in both cavities is mainly affected by many factors, such as the spacing between periodic vias, the dielectric constant and the dielectric thickness. Fig. 2 shows the effect of via spacing and dielectric constant on the transmission coefficients where d represents the spacing between vias and ε denotes relative permittivity. In the simulation of Fig. 2, only one dielectric is used in the top



(a)



(b)



(c)

Figure 3: (a) Side view of the fabricated boards. (b) $|S_{21}|$ of the first board. (c) $|S_{34}|$ of the second board.

and bottom plane pairs. Increasing the relative permittivity is undesirable due to upper cutoff frequency and MFSTC are both deceased. Minimizing the spacing between shoring vias is one of typical ways to improve the performance of noise suppression. Reducing the spacing between shoring vias not only make the frequency range of same transmission coefficients wider, but also enhance the upper cutoff frequency.

3. SSN suppression in multiple plane pairs

Actually, SSN can be excited in every plane pairs in multilayer PCBs. Previous techniques of noise suppression either cannot effectively minimize the SSN in multiple plane pairs, or employ too much metal layers. In this section shorting via arrays are combined with embedded capacitance to reduce metal layers and enhance the SSN suppression in multiple plane pairs.

Further inspecting Fig. 1(b), we can observe that S_{21} and S_{34} of the 3-layer boards also have the same suppression characteristics with that of 0.05mm thick 2-layer board in low-frequency range. This reveals that if one of the plane pairs has excellent noise suppression performance in shorted multilayer PCBs, it can achieve SSN suppression simultaneously in several plane pairs in low-frequency range. As we know, excellent noise suppression performance can be realized by employing thin dielectric substrate or high dielectric constant materials in one solid plane pairs. Based on this knowledge, embedded capacitance is adopted in the fabricated multilayer PCBs.

Two same boards are fabricated with test ports placed at top and bottom plane pairs respectively. The side view of the boards is shown in Fig. 3(a). Ports 1 and 2 are the test ports of first board. Ports 3 and 4 are the test ports of second board. To simplify the illustration, four test ports are depicted in the same figure once again. Port 1 and port 3 are located at (6.5 mm, 6.5 mm). Port 2 and port 4 are placed at (30.5 mm, 38.5 mm). The thickness of embedded capacitance is 14 micron, the dielectric constant is 16 and loss tangent is 0.005. The size of fabricated board is 45 mm $\times$ 45 mm, with d=8 mm, h_1=0.8 mm, and h_2=0.5mm. The dielectric substrates in top and bottom plane pairs are FR4 with a dielectric constant of 4.4 and a loss tangent of 0.02.

The simulated and measured results are shown in Figs. 3(b) and (c). The S_{21} and S_{34} of same boards without the shorting via arrays are also given in Figs. 3(b) and (c) for reference. From Figs. 3(b) and (c), we can observe that SSN have been suppressed below -40dB from near DC to 4.5GHz simultaneously in top and bottom plane pairs. Moreover, measured S_{21} and S_{34} keep almost the same below 1.5 GHz. Due to only one dielectric substrate is used in [11], the upper cutoff frequency of P-G via pairs can be accurately estimated by $\lambda/4$ waveguide resonator principle. However, in the designed multilayer PCBs, two different dielectric substrates are used. It is much more complicated than the situation of only one dielectric substrate to accurately analyze the upper cutoff frequency. Fortunately, due to the thickness of embedded capacitance layer is far smaller than that of the other dielectric layers, dielectric substrates in top and bottom plane pairs are dominant. Therefore, the upper cutoff frequency can also be approximately predicted by [11]

$$f_{upper} \approx c/4d\sqrt{\varepsilon_r}\ , \qquad (1)$$

where c is the light speed in vacuum and ε_r is the relative permittivity of dielectric used in top and bottom cavities. The upper cutoff frequency of the designed board predicted by (1) is 4.47 GHz, which is close to the measured 4.5 GHz.

4. Conclusions

In this paper, the low-frequency performance of 3-layer PCB shorted by via arrays is investigated firstly. Same transmission coefficients in low-frequency range are observed in two plane pairs of the shorted 3-layer PCB. Then embedded capacitance is utilized and combined with shorting via arrays to enhance the noise suppression simultaneously in multiple plane pairs. The Measured -40 dB suppression bandwidth of the fabricated board is from almost DC to several Giga Hz. Both the simulation and measurement are given which are consistent with each other.

Acknowledgements

This work was supported by the National Natural Science Fund for Creative Research Groups（60821062）and the National Basic Research Program (2009CB320202) of China.

References

[1] M. Swaminathan, J. Kim, I. Novak, J. P. Libous, Power distribution networks for system-on-package: status and challenges, *IEEE Trans. Adv. Packag.*, vol. 27, no. 2, pp. 286-300, 2004.

[2] A. C. Scogna, A. Orlandi, V. Ricchiuti, Signal and power integrity analysis of differential lines in multilayer printed circuit boards with embedded electromagnetic bandgap structures, *IEEE Trans. Electromagn. Compat.*, vol. 52, no. 2, pp. 357-364, 2010.

[3] S. Shahparnia, O. M. Ramahi, Electromagnetic interference (EMI) reduction from printed circuit board (PCB) using electromagnetic bandgap structures, *IEEE Trans. Electromagn. Compat.*, vol. 46, no. 6, pp. 580-587, 2004.

[4] V. Ricchiuti, Power-supply decoupling on fully populated high-speed digital PCBs, *IEEE Trans. Electromagn. Compat.*, vol. 43, pp. 671–676, 2001.

[5] T. Kamgaing, O. M. Ramahi, A novel power plane with integrated simultaneous switching noise mitigation capability using high impedance surface, *IEEE Microw. Wireless Compon. Lett.*, vol. 13, no. 1, pp. 21–23, 2003.

[6] R. Abhari, G. V. Eleftheriades, Metallo-dielectric electromagnetic bandgap structures for suppression and isolation of the parallel-plate noise in high-speed circuits, *IEEE Trans. Microw. Theory Tech.*, vol. 51, no. 6, pp. 1629-1639, 2003.

[7] T. L. Wu, C. C. Wang, Y. H. Lin, T. K.Wang, G. Chang, A novel power plane with super wideband elimination of ground bounce noise on high speed circuits, *IEEE Microw. Wireless Compon. Lett.*, vol. 15, no. 3, pp. 174–176, 2005.

[8] D. Chung, T. H. Kim, C. Ryu, E. Engin, M. Swaminathan, J. Kim, Effect of EBG structures for reducing noise in multi-layer PCBs for digital systems, in *Proceedings of the IEEE 15th Topical Meeting on Electrical Performance of Electronic Packaging*, pp.253-256, 2006.

[9] M. S. Zhang, Y. S. Li, C. Jia, L. P. Li, Signal integrity analysis of the traces in electromagnetic-bandgap structure in high-speed printed circuit boards and packages, *IEEE Trans. Microw. Theory & Tech.*, vol. 55, no. 5, pp. 1054-1062, 2007.

[10] J. Fang, J. Zhao, and J. Zhang, Shorting via arrays for the elimination of package resonance to reduce power supply noise in multilayered area array IC packages, in *Proc*. *IEEE Symp*. *ICP Design Integr*., pp. 116–119, 1998.

[11] M.-S. Zhang, J.-F. Mao, Y.-L. Long, Power noise suppression using power-and-ground via pairs in multilayered printed circuit boards, *IEEE Trans*. *Compon*. *Packag*. *Manuf*. *Technol*., vol. 1, no. 3, pp. 374-385, 2011.

Fast and Accurate Modeling of PCB Interconnection Lines for High-Rate Signal Integrity Time-Domain Measurement

Thomas Eudes[1]*, Blaise Ravelo[1] and Rabee Al Hayek[2]

[1]IRSEEM, EA 4353, at the graduate School of Engineering ESIGELEC,
Av. Galilée, BP 10024,
76801 Saint-Etienne du Rouvray CEDEX, France
Phone : +33 (0)2 32 91 59 71 / Fax : +33 (0)2 32 91 58 59
[2]LeCroy SARL, 19 Avenue de Norvège, 91953 Courtaboeuf, CEDEX, France.
*corresponding author, E-mail: eudes@esigelec.fr

Abstract

This paper presents an accurate modeling and measurement technique of signal integrity (SI) for high-rate PCB interconnection. This model is based on the reduced transfer function extracted from the electromagnetic (EM) behavior of the interconnect line RLCG-parameters. So, the transfer function established takes into account both the frequency dispersion effects and the different propagation modes. In addition, the transfer function includes also the load and source impedance effects. Then, the SI analysis is proposed for high-speed digital signals through the developed model. To validate the model understudy, a prototype of microstrip interconnection with $w = 500$ µm and length $d = 33$ mm was designed, simulated, fabricated and tested. Then, comparisons between the frequency- and time- domain results from the model and from measurements are performed. As expected, good agreement between the S-parameters form measurements and the model proposed is obtained from DC to 8 GHz. Furthermore, a de-embedding method enabling to cancel out the connectors and the probe effects are also presented. Finally, an innovative time-domain characterization is proposed in order to validate the concept with a 2.38 Gbit/s-input data signal.

1. Introduction

Over the last 50 years, the tremendous growth of the microelectronics industry has lead to an incessant increase of operating frequencies and integration scale densities of the chips and the electronic systems [1]. The combination of the functional diversification ("More than Moore") and the integration technologies ("More Moore") lead to new electromagnetic compatibility (EMC) challenges in order to make coexisting these micro-systems in restricted environments [1-2]. This arrangement of technologies is the worthwhile and strategic work to target in order to obtain a high value system [2-4]. In addition to this constant increase in density, since the digital systems reach very high data rates, the fidelity of these RF-digital signals must be taken into account by designers [3-6], [11]. In order to preserve the acceptable functioning of modern high speed digital electronics, since the early 1990s, critical requirements on the signal integrity (SI) were established [3], [5-6]. It is widespread that all electronic products have the same configuration, there are drivers that outputting signals to receivers through the interconnects [6]. This statement illustrates that the effects of interconnection lines cannot be neglected [7-8], for integrated circuits (ICs) [9] and printed circuit boards (PCBs) [10-11].

Subsequently, one of the most important degradations in such systems is linked to the interconnection modeling for high-speed applications [1-3], [6], [12]. For this reason, more and more accurate interconnection network models are necessary to balance correctly the signals at different stage of the electronic boards [10-12]. A fast and accurate modeling of PCB TLs (Printed Circuit Boards Transmission Lines) for high-rate digital-mixed signal interconnects has been recently performed [13-14]. Whereas PCBs or TLs are well-known since the early of 1980s [15], some improvements seem to be still required [11] for the better understanding of the physical behavior [16] and the signal integrity forecasting for modern applications [17-22]. Indeed, facing to the widespread microwave theory, the PCB interconnects require faster and more accurate broadband models [18] and measurement techniques [23]. Therefore this field of investigation is extremely attractive, in particular for differential TLs or multilayer TLs [17] and time domain analysis [24-25]. Undeniably, over the last five years many enhancements about the knowledge of TLs behavior have been highlighted [16-26]. Despite this technical progress, a major issue is inherent to the time-domain prediction [27] and the calibration process [23]. In fact, the de-embedding technique is the critical point in order to accomplish a good agreement with the models [28]. Consequently, the ABCD matrix is one parameter which allows one to explore this bottleneck [17], [29], particularly for estimating the transient responses [25-28]. This statement motivates us to develop simpler and faster models to forecast the transient responses for digital interconnection lines on PCBs to help designers for high-speed applications [13-14], [30]. Moreover, as exposed above, interconnects

play an important role in designing modern electronic and microelectronic systems. So the degradations engendered by these interconnects can be partially reduced by the repeaters insertion [31] or completely reduced using the NGD concept as recently introduced [32-35].

For the better understanding, this paper is outlined as follows. *Section 2* offers the theoretical approach of extracting the RLCG model of microstrip lines. First of all, the characteristic impedance and the propagation constant including the frequency dispersion and propagation modes effects are established in function of the geometrical and physical properties of the interconnect line. Then the overall voltage transfer function of interconnected electronic systems is extracted, including source impedance and load impedance effects. In order to demonstrate the relevance of this model, *Section 3* presents frequency- and time-domain investigations performed with an original "omega" shape interconnect line. The validation process will be presented by considering frequency-/time-domains measurements achieved with the innovative improved TDR / TDT (Time-Domain Reflectometry / Time-Domain Transmissiometry) equipment introduced in [36-41]. This allows one to illustrate the evidence of the effects of connectors and the de-embedding process consequences. Finally, the conclusion of the paper is offered in the last section.

2. Theoretical approach

This section is structured in two paragraphs. First, we recall the characterization theory of microstrip lines including the extraction method of per unit length parameters *R*, *L*, *C* and *G*. Then, knowing the RLCG-model of the line, the analytical expressions of the transfer function and the access impedances of the line are introduced in the second paragraph.

2.1. Electromagnetic parameters extraction of a single transmission line (TL)

One considers a microstrip TL, of length *d*, with EM (Electromagnetic) parameters propagation constant $\gamma(\omega)=\alpha(\omega)+j\beta(\omega)$ (with $j=\sqrt{-1}$) and characteristic impedance, $Z_c(\omega)$, defined from physical properties (permittivity ε_r, dielectric loss tangent $tan\delta$, metal resistivity ρ…) and geometrical properties (width *w*, metallization thickness *t* and substrate height *h*) in function of the frequency as sketched on Figure 1.

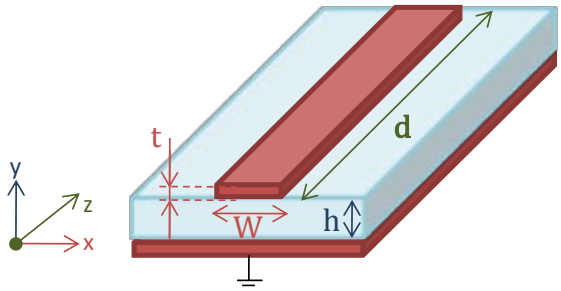


Figure 1: Geometrical representation of a microstrip TL.

According to the microwave theory [15], the well-known microstrip line synthesis and analysis relations [20], which are used in the EMDS (Electromagnetic Design System) environment of ADS (Advanced Design System) simulation tool, permit to extract the characteristic impedance:

$$Z_c=\frac{\eta_0}{2\pi\sqrt{\varepsilon_{eff}}}\ln\left[\frac{h\cdot F(w/h)}{w}+\sqrt{1+\frac{4h^2}{w^2}}\right], \quad (1)$$

where

$$F(w/h)=6+(2\pi-6)\cdot\exp\left[-\left(\frac{30.66h}{w}\right)^{0.7528}\right], \quad (2)$$

η_0 is the air impedance and ε_{eff} is the effective relative permittivity of the medium. In order to reach a better accuracy, this model must be valid in the wide frequency bandwidth. For this reason, frequency dispersion effects can be taken into account if the characteristic impedance is considered as follows:

$$Z_c(f)=Z_c\cdot\sqrt{\frac{\varepsilon_{eff}}{\varepsilon_r(f)}}\cdot\frac{\varepsilon_r(f)-1}{\varepsilon_{eff}-1}, \quad (3)$$

with

$$\varepsilon_r(f)=\varepsilon_r-\frac{\varepsilon_r-\varepsilon_{eff}}{1+g\cdot\left(f/f_p\right)^2}, \quad (4)$$

$$g=\frac{\pi^2}{12}\cdot\frac{\varepsilon_r-1}{\varepsilon_{eff}}\cdot\sqrt{\frac{Z_c}{\eta_0}}, \quad (5)$$

$$f_p=\frac{Z_c}{2\cdot\mu_0\cdot h} \quad (6)$$

and by replacing $u=w/h$, ε_{eff} is given by:

$$\varepsilon_{eff}=\frac{\varepsilon_r+1}{2}+\frac{\varepsilon_r-1}{2}\cdot\left(1+\frac{10}{u}\right)^{-a(u)b(\varepsilon_r)}, \quad (7)$$

$$a(u)=1+\frac{1}{49}\ln\left(\frac{u^4+\left(u/52\right)^2}{u^4+0.432}\right)+\frac{1}{18.7}\ln\left(1+\left(\frac{u}{18.1}\right)^3\right), \quad (8)$$

$$b(\varepsilon_r)=0.564\cdot\left(\frac{\varepsilon_r-0.9}{\varepsilon_r+3}\right)^{0.053}. \quad (9)$$

In this reminder, it is worthy of note to mention that a particular point of attention should be considered regarding the effective width w_{eff} of the structure. Indeed, a conformal transformation should be performed with respect of the value of *u* [15] as follows:

$$w_{eff} = \begin{cases} w + \frac{1.25}{\pi} \cdot \left(1 + \ln\left(\frac{2h}{t}\right)\right), & if \quad u < \frac{1}{2\pi} \\ w + \frac{1.25}{\pi} \cdot \left(1 + \ln\left(\frac{4\pi w}{t}\right)\right), & if \quad u \geq \frac{1}{2\pi} \end{cases} . \tag{10}$$

One also considers the propagation mode effects, hence the propagation constant in function of the frequency can be written, by denoting c the vacuum light celerity, as:

$$\gamma(f) = \alpha_c(f) + \alpha_d(f) + j\frac{2\pi f}{c}\sqrt{\varepsilon_r(f)}\,, \tag{11}$$

includes the metallic conductor and the dielectric losses respectively given by:

$$\alpha_c(f) = 1.38 \cdot \left\{1 + \frac{h}{w_{eff}} \cdot \left[1 + \frac{1}{\pi} \cdot \ln\left(\frac{2h}{t}\right)\right]\right\} \cdot \frac{R_s(f)}{h \cdot Z_c(f)} \cdot \frac{32 - \left(\frac{w}{h}\right)^2}{32 + \left(\frac{w}{h}\right)^2} \tag{12}$$

$$\alpha_d(f) = 27.3 \cdot \frac{\varepsilon_r}{\varepsilon_r - 1} \cdot \frac{\varepsilon_{eff} - 1}{\sqrt{\varepsilon_{eff}}} \cdot \frac{\tan(\delta)}{\frac{2\pi f}{c}} \tag{13}$$

with

$$R_s(f) = \sqrt{\pi \cdot f \cdot \mu_0 \cdot \rho} \tag{14}$$

For the calculation including the radiating losses, more explicit analytical expressions of the propagation constant real part or the per unit length losses constant $\alpha(f)$ is presented in [15-16]. It is noteworthy that from this statement one can also extract straightforwardly the RLCG parameters of any interconnect lines by substituting [13]:

$$R(f) = \Re\{\gamma(f) \cdot Z_c(f)\} \cdot d\,, \tag{15}$$

$$L(f) = \frac{\Im\{\gamma(f) \cdot Z_c(f)\}}{\omega} \cdot d\,, \tag{16}$$

$$C(f) = \frac{\Im\left\{\frac{\gamma(f)}{Z_c(f)}\right\}}{\omega} \cdot d\,, \tag{17}$$

$$G(f) = \Re\left\{\frac{\gamma(f)}{Z_c(f)}\right\} \cdot d\,, \tag{18}$$

2.2. Voltage transfer function determination of a TL

Getting an accurate voltage transfer function (VTF) of an interconnection line yields to determine the domain of validity of the presented equations (1) to (14). The simpler approximation that one can provide is to bound the upper frequency, f_{max}, in function of the substrate height [11] as:

$$f_{max} \leq \frac{c}{10 \cdot h \cdot \sqrt{\varepsilon_r}}\,. \tag{19}$$

In this case one can assume that the TL offers quasi-TEM solution for propagating. Hence, the TL is characterized by the following ABCD matrix [15]:

$$[M_{TL}] = \begin{bmatrix} \cosh(\gamma(\omega) \cdot d) & Z_c(\omega) \cdot \sinh(\gamma(\omega) \cdot d) \\ \frac{\sinh(\gamma(\omega) \cdot d)}{Z_c(\omega)} & \cosh(\gamma(\omega) \cdot d) \end{bmatrix} \tag{20}$$

By considering a real electronic system like two logic gates connected together through a PCB interconnection line, as depicted on Figure 2, one proposes evaluating the SI.

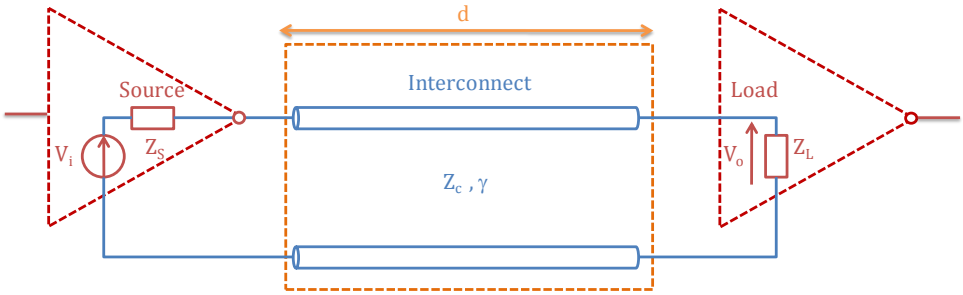


Figure 2: Circuit diagram representing interconnect line driven by source gate with impedance Z_S and loaded by input impedance Z_L.

Since, the SI assessment is based on the equivalent analog bandwidth of a considered input signal. Consequently, the RLCG-interconnection VTF should present the same bandwidth, this becomes challenging especially for high-rate signal due to important rise times [13]. Indeed, the equivalent frequency bandwidth BW for a trapezoidal signal is related to the 10% to 90% rise time, $t_{r\,90\text{-}10}$, as:

$$BW \approx \frac{0.35}{t_{r\,90-10}}\,. \tag{21}$$

As a result, the frequency-domain of validity of the VTF must satisfy relations (19) and (21). So, the overall TL transfer matrix M_{ij} including the source Z_S, and load Z_L,

impedances within the frequency band of interest is given by the matrix product expressed in (22). Afterwards, SI parameters can be established straightforwardly from the impedance matrix and the transient responses [14].

$$\begin{bmatrix} M_{11}(\omega) & M_{12}(\omega) \\ M_{21}(\omega) & M_{22}(\omega) \end{bmatrix} = \begin{bmatrix} 1 & Z_S(\omega) \\ 0 & 1 \end{bmatrix} \times [M_{TL}] \times \begin{bmatrix} 1 & 0 \\ \frac{1}{Z_L(\omega)} & 1 \end{bmatrix} \quad (22)$$

In fact, the VTF denoted $H(j\omega)$, the input impedance $Z_{in}(j\omega)$, the output impedance $Z_{out}(j\omega)$ and the transfer impedance $Z_T(j\omega)$ of the considered system of the Figure 2 are respectively summarized in Table 1:

Table 1: Summary of extracted frequency-domain SI parameters.

SI parameters	Expression
$H(j\omega)$	$\frac{1}{\left[\frac{Z_c(j\omega)}{Z_L(j\omega)}+\frac{Z_S(j\omega)}{Z_c(j\omega)}\right]\cdot\sinh(\gamma(j\omega)\cdot d)+\left[1+\frac{Z_S(j\omega)}{Z_L(j\omega)}\right]\cdot\cosh(\gamma(j\omega)\cdot d)}$
$Z_{in}(j\omega)$	$\frac{\left(Z_c^2(j\omega)+Z_L(j\omega)\cdot Z_S(j\omega)\right)\cdot\sinh(\gamma(j\omega)\cdot d)+Z_c(j\omega)\cdot(Z_L(j\omega)+Z_S(j\omega))\cdot\cosh(\gamma(j\omega)\cdot d)}{Z_L(j\omega)\cdot\sinh(\gamma(j\omega)\cdot d)+Z_c(j\omega)\cdot\cosh(\gamma(j\omega)\cdot d)}$
$Z_{out}(j\omega)$	$\frac{Z_c(j\omega)\cdot Z_L(j\omega)\cdot\cosh(\gamma(j\omega)\cdot d)}{Z_L(j\omega)\cdot\sinh(\gamma(j\omega)\cdot d)+Z_c(j\omega)\cdot\cosh(\gamma(j\omega)\cdot d)}$
$Z_T(j\omega)$	$\frac{Z_c(j\omega)\cdot Z_L(j\omega)}{Z_L(j\omega)\cdot\sinh(\gamma(j\omega)\cdot d)+Z_c(j\omega)\cdot\cosh(\gamma(j\omega)\cdot d)}$

3. Frequency- and time-domain investigations

As concrete proof-of-concept, the "**omega**" shape microstrip interconnect displayed in Figure 3 was considered and characterized by the TDR/TDT techniques. The equipment used in this experiment applies de-noising algorithms [42] on all the 40-GHz instantaneous bandwidth TDR/TDT traces. This allows performing straightforwardly and accurately the de-embedding of the SMA connectors in [36]. The interconnect-under-test (IUT) presents a width $w = 0.5$ mm, and a length $d = 32.944$ mm printed on the FR4-epoxy substrate, of height $h = 1.6$ mm, having relative permittivity $\varepsilon_r = 4.4$. Figure 4 represents the schematic diagram of the circuit tested by considering an interconnection with complex form. This interconnect corresponds to the length of PCB interconnections for mixed-circuit as PLL or clock distribution [43].

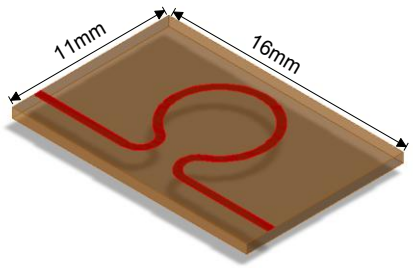


Figure 3: Interconnect microstrip line under test.

EM full-wave simulations of the 3-D structure represented by the black box shown in Figure 4 were performed in the EM design system environment, "Momentum", of ADS microwave/electronic tool. This IUT was also modeled with the method proposed in *Section 2*.

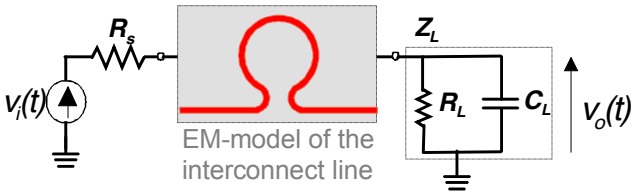


Figure 4: Schematic diagram used for the EM/circuit co-test.

3.1. Time-domain de-embedding technique supplied by the SPARQ

When characterizing any IUT, connectors are required; nonetheless, the impact of these later cannot be neglected. For this reason, de-embedding connectors is essential for assessing the signal integrity of an interconnected electronic system as presented in Figure 4. Figure 5 illustrates the effectiveness of the de-embedding technique by considering a digital-mixed input v_i with 1 Gbit/s (Gbps) rate and 0.3-ns rise-time propagating trough the designed IUT. The degradation of SI parameters is summarized below, in Table 2. It is noteworthy that le de-embedded signal, virtually without connectors, can be accurately restored.

Table 2: SI parameters of the transient results.

SI Parameter	IUT with connectors	IUT virtually without connectors
Rise-time (ps)	30	30
Amplitude attenuation (dB)	-1.04	-0.94
50%-Time-delay (ps)	30	20

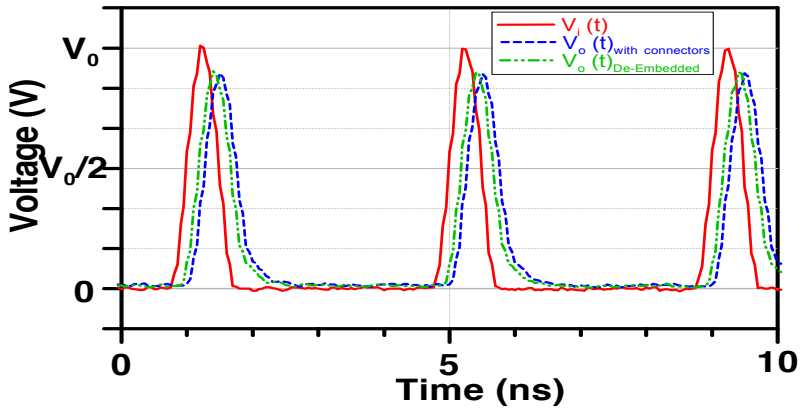


Figure 5: Measured transient results of the IUT shown in Figure 3.

3.2. Assessing the de-embedding effects

At present time, the de-embedding process of the SPARQ is under consideration. First, the IUT is characterized with using a VNA (Vector Network Analyzer) within the frequency-domain from 100 kHz to 8.5 GHz. The calibration was made in SOLT including port extension (open and short) of the universal test fixture for PCB, as presented by the photograph in Figure 6. Afterwards, comparison was made with the SPARQ measurement in the time-domain for de-embedding ports 1 and 2.

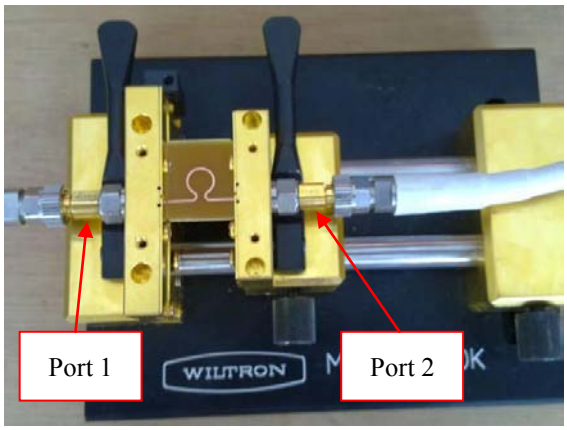


Figure 6: Universal test fixture used for the IUT characterization.

The ports are de-embedded via an algorithm that uses S-parameter measurement, and thus the S-parameters for these components must be known prior to the time of measurement. Hence, SPARQ calculates first the gated-port's S-parameters and then uses them in de-embedding connectors [36, 37]. Table 3 proposes the comparison between the time delays engendered by the connectors obtained from VNA with port extension (SOLT calibration) and TDR/TDT measurement performed with the SPARQ. Then, the S-parameters were also obtained with the SPARQ measurement within the time-domain including the "*gating*" process for de-embedding connectors [36-37], [41]. Hereafter, magnitude of the S_{11} (a), S_{21} (b) and phase of the S_{21} (c) are offered in Figure 7, from the EM simulation (black continuous curves), the proposed model (blue dashed curves), the VNA measurement (green dashed curves) and the SPARQ measurement (red continuous curves).

Table 3: Port extension for de-embedding connectors.

Port	VNA	SPARQ
Port 1	91.4 ps	90 ps
Port 2	90.5 ps	89 ps

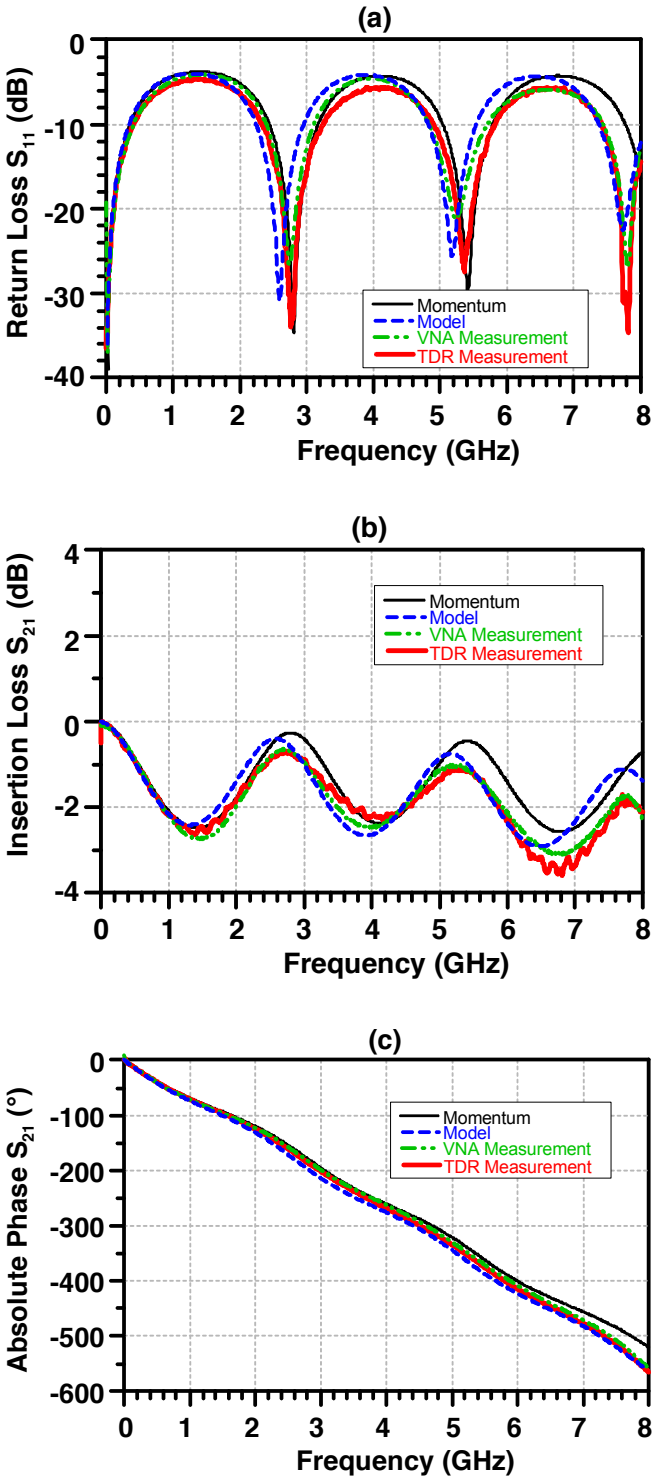


Figure 7: Comparisons of S_{11}-amplitude (a) and S_{21}-amplitude (b) and S_{21}-phase (c) from the EM model obtained from momentum, the developed model, the VNA measurement and the TDR/TDT measurement.

In order to show the relevance of this de-embedding technique, the transient transfer impedance Z_T is compared between the measurement from SPARQ (red continuous curve) and from the VNA (blue dashed curve). As depicted on Figure 8, a good agreement is established among the two results.

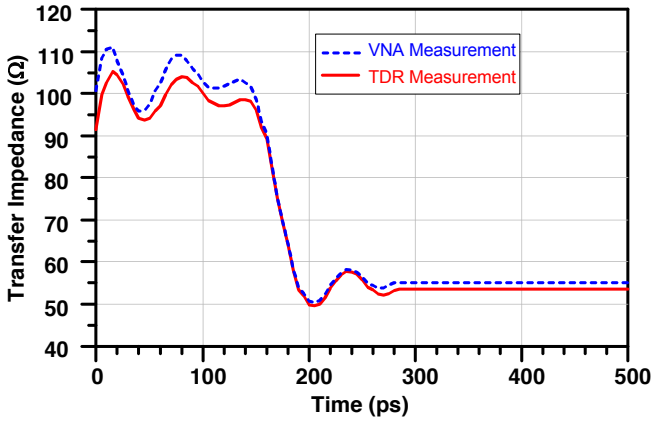


Figure 8: Time-domain transfer impedances obtained from the VNA measurement and the TDR/TDT measurement.

3.3. Application to the signal integrity forecasting

Using the SI Studio feature to simulate a noisy digital-mixed input v_{in} with 2.38-Gbit/s rate and 42-ps rise-time. Then, in order to emulate SI parameters degradation by considering $R_s = 20\ \Omega$, $R_L = 500\ \Omega$ and $C_L = 2$ pF, the Virtual-Probing was performed [44].

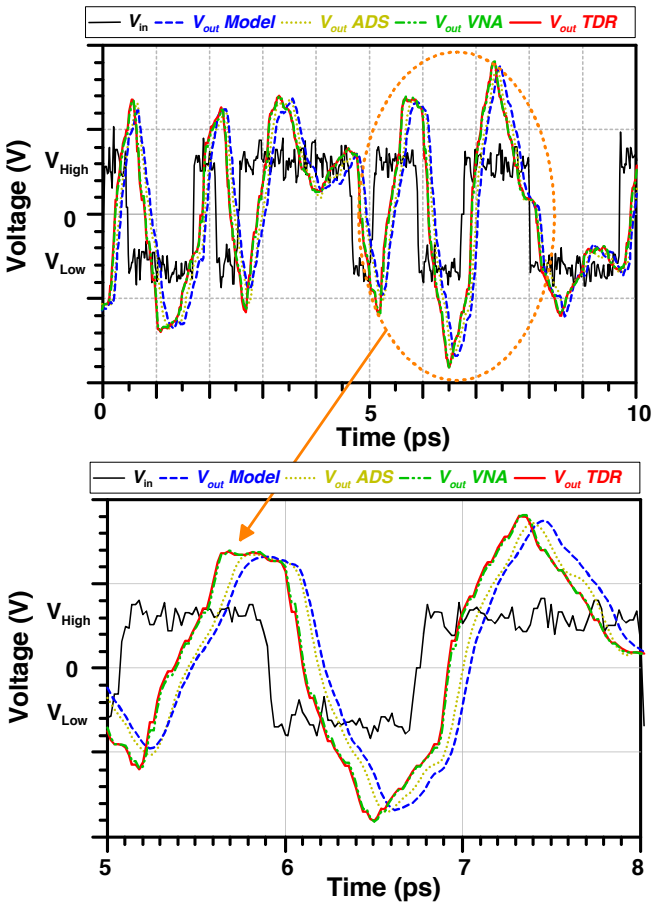


Figure 9: Comparisons of the responses of the circuit shown in Figure 3 obtained with different techniques for an NRZ noisy 2.38 Gpbs input signal.

Indeed, the SI Studio capability allows one to forecast the transient response of the system as shown by Figure 9. In addition, comparisons were made between the transient responses obtained from SI Studio with the VNA (green dashed curves) and the SPARQ measurements (red continuous curves) and between the simulations obtained from the developed model (blue dashed curves) and from ADS (ocher dashed curves). An excellent correlation was found between the VNA results and the SPARQ measurements that give evidence of the de-embedding method efficiency. In addition a very good agreement is established between the developed theoretical model and the measurements.

4. Conclusions

A modeling method of microstrip interconnections with reduced VTF is successfully introduced. The theoretical analyses of the interconnections are recalled. Then, basic expressions of the VTF and access impedances including the driven gate and loaded gate are established.

In order to validate the model established, a particular shape microstrip interconnect was characterized, designed and measured. Investigations both with frequency- and time-domain equipments were achieved in order to characterized PCB-interconnects. The de-embedding technique efficiency of the SPARQ Signal Integrity Network Analyzer was also exposed. The potential use for signal integrity forecasting was clearly shown. An excellent agreement was found between modern and complicate electronic simulation tools and the SI studio and Virtual-Probing environments from SPARQ measurements.

In addition, the interest of developed de-embedding technique can be applied to the investigation of microelectronic systems, as well bounding wires or lead frame effects compensation. In the continuation of these works, the 3D interconnect couplings in-package effects will be investigated.

Acknowledgements

These research works have been implemented within the frame of the "Time Domain Electromagnetic Characterization and Simulation for EMC" (TECS) project which is part-funded by the Haute-Normandie Region and the ERDF via the Franco-British INTERREG IV-A program. Singular acknowledgments are made to LeCroy SARL for the measurements with the SPARQ that were performed and for supplied the expertness in time-domain de-embedding techniques.

References

[1] International Technology Roadmap for Semiconductors Update Overview 2011. Available [Online]: http://www.itrs.net/Links/2011ITRS/Home2011.htm

[2] B. Bottom, "Assembly and Packaging White Paper on System Level Integration," *ITRS white papers*, 2009. Available [Online]: http://www.itrs.net/papers.html

[3] F. Jun, Y. Xiaoning, J. Kim, B. Archambeault, and A. Orlandi, "Signal Integrity Design for High-Speed Digital Circuits: Progress and Directions," *IEEE Trans. EMC*, Vol. 52, No. 2, pp. 392-400, May 2010.

[4] J. F. Buckwalter, "Predicting Microwave Digital Signal Integrity," *IEEE Trans. Advanced Packaging*, Vol. 32, No. 2, pp. 280-289, May 2009.

[5] J. Kim, and E. Li, "Special Issue on PCB Level Signal Integrity, Power Integrity, and EMC," *IEEE Trans. EMC*, Vol. 52, No. 2, pp. 246-247, May 2010.

[6] E. Bogatin, "Essential Principles of Signal Integrity," *IEEE Microwave Magazine*, Vol. 12, No. 5, Aug. 2011.

[7] Y. I. Ismail, and E. G. Friedman, "Effects of Inductance on the Propagation, Delay and Repeater Insertion in VLSI Circuits", *IEEE Trans. VLSI Systems*, Vol. 8, No. 2, pp. 195-206, Apr. 2000.

[8] A. Deutsch, G.V . Kopcsay, P. Restle, G. Katopis, W. D. Becker, H. Smith, P. W. Coteus, C. W. Surovic, B. J. Rubin, R. P. Dunne, T. Gallo, K. A. Jenkins, L. M. Terman, R. H. Dennard, G. A. Sai-Halasz, and D. R. Knebel, "When are transmission-line effects important for on-chip interconnection", *IEEE Trans. MTT*, Vol. 45, No. 10, pp. 1836-1846, Oct. 1997.

[9] M. Celik, L. Pileggi, and A. Odabasioglu, *IC Interconnect Analysis*, Kluwer Academic Publisher, Dordrecht, Germany, 2002.

[10] M. Zolog, and D. Piticã, "Controlling the Signal Integrity through the Geometry of the Microstrip on the Digital PCBs," *Electronic System-Integration Technology Conference (ESTC)*, Berlin, Germany, Sep. 2010.

[11] F. W. L. Kung and H. T. Chuah, "System Modeling of High-Speed Digital Printed Circuit Board Using SPICE," *Progress In Electromagnetics Research*, Vol. 20, pp. 179-211, 1998.

[12] T. Granberg, "*Handbook of Digital Techniques for High Speed Design*," Pentrice Hall Modern Semiconductor Design Series, Ed. by Pentrice Hall, Chapter 1, pp. 3-16, 2004.

[13] T. Eudes, B. Ravelo, and A. Louis, "Transient Response Characterization of the High-Speed Interconnection RLCG Model for the Signal Integrity Analysis," *PIER J.*, Vol. 112, 183-197, Jan. 2011.

[14] T. Eudes, B. Ravelo, and A. Louis, "Experimental validations of a simple PCB interconnect model for high-rate signal integrity," *To be published in IEEE Trans. EMC. doi: 10.1109/TEMC.2011.2165216*, pp. 1-8, Sept. 2011.

[15] G. L. Matthaei, L Young, and E. M. T. Jones, *Microwave Filters, Impedance Matching and Coupling Structures*, Artech House Microwave Library, Norwood, MA, Ed. by Artech House, 1980.

[16] P. G. Huray, *The Foundations of the Signal Integrity*, Ed. by Wiley and Sons Inc., Hoboken, NJ, 2010.

[17] J. Cho, E. Song, H. Kim, S. Ahn, J. S. Pak, Ji. Kim and Jo. Kim "Mixed-Mode ABCD Parameters: Theory and Application to Signal Integrity Analysis of PCB-Level Differential Interconnects," *IEEE Trans. EMC*, Vol. 53, No. 3, pp.1-9, Aug. 2011.

[18] J. H. Kim, D. Oh, and W. Kim, "Accurate Characterization of broadband Multiconductor Transmission Lines for High-Speed Digital Systems," *IEEE Trans. Advanced Packaging*, Vol. 33, No. 4, pp. 857-867, Nov. 2010.

[19] A. Koul, P. K. R. Anmula, M. Y. Koledintseva, J. L. Drewniak and S. Hinaga, "Improved Technique for Extracting Parameters of Low-Loss Dielectrics on Printed Circuit Boards," in Proc. of *IEEE EMC Symp.*, pp. 191-196, Aug. 2009.

[20] K. S. R. Krishna, J. L. Narayana and L. P. Reddy, "ANN Models for Microstrip Line Synthesis and Analysis," *Int. J. Elect. Syst. Sci. Eng.*, Vol. 1, pp.196-200, 2008.

[21] J. Lilja, R. Mäkinen, V. Pynttäri, P. Mansikkamäki, and M. Kivikoski, "Application of Thin-Film RCLG Model for the Modeling of Inkjet Printed Microstrip Lines", in Proc. of *12th Workshop on SPI*, pp. 1-4, May 2008.

[22] Y. Shlepnev, "Modeling Frequency-Dependent Conductor Losses and Dispersion in Serial Data Channel Interconnects," *Simberian Inc.*, 2007. Available [Online]: http://www.simberian.com

[23] M. Resso, and E. Bogatin, *Signal Integrity Characterization Techniques*, Int. Engineering Consortium, Ed. by IEC Publications, 2009.

[24] N. Nakhla, M. Nakhla, and R. Achar, "A General Approach for Sensitivity Analysis of Distributed Interconnects in the Time Domain," *IEEE Trans. MTT*, Vol. 59, No. 1, pp. 46-55, Jan. 2011.

[25] S. Roy, and A. Dounavis, "RLC Interconnect Modeling using Delay Algebraic Equations," in Proc. of *IEEE CAS Workshop*, Dallas, CO, Oct. 2009.

[26] S. Gupta, A. Parsa, E. Perret, R. V. Snyder, R. J. Wenzel and C. Caloz, "Group-Delay Engineered Noncommensurate Transmission Line All-Pass Network for Analog Signal Processing," IEEE Trans. MTT, Vol. 58, No. 9, pp. 2392-2407, Sept. 2010.

[27] J. L. Naredo, J. A. Gutérrez, F. A. Uribe, J. L. Guardado and V. H. Ortiz, "Frequency Domain Methods for Electromagnetic Transient Analysis," in Proc. of *IEEE Power Engineering General Meeting*, pp. 1-7, June 2007.

[28] P. Wittwer and P. J. Pupalaikis, "A general Closed-Form Solution to Multi-Port Scattering Parameter Calculations," in Proc. of the *72nd ARFTG Microwave. Meas. Symp.*, pp. 137-143, Dec. 2008

[29] D. A. Frickey, "Conversions Between S, Z, Y, h, ABCD and T Parameters which are Valid for Complex Source and Load Impedances," *IEEE Trans. MTT*, Vol. 42, No. 2, pp. 205-216, Feb. 1994.

[30] B. Ravelo and T. Eudes, "Fast estimation of RL-loaded microelectronic interconnections delay for the signal integrity prediction," *To be published in Int. J. Numer. Model. DOI: 10.1002/jnm.838*.

[31] V. Adler, E. G. Friedman, "Repeater Design to Reduce Delay and Power in Resistive Interconnect," *IEEE Trans. on CAS II*, Vol. 45, No. 5, May 1998.

[32] B. Ravelo, A. Perennec, and M. Le Roy, "New Technique of Inter-Chip Interconnect Effects Equalization with Negative Group Delay Active Circuits", *VLSI*, Chap. 20, INTECH Book, Ed. by Z. Wang, 409-434, Feb. 2010.

[33] B. Ravelo, A. Perennec, and M. Le Roy, "Experimental Validation of the RC-Interconnect Effect Equalization with Negative Group Delay Active Circuit in Planar Hybrid Technology," in Proc. of *13th IEEE Workshop SPI*, Strasbourg, France, May 2009.

[34] B. Ravelo, A. Pérennec, M. Le Roy, and Y. Boucher, "Active Microwave Circuit with Negative Group Delay," *IEEE MWC Lett.*, Vol. 17, No. 12, pp. 861-863, Dec. 2007.

[35] T. Eudes and B. Ravelo, "Cancellation of Delays in the High-Rate Interconnects with UWB NGD Active Cells," *Applied Physics Research*, Vol. 3, No. 2, Nov. 2011.

[36] A. Blankman, "De-embedding Gigaprobes® Using Time Domain Gating with the LeCroy SPARQ," *LeCroy SPARQ Application Note*. Available [Online]: http://www.lecroy.com/sparq/

[37] A. Blankman, "LeCroy SPARQ S-Parameter Measurement and Methodology," *LeCroy Technical Brief*, Rev. 3, July 2011. Available [Online]: http://www.lecroy.com/support/techlib/

[38] A. Blankman, "SPARQ S-Parameter Measurements with Impulse Response Time Limiting," LeCroy Technical Note, Rev. 2, June 2011. Available [Online]: http://www.lecroy.com/support/techlib/

[39] P. J. Pupalaikis, "SPARQ Dynamic Range," *LeCroy Technical Brief*. Available [Online]: http://www.lecroy.com/support/techlib/

[40] M. Schnecker, M. Miller and J. Schachner, "Signal Integrity Measurement in High Bit Rate Systems," Presented at *DesignCon2009*, Santa Clara, CA, US, Feb. 2009.

[41] J. Kenney and P. J. Pupalaikis, "Timing Measurement Problems and Solutions in Source Terminated Memory Systems with Inaccessible Probing Points," in Proc. of *DesignCon2010*, Santa Clara, CA, US, Feb. 2010.

[42] P. J. Pupalaikis, "Wavelet Denoising for TDR Dynamic Range Improvement," in Proc. of *DesignCon2011*, Santa Clara, CA, US, Feb. 2011.

[43] "240-Pin PC-6400/PC-5300/PC-4200/PC-3200 DDR2 SDRAM Registered DIMM Design Specification," JEDEC Standard, No. 21C, Rev. 4.04, Jan. 2010. Available [Online]: http://www.jedec.org

[44] Signal Integrity Studio, Available [Online]: http://www.lecroy.com/sistudio/sistudio.aspx?mid=1084&modelid=6261

3D-Modelling of an Aperture Illuminated by a HF Electromagnetic Source For EMC Application

[2]Zakia Abidi, [1]Mohamed Djennah, , [2]Bernard BANDELIER, and [2]Françoise Rioux-Damidau

[1] Laboratory Signal and Image – Polytechnic School of Algiers - Algeria
[2]IR4M, University Paris XI, UMR CNRS 8081, Bat 220, 91405 Orsay France
zakia.abidi@u-psud.com , mdjennah@hotmail.com

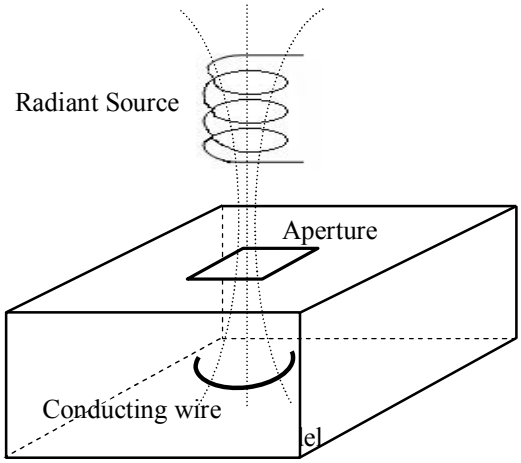
Abstract:

In this paper, we present a numerical method for determining the penetration of electromagnetic fields through a small aperture in a metal enclosure having inside it a conducting component. To solve the problem of coupling between the radiated electromagnetic field and the metallic enclosure, we develop a variational formulation in the interior region and an integral formulation in the exterior region by using the equivalent electric current on the exterior surface of the enclosure. The numerical results obtained with this method show the influence of the characteristic parameters (ó,ε,μ) and of the thickness of enclosure on the penetration of electromagnetic field inside the enclosure.

I. INTRODUCTION

Nowadays, more and more of electronics is embarked on board of terrestrial or air vehicles with electronic components functioning at frequencies higher and higher. The multiplication of the feasibility of electromagnetic sources and of their increasing power thus generates new types of bad function of the electrical appliance and problems of incompatibility inter-equipment, which can go until their destruction. Electromagnetic compatibility, according to its "fundamental principles", is thus analyzed in terms of emission (to not disturb the environment) and of immunity (to not be disturbed). The two aspects occur at the same time in conduction (currents and parasite tensions) and in radiation (electric and/or magnetic fields). Consequently, in the scenario of an EMC problem, one will find three actors: a source of disturbance (for example the equipment itself in the case of a problem of emission, or its environment in the case of immunity), a connection (for example by conduction, radiation, cross talk…) and a victim of the coupled disturbances (for example the equipment itself in the case of problem of immunity).

In our study we are interested in the radiated electromagnetic field. On figure 1 we present a configuration of a problem model related to the EMC, The metal enclosure with a small rectangular opening lit by the electromagnetic radiation of a source located in the exterior region, considered as harmonic in time.



This problem was the subject of some works by using various numerical models [1][2][3] [4]. In our study, we first apply the finite element method inside and on enclosure and next we express the external field by an integral representation.¶ This one is a function of the equivalent electrical currents K carried by the external surface of the enclosure. These surface currents represent the jump of the tangential component of the magnetic field:

$$[\, n \times h \,]_{\Gamma} = K \qquad (1)$$

We realize the coupling of the two regions by computing an integral-differential operator R binding the traces of tangential component of the electric field and that of its rotational [5]:

$$R(n \times e) = n \times curl\,(e) \qquad (2)$$

This term represents the border term in the variational formulation of the problem. We compute the operator R by using K as an

intermediate unknown factor between the interior problem and the exterior problem.

II. FORMULATION

The physical system is defined by the following equations:

- in the enclosure without the conducting wire :

$$i\omega\mu_0 h + curl(e) = 0 \quad (3)$$

$$-i\omega\varepsilon_0 e + curl(h) = 0 \quad (4)$$

- in conducting wire:

$$i\omega\mu_c h + curl(e) = 0 \quad (5)$$

$$-(\sigma_c + i\omega\varepsilon)\, e + curl(h) = 0 \quad (6)$$

- in the exterior region without source:

$$i\omega\mu_0 h + curl(e) = 0 \quad (7)$$

$$-i\omega\varepsilon_0 e + curl(h) = 0 \quad (8)$$

and moreover we take in all system:

$$div\,\mu h = 0 \;;\; div\,\varepsilon e = 0 \quad (9)$$

With these equations, we take into account the conditions at infinite:

$$e = 0\,(1/r) \quad (10)$$

$$h = 0\,(1/r) \quad (11)$$

We take $(\varepsilon, \mu, \sigma)$ as constant scalar functions in each different region, where h and e are respectively the magnetic and electric fields intensities, ó is the electric conductivity, ε is the electric permittivity and μ is the magnetic permeability.

III. VARIATIONAL PROBLEM

With the object of evaluating the electromagnetic field inside the enclosure and in particular of calculating the induced voltage in the conducting wire, we formulate our problem in electric field:

$$\frac{1}{\mu} curl\, curl(e) + i\omega(\sigma + i\omega\varepsilon)e = 0 \quad (12)$$

Multiplying equation (13) by a test function e' and integrating it on the volume of the domain occupied by the enclosure p, we have:

$$\int_\Omega curl(e)\cdot curl(e')\,d\Omega + \int_\Gamma (n\cdot curl(e))\,e'\,d\Gamma + i\omega\mu(i\omega\varepsilon - \sigma)\int_\Omega e\cdot e'\,d\Omega = 0 \quad (13)$$

Where Γ is the border of Ω and n is the unit outward normal to Γ.

The total electric field e is composed theoretically of two parts, one of reaction e^r and the other of source e^s:

$$e = e^s + e^r \quad (14)$$

With this decomposition, we can write (13) as an integral equation where er is the unknown in the first term and where second member is function of es.

In another way, the conducting wire intervenes as an integral term in the problem formulation. We suppose that the ray of the wire is very small compared with the dimensions of the enclosure and as the length is small we can take it as one or two edges as a sequence of mesh edges. We can write the wire term in the variational formulation as :

$$T_{Wire}\int_\Gamma (n\times\nabla\times e)\,d\Gamma\cdot e' = \frac{-\partial}{\partial t}\int_S (n\times h)\cdot e'\,dS \quad (15)$$

$$n\times e = \rho\,(n\times h)\times n \quad (16)$$

where S is the surface enclosing the wire and ρ is the surface impedance of the wire.

Equation (15) becomes:

$$T_{Wire} = \frac{\partial}{\partial t}\int_w \frac{1}{Z_w}\cdot e_{ij}\cdot e'_{kl}\,dl \quad (17)$$

With

$$Z_w = \frac{1+j}{2\pi a}\cdot\sqrt{\frac{\omega\mu}{2\sigma}} \quad (18)$$

where a is the wire radius, and Z is the wire impedance per unit length in (Ω /m)

IV. CALCULATION THE BORDER TERM

The integral term on the integral equation (15) is called border term. At this stage, it should be noted on the first hand that we cannot solve the problem without identifying the jump of the tangential component of the magnetic field on
On the other hand, the solution of the interior problem could not be the solution of the problem set in the open space R3. Only the border term enables us to take account of the behavior of the field in the exterior region. To treat the border term, we first of all will formulate the external problem and will express its solution according to the traces of the field on the border . The system of equations (7)-(10) governs the behavior of the magnetic field in the exterior region. We indicate by e0 the trace of the tangential component of electric field on
problem can be written in the following integral form:

$$e(x) = \mu_0 \int_\Gamma K(y) \cdot G(x,y)\, dy \qquad (19)$$

where K represents the jump of the tangential component of the magnetic field:

$$[n \wedge h] = K \qquad (20)$$

The equivalent surface current K, introduced on , is fictitious. It is also an intermediate unknown used to couple the exterior and the interior problems. To keep the electric field e like only unknown actor on , we will have to express K according to e:

$$[n \wedge h] = R(e). \qquad (21)$$

$$\nabla \times e(x) = \mu_0 \cdot \int_\Gamma K(y) \times \nabla G(x,y)\, dy$$

$$= e_0 \quad n \times e(x) = \mu_0 \cdot \int_\Gamma n \times K(y) \cdot G(x,y)\, dy$$

$$\langle e'_e, K' \rangle = \langle e_0, K' \rangle = \frac{1}{4\pi} \iint_\Gamma \iint_\Gamma \frac{K(y) \cdot K'(x)}{|x-y|}\, dxdy$$

Our aim now is to calculate R. This computation is based on a variational formulation:

V. NUMERICAL IMPLEMENTATION

In order to numerically solve the problem, the volume of study is cut in tetrahedral elements and the electric field vector E is described in terms of basic functions Wij associated to the edges of these elements.

$$e = \sum_{i=1}^{N} W_{ij} \cdot e_i \qquad (22)$$

$$W_{ij} = \lambda_a \nabla \lambda_b - \lambda_b \nabla \lambda_a \qquad (23)$$

where N is the total number of edges of the mesh, Wij is the vector basis function associated with edge (ij) and eij is the problem unknown which represents the circulation of the electric field along the edge (ij). λi is the barycentric coordinate of tetrahedra associated with the node i.

We have developed the currents K on the basic function:

$$\omega_i(x) = n(x) \times grad\ \lambda_i \qquad (24)$$

and we have:

$$K(x) = \sum_i P_i \cdot \omega_i(x) \qquad (25)$$

where:

i : described the vertex of Γ.
P_i : the value of K in vertex i.
λ_i : the barycentric coordinate.
$n(x)$: normal vector on Γ.

Our variational formulation can be rewriten like the following linear forms:

$$M_{GR} \cdot e_V = S_V \qquad (26)$$

$$M_{GC} \cdot e_C = S_C \qquad (27)$$

where:

$$M_{GV} = M_1 + R + j\omega\sigma\mu \cdot M_2$$

$$M_{GC} = M_1 + R$$

R : is a full matrix with dimension (nbat × nbat); it represents the edge term of the approached variational problem.

M1 and M2. are two matrices; their dimensions are (nbat × nbat); an element of these matrices is zero

only if (ij) and (kl) do not belong to the same tetrahedron.

VI. NUMERICAL RESULTS :

A. Representation of a grid mesh

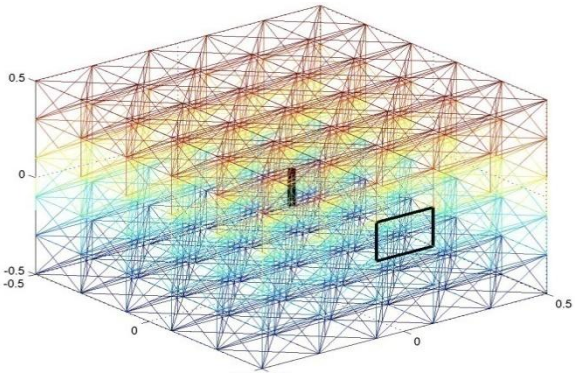


Fig.2. Tetrahedral grid of the enclosure

Number of internal nodes	489
Number of frontier nodes	302
Number of internal edges	3190
Number _of frontier edges	900
Number_of faces	600
Number of tetrahedral	3000

B. Representation of the fields:

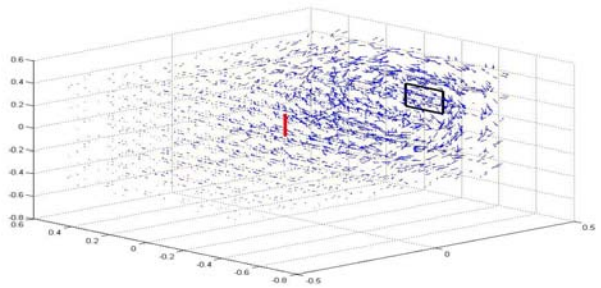


Fig.3. Magnetic field *h*, *f* = 1 MHz

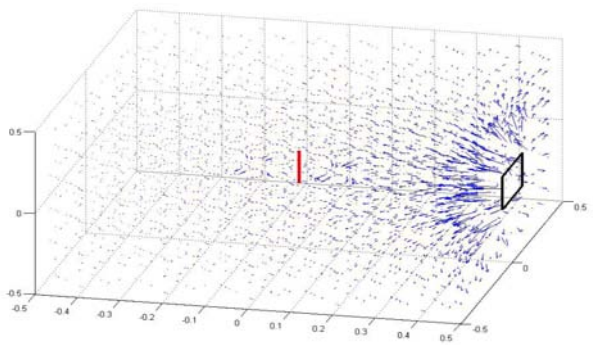


Fig.4. Electric field *e* *f* = 1 MHz

C. iso-value of electromagnetic field according to plan (YOZ) (Real Part):

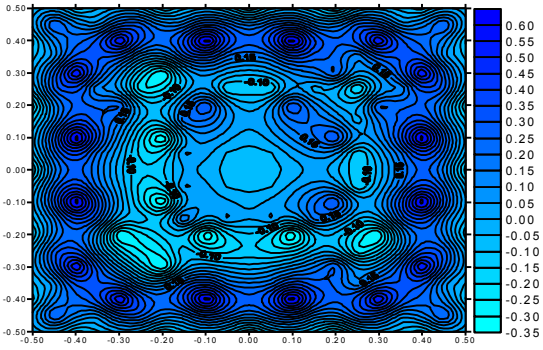


Fig.5. *f* =1 GHz, DD=0.7, RHO=1.6672 10^{-8}
J_s = 100, R=0.2 , VN1= -1, VN2= 0, VN3=0

The real part of the electric field according to plan (YOZ) X=0.1

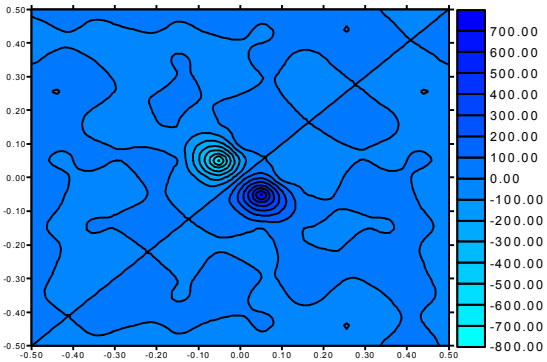


Fig.6. *f* =1 GHz, DD=0.7, RHO=1.6672 10^{-8}

J_s = 100, R=0.2 , VN1= -1, VN2= 0, VN3=0

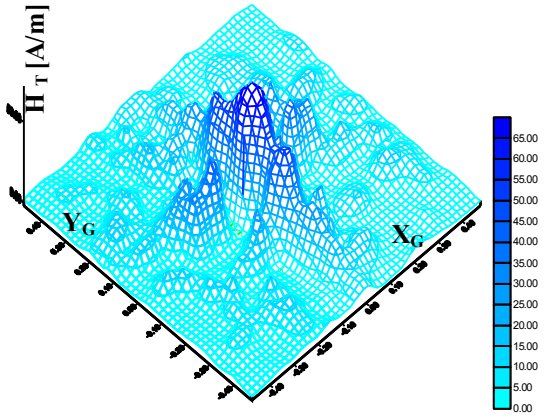


Fig.7. Representation of total magnetic field in *f* =50 MHz

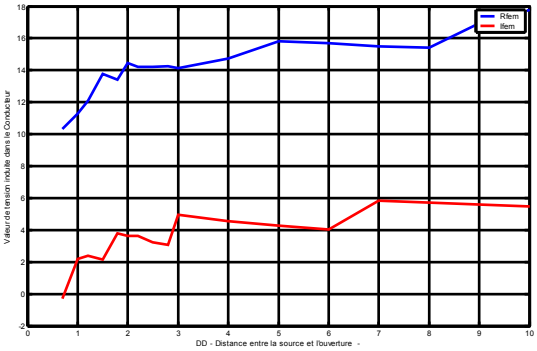


Fig.8. Variation of induced voltage in conducting wire according to distance DD between source and aperture.

CONCLUSION

In this article we have some numerical results to evaluate the penetration of the electromagnetic field in a metal enclosure. We considered a radiant electromagnetic source in front of an aperture of the enclosure at a limited distance DD. We realize a coupling between the boundary integral method outside and the finite element method inside the enclosure to solve our problem. The numerical results show the contribution of each parameter of the problem in the evaluation of the electromagnetic energy penetrating in the enclosure, On the one hand, according to the electromagnetic parameters: (electric conductivity and permittivity (magnetic permeability (addition, according to the density of the current source, the geometrical position and the frequency of the radiant source. The numerical results show the variation in the values and the form of electromagnetic energy in each point inside the enclosure while varying at each time only one parameter. Considering the number of parameters we cannot expose all the results in this paper.

REFERENCES

[1] W.P.Carpes, L. Pichon, Razek "Analysis of the Couplingof an Incident Wave with a Wire inside a Cavity using an FEM in Frequency and Times Domains" IEEE Transaction on Electromagnetic Compatibility.Vol 44, No3 August 2002.

[2] F.Paladian, P.Bonnet, M.Klingler "A frequency-domain prediction model using measured scattering parameters of electrically short lines to determine the per unit length parameters matrices of multiconductor transmission lines" 14th International Zurich Symposium & Technical Exhibition on Electromagnetic Compatibility, Zürich (Suisse), February 2001, Actes du Colloque, pp.293-298.

[3] D. Lecointe, W. Tabbara, J. Lasserre " Aperture Coupling of Electromagnetic Energy to a Wire inside a Rectangular Metallic Cavity " IEEE AP-S Antennas Propagation Soc. Int. Symp, Vol. 3, pp.1571-1574, 1992.

[4] T. Yang, J. L. Volakis "Coupling to Wires in Cavity Enclosure Using Iterative Algorithm" Radiation Laboratory, EECS, Dept. The University of Michigan, ElectroScience Labo. The Ohio State University, Columbus, OH43212, 2004.

[5] M. Djennah, F. Rioux-Damidau, B. Bandelier "Computation of electric charges and eddy currents with an e formulation" Journal IEEE Transaction Magnetic 1997, Vol 32, pp 1322-25.

INFLUENCE OF THE LINE CONFIGURATION AND THE SHIELDING WIRE ON THE OVER VOLTAGES INDUCED ON OVERHEAD POWER DISTRIBUTION LINES CAUSED BY INDIRECT LIGHTNING STROKES

Nassima M'ziou[1*] Ahmed Boubakeur[2], Mahdi Izadi[3]

[1]trical Engineering .Mohamed Khider ,University . Biskra. Algeria
[2] L..E/High Voltage Laboratory, Ecole Nationale Polytechnique, Algiers.
Algeria Dépt. of Elec
[3] Malaysia University

[*]E-mail: mziou_nas@yahoo.fr

Abstract: The major aim of this study is the computation of the voltages induced by an external transient electromagnetic excitation, especially due to the lightning discharge coupling to overhead power line. In this paper we propose an original method which is the hybrid method for evaluating the electromagnetic field radiated by lightning. The proposed method is the combination of the images method and finite difference time-domain (FDTD) method. We calculate firstly the magnetic field with images method using the Simpson technique and, secondly, based partially on the finite difference time-domain method, we calculate the electric field. We present the coupled model used for the calculation of lightning induced overvoltages given in the Agrawal approach. The algorithm applied to multi-conductors lines above a perfectly conducting ground. After we present the influence of the line configurations and the presence of shielding wire on the induced voltage.

Key words: Lightning, electromagnetic field, FDTD method, induced voltage, power lines, vertical configuration, triangular configuration, shielding wire.

I INTRODUCTION

The evaluation of the effects of lightning strike has been a special concern in our modern society due to the use of highly susceptible equipment, such as electronic devices and systems, for a wide variety of applications. Lightning flash between cloud and ground generates transient electromagnetic fields, which can result in extremely high voltages induced in the vicinity of lightning strike. When a building is struck by lightning, the resulting transient current and voltage can cause dangerous effects. To analyze the effects of indirect lightning strikes on lines or various kinds of circuits, it is necessary to go through the following steps:

1) The development of lightning return-stroke models, which means the modeling of the spatial–temporal distribution of the current in the lightning channel [1], [2].
2) The calculation of the electromagnetic field radiated by such a current distribution including propagation effects over a soil with finite conductivity.
3) The evaluation of voltages resulting from the coupling between the electromagnetic field and the line conductors.

.

In order to calculate the lightning induced overvoltages, the Agrawal model and its equivalent formulation is used. We are interested in computing radiated lightning electromagnetic field with a hybrid method which is the combination of two methods: the Simpson method to obtain the magnetic field and the FDTD method to evaluate the electric field and the induced voltage.

II LIGHTNING RETURN STROKE MODELS

These models specify the spatial–temporal distribution of the channel current based on the current at the channel base, since it is only the channel-base current that can be measured directly and for which experimental data are available [3]. These models are also called "engineering models" due to their simplicity that

Nassima M'ziou: mziou_nas@yahoo.fr

permits the return-stroke current to be related to a channel-base current known from measurements in a straight form.

The most popular of these models are probably the transmission line (TL) model [4], the traveling current source
(TCS)model [5], the modified TL (MTL) model [6]–[8], theDiendorfer–Uman (DU) and the modified Diendorfer–Uman (MDU) models [9], [10]. All these models have been analyzed in detail in [11], and it is concluded that, for most engineering coupling calculations, any one of the models is adequate. The engineering models are expressed by the following generalized current equation:

$$i(z',t) = u(t - z'/v_f)P(z')i(0, t - z'/v_f) \quad (1)$$

Where u the Heaviside function is equal to unity for $t \geq z'/v_f$ and zero otherwise, $P(z')$ is the height dependent current attenuation factor (Table.1), and v_f is the current-wave propagation speed. i(0, t) is the channel base current which is represented by two Heidler functions:

$$i(0,t) = \frac{I_{01}}{\eta_1}\frac{(t/\tau_{11})^{n_1}}{1+(t/\tau_{11})^{n_1}}\exp(-t/\tau_{12}) + \frac{I_{02}}{\eta_2}\frac{(t/\tau_{21})^{n_2}}{1+(t/\tau_{21})^{n_2}}\exp(t/\tau_{22}) \quad (2)$$

$$\eta_1 = \exp^{(\tau_{11}/\tau_{21})(n_1\tau_{12}/\tau_{22})^{1/n_1}}$$

Where I_{01} , I_{02} τ_{11} , τ_{12} , τ_{21} , τ_{22} are constants.

Table 1: $P(z')$ and v_f for different return stroke models [12].

Model	$P(z')$	v_f
BG	1	∞
TL	1	v
TCS	1	-c
MTLL	1-z'/Htot	v
MTLE	$\exp(-z'/\lambda)$	v

Where the factor λ is the decay constant, z' is the coordinate directed along the channel, v is the speed of propagation of the return stroke wave front and c is the speed of light.
In Table.2 we list the parameters of the Heidler function.

Table 2: Channel Base Current Parameters [13].

I_{01} **(KA)**	τ_{11} **(μs)**	τ_{21} **(μs)**	$\mathbf{n_1}$	I_{02} **(KA)**	τ_{12} **(μs)**	τ_{22} **(μs)**	$\mathbf{n_2}$
10.7	0.25	2.5	2	6.5	2.1	230	2

Fig.1 represents the time-variation of the channel base current

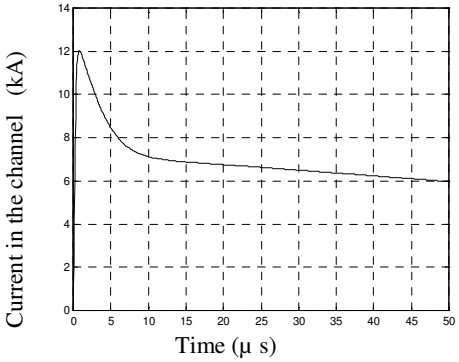


Fig.1 Time-variation of the channel- base current.

III ELECTROMAGNETIC FIELD ASSOCIATED TO LIGHTNING

Assuming a perfectly-conducting ground, the computation of the electromagnetic fields can be greatly simplified. The components of the electric and the magnetic fields produced by a short vertical section of infinitesimal channel dz' at height z' carrying a time-varying current i (z', t) that can be computed in the time domain using the following relations.

$$dE_r(r,\phi,z',t)=\frac{dz'}{4\pi\varepsilon_0}.\left[\frac{3r(z-z')}{R^5}.\int_0^t i(z',\tau-\frac{R}{c})d\tau + \frac{3r(z-z')}{cR^4}.i(z',t-\frac{R}{c}) - \frac{r(z-z')}{c^2R^3}.\frac{\partial i(z',t-\frac{R}{c})}{\partial t}\right] \quad (3)$$

$$dE_z(r,\phi,z,t)=\frac{dz'}{4\pi\varepsilon_0}.\left[\frac{2(z-z')^2-r^2}{R^5}.\int_0^t i(z',\tau-\frac{R}{c})d\tau + \frac{2(z-z')^2-r^2}{cR^4}.i(z',t-\frac{R}{c}) - \frac{r^2}{c^2R^3}.\frac{\partial i(z',t-\frac{R}{c})}{\partial t}\right] \quad (4)$$

$$dH_\phi(r,\phi,z,t)=\frac{dz'}{4\pi}.\left[\frac{r}{R^3}.i(z',t-\frac{R}{c})+\frac{r}{cR^2}.\frac{\partial i(z',t-\frac{R}{c})}{\partial t}\right] \quad (5)$$

$$R=\sqrt{r^2+(z-z')^2}$$

where ε_0 and μ_0 are the permittivity and permeability of the vacuum respectively. c is the light speed. R is the distance from the dipole to the observation point, and r is the horizontal distance between the channel and the observation point.

IV THE HYBRID METHOD PRESENTATION

A. Formulation of the method

The magnetic flux density is obtained by integrating (5) using a numerical integration which is the Simpson method.

The electric field is calculated by a simplified approach based on the FDTD method, it's given by the following expression:

$$\nabla \times \vec{B} = \mu \left(\vec{J} + \frac{\partial \vec{D}}{\partial t} \right) \quad \left(\sigma \vec{E} + \varepsilon \frac{\partial \vec{E}}{\partial t} \right) \qquad (6)$$

Where μ is the permeability, σ is the conductivity, ε is the permittivity, $\vec{J}$ is the current density vector, and $\vec{D}$ is the electric flux density vector.

Finally, the electric field component:

$$E_z\left(m,n,p,k+\frac{1}{2}\right) = E_z\left(m,n,p,k-\frac{1}{2}\right) + \frac{c^2\Delta t}{\delta l}\left[B_y(m+n\ \ 1,p,k) - B_y(m,n-1,p,k) + B_x(m,n,p-1,k) - B_x(m,n,p+1,k)\right] \qquad (7)$$

$$E_x\left(m,n,p,k+\frac{1}{2}\right) = E_z\left(m,n,p,k-\frac{1}{2}\right) + \frac{c^2\Delta t}{\delta l}\left[B_z(m,n,p+\ \ 1;k) - B_z(m,n,p-1,k) + B_y(m-1,n,p,k) - B_y(m+1,n,p,k)\right] \qquad (8)$$

$$E_y\left(m,n,p,k+\frac{1}{2}\right) = E_y\left(m,n,p,k-\frac{1}{2}\right) + \frac{c^2\Delta t}{\delta l}\left[\ B_x(m+1,n,p,k) - B_x(m-1,n,p,k) + B_z(m,n-1,p,k) - B_z(m,n+1,p,k)\right] \qquad (9)$$

Thus, the electric field is calculated at instant $(k+1/2)$ taking into account the electric field at instant $(k-1/2)$.

In order to avoid numerical instabilities, the time increment should be bounded by the grid size values. A typical choice of Δt is $\Delta t \leq \Delta l / 2c$ and $\Delta l < \lambda e$ where λe is the wavelength.

The obtained results by the hybrid method using the MTL model; example shown in Table.2 is shown in figures 2 and 3.

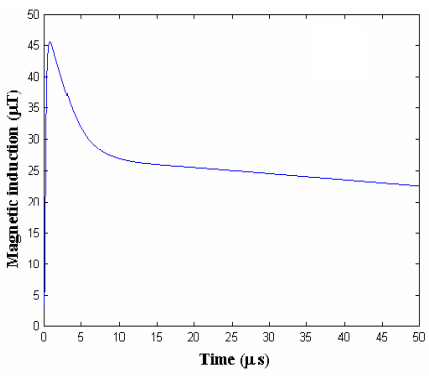


Fig. 2 The magnetic field at 50 m from a lightning return stroke

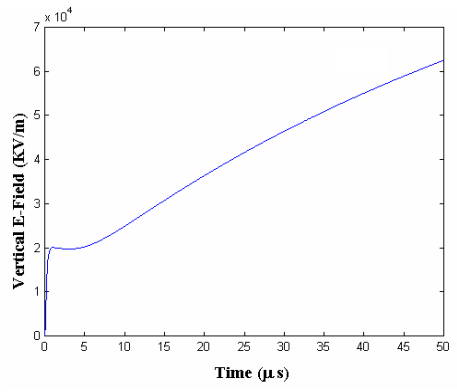


Fig. 3 The electric field at 50 m from a lightning return stroke

V THE VOLTAGE INDUCTION ON AN OVERHEAD LINE ACCORDING TO AGRAWAL MODEL

Starting from Maxwell's equations and adopting the transmission line assumption, it is possible to derive a pair of equations describing the coupling of an external electromagnetic field and a single conductor line. These equations can be written in different equivalent formulations. The formulation we adopt in this paper is the one proposed by Agrawal and al. The Agrawal model is expressed by the following equations (see Figs. 4 and 5 for the parameter definition) for which the case of a lossless line, is given by:

$$\frac{\partial u^s(x,t)}{\partial x} + L' \frac{\partial i(x,t)}{\partial t} = E_x^i(x,h,t) \qquad (10)$$

$$\frac{\partial i(x,t)}{\partial x} + C' \frac{\partial u^s(x,t)}{\partial t} = 0 \qquad (11)$$

In which:

$i(x,t)$ is the induced current;

L' and C' are respectively the inductance and the capacitance per unit length of the line;

$E_x^i(x,h,t)$ is the horizontal component of the incident electric field along the x axis at the conductor's height h;

$$u^s(x,t) = -\int_0^h E_z^s(x,z,t)dz \qquad (12)$$

Where $E_z^s(x,z,t)$ is the vertical component of the scattered electric field. The scattered voltage is related to the total line voltage $u(x,t)$ by the following expression

$$u(x,t) = u^s(x,t) + u^i(x,t) \qquad (13)$$

$i(x,t)$ is the induced current;

L' and C' are respectively the inductance and the capacitance

$u^s(x,t)$ is the scattered voltage, related to the induced voltage $u(x,t)$, by the following expression:

The boundary conditions for the scattered voltage are :

$$u^s(0,t) \quad -R_0(0,t) + u^i(0,t) \qquad (14)$$

$$u^s(L,t) \quad -R_L(L,t) + u^i(L,t) \qquad (15)$$

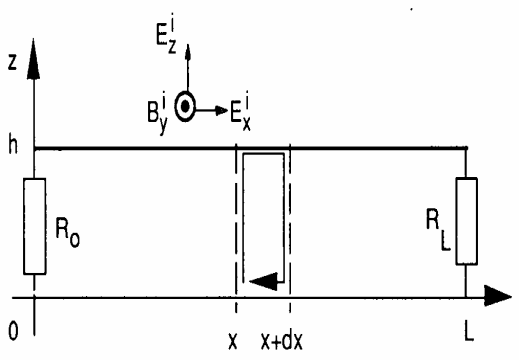


Fig. 4 Geometry used for the calculation of overvoltages induced on an overhead power line by an indirect lightning return-stroke

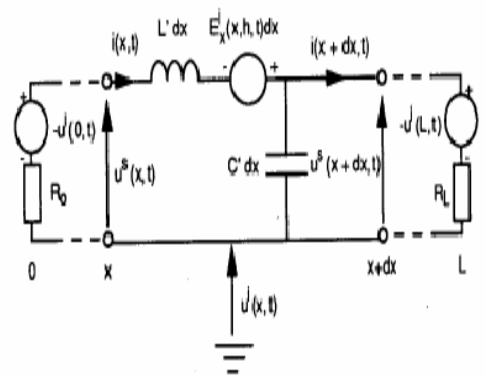


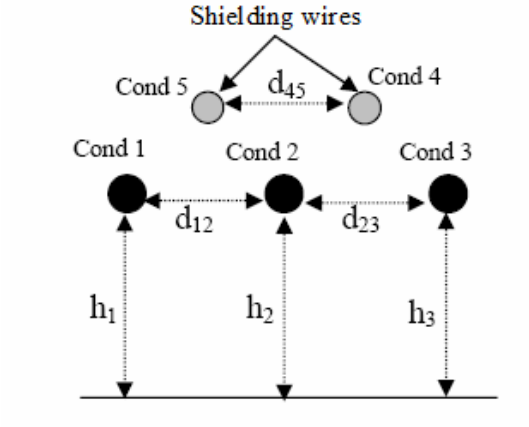
Fig. 5 Differential equivalent coupling circuit according to the Agrawal and al. for a lossless single wire overhead line

VI SIMULATED RESULTS

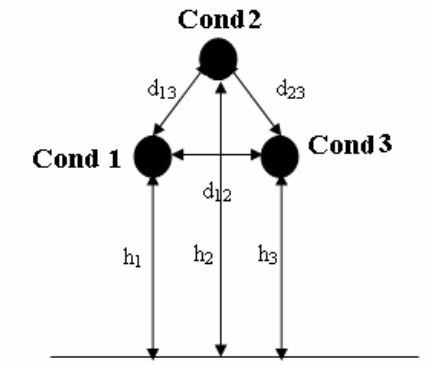
A. Influence of the line configuration

We consider now three phase line in two configurations: horizontal configuration and triangular configuration as shown in Fig.6 where their geometric parameters are listed in Table 3. For the calculation of the electromagnetic field, the channel-base current (peak value of 12 kA as shown in Fig.1and a maximum front-steepness of 40 kA / μ s), and input it to the modified transmission line with exponential decay (MTLE) model, assuming the ground as a perfect conductor and return- stroke a velocity of $1.3*10^8$ m/s.

In this paper the hybrid method composed of the Simpson method and the FDTD method is applied for the calculation of the electromagnetic field. Fig.7 represents the induced voltage on an overhead three phases lines for the horizontal and triangular configuration without the shielding wires.



a- Horizontal configuration

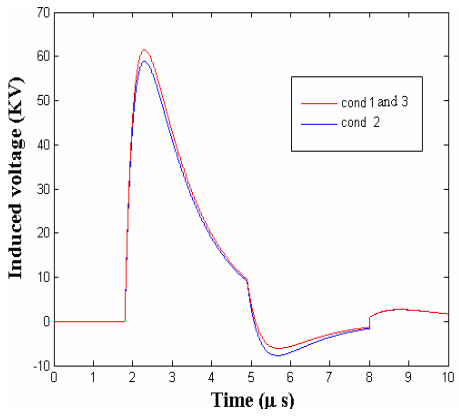


b- Triangular configuration

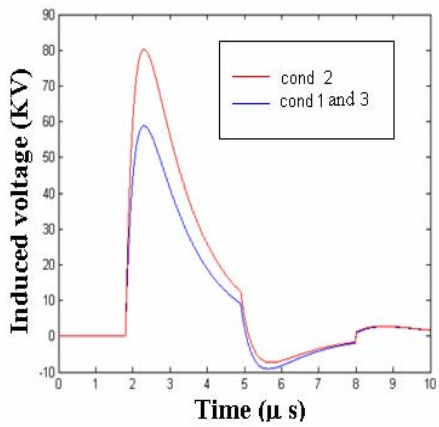
Fig.6 Different configurations of three phases lines

Table 3: Geometrical parameters of three phases lines for horizontal and triangular configurations [13]

Line Parameters	Horizontal configuration	triangular configuration
Conductor radius (mm)	9.14	9.14
h_1 (m)	10	10
h_2 (m)	10	13.7
h_3 (m)	10	10
d_{12} (m)	3.7	4.14
d_{23} (m)	3.7	4.14
d_{31}(m)	7.4	3.7
Shielding wire radius (mm)	3.96	-
h_4 (m)	13.05	-
h_5 (m)	13.05	-
d_{45}(m)	3.7	-



a- Horizontal configuration



b- Triangular configuration

Fig.7 Induced voltage on an overhead three phase line

B. Influence of the shielding wire

In order to illustrate the effect of the shielding wire (the 4th & 5th conductors for the horizontal configuration) we have considered the three phases lines with the shielding wire, the induced voltage is illustrated in Fig.8.

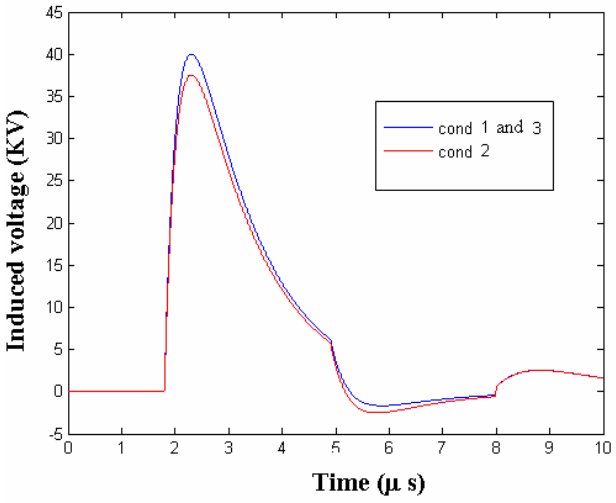


Fig. 8 Induced voltage on an overhead a three phases lines with a shielding wire
Horizontal configuration

VII CONCLUSION

The hybrid method which is a combination between a Simpson method and FDTD method was presented initially in this paper. The hybrid approach makes a good alternative for the calculation of the nearest electromagnetic field radiated by the lightning channel since it allows the calculation of the electric field by the FDTD method without concern of the memory problems and the calculation precision. It depends only on a good choice of the calculation steps.
The induced voltage on overhead three phases lines was evaluated. We have considered two configurations of three phases lines: horizontal configuration and triangular configuration without shielding wire. We can observe that the horizontal configuration the induced voltage is less than the triangular configuration because the conductor 3 (triangular configuration) is higher than the conductors 1 and 2 (horizontal configuration).
We can observe that the presence of the shielding wires reduce the induced voltage.

REFERENCES

[1] Yoshihiro Baba, Satoru Miyazaki, and Masaru Ishii "Reproduction of Lightning Electomagnetic Field Waveforms by Engineering Model of Return Stroke", IEEE Trans. Electromagn. Compat, Vol 46, N° 1, pp 130-133, Feb 2004.
[2] Chunshan Yang and Bihua Zhou "Calculation Methods of Electromagnetic Fields Very Close to Lightning", IEEE Trans. Electromagn. Compat, Vol 46, N° 1,pp 133-141, Feb 2004.
[3] C. A. Nucci, G. Diendorfer, M. A. Uman, F. Rachidi, M. Ianoz, and C. Mazzetti, "Lightning return stroke current models with specified channel-base current: A review and comparison," J. Geophys Res. vol. 95, pp. 20395–20408, Nov. 1990.
[4] M. A. Uman andD.K.McLain, "Magnetic field of lightning return stroke," J. Geophys. Res., vol. 74, pp. 6899–6910, 1969.
[5] F. Heidler, "Traveling current source model for LEMP calculation," presented at the 6th Symp. Tech. Exhib. Electromagn. Compat., Zurich, Switzerland, Mar. 5–7, 1985
[6] C. A. Nucci, C. Mazzetti, F. Rachidi, and M. Ianoz, "On lightning return stroke models for LEMP calculations," presented at the 19th Int. Conf. Lightning Protection, Graz, Austria, Apr. 1988.
[7] C. A. Nucci and F. Rachidi, "Experimental validation of a modification to the transmission line model for LEMP calculations," presented at the8th Int. Symp. Tech. Exhib. Electromagn. Compat., Zurich, Switzerland, 1989.

[8] V. A. Rakov and A. A. Dulzon, "A modified transmission line model for lightning return stroke field calculations," presented at the 9th Int. Symp. Tech. Exhib. Electromagn. Compat., Zurich, Switzerland, 1991.
[9] G. Diendorfer and M. A. Uman, "An improved return stroke model with specified channel-base current," J. Geophys. Res., vol. 95, no. D9,pp. 13621–13644, Aug. 1990.
[10] R. Thotappilil, D. K. McLain,M.A.Uman, andG.Diendorfer, "Extension of the Diendorfer–Uman lightning return stroke model to the case of a variable upward return stroke speed and a variable downward discharge current speed," J. Geophys. Res., vol. 96, no. D9, pp. 17143–17150, Sep. 1991.
[11] C. A. Nucci, "Lightning-induced voltages on overhead power lines. Part I: Return-stroke current models with specified channel-base current for the evaluation of the return-stroke electromagnetic fields," Electra, no. 161, pp. 75–102, Aug. 1995.
[12] V.A.Rakov, M.A. Uman, «Review and evaluation of lightning return stroke models including some aspects of their application », IEEE Transactions on Electromagnetic Compatibility, vol. 40, no. 4, pp. 403–426, Nov. 1998.
[13] Rachidi, "Effets électromagnétiques de la foudre sur les lignes de transmission aérienne, modélisation et simulation » Thèse de Doctorat, Ecole polytechnique Fédérale de Lausanne, 1991.
[14] C. Sartori, J. Cardoso "An analytical-FDTD method for near LEMP calculation", IEEE Transaction on magnetics, Vol. 36, n°4, pp. 1631-1634. july 2000.
[15] M. Rubenstein and M.A. Uman, "Transient electric and magnetic fields associated with establishing a finite electrostatic dipole, revised", Transaction on Electromagnetic Compatibility, Vol. 33, n°4, pp. 312-320. nov. 1991.
[16] M. N. O. Sadiku, "Numerical techniques in electromagnetics", Boca Ration, FL: CRC Press, 1992, ch. 3.
[17] C. Nucci, "Lightning-induced voltages on over head power lines", in Electra, pp. 74-102, 1995.

Electromagnetic Simulation of a Magnetically-Coupled ZOR on YIG Thin Film

Aziza Zermane[1,2], Bruno Sauviac[1], Bernard Bayard[1], Abdelmadjid Benghalia[2]

[1]Université de Lyon, F-69000, Lyon, France
Université de Saint Etienne, F-42000, Saint-Etienne, France
TELECOM Saint-Etienne, école associée de l'institut TELECOM
Laboratoire LT2C (Laboratoire Telecom Claude Chappe)

[2]Université Mentouri de Constantine, A-25000 Constantine, Algérie
Laboratoire LHS (Laboratoire des Hyperfréquences et Semi-conducteurs)

*corresponding author: zermaneaziza@yahoo.fr

Abstract

The objective of this work is to study numerically the behaviour of a magnetically-coupled zeroth order resonator (ZOR) realized on a YIG (Yttrium Iron Garnet) thin film. We are focusing on the effects on the resonant frequency and the insertion losses when changing the magnetic bias and the thickness of the YIG. This study presents for the first time a tunable ZOR with a coplanar structure designed on a YIG thin film. The proposed resonator is designed to be tuned over the 3.5-4.5 GHz frequency band; insertion loss is lower than 2dB and return loss is better than 10 dB. The length of the proposed device is 4.4 mm, which is very small compared to a traditional half wave resonator.

1. Introduction

The concept of the Composite Right-Handed Transmission Line (line with traditional propagation) and Left-Handed Transmission Line (line having a negative phase velocity) was proposed by UCLA group [1]. An equivalent circuit approach was also developed by Eleftheriades and al [2]. This approach takes into account the parasitic Right-Handed (RH) effects naturally occurring in a practical Left-Handed (LH) structure. So the CRLH notation (Composite Right Left Handed) is more general than the LH notation. The CRLH approach describes in a simple manner the fundamentally right-handed and left-handed nature of metamaterials [3, 1].

The first zeroth-order resonator (ZOR) is proposed by Sanada and al [4]; it is realized in microstrip configuration. Based on the proposed unit cell, a practical application is realized for antennas [5]. A coplanar waveguide (CPW) have the advantage that line and ground are located in the same plane, and it can be easily fabricated at low cost by using a simple lithography process. Some researchers studied and realized zeroth-order resonators in a coplanar waveguide technology [6, 7, 8].

Recently, ferrite materials have been used in metamaterials and in meta-line too. Tsutsumi and Abdalla proposed a non-reciprocal left-handed transmission line in microstrip and in coplanar waveguide configurations with a ferrite substrate [9, 10]. All of them employed a bulk ferrite. Our objective is to prove that it is possible to make a tunable CRLH ZOR with a 20µm ferrite film only. As the manufacturing process developed in LT2C laboratory allows making YIG thin films, then it will be possible for us to prospect for collective fabrication in order to reduce the production costs.

2. Theory

Zeroth-order resonator (ZOR) is one of the very interesting applications of metamaterials [1]. The interest lies in the fact that the resonant frequency is independent from the physical length of the resonator. Due to metamaterials properties, negative and zero resonances are possible. The proposed resonator is designed in coplanar waveguide configuration realised using an interdigital capacitor (IDC) and a short-circuited stub inductor (SSI).

The ferrite substrate has a relative dielectric permittivity close to 15, a saturation magnetization equal to M_s =1780 Gauss and a ferromagnetic resonance (FMR) line width ΔH=20 Oe. It is supposed to be saturated and the internal bias field is supposed to be uniform. In this work our magnetic layer is magnetized in a direction perpendicular to the propagation direction (figure 1(b)).

The physical parameters of our resonator and the theoretical developments used for modelling were presented in reference [4].

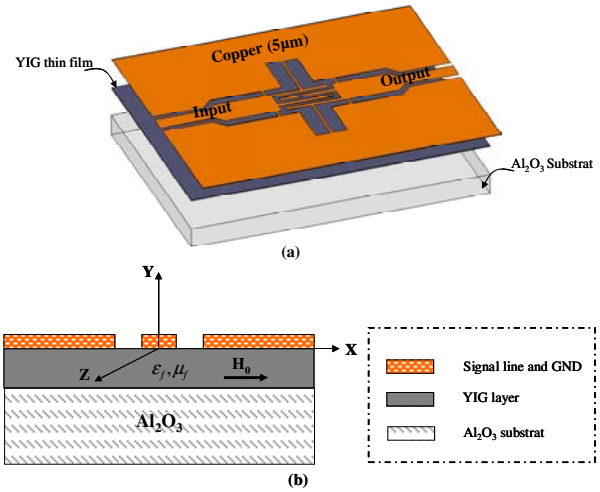


Figure 1: Physical configuration of the magnetically-coupled ZOR, (b): in Cross section.

As the material is supposed to be saturated, the ferrite is modeled using Polder's tensor. According to the direction of the DC magnetic bias presented in the previous figure, the permeability tensor has the following form:

$$[\overline{\overline{\mu_f}}] = \begin{bmatrix} 1 & 0 & 0 \\ 0 & \mu_f & +jk \\ 0 & -jk & \mu_f \end{bmatrix}, \quad (1)$$

The elements of the permeability tensor depend on the frequency:

$$\mu_f = 1 + \frac{\omega_0 \omega_M}{\omega_0^2 - \omega^2}, \quad (2)$$

$$k = \frac{\omega \omega_M}{\omega_0^2 - \omega^2}, \quad (3)$$

Where

$$_M = \gamma \mu_0 M_S, \quad _0 = \gamma \mu_0 H_0$$

and $\gamma = 176 \quad 10^9 \; rad\, S^{-1} \quad T^{-1} \qquad (\Leftrightarrow 28GHz/T)$

3. Numerical results

The results which enabled us to launch manufacture thereafter were obtained starting from 3D electromagnetic simulations. For example, we present the results obtained from a structure using 20µm YIG layer thickness only. In the case of the applied field of 250kA/m, the resonant frequency is equal to 3.67GHz, at this frequency the insertion loss is about 1.8dB. We observe that the phase of transmission coefficient is close to zero near the resonant frequency (figure 2).

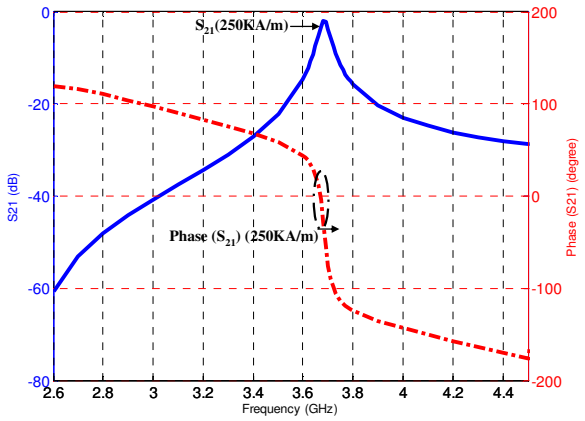


Figure 2: Transmission characteristics and the phase of S_{21} of the resonator under H_0=250kA/m.

To show the tunable property of the proposed CRLH CPW ZOR, our resonator has been analyzed numerically for different values of DC magnetic bias. The results obtained are shown in figure 3. We observe that the resonant frequency varies with applied field. This is a very interesting result, especially because of the thickness of ferrite which is 20µm only.

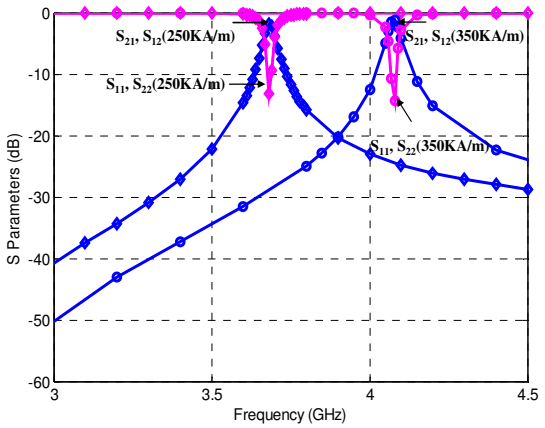


Figure 3: Transmission characteristics of resonator at H_0=250kA/m and H_0=350kA/m.

Now it is proposed to vary the thickness of YIG (h_f) and observe the influence of this parameter to the frequency response of the resonator for the same value of applied magnetic field.

Structures with different thicknesses of ferrite 40, 60, 80 and 100 microns were simulated with HFSS. These structures were polarized by a magnetic field of about 150 kA/m.
Figure 4 shows the performance of the resonator according to the thickness of the magnetic layer (YIG).

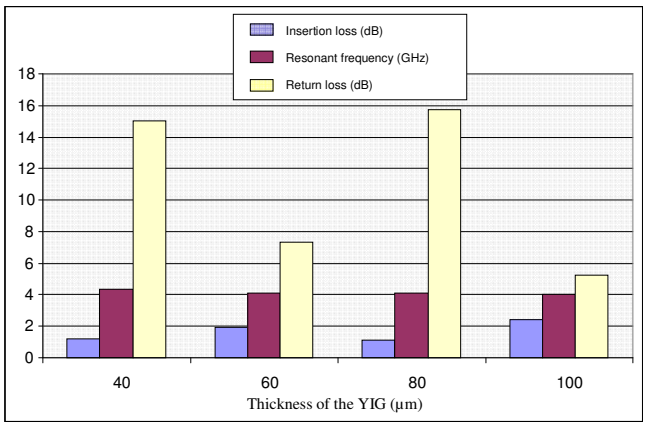


Figure 4: Performance of the inductively-coupled zero-order resonator according to the YIG thickness.

We note that the resonant frequency slightly decreases when the thickness of the magnetic layer increases from 40 to 100 µm. The values of insertion loss and reflection have a non-regular variation in a structure to another. Values of return loss show that the structure is not perfectly matched - in all cases - and that the input impedance depends on the thickness of the magnetic film. Considering this approximate matching, the level of insertion losses is very interesting. The value is indeed less than 2 dB and do not increase when the thickness is low (as it can be seen in other magnetic planar device like isolators or circulators).
In conclusion, we can say that it is feasible to realize a tuned magnetically-coupled composite right/left handed resonator with a YIG thin film, and moreover that this structure is promising.

4. Conclusions

A CRLH CPW ZOR on the YIG thin film has been studied numerically using a three dimensional electromagnetic simulation. The tunable propriety has been validated numerically for the magnetically-coupled line CRLH CPW ZOR with a 20µm ferrite film only. This result shows the possibility of modifying the agreement of the device by an external intervention (magnetic field). Moreover, the level of insertion loss in the device is promising, considering the presence of the ferrite. The proposed device can be applied in many filters, for example when multiband devices are necessary.

References

[1] C. Caloz, A. Sanada, T. Itoh, Microwave circuits based on negative refraction index material structures, *33rd European Microwave Conference, Munich,* pp. 105–110, 2003.

[2] G.V. Eleftheriades, A.K. Iyer, P.C. Kremer, Microwave Planar negative refractive index media using periodically L-C loaded transmission lines, *IEEE. Trans. Microw. Theory Tech* 50: 2702–2712, 2002.

[3] C. Caloz, A. Sanada, T. Itoh, Microwave applications of transmission-line based negative refractive index structures, *Microwave Conference, Asia Pacific ,* 2003.

[4] A. Sanada, C. Caloz, T. Itoh, Novel zeroth-order resonance in composite right/left-handed transmission line resonators, *Microwave Conference, Asia Pacific,* 2003.

[5] C. Caloz, T. Itoh, A. Renning, CRLH metamaterial leaky-wave and resonant antennas, *IEEE. Antennas and Propagation Magasing* 50: 25–39, 2008.

[6] A. Zermane, B. Sauviac, B. Bayard, B. Payet-Gervy, J.J. Rouseau and A. Benghalia, Modeling and measurement of a zeroth-order-resonator and a composite right-left-handed transmission line in coplanar technology, *Progress In Electromagnetic Research C,* 14: 33–43, 2010.

[7] C. Li, K.Y. Liu, F. Li, Modeling and measurement of a zeroth-order-resonator and a composite right-left-handed transmission line Analysis of composite right/left-handed coplanar waveguide zeroth-order resonators with application to a band-pass filter in coplanar technology, *PIERS Online,* 3: 599–602, 2007.

[8] L. Li, D. Uttamchandani, Demonstration of tunable RF MEMS bandpass filter using silicon foundry process, *Journal of Electromagnetic Wave and Application* 23: 405–413, 2009.

[9] M. Tsutsumi, T. Ueda, Nonreciprocal left-handed microstrip lines using ferrite substrate, *IEEE. MTT-S Int. Microwave Sym. Dig* 1: 249–252, 2004.

[10] M. Abdalla, Z. Hu, Nonreciprocal left-handed coplanar waveguide on ferrite substrate with only shunt inductive load, *Proceeding of Metamaterials*, 2007.

Electromagnetic compatibility in hospitals for electromedical equipment and personal communication systems

S. de Miguel[1], M.A. Martín[2], J. del Pozo[1], V. Febles[2], J. García[1], D. S. Suárez[2], J.C. Fernández de Aldecoa[2], V. Ramos[1]

[1]Telemedicine and eHealth Research Unit, Health Institute Carlos III (ISCIII), Madrid, Spain
[2]Engineering Subdepartment, Canary University Hospital Consortium, La Laguna (Tenerife), Spain
*corresponding author, E-mail: sdemiguel@isciii.es

Abstract

This paper analyzes the signals of the different wireless communications systems in a healthcare center, the Canary University Hospital Consortium (CUHC), in order to evaluate the electromagnetic (EM) conditions. The results of the assessment are represented through 2D contour maps. The proposed graph survey aims to provide a methodology of studying the electromagnetic environments that could help in the design of healthcare centers, in the installation of new radiofrequency systems based on wireless technology, or in the evaluation of the safety conditions of workers, patients, and people in general.

1. Introduction

A large hospital currently presents a great variety of wireless telecommunications systems that generate electromagnetic (EM) fields with different features and intensities. These systems range from medical equipment with telemetry systems to the usual wireless communication systems, such as healthcare professional tracking devices (pagers), terrestrial trunked radio (TETRA), digital enhanced cordless telecommunications (DECT), wireless local area networks (WLAN), and conventional mobile phones.

An important issue to consider when a new wireless system or a new electrical device is being installed in a healthcare center is to identify the main radiation sources and predict the intensity of the EM fields. A high level signal can compromise the safety conditions of people in hospitals, and can affect the proper working of the communication systems and the sensitive medical devices. The safety in hospitals must be compatible with the requirements of coverage and quality of service of the communication systems and the sensitive medical devices.

There are two aspects that should be analyzed and considered to assure a proper, reliable and safe usage of the wireless communication technologies and medical equipment in healthcare environments. The first is the compatibility and possible interferences between the different types of signals that share the same transmission band [1]. The second is the compliance with exposure level thresholds [2], to quantify and analyze the risk of continued exposure caused by the use of wireless technologies [3, 4]. Due to the potential health effects of EM radiation; various studies delve into the consequences of the exposure to wireless communication devices [5].

On the other hand, the contribution of certain medical devices must also be considered. Medical devices can generate EM fields that disrupt the radio environment of hospital areas where they are located. It is also possible that in certain areas of the healthcare center, high frequency signals are detected as a result of pollution caused by broadcast commercial radio stations or communications systems that use commonly used frequency bands (walkie-talkies, radio ham or broadcast of security forces and civil protection), in addition to those received by mobile operator base stations.

Nowadays there are an increasing number of sensor networks and personal medical devices in healthcare environments that have to coexist with a considerable range of wireless communication systems. These devices work in wireless channels and are vulnerable to malicious attacks, as a result, personal and control information could be intercepted, harming the health of the patient.

The study of EM conditions in the range of personal communication frequencies assures the proper and secure working of implantable devices and sensor networks, avoiding malfunction.

Large hospitals, especially if they are not new, generally consist of several old buildings of different nature and constructive characteristics. Thus, it is difficult to establish standards for EM fields measurements, even different areas of the hospitals are dedicated to the same health-care activities and similar electro-medical equipment are used.

This paper analyzes the signals of the different wireless communications systems in two floors of the Canary University Hospital Consortium (CUHC), and presents a methodology for the generation of 2D contour maps that provide a graphical, immediate and accurate representation of the EM fields.

This work aims to provide a global and immediate overview through 2D contour maps in order to assure the compliance with the exposure levels to EM fields. As a possible tool, the proposed methodology can be used to analyze and study health and safety conditions, and the EM compatibility in healthcare environments. As a consequence, improvements can be performed to encourage and guarantee a better level of protection for the health and safety of workers patients, and people in general.

2. Methods and materials

The measurements have been carried out using a Rhode & Schwartz FSH6 spectrum analyzer and a Rhode & Schwartz HL040 log periodic antenna.
The spectrum analyzer allows measurements of the electric field, and the characterization, identification and monitoring of the signals in the environment under study. This model of the spectrum analyzer has the following characteristics:

- Frequency range: from 100 kHz to 6 GHz.
- Detection limits: –120 dBm to +20 dBm.
- Resolution bandwith: 100 Hz to 1 MHz.



Figure 1: R&S FSH6 Spectrum Analyzer

The HL040 log periodic antenna is a directive antenna that allows the identification of the radiation sources and collect data in the direction of maximum radiation.
The antenna presents the following features:

- Frequency range: from 400 MHz to 3.6 GHz.
- Polarization linear.
- Gain: 5 dBi to 7 dBi.



Figure 2: Spectrum Analyzer and log periodic antenna

The values of the electric field strength have been measured in the points of the 9th and 10th floors belonging to a predefined grid. These points have been selected in function of several factors: the position of the radiation sources, the location of the medical devices, the type of activities performed, etc. Figure 3 is the map of each floor, obtained with AUTOCAD software, where the points of measure are marked.

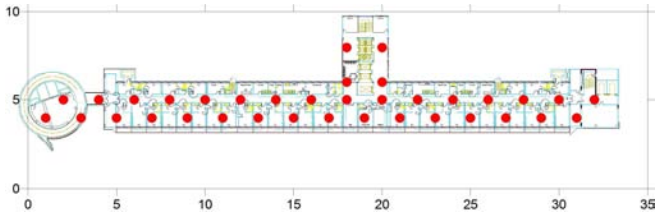


Figure 3: Map of each floor and measuring points.

The length of each floor is 35 meters, and a grid of 5 x 5 m^2 is set. The measurements have been carried out in the vertices of each square that belongs to the grid.
The floors 9th and 10th have been considered because they are the most exposed to the radiation sources. These floors are just below the 11th floor where the radiation sources of the short range communication systems are situated.
The 9th floor is dedicated to surgery and neurology, and the 10th floor is the unit for infectious patients and is also dedicated to digestive specialization.
Systematic measurements have been performed on two floors for four different frequencies:

- 900 MHz, the Global System for Mobile Communications (GSM) frequency band,
- 1800 MHz, the Digital Cellular Service (DCS) frequency band,
- 2.14 GHz, the Universal Mobile Telecommunications System (UMTS) frequency band,
- 2.42 GHz, the common Wi-Fi frequency.

The radiation sources for personal communications, such as mobile phone antennas, and Wi-Fi access points, are the main elements that have to be considered in calculating the electric field strength. A global view of the building and the main antennas of mobile telephony, the FM commercial radio, and short range mobile communication systems can be observed in Figure4.



Figure 4: Location of the antennas around the hospital

For the mobile phone frequencies (900 MHz, 1800 MHz and 2,14 GHz), the first step is to define exactly where the antennas are situated around the hospital [6]. The map as follows shows the frequencies and the position of the mobile phone antennas regarded:



Figure 5: Position of the mobile phone antennas around the hospital.

Regarding the short range communications systems, the Wi-Fi system has been analysed. To measure the electromagnetic conditions for Wi-Fi frequency the location of the access point must be known.

The radiation sources for short range communications systems (pager, TETRA, and Wi-Fi) are situated on the roof of the building, so the higher floor is the most exposed to the radiation for these frequencies. The next figure shows the location of the access point on the roof of the building:

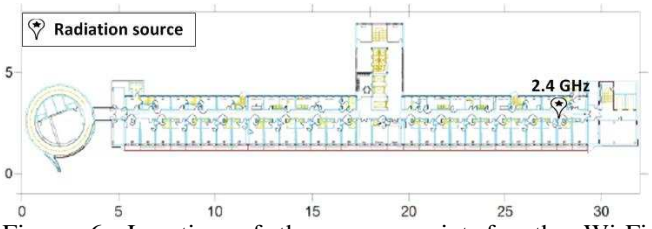


Figure 6: Location of the access point for the Wi-Fi frequency.

Data collected were transferred to the graphic software Surfer 10 to draw 2D contour maps. Surfer is a contouring and 3D surface mapping program that runs under Microsoft Windows. The software allows the representation of the input data through different types of maps including contour, vector, wireframe, image, shaded relief, and surface maps. This program displays maps over any contour range and interval, and specifies the contour levels and contour line properties on the map. Surfer maps allow the usage of different colours to represent different electric field levels.

3. Results

Table 1 and Table2 present schematically the most common statistical values of the results of the measurements: the minimum, maximum values, the mean, and the standard deviation.

Table 1: Summary of the experimental results of the electric field on the 9th floor.

dBµV/m	900 MHz	1,8 GHz	2,14 GHz	2,42 GHz
Mín.	73.59	68.84	69.47	70.52
Máx.	109.42	97.46	93.33	80.03
Mean	89.22	79.59	81.19	72.95
Std.	9.11	7.68	7.44	2.29

Table 2: Summary of the experimental results of the electric field on the 10th floor.

dBµV/m	900 MHz	1,8 GHz	2,14 GHz	2,42 GHz
Mín.	77.61	67.78	69.07	63.79
Máx.	99.83	97.50	95.49	80.15
Mean	86.85	78.63	78.93	72.27
Std.	7.65	7.92	7.70	2.85

Figure7 shows the 2D contour map of the data set in each floor, and the location of the access point of the Wi-Fi frequency. The graphs of Figure7 have been obtained with Surfer software.

A characteristic feature for all the graphs of Figure7, is a local increase of the electric field strength that matches with the location of the lift and the stairs. In these areas there is a greater exposure to the EM radiation than the rest of the points of the same floor.

4. Discussion

After measuring and calculating the EM conditions in these areas of the hospital, it is quite important to carry out a study of the results and to check if the obtained values are under the thresholds of the recommended exposure levels.

International and national bodies have set different limit values for permissible electromagnetic radiation levels in various standards and regulations.

The obtained EM levels are below the security threshold stated by ICNIRP-98 [7]. It means electric field levels in healthcare environments are apparently safe according with the health and safety requirements regarding the exposure of patients, staff and general public to the risks arising from electromagnetic fields.

The lower and more restrictive value of these thresholds is 3 V/m, in compliance with the International Electrotechnical Commission Standard of Electromedical Devices [1]. Examining the experimental and simulation results, the maximum value of the electric field for all the analyzed frequencies is much lower than the 3 V/m.

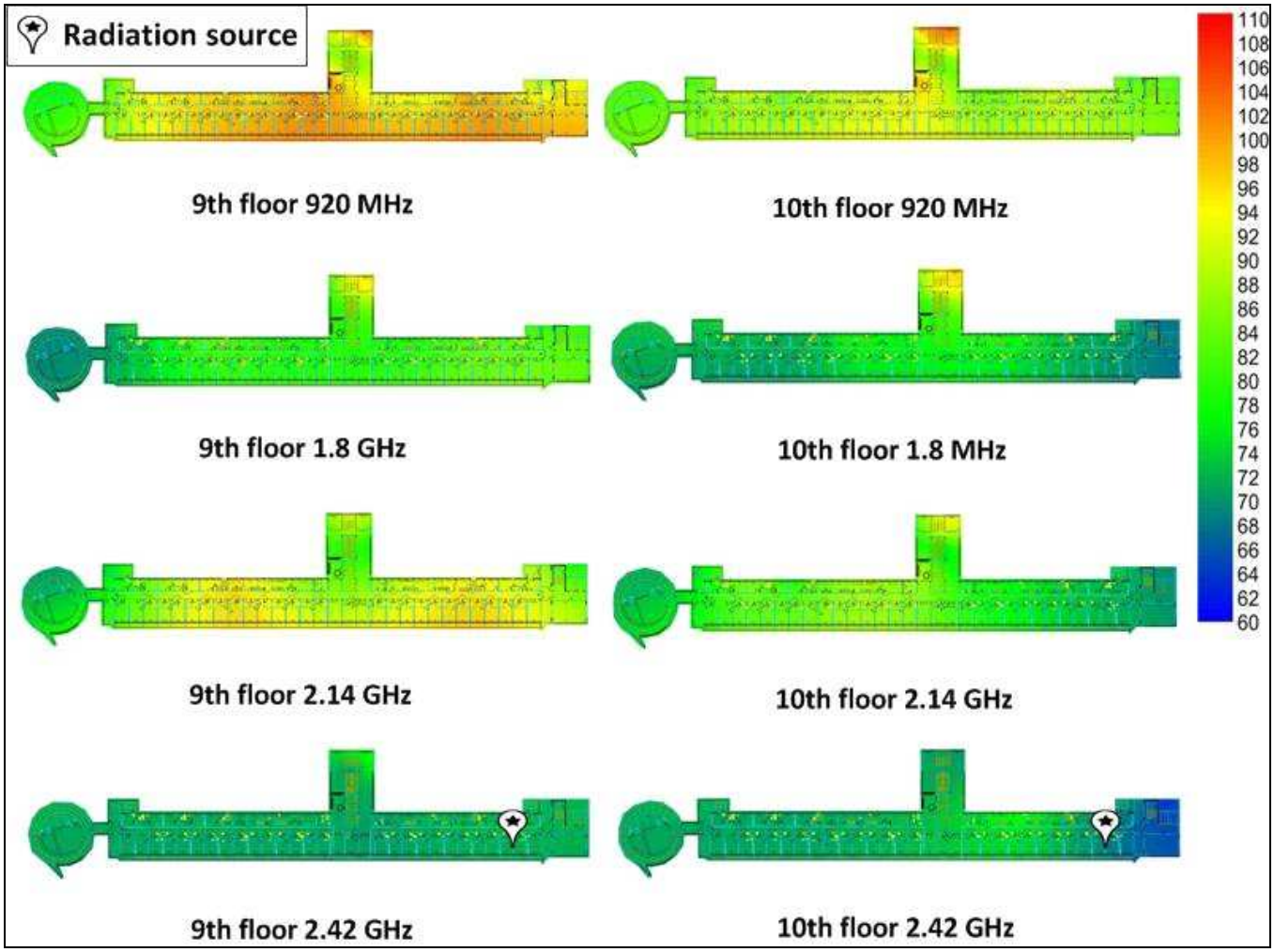


Figure7: 2D contour maps of the experimental values of the electric field (dBμV/m)

5. Conclusions

The proposed procedure is useful to compare the obtained results (Table1 and Table2) with the thresholds of the recommended exposure levels [7], and the thresholds for the safety and basic performance of the electromedical equipment [1]. The maximum value obtained is much lower than the more restrictive threshold that is established in the International Electrotechnical Commission Standard of Electromedical Devices [1].

The computation of 2D contour maps of EM fields in a healthcare center provides a global, immediate and accurate vision that can help to avoid EM interferences on electro medical equipment, and monitor the exposure to EM fields of the staff, the patients and the general public. This basic premise should be compatible with a sufficient signal level in wireless systems operating in a healthcare center.

The analysis and study of EM conditions in a healthcare environment using 2D contour maps could be helpful for the following purposes:

- To detect the over-exposed points to electromagnetic radiation and areas with greater absorption levels.
- To avoid potential harm to patients due to the interferences on electromedical equipment and on implantable personal devices.
- To achieve emission levels under of the recommended thresholds, but enough to assure a proper quality of service of wireless communication systems.
- To plan and design new high-tech healthcare centers.
- To monitor properly the exposure to electromagnetic fields of health staff, patients and the general public.

Acknowledgments

This work was supported by the project "Electromagnetic Safety and Protection of Patients", DGPY 1445/08 (PI08/90185), belonging to the National Plan of Research Development and Innovation 2008-2011.

References

[1] International Electrothecnical Commission (IEC) Standard IEC 60601-1-2 Electromedical devices. 2007.

[2] Directive 2008/46/EC of the European Parliament and the Council of 23 April 2008 amending Directive 2004/40/EC on minimum health and safety requirements regarding the exposure of workers to the risks arising from physical agents (electromagnetic fields). Off J Eur Union 2008, L114/88.

[3] N. Carranza, V. Febles, J. A. HernÁndez, J. L. Bardasano, J. L. Monteagudo, J. C. Fernández de Aldecoa and V. Ramos, "Patient safety and electromagnetic protection: a review," Health Phys, Vol. 100, No. 5, 530-541, 2011.

[4] N. Carranza, J. García, V.M. Febles, J.C. Fernández de Aldecoa, J.L. Monteagudo and V. Ramos, "Evaluation of electromagnetic compatibility and safety assessment in healthcare environments," VIII International Symposium and Exhibition On Electromagnetic Compatibility and Electromagnetic Ecology, San Petersburg , Russia, June 2009, 253-256.

[5] Carranza N, Febles V, Hernandez JA, Bardasano JL, Monteagudo JL, Fernández de Aldecoa JC, Ramos V, "Patient safety and electromagnetic protection: a review", Health Physics 100(5):530-541; 2011.

[6] Information service of radioelectric installations and exposure level: http://geoportal.mityc.es/visorCartografico/index.jsp. Last access in December 2010.

[7] ICNIRP (1998) Guidelines for limiting exposure to protection time-varying electric, magnetic and electromagnetic fields (up to 300 GHz). International Commission on Non-Ionizing Radiation.

Design and Calibration of a Wideband TEM-Cell for Material Characterization

SK Yee1[1], A Kazemipour2[2], A. Sayegh[3], MZ Mohd Jenu[4]

[1,2,3,4]Center for Electromagnetic Compatibility, Faculty of Electrical and Electronic Engineering, Universiti Tun Hussein Onn Malaysia
*corresponding author, E-mail: skyee@uthm.edu.my

Abstract

A wideband TEM cell which is operated based on transmission/reflection method is designed for dielectric measurement. It is operated in between 50MHz – 800MHz. This cell is compact, easy to fabricate and useful for measuring porous samples such as concrete. The classic dielectric measurement set-up is usually based on rectangular TE_{10}-mode waveguides which become very large, expensive and non-practical for lower frequencies. As for a classic coaxial cell, the electromagnetic field is not uniform and it is difficult to obtain sample in toroidal shape in coaxial cells. These problems are overcome using this proposed TEM-cell. Wideband matching is obtained using a coaxial to waveguide connector based on a tapering technique. A specific calibration is used and the complex permittivity and permeability are calculated from the measured S-parameters. Preliminary experimental results are presented.

1. Introduction

Dielectric properties measurement at microwave frequencies is required to illustrate how electromagnetic waves propagate through materials [1]. Various methods have been used for the measurement of dielectric properties [2], including both time and frequency domain methods.

The existing systems are mainly based on coaxial probes, free space, transmission/reflection methods using waveguide or coaxial cells and resonance techniques [3]. Waveguide has the advantage of high power handling capability and low loss but it requires the sample to be machined out to fit the cross section of the waveguide. A waveguide with specific dimensions can only be used for dielectric measurements in a narrowband of the frequency range. Practically waveguides are not appropriate for lower frequencies due to the large size.

The coaxial line technique is wideband enough but is not easy for dielectric measurements of heavy and porous materials such as concrete because the specimen need to be in a toroidal shape which is hard to achieve. Besides that it does not provide a uniform electromagnetic (EM) wave.

In the resonant techniques, the amount of frequency shift in the resonant mode of the cavity determines the dielectric properties of the specimen. The disadvantage of this method is that the measurements cannot be carried out over a range of frequencies without changing the cavity dimensions.

In the free space method a perfect normal plane wave is hard to achieve and the diffraction effect of the sample edges cannot be avoided.

In this paper, a novel wideband TEM-cell based on a parallel plate is presented, suitable for the transmission/reflection method. A specimen of dielectric material is put between two parallel plates. The scattering parameters (S-parameters) of the two port line are measured using avector network analyzer. Complex permittivity and permeability can be determined from the measured S-parameters using the Nicolson-Ross-Weir (NRW) method [4]. Section 2 describes the design of the parallel plate cell. Before directly apply the NRW conversion, a specific calibration as described in Section 3 will be executed. For better illustration, the experimental setup of the dielectric measurement is shown in Section 4. In order to validate the functionality of the wideband TEM-cell, the dielectric properties of Teflon is measured and shown in Section 5.

2. Parallel Plate Cell Design

The wideband TEM cell is optimized to operate from 50MHz up to 800MHz. This cell is design to be large enough to immerse the sample between the two plates [5]. The width, w and distance between the two plates, d are set to 10.6cm and 2cm respectively to achieve a characteristic impedance approximate to 50ohm in free space. At first the values are calculated based on eq. (1) [6] which are valid in an ideal situation where the fringing field can be neglected. It is then further optimized in CST MICROWAVE STUDIO®

$$Z_{plate} = \frac{V}{I} = \frac{\eta d}{w} \tag{1}$$

where V is the voltage of the top plate with respect to bottom plate, I is the total current on the top plate, η is the intrinsic impedance of the medium between the parallel plate, d is the separation distance between the two plates and w is the width of both the two plates.

The cell is connected to a network analyzer through an N-type coaxial port. The coaxial port is designed so that it produces 50ohm impedance. Its characteristic impedance can be calculated based on.

$$Z_o = \frac{\eta}{2\pi} \ln(\frac{b}{a}) \tag{2}$$

where Z_0 is the characteristic impedance of the connector medium, and a and b represent the radius of inner conductor and outer conductor respectively.

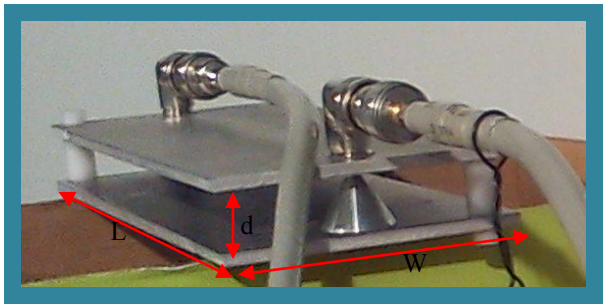


Figure 1: Fabricated wideband TEM cell

The highlight of the cell is the inner conductor of input coaxial line which is extended in form of conical shape [5] in order to achieve wideband.

The cell is machined out of aluminium plate and two halves are held together by two plastic screws. This cell provides an easy way to remove and insert the sample.

The design of the cell is similar as the design of a classical parallel plate capacitor [7]. However the operating concept behind both structures (wideband TEM cell and parallel plate capacitor) is totally different.

In the parallel plate capacitor method, the plates are connected to the network analyzer to measure its capacitance. Parallel plate capacitor model is proposed in the work to relate the capacitance to the material sandwiched in between two parallel plates [7]. This method cannot be used to calculate the relative permeability of the material moreover the operating frequency of the model is much lower, which is below 40MHz.

On the other hand, the wideband TEM cell proposed here works at frequencies which is much higher (50MHz to 800MHz). The relative permittivity and relative permeability of the material are calculated based on the application of NRW conversion.

3. Specific Calibration

NRW is widely used to convert the S-parameters to their associated relative permittivity and relative permeability [8]. This technique, it requires the calibration plane to be on the surface of the dielectric material as shown in Fig. 3. However in this cell, it is difficult to have the calibration plane on the surface of the dielectric material because of its open-structure. Hence in order to obtain the S^B-parameter, the cell is modelled as 3 sections. The transmission matrix of sections A, B and C will be cascaded together to reach the overall S-matrix which can be measured in the experiment [9]. The S-matrices for sections A and C will be deduced based on the measurement when the dielectric is removed.

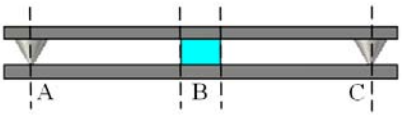


Figure 2: Cross section of the TEM parallel plate cell when the dielectric is inserted at the centre of the cell.

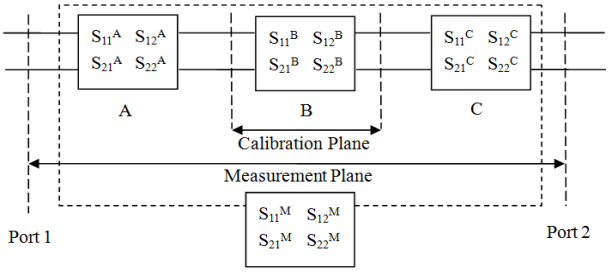


Figure 3: The parallel plate cell model is illustrated as 3 cascaded networks.

4. Measurement System Set up

In order to validate the functionality of the cell, Teflon is used as the first specimen. It is placed at the centre of the cell for the dielectric measurement. Fig. 4 shows the configuration of the measurement system setup. This system consists of the wideband TEM-cell, coaxial cables, a network analyzer and the material under test. The measurement is carried out with absorbers placed beside the structure to avoid reflections from the surrounding environment.

Port 1 and port 2 are connected to the network analyzer through coaxial cable. The sample is placed at the centre of the cell. It should be far away from the feeding ports due to non-uniformity of the field near the ports. S-Parameters are measured and the permittivity and permeability of dielectric material are obtained based on the NRW conversion technique. The results are illustrated in Section 5.


Figure 4: Experimental setup for a dielectric measurement.



Figure 5: The internal layout shows how the parallel plate cell is placed.

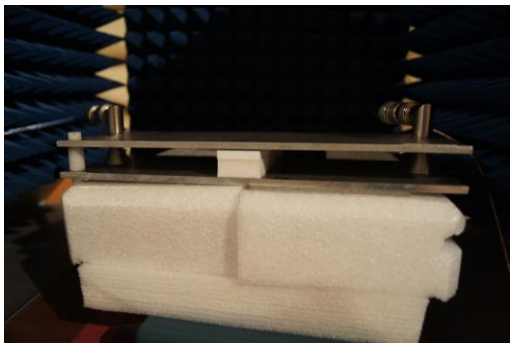


Figure 6: The Teflon is placed at the centre of the parallel plate cell for measurement.

5. Result and Discussion

5.1. Verification Using Teflon

A 3cm width of Teflon with relative permittivity, $\varepsilon_r \sim 2$ and relative permeability, $\mu_r=1$ is placed at the centre of the cell. The height of the Teflon is nearly 2cm so that the Teflon can be easily put in between the two plates. The measured S-parameter with and without the Teflon will be used for the relative permittivity and permeability calculation. In order to validate the result, the same structure is created in CST MICROWAVE STUDIO®, both of the results are shown in Fig. 7 and Fig. 8.

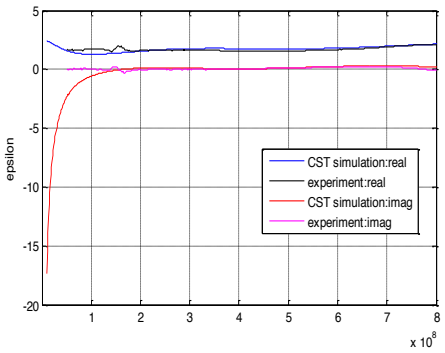


Figure7: Relative permittivity (epsilon) comparison between experiment and simulation results for Teflon.

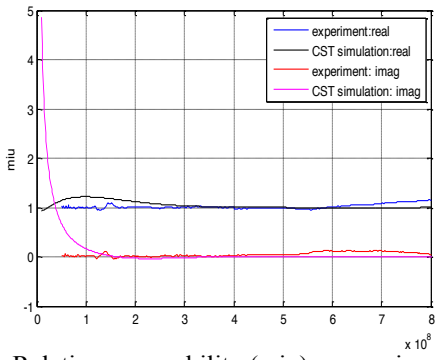


Figure 8: Relative permeability (miu) comparison between experiment and simulation results for Teflon.

The experimental result is in good agreement with the simulation result and also the published data for Teflon. The fluctuation of the experimental results is believed to be due to imperfect contacts in the preliminary prototype and parasitic coupling effects [5].

6. Conclusion

A wideband TEM-cell is designed with a novel feeding section of conical shape. This feeding successfully upgrades the parallel plate to a wideband cell and provides better matching. The specific calibration successfully solves the limitation of the parallel plate which only provides calibration plane at the edge of the plane instead of the surface of the dielectric material. The dielectric measurement for Teflon indicates that this cell has the potential to be used as equipment for dielectric measurements. The fluctuations of the results are believed to be due to coupling effects and also the placement of the coaxial cable during the measurement.

Acknowledgements

The authors would like to thank the technicians in mechanical department for machining out the cell.

References

[1] R. Collier and D. Skinner, Microwave Measurement, 3rd ed., IET, Gateshead, London, UK, 2007.

[2] Weng Cho Chew, Kenneth J. Olp, and Gregory P. Otto, "Design and calibration of a large broadband dielectric measurement cell," *IEEE Transactions on Geoscience and Remote Sensing*, vol.29, pp. 42-47, Jan. 1991.

[3] Clarke, R N, A P. Gregory, D. Cannell, M. Patrick, S. Wylie, I. Youngs, and G. Hill, "A guide to the characterization of dielectric materials at RF and microwave frequencies," National Physical Laboratory, NPL, Rep. 0904457389, 2003.

[4] Rohde & Schwarz, "Measurement of dielectric material properties," Application centre Asia pacific. RAC0607-0019, 2006.

[5] Kazemipour, A, D. Allal, A. Litwin and M.Bourghes, "Wideband TEM Parallel-plate cell for SAR-probe calibration," in *proc. Electromagnetic Measurement, Daejeon, Korea*, 2010, pp. 710-711.

[6] M. Pozar, D., *Microwave Engineering*, 3rd ed., Amherst, John Wiley & sons, Inc., US, 2004.

[7] Jason Jon Yoho, (1998) *Design and Calibration of a RF Capacitance Probe for Non-Destructive Evaluation of Civil Structures*. Published thesis. Virginia Polytechnic Institute and State University

[8] D.k.Ghodgaonkar, V.V.Varadan, V.K.Varadan, "Free-Space Measurement of Complex Permittivity and Complex Permeability of Magnetic Material at Microwave Frequencies," *IEEE Transaction on Instrumentation and Measurement*, vol. 39, No. 2, pp. 387-394, April 1990

[9] Robert E. Collin, *Foundations for Microwave Engineering*, 2nd ed., IEEE Press Classic Reissue, 2000.

Transfer of orbital angular momentum on macroscopic object in the UHF band

Ronan Niemiec[1,2], Christian Brousseau[1], Olivier Emile[2], and Kouroch Mahdjoubi[1]

[1]UMR 6164 IETR, Université de Rennes 1, 35042 Rennes Cedex, France
[2] URU 435 Physique des Lasers, Université de Rennes 1, 35042 Rennes Cedex, France
*corresponding author, E-mail: ronan.niemiec@univ-rennes1.fr

Abstract

We report on the exchange of orbital angular momentum between an electromagnetic microwave and a macroscopic object. Using a quadrupole wire antenna at frequency *f = 870 MHz*, we induce a torque on a suspended copper strip. The induced torque on the strip is of the order of 10^{-8} *Nm*. A linear dependence of the acceleration of the strip on the radiated power, up to 8.10^{-4} °/*s*², is observed and rotations of a few degrees are measured.

1. Introduction

An electromagnetic (EM) wave is defined by its magnitude, its wave vector, its frequency and its angular momentum. Angular momentum is the mechanical property of an EM wave and can be decomposed in two components:

- The intrinsic component which is the Spin Angular Momentum (SAM), associated to the wave polarization,
- The extrinsic part which is the Orbital Angular Momentum (OAM), which represents the spatial distribution and depends on the gradient of the EM fields.

Since the pioneering experiment of Beth in 1935 [1], it is well known that the circular polarization of EM waves can induce rotation of macroscopic birefringent plates. This effect has since been experimentally confirmed either at macroscopic scale, both in optics [1, 2] and microwaves [3, 4], or at microscopic scales [5] in optics only. In 1949, Carrara [3] measured rotations of few degrees of various absorbing macroscopic objects, like 3cm size-disks and squares, using circularly polarized waves at a frequency of *9.36 GHz* with a mean power of *50 W*. More refining experiments have been conducted by Allen in 1966 [4], at a frequency of *9.3 GHz*. Continuous rotation of a small dipole, delicately suspended in a circular waveguide, has been observed using an incident circular polarized wave of low power (less than *1 W*).
On the other hand, according to the Maxwell equations, electromagnetic fields can also carry orbital angular momentum (OAM) when the wavefronts are twisted regarded to the direction of propagation. In 1992, Allen *et al.* [6] showed that light beams with an azimuthal phase dependence $exp(i.l.\varphi)$, carry an orbital angular momentum of $l.\hbar$ per photon, where $\hbar$ is the reduced Planck constant, and *l*, an integer number called the "topological charge" [7]. From these studies, an analogous adventure can be considered for the orbital angular momentum (OAM) of an EM field to rotate objects. Indeed, transfer of OAM has already been observed on microparticles [8]. However, in the macroscopic domain, no direct evidence of OAM transfer from an EM wave has ever been observed. Besides, in the microwave or in the radiofrequency domain, such an effect would be easier to evidence since the angular momentum carried by the EM wave could be much higher for a given power. For example in Carrara's experiment [3], the induced torque was indeed observed with the naked eyes.
In this paper, we report the experimental observation of the OAM transfer from an EM wave to a macroscopic object suspended by a torsion pendulum, in the radiofrequency domain. In a first part, the experimental setup is described and characterized. In a second part, experimental results are presented and discussed. Finally, a conclusion is presented and some improvements are proposed.

2. Experimental Setup

In 1987, Vul'fson [9] proposed an experimental setup to measure the angular momentum of EM radiation with a wavelength of the order of *1-1.5 cm*, using a torsion pendulum. However, such an experimental setup has not been realized yet.
Torsion pendulum is a very popular tool that has been used for over more than two centuries for fundamental measurements [10, 11] and is still the most sensitive tool for measuring weak torques. It has also been used in photon spin angular momentum transfer to a macroscopic object [1-4]. The schematic diagram we used to measure angular momentum in the UHF range is presented in Fig.1 showing in particular the suspended receiving ring, which is the detector of the angular momentum.

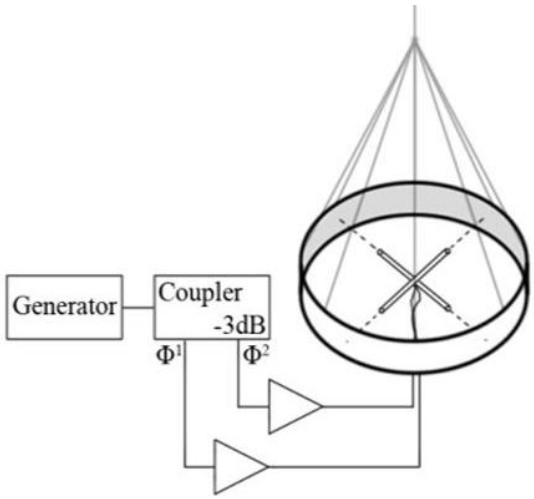


Figure 1: Schematic diagram of the experimental set-up, as inspired from Vul'fson's proposal [9], showing the RF frequency generator, the *-3dB* coupler, the power amplifiers, the antennas and the copper detector ring.

. This experimental system is composed of:

- a RF frequency signal synthesizer (Generator),
- a *-3 dB* coupler,
- two power amplifiers,
- two dipole antennas.

Orbital angular momentum is detected by a light copper ring which has the following dimensions:

- internal radius R_1: *15.4 cm*,
- height h_r: *5 cm*,
- thickness: *156 μm*.

From these parameters, the inertial momentum J can be determined using the following equation:

$$J = \frac{1}{2}.M.\left(R_2^2 + R_1^2\right), \qquad (1)$$

where:

$$M = \rho.\pi.h_r.\left(R_2^2 - R_1^2\right), \qquad (2)$$

Where R_1 and R_2 are respectively the internal and the external radius of the ring, h_r, the height of the ring, and ρ, the copper density equals to $8.94\ g.cm^{-3}$. Therefore, the inertial momentum is evaluated to be $J = 8.4\ 10^{-4}\ kg.m^2$.
The ring is suspended to the ceiling of the room with an ordinary cotton thread. This thread has a length of *2 m* and a diameter of *0.5 mm*. It is then attached to the ring by eight branches of cotton thread. The torsion constant of this suspension has been then deduced from the *12 min* period of the free oscillation of the pendulum and equals to $\Gamma = 2.3\ 10^{-10}\ Nm/°$.
From Fig.2, one can see the two dipole antennas at the center of the ring, which are orthogonal to each other. These antennas are supplied from a common frequency synthesizer with a phase shift of $\pm \pi/2$. These two dipole antennas are made from a copper wire that has a diameter of *2 mm* and a length of *17 cm*.

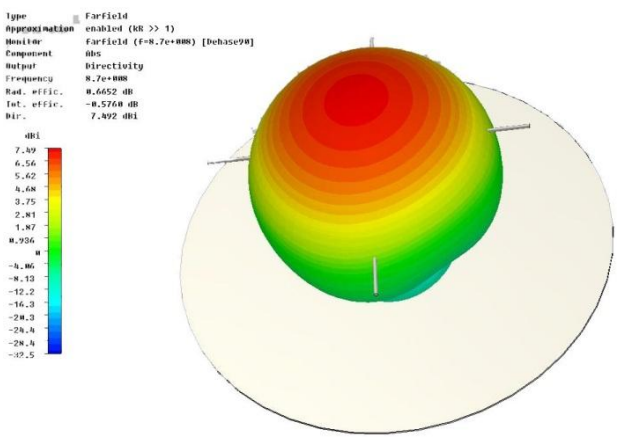


Figure 2: 3D radiation pattern of the two crossed dipole antennas in the far field, at the frequency of *f = 870 MHz*.

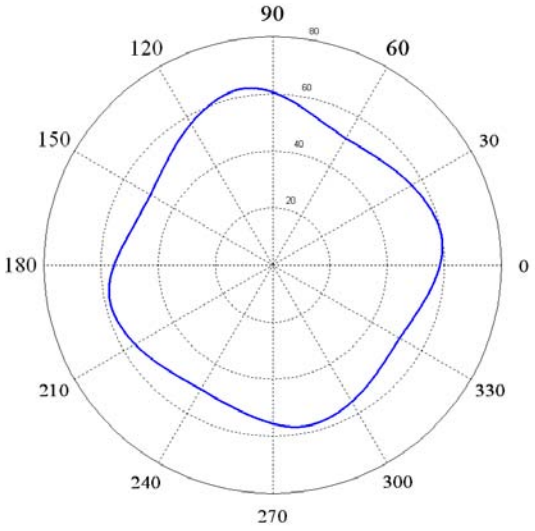


Figure 3: Electrical field radiated by a turnstile antenna composed of two crossed dipoles excited in phase quadrature, at the distance of *15.4 cm*. Transmitted power is equal to *1 W*. The field is calculated at the frequency of *f = 870 MHz* and in the plane of antennas. Pattern dissymmetrical defect is due to a small difference on the size of the realized dipoles.

This type of antenna is known as turnstile antenna, whose principal characteristic is an isotropic radiation pattern. Thus, the electric field is constant all over the copper ring, ensuring a global symmetry of the system [12].
Fig.2 and Fig.3 present, respectively, the 3D radiation pattern and the E field radiated by the turnstile antenna in the far field. The latter is calculated in the plane of antennas, at a distance of *15.4 cm* to the center and at a frequency of *870 MHz*. These results are computed using CST numerical electromagnetic software. Small variations are observed along the radiation pattern due to a small difference on the antenna size.

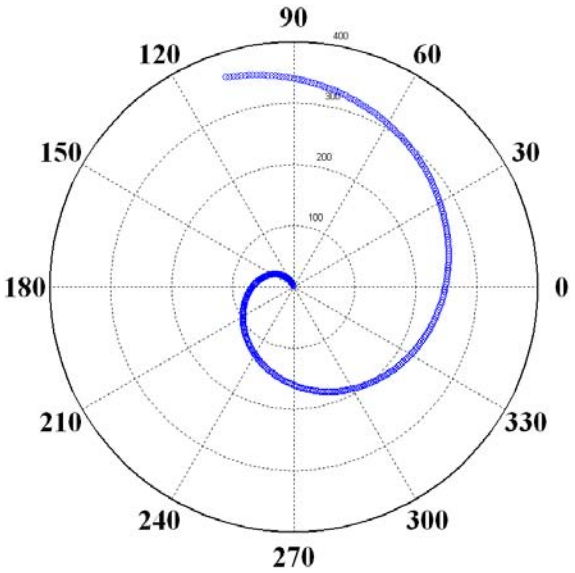


Figure 4: Phase variation of the radiated EM field as a function of the azimuth angle (*Phi* angle), in the plane of antennas and at the frequency of *870 MHz*.

The measured SWR is around *1.3* for each antenna. These antennas, having a power supply with a $\pi/2$ phase shift, are often used for circular polarization applications (e.g. satellite communications), because the far field radiation pattern in front of the antennas has a circular polarization. The turnstile antenna is also used in broadcast applications, where there is a need for horizontal (linear) polarization with uniform (isotropic) radiation pattern around the antenna. However, in our case, we are interested in the EM field in the plane of the antennas only.

In the near field and in the plane of the antennas, the radiated electromagnetic field is near-isotropic (Fig.3) and has a 2π phase rotation as a function of the azimuth angle (*Phi* angle). This is in fact, the characteristic behavior of an EM wave carrying an orbital angular momentum with a topological charge *l* equal to *l=1* (Fig. 4).

These dipoles are supplied from a CW (Continuous Wave) frequency synthesizer through a *-3 dB* coupler (power divider) having a $\pi/2$ phase shift. A picture of this *-3 dB* power-divider/phase-shifter is shown in Fig.5. Then, the RF signals, which are now in phase quadrature, are amplified by two *40 dB* gain power amplifiers before being supplied to the antennas, through 2 coaxial cables of *5 m* long.

Finally, the gain and phase induced by the electronic parts (amplifiers, cables, connectors, …) between the output of the RF frequency synthesizer and the inputs of each antenna, have been measured using a vector network analyzer. Measurements are summarized in Table 1. Gains of the two transmission lines (TL1 and TL2) are very close to each other, with a difference of *0.8 dB*. The phase difference is equal to *85.8°*, which is slightly smaller than the desired *90°*, despite the difference of lengths of the two output ports of the *-3 dB* coupler. But, we will see in the next part that it is good enough for our experiment.

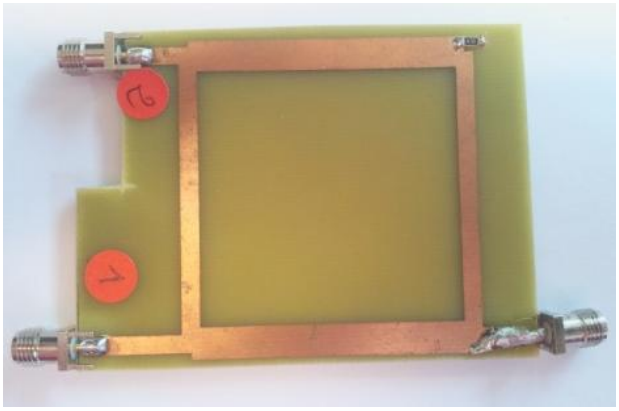


Figure 5: Picture of the *-3 dB* coupler/power divider with a $\pi/2$ phase shift between outputs 1 and 2. The output port 2 is slightly shorter than port 1 to compensate for the phase discrepancy between the transmission lines (amplifiers + coaxial cables) used to feed the dipole antennas

Table 1: Gain and phase introduced by the electronic parts between the output of the RF frequency synthesizer and the inputs of the antenna 1 (TL1) and the antenna 2 (TL2).

	TL1	TL2
Gain (dB)	39.8	40.6
Phase (deg.)	178.6	-95.6

Special care has been taken to avoid spurious effects. The experimental setup is confined in an anechoic chamber. Besides, the suspension and the experimental setup have been isolated from any mechanical vibration. Rotation of the ring is recorded via a webcam connected to a computer located outside of the anechoic chamber. Fig.6 and Fig.7 show pictures of the experimental setup placed in the anechoic chamber.

3. Fields

The electric field radiated by one dipole antenna alone writes in the far field:

$$E_{\theta,1} = \frac{L}{4.\varepsilon_0.c.\lambda}.\frac{\cos\left(\frac{\pi}{2}.\sin\theta\right)}{\sin\theta}.I_0.e^{j.(\omega t-kr)} \quad , \quad (3)$$

$$E_{\theta,1} \approx \frac{L}{4.\varepsilon_0.c.\lambda}.\sin\theta.I_0.e^{j.(\omega t-kr)}$$

where λ is the wavelength of the electric field, *k*, the wave vector, *L*, the length of the antenna, *c*, the velocity of light, ε_0, the dielectric constant, ω, the angular frequency of the current in the dipole, I_0, its amplitude, (r, θ), the usual polar coordinates, and *j* is the usual complex number. Note that the estimated electric field lies in the plane of the antennas and is thus tangential to the copper ring.



Figure 6: Picture of the experimental set-up showing the suspended detector ring in the anechoic chamber.

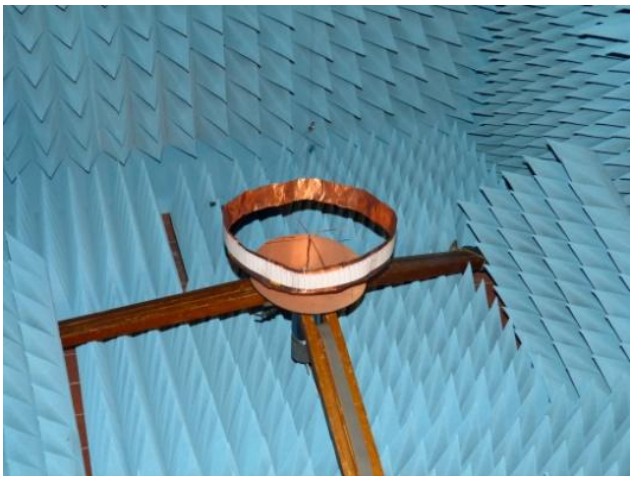


Figure 7: Experimental set-up showing the antennas and the suspended ring in the anechoic chamber.

Since there is a phase of $\phi = \pi/2$ to the signal sent to the second antenna, its radiated electric field can be written:

$$E_{\theta,2} \approx \frac{L}{4.\varepsilon_0.c.\lambda}.\cos\theta.I_0.e^{j.(\omega t - kr - \pi/2)}, \quad (4)$$

This leads to a total electric field which also lies in the plane of the antennas:

$$E_\theta \approx e^{-j.\theta}.\frac{L}{4.\varepsilon_0.c.\lambda}.\frac{1}{r}.I_0.e^{j.(\omega t - kr)}, \quad (5)$$

Note the phase factor *exp(-jθ)* in this expression. Actually, this factor leads to a spatial modulation of the phase of the field. In such an electric field, the phase fronts are twisted and the orbital momentum is $\hbar$ per photon.

4. Measurements

The antennas have been excited with powers, varying from *1.5 W* up to *25 W*. The corresponding rotation of the pendulum has been recorded and is displayed as a function of time on Fig. 8. For the sake of clarity, the rotations for four radiated powers (*3 W*, *6 W*, *8 W* and *25 W*) have been plotted with a fit of the experimental data with parabolas.

As one can see, the rotation of the pendulum is a uniformly accelerated rotation within a very good approximation. To our knowledge, it is the first direct observation of the transfer of electromagnetic orbital angular momentum to a macroscopic object. For a longer time of observation, the restoring torque of the thread becomes no longer negligible and this leads to damped oscillations. As expected, the rotation becomes more important as the power is increased.

An inversion of the rotation of the pendulum is also experimentally observed for a reversing of the phase shift from $+\pi/2$ to $-\pi/2$. This is equivalent to remove the minus sign just in front of θ in Eq. 5. Thus, it corresponds to the change from $+\hbar$ to $-\hbar$ OAM carried per photon. Then, the sign of the torque should also be reversed as we can see in Fig. 8.

Besides, we can also observe in Fig. 8, that the two recordings of the rotation for both directions are nearly perfectly symmetric.

Finally, when the two dipoles are in phase ($\phi = 0$), no rotation is observed, meaning that parasitic effects such as, radiation pressure due to a misalignment of the pendulum regarding the antennas, or reflection from the walls or the ground of the chamber, are negligible in our experimental setup.

Based on the measurement of the angle of rotation as a function of time reported in Fig. 8, angular acceleration transferred by the electric field to the strip as a function of the applied power has been estimated. Since the applied torque is $\hbar$ per photon, the total torque should be proportional to the number of photons, and thus the angular acceleration should depends linearly on the applied power. Indeed, the experimental results show a nearly perfect linear dependence on the applied power. Moreover, the linear dependence holds over more than one order of magnitude, from *1.5 W* to *25 W*.

The symmetry between both directions of rotation is also verified. The linear coefficient deduced from the fitting of the experimental data is exactly the inverse for one direction of rotation and for the other direction.

From Fig. 8, for a power of *25 W*, we can deduce an angular acceleration of $a = 6.4x10^{-4}$ °/s^2.

This corresponds to an applied torque Γ applied to the ring by the EM microwave radiation due to the OAM:

$$\Gamma = J.a = 4.71\times10^{-9} \text{ Nm} \quad (6)$$

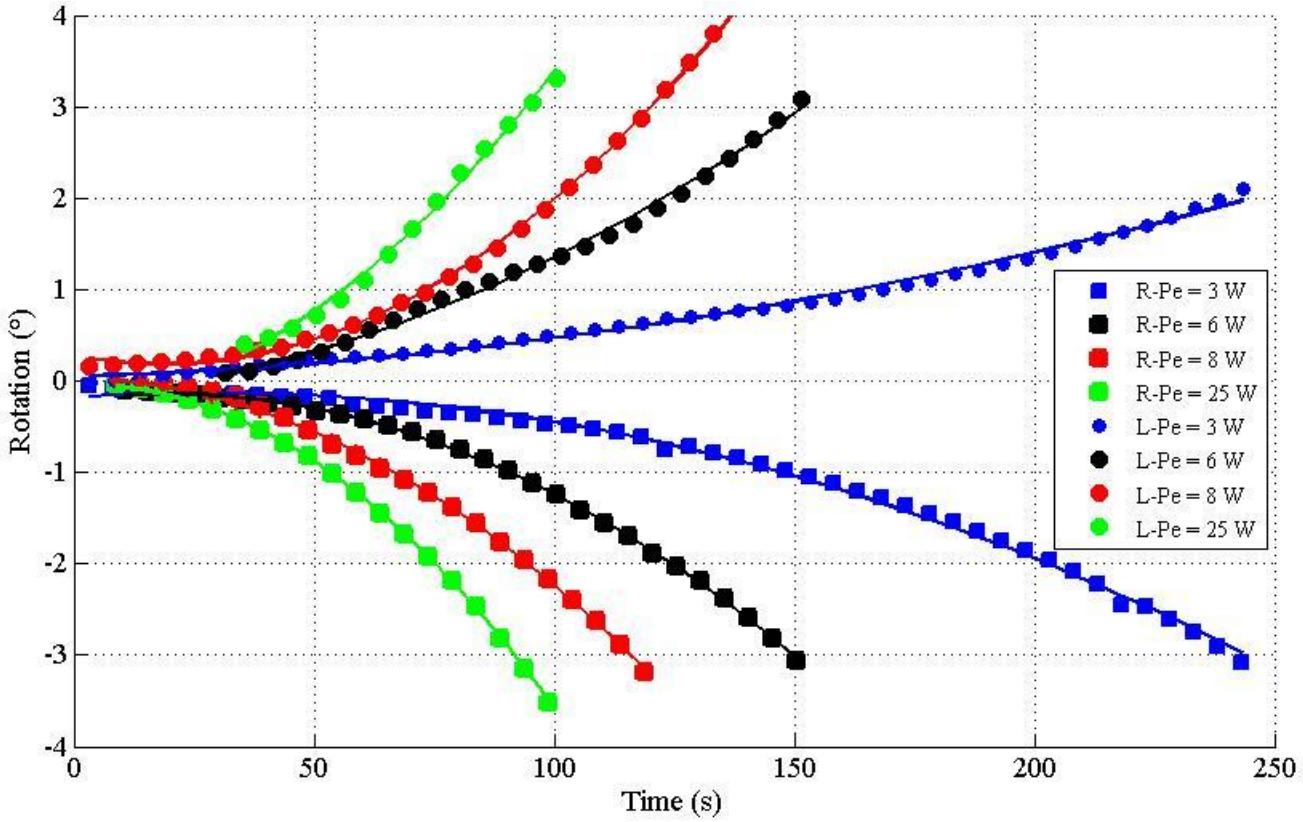


Figure 8: Angular rotation as a function of time for a $-\pi/2$ ("R"curves) and $+\pi/2$ ("L"curves) phase shift between the antennas and for different transmitted powers P_e (*3 W*, *6 W*, *8 W* and *25 W*).

5. Discussions

Thanks to the very high sensitivity of the torsion pendulum, we have been able to detect an applied torque of the order of $\Gamma = 10^{-9}\ Nm$ due to the transfer of orbital angular momentum of the photon. By improving the suspension mechanism, as well as the thread suspension [13], like using spider draglines, and by inserting the experimental setup in a vacuum chamber to reduce the damping coefficient, a detection of a torque of the order of $\Gamma = 10^{-14}\ Nm$ seems within reach. The absorbing object could be either an absorbing ring or strip in the case a spherical wave, or an adapted absorbing plate in the case of a plane wave. This would correspond to electromagnetic fields carrying orbital angular momentum in the microwatt range or lower. This may be an alternative way to detect orbital angular momentum in the radio domain [14, 15] or even in astronomy [16].

6. Conclusions

To conclude, we have experimentally observed the transfer of angular orbital momentum from an electromagnetic wave to a macroscopic object using a torsion pendulum, at the frequency of *870 MHz*.

A microwave field has been generated using a linear quadrupole antenna (turnstile antenna) with a controlled ~~de~~phasing between the antennas. A phase rotation of 2π is observed on this electromagnetic field, in the plane of the antennas, characteristic phenomenon of a EM field carrying an angular orbital momentum of $\hbar$ per photon. The accelerating regime of the pendulum has been isolated and it is possible to switch the direction of the rotation simply by inverting the phase shift between the two dipole antennas. It would be now stimulating to try to detect microwave electromagnetic field carrying more than one $\hbar$ per photon.

Acknowledgements

We would like to thank K. Wang, T. Teko, and A. Adibi for early interest, and D. Levalois and R. Legave for technical assistance. This work was supported by the University of Rennes 1 via a "défi émergent" action, the French Ministry of Defense (DGA) and the council of Brittany (Région Bretagne).

References

[1] R.A. Beth, Mechanical detection and measurement of the angular momentum of light, *Physical Review*, 50: 115−125, 1936.

[2] G. Delannoy, O. Emile, A. Le Floch, Direct observation of a photon spin-induced constant acceleration in macroscopic systems, *Applied Physical Letters*, 86: 081109, 2005.

[3] N. Carrara, Torque and angular momentum of centimetre electromagnetic waves, *Nature*, 164: 882−884, 1949.

[4] P.J. Allen, A radiation torque experiment, *American Journal of Physics*, 34: 1185−1192, 1966.

[5] M.E.J. Friese, T.A. Nieminen, N.R. Heckenberg, H. Rubinsztein-Dunlop, Optical alignment and spinning of laser-trapped microscopic particles, *Nature*, 394: 348−350, 1998.

[6] L. Allen, M.W. Beijersbergen, R.J.C. Spreeuw, J.P. Woerdman, Orbital angular momentum of light and the transformation of Laguerre-Gaussian laser modes, *Physical Review A*, 45: 8185−8189, 1992.

[7] M. Padgett, R. Bowman, Tweezers with a twist, *Nature Photonics* 5: 343−348, 2011.

[8] H. He, M.E.J. Friese, N.R. Heckenberg, H. Rubinsztein-Dunlop, Direct observation of transfer of angular momentum to absorptive particles from a laser beam with a phase singularity, *Physical Review Letters*, 75: 826−829, 1995.

[9] K.S. Vul'fson, Angular momentum of electromagnetic waves, *Soviet Physics Uspekhi*, 30 (8), pp. 724-728, August 1988.

[10] H. Cavendish, Experiments to determine the density of earth, *Philosophical Transactions of the Royal Society*, London 8: 469, 1798.

[11] C.A. Coulomb, *Mémoires de Coulomb*, édité par les soins d'A. Potier, Imprimeur Gauthier-Villars, Paris 1884.

[12] S.G.M. Darwish, K.F.A. Hussein, H.A. Mansour, Circularly polarized crossed-dipole turnstile antenna for satellites, *Proceedings of the Twenty-First NRSC2004 - National Radio Science Conference*, June 2004, Monterey, California, USA.

[13] O. Emile, A. Le Floch, A. Vollrath, Time-resolved Torsional relaxation of spider draglines by an optical technique, *Physical Review Letters*, 98: 167402, 2007.

[14] H. The, B. Thidé, J.T. Mendoça, T.D. Carozzi, J. Bergman, W.A. Baan, S. Mohammadi, B. Eliasson, Detecting orbital angular momentum in radio signals, *arXiv.org*, astro-ph(0805.2735), 18 May 2008, http://arxiv.org/abs/0805.2735.

[15] S.M. Mohammadi, L.K.S. Daldorff, R.L. Karlsson, B. Thidé, K. Forozesh, T.D. Carozzi, and B. Isham, Orbital angular momentum in radio - A system study, *IEEE Transactions on Antennas and Propagation*, 58: 565, 2010.

[16] N.M. Elias, Photon orbital momentum in astronomy, *Astronomy & Astrophysics*, 492: 883, 2008.

Fresnel Field to Far Field Transformation Based on Two-Dimensional Fourier Series Expansion

Yury V. Krivosheev, Alexander V. Shishlov, Aleksey K. Tobolev and Irina L. Vilenko

Company "Radiofizika", Moscow, Russia
E-mail: jscapex@online.ru

Abstract

A method of Fresnel field to far field transformation based on two-dimensional Fourier series expansion is presented. According to the method, far field can be reconstructed from several sections of the field in Fresnel region. Computer simulation and experimental verification results are given. Relationship to other results of antenna measurements theory is considered.

1. Introduction

Reconstruction of antenna characteristics from Fresnel region measurements is an important problem of the antenna engineering. Particularly, it is important when one has an anechoic chamber with test facility for far field measurements, but far field distance of an antenna under test (AUT) is larger than the length of an anechoic chamber.

For far field reconstruction from measurements in Fresnel region classical methods of far-field reconstruction from near-field measurements can be used. It is known that in this case measurements can be carried out only in a limited angular sector [1,2]. However, it requires $\lambda/2$ spacing between samples, so the amount of measurements can be large.

In the literature several methods of far field reconstruction specific to Fresnel region have been proposed. In these methods the spacing between samples is much larger than $\lambda/2$, which allows to reduce measurements time.

In [3,4] a solution of three-dimensional problem based on pseudosampling representation of the field was found. The presented method is convenient for both computation and practical realization. A disadvantage of the method is that the far field can be reconstructed only in angular directions close to the normal of the aperture.

In [5,6] a method based on one-dimensional Fourier series expansion of phase exponential was presented. The solution is also convenient to use (e.g. [7]), but is applicable only to linear antennas elongated in one direction, because in [5,6] only a two-dimensional problem was considered. However, the method is not limited only to the directions close to the normal of the aperture.

In [8] a generalization of [5,6] to three-dimensional case based on Bessel functions expansion was considered. The proposed representation is less convenient in practical sense, because it requires to measure field in an irregular angular grid.

In [9] a solution to three-dimensional problem based on [5,6] was proposed, which utilizes two-dimensional Fourier series expansion. As opposed to Bessel functions expansion, this method requires to carry out measurements in a regular angular grid, which makes it convenient to use in practice. Also, for the directions close to the normal of the aperture the expansion presented in [9] tends to the expansion in [4]. Thus, a method of two-dimensional Fourier series expansion can be considered as a generalization of method [4] for reconstruction of the far field in the directions which are not close to the normal of the aperture. Also in [9] several issues concerning practical implementation of the method were discussed.

Method [9] was further developed in papers [10–12], where measurements on non-spherical surface were considered [10], a Fresnel field to Fresnel field transformation was presented [11] and an alternative approach to expansion coefficients calculation was given for far field reconstruction from measurements at smaller distances [12].

In the current paper a method of Fresnel field to far field transformation based on two-dimensional Fourier series expansion is presented [9]. New results are given, such as vector form of the formulas for arbitrary point in far zone (in [9] only points with either small azimuth or small elevation were considered) and relationship of the method to other results of antenna measurements theory. Formulas for such characteristics as gain and EIRP and configuration of the measurement system are presented. Also the results of numerical simulation and experimental verification are given.

2. Mathematical model

Consider an antenna with dimensions at least several wavelengths. Let the antenna be in the left half-space near the z=0 plane (Fig.1). Then we need to choose a rectangle T_xxT_y in the z=0 plane, which must be at least as large as the antenna. Also let the antenna be positioned in such way that the center of the rectangle coincides with the origin.

To describe the field at z>0 mathematically we'll use Kirchhoff integral with the Green's function, chosen to eliminate either the term with the derivative of the field, or the term with the field. Also the field at z=0 outside the

T_xxT_y rectangle is neglected. Then the electric field in an arbitrary point in the right half-space for which $kr \gg 1$ can be written in terms of the field at z=0 plane as:

$$\mathbf{E}(u,v,r) = j \iint_{T_x \times T_y} \mathbf{E}(x,y,0) \times \frac{W(x,y) e^{-jkR(x,y)}}{\lambda R(x,y)} dxdy \text{, or} \quad (1)$$

$$\mathbf{E}(u,v,r) = -\frac{1}{2\pi} \iint_{T_x \times T_y} \frac{\partial \mathbf{E}}{\partial z}(x,y,0) \frac{e^{-jkR(x,y)}}{R(x,y)} dxdy \text{ , (2)}$$

where **E** is complex electric field amplitude; λ is wavelength, k=2π/λ; u=sinα, v=cosα sinβ, w=cosα cosβ are direction cosines of the direction of observation, β and α are azimuth and elevation of the direction of observation, r is the distance between the origin and observation point; U, V, W and R are directional cosines and length of the vector between integration point and observation point.

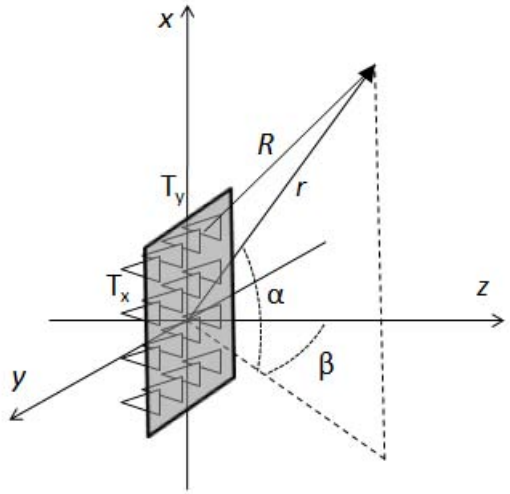


Figure 1: Antenna and the reference frame.

Under the condition $kR \gg 1$, the error of (1) and (2) is determined by the same integrals over the region $\mathbb{R}^2 \setminus T_xxT_y$. If the rectangle T_xxT_y includes all points with significant (large enough) amplitude of the field, then the error is small.

The further analysis will be based on (2). Analysis can be carried out based on (1) as well. As it will be shown, the result will change insignificantly in this case.

Let us make a simplification for the case, when the observation point is at least as far as in the Fresnel region, i.e.:

$$r > 0.62\sqrt{D^3/\lambda} \text{ .} \quad (3)$$

In this case (2) can be rewritten in the following way:

$$\mathbf{E}(u,v,r) = -\frac{e^{-jkr}}{2\pi r} \iint_{T_x \times T_y} \frac{\partial \mathbf{E}}{\partial z}(x,y,0) \times e^{-j\Phi_r(x,y,u,v)} dxdy \text{ ,} \quad (4)$$

where

$$\Phi_r(x,y,u,v) = k\sqrt{(ru-x)^2 + (rv-y)^2 + r^2(1-u^2-v^2)} - kr \approx -k(xu+yv) + \frac{k}{2r}\left(x^2(1-u^2) + y^2\left(1-v^2\right) - 2xyuv\right)$$

$$= \Phi^{(1)}(x,y,u,v) + \Phi_r^{(2)}(x,y,u,v) \text{ ,} \quad (5)$$

$$\Phi^{(1)}(x,y,u,v) = -k(xu+yv) \text{ ,} \quad (6)$$

$$\Phi_r^{(2)}(x,y,u,v) = \frac{k}{2r}\left(x^2(1-u^2) + y^2\left(1-v^2\right) - 2xyuv\right) . \quad (7)$$

3. Field transformation

We consider the following problem: given field measurements at a sphere r_1 in the Fresnel region, we need to determine field values at a sphere r_2. The problem of reconstructing far field corresponds to $r_2 \to \infty$.

3.1. Transformation theory

Consider the following representation of exponential of the phase function from (4) for the sphere r_2:

$$e^{-j\Phi_{r2}(x,y,u,v)} = g(x,y,u,v) e^{-j\Phi_{r1}(x,y,u,v)} \text{ ,} \quad (8)$$

where

$$g(x,y,u,v) = \exp\left(j\frac{k}{2}\left(\frac{1}{r_1} - \frac{1}{r_2}\right) \times \left(x^2(1-u^2) + y^2\left(1-v^2\right) - 2xyuv\right)\right) \quad (9)$$

Let us expand (9) into Fourier series as a function of (x,y) at a rectangle [$-T_x$/2,T_x/2]x[$-T_y$/2,T_y/2] for fixed u and v:

$$g(x,y,u,v) = \sum_{m,n} k_{mn}(u,v) e^{jm\frac{2\pi}{T_x}x} e^{jn\frac{2\pi}{T_y}y} \text{ ,} \quad (10)$$

where

$$k_{mn}(u,v) = \frac{1}{T_x T_y} \iint_{T_x \times T_y} e^{j\frac{k}{2}\left(\frac{1}{r_1} - \frac{1}{r_2}\right)\left(x^2(1-u^2) + y^2\left(1-v^2\right) - 2xyuv\right)} \times e^{-jm\frac{2\pi}{T_x}x} e^{-jn\frac{2\pi}{T_y}y} dxdy \text{ .} \quad (11)$$

Substitute (10) into (8) taking into account denotations (6) and (7):

$$e^{-j\Phi_{r2}(x,y,u,v)} = \sum_{m,n} k_{mn}(u,v) e^{jm\frac{2\pi}{T_x}x} e^{jn\frac{2\pi}{T_y}y} e^{-j\Phi_{r1}(x,y,u,v)} \approx \sum_{m,n} k_{mn}(u,v) e^{-j\Phi^{(1)}(x,y,u+m\Delta u, v+n\Delta v)} e^{-j\Phi_{r1}^{(2)}(x,y,u,v)} \text{ .} \quad (12)$$

where

$$\Delta u = \lambda / T_x \text{ , } \Delta v = \lambda / T_y \text{ .} \quad (13)$$

For r_1 in the Fresnel region, in the vicinity of u, v the following inequality takes place:

$$\left|\Phi_{r_1}^{(2)}(x,y,u,v) - \Phi_{r_1}^{(2)}\left(x,y,u+m\Delta u, v+n\Delta v\right)\right| \ll 1. \quad (14)$$

With (14), the relation (12) can be rewritten as:

$$e^{-j\Phi_{r2}(x,y,u,v)} \approx \sum_{m,n} k_{mn}(u,v) e^{-j\Phi_{r1}(x,y,u+m\Delta u, v+n\Delta v)}. \quad (15)$$

Note, that physical interpretation of (15) is representation of a spherical wave with center in (u,v,r_2) as a linear combination of spherical waves with centers in $(u+m\Delta u, v+n\Delta v, r_1)$, the representation taking place at a rectangle T_xxT_y.

Now substitute (15) into (4). After changing order of summation and integration, we have:

$$\mathbf{E}(u,v,r_2) \approx e^{-jk(r_2-r_1)} \frac{r_1}{r_2} \times \sum_{m,n} k_{mn}(u,v) \mathbf{E}(u+m\Delta u, v+n\Delta v, r_1). \quad (16)$$

In sum (16) only several terms contribute significantly, so other terms can be dropped. This issue will be considered in more detail below.

Note, that a formula analogous to (16) was originally obtained in [13] for a two-dimensional problem and later in [14] for a three-dimensional problem for the case when antenna is illuminated by a nonplanar wave. However in these publications the formulas were applied only to nonplanar waves of a compact range.

Now let us consider a point u_2, v_2, which is located between nodes $u_1+m\Delta u$, $v_1+n\Delta v$. Let the node u_1, v_1 be the closest node of the mentioned grid's nodes to u_2, v_2. Expression (8) can be rewritten as:

$$e^{-j\Phi_{r2}(x,y,u_2,v_2)} = g(x,y,u_1,v_1,u_2,v_2) e^{-j\Phi_{r1}(x,y,u_1,v_1)}. \quad (17)$$

After transformations similar to (10)-(16), we obtain:

$$\mathbf{E}(u_2,v_2,r_2) \approx e^{-jk(r_2-r_1)} \frac{r_1}{r_2} \sum_{m,n} k_{mn}(u_1,v_1,u_2,v_2) \times \mathbf{E}(u_1+m\Delta u, v_1+n\Delta v, r_1), \quad (18)$$

where

$$k_{mn}(u_1,v_1,u_2,v_2) = \frac{1}{T_x T_y} \iint_{T_x \times T_y} e^{j\Phi_{r1}^{(2)}(x,y,u_1,v_1) - j\Phi_{r2}^{(2)}(x,y,u_2,v_2)} \times e^{jk(x(u_2-u_1)+y(v_2-v_1))} e^{-jm\frac{2\pi}{T_x}x} e^{-jn\frac{2\pi}{T_y}y} dxdy. \quad (19)$$

Note, that in (18) the largest contribution into sum is made by the field samples near (u_2,v_2), because coefficients (19) have largest magnitudes in this area.

Thereby, using field values in the angular grid $u_1+m\Delta u$, $v_1+n\Delta v$ on a sphere in Fresnel region or far region, one can reconstruct field values in every points of the half-space in Fresnel region or far region. Formulas (18),(19) can also be generalized for the case when r_1 and/or r_2 are in antenna near zone. This issue will be considered in the following publications. Also, (18),(19) can be applied at closer distances than indicated by (3). In [12] it was shown that these formulas can be applied under the following conditions:

$$\frac{D^4}{50\lambda r^3} << 1, \ \frac{D}{4r} << 1. \quad (20)$$

Note, that if we base the formulas on (1) instead of (2), then (18) turns into:

$$\mathbf{E}(u_2,v_2,r_2) \approx e^{-jk(r_2-r_1)} \frac{r_1}{r_2} \sum_{m,n} \frac{w_2}{w_{1,mn}} k_{mn}(u_1,v_1,u_2,v_2) \times \mathbf{E}(u_1+m\Delta u, v_1+n\Delta v, r_1), \quad (21)$$

where

$$w_{1,mn} = \sqrt{1-(u_1+m\Delta u)^2-(v_1+n\Delta v)^2}. \quad (22)$$

The formula for coefficients in this case remains the same – (19). Formula (21) is also very close to (18), since $w_2/w_{1,mn}$ are close to 1. Numerical simulation also shows that the formulas work equally well.

The formulas can also be applied to samples equally spaced in azimuth-elevation coordinates. Let us show it for the case when either $\alpha \approx 0$ or $\beta \approx 0$. In this case the phase doesn't have an xy term, so the two-dimensional integral (19) becomes a product of two one-dimensional integrals and the formula takes simpler form.

First, consider $\alpha \approx 0$ (when field is measured in azimuth sections). Then field values are given in a rectangular grid in α-β:

$$\alpha = \alpha_1 + m\Delta u, \beta = \beta_1 + n\Delta v, \ \alpha_1 \approx 0. \quad (23)$$

These angles correspond to the following u and v:

$$u \approx \alpha_1 + m\Delta u, v = \sin(\beta_1 + n\Delta v), \quad (24)$$

i.e. v spacing becomes smaller when azimuth increases. Based on (13), to have a smaller spacing for v we need to increase the area for integration: $\tilde{T}_y = T_y / \cos(\beta)$. Substituting it into (19) yields:

$$k_{mn} = \frac{1}{T_x T_y} \int_{-T_x/2}^{T_x/2} e^{j\frac{k}{2}\left(\frac{1}{r_1}-\frac{1}{r_2}\right)x^2 + jkx(\alpha_2-\alpha_1)} e^{-jm\frac{2\pi}{T_x}x} dx \times \int_{-T_y/2}^{T_y/2} e^{j\frac{k}{2}\left(\frac{1}{r_1}-\frac{1}{r_2}\right)y^2 + jky(\beta_2-\beta_1)} e^{-jn\frac{2\pi}{T_y}y} dy. \quad (25)$$

Using same considerations one can obtain the formula for $\beta \approx 0$ (elevation section):

$$k_{mn} = \frac{1}{T_x T_y} \int_{-T_x/2}^{T_x/2} e^{j\frac{k}{2}\left(\frac{1}{r_1}-\frac{1}{r_2}\right)x^2 + jkx(\alpha_2-\alpha_1)} e^{-jm\frac{2\pi}{T_x}x} dx \times \int_{-T_y/2}^{T_y/2} e^{j\frac{k}{2}\left(\frac{1}{r_1}-\frac{1}{r_2}\right)y^2/\cos^2\alpha_1 + jky(\beta_2-\beta_1)/\cos\alpha_1} e^{-jn\frac{2\pi}{T_y}y} dy. \quad (26)$$

Also note, that all formulas were written in vector form so far. However, one doesn't need to measure all three components of the field. Firstly, it is not necessary to measure radial component since in Fresnel region it is small and in addition its influence on far field is reduced due to the fact that in (18) radial components are almost orthogonal to transversal components of the far field.

Also, (18) can be used in scalar form separately for co and cross components of the field. It is also due to the fact that in (18) only points with close angular directions are used, so basis vectors of co and cross polarizations are almost orthogonal, regardless of which pair of co and cross polarizations is used.

3.2. Analogies

Let us draw several analogies with other results of antenna measurements theory. First, let us apply (18),(19) for $r_1 = r_2$. In this case the formulas become interpolation formulas with sampling functions; the coefficients tend to:

$$k_{mn}(u_1,v_1,u_2,v_2)\big|_{r_1=r_2} \approx \operatorname{sinc}\left(\frac{\pi}{\Delta u}(u_2-(u_1+m\Delta u))\right) \times \operatorname{sinc}\left(\frac{\pi}{\Delta v}(v_2-(v_1+n\Delta v))\right). \quad (27)$$

This result was achieved in [15], [16]. Note, that there is a small difference between formulas, which is due to different mathematical models of the field. We consider models (1) and (2) more appropriate, because in the model used in [15] equivalent magnetic currents on the virtual aperture were not taken into account. However, numerical simulation shows that both models work equally well.

Note, that field interpolation formulas can be used in the far field reconstruction problem the following way. The field can be reconstructed with (18),(19) in sparse angular grid with spacing Δu, Δv from (13). Then interpolation formulas can be applied to determine field values between nodes of the grid.

Also the formulas similar to those obtained in the previous section can be found based on field integration on a spherical surface. To obtain such representation one can apply interpolation formulas to the field on a sphere, at which the measurements take place. Let us show this approach in scalar approximation. The field on a sphere $r_2>r_1$ in direction u_2, v_2 can be represented using field on a sphere r_1 in the Fresnel region:

$$E(u_2,v_2,r_2) = j\iint E(u,v,r_1)\frac{r_1^2 e^{-jk\Delta r(u,v)}}{\lambda\Delta r}d\Omega, \quad (28)$$

where $\Delta r(u,v)= |\mathbf{r}_2(u_2,v_2)-\mathbf{r}_1(u,v)|$.

Using formulas for field interpolation in Fresnel region it can be rewritten as (with $u_1= v_1=0$ for simplicity):

$$E(u_2,v_2,r_2) = j\iint \sum_{m,n} E(m\Delta u,n\Delta v,r_1) \times \frac{\sin((u-m\Delta u)\pi/\Delta u)}{(u-m\Delta u)\pi/\Delta u}\frac{\sin((v-m\Delta v)\pi/\Delta v)}{(v-m\Delta v)\pi/\Delta v} \times \frac{r_1^2 e^{-jk\Delta r(u,v)}}{\lambda\Delta r(u,v)}d\Omega \quad (29)$$

After changing the order of summation and integration and regrouping, the formula can be written as:

$$E(u_2,v_2,r_2) = e^{-jk(r_2-r_1)}\frac{r_1}{r_2} \times \sum_{m,n}\tilde{k}_{mn}E(m\Delta u,n\Delta v,r_1), \quad (30)$$

where

$$\tilde{k}_{mn} = j\iint \frac{\sin((u-m\Delta u)\pi/\Delta u)}{(u-m\Delta u)\pi/\Delta u} \times \frac{\sin((v-m\Delta v)\pi/\Delta v)}{(v-m\Delta v)\pi/\Delta v}\frac{r_1 r_2 e^{jk(r_2-r_1)-jk\Delta r(u,v)}}{\lambda\Delta r(u,v)}d\Omega. \quad (31)$$

Despite the difference between formulas (31) and (19), numerical evaluation shows that the coefficients coincide with high precision. Note, that a similar approach was used in near field to far field transformation in [17], where measurements on cylindrical surface were considered.

Finally, let us show that formulas obtained in [4], are a special case of (18) and (19) when $u_1=u_2\approx 0$, $v_1=v_2\approx 0$, $r_2\to\infty$. In the notations of this paper, the formulas from [4] can be written as:

$$\mathbf{I}(s\Delta u,t\Delta v,r_2) \approx \sum_{m,n}\hat{k}_{mn}\mathbf{I}((s+m)\Delta u,(t+n)\Delta v,r_1), \quad (32)$$

where $\mathbf{I}$ is a vector potential, and $\hat{k}_{mn}$ are:

$$\hat{k}_{mn} = \frac{1}{T_x T_y}\int_{-T_x/2}^{T_x/2} e^{j\frac{k}{2r_1}x^2} e^{-jm\frac{2\pi}{T_x}x}dx \times \int_{-T_y/2}^{T_y/2} e^{j\frac{k}{2r_1}y^2} e^{-jn\frac{2\pi}{T_y}y}dy. \quad (33)$$

With small u and v the vector potential $\mathbf{I}$ defined in [4] is proportional to the electric field vector $\mathbf{E}$. One can see that formulas (25) and (26) tend to (33) when $u_1=u_2\approx 0$, $v_1=v_2\approx 0$, $r_2\to\infty$. Note, that (25) uses azimuth and elevation angular variables as opposed to (33), which uses u and v; it makes (25) more precise for directions distant from the normal to the aperture.

3.3. The amount of sections

The k_{mn} coefficients rapidly decrease with m and n, as can be seen from Fig.2. Also, field in Fresnel region decreases as the observation point moves away from field maximum. Therefore, in sums (16), (18) a finite number of terms can be used. Let us estimate minimum amount of terms for correct far field reconstruction.

At first, consider a well-focused antenna with maximum along Z-axis, when central azimuth section is reconstructed. For field reconstruction M azimuth sections of the field in the Fresnel region are measured. To estimate $M_{\min}$ let us use a stationary phase method. The integrals defining k_{mn} and $E(m\Delta u,n\Delta v,r_1)$ have a stationary phase point under conditions $|m|\le T_x^2/(2\lambda r_1)$ and $|n|\le T_y^2/(2\lambda r_1)$. Hence, estimation for the amount of sections is [9]:

$$M_{\min} = 2\left\lfloor \frac{T_x^2}{2\lambda r_1}\right\rfloor + 1. \quad (34)$$

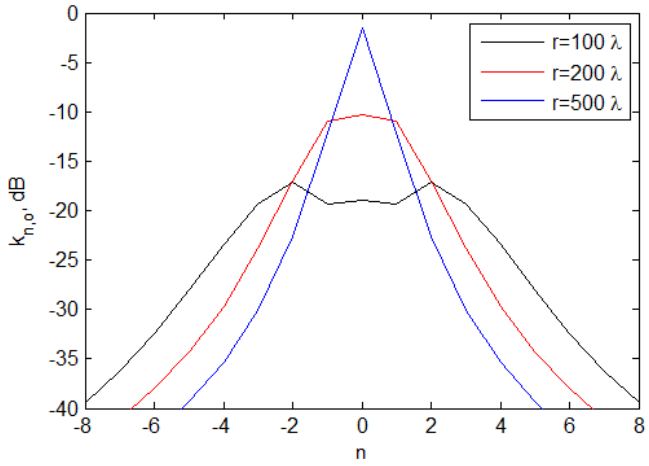


Figure 2. Magnitudes of $k_{n,0}$ coefficients for antenna with size 30 λ and different r.

However, the amount of n-terms shouldn't be limited with this estimation. It is due to contribution of the points with largest field amplitudes in Fresnel region to sums (16), (18) even for points distant from field maximum in far zone. Such terms have small k_{mn} but large $E(u+m\Delta u,v+n\Delta v,r_1)$, so they should also be included into the summation.

A similar effect takes place when a reconstructed section doesn't go through field maximum: in this case in addition to (34) it might be required to measure the sections which go through Fresnel field maximum. Also (34) cannot be applied to badly focused antennas (e.g. antennas with contoured beams), because estimation of the size of Fresnel field maximum made above might be incorrect in this case.

Note, that formula (34) is an estimation, which means that to obtain a more precise result it might be required to measure several additional sections.

3.4. Gain, EIRP and *G*/*T* calculation

Using the presented field transformation formulas it is possible determine antenna gain [10]. Since Poynting vector can be expressed as $\Pi=|E|^2/(60\pi)$, antenna gain can be determined by:

$$G(u,v)=\frac{4\pi r_2^2\Pi}{P}=\frac{|E(u,v,r_2)|^2\,r_2^2}{60P}, \qquad (35)$$

where P is antenna input power, $r_2>2D^2/\lambda$.

Substituting (18) to (35), gives:

$$G(u,v)=\frac{\left|r_1\sum_{m,n}k_{mn}E(u+m\Delta u,v+n\Delta v,r_1)\right|^2}{60P}. \qquad (36)$$

In (35), (36) the symbol E designates field amplitude at the given polarization, expressed in V/m. Since in practice the field is measured in non-calibrated units, one can use an auxiliary standard antenna with a known gain for calibration.

It is more convenient to use a standard antenna with far field distance smaller than r_1. In this case the AUT gain is:

$$G(u,v)=\frac{P_0G_0}{P}\times\left|\frac{1}{E_0}\sum_{m,n}k_{mn}E(u+m\Delta u,v+n\Delta v,r_1)\right|^2, \qquad (37)$$

where P_0, G_0, E_0 are input power, gain and measured non-calibrated field amplitude of the standard antenna.

If the AUT is an active antenna, one can determine its EIRP:

$$PG(u,v)=P_0G_0\times\left|\frac{1}{E_0}\sum_{m,n}k_{mn}E(u+m\Delta u,v+n\Delta v,r_1)\right|^2. \qquad (38)$$

Formulas (37),(38) are for a transmitting AUT. A similar formula for antenna gain can be written for a receiving AUT (according to reciprocity principle, measurements in transmitting mode and in receiving mode are equivalent). If an auxiliary transmitting antenna is working with a constant power, AUT gain is:

$$G(u,v)=G_0\times\left|\frac{1}{E_0}\sum_{m,n}k_{mn}E(u+m\Delta u,v+n\Delta v,r_1)\right|^2. \qquad (39)$$

The AUT noise quality G/T can be determined using [18]:

$$\frac{G(u,v)}{T}=\frac{4\pi k\Delta f}{\lambda^2}\frac{4\pi r_1^2}{P_tG_t}\times\frac{1}{2N}\left|\sum_{m,n}k_{mn}E(u+m\Delta u,v+n\Delta v,r_1)\right|^2, \qquad (40)$$

where k is Boltzmann constant, Δf is effective bandwidth, P_t and G_t are power and gain of the transmitting antenna, N is noise power at AUT.

4. Computer simulation results

In this section the results of computer simulation are presented. For simulation an axisymmetrical reflector antenna was used, D=30λ ($2D^2/\lambda$=1800λ). Using PO approximation several azimuth sections of Fresnel field at 200λ and a central section of far field were calculated. Elevation spacing was 1.8°. Based on (18), (19) far field was reconstructed and compared to the calculated far field. Fig.3 shows the results of field reconstruction using 7 sections of Fresnel field (according to (34)) and 11 sections, and a central section of the Fresnel field. For the first case the gain error was 0.03 dB, first side lobe level error was 0.4 dB. For the second case the gain error was 0.01 dB, first side lobe level error was 0.07 dB.

5. Configuration of the measurement system

To carry out measurements the AUT is adjusted to a positioner, which must be able to rotate in both azimuth and elevation (Fig.4). Measurement system configuration for AUT in receiving mode is shown in Fig.5.

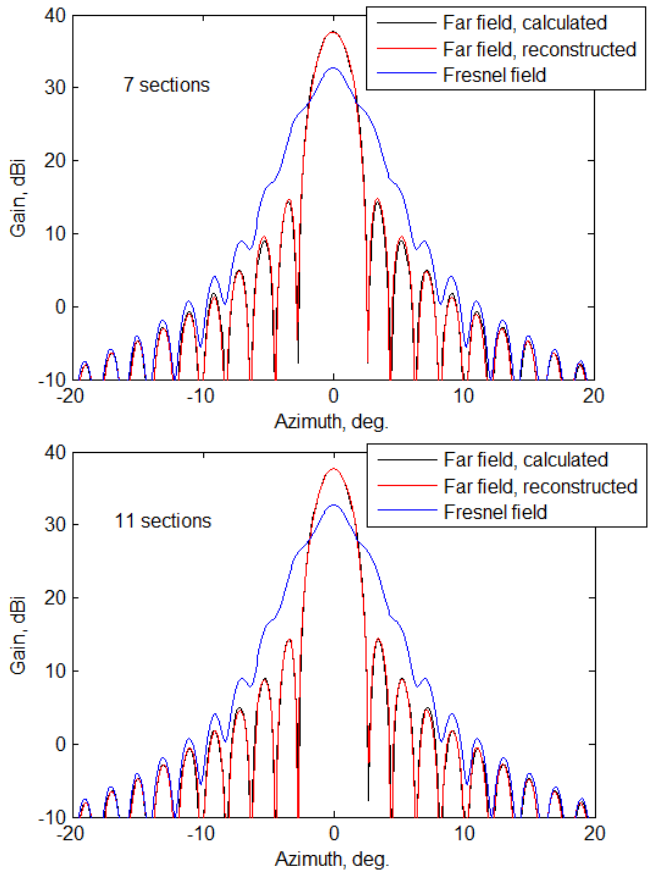


Figure 3: Computer simulation results using 7 sections and 11 sections in Fresnel region.

The AUT 5 receives the signal transmitted by an auxiliary antenna 2. For phase measurements a reference channel with an auxiliary receiving antenna 3 is used. Amplitude and phase of the received signal are registered in circuit analyzer 10 and stored in computer 12 for current positioning angles. The measurements take place when the positioner gradually changes its azimuth with a fixed elevation. After the section is measured, positioner changes elevation and then the measurements continue. After that the data are processed using (18) and (19) or (25)/(26).

For gain measurements the input of the mixer 7 is switched to a standard antenna 6 and then field amplitude in the maximum of standard antenna's radiation pattern is measured. Antenna gain is determined using (39). To measure gain or EIRP of a transmitting antenna the configuration shown in Fig.5 is modified accordingly.

6. Experimental verification

For verification of the method a set of experiments was carried out [9]. Field patterns of an offset reflector antenna with D=0.6 m at f=12.5 GHz ($2D^2/\lambda$=30m) with linear polarization were measured in an anechoic chamber. The measurements were taken at different distances: in far region at 76 m and in Fresnel region. In Fresnel region several elevation sections of the field with azimuth spacing 2° were taken. Then reconstructed far field was compared to measured far field.

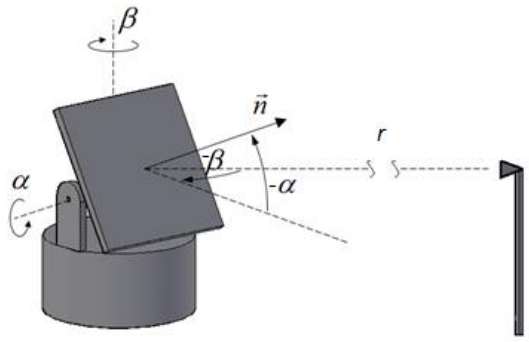


Figure 4: Antenna on a positioner.

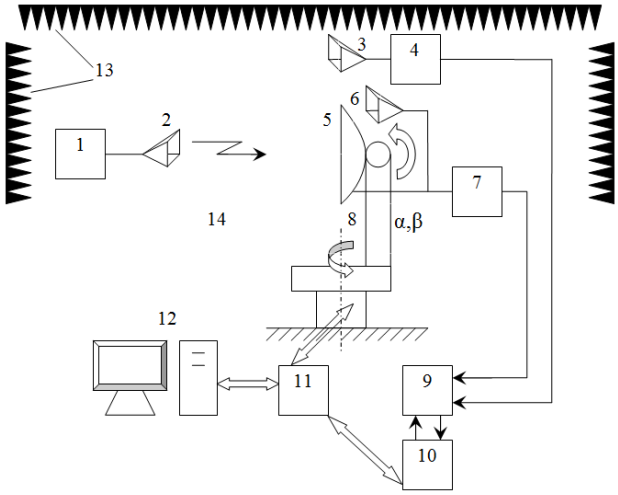


Figure 5: Configuration of the measurement system (simplified): 1 – generator; 2 – auxiliary transmitting antenna; 3 – reference channel antenna; 4 – reference channel mixer; 5 – AUT; 6 – standard antenna; 7 – measurements channel mixer; 8 – positioner; 9 – amplification an commutation unit; 10 – vector circuit analyzer; 11 – controller; 12 – computer; 13 – RAM; 14 – anechoic chamber.

In Fig.6 the results of far field reconstruction using 7 sections measured at 4 m and using 9 sections at 2.5 m are given. Comparing the reconstructed and measured radiation patterns one can see that the quality of reconstruction is good and the error is less than 3 dB in the dynamic range up to -50 dB. Error of maximum side lobe level reconstruction is 1 dB and 0.3 dB for 4 m and 2.5 m measurements.

Fig.7 shows the results of cross-polarization reconstruction using measurements at 7.6 m. The reconstructed pattern also agrees with the measured one.

The method described in this article has been used for antenna measurements in an anechoic chamber in company Radiofizika (measurements distance up to 80 m) for several years. Using this method many antennas were tested, with far field distance of hundreds of meters and even kilometers. Fig.8 shows the increase of maximum size of antennas, which can be tested in the anechoic chamber of Radiofizika, that is gained when Fresnel field measurements instead of far field measurements are used. The lower curve corresponds to the standard far field criterion $r>2D^2/\lambda$, the higher curve corresponds to criterion (20).

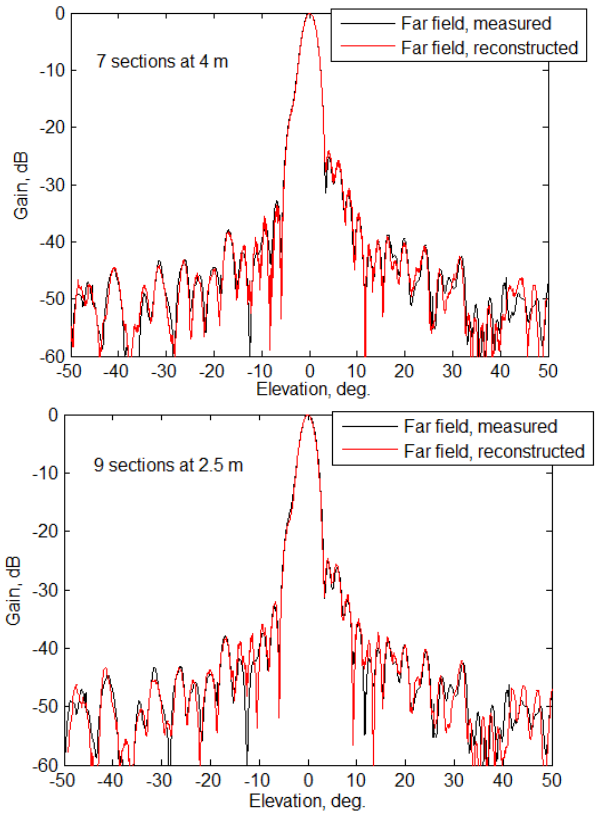


Figure 6. Experimental verification results (co-polarization).

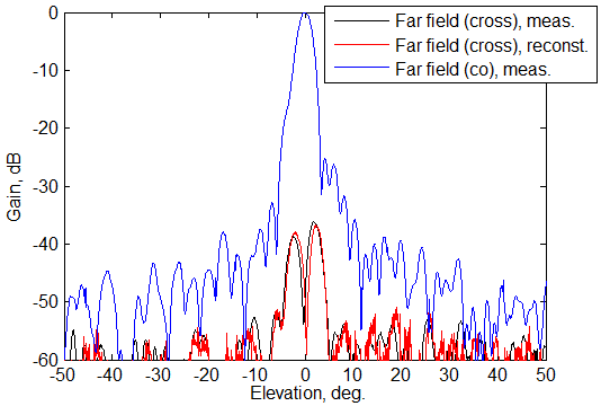


Figure 7. Experimental verification results (cross-polarization).

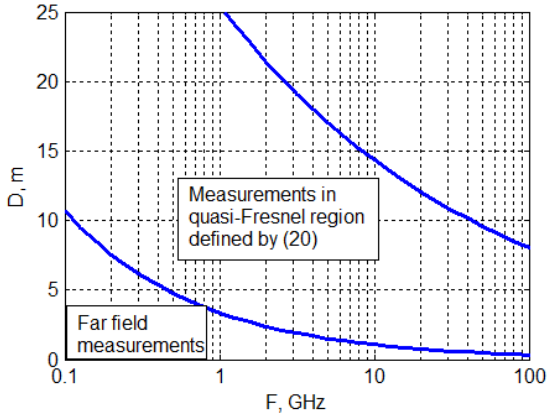


Figure 8. Maximum size of antennas, which can be tested in the anechoic chamber of Radiofizika, versus frequency.

Fig.9 demonstrates the example of far field reconstruction for a reflector antenna (D=3.8m). The antenna adjusted on a positioner is shown in Fig.10. Far field distance of the antenna at f=6.25 GHz is 600m. Measurement distance was 76 m, i.e. 8 times less.

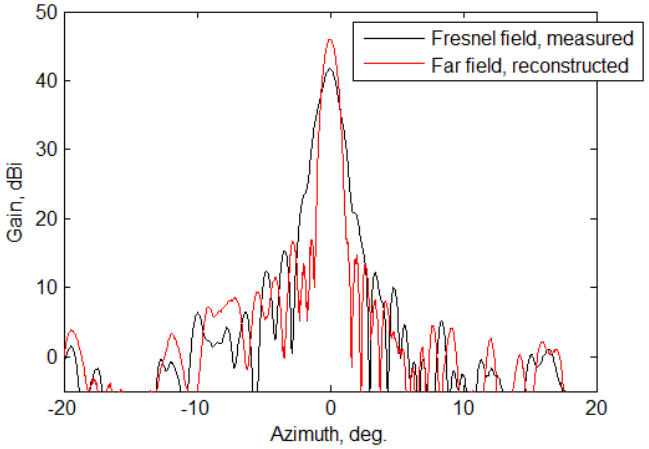


Figure 9. Reconstructed far field and central section of the measured Fresnel field for antenna D=3.8m, f=6.25GHz.



Figure 10. C-band reflector antenna (D=3.8m) on a positioner.

7. Conclusions

Fresnel field to far field transformation based on two-dimensional Fourier series expansion was presented. The method was compared to other results from antenna measurements theory. The results of computer simulation and experimental verification were presented. The results

suggest that the method ensures good quality of far field reconstruction. The method has been used in practice in an anechoic chamber of company Radiofizika for over 12 years for measurements of large-size antennas, and it has obvious advantages over outdoor far field measurements.

References

[1] R. Mittra, W. Imbriale, Gain and pattern measurements of large aperture antennas in the Fresnel zone, *Proc. IEEE APS Digest*, 1969, vol. 7, pp. 40-42.

[2] Yu.A. Kolosov, A.P. Kurochkin, Radiation pattern reconstruction using field known in a limited angular sector, *Antennas*, vol.16, 1972, pp. 25-37 (in Russian).

[3] G. D'Elia, G. Leone, R. Pierri, A new approach in the near field-far field transformation. *Proc. IEEE APS Digest*, Houston, USA, 1983, pp. 495-498.

[4] G. D'Elia, G. Leone, R. Pierri, G. Schirinzi, New Method of Far-Field Reconstruction from Fresnel Field, *Electronics Letters*, vol. 20, no. 8, Apr. 1984, pp. 342-343.

[5] G. Evans, Far Field Correction for Short Antenna Ranges, *Proc. AMTA Symposium*, 1985, pp. 34.1–34.9.

[6] G. Evans, *Antenna Measurement Techniques*, Artech House, 1990.

[7] M. Sierra-Castañer, S. Burgos, Fresnel zone to far field algorithm for rapid array antenna measurements, *Proc. EuCAP Symposium*, Rome, Italy, April 2011, pp. 3251-3255.

[8] K. Wu, S. Parekh, A method of transforming Fresnel field to far field for circular aperture antennas, *Proc. IEEE APS Digest*, May 1990, pp. 216–219.

[9] I.L. Vilenko, A.A. Meduhin, Yu.A. Suserov, A.K. Tobolev, A.V. Shishlov, Reconstruction of antenna radiation pattern by using data of measurements in a Fresnel region with test facility intended for far-field measurements, *Antennas*, vol. 1(92), pp. 46–52, 2005 (in Russian).

[10] S.-S. Oh, J.-M. Kim, J.-H. Yun, Antenna measurement on cylindrical surface in Fresnel region using direct far-field measurement system, *ETRI J.*, vol. 29, no. 2, pp. 135–142, 2007.

[11] S.-S. Oh, J.-H. Yun, New Method for Predicting the Electromagnetic Field at a Finite Distance Using Fresnel Field Transformation, *IEEE Antennas and Wireless Propagation Letters*, vol. 7, pp. 291–293, 2008.

[12] Yu.V. Krivosheev, A.V. Shishlov, Development of the method of antenna radiation pattern reconstruction using measurements in the Fresnel zone, *Proc. Radars and Communication*, Moscow, Russia, November 2010, pp. 320-324 (in Russian).

[13] L. D. Bakhrakh, I. V. Kaplun, A. P. Kurochkin, Determination of Parameters of Antennas Illuminated by a Nonplanar Wave, *Radio Engineering and Electronic Physics*, vol. 20, Dec. 1975, pp. 1-8. Translation from Russian.

[14] L.D. Bakhrakh, S.D. Kremenetskiy, A.P. Kurochkin, V.A. Usin, Ya.S. Shifrin, *Near field antenna measurements*, Nauka, 1985 (in Russian).

[15] O. Bucci, G. Franceschetti, G. D'Elia, Fast analysis of large antennas – A new computational philosophy, *IEEE Transactions on Antennas and Propagation*, vol. 28 , 1980, pp. 306 – 310.

[16] G. D'Elia, G. Leone, R. Pierri, D. Valentino, Numerical evaluation of the near field using sampling expansions, *Proc. IEEE APS Digest*, 1982, vol.20, pp. 241 – 244.

[17] O. Bucci, C. Gennarelli, Use of sampling expansions in near-field-far-field transformation: the cylindrical case. *IEEE Transactions on Antennas and Propagation*, vol. 36, 1988, pp. 830 – 835.

[18] E.N. Egorov, *Basics of microwave electronics*, 1983 (in Russian).

Wideband Calculable Antenna for EMC Measurements

Syarfa' Zahirah Sapuan*, Alireza Kazemipour, Mohd Zarar Mohd Jenu,

Center for Electromagnetic Compatibility, Universiti Tun Hussein Onn Malaysia (UTHM), Malaysia
* syarfa@uthm.edu.my

Abstract

An optimized wideband biconical antenna is presented for EMC measurement which potentially can be used as standard-reference antenna. The antenna is "direct-fed" (no Balun needed) with optimized dimension to match with 50Ω coaxial cable from 200MHz to 2GHz. Balun itself has an important contribution on E-field measurement uncertainty, therefore, this antenna can improve the measurement accuracy. Meanwhile, the antenna has a fixed phase-center for the various frequencies and the related uncertainties can be removed. The antenna factor (AF) of the antenna has been evaluated using analytical and numerical method. Experimental "Standard Antenna Method SAM" has been used to verify the theoretical results and a good agreement is stated.

1. Introduction

E-field measurement together with the magnetic field, are the basis of every experimental study in the domain of ElebtroMagnetic Compatibility EMC. The measuring device is generally an antenna which itself should be calibrated for the accurate measurements. The antenna can be calibrated by using different methods such as standard antenna method (SAM) or standard site method (SSM). Both methods require a reference antenna and/or reference site. Usually, measurement calibration techniques have been used to determine the antenna factor (AF), antenna gains (G) and its input impedance Z_{ant}. The most important antenna parameter for EMC is the AF which is defined as the ratio of the electric-field (E) of a plane-wave incident on the antenna to the detected output voltage (V):

$$E = AF\ (dB/m)\ .\ V \qquad (1)$$

The calibration process is long in time and expensive and the accuracy is highly depended on the reference/site quality. Therefore, a well-calculated antenna can be preferable in order to achieve good accuracy and less cost.

Half-wavelength dipole has well-known calculable radiation characteristic and can be used as a "calculable standard" for EMC calibration with low uncertainty level [1-3]. However, dipole antenna is a narrowband antenna and for different frequencies its length should be adjusted to the relevant half-wavelength. This fact increased the calibration time and cost. Therefore, it is helpful to focus on calculable wideband antenna.

The suggested biconical antenna here, is "direct-fed" (no Balun needed) (Fig. 1) with optimized dimension to match to 50Ω coaxial cable from 200MHz to 2GHz. Balun itself has an important contribution on E-field measurement uncertainty, therefore, this antenna can improve the measurement accuracy. Meanwhile, the antenna has a fixed phase-center for the various frequencies and the related uncertainties can be removed.

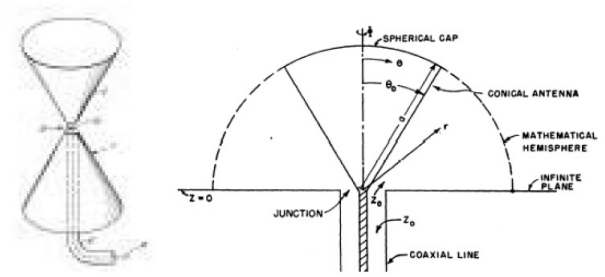


Figure 1: Biconical antenna with direct coaxial fee

2. Theory

The input impedance and radiation pattern of a conical antenna (with perfect direct coaxial-feed) is evaluated analytically by using Bessel's functions [4, 5]. The input impedance (R_{in} + jX_{in}) is deduced as a function of antenna size (*a*) and flare angle (θ) by simplifying and developing/simplifying the long Bessel's functions. An optimized 50Ω wideband antenna can be achieved by choosing the flare-angle around 60-70 degrees. The analytical results are compared with CST numerical simulation together with the experimental results (Fig. 2)
It's to mention that the 'feed gap-effect' is not taken into account in the analytical and antenna pattern. For the low frequencies the coupling effects antenna to ground plane and for the higher frequencies the feed-gap effects can affect the measurement results of impedance and AF.

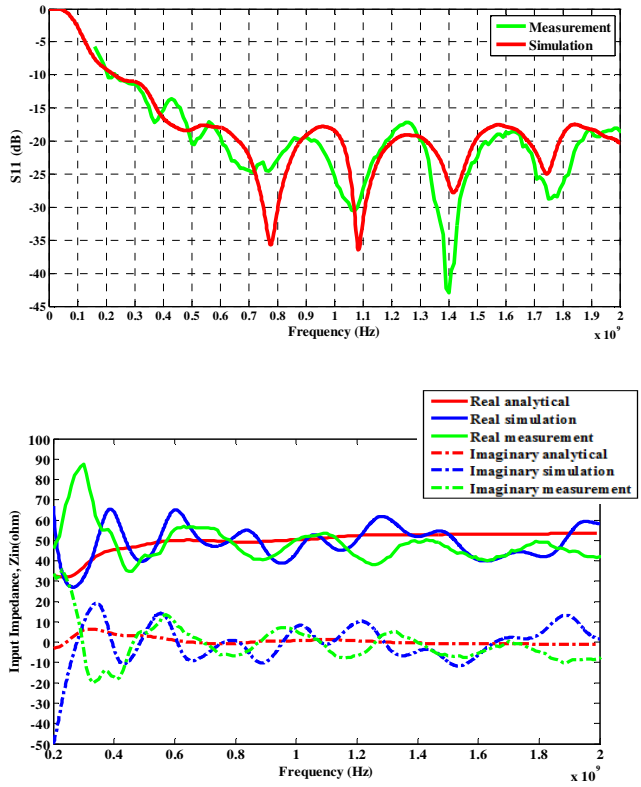


Figure 2: Input Impedance ($Z_{in} = R_{in} + jX_{in}$) and Γ ($S_{11}$) of the antenna

In the literature, the antenna usually supposed perfectly-matched (Rr = 50Ω), then the (AF) can be evaluated based on the effective-length (L_e) and the antenna gain (G) :

$$(AF)^{-1} \sim Le = \frac{\lambda}{\pi}\sqrt{\frac{GRr}{120}} \qquad (2)$$

For a real antenna which the input impedance is a complex value ($R_{in} + jX_{in}$) and not perfectly matched to 50Ω, the AF formula should be corrected to take into account the internal power reflections:

$$AF = \frac{|E|}{V} = \frac{2\pi}{\lambda}\sqrt{\frac{120}{D\,|1-\Gamma^2|R_{load}}} \qquad (3)$$

In which, R_{load} is usually a 50Ω coaxial connector, D is the antenna directivity and Γ is the input reflection-coefficient of the antenna.

3. Results

D and Γ can be driven from analytical and/or simulation methods and therefore, the (AF) will be deduced theoretically. The results are compared with the experimental ones which performed with Standard Antenna Method (SAM) (Table 1)

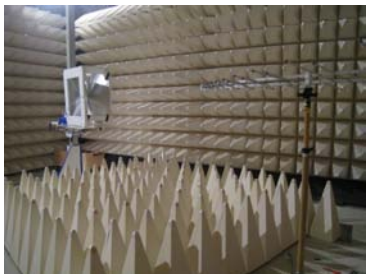
As shown in Table 1, the analytic AF gives a good agreement with simulation and measurement results. However, SAM can cause up to 3dB error and uncertainty on (AF) especially at low frequency due to the coupling effect, the reference antenna uncertainty and semi-anechoic chamber conditions (Fig 3). The reference antennas used in these measurements are usually standard dipole, standard horn or standard log-periodic antenna. These standard antennas have an already-calibrated gain (G) and (AF) which contains sometimes high uncertainty level because of the measurement condition and especially their frequency-dependent variable phase-center.

Table 1: Antenna Factor "AF" (dB/m): analytical, simulation and measurement results.

F (MHz)	AF (Analytical)	AF (Simulation)	AF (measurement)
200	15.8	16.1	15.6 ± 1
300	17.7	17.6	21.5 ± 1
400	19.9	21.8	22.3 ± 1
500	21.9	21.9	22.6 ± 0.5
600	24.1	24.0	23.6 ± 0.5
700	25.1	25.3	25.8 ± 0.5
800	24.6	24.7	25.8 ± 0.5
900	24.9	25.0	26.2 ± 0.5
1000	27.0	27.1	25.3 ± 0.5
1100	26.7	26.5	27.2 ± 1
1200	26.7	27.1	27.4 ± 1
1300	27.7	27.9	28.6 ± 1
1400	28.0	28.4	27.7 ± 1
1500	28.0	28.4	28.3 ± 1
1600	28.5	28.8	28.9 ± 1
1700	29.1	29.5	28.8 ± 1
1800	29.2	29.9	30.3 ± 1
1900	29.6	30.1	29.7 ± 1



(a)



(b)

Figure 3: (a) Antenna prototype and the (b) measurement SAM set-up

4. Conclusions and perspectives

An optimized wideband biconical antenna is presented for EMC measurement which can be used as standard-reference antenna because of its calculable characteristics. The antenna is optimized to match with 50Ω coaxial cable from 200MHz to 2GHz. Theoretical and experimental results of the antenna input impedance and the Antenna-Factor show good agreement.

Better coaxial connector with a high-quality soldering junction can reduce the feed-gap effects, as for the antenna-ground coupling, analytical study is in progress [6] to take into account its effect on the AF and the related uncertainties Equations.

References

[1] M. Alexander, "Using the calculable dipole antenna for antenna calibration and validation of EMC test sites" APEMC 2010, pp. 782-785.

[2] A. Kazemipour and X. Begaud “Calculable dipole antenna for EMC measurements with low-loss wide-band balun from 30 MHz to 2 GHz” .*Journal of Electromagnetics*.25.187-202, 2005.

[3] A. Kazemipour and X. Begaud, “Feasibility of a Wideband Calculable Standard Antenna for EMC Measurements,” Precision Electromagnetic Measurements Digest, 2008. CPEM 2008. 8-13 June 2008

[4] C. Papas and R. King, "Input impedance of wide-angle conical antennas fed by a coaxial line," *Proceedings of the IRE,* vol. 37, pp. 1269-1271, 1949.

[5] C. Papas and R. King Radiation from wide-angle conical antennas fed by a coaxial line”, *Proceedings of the IRE*.39.49-51. ,1951.

[6] A. Kazemipour, X. Begaud, “A Simple closed-form formula for the Mutual impedance of dipoles”. *Microwave and Optical Technology Letters*. Wiley. 34. No 5 (2002), 371 – 374.

On the Evaluation of the Shielding Effectiveness of Electrically Large Enclosure

Angelo Gifuni[1], Antonio Sorrentino[1], Alessandro Fanti[2*], Giuseppe Ferrara[1], Maurizio Migliaccio[1], Giuseppe Mazzarella[2], and Federico Corona[1]

[1]Dipartimento per le Tecnologie, Università degli Studi di Napoli Parthenope,
Centro Direzionale Isola C 4, Napoli, Italy
[2]Dipartimento di Ingegneria Elettrica ed Elettronica Pad. B, Università degli Studi di Cagliari
Piazza d'Armi 09123 Cagliari, Italy
*Alessandro Fanti, E-mail: alessandro.fanti@diee.unica.it

Abstract

The shielding effectiveness (SE) has become a fundamental step in testing active or passive electric devices. The Reverberating Chamber (RC) is a well-established method for determining the SE since has the advantage to expose the material to a more realistic environment. In this paper the SE_e of electrically large enclosure with a metallic mesh grid in a RC is evaluated. Enclosures made with metallic mesh are considered. In particular, it is shown that the SE of a material is unable to provide complete information for the SE_e of electrically large enclosure made with the same material. Moreover, this latter one is related to the loading conditions within the enclosure itself. Measurements accomplished at RC of the Università di Napoli Parthenope (formerly Istituto Universitario Navale, IUN) confirm the physical soundness of the proposed approach.

1. Introduction

The importance of electromagnetic interference (EMI) and electromagnetic compatibility (EMC) in daily environment rises from the fact that the environment is electromagnetic hostile. The increasing use of electronic devices makes the EMI and EMC issues of great relevance in such environments in which more devices are used in disparate contexts. The enclosure are great of importance for controlling the emission of such electronic systems. On the other hand, they increase immunity of the devices subject to strong electromagnetic interference. A measure of the efficiency of an enclosure is the shielding effectiveness (SE_e), i.e. the ability of attenuating the sources of electromagnetic disturbance. Usually, the nested reverberating chamber (RC), with the mode-stirred method, is employed to characterize the enclosures [1-2]. Nested RCs have been used in the past to determine the SE of material [3]. The RC is an electrically large chamber which uses several stirring technique to randomize the input electromagnetic field in order to expose the device under test to a more realistic environment [1].

The SE_e of an enclosure is defined as follows [1-2]

$$SE_e = -10\log_{10}\left(\frac{P_{in}}{P_{out}}\right) \quad (1)$$

where P_{in} is the power received by the receiving antenna placed in RC and P_{out} is the power received by a receiving antenna placed in the enclosure. Therefore, the SE_e relates the interior fields to the external incident field. The SE_e is a fundamental step in establishing the EMC of active or passive devices.

Among the different enclosures used to shield the electronic devices, the metallic meshes are potentially attractive as electromagnetic shield enclosure because of their reduced weight per unit area compared to metallic box. However, the metallic mesh often forms parts of enclosures, as it allows the aeration of the electronic circuits, which are shielded by enclosures themselves. The electromagnetic behavior of wire meshes has been previously addressed in [4-5].

In this paper, an electrically large enclosure is placed in an RC and measurements of the SE_e are accomplished. This type of configuration is essentially a nested RC [3, 6]. Clearly, the walls of the enclosure are regarded as reciprocal walls. In Fig.1 is shown a sketch of the measurement set-up. It includes two antennas in the RC and a small monopole probe, which is placed on one interior wall of the enclosure. In Section 3, the experimental set-up is further discussed. Being the walls made of metallic mesh, the enclosure within the RC has no stirrers inside since all points into the enclosures statistically have the same fields level; indeed it is uniformly and randomly excited from all sides. As matter of fact, no paddles within the enclosure are needed as long as the SE_e is weak or moderate. Following the mathematical model developed in [7] this paper shows that the SE_e of the enclosure is smaller than the one obtained by a same material exposed to a RC electromagnetic field. Further, the SE_e is depending on the loading conditions of the enclosure. Measurements accomplished at RC of the

Università di Napoli Parthenope (formerly Istituto Universitario Navale, IUN) confirm the physical soundness of the proposed approach and its applicability from an operational point of view.

2. Mathematical Model

In this section, two equivalent mathematical models for SE_e, based on the power balance, are shown. An approach followed for measuring the SE_e of electrically large enclosure is based on the RC technique. It is assumed that the field is uniform and isotropic inside and outside the enclosure. Following the power balance theory, the SE_e of an electrically large enclosure can be expressed as follows [1-2]

$$\mathrm{SE_e} = 10\log\left(\frac{4\pi V}{\langle\sigma_t\rangle\lambda Q}\right) \tag{2}$$

where V and Q are the volume and the quality factor of the enclosure, respectively, λ is the working wavelength, and σ_t is the average transmission cross section (TCS) of the enclosure walls. $\langle\ \rangle$ indicates an incidence angle average over 4π steradians.

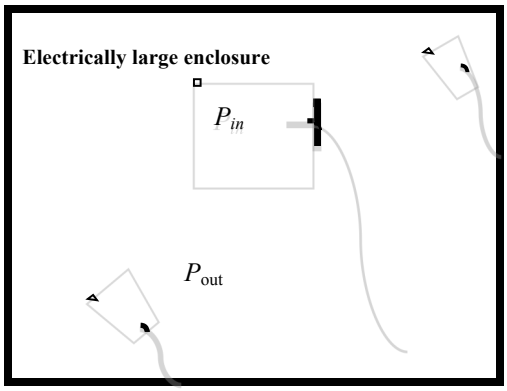


Figure 1: Illustration of the RC set-up measurements

From power balance it can be written [7]:

$$(S_o\sigma_t - S_i\sigma_t) = S_i(\sigma_{w,i} + \sigma_{a,i} + A_e) \tag{3}$$

whence [7]

$$\mathrm{SE_e} = \frac{P_{in}}{P_{out}} = \frac{\sigma_t + \sigma_{w,i} + \sigma_{a,i} + A_e}{\sigma_t} \tag{4}$$

where S_i and S_o are the incident power density inside and outside the enclosure, respectively; $\sigma_{w,i}$ is the total average absorption cross section (ACS) of the enclosure wall when the field impinges from the inner, $\sigma_{a,i}$ is the average ACS of the load, A_e is the effective area of the receiving antenna inside the enclosure [2], and σ_t is the one in eq. (2).
It must be noted that the trend of SE_e given by eq. (2), for different frequency range is not straightforward to draw, particularly for enclosure where σ_t is very sensitive to the frequency changes. Further, Q factor in eq. (2) is inversely proportional to σ_t. Equation (4) improves the comprehension of the SE_e of an enclosure; by setting

$$\sigma_{ae,i} = \sigma_{w,i} + \sigma_{a,i} + A_e \tag{5}$$

eq. (4) becomes

$$\mathrm{SE_e} = \frac{\sigma_t + \sigma_{ae,i}}{\sigma_t} \quad . \tag{6}$$

If the enclosure is unload, i.e. $\sigma_{a,i} = 0$, then

$$\sigma_{ae,i} = \sigma_{w,i} + A_e \quad . \tag{7}$$

In the case of a metallic mesh enclosure, the behavior of SE_e can be simply described by observing that the transmission cross section grows more rapidly with increasing of the frequency respect to $\sigma_{ae,i}$. In particular, at low frequencies, σ_t is smaller than $\sigma_{ae,i}$. Hence, a SE_e greater than 1 is expected. On the other hand, as the frequency gradually increases, the transmission cross section increases faster than $\sigma_{ae,i}$. Therefore, a value of SE_e about equal to 1 (0 dB), is obtained. Accordingly, a decreasing trend of SE_e, with frequency is expected. In [7], it is shown that SE_e can be expressed as follows

$$\mathrm{SE_e} = \mathrm{SE}\cdot(1-\mathrm{R}) + \frac{\mathrm{A_e}}{\sigma_\mathrm{t}} \tag{8}$$

where $\sigma_{a,i}$ has been assumed equal to zero; SE is the shielding effectiveness of the wall material; R is the reflectivity of the enclosure walls when the field impinges from the inner of the enclosure [8]. σ_t can be expressed as follows [7]

$$\sigma_\mathrm{t} = \frac{\sigma_{\mathrm{t,gA}}}{\mathrm{SE}} \tag{9}$$

where $\sigma_{t,gA}$ is the TCS of the total geometric area of the wall enclosure when they are considered perfectly transmitting; clearly, σ_t is attendant to the same geometric area. The SE can be achieved as follows [7]:

$$\mathrm{SE} = (1-\mathrm{R}) + \frac{\sigma_{\mathrm{w,i}}}{\sigma_{\mathrm{a,gA}}} \tag{10}$$

where $\sigma_{a,gA}$ is the total geometric area of the enclosure walls when they are considered perfectly absorbing [7]. It

is important to note that $\sigma_{a,gA} \equiv \sigma_{t,gA} = S_g/2$ where S_g is the surface area of enclosure walls.

Although the losses were negligible by setting $\sigma_{w,i}=0$ in eq. (10), pioneering results about R (SE) of metallic mesh grids have been carried out in [9]. In this paper, initial results of SE_e are predicted by using (8)-(10) and R (SE) measurements [9]; a comparison with measured SE_e is shown as well.

3. Experiment Results

In this section, a meaningful set of experimental results is shown. Before that, a brief description of the calibration procedure is first summarized. For the evaluation of SE_e, the power levels in the enclosure are monitored by a small probe placed on one of the enclosure wall. Hence, large reflection at the antenna terminal can occur due to the mismatch between the probe and the coaxial cable used to deliver the field to the probe terminal. To overcome this issue, a correction of the SE_e is accomplished. As matter of fact, two separate calibrations were performed (continuous stirring chamber): a transmission one and a reflection procedure. The two measurements are taken in two separate steps. Hence, the scattering coefficients $\dot{S}_{12}$ and $\dot{S}_{22}$ are measured. Port1 is permanently connnected to the horn antenna in RC. Port2 is in succession connected to the horn antenna in RC (horn-horn, hh) and to monopole antenna on the enclosure wall (horn-monopole, hm) according to Fig.1. Therefore, SE_e is achieved as follows

$$SE_e = \left\langle \left| \dot{S}_{12} \right|^2 \right\rangle_{hh} - \left\langle \left| \dot{S}_{12} \right|^2 \right\rangle_{hm} + \left(1 - \left| \left\langle \dot{S}_{22} \right\rangle \right|^2 \right) \qquad (11)$$

All the terms in eq. (11) are taken in dB values.

This correction has been accomplished to avoid the strong mismatch error affecting measurements that have been accomplished in the RC of the IUN. It is a 8 m^3 metallic chamber wherein three mechanical stirrers are present. The first one (S1), placed on the left of the entrance door, has a rectangular shape of about 1.84mx0.45m size; the second stirrer (S2) and the third stirrers (S3) have a Greek-cross shape. The former one has bars of about of 1.84mx0.25m size; it is placed in front of the entrance door. The (S3) stirrer has bars of about of 1.20mx0.18m size and it is placed in the ceiling. The S1, S2 and S3 stirrers work in continuous mode with a maximum speed of 190, 390 and 320 rate per minute (rpm), respectively. In Figure 2 a sketch of the IUN RC with a particular of the enclosure employed in the measurements, is shown.

In all experiments the transmitting and the receiving antenna used in the RC are both Ets-Lindgren double-ridged waveguide horn certified to work in the 1 – 18 GHz frequency range. An Agilent Technologies Vector Network Analyzer (VNA) is used in experimental tests. Measurements by shifting the measuring frequency in the designed bandwidth (1 – 18 GHz) by steps of 200 MHz are accomplished. 3000 independent samples are acquired at each frequency point. It must be noted that the statistically independence of the acquired samples, provided by the vibration of IUN RC walls that add up to the mechanical stirring, has been verified by the autocorrelation function (not shown to save space). The scattering coefficient S_{21} is measured and an off-line data analysis is accomplished. The software used to acquire and to off-line analyze the data is developed in LabVIEW, a graphical development environment of the National Instruments (NI).

In order to validate the theoretical model with the proposed procedure, two different-size enclosures of metallic grid, have been employed. Both the enclosures are cubic boxes of 49 cm side size. The first enclosure is made with metallic grid and its mesh size is 5 mm, see Fig. 3; the second is made with metallic fabric and its mesh size is 1 mm: the latter has a foam structure as a support, see Fig. 2. They have been placed on foam support within the RC during the measurements; the clearance from the chamber floor is 50 cm. This approach is essentially a nested RC. The stirrers within RC accomplish the randomization of the electromagnetic field. Hence, the uniformity and isotropy of the field inside the enclosure can be assumed since it is uniformly and randomly excited from all sides. In any case, when SE_e values increase until 10 dB about, a conventional stirrer must be placed within the enclosure; by experience, this concept is very more stringent for monopole mismatch measurements. It is important to note that for such measurements the enclosure is excited by monopole itself and that for the frequency points where the mismatch is very strong, the residual error about S_{22} parameter, can significantly affect the achieved SE_e, see eq. (11).

The losses inside the enclosure reduce the impedance mismatch of the probe monopole. In any case, if the assumed hypothesis of uniformity and isotropy of the field deteriorates, then the quality of expected results deteriorates as well. In particular, that problem occurs at lower frequencies in the employed frequency range, where the modal behavior of the enclosure is not negligible.

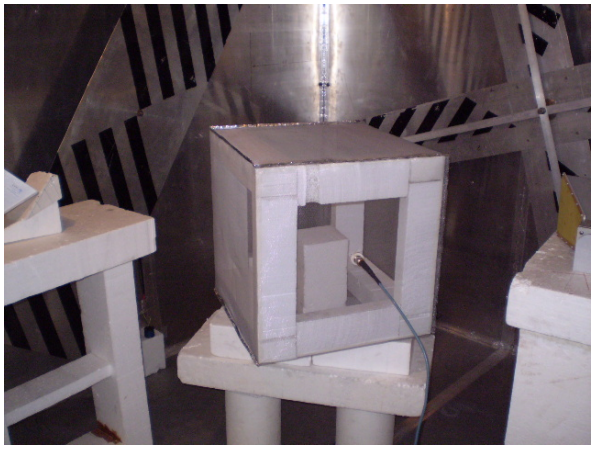


Figure 2: A sketch of the IUN RC with a particular of the enclosure made with mesh size of 1 mm.

In Fig. 4 is shown the SE_e obtained with the enclosure made with a mesh size of 5 mm. The SE_e of the enclosure with the correction due to mismatch of the probe (blue line) and without it (black line) is shown. As expected, according to the theoretical model, the SE_e shows a decreasing behavior with the frequency. It must be noted that when the black and blue line have the same value, i.e. around 3 GHz and from 6 to 8 GHz, the return loss on the receiving antenna is always smaller than 10 dB, see Figure 5.



Figure 3: 5 mm metallic mesh enclosure used for the experiments.

A visual comparison with the results obtained in [9] shows a value of SE_e smaller than SE, to witness that a shielding reduction is obtained when an enclosure is employed.
In Fig. 6 is shown the SE_e obtained with the enclosure made with a mesh size of 1 mm.

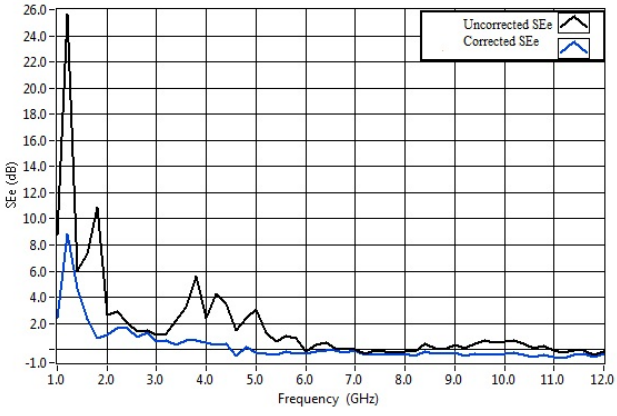


Figure 4: SE_e from measurements of 5 mm mesh size enclosure.

In conclusion, the SEe of an enclosure with wall of metallic grids decreases with the increasing of the frequency. Moreover, the SE_e is smaller than the corresponding one obtained with the same material of which the enclosure is made [9]. The SE_e of an enclosure tends to the one of a metallic grid if a load is placed within the enclosure [9].
In Fig.7 is shown a comparison between the shielding effectiveness of the enclosure made with metallic mesh of 1 mm with a piece of absorber (blue line) and without it (black line).

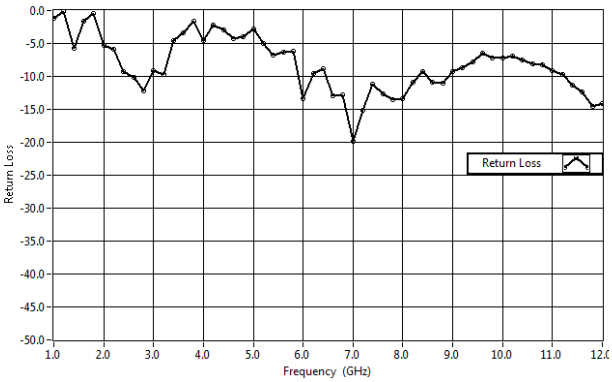


Figure 5: Return Loss, enclosure built with metallic mesh whose side is 5 mm.

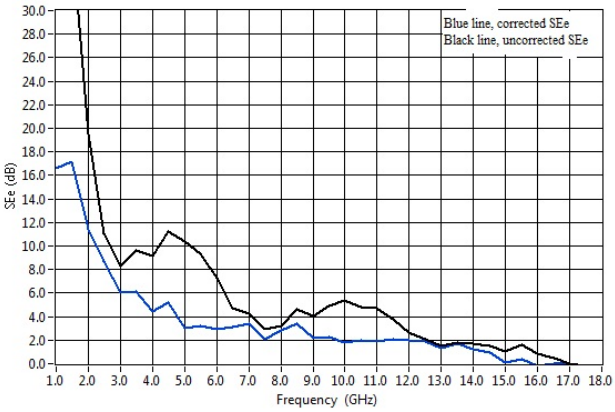


Figure 6: SE_e from measurements of 1 mm mesh size enclosure.

The absorber is of the Emerson-Cuming, its dimensions are 9 cm x 9 cm x 9 cm, and it is place on a foam support, see Fig.3. As expected, the loading effect improves the SE_e of the enclosure that increases from 2 to 10 dB about. In particular, apart from the effect due to the mismatch of the monopole, at lowest frequency, σ_t becomes smaller than $\sigma_{ae,i}$; also, $\sigma_{w,i}$ is negligible with respect to σ_t, but it has no zero value.

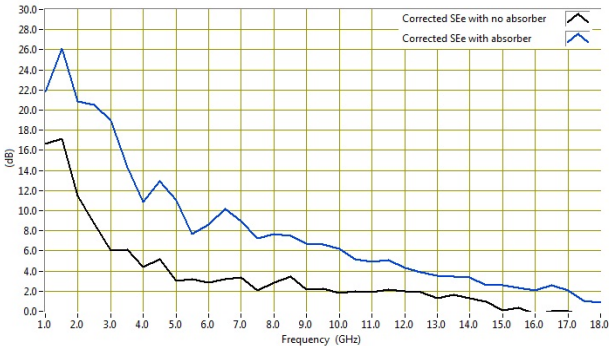


Figure 7: Enclosure made with metallic mesh of 1 mm side dimension. Difference between the SE_e with the absorber (blue line) and without it (black line) inside the enclosure.

4. Comparisons and Discussion

In this Section, the comparison between the expected results of SE_e and the measured ones is discussed. The former are achieved according to (8)-(10); the experimental measurements of R (SE), reported in Figs. 8 and 9, are the same as in [9]. One specifies that those measurements were available for the paper, and that the frequency step is 1 GHz. For the enclosure with mesh size of 5 mm, the expected SE_e is about zero dB over the whole frequency range from 1 to 18 GHz. This agrees well with experimental results in Fig. 4, in particular from 2 GHz up. Fig. 10 shows the expected results for $\sigma_{w,i}+A_e$ (black line) and $\sigma_{w,i}$ (blue line). In Fig. 11 SE_e for the enclosure with mesh size of 1 mm is shown. The calculation of A_e takes into account the developing of the model (6) [7].
The estimate of $\sigma_{w,i}$ has been simplified; indeed, it has been estimated by considering the solid part of inner total area of the wall enclosure. Clearly, the losses have been estimated by considering a field uniform and isotropic [7], [10]. For the enclosure with mesh size of 1 mm, the ratio between solid area and surface total area is equal to 0.6.

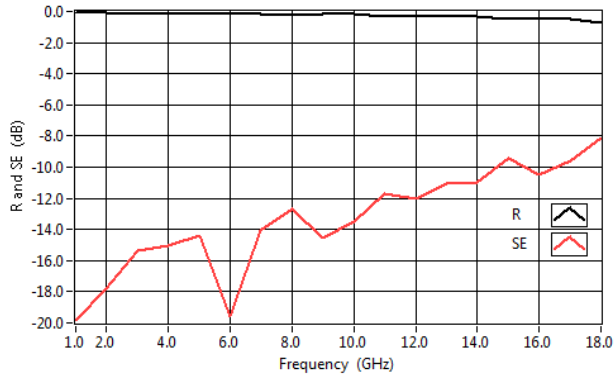


Figure 8: Reflectivity (black line) and SE (red line) vs. frequency of a 1 mm side dimension mesh grid.

Results in Fig. 11 shown that the expected SE_e appreciably differs from measured one from 1 to 5 GHz, and the result mismatch decreases as the frequency increases. The authors think that the mismatch of the results at lower frequencies in the employed frequency range is due to the fact that the modal behavior of the enclosure is not negligible, so that the necessary property of uniform and isotropy of the field are no more fully satisfied.
Uniformity and isotropy of the field can be improved by a mechanical stirred installed inside the enclosure; however, at frequencies where the modal density is inadequate, it is not possible to obtain field uniformity and isotropy within the enclosure.

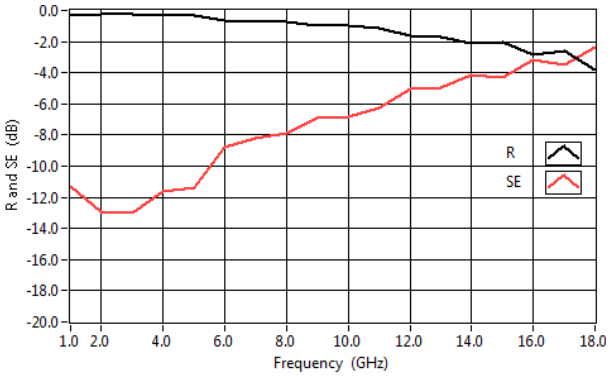


Figure 9: Reflectivity (black line) and SE (red line) vs. frequency of a 5 mm side dimension mesh grid

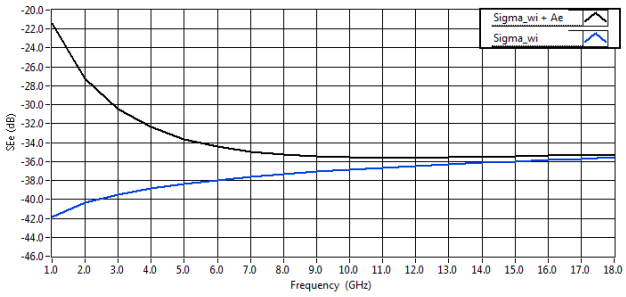


Figure 10: Expected results for $\sigma_{w,i}+A_e$ (black line) and $\sigma_{w,i}$, (blue line) for the enclosure with mesh size of 1 mm

Different conditions of field affect the estimate of all the parameters in (4); that is, both the estimate of $\sigma_{w,i}$ and A_e would turn out to be affected; however, at lower frequencies the effective area of the monopole is significantly greater than $\sigma_{w,i}$, and it can assume appreciably values higher from the expected ones. Also, at the frequency points where the mismatch is very strong, the correction in eq. (11) can turn out been affected.

Finally, another reason for mismatch of the results can be the accuracy of the R (SE) measurements.

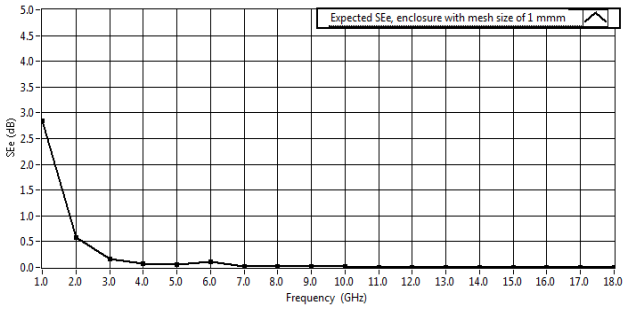


Figure 11: Expected SE_e for the enclosure with mesh size of 1 mm

Both models (2) and (7) have been developed under conditions of uniformity and isotropy of the field; in principle, they could be applied in different field conditions as well; but that is very difficult, as the estimates of the parameters requires the accurate knowledge of the field structure inside an enclosure.
It is well known that the leakage for an enclosure can be low, but it cannot be zero. Therefore, it is important to note that an enclosures must be made with material having both high SE and low R [11], where the latter refers to internal side of the enclosure walls

5. Conclusions

In this paper a different form of the SE_e of an enclosure made with metallic grids has been proposed and successfully tested by measurements accomplished at IUN RC. Measurements have been accomplished for the first time on enclosure totally made with square metallic mesh and they have been proved that the SE_e of an enclosure is always smaller than the SE of a material. Further, the SE_e of such enclosures is decreasing with the increasing of frequency. Finally, by loading the enclosure with absorbing material, it has been noted that the SE_e tends to the one of the wall metallic grid.

Acknowledgement

The authors thank Mr. Giuseppe Grassini of the Electrical and Electronic Measurements Lab (at Department of Technology, University of Napoli Parthenope) for helping in conducting the experiments that have been used in this paper.

References

[1] Holloway C. L., D. A. Hill, M. Sandroni, J. M. Ladbury, J. Coder, G. Koeple, A, C, Marvin, and Y. He, “Use of Revereration Chambers to Determine the Shielding Effectiveness of Physical Small, Electrically Large Enclosures and Cavities,” *IEEE Trans. On. Electromag. Compatibility*, Vol. 50, No. 4, pp. 770-782, 2008.

[2] Hill D. A., M. T. Ma, A. R. Ondrejka, B. F. Riddle, M. L. Crawford, and R. T. Johnk, “Aperture Excitation of Electrically Large, Lossy Cavities,” *IEEE Trans. On. Electromagn. Compatibility*, Vol. 36, No. 3, pp. 169-178, 1994.

[3] Holloway C. L., D. A. Hill, J. Ladbury, G. Koepke, R. Gracia, “Shielding Effectiveness Measurements of Materials Using Nested Reverberation Chamber,” *IEEE Trans. On. Electromag. Compatibility*, Vol. 45, No. 2, 350-356, 2003.

[4] K.F.Casey, “Electromagnetic Shielding Behavior of Wire Mesh Screens”, *IEEE Trans. On. Electromag. Compatibility*, Vol. 30, No. 3, pp.298-306, 1988.

[5] V. M. Primiani, F. Moglie, A. P. Pastore, “Field penetration through a Wire Mesh Screen Excited by a Reverberation Chamber Field: FDTD Analysis and Experiments”, *IEEE Trans. On. Electromag. Compatibility*, Vol. 51, No. 4, pp.883-891, 2009.

[6] A. Gifuni, M. Migliaccio, “Used of Nested Reverberating Chambers to Measure Shielding Effectiveness of Nonreciprocal Samples Taking into Account Multiple Interactions”, *IEEE Trans. On. Electromag. Compatibility*, Vol. 50, No. 4, pp. 783-786, 2008.

[7] A. Gifuni, “Electrically Large Enclosures Under the Effect of the Losses: Relation Between the Shielding Effectiveness of an Enclosure and the Wall Material,” submitted to *IEEE Trans. On Electromagnetic Compatibility* .

[8] A.Gifuni, "On the Measurement of the Absorption Cross Section and Material Reflectivity in a Reverberation Chamber," *IEEE Trans. Electromagn. Compat.,* vol.51, pp. 1047-1050, 2009.

[9] A. Gifuni, A. Sorrentino, G. Ferrara, M. Migliaccio, A. Fanti, G. Mazzarella, “Measurements on the Reflectivity of Materials in a Reverberating Chamber”, *Proceeding on Antenna and Propagation Conference* (LAPC), pag.1-4, 2011.

[10] D. A. Hill, "A Reflection Coefficient Derivation for the *Q* of a Reverberantion Chamber," *IEEE Trans. Electromagn. Compat.*, vol.38, pp.591-592, November 1996.

[11] N. F. Colaneri and L. W. Shacklette, "EMI Shielding Measurements of Conductive Polymer Blends," *IEEE Trans. Instrum. Meas.*, vol.41, pp.291-297, April 1992.

Diffraction by a lossy 90° dielectric wedge

Gianluca Gennarelli[1], Giovanni Riccio[1]

[1]Department of Electronic and Computer Engineering, University of Salerno, Fisciano (SA), Italy
*corresponding author, E-mail: griccio@unisa.it

Abstract

This study concerns the plane wave diffraction by a 90° dielectric wedge in the case of normal incidence with respect to the edge. The material forming the wedge has a finite conductivity. The here adopted approach is based on a Physical Optics approximation for the equivalent electric and magnetic surface currents involved in the radiation integrals used to represent the fields scattered in the inner region of the wedge and the surrounding space. Uniform asymptotic evaluations of such integrals allow one to obtain closed form expressions for the diffracted field, thus resulting easy to handle and compute. Numerical comparisons with Finite Difference Time Domain and Finite Element Method results validate the approach.

1. Introduction

The canonical problem of the electromagnetic diffraction by dielectric wedges assumes great significance when modeling propagation scenarios involving man-made structures. For instance, the ruptures into structures and infrastructures caused by natural disasters can be represented in the form of a wedge-shaped fracture. They modify the electromagnetic response of the scene under investigation and the Geometrical Theory of Diffraction (GTD) can be used as efficient tool for describing this occurrence.

Diffraction by a wedge is a well-covered topic in the scientific literature, but the available results mainly concern impenetrable structures. In the case of penetrable wedges, the available methodologies provide approximate analytical or heuristic solutions, or attempt to solve the problem in an exact sense by combining analytical and numerical techniques to evaluate integral equations (see [1]-[5] as interesting bibliography). In this framework, a Uniform Asymptotic Physical Optics (UAPO) solution for predicting the field diffracted by a lossless 90° dielectric wedge has been recently presented in closed form by the authors [6].

This work deals with the evaluation of the electromagnetic field in presence of a right-angled wedge consisting of a dielectric having finite conductivity. In particular, a solution for the diffracted field is obtained in the case of an electric polarized plane wave normally incoming from the free-space surrounding the structure. The diffraction problem is split into two sub-problems concerning the inner region of the wedge and the surrounding space. For each of them, equivalent electric and magnetic PO surface currents lying on the corresponding faces of the wedge are assumed as sources in the radiation integrals. Useful approximations and integral representations followed by uniform asymptotic evaluations of the resulting integrals lead to closed form formulas for the diffracted field. These last are given in terms of the transition function of the Uniform Theory of Diffraction (UTD) [7] and the Fresnel's reflection and/or transmission coefficients of the structure.

2. Problem statement and UAPO approach

The geometry of the diffraction problem is illustrated in Fig. 1. A linearly polarized electromagnetic plane wave having the electric field parallel to the edge illuminates the wedge at normal incidence. The material forming the wedge is assumed nonmagnetic ($\mu_r = 1$), and characterized by the complex relative permittivity $\varepsilon_c = \varepsilon_r(1 - j\tan\delta)$, where ε_r is its real part and $\tan\delta$ denotes the effective electric loss tangent. According to the apex angle, the wedge surfaces are denoted by S_0 and $S_{\pi/2}$. In the adopted polar coordinate system (ρ,ϕ) , they are located at $\phi = 0$ and $\phi = 3\pi/2$, respectively, and divide the space into the outer region $(0 < \phi < 3\pi/2)$ and the inner region $(3\pi/2 < \phi < 2\pi)$. The angle ϕ' defines the incidence direction and its considered values ensure that both faces are illuminated $(\pi/2 < \phi' < \pi)$. The $e^{j\omega t}$ time dependence is assumed throughout the work.

The approach uses the radiation integral for evaluating the field $\underline{E}^s$ scattered at the observation point P in the inner and outer regions:

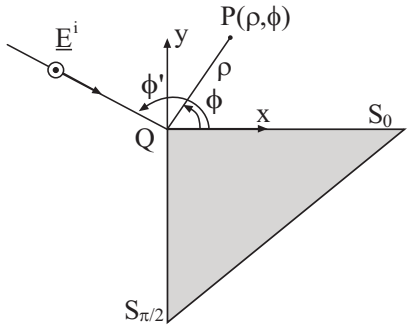


Figure 1: Geometry of the diffraction problem.

$$\underline{E}^s \cong -jk\iint_S \left[\left(\underline{\underline{I}}-\hat{R}\hat{R}\right)(\zeta \underline{J}_s)+\underline{J}_{ms}\times\hat{R}\right]G(\underline{r},\underline{r}')\,dS \quad (1)$$

where $S = S_0 \cup S_{\pi/2}$, $\underline{J}_s$ and $\underline{J}_{ms}$ are the equivalent electric and magnetic surface currents lying on S. Moreover, $G(\underline{r},\underline{r}')$ is the Green's function, ζ and k are the impedance and propagation constant of the medium in the considered observation region, $\underline{r}$ and $\underline{r}'$ fix the observation and source points, respectively, $\hat{R}$ is the unit vector from the radiating element at $\underline{r}'$ to P, and $\underline{\underline{I}}$ is the (3x3) identity matrix.

Now it is possible to use the approximation $\hat{R} \simeq \hat{s}$ in (1), $\hat{s}$ being the unit vector in the diffraction direction. Then, by taking into account the linearity of the integral in (1) and using the PO approximation for $\underline{J}_s = \underline{\tilde{J}}_s e^{jq}$ and $\underline{J}_{ms} = \underline{\tilde{J}}_{ms} e^{jq}$ (q is a phase factor depending on the field impinging over S), the scattered field can be rewritten as:

$$\begin{aligned}
&\underline{E}^s = \underline{E}^s_0 + \underline{E}^s_{\pi/2} \cong \\
&-\frac{jk}{4\pi}\left[\left(\underline{\underline{I}}-\hat{s}\hat{s}\right)\zeta\underline{\tilde{J}}_{s_0}+\underline{\tilde{J}}_{ms_0}\times\hat{s}\right]\iint_{S_0} e^{jq_0}\frac{e^{-jk|\underline{r}-\underline{r}'|}}{|\underline{r}-\underline{r}'|}\,dS_0 + \\
&-\frac{jk}{4\pi}\left[\left(\underline{\underline{I}}-\hat{s}\hat{s}\right)\zeta\underline{\tilde{J}}_{s_{\pi/2}}+\underline{\tilde{J}}_{ms_{\pi/2}}\times\hat{s}\right]\iint_{S_{\pi/2}} e^{jq_{\pi/2}}\frac{e^{-jk|\underline{r}-\underline{r}'|}}{|\underline{r}-\underline{r}'|}\,dS_{\pi/2} \\
&= \left[A_0 I_0 + A_{\pi/2} I_{\pi/2}\right] E^i\,\hat{z}
\end{aligned}$$

in which I_0 and $I_{\pi/2}$ represent the integrals over S_0 and $S_{\pi/2}$. The terms A_0 and $A_{\pi/2}$ are introduced to put in evidence the incident field E^i at the diffraction point Q on the edge.

According to the approach in [6], the original problem is decomposed into two sub-problems related to the outer region and the inner region, respectively. For each of them, the diffracted field is obtained by performing uniform asymptotic evaluations of I_0 and $I_{\pi/2}$. Accordingly, the edge diffracted field $\underline{E}^d = E^d \hat{z}$ results expressed by:

$$\begin{aligned}
E^d &= \left[A_0 I_0^d + A_{\pi/2} I_{\pi/2}^d\right] E^i \frac{e^{-jk\rho}}{\sqrt{\rho}} = \\
&= \left[D_0 + D_{\pi/2}\right] E^i \frac{e^{-jk\rho}}{\sqrt{\rho}} = D E^i \frac{e^{-jk\rho}}{\sqrt{\rho}}
\end{aligned} \quad (3)$$

where $I^d_{0,\pi/2}$ are the diffraction contributions resulting from the asymptotic evaluations of $I_{0,\pi/2}$. The UAPO diffraction coefficient D is expressed as superposition of two terms related to S_0 and $S_{\pi/2}$, respectively. It is in closed form, and contains the transition function $F_t(\cdot)$ of the UTD [7] and the Fresnel's reflection (R) and/or transmission (T) coefficients involved in the propagation mechanisms.

3. UAPO diffraction coefficients

The expressions of the UAPO diffraction coefficients relevant to the outer and inner regions are reported in this section.

3.1. Outer region

The considered incidence direction fixes two reflection boundaries in correspondence of the specular reflection directions relevant to S_0 and $S_{\pi/2}$, where the Geometrical Optics (GO) fails.

The asymptotic evaluation of I_0^{out} gives:

$$\begin{aligned}
D_0^{out} &= \frac{e^{-j\pi/4}}{2\sqrt{2\pi k_0}}\left[\sin\phi'\left(1-R_0\right)-\sin\phi\left(1 \quad R_0\right)\right] \\
&\cdot\frac{F_t\left[\frac{k_0\rho}{2}\left(\frac{\cos\phi+\cos\phi'}{\sin\phi'}\right)^2\right]}{\cos\phi+\cos\phi'}
\end{aligned} \quad (4)$$

(2)

For what concerns the diffraction contribution relevant to $S_{\pi/2}$, it results:

$$\begin{aligned}
D_{\pi/2}^{out} &= \frac{e^{-j\pi/4}}{2\sqrt{2\pi k_0}}\left[\cos\phi\left(1+R_{\pi/2}\right)-\cos\phi'\left(1-R_{\pi/2}\right)\right] \\
&\cdot\frac{F_t\left[\frac{k_0\rho}{2}\left(\frac{\cos\left(3\pi/2-\phi\right)+\cos\left(3\pi/2 \quad \phi'\right)}{\sin\left(3\pi/2-\phi'\right)}\right)^2\right]}{\cos\left(3\pi/2-\phi\right)+\cos\left(3\pi/2 \quad \phi'\right)}
\end{aligned} \quad (5)$$

3.2. Inner region

According to [8], the wave penetrating into a lossy dielectric material attenuates in the direction normal to the surface and travels along a different direction. Two transmission boundaries are originated inside the wedge.

The asymptotic evaluation of I_0^{in} provides:

$$\begin{aligned}
D_0^{in} &= \frac{\left(k_d/k_0\right)e^{-j\pi/4}}{2\sqrt{2\pi k_d}}T_0\left[-\frac{\left(\left|\underline{\beta}_{t,0}\right|\cos\gamma_0^t + j\left|\underline{\alpha}_{t,0}\right|\right)}{k_0\sqrt{\varepsilon_c}}+\sin\phi\right] \\
&\cdot\frac{F_t\left[\frac{\beta_d\rho}{2}\frac{\left(\left(\beta_d/k_0\right)\cos\phi+\cos\phi'\right)^2}{\left(\beta_d/k_0\right)^2-\cos^2\phi'}\right]}{\left(\beta_d/k_0\right)\cos\phi+\cos\phi'}
\end{aligned} \quad (6)$$

where $k_d = \beta_d - j\alpha_d$ is the complex propagation constant, in which

$$\beta_d = k_0 \sqrt{\frac{\varepsilon_r}{2}} \sqrt{\sqrt{1+\tan^2\delta}+1} \tag{7}$$

$$\alpha_d = k_0 \sqrt{\frac{\varepsilon_r}{2}} \sqrt{\sqrt{1+\tan^2\delta}\quad 1} \tag{8}$$

Moreover, $\underline{\beta}_{t,0}$ and $\underline{\alpha}_{t,0}$ denote the propagation and attenuation vectors (see [8] for their expressions) associated to the plane wave transmitted through S_0, and γ_0^t is the angle between them.

The diffraction contribution relevant to $S_{\pi/2}$ is given by:

$$D_{\pi/2}^{in} = \frac{(k_d/k_0)\mathrm{e}^{-j\pi/4}}{2\sqrt{2\pi k_d}} T_{\pi/2} \cdot \left[\frac{\left(\left|\underline{\beta}_{t,\pi/2}\right| \cos\gamma_{\pi/2}^t - j\left|\underline{\alpha}_{t,\pi/2}\right| \right)}{k_0\sqrt{\varepsilon_c}} + \cos\phi \right] \cdot \frac{F_t\left[\frac{\beta_d \rho}{2} \frac{\left((\beta_d/k_0)\sin\phi + \sin\phi'\right)^2}{(\beta_d/k_0)^2 - \sin^2\phi'} \right]}{(\beta_d/k_0)\sin\phi + \sin\phi'} \tag{9}$$

where $\underline{\beta}_{t,\pi/2}$, $\underline{\alpha}_{t,\pi/2}$ and $\gamma_{\pi/2}^t$ are pertinent to the transmission through $S_{\pi/2}$.

4. Numerical results

Numerical tests are reported in this section to demonstrate the effectiveness of the UAPO-based approach. A plane wave impinging at $\phi' = 150°$ and a circular observation path with radius $\rho = 5\lambda_0$, λ_0 being the free-space wavelength, have been considered.

The UAPO-based results for the total field patterns have been computed and compared in Figs. 2-5 with those obtained by means of two reliable numerical solvers. The former is the RF Module of Comsol Multiphysics [9], a commercial tool based on the Finite Element Method (FEM). The latter is an in-house code based on the Finite Difference Time Domain (FDTD) technique [10]. Such a code implements the total field/scattered field (TF/SF) technique to generate an accurate incident numerical plane wave. The outer boundaries of the computational domain are terminated with a Uniaxial Perfectly Matched Layer (UPML) [11] backed with a PEC wall.

Results plotted in Figs. 2-5 show that the total field patterns obtained by means of the UAPO approach are continuous at the GO shadow boundaries. Moreover, they turn out to be in very good agreement with the FDTD and COMSOL results in the inner and outer regions. Note that the vertical solid line reported at $\phi = 270°$ in all the figures corresponds to $S_{\pi/2}$.

5. Conclusions

UAPO solutions have been proposed for the diffraction problem relevant to an electric polarized plane wave illuminating both the external faces of a lossy dielectric wedge. They are formulated in the UTD framework and expressed in terms of the GO response of the structure. According to the performed numerical tests, they give accurate results for the total field in the dielectric material and the surrounding space. Moreover, they are user-friendly analytical solutions and it is very simple to implement them in computer simulators.

References

[1] R. E. Burge et al., Microwave scattering from dielectric wedges with planar surfaces: a diffraction coefficient based on a physical optics version of GTD, *IEEE Trans. Antennas Propag.*, 47: pp. 1515–1527, 1999.

[2] J. F. Rouviere, N. Douchin, P. F. Combes, Diffraction by lossy dielectric wedges using both heuristic UTD formulations and FDTD, *IEEE Trans. Antennas Propag.*, 47: pp. 1702–1708, 1999.

[3] M. A. Salem, A. H. Kamel, A. V. Osipov, Electromagnetic fields in presence of an infinite dielectric wedge, *Proc. R. Soc. Lond.* A, 462: pp. 2503-2522, 2006.

[4] C. H. Seo, J. W. Ra, Plane wave scattering by a lossy dielectric wedge, *Microwave Opt. Technol. Lett.*, 25: pp. 360-363, 2000.

[5] S. Y. Kim, J. W. Ra, S. Y. Shin, Diffraction by an arbitrary-angled dielectric wedge: part I–physical optics approximation, *IEEE Trans. Antennas Propag.*, 39: pp. 1272–1281, 1991.

[6] G. Gennarelli, G. Riccio, A uniform asymptotic solution for diffraction by a right-angled dielectric wedge, *IEEE Trans. Antennas Propag.*, 59: pp. 898–903, 2011.

[7] R. G. Kouyoumjian, P. H. Pathak, A uniform geometrical theory of diffraction for an edge in a perfectly conducting surface, *Proc. IEEE*, 62: pp. 1448-1461, 1974.

[8] C. A Balanis, *Advanced Engineering Electromagnetics*, Wiley, New York, 1989.

[9] COMSOL Multiphysics® v. 3.5a, Users' Guide, RF Module, 2008.

[10] A. Taflove, S. C Hagness, *Computational Electromagnetics: The Finite Differnce Time Domain Method*, Artech House, Norwood, 2000.

[11] S. D. Gedney, An anisotropic perfectly matched layer absorbing medium for the truncation of FDTD lattices, *IEEE Trans. Antennas Propag.*, 44: pp. 1630-1639, 1996.

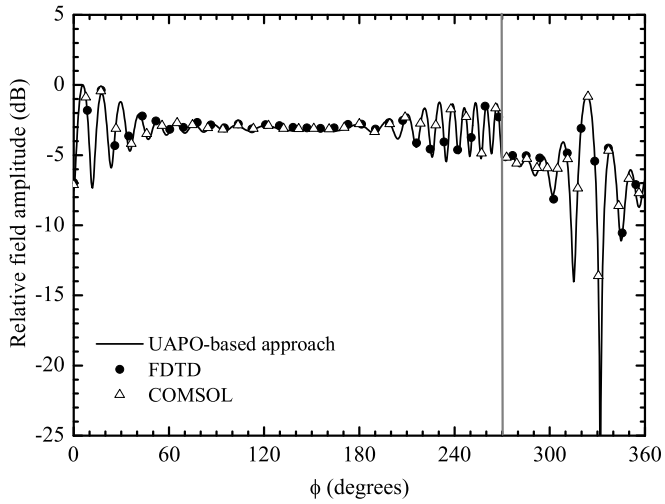


Figure 2: Relative amplitude of the total field when $\varepsilon_r = 2$ and $\tan\delta = 0.01$.

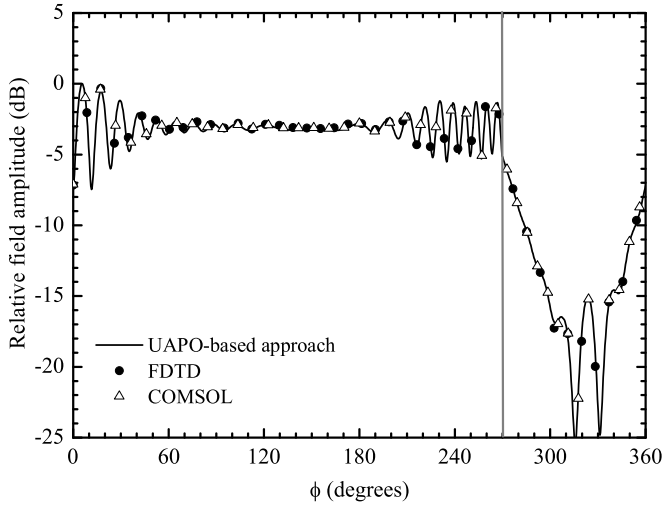


Figure 3: Relative amplitude of the total field when $\varepsilon_r = 2$ and $\tan\delta = 0.1$.

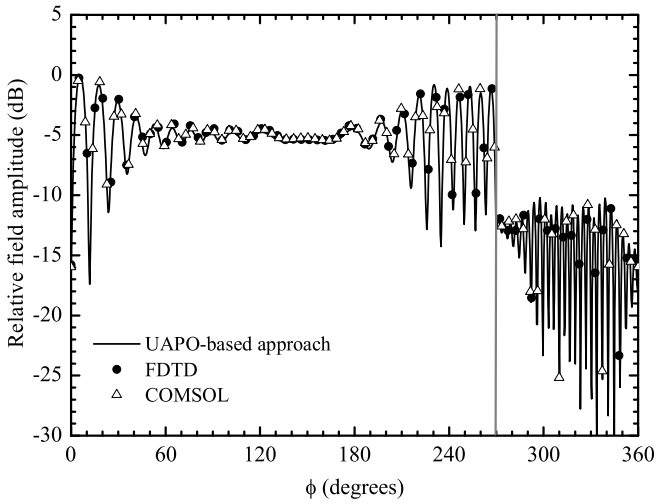


Figure 4: Relative amplitude of the total field when $\varepsilon_r = 10$ and $\tan\delta = 0.01$.

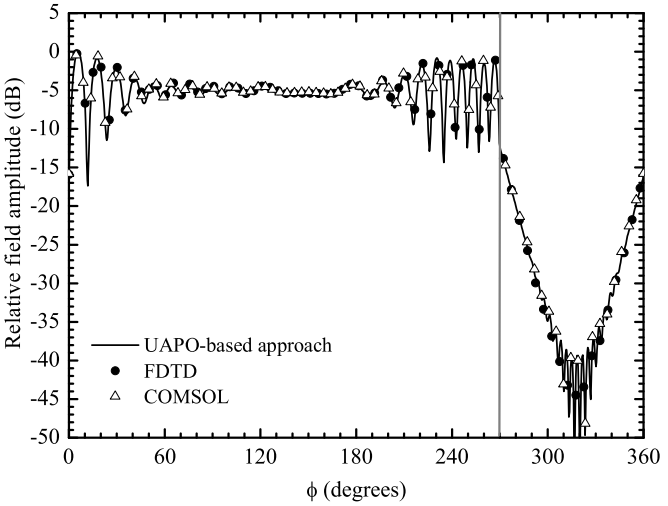


Figure 5: Relative amplitude of the total field when $\varepsilon_r = 10$ and $\tan\delta = 0.1$.

MESUA: A model dedicated to radar detection in bistatic and/or monostatic mode

Ngoc Truong Minh Nguyen[1,*], David Lautru[1], Hélène Roussel[1],

[1]UPMC Univ Paris 06, UR2, L2E, F-75005, Paris, France
*corresponding author, E-mail: minhn2t@yahoo.com

Abstract

In this paper, a 3-D model called MESUA (Model for Electromagnetic Scattering for Urban Areas) is proposed in order to characterize the field scattered by an urban area, which is composed of a group of buildings, for both monostatic and bistatic radar configurations. This model is based on a ray-tracing technique combined with the asymptotic Uniform Theory of Diffraction (UTD). It is useful not only in elucidating mechanisms of ray propagation through the observed area, but also in evaluating the amplitude and the phase at any point in the far-zone scattered field above the ground. In order to validate our model, some comparisons with the commercial software XGTD® are presented. Moreover, our model is tested against 33-37 GHz indoor measurements conducted in the anechoic chamber of the "ElectroMagnetic Effects Research Lab" (EMERL) in Singapore. These latter comparisons have shown that the model can predict precisely the location of a target placed between two metallic plates representing walls.

1. Introduction

Synthetic Aperture Radar (SAR) imaging of urban areas has received much interest in recent years with some promising applications [1-3]. A major challenge is to give a fast and accurate ElectroMagnetic (EM) model in order to provide the synthetic data for imaging algorithms. The faster the information retrieval process, the more effective the actions to reach required objectives. In addition, in a way to evaluate the best bistatic radar configuration, it is necessary, at the beginning, to develop a three-dimensional model to predict the diffracted field by a scenario.

This information can be employed for many uses such as infrastructure development planning, physical environment protection, and traffic surveillance. Many models have been proposed for the propagation prediction in urban medium [4-6].

Due to this issue, a bistatic EM model used to determine the scattered field by an urban area is developed in this paper. A ray-tracing approach with particular attention on multiple wall reflections and diffractions on building edges compounding with the high-frequency asymptotic methodology Uniform Theory of Diffraction (UTD) [7] is used to calculate the scattered field.

2. The model

2.1. The model

2.1.1. Radar configuration

The radar configuration used in our model is illustrated in Fig. 1. The transmitter and the receiver are co-localized or separated in order to perform monostatic or bistatic configurations. (θ_i, Φ_i) are the elevation and azimuth angles of the incident wave; ($\vec{k}_i$,$\vec{v}_i$,$\vec{h}_i$) is the polarization base for the incident wave. We keep the same definition for the scattering wave with the subscript *s*. This configuration is taken into consideration with the purpose of improving the radar capacity of detection and identification, and thus to increase the detection capability of a target [8].

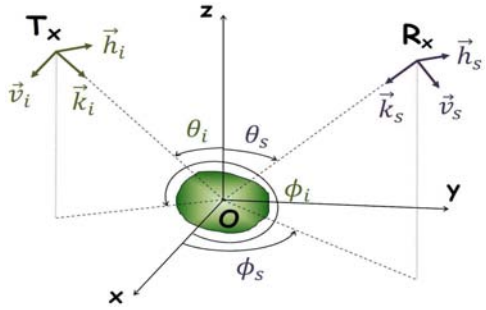


Figure 1: Bistatic scattering configuration.

2.1.2. Geometrical representation of urban areas

The backscattered fields from urban areas are dominated by multiple reflections from building walls, roofs and diffractions from building edges. A canonical representation of urban areas including the effects related to the reflections and diffractions is chosen. Indeed, this representation is justified because in the frequency band of interest, the elements composing of urban areas (buildings, cars, …) are always much more larger than the incident wavelength. Furthermore, the roughness of the ground is not taken into account because it is small compared to the incident wavelength. Buildings are depicted by parallelepipeds with flat or inclined roofs placed at deterministic positions on a dielectric L_xxL_y-sided plane representing the air-ground interface (see Fig. 2). The permittivities of the buildings and the ground depend on the building compositions and the soil moisture. They are defined by the real and imaginary parts of its complex relative permittivities ε_b and ε_r. The relative permeabilities of the buildings μ_b and the ground μ_r are equal to one.

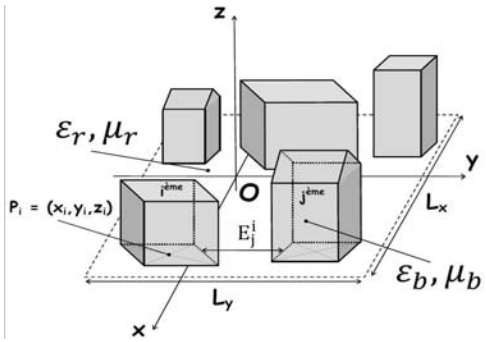


Figure 2: Representation of an L_xxL_y-sided urban area.

2.1.3 *Ray-tracing*

A ray-tracing algorithm is used to determine the geometrical paths of rays inside the illuminated area. Rays are first traced from the source points to the project. When they intercept building facets or the ground, they are specularly reflected and continue to be propagated up to the maximum number of reflections which is defined in advance or when they hit the study area boundary. However, in order to integrate all the diffraction effects on the building edges where the field becomes discontinuous, the intervals between rays should be reduced and as a consequence increase computing time. To avoid it, we develop a hybrid ray-tracing method which can refine the ray mesh with the aim of including diffraction effects due to the edges of buildings. This adaptive subdivision adjusts the distance between two adjacent rays following different paths through the geometry (i.e. they intercept two different buildings or two adjacent sides of a building, it means that we can generate a tertiary ray between the two previous ones which might be intercepted by an edge). A pre-defined criteria of diffraction is needed when we use this method.

Examples of how the rays launched from the source points on the transmitter used to identify diffracting edges are shown in Fig. 3. If we consider two adjacent rays number 1 and 2, the ray number 1 is reflected by facet 1 while the other is reflected by facet 6. This means that there exists a diffracting edge lying between these two rays. It is accordingly quite simple to locate a diffraction point on the edge and then to construct the path followed by the incident field. Another situation is shown for the two other rays number 3 and 4. These two rays hit the same building but different facets (facets 10 and 9), so a diffracting edge should be situated between them.

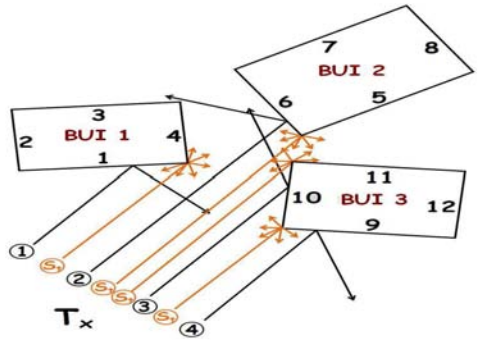


Figure 3: Identifications of the rays intercepting diffracting edges.

2.1.4 *Calculation of the scattered field*

Considering a reflection at a point O, the reflected field at a point M (after reflection) is obtained as the sum of two components, vertical and horizontal to the reflection plane, which are functions of the transmitted field, the reflection coefficients and the propagation delay. If we assume that the harmonic time dependence is $e^{j\omega t}$, the reflected field is then given by :

$$\begin{pmatrix} E_v^r(M) \\ E_h^r(M) \end{pmatrix} = \begin{pmatrix} R_v & 0 \\ 0 & R_h \end{pmatrix} \begin{pmatrix} E_v^i(O) \\ E_h^i(O) \end{pmatrix} e^{-j\vec{k}\cdot\vec{OM}} \quad (1)$$

where R_v, R_h are the Fresnel vertical and horizontal reflection coefficients. Thus,

$$\vec{E}^r(M) = E_v^r(M)\vec{v_r} + E_h^r(M)\vec{h_r} \quad (2)$$

In the case of a diffraction at a point O (the intersection of a ray with a building edge), the formulation of the diffracted field at a point M (after diffraction) is expressed by using the UTD and given by :

$$\begin{pmatrix} E_v^d(M) \\ E_h^d(M) \end{pmatrix} = \begin{pmatrix} D_v & 0 \\ 0 & D_h \end{pmatrix} \begin{pmatrix} E_v^i(O) \\ E_h^i(O) \end{pmatrix} \frac{e^{-j\vec{k}\cdot\vec{OM}}}{\sqrt{\left\|\vec{OM}\right\|}} \quad (3)$$

where D_v, D_h are the heuristic vertical and horizontal UTD coefficients of diffraction. Thus,

$$\vec{E}^d(M) = E_v^d(M)\vec{v_d} + E_h^d(M)\vec{h_d} \quad (4)$$

Finally, the total electric field at a given point M (the receiver) will be obtained after some mechanisms of multiple reflections or diffraction(s)-reflection(s) or reflection(s)-diffraction(s). In this study, we take into account only the first order of diffraction, for higher order diffraction, we consider that the signal is weak enough to be neglected. However, the number of reflections can be modified.

2.2. Validation

To validate the model, we firstly compare it with the commercial software XGTD®[9] and later with a set of measurements in the anechoic chamber.

2.2.1 *Comparisons with the software XGTD®*

A simple configuration (see Fig. 4) is conceded for validation. It consists of a right-angled wedge ($\alpha = 90°$) illuminated perpendicularly to its edge by an incident plane wave. The wedge is perfectly conducting or dielectric (concrete of relative permittivity $\varepsilon_r = \varepsilon'_r - j.60\sigma\lambda_s$ where in the computations, relative dielectric permittivity $\varepsilon'_r = 7.3$ and conductivity $\sigma = 0.2$ S/m). The operating frequency is 10 GHz. The diffracted angle Φ varies from 0° to 270°. The diffracted field is calculated at points placed on an arc of radius 3m from the tip of wedge. Once again, the comparisons between our model and the software are in good agreement for both polarizations and materials. However, in the case of an incident angle $\Phi' = 120°$ for the dielectric wedge, there are some small discrepancies for both, vV- and hH-, polarizations between our computed results and those from XGTD®. These divergences come

from that the diffraction coefficients are calculated according to different references. (See Fig. 5 for an incident angle Φ' = 45° and Fig. 6 for an incident angle Φ' = 120°).

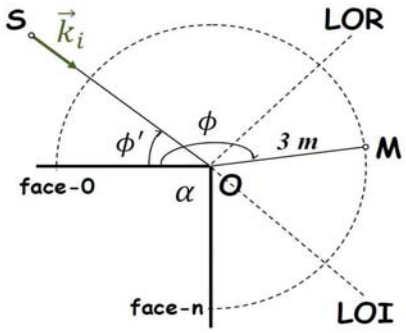
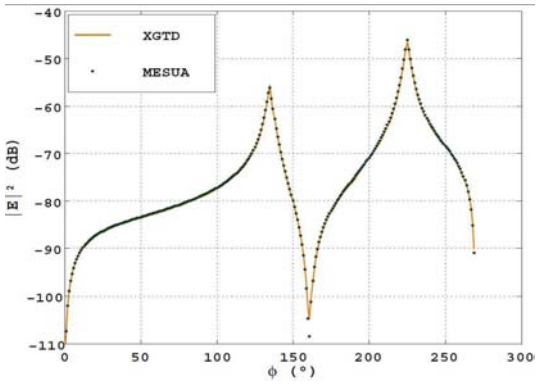
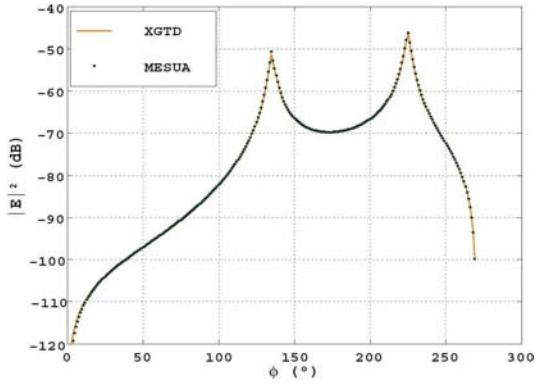


Figure 4: Configuration used for diffraction comparisons.

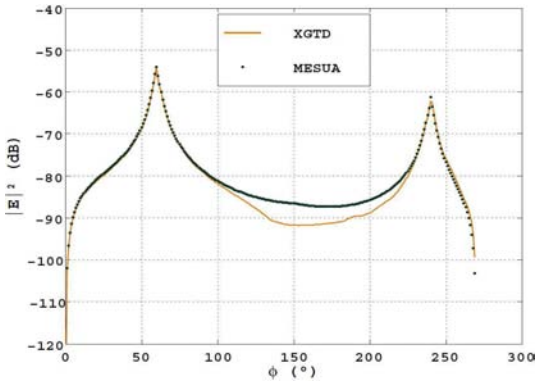


(a) Polar vV

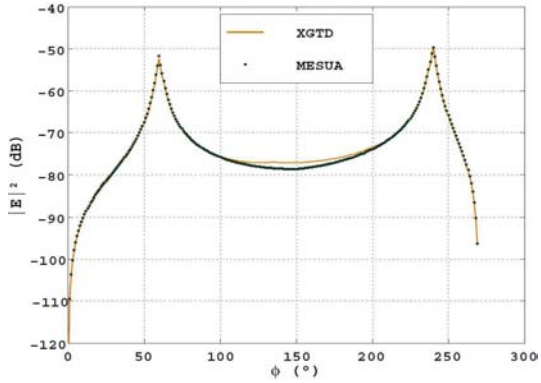


(b) Polar hH

Figure 5: Diffraction on a concrete wedge for an incident angle Φ' = 45°, f = 10 GHz.



(a) Polar vV



(b) Polar hH

Figure 6: Diffraction on a concrete wedge for an incident angle Φ' = 120°, f = 10 GHz.

2.2.2 *Comparisons with measurements*

To better demonstrate the pertinence of the UTD ray-tracing approach in urban areas, we have done some measurements in anechoic chamber with the objective of comparing with our model. Three comparisons composed of two metallic walls with or without target are considered (see Fig. 7). Two identical BBHA 9170 broadband horn antennas 14-40 GHz are used as the transmitter and the receiver. The total half-power beam-width of the antenna is 13°x15°. In all cases, they are put side-by-side at a height of 2m upon the ground and both are vertically polarized. The slope angle between the normal of the antennas and the ground is 18°. The working frequency band is from 33 to 37 GHz with a step of 5 MHz. The direct path between two antennas which corresponds to the cable length is 1.62m.

In the first case, two metallic plates of heights 1.2m and 1.5m are put at 1.5m and 3.5m respectively from the antennas as in Fig. 7. The comparison between the measured and simulated range profiles obtained for this configuration is shown in Fig. 8. Note that we succeed in retrieving all the peaks obtained by measurements. The first two peaks (number 1 and 2) correspond to the direct diffractions from wall 1 and wall 2. The next five peaks numbered 4, 6, 8, 10 and 12 are due to multiple bounces between two walls (equivalent to 4, 6, 8, 10 and 12 reflections) (see Table 1). For example, the first peak stands for the direct diffraction from the transmitter to the wall 1 and backwards to the receiver as shown in Fig. 9. The distance between the antennas and the top of the first wall is 1.72m, added to 1.62m cable length so that in the range profile it appears at the distance of 1.72 + 1.62 = 3.34m. The other peaks are obtained in the same way.

We observe here a significant difference in magnitude between simulations and measurements. This is due to two approximations inhere in our model : the first is that we have not treated the antenna sidelobes because it would increase considerably the computation time and secondly we have considered a non-canonical shape for the walls and the target instead of a more realistic representation (i.e. the metallic bars attached to the wall plates can cause undesired effects on the received field).

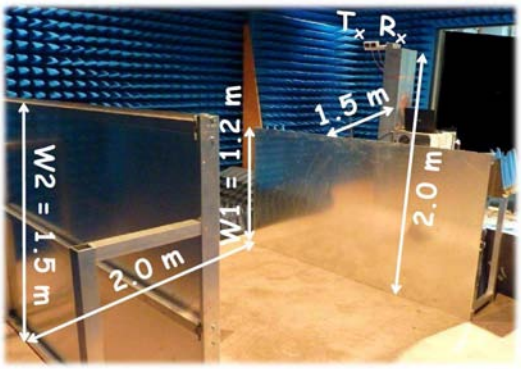


Figure 7: The configuration of indoor measurements.

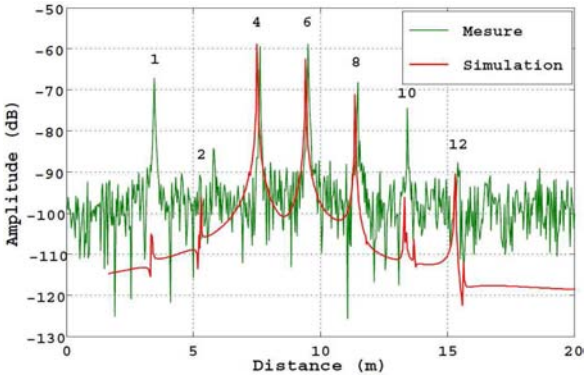


Figure 8: Measured and simulated range profiles for the first case.

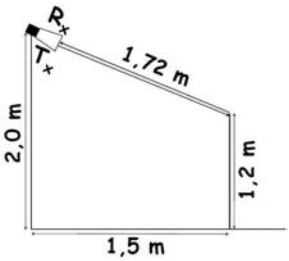
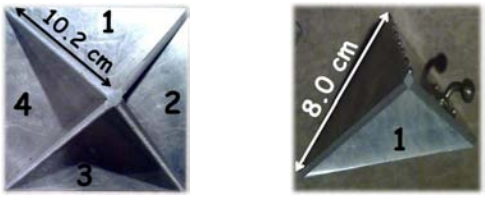


Figure 9: The example of the first peak retrieval in the range profile.

Peak number	(1)	(2)	(4)	(6)	(8)	(10)	(12)
Interaction index	001	001	400	600	800	1000	1200
Measurement (m)	3.45	5.25	7.61	9.53	11.48	13.42	15.41
Computing (m)	3.38	5.21	7.50	9.41	11.36	13.35	15.34

Table 1: Comparison between the positions of the peaks due to multi-reflection on walls, measured and calculated.

In the second case, we place a 4-in-1 corner reflector (CR) (the right-angled size is 10.2cm), as shown in Fig. 10(a), between two walls at the position of 2.23m from the antennas. The open angle 1 of the CR is towards to the second wall. In this case, besides all the effects appearing in the first configuration, we have some more interactions corresponding to the target. Their interaction indices 230, 430, 630, 830, 1030 (see Table 2) and correspond to peak numbers 3, 5, 7, 9 and 11 in Fig. 11. For better understanding, an index "430" means that the ray undergoes four times of reflections on the walls, three times of reflections on the target and no diffraction as shown in Fig. 12. These five peaks are the results of the reflections on the walls and on the two open angle 1 and 3 of the CR. More precisely, the indices 230, 630 and 1030 are relevant to the open angle 1 while the two others 430 and 830 are due to the opposite open angle. Besides that, there exists three indices 421, 621 and 821 corresponding to peaks 50, 60 and 90. Nevertheless, there is only a few number of received rays associated to these interactions so their amplitudes are too small to be detected as in measurements.



(a) (b)

Figure 10: (a) The 4-in-1 (b) The 1-in-1 corner reflector.

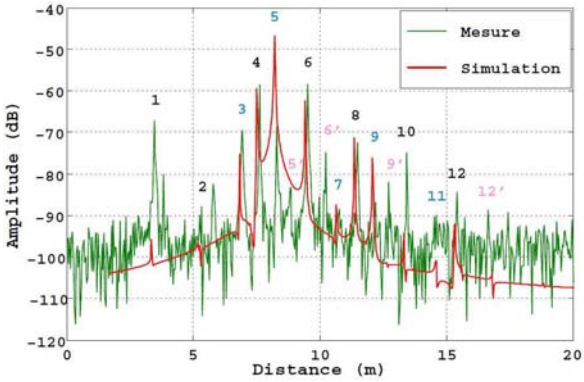


Figure 11: Measured and simulated range profiles for the second case.

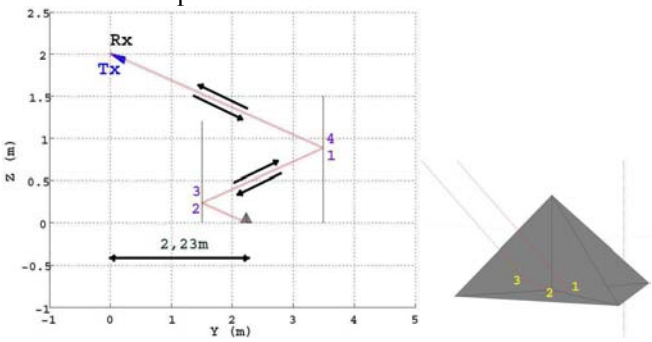


Figure 12: A ray undergoing four times of reflections on the walls, three times of reflections on the target and no diffraction. (a) The side view. (b) Target reflections.

Peak number	(3)	(5)	(7)	(9)	(11)
Interaction index	230	430	630	830	1030
Measurement (m)	6.94	8.29	10.76	12.19	14.59
Computing (m)	6.83	8.21	10.65	12.08	14.59

Table 2: Comparison of the multi-bounces (on 4-in-1 CR) peaks' ranges between the measurement and computing.

For the third configuration, we change only the target to a 1-in-1 CR (the right-angled size is 8.0cm) in order to identify the peaks due to the previous target (see Fig. 10(b)). The open angle 1 of the CR is towards to the second wall. Unlike the preceding case, we do not observe in Fig. 13 the interactions indices 430 and 830 because of the target shape which does not show up trihedral effect on his backside (see

Table 3). Once again, the same analysis as the previous case is conducted to explain the appearances of two peaks 50 and 90. Then again, as a consequence of the target shape, the peak number 60 is not observed in this case.

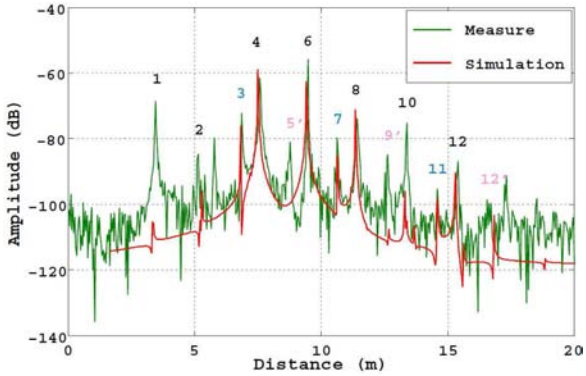


Figure 13: Measured and simulated range profiles for the third case.

Peak number Interaction index	(3) 230	(7) 630	(11) 1030
Measurement (m)	6.86	10.65	14.59
Computing (m)	6.83	10.65	14.59

Table 3: Comparison of the multi-bounces (on 1-in-1 CR) peaks' ranges between the measurement and computing.

2.3. Evaluation of the detection capacity of MESUA

In order to get a full view of the observed area, what we are interested in is the spot of the incident wave on the ground which should entirely illumine the study scenario. According to this reason, the size of the transmitter depends on each simulation. Furthermore, the transmitter is placed at a height of 700m upon the ground and the incident angles are (θ_i, Φ_i). The receiver is a pixel of 1mx1m square aperture moving on a half-sphere of radius 5000m centred at the origin point O (see Fig. 14). The transmitted electric field is fully polarized and its amplitude is 1V/m. The frequency of interest is 10 GHz. The building relative permittivity is that of concrete and is equal to ε_b = 7.3 - j*0.36. For the ground, we choose ε_r = 28.5 - j*12.84 corresponding to moist soil.

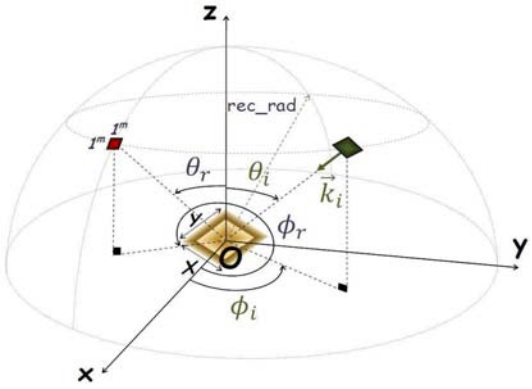


Figure 14: The radar configuration for the simulation.

In a previous paper, we proposed studies on the influence of the shape of the building and their density on the scattered field on a half-sphere [10]. These analysis allowed us on the one hand to identify the directions where the scattered field is maximum et on the other hand to show that when the building density increases, the effects of diffrations are more considerable. In this part, we focus our attention on the ability to detect a target placed among buildings. That's why, in this case, we consider a crossroad formed by twelve buildings as shown in Fig. 15. At the beginning, we study this area without the object (i.e. a car), and then we add a target in a street in order to evaluate the ability of detection by using the software MESUA.

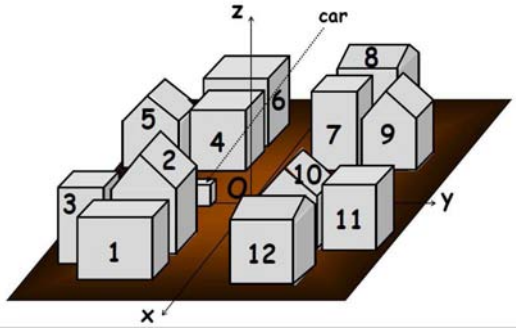
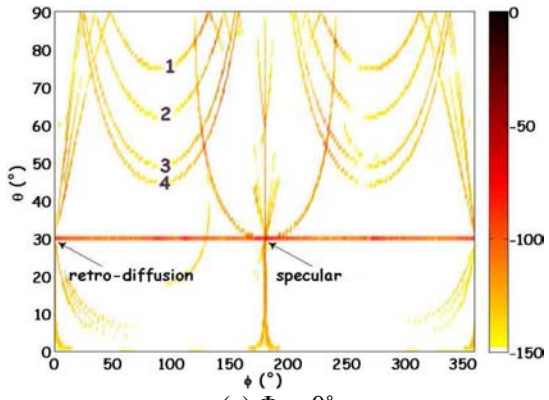
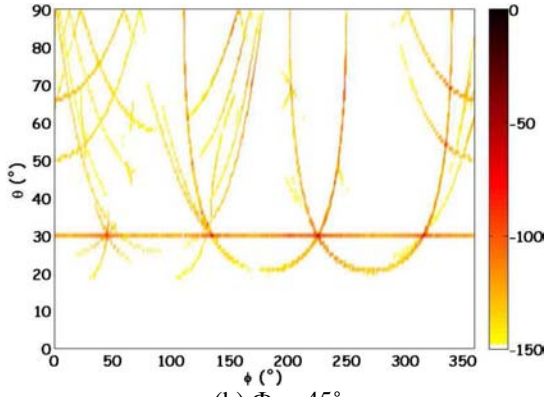


Figure 15: A crossroad formed by twelve buildings, six with flat-roof and six with inclined-roof.

In Fig. 16, we present the scattered field by this scene for two different incident angles (θ_i = 30°, Φ_i = 0°) and (θ_i = 30°, Φ_i = 45°). We treat this configuration with a number of reflection N_r = 6 and that of the diffraction N_d = 1.



(a) Φ_i = 0°

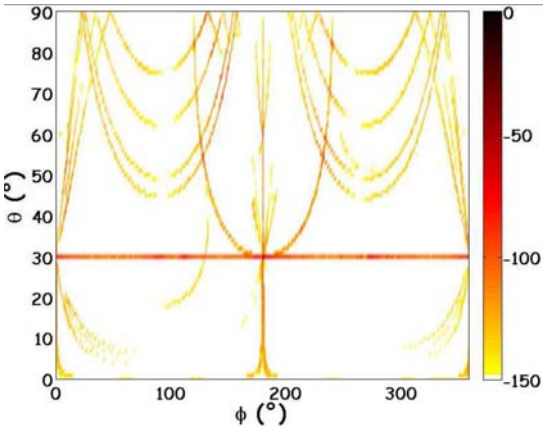


(b) Φ_i = 45°

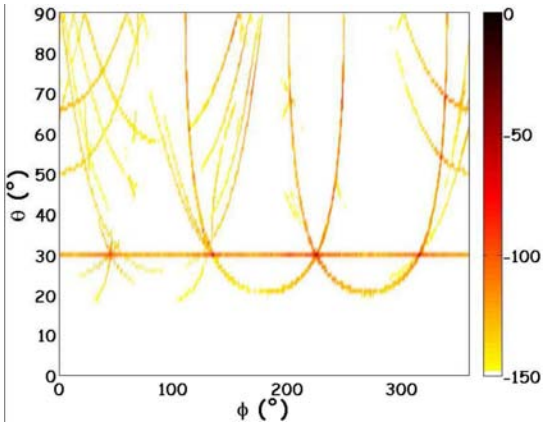
Figure 16: The field strength received by a crossroad formed by twelve buildings with two different incident angles of the transmitter (in case of no object).

We will now put a car represented by a rectangular metal sized 4m x 1.5m x 1.5m in the street parallel to the axis Oy

at the position P_{target} and incline an angle $\alpha = 90^\circ$ compared with the Ox axis. The fact is that the target is represented by the parallelepiped and its angle of inclination with the axis Ox is 90°, so the field due to the diffraction by the target is the same direction as that of the buildings with flat-roofs. In other words, the curves indicating the directions of reflection and diffraction of the target are superimposed on those of the buildings. Therefore, we can not directly observe the presence of the target in Fig. 17.



(a) $\Phi_i = 0^\circ$

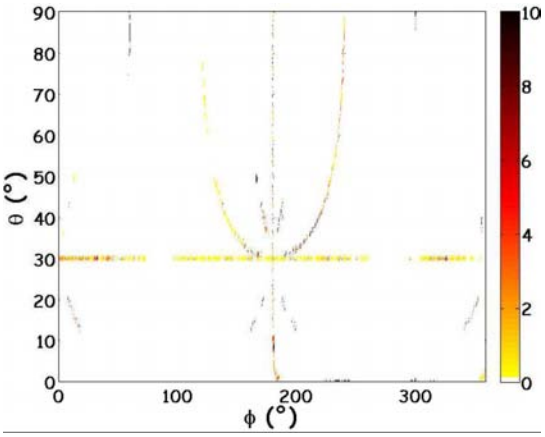


(b) $\Phi i = 45^\circ$

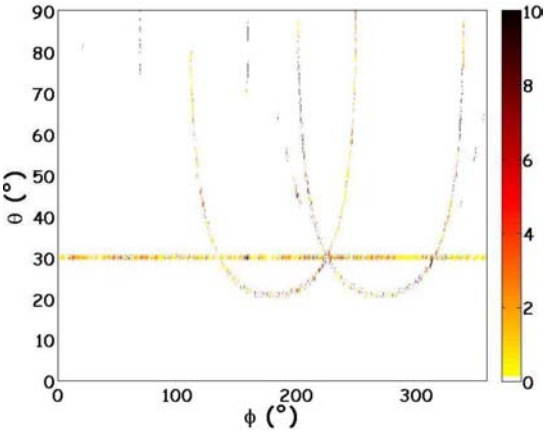
Figure 17: The field strength received by a crossroad with two different incident angles of the issuer (in case of the presence of a target on the street).

In order to detect the appearance of the target in the considered crossroad, we have to subtract these fields to those calculated previously in the case without target. In Fig. 18, we present the modulus of the difference between these diffused two fields. All the figures are represented in same scale from 0dBm to 10dBm.

We can see that this difference is linked to the presence of the target. In addition, we observe for both cases in Fig. 18, there is a parabolic curve and a vertical line $\Phi_r = 180^\circ$ (for the incident angles $\theta_i = 30^\circ$ and $\Phi_i = 0^\circ$) or two parabolic curves (for the incident angles $\theta_i = 30^\circ$ and $\Phi_i = 45^\circ$). This means that the target in the illuminated area has a parallellepiped form. In addition, the small traces corresponding to the buildings interaction caused by the presence of the target.



(a) $\Phi i = 0^\circ$



(b) $\Phi i = 45^\circ$

Figure 18: The difference between the two scattered fields by a crossroad in cases of with and without the presence of a target in a street.

3. Discussion

All the cases simulated previously were run on an Intel® Core(TM)2 Duo CPU, T7700 @2.40 GHz with 3.5GB of RAM. The total computation time for a crossroad with the target is about one hour and a half when we consider 3600 incident rays. In case of the scene with the target, the calculation time does not increase signicantly. Most of the CPU time is spent on finding the diffracting edges, the third-order combination ray paths related to the diffraction, such as R-R-D, R-D-R, D-R-R, etc. and higher order mechanisms. The simulation time really depends on the maximum number of interactions we choose to include.

When the ground roughness is small enough to be neglected, the dominant component of the EM scattering returns to the receiver from the group of buildings is the double-scattering (wall-ground or ground- wall mechanisms).

The software MESUA can predict precisely the presence of a target as well as its orientation angle.

4. Conclusions

We have defined a three-dimensional EM model to characterize in an effcient and accurate way the scattered field by an urban area in high-frequency range. This field

depends on the polarization of the incident wave, the geometry and the materials composing of the buildings and the ground. With our model, the diffracted field by an urban area is obtained for a deterministic distribution of buildings. To obtain an average value of the diffracted field in a given direction, it should be calculated for several possible configurations and take the mean value.

In the future work, an activity is ongoing to perform more complete simulations of urban areas to include also features like building balconies, trees, cars, … and that, from early studies, such details do not significantly contribute to the far field. This would be of much interest to the community performing parameter reconstructions from SAR data.

Acknowledgements

The authors would like to thank Mr Liu Weixian, Mr Feng HongChuan, Mr Sun Hongbo and Ms Xiao Yi from the Temasek Laboratories of Nanyang Technological of University (NTU), Singapore who has contributed the measurements to compare to our model. All the measurements were done in the anechoic chamber of the "ElectroMagnetic Effects Research Lab" (EMERL) of NTU.

References

[1] Gierull, C. H., "*Statistical analysis of multilook SAR interferrograms for CFAR detection of ground moving targets"*, IEEE Trans. on Geosci. and Remote Sens., Vol. 42, No. 4, 691-701, Apr. 2004.

[2] Tison, C., J.-M. Nicolas, F. Tupin, and H. Maitre, "*New statistical model for Markovian classification of urban areas in high-resolution SAR images"*, IEEE Trans. on Geosci. and Remote Sens., Vol. 42, No. 10, 2046-2057, Oct. 2004.

[3] Garestier, F., P. Dubois-Fernandez, X. Dupuis, P. Paillou, and I. Hajnsek, "*PolInSAR analysis of X-Band data over vegetated and urban areas"*, IEEE Trans. on Geosci. and Remote Sens., Vol. 44, No. 2, 356-364, Feb. 2006.

[4] De Adana, F. S., O. G. Blanco, I. G. Diego, J. P. Arriaga, and M.F. Catedra, "*Propagation model based on ray tracing for the design of personal communication systems in indoor environments"*, IEEE Trans. on Vehicular Techno., Vol. 49, No. 6, 2105-2112, Nov. 2000.

[5] Degli-Esposti, V., "*A diffuse scattering model for urban propagation prediction"*, IEEE Trans. on Ant. and Propa., Vol. 49, No. 7, 1111-1113, Jul. 2001.

[6] Chang, P. C., R. J. Burkholder, J. L. Volakis, R. J. Marhefka, and Y. Bayram, "*High-frequency EM characterization of through-wall building imaging"*, IEEE Trans. on Geosci. and Remote Sens., Vol. 47, No. 5, 1375-1387, May 2009.

[7] El Sallabi, H. M. and P. Vaikikainen, "*Improvements to diffraction coefficient for non-perfectly conducting wedge"*, IEEE Trans. On Ant. and Propa., Vol. 53, No. 9, 3105-3109, Sep. 2005.

[8] Ben Kassem, M. J. and A. Khenchaf, "*Bistatic mapping radar BiSAR"*, OCEANS 2003 Proceedings, Vol. 5, 2754-2760, Sep. 2003.

[9] XGTD®, Remcom, Inc., 2010, XGTD version 2.5.16 User's Manual.

[10] N. T. M. Nguyen, D. Lautru, and H. Roussel, "*A 3D model to characterize high-frequency scattering by urban areas for monostatic and bistatic radar configurations"*, PIER B, Vol. 30, 83-102, 2011.

The Reconstruction of Objects Buried in a Stratified Medium with Rough Interfaces

Ö. Özdemir[1] and H. Haddar[2]

[1]Istanbul Technical University, Turkey
[2]INRIA Saclay Ile de France & CMAP, France
*corresponding author, E-mail: ozdemiroz3@itu.edu.tr

Abstract

A reciprocity gap linear sampling method (RG-LSM) and the Approximate Transmission Condition (ATC)-based method is proposed to image object buried under a stratified media with rough interfaces. First the Approximate Transmission Condition is employed to obtain the field values and its normal derivative on the boundary of the medium which the object is located from the data measured on the outermost boundary. Then with the use of that reconstructed field values, RG-LSM is applied to image the object. Our method is particularly suited for configurations where the layers are thin with respect to the wavelength (skin, wall, coatings, etc...).

1. Introduction

Reconstruction of objects buried in layered medium has been very popular subject in many areas and constitutes an inverse scattering problem. They have very important practical applications such as mine detection, tumor cells recognition, etc. Several techniques have been developed to image buried objects[1-3]. Among these methods, Reciprocity Gap-Linear Sampling Method (RG-LSM)[3] seems more attractive since it does not require the knowledge of Green'function of background medium. On the other hand, the concept of approximate (or asymptotic) models is commonly used in scattering problems in which layered medium is involved, such as geophysics, underground imaging, etc [4-6]. Even though the asymptotic models of thin layer is widely used for direct scattering problems, they are not restricted only those problems, they can also be applied to the inverse scattering problems. With this aim, in our recent work [6] we have derived the Approximate Transmission Condition that account for general curvilinear behavior of the transmission layer and show that they can be used in determination of the field distributions on the one of the boundary from the known field data.

In this framework, we propose a new fast method which is based on Approximate Boundary Condition and RG-LSM to reconstruct the object buried under stratified medium with rough interface. RG-LSM needs the knowledge of the field values and its normal derivative on the boundary of the medium where the object is buried. In multi-layered media, however, these data cannot be simply obtained by measurement since the boundary is inaccesible. To solve this problem, ATC is employed to reconstruct these data from the field distributions measured on the outer boundary.

This paper is organized as follows: Section II gives overview of Approximate Boundary Condition. The outline of the Reciprocity Gap-Linear Sampling Method is given in Section III and then the numerical result is presented to show the feasibility of the proposed method.

2. Approximate Transmission Condition

Let us consider a thin layer (Ω_δ) of thickness δ with wavenumber k, see Figure 1. Let $\partial\Omega_+$, and $\partial\Omega_-$ be the outer and inner boundary of the thin layer, respectively Let u_+ and $\frac{\partial u_+}{\partial n}$ be the field and its normal derivative at the $\partial\Omega_+$. In the same manner, u_- and $\frac{\partial u_-}{\partial n}$ stand for the field and its normal derivative at the $\partial\Omega_-$. The problem we would like to solve is to compute u_- and $\frac{\partial u_-}{\partial n}$ from the knowledge of u_+ and $\frac{\partial u_+}{\partial n}$. Our goal is to solve this problem in an approximate way when δ is sufficiently small, by using an asymptotic development of the solution with respect to δ. To give the expression of ATC , first we shall set, $[u] := u_+ - u_-$ and $\langle u\rangle := \frac{1}{2}\{u_+ + u_-\}$ Then the ATC can be written in the form

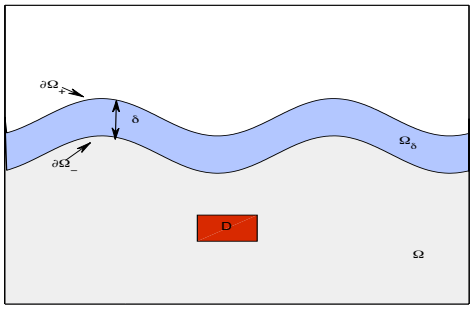


Figure 1: Geometry of three-layered medium

$$\begin{aligned}[u] &= \mathcal{Z}_{11}^{(\ell)}\langle u\rangle + \mathcal{Z}_{12}^{(\ell)}\left\langle \tfrac{\partial u}{\partial n}\right\rangle + O(\delta^{\ell+1}) \\ \left[\tfrac{\partial u}{\partial n}\right] &= \mathcal{Z}_{21}^{(\ell)}\langle u\rangle + \mathcal{Z}_{22}^{(\ell)}\left\langle \tfrac{\partial u}{\partial n}\right\rangle + O(\delta^{\ell+1})\end{aligned} \tag{1}$$

where $\mathcal{Z}_{ij}^{(\ell)}$ denotes some boundary operator. The transmission conditions obtained from (1) after neglecting the $O(\delta^{\ell+1})$ term will be referred to as the ATC of order $\ell+1$.

The fourth order condition corresponds with

$$\begin{aligned}
\mathcal{Z}_{11}^{(3)} &= -\tfrac{\delta^3}{12}\left(3\mathcal{C}\tfrac{\partial^2}{\partial s^2}+\mathcal{C}k^2+\mathcal{C}'\tfrac{\partial}{\partial s}\right),\\
\mathcal{Z}_{12}^{(3)} &= \delta+\tfrac{\delta^3}{12}\left(\tfrac{\partial^2}{\partial s^2}+k^2-2\mathcal{C}^2\right),\\
\mathcal{Z}_{21}^{(3)} &= \mathcal{Z}_{21}^{\delta,2}-\tfrac{\delta^3}{12}\left(\left(\tfrac{\partial^2}{\partial s^2}+k^2\right)\left(\tfrac{\partial^2}{\partial s^2}+k^2\right)+\tfrac{\partial}{\partial s}\mathcal{C}^2\tfrac{\partial}{\partial s}\right),\\
\mathcal{Z}_{22}^{(3)} &= -\mathcal{C}\delta-\tfrac{\delta^3}{12}\left(\tfrac{\partial^2}{\partial s^2}\mathcal{C}+2\mathcal{C}k^2-\mathcal{C}\tfrac{\partial^2}{\partial s^2}-\mathcal{C}'\tfrac{\partial}{\partial s}\right),
\end{aligned} \tag{2}$$

where s is the curvilinear abscissa and $\mathcal{C}$ denotes the curvature of Γ defined as $\Gamma=\frac{1}{2}(\partial\Omega_+ + \partial\Omega_-)$, i.e., the parallel interface located half way between the two boundaries and $\mathcal{C}'$ denotes the derivative of $\mathcal{C}$ with respect to s. From the measured data on the outer boundary $\partial\Omega_+$, the electromagnetic field on the inner boundary $\partial\Omega_-$ can be determined by the solution of ATC.

3. Reciprocity Gap Sampling Method

For the sake of simplicity, in this section we assume the background is two layered medium(without thin layer, only upper medium and the one object D is buried). Let v be a field satisfying the Helmholtz equation in Ω with downward propagating condition. We define the *Reciprocity Gap* between $u(\cdot;x_0)$ and v by

$$\mathcal{R}(u(\cdot;x_0),v) := \int_{\partial\Omega_-}\left(u(x,x_0)\frac{\partial v}{\partial\nu_x}(x)-v(x)\frac{\partial u}{\partial\nu_x}(x,x_0)\right)ds(x). \tag{3}$$

where $u(.;x_0)$ is the total field due to point source is located at x_0. Notice that if there are no obstacles ($D=\emptyset$), then $\mathcal{R}(u(\cdot;x_0),v)=0$. We now introduce a sufficiently rich parametrization of the set of admissible functions v by choosing v to be a *single layer potential* defined by

$$v=s_g := \int_\Lambda g(y)\Phi(x,y)ds(y) \tag{4}$$

where g is an unknown potential and where

$$\Phi(x,y)=\frac{i}{4}H_0^{(1)}(k_1|x-y|)$$

$H_0^{(1)}$ is the Hankel function of the first kind with the order zero and Λ is a straight horizontal line in the upper medium.

The RG-LSM amounts to find an approximate solution $g_z\in L^2(\Lambda)$ to the (integral) equation

$$\mathcal{R}(u(\cdot;x_0),s_{g_z})\simeq\mathcal{R}(u(\cdot;x_0),\Phi(\cdot,z)) \quad for\ all\ \ x_0, \tag{5}$$

where z is a parameter, so-called sampling point, lying in the search domain in Ω. In other words, for a given sampling point $z\in D$ on would like to test whether there exists a *regular solution* to the Helmholtz equation in Ω, namely s_{g_z}, whose reciprocity gap with $u(\cdot;x_0)$ coincides with reciprocity gap of a singular solution, namely $\Phi(\cdot,z)$, with the same fields and for all sources x_0.One can easily guess that this would not be true when z is outside D since $u(\cdot;x_0)$ and s_{g_z} satisfy the same Helmholtz equation outside D while $\Phi(\cdot,z)$ satisfies the equation with $-\delta_z$ source term. The method then stipulates that given an approximate solution to (5) the norm of $\|g_z\|$ would be much larger for z outside D than for z inside D.

From the practical point of view (5) can be written in the form

$$\mathcal{A}g_z\simeq\phi(.,z) \tag{6}$$

where $\mathcal{A}$ is the integral operator with kernel,

$$A(x_0,y)=\mathcal{R}(u(\cdot,x_0),\Phi(x,y))\ y\in\Lambda, \tag{7}$$

and where with

$$\phi(x_0,z)=\mathcal{R}(u(\cdot,x_0),\Phi(\cdot,z))\ z\in\Omega. \tag{8}$$

To construct an approximate solution to the ill-posed equation (6), one can use the Tikhonov regularization by solving

$$(\alpha+A^*A)g_{z,\alpha}=A^*\phi(.,z) \tag{9}$$

where α is the regularization parameter and $\mathcal{A}^*$ is the adjoint of $\mathcal{A}$.

The numerical procedure to locate the target object is then the following : uniform sampling points $\{z_i\}_{i=1,\dots,N}$ of the probed region are considered and then for each point z_i,

$$\mathcal{G}(z_i)=\|\phi(.,z_i)\|_{L^2}/\|g_{z_i,\alpha}\|_{L^2} \tag{10}$$

is computed. Then the contours of the function $z_i\to\mathcal{G}(z_i)$ are visualized. As explained above, the values of $\mathcal{G}$ are expected to be much smaller where z_i does not belong the scatterers.

4. Numerical Results

This section is devoted to the validation of the feasibility of the proposed method. Measurement field are obtained synthetically by solving the forward scattering problem using an integral equation method. In the example the frequency of the exciting sources is chosen as $f=300MHz$ which corresponds $k_0=2\pi$.

Three layered medium having sinusoidal interfaces is considered, Figure 1. Thickness of the thin layer is chosen as $\delta=0.1\lambda_0$ and its index as $n_\delta=2.5+0.2i$ Perfectly conducting rectangle-shaped object with dimensions $\lambda_0\times\lambda_0/2$ is buried in a lower homogeneous medium with index $n=1.2+0.2i$. 40 point sources are uniformly placed on a line with the length $4\lambda_0$, at a distance of $1.1\lambda_0$ from the interface and measurements are done on upper boundary $\partial\Omega_+$ and the reconstruction domain is chosen as $4\times4m^2$ and contains 40×40 pixels. Λ is chosen as a straight line having a $2\lambda_0$ length at a distance of $0.5\lambda_0$ from the interface and 40 discrete number on it.

The reconstructed object by proposed method is depicted in Figure 2. As it can be seen from the figure,

since the sources and the measurements are placed on the only upper layer but not all over the object, only the upper boundary of the object is clearly identified, but not the lower part of the object. Even so, the location of the object is still distinguished.

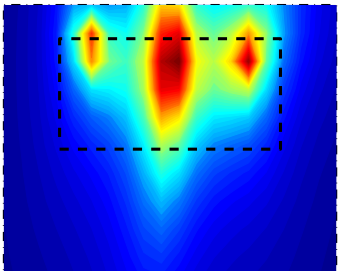


Figure 2: Reconstructed perfectly conducting rectangular object

5. Conclusion

We propose a fast method to image the objects buried under a stratified medium with arbitrary interfaces. The method is based on Approximate Transmission Condition and Reciprocity Gap-Linear Sampling Method. The field distributions on the lower interface of the thin layer is determined from the measument data on the upper boundary of the layer by the use of ATC and then RG-LSM method is carried out to image the object. Our approach can be also effectively used in other imaging algorithms,besides RG-LSM, related to objects buried under stratified medium This topic is the subject of a work under progress.

Acknowledgement

This work was supported by The Scientific and Technological Research Council of Turkey (TUBITAK) under Grant 108E173.

References

[1] T. J. Cui, W. C. Chew, A. A. Aydiner, and S. Y. Chen, "Inverse scattering of 2-D dielectric objects buried in a lossy earth using the distorted Born iterative method," *IEEE Trans. Geosci. Remote Sens.*, Vol. 39, No. 2 339–346, 2001.

[2] P. M. van den Berg and R. E. Kleinman, "A contrast source inversion method," *Inv. Probl.*, Vol. 13, No. 6 1607–1620, 1997.

[3] D. Colton and H. Haddar, "An application of the reciprocity gap functional to inverse scattering theory," *Inverse Problems*, Vol. 21, 383–398, 2005.

[4] T. B., A. Senior and J. L. Volakis, *Approximate boundary conditions in electromagnetics*, IEE Electromagnetic Waves Series, 1995.

[5] A. Karlsson,"Approximate boundary conditions for thin structures," *IEEE Trans. Antennas. Propagat.*, Vol. 57,No. 1, 144–148, 2009.

[6] Ö. Özdemir, H. Haddar and A. Yaka," Reconstruction of the electromagnetic field in layered media using the concept of approximate transmission conditions," Trans. Antennas. Propagat, Vol. 59, No. 8, 2964–2972, 2011.

Electromagnetic Scattering by 3D Dielectric Objects Buried Under 2D Rough Surfaces

Yasemin Altuncu

Department of Electrical and Electronics Engineering,
Nigde University, Nigde, Turkey
E-mail: yaltuncu@nigde.edu.tr

Abstract

In this paper, the solution of a direct scattering problem related to 3D arbitrary shaped dielectric objects buried under 2D locally rough surface is considered. A method based on the solution of an electric field integral equation including the dyadic Green's function of two-half space media with rough interface is proposed. The required Green's function is achieved using buried object approach (BOA) which also involve the solution of another electric field integral equation including the dyadic Green's function of two-half space media with planar interface. The computation of this well-known Green's function is required the time-consuming Sommerfeld integrals. To enhance the computational efficiency of the proposed method and to avoid the numerical calculations of Sommerfeld integrals, the dyadic Green's function is derived in closed-form by using DCIM.

1. Introduction

Electromagnetic scattering by 3D dielectric or conducting objects embedded in a layered media is very important in many practical applications of wave propagation. Therefore, a wide range of studies have been made about this issue in the past few decades [1]-[2]. However, most of them investigate the scattering problem related to bodies buried under planar interface while the surface roughness must also be taken into account in real applications.

In this paper, we present a method for the scattering of electromagnetic waves in the presence of the 3D arbitrary shaped dielectric bodies embedded into a semi-infinite medium with a 2D rough surface. The method is based on the solution of an electric field integral equation including dyadic Green's function of background medium. Hence, the background medium consist of two-half spaces with rough boundary, to obtain its Green's function is a complex and difficult problem in itself. By using the buried object approach (BOA) which based on the assumption that the areas bordered by the rough surface and a fictional plane through the center of roughness constitute 3D dielectric bodies, this problem has been converted to a scattering problem of 3D dielectric objects placed into both sides of the fictional plane [3]. Then, the desired Green's function can be obtained by the solution of another electric field integral equation including dyadic Green's function of two-layered media with planar interface. The dyadic Green's function of two-layered media is required the solution of slow converging and time consuming Sommerfeld integrals. To avoid the numerical calculation of the Sommerfeld integrals and obtain the dyadic Green's function in closed-form, two-level approximation as an application of discrete complex image method (DCIM) has been is used in present work. A three-level approximation as an extension of two-level approximation is proposed in [5] to eliminate the some limitations of it. In [6] 2D-DCIM is presented to obtain the closed-form spatial Green's function for arbitrary locations of the source and fields. This is more efficient than 1D-DCIM when the source and field points are in different layers. The methods presented in the last two works can be applied our method to improve the efficiency and the range of the validity.

In Section 2, the electric field integral equations which are required to get the scattered field from 3D objects buried under 2D rough surface are given. The procedure to obtain the closed-form of the electric fields Green's function is presented in Section 3. The conclusions regarding the method described in Section 4.

2. Formulation of the problem

The geometry of the addressed problem is illustrated in Fig. 1. Here, a 3D dielectric body is buried into the lower half-medium having 2D locally rough surface. An electromagnetic wave source located into the upper half-medium illuminate the rough surface. The main goal of this study is to discover the effect of buried dielectric object as well as the roughness on the electromagnetic wave propagation originated from this source. In this work, we investigate the scattering due to a plane wave.

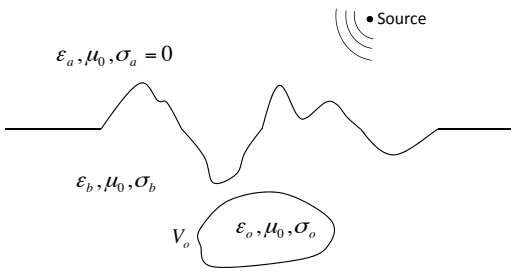


Figure 1: Geometry of the problem.

The electric field at any point $\mathbf{r}(x, y, z)$ can be described as a summation of two fields, namely,

$$\begin{aligned}\mathbf{E}(\mathbf{r}) &= \mathbf{E}_o(\mathbf{r}) + \mathbf{E}_s(\mathbf{r}) \\ &= \mathbf{E}_o(\mathbf{r}) + k_b^2 \int_{V_o} \bar{\bar{G}}^E(\mathbf{r}, \mathbf{r}') \upsilon(\mathbf{r}') \mathbf{E}(\mathbf{r}') d\mathbf{r}' \end{aligned} \quad (1)$$

where $\mathbf{E}_s(\mathbf{r})$ is the scattered field from $3D$ object embedded into the lower medium and $\mathbf{E}_o(\mathbf{r})$ is the total field in the absence the object but the presence of the roughness. Additionally, in Equation (1), k_b is the wavenumber of the lower medium, $\upsilon(\mathbf{r})$ is the the object function defined by $\upsilon(\mathbf{r}) = k(\mathbf{r})/k_b(\mathbf{r}) - 1$, V_o is the volume of the scattered object and $\bar{\bar{G}}^E(\mathbf{r}, \mathbf{r}')$ is the electric field dyadic Green's function of the two-half space media with rough interface. If $\bar{\bar{G}}^E(\mathbf{r}, \mathbf{r}')$ and $\mathbf{E}_o(r)$ are known, the scattered field can be obtained by solving the above integral equation numerically via Method of Moment (MOM). Since $\mathbf{E}_o(\mathbf{r})$ is the total electric field at point $\mathbf{r}(x, y, z)$ due to the plane wave and $\bar{\bar{G}}^E(\mathbf{r}, \mathbf{r}')$ is the total electric field at point $\mathbf{r}(x, y, z)$ due to the point source at point $\mathbf{r}'(x', y', z')$ in the presence of the rough surface, they are identical to each other except the sources creating them. So, they are calculated by similar way using BOA which is based on the assumption that the areas bordered by the rough surface and a fictional plane through the center of roughness constitute $3D$ dielectric bodies buried into both sides of the plane as illustrated in Fig. 2. Thus, $\mathbf{E}_o(r)$ and $\bar{\bar{G}}^E(\mathbf{r}, \mathbf{r}')$ are calculated by solving the problems of scattering from objects buried in two half-spaces media with planar interface.

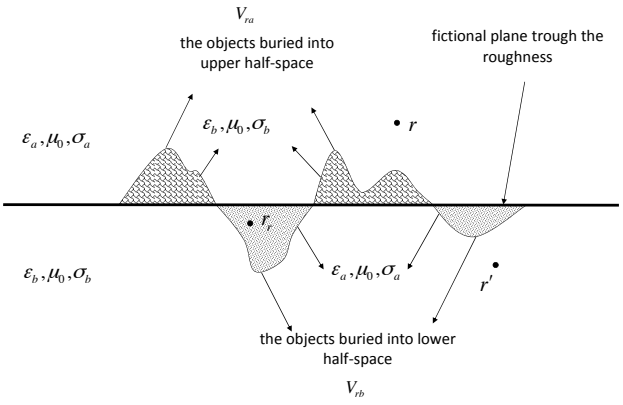


Figure 2: The BOA model of the rough surface.

In this new context, the field $\mathbf{E}_o(\mathbf{r})$ is written as the summation of two fields, namely,

$$\begin{aligned}\mathbf{E}_o(\mathbf{r}) &= \mathbf{E}_{oi}(\mathbf{r}) + \mathbf{E}_{os}(\mathbf{r}) \\ &= \mathbf{E}_{oi}(\mathbf{r}) + k_i^2 \int_{V_{ri}} \bar{\bar{G}}_o^E(\mathbf{r}, \mathbf{r}_r) \upsilon_{ri}(\mathbf{r}_r) \mathbf{E}(\mathbf{r}_r) d\mathbf{r}_r, i = a, b \end{aligned} \quad (2)$$

where $\mathbf{E}_{oi}$ is the total field in the absence of the roughness and it can be easily obtained by using the classical rules of the reflection and transmission of plane waves from planar interfaces. $\mathbf{E}_{os}$ is the scattered field from $3D$ objects modeling the rough surface. Analogously, $\bar{\bar{G}}^E(\mathbf{r}, \mathbf{r}')$ is also summation of two terms as follows,

$$\begin{aligned}\bar{\bar{G}}^E(\mathbf{r}, \mathbf{r}') &= \bar{\bar{G}}_o^E(\mathbf{r}, \mathbf{r}') + \bar{\bar{G}}_s^E(\mathbf{r}, \mathbf{r}') \\ &= \bar{\bar{G}}_o^E(\mathbf{r}, \mathbf{r}') + k_i^2 \int_{V_{ri}} \bar{\bar{G}}_o^E(\mathbf{r}, \mathbf{r}_r) \upsilon_{ri}(\mathbf{r}_r) \bar{\bar{G}}^E(\mathbf{r}_r, \mathbf{r}') d\mathbf{r}_r \\ i &= a, b. \end{aligned} \quad (3)$$

Here, $\bar{\bar{G}}_o^E$ is the Green's function of two layered medium with planar interface and $\bar{\bar{G}}_s^E(\mathbf{r}, \mathbf{r}')$ is the contributions of the roughness to the desired total Green's function $\bar{\bar{G}}^E(\mathbf{r}, \mathbf{r}')$. In Equation (2) and (3), k_i is the wavenumber of the medium in which the related objects are buried, υ_{ri} is the object function corresponding to these object and they can be written as:

$$k_i = \begin{cases} k_a, & \text{if } z > 0 \\ k_b, & \text{if } z < 0 \end{cases} \quad (4)$$

$$\upsilon_{ri}(\mathbf{r}_r) = \begin{cases} k_b/k_a - 1, & \text{if } \mathbf{r}_r \in V_{ra} \\ k_b/k_a - 1, & \text{if } \mathbf{r}_r \in V_{rb} \\ 0, & \text{if } \mathbf{r}_r \notin V_{ri} \end{cases}. \quad (5)$$

Once the dyadic Green's function of two-half space media $\bar{\bar{G}}_o^E(\mathbf{r}, \mathbf{r}')$ is found, the integral equations in Equation (2) and (3) are solved numerically by using MOM to obtain $\mathbf{E}_o(\mathbf{r})$ and $\bar{\bar{G}}^E(\mathbf{r}, \mathbf{r}')$, respectively. To enhance the computational efficiency of the solution, $\bar{\bar{G}}_o^E(\mathbf{r}, \mathbf{r}')$ is obtained in closed-form by using Discrete Complex Image Method (DCIM) which is explained in the next section.

3. Closed-Form Green's Function of Two-Half Space Media

Consider a two-layered medium perpendicular to $z-$ axis with a dipole source, as shown in Fig. 3. Since the electromagnetic properties of the mediums are constant along all directions except z, this geometry is cylindrically symmetric. The dipole is represented by current density $\mathbf{J} = \hat{\alpha} I\ell\delta(r)$ with arbitrary orientation $\hat{\alpha}$ and current moment $I\ell$.

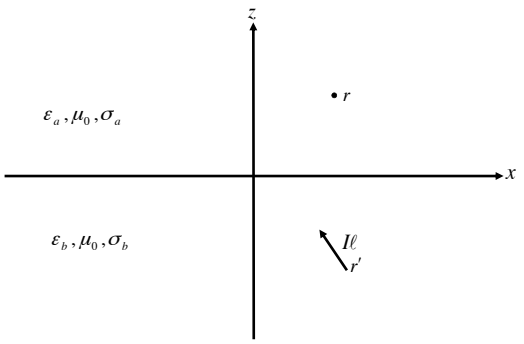


Figure 3: Two-half space media with an arbitrary oriented dipol.

In general, any spatial Green's function for two-half space media is expressed in terms of spectral Green's function via Sommerfeld integrals, namely,

$$\bar{\bar{G}}(\rho, z; z') = \frac{1}{4\pi}\int_{SIP} \tilde{G}(k_\rho, z; z') H_0^{(2)}(k_\rho \rho) k_\rho dk_\rho \quad (6)$$

where $\tilde{G}$ is the spectral domain Green's function which can be written analytically. $H_0^{(2)}$ is the zeroth order Hankel function of second kind and SIP is the Sommerfeld integration path.

The spatial Green's function for electric field which is needed for our purpose can be expressed in terms of vector and scalar potential Green's function via Mixed Potential Integral Equation (MPIE) as follows,

$$\bar{\bar{G}}^E = -j\omega\mu_0(\bar{\bar{G}}^A - \frac{1}{k_i^2}\nabla\nabla'\bar{\bar{G}}^Q). \quad (7)$$

In Equation (7), $\bar{\bar{G}}^A$ is the vector potential Green's function and $\bar{\bar{G}}^Q$ is the scalar potential Green's function.

According to the procedure followed in this study, first the potential Green's functions obtain in closed-form by using DCIM. Then the electric field Green's function is obtained in closed-form by analytical differentiations of these closed-form potential Green's function [7] using Equation (7). For that reason, let us first consider how the closed-form Green's function of potentials are achieved.

3.1. Closed-Form Green's Function of Potentials

According to the traditional form, the vector potential Green's function can be described as

$$\bar{\bar{G}}^A = (\hat{x}\hat{x} + \hat{y}\hat{y})G_{xx} + \hat{z}\hat{x}G_{zx} + \hat{z}\hat{y}G_{zy} + \hat{z}\hat{z}G_{zz} \quad (8)$$

and scalar potential Green's functions $G_{x,y}^Q$ and G_z^Q. Any component of spatial Green's functions of vector and scalar potentials are represented by Sommerfeld integral with kernel of spectral Green's function as given in Equation (6). The spectral Green's function which were derived in numerous works [8] are acquired analytically. For example, when both the observation and source points are in the upper medium, Green's function of the potentials are represented as follows

$$G_{xx} = \frac{\mu_0}{4\pi}\{\frac{e^{-jk_a|r-r'|}}{|r-r'|} + \int_{-\infty}^{\infty}\frac{1}{j2k_{z_a}}[\Gamma^{\perp}e^{-jk_{z_a}(z+z')}]H_0^{(2)}(k_\rho\rho)dk_\rho\} \quad (9)$$

$$G_{zx} = \frac{-\mu_0}{4\pi}\frac{\partial}{\partial x}\int_{-\infty}^{\infty}\frac{1}{j2k_{z_a}}[\frac{k_{z_a}}{k_\rho^2}(\Gamma^{\parallel}-\Gamma^{\perp})e^{-jk_{z_a}(z+z')}] H_0^{(2)}(k_\rho\rho)dk_\rho\} \quad (10)$$

$$G_{zy} = \frac{-\mu_0}{4\pi}\frac{\partial}{\partial y}\int_{-\infty}^{\infty}\frac{1}{j2k_{z_a}}[\frac{k_{z_a}}{k_\rho^2}(\Gamma^{\parallel}-\Gamma^{\perp})e^{-jk_{z_a}(z+z')}] H_0^{(2)}(k_\rho\rho)dk_\rho\} \quad (11)$$

$$G_{zz} = \frac{\mu_0}{4\pi}\{\frac{e^{-jk_a|r-r'|}}{|r-r'|} - \int_{-\infty}^{\infty}\frac{1}{j2k_{z_a}}[\Gamma^{\parallel}e^{-jk_{z_a}(z+z')}]H_0^{(2)}(k_\rho\rho)dk_\rho\} \quad (12)$$

$$G_{x,y}^Q = \frac{1}{4\pi\epsilon_a}\{\frac{e^{-jk_a|r-r'|}}{|r-r'|} + 2\int_{-\infty}^{\infty}\frac{1}{j2k_{z_a}}[\frac{k_a^2\Gamma^{\parallel}+k_{z_a}^2\Gamma^{\perp}}{k_\rho^2}e^{-jk_{z_a}(z+z')}] H_0^{(2)}(k_\rho\rho)dk_\rho\} \quad (13)$$

$$G_z^Q = \frac{1}{4\pi\epsilon_a}\{\frac{e^{-jk_a|r-r'|}}{|r-r'|} + 2\int_{-\infty}^{\infty}\frac{1}{j2k_{z_a}}[\Gamma^{\perp}e^{-jk_{z_a}(z+z')}]H_0^{(2)}(k_\rho\rho)dk_\rho\} \quad (14)$$

where

$$\Gamma^{\parallel} = \frac{\epsilon_a k_{z_b} - \epsilon_b k_{z_a}}{\epsilon_a k_{z_b} + \epsilon_b k_{z_a}}, \Gamma^{\perp} = \frac{\mu_b k_{z_a} - \mu_a k_{z_b}}{\mu_b k_{z_a} + \mu_a k_{z_b}}$$

$$\rho = \sqrt{(x-x')^2 + (y-y')^2}, k_\rho = \sqrt{k_x^2 + k_y^2}$$

For other locations of source and field points, similar expressions are generated. Since would occupy too much space, these expressions are not given here.

In Equation (8-14) any of the expressions in the square brackets are approximated as a summation of complex exponentials by using two-level approximation [4] as application of DCIM as follows

$$\tilde{G} \cong \sum_{n=1}^{N_1} a_{1n}e^{-b_{1n}k_{z_a}} + \sum_{n=1}^{N_2} a_{2n}e^{-b_{2n}k_{z_a}}. \quad (15)$$

Here the coefficients a_{1n} and a_{2n} and exponents b_{1n} and b_{2n} obtained using Generalized Pencil of Functions (GPOF) method, N_1 and N_2 are the number of the exponentials used in the approximation. By using approximate spectral expressions in Equation (8-14) and by means of Sommerfeld identity

$$\frac{e^{-jkr}}{r} = \int_{-\infty}^{\infty}\frac{e^{-jk_z z}}{j2k_z}H_0^{(2)}(k_\rho\rho)dk_\rho \quad (16)$$

any of the spatial Green's function of potentials is written in closed-form such as in the following expression

$$G \cong \text{direct term} + \sum_{n=1}^{N_1} a_{1n}\frac{e^{-jk_a r_{1n}}}{r_{1n}} + \sum_{n=1}^{N_2} a_{2n}\frac{e^{-jk_a r_{2n}}}{r_{2n}} \quad (17)$$

where $r_{1n} = \sqrt{\rho^2 - b_{1n}^2}$ and $r_{2n} = \sqrt{\rho^2 - b_{2n}^2}$. The direct term showing in Equation (17) can be calculated analytically without the need for DCIM.

Once, all components of the spatial domain potential Green's function are acquired in closed-form by DCIM, the spatial domain electric field Green's functions derived from analytical differentiations of these closed-form potential functions through the Equation (7)

4. Conclusions

In this work the scattering problem belong to 3D dielectric object embedded into a semi-infinite medium with 2D rough surface is considered. The proposed method involve the solution of an integral equation enclosing the Green's function of background medium which is the rest of the overall geometry when the buried dielectric object is removed. The background space Green's function is also involve a solution of another electric field integral equation enclosing the dyadic Green's function of two-half space. The closed-form Green's function of electric field are derived from the analytical differentiations of the closed-form Green's function of vector and scalar potentials which obtained by using DCIM. This improve the computational efficiency of the method. The method presented here can be applied any arbitrary shaped 3D dielectric or conducting objects buried beneath 2D rough surface with arbitrary fluctuation.

Acknowledgement

This work is supported by The Scientific and Technological Council of Turkey (TUBITAK) grant 108E175.

References

[1] Cui T.J., Wiesbech W. and Herschlein A., Electromagnetic scattering by multiple three-dimensional scatterers buried under multilayered media, *IEEE Trans. Geosci. Remote Sens.* vol.36, no.2, 1998.

[2] Song L., Liu H.L., A new approximation to three-dimensional electromagnetic scattering, *IEEE Geosci. Remote Sens. Letters* vol.2, no.2, 2005.

[3] Altuncu Y., Yapar A. and Akduman I., On the scattering of electromagnetic waves by bodies buried in a half-space with locally rough interface,*IEEE Trans. Geosci. Remote Sens.*, vol.44, no.6, 2006.

[4] Aksun M.I., A robust approach for the derivation of closed-form Green's functions, *IEEE Trans.Microwave Theory Tech.*, vol.44,no.5,1996.

[5] Alparslan A. Aksun M.I. and Michalsky K.A., Closed-form Green's functions in planar layered media for all ranges and materials, *IEEE Trans.Microwave Theory Tech.*, vol.58,no.3,2010.

[6] Yuan M., Zhang Y., De A., Ji Z. and Sarkar T.K., Two-Dimensional Discrete Complex Image Method (DCIM) for Closed-Form Green's Function of Arbitrary 3D Structures in General Multilayered Media, *IEEE Trans. Antennas Propagat.* vol.56, no.5,2006

[7] Dogan M., Aksun M.I., Swan A.K.,Goldberg B.B. and Unlu M.S., Closed-form representations of field components of fluorescent emmiters in layered media, *J. Opt. Soc. Am.A* vol.26, no.6,2009.

[8] Michalsky K.A., On the scalar potential of a point charge associated with a time-harmonic dipole in a layered medium, *IEEE Trans. Antennas Propagat.* vol.35, no.11,1987.

A Novel Multiband Fractal Antenna

Crislane Silva*, Lidiane Araujo, Antonio Belfort and Marcos de Melo

Department of Electronic and Systems, Federal University of Pernambuco, Pernambuco, Brazil
*corresponding author, E-mail: crislanepns@hotmail.com

Abstract

A novel fractal geometry is here investigated for antennas applications. The proposed geometry is obtained by introducing narrow slots in X shape in square patches, so that successive iterations can be obtained. Antennas with this geometry will produce currents that will flow near the edges of the squares which have been defined by slots. As a result, resonances occur at frequencies which correspond to the dimensions of the fractal generator in different scales. A novel fractal dipole antenna is then studied in this paper and simulation results for the return loss, surface current distribution, radiation pattern and input impedance are here reported. Results show that it can operate as a multiband antenna.

1. Introduction

Fractal structures have been used recently in antenna design aiming either to reduce its size or to achieve multiband characteristics. The capacity to reduce size can be seen in the Koch monopole fractals [1]-[3]. The Koch fractal monopoles exhibit lower resonant frequencies than the Euclidean monopoles of the same height. As a result, monopoles and dipoles with reduced dimensions can be constructed. The Sierpinski [4,5] fractal geometries (triangle and carpet) and Minkowski [6,7] as well, on the other hand, are normally used to design monopole and dipole antennas with multiband characteristics.

It has been observed that the surface current in these structures always flow in regions near the edges of the antenna, regardless of the iteration being considered. This means that if narrow slots were introduced in antennas patches in X shape, this would force currents to flow on their edges creating, as a result, squares in different scales. This paper, therefore, investigates the performance of a new fractal dipole antenna (fractal X) that uses such squares in the definition of successive iterations. Simulation results for radiation patterns, current densities, input impedance and return loss were carried out by software CST Microwave Studio and it are here reported in the 0-15.6 GHz range. They strongly indicate that operation multiband can be achieved with the antenna.

2. Description of the fractal dipole

Iteration 0, the generator (iteration 1) and iteration 2 are shown in Fig. 1. The initializer is a single square and the transformation that creates the fractal X consists in introducing narrow slots having the shape of x. A new geometry is then created which is now considered to be the fractal generator, also called iteration 1. Iteration 2 is obtained by reproducing the geometry of iteration 1 in reduced scale, and so on for higher iterations.

The slots in X shape have lengths slightly smaller than the side of the square created in each iteration and, as a consequence, the currents are diverted to the edges of the slots yielding new resonances. For iteration 1, the squares have diagonals with dimension approximately half the one of the square of iteration 0. Therefore one would expect that the corresponding resonance frequency is next to twice the first one. This repeats for successive higher iterations.

3. Simulation Results

3.1. Return Loss

The corresponding dipole here investigated is in the *y-z* plane and the diagonals of the squares are 23 mm, 10.44 mm and 4.74 mm for iterations 0, 1 and 2, respectively. The patches lie on a dielectric layer of thickness 1.27 mm and ε_r=2.2. The input return loss with frequency, relative to 50 Ω, of the new proposed antenna with the shape of the iteration 2 was simulated in the 0 – 15.6 GHz range and the results are shown in Fig. 2. The dipole of the initializer resonates at 2.24 GHz. The next two iterations allow the antenna to resonate at 5.74 GHz and 15.13 GHz, corresponding to the squares built for iterations 1 and 2, respectively. Both resonances exhibit return losses below -10 dB, as one can see from Fig. 2.

Therefore, the dipole with iteration 2 produces three resonances with return losses below -10dB referenced to 50 Ω, which confirms its performance as a multiband antenna. Figs. 3 and 4 show the real and imaginary parts of the input impedance along the whole band. Near the three resonance bands the real part of the input impedance approaches 50 Ω and the imaginary one approaches 0 Ω.

One point to be mentioned is that the distance the slot starts from the edge of the square created in each iteration influences the return loss results.

3.2. Surface current

Figs. 5, 6 and 7 show simulation results for the surface current of the fractal X dipole with the shape of iteration 2.

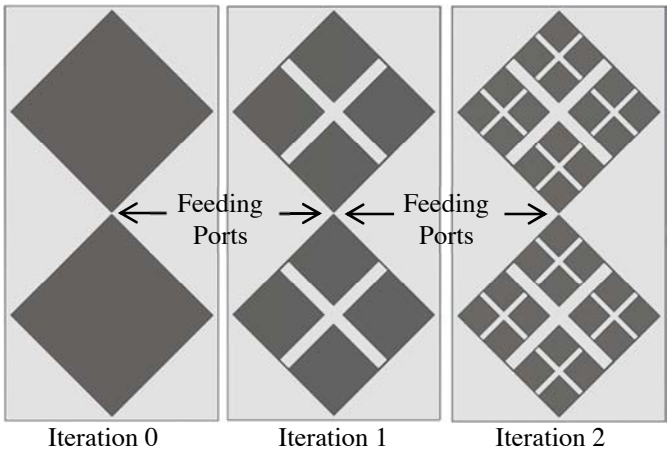


Figure 1: The novel fractal dipoles.

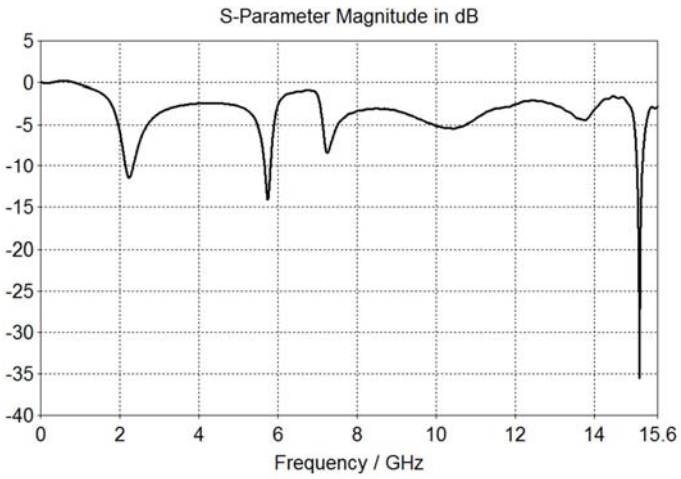


Figure 2: Return loss for iteration 2 of the novel fractal dipole.

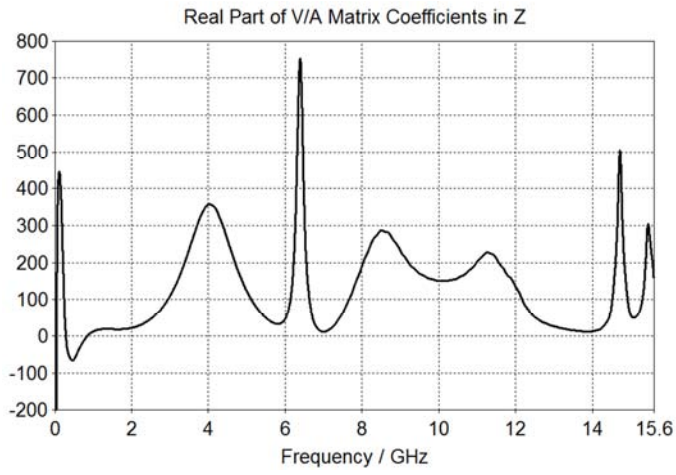


Figure 3: Real part of the input impedance for iteration 2 of the new fractal dipole.

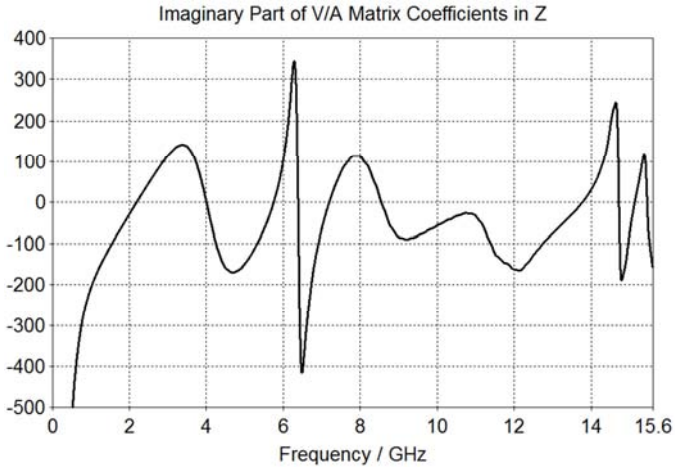


Figure 4: Imaginary part of the input impedance for iteration 2 of the new fractal dipole.

The illumination is at peak values for frequencies of 2.24 GHz, 5.74 GHz and 15.13 GHz, which are the resonance frequencies for iterations 0, 1, and 2, respectively.

The slots yield a new path for the currents which turns out to be the edges of the squares created. Each square resonates at a frequency which will depend on its dimensions.

Surface currents revel for each resonance frequency a behavior that might explain the very good return loss achieved at 15.13 GHz band. The dipole formed by the two smallest squares are not the only resonators in the whole dipole.

Remarkable current densities can be observed of the square patches away from the feeding ports. This suggests that radiator occurs strongly at that frequency.

This contributes for less power being reflected back to the R.F. generator. The same reasoning can be applied at 5.74 GHz. In this case weaker current densities are noticed. This accounts for an increase in the return loss, coming close to -15 dB. At 2.24 GHz, the weaker densities can be seen and, therefore, less radiation is expected, which means more power being reflected.

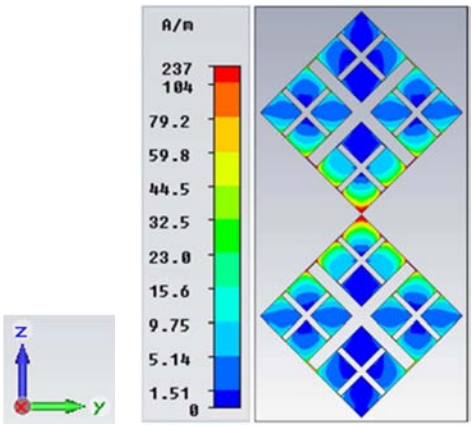


Figure 5: Surface current over the new fractal dipole for iteration 2 at the frequencies 2.24 GHz.

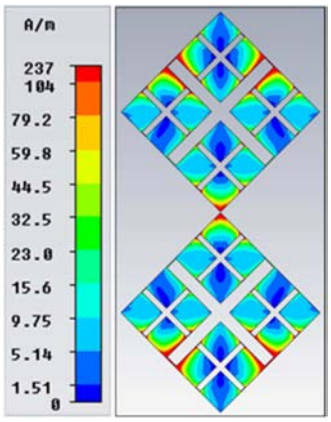


Figure 6: Surface current over the new fractal dipole for iteration 2 at the frequencies 5.74 GHz.

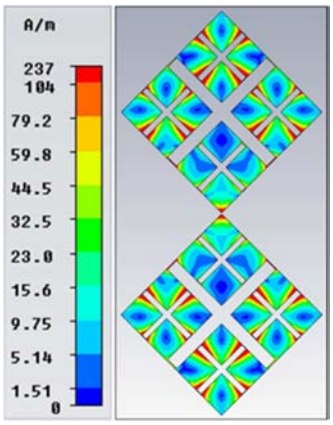


Figure 7: Surface current over the new fractal dipole for iteration 2 at the frequencies 15.13 GHz.

3.3. Radiation Patterns

The radiation patterns for the dipole are displayed in Fig. 8. Simulations were carried out for dipole in the iteration 2 at 2.24 GHz, 5.74 GHz and 15.13 GHz, for $\varphi = 0°$, $\varphi = 90°$ and $\theta = 90°$. For $\theta = 90°$, the radiation patterns are very similar at the three frequencies. For $\varphi = 0°$, they show some degree of similarity, as would be expected from a fractal antenna. Similarity happens to $\varphi = 90°$ as well. The well-known single linear dipole presents more lobes as frequency increases. One verifies similar behavior to the investigated dipole here, but in this case even more lobes are observed due to more radiator elements as the order of iteration increases.

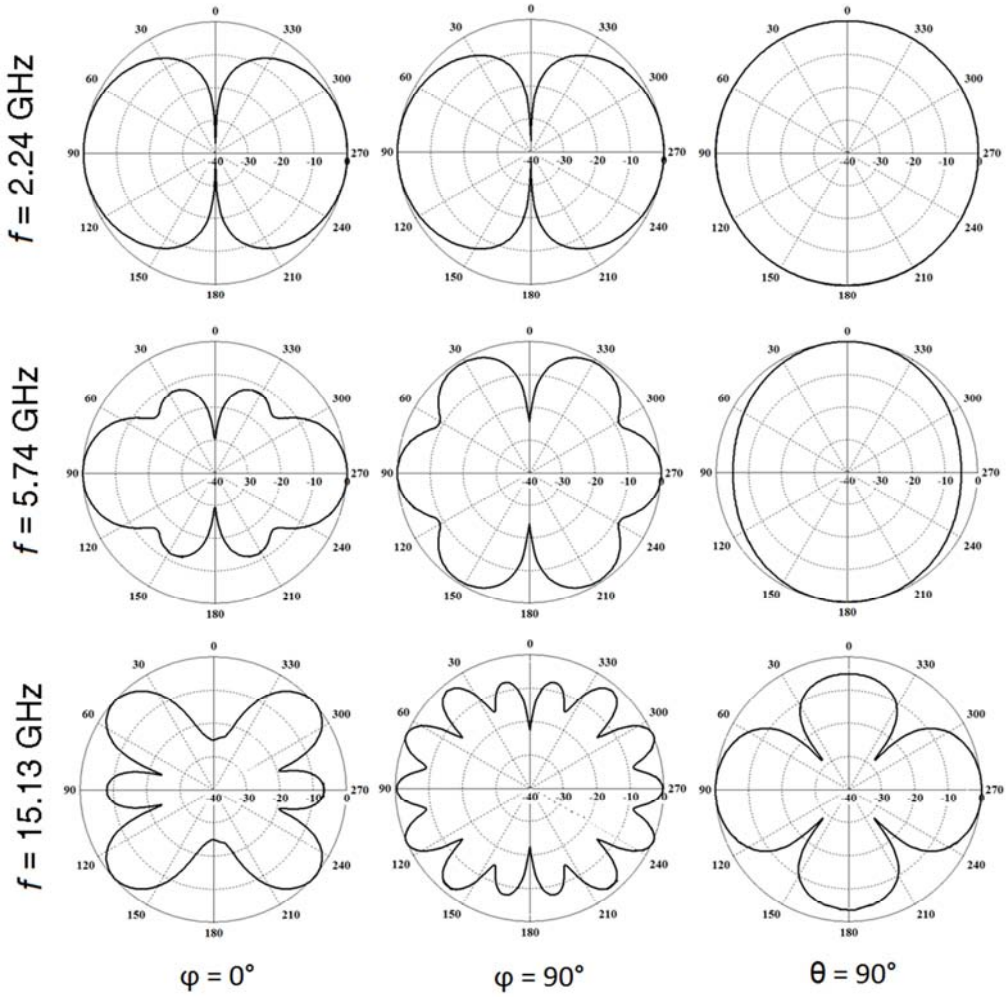


Figure 8: Radiation patterns for the new proposed fractal dipole at the frequencies 2.24 GHz, 5.74 GHz and 15.13 GHz.

4. Conclusions

The inclusion of slots in the design of fractal X has created a dipole with three resonances corresponding to the number of iterations considered. Simulation results for the input return loss at those resonance frequencies are such that the VSWR<2. The dipole can therefore operate as multiband antenna. The dimensions of the squares created by the slots for each iteration defined the resonance frequencies which are related by the scale factor of on approximately 2 used in this investigation. The radiation patterns for $\varphi = 0°$, $\varphi = 90°$ and $\theta = 90°$ exhibited some degree of similarity, what is expected from an antenna with a fractal shape. This paper has suggested that the input return loss can be controlled and resonance frequency allocated as long as slots properly dimensioned are introduced in the main structure of the dipole. The slot dimensions play an important role in the design of the antenna.

References

[1] C. Puente, J. Romeu, R. Pous, J. Ramis and A. Hijazo, "Small but long Koch fractal monopole,"Electronic Letters, January 1998, vol.34, No.1, pp. 9-10.

[2] C. Puente, J. Romeu and A. Cardama, "The Koch monopole: A small fractal antenna," IEEE Trans. Antennas and Prop., vol.48, No.11, pp.1773-1781, Nov. 2000.

[3] Steven R. Best, "On the performance properties of the Koch fractal and other bent wire monopoles," IEEE Trans. on Antennas and Propagat, vol. 51, No. 6, June 2003.

[4] Puente, J. Romeu, R. Pous, and A. Cardama, "On the behavior of the Sierpinski multiband fractal antenna", IEEE Trans. on Antennas and Propagation., vol.46, No. 4, April 1998, pp. 517-524.

[5] J. S. Castany, J. R. Robert, and C. Puente, " Mod-P Sierpinski fractal multiband antenna, "Proceeding of the Millenium Conf. on Antennas and Propagation, April 2000.

[6] G. S. Tsachtsiris, M. P. Karaboikis, C. F. Soras, and V. T. Makios, "Single and multi-element printed Minkowski monopole antennas for portable terminal devices," Automatika, vol.45, 2004, pp.33-39.

[7] S. Saleekaw, C. Mahatthanajatuphat, P. Akkaraekthalin, and M. Krairiksh, "Monopole antennas with modified Minkowski fractal geometry," Proc. Of ECT-CON, 2008, pp. 213-216.

Band-Notched Small Square Monopole Antenna Surrounded by Rotated C-Shaped Parasitic Structure for UWB Applications

Mohammad Ojaroudi[1], Nasser Ojaroudi[2], and Shervin Amiri[3]

[1]Young Research Club, Ardabil Branch, Islamic Azad University, Ardabil, Iran.
[2]Faculty of Electrical & Computer Engineering, Shahid Rajaee Teacher Training University, Tehran, Iran
[3]Scientific Member of Electrical Engineering Department of Iranian Research Organization for Science and Technology (IROST), Tehran, Iran.
*corresponding author, E-mail: m.ojaroudi@iauardabil.ac.ir

Abstract

A novel printed monopole antenna for UWB applications with frequency band-notch function is presented. By cutting an inverted T-shaped slit in the radiating patch a new resonance at higher frequencies can be achieved and provides a wide usable fractional bandwidth of more than 120% (3.08-13.23 GHz), also in order to create frequency band-stop performance, the square radiating patch surrounded by rotated C-shaped parasitic structure, that with this design, a frequency notched band of 5.03–5.97 GHz has been obtained. Simulated and experimental results obtained for this antenna show that the proposed single band-notch square monopole antenna has a good antenna gains and radiation behavior within the UWB frequency. The designed antenna has a small dimension of 12×18 mm^2.

1. Introduction

Ultra wide band (UWB) antenna technology and application developed rapidly in recent years. Its plenty of advantages, such as simple structure, small size and low cost due to have received increased attention, especially planar monopoles are extremely attractive to be used in emerging UWB applications, and growing research activity is being focused on them. Consequently, a number of planar monopoles with different geometries have been experimentally characterized [1-3].

The frequency range for UWB systems between 3.1–10.6 GHz will cause interference to the existing wireless communication systems for example the wireless local area network (WLAN) for IEEE 802.11a operating in 5.15–5.35 GHz and 5.725–5.825 GHz bands, so the UWB antenna with a band-notch function is required. Lately to generate the frequency band-notch function, modified planar monopoles several antennas with band-notch characteristic have been reported [4-8]. In [4], [5] and [6], different shapes of the slots (i.e., square ring, W-shaped and folded trapezoid) are used to obtain the desired band notched characteristics. Single and multiple [7] half-wavelength U-shaped to generate the frequency band-notch function, modified planar slits are embedded in the radiation patch to generate the single and multiple band-notched functions, respectively. In [8], band notch function is achieved by using a T-shaped coupled parasitic element in the ground plane.

A simple method for designing a novel and compact microstrip-fed monopole antenna with band-notch characteristic for UWB applications has been presented. In the proposed antenna, by inserting a rotated C-shaped parasitic structure with variable dimensions in the radiating patch a single band-stop performance can be created and also for bandwidth enhancement, we use an inverted T-shaped slit in the radiating patch. The presented monopole antenna has a small size of 12×18 mm^2. Good return loss and radiation pattern characteristics are obtained in the frequency band of interest. Simulated and measured results are presented to validate the usefulness of the proposed antenna structure for UWB applications.

2. Antenna Design

The presented monopole antenna is shown in Figure 1, which is printed on an FR4 substrate of thickness 1.6 mm, permittivity 4.4, and loss tangent 0.018.

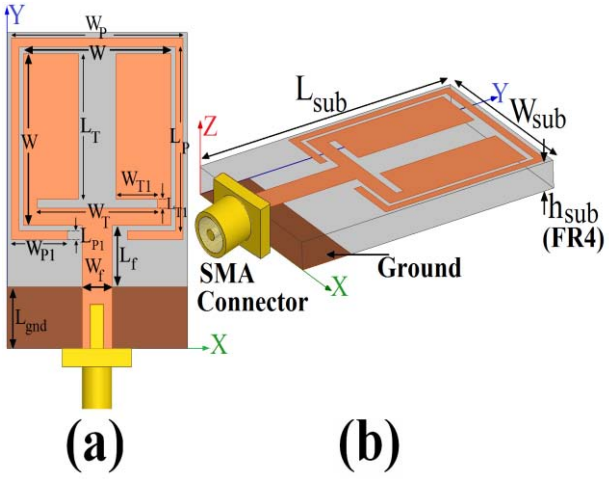


Figure 1: Geometry of the proposed antenna, (a) top view, (b) side view.

The optimized values of proposed antenna design parameters are as follows:

$W_{sub}=12mm$, $L_{sub}=18mm$, $W_f=2mm$, $L_f=3.5mm$, $W=8mm$, $W_T=3.8mm$, $L_T=8.75mm$

, $W_{T1} = 2.5mm$, $L_{T1} = 0.25mm$, $W_P = 11.4mm$, $L_P = 10.4mm$, $W_{P1} = 3mm$, $L_{P1} = 0.2mm$, , and $L_{gnd} = 3.5mm$.

3. Results and Discussions

The proposed microstrip-fed monopole antenna with various design parameters were constructed, and the numerical and experimental results of the input impedance and radiation characteristics are presented and discussed. The Ansoft simulation software high-frequency structure simulator (HFSS) [9] is used to optimize the design and agreement between the simulation and measurement is obtained.

The configuration of the various antennas structures were shown in Figure 2. Return loss characteristics for ordinary square monopole antenna, square monopole antenna with an inverted T-shaped slit in the radiating patch and the proposed antenna structure are compared in Figure 3. As shown in Figure 3, it is observed that the upper frequency bandwidth is affected by using an inverted T-shaped slit in the radiating patch and the notch frequency bandwidth is sensitive to the rotated C-shaped parasitic structure.

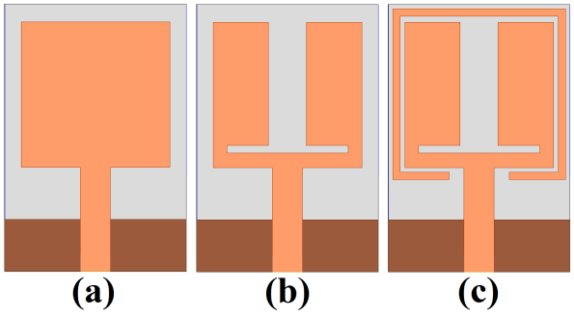


Figure 2: (a) Ordinary square monopole antenna, (b) square monopole antenna with an inverted T-shaped slit on the radiating patch, and (c) the proposed antenna.

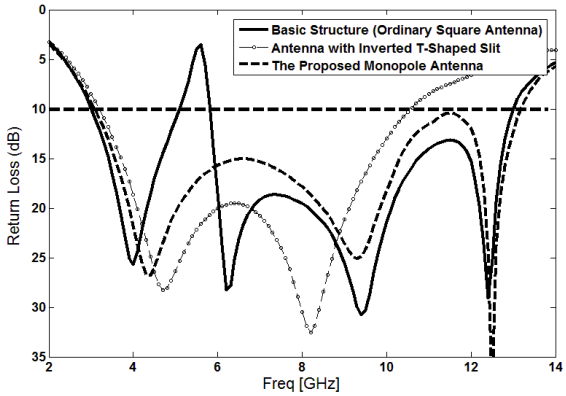


Figure 3: Simulated return loss characteristics for the antennas shown in Figure 2.

Also the input impedance of the various monopole antenna structures that shown in Fig. 2, on a Smith Chart is shown in Fig. 4.

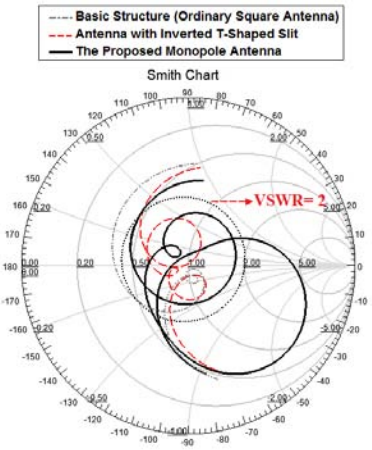


Figure 4: The simulated input impedance on a Smith chart of the various monopole antenna structures shown in Fig. 2.

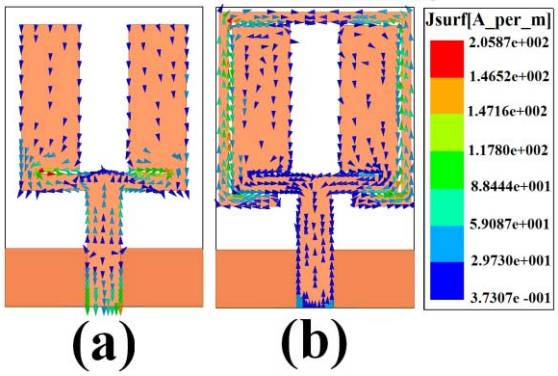


Figure.5. Simulated surface current distributions at the radiating patch (a) for the square antenna with an inverted T-shaped slit on the radiating patch at 12.3 GHz and, (b) for the proposed antenna in the at 5.5 GHz.

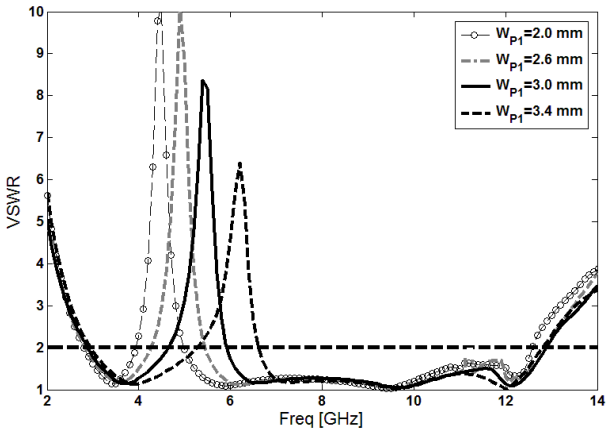


Figure 6: Simulated VSWR characteristics for the proposed antenna with different values of W_{P1} .

In order to understand the phenomenon behind this additional resonance and band notch performance, the simulated current distributions on the ground plane for the square antenna with an inverted T-shaped slit at 12.3 GHz are presented in Figure 5 (a). It is found that by using this slit, new resonance at 12.3 GHz can be achieved [2]. Another important design parameter of this structure is the

rotated C-shaped parasitic structure. Figure 5 (b) presents the simulated current distributions at the radiating stub at the notch frequency (5.5 GHz). As shown in Figure 5 (b) by inserting the rotated C-shaped parasitic structure on the radiating stub, a band-stop performance is generated [3].

The simulated VSWR curves with different values of W_{P1} are plotted in Fig. 6. As shown in Fig. 6, when the width of the W_{P1} increases from 2 to 3.4 mm, the centre of notch frequency is decreases from 6.35 to 4.28 GHz and from these results, we can conclude that the notch frequency is controllable by changing the interior height of the W_{P1}.

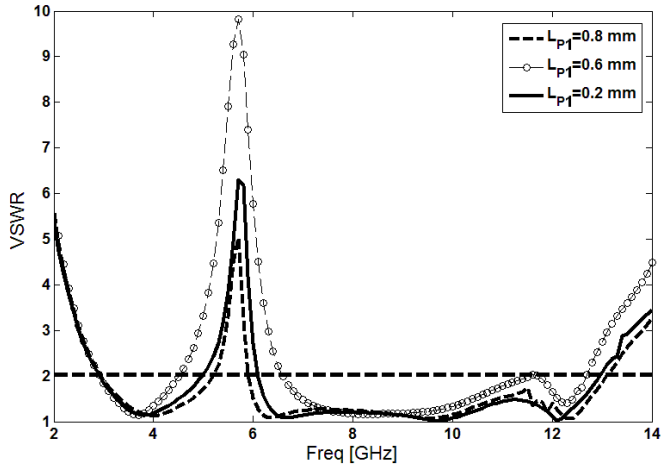


Figure 7: Simulated VSWR characteristics for the proposed antenna with different values of L_{P1}

The simulated VSWR curves with different values of L_{P1} are plotted in Figure 7. As shown in Figure 7, when the length of the L_{P1} increases from 0.2 to 0.8 mm, the filter bandwidth is varied from 0.65 to 1.75 GHz.

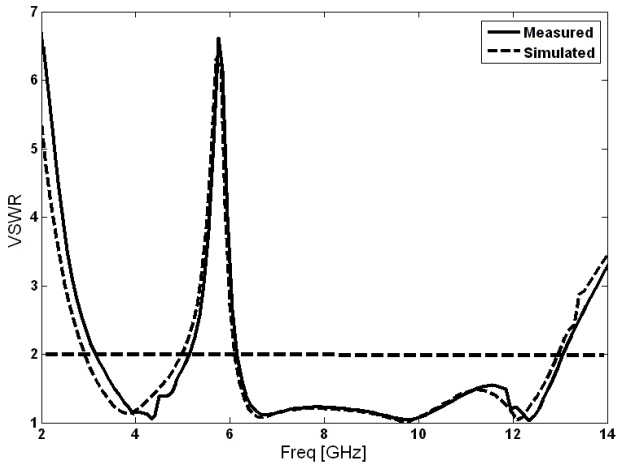


Figure 8: Measured and simulated VSWR for the proposed antenna.

The proposed antenna with optimal design, was built and tested. Fig. 8 shows the measured and simulated VSWR characteristics of the proposed antenna. The fabricated antenna has the frequency band of 3.08 to over 13.23 GHz with notched-band function around 5.03-5.97 GHz. As shown in Figure 8, there exists a discrepancy between measured data and the simulated results this could be due to the effect of the SMA port. In order to confirm the accurate return loss characteristics for the designed antenna, it is recommended that the manufacturing and measurement process need to be performed carefully.

Figure 9 shows the measured radiation patterns including the co polarization and cross-polarization in the H-plane (x-z plane) and E-plane (y-z plane). The main purpose of the radiation patterns is to demonstrate that the antenna actually radiates over a wide frequency band. It can be seen that the radiation patterns in x-z plane are nearly omnidirectional for the three frequencies.

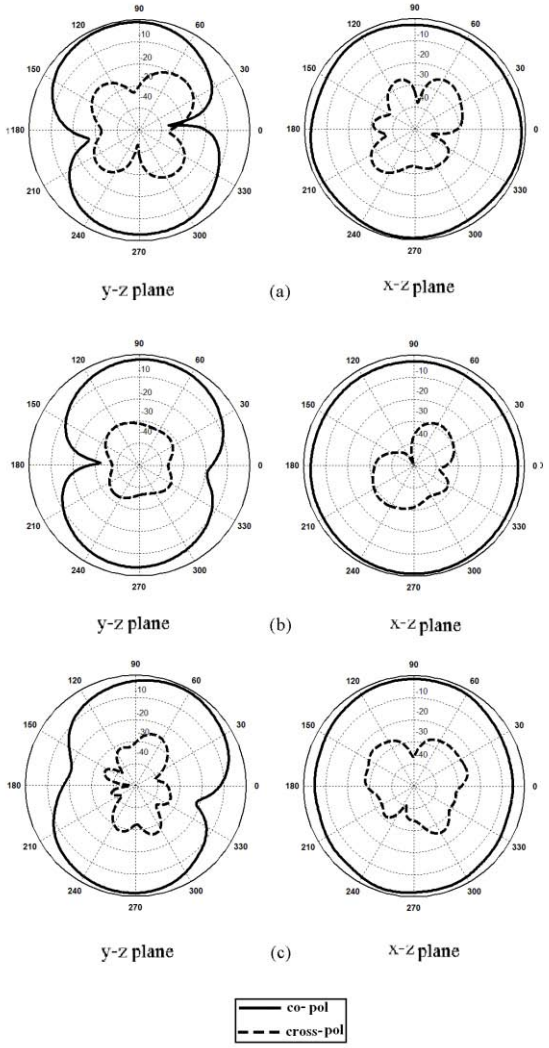


Figure 9: Measured radiation patterns of the proposed antenna (b) 4 GHz, (c) 7 GHz, and (d) 10 GHz.

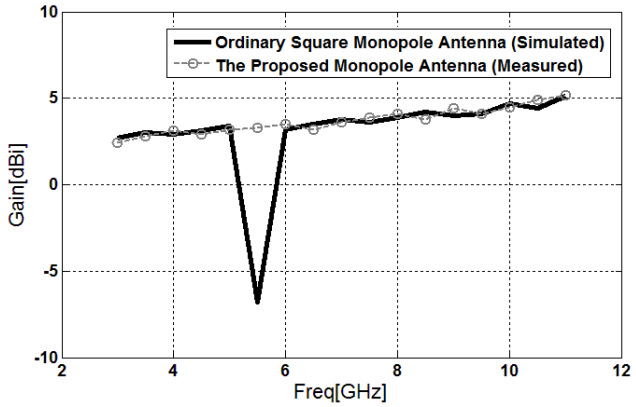


Figure 10: Maximum gain comparisons for the ordinary square antenna (simulated), and the proposed antenna (measured).

Figure10 shows the effects of the rotated C-shaped parasitic structure and the inverted T-shaped slit on the maximum gain in comparison to the ordinary square antenna without them. As shown in Figure 10, the ordinary square antenna has a gain that is low at 3 GHz and increases with frequency. It is found that by using a square radiating patch with the rotated C-shaped parasitic structure and the inverted T-shaped slit, a sharp decrease of maximum gain in the notched frequency band at 5.5 GHz are shown. For other frequencies outside the notched frequency band, the antenna gain with the filter is similar to those without it.

4. Conclusions

In this paper, a novel small square monopole antenna with band-notched characteristics and wide bandwidth capability for UWB applications is proposed. In this design, the proposed antenna can operate from 3.08 to 13.23 GHz with a rejection band around 5.03–5.97 GHz. By inserting a rotated C-Shaped parasitic structure and by cutting an inverted T-shaped slit on the radiating patch a band notch characteristic generated and also additional resonances are excited, respectively. The designed antenna has a small size. Good return loss and radiation pattern characteristics are obtained in the frequency band of interest. Simulated and experimental results show that the proposed antenna could be a good candidate for UWB application.

Acknowledgements

The authors are thankful to Microwave Technology Company staff for their beneficial and professional help. (www.microwave-technology.com).

References

[1] M. Ojaroudi, Sh. Yzdanifard, N. Ojaroudi, and M. Nasser-Moghaddasi, "Small Square Monopole Antenna with Enhanced by Using Inverted T-Shaped Slot and Conductor-Backed Plane", IEEE Transactions on Antenna and Propagation, VOL. 59, No. 2, pp. 670-674, February 2011.

[2] M. Ojaroudi, Ch. Ghobadi, and J. Nourinia, "Small Square Monopole Antenna With Inverted T-Shaped Notch in the Ground Plane for UWB Application," *IEEE* Antennas and Wireless Propagation *Letters*, Vol. 8, no. 1, pp. 728-731, 2009.

[3] A. Ghazi, M. N. Azarmanesh, and M. Ojaroudi, "Muti-Resonance Square Monopole Antenna for Ultra-Wideband Applications", Progress In Electromagnetics Research C, Vol. 14, 103-113, 2010.

[4] M. Ojaroudi, Sh. Yzdanifard, N. Ojaroudi, and R. A. Sadeghzadeh, " Band-Notched Small Square-Ring Antenna with a Pair of T-Shaped Strips Protruded Inside the Square Ring for UWB Applications", *IEEE* Antennas and Wireless Propagation *Letters*, Vol. 10, accepted to publish, 2011.

[5] M. Ojaroudi, "Printed Monopole Antenna with a Novel Band-Notched Folded Trapezoid for Ultra-Wideband Applications", Journal of Electromagnetic Waves and Application (JEMWA), Vol. 23, 2513–2522, 2009.

[6] Sh. Yazdanifard, R. A. Sadeghzadeh, and M. Ojaroudi, "ULTRA-WIDEBAND SMALL SQUARE MONOPOLE ANTENNA WITH VARIABLE FREQUENCY BAND-NOTCH FUNCTION", Progress In Electromagnetics Research C, Vol. 15, 133-144, 2010.

[7] M. Ojaroudi, Gh. Ghanbari, N. Ojaroudi, and Ch. Ghobadi, "Small Square Monopole Antenna for UWB Applications with Variable Frequency Band-Notch Function," *IEEE* Antennas and Wireless Propagation *Letters*, Vol. 8, pp. 1061-1064, 2009.

[8] R. Rouhi, Ch. Ghobadi, J. Nourinia and M. Ojaroudi, "Ultra-Wideband Small square monopole antenna with Band Notched Function," Microwave and Optical Tech. Letters, vol. 52, no.8, August 2010.

[9] Ansoft High Frequency Structure Simulation (HFSS), Ver. 13, Ansoft Corporation, 2010.

Microstrip-Fed Slot Antenna with Band-Notch Performance for UWB Wireless Communications

Nasser Ojaroudi[1], Mohammad Ojaroudi[2], and Shervin Amiri[3]

[1]Faculty of Electrical & Computer Engineering, Shahid Rajaee Teacher Training University, Tehran, Iran
[2]Young Research Club, Ardabil Branch, Islamic Azad University, Ardabil, Iran.
[3]Scientific Member of Electrical Engineering Department of Iranian Research Organization for Science and Technology (IROST), Tehran, Iran.
*corresponding author, E-mail: m.ojaroudi@iauardabil.ac.ir

Abstract

In this paper, a simple and compact ultra wideband (UWB) printed slot antenna with band-notch performance is presented. In order to increase the impedance bandwidth of the square slot antenna, we use a pair of S-shaped slots in the ground plane that with this structure UWB frequency range can be achieved. Additionally, by cutting a rectangular slot with a protruded E-shaped strip inside the slot in the radiating stub, a frequency notched band performance has been obtained. The designed antenna has a small size of 20×20 mm^2, while showing the radiation performance in the frequency band of 3.08 to over 14.3 GHz with a band rejection performance in the frequency band of 5 to 6 GHz. Simulated and experimental results obtained for this antenna show that it exhibits good radiation behavior within the UWB frequency range.

1. Introduction

Communication systems usually require smaller antenna size in order to meet the miniaturization requirements of radio-frequency (RF) units [1]. In UWB systems to improve the impedance bandwidth which do not involve a modification of the geometry of the planar antenna have been investigated, and growing research activity is being focused on them. As important compact UWB antennas, printed slot antennas have attracted more and more attention. Consequently, a number of planar slots with different geometries have been experimentally characterized [2]-[5].

The frequency range for UWB systems between 3.1–10.6 GHz will cause interference to the existing wireless communication systems for example the wireless local area network (WLAN) for IEEE 802.11a operating in 5.15–5.35 GHz and 5.725–5.825 GHz bands, so the UWB antenna with a band-notch function is required. In this paper, we present a new design of compact wideband slot antenna with variable band rejection characteristic for UWB applications. In this antenna, two S-shaped slots cut in ground plane was used for enhance of bandwidth and a modified rectangular slot with a protruded E-shaped strip inside the slot in the radiating stub was applied to generate a band notch performance. The fabricated antenna has the frequency band of 3.08 to over 14.3 GHz with a rejection band around 5-6 GHz. The size of the designed antenna is smaller than the slot antennas reported recently [2]-[5]. Good return loss and radiation pattern characteristics are obtained in the frequency band of interest.

2. Antenna Design and Configuration

The square slot antenna fed by a 50 Ω microstrip line is shown in Figure 1, which is printed on a FR4 substrate of thickness 0.8 mm, permittivity 4.4, and loss tangent 0.018. The basic antenna structure consists of a square radiating stub, a 50 Ω microstrip feed-line, and a ground plane with a rectangular slot. The square radiating stub has a width W. The radiating stub is connected to a feed line of width W_f and length L_f, as shown in Figure 1. On the other side of the substrate, a conducting ground plane with a rectangular slot is placed. The proposed antenna is connected to a 50 Ω SMA connector for signal transmission

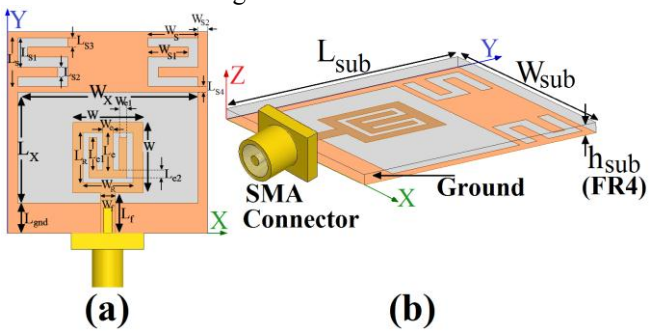


Figure.1: Geometry of proposed slot antenna, (a) top view, (b) side view.

The optimal dimensions of the designed antenna are as follows: $W_{sub}=20mm$, $L_{sub}=20mm$, $h_{sub}=0.8mm$, $W=7mm$, $W_f=1.5mm$, $L_f=4mm$, $W_X=18mm$, $L_X=11mm$, $W_S=5mm$, $L_S=5mm$, $W_{S1}=4mm$, $L_{S1}=3.5mm$, $W_{S2}=1mm$, $L_{S2}=0.5mm$, $L_{S3}=1.25mm$, $L_{S4}=0.5mm$, $W_R=5mm$, $L_R=5.5mm$, $W_e=1mm$, $L_e=3.75mm$, $W_{e1}=0.75mm$, $L_{e1}=3.25mm$, $L_{e2}=0.75mm$, and $L_{gnd}=3mm$.

3. Results and Discussion

The proposed microstrip-fed slot antenna with various design parameters were constructed, and the numerical and experimental results of the input impedance and radiation characteristics are presented and discussed. The Ansoft simulation software high-frequency structure simulator (HFSS) [6] is used to optimize the design and agreement between the simulation and measurement is obtained.

The configuration of the various antennas structures were shown in Figure 2. Return loss characteristics for ordinary square slot antenna, square slot antenna with a pair of S-shaped slots in the ground plane and the proposed antenna structure are compared in Figure 3. As shown in Figure. 3, it is observed that the middle frequency bandwidth is affected by using a pair of S-shaped slots in the ground plane and the notch frequency bandwidth is sensitive to the a protruded E-shaped strip inside the slot in the radiating stub.

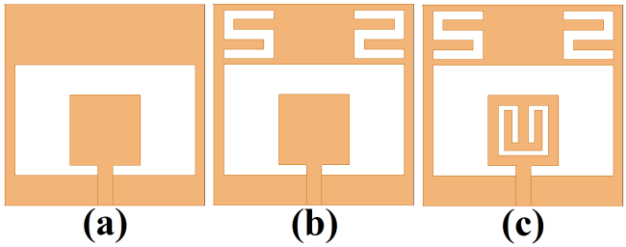


Figure 2: (a) ordinary square slot antenna, (b) ordinary square slot antenna with two S-shaped slots in the ground plane, and (c) the proposed antenna.

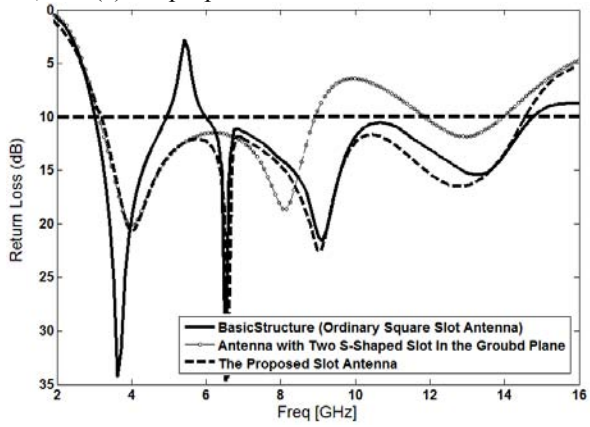


Figure 3: Simulated return loss characteristics for the antennas shown in Figure 2.

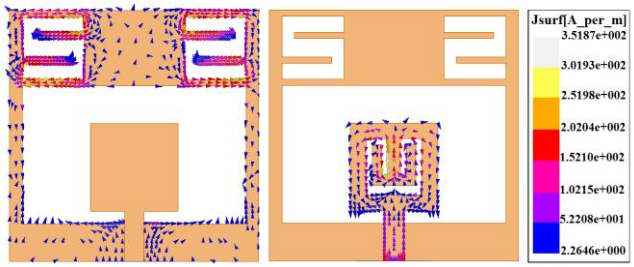


Figure 4: Simulated surface current distributions (a) for the square antenna with two S-shaped slots in the ground plane at 6.3 GHz and, (b) for the proposed antenna in the radiation stub at 5.5 GHz.

In order to understand the phenomenon behind this additional resonance and band notch performance, the simulated current distributions on the ground plane for the square antenna with two S-shaped slots at 6.3 GHz are presented in Figure 4 (a). It is found that by using these S-shaped slots, new resonance at 6.3 GHz can be achieved [2]. Another important design parameter of this structure is the rectangular slot with a protruded E-shaped strip inside the slot at the radiating stub. Figure 4 (b) presents the simulated current distributions at the radiating stub at the notch frequency (5.5 GHz). As shown in Figure 4 (b) by cutting rectangular slot with a protruded E-shaped strip inside the slot on the radiating stub, a band-stop performance is generated [3].

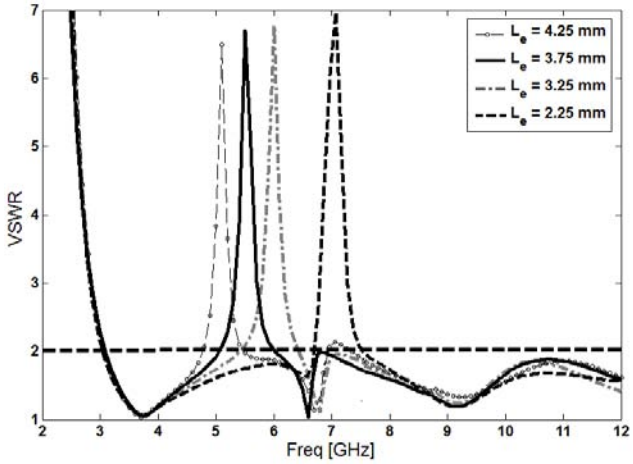


Fig. 5: Simulated VSWR characteristics for the proposed antenna with different values of L_e

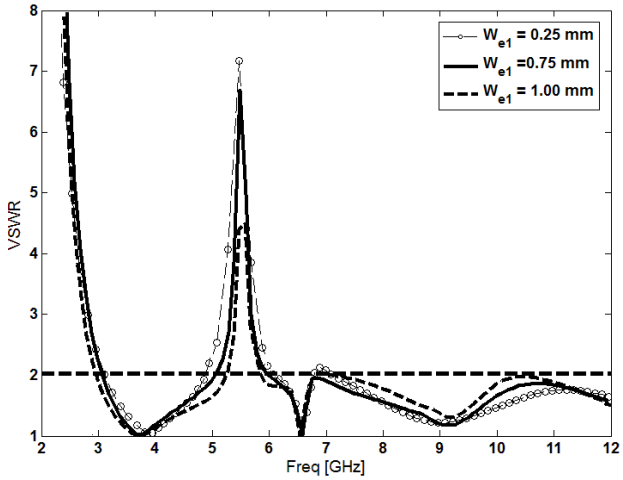


Fig. 6: Simulated VSWR characteristics for the proposed antenna with different values of W_{e1}

The simulated VSWR curves with different values of L_e are plotted in Figure 5. As shown in Figure 5, when the height of the L_e increases from 2.25 to 4.25 mm, the centre of notch frequency is decreases from 7.2 to 5.15 GHz and from these results, we can conclude that the notch frequency is controllable by changing the interior height of the L_e .

The simulated VSWR curves with different values of W_{e1} are plotted in Figure 6. As shown in Figure 6, when the width of the W_{e1} increases from 0.25 to 1 mm, the filter bandwidth is varied from 075 to 1.35 GHz.

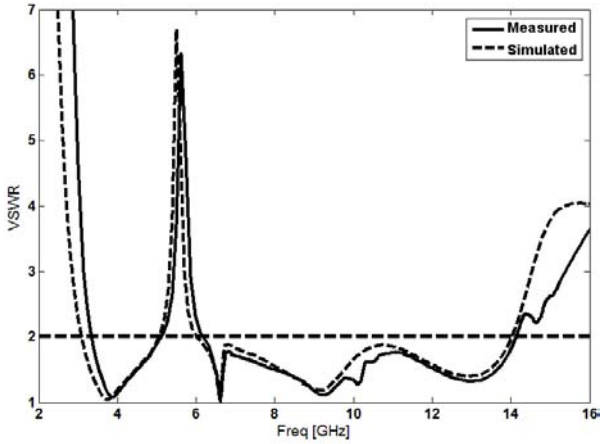


Figure 7: Measured and simulated VSWR for the proposed antenna

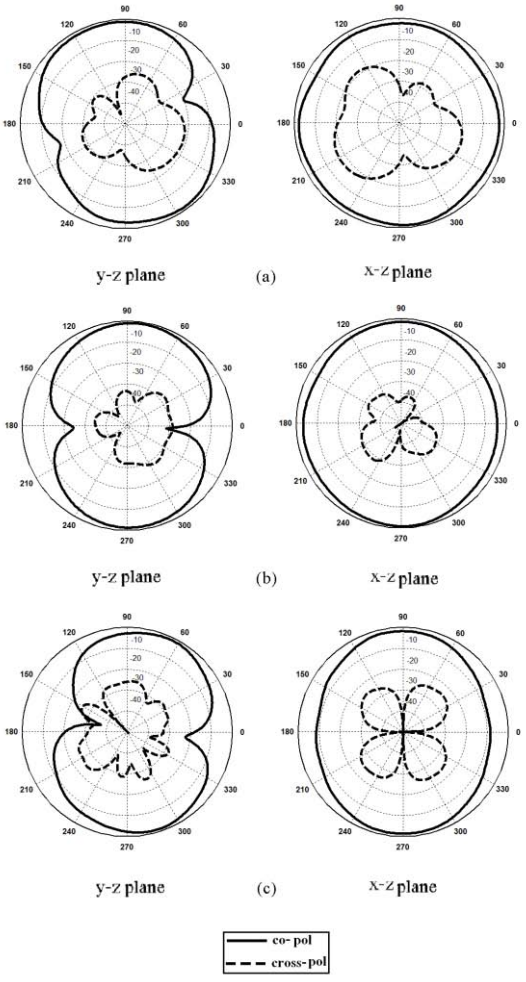


Figure 8: Measured radiation patterns of the proposed antenna (b) 4 GHz, (c) 7 GHz, and (d) 10 GHz.

The measured and simulated VSWR characteristic of the proposed antenna was shown in Figure 7. The fabricated antenna has the frequency band of 3.08 to over 14.3 GHz with a band rejection performance in the frequency band of 5 to 6 GHz. Also Figure 8 show the measured radiation patterns including the co-polarization and cross polarization in the H-plane (x-z plane) and E-plane (y-z plane). It can be seen that the radiation patterns in the plane are nearly omnidirectional for the three frequencies.

4. Conclusions

In this paper, a novel design of ultra wide band slot antenna with variable band notch function is proposed. The presented slot antenna can operate from 3.08 to 14.3 GHz with VSWR < 2 with a rejection band around 5 to 6 GHz .By using two S-shaped slots in the ground plane additional resonance at higher frequency range is excited and much wider impedance bandwidth can be produced. In order to generate a frequency band-stop performance we cut a rectangular slot with a protruded E-shaped strip inside the slot in the radiating stub. The designed antenna has a small size. The measured results showed good agreement with the simulated and good measured results. Experimental results show that the presented slot antenna could be a good candidate for UWB application.

Acknowledgements

The authors are thankful to Microwave Technology Company staff for their beneficial and professional help. (www.microwave-technology.com).

References

[1] H. Schantz, The art and science of ultra wideband antennas, Artech House 2005.

[2] M. Ojaroudi, and A. Faramarzi, “Multi-resonance Small Square Slot Antenna for Ultra-Wideband Applications,” Microwave and Optical Tech. Letters, vol. 53, no.9, September 2011.

[3] J. Y. Sze and K. L. Wong, “Bandwidth enhancement of a microstrip line-fed printed wide-slot antenna,” IEEE Trans. Antennas Propag., vol. 49, pp. 1020–1024, 2001.

[4] Y. W. Jang, “Experimental study of large bandwidth three-offset microstrip line-fed slot antenna,” IEEE Microw.Wireless Comp. Lett., vol. 11, pp. 425–426, 2001.

[5] Aliakbar Dastranj, Ali Imani, and Mohammad Naser-Moghaddasi, "Printed Wide-Slot Antenna for Wideband Applications, IEEE TRANSACTIONS ON ANTENNAS AND PROPAGATION, VOL. 56, NO. 10, pp./3097-3102, OCTOBER 2008.

[6] Ansoft High Frequency Structure Simulation (HFSS), Ver. 13, Ansoft Corporation, 2010.

Multipole theory for tight focusing of polarized light: Application to hemispherical solid immersion lens (SIL) for subsurface imaging

Thanh Xuan Hoang,[1,*] Xudong Chen,[1] and Colin J.R. Sheppard[2]

[1]Department of Electrical and Computer Engineering,
National University of Singapore, Singapore 117576, Singapore
[2]Department of Bioengineering,
National University of Singapore, Singapore 117576, Singapore
*corresponding author, E-mail: a0033737@nus.edu.sg

Abstract

Microscopy is becoming more and more important as modern technologies require smaller and better designs. Spatial resolution is often a major concern, defining how small components can be designed. Among different techniques, solid immersion microscopy is well-known to provide a high resolution and a high light collection efficiency. Due to these advantages, many researchers have analyzed electromagnetic field distributions in the focal region of the SIL by using the angular spectrum representation for the field. However, the approach needs a heavy computation of diffraction integrals. This paper presents an alternative approach using multipole theory to calculate the focused field of a hemispherical solid immersion lens. The new approach gives a better insight into the physical properties of the focused beam, and avoids evaluating diffraction integrals. Only a few multipole terms are needed to get the same approximation as the diffraction integrals, hence the proposed method is more efficient and convenient. The paper also shows a clear view on a relationship between multipole theory and the Debye potentials (DPs) Π_e, Π_m which are very convenient for calculating scattering by a sphere using the generalized Lorentz-Mie theory.

1. Introduction

SIL was firstly introduced by Mansfield and Kino in 1990 [1]. Through more than 20 years of development, SIL has been extensively employed in optical data storage, photolithography, and microscopy. The performance of the SIL has been analyzed in both theory and experiment [2, 3]. In theory, most researchers [4, 5] evaluate the focal field of the SIL by calculating diffraction integrals which are similar to the integrals of Richards and Wolf [6]. The integrals are rapidly varying products of a Bessel function and a sinusoid, and hence need a heavy load of computation. Recently, we expressed the focused field of any polarized beam in terms of multipole terms, which not only helps to gain a deeper insight into the physical properties of the focused beam but also avoids computing the diffraction integrals [7]. In our paper, we analyzed the focal field of an aplanatic optical lens for a number of different polarized beams. The aplanatic optical lens is a major component of a conventional microscope. The aplanatic optical lens and its modeling system are shown in Fig. 1, where the lens is represented by the Gaussian reference sphere (GRS).

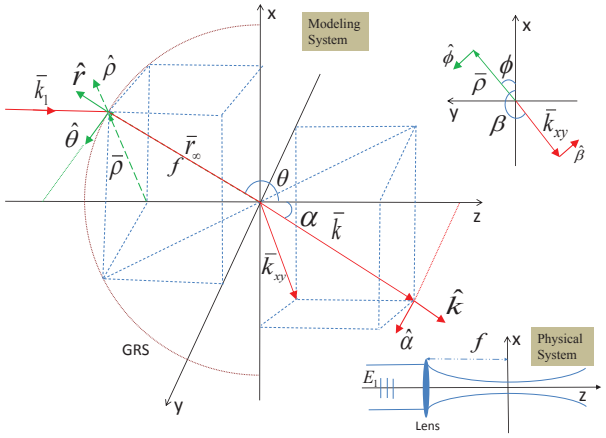


Figure 1: Aplanatic optical lens and modeling system.

Hemispherical solid immersion microscope is a modification of the conventional microscope in which a SIL is placed into the focal region. The center of the SIL coincides with the focal point of the lens, as illustrated in Fig. 2. The system configuration in Fig. 2 represents the major part of the hemispherical solid immersion microscope. The electric field inside the SIL will be derived and analyzed in this paper using the multipole theory. We will show that all the advantages of the multipole theory presented in [7] are preserved regardless of the presence of the SIL. The diffraction integrals of the focal field will also be presented for the sake of comparison.

The structure of this paper is as follows: First, we briefly give an introduction to the problem. Then, we present and solve the problem in theory for a general polarized beam. In section 3, a radially polarized beam, which can produces a smaller focal spot than focusing linearly polarized light, will be analyzed and discussed. We will give a conclusion in section 4.

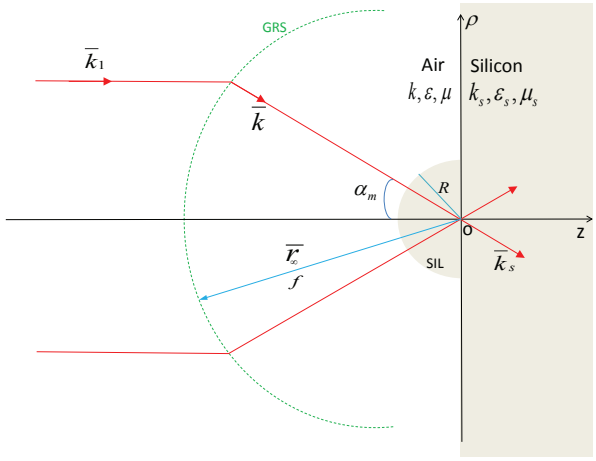


Figure 2: Hemispherical SIL configuration.

2. Theory

This section derives the focal field of the SIL. For any incident polarized beam approaching the aplanatic optical lens, the refracted field on the GRS can be estimated [5]. And the field outside the SIL can be calculated as shown in [7]. The field inside the SIL can then be calculated by considering the scattering effect of the SIL's interface. To account for the effect, it is very convenient to express the field in terms of the Debye potentials [8]. The details of deriving the field expressions are shown below.

2.1. Multipole theory

The electric field at the GRS can be in general expressed in terms of the vector electric $\mathbf{N}_l^m(\bar{r})$ and magnetic $\mathbf{M}_l^m(\bar{r})$ multipole fields as

$$\mathbf{E}(\bar{r}) = \sum_{l=1}^{\infty}\sum_{m=-l}^{l}[p_{El}^m\mathbf{N}_l^m(\bar{r}) + p_{Ml}^m\mathbf{M}_l^m(\bar{r})], \quad (1)$$

where

$$\mathbf{N}_l^m(\bar{r}) = \nabla\times\nabla\times[\bar{r}h_l^{(2)}(kr)Y_l^m(\theta,\phi)],$$
$$\mathbf{M}_l^m(\bar{r}) = ik\nabla\times[\bar{r}h_l^{(2)}(kr)Y_l^m(\theta,\phi)].$$

Since the wave at the GRS is converging, the Hankel function of the second kind is chosen. When only the field around the focal point is of interest, and taking the fact into account that the radius of the GRS is in practice much larger than the wavelength, the electric p_{El}^m and magnetic p_{Ml}^m multipole strengths (EMMSs) can be estimated in terms of the spectral amplitude of the field as shown in [7]. Equivalently, we can also estimate the EMMSs in terms of the far-field:

$$\mathbf{E}(\bar{r}_\infty) = E_\alpha\hat{\alpha} + E_\beta\hat{\beta}. \quad (2)$$

The EMMSs are as follows:

$$p_{El}^m = -\frac{i^l f e^{ikf}}{l(l+1)}c_{lm}\int_0^{2\pi}\int_0^{\pi}\left(\frac{dP_l^m(\cos\alpha)}{d\alpha}E_\alpha - im\frac{P_l^m(\cos\alpha)}{\sin\alpha}E_\beta\right)e^{-im\beta}\sin\alpha\, d\alpha d\beta, \quad (3)$$

$$p_{Ml}^m = \frac{i^l f e^{ikf}}{l(l+1)}c_{lm}\int_0^{2\pi}\int_0^{\pi}\left(\frac{dP_l^m(\cos\alpha)}{d\alpha}E_\beta + im\frac{P_l^m(\cos\alpha)}{\sin\alpha}E_\alpha\right)e^{-im\beta}\sin\alpha\, d\alpha d\beta, \quad (4)$$

where

$$c_{lm} = (-1)^m\left[\frac{2l+1}{4\pi}\frac{(l-m)!}{(l+m)!}\right]^{\frac{1}{2}},$$

and (θ,ϕ) and (α,β) respectively specify the field point and the wave propagation direction as shown in Fig. 1. The f is the focal length of the aplanatic optical lens or the radius of the GRS. Fig. 1 shows the aplanatic optical lens and its modeling system.

2.2. Debye potentials

Eq. 1 expresses the field in terms of the multipole fields. Alternatively the field can be expressed in terms of electric (Π_e) and magnetic (Π_m) Debye potentials as follows [8]:

$$E_r = \frac{i}{\omega\varepsilon}\left(\frac{\partial^2}{\partial r^2}r\Pi_e + k^2 r\Pi_e\right),$$
$$E_\theta = \frac{i}{\omega\varepsilon}\frac{1}{r}\frac{\partial^2}{\partial r\partial\theta}r\Pi_e + \frac{1}{\sin\theta}\frac{\partial}{\partial\phi}\Pi_m,$$
$$E_\phi = \frac{i}{\omega\varepsilon}\frac{1}{r\sin\theta}\frac{\partial^2}{\partial r\partial\phi}r\Pi_e - \frac{\partial}{\partial\theta}\Pi_m. \quad (5)$$

It can be proven that Eqs. (1) and (5) are related by the following equations:

$$\Pi_e = -i\omega\varepsilon\sum_{l=1}^{\infty}\sum_{m=-l}^{l}p_{El}^m h_l^{(2)}(kr)Y_l^m(\theta,\phi),$$
$$\Pi_m = ik\sum_{l=1}^{\infty}\sum_{m=-l}^{l}p_{Ml}^m h_l^{(2)}(kr)Y_l^m(\theta,\phi). \quad (6)$$

The above DPs represent the focused field incident onto the SIL, and the DPs of the transmission field can be expressed as follows:

$$\Pi_e^{in} = -i\omega\varepsilon_s\sum_{l=1}^{\infty}\sum_{m=-l}^{l}\frac{\varepsilon}{\varepsilon_s}c_l p_{El}^m h_l^{(2)}(k_s r)Y_l^m(\theta,\phi),$$
$$\Pi_m^{in} = ik_s\sum_{l=1}^{\infty}\sum_{m=-l}^{l}\frac{k}{k_s}d_l p_{Ml}^m h_l^{(2)}(k_s r)Y_l^m(\theta,\phi). \quad (7)$$

The coefficients c_l and d_l can be derived:

$$c_l = \frac{2i\sqrt{\frac{\mu_s\varepsilon_s}{\mu\varepsilon}}}{\hat{H}_l^{(1)'}(kR)\hat{H}_l^{(2)}(k_sR) - \sqrt{\frac{\mu_s\varepsilon}{\mu\varepsilon_s}}\hat{H}_l^{(1)}(kR)\hat{H}_l^{(2)'}(k_sR)},$$
$$d_l = \frac{2i\sqrt{\frac{\mu_s\varepsilon_s}{\mu\varepsilon}}}{\hat{H}_l^{(1)'}(kR)\hat{H}_l^{(2)}(k_sR) - \sqrt{\frac{\mu\varepsilon_s}{\mu_s\varepsilon}}\hat{H}_l^{(1)}(kR)\hat{H}_l^{(2)'}(k_sR)}.$$

where

$$\hat{H}_l^{(2)}(kr) = krh_l^{(2)}(kr),$$
$$\hat{H}_l^{(1)}(kr) = krh_l^{(1)}(kr)$$

are the Riccati-Bessel functions. It is observed from Eqs. (6) and (7) that the interface changes $EMMSs$ outside p^m_{El} and p^m_{Ml} into $\frac{\varepsilon}{\varepsilon_s}c_l p^m_{El}$ and $\frac{k}{k_s}d_l p^m_{Ml}$ inside the SIL, respectively. It is important to notice that the coefficients c_l and d_l are different from Mie scattering coefficients for a sphere. This difference is due to the multiple reflections inside the sphere which do not occur inside the SIL. This will be presented further in a further paper.

2.3. Focal field expressions

Eq. (7) represents the field incident onto focal region. Since there is no source in the focal region, there will be an outgoing field which is a consequence of the incoming field as visualized in Fig. 2. The DPs representing this outgoing field can be obtained from Eq. (7) by replacing $h^{(2)}_l(k_s r)$ by $h^{(1)}_l(k_s r)$:

$$\Pi^{out}_e = -i\omega\varepsilon_s \sum_{l=1}^{\infty}\sum_{m=-l}^{l} \frac{\varepsilon}{\varepsilon_s} c_l p^m_{El} h^{(1)}_l(k_s r) Y^m_l(\theta,\phi),$$

$$\Pi^{out}_m = ik_s \sum_{l=1}^{\infty}\sum_{m=-l}^{l} \frac{k}{k_s} d_l p^m_{Ml} h^{(1)}_l(k_s r) Y^m_l(\theta,\phi). \quad (8)$$

The total DPs in the focal region are then the summations of Π^{in} in Eq. (7) and Π^{out} in Eq. (8):

$$\Pi^{tot}_e = -2i\omega\varepsilon_s \sum_{l=1}^{\infty}\sum_{m=-l}^{l} \frac{\varepsilon}{\varepsilon_s} c_l p^m_{El} j_l(k_s r) Y^m_l(\theta,\phi),$$

$$\Pi^{tot}_m = 2ik_s \sum_{l=1}^{\infty}\sum_{m=-l}^{l} \frac{k}{k_s} d_l p^m_{Ml} j_l(k_s r) Y^m_l(\theta,\phi). \quad (9)$$

The field around the focus can be derived by substituting Eq. (9) into Eq. (5), to give the field expression shown in Eq. (10) (see page 4). Now, the field inside the hemispherical SIL can be estimated for any incident polarized beam. In the next section, the result will be used for the radially polarized beam as an example for comparison between the two approaches, i.e., the angular spectrum representation and the multipole approach.

3. Simulation

For the case of a radially-polarized beam, the electric field on GRS consists of only the meridional component, and the polarization is circularly symmetrical. Hence we can express the refracted field on the GRS:

$$\mathbf{E}(\bar{r}_\infty) = a(\alpha)\hat{\alpha}, \quad (11)$$

or equivalently, the E_α and E_β in Eq. (2) are as follows:

$$E_\alpha = a(\alpha), \qquad E_\beta = 0.$$

Consequently, the EMMSs of the radially-polarized beam can be obtained from Eqs. (3) and (4):

$$p^m_{El} = -\frac{i^l f e^{ikf}[\pi(2l+1)]^{\frac{1}{2}}}{l(l+1)}\delta^0_m \int_0^{\pi} a(\alpha)\frac{dP_l(\cos\alpha)}{d\alpha}\sin\alpha\, d\alpha,$$
$$p^m_{Ml} = 0, \quad (12)$$

where δ^0_m is a Kronecker tensor.

The axial dipole wave [7, 9] is a case of the radially-polarized beam for which:

$$a(\alpha) = \sin\alpha \text{ for } \alpha < \alpha_m; a(\alpha) = 0 \text{ for } \alpha > \alpha_m,$$

where α_m is the angular semi-aperture of the lens. Eq. (12) becomes:

$$p^m_{El} = -i^l \frac{f e^{ikf}[\pi(2l+1)]^{\frac{1}{2}}}{l(l+1)}\delta^0_m \int_0^{\alpha_m} \frac{dP_l(\cos\alpha)}{d\alpha}\sin^2\alpha\, d\alpha,$$
$$p^m_{Ml} = 0.$$

Then Eq. (10) can be simplified for this particular case:

$$E^{tot}_r = \frac{k_s}{\sqrt{\pi}}\sum_{l=1}^{\infty}\frac{l(l+1)}{\sqrt{2l+1}}\frac{\varepsilon}{\varepsilon_s}c_l p^0_{El}[j_{l-1}(k_s r) + j_{l+1}(k_s r)]P_l(\cos\theta),$$

$$E^{tot}_\theta = \frac{k_s}{\sqrt{\pi}}\sum_{l=1}^{\infty}\frac{l(l+1)}{\sqrt{2l+1}}\frac{\varepsilon}{\varepsilon_s}c_l p^0_{El}\left[\frac{j_{l-1}(k_s r)}{l} - \frac{j_{l+1}(k_s r)}{l+1}\right]\frac{dP_l(\cos\theta)}{d\theta},$$

$$E^{tot}_\phi = 0. \quad (13)$$

Eq. (13) expresses the field in terms of multipole terms. Alternatively, the field can be expressed in terms of angular spectrum representations as follows:

$$\mathbf{E}(x,y,z) = kfe^{ikf}\begin{pmatrix} I_1\cos\phi \\ I_1\sin\phi \\ iI_0\end{pmatrix}, \quad (14)$$

where

$$I_0 = \int_0^{\alpha_m} t_p a(\alpha)\cos\alpha J_0(k_s\rho\sin\alpha)e^{i(\Phi + k_s z\cos\alpha)}\sin\alpha\, d\alpha,$$
$$I_1 = \int_0^{\alpha_m} t_p a(\alpha)\sin\alpha J_1(k_s\rho\sin\alpha)e^{i(\Phi + k_s z\cos\alpha)}\sin\alpha\, d\alpha,$$

and t_p is the amplitude transmission coefficient, Φ is the spherical aberration due to the interface:

$$t_p = \frac{2k}{k+k_s}, \qquad \Phi = (k_s - k)R,$$
$$\rho = \sqrt{x^2+y^2}, \qquad \phi = \arctan\frac{y}{x}.$$

The electric energy densities around the focus, which are calculated by using Eqs. (13) and (14), are shown in Figs. 3-6. The Fig. 3 and Fig. 4 are plotted for the case of which (k,ϵ) and (k_s,ϵ_s) are the same. These two figures show that the two approaches agree well in absence of the SIL. This result has been presented in [7]. The Fig. 5 and Fig. 6 are plotted with the following conditions:

$$\mu_s = \mu, \qquad \epsilon_s = 12.25\epsilon,$$
$$k_s = 3.5k, \qquad kR = 2345.$$

$$E_r^{tot} = \frac{k_s}{\sqrt{\pi}} \sum_{l=1}^{\infty} \sum_{m=-l}^{l} (-1)^m \frac{l(l+1)}{(2l+1)^{\frac{1}{2}}} \left[\frac{(l-m)!}{(l+m)!}\right]^{\frac{1}{2}} \left(\frac{\varepsilon}{\varepsilon_s} c_l p_{El}^m [j_{l-1}(k_s r) + j_{l+1}(k_s r)] P_l^m(\cos\theta)\right) \exp(im\phi),$$

$$E_\theta^{tot} = \frac{k_s}{\sqrt{\pi}} \sum_{l=1}^{\infty} \sum_{m=-l}^{l} (-1)^m \frac{l(l+1)}{(2l+1)^{\frac{1}{2}}} \left[\frac{(l-m)!}{(l+m)!}\right]^{\frac{1}{2}} \left(\frac{\varepsilon}{\varepsilon_s} c_l p_{El}^m \left[\frac{j_{l-1}(k_s r)}{l} - \frac{j_{l+1}(k_s r)}{l+1}\right] \frac{dP_l^m(\cos\theta)}{d\theta} - m\frac{2l+1}{l(l+1)} \frac{k}{k_s} d_l p_{Ml}^m j_l(k_s r) \frac{P_l^m(\cos\theta)}{\sin\theta}\right) \exp(im\phi),$$

$$E_\phi^{tot} = i\frac{k_s}{\sqrt{\pi}} \sum_{l=1}^{\infty} \sum_{m=-l}^{l} (-1)^m \frac{l(l+1)}{(2l+1)^{\frac{1}{2}}} \left[\frac{(l-m)!}{(l+m)!}\right]^{\frac{1}{2}} \left(m\frac{\varepsilon}{\varepsilon_s} c_l p_{El}^m \left[\frac{j_{l-1}(k_s r)}{l} - \frac{j_{l+1}(k_s r)}{l+1}\right] \frac{P_l^m(\cos\theta)}{\sin\theta} - \frac{2l+1}{l(l+1)} \frac{k}{k_s} d_l p_{Ml}^m j_l(k_s r) \frac{dP_l^m(\cos\theta)}{d\theta}\right) \exp(im\phi). \quad (10)$$

As observed in Fig. 5 and Fig. 6, the two approaches preserve the convergence property, without the need for increasing the required number of the multipole terms. The multipole approach still needs only 6 and 15 terms to obtain almost the same approximation as the approach using angular spectrum representation in x and z directions, respectively.

With the notices that the two plots in Fig. 3 and Fig. 5 have the same shape and size, but the units of the horizontal axes in Fig. 3 and Fig. 5 are respectively kx and $k_s x$. Then we can conclude that the hemispherical SIL narrows the focal spot in the x, y directions by a factor of the refractive index of the SIL ($\frac{k_s}{k}$). The same observation is applied for Figs. 4, 6, and z direction. These results have been well-known [5].

Obviously, the dipole term ($N = 1$) in Fig. 3 gives the tightest spot, and the higher orders gradually vanish when α_m is increased [7]. This accounts for the fact that the best resolution is achieved with 4π microscopy ($\alpha_m = \pi$). In general, the dipole term gives the tightest spot in terms of volume, but means that more terms can give a tighter size in one particular direction. This approach may be exploited in improving the resolution [10].

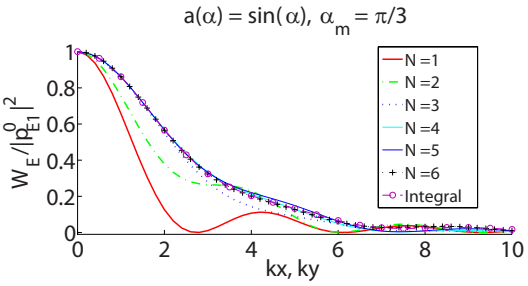


Figure 3: The convergence property along x, y directions in absence of SIL.

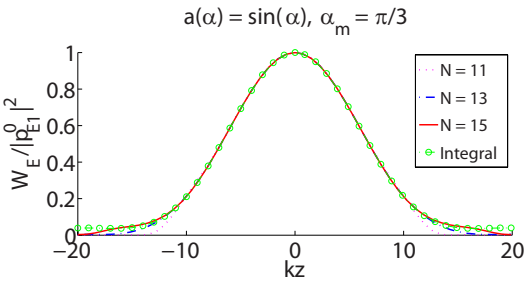


Figure 4: The convergence property along z direction in absence of SIL.

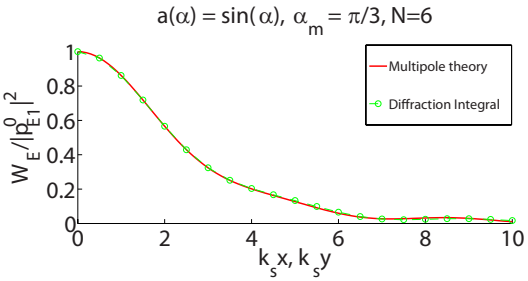


Figure 5: The convergence property along x, y directions in presence of SIL.

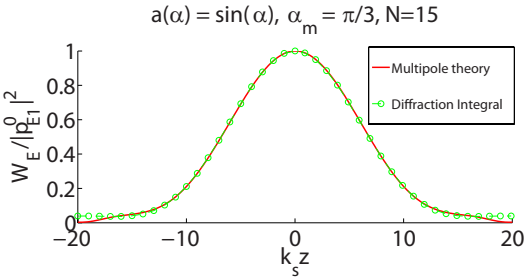


Figure 6: The convergence property along z direction in presence of SIL.

4. Conclusions

The paper presents a new alternative approach for calculating the focal field distribution of the optical hemispherical SIL-based system. The new approach is based on the multipole theory, which helps avoid the evaluation of diffraction integrals and gives deeper insights into the behavior of the polarized beam. Since a few multipole terms are sufficient for achieving very good approximation, this approach is very fast in evaluating the focal field. The paper also shows the clear relationship between multipole theory and DPs, in which the EMMSs link the two expressions. The new approach is also very useful for investigation of scattering and trapping effects.

Acknowledgement

We would like to thank Mr. Chen Rui for writing the Matlab code for the diffraction integrals.

References

[1] S.M. Mansfield, G.S. Kino, Solid immersion microscope, *Appl. Phys. Lett.* Vol. 57, No. 24, 2615-2616, 1990.

[2] Q. Wu, L.P. Ghislain, V.B. Elings, Imaging with Solid Immersion Lenses, Spatial Resolution, and Applications, *Proceedings of the IEEE* Vol. 88, No. 9, 1491-1498, 2000.

[3] S.H. Goh, C.J.R. Sheppard, A.C.T. Quah, C.M. Chua, L.S. Koh, J.C.H. Phang Design considerations for refractive solid immersion lens: Application to subsurface integrated circuit fault localization using laser induced techniques, *Rev. Sci. Instrum.* Vol. 80, 013703, 2009.

[4] K.M. Lim, G.C.F. Lee, C.J.R. Sheppard, J.C.H. Phang, C.L. Wong, X. Chen, The Effect of Polarization on a Solid Immersion Lens of Arbitrary Thickness, *J. Opt. Soc. Am. A* Vol. 28, No. 5, 903-911, 2011.

[5] A.N. Vamivakas, R.D. Younger, B.B. Goldberg, A.K. Swan, M.S. Ünlü, E.R. Behringer, S.B. Ippolito, A case study for optics: The solid immersion microscope, *Am. J. Phys.* Vol. 76, No. 8, 758-768, 2008.

[6] B. Richards, E. Wolf, Electromagnetic diffraction in optical systems. II Structure of the image field in an aplanatic system, *Proceedings of the Royal Society of London A* Vol. 253, 358-379, 1959.

[7] X.T. Hoang, X. Chen, C.J.R. Sheppard, Multipole theory for tight focusing of polarized light, including radially polarized and other special cases, *J. Opt. Soc. Am. A* Vol. 29, No. 1, 32-43, 2012.

[8] J.A. Kong *Electromagnetic Wave Theory*, EMW Publishing, Cambridge, Massachusetts, USA 2008.

[9] C.J.R. Sheppard, E.Y.S Yew, Performance parameters for focusing of radial polarization, *Optics Letters* Vol. 33, No. 5, 497-499, 2008.

[10] K.A. Serrels, E. Ramsay, R.J. Warburton, D.T. Reid, Nanoscale optical microscopy in the vectorial focusing regime, *Nature Photonics*, Vol. 2, 311-314, 2008.

Space-Efficient UWB Tapered Slot Antenna

Anatoliy Boryssenko*, and Elen Boryssenko

A&E Partnership, Belchertown, MA, USA
* E-mail: anatoliy@ae-partnership.com

Abstract

The results of parametric optimization of an ultra-wideband (UWB) tapered-slot antenna (TSA) are presented. The major design objectives included: (i) return loss 10 db and better with forward directive radiation across the 0.5…7 GHz frequency band; (ii) operation without and with backing small ground plane; (iii) small physical volume and low weight; (iv) low fabrication cost. First, the antenna equivalent circuit has been developed to guide its design process. Second, the geometrical parameterized model has been created and program in Matlab. The model provided with CAD conductor topologies imported into full-wave EM simulators. The antenna was iteratively tuned based on its equivalent circuit. Finally, the developed TSA design was fabricated at a low-cost FR-4 substrate and tested with good agreement between predicted and measured electrical features.

1. Introduction

Tapered slot (Vivaldi) antennas have been widely used from the pioneer study of Gibson [1]. Since that time of invention, TSAs have attracted lots of attention thanks of their broadband features and suitability to PCB fabrication. In particular, TSAs have been employed as an element of electronically scanning phased arrays [2], and as a single radiator and array element in numerous broadband and UWB radar, sensor and imaging [3], and communication applications.

Several versions of TSA antennas have been developed and demonstrated in operation including balanced TSA configuration (Fig. 1). This type of TSA looks most widely explored in the antenna literature, for example, [4-6]. Its design includes also a balun circuit required to feed the antenna through a coaxial connector, for example, SMA shown in Fig. 2.

Success in design of TSAs comes often from adequate understanding of their physical phenomenology [2,7]. This might guide design process towards obtaining desired electrical performance [8]. One of such useful interpretation of the TSA operation comes from its equivalent circuit that describes its operation as a cascaded impedance transformation between feed point and aperture [2]. Such a circuit model is shown in Fig. 2 developed particularly for the TSA in Fig. 1. This model includes four major transmission lines among which the section 2 has constant characteristic impedance only while wave impedances of the sections 1, 3 and 4 is gradually changed versus their lengths (Fig. 2).

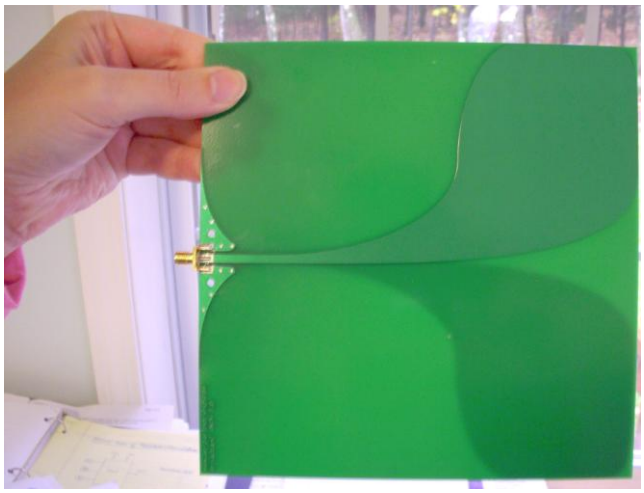


Figure 1: Tapered slot antenna on FR-4 substrate designed, fabricated and tested in this study.

From this perspective, the TSA shape needs to be designed to enable a smooth impedance transformation from the standard 50 Ohm coaxial port to 120π Ohm of free space. At the same time, severe restrictions are typically imposed on TSA geometrical dimensions mostly at degree of its forward protrusion and height that corresponds to the parameters L and C, respectively, in Fig. 3. Often this restriction is quantified as ratios L/λ and S/λ where λ is the wavelength for lowest operational frequency. A "good" TSA design tends to show $L/\lambda \approx 0.5$ and S/λ $L/\lambda \approx 0.5$.

2. Design Methodology

The physical insight [2,7,8] was employed to design the demonstrated TSA radiator with more than a decade bandwidth. The design process was guided by the antenna equivalent circuit in Fig. 2 and based on the use of an antenna parametric geometrical model in Fig. 3 developed in Matlab. The TSA geometrical model includes more parameters than other models reported in the literature [4-6]. In particular, there are dimensional parameters A-E, L and along with parameter P1-5 used to approximate smooth portion of the TSA conductors by hyper-ellipse curves.

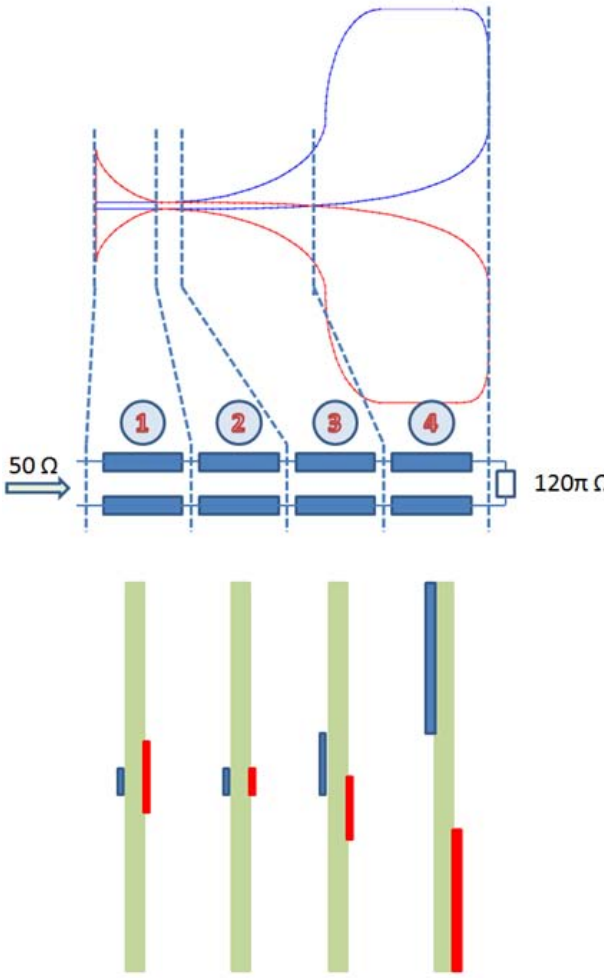


Figure 2: (Top) Equivalent circuit model of TSA formed as a cascaded transmission line transformer. (Bottom) Four major types of transmission lines implemented on two faces of antenna dielectric substrate.

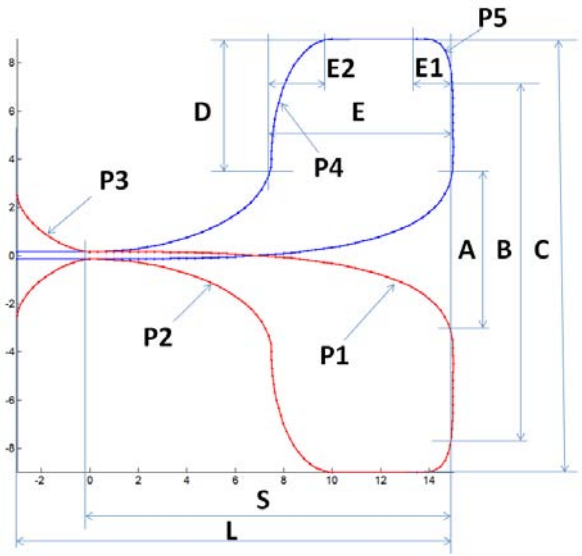


Figure 3: Geometrrcal model for TSA top (blue) and bottom (red) conductor outlines along with major geometrical dimensions A-E, S and L along with shape approximating parameters P1…5.

The proposed TSA model involves all important structural details that must be involved in shape optimization to come up with the required electrical features. In fact, this model covers a broad set of possible shapes as those illustrated in Fig. 3. The model was implemented in Matlab as a shape generator that takes as inputs the parameter from Fig. 3 and generates conductor topologies including their coding in CAD formats used to import the geometry into full-wave EM simulators and to control PCB fabrications (Fig. 5).

The final design was derived through iterative tuning facilitated by physical insight coming from the equivalent circuit (Fig. 2) and accuracy of full-wave EM simulations. Several commercial (CST) and in-house (MoM, FDTD) simulators have been used with very good agreement between them. The shape of the top and bottom conductors (Fig. 5), which is critical to meet the performance requirements, was optimized to operate without and with the backing ground plane. In this study, we have identified and manage the most critical design parameters that contribute critically to the low-frequency band cutoff and good forward directed radiation. In particular, the reported studies [4-6] omit many important details such as described in Fig. 3 by the parameter s E1, E2, P4, P5 and others.

The final design is shown Fig. 6 along with some important details of its feed implementation.

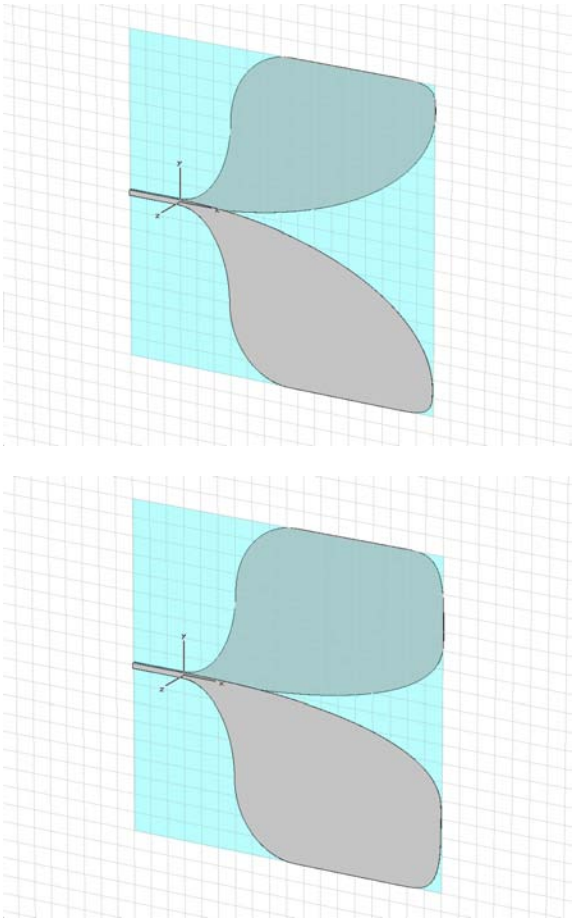


Figure 4: Examples of antenna conductor shapes generated through the parametric model in Fig. 3.

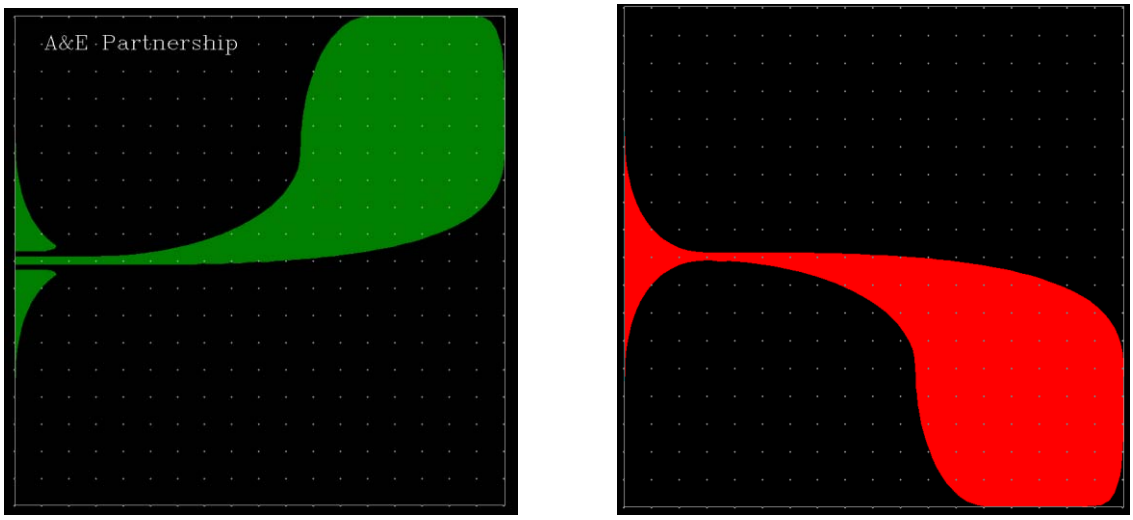


Figure 5: Optimized top, at the lef, and bottom, at the right, antenna conductors printed at the correponding faces of the antenna PCB pictured in Fig. 1.

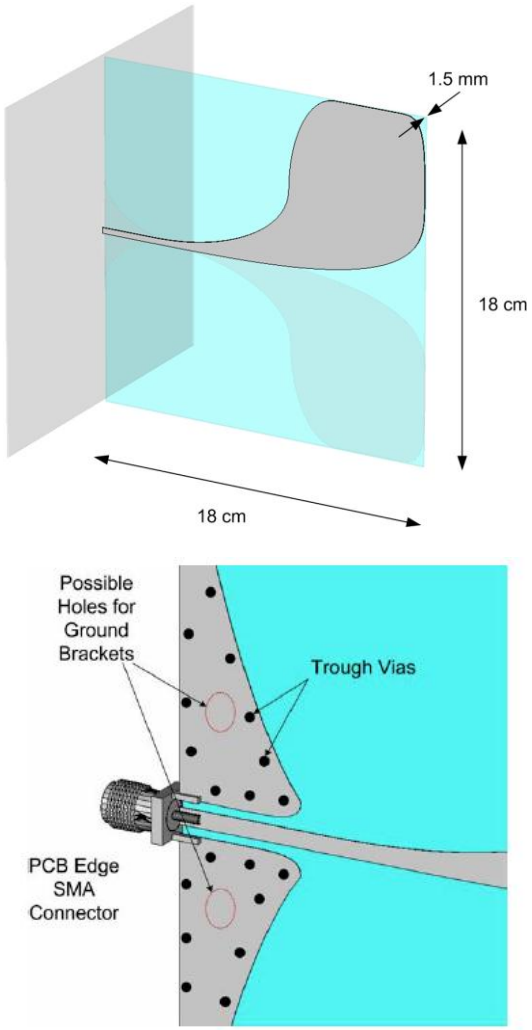


Figure 6: Antenna design with a small backing ground plane and major geometrical dimensions, at the top, and details on feed design with SMA connector, at the bottom.

3. TSA Electrical Performance

This antenna was prototyped and measured with the desired electrical features across 0.5-7.0 GHz that are close to those required and predicted in full wave simulations. These features include return losses of 10 dB and better. Antenna realized gain rises monotonically from 1.5 dBi (3dBi with ground plane) at 0.5 GHz up to 8 dBi at 7 GHz. This particular antenna was designed to use in an array for multichannel UWB imaging radar applications such as subsurface and "through-matter" vision and similar [3].

The simulated and measured return loss (S11) data in Fig. 7 are in pretty acceptable agreement. Major notable differences are observed only around 1 GHz and 2 GHz as S11 spikes of a few dB above the predicted -10 dB level. This might be attributed to variations in dielectric constant of the used FR-4 substrates that can be changed in the range 3.3-4.5. The value used in the simulation was set to 3.6. The computed 3-D radiation patterns are rendered in Fig. 4 and antenna realized gain evaluated in full-wave CST simulations is indicated in Table 1 for two cases, i.e. without and with backing ground plane.

Table 1: Realized Gain (dBi) without and with 18x18 cm ground plane (Fig. 6, top)

Freq, GHz	.5	1	2	3	4	5	6	7
W/o GRND	2	3	5	6	7	8	8	8
W/ GRND	3	4	7	6	7	8	8	8

4. Conclusions

The demonstrated design approach enables creation of the reported space efficient antenna (Fig. 1). Efficiency of space usage is quantified by the ratios of the antenna length, L, and height, C, (Fig. 3) to the largest operational wavelength, λ. The designed TSA exhibits $L(C)/\lambda = 0.3$ because of its optimized geometry while other reported

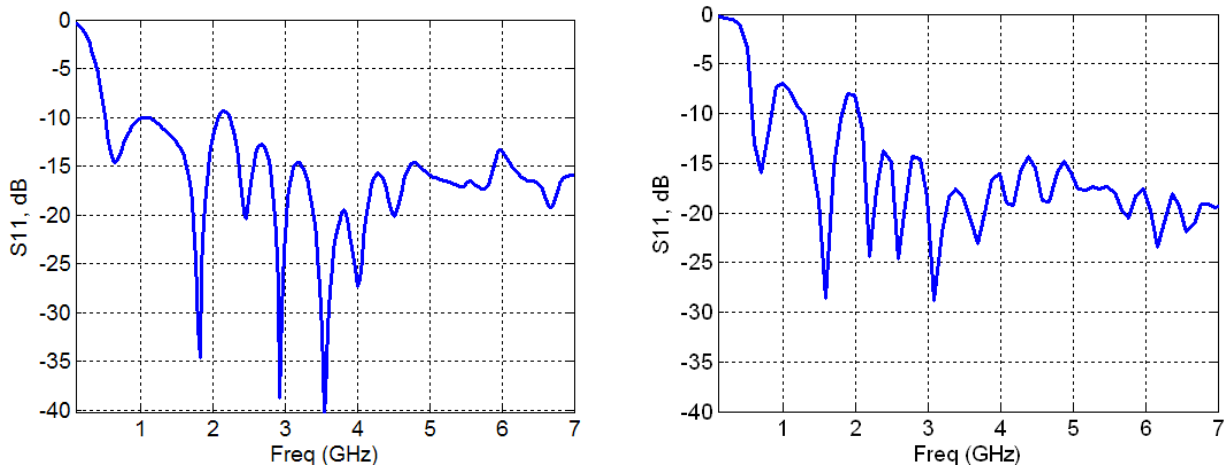


Figure7: Antenna return loss (s11) predicted in full-wave simulations, at the left, and measured with the sample in Fig. 1, at the right.

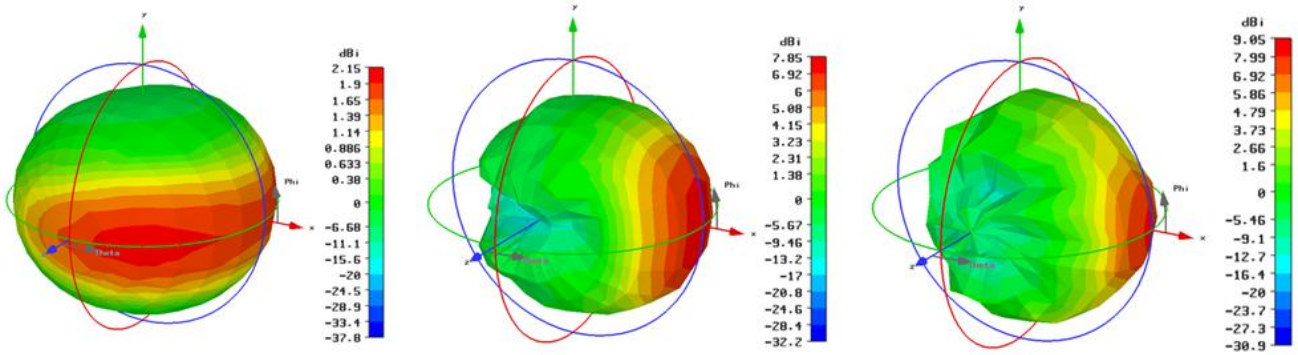


Figure 8: 3-D antenna radiation pattern predicted in CST simulations at 0.75 GHz, at the left, 4 GHz, at the middle, and 7 GHz, at the right.

TSAs, best to our knowledge, are not such space-efficient. For example, [2-3] demonstrate $L(C)/\lambda \geq 0.5$ being fabricated on expensive microwave substrates with dielectric constant exceeding 10 while the proposed design is based just on the low-cost FR-4 with dielectric constant around 4.

References

[1] P. I. Gibson, "The Vivaldi Aeriel," *9th European Microwave Con*., Brighton, UK, October 1979, 101–105.

[2] N. Schuneman, J. Irion, and R. Hodges, "Decade Bandwidth Tapered Notch Antenna Array Element," *Antenna Applications Symp*., pp. 280 – 294, 19-21 Sept. 2001. Monticello, IL.

[3] A. Boryssenko and E. Boryssenko, "Principles and Methods of Materials Penetrating UWB Radar Imagery", In *Ultrawideband Radar: Applications and Design*, Ed. by J. D. Taylor, CRC Press, to be published in May 2012.

[4] X. Qing, Z.N. Chen, and M. Y. Chia, "Parametric Study of Ultra-Wideband Dual Elliptically Tapered Antipodal Slot Antenna", *International J Ant. Propag*., Vol . 2008 ID 267197, 9 pages.

[5] A.M. Abbosh, H. K. Kan, and M. E. Bialkowski, "Design of compact directive ultra wideband antipodal antenna," *Microwave and Opt. Tech. Lett*., Vol. 84, No. 12, 2006.

[6] A.M. Abbosh, "Miniaturized Microstrip-Fed Tapered-Slot Antenna", *IEEE Ant. Wireless Propag. Letters*, Vol. 8, 2009, 690-692.

[7] A. Boryssenko, D. Schaubert, "Physical aspects of mutual coupling in finite broadband tapered slot (Vivaldi) arrays," *Int. Conf. on Antenna Theory and Techniques*, Kiev, Ukraine, 24-27 May, 2005, pp. 74 – 79.

[8] A. Boryssenko, "Taxonomical and Heuristic Studies on UWB Antenna Design Strategies", *High Frequency Electronics*, August, 2009, pp. 38, 40-42, 44-48.

Full and compact polarimetry modes using RADARSAT2 data

Boularbah Souissi[1], Mounira Ouarzeddine[2], Aichouche Belhadj-Aissa[3]

[1]Infotronic, Department of Physics, Faculty of Science, UMBB University, Boumerdes, Algeria
[3,2]Faculty of Electronics and Computational Science, USTHB University, Algiers, Algeria
*corresponding author, E-mail: m.ouarzeddine@yahoo.fr

Abstract

Recently, there has been growing interest in dual-pol systems that transmit one polarization and receive two polarizations. Souyris *et al.* proposed a DP mode called compact polarimetry (CP) which is able to reduce the complexity, cost, mass, and data rate of a SAR system while attempting to maintain many capabilities of a fully polarimetric system. This paper provides a comparison of the information content of full quad-pol data and the pseudo quad-pol data derived from compact polarimetric SAR modes. A pseudo-covariance matrix can be reconstructed following Souyris's approach and is shown to be similar to the full polarimetric (FP) covariance matrix. Both the polarimetric signatures based on the kennaugh matrix and the Freeman and Durden decomposition in the context of this compact polarimetry mode are explored. The Freeman and Durden decomposition is used in our study because of its direct relationship to the reflection symmetry.
We illustrate our results by using the polarimetric SAR images of Algiers city in Algeria acquired by the RadarSAT2 in C-band.

1. Introduction

The polarimetric radar synthetic aperture radar (PolSAR) images are formed by radar echoes of various combinations of transmitting and receiving polarizations from scattering media [1]. Single polarimetric radar systems (SP) operate with single fixed polarization antenna for both electromagnetic wave transmission and reception, for example transmitting horizontally polarized radiation and receiving horizontal polarization.

The full polarimetric SAR (FP-PolSAR) design architectures are built around the standard linear basis, i.e., horizontal (H) and vertical (V). On transmission, the radar interleaves pulses with H and V polarizations. On-receive, both polarizations are simultaneously and coherently recorded [1,2]. This quad-pol system produces the scattering matrix containing the four backscatter measurements (HH, HV, VH and VV) which allow much more information to be extracted from target scene. Indeed, FP mode has proven its increased potential compared to a single channel acquisition, but suffer from an increase in the pulse repetition frequency by a factor of two and an increase in the data rate by a factor of four over single polarization [3]. Their imaged swaths also are halved, resulting in reduced coverage and a degraded revisiting time [3]. The L-band PALSAR on board of the Japanese ALOS, for example, can only image 35-km swaths at incidence angles of less than 27° when operating in FP mode. Similarly, the Canadian Radarsat-2 offers a quad-polarimetric mode over a wider range of incidence angles (20°–40°) but a swath width of only 25 km [4].

Recently, dual-mode partially polarimetric SAR systems (DP) have been proposed such as Envisat ASAR, the Japanese L-band PalSAR, the European X-band TerraSAR-X, and the Canadian C-band RadarSAT 2, where one polarization (H or V) is transmitted, whereas two are received. These DPmodes collect only half of the full scattering matrix, either (HH, VH) or (VV, HV). This reduces both the data processing requirements and the information content of the polarimetric imagery. The acquired data set has the same coverage as for the single transmit polarization, but provides added information due to the two independent channels on-receive. From a mission standpoint, the DP imaging modes collect a wider swath width, and hence greater area coverage, as compared to quad-pol (FP) imagery. However, the per-pixel information content is less for DP imagery than for quad-pol imagery, which tends to favor quad-pol data collection [5].

Other system configurations have been also proposed and called compact polarimetry [6,7]. In these polarimetric configurations, only one transmit/receive cycle is required instead of two in a quad-pol system, reducing the pulse repetition frequency and data rates by a factor of two for a given swath width. Souyris *et al.* [6] introduced the $\pi/4$ compact polarimetric mode, in which the transmitted polarization is the superposition of linear horizontal and vertical polarizations H+V, resulting in a linear polarization oriented at 45° with respect to the horizontal. The radar receives returns in horizontal and vertical polarizations. Another hybrid DP mode is the circular transmit, linear receive (CTLR) mode [7]. As the name suggests either a left or right circularly-polarized signal is transmitted and both H and V polarizations are coherently received. The polarimetric models employed assume both reflection symmetric scattering, and a relationship between the linear coherence and the cross-polarization ratio to construct a full reflection symmetric polarization matrix from the 2×2 covariance data [6]. An equivalent covariance or coherency

matrix may be reconstructed to produce the so-called pseudo quad-pol data that accurately reproduces the full quad-pol data.

The compact polarimetry was proposed to assess various architecture designs that could be implemented on low-cost/low-mass. In that context, the comparison between FP versus DP is a subject of most importance.

This paper provides a comparison of the information content of full quad-pol data and the pseudo quad-pol data derived from compact polarimetric SAR modes. A pseudo-covariance matrix can be reconstructed following Souyris's approach and is shown to be similar to the full polarimetric (FP) covariance matrix. Both the polarimetric signatures based on the kennaugh matrix and the Freeman and Durden decomposition in the context of this compact polarimetry mode are explored. The Freeman and Durden decomposition is used in our study because of its direct relationship to the reflection symmetry.

We illustrate our results by using the polarimetric SAR images of Algiers city in Algeria acquired by the RadarSAT2 in C-band.

2. Data used

The study area is located in the west of the city of Algiers which is the capital of Algeria. It consists mainly of urban areas, agriculture fields and sea. The data was acquired on 11th April 2009 by RADARSAT2 in a fully polarimetric mode in C-band. Table 1 gives more information about he acquisition and Fig. 1 shows the RGB image of the test site.

Table 1: Polarimetric data characteristics

Frequency	C-Band (5,3 GHz)
Polarization	HH, HV, VH, VV (Single Look Complex)
Resolution	11x9 m (azimuth) * (distance)
Swath width	25 km
Mode	Fine Quad-Pol
Date of acquisition	April 11th 2009
Time of acquisition	10 :54 pm GMT
Orbit	Ascending, Ref : DT14
Incidence angle	38,34-39,81°

3. Full polarimetry theory

The fundamental quantities measured by a polarimetric SAR are the scattering matrix elements S_{tr}, where t and r are the transmit and receive polarizations, respectively. The scattering matrix representation as defined in the linear (H, V) basis is [8]:

$$S = \begin{bmatrix} S_{hh} & S_{hv} \\ S_{hv} & S_{vv} \end{bmatrix} \quad (1)$$

Rewriting this matrix in the equivalent vector in the Lexicographic basis yields:



Figure 1: The RGB image of the polarimetric data of the test site (Red:HH, Green:HV and Blue:VV).

$$\vec{k} = \begin{bmatrix} S_{hh} & \sqrt{2}S_{hv} & S_{vv} \end{bmatrix}^T \quad (2)$$

Where the superscript T indicates, the transpose operator. The scattering vector in the Pauli basis is given as:

$$\overrightarrow{k_p} = \frac{1}{\sqrt{2}}[S_{hh} + S_{vv} \quad S_{hh} - S_{vv} \quad 2S_{hv}]^T \quad (3)$$

For multilook processed 3x3 positive semi-definite hermitian coherency and covariance matrices:

$$\langle [T] \rangle = \langle \overrightarrow{k_p} \overrightarrow{k_p}^{*T} \rangle \quad (4)$$

$$\langle [C] \rangle = \langle \vec{k} \vec{k}^{*T} \rangle \quad (5)$$

Where the superscript $*T$ denotes the conjugate transpose operator. The symbol < > indicates ensemble averaging. The coherency matrix is related to the covariance matrix as [8]:

$$[C] = \frac{1}{2}\begin{bmatrix} 1 & 1 & 0 \\ 0 & 0 & \sqrt{2} \\ 1 & -1 & 0 \end{bmatrix}[T]\begin{bmatrix} 1 & 0 & 1 \\ 1 & 0 & -1 \\ 0 & \sqrt{2} & 0 \end{bmatrix}$$

$$= \begin{bmatrix} |S_{hh}|^2 & \sqrt{2}(S_{hh}S_{hv}^*) & S_{hh}S_{vv}^* \\ \sqrt{2}(S_{hv}S_{hh}^*) & 2|S_{hv}|^2 & \sqrt{2}(S_{hv}S_{vv}^*) \\ S_{vv}S_{hh}^* & \sqrt{2}(S_{vv}S_{hv}^*) & |S_{vv}|^2 \end{bmatrix} \quad (5)$$

In the case of a target characterized by reflection symmetry [9], the following relations hold:

$$\langle S_{hh}S_{hv}^* \rangle = \langle S_{hv}S_{vv}^* \rangle = 0 \quad (6)$$

Equations (5) can then be written as:

$$[C] = \begin{bmatrix} |S_{hh}|^2 & 0 & S_{hh}S_{vv}^* \\ 0 & 2|S_{hv}|^2 & 0 \\ S_{vv}S_{hh}^* & 0 & |S_{vv}|^2 \end{bmatrix} \quad (7)$$

4. Compact polarimetry theory

Compact polarimetry is a technique that allows construction of pseudo quad-pol information from dual-polarization SAR data.

If a single polarization is transmitted, whereas the two canonical orthogonal linear polarizations (H and V) are received, the 2-D measurement vector (or observable) $\vec{k}_{CP}$ is the projection of the full backscattering matrix S on the transmit polarization state. The relation between $\vec{k}_{CP}$ and S is given by [3]:

$$\vec{k}_{CP} = S\,\vec{J}_t \tag{8}$$

Where $\vec{J}_t$, represents the transmitted Jones vector. Table 2 provides examples of Jones vectors for canonical polarization states.

Table 2: Jones vector for canonical polarization states

	Polarization cases			
	H	V	RC	LC
$\vec{J}$	$\begin{pmatrix}1\\0\end{pmatrix}$	$\begin{pmatrix}0\\1\end{pmatrix}$	$\frac{1}{\sqrt{2}}\begin{pmatrix}1\\-i\end{pmatrix}$	$\frac{1}{\sqrt{2}}\begin{pmatrix}1\\i\end{pmatrix}$
(ψ,χ)	$(0°,0°)$	$(90°,0°)$	$(und,45°)$	$(und,-45°)$

In this table (ψ,χ) stands for orientation and ellipticity angles, RC and LC for Right and Left circular respectively. *Und* means undefined

The scattering vectors $\vec{k}_{CP}$ for the $\pi/4$, dual circular polarimetric (DCP), and right circular transmit, linear (horizontal and vertical) receive or hybrid (CTLR) modes are given in Table 3 [5].

Table 3: Compact polarimetry modes

Mode	Trans/Recep	$\vec{k}_{CP}$
$\pi/4$	45°/(H,V)	$[S_{hh}+S_{hv} \quad S_{vv}+S_{hv}]^T/\sqrt{2}$
DCP	RC/(RC,LC)	$[S_{RR} \quad S_{RL}]^T = [S_{hh}-S_{vv}+i2S_{hv} \quad i(S_{hh}+S_{vv})]^T/2$
CTLR	RC/(H,V)	$[S_{hh}-iS_{hv} \quad -iS_{vv}+S_{hv}]^T/\sqrt{2}$

In this table, 45° stands for linear polarization with a 45°inclination.

Fig. 2 shows the different configurations of the CP modes.

The two vectors $\vec{k}_{DCP}$ and $\vec{k}_{CTLR}$ are related by the following equation [10].

$$\vec{k}_{DCP} = \frac{1}{\sqrt{2}}\begin{bmatrix}1 & -i\\ 1 & i\end{bmatrix}\vec{k}_{CTLR} \tag{9}$$

The two vectors have equivalent polarimetric information. This case is important because it means that the analysis of the data from these two modes should generally lead to the same results.

The measured compact polarimetric vector $\vec{k}_{cp}$ and its corresponding covariance matrix C_{cp} are given by:

$$\vec{k}_{cp} = [CP_1 \quad CP_2]^T \tag{10}$$

$$[C_{cp}] = \langle \vec{k}_{cp}\vec{k}_{cp}^{*T}\rangle = \begin{bmatrix}C_{11} & C_{12}\\ C_{21} & C_{22}\end{bmatrix} \tag{11}$$

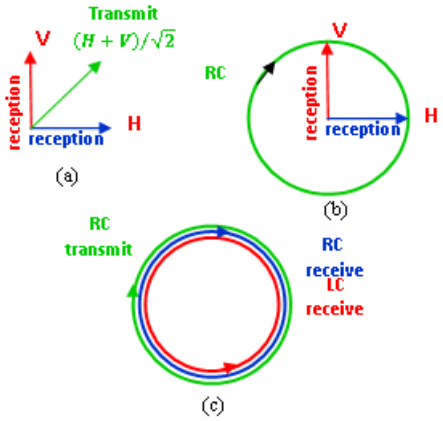


Figure 2: The three configurations of the compact polarimetry (a) $\pi/4$, (b) CTLR and (c) DCP.

Where $C_{11} = \langle |CP_1|^2\rangle$, $C_{12} = C_{12}{}^* = \langle CP_1 * CP_2{}^*\rangle$ and $C_{22} = \langle |CP_2|^2\rangle$. C_{cp} , is Hermitian and provides four measurements, two real diagonal terms and the real and imaginary parts of one of the off-diagonal terms.

The relevant 2x2 Hermitian covariance matrices become:

$$\left[C_{\frac{\pi}{4}}\right] = \langle \vec{k}_{\frac{\pi}{4}}\vec{k}_{\frac{\pi}{4}}^{*T}\rangle = \frac{1}{2}\begin{bmatrix}\langle |S_{hh}|^2\rangle & \langle S_{hh}S_{vv}^*\rangle\\ \langle S_{vv}S_{hh}^*\rangle & \langle |S_{vv}|^2\rangle\end{bmatrix} + \frac{1}{2}\langle |S_{hv}|^2\rangle\begin{bmatrix}1 & 1\\ 1 & 1\end{bmatrix} + \frac{1}{2}\begin{bmatrix}2\Re(\langle S_{hh}S_{hv}^*\rangle) & \langle S_{hh}S_{hv}^*\rangle + \langle S_{hv}S_{vv}^*\rangle\\ \langle S_{hh}^*S_{hv}\rangle + \langle S_{vv}S_{hv}^*\rangle & 2\Re(\langle S_{vv}S_{hv}^*\rangle)\end{bmatrix} \tag{12}$$

$$[C_{DCP}] = \langle \vec{k}_{DCP}\vec{k}_{DCP}{}^{*T}\rangle = \frac{1}{4}\begin{bmatrix}\langle |S_{hh}-S_{vv}|^2\rangle & \langle -i(S_{hh}-S_{vv})(S_{hh}+S_{vv})^*\rangle\\ \langle -i(S_{hh}+S_{vv})(S_{hh}-S_{vv})^*\rangle & \langle |S_{hh}+S_{vv}|^2\rangle\end{bmatrix} + \frac{1}{4}\begin{bmatrix}4\langle |S_{hv}|^2\rangle & 0\\ 0 & 0\end{bmatrix} + \frac{1}{4}\begin{bmatrix}4\langle \Im((S_{hh}-S_{vv}).S_{hv}^*)\rangle & 2\langle (S_{hh}+S_{vv})^*\rangle\\ 2\langle (S_{hh}+S_{vv}).S_{hv}^*\rangle & 0\end{bmatrix} \tag{13}$$

$$[C_{CTLR}] = \langle \vec{k}_{CTLR}\vec{k}_{CTLR}{}^{*T}\rangle = \frac{1}{2}\begin{bmatrix}\langle |S_{hh}|^2\rangle & \langle i(S_{hh}S_{vv}^*)\rangle\\ \langle -i(S_{vv}S_{hh}^*)\rangle & \langle |S_{vv}|^2\rangle\end{bmatrix} + \frac{1}{2}\langle |S_{hv}|^2\rangle\begin{bmatrix}1 & -i\\ i & 1\end{bmatrix} + \frac{1}{2}\begin{bmatrix}-2\Im(\langle S_{hh}S_{hv}^*\rangle) & \langle S_{hh}S_{hv}^*\rangle + \langle S_{hv}S_{vv}^*\rangle\\ \langle S_{hh}^*S_{hv}\rangle + \langle S_{vv}S_{hv}^*\rangle & 2\Im(\langle S_{vv}S_{hv}^*\rangle)\end{bmatrix} \tag{14}$$

The resulting compact polarimetry covariance matrices are expressed as a sum of three terms. The first term contains elements that depend only on S_{hh} and S_{vv}, the second term contains $\langle |S_{hv}|^2\rangle$ elements, and the last term consists only of co-polarization (co-pol) and cross-pol correlations.

We come up with an undetermined system of four equations (linked to the two real measurements C_{11}, C_{22} and the complex one C_{12}) and six variables:

$$\text{H}=\langle|S_{hh}|^2\rangle,\quad V=\langle|S_{vv}|^2\rangle,\quad \text{X}=\langle|S_{hv}|^2\rangle,$$
$$\text{P}=\langle S_{hh}S_{vv}^*\rangle,\quad \langle S_{hh}S_{hv}^*\rangle \text{ and } \langle S_{vv}S_{hv}^*\rangle).$$

Additional information is, therefore required to solve it. For this reason, two hypotheses related to the polarimetric behavior of the compact covariance matrix components have been introduced [6].

- The first one suppose reflection symmetry as stated in equation (6).
- The second assumption relates the co-pol correlation coefficient to the relative magnitudes of the cross-pol and co-pol responses.

$$\frac{X}{H+V}\approx\frac{1-|\rho_{h-v}|}{4} \tag{15}$$

Where $\rho_{h-v}=\frac{\langle S_{hh}S_{vv}^*\rangle}{\sqrt{\langle|S_{hh}|^2\rangle.\langle|S_{vv}|^2\rangle}}$ is the linear correlation between S_{hh} and S_{vv}.

The assumption of reflection symmetry implies that the last term is null and the covariance matrices become:

$$\left[C_{\frac{\pi}{4}}\right]=\langle\vec{k}_{\frac{\pi}{4}}\vec{k}_{\frac{\pi}{4}}^{*T}\rangle=\frac{1}{2}\begin{bmatrix}\langle|S_{hh}|^2\rangle & \langle S_{hh}S_{vv}^*\rangle\\ \langle S_{vv}S_{hh}^*\rangle & \langle|S_{vv}|^2\rangle\end{bmatrix}+\frac{1}{2}\langle|S_{hv}|^2\rangle\begin{bmatrix}1 & 1\\ 1 & 1\end{bmatrix} \tag{16}$$

$$[C_{DCP}]=\langle\vec{k}_{DCP}\vec{k}_{DCP}^{*T}\rangle=\frac{1}{4}\begin{bmatrix}\langle|S_{hh}-S_{vv}|^2\rangle & \langle-i(S_{hh}-S_{vv})(S_{hh}+S_{vv})^*\rangle\\ \langle-i(S_{hh}+S_{vv})(S_{hh}-S_{vv})^*\rangle & \langle|S_{hh}+S_{vv}|^2\rangle\end{bmatrix}+\frac{1}{4}\begin{bmatrix}4\langle|S_{hv}|^2\rangle & 0\\ 0 & 0\end{bmatrix} \tag{17}$$

$$[C_{CTLR}]=\langle\vec{k}_{CTLR}\vec{k}_{CTLR}^{*T}\rangle=\frac{1}{2}\begin{bmatrix}\langle|S_{hh}|^2\rangle & \langle i(S_{hh}S_{vv}^*)\rangle\\ \langle-i(S_{vv}S_{hh}^*)\rangle & \langle|S_{vv}|^2\rangle\end{bmatrix}+\frac{1}{2}\langle|S_{hv}|^2\rangle\begin{bmatrix}1 & -i\\ i & 1\end{bmatrix} \tag{18}$$

Here, each mode reduces to a system of four equations from the covariance matrix and five unknowns. For the $\pi/4$ and CTLR modes, the unknowns are $|S_{hh}|^2$, $|S_{vv}|^2$, $|S_{hv}|^2$, $(S_{hh}S_{vv}^*)$and $(S_{vv}S_{hh}^*)$, where the last unknown is complex. As stated in equation (17), the DCP mode depends on the Pauli basis coefficients $(S_{hh}-S_{vv})$, $(S_{hh}+S_{vv})$, and S_{hv}.

The assumption of reflection symmetry implies that the last term is null and the covariance matrices become:

$$\left[C_{\frac{\pi}{4}}\right]=\langle\vec{k}_{\frac{\pi}{4}}\vec{k}_{\frac{\pi}{4}}^{*T}\rangle=\frac{1}{2}\begin{bmatrix}\langle|S_{hh}|^2\rangle & \langle S_{hh}S_{vv}^*\rangle\\ \langle S_{vv}S_{hh}^*\rangle & \langle|S_{vv}|^2\rangle\end{bmatrix}+\frac{1}{2}\langle|S_{hv}|^2\rangle\begin{bmatrix}1 & 1\\ 1 & 1\end{bmatrix} \tag{19}$$

$$[C_{DCP}]=\langle\vec{k}_{DCP}\vec{k}_{DCP}^{*T}\rangle=\frac{1}{4}\begin{bmatrix}\langle|S_{hh}-S_{vv}|^2\rangle & \langle-i(S_{hh}-S_{vv})(S_{hh}+S_{vv})^*\rangle\\ \langle-i(S_{hh}+S_{vv})(S_{hh}-S_{vv})^*\rangle & \langle|S_{hh}+S_{vv}|^2\rangle\end{bmatrix}+\frac{1}{4}\begin{bmatrix}4\langle|S_{hv}|^2\rangle & 0\\ 0 & 0\end{bmatrix} \tag{20}$$

$$[C_{CTLR}]=\langle\vec{k}_{CTLR}\vec{k}_{CTLR}^{*T}\rangle=\frac{1}{2}\begin{bmatrix}\langle|S_{hh}|^2\rangle & \langle i(S_{hh}S_{vv}^*)\rangle\\ \langle-i(S_{vv}S_{hh}^*)\rangle & \langle|S_{vv}|^2\rangle\end{bmatrix}+\frac{1}{2}\langle|S_{hv}|^2\rangle\begin{bmatrix}1 & -i\\ i & 1\end{bmatrix} \tag{21}$$

5. Pseudo quad-pol reconstruction algorithm

The construction of the pseudo quad-pol covariance matrices from the compact polarimetry modes is based on a pair of equations that are iteratively solved for $\langle|S_{hv}|^2\rangle$ [6].

5.1. $\pi/4$ mode solution

For the $\pi/4$ mode, the solution of equations starts with the initial values of $\langle|S_{hv}|^2\rangle$ and the linear co-polarization coherence $\rho=\rho_{h-v}$.

$$\rho_{(0)}=\frac{C_{12}}{\sqrt{C_{11}C_{22}}} \tag{22}$$

$$\langle|S_{hv}|^2\rangle_{(0)}=\frac{C_{11}+C_{22}}{2}\left(\frac{1-|\rho_{(0)}|}{3-|\rho_{(0)}|}\right) \tag{23}$$

and then iterates the following equations:

$$\rho_{(i+1)}=\frac{C_{12}-\langle|S_{hv}|^2\rangle_{(i)}}{\sqrt{(C_{11}-\langle|S_{hv}|^2\rangle_{(i)})(C_{22}-\langle|S_{hv}|^2\rangle_{(i)})}} \tag{24}$$

$$\langle|S_{hv}|^2\rangle_{(i+1)}=\frac{C_{11}+C_{22}}{2}\left(\frac{1-|\rho_{(i+1)}|}{3-|\rho_{(i+1)}|}\right) \tag{25}$$

Given a value for $\langle|S_{hv}|^2\rangle=\langle|S_{hv}|^2\rangle_{(n)}$ (where n is the order of iteration), the pseudo quad-pol covariance matrix is then constructed by:

$$[C]_{pseudo\ quad}=\begin{bmatrix}C_{11}-\langle|S_{hv}|^2\rangle & 0 & C_{12}-\langle|S_{hv}|^2\rangle\\ 0 & 2\langle|S_{hv}|^2\rangle & 0\\ (C_{12}-\langle|S_{hv}|^2\rangle)^* & 0 & C_{22}-\langle|S_{hv}|^2\rangle\end{bmatrix} \tag{26}$$

The null components are the characteristic of the reflection symmetry assumption.

5.2. DCP mode solution

The iterative equations and pseudo quad-pol covariance matrix for the DCP mode are [5]:

$$\rho_{(i+1)}=\frac{C_{12}+\langle|S_{hv}|^2\rangle_{(i)}}{\sqrt{(C_{11}-\langle|S_{hv}|^2\rangle_{(i)})(C_{22}-\langle|S_{hv}|^2\rangle_{(i)})}} \tag{27}$$

$$\langle|S_{hv}|^2\rangle_{(i+1)}=\frac{C_{11}+C_{22}}{2}\left(\frac{1-|\rho_{(i+1)}|}{3-|\rho_{(i+1)}|}\right) \tag{28}$$

$$[C]_{pseudo\ quad}=\begin{bmatrix}C_{11}-\langle|S_{hv}|^2\rangle & 0 & C_{12}+\langle|S_{hv}|^2\rangle\\ 0 & 2\langle|S_{hv}|^2\rangle & 0\\ (C_{12}+\langle|S_{hv}|^2\rangle)^* & 0 & C_{22}-\langle|S_{hv}|^2\rangle\end{bmatrix} \tag{29}$$

$\langle|S_{hv}|^2\rangle = \langle|S_{hv}|^2\rangle_{(n)}$.

5.3. CTLR mode solution

The construction of the pseudo quad-pol covariance matrices CTLR mode is similar to the previous mode. The iterative equations and pseudo quad-pol covariance matrix for the CTLR mode are [5]:

$$\rho_{(i+1)} = \frac{iC_{12}+\langle|S_{hv}|^2\rangle_{(i)}}{\sqrt{(C_{11}-\langle|S_{hv}|^2\rangle_{(i)})(C_{22}-\langle|S_{hv}|^2\rangle_{(i)})}} \quad (30)$$

$$\langle|S_{hv}|^2\rangle_{(i+1)} = \frac{C_{11}+C_{22}}{2}\left(\frac{1-|\rho_{(i+1)}|}{3-|\rho_{(i+1)}|}\right) \quad (31)$$

$$[C]_{pseudo\ quad} = \begin{bmatrix} C_{11}-\langle|S_{hv}|^2\rangle & 0 & iC_{12}+\langle|S_{hv}|^2\rangle \\ 0 & 2\langle|S_{hv}|^2\rangle & 0 \\ (iC_{12}+\langle|S_{hv}|^2\rangle)^* & 0 & C_{22}-\langle|S_{hv}|^2\rangle \end{bmatrix} \quad (32)$$

$\langle|S_{hv}|^2\rangle = \langle|S_{hv}|^2\rangle_{(n)}$.

For all the three modes, it occurs that $\rho_{(n)}$ may become larger than one for certain pixels, or even that its denominator becomes the square root of a negative number. In both cases, we regularize by setting $\rho_{(n)} = 1$ and $\langle|S_{hv}|^2\rangle_{(n)} = 0$ and then halt the iteration.

Using CTLR mode would involve the same properties as those established hereafter with transmitted linear polarization [6]. The two vectors of CTLR and DCP modes have also equivalent polarimetric information, so they should generally lead to the same results. Therefore, we will limit our discussion in this paper to the π/4 mode.

5.4. Modification of the compact polarimetry reconstruction algorithm

The second assumption proposed by souyris et *al*. may not always hold [5]. Hence, an alternate method has been set out for approximating the value of X in order to derive better pseudo quad-pol representations. The construction algorithms employ for iteratively updating X:

$$\langle|S_{hv}|^2\rangle_{(i+1)} = (C_{11}+C_{22})\left(\frac{1-|\rho_{(i+1)}|}{N+2(1-|\rho_{(i+1)}|)}\right) \quad (33)$$

Where $N = (|S_{hh}-S_{vv}|^2)/|S_{hv}|^2$

The value of N is estimated from the resulting original reconstruction algorithm.

To show the performance of the reconstructed algorithm, a full quad-pol data set was used to generate the CP mode, and then the corresponding pseudo quad-pol data sets were constructed via (21)-(33) equations. The datasets used to illustrate the CP mode are the RADARSAT2 C-band fully polarimetric images of the west region of the Algiers city and an agriculture field region situated in the south of the same town. It contains symmetric and non-symmetric scattering SAR targets.

6. Linear co-polarization coherence $|\rho_{h-v}|$ mapping

6.1. Linear co-polarization coherence $|\rho_{h-v}|$ mapping

Fig. 3 displays the mapping of the degree of coherence $|\rho = \rho_{h-v}|$ for consecutive orders of estimation. The test is conducted on the same zone which is the west region of Algiers, with a 5X5 analysis window. Fig. 3.a displays the FP reference value. The first order estimate shown in Fig. 3.b produces a "milky" impression, which alters the image contrast. However, the third estimated coherence shown in Fig. 3.c is qualitatively very close to the FP coherence.
Fig. 3d displays the last estimate of the reconstructed degree coherence versus the actual degree of coherence. As expected, this figure shows very good reconstruction performances.

6.2. Quantitative assessment

For comparison, the original FP data are shown in Fig. 4a with H in red, X in green, and V in blue. The π/4 mode synthesized result is shown in Fig. 4b. We notice some differences between these two images, especially in the X intensity in some urban areas, which is noticeably lower for the CP mode. However, strong similarity does exist in polarimetric response of most of the rest of the test area.

Fig. 5 shows scatter plots detailing how well the derived pseudo-quad-pol results fit the original quad-pol. It shows also the performance of the reconstruction algorithm. Most of the points of the scatter plot fall close the one-to-one line with small spread. A small systematic overestimation of the $|S_{hv}|^2$ can be observed over this data. For every channel, an overall agreement is observed between the reconstructed and actual radiometric values.

6.3. Compact polarimetric signatures

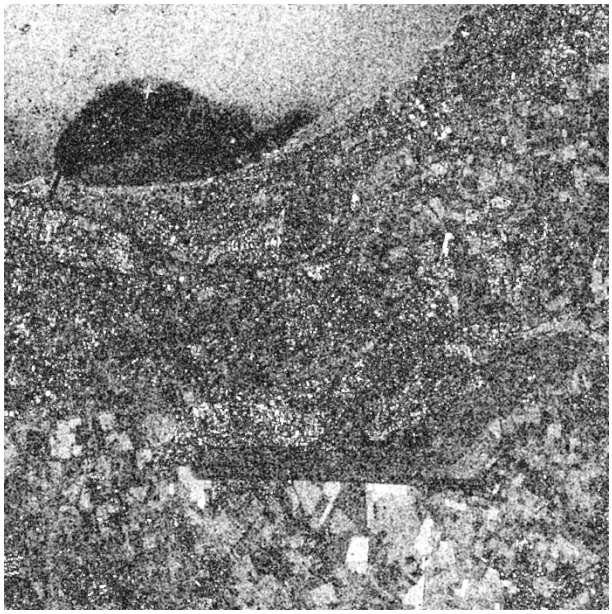
The concept of the polarization signature of a scatterer was used by Van zyl *et al*. [11] to graph the power of a return wave as a function of transmit and receive polarizations. The backscattering radar cross section is given by:

$$\sigma(\psi,\chi) = \frac{4\pi}{k^2}\overrightarrow{S_r}[K]\overrightarrow{S_t} \quad (34)$$

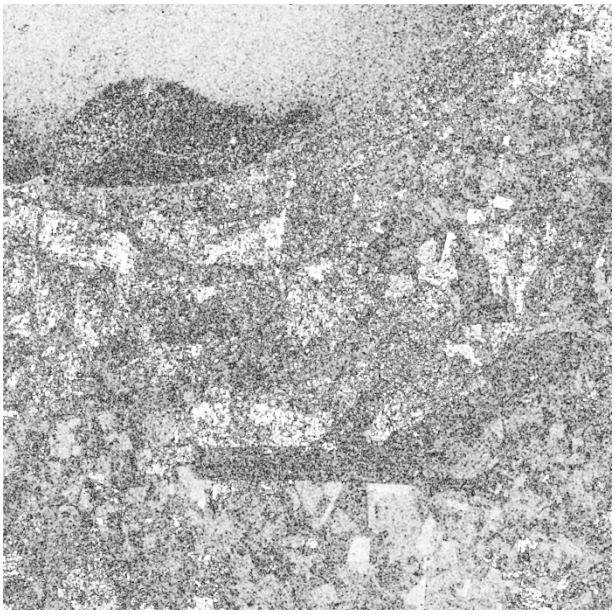
Recall that *t* and *r* denote the received and the transmitted polarizations. *k* is the transmitted wavenumber, ψ and χ are the orientation and the ellipticity angles. The first angle (ψ) ranges between 0° to 180° and the second one (χ) is defined between -45° to 45°.
$\overrightarrow{S_i}$ is the normalized Stokes vector defined as:

$$\overrightarrow{S_i} = \begin{bmatrix} 1 \\ \cos(2\psi_i)\sin(2\chi_i) \\ \sin(2\psi_i)\cos(2\chi_i) \\ \sin(2\chi_i) \end{bmatrix} \quad (35)$$

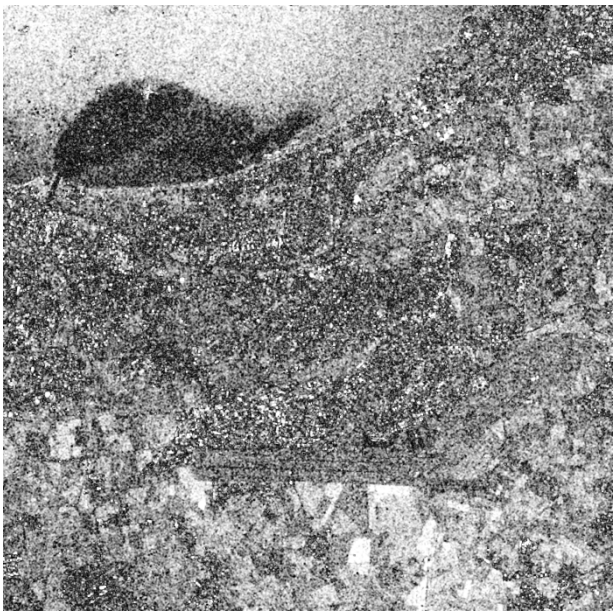
The subscript *i* denotes *r* or *t*.
The elements of the Kennaugh matrix [*K*] can be calculated



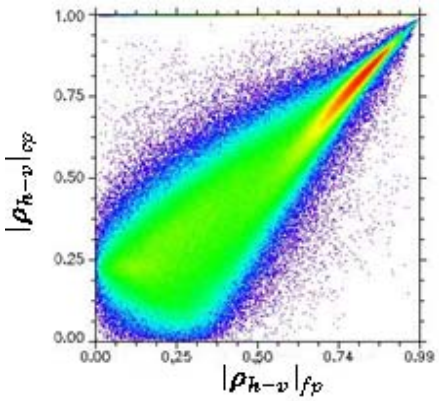
(a)



(b)



(c)



(d)

Figure 3: Degree of coherence $|\rho = \rho_{h-v}|$, (a) reference value of $|\rho_{h-v}|$ inferred from FP. (0=black, 1=white), (b)-(c) first- and second-order estimates of $|\rho_{h-v}|$, (c) reconstructed degree of coherence (3rd order estimates) versus actual degree of coherence (reference value)

from the coherency matrix $[T]$ as follows [2]

$$k_{ij} = \frac{1}{2} tr([T]\eta_{ij}) \qquad (36)$$

With $\eta_{ij} = (-1)^{-\delta_{ij}}[A]\sigma_i \otimes \sigma_j [A]^{*T}$

Where $[A] = \frac{1}{\sqrt{2}}\begin{bmatrix} 1 & 0 & 0 & 1 \\ 1 & 0 & 0 & -1 \\ 0 & 1 & 1 & 0 \\ 0 & i & -i & 0 \end{bmatrix}$ and $\delta_{ij} = \begin{cases} 0 & i \neq j \\ 1 & i = j \end{cases}$

$\sigma_{i,j} = (i, j = 0,1,2,3)$ are the four Pauli matrices given by

$\sigma_0 = \begin{bmatrix} 1 & 0 \\ 0 & 1 \end{bmatrix}$, $\sigma_1 = \begin{bmatrix} 1 & 0 \\ 0 & -1 \end{bmatrix}$, $\sigma_2 = \begin{bmatrix} 0 & 1 \\ 1 & 0 \end{bmatrix}$, and $\sigma_3 = \begin{bmatrix} 0 & -i \\ i & 0 \end{bmatrix}$

The symbol $\otimes$ denotes the standard tensorial Kronecker matrix product.

One collects coherent CP SAR imagery by transmitting a given polarized signal and then coherently receiving any pair of orthogonal polarizations. While the transmitted polarization is fixed, from the coherently received signals one may synthesize the response of any receive polarization.



(a) (b)

Figure 4: Full (a) RGB versus compact polarimetric (b) RGB color composit images, (Red:H, Green:X, Blue:V)

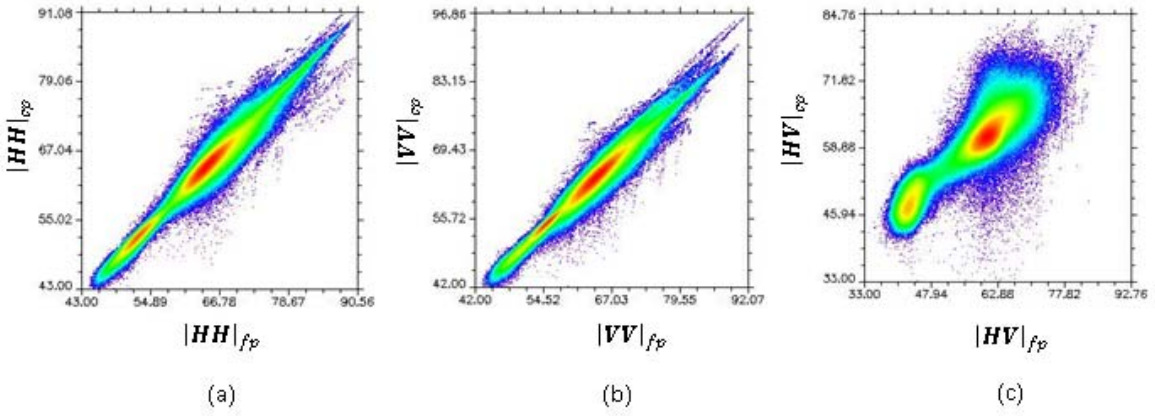


Figure 5 : Reconstruction performance for H, V and X channels. Scatter plots of (a)H_{fp}-H_{CP}, (b) V_{fp}-V_{cp} and (c) X_{fp}-X_{cp}

Therefore, the received power, as a function of the ellipticity and orientation angles of the received polarization, completely characterizes the CP response.

The two-dimensional surface plot of the received power as a function of polarization ellipticity and orientation provides a simple, graphical way to display this result.

Plots of the CP response from a variety of scattering mechanisms, e.g. rough surface, dihedral, dipole, allow for an easy visual analysis of the CP information. The results for the selected subregions shown in Fig. 6 that consist primarily of sea, grass field and urban structure are given in Fig. 7 and Fig. 8 where the quad- and CP. signatures of surface scattering and dihedral scattering representing three subregions were plotted and compared against each other.

Of note in these figures is that employing the CP- and quad-pol signatures yield essentially the same results.

As shown in these figures, the urban targets have the double-bounce reflection properties and the sea and the grass fields have the surface scattering characteristics.

6.4. Three component decomposition

Freeman and Durden [12] introduced an unsupervised classification based on a three-component scattering model under the well-known reflection symmetry condition using

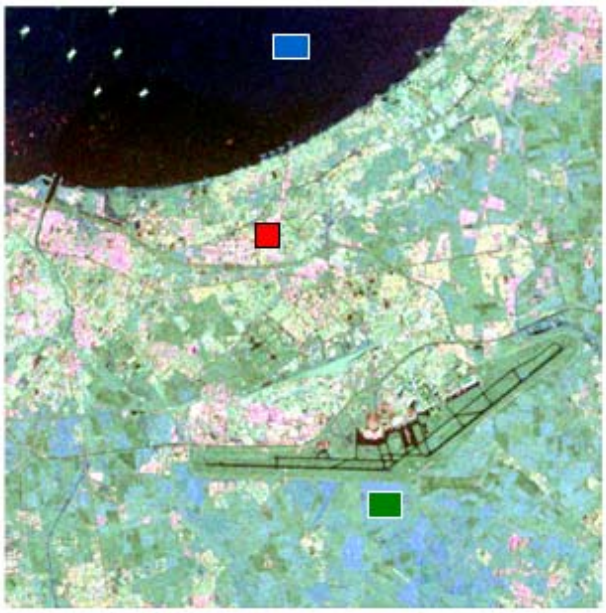


Figure 6: The selected regions of interests to generate the polarimetric signatures in full and compact modes. The three outlined areas the urban (double-bounce scattering), grass (surface scattering), and sea (Bragg surface) regions over which the polarimetric signatures are examined.

the covariance matrix. The components of the scattering matrix are analyzed to assign each pixel to one of three scattering categories of the model: surface, double-bounce scattering, and volume scattering. The mechanisms are a

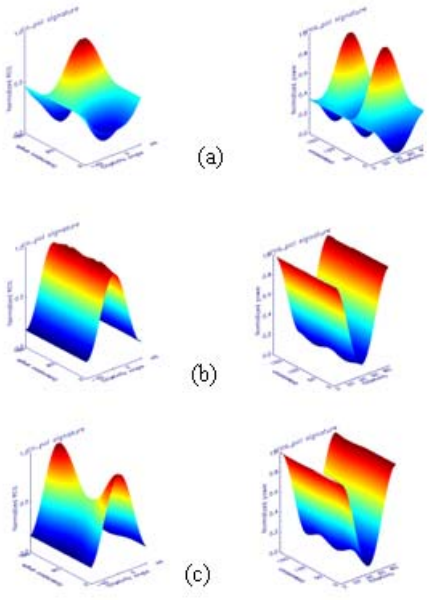


Figure 7: Co- and cross-polarimetric signatures using full polarimetric mode (a) urban region, (b) Agriculture field region, and (c) sea region.

canopy scatter from a cloud of randomly oriented dipoles, even- or double-bounce scatter from a pair of orthogonal surfaces with different dielectric constants, and Bragg scatter from a moderately rough surface.

The Freeman-Durden model for the scattering and covariance matrices are:

- For the scattering processes for slightly rough surfaces

$$[S] = \begin{bmatrix} \beta & 0 \\ 0 & 1 \end{bmatrix} \Rightarrow \langle [C] \rangle_s = \begin{bmatrix} |\beta|^2 & 0 & \beta \\ 0 & 0 & 0 \\ \beta^* & 0 & 1 \end{bmatrix} \quad (37)$$

The obtained covariance matrix terms are : $\langle |S_{hh}|^2 \rangle = |\beta|^2$, $\langle |S_{vv}|^2 \rangle = 1$, $\langle S_{hh} S_{vv}^* \rangle = \beta$, $\langle |S_{hv}|^2 \rangle = 0$ and $\langle S_{hh} S_{hv}^* \rangle = \langle S_{hv} S_{vv}^* \rangle = 0$.

Where β is a parameter related to the relative dielectric constant of the surface and the local orientation angle.

- For the double-bounce scattering

The scattering matrix and the corresponding covariance matrix are:

$$[S] = \begin{bmatrix} \alpha & 0 \\ 0 & 1 \end{bmatrix} \Rightarrow \langle [C] \rangle_d = \begin{bmatrix} |\alpha|^2 & 0 & \alpha \\ 0 & 0 & 0 \\ \alpha^* & 0 & 1 \end{bmatrix} \quad (38)$$

Where α is related to tree trunk and ground reflection coefficients for horizontal and vertical polarizations.

- For a cloud of identical particles with random orientations and very thin horizontal cylinders like needle scatterers, the volume scattering averaged covariance matrix is given by

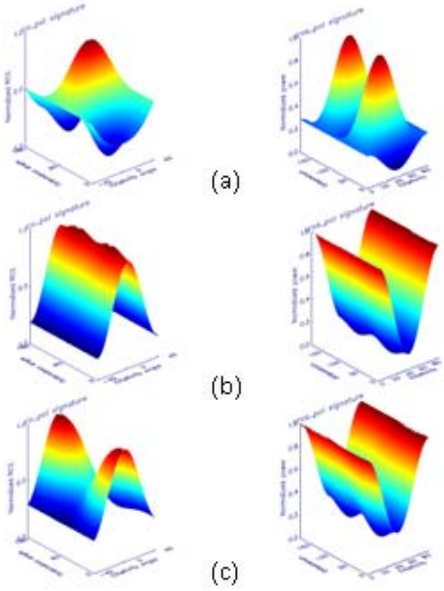


Figure 8: Co- and cross-polarimetric signatures using compact polarimetric mode (a) urban region, (b) Agriculture field region, and (c) sea region.

$$\langle [C] \rangle_v = \begin{bmatrix} 1 & 0 & 1/3 \\ 0 & 2/3 & 0 \\ 1/3 & 0 & 1 \end{bmatrix} \quad (39)$$

Finally, the covariance matrix of these models of the decomposition has the following form:

$$\langle [C] \rangle = f_s \langle [C] \rangle_s + f_d \langle [C] \rangle_d + f_v \langle [C] \rangle_v \quad (40)$$

Where f_s, f_d, and f_v, are the coefficients of the surface, double-bounce and volume scattering respectively.
The model for the total backscatter is

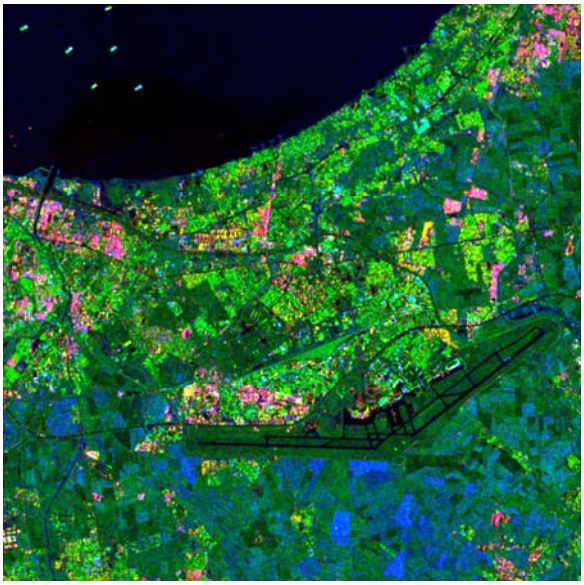
$$\langle [C] \rangle = \begin{bmatrix} C_{11} & 0 & C_{13} \\ 0 & 0 & 0 \\ C_{13}^* & 0 & C_{33} \end{bmatrix} \quad (41)$$

Where $C_{11} = f_s|\beta|^2 + f_d|\alpha|^2 + \frac{3}{8}f_v$,
$C_{12} = f_s\beta + f_d\alpha + \frac{1}{8}f_v$, $C_{33} = f_s + f_d + \frac{3}{8}f_v$
Finally, we estimate the contribution of each scattering mechanism to the span

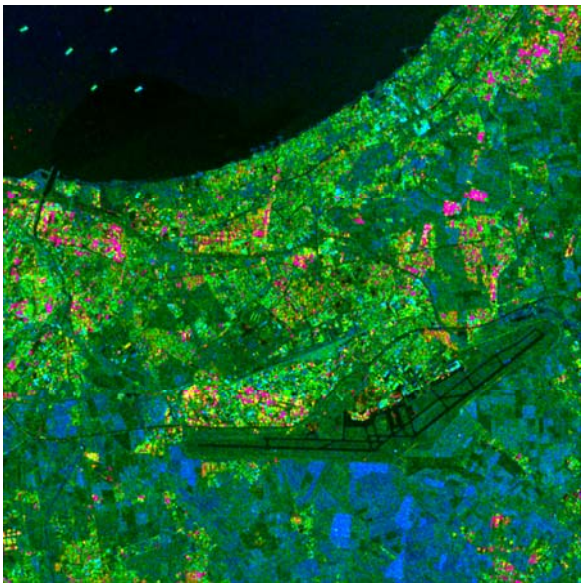
$$span = |S_{hh}|^2 + 2|S_{hv}|^2 + |S_{vv}|^2$$
$$= P_s + P_d + P_v \quad (42)$$

With $P_s = f_s(1 + |\beta|^2)$, $P_d = f_d(1 + |\alpha|^2)$ and $P_v = f_v$

Fig. 9a and 9b shows the result of applying the Freeman-Durden decomposition to the polarimetric data. In each figure, the contributions of each of the three scattering mechanisms to the total power are shown for each pixel, with surface scatter colored blue, volume scatter green, and double-bounce red. The relative strength of each color in the resulting RGB images can be related to the relative strengths of the scattering mechanisms.
The blue areas are dominated by single-bounce surface, or grass, backscatter whereas the red areas are dominated by double-bounce backscatter from man-made structures. The green areas are volume backscatter from forest canopy. The black linear patterns are the airport runways with low backscatter from their smooth surfaces.
Double bounce scattering events can, however, originate from many natural situations. Among these situations are forest ground-trunk scattering interactions and scattering from abrupt, steep cliff. Man-made structures not aligned in the azimuth direction introduce higher cross-pol returns. This explains the observed strong volume scattering areas in green color which is defined by the strength of $|S_{hv}|^2$.
The agreement between the CP data and the FP data can be tested using a scatter plot which represents the comparison between them as shown in Fig. 10 The three CP- and FP-components are seen to be highly correlated**.**



(a)



(b)

Figure 9: Freeman-Durden image, the red channel is f_d, the green channel is f_v, and the blue channel is f_s (a) RGB-full polarimetric image. (b) RGB-compact polarimetric image

7. Conclusion

In this study, we have investigated to what extent the CP mode permits to reconstruct the FP information from a single linear transmitted polarization and a reception of two orthogonal polarizations. However, the key property used to estimate the FP information is reflection symmetry, which reveals a complete decorrelation of copolarized and cross-polarized backscattering coefficients.

We have investigated also the CP mode discriminating capability using polarimetric signatures which provide a complete, easy graphic means to analyze the scattering mechanism information in any mode. In particular, we showed that the CP signature plots compare well to their corresponding quad-pol.

The Freeman-Durden decomposition based on the symmetry of the geophysical media is derived for the CP- and FP-mode. The results indicate that the generated

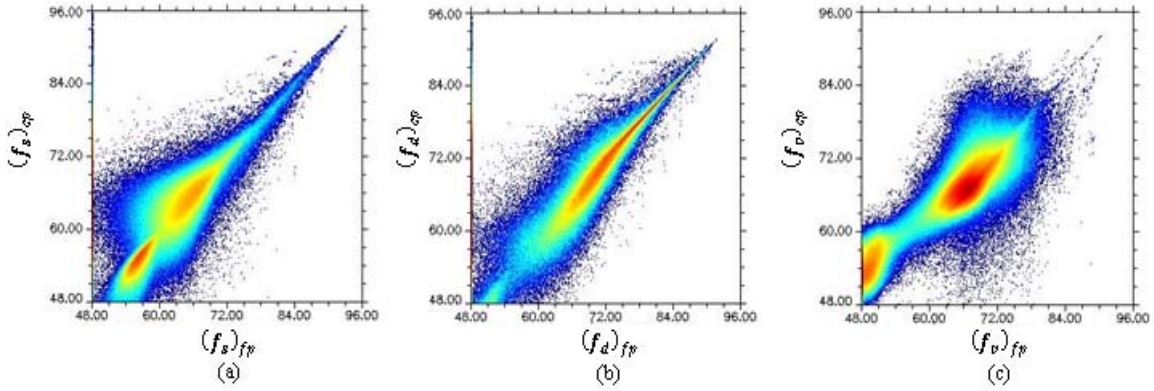


Figure 10: (a)-(c) scatter plots of the reconstruction performance for odd ($(f_s)_{fp}$-$(f_s)_{cp}$), double($(f_d)_{fp}$-$(f_d)_{cp}$) and volume scattering ($(f_v)_{fp}$-$(f_v)_{cp}$)parameters

pseudo quad-pol compares well to the original quad-pol imagery.

As a conclusion, a Compact polarimetry SAR cannot be "as good as" a fully polarimetric system because an FP-SAR measures the 4x4 covariance scattering matrix of the scene, whereas a CP-SAR has access only to the 2x2 covariance matrix of the backscattered field. However, in many applications, the results enjoyed from a CP radar are equivalent to those from an FP radar. Consequently, Compact polarimetry showed promise of being able to reduce the complexity, cost, mass, and data rate of a SAR system while attempting to maintain many capabilities of a fully polarimetric system and it affords more target information than a single-pol system, while not suffering as much from the drawbacks of a quad-pol system.

Acknowledgements

The authors would like to thank the Canadian Space Agency for kindly providing the polarimetric RADARSAT2 data used in this paper in the frame of the SOAR program under the #1670 project.

References

[1] W.-M. Boerner, H. Mott, E. Luneburg, C. Livingstone, B. Brisco, R. J. Brown, and J. S. Paterson, "Polarimetry in radar remote sensing: Basic and applied concepts," in *Principles and Applications of Imaging Radar*, 3rd ed, vol. 2. F. M. Henderson and A. J. Lewis, Eds. Hoboken, NJ: Wiley, 1998.

[2] R. Touzi, W.-M. Boerner, J.-S. Lee, and E. Lueneburg, "A review of polarimetry in the context of synthetic aperture radar: Concepts and information extraction," *Can. J. Remote Sens.*, vol. 30, no. 3, pp. 369–379, 2004.

[3] P. Dubois-Fernandez, J.-C. Souyris, S. Angelliaume, and F. Garestier, "The compact polarimetry alternative for spaceborne SAR at low frequency," *IEEE Trans. Geosci. Remote Sens*, vol. 46, pp. 3208-3222, 2008.

[4] M-L. Truong-Loï, A. Freeman, P. C. Dubois-Fernandez and E. Pottier, "Estimation of Soil Moisture and Faraday Rotation From Bare Surfaces Using Compact Polarimetry, " *IEEE Trans. Geosci. Remote Sens*, vol. 47, no. 11, Nov. 2009

[5] M. Nord, T. L. Ainsworth, J. –S. Lee, and N. Stacy, "Comparison of Compact Polarimetric Synthetic Aperture Radar Modes, " *IEEE Trans. Geosci. Remote Sens.*, vol. 47, no. 1, pp. 147–188, Jan. 2009.

[6] J.-C. Souyris, P. Imbo, R. Fjørtoft, S. Mingot, and J.-S. Lee, "Compact polarimetry based on symmetry properties of geophysical media: The π/4 mode," *IEEE Trans. Geosci. Remote Sens.*, vol. 43, no. 3, pp. 634–646, Mar. 2005.

[7] K. Raney, "Hybrid polarimetric SAR architecture," *IEEE Trans. Geosci.Remote Sens.*, vol. 45, no. 11, pp. 3397–3404, Nov. 2007.

[8] S. R. Cloude and E. Pottier, "A review of target decomposition theorems in radar polarimetry," *IEEE Trans. Geosci. Remote Sens.*, vol. 34, no. 2, pp. 498–518, Mar. 1996.

[9] S. V. Nghiem, S. H. Yueh, R. Kwok, and F. K. Li, "Symmetry properties in polarimetric remote sensing," *Radio Sci.*, vol. 27, no. 5, pp. 693–711, Oct. 1992.

[10] M-L. Truong-Loï**,** "Potentiels d'un système RSO basse fréquence opérant en polarimétrie compacte," Ph.D. dissertation, Univ. Renne1, Renne, France, 2010.

[11] J. J. van Zyl, H. A. Zebker, and C. Elachi, "Imaging radar polarization signatures: Theory and observation," *Radio Sci.*, vol. 22, no. 4, pp. 529–543, 1987.

[12]A. Freeman and S. L. Durden, "A three-component scattering model for polarimetric SAR data," *IEEE Trans. Geosci. Remote Sens.*, vol. 36, no. 3, pp. 963–973, May 1998.

Quad band CPW Antenna for PCS, Bluetooth, WiMAX and WLAN Applications

Masoumeh Darvish[1] and Hamid Reza Hassani[2]

[12]Department of Electrical and Electronic Engineering, Shahed University, Tehran, Iran.
*corresponding author, E-mail: hassani@shahed.ac.ir

Abstract

A small-size and low cost multi-band CPW monopole antenna is presented. The base of the proposed antenna is a cross shaped CPW strip. By adding several narrow strips at the end of the base strip, acting as resonance paths, located symmetrically along the axis of the antenna, multiband behavior is obtained. By changing the length of the resonant strips, the proposed multi-band antenna can easily be tuned to cover the required frequency bands. A designed quad-band antenna on a substrate size of 20 × 32 mm2 covers the frequency bands 1.9, 2.4, 3.5 and 5.2 GHz. This includes the PCS, Bluetooth, WLAN and WiMAX frequency ranges. The proposed antenna has omnidirectional radiation pattern across all relevant bands.

1. Introduction

In recent years, wireless local area networks (WLAN) and worldwide interoperability for microwave access (WiMAX) have evolved at very high rate for modern communication systems. There are other frequency bands, such as PCS and Bluetooth that are also important. Designs of compact antennas that can operate at these frequency bands are highly desirable. Different studies have paid attention to the planar antennas operating at WLAN and WiMAX frequency bands. In comparison to non-printed antennas, printed antennas due to their small size, low profile, lightweight, and low cost are more attractive [1]. Among different structure of printed antennas, printed coplanar waveguide (CPW)-fed antenna is more appropriate for WLAN and WiMAX applications, due to its omnidirectional radiation coverage, little dependence of the characteristic impedance on substrate height, single metallic layer structure, easy integration to monolithic microwave integrated circuits, and comparatively higher bandwidth [2]. Several techniques to obtain multi-band CPW antenna is reported in the literature. In [3], an LI-shaped-monopole antenna consisting of an I-shaped monopole and an L-shaped meandered one is reported. A distinct triple-band resonator-loaded antenna employing a symmetrical CPW feed for Wi-Fi and WiMAX applications is proposed in [4]. In [5] a planar compact inverted L-shaped monopole antenna with an L-shaped parasitic strip for multi-band WiMAX communication is presented. A dual-band design of a CPW-fed monopole antenna consisting of a compact rectangular patch and a couple of twin embedded slots is presented in [6]. By properly selecting the shapes and dimensions of these embedded slots, dual-band impedance bandwidths can be achieved.

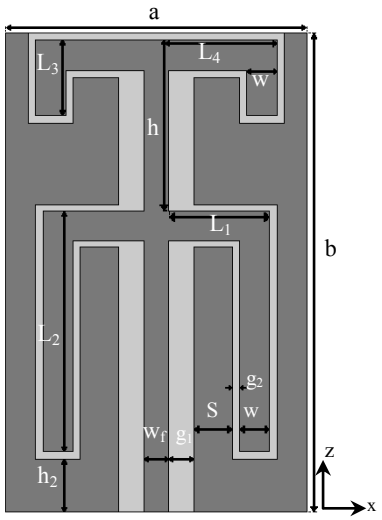
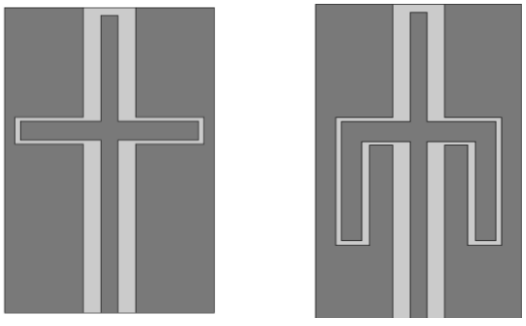


Figure 1: Geometry of the proposed CPW monopole antenna.



(a) (b)

Figure 2: (a) The basic antenna structure, (b) the modified structure

Table 1: Parameters of the antenna (Unit: mm)

parameter	Value	Parameter	Value
w	2	h_2	3.5
w_f	1.6	g_1	1.7
L_1	6.7	g_2	0.5
L_2	16	S	2.25
L_3	5	a	20
L_4	7.2	b	31.8
h	11.3		

Another technique to create multiband antennas is to provide a wideband behavior and then introduce notches to obtain the multiband behavior. In [7] a triple-band monopole antenna that is suited for WiMAX and WLAN operation is reported. Two thin bent slots, half-guided wavelength at the center frequency of the rejected band, are etched on the radiating patch, creating the dual band-notched feature. In this way, the undesired frequencies can be restricted to the notch band without affecting the radiation performance of the antenna.

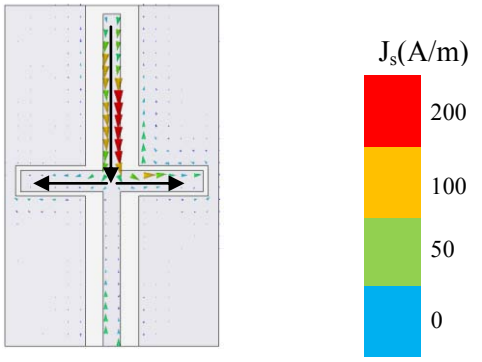
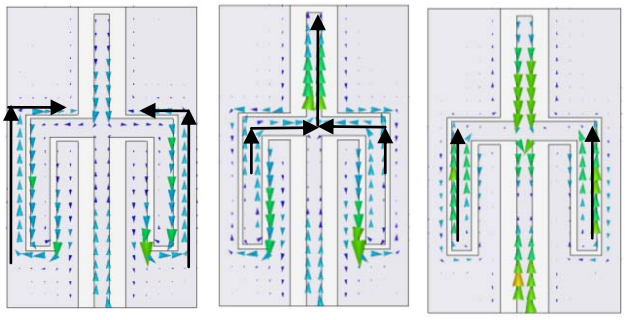


Figure 3: The current distribution on the basic antenna structure at 3.5 GHz.



(a) (b) (c)

Figure 4: The current distribution on the modified structure at (a) 2.4, (b) 3.5 and (c) 5.2 GHz.

In [8] a CPW-fed wideband planar monopole antenna with symmetrical slope ground plane for multiband wireless communication systems is presented. This structure can cover DCS, PCS, 3G, and Bluetooth bands and the antenna has an overall dimension of 40 × 80 mm^2.

According to the literature review of antennas, the proposed multi-band antennas are capable to operate up to quad-band behavior. The various designs reported for multi-band antenna have complicated structures or are large in overall substrate dimension. In this paper, a small size quad-band CPW antenna for PCS, Bluetooth, WLAN and WiMAX systems is introduced which consists of a folded slot and a CPW-fed structure such that only a single-layer substrate is required for the antenna. The base structure of the antenna is a cross shaped strip made up of an open end vertical strip along with a horizontal strip. To increase the number of the resonant bands, extra strips can be added to the base structure. The proposed antenna is simulated through two commercially available software packages of Ansoft HFSS (finite element method) and CST Microwave Studio (finite integration technique). Results are provided and compared.

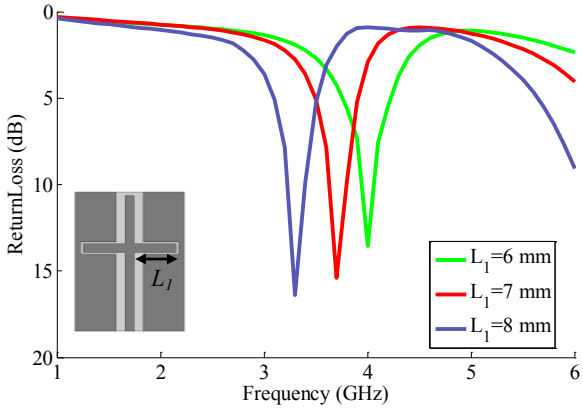


Figure 5: Loss of the basic antenna structure for various L_1.

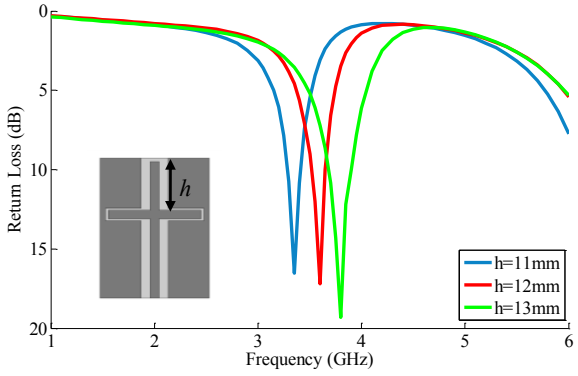


Figure 6: Loss of the basic antenna structure for various h.

2. Antenna design

The geometry of the proposed multiband coplanar waveguide (CPW) monopole antenna with open end is shown in Fig. 1. This antenna has a simple structure with only one layer of low cost FR4 substrate of thickness 1 mm and ϵ_r = 4.4. The antenna is symmetrical with respect to the longitudinal direction.

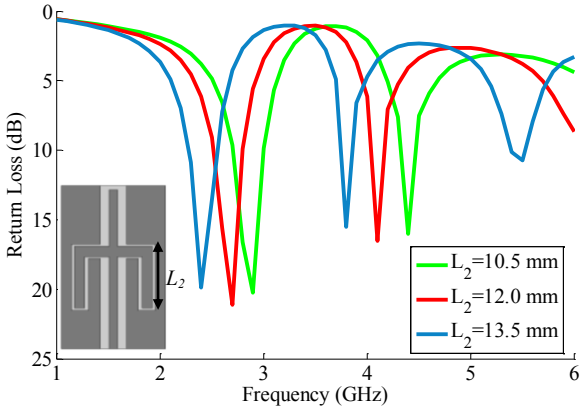


Figure 7: Return Loss of the modified structure for various lengths L_2. L_1=6.7 mm.

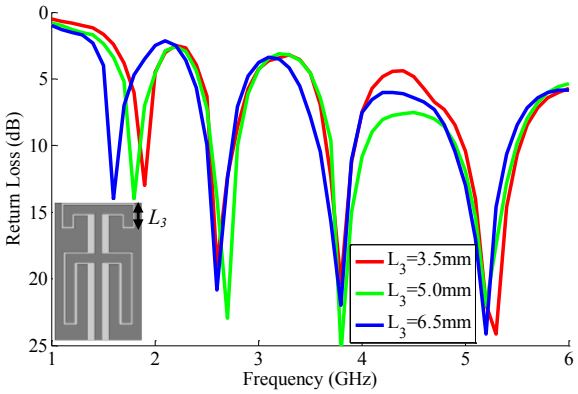


Figure 8: Return Loss of the proposed antenna structure of Fig. 1 for various length L_3. L_1=6.7 mm, L_2=16 mm

The base structure of the proposed antenna is a cross shaped CPW strip. Based on the dimensions chosen, this basic structure can produce a resonance in the WiMAX band at 3.5 GHz. The structure of this basic antenna is shown in Fig.2 (a).

Fig. 3 shows the simulated current distribution of the basic antenna structure at the center resonant frequency of 3.5 GHz. It is obvious that the current is at a minimum at the ends of the horizontal strip as well as at the top end of the vertical strip. This shows that the effective length of the strips at resonance should be half wavelength and the following formula applies

$$L = \frac{\lambda_0}{2\sqrt{\varepsilon_r}} \qquad (1)$$

Where L=L1+h. By inserting two vertical strips at the end of the horizontal arm of the cross, a modified cross is made, as shown in Fig. 2(b). This results in two extra resonant frequencies at 2.4 GHz and 5.2 GHz. Fig. 4 shows the relevant current distribution at the resonant frequencies of each band. Also shown on each picture is the effective current path. Based on the new current path, one can show that in formula (1) the effective length should be modified to L=mL1+nh+qL2 for the structure shown in Fig. 2(b). At various frequency bands the integers (m, n, q) should be set (1, 0, 1) for 2.4 GHz, (1, 0.75, 0.25) for 3.5 GHz and (0, 0, 0.85) for 5.2 GHz.

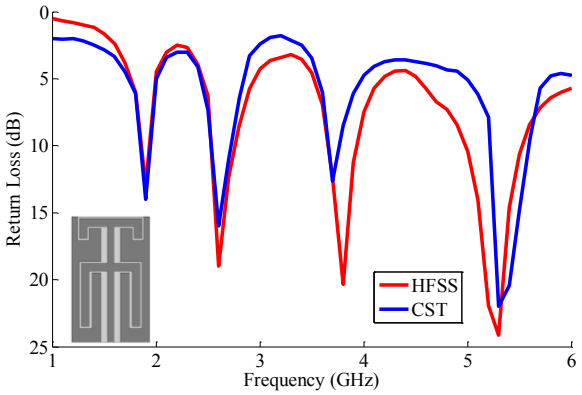


Figure 9: Return Loss of the modified structure for various lengths L_2. L_1=6.7 mm.

It is seen that on the modified structure over all the three frequency bands very similar surface current distributions are obtained. This characteristic agrees with the results of next section that similar radiation patterns are obtained at the three frequency bands.

Finally addition of a T-shaped strip with open ended slot on top of the modified cross shape adds another resonant frequency at 1.9 GHz. The structure of this antenna is that of Fig. 1. By properly choosing the length, L1, L2 and L3 an antenna with quad resonant bands at the desired frequencies can be achieved. The parametric study of these structures and radiation patterns, are studied and the results are presented next. Details of the proposed multiband antenna structure are shown in Fig. 1 and the relevant parameters are given in Table.1.

3. Results and discussion

The base (main) structure of the proposed antenna is a cross shaped CPW antenna that consists of a horizontal and a vertical strip as shown in Fig. 2(a). This structure, by properly choosing the length L_1 can produce a resonance at 3.5 GHz. Fig. 5 shows the return loss of the base antenna for various lengths L_1. From this figure, it can be seen that by increasing the length L_1 of the horizontal arm of the cross shaped antenna, the centre frequency of the resonant frequency decreases.

The effective current path at 3.5 GHz for the cross shaped antenna, as shown in Fig. 3, includes both h and L_1 parameters. Fig. 6 shows the return loss of the same cross shaped antenna for various values of h parameter. From this figure, it is noticed that by increasing the h the resonant frequency of the band decreases.

The second step towards obtaining the multiband antenna structure is to add vertical strip at the end of the horizontal

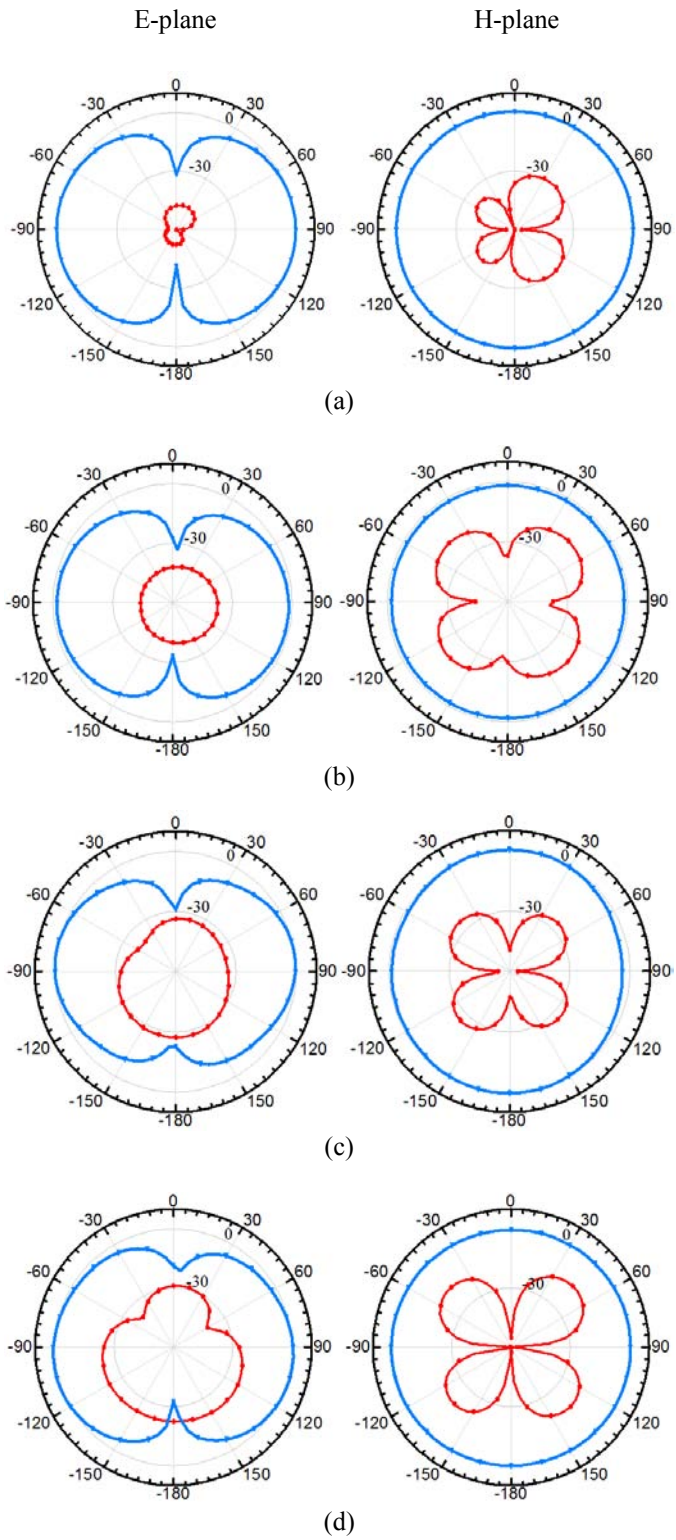


Figure 10: Simulated (Co-Pol) and (Cross-Pol) E-plane and H-Plane radiation patterns of the proposed antenna at: (a) 1.9 GHz, (b) 2.4 GHz (c) 3.6 GHz (d) 5.2 GHz

strip of the cross shaped CPW antenna, leading to the modified structure shown in Fig. 2 (b). The added strips can add two extra resonant frequencies at 2.4 GHz and 5.2 GHz as shown in Fig. 7. By increasing the length L_2 of the added strip, these resonances move to the lower frequencies and appear at the desired frequencies of 2.4 GHz and 5.2 GHz where a good tri-band performance at 2.4, 3.5 and 5.2 GHz can be seen.

Finally if an open end horizontal slot with T-shaped strip on top of the antenna is added to the structure of the Fig. 2(b) the proposed antenna of Fig. 1 with quad band behaviour can be obtained. Fig. 8 shows the return loss of the quad band antenna. The added resonance at 1.9 GHz is because of

the horizontal strip. By increasing the length L_3 of the proposed antenna, the resonant frequency at 1.9 GHz decreases.

Quad resonances are obtained at 1.9, 2.4, 3.5 and 5.2 GHz bands. To check the validity of the simulation results, the structure is also studied through the CST microwave studio software. The simulated return loss of the proposed antenna as obtained through CST and HFSS are shown in Fig. 9. It can be observed that CST results reasonably agree with the HFSS results with an acceptable frequency discrepancy.

The far-field E-plane and H-plane radiation patterns at frequencies of 1.9, 2.4, 3.5, and 5.2 GHz for the proposed antenna are shown in Fig. 10. The results, in general, show that the proposed antenna has a stable monopole-like radiation pattern in the E-plane and omnidirectional pattern in the H-plane. Also shown in this figure is the Cross-polarization in the E- and H-planes. These results show the low cross polarization at all four resonant bands.

4. Conclusions

A quad band CPW monopole antenna has been presented. Two full wave simulation software packages, HFSS and CST have been used to verify the simulation results of the designed antenna. The basic structure for the antenna has been presented. This structure gives a resonance at 3.5 GHz band. By adding other strips at the end of the basic antenna, triple resonant bands at 1.9, 2.4 and 5.2 GHz are obtained. The low-cost antenna is only 31.8 × 20 mm^2 in size. All resonant bands have return loss well above 10 dB. A good radiation performance is also achieved.

References

[1] C.-C. Lin, S.-W. Kuo, and H.-R. Chuang, "A 2.4-GHz printed meander line antenna for USB WLAN with notebook-PC housing," *IEEE Microw Wirel Compon Lett*., vol. 15, pp. 546–548, 2005.

[2] P.C. Bybi, G. Augustin, B. Jitha, C.K. Aanandan, K. Vasudevan, and P. Mohanan, "A quasi-omnidirectional antenna for modern wireless communication gadgets," *IEEE Antennas Wirel Propag Lett*., vol. 7, pp. 505–508 , 2008.

[3] Y., Lee, and Y.M., Seo, "Triple-band CPW-fed compact monopole antenna for GSM/PCS/DCS/WCDMA applications," *Electron. Lett*.,vol. 45, no. 9, pp. 447-448, 2009.

[4] S. Chaimool and K.-L. Chung, “CPW-fed mirrored-L monopole antenna with distinct triple bands for WiFi and WiMax applications,” *Electron. Lett*., vol. 45, no. 18, pp. 928–929 , 2009.

[5] J.-H. Lu and B.-J. Huang, “Planar multi-band monopole antenna with L-shaped parasitic strip for WiMax application,” *Electron. Lett*., vol. 46, no. 10, pp. 671-672, 2010.

[6] Liu, W.-C., C.-M. Wu, and N.-C. Chu, “A compact CPW-fed slotted patch antenna for dual-band operation,” *IEEE Antennas Wirel Propag Lett*., vol. 9, pp. 110–113, 2010.

[7] H.-W. Liu, C.-H. Ku, and C.-F. Yang, “Novel CPW-Fed planar monopole antenna for WiMAX/WLAN applications,” *IEEE Antenna Wirel Propag Lett*., vol. 9, pp. 240–243, 2010.

[8] J.-Y. Jan and T.-M. Kuo, “CPW-fed wideband planar monopole antenna for operations in DCS, PCS, 3G, and Bluetooth bands,” *Electron. Lett.,* vol. 41, no. 18, pp. 991-993, 2005.

Multi Band Monopole Antenna for MIMO Systems

Masoumeh Darvish and Hamid Reza Hassani

Department of Electrical and Electronic Eng., Shahed University, Tehran, Iran
hassani@shahed.ac.ir

Abstract

A novel multiband CPW-Fed monopole antenna for multi-input multi-output (MIMO) application is presented. The proposed antenna covers quad frequency bands including UMTS, WLAN and WiMAX application, centered at 2, 2.5, 3.5 and 5.5 GHz. A two element array of such antenna suitable for MIMO application is presented. The antenna element and array of the two orthogonal element of the proposed antenna was fabricated and tested. The array has low mutual coupling, low envelope correlation, high efficiency and good radiation patterns over all the relevant frequency bands.

1. Introduction

Due to their ability to increase the channel capacity and reduce multipath fading, there is a great interest in using multi-input multi-output (MIMO) systems in the wireless communication. Among the antennas which are used for MIMO application, printed antennas are more appropriate due to their small size and low cost. Furthermore, because of the omnidirectional pattern of printed monopole antennas, they are more attractive for MIMO application. The design of a single-band four-element printed monopole antenna for UMTS mobile phone application is given in [1]. To achieve maximum channel capacity the array is also required having high gain [2].

Rapid developments in the wireless communication systems demand novel antenna designs that can be used in more than one frequency bands. The design of a dual-band back-to-back printed monopole antenna operating at UMTS and 2.4 GHz WLAN is reported in [3]. A tri-band E-shaped printed monopole antenna loaded with two U-shaped resonance paths suitable for MIMO systems for WLAN application, covering 2.4, 5.4 and 5.8 GHz is reported in [4]. This antenna cannot cover the WiMAX frequency band.

In this paper, a multi band CPW-Fed monopole antenna suitable for MIMO application is presented. The array structure of the antenna is also presented. Each of the elements consists of a CPW-Fed fork-shaped strip to which is added an inverted U-shaped strip on top of the structure. Due to its two resonance paths, the base forked-shaped structure provides two frequency bands. When this antenna is loaded with an inverted U-shaped strip, new resonance paths is created, which provide three frequency bands. Finally unequal arms in the base fork-shaped structure, can add another resonant band, which cause the antenna to operate in four separate resonant bands.

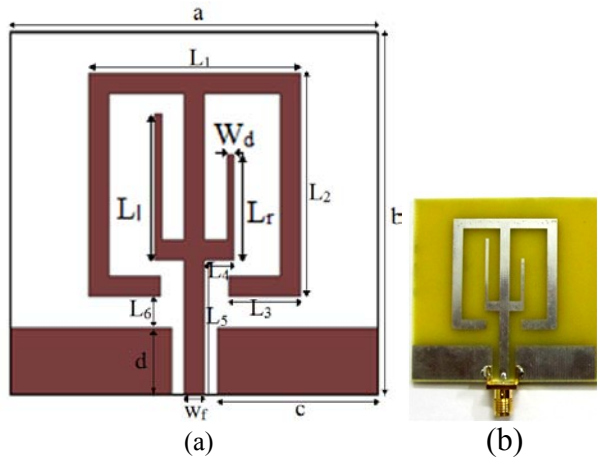


Figure 1: (a) Geometry of the proposed quad band MIMO antenna with asymmetric arms and (b) a fabricated prototype.

Table 1: Parameters of the proposed antenna

parameter	value [mm]	parameter	value[mm]
a	54	L_4	4.3
b	52	L_5	22
c	23.7	L_6	4.6
d	10	w_f	3
L_1	31	L_l	21
L_2	33	L_r	15.5
L_3	10.5	w_d	1

2. Antenna design

The configuration of the proposed quad band antenna is shown in Fig. 1. The antenna is printed on an FR4 substrate with relative permittivity $\epsilon r = 4.4$ and thickness h = 1 mm and is fed by a CPW transmission line with 50 Ω impedance. The optimal antenna dimensions are listed in Table 1. The base structure is a three branch fork like strip with an inverted U-shape strip on top of it. This structure

can provide three resonant bands at 2.4, 3.5 and 5.5 GHz due to three resonance paths. By making the arms of the three branch fork like strips unequal resonant band at 2 GHz can be created due to creating a new resonance path. The proposed antenna can cover 2, 2.5, 3.5 and 5.5 GHz suitable for UMTS, WiMAX and WLAN applications.

3. Discussion

The simulated and measured return loss for the proposed quad band antenna is shown in Fig. 2. Good agreement between these two results can be seen. Fig. 3 is shown the current distribution of the antennas at 2 and 3.5 GHz. As can be seen, two arms with unequal size have two different resonance path from feed point to end of the arm.

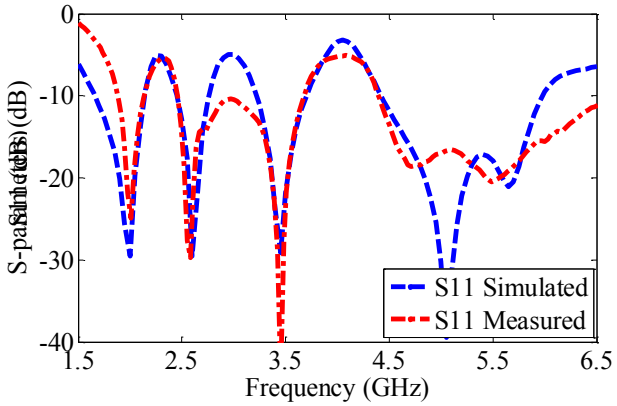


Figure 2: Simulated and measured S11 of the proposed antenna.

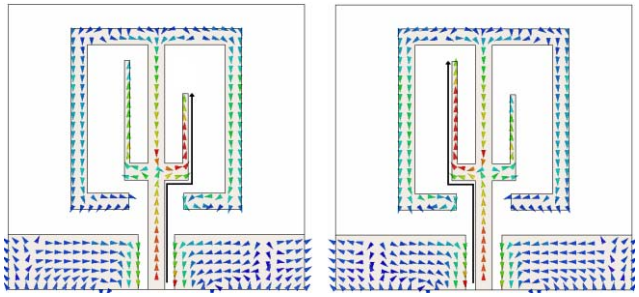


Figure 3: Current distribution of the proposed antenna with asymmetrical arms.

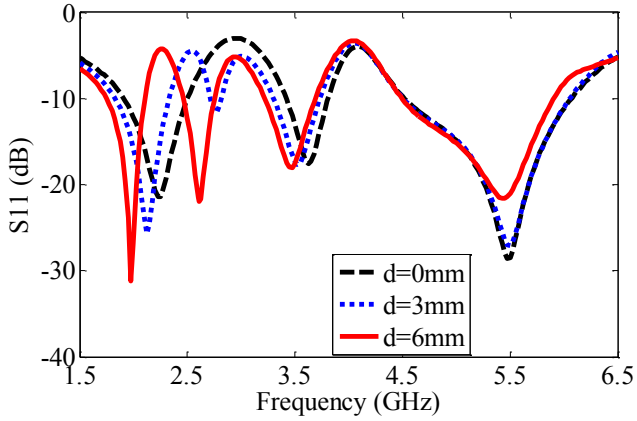


Figure 4: Reflection coefficient for various d.

Fig. 4 was shown studying the effect of the creating asymmetric arms on the return loss of the antenna. This figure shows that if the difference between the left arm and the right arms ($d = L_l - L_r$) is zero, the antenna resonate in three resonant bands. By increasing this difference, d = 3 mm, a resonance at 2.7 GHz created but it has low impedance matching with return loss -10 dB at centre frequency. By using d = 6 mm, a centre frequency of the created band, decrease to 2.6 GHz and the impedance matching improved with return loss of -22 dB and also good impedance matching in all quad frequency bands.

Radiation patterns with co- and cross- polarization in the E- and H- planes are shown in Fig. 5. It is seen that the E-plane patterns are monopole-like for operation at all frequencies, while the H-plane patterns are nearly omnidirectional.

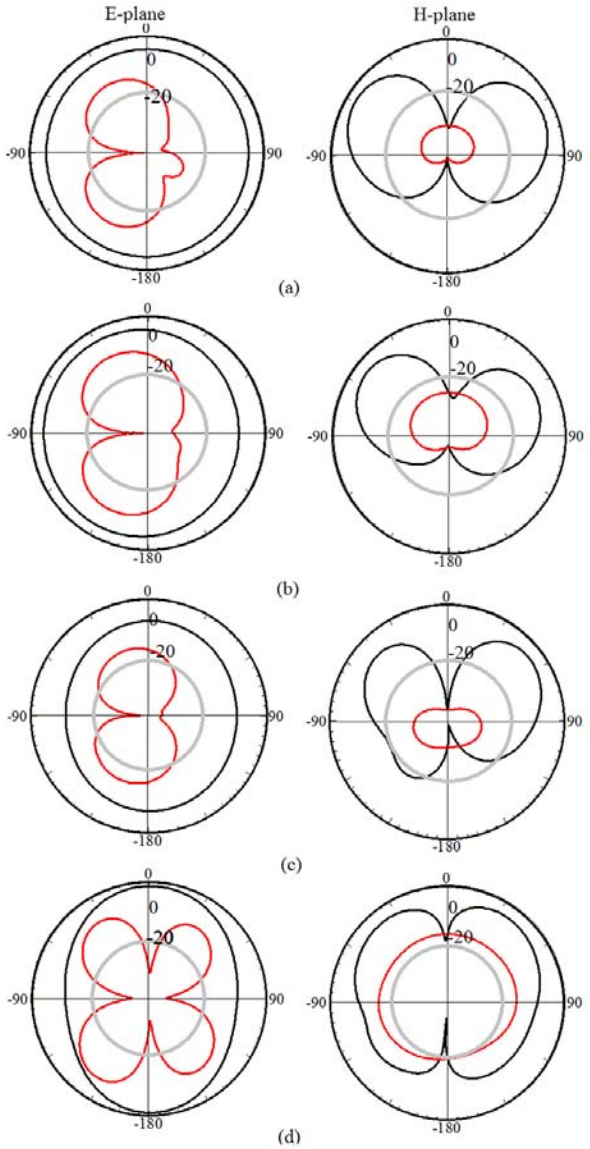


Figure 5: Radiation pattern of the proposed antenna at (a) 2, (b) 2.5, (c) 3.5, and (d) 5.5 GHz.
(—— Co-polar and —— Cross-polar)

To design a MIMO structure from this proposed antenna, two elements are placed beside each other. In a MIMO antenna high radiation efficiency, high peak gain, low envelope correlation, and high isolation between the signal ports is required. The various configurations of such antennas in relation to each other are investigated and based on the least correlation and mutual coupling, the most suitable configuration for MIMO application is presented. The proposed configuration consists of two orthogonal elements as shown in Fig. 6. These two elements are placed in orthogonal configuration with 0.2λg distance between each other, and due to the polarization diversity that is achieved from this configuration, the correlation and coupling is decreased.

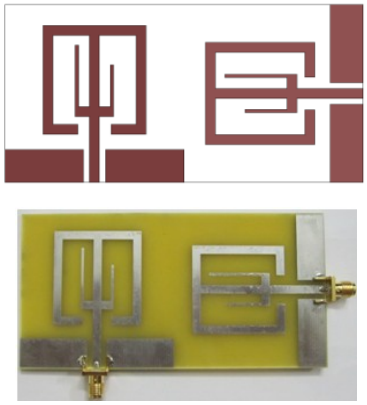


Figure 6: Quad-band MIMO printed monopole antenna with asymmetric arms and a fabricated prototype

Fig. 7 shows the reflection coefficient and mutual coupling of the proposed MIMO antenna. The impedance bandwidth meets the required bandwidth specification for UMTS, WiMAX and WLAN operation with reflection coefficient below -10 dB. Also S12 is less than -20 dB, thus the mutual coupling of this structure is low and these two antennas are approximately independent. Good agreement between simulated and measured results achieved.

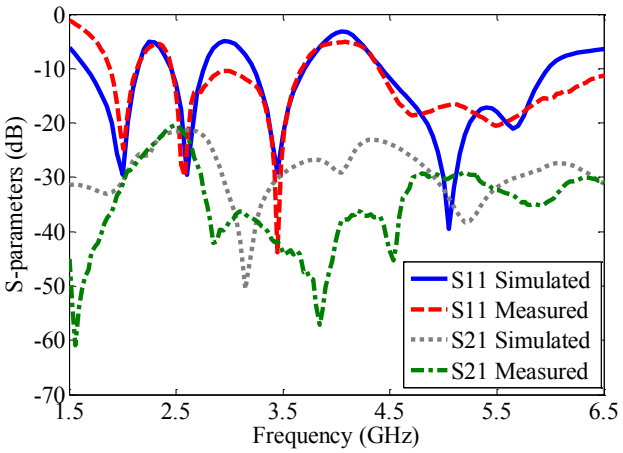


Figure 7: Simulated and measured S-parameters of the proposed antenna.

The envelope correlation can be computed from s-parameters using the following formula [4]:

$$\rho_e = \frac{|S_{11}^* S_{21} + S_{12}^* S_{22}|^2}{|(1-|S_{11}|^2 - |S_{21}|^2)(1-|S_{22}|^2 - |S_{12}|^2)|} \quad (1)$$

Fig. 8 shows envelope correlation of the proposed MIMO antenna. As can be seen, the envelope correlation of this structure is less than 0.005, so the proposed antenna is appropriate for the MIMO applications.

Table 2 give the simulated gain and radiation efficiency of the antenna array structure of Fig. 6. The radiation efficiency decreases with frequency, but is always higher than 85%. The low mutual coupling shown in Fig. 7 the low envelope correlation shown in Fig. 8 confirm that the proposed antenna is a good candidate for use in MIMO applications.

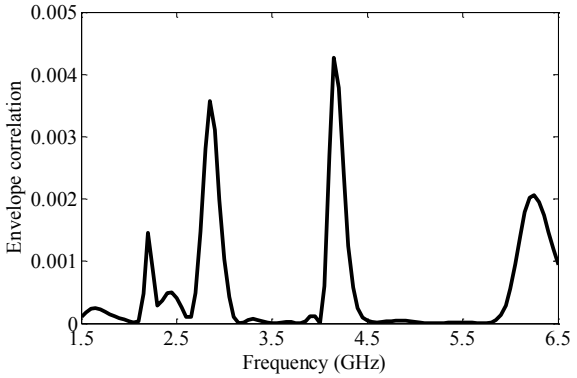


Figure 8: Envelope correlation of the proposed MIMO antenna.

Table 2: Gain and radiation efficiency results

frequency [GHz]	Gain [dBi]	radiation efficiency [%]
2	0.05	85
2.5	1.13	87
3.5	2.54	88
5.5	3.63	94

4. Conclusions

A quad-band CPW-fed monopole antenna suitable for MIMO application has been presented. The antenna parameters for UMTS, WIMAX and WLAN application are given. The proposed MIMO array configuration with element spacing of λg/5 provides less than -22 dB mutual coupling, envelope correlation of lower than 0.008 and efficiency of higher than 85% over all frequencies. The proposed antenna has also fabricated and tested. Good agreement between simulated and measured results obtained.

Acknowledgements

This work was supported by Research Institute for information and communication technology, ICT-ITRC.

References

[1] Y. Ding, Z. Du, K. Gong, and Z. Feng, “A four-element antenna system for mobile phone,” *IEEE antennas and wireless propagation letters*, Vol. 6, 655-658, 2007.

[2] A. R. Mallahzadeh, S. Es’haghi, and H. R. Hassani, “Compact U-array MIMO antenna designs using IWO algorithm,” *Int. J. RF Microw. Comput.-Aided Eng*., Vol. 19, 568–576, Jul. 2009.

[3] Y. Ding, Z. Du, K. Gong, and Z. Feng, ”A novel dual-band printed diversity antenna mobile terminals,” *IEEE Trans. Antennas Propag*. Vol. 55, No. 7, 2088-2096, July 2007.

[4] S. Mohammad Ali Nezhad, and H.R. Hassani, "A novel tri-band E-shaped printed monopole antenna for MIMO application," *IEEE antennas and wireless propagation letters,* Vol. 9, 576-579, 2010.

Compact PCB-Embedded GPS Antenna Loaded with Lumped Elements

Jungho Ahn[1,2], Junho Choi[2], Seunghwan Kim[1], and Young-Sik Kim[2]

[1]Mobile Communication Division Samsung Electronics Co., Ltd., Gyeonggi-do, 443-742, Korea
[2]Department of Computer and Radio Communications Engineering Korea University, Seoul, 136-713, Korea
*corresponding author, E-mail: yskim@korea.ac.kr

Abstract

In this paper, a compact PCB-embedded GPS antenna loaded with lumped elements is presented. The proposed antenna consists of a T-shaped FIPA, two chip capacitors, and one chip inductor. The antenna size is 8 mm × 5 mm with a ground size of 70 mm × 40 mm. The proposed antenna is designed and examined via simulation and experiment. The bandwidth under VSWR of 1:3 is 26 MHz from 1569 MHz to 1595 MHz. The measured gain is +2.1 dBi at 1575 MHz.

1. Introduction

Since commercial mobile phones with a single-band internal antenna have been introduced in 1998, mobile terminals are getting smaller and slimmer because of consumer's needs. A mobile phone can usually provide various wireless services using one main antenna and several sub-antennas, such as GPS, BT, Wi-Fi, DMB, and so on. Hence, the space for internal antennas is limited to set it up due to a mobile phone size. Antenna miniaturization is an important issue because several antennas are often packed into one mobile phone.

Recently, various design methods for an internal sub-antenna have been demonstrated [1]-[4]. Among them, the printed antenna has an attractive feature owing to a compact size at a fixed operating frequency [5]-[6]. As the printed antenna has a simple planar structure, the antenna is suitable to be printed on the system circuit board of a mobile phone and feasible to be fabricated at a low cost for practical applications.

In this paper, a small GPS antenna embedded on a printed circuit board (PCB) for use in a mobile phone is proposed. The proposed antenna consists of a conventional T-shaped PIFA with three reactive elements, which are two chip capacitors and one chip inductor. The proposed antenna has be implemented on a PCB ground and tuned to the GPS frequency via appropriate capacitances. Further, these antennas can be positioned anywhere on a PCB. The details of the antenna design, and simulated and measured results are presented.

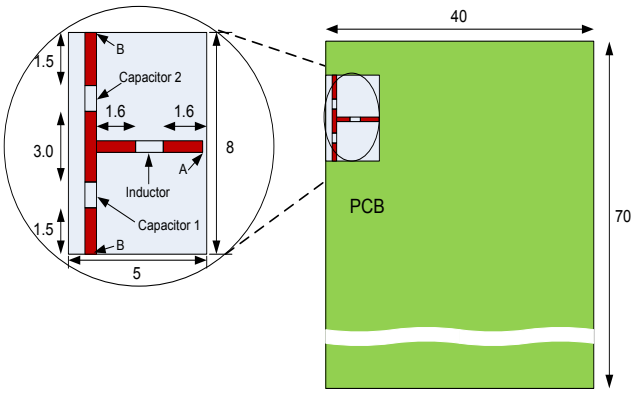


Figure 1: Dimensions of the proposed antenna (line width: 0.5, unit: mm).

2. Antenna Design

The proposed antenna is based on a PIFA type antenna. The configuration of the proposed T-shaped GPS antenna is shown in Fig. 1. The antenna is designed on an FR-4 substrate with a thickness of 0.8 mm and a dielectric constant of 4.4, that is generally used to a system circuit board of a usual mobile phone. The antenna utilizes a small portion (8 mm × 5 mm) of a ground plane (70 mm × 40 mm) and is placed at an off-centered position.

The main path length of each folded stripline is 9.6 mm, which is about $\lambda_0/20$. Without capacitors, the resonance occurs at a frequency of 5.6 GHz via the HFSS simulation [7]. To reduce the resonant frequency to the GPS frequency (~ 1575.42 MHz) while maintaining the same antenna size, two chip capacitors are inserted into the T-shaped antenna. Thus, each capacitor is placed at each arm of a T-shape. One chip inductor is utilized to achieve good matching condition at the input port. The antenna is fed at point A and shorted with the ground plane at point B, as shown in Fig. 1. As the feeding signal of the antenna is applied to point A, the signal splits at the T-junction and returns through the

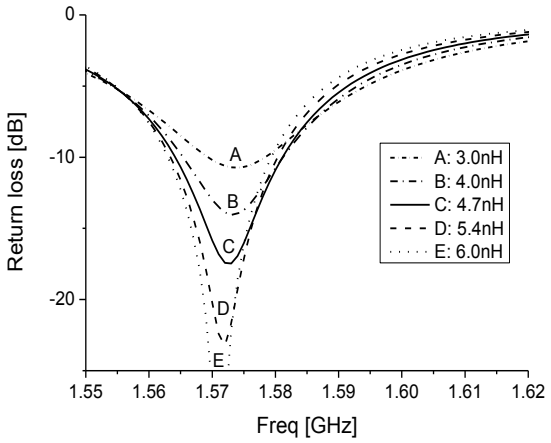
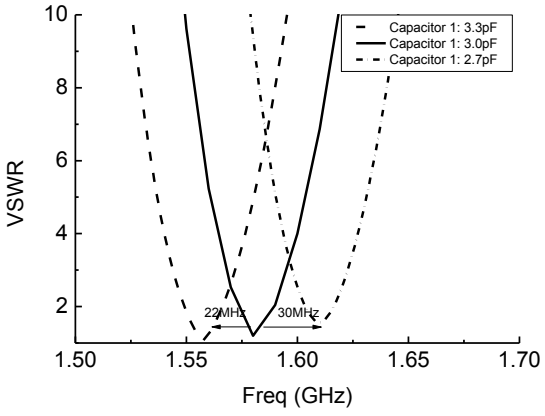
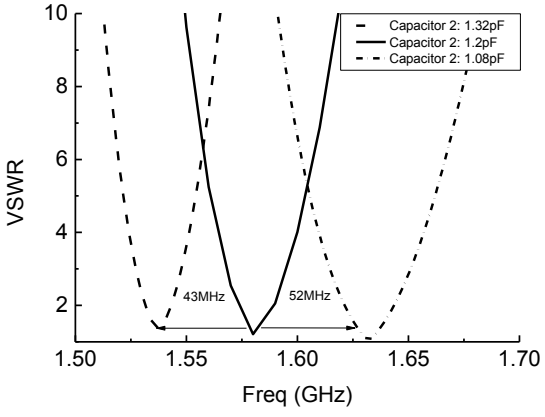


Figure 2: Simulated return losses of the proposed antenna with different inductances.



(a)



(b)

Figure 3: Simulated VSWRs of the proposed antenna. (a) capacitor 1 and (b) capacitor 2.

ground plane. The detailed antenna dimensions are also depicted in Fig. 1.

Firstly, the input inductance has been studied. The simulated results of the return losses are shown in Fig. 2.

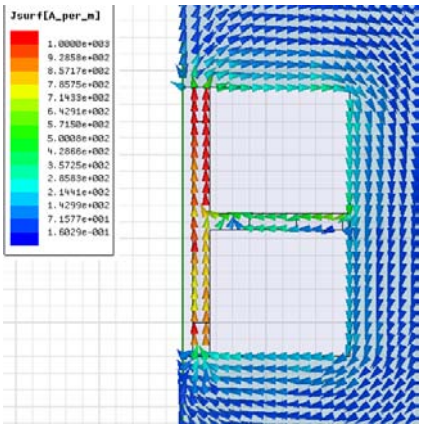


Figure 4: Simulated current distribution of the proposed antenna.

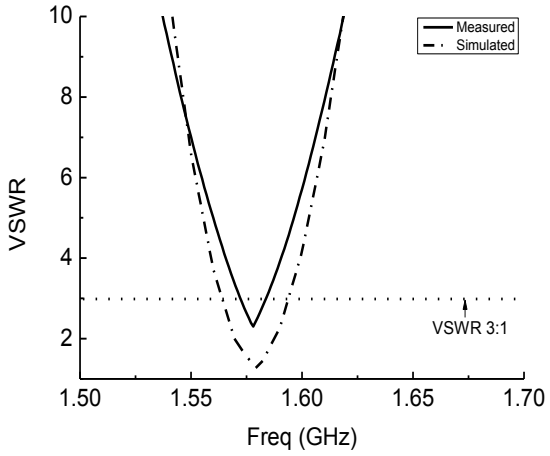


Figure 5: Measured and simulated VSWRs of the proposed antenna.

The input inductor has a little influence on a resonant frequency of the proposed antenna. It can be stated that the input inductor may work on an antenna Q-factor.

Secondly, two capacitors (capacitors 1 and 2) with fixing an input inductance of 4.7 nH have been investigated. Fig. 3 shows simulated VSWRs. Although the antenna is configured symmetrically, the capacitance of capacitor 1 has less influence on a resonant frequency of the proposed antenna than that of capacitor 2. It is worth noting that the capacitance of C1 should be about 2.5 times larger than that of C2 to achieve the optimum performance.

3. Results and Discussions

Fig. 4 shows simulated current distribution of the proposed antenna. The current flows largely on the bar of the T-shape and returns through the antenna ground plane. It may be noted that the proper ground plane may influence the antenna performance.

Fig. 5 shows the measured and simulated VSWRs of the proposed antenna. Good agreement between the measured and simulated results can be observed. The proposed antenna has a bandwidth (3:1 VSWR) of 30MHz (1564 ~ 1594 MHz) which satisfies the operating bandwidth of the GPS band.

Fig. 6 shows the measured radiation patterns in an anechoic chamber. The proposed antenna shows an omni-directional radiation pattern in the x-y plane. The measured peak gain is 2.1 dBi at the broadside direction (z-axis). The measured peak and average gain, and radiation efficiency are listed in Table I.

Table 1: Lumped Elements and Measured Results.

L1	C2	C3	Peak Gain	Average Gain
4.7 nH	3.0 pF	1.2 pF	2.1 dBi	-3.6 dBi

4. Conclusion

In this paper, a printed GPS antenna for an internal mobile phone has been proposed. The antenna has a compact structure and is easy to print on the PCB ground of a mobile phone because of a small area of 8 mm × 5 mm. For size reduction, this antenna uses one inductor and two capacitors. The inductor at the input port influences an antenna Q-factor, while two capacitors on the bar of the T-shape have an effect on the resonant frequency of an antenna. Although the antenna has a simple structure and compact volume, it has good radiation characteristics and high efficiency. The proposed antenna may be especially applicable for modern thin mobile phones as an internal antenna.

References

[1] Y. -S. Wang, and S. -J. Chung, A short open-end slot antenna with equivalent circuit analysis, *IEEE Trans. Antennas propag.*, vol. 58, no. 5, pp. 1771-1775, May 2010.

[2] M. C. Scardelletti, and G. E. Ponchak, and S. Merritt, and J. S. Minor, and C. A. Zorman, Electrically small folded slot antenna utilizing capacitive loaded slot lines, *in Proc. IEEE Radio Wireless Symp.*, pp. 731-734, Jan 2008.

[3] H. Choi, S. Jeon, L. Yang, D. Yun and H. Kim, GPS antenna using a system ground as a radiator, *in Proc. IEEE Int. Workshop on Antenna Technology Small Antennas and Novel Meta-materials, Radio Wireless Symp.*, pp. 235-238, Apr 2011.

[4] J. Villanen, and P. Vainikainen, Optimum dual-resonant impedance matching of coupling element based mobile terminal antenna structures, *Microwave and Optical Technology Letters, USA*, vol. 49, pp. 2472-2477, October 2007.

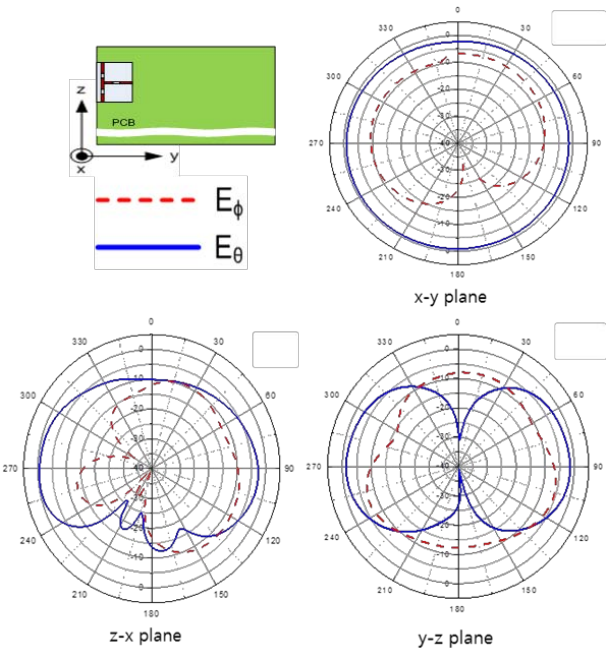


Figure 6: Measured radiation patterns of the proposed antenna.

[5] V. Pathak, S. Thornwall, M. Krier, S. Rowson, G. Poilasne, and L. Desclos, Mobile Handset System Performance Comparison of a Linearly Polarized GPS Internal Antenna with a Circularly Polarized Antenna, *IEEE Antennas and Propagation Society International Symposium, Columbus, Ohio, USA*, vol. 3, pp. 666-669, June 2003.

[6] C. R. Rowell, and R. D. Murch, A Capacitively Loaded PIFA for compact Mobile Telephone Handsets, *IEEE Trans. Antennas propag.*, vol. 45, no. 5, pp. 837-841, May 1997.

[7] HFSS Ansoft Corp. 2005, ver.12.0

A compact dual-band dual-port diversity antenna for LTE

Lila Mouffok*, Anne Claire Lepage, Julien Sarrazin, and Xavier Begaud

Institut Telecom, Telecom ParisTech- LTCI CNRS UMR 5141 Paris, France
*corresponding author, E-mail: lila.mouffok@telecom-paristech.fr

Abstract

The design of a compact dual-band dual-port antenna system is presented. It operates in two frequency bands, 790-862 MHz and 2500-2690 MHz, thereby making it suitable for Long Term Evolution (LTE) handheld devices. The proposed system is composed of two orthogonal inverted-F antennas (IFA) to perform diversity in mobile terminals. A good agreement is observed between simulated and experimental results. The high antenna diversity capability of the proposed system is highlighted with the calculation of envelope correlation coefficient, mean effective and diversity gains for different environment scenarii.

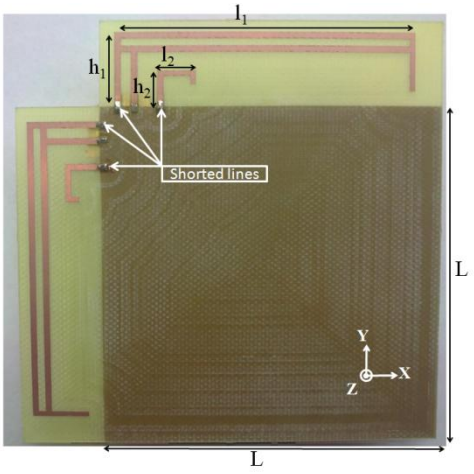
1. Introduction

The use of multiple antennas can improve reliability and increase the channel capacity [1]. However, for wireless mobile devices, the available space is limited. Therefore, compact antenna systems are required. Recently, a variety of compact antennas for MIMO (Multiple-Input Multiple-Output) systems have been presented. An internal loop antenna with distributed feed which operates in LTE 700 MHz and GSM 800 MHz bands is presented in [2]. In this solution the two operating bandwidths are close. A dual port ferrite antenna is presented in [3] which operates in LTE 700 MHz but with low gain (-8 dBi). In [4], to achieve compactness, a PIFA is top loaded with a dielectric sheet. This solution covers the bands: 1710-1880 MHz, DCS 1800 MHz, and 2.5-2.69 GHz. Significant research has been made on dual-port and multiband antennas. However, there are few solutions covering two bands which are separated by more than an octave such as LTE bands (790-862 MHz and 2.5-2.69 GHz), with implementation of MIMO, for handheld devices.

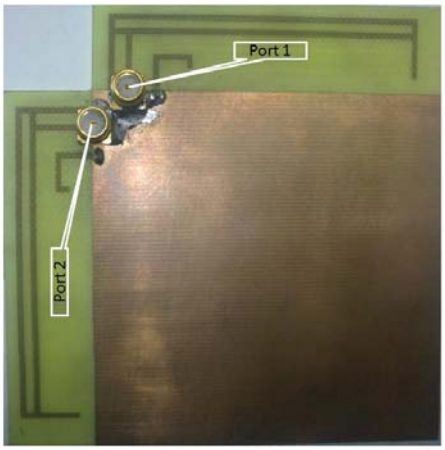
Thus, the objective of the work presented in this paper is to propose a compact antenna system for mobile devices that operates in the above mentioned bands.

2. Antenna design

The proposed structure is printed on FR4 substrate with ε_r=4.4, tan δ=0.019, and thickness of 0.7 mm (fig.1). The dimensions of the ground plane are L*L=70*70 mm^2 (λ_{01}/5 * λ_{01}/5) where λ_{01} is the free space wavelength of the lower band central frequency (f_1=816 MHz). The structure is composed of two identical elements shaped IFA (Inverted-F Antenna) located orthogonally to each other. The longer monopole allows operation on the lower band. It is connected to the ground plane with a metallic via hole to improve impedance matching. Its dimensions are l_1=60 mm (λ_{01}/6), and h_1=16 mm (λ_{01}/22). The shorter L shaped monopole controls the higher band operation with dimensions of l_2=7.6 mm (λ_{02}/15) and h_2=8.4 mm (λ_{02}/13) where λ_{02} is the free space wavelength of the higher band central frequency (f_2=2.6 GHz). The two monopoles are fed by two 50 Ohms SMA connectors (fig.2.b).



(a)



(b)

Figure 1: Photography and dimensions of the realized structure: (a) top view, (b) Bottom view.

3. Experimental results and discussions

The proposed structure has been simulated with the transient solver of CST Microwave Studio® and a prototype has been fabricated. Simulated and measured S-parameters are compared in Fig.2. A similar behavior between simulations and measurements is obtained. The structure operates in two bands ($|S_{11}| < -6$ dB): the lower band is about 10% (777-865 MHz) and the higher one about 7 % (2.51-2.70 GHz). The mutual coupling between the two ports is less than -6 dB in the lower band and -13 dB in the higher one.

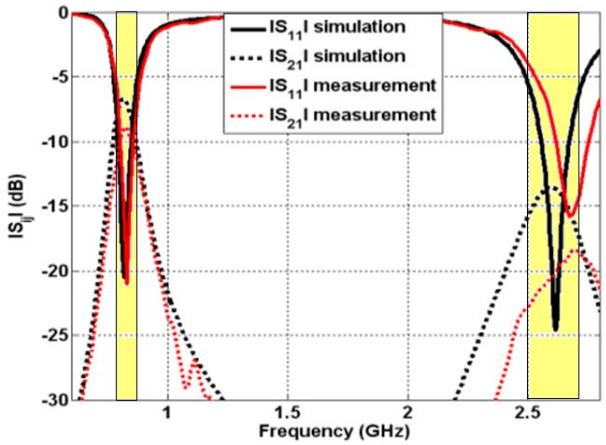


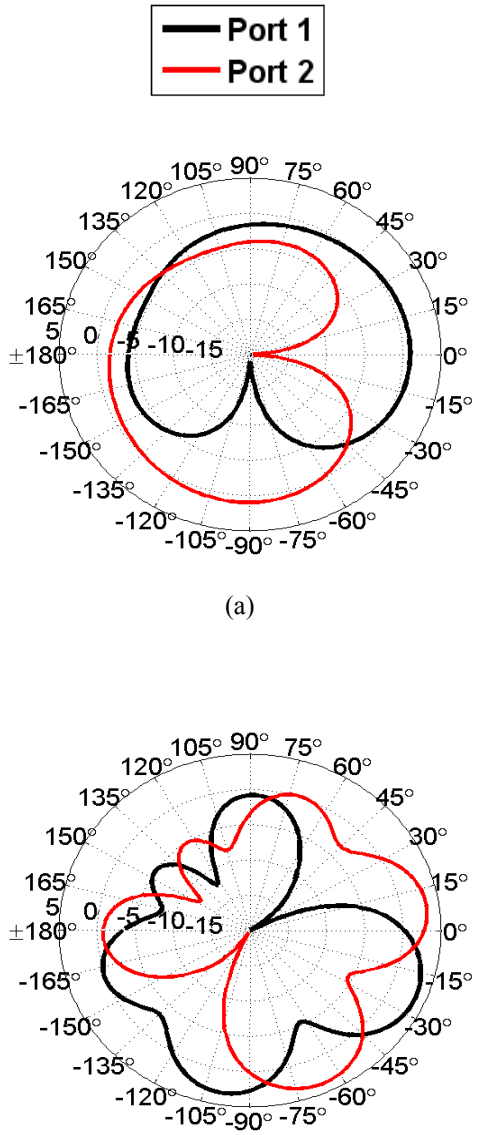
Figure 2: Simulated and measured S-parameters.

Fig.3 shows the simulated radiation patterns of each antenna in the XY plane for the two bands. For the lower band, quasi-orthogonality between the patterns can be observed. The maximum realized gain is about 1 dB at 0° for the port 1 and 1 dB at -90° for the port 2. The realized gain, by definition, takes into account the reflection coefficient at each port.

For the higher band, the maximum realized gain is 3.5 dB. At 2.6 GHz, even if patterns are not orthogonal, the two monopoles present minimum and maximum gain in different directions. This is well-suited to provide high diversity capabilities.

Fig.4 compares the simulated and measured co-polar and cross-polar radiation patterns in the E plane (YZ plane) and H plane (XZ plane) respectively. Because both ports are symmetrical, we only present radiation patterns for port 1 at 816 MHz and 2.6 GHz. For both planes and both bands, it is found that the simulated and the measured radiation patterns are in good agreement.

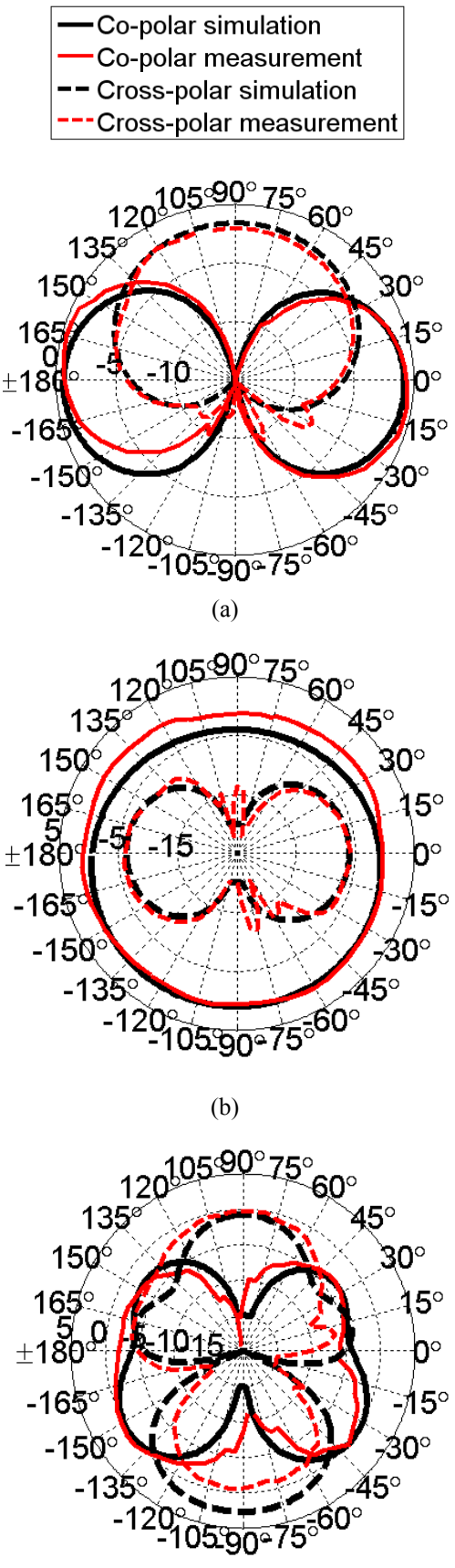
In the lower band, the measured cross-polar level is about 10 dB lower than the co-polar level in the H plane but it increases in the E plane at 90° direction. This is due to the coupling with the second radiating element.



(a)

(b)

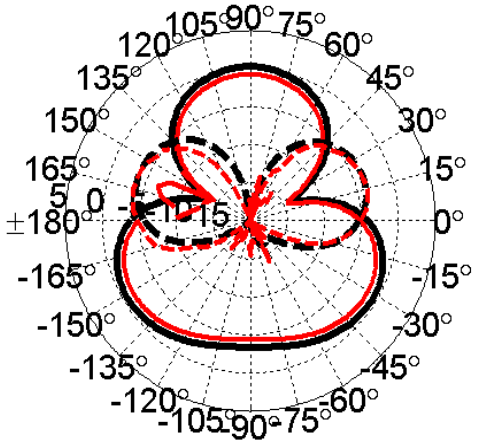
Figure 3: Realized total gain (dB) in the XY plane for the two bands: (a) at 816 MHz (b) at 2.6 GHz.



(a)

(b)

(c)



(d)

Figure 4: Simulated and measured radiation patterns: (a) in the E plane at 816 MHz, (b) in the H plane at 816 MHz, (c) in the E plane at 2.6 GHz, (d) in the H plane at 2.6 GHz.

4. Evaluation of the diversity performance

In this section, we propose to evaluate the diversity performance of the proposed antenna by calculating the envelope correlation coefficient, the mean effective gain and the diversity gain while taking into account the propagation environment.

The envelope correlation coefficient ρ_e quantifies the similarity between the radiation patterns of the two monopoles. The lower the correlation, the better the diversity performance. Vaughan shows in [5] that this coefficient can be expressed by:

$$\rho_e = \frac{\left| \int_\Omega \left(E_{1\theta} E_{2\theta}^* p_\theta + XPD\, E_{1\varphi} E_{2\varphi}^* p_\varphi \right) d\Omega \right|^2}{\int_\Omega \left(E_{1\theta} E_{1\theta}^* p_\theta + XPD\, E_{1\varphi} E_{1\varphi}^* p_\varphi \right) d\Omega \int_\Omega \left(E_{2\theta} E_{2\theta}^* p_\theta + XPD\, E_{2\varphi} E_{2\varphi}^* p_\varphi \right) d\Omega}$$

$E_{1\theta}(\Omega)$, $E_{1\varphi}(\Omega)$, $E_{2\theta}(\Omega)$, $E_{2\varphi}(\Omega)$ are complex electric fields along θ and φ radiated by the antenna fed by two different ports. The solid angle Ω is defined by θ [0: π] in elevation and φ [0:2π] in azimuth. $p_\theta(\Omega)$ and $p_\varphi(\Omega)$ are the Angle-of-Arrival (AoA) distributions of incoming waves. The parameter XPD is the cross-polarization discrimination of the incident field and is defined as XPD= S_φ/S_θ (where S_φ and S_θ represent the average power along the spherical coordinates φ and θ). The environment depends strongly on the arrival angles distribution and on XPD. The most common distributions proven by measurements are Gaussian and Laplacian distributions [6]. Thus, we consider different distributions in elevation, while in azimuth plane the distribution will be uniform, as demonstrated by the two main measurement campaigns in the literature [6], [8]. In order to obtain more realistic results, different environments are considered. Each environment is characterized by typical values of XPD, mean angle of incident wave

distribution (θ_i) and standard deviation of wave distribution (σ).
These values were deduced from several measurements [6], [7], [8] for different environments: isotropic, indoor, and outdoor. The isotropic environment is defined by XPD=0 dB, $p_\theta(\Omega)=p_\varphi(\Omega)=1$, the indoor environment by XPD=1 dB, $\theta_i= 20°$, $\sigma =30°$ and the outdoor environment by XPD=5 dB, $\theta_i= 10°$, $\sigma =15°$.

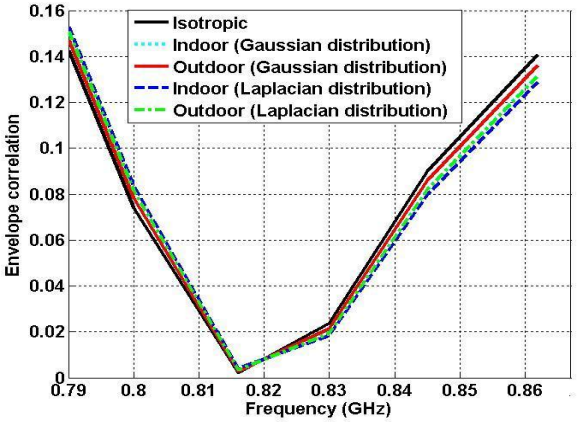
The envelope correlation coefficient of the proposed structure has been calculated from simulated radiation patterns. Results are given in Fig.5.
For the lower band, the correlation coefficient is higher at extremities than at the center of the band, for all environments (see Fig. 5a). Note that correlation takes into account the radiation, matching and isolation level at each frequency. According to S-parameters levels, the correlation is more or less higher. Since $|S_{11}|$ variation over the whole band is more significant (from -6 dB to -20 dB) than $|S_{21}|$ variation (from -6 to -8 dB), ρ_e variation depends mainly on $|S_{11}|$ variation. Thus, the lower $|S_{11}|$ is, the lower ρ_e is.
For the higher band, the maximum value is below 0.08 which is less than in the lower band, thanks to a better isolation (<-13 dB). However, the ρ_e levels remain below 0.16 for the two bands which largely satisfies the condition ($\rho_e<0.5$) to provide high diversity capabilities [5].

In the following part, we evaluate the Mean Effective Gain (MEG) which was introduced by Taga [9]. It is defined as the ratio between the mean received power of antennas over the random route and the total mean incident power. When each monopole receives the same quantity of power, the MEG ratio of the two monopoles is equal to one, which means that no performance deterioration is expected due to some power imbalance [10]. The mathematical expression is given by the following equation:

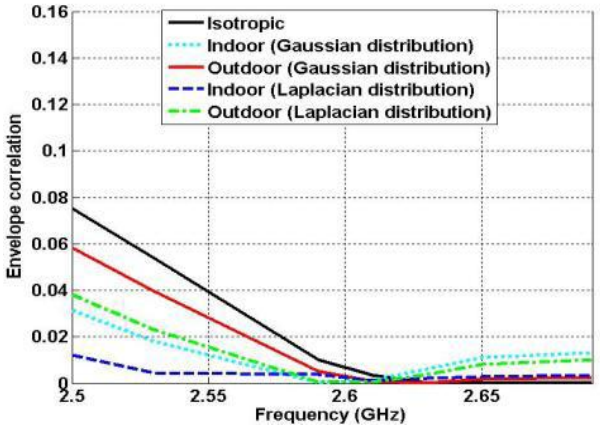
$$MEG = \int_{\Omega} \left(\frac{XPD}{XPD+1} G_\theta p_\theta + \frac{1}{XPD+1} G_\varphi p_\varphi \right) d\Omega$$

Where G_θ and G_φ are the θ and φ components of the antenna power gain pattern respectively.
The calculated mean effective gains of the monopoles from simulated radiation patterns in the two bands are presented in Table I. It can be seen that the ratio of MEG_1, determined at port 1, over MEG_2, determined at port 2, is almost equal to 1, which satisfied equal contribution of the two monopoles to receive the same quantity of power. This is due to the fact that the proposed structure is completely symmetric and that the Gaussian and Laplacian angular distributions are taken only along the elevation as presented in [6].
Finally, the efficiency of the diversity is usually presented in terms of diversity gain (DG). It can be defined as the difference between the signal-to-noise ratio (SNR) of the combined signals and the SNR of a single antenna. In theory, the maximum gain estimated for diversity of two antennas is 10.2 dB [11]. It can be seen in Table 1 that calculated DG is about 10 dB across the whole desired bands, which is very satisfactory.

From the results shown in Fig.5 and Table 1, it is found that the received signals satisfy the conditions $\rho_e < 0.5$, $MEG_1/MEG_2 \approx 1$ and allows a diversity gain of 10 dB. These values fit the diversity requirements of MIMO systems.



(a)



(b)

Figure 5: Envelope correlation for different environments of the proposed structure: (a) in the lower band (b) in the higher band.

Table 1: Diversity performances of the proposed antenna.

	MEG_1/MEG_2		Gain diversity (dB)	
	816 MHz	***2.6 GHz***	***816 MHz***	***2.6 GHz***
Isotropic	-4.33/-4.35	-4.93/-4.91	9.9	9.9
Indoor Gaussian	-5.03/-5.05	-5.17/-5.15	9.9	10
Outdoor Gaussian	-7.63/-7.64	-7.18/-7.15	9.9	9.9
Indoor Laplacian	-5.04/-5.05	-5.17/-5.15	9.9	10
Outdoor Laplacian	-7.63/-7.64	-7.18/-7.15	9.9	9.9

5. Conclusions

In this paper, a compact dual-band dual-port system for handheld devices has been proposed. The radiation element has an advantage to be only 60*16 mm^2 ($\lambda_{01}/6 * \lambda_{01}/22$), thus it can be easily implemented in mobile terminals. In addition, it covers two bands which are separated by more than an octave. The system provides good diversity capabilities thanks to a low correlation coefficient ($\rho_e < 0.2$), an equal amount of received power between the two radiating elements ($MEG_1/MEG_2 \simeq 1$), and a diversity gain equal to 10 dB for different environments: isotropic, indoor and outdoor. Consequently, the presented design is suitable for MIMO communication applications.

Acknowledgements

The research leading to these results has received funding from the European Community's Seventh Framework Program (FP7/2007-2013) under grant agreement SACRA n° 249060.

References

[1] G. S. Foschini, M. J. Gans, On limits of wireless communications in a fading environment when using multiple antennas, *Wireless Personal Communications*, Vol. 6, 311–335, 1998.

[2] S. J. Eom, J. H. Lee, A. Kim, S. O, Park, Broadband internal antenna for 700 MHz LTE application with distributed feeders, *IEEE Microwave conference, APMC, Asia Pacific*, 1845–1848, 2009.

[3] J. Lee, Y. K. Hong, S. Bae, G.S. Abo, W.M Seong, G. H. Kim, Miniature Long-Term Evolution (LTE) MIMO ferrite antenna, *IEEE Antennas Wireless Propag. Lett.*, Vol.10, 603–606, 2011.

[4] A. N. Kulkarni, S. K. Sharma, A compact multiband antenna with MIMO implementation for USB Size 4G LTE wireless devices, *IEEE International Symposium on Antennas and Propag. (APSURSI),* vol.10, 2215–2218, 2011.

[5] R. J. Vaughan, J. B. Andersen, Antenna diversity in mobile communication, *IEEE Trans. on Vehicular Technology*, vol. 36, 149–172, 1987.

[6] K. Kalliola, K. Sulonen, H. Laitinen, O. Kivekas, J. Krogerus, P. Vainikainen, Angular power distribution and mean effective gain of mobile antenna in different propagation environments, *IEEE Trans. on Vehicular Technology* , vol.51, 823– 838, 2002.

[7] Z. Ying, T. Bolin, V. Plicanic, A. Derneryd, G. Kristensson, Diversity antenna terminal evaluation, *IEEE Antennas and Propagation Society International Symposium, vol. 2A*, 375– 378, 2005.

[8] F. Adachi, M. Feeney, , J. Parsons, A. Williamson, Cross correlation between the envelopes of 900 MHz signals received at a mobile radio base station site, *Communications, Radar and Signal Processing, IEE Proceedings F* , vol. 133, 506-512, 1986.

[9] T. Taga, Analysis for mean effective gain of mobile antennas in land mobile radio environments, *IEEE Trans. on Vehicular Technology*. vol. 39, 117-131, 1990.

[10] T. W. C. Brown, Antenna diversity for mobile terminal, Ph.D. dissertation, Univ. Surrey, Surrey, U.K., 2002

[11]A. Diallo, C. Luxey, Estimation of the diversity performance of several two-antenna systems in different propagation environments, *Antennas and Propagation Society International Symposium*, 2642–2645, 2007.

Ionospheric Depletion Detection for Indian SBAS, GAGAN

Prachi Joshi[1], P.R.Mahapatra[2], A.S. Ganeshan[3], S. Nirmala[4]

[12]Indian Institute of Science, Bangalore, India
[34]ISRO Satellite Center, Bangalore, India
*Prachi Joshi, E-mail: prachi@aero.iisc.ernet.in

Abstract

To meet the increasing demand of accuracy, integrity, availability and continuity; the key parameters for satellite based navigation for civil aviation, nations like the US, Europe and Japan have developed and deployed SBAS (WAAS, EGNOS and MSAS respectively). A similar program called GAGAN (GPS Aided GEO Augmented Navigation) has been taken up by the Government of India to provide precision approach service for aircraft operations over the Indian airspace [1]. Ionosphere is made up of free ions which introduce a considerable delay in the passing signal; hence it is the major source of error in GPS measurements. In particular the tropical region is characterized by strong ionospheric disturbances such as depletion and scintillation, which strongly affect SBAS performance. This paper discusses a methodology for real time detection of ionospheric depletion for GAGAN. Sample results of the detection algorithm are presented.

1. Introduction

GPS is a satellite based navigation system which is useful for providing co-ordinates of a user's position. It plays an important role in aircraft, boats/ships and vehicles on ground. Position determination using GPS technology involves calculation of transit time of the electromagnetic signal from the satellite to the receiver. The signal follows a straight line path in vacuum but after entering the earth's atmosphere a number of errors are introduced due to the refractive indices of various layers of the atmosphere. In addition to this there are errors on the measured pseudorange caused due to Ephemeris, Clock, Multipath, Troposphere and Receiver noise, out of which the largest source is the ionosphere, which is more dominant over the equatorial and low latitude regions,

1.1. Ionosphere

Ionosphere ranges from about 60 km to 1000 km above the earth's surface. There are two main processes namely, photo ionization and recombination occurring constantly in the ionosphere [5]. Due to these processes, ionosphere consists of free ions and electrons, which interfere with the electromagnetic signals and introduce a delay.

In the current operating mode of the GPS system, the major source of positioning error is the ionosphere. The delay due to ionosphere is dependent on the integral of the density of electrons along the path of the signal, called the Total Electron Count (TEC). A single-frequency GPS receiver, as used in most civilian applications, needs to estimate the error caused due to the ionosphere in order to remove the delay from the observed total propagation delay. The nature of ionospheric activity varies over day and night. It also varies with latitude of the region. Low-latitude regions (e.g., India, Brazil) have a more dynamic and anomalous ionosphere than the mid (e.g. U.S.) and high-latitude regions. This requires a fresh look at ionospheric behavior for the regional implementation of SBAS (Satellite Based Augmentation System).

2. SBAS: Satellite Based Augmentation System

This is a recent development in the field of navigation. It plays an important role in augmenting the existing GPS technology and improves its accuracy. It provides integrity, continuity and availability to the user.
SBAS employs the following method for correcting errors. There are reference stations with dual frequency receivers built at pre-surveyed locations with known co-ordinates. It is at these reference stations that the pseudo-range and carrier phase at both L1 and L2 frequencies are measured. The measurements are sent to the Master Stations, where errors in the received data like ionospheric delay, ephemeris and clock errors for each GPS satellite are computed. The Master station also computes error bounds for ionospheric delay called Grid Ionospheric Vertical Errors (GIVEs) and for clocks and ephemeris called User Differential Range Errors (UDREs). [3]

The mechanism followed in SBAS for ionospheric corrections is based on the assumption that the ionospheric delay occurs at a hypothetical surface covering the earth at an altitude of 350 km. The surface is divided into a grid of 5°x5° in latitude and longitude and the vertices of this grid are the IGPs (Ionospheric Grid Points). The IPP (Ionospheric Pierce Points) are points where the LOSs for the visible satellites to the receiver crosses this surface. The slant delay calculated over the path of the signal is converted to equivalent vertical delay at the IPPs. The GIVE (Grid Ionospheric Vertical Error) and GIVD (Grid

Ionospheric Vertical Delay), which are respectively the vertical error and delay at IPPs fitted to the grid points, are uplinked to the Geostationary satellites.

GAGAN: Indian SBAS

GAGAN or Geo Aided GPS Augmentation Navigation is an SBAS over the Indian region, which has been taken up in India by Airport Authority and ISRO. It consists of: 15 INRES (Indian Reference Stations), 2 INMCC (Indian Mission Control Centre), 3 INLUS (Indian Navigation Land Uplink Station) and 3 Geostationary satellite payload.

3. Depletion

It is a phenomenon where the plasma density of a region falls below the average plasma density for a certain period and then returns back (or close) to its original value [4]. These are generated due to plasma instability processes in the F region of the ionosphere. As a result, there is a sudden decrease in the TEC in that region, which could affect the accuracy of the error prediction by the SBAS corrections.
Depending on the variations of electron density, the earth's ionosphere can be distributed into three main regions, the equatorial region from +30° to -30° from the equator, the high-latitude beyond 60° towards the poles, and mid-latitude which lies in between both these regions. Of these the equatorial region is the most dynamic region with respect to ionospheric disturbances. Diurnal observations of the ionosphere suggest that depletions are more common during the post sunset period. [6] India lies over the equatorial anomaly region. Hence it is important to study the depletion events over the Indian region and compute their parameters such as depth (maximum decrease in the TEC value) and duration (period for which a depletion event has occurred). A depletion detector has been developed by the authors to study the depletion occurrences over the Indian region.

3.1. Scintillation

Scintillations are rapid fluctuations of the phase and amplitude of satellite radio signals and may have a considerable effect on the performance of satellite geodesy, navigation and communication systems. In the case of GNSS, scintillations may reduce the accuracy of the pseudorange and phase measurements. At times the amplitude scintillation may be so intense that the receiver loses lock to the signal. The magnitude of scintillation along a line of sight can be measured through a parameter called S4 index, which is a function of the signal strength. Scintillations are observed to occur within depletions. Solar activity plays a major role in variations of the total electron count of the ionosphere. Solar maximum conditions have been observed to be associated with high values of scintillation [4]. Effort was made to utilize S4 index to detect the depletions.

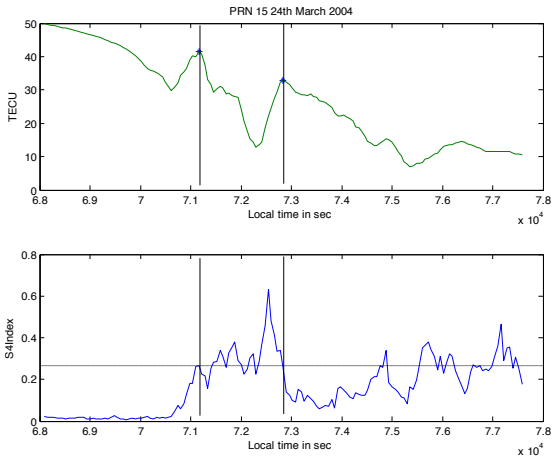


Figure 1: Correlation of S4Index with depletion. S4 Index above 0.25 is considered to be moderate disturbance.

3.1.1. Detection of ionospheric depletion

To study the impact of depletions on the SBAS corrections, it is mandatory to develop a depletion detector and study its behavior over Indian region. An attempt in this direction has been reported in [2] over the South-American region.
A study has been made on an existing real time algorithm for detecting Ionospheric Depletions for SBAS developed in [2]. This algorithm detects the beginning of the depletion using a first derivative check and the end of the depletion using a combination of a first and a second derivative check. This algorithm was implemented and tested, on real TEC data for days with moderate scintillation activity over the Indian region. It detects depletions using the above mentioned thresholds on derivatives. It rejects very small depletions, due to their insignificance to the error contribution for SBAS system and to reduce false detections.
In the adjoining figure, implementation of [2] is made, on a plot with real TEC data recorded by an Indian station on 24th March 2004. The start of the depletion is accurately detected but the end of the depletion is incomplete which is evident from the figure. The Y-axis represents the measured slant TEC for a given line of sight, and the X-axis has local time in seconds.

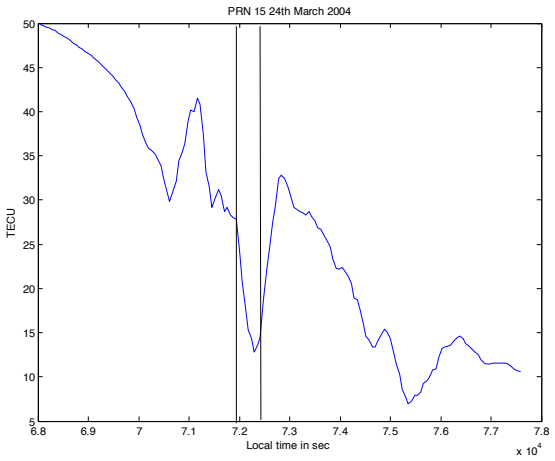


Figure 2: Implementation of the algorithm proposed by [2] on Indian data on 24th March 2004

3.1.2. An improved algorithm for depletion detection

Here an improved algorithm for detecting the beginning and end of significant depletion episodes with high accuracy is being proposed. As the depletion phenomenon manifests itself as a relatively sudden dip in the TEC plot, the algorithm works on this plot to first locate the points of maxima. In principle, all stretches of the TEC plot between two successive maxima should be classified as depletion. However, in order to eliminate rapid, low-amplitude and high-frequency variations of the TEC curve, including noise fluctuations, it is necessary to apply appropriate thresholds to both the TEC variation and its rate. A combination of TEC and TEC-rate thresholds to capture the start and end of those depletion episodes has been evolved. The nature of TEC variation associated with depletion shows a high degree of variability. Additional difficulties arise in case of complex depletion histories such as those with secondary depletions (i.e. depletions within depletions). Our thresholding scheme is able to account for such special cases. Problems also arise due to missing or inaccurate data points on the TEC curve, as these would give rise to false extrema in both amplitude and slope. The algorithm includes mechanisms for handling data dropouts, outliers, and flagged data.

3.1.3. Thresholds used in the algorithm for precise detection

The algorithm uses several thresholds in order to report detection of only significant depletion cases (the significance being dependent on the error contribution to the SBAS of that region). On the basis of our analysis of the depletion patterns over the Indian region, we selected a value to filter out the small fluctuations in TEC. For deciding the range of the slope, the average of all starting slopes of the depletions was computed, which was taken as the minimum value. Similarly the average of the ending slopes of the depletions was computed and plugged in as the maximum value. In addition to these the maxima (peaks) are selected if they happen to be above a certain value to avoid selection of trivial variations of the TEC plot. This criterion is based on the observation that since depletion creates a deficiency of electron count, the TEC value actually rises before the event in order to create that abyss.

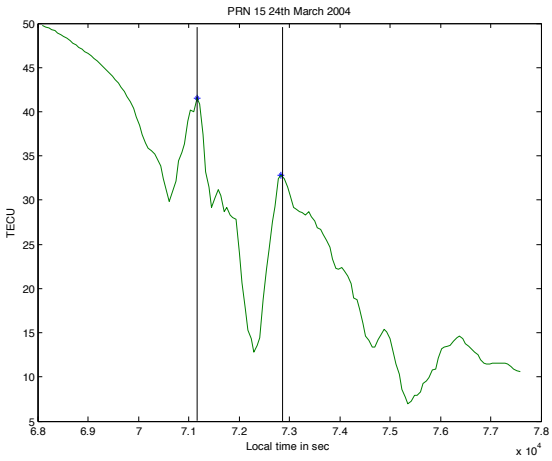


Figure 3: Implementation of the our algorithm on Indian data on 24th March 2004

In the above figure, a plot showing detection of depletion using our improved algorithm is presented. The data is the same as that in Figure 2. Clearly, from the figure the start and end points of the depletion are accurately detected. Here, again the Y-axis represents the measured slant TEC for a given line of sight, and the X-axis has local time in seconds.

3.1.4. Data Handling

Real time data has missing data values due to signal outage or device errors. The data points need to be fitted to a curve in order to compute temporal derivatives and double derivatives of the total electron count. But before that the missing data points need to be interpolated. Here, we have used a sixth order polynomial fit (Gaussian method) to get an appropriate curve fitting for the TEC data. After that the plot has been smoothed using moving average technique.

The figure 4 below shows the plot of TEC vs Time of a particular PRN with data dropouts and outliers. The next plot (Figure 5) shows the same data after it has been fitted and smoothed.

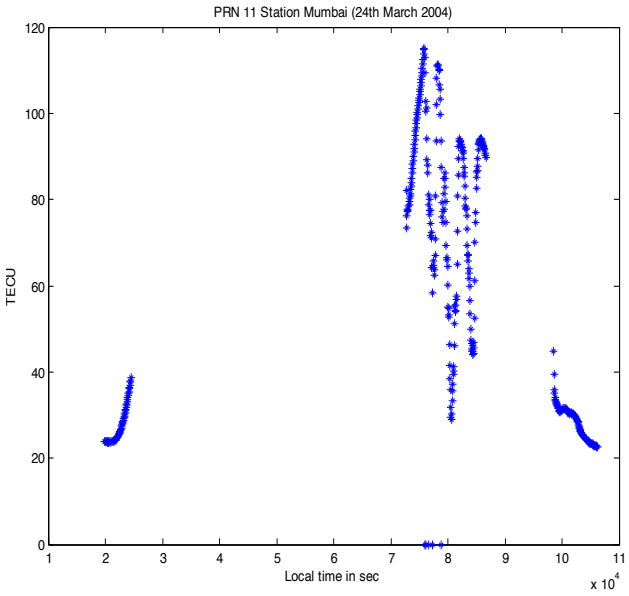


Figure 4: Plot of TECU vs Local time (Mumbai station) with missing data and data outliers on data of 24th March 2004

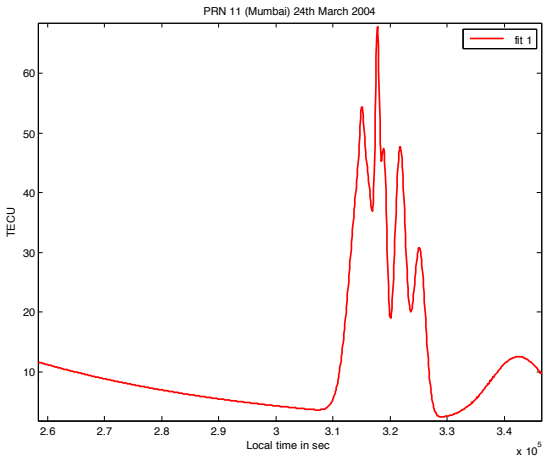


Figure 5: Plot of TECU vs Local time (Mumbai station) on data of 24th March 2004 after curve fitting and smoothing

4. Discussion

Implementation of the detection algorithm requires us to set a few thresholds in order to reject cases of insignificance. The values of these parameters on the basis of the region need to be analyzed and derived with more data. For example, in an equatorial region the depth values may be required to set high owing to more severe ionospheric conditions prevailing there. But if the same values are used for low-latitude regions, the detection algorithm may filter out all the depletions. Also, it is the sensitivity of the ionospheric model which decides the limit of the threshold for a potentially error causing depletion.

The algorithm was tested with real TEC data from various stations over the Indian region. It provides complete detection of depletion (whenever it existed). Nevertheless for a more profound analysis it is required that the algorithm be tested on a larger set of data, with varying threshold values.

5. Conclusions

Given the dynamic nature of ionosphere, occurrence of events like depletions and scintillations that cause the SBAS to give erroneous information, are unpredictable. As the Indian region falls in an area of high ionospheric activity, detection of aberrations which may impact GAGAN performance is of utmost importance. This algorithm can be employed to detect ionospheric depletions automatically, thus, providing it with information to provide accurate error estimation to the user. Using this algorithm the ionospheric characteristics relating to depletion namely, latitude of occurrence, maximum/minimum depth of a depletion and average duration of depletion occurring in a region may also be studied, which would be useful for designing an iono-model for that region.

Acknowledgements

We are deeply grateful to ISAC, Bangalore for providing us insightful information, reading materials relevant to this project and most importantly, real time TEC data to test our work.

References

[1] Kibe, S.V., “Indian plan for Satellite-based Navigation Systems for Civil Aviation,” Curr. Sci., Vol. 84, No. 11,10 June 2003.

[2] Bakry, El-Arini, “Description of a Real-Time Algorithm for detecting Ionospheric Depletions for GNSS/SBAS and the Statistics of Depletions in South America during the Peak of the Current Solar Cycle,” in Serminar on Ionosphere and its Effects on GNSS Systems, Santiago, Chile, 14-16 April 2008.

[3] Suryanarayana Rao, K.N., “GAGAN- The Indian satellite based augmentation system,” IJRSP, Vol. 36, pp. 293-302, August 2007.

[4] Valladares, C.E., Villalobos, R., Sheehani, and Hagan, M.P., “Latitudinal extension of low-latitude scintillations measured with a network of GPS receivers,” AnGeo ., Vol. 22, 3155-3175,2004.

[5] Close, Sigrid, “Introduction to Ionospheric Physics”

[6] Dasgupta, A. , Paul, A. , Das, A. , “Ionospheric total electron count (TEC) studies with GPS in the equatorial region, ” IJRSP, Vol. 36, August 2007, pp. 278-292.

Photonic band gaps in 2D photonic crystals composed of core-shell particles

Amel Labbani* And Abdelmadjid Benghalia

Laboratoire Hyperfréquences et Semi-conducteurs, Faculté des Sciences de l'ingénieur
Université Mentouri, Constantine Route d'Ain El Bey, Constantine 25000, Algérie
*corresponding author, E-mail: labbame@yahoo.fr

Abstract

Photonic crystals (PC's) made of SiO_2 rods covered with air shell layer in 2D hexagonal and square lattices are investigated. We study the different aspects of the complete photonic band gap using the finite difference time domain (FDTD) method. The rods are embedded in TiO_2 background medium with a high dielectric constant. Such photonic lattices present complete photonic band gaps (CPBG).We study the effect of the thickness of the shell layer on these gaps. Our results show that the existence of air shell layer leads to larger complete photonic gaps. We believe that the present results are significant to increase the possibilities for experimentalist to realise a sizeable and larger CPBG.

1. Introduction

During recent years, photonic band gaps (PBG) structure also called photonic crystals (PC's) [1-3] have attracted much interest after the pioneering work of Yablonovitch and John[4,5]. They scatter photons in manner similar to the scattering of electrons in semiconductor. These structures are periodic modulation of dielectric permittivity with lattice spacing comparable to the wavelength of light [6]. One of the most important properties of the PC's is their ability to control and manipulate the propagation of electromagnetic (EM) waves in confined space [1].This will give many applications of photonic crystals, such as waveguides and communication component [7-8]. If the band gap exists for both polarizations and all directions, the crystal is said to have a complete photonic band gap (CPBG). Electromagnetic wave with frequencies within a CPBG is completely reflected since it cannot propagate inside the crystal. Various photonic band gap structures have been manufactured in two (2D) and three dimensions (3D) but for frequencies in both near-infrared and microwave regions. 2D structures have received some increasing attention because they are easier to fabricate than 3D ones and may be employed in optical and electronic devices. The creation of a gap depends on many factors such as refractive index contrast, lattice type, period, and filling factor.

Recently, the studies on the PBG are not limited in the ordinary photonic crystal only. Much attention has thus been drawn towards a new type of photonic crystal. Trifonov et al.[9] have analysed the existence of an interfacial (or cladding) layer affects the properties of the PBG in 2D photonic crystal. Xiao et al,[10] have studied the effect of the variation of a rod's dielectric constant on the PBG in a 2D square lattice. Babin et al [11], have analysed the effect of multi-layers particles on PBG. This new type of composite photonic crystal mentioned above can be called core-shell or rods with cladding.

In this paper, we study the modification of the complete photonic band gap (CPBG) spectrum when the thickness of the shell layer varies. For this study, 2D hexagonal and square lattices of circular SiO_2 rods in TiO_2 matrix have been considered. The rods are covered by thin interfacial layer (air). This investigation aids greatly to design photonic crystals with predefined properties.

Titanium dioxide have attracted much attention in the past as their chemical stability, high refractive index allow their use as components in optoelectronic devices, sensors, and photocatalysts [12].

2. Design parameters of the photonic crystal

To analyse the variation of CPBG size with varying the thickness of the interfacial layer, we consider the following two structures:

i) photonic crystal composed of hexagonal lattice of circular SiO_2 rods surrounded by air in TiO_2 matrix as shown in figure 1(a).
ii) photonic crystal composed of square lattice of circular SiO_2 rods covered by air in TiO_2 matrix as shown in figure 1(b).

Figure 1(c) shows the diagrammatic presentation of regular core-shell rod. Parameters r_c and r_s denote the inner rods and the outer radius of the interfacial layer respectively. The thickness of the shell layer is then $t_s = r_s - r_c$ Parameter a is the space between the centres of two nearest-neighbour rods. Note that $t_s=0$ yields yield rods without interfacial layer.

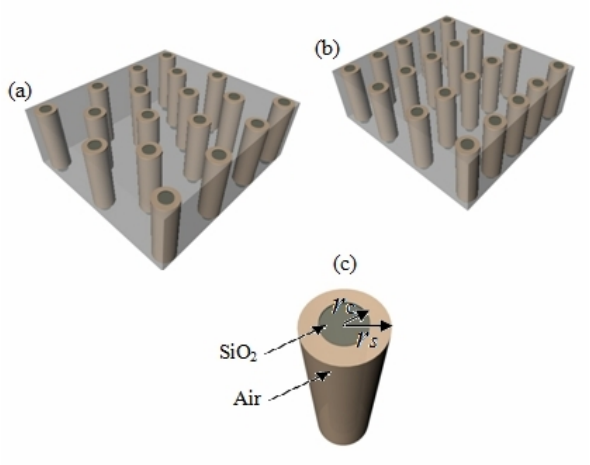


Figure: 1 Schematic representation of the studied 2D core-shell photonic crystal; (a) hexagonal lattice; (b) square lattice; (c) the diagrammatic presentation of a regular core-shell rod.

3. Numerical analysis and results

The photonic bands of 2D photonic crystals were calculated by the finite difference time domain (FDTD) method [12]. The PBGs for TE and TM polarization modes were calculated along the Γ-M-K- Γ edge for the Brillouin zone.

3.1. Hexagonal lattice

We start our study by calculating band structures of circular rods in TiO_2 matrix with hexagonal structure. First we consider that SiO_2 rods with radius r=0.46a are not covered by air layer (t_s= 0).

Parameters ε_{Sio2} and ε_{TiO2} denote the dielectric permittivity of SiO_2 and TiO_2 respectively. The values of the parameters are: ε_{Sio2} = 2.13 ε_{TiO2}=9 at λ = 520nm. Results are presented in terms of frequencies $wa/2\pi c$, where a is the lattice constant, c the speed of light in a vacuum and , λ the vacuum wavelength.

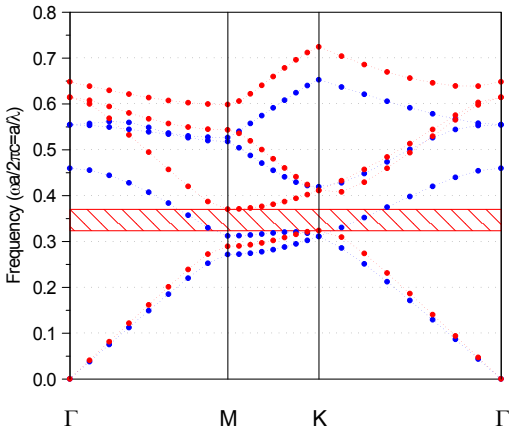


Figure 2: Photonic band structure for hexagonal lattice of circular SiO_2 rods in TiO_2 matrix.

Figure 2 shows that there is one gap for TM modes extends from 0.3230 ($\omega a/ 2\pi c$) to 0.3698 ($\omega a/ 2\pi c$), with $\Delta w/w_g$ = 13.5%, and there is no gaps for TE modes.

No let us consider that the air layer exists between the SiO_2 and TiO_2 matrix. The internal radius and the thickness of the shell layer are r_c = 0.08a, t_s = 0.36a respectively.

The band diagram is plotted in Fig. 3(a). Only one CPBG exists and its relative width of $\Delta w/w_g$ = 1.73%, where Δw and w_g are the frequency width and the middle frequency of the gap, respectively. Let's consider now the external radius r_s = 0.455a, t_s = 0.375a and r_c remains constant. Figure 3(b) shows the dispersion relation of this structure. As can be seen, the CPBG exists and its relative width is $\Delta w/w_g$ = 2,93%. The obtained results show that Δw increases when the thickness of the air layer between the rods and TiO_2 increases.

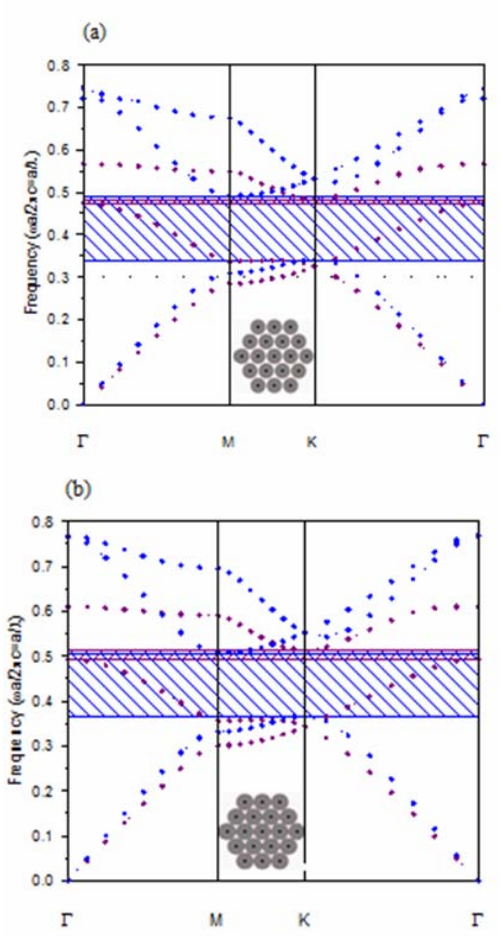


Figure 3: Photonic band structure for TE and TM polarization modes in 2D hexagonal lattice of SiO_2 rods covered with air shell layer for (a) t_s = 0.36a (b) t_s =0.375a.

3.2. Square lattice

In this section, PCs with a square lattice is considered. This configuration is analogous to the one described above except for a square lattice. First of all we consider the case where there is no shell layer. Similar to the previous case there is no CPBG.

We can see from Fig.4 that there is only one tiny photonic band gap in TE polarization modes in the frequency ranges of 0.2630 ($\omega a/ 2\pi c$) and 0.26954 ($\omega a/ 2\pi c$), with $\Delta w/w_g$ =2.45%, and there is no gaps for TM modes.

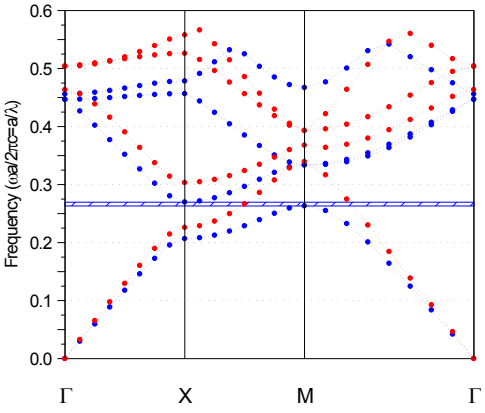


Figure 4 : Photonic band structure for square lattice of circular SiO_2 rods in TiO_2 matrix.

We think it would be interesting to see how the shell layer thickness affects the CPBC with square lattice structure of SiO_2 rods covered by a thin air layer.

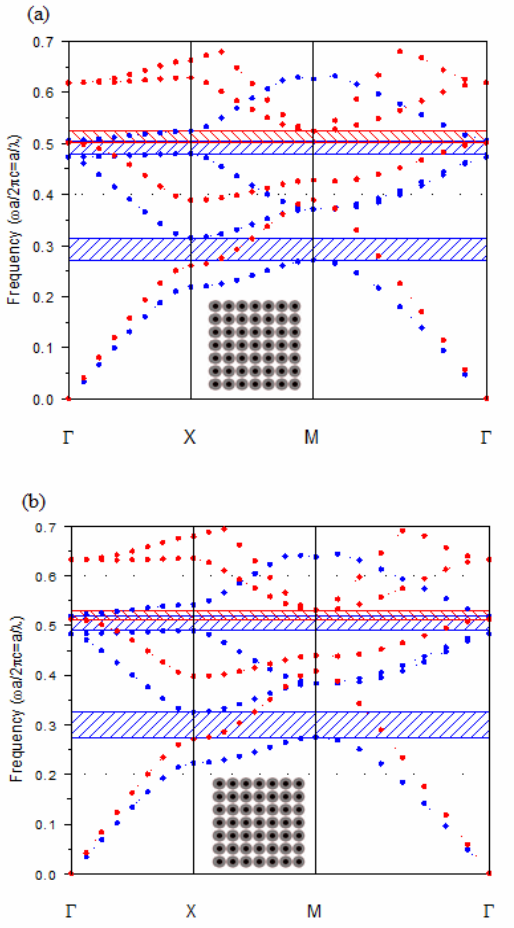


Figure 5: Photonic band structure for TE and TM polarization modes in 2D square lattice of SiO_2 rods covered with air shell layer for (a) t_s = 0.428a (b) t_s = 0.435a.

We have calculated the PBG for the square arrangement of SiO_2 core - air shell particles as shown in Fig. 1(b). For r_s = 0.468a and t_s = 0.428a, only one tiny CPBG is found in the frequency range (0.50518-0.50085)$\omega a/2\pi c$. Photonic band calculations demonstrated that for r_s = 0.475a, and t_s = 0.435a, the value of $\Delta w/w_g$ = 11.25%. Figure 5 (a) clearly illustrate that the width is reduced from that in Fig. 5 (b). After calculations we found that the thickness of the interfacial layer leads to improvement of width of CPBG.

4. Conclusions

Complete photonic band gaps in 2D hexagonal and square lattices considering an interfacial layer between the SiO_2 rods in TiO_2 matrix have been studied.

Our results show that changing the thickness of the shell with respect to the core, one can tune and control the CPBG. Hence it seems that the full PBG width is affected by the shell layer thickness. The relative width of CPBG increases with increasing the shell layer thickness. Therefore the existence of the air shell layer causes an enlargement in the CPBG. Therefore, in order to obtain the largest CPBG, we should suitably choose the thickness of the air shell layer.

References

[1] J.D. Joannopoulos, S. G. Johnson, J. N. Winn, and R. D. Meade, *Photonic Crystals: Molding the Flow of Light*, Princeton : Princeton University Press, 2008.

[2] C.M. Soukoulis, *Photonic Band Gaps and Localization*, Proceedings of the NATO ARW, Plenum, New York, 1993.

[3] J. D. Joannopoulos, P. R. Villeneuve and S. Fan, Photonic crystals: putting a new twist on light, *Nature*, pp. 143-147, 1997.

[4] E. Yablonovitch, Inhibited spontaneous emission in solid-state physics and electronics, *Phys. Rev. Lett.* pp. 2059-2061, 1987.

[5] S. John, Strong localization of photons in certain disordered dielectric superlattices, *Phys. Rev. Lett.* pp. 2486-2488, 1987.

[6] K. Sakoda, *Optical Properties of Photonic Crystals*, Springer, Berlin, 2001.

[7] P.E. Barclay, K. Srinivasan, O. Painter, Design of photonic crystal waveguides for evanescent coupling to optical fiber tapers and for integration with high-Q cavities, *Journal of the Optical Society of America B-Optical Physics*, pp. 2274-2284, 2003.

[8] P.E. Barclay, K. Srinivasan, M. Borselli, O. Painter, Efficient input and output fiber coupling to a photonic crystal waveguide, *Optics Letters*, pp. 697-699, 2004.

[9] T. Trifonov, L. F. Marsal, A. Rodríguez, J. Pallarès, and R. Alcubilla, Analysis of photonic band gaps in two-dimensional photonic crystals with rods covered by a thin interfacial layer, *Phys. Rev. B*, pp. 195108, 2004.

[10] H. Xiao, D.Z. Yao and C.X. Wang, Analysis of the peculiar shift of the low-frequency end of a variable photonic band gap, *Appl. Phys. B*, pp. 463-467, 2007.

[11] V. Babin, P. Garstecki and R. Hołyst, Multiple photonic photonic band gaps in the structures composed of core- shell particles. J. Appl. Phys. pp.4244, 2003.

[12] P. Chrysicopoulou, D. Davazoglou, Chr. Trapalis and G. Kordas, Optical properties of very thin (<100nm) sol-gel TiO_2 films, *thin solid films*, pp. 188–193, 1998.

[13] A. Taflov, S. C. Hagness, *Computational Electro--dynamics: the finite-difference time- domain Method*, 2 edition, Boston: Artech House Publishers, 2000.

High-voltage Tesla coil discharges guided and triggered by femtosecond laser filaments in air

Yohann Brelet[1], Aurélien Houard[1], Benjamin Forestier[1], Yi Liu[1], Bernard Prade[1], Jérôme Carbonnel[1], Yves-Bernard André[1] and André Mysyrowicz[1,*]

[1]Laboratoire d'Optique Appliquée, ENSTA ParisTech-Ecole Polytechnique-CNRS, 91761, Palaiseau, France
*corresponding author, E-mail: andre.mysyrowicz@ensta-paristech.fr

Abstract

Triggering and guiding of Tesla coil high-voltage sparks discharges in air with plasma filaments generated by femtosecond laser pulses are demonstrated experimentally. Sparks discharges are established between a high-voltage electrode (HVE) fixed at the top of the Tesla coil resonator and a second electrode connected to the ground. We have observed meter long guided sparks discharges when the plasma column created by an intense femtosecond laser beam connects both electrodes.

1. Introduction

Intense ultrashort laser pulses propagating through atmosphere give rise to spectacular non-linear effects. Owing to a dynamical competition between non-linear optical Kerr self-focusing, and multiphoton ionization induced defocusing, a contracted beam of high peak intensity is formed over long distances. It leaves in its wake a long thin column of weakly ionized plasma (electron density ~ 10^{16} cm^{-3}). This process is usually referred to as filamentation [1]. Filaments are of great interest for remote guiding and triggering of high voltage discharges. It has already been reported that electric discharges triggered by such straight conductive plasma columns can carry high currents with reduced losses [2]. The guided discharge plasma columns can also find an application as virtual plasma antennas for RF transmission [3].

In this paper, we report experiments of laser guided discharges obtained in air by high voltage bursts delivered by a compact Tesla coil. In a first part, we briefly present a review of Tesla coil theory, together with computational results. In a second part, we describe our compact Tesla coil and show that it operates according to the theory. Finally, we show results concerning long laser triggered electric discharges in air.

2. Background description

The experimental setup is illustrated in Fig. 1. The fs laser is a Ti:Sapphire Chirped-Pulse Amplification chain [4] delivering pulses of 300 mJ energy at 800 nm with a repetition rate of 10 Hz. In our experiments, the 50 fs pulse is stretched temporally to 700 fs in order to avoid damages on steering mirrors and focusing lens.

The discharges are generated with a home-made Tesla coil consisting in an elevator transformer. The coupled resonance of the two series R L C circuits (see Fig. 2) at radiofrequencies allows obtaining voltage burst with amplitude of 250 kV at the output.

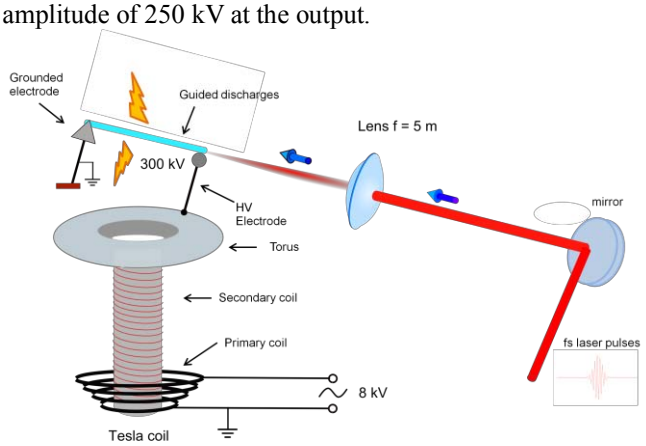


Figure 1: Experimental setup. Our Tesla coil delivers voltage up to 250 kV. The fs laser beam is focused and aligned to be in contact with the high voltage electrode.

In the following, index values i = 1 and 2 denote the primary and secondary circuit respectively. The primary circuit is constituted of C_1, R_1, L_1 and the secondary circuit is composed of C_2, R_2, L_2. Two cycles of operation are observed. First, the capacitor C_1 is charged to a potential V_C supplied by a HV generator which can deliver a voltage up to 8 kV.

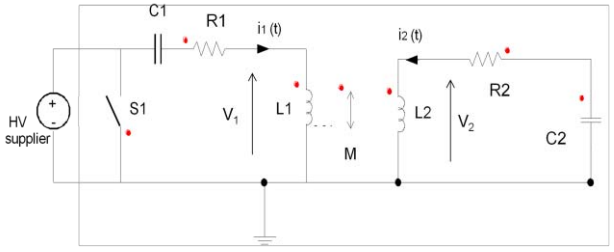


Figure 2: Coupled resonant RLC lumped circuits describing a classical Tesla coil.

Then, when switch S_1 closes, C_1 discharges through the primary circuit and a free oscillatory behavior of the Tesla coil is launched via the magnetic flux represented by the

mutual inductance M. This initializes HV discharges from the tip of the electrode on the torus top end (see Fig. 1). Our Tesla coil is built with the following component values: $C_1 \approx 38$ nF, $L_1 \approx 60$ µH, $C_2 \approx 48$ pf and $L_2 \approx 50$ mH, such that both circuits are tuned to the same resonance frequency,

$$f_2 = f_1 = \frac{1}{2\pi\sqrt{L_1 C_1}} = 105\,kHz.$$

The transformation ratio of the Tesla is of about 25-30, meaning that its output delivers nearly 250 kV.

In Fig. 3, we show a sequence of photographs realized with the original Tesla coil built with a mechanical rotary switch S_1. Laser beam propagates from left to right. One can clearly see a well-formed ~ 1 m long forward guided discharge between the HVE of the Tesla coil and the grounded electrode. The drawback of this configuration is the important jitter (>100-200 µs) of the mechanical rotary switch used in the circuit.



Figure 3: Femtosecond laser-induced guided discharges at t = {33, 66, 133} ms, from top to bottom. HV discharges are initialized by the origin rotary spark gap.

For the experiments we have in mind, it is imperative to reduce the jitter to synchronize the Tesla with the discharge triggering laser pulse. In the following subsection, we present a practical realization of the switch S_1 represented in Fig. 2.

2.1. Solid state switch

A convenient solution consists in implementing a solid state electronics device. This allows stable repetitive formation of guided discharges since the laser pulse arrival time can be tuned to the maximum of the voltage on the secondary Tesla loop. It is based on a push-pull triac configuration of two thyristors allowing transmission of high alternating currents occurring in the cycle where C_1 supplies its stored energy in the primary circuit (see Fig. 4).

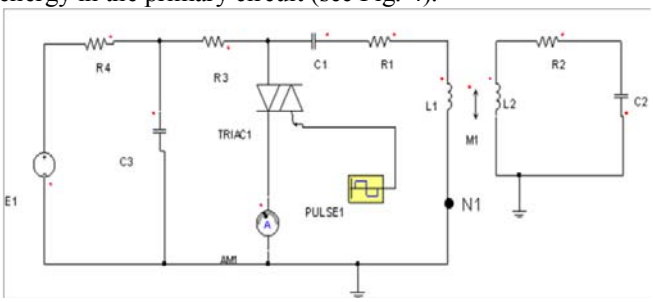


Figure 4: Electrical scheme of our Tesla coil. Low-Pass RC filter is constituted of {R_3 = 20 kΩ; R_4 = 20 kΩ; C_3 = 180 nF}. E_1 is a 30 kV-30 mA DC bias supply. Triac is turned on with the laser trigger pulse on its gate. A is a classical Rogowski current probe giving waveform of $i_1(t)$ as it will be shown later for instance.

Furthermore, to avoid any high-frequency feedback currents due to the short-circuit when S_1 closes, , we added a RC low-pass filter towards the DC supply, as shown in Fig. 4.

3. Tesla coil theory and experimental verification

In this section, we give a brief model of Tesla coil systems. By applying Kirchhoff's rule to the loops appearing in Fig. 2, we establish a system of two differential equations coupling the currents $i_1(t)$ and $i_2(t)$:

$$\begin{aligned} &\frac{1}{C_1} i_1(t) + R_1 \frac{di_1(t)}{dt} + L_1 \frac{d^2 i_1(t)}{dt^2} + M \frac{d^2 i_2(t)}{dt^2} = 0, \\ &\frac{1}{C_2} i_2(t) + R_2 \frac{di_2(t)}{dt} + L_2 \frac{d^2 i_2(t)}{dt^2} + M \frac{d^2 i_1(t)}{dt^2} = 0, \end{aligned} \qquad (1)$$

where $M = k\,(L_1 L_2)^{1/2}$ is the mutual inductance and $k \approx 0.2$ is the coupling coefficient. Solving these coupled equations with appropriate initial conditions [5], we obtain a closed solution form in good agreement with a Runge-Kutta numerical integration.

In the absence of secondary circuit, the primary voltage and current oscillate at their own frequency $\omega_1 = 1/\,(L_1 C_1)^{1/2}$ defined by the lumped elements of the primary circuit as defined above. When the secondary circuit is included, energy is coupled from the primary to the secondary circuit. Once the whole energy is transferred, the process reverses and energy goes back to the primary circuit. This free

energy oscillation between the two circuits runs until S_1 opens or until damping due to losses cancels the energy. From an electromagnetic point of view, it has been shown that the Tesla structure radiates energy like a resonant dipole antenna, and the field distributions of the Tesla coil possess characteristics of helical resonators [6].

In Fig. 5 we compare the primary current $i_1(t)$ measured with a Rogowski coil, and the numerical solution of Eqs (1).

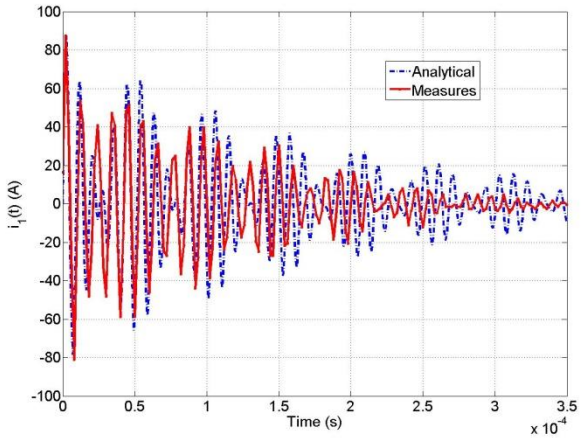


Figure 5: Temporal waveform of i_1 in the primary circuit of the Tesla coil over the range $t \in [0; 350]$ µs and computed with a measure and the closed solution of Eqs (1). C_1 is initially charged at the potential $Vc \approx 4$ kV DC.

The two curves are in very good agreement and show that the signal decays at a rate determined by the quality factor $Q_i = 1/ R_i \times (L_i/ C_i)^{1/2}$ of the circuits. Fig. 6 displays the spectrum of the temporal waveforms $V_1(t) = -L_1 di_1/dt$ both from numerical solution of Eqs (1) and from measurement. The two characteristic frequencies, corresponding to the envelope and the carrier appear at 95 kHz and 115 kHz, and lie on either side of the central resonant frequency $\omega_r \approx 105$ kHz.

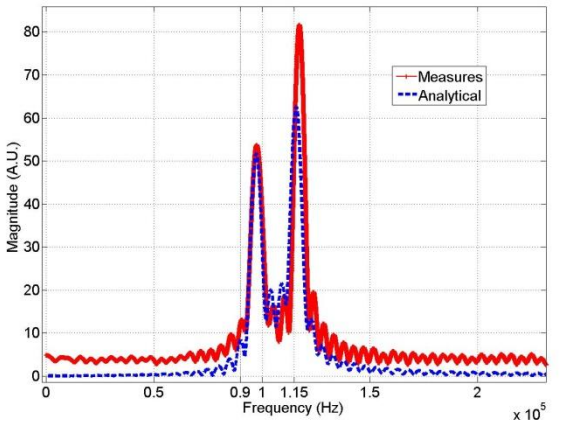


Figure 6: Spectrum of the temporal waveform $V_1(t) = -L_1 di_1/dt$, where $i_1(t)$ is shown in Fig. 5.

Fig. 7 gives the computed temporal waveform of the output voltage of the Tesla coil. As expected, the output signal is also amplitude modulated, with a phase shift of the current, due to inductive behavior. The peak value reaches ~200 kV and corresponds to the potential reached at the tip of the high voltage electrode. Note that the highest voltage is reached during the first beat envelope after a delay of ~ 25 µs.

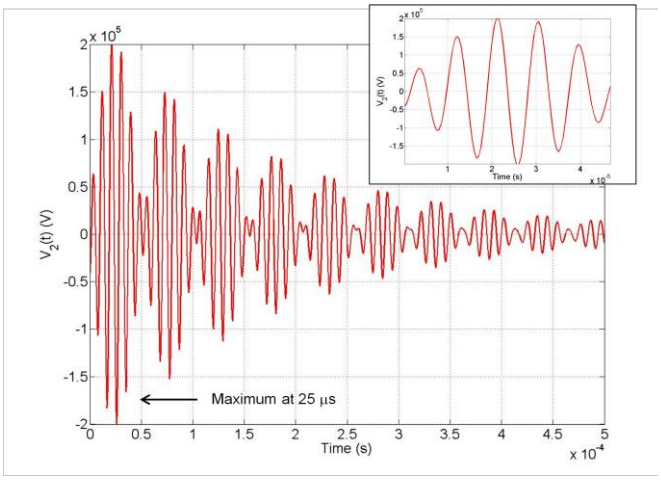


Figure 7: Temporal waveform of $V_2(t)$ voltage at the output of the Tesla coil over the range $t \in [0; 500]$ µs and computed with the closed solution of Eqs (1). Input voltage $Vc = 8$ kV DC. Inset is a zoom at $t \in [0; 50]$ µs.

4. Experimental results with spontaneous discharges

First, experiments were conducted without laser, to ensure that the triac works with spontaneous discharges bridging the gap between HVE and grounded electrode. To switch S_1 on, we send a TTL rising edge to the gate of the triac.

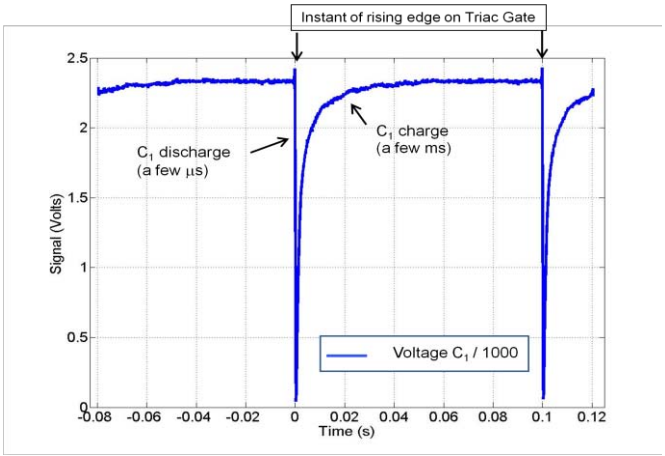


Figure 8: Tesla coil typical voltage measured at C_1 terminals. F = 10 Hz. $Vc \approx 2$ kV DC.

The voltage in the primary circuit was recorded with a North-Star HV high impedance probe (400 MΩ).
The HV probe connected to the C_1 terminals returns its typical voltage as displayed in Fig. 8. Two cycles of charge/

discharge of C_1 are shown. We are able to control easily the frequency and the starting time of the HV discharges with an accuracy of a few hundreds of ns.
In order to overcome the difficulty of measuring the very high voltage in the secondary circuit [7], we placed a remote (~ 1.8 meter) copper disk with 80 mm diameter, acting like a receiver antenna, and connected to an oscilloscope.
Fig. 9 is a trace of the typical electric field produced by the Tesla coil and recorded with the antenna. As discussed in the theory section, it shows that maximum output voltage occurst 25 µs after C_1 discharge has begun. The measured waveform is in good agreement with the calculation.

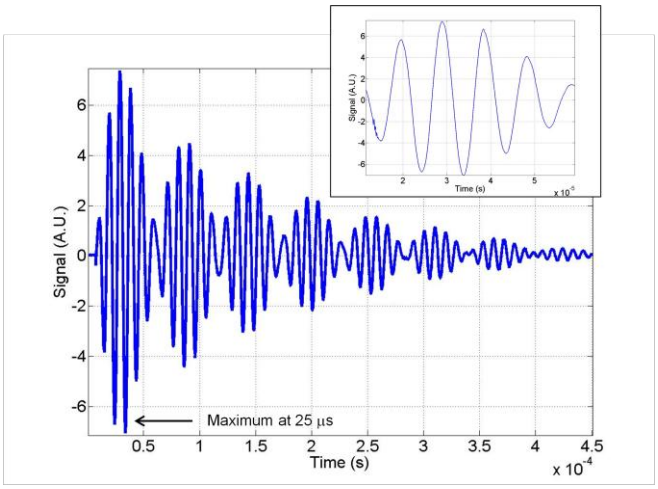


Figure 9: Signal emitted by the Tesla coil and capture with the antenna. Illustration of the normal output voltage. Input voltage Vc ≈ 7 kV DC (just below threshold) and D ≈ 16 cm. Inset is a zoom at t ∈ [0; 50] µs.

In Fig. 10 by contrast, one can clearly see that when a natural HV discharge occurs, the energy stops ringing between primary and secondary circuits of the Tesla coil. Its EM radiation is turned off at the first beating because the whole energy is released towards the ground through the ionized channel defined by the spontaneous HV discharge.

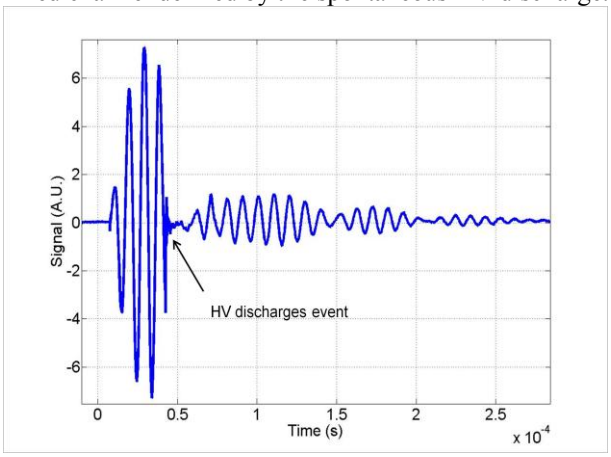


Figure 10: Signal emitted by the Tesla coil and capture from the antenna. Illustration of the output voltage when a HV discharge is initiated. Input voltage Vc ≈ 7 kV DC (just above threshold) and D ≈ 16 cm.

This result means that guided HV discharges can carry high power, and should show interesting abilities in antennas applications, for instance.

4.1.1. *Guided and triggered discharges*

To synchronize the laser pulse we used a photodiode sensitive to 800 nm. This signal displayed on the oscilloscope is used as a time reference, enabling to adjust the delay of the gating signal applied to the triac.

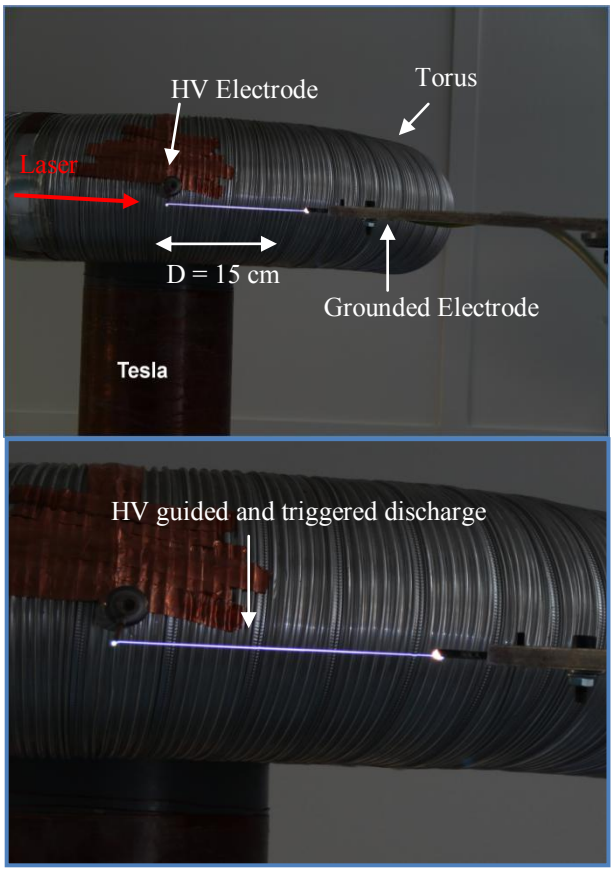


Figure 11: Femtosecond laser-induced guided and triggered discharge. D = 15 cm between electrodes. Overview description (top) and zoom (bottom). HV discharges are initialized by the solid-state switch. Vc ≈ 6 kV DC.

We optimized the triggering of HV discharges in such a way that laser pulse bridges the gap between the electrodes when the voltage across the secondary circuit has peaked, i.e. 25 µs in our Tesla coil system. Hence, the triac S_1 must be set on 25 µs before the laser pulse arrival on the HVE tip. Therefore, precise adjustement of this delay between the laser beam arrival at HVE tip and S_1 closing is empirically done, such that maximum voltage is collected by the laser induuced plasma filaments to the remote grounded electrode.
Results displayed in Fig. 11 are time-integrated images of the visible radiation emitted by the HV guided discharges, recorded perpendicularly to the laser beam transverse direction with a standard CCD camera. The primary voltage

was held at Vc ≈ 6 kV DC. These photographs exhibit a fully developped and perfectly straigth HV triggered discharge channel along the laser propagation direction, with a gap of, and performed with a 300 mJ, 700 fs IR laser pulse at 10 Hz repetition rate. The gap D = 15 cm between the electrodes is entirely bridged.
Several remarks can be made. First, the typical Tesla coil EM radiation shown in Fig. 9 is quenched when an HV guided and synchronized discharge appears, leading to the same waveform as in absence of laser filaments (as depicted in Fig. 10). Next, the HV guided discharge takes place within a few μs after laser has entered the HV gap region. This behavior is consistent with ref. [8]. Lastly, the breakdown voltage threshold is significantly reduced due to the pre-ionization of the air gap by the laser induced plasma filaments.

Understanding of mechanisms of formation (laser connection with negative-positive leader, depending on the polarity of the HVE) of those HV guided discharges has been performed by several groups through previous experiments with streak cameras [8-9]. But, the guiding and triggering of HV discharge being a complex interplay between plasma physics, hydrodynamic and air chemistry processes, it has yet to be examinated.
We also note that weaker backward guided HV fragrances have been observed. This phenomenon exists mainly because filaments are produced even several tens of centimeters before the lens focus [10], which is set here at the HVE tip. Pictures also indicate that laser induced plasma filaments enhances the luminence of the discharges, as compared with unguided spontaneous discharges. Finally, once the delay was accurately adjusted, we measured a probability of guided and triggered HV discharges higher than 80 % at the laser 10 Hz repetition rate.

5. Conclusions

In this paper, we have covered a descriptive overview of a Tesla transformer and have compared solutions from the governing coupled differential equations describing the Tesla circuit with experimental measures.
Preliminary discharges generated with the Tesla coil built with a rotating spark gap device and guided with laser induced plasma filaments have been presented. Since precise triggering of the HV burst was not possible with the latter rotary device, we implemented an alternative solution based on a solid-state semiconductor element. We have then described an efficient and helpful bench Tesla coil HV discharges, controlled by the solid-state component, and guided and triggered by fs laser induced plasma filaments.

Acknowledgements

This project is supported by the French Direction Générale de l'Armement (grant n° 2007 95 091). The authors would also like to thank F. Galet and J. E tivant for their technical assistance.

References

[1] E. T. Nibbering, P. F. Curley, G. Grillon, B. Prade, M. Franco, F. Salin and A. Mysyrowicz, Conical emission from self-guided femtosecond pulses in air, *Opt. Lett.* 21 (1): 62-65, 1996.

[2] A. Houard, C. D'Amico, Y. Liu, Y. B. André, M. Franco, B. Prade, A. Mysyrowicz, E. Salmon, P. Pierlot, and L. M. Cleon, High current discharges in air induced by femtosecond laser filamentation, *App. Phys. Lett.* 90 (17), 2007.

[3] B. Forestier *et al.*, Radiofrequency conical emission from femtosecond filaments in air, *Appl. Phys. Lett.* 96: 141111-141113, 2010.

[4] D. Strickland and G. Mourou, Compression of amplified chirped optical pulses, *Opt. Commun.* 56: 219−221, 1985.

[5] K. D. Skeldon, A. I. Grant and S. A. Scott, A high potential Tesla impulse generator for lecture demonstrations and science exhibitions, *Am. J. Phys.* 65 (8): 744−754, 1997.

[6] K. L. Corum and J. F. Corum, RF coils, helical resonators and voltage magnification by coherent spatial modes, *Micro. Revija.* : 7:36−44, 2001.

[7] D. G. Bruns, A solid-state low-voltage Tesla coil demonstrator, *Am. J. Phys.* 60 (9): 797−803, 1992.

[8] T. Fuji, M. Miki, N. Goto, A. Zhidkov, T. Fukuchi, Y. Oishi and K. Nemoto, Leader effects on femtosecond-laser-filament-triggered discharges, *Phys. Plasmas* 15: 0131071−0131075, 2008.

[9] R. Ackermann *et al.*, Influence of negative leader propagation on the triggering and guiding of high voltage discharges by laser filaments, *Appl. Phys. B* 82: 561−566, 2006.

[10] M. Rodriguez *et al.*, Triggering and guiding megavolt discharges by use of laser-induced ionized filaments, *Opt. Lett.* 27 (9): 772−774, 2002.

Femtosecond laser filament guided electric discharge as an RF plasma virtual antenna

Benjamin Forestier[1], Aurélien Houard[1*], Yohann Brelet[1], Jérôme Carbonnel[1], Bernard Prade[1], Yves-Bernard André[1], Michel Pellet[2] and André Mysyrowicz[1]

[1] Laboratoire d'Optique Appliquée, ENSTA ParisTech, Ecole Polytechnique, CNRS, 91761 Palaiseau, France.
[2] Ministère de la Défense, F-00457 Armées, France.
[*]corresponding author, E-mail: aurelien.houard@ensta-paristech.fr

Abstract

We demonstrate the coupling of a radiofrequency signal into a guided atmospheric discharge initiated by a femtosecond laser filament. The radiation efficiency of this virtual plasma antenna is compared to a classic copper monopole of same dimension.

1. Introduction

Plasma antennas have been studied since the 70s for radiofrequency telecommunications applications in the domain of defense [1]. Those virtual antennas are generally monopole antennas in which the radiating element is a plasma column obtained in a low pressure discharge tube filled with noble gas. The main drawback in this scheme lies in the presence of the tube which limits the stealth of the antenna. An interesting alternative has been demonstrated by Dwyer *et al*., who used a nanosecond laser to initiate a long atmospheric discharge plasma column and demonstrate emission at 112 MHz [2]. To improve the concept, the use of femtosecond lasers associated with the formation of plasma filaments seems promising. Indeed, contrary to a nanosecond setup presented in [2] where laser energy of 15 J/m was needed to guide a discharge, using femtosecond pulses reduces this energy to 0.12 J/m allowing the prospect of long monopole antenna.

When powerful laser pulses with femtosecond duration is loosely focused in air, a long and uniform weakly ionized plasma string is produced in a process called filamentation. Laser energy loss during filamentation is small since the intensity in the filament core is clamped close to the minimum required for ionization while the short pulse duration prevents reabsorption by the self generated plasma [3]. The resulting plasma is much longer and continuous than the one produced with nanosecond pulse, and the energy necessary is also considerably reduced [4].

In this work we first demonstrate the coupling of a radiofrequency signal inside the high conductivity plasma column formed by the laser guided discharge. In a second phase we show that the plasma column can radiate this injected signal, behaving like a monopole emitting antenna.

2. Experimental setup

The ENSTAmobile laser was used to create the plasma filament in air. This Chirped Pulse Amplified laser chain can deliver nominally 50 fs pulses with a peak power of 7 TW at a repetition rate of 10 Hz. In this experiment the laser beam with energy of 250 mJ and pulse duration of 350 fs was focused in air by a 3 m focal convex lens. A continuous plasma column of 50 cm was then formed in air around the geometrical focus of the beam. This weakly ionized plasma column has an electron density of 10^{16} e^-/cm^3, and a recombination time of about 10 ns.

The filament plasma column was used to trigger a reproducible and perfectly linear electric arc with high conductivity. The discharge was obtained by applying DC voltage of 40 kV between two sharp metallic electrodes separated by 50 mm. The filaments were touching both electrode tips to close the circuit. The low density plasma from the filament served as a precursor and preferential path for the electric arc [4-5]. It decreased the breakdown voltage by ~30%.

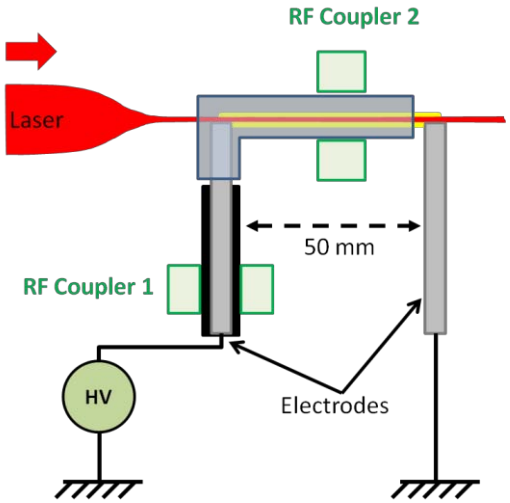


Figure 1: Experimental setup. Laser guided discharges are obtained inside a glass tube, between the two metallic electrodes separated by 50 mm.

Two different couplers were used in the experiment to inject or to detect RF signal in the circuit. Coupler 1 consists in a metallic coil of few turns placed around the high voltage cable. Coupler 2 is a resonant inductive cavity similar to the one described in ref [6]. Coupler 1 presents a higher coupling efficiency between 100 MHz and 1 GHz but it radiates strongly, making the characterization of the plasma radiation difficult, while coupler 2 is shielded and does not emit any radiation by itself. A glass tube was added around the discharge gap to avoid direct arcing on RF coupler 2 (see blue cylinder in Fig. 1).

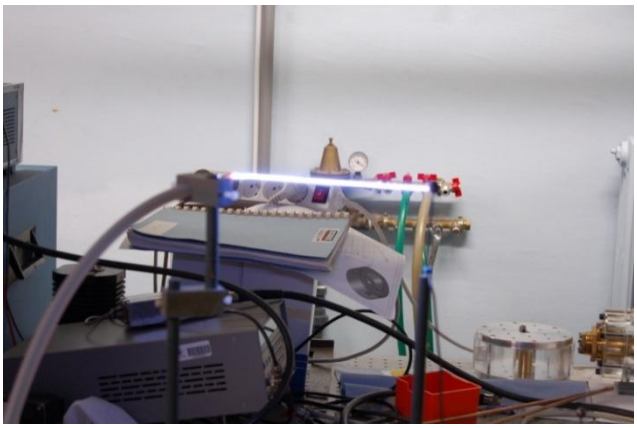


Figure 2: Picture of a filament guided electric discharge of 20 cm, obtained with an applied voltage of 50 kV.

3. Results

3.1. Coupling RF signal inside the plasma

In the first experiment we checked that a RF signal could be injected inside the laser guided plasma discharge. A continuous signal at 1 GHz with 2W power was injected through coupler 1, while coupler 2 was connected to a fast oscilloscope with a 1 GHz bandwidth. The measured signal is presented in Fig. 3 (red curve). The laser filament was formed between the electrodes at time t = 0 s, initiating the discharge within a few 100 ns. As described in ref [6], coupler 2 is equivalent to a derivative current monitor with a maximum efficiency at 1.5 GHz. The measured signal is then related to the current circulating inside the plasma. At t = 0 s the current presented slow oscillations corresponding to the development of the discharge. These oscillations are rapidly damped after 1 µs, but a 1 GHz modulation on the signal remains for almost 10 µs.
To observe more clearly this modulation a frequency filter at 1 GHz with a 10 MHz bandwidth was applied to the signal. The result is presented in Fig. 3 (black curve). On can clearly see the amplification of the 1 GHz component at t = 0 s followed by a slow decay over 10 µs. This slow decay corresponds to the lifetime of the arc, limited by the power supply energy storage capacity.

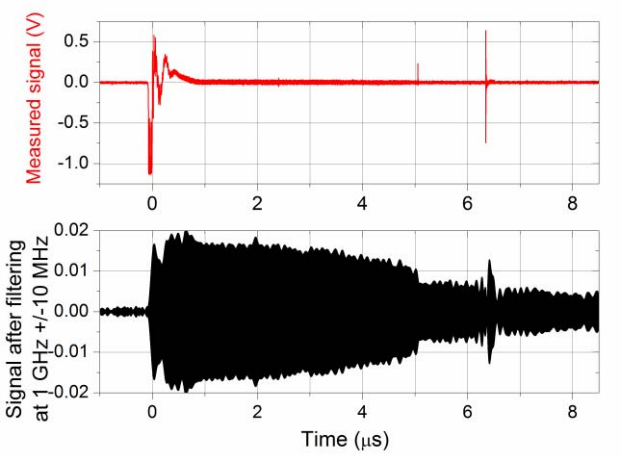


Figure 3: Current measured inside the plasma during the discharge when a 1 GHz signal is injected with coupler 1 (top). Same signal after application of a frequency filter at 1 GHz with a 10 MHz bandwidth (bottom).

The spectrum of the current signal obtained by direct Fourier transformation is also presented in Fig. 4. The injected 1 GHz component is again clearly visible.
Other measurements have been made in the same conditions with a signal at 0.5, 0.8 and 1.1 GHz showing a similar behavior.

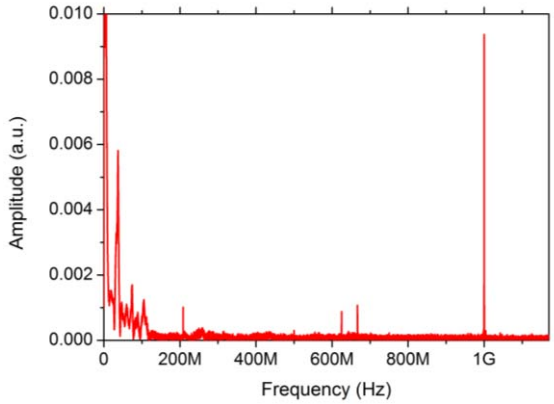


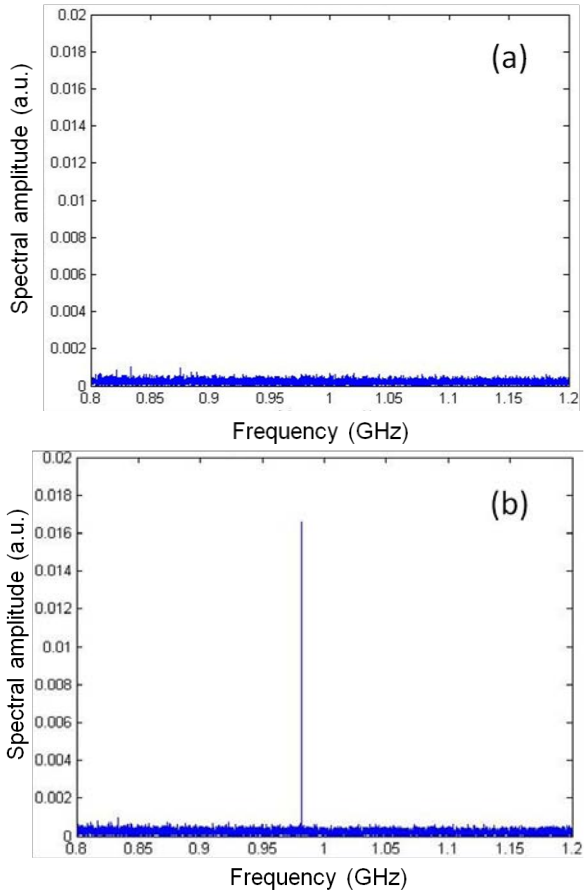
Figure 4: Spectrum of the current signal presented in Fig. 3 obtained by Fourier transformation.

3.2. RF Emission from the plasma antenna

In the second experiment the emission from the high density plasma column seeded by the RF signal has been characterized. For this experiment, to minimize radiation from the high voltage cables, coupler 2 was used to inject the signal directly inside the plasma antenna. Detection of the radiated signal was performed with a planar integrated antenna (described in ref [7-8]) placed 1.5 m away from the plasma emitting antenna. The frequency of the injected signal was 0.97 GHz.
The spectrum of the antenna signal in the frequency range 0.8 – 1.2 GHz is presented in Fig. 5. Fig. 5(a) shows the measured spectrum when the RF generator and the high voltage were operating, but no laser filament was present to initiate the discharge. Fig. 5(b) shows the measured

spectrum when the filament initiated the high density plasma column. A significant noise due to the discharge is present over the whole frequency range, but the injected RF component at 0.97 GHz is clearly observed. For comparison, a measurement has been made replacing the plasma column by a copper tube of 50 mm length equivalent to a monopole antenna (Fig. 5(c)). We find that the plasma column emission efficiency is about 4 times smaller than the one of the metallic monopole antenna.

The main limitation in the experiment was related to the apparition of corona discharges in the electrical circuit. With voltage higher than 30 kV, the formation of corona is difficult to avoid in DC mode. These corona generate a significant noise in the measurements and degrade the stability of the discharge in terms of jitter and current amplitude. To improve the results, the development of a pulsed high voltage generator should allow discharges without corona.



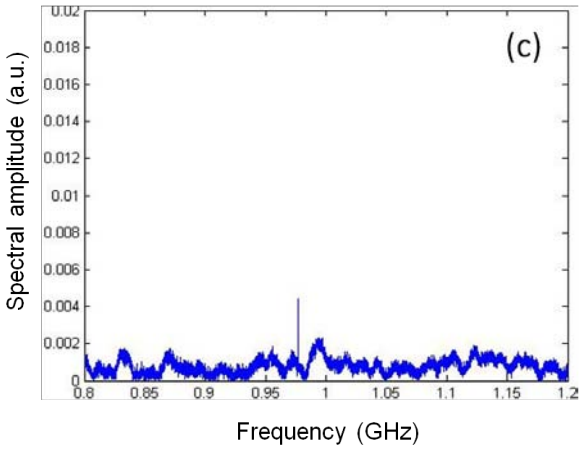


Figure 5: Spectrum detected with the antenna in absence of laser filament (a), when the plasma is replaced by a metallic tube (b) and with the laser guided discharge (c).

4. Conclusions

In this paper, we have demonstrated the possibility of using an atmospheric discharge initiated by femtosecond laser filament as a virtual antenna emitting in the radiofrequency domain.

Acknowledgements

We acknowledge financial support from DGA through grant N°200795091. We thank Kevin Verhaeghe from DGA for his technical support in the experiments.

References

[1] D.C. Jenn, "Plasma Antennas: Survey of techniques and the current state of the art", Naval Post Graduate school, Technical report, 2003.

[2] J.T. Dwyer, On the Feasibility of using an atmospheric discharge plasma as an RF antenna, *IEEE Transactions on Antennas and Propagation* 32: 141-146, 1984.

[3] A. Couairon and A. Mysyrowicz, Femtosecond filamentation in transparent media, Phys. Rep. 441: 47-189, 2007

[4] B. Forestier *et al*., Triggering, guiding and deviation of long air spark discharges with femtosecond laser filament, *to appear in AIP Advances*, March 2012

[5] A. Houard *et al*., High Current Permanent Discharges in Air Induced by Femtosecond Laser Filamentation, *Appl*. *Phys*. *Lett*. 90: 171501 (2007)

[6] B. Zhou *et al*., Measurement and control of plasma oscillations in femtosecond filaments, *Phys*. *Rev*. *Lett*. 106: 255002, 2011.

[7] E. Guillanton, J.Y. Dauvignac, C. Pichot, and J. Cashman, A new design tapered slot antenna for ultra-wideband applications, *Microw*. *Opt*. *Technol*. *Lett*. 19: 286-289, 1998.

[8] B. Forestier *et al*., Radiofrequency conical emission from femtosecond filaments in air, *Appl*. *Phys*. *Lett*. 96: 141111-141113, 2010.

VHDL-AMS modeling of VCSEL light transmission through the graded-index optical fiber

Fatima Zohra Baouche [1,2], Farida Hobar[1], Yannick Hervé [2*]

[1]laboratory of Microsystems and instrumentations (LMI), Department of Electronics, University of Constantine, Algeria
[2] InESS-UMR 7163 ULP/CNRS laboratory, National High School of Physics, University of Strasbourg, France
* Corresponding author Yannick Hervé, E-mail address: yrv@wanadoo.fr

Abstract

In this paper we aimed to model the light transmission of a Vertical-Cavity Surface-Emitting Laser diode (VCSEL) in the graded-index optical fiber, taking into account the attenuation and the dispersion influence on light characteristics. For this we used the VHDL-AMS language. Thanks to its multidisciplinary characteristics, it allows us to study several domains in the same model, such as, electrics, optics, optoelectronics and thermal influence. Our objective is to find the performance of GI fiber and to know their limits in length.

1. Introduction

Metallic and non-metallic wave guides were fabricated to guide light, but they have enormous losses and they were not suitable for telecommunication systems. During 1950s, the optical fibers with large diameters were used in endoscopes to see the inner parts of the human body [1]. Since its invention in the early 1970s in the laboratories of the U.S.A Company Corning Glass Works [2], the use of and demand for optical fiber have grown tremendously. With the explosion of information traffic due to the Internet, electronic commerce, computer networks, multimedia, voice, data, and video, the need for a transmission medium with the bandwidth capabilities for handling such vast amounts of information is paramount.
Fiber optics are a medium for carrying information from one point to another in the form of light. Fiber consists of a core and cladding, of the transparent materials are made of glass or plastic. A protective coating of plastic surrounds the cladding. It is important that the core refractive index n_c, is greater than the cladding refractive index n_g. It is known that, the optical fibers have many advantages such as large bandwidth, light weight, small diameter, low transmission loss, dielectric waveguide because optical fibers are made from silica which is an electrical insulator, signal security i.e. the transmitted signal through the fibers does not radiate, Long-distance signal transmission and designed for future applications needs [3].
This study based on VHDL-AMS (Very High Speed Integrated Circuit Hardware Description Language Analog Mixed Signal [4]) simulation. The model of each component in the chain will have an input from one or more of the areas mentioned above and a number of parameters intrinsic to the component to simulate the output variables of the model also may belong to different areas. For this we made a study theoretical physics, before the use of a specialized computer tool were then required to help establish low-level models based on fundamental equations of components or more abstract models with sufficient performance for the purpose.

2. VCSEL model

We have begin to modelling the transmission block, which is a VCSEL laser diode using the two rate equations of the variation in the carrier and the photon number [5] taking into account the various domains, such as the electrical, the optical domain and the thermal domain.
In Fig. 1, we show the results for the static response of the VCSEL versus injection current. We notice that under the emission threshold current 1.5 mA, the carrier number is proportional to I_d however, when I_d is greater than I_{th} the lasing starts and the carrier number stabilizes at a constant value to the lasing threshold of the call (N_{th}), while the number of photons increases almost linearly.

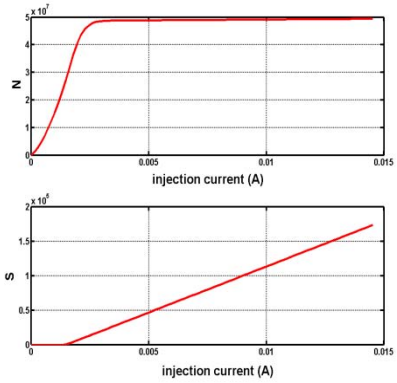


Figure 1: DC response of the carrier and photon number, versus injected current.

We started the simulation of the opto-electro-thermal model in a static analysis to find the graphics curves of $P_{opt}(I)$ for several temperature. In Fig. 2 the schematic of the optical power as a function of T is shown. Notice that, a temperature change causes a variation of the threshold current and also the optical power is given by Eq. (1) [6], under the emission threshold I_{th}, the optical power is not emitted, when I_d exceeds I_{th}, the laser effect is started and

the optical power increases almost linearly; it reaches its maximum for a temperature of 25 ° C.

$$P_{opt}(T) = \eta(T)(I - I_{th}(T)) \quad (1)$$

where $P_{opt}(T)$ is the optical output power, I is the injection current, $\eta(T)$ is the temperature dependence differential slope efficiency, and $I_{th}(T)$ is the threshold current as a function of temperature.

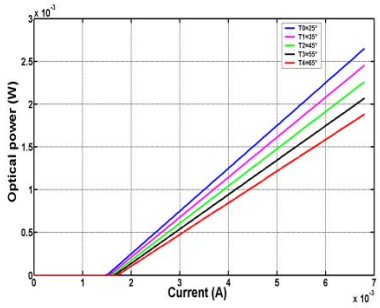


Figure 2: Optical powers of the VCSEL versus injected current for several temperatures.

The results of the dynamic response of VCSEL using a frequency sinusoid source are shown in Fig. 3. We can see that the dissipation power which is equal of subtracting between electrical power and optical power, causes a temperature elevation of physical process in a laser diode.

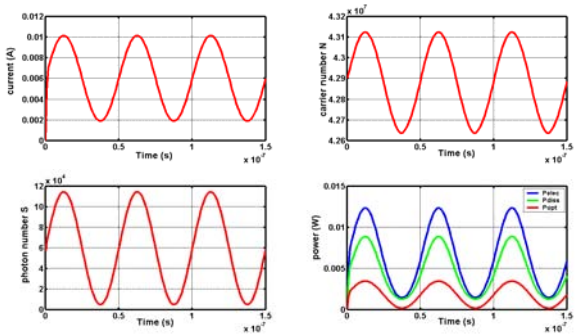


Figure 3: Dynamic response of a VCSEL versus time using a sinusoidal source.

3. Graded-index fiber Model

The fibers used in our work are the graded-index (GI). Modelling this component aims to account for the influence of his opto-geometric parameters on spectral and temporal characteristics of the propagating signal. The important effects to take into account in these models are attenuation, modal dispersion and chromatic dispersion. We also modeled two couplings, the connector VCSEL-fiber and the connector Fibre1-Fibre2 which connected the optical fibers to each other.

model of the graded index fiber, with a numerical aperture of 0.275, a wavelength of 1300 nm, a center refractive index of 1.5, a cladding refractive index of 1.474, a vacuum refractive index of 1, a profile exponent of 2, a core radius of 25 µm and a cladding radius of 60 µm.

Data from Fig. 4, shows that the core refractive index varies according to a parabolic profile during the core diameter of the fiber. n_c is maximal at the core center and when the light comes to the core-cladding junction, n_c takes the value of n_g.

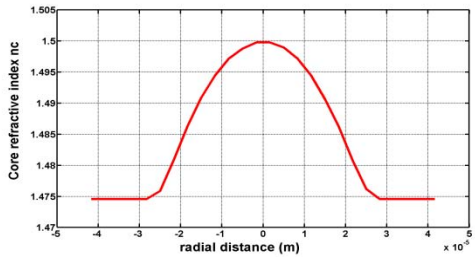


Figure 4: Simulation results of the core refractive index of the graded-index fiber.

Dispersion, expressed in terms of the symbol τ_{tot}, is defined as pulse spreading in an optical fiber. As a pulse of light propagates through a fiber, elements such as numerical aperture, core diameter, refractive index profile, wavelength, and laser line-width cause the pulse to broaden. This poses a limitation on the fiber overall bandwidth. It is measured in time, typically nanoseconds or picoseconds. Dispersion is generally divided into two categories: modal dispersion (τ_{mod}) and chromatic dispersion (τ_c). Modal dispersion is defined as pulse spreading caused by the time delay between lower-order mode sand higher-order modes.

Chromatic dispersion is typically expressed in units of nanoseconds or picoseconds per (km-nm).

In Fig. 5, we cane that the total dispersion rise with increasing the fiber length according to Eq. (2), (3) and (4) [7-8]:

$$\tau_{tot} = \sqrt{\tau_\mathrm{mod}^2 + \tau_c^2} \quad (2)$$

$$\tau_c = T_c L \Delta\lambda \quad (3)$$

$$\tau_{\mathrm{mod}} = L.D_{\mathrm{mod}} \quad (4)$$

where T_c is the chromatic dispersion coefficient, consists of two parts, material dispersion D_M and waveguide dispersion D_G, it is expressed in units of (ps / nm · km), $\Delta\lambda$ is laser diode spectrum, and the D_{mod} is the modal dispersion coefficient, it is expressed in units of (Ps / Km).

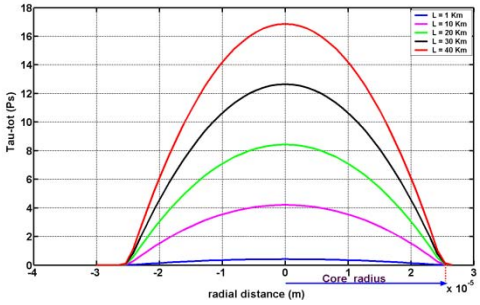


Figure 5: Simulation results of fiber total dispersion versus radial distance for several lengths.

The core a graded index fiber is composed of several layers, each with a refractive index, slightly different from the previous one. The core index decreases from the centre axis to the core-cladding interface, according to a parabolic law. The light rays are not reflected to the

encounters with the cladding, but follow the trajectories almost sinusoidally and deviated gradually each time they cross a new layer, thus decreasing the amount of modal dispersion. In Fig. 6, we show the simulation results of light transmission through the GI fiber for several lengths. The graphs show the optical powers to the output of each component. The powers represented are respectively: $P_{opt\text{-}VCSEL}$ to the VCSEL output, $P_{opt\text{-}C\text{-}VCSEL\text{-}F1}$ to the output of VCSEL-fiber connector, $P_{opt\text{-}F1}$ to the first fiber output, $P_{opt\text{-}C\text{-}F1\text{-}F2}$ at the output of the Fibre1-Fibre2 connector and $P_{opt\text{-}F2}$ which is to the second fiber output. we can see that, the $P_{opt\text{-}VCSEL}$ and $V_{CSEL\text{-}C\text{-}F1}$ do not change as a function of the fiber light, by cons $P_{opt\text{-}F1}$, $P_{opt\text{-}C\text{-}F1\text{-}F2}$ and F2-Popt, are decreased with increasing fiber length, for example $P_{opt\text{-}F2}$ is decreased to 1 µW for L = 40 km. According to the representative graphs, we notice that the optical power is reduced at the output of each component compared to the previous one. The light energy transmitted through the VCSEL, is not totally recovered at the fiber output. This attenuation is due to several phenomena, such as, the dispersion, the absorption by the impurities, the scattering by impurity or by interface defects of core-cladding and Rayleigh scattering [9], the loss of the coupling (VCSEL-fiber and fiber-fiber).

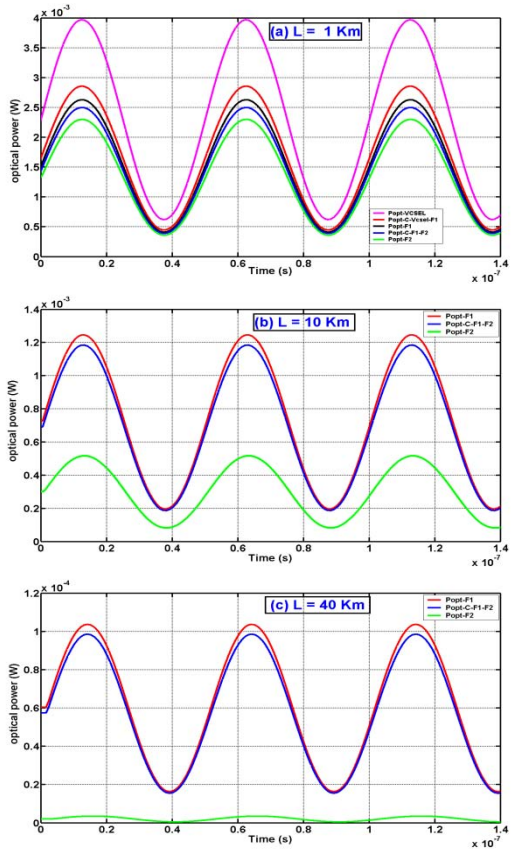


Figure 6: Simulation results of the light transmission in graded-index fiber versus time for several lengths.

The GI fibers are specially designed for telecommunications. The GI fiber core is not homogeneous, the refractive index value, decreases from the axis until it reaches the cladding index value. The propagation principle in a graded index fiber is based on a focusing the light beam is continuously deflected towards the fiber optical axis. This deviation causes the optical signal to have a sinusoidal signal form.

4. Conclusion

In this paper, we modeled the optical transmission of a VCSEL laser diode through GI fiber. We have also focused to find the basic characteristics of each component and the influence of parasites parameters and to find the transmission limitations according to the length. We used as transmission block , the electro-opto-thermal model of the VCSEL diode created by the VHDL-AMS based on two rate equations of the carrier number, and of the photon number.

Implementation as VHDL-AMS language, allows us to support the modelling steps and simulation needed to implement the design top-down. This language allows describing all the steps, beginning with the high level functional to the modelling of noise, instead of using multiple tools. In addition, it supports the multi abstraction: the blocks can be simulated with different description levels. Our models are useful in the design and simulation of an optical transmission system by adding a photodiode model, as receiving block.

References

[1] P.L. chu, Fiber optic devices and systems, Electrical engineering, vol II: 10 pages.

[2] K. Fidanboylu, H. S. Efendioğlu, Fiber optic sensors and their applications, 5th International Advanced Technologies Symposium (IATS'09): 1-6, 2009.

[3] N. Massa, Fiber optic telecommunication, fundamentals of photonics, Module 1.8: 293-347.

[4] Hervé Y. VHDL-AMS application et enjeux industriels. Dunod éditeur. Collection Sciences-sup: ISBN 2100058886, Paris, 2002.

[5] R. Pant, M. A. Neifeld, M. B. Steer, H. Kanj and A. C. Cangellaris, Electrical package impact on VCSEL-based optical interconnects, Optics communication, 245(1-6): 315-332, 2005.

[6] P. V. Mena, J. J. Morikuni, S.-M. Kang, et al. A Simple Rate-Equation-Based Thermal VCSEL Model, Journal of Lightwave Technology, Vol. 17(5): 865-872, 1999.

[7] A.J. Liu, H.W. Qu, W. Chen, et al. Graded index profiles and loss-induced single-mode characteristics in vertical-cavity surface-emitting lasers with petal-shape holey structure, Chin. Phys. B 2011: 20(2): 024204-1/-8, 2011.

[8] Telecommunication standardization sector of ITU, Characteristics of a 50/125 µm multimode graded index optical fiber cable. G.651 (02/98).

[9] K. Tsujikawa, T. Katsusuke and O. Masaharu , Rayleigh Scattering Reduction Method for Silica-Based Optical Fiber, J.Lightwave thechnology, 18(11): 1528-1532, 2000.

ADVANCED ELECTROMAGNETICS SYMPOSIUM, AES 2012, 16 – 19 APRIL 2012, PARIS – FRANCE

Simulation of the propagation of the solitons in presence of the Raman effect and the third-order dispersion in the optical fiber links

Lyes Bahloul*, L. Cherbi, W. Medellel, and A.Bellil

Laboratory of instrumentation (LINS), University of Sciences and Technology Houari Boumedienne (USTHB), Algeria

*lyes_86@live.fr

Abstract

We resolve numerically the nonlinear Schrödinger equation using the SSFM (Split Step Fourier Method) in order to generate and stabilize soliton pulses by searching the best balance between the GVD (Group Velocity Dispersion) and the nonlinear effects when ultra short pulses are launched through the fiber. After that, we study the influence of the Raman and TOD (third order dispersion) effects on these solitons.

1. Introduction

Optical solitons play a major role in large amount of data communication through the optical fibers [2][3], so far it's considered as the best way of transmission because they are defined as pulses which don't vary during propagation, that's why they are being majorly used in transmission across trans-oceanic and trans-continental distances.

2. The used Numerical model

The propagation of an impulsion through the optical fiber is governed by the Schrödinger equation, which is written as follows [1], [2], [4]:

$$\frac{\partial A}{\partial z} + j\frac{\beta_2}{2}\frac{\partial^2 A}{\partial t^2} - \frac{\beta_3}{6}\frac{\partial^3 A}{\partial t^3} = j\gamma|A|^2 A - \frac{\alpha}{2}A \qquad (1)$$

With:

A: the envelope of the pulse.

β_2 : The group velocity dispersion.

β_3 : The third order dispersion.

γ : The nonlinear coefficient.

α : The attenuation.

In the case of anomalous dispersion (β_2<0) and with a certain agreement between the input power and the chromatic dispersion in such a way that: $\frac{\gamma P_0 {T_0}^2}{|\beta_2|} = 1$, we generate an optical soliton, this one is defined physically as a pulse that doesn't change during its propagation even for long distances, mathematically the soliton is a solution of the Schrödinger equation which has this form [2]:

$$u(\varepsilon,\tau)=\mathrm{sech}(\tau)\exp\left(j\frac{\varepsilon}{2}\right) \qquad (2)$$

With:

$\tau=\frac{t}{T_0}$

$\varepsilon=\frac{z}{L_d}$ (L_d: the dispersion length).

$u=\frac{A}{(P_0)^{1/2}}$

To simulate this propagation we used the SSFM method [1] which is considered as pseudo spectral method that allows the resolution of the nonlinear Schrödinger

equation, with the purpose to follow the evolution of the pulse in the temporal and the spectral domain.

Its principle is based on dividing the fiber into several small fractions « h » and assumes that in each fraction the linear and the nonlinear effects act separately as shown in figure 1:

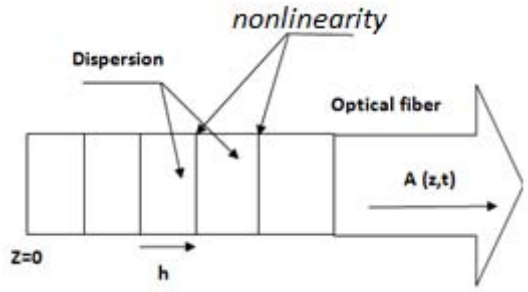


Figure 1: schematic illustration of the SSFM method.

In this method the linear and nonlinear effects are characterized by the (D and N) operators as follows:

$$\mathrm{D} = -\frac{i\beta_2}{2}\frac{\partial^2}{\partial t^2} + \frac{\beta_3}{6}\frac{\partial^3}{\partial t^3} - \frac{\alpha}{2} \qquad (3)$$

$$\mathrm{N}=i\gamma\left(|A|^2 + \frac{i}{\omega_0}\frac{1}{A}\frac{\partial}{\partial t}\left(|A|^2 A\right) - T_r\frac{\partial |A|^2}{\partial t}\right) \qquad (4)$$

With: $\frac{\partial}{\partial t} = j\omega$

The introduction of these effects is done in two steps:

2.1. The dispersive step

As the differential operator $\frac{\partial}{\partial t}$ is equivalent to a multiplication by jω in the space of frequencies, and for more simplicity, the operator D is calculated in the Fourier domain and the pulse is written as follows in the temporal domain:

$$A(z+h,t)=TF^{-1}[\exp(h.D)(TF(A(z,t))] \qquad (5)$$

$$A(z+h,t)=TF^{-1}[\exp(j\frac{\beta_2}{2}\omega^2 h)(TF(A(z,t) \qquad (6)$$

2.2. The nonlinear step:

The N operator is applied directly in the temporal domain and the pulse is given in this case by the follow equation:

$$A(z+h,t)=\exp(hN).A(z+h,t) \qquad (7)$$

$$A(z+h,t)=\exp(j\gamma|A|^2 h).A(z+h,t) \qquad (8)$$

By repeating these two operations many times, we have access to the electrical field of the pulse according to the distance of propagation and we achieve a numerical simulation of the propagation of the light in an optical fiber.

3. Results and interpretations

3.1. The soliton

To simulate the propagation of the soliton pulse, we used an optical fiber and an hyperbolic sine pulse which have the following characteristics:

- T_0=0.56 ps.
- P=22.5 watt.
- γ=3 $\mathrm{W}^{-1}/\mathrm{Km}^{-1}$
- β_2=-22 $\mathrm{ps}^2/\mathrm{Km}$
- L_d=L_n= 0.0148Km.
- L=100Km.

We have neglected the fiber losses, and the carrier frequency that we used is 1550nm.

Figure 2 shows the shape of the pulse at the input of fiber.

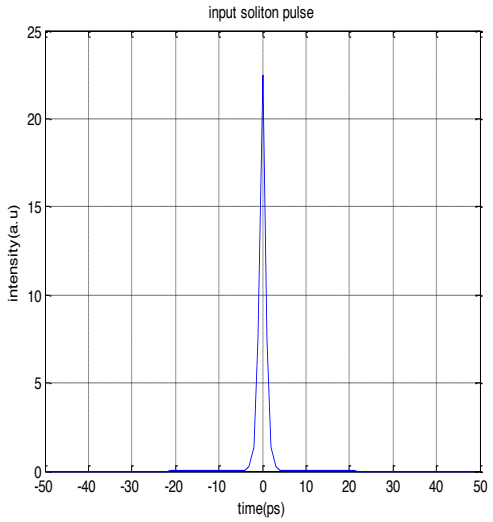


Figure 2: The input soliton in the temporal domain.

Figure 3 gives the comparison between the input and the output soliton pulse in the temporal domain, we can easily see that there is no difference between them; this result is in agreement with theoretical assumptions.

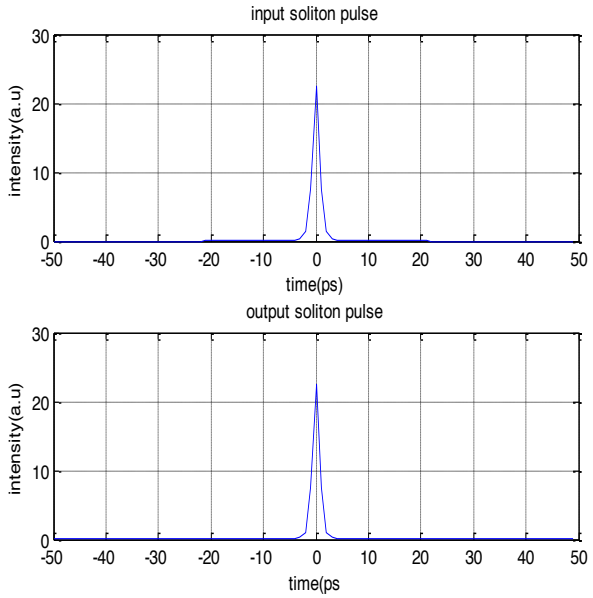


Figure 3: the input and the output soliton in the temporal domain.

The next figure shows the evolution of the shape of the pulse through all the distance of propagation.

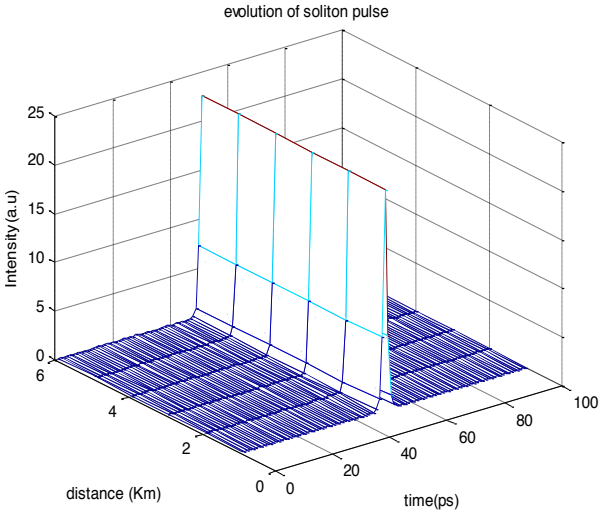


Figure 4: the evolution of the soliton through the fiber in the temporal domain.

In this figure we can clearly see that the pulse keeps the same shape at any point of the fiber from the input to the output of the fiber.

Figure 5 shows the input and the output spectrum of this pulse, also here we see that the shape of spectrum doesn't change through the propagation, but we have just small and negligible perturbations and we have also attenuation in its intensity.

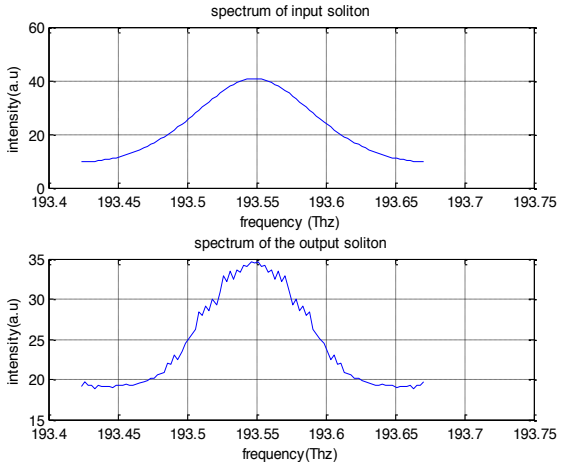


Figure 5: the input and the output soliton in the frequency domain.

3.2. Higher-Order Effects

On the previous section we didn't study the higher effect (TOD and SRS) on the propagation of soliton; we have just seen how to use the GVD and nonlinear effect to generate the soliton. In the next section we see the influence of these effects on the propagation of soliton.

3.2.1 The TOD effect on soliton propagation

In general this effect is neglected in presence of the GVD, however its effects may occur when the GVD is small or zero, that's why we consider the following parameters for our simulation:

- T_0=0.56 ps.
- P=0.203 watt.
- ɣ=3 W^{-1}/Km^{-1}
- β_2=0 ps^2/Km.
- L_{d3}=L_n=1.64 Km.
- L=150Km.
- β_3=0.11ps^3/Km

Figure 6 shows the input and the output pulse in the time domain, we see clearly that we have a shift of a few picoseconds and also an attenuation of the pulse.

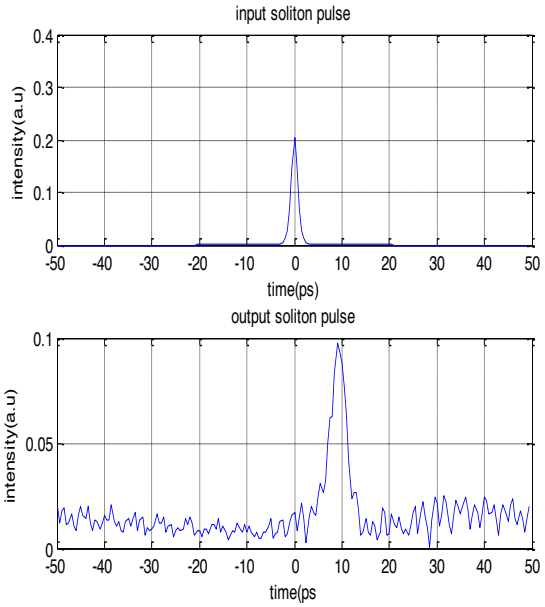


Figure 6: the input and the output soliton in the temporal domain under the TOD effect.

Physically speaking, we can say that the TOD slows down the soliton and as a result, the soliton peak is delayed by an amount that increases linearly with distance.

Figure 7 shows the evolution of the delayed of the pulse in the time domain; we see clearly that its increase with the distance of propagation.

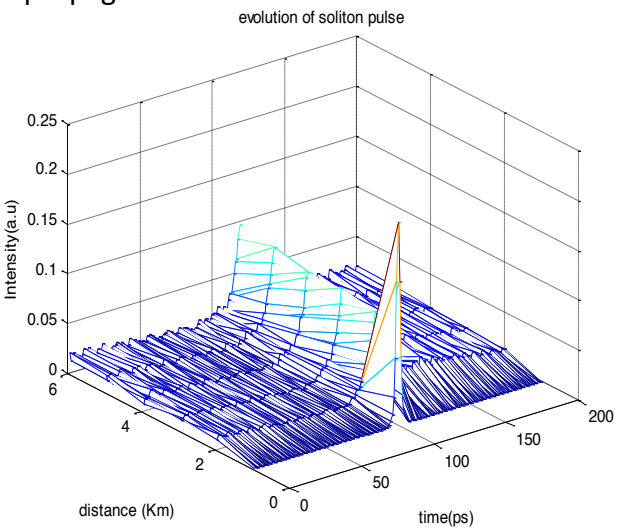


Figure 7: the temporal shift of the pulse through the optical fiber.

The next figure shows the spectrum of input and output soliton under the TOD effect; we see a splitting of the spectrum into two well-resolved spectrum peaks. These peaks correspond to the outermost peaks of the SPM-broad end spectrum.

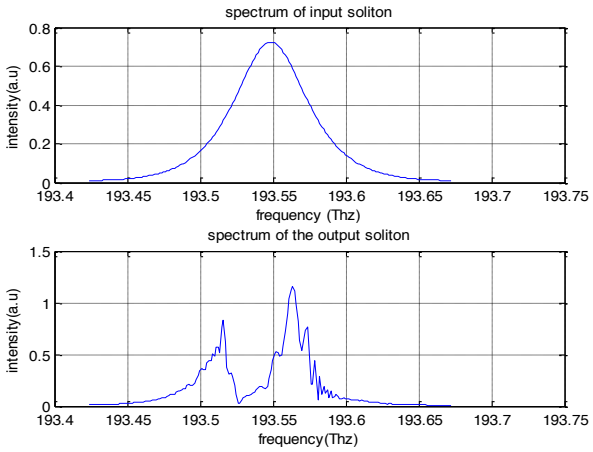


Figure 8: The input and the output soliton in the spectral domain under the TOD effect.

Figure 9 shows the generation of the two frequencies from the carrier according to the length of the fiber.

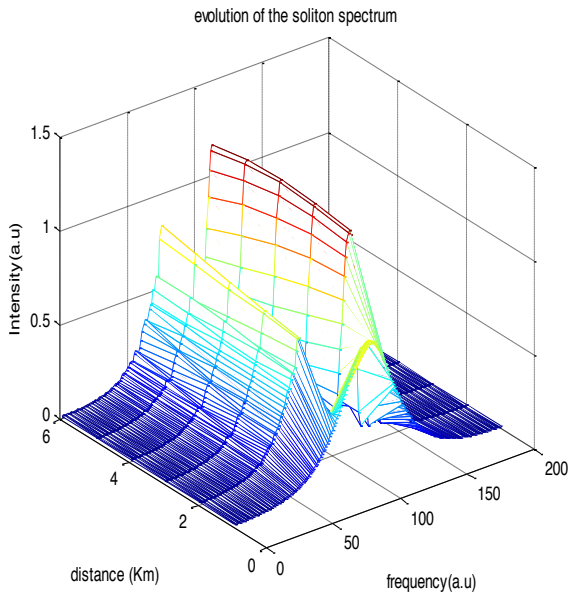


Figure 9: the splitting of the carrier along the distance of propagation.

3.2.2 The Stimulated Raman scattering effects on soliton propagation

When the pulses are very short and energy, they have a large enough spectrum that during the propagation the Raman gain amplifies the low spectrum components with the energy carried by high frequencies which play the role of pump. This process is known as the self frequency shift.

To see this effect, we use the following parameters:

- T_0=0.56 ps.
- P=22.5 watt.
- ɣ=3 W^{-1}/Km^{-1}
- β_2=-22 ps^2/Km.
- L_d=L_n=0.0148 Km.
- L=7.5Km.
- Tr=5fs.

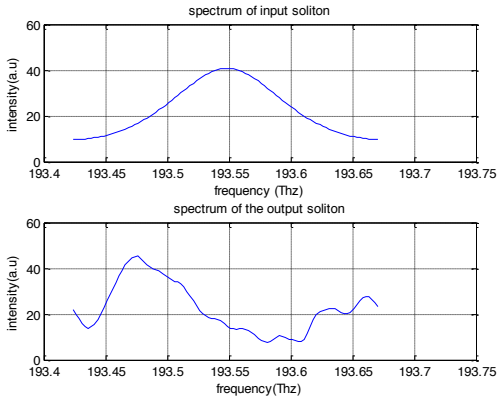


Figure 10: the input and the output soliton in the spectral domain under the SRS effect.

Figure 10 represents the input and the output spectrum of the pulse; it shows the frequency shift of soliton spectrum to lowers frequencies. In the next figure we see a temporal drift; it's caused by the difference in the group velocity due to the chromatic dispersion of the fiber.

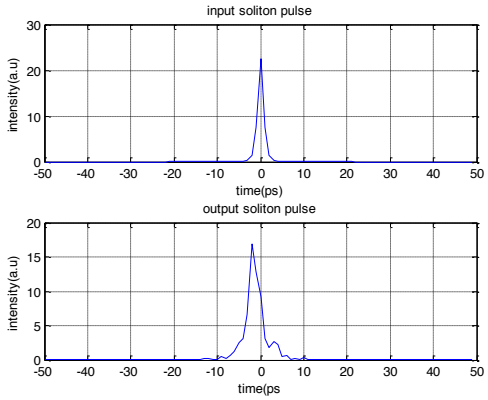


Figure 11: the input and the output soliton in the temporal domain under the SRS effect

4. Conclusion

In this work, we are arrived to generate and study a soliton pulses according to the transmission distance by resolving the propagation equation in optical fiber taking in consideration the dispersion and the nonlinear effects using The SSFM method, and ensuring the balance between these two effects. After that, we have studied the influence of the TOD and the SRS on the temporal shape and spectrum of generated solitons according of many features of both lunched pulse and the fiber, and this for the reason that these effects are very important, so we can't ignore them. However we can affirm that the optical solitons are by far the light pulses which are the most appropriate for long distances transmission trough optical fibers.

References

[1] Patrick L. Nash, A new fourth-order Fourier–Bessel split-step method for the extended nonlinear Schrödinger equation, Department of Physics and Astronomy, The University of Texas at San Antonio, October 2007

[2] Govind.P.Agrawell, Non Linear Fiber optics, Academic press, (third edition), 2001.

[3] Govind P. Agrawal , Fiber-Optic Communications Systems, John Wiley & Sons, 2002

[4] Julien FATOME, Propagation d'impulsions ultra-courtes à 160-Gb/s dans des lignes de fibres optiques gérées en dispersion, doctorat en physique, Université de Bourgogne - 2004- France

Significance of Quantum Communication in LEO Satellite Transmission Networks

Skander Aris[1], Abderraouf Messai[1], Hatem Mokhtari[1], Nadjim Merabtine[2], Mosleh M. Alharti[2], and Malek Benslama[1]

[1] LET Laboratory, Department of Electronics, Constantine University. Algeria
[2] Electrical Engineering Departments, Faculty of Engineering, Taif University. Saudi Arabia
*corresponding author, E-mail: arisskander@yahoo.fr

Abstract

Quantum cryptography is a hot extraordinary topic that covers a wide range of expertise, ranging from fundamental physics to industrial applications. The objective of this research should result in increasing the security of our transmissions, all the more with regard to trade information. The purpose of this work was to study the satellite communications and coupled with quantum transmission. We began with a study of state and pose the problematic problem of free space without quantum transmissions and quantum cryptography. We then reviewed to purpose the BB84 protocol lake away of transmission between the satellite and earth station by giving its principles, so that the study of different problem of free space by considering the theoretical limits. Thus, we focus on a comprehensive survey on the quantum error rate given their importance in implementations of key exchange systems. These points are thus the primary aim of our study. We will try to highlight the practical limitations of quantum cryptography. These limits are coupled with techniques borrowed from signal processing with pure quantum theories to develop methods for correcting errors in the field of quantum transmission.

1. Introduction

The quantum modern global satellite systems really is a big step into the world of communications over secrete service links between people all over the surface of the earth, how it is a major concern of all researchers to improve the performance of the Quantum Cryptography [1, 2]. It is the latest scientific revolution with real world telecommunication after a communication network to global satellite systems may offer different services to the users. Altitude orbit is considered that essential parameter in the satellite network. This explains why the constellation defined in him; he is in four kinds of orbits: LEO, MEO, HEO, and GEO satellite.

The main goal of this paper is to develop a prototype approach of optical laser satellite communication terminal applications on micro-satellites in LEO and space-to-ground constellations. Micro-satellite constellations in LEO orbits can inter-communicate and communicate with the ground station using laser beams as the carrier (Figure 1) [3].

The onboard laser communication equipment takes the form of a terminal including an optical or quantum transmitter and a receiver.

Quantum satellite transmissions offer many advantages for secure communications, e.g. eavesdropper's problems, confidentiality of keys, resistance to traffic analysis, high speed transmission. The principal of quantum information is encoded in two or three states (two or three qubits), using the correlation between more particles (photons, atoms) [4]. Quantum Key Distribution (QKD) is one of the more essential researches methods of modern information processing that emerged from the properties of "Superposition of states" and "Teleportation systems" [5].

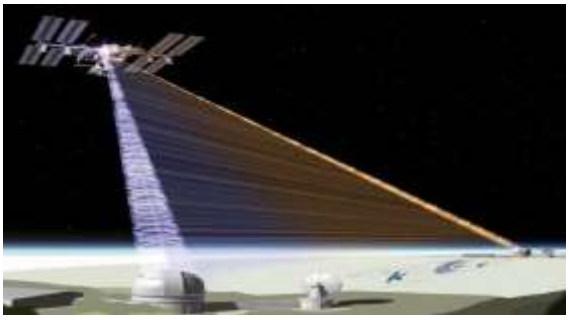


Figure 1: The LEO satellite constellation and ground station.

In this regard, some of the most outstanding problems included:

a) Atmospheric turbulence which leads to wave front distortion [5], b) Environmental vibration effects which lead to pointing errors, c) The absorption, scattering and reflection of radiation in the lower layers.

The most aggressive quantum key distribution network is shown in [6], in addition, the quantum network based on optical fiber and classical communication network are involved in such modern network [7]. Furthermore, QKD can be integrated with IP address so as to secure internet traffic, which has been stated in future research paper. The realization of Quantum Key Distribution Low Earth Orbit network depends on the technology of satellite transmission. As communication has many advantages compared to satellites telecommunications, such as that its cost is relatively much lower, the maintenance is simple and convenient and it is in favor of environment protection.

Once quantum communications Satellites can be practically performed and is in wide use, our scheme is undoubtedly more feasible than the idea to distribute entangled photons using satellites. Generally, on the basis of the obtained results, design recommendations were made for developing and enhancing current and future free space QKD links in the LEO. Additionally, it is noteworthy to say that such recommendations could be potentially adapted in the coming GEO links. Essentially, specific suggestions for future research are included, where the overall study may be useful to researchers working in similar free space quantum communication links.

2. Simple Quantum Satellite Networks

The quantum photon emitter is placed at the station. The laser link to the top receiver on the satellite using the BB84 protocol can be used to run the negotiation of shared secret key, see Figure 2.

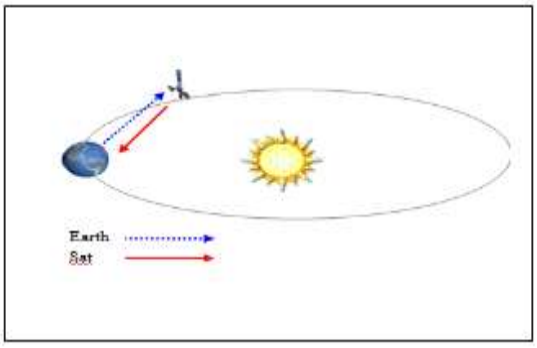


Figure 2 : Simple quantum satellite scenario.

To get things really integrated in this proposal is in the system-space satellite station transmitter pairs of entangled photons are placed on the satellite. This is the most interesting use of technology pairs of entangled photons integer in BB92or BB84 protocol [7]. The most aggressive quantum key distribution network is shown in figure 3, in addition, the quantum network based on optical fiber and classical communication network are involved in such network [3].

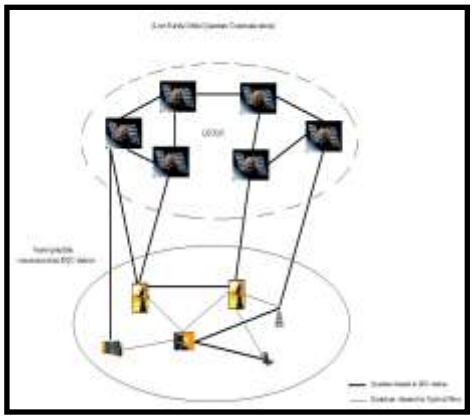


Figure 3: Global Quantum Key Distribution LEO network [4].

Some desirable attributes in QKD network are safe management of keys, quantum authentication, efficient transmission of key and robustness etc. Furthermore, such QKD can be integrated with IP address so as to secure internet traffic, which has been stated in future research paper.

3. Objectives of space communication

In our point of view, the quantum computing algorithms can be used to affirm our free-space communication in the following four ways [8]:

1. Open-space communication: usually “horizontal” telecommunication that happens below 100km height. For channel, the space is used instead of optical cable.
2. Earth-satellite communications: it happens through greater heights than the Open air communication, usually between 300 and 800 km altitude. Signal encoding and decoding is used to produce quantum error correction that allows operation in noisy environment.
3. Satellite transmission: Quantum algorithms improve that the effective bandwidth, thus the brand is better utilized as in traditional cases [9].
4. Inter-satellite communication (Handover inter satellite systems): the communication between satellites where the channel is the free-space. Any kind of coding and encoding can be used, to increase stability [10].

Much as satellite communication systems is viewed as an alternative solution to the realization of relatively long-distance secure key exchange, obtainment of global scale key exchange is still challenging. This is owed to the fact that long-distance propagation of the optical beam is affected by several atmospheric and geographical problems.

4. Research contribution

Based on the objectives stated in last section, the contributions from this work are detailed in the following subsections:

A- Mathematical Model for the BB84 Protocol:

Since the discovery of the concept of quantum cryptography, various protocols have been proposed for use in quantum communication links. Of the many protocols that have been proposed, BB84 is considered the most developed let alone the recently proposed B92 variant. These protocols are assumed to have different deficiencies and are thus differently suited for secure information interchange. In order to determine the suitability of the two protocols for quantum communication, a mathematical model should be developed for possible analysis of related links. With regard to the above point of view, the contribution made in this part of the study includes the development of a mathematical model for analyzing the performance of BB84 protocol over satellite-based quantum communication links between a ground station and a satellite in the LEO [11].

The developed model takes into account the various atmospheric phenomena such as absorption, scattering and turbulence which can significantly limit the performance of free space links. Moreover, the expressions of the quantum bit rated are given based on ideal single-photon sources and single-photon sources with Poison distribution. Using the developed theoretical model, it is possible to analyze the performance of the quantum protocol in the LEO domain [12, 13].

B- Mathematical Model for the Physical Layer Limitation in Satellite-Based QKD systems:

Quantum optical communication offers an attractive solution to ensure secure distribution of the key information. However, satellite vibration is a major cause of pointing errors, a phenomenon whose effect can lead to misalignment between the transmitter and receiver, hence resulting in the problem of pointing errors. In the end, the occurrence of pointing errors can lead to link outages. As pointed in the objectives such an occurrence should be modeled. Thus, the contribution made in this part of the study includes a newly developed QBER mathematical model which takes into account the effect of satellite vibration. In line with the above, it is noteworthy to affirm that this is the first model developed in an attempt to address the problem of pointing errors due to satellite vibration, in the research discipline of quantum cryptography. Moreover, using the developed model, the effect of satellite vibration was studied by way of simulation. For the derived model we define the QBER as a function of satellite vibration amplitude. Moreover based on the numerical simulation carried out, we a plot of the QBER as a function of satellite vibration amplitude is presented. The obtained result shows that the vibration amplitude has greater effect on the QBER. Generally, the obtained result reveals that an increase in the vibration amplitude leads to a corresponding increase in the QBER, an outcome which can reduce the amount of generated secure communication key rate, after the procedures of error correction and privacy amplification.

5. Research solution

The bit error rate (BER) for the classical space links communications is very high (usually in the order of 10^{-1}) because of noisy deep space, however, TCP/IP can tolerate bit error rate in the order 10^{-5} only. FEC (Forward Error Correction) compensate for the errors to some extent but only by trading bandwidth (FEC requires more data to detect bit error and recover from it). Some characteristics of the satellite communicating and earth links in Space scenario make the direct use of terrestrial protocol stack TCP/IP infeasible [12]. I have tried to cover the essential characteristics of satellite, and Surface station:

- Very High and Variable Propagation Delay: Communication using electromagnetic waves having the speed of light takes time in minutes or even hours in deep space due to the astronomical distances;
- Security: Security and integrity of data is a big issue for data flowing through the deep space that is vulnerable or open to attack. High Latency has to be taken into consideration before using the proper algorithm otherwise communication will be severed.
- Noise: High Signal to Noise can be achieved by using lower loss receivers, with more performance improvement by using Reed –Solomon, Turbo Decoder.
- The performance of a quantum key distribution is evaluated by calculating the quantum bit error rate (*QBER*).

The error rate in quantum optical transmission is generally expressed as the ratio of wrong bits to the total amount of detected bits. We call this quantity quantum bit error rate (QBER). It is equivalent to the ratio of the probability of getting a false detection to the total probability of detection per pulse:

$$QBER = \frac{P_{opt}P_{phot} + P_{dark}}{P_{phot} + 2P_{dark}} \cong P_{opt} + \frac{P_{dark}}{P_{phot}} \qquad (1)$$
$$= QBER_{opt} + QBER_{\det}$$

We consider free space quantum communication:

$P_{opt} \cong 0$, $QBER_{opt} = 0$.

Whit:

$P_{dark} = n_{dark}\Delta\tau$, and $P_{phot} = q\nu\mu n_t n_d$ we obtain:

$$QBER_{\det} = \frac{n_{dark}\Delta t}{q\nu\mu n_t n_d} \qquad (2)$$

P_{dark}, P_{phot}, are the probabilities to get a dark count, to detect a photon. n_{dark} is the dark count rate of the detector and $\Delta\tau$ is the detection time window. This formula applies for a setup with two detectors.

Since a dark count will with a 50% chance not lead to an error, but just to an additional count, there is a factor two in the denominator, but not in the numerator. Note that the QBER is dependent of the factor q, the last one is a systematic factor depending on the chosen implementation. It cannot be bigger than 1/2 due to the fact that half of the time the randomly chosen bases of Alice and Bob are not compatible. The second part, $QBER_{\text{det}}$, is due to the dark count rate of the photon counters and increases with decreasing transfer efficiency η_t. Hence $QBER_{\text{det}}$ is the determining factor for longer transmission distances. The detector dark count rate finally limits in combination with the losses in the fibres the transmission distance. Since fibre losses have already attained the physical limits, the detectors deserve a thorough discussion. It is known that when the atmosphere is clear there is very high transmittance in certain windows.

Higher than 10 km above sea level the atmosphere becomes rarefied, and absorption and scattering can be neglected. In clear weather the transmittance can be improved to 65% by selecting a proper wavelength, but in bad weather when there are clouds, rain or fog, noise and losses increase so quickly that QKD fails. This is the problem encountered in all free-space communication [14].

If the ground station can be established on a high mountain, most losses caused by the atmosphere can be avoided. The divergence half-angle θ of a Gaussian beam with radius $\omega 0$ *(1/e2)* is given by [3, 14]:

$$\vartheta = \frac{\lambda}{\pi\omega_0} \qquad (3)$$

Where λ is the laser wavelength and $\omega 0$ is equal to half the diameter D of the collimating telescope [4]. Considering the satellite's allowed payload, we take D = 10 cm, transmission distance L = 1000 km and λ = 650 nm. After propagation over 1000 km the spot size becomes 8m in diameter (it should be less than 10m to account for atmospheric turbulence). In order to receive the signals from the satellite with accuracy better than 5μrad is required. If we intercept a large Gaussian beam of diameter 2ω with a small telescope (D) then the collected fraction is:

$$\eta_{atmos} = 1 - Exp[-\frac{D^2}{2\omega^2}] \cong \frac{D^2}{2\omega^2} \qquad (4)$$

Here, we take D = 1m so the losses are 17 dB. The transmittance number of photons per pulse 0.1 and coupling efficiency 60%, then the number of signal photons received by the ground station is 10−4 per pulse. At present, the dark count of silicon-based is about 25 counts s−1 which will cause 2.5 × 10−7counts pulse if the width of the time gate is 10 ns, which contributes less than 0.2% to the error rate. Compared with *QBER* formula in the quantum transmissions:

$$QBER_{\det} = \frac{n_{dark}\Delta t}{qv\mu n_t n_d n_{atmos}} \qquad (5)$$

6. Discussion

According to the expression president the quantum error rate is a function of the average number μ of photon in an impulse. We will evaluate the expression of the *QBER* for various values of μ.

The figure 4 present the various values of contrast C of the interferometer, an estimate of the error rate in the absence of spy on the channel according to his length. Indeed, the device of detection presented in this paper being entirely fiber, it is difficult to control the fluctuations of phase in optical fibers connecting each detector. The direct consequence of these fluctuations is a variation of the contrast of the interferometer.

Several measurements were taken and give a value of oscillating contrast between [0, 7 and 0, 9].

In the worst of the cases, the value of contrast is 0, 7. In this case, the error rate is greater than 13% some is the length of the channel, which does not guarantee an unconditional safety.

QBER (μ = 0.1)

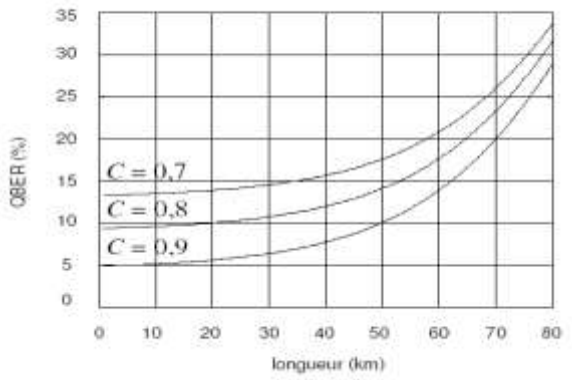


Figure 4: Quantum Error Rate as function altitude and contrast.

The average value of the contrast of our system of detection is 0, 8. Figure 4 presents the evaluation of the error rate in this case. The confidentiality of a transmission is then guaranteed since the error rate is lower than 11% when the length of the channel does not exceed more than 30 km. In the best of the cases, the value of contrast is worth 0, 9. A transmission having for goal to constitute a key of encoding can be regarded as confidential as long as the length of the channel does not exceed 50 km. By modifying the interferometer device in order to refine its contrast using a loop of control in phase, it is possible to approach the usual values for a quantum system of key distribution.

7. Conclusions

The realization of Quantum Key Distribution Low Earth Orbit network depends on the technology of satellite transmission. As communication has many advantages compared to satellites telecommunications, such as that its cost is relatively much lower, the maintenance is simple and convenient and it is in favor of environment protection. Once quantum communications Satellites can be practically performed and is in wide use, our scheme is undoubtedly more feasible than the idea to distribute entangled photons using satellites. Generally, on the basis of the obtained results, design recommendations were made for developing and enhancing current and future free space QKD links in the LEO. Additionally, it is noteworthy to say that such recommendations could be potentially adapted in the coming GEO links. Essentially, specific suggestions for future research are included, where the overall study may be useful to researchers working in similar free space quantum communication links.

Acknowledgements

As part of the national research project J 0200920100180: Modeling and channels to improve satellite network performance. "Ad Hoc" network applications by introducing the antenna processing.

References

[1] Y. Kawaguchi, T. Tsukahara, M. Motozawa, Experimental and numerical investigations of turbulent drag reduction phenomena by additives, *Proc. ASCHT09*, Jeju, Korea, pp. 23−32, 2009.

[2] Merabtine, N. Aris, S and Benslama, M. "a Contribution to a Communication Quality Improvement by a Hand Check Survey", *Journal of Mobile Communication*, 1(1-4), pp: 21-25, 2006.

[3] Arnon, S. "Performance limitation of laser satellite communication due to vibrations and atmospheric turbulence: down-link scenario", *Int. J. Satell. Commun. Network*. 2003; 21:561–573.

[4] Aris,S. Messai, A. Merabtine, N. Alharti, M and Benslama, M. "Study of LEO Satellite Constellation Systems Based on Quantum Communications Networks*", in Proceedings of 5th International Symposium on I/V Communications and Mobile Networks*– ISIVC'10. 30-3 October. Rabat, Morocco. 2010.

[5] Bacsardi, L. "Using Quantum Computing Algorithms in Future Satellite Communication", *Acta Astronautica*, Vol 57. Issue 2-8., pp 224-229-2005.

[6] Miao, L et al, "Background noise of satellite-to-ground quantum key distribution", *New Journal of Physics*, 7 (2005) 215.

[7] Shapiro, J.H. "Near-field turbulence effects of quantum key distribution". *Phys. Rev. A*, vol. 67, no.2 022309-2003.

[8] Z. J. Zhang: Multiparty quantum secret sharing of secure direct communication, *Physics Letters A* 342 (2005), pp 60-66.

[9] Steffen M., Vandersypen L., Chuang I.,''Toward quantum computation, a five qubit quantum processor, *IEEE MICRO* 21 (2) (2002), pp 24- 34.

[10] Shor P.W, ''Polynomial time algorithms for prime factorization and discrete logarithms on a quantum computer,'', *SIAM Journal of Science and statistical Computing* 26 (1996) 1484.

[11] Steane A.M.,'' Error correcting codes in quantum theory'', *Physical Review Letters*, pp 77-793, 1996.

[12] C. Gobby, Z. L. Yuan et A. J. Shields, "Unconditionally secure quantum key distribution over 50 km of standard telecom fibre", *Electron. Lett.* 40, 1603 (2004).

[13] S. Fasel, N. Gisin, G. Ribordy et H. Zbinden, "Quantum key distribution over 30 km standard fiber using energy-time entangled photon pairs", *Eur. Phys. J. D* 30, 143 (2004).

[14] S. Aris, A. R. Messai, M. Benslama, N. Merabtine, M. M-Elharti, Integration of Quantum Cryptography through Satellite Networks Transmission. *American Journal of Applied Sciences*, No.8 (1): pp 71-76, 2011.

[15]

Exact solution of coupled differential equations of stimulated Brillouin scattering

J. Malekzadeh[1], F. M. Akbari[2]

1&2 Electrical Engineering Department, Sharif University of Technology
Azadi Avenue, Tehran, Iran
[1]jaber_malekzadeh@yahoo.com

Abstract

Characteristics of steady state Stimulated Brillouin Scattering (SBS) in an optical fiber can theoretically be explained by the system of two coupled differential equations. In this paper, these two coupled differential equations are solved analytically and exact analytical solutions are presented. The exact solution is compared with approximation solution as well.

1. Introduction

It is well known that an intense laser light wave propagating in a material medium will result in many nonlinear physical processes that can lead to light scattering. The dominant nonlinear effect in light wave systems is stimulated Brillouin scattering (SBS) [1]. Recently, Brillouin scattering exhibits great potential in the fields of distributed fiber sensing and Slow-light.

Previously works based on the steady state coupled differential equations have derived the analytical expression neglecting the attenuation for the power distribution of Brillouin scattering [2]. Thereby, the effects of pump depletion or attenuation are ignored in many works concerning about the analysis of SBS [3,4]. However, the attenuation in long distance fiber is very serious. Therefore, the analytical solution neglecting the fiber attenuation is not explicit enough.

In this paper, the steady state Brillouin scattering in a long single mode optical fiber is analyzed, and the analytical solutions with the attenuation coefficient are obtained for the first time. Using the new method, the Brillouin threshold and depletion and saturation phenomena in a standard single mode fiber (SSMF) with a length of 15*km* are analyzed. Also, with these solutions, a slow-light based on SBS is investigated.

2. Theory

SBS can be described as a three-wave-interaction of a pump wave, a Stokes wave, and an acoustic wave. A counter propagating signal wave at the Stokes wave's frequency is amplified by the pump wave. Besides the amplification, the phase of the signal wave is changed due to the SBS. A signal wave and a pump wave propagating in a fiber as Brillouin medium can be described by:

$$\frac{\partial E_s}{\partial Z} = -\left(\frac{g_B}{2A_{eff}}\Delta K_{eR}P_P - \frac{\alpha}{2}\right)E_s + j\left(\frac{g_B}{2A_{eff}}\Delta K_{eI}P_P\right)E_s, \quad (1)$$

$$\frac{\partial E_P}{\partial Z} = -\left(\frac{g_B}{2A_{eff}}\Delta K_{eR}P_s + \frac{\alpha}{2}\right)E_P, \quad (2)$$

Where E_S and E_P are the electric field components of the signal or Stokes and the pump wave and P_S and P_P are the corresponding powers. A_{eff} is the effective core area, α is the fiber attenuation and g_B stands for the SBS gain coefficient. The phase mismatch terms ΔK_{eR} and ΔK_{eI} describe the gain distribution and the phase development according to the SBS. Since we use a cw-wave, we neglected all terms regarding the pump wave's phase [4,7]. By expressing the electric fields in terms of their powers and phases $E_S(z)=P_S(z)e^{i\varphi_S(z)}$ equations (1) and (2) can be transformed to a more easily system of equations:

$$\frac{\partial P_p}{\partial Z} = -\left(\frac{g_B}{A_{eff}}\Delta K_{eR}P_s + \alpha\right)P_p, \quad (3)$$

$$\frac{\partial P_s}{\partial Z} = -\left(\frac{g_B}{A_{eff}}\Delta K_{eR}P_p - \alpha\right)P_s, \quad (4)$$

$$\frac{\partial \varphi_s}{\partial Z} = \frac{g_B}{2A_{eff}}\Delta K_{eI}P_p, \quad (5)$$

We have solved analytically these three equations and presented exact analytical solutions for P_S, P_P, and φ_S.

By dividing the equation (4) to (3) we have:

$$\frac{\partial P_S}{\partial P_P} = \frac{(\Delta g_\alpha P_P - 1)P_S}{(\Delta g_\alpha P_S + 1)P_P}, \quad (6)$$

Where $\Delta g_\alpha = g_B / \alpha A_{eff}\, \Delta K_{eR}$, the integration of (6) gives the following expression:

$$P_S e^{\Delta g_\alpha P_S} = \frac{C}{P_P} e^{\Delta g_\alpha P_P}, \qquad (7)$$

Where C is a constant, using Lambert function together with equation (7), we derive the expressions of P_P and P_S:

$$P_S = \frac{1}{\Delta g_\alpha} W\left(\frac{\Delta g_\alpha C}{P_P} e^{\Delta g_\alpha P_P}\right), \qquad (8)$$

$$P_P = -\frac{1}{\Delta g_\alpha} W\left(-\frac{\Delta g_\alpha C}{P_S} e^{-\Delta g_\alpha P_S}\right), \qquad (9)$$

Where W is Lambert function.

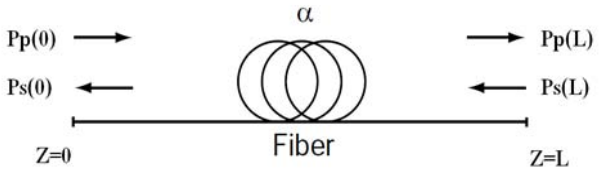


Figure 1: Propagation conditions of the pump and Stokes wave along the fiber.

The conditions of P_P and P_S along the fiber with the length L is illustrated in Fig. 1. According to Fig. 1 we have boundary value problem. Thus, the solution of the equation (9) at $z=L$ have two unknown variables, $P_P(z=L)$ and C. The integration of (3) and substituting (8), gives the following expression:

$$\int_{P_P(0)}^{P_P(L)} \frac{dP_P}{\left(W\left(\frac{\Delta g_\alpha C}{P_P} e^{\Delta g_\alpha P_P}\right)+1\right) P_P} = -\alpha L, \qquad (10)$$

Now equations (10) and (7) can be easily solved by Newton-Raphson method and we can get $P_P(z=L)$ and C. Also, we can obtain $P_S(z=0)$.

To solve equation (5) it is better to dividing it by equation (3) which then leads to following relation:

$$\frac{d\varphi_S}{dP_P} = -\frac{1}{2\alpha} \frac{\Delta g_I}{\left(\Delta g_\alpha P_S + 1\right)}, \qquad (11)$$

Where $\Delta g_I = \frac{g_B}{A_{eff}} \Delta K_{eI}$, the integration of (11) and substituting (8), gives the following relation:

$$\varphi_S(0) = -\frac{\Delta g_I}{2\alpha} \int_{P_P(L)}^{P_P(0)} \frac{dP_P}{W\left(\frac{\Delta g_\alpha C}{P_P} e^{\Delta g_\alpha P_P}\right)+1} + \varphi_S(L), \qquad (12)$$

By introducing $P_P(z=L)$ and C into this equation, the phase of Stokes wave at fiber input ($z=0$) can be obtained.

3. Simulation and Discussion

Using this new method, the Brillouin threshold and depletion and saturation phenomena in a standard single mode fiber (SSMF) with a length of 15km are analyzed and is shown in Fig. 2. As can be seen from diagram, the SBS activity starts at a Brillouin threshold of approximately 15mW. Above this power value the backscattered Stokes-wave rapidly increases whereas the transmitted pump power reaches the saturation regime.

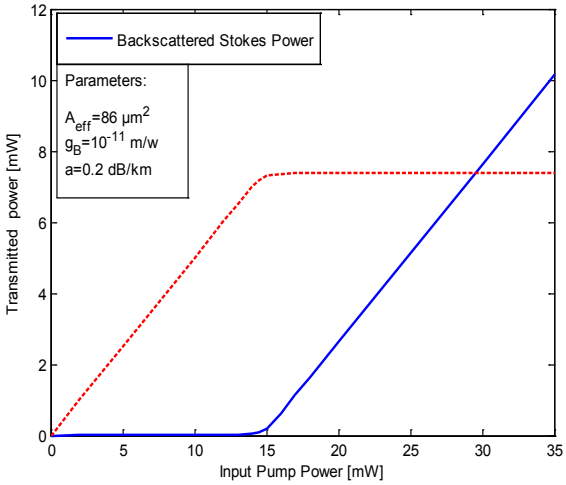


Figure 2: Stokes power and transmitted power versus launched power. It is seen that depletion and saturation occur at around 15mW launching power.

The Brillouin threshold is commonly calculated by [3,8]:

$$P_P^{th} = 19 \frac{K_B A_{eff}}{g_{B\max} L_{eff}}, \qquad (13)$$

Where K_B is a polarization factor, $g_{B\max}$ is the maximum value of the Brillouin gain coefficient in the line center and L_{eff} and A_{eff} denotes the effective length and effective area of the fiber. The calculated and measured Brillouin thresholds of several SSMF with different length are shown in Table 1. This table shows that the measured Brillouin thresholds are in good agreement with the calculated thresholds by equation (13).

Table 1: Calculated and measured Brillouin threshold of several SSMF with different length

Length (km)	P_P^{th} (calculated)	P_P^{th} (measured)
5	36.59	36.2
10	20.39	20.1
15	15.08	14.8
20	12.50	12.3

According to the Kramers-Kronig relations pulses are slowed down inside the gain bandwidth of SBS. Thus, SBS can be used to obtain a slow-light [5,6]. Using exact solution

of coupled equations, for simulation of a slow-light based on SBS a fiber length of 15km, pump powers 10mW, 15mW and 17mW, a signal input power 2μW and a temporal pulse FWHM width of 160ns were chosen. In figure (3) the normalized time functions of delayed pulses in comparison to the reference pulse are additionally shown. Also, in a SBS slow-light the maximum achievable time delay saturates at high pump powers and hence, is limited by the pump depletion. In the saturation regime the time delay does not increase any further but distortion increase, as can be seen in Fig. 3.

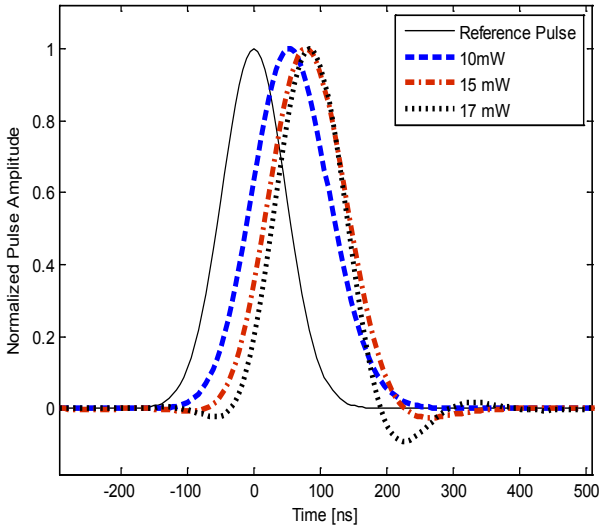


Figure 3: Normalized time functions of delayed pulses and reference pulse in SSMF with a length of 15km.

4. Conclusions

We have solved analytically two coupled differential equations of SBS and the exact analytical solutions are presented. The phenomena of power saturation and depletion have been illustrated using theoretical solution. Finally, a SBS slow-light was simulated and delayed pulses for different pump power were shown.

References

[1] C.L. Tang, Saturation and Spectral Characteristics of the Stokes Emission in the Stimulated Brillouin Process, *J. Appl. Phys.* 37, 2945, 1966.

[2] L. Chen, X. Bao, Analytical and numerical solutions for steady state stimulated Brillouin scattering in a single-mode fiber, *Opt. Commun*. vol. 152,pp. 65-70, 1998.

[3] G. Agrawal, *Nonlinear Fiber Optics*, Academic Press, San Diego, 2007.

[4] R.W. Boyd, *Nonlinear Optics*, Academic Press, San Diego, 2003.

[5] Kwang Yong Song, Miguel González Herráez and Luc Thévenaz, Observation of pulse delaying and advancement in optical fibers using stimulated Brillouin scattering, *Opt.Express*, vol. 13, no. 1, pp. 82-88, 2005.

[6] Y. Okawachi, M. S. Bigelow, J. E. Sharping, Z. M. Zhu, A. Schweinsberg, D. J. Gauthier, R. W. Boyd, and A. L. Gaeta, Tunable all-optical delays via Brillouin slow light in an optical fiber, *Phys. Rev. Lett.*, vol. 94, no. 15, p. 153902, 2005.

[7] A. Wiatrek, R. Henker, S. Preu, M. J. Ammann, A. T. Schwarzbacher, and T, Schneider, Zero-Broadening Measurement in Brillouin Based Slow-Light Delays, *Opt.Express*, vol.17, no. 2,pp. 797-802, 2009.

[8] T. Schneider, *Nonlinear Optics in Telecommunications*, Heidelberg: Springer-Verlag, Berlin, 2004.

ANFIS-based Estimation of Auditory Brainstem Response Changes in Rabbits Due to GSM-900 Radiation Exposure

Theodoros N. Kapetanakis[1], Ioannis O. Vardiambasis[1*]
Antigoni Kaprana[2], and Melina P. Ioannidou[3]

[1] Department of Electronics, Chania Branch, Technological Educational Institute (TEI) of Crete, Greece
[2] ENT Department, University Hospital of Crete, Heraklion, Greece
[3] Department of Electronics, Alexander Technological Educational Institute of Thessaloniki, Greece
* ivardia@chania.teicrete.gr

Abstract

A neuro-fuzzy system (ANFIS) is developed to estimate GSM-900 radiation exposure time needed to cause specific electrophysiological time-related changes in auditory pathway. The proposed system is exploiting the available experimental results of [1], for auditory brainstem response changes in rabbits due to mobile phone radiation exposure. This paper proves, on one hand the short-term effect of mobile phone usage to the subject auditory pathway, and on the other hand the possibility of building an automated system to detect the radiation exposure auditory brainstem responses. This system can be very useful, as it provides reliable exposure assessment, even though it is unsafe to extrapolate neurological data from non human in vivo experiments.

1. Introduction

International scientific research confirms that electromagnetic fields are biologically active in animals and humans, and in some cases can cause discomfort and disease [2]. Especially radiofrequency radiation from mobile phone use has been associated in many studies to an increased risk for brain tumors. Experimental radio frequency (RF) dosimetry indicates that, in common usage approximately one half of the mobile's output power is absorbed by tissues on the side of the head close to the handset. In conjunction with the high number of mobile phone users and the relative high specific absorption rate (SAR) close to the ear, it is clearly that the auditory system must be particularly examined for possible adverse effects from the EM radiation.

A number of studies have been carried out investigating the effect of mobile phone radiation on the auditory system. In a recent experimental animal study [1], the possible electrophysiological time-related changes in auditory pathway during mobile phone electromagnetic field exposure were investigated. In this work, we will further use the data sets acquired in [1] through the experimental study, in order to implement an ANFIS network.

The rest of the paper is organized as follows. In Section 2, the experimental procedure is described and details about the auditory brainstem response are given. In Section 3, the fundamental ANFIS network architecture is presented, along with the configuration used to train the network. Finally, in Section 4, characteristic results are presented and discussed.

2. Experimental study

Auditory brainstem response (ABR) is an electrical signal evoked from the brainstem and the central auditory pathway after sound stimulation of the ear. The procedure is to generate a brief click or tone pip from earphones and to measure the elicited neuronal action potentials by surface electrodes, typically placed at the vertex of the scalp and ear lobes. The amplitude (microvoltage) of the signal is averaged and charted versus time (msec), similarly to electroencephalography. ABR audiometry provides a unique method for non-invasive study of the pathophysiology of the human or other mammal hearing system. Since 1971 [3], the ABR recording method has been standardized and used increasingly in otorhinolaryngology clinics to evaluate symptoms and problems related to the auditory pathway. The ABR signal is characterized by a series of vertex positive peaks labeled from I to VII. The latencies of the first five peaks, which represent brainstem transmission time and therefore brainstem auditory processing, are the most important parameters for evaluation and diagnosis by medical experts. The analysis of ABRs is usually conducted manually, following a four-step procedure: determination of the responses' presence, detection of the main peaks, estimation of the different latencies between I, II, III, IV, and V peaks, and diagnosis of the possible problem [4].

As described in [1], twenty eight rabbits under general anesthesia were radiated via a power- and frequency-adjustable radio transmitter, which was designed and manufactured according to the needs of the experiment for GSM-900 mobile phone emission simulations, as described in Fig. 1. The transmitter was placed near the ear of each subject and the antenna was placed in the entrance of the external auditory bony canal, as shown in Fig. 2. ABRs were recorded during radiation (real time measurements) at

regular time intervals (at 1, 15, 30, 45, and 60 minutes), using the EP25-Eclipse platform (Interacoustics).

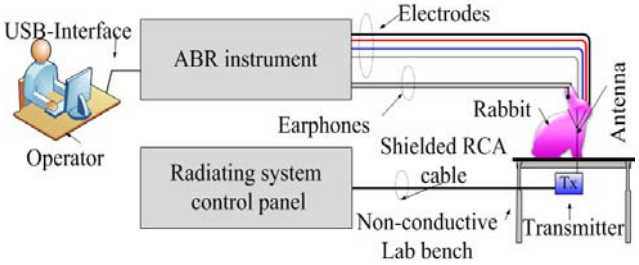


Figure 1: The block diagram of the experimental procedure in [1].

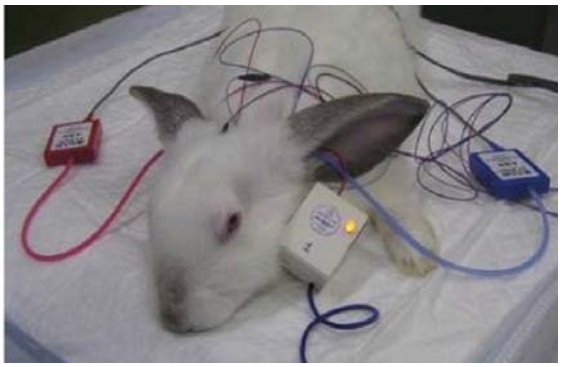


Figure 2: One of the subjects anesthetized during the experiment [1; Fig.1b]. The needle electrodes, the inserted earphones and the radio transmitter in place are shown.

3. Adaptive Neuro-Fuzzy Inference System

The ANFIS (Adaptive Network-based Fuzzy Inference System), originally proposed in [5], has emerged as the combination of two powerful intelligent techniques: the artificial neural networks and the fuzzy logic approach, which have been adopted and tested to solve many real-world problems in recent years. This combination of fuzzy logic and neural networks into adaptive network architecture is the main fact making ANFIS so attractive in our investigation. Specifically, ANFIS integrates the greater learning capability of neural networks with a fuzzy logic approach to construct a fuzzy inference system, with membership function (MF) parameters, which are tuned using a back-propagation algorithm either alone or in combination with a least squares method.

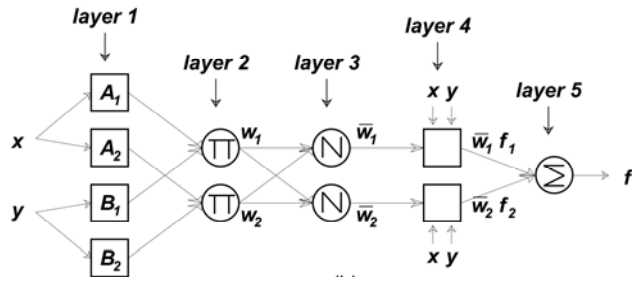


Figure 3: Equivalent ANFIS architecture, of a two-input first-order Sugeno fuzzy model with two rules.

As the a priori knowledge is not excluded, a better starting point for training the ANFIS is generally provided. Thus the convergence time is reduced and the results are improved. Since this type of neuro-fuzzy structure has proven to be a universal function approximator [5]-[6], we have decided to use it for this problem.

3.1. General architecture of ANFIS

ANFIS consists of two parts: the antecedent part and the conclusion one. They are connected to each other by rules in network form. The architecture of the ANFIS network (Surgeno fuzzy model) is shown in Fig. 3. It is structured in five layers, which are explained below. Additionally, the rule set with two fuzzy if-then rules for the above network is the following:

$$\begin{aligned} &\text{Rule 1: If } x \text{ is } A_1 \text{ and } y \text{ is } B_1, \text{ then } f_1 = p_1 x + q_1 y + r_1, \\ &\text{Rule 2: If } x \text{ is } A_2 \text{ and } y \text{ is } B_2, \text{ then } f_2 = p_2 x + q_2 y + r_2. \end{aligned} \quad (1)$$

Layer 1: Every node i in this layer is an adaptive node with a node function:

$$O_{1,i} = \mu_{A_i}(x); \text{ for } i=1,2, \text{ or } O_{1,i} = \mu_{B_{i-2}}(y); \text{ for } i=3,4 \quad (2)$$

where x (or y) is the input to node i and A_i (or B_{i-2}) is a linguistic associated with this node. Here the membership function for A_i can be any appropriate parameterized membership function such as the generalized bell function, the Gaussian function, or the sigmoid function.

Layer 2: Every node in this layer is a fixed node labeled Π, whose output is the product of all the incoming signals and represents the firing strength of a rule, or in other words perform the fuzzy AND function:

$$O_{1,i} = w_i = \mu_{A_i}(x) \cdot \mu_{B_i}(y); \; i=1,2. \quad (3)$$

Layer 3: Every node in this layer is a fixed node labeled N. The ith node calculates the ratio of the ith rule's firing strength to the sum of all rules' firing strengths. The output of this layer is called normalized fire strength:

$$O_{3,i} = \bar{w}_i = w_i / (w_1 + w_2); \; i = 1,2 \quad (4)$$

Layer 4: Every node i in this layer is an adaptive node with a node function:

$$O_{4,i} = \bar{w}_i f_i = \bar{w}_i (p_i x + q_i y + r_i), \quad (5)$$

where $\bar{w}_i$ is a normalized firing strength from layer 3 and (p_i, q_i, r_i) is the parameter set of this node. Parameters in this layer are referred to as consequent parameters.

Layer 5: The single node in this layer is a fixed node, which computes the overall output as the summation of all incoming signals:

$$\text{Overall Output} = O_{5,i} = \sum_i \bar{w}_i f_i = \left(\sum_i w_i f_i \right) \Big/ \sum_i w_i . \quad (6)$$

3.2. ANFIS configuration and training

The ANFIS network used in this paper is the Sugeno-type

FIS structure, shown in Fig. 4, with inputs: a) the absolute latency of wave I, II, III, IV, or V (baseline ABR recordings without radiation exposure), and b) the exposure time to GSM-900 radiation. The output of the network is the absolute latency of the corresponding wave after the given radiation exposure time.

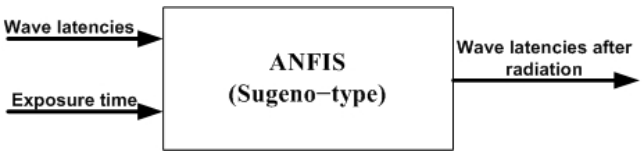


Figure 4: ANFIS inputs-output block diagram.

In the herein simulation we have followed the hybrid training algorithm, which combines the steepest descent and the least-squares methods, in order to achieve fast parameter identification (detailed information about this algorithm can be obtained from [6]). The type and number of MFs assigned to each input variable is chosen by the trial-and-error procedure (similarly to the function of neural networks), in order to achieve a desired performance level [5]. During this procedure we have tried 6 different MFs, namely: the Gauss, the Gaussian combination (gauss2), the difference between two sigmoid membership functions (dsig), the Gbell, the Π-shaped, and the product of two sigmoidally shaped membership functions. Based on the performance of each MF, we have selected either the Gauss MF (in order to evaluate the latencies of waves I, III, and IV), or the gauss2 MF (in order to evaluate the latencies of waves II and V) [5]-[7]. For the selected MFs, Table 1 shows the achieved training performance.

In order to determine the end of the training algorithm, a stopping criterion have to be designated. During the training procedure, the feedforward and reverse pass calculations are repeated per epoch (which is a single pass through the entire training set, followed by testing of the verification set), until: (a) the parameters are stabilized, (b) the respective error function is minimized, or (c) the maximum number of epochs is reached [5]-[8]. In this paper, the following RMS error function (*RMSE*) is used as error function:

$$RMSE = \sqrt{\frac{1}{N}\sum_{j=1}^{N}\left(P_j - T_j\right)^2}\ , \qquad (7)$$

where P_j is the value predicted for case j; and T_j is the target value for the same case. In order to have perfect fit, P_j has to be equal to T_j and *RMSE* has to be equal to 0. Thus, *RMSE* ranges from 0 to infinity, with 0 corresponding to the ideal case.

Table 1: ANFIS number of rules and training performance of the selected membership functions.

Input	Rules	MF type	*RMSE*
Wave-I	64	Gauss	1.384×10^{-2}
Wave-II	49	Gauss2	6.520×10^{-2}
Wave-III	64	Gauss	2.347×10^{-2}
Wave-IV	25	Gauss	1.125×10^{-1}
Wave-V	64	Gauss2	9.494×10^{-2}

4. Results

A number of training and checking tests were performed in order to achieve the best performance of the ANFIS network. The *RMSE* is shown in Fig. 5, versus the number of the dsig MFs (composed of difference between two sigmoidal membership functions), used by ANFIS in order to evaluate the latencies of waves I-V. Obviously 8 dsig MFs suffice to minimize and stabilize the training *RMSE*. Moreover, Fig. 6 depicts the *RMSE* versus the number of Gauss MFs, which are used by ANFIS in order to evaluate the latencies of waves I-V. Apparently 9 Gauss MFs suffice to minimize and stabilize the training *RMSE* [5]-[7].

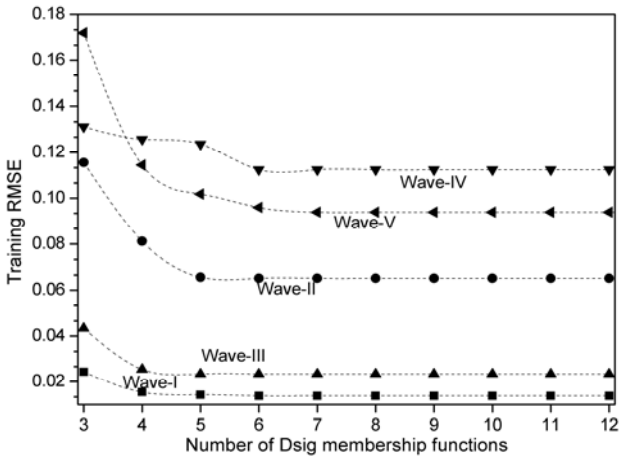


Figure 5: *RMSE* versus the number of Dsig membership functions used by ANFIS in order to evaluate the latencies of waves I-V.

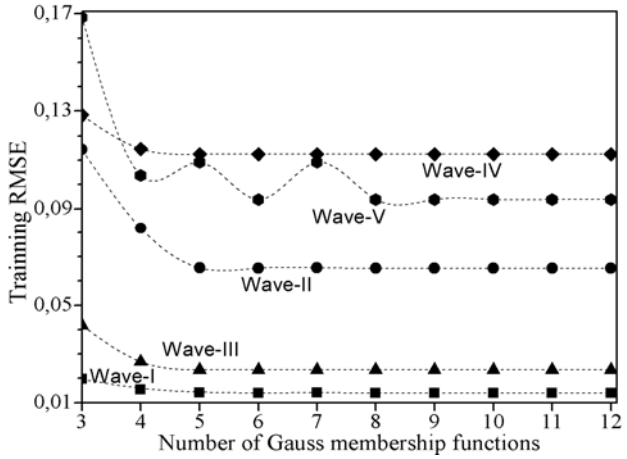


Figure 6: *RMSE* versus the number of Gauss membership functions used by ANFIS in order to evaluate the latencies of waves I-V.

Thereafter, in order to evaluate the trained ANFIS network, we compare its output with the corresponding experimental data. In all cases, ANFIS reproduced exactly the known data, as shown in Figs. 7-8. Especially in Fig. 7, the ANFIS-predicted latencies for wave-III coincide with the experimental data for 0, 1, 15, 30, 45, and 60 minutes of radiation exposure (where 0 corresponds to the baseline

recordings without exposure), for three different subjects. This network, using 8 Gauss MFs to each input variable, was trained for 37 epochs.

Similarly, in Fig. 8, the ANFIS-predicted wave latencies coincide with the corresponding ABR recordings (real experimental values) from a randomly selected subject.

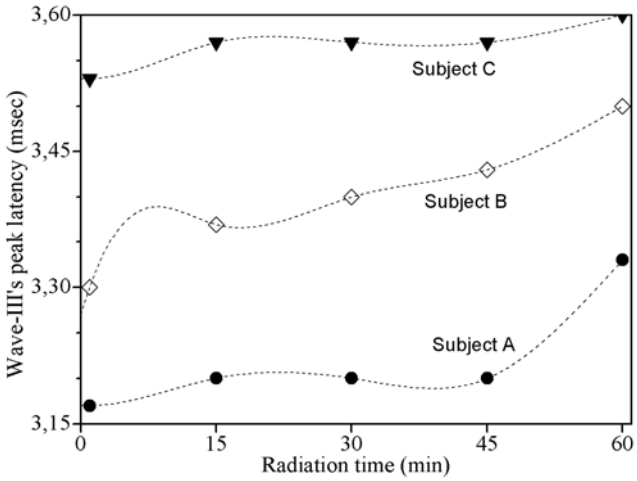


Figure 7: Coinciding experimental and ANFIS predicted values (at 1, 15, 30, 45, 60 minutes of radiation) for the latency of wave-III's peak, for three different individual subjects.

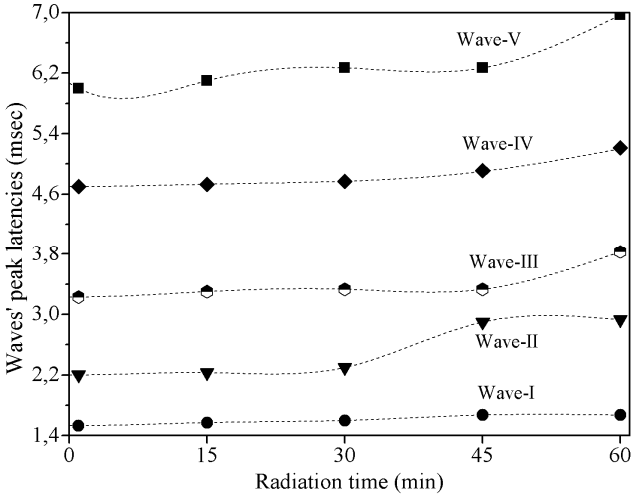


Figure 8: Coinciding experimental and ANFIS predicted values for the latencies of waves I-V, at 1, 15, 30, 45, 60 minutes of radiation.

5. Conclusions

The wide and growing usage of cellular phones has raised questions about the possible health risks associated with RF electromagnetic fields. Since it is very difficult to accurately measure and quantify the RF exposure level for all individuals, it would be helpful for epidemiologists and cellular phone users to obtain a time estimate of specific radiation exposure generating health problems. In this context, a neuro-fuzzy system was developed to estimate GSM-900 radiation exposure time causing specific electrophysiological time-related changes in auditory pathway. The system was trained and evaluated, exploiting available experimental results in [1] for auditory brainstem response changes in rabbits due to mobile phone radiation exposure. The coincidence between the real experimental and the ANFIS predicted values for the ABR wave latencies was remarkable. Thus, we have proved not only the existence of short-term effects to the auditory pathway of subjects using mobile phones, but also the capability of building an automated system to detect or satisfactory predict the radiation exposure auditory brainstem responses. Such a system, providing reliable exposure assessment, could be very useful even though it is unsafe to extrapolate neurological data from non human in vivo experiments.

Acknowledgement

This work was funded by the Research Committee of Alexander Technological Educational Institute of Thessaloniki, Greece.

References

[1] A.E. Kaprana, T.S. Chimona, C.E. Papadakis, S.G. Velegrakis, I.O. Vardiambasis, G. Adamidis, and G.A. Velegrakis, "Auditory brainstem response changes during exposure to GSM-900 radiation. An experimental study", *Audiology & Neurotology*, vol. 16, no. 4, pp. 270-276, 2011.

[2] A.E. Kaprana, A.D. Karatzanis, E.P. Prokopakis, I.E. Panagiotaki, I.O. Vardiambasis, G. Adamidis, P. Christodoulou, and G.A. Velegrakis, "Studying the effects of mobile phone use on the auditory system and the central nervous system: A review of the literature and future directions", *European Archives of OtoRhinoLaryngology*, vol. 265, no. 9, pp. 1011 - 1019, Sep. 2008

[3] D. Jewett and J. Williston, "Auditory-evoked far fields averaged from the scalp of humans", *Brain*, vol. 94, pp. 681-696, 1971.

[4] J. Tian, M. Juhola, and T. Gronfors, "Latency estimation of auditory brainstem response by neural networks", *Artificial Intelligence in Medicine*, vol. 10, pp. 115-128, 1997.

[5] J.-S.R. Jang, "ANFIS: adaptive-network-based fuzzy inference systems", *IEEE Trans Systems, Man Cybernetics*, vol. 23, no. 3, pp. 665-685, May 1993.

[6] J.-S.R. Jang, C. Sun, and E. Mizutani, *Neuro-Fuzzy and Soft Computing: A computational approach to learning and machine intelligence*, Prentice-Hall Inc., 1997, pp. 335-345.

[7] J.-S.R. Jang and N. Gulley, "MATLAB fuzzy logic toolbox user's guide", version 2.2.13, *The MathWorks Inc.*, 2011.

[8] K. Erenturk, "ANFIS-based compensation algorithm for current-transformer saturation effects", *IEEE Trans Power Delivery,* vol. 24, no. 1, pp. 195-201, 2009.

Measuring kinetics of enzymatic hydrolysis of acetylcholine in presence of high voltage pulses by dielectric characterization

C. Gilbert[1] and O. Meyer[1*]

[1] LGEP, Supélec, CNRS UMR-8507, UPMC Paris 06, Paris Sud 11 ; 11 rue Joliot Curie, F91192 Gif-sur-Yvette, France
* olivier.meyer@upmc.fr

Abstract

In this work we observe hydrolysis of acetylcholine kinetics in the presence of an enzyme, with a wide broadband dielectric spectroscopy (40Hz – 4GHz) with or without pulses excitations. We also follow an in vitro reaction with an electrical marker and can observe the consequences of high voltage (increasing to 1kV in around 20ns) pulses on this marker.

1. Introduction

The biochemical system studied is the hydrolysis of acetylcholine chloride in the presence of the enzyme acetylcholinesterase (AChE) specific to its degradation, choline chloride and acetic acid (Figure 1), in aqueous medium [1]. The acetylcholine is the primary neurotransmitter in the human body (figure 2). Roughly, the hydrolysis reaction occurs after the transmission of nervous information from one neuron to another. It allows purging the transmission channel of neurotransmitters who have accomplished their task and therefore block new entrants. The hydrolysis reaction can also re-form new radicals recovered in the synapses to synthesize new neurotransmitters.

The biochemical system studied is highly ionic, by the nature of the compounds characterized, and by adding a buffer (phosphate buffer pH 7.5), necessary to stabilize the reaction. The ionic character of molecules studied, limits the extent possible conduction phenomena at low frequencies. The need to observe the reaction in aqueous solution makes it impossible to discriminate the elements present by measuring their dipole moment (microwave frequency band), the water molecules themselves being dipolar in nature and the large majority. We then referred to a study of the effects of conduction and adsorption on the electrodes at low frequencies to observe the evolution of the kinetics of the hydrolysis reaction first and then vacuum in the presence of pulse trains of high amplitude (nanopulses below 1kV).

2. Chemical reaction & experimental set-up

The objective is to find the thresholds of electromagnetic pulses to be applied to modify the behavior of the studied biochemical reaction. The acetylcholine is the primary neurotransmitter in the human body [1]. The hydrolysis reaction occurs after the transmission of nervous information from one neuron to another. It allows one hand to purge the transmission channel of neurotransmitters have completed their task and therefore blocking new entrants, on the other hand the radical reform of choline then recovered by the synapses in order to synthesize new neurotransmitters.

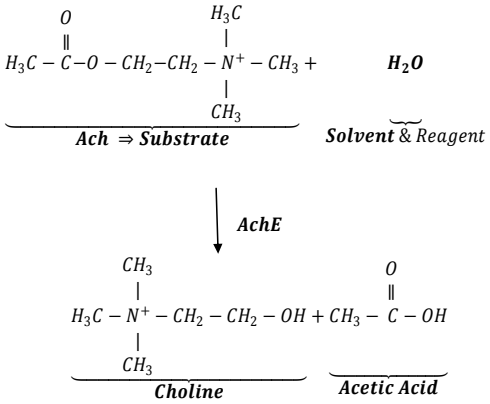


Figure 1: Hydrolysis reaction.

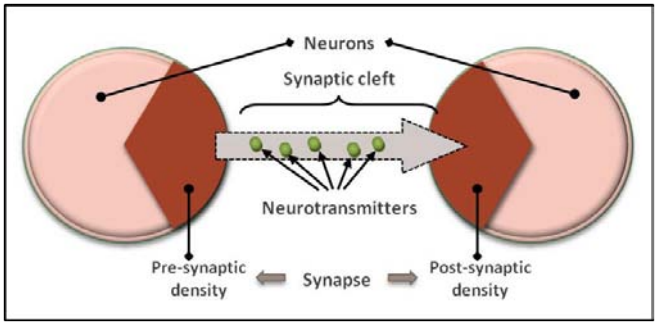


Figure 2: Simplified diagram of neural transmission between two neurons.

The experimental device (Figure 3) [2-4], has two impedance analyzers (Agilent 4294A and 4291A) and a network analyzer (Agilent PNA-C) covering a frequency band 40Hz to 18GHz in APC7. The measuring chamber is a coaxial discontinuity gold plated cylinder (by electrolytic bath). The cell characterization is a discontinuity gold

plated coaxial cylinder (by electrolytic bath). The electrodes underwent a submicron polishing so as to limit the anodic reactions at the electrodes. These reactions could lead to measure a faradic current which mask electrical the parameters of the electrolytes. The measuring chamber is connected to an electromagnetic switch analyzers broadband. All is controlled automatically by computer (switching, acquisition and calculation). The direct problem (calculation of the admittance of the whole measuring chamber and liquid) is calculated by mode matching to present both sides of the interface coaxial measuring chamber (TEM modes and evanescent TM_{0n} coaxial TM_{0m} in the cylindrical guide) [5].
The complex permittivity is obtained by numerical solution of the inverse problem by approximation and minimization of the difference between direct calculation and measurement [1,3,5]. The pulses supplied by a generator (Kentech) of 1kV (maximum) are defined by a rise time of the order of 2 to 3ns.

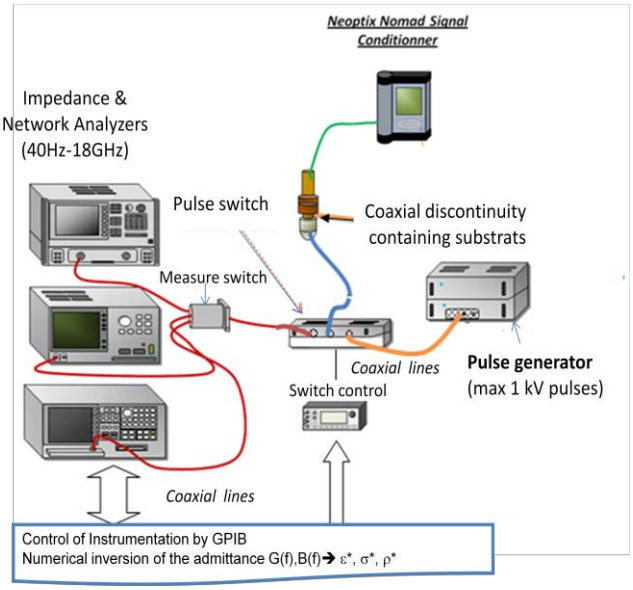


Figure 3: Instrumentation for electric and dielectric broad band characterization of liquids excited by high voltage pulses

2.1. Results

2.1.1. Validation of permittivity and conductivity measurements on liquids and common salts.

Figure 4 shows the good agreement for the method for measuring permittivity at high frequencies of liquids (ethanol in this example) between measures and results of literature.

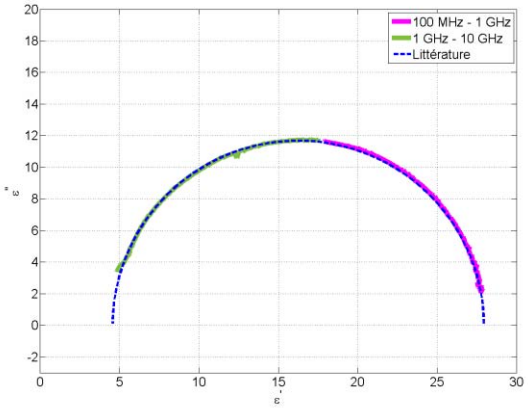


Figure 4: Validation permittivity of ethanol (95%).

Consider a charged particle and its ionic atmosphere or solvent molecules surrounding it. Under the effect of the applied field, the charged particle will move to "follow". The uncharged solvent molecules will not be subject to this effect, but their hydrogen bonds, if the solvent is water will move towards the charged particle moving. Thus, there is symmetry breaking.

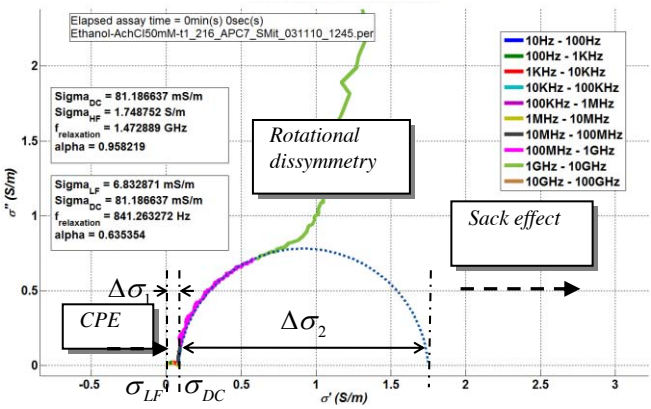


Figure 5: Example of data represented into conductivity Argand chart can be fitted by an adapted Cole-Cole model 50mM AchCl in ethanol.

The theory describing this relaxation is called the Onsager-Falkenhagen. It emphasizes that an electric field relaxation appears, partially offsetting the applied electric field. This theory plays an important role in modeling the conductivity of electrolytes in solution, which varies depending on their concentration. It can be shown that the more the ion concentration in solution is important, the more the interactions ion/ion are present, and the molar conductivity weakens. When an external electric field is applied to a sufficiently high frequency (beyond the relaxation frequency of the solvent), the ionic atmosphere is no longer able to keep the charged particle and the conductivity of the solution increases. This effect is called the Sack effect. An example of visualization of this effect is given in figure 5 of the mixture of salt Ach-Cl in ethanol.

Measured data represented into conductivity Argand chart (an example is given figure 5) are fitted by an adapted Cole-Cole model like equation 1.

$$(*)\circ\ \sigma^*(\omega) = \sigma_{LF} + \sum_i \frac{\Delta\sigma_i \left(j\varpi\tau_i\right)^\alpha}{1+\left(j\varpi\tau_i\right)^\alpha} \quad (1)$$

$$\sigma^*(\omega) = 1/(\varepsilon_0\varepsilon_r(\omega)^*) \quad (2)$$

Typically, data can be fitted with two relaxations: in the lower frequencies we found Surface phenomenon like CPE – Adsorption on electrodes, and in higher frequencies we found rotational dissymmetry zone (i.e. bulk or solvent relaxation) and then Sack effect beyond solvent relaxation.
In the high frequency area, conductivity relaxation is equal to dipolar relaxation for Debye like model.
The solvent has properties different from its solute in this experiment.
Figure 6 shows the quality and validity of conductivity measurements on common salts (ions) solvated in water double distilled, for different concentrations compared with results extracted from the literature [6]. It also shows the variation of relaxation frequency of the bulk and the relaxation frequency of the double layer capacitance shown on the representation of static conductivity. Subjected to an electric field, each ion or molecule orientational and directional characteristics differ depending on its nature (size, charge, polar, non-polar, etc).

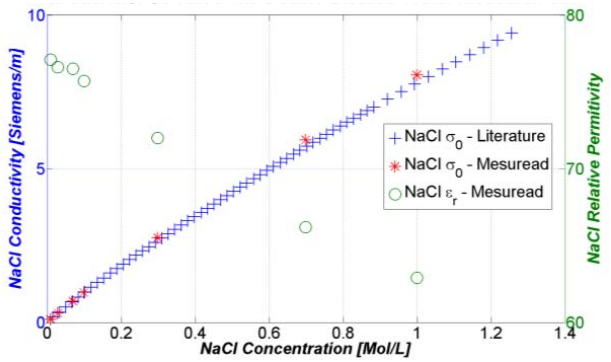


Figure 6: Validation of the conductivity measurement by various NaCl solvated in double distilled water measurement.

2.1.2. *Products and substrates*

The observed results show a significant difference between the conductivity of broadband acetylcholine chloride in buffer pH 7.5 (figure 7) and the product of the reaction (ie, Choline chloride and acetic acid in the same buffer pH 7.5) due to the adsorption of species on the electrode (figure 8 for the result of the hydrolysis to be compared to a measure of the stoichiometric mixture Choline chloride (CHCl) + 50 mM acetic acid + buffer, figure 9). Representation is most relevant to show the marker reaction is the complex conductivity ($\sigma^* = j\omega\varepsilon\varepsilon_0{}^*$) over a wide frequency band. The value of the static conductivity (σ_{DC}) results over the nature of the conjugate base (here chlorine) that characterized the molecule. Changing in Argand diagrams is characteristic of the appearance of acetic acid [3].

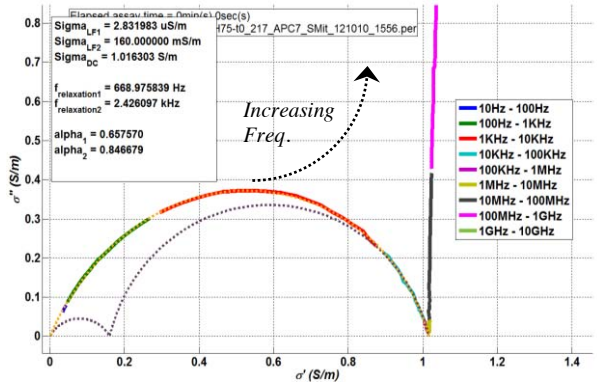


Figure 7: Initial substrate (pH 7.5 buffer + 50 mM Achcl).

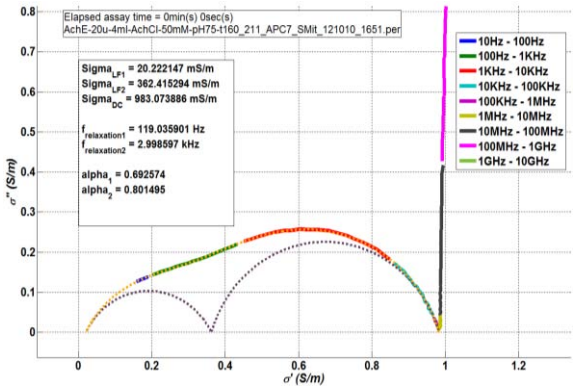


Figure 8: Final product after 57 min reaction.

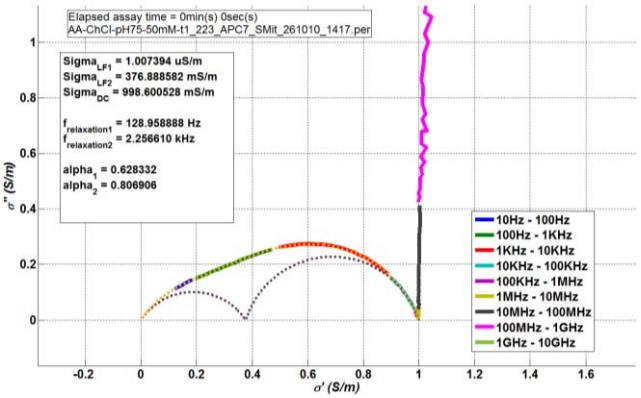


Figure 9: Result for the stoichiometric mixture Choline chloride (CHCl) + 50 mM acetic acid + buffer.

2.1.3. *Founding a marker of the reaction*

To characterize the progress of the reaction, it is initially necessary to determine a reliable marker. As we have previously set out the measurement of the static conductivity does not reflect the evolution of the reaction as it reflects the majority of the chlorine ion mobility in the substrate and product. The deconvolution of Argand diagrams of conductivity extracted two phenomena, the most important

is the circle at higher frequencies around a few hundred kHz, a relaxation was attributed mainly to the phenomenon of double layer capacitance [3-5]. The second phenomenon, at lower frequencies, is mainly attributed to adsorption of acetic acid and acetates ions (Figures 7-9). Marking the progress of the reaction will emphasize the production of acetic acid which is the exploitable broadband impedance characterization. The final selected marker (which characterizes quite well the evolution of the reaction mixture) will be the value of the imaginary conductivity, σ" at the relaxation frequency of the phenomenon of electrical double layer. The second relaxation phenomenon decreases in proportion to the amount of acetic acid. Indeed, the adsorption of acetic acid is dominant over the choline chloride ions and naturally adsorbed on the electrode. To validate this marker, we performed measurements of changes in response to different concentrations of enzyme (Figure 10).

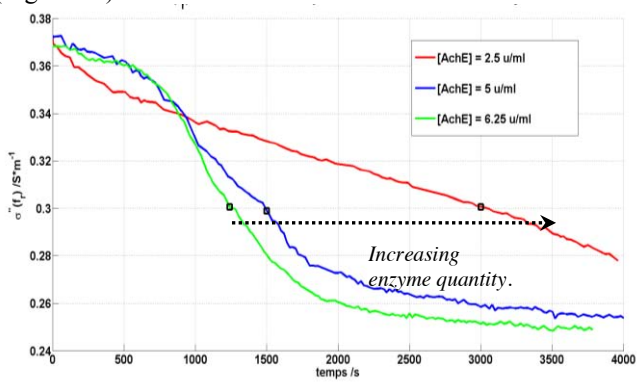


Figure 10: Evolution of σ"(Fr2) as a function of enzyme concentration

Conventionally, the more enzymes, the more quickly the reaction proceeds to the extent that it is not saturated with enzyme. This measure clearly shows the linear relationship between the amount of enzyme and reaction time. Figure 2, for the blue curve, the amount of enzyme is two times higher than for the red curve, but the conductivity value reached in mid-term is two times faster.

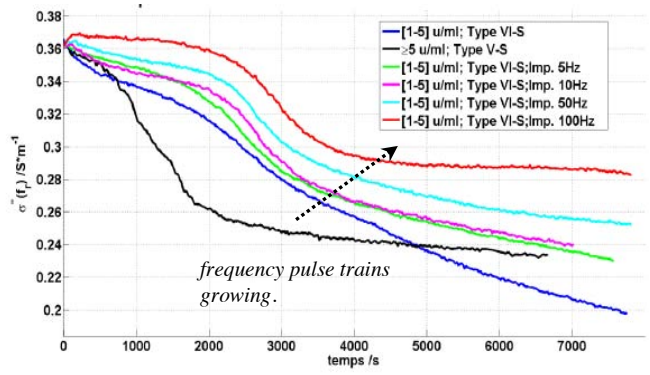


Figure 11: Evolution of the marker σ "(Fr2) for the duration of the reaction for different repetition frequencies of pulses trains (320V pulses).

Now that we have defined a marker for monitoring response reliably, we are also able to characterize the evolution of the kinetics under continuous and pulsed alternating fields.
The measurements for different values of repetition frequency of the pulse train show that the reaction appears to be more and more inhibited with increasing the pulse repetition frequency (figure 11: 320V, frequency repeat from 5 Hz to 100 Hz), with a rise in temperature controlled below 1°C. A similar characterization was performed on mixtures subjected to a field at 2.45 GHz without changing the rate of reaction (at constant temperature).

2.2. Conclusion

We were able to identify a marker of electrical hydrolysis reaction. The marker of in situ monitoring of the reaction allowed us to observe a noticeable effect of inhibition of the reaction under pulse-type nanopulses in athermal condition. These results show the usefulness of the proposed approach to observe the thermal or sub-thermal effects on biological systems in vitro. We also demonstrated that the application of a field at 2.45 GHz CW in the limit of the thermal heating of the solution (ΔT <3 ° C) does not act as a catalyst for the reaction of hydrolysis in the absence of enzyme AchE, there is no inhibitory effect in presence of this enzyme.

Acknowledgements

This study was funded by DGA "Exploratory and Innovation Research" contract, REI DGA No. 05.34.054. We thank R. Vézinet from the CEA DAM (Gramat, France) who allowed us to use the Kentech generator for this work.

References

[1] J. Massoulié, The origin of the molecular diversity and functional anchoring of cholinesterases, *Neuro Signals*, Vol. 11, 130-143, 2002.

[2] O. Meyer, M. Delmotte, J-C. Lacroix, R. Weil, A. Loupy, F. Maurel, A. Fourrier-Lamer., How broad band (from radio frequency to microwaves) dielectric parameters describe synthetic chemical reactions, *J. Phys. Org. Chem.*, 21, pp. 738-746 2008.

[3] C. Gilbert, Instrumentation hyperfréquence pour l'étude de cinétiques de réactions biochimiques en présence d'un champ électromagnétique de forte intensité. Interprétation physique des résultats, *PhD thesis of UPMC*, Paris, 29/04/2011.

[4] C. Gilbert, O. Meyer, Cast and accurate dielectric characterization technical to get various electrolytic parameter, *PIERS 2011*, Marrakech, 20/03/2011

[5] N. Belhadj-Tahar and A. Fourrier-Lamer, Broad-band analysis of a coaxial discontinuity used for dielectric measurements, *IEEE Trans. Mic. Theory and Tech.*, Vol. MTT-34, 3, pp. 346-350 (1986).

[6] W. M. Haynes, *CRC Handbook of Chemistry and Physics*. (éd. Version 2011). (W. M. Haynes, Éd.) Boulder, USA: CRC Press. (2010).

Glucose quantification in highly scattering media using diffuse reflectance polarimetry

E.T. Aksenov , G.A. Kafidova*, D.V. Mokrova, V.M. Petrov

St. Petersburg State Polytechnical University, St. Petersburg, Russia
*corresponding author, E-mail: gkafidova@gmail.com

Abstract

Method of optical polarimetry is well known, but earlier it was mainly used to low scattering media. For example a standard sensing site for glucose quantification is the aqueous humor of the eye. In this paper we consider the possibility of measuring the glucose concentration by detecting polarization of the backscattered laser light. As object of research a human finger have been chosen.

1. Introduction

More than 9 million people in Russian Federation, 17 million in the U.S. and 346 million worldwide suffer from diabetes. Thus, this disease is global medical problem of modern society. According to World Health Organization in 2030, the number of diabetics will exceed 500 million people. Effective way of definition of a critical condition especially at people being in risk group (age over 40 years old, overweight) is a real-time monitoring of blood glucose concentration.

Currently, there are dozens of commercially available blood glucometers, but for the measurement using such devices it is necessary to taking of a blood sample. Therefore, to avoid introducing infection into the body, it is necessary to strictly observe the rules of antiseptic. Given the fact that control of blood sugar levels of diabetic should carry up to 8 times a day, the problems associated with discomfort and the risk of infection becomes clear. All this leads to the fact that the patient tends to either limit the number of procedures, or avoid them altogether. The result is a deterioration in his condition until death.

Thus, the development of methods of noninvasive and continuous (or repeated) monitoring of blood glucose concentration is one of the priorities of modern biomedical diagnostics.

The development of coherent-optical methods for the study and diagnosis of biological objects makes it possible to create a non-invasive sensors of blood glucose concentration dynamics. These methods have several advantages: non-ionizing radiation is used for the control, additional chemical reagents does not require in the process of measurement, measurement can be conducted in a continuous mode, and repeated many times, the measurement results are displayed in real time. In addition, measurement procedure does not cause discomfort to the patient.

2. Glucose quantification in highly scattering media

In this paper polarimetric technique for detecting the dynamics of blood glucose concentration is considered and the possibility of creating a non-invasive sensor based on it is justified.

2.1. Theory

Changes in blood glucose concentration leads to a change in the optical characteristics of human tissues, including skin. It is known that glucose concentration increasing leads to a decrease in the scattering coefficient of tissues [1, 2], which is determined by the difference in refractive index of extracellular fluid and cell membranes. Glucose concentration increasing in the extracellular fluid leads to an increase in the refractive index, which in turn reduces the scattering coefficient of tissue. In addition, glucose, since their chirality, rotates the polarization plane of linearly polarized light. This property is the basis for all modern high-sensitivity polarimetric methods. In [3, 4] is proposed to carry out polarimetric measurements (in transmitted light) in the liquid contained in the anterior chamber of the eye (aqueous humor), as it has a low coefficient of scatter. However, this method of measurement susceptible to substantial errors caused by the birefringence of the cornea and the eye movement [5, 6]. Using human skin as an object of study in the polarimetric measurements was limited to a strong depolarization of the light passing through the skin. Nevertheless, substantial preservation of light polarization in biological tissue samples is demonstrated for the reflection geometry [7]. In view of the fact that part of the incident linearly polarized light is scattered in the opposite direction, and under certain conditions, preserves the polarization becomes possible to measure the direction of light polarization. The results of such measurements and corresponding theoretical models of the scattering of polarized radiation in containing glucose turbid media were considered in [8-10].

Polarimetric quantification of glucose, as noted, based on optical rotatory dispersion, in which chiral molecules contained in aqueous solution rotate the plane of polarization of linear-polarized light passing through the

solution. The angle of rotation is directly proportional to the concentration of optically active molecules, the length of the solution layer, and a constant of the substance, called the specific rotation. The resulting angle is given by

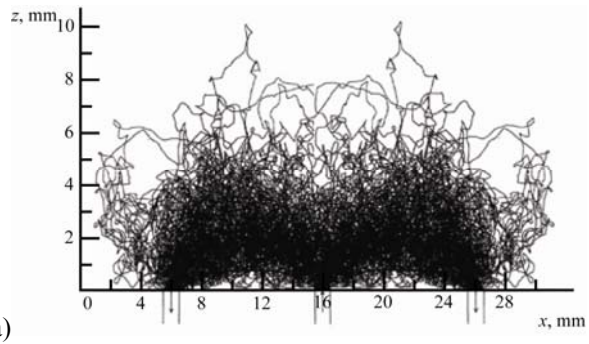
$$\varphi = \alpha_\lambda LC, \quad (1)$$

where α_λ has the dimension [deg•dm^{-1}•g^{-1}•l] and represents the specific rotation at wavelength λ, L — length of the sample in dm, C — concentration in g/l. Glucose in the human body is dextrorotatory and has a specific rotation 52.6 for the D-sodium line with a wavelength of 589 nm. At physiological concentrations and the sample length of 1 cm angle of rotation of the polarization plane is about 0,005°.

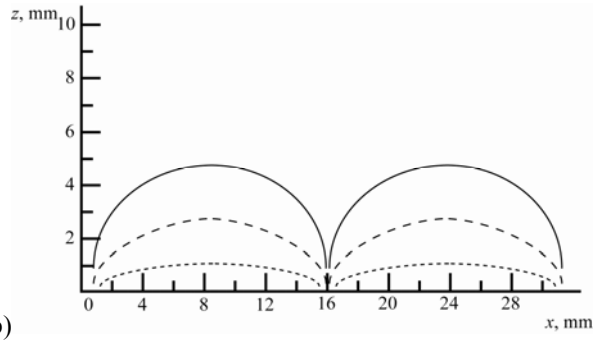
Propagation of light in biological tissue is complex. For each observation point of the scattered light at the tissue surface, the ensemble of effective optical paths that light travels from the source to this point, characterized by different optical paths, and the corresponding trajectories occupy a spatial region that has a «banana» shape. The cross section of such a distribution for different distances between the source and observation point is shown in Fig. 1a. Here are the results of Monte Carlo simulation and analytical calculations of paths of photon migration in homogeneous semi-infinite field, carried out in [11]. Under certain conditions of irradiation and detection (strongly scattering medium with small absorption, the distance between the source and observation point at least three times greater than the mean free path of the scattering medium). To calculate the statistical properties of an ensemble of effective optical paths the diffusion approximation can be used. If a strong absorption (in particular in human skin), the form of most likely trajectory can be written as

$$z_{\text{mod}}(x) \approx \sqrt{\frac{2x(r-x)}{\sqrt{3\mu_a\mu_s(1-g)r}}}, \quad (2)$$

where r — the distance between the source and observation point, the x — axis is directed along the surface, z — perpendicular to the surface, μ_a, μ_s - absorption and scattering coefficients, g - anisotropy factor. The maximum penetration depth $z_{\text{mod}}^{\max} \approx \sqrt{r/2k}$ with $x = r/2$.



a)



b)

Figure 1: The trajectories of the photons, the results of simulation (a), the analytical "banana" geometry (b) [11]. The optical parameters of the scattering medium: μ_a=0,02 mm^{-1}, μ_s=10 mm^{-1}, g=0,85.

It is known [12] that the dermis of human skin has a length of depolarization l_p=0,43 mm (476-514 nm) and 0.46 mm (633 nm). Moreover, in [13] established experimentally that the linear polarization is maintained within 2.5 of the photon transport mean free path l_{tr}. Thus, skin has μ_a=0,4 cm^{-1} and μ_s'=20 cm^{-1}, l_{tr}=0,48 mm in red and near-IR radiation. Consequently, the light can propagate in the skin over the length of 1.2 mm, while maintaining the linear polarization. Thus, we can assume that the light passing along the considered trajectory could reach the receiver maintaining polarization, with the polarization vector is rotated by an angle corresponding to the concentration of glucose contained in the skin capillary bed.

2.2. Methodology

Since the rotation angle of the polarization vector that meets glucose concentration in the blood is small, it is necessary to have a high sensitivity polarimeter. One way to improve sensitivity is to use a differential set. Consider the principle of its operation (Fig. 2). Two light beams with intensity I_0 passes through a polarizer 1 with a transmittance T_1, a cuvette 2 with transmittance T_2 and fall to the analyzer 3 (transmittance T_3) [14]. Analyzers of the two polarized beams are oriented so that its plane of oscillation rotated at angles ± 45º relative to the plane of the polarizer, so that the angle between the planes of the analyzers is 90º. The introduction of an optically active liquid in the cuvette leads to the rotation of the plane of both beams, which reduces the intensity of the beam in one channel (eg, I'_3) and increases in another (I_3).

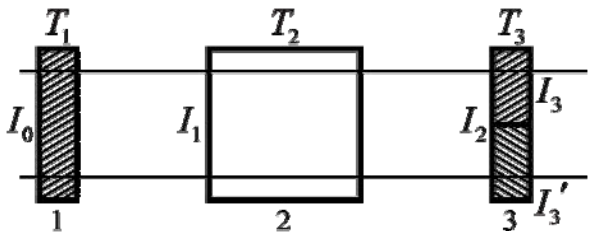


Figure 2: Optical scheme of a differential polarimeter.

Subtracting one signal from another, we obtain the intensity difference $\Delta I = I_3 - I'_3$, proportional to twice the value of the angle of polarization plane rotation. This value is defined as

$$\Delta I = T_1 T_2 T_3 I_0 \sin 2\varphi . \quad (3)$$

Equation (3) shows that the $I \sim 2\varphi$, therefore, considered two-channel differential polarimeter scheme is two times more sensitive then the single-channel. In addition, the scheme proposed here involves the use of the maximum slope of the transmission curve of the polarizer, not a traditional setting of the optical system, "the darkness", which should also increase the sensitivity of the optical sensor.

Equation (3) also shows that the ΔI depends not only on the measured angle φ, but also on the transmission coefficient T_2, depending on the optical properties of the liquid (the coefficients of T_1 and T_3 can be assumed to be constant). In order for the measured parameter was dependent only on φ, find the sum of

$$I_+ = I_3 + I'_3 = T_1 T_2 T_3 I_0 . \quad (4)$$

Divide (3) on (4), then

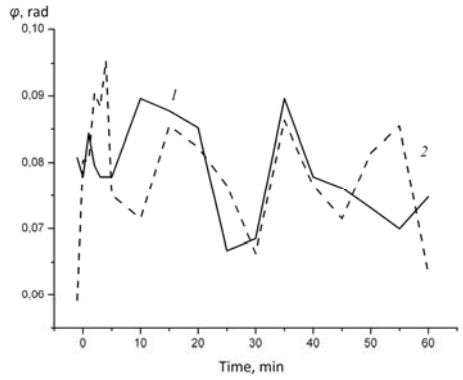
$$K = \Delta I / I_+ = \sin 2\varphi . \quad (5)$$

It is seen that the photoelectric signals processed in accordance with (3)-(5), give a signal proportional to the measured angle φ, but not dependent on T_2. The latter is important because the transmittance of the object can be changed, in particular, if the point of the study is changing.

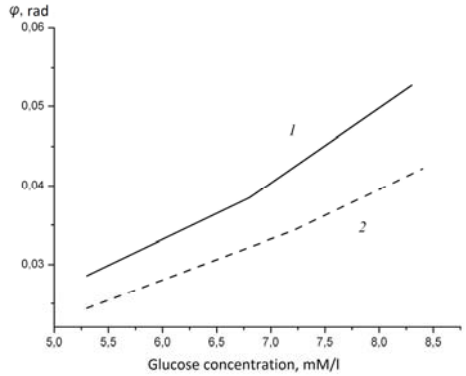
Laboratory model of non-invasive differential glucometer was constructed to detect the polarization of the reflected by skin super-ficial layers light. The depth of the light penetration allows to detect the intensity of light reflected by the microvasculature blood at a distance of about 500 microns from the skin surface.

2.3. Results

To test the possibility of non-invasive measurement of glucose concentration in blood full-scale experiment was carried out. Right index finger pad was chosen as the test object. It was illuminated focused beam of polarized laser radiation with a wavelength of 650 nm and output power of 20 mW. The scattered radiation was detected by two photodiodes conjugated with the analyzers. Received signals further processing was carried out as described above. The measurements were performed before eating (corresponding to "-1" minute on the graph) and within 60 minutes after oral administration of 25 g white sugar (corresponding to 0 minutes on the graph) for the two persons - relatively healthy volunteers 22 and 26 years. The result of this experiment is shown in Fig. 3 a.



a)



b)

Figure 3: A rotation angle of the polarization plane of the probe light beam on time (a) and on the glucose concentration in blood (b) of the two volunteers, *1*, *2* - the subjects in the age of 22 (*1*) and 26 (*2*) years.

3. Discussion

As is well known sucrose — a disaccharide consisting of two monosaccharides — α-β-glucose and fructose, and belongs to the so-called simple sugars that require only a slight digestion in the intestine, or not required at all. Therefore, as soon as sucrose reaches the intestine, it immediately enters the blood stream. Increased blood sugar

levels caused by the sudden entering of sugar, triggers the mechanism hormone insulin releasing, needed to support these sugars to the cells of the body. Sugar is rapidly consumed, leading to a sharp drop in blood sugar levels to the lowest mark (a condition also known as hypoglycemia or sweet sadness). This decrease in blood sugar causes the release of stress hormones that release stored sugar from the liver, again raising the blood sugar level. Thus, the introduction of sugar leads to a periodically change in the concentration of glucose in the blood, which can be seen in the above graphs in both subjects. It should also be noted that in general the dynamics of polarization is similar to both persons.

To directly determine the glucose concentration in blood using the proposed method will require individual calibration, which was proved in an experiment, where standard mobile glucometer indications were used as referential values (Accu Chek Active). As can be seen from the obtained results (Fig. 3b), the correlation coefficient between the concentration of glucose in the blood and the angle of rotation of the polarization of backscattered radiation varies from person to person. It is caused by individual features of the human skin structure.

4. Conclusions

So, the possibility of non-invasive detection of the glucose concentration dynamics in human blood by polarimetry of backscattered linearly polarized laser light is proved in the paper.

The photons trajectories in the human skin are analyzed. The possibility of creation a recording system, consisting of the probe light channel, and two symmetrically placed receiver channels, is founded. On this basis, the concept of a glucometer based on the differential scheme is proposed and briefly analyzed.

As a result, a laboratory model of a differential non-invasive optical coherence glucometer, allowing to measure the dynamics of glucose concentration in the blood from the change of polarization of the probing laser radiation scattered by the skin, has been developed and created. Experimental studies of glucometer, which is only preliminary, confirm its performance and practical perspective.

Acknowledgements

This work is supported by The FCP "Research and development in priority areas of Scientific and Technological Complex of Russia for 2007-2013" CS№16.512.11.2115.

References

[1] M. Kohl, M. Cope, Influence of glucose concentration on light scattering in tissue-simulating phantoms, *Opt. Lett.* Vol. 19, pp. 2170–2172, 1994.

[2] J. T. Bruulsema, J. E. Hayward, T. J. Farrell, M. S. Patterson, L. Heinemann, M. Berger, T. Koschinsky, J. Sandahl-Christiansen, H. Orskov, M. Essenpreis, G. Schmelzeisen-Redeker, D. BÃcker., Correlation between blood glucose concentration in diabetics and noninvasively measured tissue optics scattering coefficient, *Opt. Lett.* Vol. 22, pp. 190–192, 1997.

[3] Chien Chou, Chien-Yuan Han, Wen-Chuan Kuo, Yeu-Chuen Huang, Ching-Mei Feng, Jenn-Chyang Shyu Chou, C., Noninvasive glucose monitoring in vivo with an optical heterodyne polarimeter, *Appl. Opt.* Vol. 37, pp. 3553–3557, 1998.

[4] B.D. Cameron, G.L. Cote, Noninvasive glucose sensing utilizing a digital close-loop polarimetric approach, *IEEE Trans. Biomed. Eng.* Vol. 44, pp. 1221–1227, 1997.

[5] J.M. Bueno, F.V. Martin Measurements of the corneal birefringence with a liquid-crystal imaging polariscope, *Appl. Opt.* Vol. 41, pp. 116–124, 2002.

[6] S.B. Justin, B.D. Cameron, T. Sangeeta Justin, S.B. Effect of temperature, pH, and coreal birefringence on polarimetric glucose monitoring in the eye, *J. Biomed. Opt.* Vol. 7, pp. 321–328, 2002.

[7] R. C. N. Studinski, I. A. Vitkin, Methodology for examining polarized light interactions with tissues and tissuelike media in the exact backscattering direction, *Journal of Biomedical Optics* 5(3), pp. 330–337, 2000.

[8] M. Mehrubeoglu, N. Kehtarnavaz, Effect of molecular concentrations in tissue-simulating phantoms on images obtained using diffuse reflectance polarimetry, *Opt. Express* Vol. 3, pp. 286–297, 1998.

[9] X.D. Wang, G. Yao, L.H. Wang, Monte Carlo model and single-scattering approximation of the propagation of polarized light in turbid media containing glucose, *Appl. Opt.* Vol. 41, pp. 792–801, 2002.

[10] B.D. Cameron, Yanfang Li, Polarization-Based Diffuse Reflectance Imaging for Noninvasive Measurement of Glucose, *Journal of Diabetes Science and Technology* Vol. 1, pp. 873–878, 2007.

[11] R.C.N. Studinski, I.A. Vitkin, Methodology for examining polarized light interactions with tissues and tissuelike media in the exact backscattering direction, *Journal of Biomedical Optics* Vol. 3, pp. 330–337, 2000.

[12] L. O. Svaasand, Ch. J. Gomer, Dosimetry of laser radiation in medicine and biology, *SPIE Inst. Advanced Opt. Techn.* Vol. IS5, pp. 114–132, 1995.

[13] M. R. Ostermeyer, D.V. Stephens, L. Wang, S.L. Jacques, Nearfield polarization effects on light propagation in random media, *OSA TOPS on Biomedical optics spectroscopy and diagnostics*, pp. 20–25, 1996.

[14] V.A. Dubrovsky, S. Deev, Differential optical polarimeter, *Proceedings of the Academy of Sciences. Physical series.* № 6, pp. 156-161, 1995.

ELU-1:Emotions Language Unified is a BCI for communication support for patients with chronic motor disabilities

A. Fanti[1*], M. Franceschelli[1], P.Maxia[2], D. Salpietro[2],

[1]Dept. of Electrical and Electronic Engineering, University of Cagliari, Italy.
[2]Centro Don Orione, Bergamo, Italy.
*corresponding author, E-mail: alessandro.fanti@diee.unica.it

Abstract

In this paper the results of Project ELU-1 are reported. The objective of ELU-1 is to design an integrated, non-invasive, low cost system for the monitoring of "responses" in patients with chronic motor disabilities by exploiting a correlation of different signal types, e.g., EEG, EOG, EMG and biofeedback.

One of the main achievements of this project is the ability to provide evidence of sustained behavioral responses, reproducible and intentional to visual, audio, tactile and olfactory stimuli with a low cost, portable system.

This system can be used both for diagnosis and communication support for brain injured people.

1. Introduction

Patients diagnosed as vegetative may have periods of wakefulness but seem to be unaware of themselves or the environment. Although functional MRI (fMRI) studies have shown that some of these patients are consciously aware, issues of expense and accessibility preclude the use of fMRI assessment in most of these individuals [1].

We aimed to assess bedside detection of awareness with a biofeedback signal composed by a combination of electroencephalography (EEG) [1, 2]; Electrooculography (EOG) [3] and Electromyography (EMG) [4] techniques in patients in a vegetative state.

This solution relates in general to the field of brain computer interface ("BCI"). More specifically, the solution is composed by off-the-shelf biopotentials acquisition systems by which a user may control an external device with signals produced in response to a collective manifestation of electroencephalography, electromyography, electrooculography and others.

2. Description of the ElU-1 system

ELU-1 is a software that augments off-the-shelf biopotentials acquisition systems such as OCZ NIA, EMOTIC EPOC or Mindware vy NeuroSky. These input devices, such as the OCZ NIA, are able to produce an input signal related to biopotentials that varies accordingly. This signal is processed by a plurality of bandpass filters at Low (?), Mid(?) and High(?) frequencies. The output of this filters is thus related to the biopotentials. The ELU-1 software

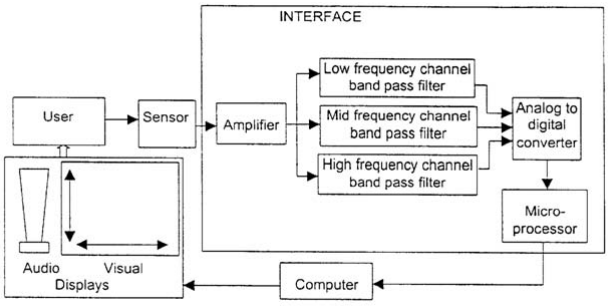


Figure 1: Schematic Block diagram of OCZ NIA BCI device.

elaborates the filters output into control signals to control an external device. ELU-1 integrates a method to analyzes the filters outputs with respect to a plurality of gesture models to detect the gestures being made by the user. Some examples of this gestures include detecting a short eyebrow lift, a long eyebrow lift, a jaw clench, a short eyebrow drop, right and left eye glances and multiple eye blink performed by the user. We now show an example of how ELU-1 generates the external device control signals. Consider the electrical response with respect to an eye blink measured as a continuous analog signal.

In Figure 2, this a of three rapid, consecutive volitional blinks creates a unique pattern of three evenly spaced small pulses in the high frequency channel time history which is discriminated by a simple state machine algorithm. In this way, a control signal in response to three consecutive eye blinks is generated and given as output. This kind of gesture recognition has been implemented for a plurality of gestures.

The main innovation of ELU-1 consists in its ability to provide evidence of sustained behavioral responses, reproducible and intentional to visual, audio, tactile and olfactory stimuli with a low cost, portable system to detect responses of patients affected by low level neurological states (LLNS). This has been achieved by the use of off-the-shelf devices for data acquisition (TiA) such as the OCZ NIA for the EEG, EMG and EOG signal and the development of the software ELU-1 as BCI output (TiC) to elaborate and visualize "the responses" or "decisions" taken by patients on a screen as markers and events (TiD) modules.

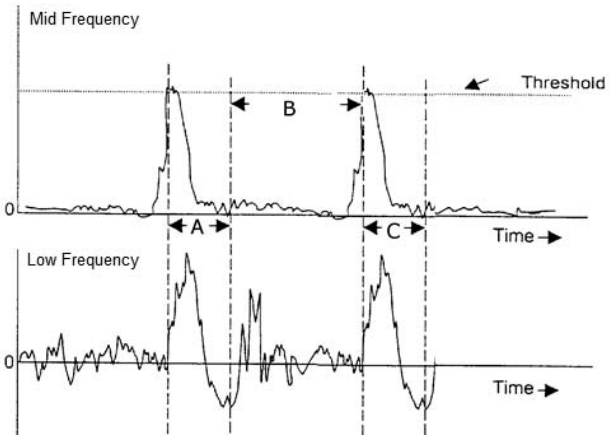


Figure 2: This is the gesture of three rapid -revisited by ELU-1.



Figure 3: ELU-1 EX Graphical User Interface.

3. Description of the ELU-1 system trials

The proposed trials were undertaken at the vegetative states department of Centro Don Orione, Bergamo, Italy. Twenty patients with traumatic brain injury and non-traumatic brain injury who met the GOS/GCS/LCF/DRS and CRS-R definitions for patients with disorders of consciousness were recruited. A novel 3-signal (EEG/EMG/EOG) motor imagery task for both ocular and facial muscles has been developed to train the proposed brain-computer interface to detect command-following in absence of overt behavior. Patients completed the task consisting in the execution of simple commands such as eye coordination motions, the reminding of strong emotions, the feeling of calm, stressed, frustrated and meditative states and the imagination of movements of their right-hand and toes. The command-specific responses of EMG/EOG/EEG of each patient were analysed for robust evidence of appropriate, consistent, and statistically reliable markers of motor imagery, similar to those noted in healthy, conscious control. The adopted sensors were able to give a representation of brain wave frequencies corresponding to stress or calm states, thus measuring emotional states in absence of any body movement. To perform the evaluation, the standard scales such as GOS/GCS/LCF/DRS and CRS-R, have been revised. In particular, motor responses

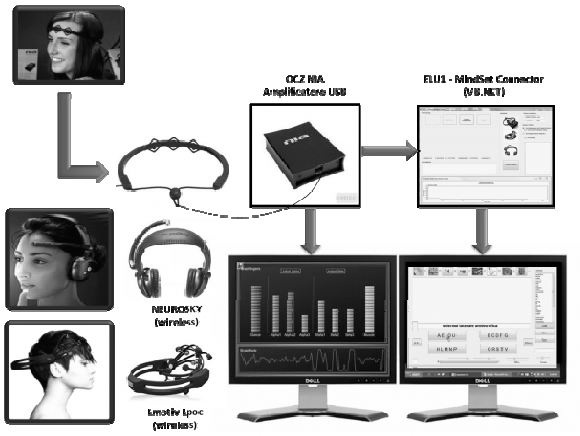


Figure 4: Figure 1. Some examples of off-the-shelf devices for EEG and related visualization software.

have been substituted by brain activity for patients who were given training to control their EEG/EMG/EOG signals for the triggering of logic gates. ELU-1 can function both in a mono-directional and bi-directional modes. In the mono-directional mode, a computer receives signals directly from brain activity, such as EEG, EMG, EOG. In the bi-directional mode, by combining the input channels with one or more feedback channels to the individual, it allows information exchange between the person and the environment, i.e., the opening or closing of a logic gate.

4. Clinical results

We assessed 15 patients diagnosed in the vegetative state, and 5 with residual cognitive function and conscious awareness. Nine (60%) of 15 patients could repeatedly and reliably generate appropriate EEG/EOG/EMG responses to two distinct commands. The performed tests were able to demonstrate the ability of patients to control the amplitude of some brain waves exploiting them as control signals for the activation of external devices. All the 20 patients that took the test had language alteration at various levels: comprehension (¡30%), production (100%), repetition (100%), construction of sentence (n.a). In the 75% of patients intentional and sustained responses have been documented. In 3 cases it has been possible to use ELU-1 to play videogames. In 2 cases it has been possible to use a computer for writing. In 75% of patients a good residual hearing capability was detected, even in those cases for which negative results were reported by the evoked potentials method, 5 patients were not able to keep their eyes open. The tests have highlighted that the use of combined signals from EEG and EOG with audio feedback, i.e., simple ”beeps” associated to the frequency of EOG pulses, have improved the attention/collaboration of patients.

5. Discussion

The combination of 3-signals (EEG, EOG and EMG) exploited in ELU-1 allows the design of a cheap, portable,

widely available and objective brain computer interface. ELU-1 can be used as portable support for communication to allow patients with serious brain damage to communicate in a simple and cheap way.

The outcome of this project could allow the widespread use of this bedside technique to give individuals with communication disabilities a voice and a way for a more fulfilled, integrated and independent life.

6. Conclusions

The combination of 3-signals (EEG, EOG and EMG) exploited in ELU-1 allows the design of a cheap, portable, widely available and objective brain computer interface. ELU-1 can be used as portable support for communication to allow patients with serious brain damage to communicate in a simple and cheap way. The outcome of this project could allow the widespread use of this bedside technique to give individuals with communication disabilities a voice and a way for a more fulfilled, integrated and independent life.

Acknowledgement

The authors thank Dott. G.B. Guizzetti and his staff of the department of Centro Don Orione (Bergamo, Italy) for helping in conducting the experiments that have been used in this paper; and this paper has been supported by "Regione Lombardia (Italy)", through the grant of the project "Sostegno alla comunicazione" 300/10, Call families 2010.

References

[1] Adrian M. Owen, Martin R. Coleman, Melanie Boly, Matthew H. Davis, Steven Laureys,Dietsje Jolles, John D. Pickard, "Detecting Awareness in the Vegetative State", Science 8 September 2006,Vol. 313 no. 5792 p. 1402.

[2] 2. Schetinin V., Schult J., "Learning Polynomial Networks for Classification of Clinical Electroencephalograms". Soft Computing, Springer, 10: 4, 397-403, 2005. (ISI 0.52)

[3] 3. Y. Punsawad, Y. Wongsawat and M. Parnichkun., "Hybrid EEG-EOG Brain-Computer Interface System for Practical Machine Control." International Conference of Engineering in Medicine and Biology Society (EMBC). Pp. 1360-1363, 2010.

[4] 4. Leeb, R., Sagha, H., Chavarriaga Lozano, R.,; Milln, Jos del R. "A hybrid BCI based on the fusion of EEG and EMG activities". Journal of Neural Engineering, vol. 8, num. 2, Institute of Physics, 2011.

3D Computer modeling of an MRI antenna steeped in a dielectric substrate

[1]Zakia ABIDI, [2]Mohammed DJENNAH, [1]Bernard BANDELIER and [1]Françoise Rioux-Damidau

[1]IR4M Paris 11 University UMR 8081 CNRS, Bât 220 Orsay, France

Tel.: +33169157978; Fax : +33169154 E-mail: {zakia.abidi,Bernard.bandelier,francoise.rioux}@u-psud.fr

[2] Electrical and Computer Engineering department 10 Hassen Badi Avenue, BP 182, El-Harrach 16200 Algiers Algeria Tel.: +213552467773; Fax: 21321522973; E-mail: mdjennah@hotmail.com

Abstract

A numerical technique, based on the combination of a finite element method and a boundary integral method has been developed to compute the induced signal in MRI antennas. This signal rises from a free movement of precession of the transverse magnetization of the sample to explore. In our modeling, the transverse magnetization represents the magnetic source field. Its flux embraces the antenna to give rise to a sinusoidal current which is very quickly attenuated in time (a few ms); it represents the signal containing all the informations of the sample. We here want to find the geometrical and electromagnetic characteristics of the antennas which permit to have a signal to noise ratio as great as possible. In our computation, we have taken into account leading factors such as the distance between the probe and the organ to be explored and also the geometrical and electromagnetic characteristics of the probe.

Keywords: MRI antennas, boundary integral method, finite element method

1. Introduction

Magnetic resonance imaging (MRI) is a very interesting exploration tool. Its utility on a patient is such as it gives a spectacular development since many years. However, detection by nuclear magnetic resonance poses a critical problem of sensitivity because the received signal is accompanied by interfering signals and noises of various origins. The main sources of noises in carefully designed MRI antenna are the internal noise of the coil itself and the noise inductively coupled to the antenna by the sample. To improve the signal-to-noise ratio, printed circuit antennas made of thin metallic layers put on a dielectric substrate are used. Our goal is to model these antennas to obtain the electric and magnetic fields and the surface current density on the conducting layer and, finally, the resonance frequency. Previous works [1],[2] have studied different models of printed circuit antennas made of thin metallic layers put on a dielectric substrate using an integral equation on both sides of the boundary and where the unknowns were the electrical and magnetic fields (E,H) on the whole boundary of the system and the surface current J on the metallic layer. But, because of the choice of degrees of freedom for E, H and J, Ohm's law was weakly satisfied and the method was not efficient for a large range of frequencies and geometries. In this paper, we propose a novel approach which associates a finite element method and a boundary integral method to model these antennas. We only consider the tangential components of the electric field e and the magnetic field h. The jump of H over the metal is the surface current density J which is the useful signal to obtain the image in MRI.

2. Physical Model

Our system is made of the body to explore and of the antenna close enough to the body surface in order to have a maximum intensity of the electromagnetic field. The whole is in MRI environment: a static magnetic induction B0, a radiofrequency magnetic induction B1 and a system giving field gradients on the three directions of space. In MRI, the useful signal comes from the induced body magnetization M at the time when this one returns to equilibrium with a free precession movement of pulsation ω and a decreasing time T2, as soon as the radio frequency magnetic field is extinguished; it then produces into the antenna a RF electromagnetic source field. The magnetization M of the body to explore is given by the solution of Bloch equations [3] and we are interested by the component Mxy which is the projection of M on the reading plane (xoy)

$$\boldsymbol{M(t)} = \boldsymbol{M}_{xy}(t) + \boldsymbol{M_z}(t) = M_0 e^{-\left(i\omega+\frac{1}{T_2}\right)t} \quad (1)$$

$$M_0\left(1 - e^{\frac{-t}{T_1}}\right) \quad (2)$$

where: $\omega = \gamma B_{01}$.

B_{01} is the amplitude of the RF magnetic induction $\mathbf{B_1}$, γ is the magnetogyric ratio,T_1 and T_2 are respectively the longitudinal and transversal relaxation times,

M_0 is the magnetization at the equilibrium.

Hydrogen imaging is most widespread because of its abundance on biological texture. The magnetization of pure water at 300 K with B01 = 1 T is about 0.00032 A/m.

Equation (2) gives the source vector potential Asfor a continuous distribution of magnetization M through a body with a volume v and a surface γ with its unit outward normal vector nb[4]:

$$\boldsymbol{A^s} = \frac{\mu_0}{4\pi}\int_v \frac{curl\,\boldsymbol{M}}{r}\,dv + \int_\Gamma \frac{\boldsymbol{M}\times n_b}{r}\,d\gamma \quad (3)$$

We consider that **M** is constant throughout the body:

$$curl\,\boldsymbol{M} = 0 \quad (4)$$

The magnetic source flux density $\mathbf{B^s}$ is represented by :

$$\boldsymbol{B^s} = \nabla \times \boldsymbol{A^s} \quad (5)$$

Faraday's law relates the electric source field intensity $\mathbf{e}^s$ to the time rate of change of $\mathbf{B}^s$:

$$\nabla \times \left(\boldsymbol{E}^s + \frac{\partial \boldsymbol{A}^s}{\partial t} \right) = 0 \qquad (1)$$

Hence, the electric source field $\mathbf{e}^s$ can be written as:

$$\boldsymbol{E}^s = -\frac{\partial \boldsymbol{A}^s}{\partial t} - \nabla\varphi \qquad (2)$$

where φ is the scalar potential.

We can deduce the electromagnetic source field $(\mathbf{E}^s,\mathbf{H}^s)$ from the transverse component $\mathbf{M}_{xy}$ of magnetization $\mathbf{M}$

$$\begin{cases} \boldsymbol{E}^s = \dfrac{\mu_0 (i\omega + \frac{1}{T_2})}{4\pi} \displaystyle\int_{\Gamma b} \frac{\boldsymbol{M}_{xy} \times n_b}{r}\, d\Gamma \\ \boldsymbol{H}^s = \dfrac{\mu_0 (i\omega + \frac{1}{T_2})}{4\pi} \displaystyle\int_{\Gamma b} \frac{(\boldsymbol{M}_{xy} \times n_b) \times r}{r^3}\, d\Gamma \end{cases} \qquad (3)$$

and we have:

$$(\boldsymbol{E}^s, \boldsymbol{H}^s) = (\boldsymbol{e}^s, \boldsymbol{h}^s) e^{-\left(i\omega + \frac{1}{T_2}\right)t} \qquad (4)$$

The electromagnetic fields generated by such a source must have the same time dependence as the source but can differ in phase thus: $(\boldsymbol{E}, \boldsymbol{H}) = (\boldsymbol{e}, \boldsymbol{h}) e^{-\left(i\omega + \frac{1}{T_2}\right)t}$

The signal pick up from MRI antennas is directly depending on the radiofrequency magnetic induction field B1 by each current unity which the antenna can send in a given space point. An expression for B1/i (or induction coefficient) can be given on the antenna axis having an equivalent radius a as a function of the antenna distance z by [5]:

$$\frac{\boldsymbol{B_1}}{i} = \frac{a^2}{(a^2 + z^2)^{3/2}} \qquad (5)$$

z is a determining factor in the design of the antennas. A very weak distance would cause the increase in the intensity of the noise. This factor does not directly appear in the equations which govern our physical system; it intervenes like a variable parameter in the calculation of the field's source.

3 .Formulation and method

In this section, we present a FEM-BIM formulation to model the antenna, the configuration of which is shown in Fig.1, where is a dielectric substrate of permittivity ε; its boundary is Γ. A part Γm of Γ is covered by a metallic layer (which may have slits) of small thickness d and conductivity σ and the other part of Γ is Γd. $\vec{n}$ is the unit outward normal vector to Γ and $\overrightarrow{n}$ is the unit outward normal vector to γ0 tangent to Γ. The antenna is embedded in a source field (Es,Hs) generated by a magnetization defined in (8).

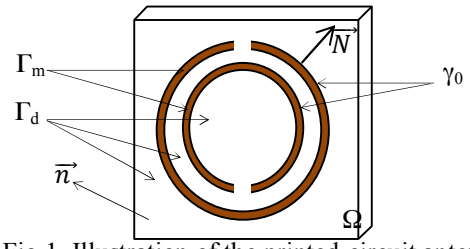


Fig.1. Illustration of the printed-circuit antenna and the different computational regions

The system thus defined is governed by Maxwell equations where á = 1/T_2:

$$\begin{cases} curl\, \boldsymbol{h} = (\sigma + i\varepsilon)\boldsymbol{e} & (6) \\ curl\, \boldsymbol{e} = -\mu \boldsymbol{h} & (7) \end{cases}$$

3.1. Variational formulation in Ω:

Variational formulation of Maxwell equations is obtained by respectively multiplying (10) and (11) by a test functions e' and h' and integrating on domain Ω:

$$\frac{1}{\mu} \int_\Omega curl\, \boldsymbol{e} \cdot curl\, \boldsymbol{e}' - (\sigma + i\varepsilon) \int_\Omega \boldsymbol{e} \cdot \boldsymbol{e}' = \int_\Gamma (n \times \boldsymbol{h}) \cdot \boldsymbol{e}' \qquad (8)$$

$$\frac{1}{\sigma + i\varepsilon} \int_\Omega curl \cdot curl \cdot \mu \int_\Omega \cdot = \int_\Gamma (n \times e) \cdot \qquad (9)$$

3.2. Formulation of the boundary terms:

The Stratton-Chu formulae [4] give an integral representation of the magnetic and electrical fields (e,h). Outside Ω, for Ã In fact, we are interested by the tangential components of the electromagnetic fields on Γ, in order to establish a variational formulation in which they are the unknown quantities. For this reason, we compute the limit of the tangential component of the electric field $x \to x_0$ when $\to_0$ Ã and $\in \mathbb{R}^3$ Ù using the potential property issued from [6]. We note gradx the gradient derived by x variable and divΓ the surface divergence and we have:

$$\lim_{x \to x0} n(x_0) \times curl \int_\Gamma G(x,y)\boldsymbol{e}(y) = \frac{\boldsymbol{e}(x_0)}{2} \times n(x_0) + \int_\Gamma grad_x\, G(x_0,y) \times \boldsymbol{e}(y) \qquad (10)$$

and somewhat similar with **h**. We then obtain the tangential trace of the electromagnetic fields **e** and **h** on the external face of Γ, x Ã

$$\frac{n \times \boldsymbol{e}}{2}(x) + n(x) \times \boldsymbol{e}^s(x) + \frac{i}{\varepsilon_0 \alpha} n(x)$$

$$+ grad_\Gamma \int_\Gamma G(x,y)\, div(n \times \boldsymbol{h}_a)_y \, d\alpha\mu_0 n(x)$$

$$+ \int_\Gamma G(x,y)\, n \times \boldsymbol{h}_a)_y \, d n(x)$$

$$+ \int_\Gamma grad_x G(x,y) \times (n \times \boldsymbol{e})_y \qquad (4)$$

$$\frac{n \times \boldsymbol{h}_a}{2}(x) + n(x) \times \boldsymbol{h}^s(x)$$

$$+ \frac{i}{\mu_0 \alpha} n(x) \times grad_\Gamma \int_\Gamma G(x,y) div(n \times e)_y$$

$$+ \alpha\varepsilon_0 n(x) \times \int_\Gamma G(x,y)\, n \times e)_y \, n(x)$$

$$+ \int_\Gamma grad_x G(x,y) \times (n \times \boldsymbol{h}_a)_y \qquad (5)$$

where $G(x,y) = e^{-ik\|x-y\|}/\|x-y\|$ is the Green function in the air for the Helmoltz equation and k is the wave number and $\boldsymbol{h}_a$ is the tangential component of h on Γ in the air side.

We assume that the metallic layer is very much smaller than the skin-depth so that the current is constant over the thickness. We then adopt a surface model. The surface current density circulating on Γm is given by Ohm's law:

$$J = \sigma d \boldsymbol{e} \qquad (17)$$

So, boundary Γ is considered as a thin shell of thickness d.

We consider that $\tilde{A} = \tilde{A}_m \cup \tilde{A}_d$ and the jump of the tangential component of the magnetic field across Γm is the surface current density:

$$n \times \boldsymbol{h}_a - n \times \boldsymbol{h} = \boldsymbol{J} \quad on \quad \tilde{A}_m \qquad (6)$$

3.3. Variational formulation of boundary terms

By respectively multiplying (15), (16) and (17) by a tangential test fields h', e' and J' defined in the same functional space of the fields and by integrating on Γ, we obtain:

$$\int_\Gamma (n \times \boldsymbol{e}(x))\boldsymbol{h}(x) = \int_\Gamma (n \times \boldsymbol{h})_x \boldsymbol{e}^s(x)$$

$$+ \frac{i}{\varepsilon_0 \alpha}\left(\int_\Gamma \int_\Gamma G(x,y) div(n \times \boldsymbol{h})_y \, div(n \times \boldsymbol{h})_x\right.$$

$$+ \int_\Gamma \int_\Gamma G(x,y) div(n \times \boldsymbol{h})_y \, div \boldsymbol{J}$$

$$\left. + \int_\Gamma \int_{\gamma_0} G(x,y) div(n \times \boldsymbol{h})_y \boldsymbol{J} \times N \right)$$

$$+ \alpha\mu_0 \left(\int_\Gamma \int_\Gamma G(x,y)(n \times \boldsymbol{h})_y \, n \right.$$

$$\left. + \boldsymbol{h}_x \times \int_\Gamma \int_\Gamma G(x,y)(n \times \boldsymbol{h})_y \boldsymbol{J}\right)$$

$$+ \int_\Gamma \int_\Gamma gradx\, G(x,y)$$

$$\times (n \times \boldsymbol{e})_y \times (n \times \boldsymbol{h})_x \qquad (7)$$

$$\int_\Gamma (n \times \boldsymbol{h}(x))e(x) = \int_\Gamma J(x) \times e(x)$$

$$+ \int_\Gamma (n \times \boldsymbol{h}^s(x))e(x)$$

$$+ \alpha\varepsilon_0 \int_\Gamma \int_\Gamma G(x,y)(n \times e)_y \, n$$

$$\times e)_x$$

$$+ \int_\Gamma \int_\Gamma grad\, G(x,y)_y \times ((n \times e)$$

$$\times n \times \boldsymbol{h})_x$$

$$+ \int_\Gamma \int_\Gamma grad\, G(x,y)_y \times (n \times e \times J)_x$$

$$+ \frac{i}{\mu_0 \alpha} \int_\Gamma \int_\Gamma G(x,y)\, div\, n \times e)_y \, div(n \times e)_x \qquad (8)$$

$$\int_\Gamma J \times J^{(x)} = \int_\Gamma \sigma de(x) \times J(x) \qquad (9)$$

$$\frac{1}{\sigma - \varepsilon \propto}\int_{\Omega} curl\, h \cdot curl\, h^{*} - \mu \propto \int_{\Omega} h \cdot h^{*}$$
$$- \frac{2}{\varepsilon_0 \alpha}\left(\int_{\Gamma}\int_{\Gamma} G(x,y) div(n \times h^{*})_y\, div(n \times h^{*})_x - \int_{\Gamma}\int_{\Gamma} G(x,y) div(n \times h^{*})_y\, div J + \int_{\Gamma}\int_{\gamma_0} G(x,y) div(n \times h^{*})_y J.N\right)$$
$$- 2\alpha\mu_0\left(\int_{\Gamma}\int_{\Gamma} G(x,y)(n \times h^{*})_y . (n \times h^{*})_x - \int_{\Gamma}\int_{\Gamma} G(x,y)(n \times h^{*})_y . J\right)$$
$$+ 2\int_{\Gamma}\int_{\Gamma} gradx\, G(x,y) \times (n \times e)_y . (n \times h^{*})_x = 2\int_{\Gamma} (n \times h^{*})_x e^{s}(x) \qquad (22)$$

$$\frac{1}{\mu \propto}\int_{\Omega} curl\, \boldsymbol{e} \cdot curl\, \boldsymbol{e}^{*} - (\sigma - \varepsilon \propto)\int_{\Omega} \boldsymbol{e} \cdot \boldsymbol{e}^{*}$$
$$- \int_{\Gamma} \boldsymbol{J}(x) . \boldsymbol{e}^{*}(x) + 2\alpha\varepsilon_0 \int_{\Gamma}\int_{\Gamma} G(x,y)(n \times \boldsymbol{e})_y (n \times \boldsymbol{e}^{*})_x - 2\int_{\Gamma}\int_{\Gamma} grad\, G(x,y)_y . \left((n \times \boldsymbol{e}^{*}) \times (n \times \boldsymbol{h})\right)_x - 2\int_{\Gamma}\int_{\Gamma} grad\, G(x,y)_y . ((n \times \boldsymbol{e}^{*}) \times \boldsymbol{J})_x + \frac{2}{\mu_0 \alpha}\int_{\Gamma}\int_{\Gamma} G(x,y)\, div(n \times \boldsymbol{e})_y\, div(n \times \boldsymbol{e}^{*})_x = 2\int_{\Gamma} (n \times \boldsymbol{h}^{s})_x \boldsymbol{e}^{*}(x) \qquad (23)$$

Replacing (19) and (20) in (13) and (12) and taking into account (21) we obtained the variational problem defined by the three equations (22), (23) and (21).

The current J must be defined in the same functional space that e and must be discretized with the same basis functions that e. Also, J must be defined in the same functional space that(n × h) and be discretized with the same basis functions that(n × h). It seems to be incompatible. To avoid this problem, we have to compute e and J. For this reason we take J as a state variable on Γm and e on Γd

4. Computational Method

To solve the variational problem we adopt a numerical approach with finite element method. The volume of the antenna (Ω) is meshed with tetrahedra and its boundary Γ is meshed in a finite union of triangles which corresponds to the faces of the tetrahedra. Fields e and h are discretized with Whitney elements [7] where the basis functions are the circulation of the fields along the edges.

5. Numerical results

Based on the presented FEM-BEM formulation, a computer program was written for the analysis of the printed-circuit antenna used in MRI. The antenna geometry is supplied to this program in an input file that contain lists of the nodes and their (x,y,z) coordinates, the nodes forming each tetrahedron, the nodes on metallic boundaries, and all information about mesh grid . We have made a first simulation of the body with a sphere with a median induced magnetization M0. By varying the distance between the antenna and the sphere, we traced the arrows of the current solution of the problem. Following figures shown mesh of the antenna and the current on the metallic layers

We take a dielectric with radius equal to 8 cm and height equal to 1.6mm, it is covered with two metallic layers one on the upper face and the second one on the lower face, the slits of the two layers being opposite. The layers are made of copper with thickness d=35µm. Their width is 1.0 cm and the size of the slits is 1.0 cm×0.5 mm. M0=32. 10-03 (A/m), and T2=0.1s.

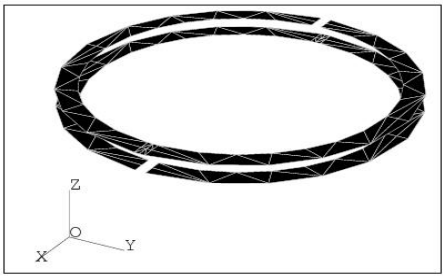


Fig. 2. Mesh of the metallic layer of the antenna

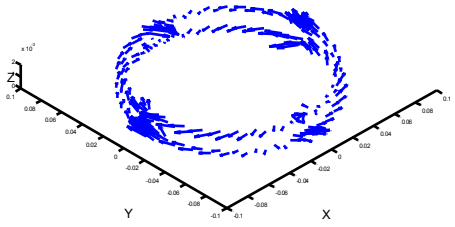


Fig.3. Induced signal on the metallic layers

To validate our computational code, we have computed the voltage on the slits and the magnetic field on

the antenna for several values of the frequency. Fig.4. shows the resonance curve from which we have calculated the numerical resonance frequency (f0=209 MHZ) and compare it with the experimental value obtained in our laboratory (fexp=200 MHZ) so the two values are comparable.

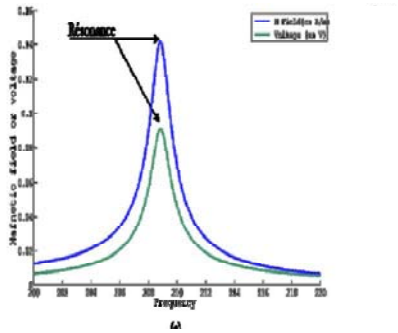


Fig.4. The resonance curve at permittivity ε=5

6. Conclusion

In this paper, we present a finite element–boundary element (FEM-BIM) formulation for printed-circuit antennas used in MRI environment. We here consider the variation in $e^{-(i\omega+\frac{1}{T_2})t}$ of the fields which is a multiplying term to the Maxwell equations, so we do not need a numerical scheme in time. From ten to one hundred MHz, the bandwidth of the frequency resonance of biological tissue, the induced signal is globally supported by the surface Γof the antenna that is why a Stratton-Chu integral formula is adopted in our computation.

The presented method gives good results in a small CPU time. The FEM coupled with BIM is more robust than BIM alone used in [1] and [2].The condition number of the matrix is improved. Our computational code is valid for a range of the frequency where MRI antennas are working from 10 MHZ to 10 GHZ but the frequency range of the code defined in [1] and [2] is a few MHZ.

The induced signal is characterized by a very low intensity and a very fast attenuation.¶ This requires a particular numerical processing.¶ The ` pseudo-period' of Mxy is T=2 ãB0 = 3.10 -7 second for protons subjected to a field of 0.5T. ¶The duration of 'relaxation' being about 5 T1, Mxy doing between 106 and 107 rotations; our work represents a new approach in this field.

In our computation, we don't take into account physical phenomena, such us, inductive and capacitive effects between antenna and the organ. These effects accentuate when the distance is towards zero. These effects essentially contribute in the identification of noise and can be quantify by experimental measurements.

References

[1] N.El Alami, B. Bandelier, F.Rioux-Damidau "Field and Current Formulation for Radio Frequency Antennas" IEEE Transactions on Magnetic , Vol 46,NO.8. AUGUST 2010. pp 3325-3328

[2] B.Kebaili, B.Bandelier,and F.Rioux-Damidau, "Modelling a Thin Shell System Submitted to an Electromagnetic wave", IEEE Transactions on Magnetic., vol 37, 2001, pp.3277-3280

[3] A.Alaux,"l'Image par Resonance Magnétique "SAURAMPS MEDICAL, 1994

[4] J.A. Stratton, Electromagnetic Theory, Mac Graw Hill, New York, 1941

[5] S.Lambert, « Modélisation et caractérisation d'antennes supraconductrices pour la micro IRM du cerveau de souris à 4.7 T » Ph.D Thesis. Université de Paris Sud 11, 2011.

[6] V.Levillain"Couplage elements finis-équations integrals pour la resolution des equations de Maxwell en milieu hétérogène", PhD Thesis, Polytechnique, Palaseau, 1991.

[7] J.C.Nédélec,"Mixed Finite Elements in R3", Numer. Math., vol.35, 1980,pp.315-341.

Retrieval of the relevant parameters of natural multilayer systems

Demetrio Macías[1*], Ana Luna[2], Diana Skigin[2], Alexandre Vial[1], and Marina Inchaussandague[2]

[1]Institut Charles Delaunay-Laboratoire de Nanotechnologie et d'Instrumentation Optique,
Université de Technologie de Troyes, France
[2]Grupo de Electromagnetismo Aplicado, Departamento de Física, FCEN,
Universidad de Buenos Aires, and IFIBA, CONICET, Argentina
*corresponding author, E-mail: demetrio.macias@utt.fr

Abstract

Ceroglossus suturalis beetles show iridescent coloration produced by multiple reflections from the epicuticle of their elytra, which is a multilayer that alternates materials of different optical density. By means of scanning and transmission electron microscopy techniques we obtain the significant geometrical parameters such as the number of layers and their thicknesses. We investigate the reflected response of the *Ceroglossus suturalis* beetle, and apply evolution strategies to retrieve the real and imaginary parts of the refraction index of the materials comprising the multilayer system. We show that this kind of algorithms have a great potential as a tool to investigate natural photonic structures.

1. Introduction

There are two main ways of achieving coloration in the biological world: pigmentary and structural. Pigmentary colors have a chemical origin and are produced by the selective absorption of natural light, and structural colors have a physical origin and are produced by the interactions of natural light with microstructures. In general, color results from a combination of pigmentary and structural effects [1, 2]. Structural color is created by interference, diffraction and scattering of light by the microstructures present in the cover tissues of animals and plants. When iridescent colors are produced, the hue changes with viewing angle, and the color is very intense and highly saturated [3, 4]. Coleoptera (the order to which the *Ceroglossus suturalis* belongs) are the most colorful specimens in the animal world, and this color originates at their surface, which is generally covered by a cuticle. A large variety of microstructures can be found within the cuticle of these beings, and then many color effects are produced [3, 4].

In addition to the structure, the refraction indices of the materials involved determine the structural color in biological structures. Therefore, a key aspect in the investigation of such systems is the knowledge of the constitutive parameters of the materials that compose biological tissues [5]. Only a few works reported methods to retrieve the complex refractive indices of such systems. For instance, an effective medium theory has been applied to a multilayer film to determine the anisotropic index of refraction of the cuticle material of the wings of butterfly *Morpho Menelaus* [6]. Measurements using index-matching techniques have been used to find the refractive index of the cuticle material comprising the microstructure of *Morpho* butterfly scales [7]. Also, the complex refractive indices of the natural multilayer reflector in the beetle *Chrysochroa raja* were found by the application of a known optical characterization technique [8]. In [9] the authors have proposed an iterative procedure, based on Cauchy's and Fresnel's equations, to retrieve the refraction index from experimental data, and Leertouwer *et al*. used Jamin-Lebedeff interference microscopy to measure the wavelength dependence of the refractive index of butterfly wing scales and bird feathers [10].

To properly analyze the reflected response and compare experimental with theoretical results, it is necessary to accurately know the values of the refractive indices of the materials that comprise the microstructures. Besides, most structurally colored biological systems contain absorbing pigments [11], which implies an increase in both the real and imaginary parts of the refraction index. Stochastic optimization techniques appear as very promising tools to be applied for this purpose. Although not in the context of natural systems, some illustrative examples of the successful use of this approach can be found in the works by Djurisic *et al*. [12] and by Vial *et al*. [13]. The authors of these references used stochastic methods together with a Drude-Lorentz-like model to characterize the optical constants of some metals.

In this paper we study the structural color generation in *Ceroglossus suturalis* beetles. In particular, we investigate the possibility of retrieving, from experimental o numerical data, accurate values of the refraction indices of the component materials of this natural multilayer system. For this, we employ a bio-inspired optimization technique known as evolution strategies. In Section 2 we show and characterize the sample under study. In Section 3 we outline the approach used to retrieve the constitutive parameters of interest and give the theoretical details of the methods employed. Some examples to illustrate the inversion method proposed are shown in Section 4. In particular, results of optimized values of the real and imaginary parts of the refraction indices and the corresponding reflectance spectra of the multilayer system are given. The performance of the method is assessed by means of the fitness function. Fi-



Figure 1: Samples of a green and a brown specimen of *Ceroglossus suturalis* beetles.

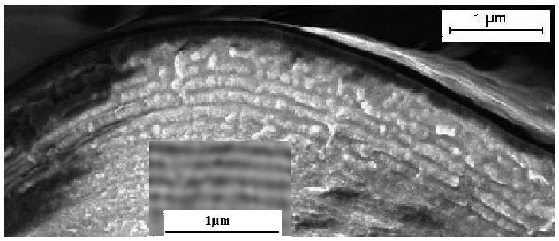


Figure 2: SEM image of a transversal cut of the cuticle of a green *Ceroglossus suturalis* specimen. Inset: TEM image.

nally, concluding remarks are provided in Section 5.

2. Sample characterization

Ceroglossus suturalis beetles mostly live endemically in the Argentinean Patagonia and in the south of Chile, in the forest. They exhibit a characteristic iridescent coloration that can vary between yellow-green and brown-copper, as shown in Fig. 1. The structural arrangement that produces color in this species is a periodic multilayer composed of alternating layers of materials with different optical density, located in the epicuticle [14]. Scanning (SEM) and Transmission (TEM) Electron Microscopy images of a transversal cut of the cuticle are shown in Fig. 2, in which the periodic multilayer system becomes evident. Each period comprises two layers of different materials. A total of 9 periods was found in the green specimen, the layers' thicknesses being 100 nm and 60 nm, whereas for the brown beetle the multilayer consists of 20 periods, and the layers' thicknesses are 120 nm and 70 nm. These values were obtained after an exhaustive study and analysis of several SEM and TEM images using the *ImageJ* software [15]. The parameter extraction was completed with a statistical analysis.

3. Theoretical approach

The essential idea of the inversion method proposed in this contribution is illustrated in Fig. 3. The pink arrows in the flux diagram show the basic steps to obtain an optical signal from a biological sample, e.g. reflectance spectrum, etc. On the other hand, the black arrow illustrates the important role played by the characterization of the sample microstructure, through different microscopy techniques, in the establishement of an adecuate geometrical model. Once this is done, a rigorous electromagnetic method (analytical or numerical) is developed to calculate an optical signal for different geometrical and constitutive parameters of the system. As indicated by the blue arrow, this should lead to a theoretical curve that in principle agrees with the experimental one. The main objective in this work is to retrieve the constitutive parameters of the system from this information. To solve this special inverse problem, we make use of an heuristic optimization technique coupled to the forward electromagnetic solver that is described in the following paragraphs.

In the case of the *Ceroglossus suturalis* the iridescent response is clearly governed by the periodic multilayer structure present in the epicuticle. As observed in Fig. 2, the layers exhibit imperfections such as surface roughness and non-uniform thickness, and their distribution is not perfectly periodic. However, as a first approach a periodic planar multilayer model appears as a suitable model to represent such system. A sketch of the simplified structure is shown in Fig. 4, where it can be observed that each period comprises two layers of different refraction indices and thicknesses. An electromagnetic method for one-dimensional periodic multilayer systems based on the 4x4 transfer matrix method [16] is then used to find the solution of the direct problem, i.e., the scattered electromagnetic response given all the parameters of the structure. The basis of this approach is to combine Maxwell equations with the corresponding constitutive relations to obtain a differential system for the unknown electric and magnetic field components in each layer. For structures with traslational invariance and assuming plane wave illumination, this system can be reduced to a 4x4 differential system, whose unknowns are the tangential components of the electric and the magnetic fields. Then, the field components are propagated from one side to the other of each layer, and also the boundary conditions at each interface are imposed. This procedure ends with a 4x4 matrix system for the unknown amplitudes outside the structure, i.e., transmitted and reflected.

3.1. Retrieving some relevant constitutive parameters: stochastic optimization

This section is devoted to describe the inversion procedure that we employ to retrieve some constitutive parameters of the multilayered structure shown in Fig. 4. As stated in the previous section, the computation of the reflected and transmitted fields can be done in a straightforward manner through the 4x4 method. Nevertheless, the relationship between the geometrical and material features of the microstructure and the reflected/transmitted field is not a trivial one. As a consequence, the establishment of an inversion scheme directly from the forward model is a formidable

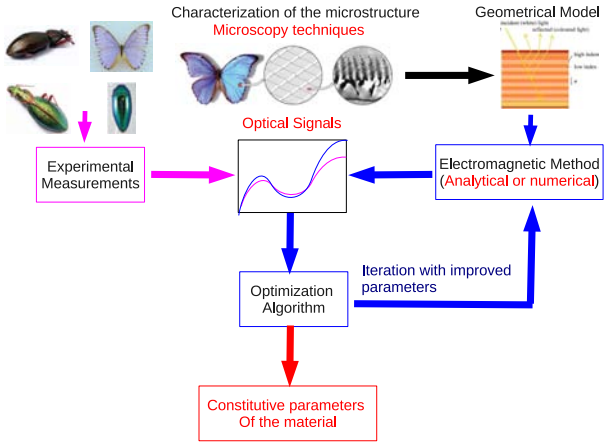


Figure 3: Scheme of the procedure proposed to retrieve the relevant parameters of biological microstructures.

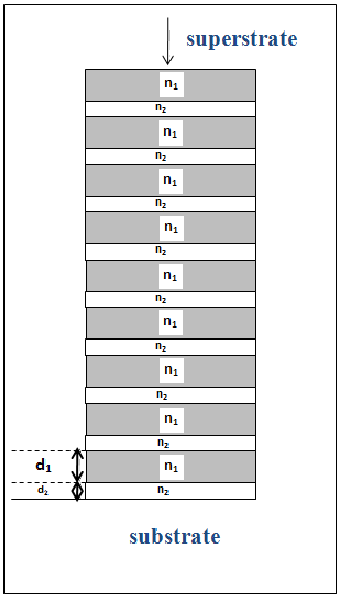


Figure 4: Periodic multilayer system.

task itself. One way to overcome this situation is to reformulate the original inverse problem in terms of approximation theory. For this, we employ the functional

$$f(\mathbf{p}^T) = \|I^{\exp}(\lambda) - I^{\text{the}}(\lambda|\mathbf{p}^T)\|_2^2, \qquad (1)$$

where $\|\|_2$ is the Euclidean Norm, $I^{\exp}(\lambda)$ and $I^{\text{the}}(\lambda|\mathbf{p}^T)$, respectively, represent the spectrum measured experimentally and the spectrum generated with a previously established analytical or numerical model. Also, the components of the vector $\mathbf{p}^T$ are the parameters of interest to retrieve. At least in principle, the minimization of the functional (1) should lead, if the solution is unique, to recover them, which in the present context are the dielectric constants, real and imaginary parts, of the multilayered structure studied.

3.2. Evolution strategies

We have found in previous contributions that evolution strategies, a variant of the so called evolutionary algorithms, are a suitable and versatile tool for the optimization of functionals similar to (1) [17, 18]. Since there are no visible restrictions to employ them in the present work, for the sake of completeness we will succinctly describe their operational principles in the next paragraph. For a more detailed depiction, we refer the interested reader to the excellent Beyer's work [19].

The first step prior to the beginning of the optimization process is the random generation of an ensemble of vectors $\mathbf{p}^T$ that will conform the initial population $P_\mu^{\langle g \rangle}|_{g=0}$, where μ is the number of elements within the population and g is the associated iteration of the algorithm. A canonical evolutionary optimization algorithm is based on the application, over a defined number of iterations, of two "genetic" operators with well defined roles. The first is the Recombination, which explores the search space through the exchange of information between different elements of the population. The second operator is the Mutation, which is used to explore the search space through the introduction of random variations in the population. The application of these genetic operators over the initial population leads to the generation of a secondary population $P_\lambda^{\langle g \rangle}$ of λ elements. It is at this stage of the evolutionary loop that the link between the physics of the problem studied and the optimization algorithm is established. As we stated in previous paragraphs, in the present work this is done through the minimization of the functional (1), which can also be interpreted as a measure of the closeness between the reflectance data and those computed with a previously established model. Each element of the secondary population will be evaluated, and only those elements of $P_\lambda^{\langle g \rangle}$ that minimize the Euclidean norm will be retained, through some selection scheme, as part of the population $P_\mu^{\langle g+1 \rangle}$ for the next iteration of the evolutionary loop. The procedure is repeated until a defined termination criterion has been achieved. The respective sizes of the initial and the secondary populations, $P_\mu^{\langle g \rangle}$ and $P_\lambda^{\langle g \rangle}$, remain constant throughout the entire search process.

4. Results and discussion

As a first example, we illustrate the inversion scheme proposed in this work. For this, we will consider the target spectrum depicted with a solid blue line in Fig. 5. Although this information could be experimentally measured, we generate it numerically through the 4x4 Method previously described. The incident field is assumed to be a p- or s-polarized plane wave. Furthermore, we fixed the dielectric constant of one layer to ϵ_1=(2.3829+ i 0.434) (this value remained the same throughout the optimization process), and we assumed ϵ_2= (2.8215+ i 0.1008), as reported by Noyes *et al*. for the *Buprestid* beetle [8], which presents a periodic multilayer structure similar to that of the

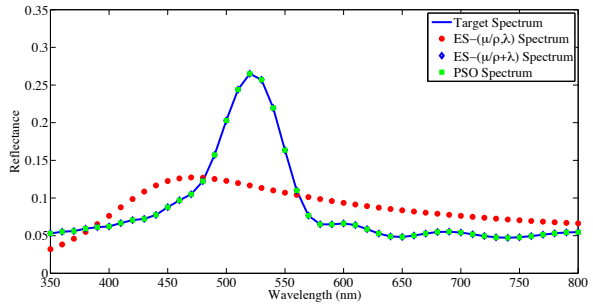


Figure 5: Target reflectance spectrum and optimized spectra obtained with different evolution strategies.

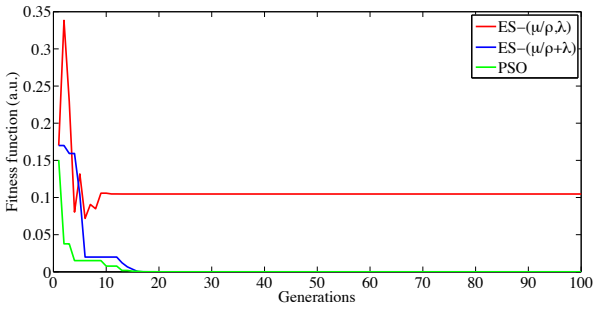


Figure 6: Convergence behavior of the Non-Elitist strategy (red), Elitist strategy (blue), and PSO (green).

Ceroglossus suturalis. Our goal is to retrieve this value of ϵ_2 directly from the reflectance spectrum.

Throughout our numerical experiments we set the size of the initial and the secondary populations to $\mu = 14$ and $\lambda = 100$, respectively. Furthermore, we fix the number of elements to be recombined to $\rho = 2$. The number of generations in the evolutionary loop was set to $g = 100$ and it provided the termination criterion. In this example, each element of the population was a randomly generated value of ϵ_2. Also, to define the search space, we set the lower and upper bounds $-10 \leq \mathrm{Re}\{\epsilon_2\},\ \mathrm{Im}\{\epsilon_2\} \leq 10$.

The Non-Elitist, $(\mu/\rho,\lambda)$, and the Elitist, $(\mu/\rho,+\lambda)$, evolution strategies (ES) were tested for their relative success looking for the solution from twenty different initial states. The main difference between these selection schemes is that the former choices the best elements only from the mutated population. The latter, on the other hand, selects the best elements from an intermediate population generated from the junction of the initial and mutated populations. Consequently, a promising element belonging to the first initial population can survive throughout the entire optimization process. Although this attribute of the Elitist strategy guarantees a monotonic decrement or increment of the fitness function, it can also make it prone to premature convergence into a local optimum.

Some typical results are shown in Fig. 6, where the red and blue solid curves represent the convergence behavior of the Non-Elitist and the Elitist strategies, respectively.

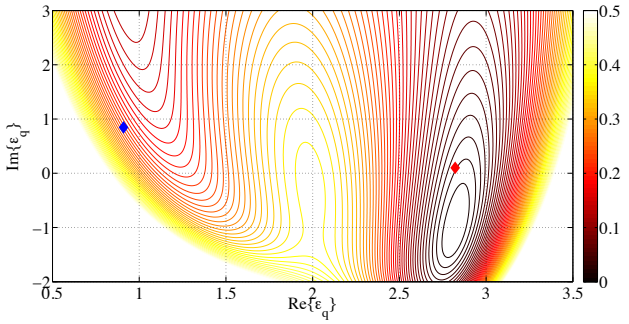


Figure 7: Topology of the fitness function.

The oscillating behavior is representative of the Non-Elitist strategy and can be interpreted as a temporary deterioration of the fitness value throughout the optimization process. In certain situations, this feature can be advantageous to avoid a premature convergence into a local optimum. However, this was not the case for this example and the Non-Elitist strategy did not converge to the target spectrum in any of the original twenty trials. On the other hand, the Elitist strategy converged to the target solution in fifteen trials. This result suggests that the Elitist strategy could be the most suitable method for this inverse problem. However, further work is required to have concluding results. The spectra associated to the parameters retrieved with the Elitist (blue symbols) and the Non-Elitist (red symbols) strategies are shown in Fig. 5, where we have used the same colors as in Fig. 6 to facilitate the visualization. It is evident that the Non-Elitist strategy converged to an undesired solution, i.e., to a local optimum of the fitness function.

For the sake of completeness, we compared the results obtained with the Elitist strategy with those of another bio-inspired optimization technique known as Particles Swarm Optimization (PSO). In essence, this algorithm mimicks the collaborative behavior of a population of individuals during their search for food [20, 21]. In order to compare the ES and the PSO in an objective manner, we considered a swarm of size $\mu = 114$ elements. Also, we fixed the number of iterations of the PSO to $g = 100$. Under these conditions, the Elitist strategy $(\mu/\rho+\lambda)-$ES and the PSO evaluate the fitness function the same number of times. Typical results of our numerical experiment are depicted with the solid green curve in Fig. 6. The convergence behavior shows that the dynamics of the $(\mu/\rho+\lambda)-$ES and the PSO are quite similar and their respective fitness values after twenty generations are quite close. It should be mentioned that the PSO retrieved the target parameters in the twenty trials. With respect to Fig. 5, the green squares show that the spectrum generated with the parameters retrieved by the PSO is indistinguishable from that generated with the Elitist ES. The fact of obtaining similar results with methods of different natures provides some confidence in our approach. A further study employing the PSO is the subject of a future publication.

To get more insight into the behavior of the different

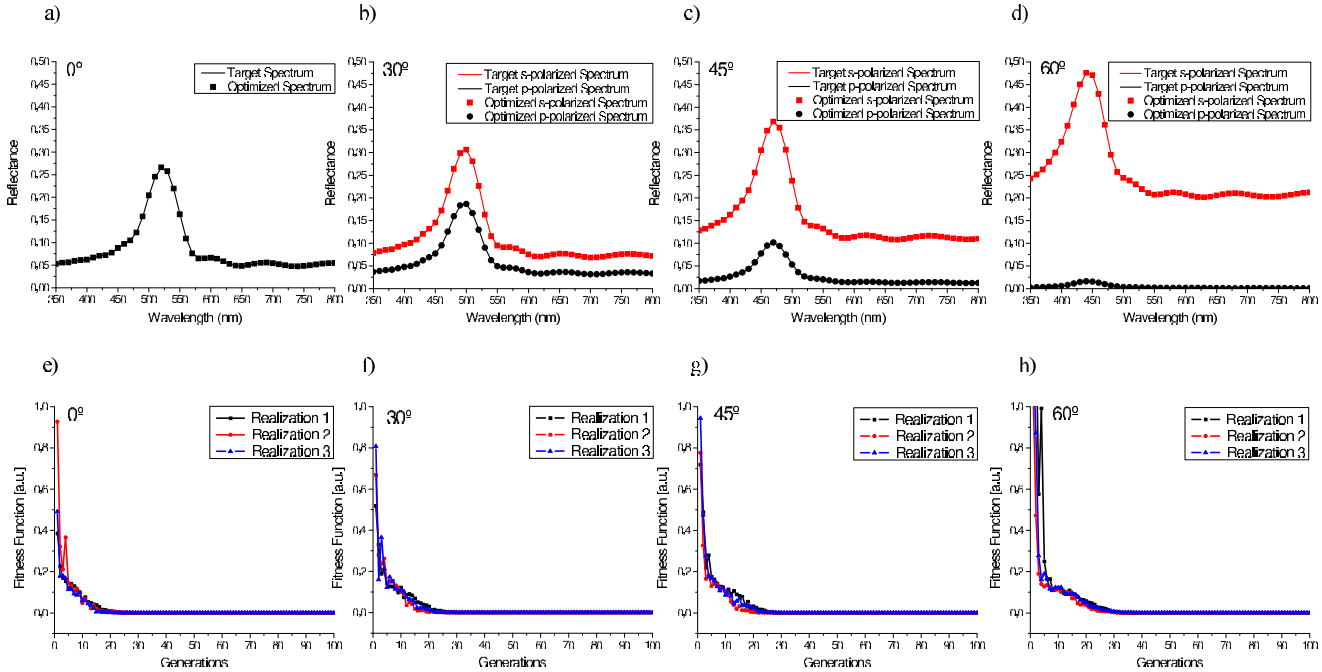


Figure 8: (a)-(d) Target reflectance spectra for different incidence angles and for both polarization modes (solid lines), and their corresponding optimized spectra (symbols) obtained using the Non-Elitist strategy. (e)-(h) Fitness functions for a few realizations for each one of the incidence angles considered.

optimization strategies, in Fig. 7 we show the topology of the fitness function as a function of the real and imaginary parts of the dielectric permittivity, for the same parameters used in Fig. 5. Both optima are marked with diamonds in the figure. The red one represents the desired solution that we are looking for and where the minimum value of the fitness function –for the permitted range of dielectric constants– is achieved. Furthermore, this is the optimum found by the Elitist Strategy $(\mu/\rho + \lambda)$ and the PSO. The contour lines in its vicinity are dark, and increase in value (become yellow) as we move away from it. On the other hand, the blue diamond corresponds to the local optimum to which the Non-Elitist ES converged. Although the fitness function also decreases in its vicinity, its value is not as low as for the other optimum. During the optimization process, the algorithm may converge to this undesired solution, and this should be avoided.

With the following example we intend to highlight the potential of evolution strategies to retrieve simultaneously several unknown parameters of the system. In particular, we applied the Non-Elitist strategy to find the dielectric constants of both materials that comprise the natural multilayer system. This means that we have now four unknowns to be found: the real and imaginary parts of both dielectric permittivities. We consider the same parameters of the structure as those of the previous example, but without fixing any of the dielectric constants. Then, for this example the search space was defined as $-10 \leq \mathrm{Re}\{\epsilon_i\},\ \mathrm{Im}\{\epsilon_i\} \leq 10$, with $i = 1, 2$.

In Figs. 8 (a)-(d) we plot the target reflectance spectra for different incidence angles and for both polarization modes (solid lines), together with the corresponding optimized spectra (symbols) obtained using the Non-Elitist strategy. The target curves have been calculated for $\epsilon_1 = (2.3829 + i0.434)$ and $\epsilon_2 = (2.8215 + i0.1008)$. It can be observed that there is an excellent agreement between the target and the retrieved reflectance for all incidence angles. In order to get more insight on the accuracy of the retrieved solution, in Figs. 8(e)-(h) we plot the corresponding fitness functions for a few realizations in each case. It can be noticed that for 30-40 generations, all realizations achieved the right values (we show only three examples in each case for the sake of clarity). The preliminary results obtained with the Elitist strategy and the PSO agree with those showed in Figs. 8. This numerical evidence suggests that the solution found with the three inversion schemes is the global optimum, within the search space defined in this contribution. Nevertheless, this work is still in progress and at this stage we are unable to draw conclusive results.

5. Conclusions

We have proposed evolution strategies as a tool to retrieve the relevant parameters of natural photonic structures. In particular, we investigated the *Ceroglossus suturalis* beetle, which exhibits an iridescent coloration produced by the interaction of light and the multilayer structure present in its epicuticle. We have shown examples in which the refraction indices of the materials that compose the periodic bilayered structure are obtained. If one of the indices is fixed,

the Elitist strategy and the Particles Swarm Optimization methods successfully converge to the right values of the real and imaginary parts of the other refraction index. However, the Non-Elitist strategy algorithm arrives to a non-desired local optimum. On the other hand, if both refraction indices are unknown, the Non-Elitist strategy converges to the right values. There are still many improvements that could be done within the optimization algorithms proposed, to guarantee the convergence to the global optimum in all cases. However, we have shown that this approach constitutes a promising tool for the determination of refraction indices of the materials involved in biological structures. Currently, work is in progress to include, in the evolutionary loop, a Debye's or a Cole-Cole model to describe the frequency-dependent dielectric permitivitty of the layers.

Acknowledgement

D. S., A. L. and M. I. acknowledge partial support from Consejo Nacional de Investigaciones Científicas y Técnicas (CONICET PIP 112-200801-01880) and Universidad de Buenos Aires (UBA-20020100100533).

References

[1] A. Parker, 515 million years of structural colour, *J. Opt. A, Pure Appl. Opt.* 2: R15–R28, 2000.

[2] P. Vukusic and J. R. Sambles, Photonic structures in biology, *Nature* 424: 852–855, 2003.

[3] S. Berthier, *Iridescences, the physical colours of insects*, Springer Science+Business Media, LLC, 2007.

[4] S. Kinoshita, *Structural colors in the realm of nature*, World Scientific Publishing Co., 2008.

[5] P. Vukusic and D. G. Stavenga, Physical methods for investigating structural colours in biological systems, *J. R. Soc. Interface* 6: S133–S148, 2009.

[6] S. Berthier, E. Charron and A. Da Silva, Determination of the cuticle index of the scales of the iridescent butterfly Morpho menelaus, *Opt. Commun.* 228: 349–356, 2003.

[7] P. Vukusic, J. R. Sambles, C. R. Lawrence, and R. J. Wootton, Quantified interference and diffraction in single Morpho butterfly scales, *Proc. R. Soc. Lond. B* 266: 1403, 1999.

[8] J. A. Noyes, P. Vukusic and I. R. Hooper, Experimental method for reliably establishing the refractive index of buprestid beetle exocuticle, *Opt. Express* 15: 4351–4357, 2007.

[9] S. Yoshioka and S. Kinoshita, Direct determination of the refractive index of natural multilayer systems, *Phys. Rev. E* 83: 051917, 2011.

[10] H. L. Leertouwer, B. D. Wilts and D. G. Stavenga, Refractive index and dispersion of butterfly chitin and bird keratin measured by polarizing interference microscopy, *Opt. Express* 19: 24061–24066, 2011.

[11] H. M. Fox and G. Vevers, *The nature of animal colours*, Sidgwick and Jackson, London, UK, 1960.

[12] A. B. Djurišic, J. M. Elazar and A. D. Rakic, Modeling the optical constants of solids using acceptance-probability-controlled simulated annealing with adaptive move generation procedure, *Phys. Rev. E* 55: 4797–4803, 1997.

[13] A. Vial, A. S. Grimault, D. Macías, D. Barchiesi and M. Lamy de la Chapelle, Improved analytical fit of gold dispersion : application to the modelling of extinction spectra with the FDTD method, *Phys. Rev. B* 71: 085416-085422, 2005.

[14] A. Luna, D. Skigin, M. Inchaussandague and A. Roig Alsina, Structural color in beetles of South America, *Proc. SPIE* 7782: 778205, 2010.

[15] *ImageJ* is a public domain, Java-based image processing program, http://rsbweb.nih.gov/ij/.

[16] P. Yeh and A. Yariv, *Optical Waves in Crystals*, Wiley, 1984.

[17] D. Macías, A. Vial and D. Barchiesi, Application of evolution strategies for the solution of an inverse problem in near-field optics, *J. Opt. Soc. Am. A* 21: 1465–1471, 2004.

[18] D. Macías, G. Olague and E. R. Méndez, Inverse scattering with far-field intensity data: random surfaces that belong to a well-defined statistical class, *Waves in Random and Complex Media* 16: 545–560, 2006.

[19] H. G. Beyer, *The Theory of Evolution Strategies*, Springer-Verlag, 2001.

[20] J. Robinson and Y. Rahmat-Samii, Particle swarm optimization in electromagnetics, *IEEE Transactions on Antennas and Propagation* 52: 397–407, 2004.

[21] R. Poli, J. Kennedy and T. Blackwell, Paticle swarm optimization: an overview, *Swarm Intelligence* 1: 33–57, 2007.

Actin Filaments Can Serve as Nonlinear Electrical Network

Dalibor L Sekulic[1*], and Miljko V Sataric[1]

[1]Faculty of Technical Sciences, University of Novi Sad, Novi Sad, Serbia
*corresponding author, E-mail: dalsek@yahoo.com or dalsek@uns.ac.rs

Abstract

In this paper, we establish a model of actin filaments as nanobioelectronics nonlinear transmission line based on polyelectrolyte features of biopolymers. Each actin monomer is an electric element with a capacitive, inductive, and resistive property due to the molecular structure of the actin filament. In the continuum limit and weak amplitude limit, the perturbed nonlinear Schrödinger equation is derived for the propagation of solitary ionic waves along a filament. From the analytical analysis and numerical simulations, we can conclude that actin filaments can function as biomolecular "electrical wires". This ability of actin filaments to conduct electrical signals may have important implications in the coupling of intracellular signals.

1. Introduction

The cytoplasm of eucaryotic cells is spatially organized by a network of protein filaments known as the cytoskeleton. This network contains three principal types of filaments: actin-based filaments, see Fig. 1, tubulin-based filaments called microtubules, and intermediate filaments. All three types of filaments are formed as helical assemblies of subunits that self-associate using a combination of end-to-end and side-to-side protein contacts. Each actin monomer (globular, G- actin), see Fig. 2, has tight binding sites that mediate head-to-tail interactions with two other actin monomers, so actin monomers polymerize to form filaments (filamentous, F- actin), see Fig. 1. Because all the actin monomers are oriented in the same direction, F-actin have a distinct polarity and their ends (called the plus and minus ends) are distinguishable from one another. Here we are dealing with F-actin which represents polymerized two-stranded helical chain of G-actin. We take the length of an actin monomer is typically $l = 5.4$ nm and the radius of the actin filament is approximately $R = 2.5$ nm [1].

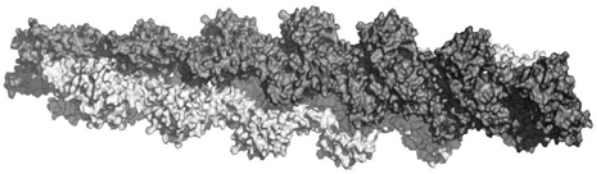


Figure 1: The sketch of F-actin helicoidally polymerized with discernible monomers.



Figure 2: Ribbon diagram of an actin monomer [2].

Much of the research on F-actin systems has focused on their mechanical properties. However, actin filaments are polyelectrolytes and therefore may have electrochemical properties of biological significance. This phenomenon is further manifested by the extensive changes in electric dipole moment observed in actin filament oriented by shear flow and a nonlinear electro osmotic response to weak osmotic stress [3].

Recently, it has been proposed that cytoskeletal elements including microtubules and F-actin are involved in facilitating the propagation of electrical signals in the cell. Lin and Cantiello [2] have experimentally demonstrated that actin filaments are good conductors of electrical signals. Electrical currents were observed about the surface of an F-actin under both high and low counter ionic strength conditions. Counter ionic waves were highly nonlinear and remained long after the electrical stimulation of F-actin ceased.

On the basis of such concept, we established the model where these cytoskeletal cylindrical polymers can be viewed as "coaxial cables" having the features of nonlinear transmission lines (NLTLs). These lines in general could be sequenced in ladders of repeated identical electric elementary units (EEU) which possess specific values of capacity, inductivity, and resistivity.

On the other hand, the concept of molecular communications has been introduced in the recent years. Following the bio-hybrid approach, molecular communication is inspired by the communication mechanisms that naturally occur amongst living cells, and it is defined as the transmission of information using molecules [4]. In molecular motor transport, a sender

(nanoscale component) releases information molecules, and molecular motors transport the information molecules along protein filaments to a receiver (nanoscale component) up to hundreds of micrometers away. We believe that a bio-inspired molecular communication system using a network of cytoskeletal filaments will govern the development of future nanonetwork communications.

In this paper, we explain the polyelectrolyte character of F-actin and develop a model based on the transmission line analogy with capacitive, inductive, and resistive components. The physical signi□cance of each of the components, for each section of the electrical network, will be described below. This way we will investigate the nature of nonlinear ionic waves propagating along an actin □lament in solutions containing counter-ions as would be found under realistic physiological conditions. Also, we numerically analyzed the pertaining voltage equation.

2. Characterization of F-actin

In as much actin filaments are mostly negatively charged on their outer surface they are true polyelectrolyte polymers. This is the consequence of the fact that numerous amino acids forming actin monomer have many negatively charged residues under physiological conditions. Manning [5] showed that highly charged cylinder-like polymers exert strong attraction on their counter ions so that a certain fraction condenses onto the polymer surface forming the so-called ionic cloud. An important point is that, because of the helical structure of F-actin, the distribution of counter ions will be nonuniform along the polymers length [1].

In order to use the polyelectric theory for F-actin chain, we start from the so-called Bjerrum length, λ_B, the distance where the thermal □uctuations of ions are balanced by Coulomb interactions between their charges. For monovalent ions it yields

$$\frac{e^2}{4\pi\varepsilon_0\varepsilon\lambda_B} = k_B T. \qquad (1)$$

Here, e is the charge of an electron, ε_0 the permittivity of vacuum, ε_r the relative permittivity of cytosol and k_B is Boltzmann□s constant. At the physiological temperature T = 310 K and taking ε_r = 80, it is easy to □nd from Eq. (1) that λ_B = 0.67 nm.

Counter ion condensation occurs when the mean distance between intrinsic polymer charges is such that λ_B/β > 1 [6]. Each actin monomer carries an effective excess of 11 negative charges. Assuming an average of 370 monomers per μm, one □nds that there is approximately □4e/μm. So linear charge spacing of β = 2.5×10^{-10} m is giving $\lambda_B/\beta \sim 2.7 > 1$. Thus the majority of counter ion population is predominantly constrained within the layer of thickness λ_B around F-actin □lament.

Now we will introduce the electrical components which are ingredients of respective nonlinear circuit which simulates the conductive properties of an F-actin in solution. The described cloud of counter ions with thickness λ_B is wrapped around F-actin. This cloud provides both resistive and capacitive components for ionic currents con□ned in this layer resembling the role of coaxial cable in electrical engineering. The inductive component to the electrical properties of ionic waves along F-actin is due to its double-stranded helical structure that induces the ionic □ow in a solenoidal manner following the winding troughs of local electric potential.

2.1. Capacitance of an electric elementary unit of F-actin

In continuum model, F-actin as a polyelectrolyte is represented by a volume which is bounded by a charged cylindrical surface in contact with an electrolyte whose dielectric constant is assumed to be time invariant and uniform. In an earlier papers [1, 6, 7], a detailed Poisson-Boltzmann approach was used to estimate the capacitance of elementary capacitance attributed to one F-actin monomer, see Fig. 3. Here, we adopt the same expression

$$C_0 = \frac{2\pi\varepsilon l}{\ln\left(1+\frac{\lambda_B}{R}\right)} = 2\times10^{-16}\,\mathrm{F}, \qquad (2)$$

where l = 5.4 nm is typical length of an actin monomer, and R = 2.5 nm is approximate radius of the actin filament. The permittivity, ε, is given by $\varepsilon_0\varepsilon_r$, where ε_r is the relative permittivity, which we take to be that of cytosol, i.e., ε_r =80.

This result is a pretty rough estimation which ignores the local peaks and troughs due to globular shapes of actin monomers. These troughs wind helically along F-actin. This circumstance will be taken into account by assuming that the charge on this capacitor varies in a nonlinear way with voltage much like the charge-voltage relation for a reversed-biased pn diode junction. Thus, for the n-th monomer, we suppose [8]

$$q_n = C_0\left(V_n - \alpha V_n^2 + \beta V_n^3\right), \qquad (3)$$

where C_0 is the linear capacitance of the capacitor, and α and β designate the nonlinear coef□cients of the capacitor.

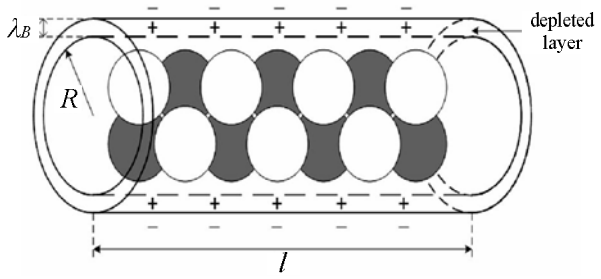


Figure 3: The rough shape of cylindrical capacitor with characteristic dimensions.

2.2. Inductance of an electric elementary unit of F-actin

In F-actin the monomers are arranged in head to head order to form actin dimers resulting in alternating distribution of electric dipole moments along the length of the □lament, see Fig. 4. This fact, together with the winding troughs, would be the reason that F-actin may be thought of as a □solenoid□ This solenoid □ow geometry leads to an

equivalent electrical element possessing self-inductance. Thus, we may roughly estimate an effective inductance for the length of one monomer in solution by [1]

$$L = \frac{\mu N^2 A}{l} = 1.7 \times 10^{-12}\,\mathrm{H}, \qquad (4)$$

where $A = \pi(R+\lambda_B)^2$ is the cross-sectional area of the effective coil, and l is the length of the F-actin. N is the total number of effective turns of the coil, in this case it is the number of windings of the helical distribution of ions around the filament.

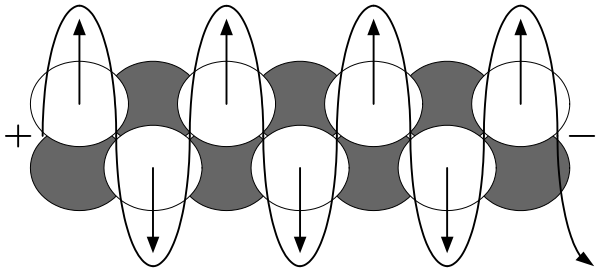


Figure 4: Schematic shape of F-actin monomers with pertaining dipole moment and winding current.

2.3. Resistance of an electric elementary unit of F-actin

The current trough layer of ionic cloud about F-actin can be divided into two components, longitudinal and transversal [7]. If we suppose that the connectivity of ionic cloud is homogenous, then the expression for longitudinal resistivity along one monomer reads:

$$R_1 = \rho\frac{l}{A_1}; \quad A_1 = 2\pi R\lambda_B. \qquad (5)$$

While the transversal component is:

$$R_2 = \rho\frac{\lambda_B}{A_2}; \quad A_2 = 2\pi Rl. \qquad (6)$$

These resistors are shown in Fig. 5. Due to lack of experimental evidences, we adopt the theoretical estimated conductivity of solution with counter ions in cytosol [1]. Using the values of conductivity, σ = 1.21 $(\Omega\,\mathrm{m})^{-1}$, and parameters as before, we get:

$$R_1 = 2\times 10^8\,\Omega, \text{ and } R_2 = 3\times 10^6\,\Omega. \qquad (7)$$

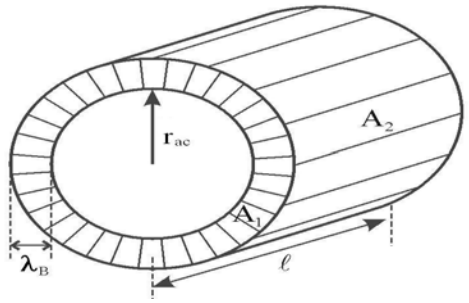


Figure 5: The representation of two elementary resistors, transversal and longitudinal.

3. Model of F-actin as nonlinear electrical transmission line

On the basis of already estimated components of electric elementary units, actin monomer, we are now able to establish a corresponding electrical model. A typical section scheme is shown in Fig. 6.

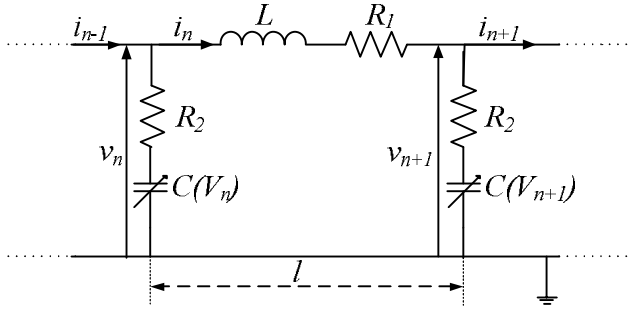


Figure 6: Schematic representation of the nonlinear transmission line for ion propagation along F-actin.

We expect a potential difference between the F-actin charged surface with condensed counterions and ions laying along coaxial cylinder at one Bjerrum length away. These Bjerrum ions are responsible for time dependant current which makes the inductance, L. In series with L should be inserted resistive component, R_1, see Fig. 6. In parallel to these components, there exists a resistance, which we denote R_2, acting between the Bjerrum ions and the surface of the filament. In series with this resistance, we have a nonlinear voltage-dependent capacitance, $C(V_n)$.

By applying the Kirchhoff current law at node n whose voltage with respect to the ground is v_n, and applying the Kirchhoff voltage law across the two inductors connected to this node, we obtain:

$$i_{n-1} - i_n = \frac{dq_n}{dt}, \qquad (8)$$

$$v_n - v_{n+1} = L\frac{di_n}{dt} + R_1 i_n. \qquad (9)$$

Similarly, if the voltage across the capacitor is V_b+V_n, where V_b is the bias voltage of the capacitor, we have:

$$v_n = R_2(i_{n-1} - i_n) + V_b + V_n. \qquad (10)$$

From Eq. (9) we have:

$$\begin{aligned} L\frac{di_{n-1}}{dt} &= v_{n-1} - v_n - R_1 i_{n-1}, \\ L\frac{di_n}{dt} &= v_n - v_{n+1} - R_1 i_n. \end{aligned} \qquad (11)$$

From (8) we have

$$L\frac{d^2 q_n}{dt^2} = L\frac{di_{n-1}}{dt} - L\frac{di_n}{dt}, \qquad (12)$$

and including Eqs. (11) in Eq. (12), we get:

$$L\frac{d^2q_n}{dt^2} = v_{n-1} - 2v_n + v_{n+1} + R_1(i_n - i_{n-1}). \quad (13)$$

Replacing the expressions for the voltages v_{n-1}, v_n and v_{n+1} from Eq. (10) to Eq. (13), we obtain that voltages of the adjacent nodes on this lossy NLTL are related via partial differential equation as follows

$$\begin{aligned}
&\left(LC_0\frac{d^2}{dt^2} + R_1C_0\frac{d}{dt}\right)\left(V_n - \alpha V_n^2 + \beta V_n^3\right) = \\
&\left(1 + R_2C_0\frac{d}{dt}\right)\left(V_{n-1} - 2V_n + V_{n+1}\right) \\
&- R_2C_0\alpha\frac{d}{dt}\left(V_{n-1}^2 - 2V_n^2 + V_{n+1}^2\right) \\
&+ R_2C_0\beta\frac{d}{dt}\left(V_{n-1}^3 - 2V_n^3 + V_{n+1}^3\right)
\end{aligned} \quad (14)$$

Applying the reductive perturbation method [9], we expand each Fourier component of $V_n(t)$ in a power series in the small quantity ش

$$V_n(t) = \sum_{l=1}^{\infty}\left(\sum_{m=1}^{\infty} ش^m V_l^{(m)}(\xi,\tau)\right)e^{il\theta} + \text{c.c}, \quad (15)$$

where c.c. stand for complex conjugate. Here

$$\xi = ش(n - v_g t), \quad \tau = ش^2 t, \quad \theta = kn - \omega t, \quad (16)$$

where v_g is the group velocity. The resistances are rescaled to

$$R_1 \to ش^2 R_1, \quad R_2 \to ش^2 R_2. \quad (17)$$

A Taylor expansion allows us to write

$$\begin{aligned}
&v_{n-1} - 2v_n + v_{n+1} = \\
&\sum_{m=1}^{\infty} ش^m\left(\sum_{l=1}^{\infty}\left(\sum_{p=0}^{\infty}\frac{(-1)^p ش^p}{p!}\frac{\partial^p V_l^{(m)}(\xi,\tau)}{\partial\xi^p}\right)e^{il(\theta-k)}\right) \\
&- 2\sum_{m=1}^{\infty} ش^m\left(\sum_{l=1}^{\infty} V_l^{(m)}(\xi,\tau)e^{il\theta}\right) \\
&\sum_{m=1}^{\infty} ش^m\left(\sum_{l=1}^{\infty}\left(\sum_{p=0}^{\infty}\frac{ش^p}{p!}\frac{\partial^p V_l^{(m)}(\xi,\tau)}{\partial\xi^p}\right)e^{il(\theta+k)}\right) + \text{c.c.}
\end{aligned} \quad (18)$$

After substituting Eqs. (15) and (18) into Eq. (14) and using Eqs. (16) and (17), we can transform Eq. (14) into a chain of equations in different orders of the small parameter ش and we can obtain at order $ش^1$ (also with the aid of the results of order ش), and for $l = 1$, the following equation:

$$i\frac{\partial V}{\partial t} + P(\omega)\frac{\partial^2 V}{\partial\xi^2} + Q(\omega)|V|^2 V = -i\Gamma V, \quad (19)$$

where the values of the coefficients are

$$\begin{aligned}
&P(\omega) = -\frac{\omega}{2}, \quad Q(\omega) = \alpha^2\omega\left(\frac{3\beta}{2\alpha^2} + \frac{\omega_c^2}{\omega^2} - 2\right), \\
&\Gamma = \frac{R_1}{2L} + 2\frac{R_2}{L}\sin^2\left(\frac{k}{2}\right),
\end{aligned} \quad (20)$$

with $\omega_c = 2(LC_0)^{-1/2}$ being the cutoff angular frequency. In addition, $P(\omega)$, $Q(\omega)$ and Γ are the coefficients of dispersion, nonlinearity and dissipation, respectively. The corresponding linear dispersion law of the elementary solution is given by

$$\omega = \omega_c \sin\left(\frac{k}{2}\right). \quad (21)$$

Thus, propagation the time-space voltage of ionic pulses along actin filaments can be described with a lossy nonlinear Schrödinger (NLS) equation (19).

With the dissipation disregarded, ة =0, Eq. (19) reduces to the standard NLS equation, which possess in□nitely many symmetries and conservation laws such as the total pulse intensity and total energy. A well-known soliton solution of the standard NLS equation is of the form [10]

$$V(\xi,t) = A\,\text{sech}\left(A\sqrt{\frac{Q}{2P}}\xi\right)e^{i\frac{A^2Q}{2}t}, \quad (22)$$

where A is real constant. When ة □0, the perturbed term iة V is considered as the loss for ة >0. Consequently, the conservation quantities always change, say, the total pulse intensity satis□es the following equation:

$$\frac{dI}{dt} = -2\Gamma I, \quad (23)$$

here, we take ة >0. It implies that the amplitude and width of the pulse will be changed due to the perturbed term. As far as we know, there are two different views on the decay rate of soliton amplitude. One holds that the amplitude of the bright soliton of Eq. (22) will decay exponentially as $e^{(-2ة\,t)}$ [11, 12]:

$$V(\xi,t) = Ae^{-i2\Gamma t}\,\text{sech}\left(A\sqrt{\frac{Q}{2P}}e^{-i2\Gamma t}\xi\right)e^{i\frac{A^2Q\Gamma}{8}\left(1-e^{-4\Gamma t}\right)}. \quad (24)$$

Here we mention one of possible numerical solutions of Eq. (19) for the speci□c set of the values of estimated resistive components of the EEU. Fig. 7 depicts the evolution of intensity pro□les $|V|^2$ of the solution of perturbed NLS equation. Under the action of perturbation of iة V, the amplitude and energy of soliton decay with time t exponentially. For larger ة values, both of them decay faster. And the phases of soliton are also changed by perturbation.

Numerical solution is apparent that localized solitonic pulse-like wave propagates with decreasing amplitude along distances of hundreds EEUs with constant velocity. This velocity can be estimated from Fig. 7 as follows:

$$v \approx \frac{\Delta x}{\Delta t} \approx \frac{300l}{\Delta t} = \frac{300 \times 5.4\text{ns}}{200\text{ns}} = 8.1\frac{\text{m}}{\text{s}}. \qquad (25)$$

The range of this soliton-like waves is $300 \times l = 300 \times 5.4$ nm = 1.62 μm which is of the order of cell's diameter.

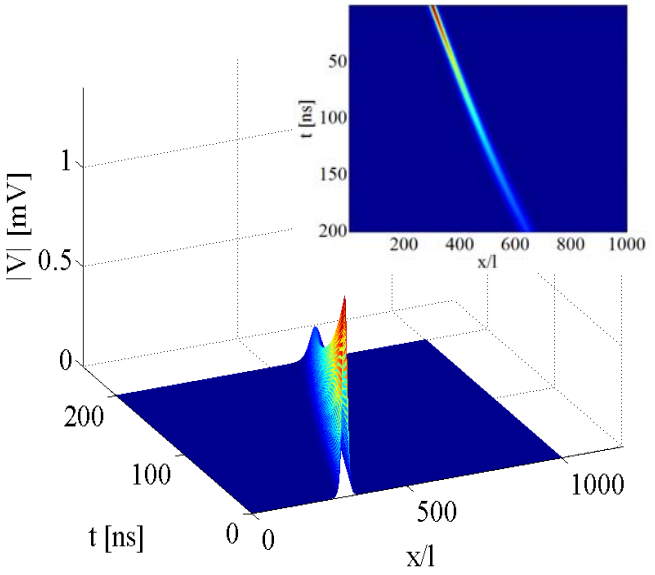


Figure 7: One of possible numerical solutions of pertaining voltage equation for the specific set of the values of estimated resistive components.

4. Conclusions

Strongly reliant on the polyelectrolyte concept, we elaborated a new model for ionic waves along actin filaments in cell. The background for the model is the molecular structure and geometry of F-actin and its interaction with solvent ions. In that context, F-actin filament surrounded by ions from cytosol is considered as an nonlinear electrical transmission line with *R*, *L* and *C* elements estimated on the basis of available experimental data and known geometry. The important feature of nonlinearity of F-actin capacitance was arisen naturally from rough landscape of its surface.

In the continuum limit and weak amplitude limit, the perturbed nonlinear Schrödinger equation is derived for the propagation of solitary ionic waves along F-actin. Our numerical solution of pertaining voltage equation has the shape of soliton-like pulse, which progresses with an almost constant velocity and only a decay of its initial amplitude. The velocity of propagation of soliton localized pulses was estimated to be several m/s, which are very reasonable values. It depends on the characteristic properties of the electrical circuit model.

We believe that these findings may have important consequences for our understanding of the signaling and ionic transport at intracellular level.

Acknowledgements

The authors would like to thank the Ministry of Education and Science of Serbia, Grant III43008, for the financial support of this work.

References

[1] M. V. Satarić, N. Bednar, B. M Satarić, G. Stojanović, Actin filaments as nonlinear RLC transmission lines, *International Journal of Modern Physics B* 23: 4697–4711, 2009.

[2] E. C. Lin, H. F. Cantiello, A novel method to study the electrodynamic behavior of actin filaments. Evidence for cable-like properties of actin, *Biophysical Journal* 65: 1371–1378, 1993.

[3] H. F. Cantiello, C. Patenaude, K. Zaner, Osmotically induced electrical signals from actin filaments, *Biophysical Journal* 59: 1284–1289, 1991.

[4] I. F. Akyildiz, J. M. Jornet, M. Pierobon, Nanonetworks: A new frontier in communications, *Communications of the ACM* 54: 84–89, 2011.

[5] B. O'Shaughnessy, Q. Yang, Manning-Oosawa counter ion condensation, *Physical Review Letters* 94: 048302.1–4, 2005.

[6] D. L. Sekulić, B. M. Satarić, J. A. Tuszynski, M. V. Satarić, Nonlinear ionic pulses along microtubules, *European Physical Journal E: Soft Matter* 34: art. no. 49, 2011.

[7] M. V. Satarić, D. L. Sekulić, M. V. Ivanov, Solitonic ionic currents along microtubules, *Journal of Computational and Theoretical Nanoscience* 7: 2281–2290, 2010.

[8] D. L. Sekulić, M. V. Satarić, M. B. Ivanov and J. S. Bajić, Soliton-like pulses along electrical nonlinear transmission line, *Electronics and Electrical Engineering* 122: 2012, in press.

[9] K. Tse Ve Koon, J. Leon, P. Marquie, P. Tchofo-Dinda, Cutoff solitons and bistability of the discrete inductance capacitance electrical line: Theory and experiments, *Physical Review E* 75: 066604.1–8, 2007.

[10] M. V. Satarić, R. Makula, On the role of the soliton mechanism in the electron transfer along the quasi-one-dimensional structures, *Physica Status Solidi (B) Basic Research* 116: 617–632, 1983.

[11] D. Cai, A. R. Bishop, N. Gronbech-Jensen, B. A. Malomed, Dark shock waves in the nonlinear Schrödinger system with internal losses, *Physical Review Letters* 78: 223–226, 1997.

[12] A. Hasegawa, Y. Kodama, Signal transmission by optical solitons in monomode fiber, *Proceedings of the IEEE* 69: 1145–1150, 1981.

Effects of RF/ MW Emitted from Mobile-Phone Base-Stations on Plant Growth using Chlorophyll a Fluorescence and Vegetative Growth

S. T. Kafi[1], A. M. Ahmed[1], Samah Osman[2], Ahmed Bakheit[2] and **A. K. Sabir Ali[3]**

[1]Department of Medical Physics, Faculty of Science and Technology,
Al Neelain University, Khartoum, Sudan.
[2]Department of Laser and Optics, Faculty of Science and Technology,
Al Neelain University, Khartoum, Sudan.
[3]Department of Biology and Environmental Sciences, Faculty of Science
and Technology, Al Neelain University, Khartoum, Sudan.

Corresponding author: stawer.kafi@gmail.com

Abstract:

The objectives of the present study are to investigate the effects of radiation emitted from mobile-phone base–stations on plants growth by using fluorescence emission spectra. Five plants: Dura"*Sorghum bicolor"*, Sunflower "*Helianthus annuus*", Roselle "*Hibiscus sabdariffa*", Maize "*Zea mays*" and Aubergine "*Solanum americanum*" were selected for this experiment. The plants were grown under three levels of irradiation i.e. 0.08 mW/cm^2 and 0.16 mW/cm^2, while the control was set free of radiation exposure. The chlorophyll fluorescence emission of the intact leaf was measured using a blue LED which emits 450 nm and recorded via USB2000 spectrophotometer from Ocean Optics Company (USA). Spectroscopic parameters calculated are the P. I. R and A. R The vegetative growth parameters of plants were monitored: height and width of leaf, fresh and dry weights,. The data obtained revealed that increase in radiation intensity is associated with poor growth parameters in all studied plants. The response of each plant depends on its tolerance to the increase of RF/MW radiation. All growth parameters revealed signs of damage on leaves of the exposed plants.

Key words: Base-station, RF/MW, Plants, LED, P. I. R and A. R.

Introduction:

There is considerable evidence which proves, beyond reasonable doubt, that microwave radiation from mobile phones and wireless telecommunications cause a significantly increased risk on biological systems of both humans and plants e.g. brains, genes and plants' growth stress [1, 2 and 3]. Plant tissues absorb the energy of the electromagnetic radiation in the visible region by the photosynthetic pigments. This energy is used for the photosynthetic processes [4, 5]. The liberalization and privatization of the telecommunication sector, policies, regulations and plans adopted by the Government of the Sudan have created a capital–attracting, pro-competitive policy environment that have fostered the build–up of a modern, fully–digital infrastructure in the country and furnished a climate suited to enhance ICTs development nationwide. Accordingly, the number of mobile subscribers in Sudan has increased dramatically in the last decades from only 292 users in 1998 to 17784190 users in 2010 [6]. There are thousands of

mobile-phone base-stations installed all over the country. Since wireless communication uses radiofrequency (RF) and microwave (MW) electromagnetic fields, exposure to these fields result if not controlled by safety protocols, in environmental contamination and health hazards. Chlorophyll a *(Chl a)* induced-fluorescence emission from intact leaves is a well known technique for the study of plants classification, growth, stress …etc. The objectives of the present study are to investigate the effects of radiation emitted from mobile-phone base–stations on plants growth by using LED (450nm) on five conventional plants grown in Sudan i.e. Dura, Sunflower, Roselle, Maize and Aubergine.

Materials and Methods:

Tested plants

Dura is cultivated in Sudan for it constitutes the main staple food and also used for livestock feed. For food use, the grain may be roughly ground and as a mush or porridge, or made into flour. The grain is also a source of native beers, particularly in Africa. [7] . Sunflower is an annual plant native to the Americas. The plant is grown in Sudan for its oil (a widespread cooking ingredient) and as an ornamental plant [8]. Maize known as corn in some countries is a cereal grain domesticated in Mesoamerica and from there it spread to the rest of the world [9]. Maize in Sudan is currently a secondary crop, although it is used as a food staple in some parts of the southern states. But the government is trying to encourage expanded, larger-scale production to capture export markets [10]. Rossele is an important commercial kenaf species grown for its calyx (herbal tea), pigments, fibres and oil. Its fibres were reported to be superior to that of jute and its seeds' oil content are similar to kaok and cotton seeds [11]. Egg plant Aubergine is a delicate perennial plant often cultivated as an annual for its fleshy and meaty texture, fruit. The plant is native to the Indian subcontinent .[12 and 13]. The plant is a popular salad ingredient in the Sudanese meals.

Thirty seeds of each of the five tested plants were sown in three pots (i.e. 10 seeds/pot) that were filled with a mixture heavy clay soil and sand (mixed with equal ratios) to about 10 cm from the top. The clay soil was brought from the Blue Nile Bank near Khartoum and mixed with dry plants leaves as an organic–fertilizer. The average diameter of the pots is about 26 cm. After successful germination and establishment, the seedlings were thinned to leave the best three healthy seedlings in each pot. Three sets were grown for each plant species: at 0.16 mW/cm^2; at 0.08 mW/cm^2 and the control which was completely isolated. The plants were irrigated daily at six o'clock pm till the flowering of the plants. The following parameters were measured: germination, height of plants, width of leaves, fresh and dry weights of plants, % dry weight.

RF/MW radiation exposure

A mobile phone base-station installed on the roof of the Faculty of Science building was used as a source of radiation in this experiment As a precautionary measure, the Expert Group on Health Effects of Electromagnetic Fields [14] recommended that power lines and power installations should be sited away from heavily populated areas to keep

exposures to people low. This base station belongs to Zain, Sudan Telecommunication Company and emits RF/MW radiation frequency between 800 and 900 MHz. The power density varies due to distance from base of the tower. The power density was measured using a RF-strength metre, Alpha Inc. No. 9912-00 b, USA.

Spectroscopic Measurements

Spectroscopy measurements of chlorophyll fluorescence of plant material were performed by irradiating the leaves with a blue light emitting diode (LED) operating at a wavelength of 450 nm, and output power 60μW. Plant leaf was placed a distance between source of excitation and a fiber optic which was connected to a high-resolution Ocean Optic spectrometer. A compact software controlled spectrometer (USB 2000/origin lab Dunedin, USA/Northampton, USA) was used for recording the fluorescence signal emitted by the plants intact leaf. The resolution of the spectrometer was 1.34 nm FWHM, and its detector covers the wavelength range from 350-1100 nm. The whole setup was coupled to laptop computer; and the recorded data were then analyzed using ORIGIN 6.1 computer program. The software uses an algorithm curve fitting with a combination of Gaussian spectral functions to analyze the spectra. Spectroscopic parameters calculated after the Guassian fit of the curve were the peak fluorescence intensity and peak wavelength for PSII and PSI complexes i.e. $I_F(685)$ and $I_F(734)$ respectively, the peak intensity ratio P.I.R. and area A.R. The latter two parameters when plotted versus time provide information about the plant growth. The measurements of the fluorescence started at the middle of the third week after sowing, and were taken from different leaves in each pot. Fluorescence signals from intact leaves of the tested plants were recorded daily, and averaged per week.

Results Analysis and Discussion

Spectroscopic data

Fluorescence data obtained are summarized in Fig. (1a-e), which shows the fluorescence spectra together with P.I.R and A.R for each type of plants.

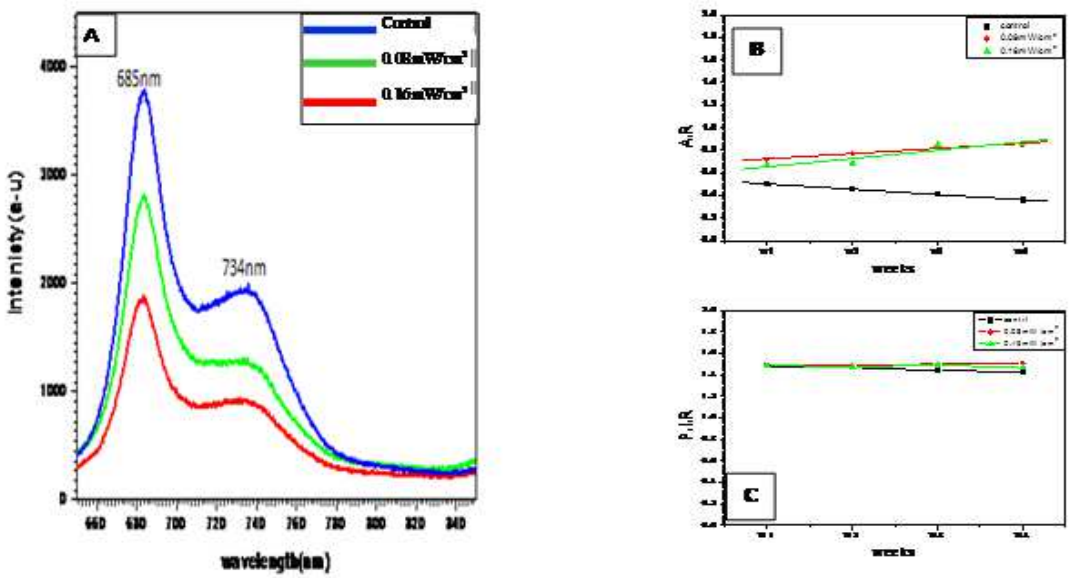


Fig. (1-a): Dura: (A). Fluoresce spectra (B). A. R and (C). P. I.R

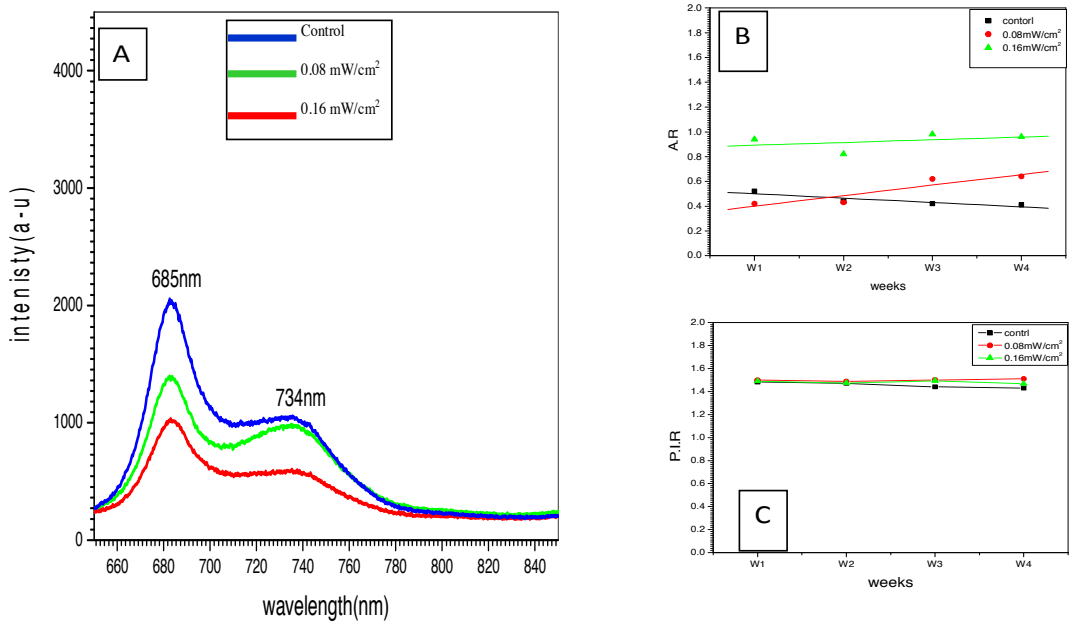


Fig. (1-b): Sunflower

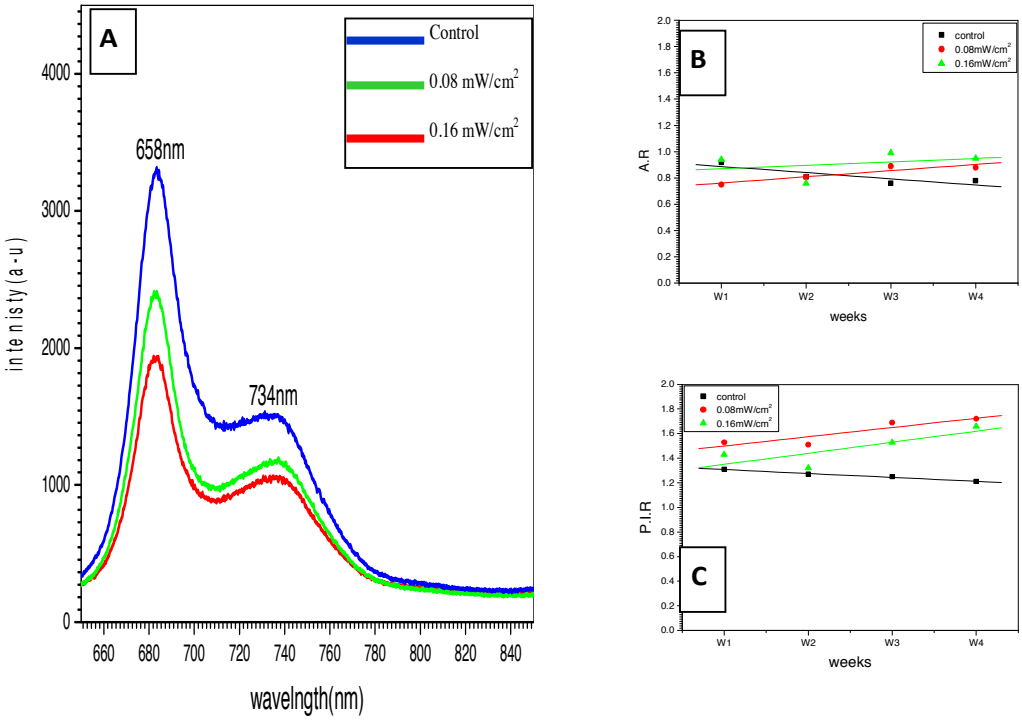


Fig. (1-c): Maize

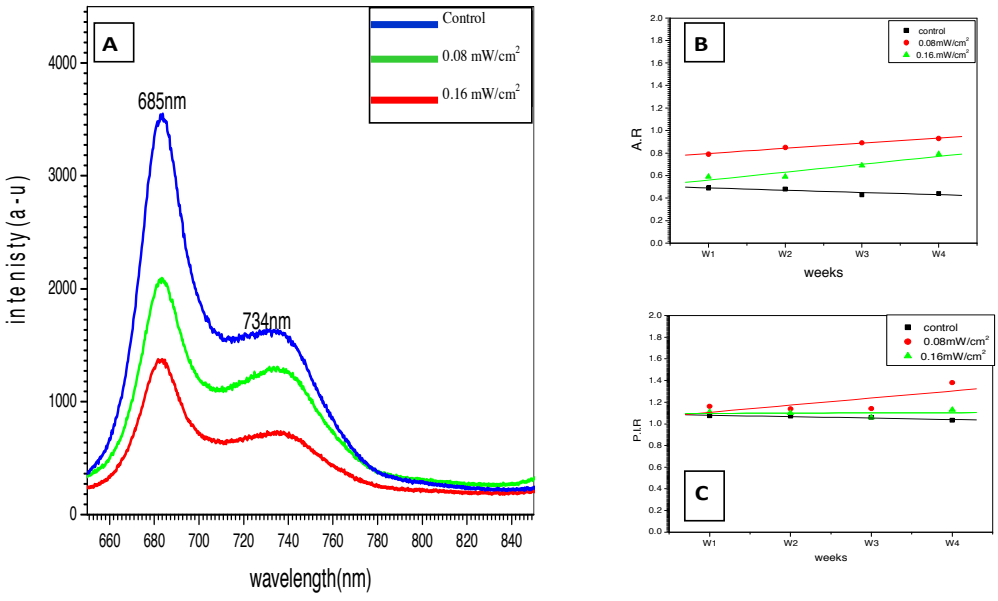


Fig. (1-d): Roselle

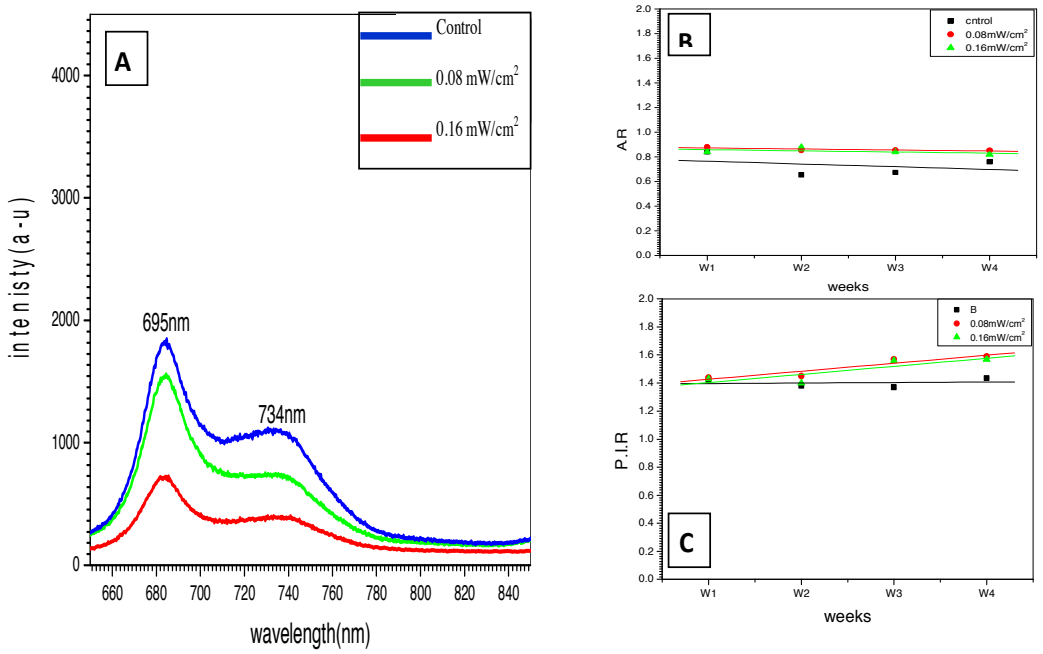


Fig. (1-e): Aubergine

From spectra shown in Fig.(1:a-e), the highest fluorescence intensity was recorded by the control plants, followed by the group exposed to 0.08 mW/cm^2 and 0.16 mW/cm^2 respectively. Since the fluorescence intensity is proportional to the number of fluorescing molecules, then the amount of chlorophyll content of plants under free radiation exposure is higher than that of the exposed plants. Similar results were obtained by [15 and 16] working with gamma irradiation on chickpea and cotton respectively. In addition, the values of P.I.R and A.R. were lower for the control group of plants compared to those exposed to 0.08mW/cm^2 and 0.16 mW/cm^2 respectively. According to [4], lower values of these parameters is an indication to higher chlorophyll content in plant leaves. Generally the maximum peak wavelengths of intact leaves center around 685 and 734 nm respectively, but slight deviations from these values occur depending on the internal leaf structure of each plant. The P. I. R and A. R parameters measured followed a linear relation with time for all tested plants, which indicates regularity of the changing effects.

Vegetative data

Germination response to RF/MW radiation

Seed germination of all tested plants began two days after sowing and by 14 day, it was completed (see Table (1)). The results indicated that the seeds of the five plants germinated best in the absence of RF/MW while exposure delays germination for all

tested plants. These results are in conformity with [17]. Other authors e.g. [18, 19], have shown that microwave radiation either promotes or has no effect on germination and plant growth.

Table (1). Germination percentage of the five tested plants (±SD)

Plant	Germination (%)								
	Control			0.08 mW/cm^2			0.16 mW/cm^2		
	Day2	**Day7**	**Day14**	**Day2**	**Day7**	**Day14**	**Day2**	**Day7**	**Day14**
Dura	**85±2.1**	**100±0.0**	-	**75±2.5**	**80±2.3**	**98±1.8**	**60±3.8**	**80±3.4**	**100±0.0**
Sunflower	**90±3.2**	**100±0.0**	-	**70±3.3**	**85±3.0**	**95±2.0**	**50±4.0**	**75±2.8**	**98±1.7**
Maize	**90±2.2**	**100±0.0**	-	**80±4.1**	**85±2.9**	**97±1.9**	**70±3.2**	**89±3.3**	**100±0.0**
Roselle	**88±1.9**	**100±0.0**	-	**60±3.0**	**80±2.8**	**90±3.0**	**55±5.0**	**85±1.0**	**98±1.1**
Aubergine	**85±2.8**	**98±1.6**	-	**55±4.4**	**90±4.0**	**98±2.1**	**65±2.9**	**90±1.0**	**99±0.3**

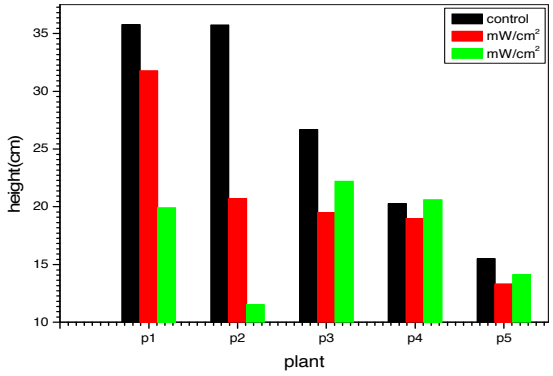


Fig (2). Effect of MW/FR on height of plants.

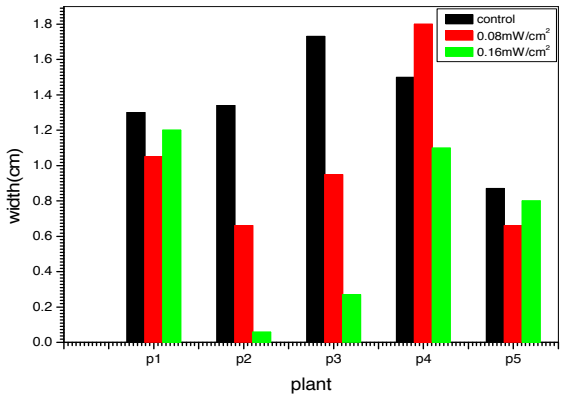


Fig (3) Effect of MW/FR on width of leaves

(P1: Dura, P2: Sunflower, P3: Maize, P4:Roselle, P5: Aubergine).

Fig. (2) Showed that microwave negatively affects the height of the five tested plants i.e. stunted dwarf growth was associated with high microwave strength. The control scored the maximum height followed by 0.08 mW/cm^2 and at 0.16 mW/cm^2, respectively. Similar results were obtained for the width of the plants (Fig. 3).

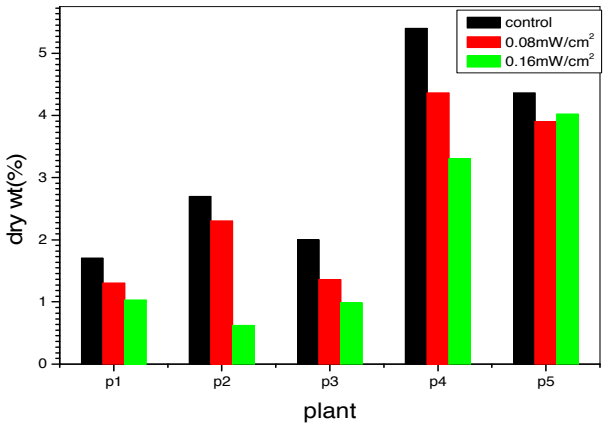


Fig. (4): Ratio of fresh to dry weights for all tested plants

Symptoms of growth damage such as leaf necrosis, leaf tip burn, and leaf folding were evident on plants grown at 0.08 mW/cm^2 and at 0.16 mW/cm^2. The extent of damage depends on the level of radiation exposure. These observations were in agreement with [20] who reported that microwave radiations caused burns along the vascular system of maize seedlings and damage the photosynthetic system. The five plants grown at 0.16 mW/cm^2 radiation were more susceptible to be attacked by insects e.g. Aphids, destructive insects that feed on plants cell sap [21], and aubergine exposed to the highest radiation dose was infected by tomato leaf curl virus (TLCV), a virus associated with the Family Solanaceae and causes much damage to the crops [22].

Conclusions

Spectroscopic and vegetative measurements were found to be consistent with each other for all experimented plants. Signs of damage were evident on plants exposed to RF/MW radiation. These effects include delay germination; dwarf stunted plants, decreasing length and width of leaves and fresh and dry weights, acceleration of flowering in some of tested plants and weakening of the plants' immune systems. Installation of base-stations should consider safety regulations that insure minimal risk to plants, animals and humans. Further studies on the effects of RF/MW radiation on plants in correlation with intensity levels and exposure time are proposed.

Acknowledgement

The authors would like to thank Al Neelain University, Khartoum, Sudan for financial support for this project and Mr. Ayman Elshayeb for the help he offered .

References

[1] Havas M., Analysis of Health and Environmental Effects of Proposed San Francisco Earthlink Wi-Fi Network.mhavas@trentu.ca 2007.

[2] Cumarsáide, A. R. and Nádúrtha M. A. Health Effects of Electromagnetic Fields. Expert Group on Health Effects of Electromagnetic Fields, 2005.

[3] Kumar A. A., P. Mishra, K. Kumari1, K. C. S Panigrahi. Environmental stress influencing plant development and flowering. www.niser.ac.in/~aaram01/env_**stress**.pdf 2011.

[4] Ndao, A.S., Konte, A., Biaye, M., Faye, M.E., Faye, N.A.B. and Wague, A., J. Fluorescence, 5(2) (2005) 123-129.

[5]Blankenship, R.E. "Molecular Mechanisms of Photosynthesis". (Blackwell Science, Arizona, USA, 2002).

[6]Reserch and mobile Sudan-Telecoms, mobile and forcasts. *Bussiness Wire*, 2011. (www.sudannas.com/vb).

[7] Magnuss, J. R., Markle, G. M. and Compton, G. C. Food and crops of the United States. Interregional Research Project. IR-4, IR Bul. 1(Bul. 828. *New Jersey Agricultural Experimental Station* 1971. http://www.hort.purdue.edu/newcrop /crops/ Sorghums Forage.html).

[8] Shell, G.S.G., A.R.G. Lang, and P.J.M. Sale. Quantitative measures of leaf orientation and heliotropic response in sunflower, bean, pepper and cucumber. *Agricultural Meteorology*, 15(1), 25-37. 2003.

[9] E. L. Sturtevant (1894). Notes on Maize. Bulletin of the Torrey Botanical Club, Vol. 21, Lancaster, PA August 20(8), page 1.

[10] Alexander, M. Country Focus: Sudan. Drought, unrest sparks wheat and food sorghum shortages in Sudan. (2001).World-grain.com.

[11] El-Saidi and Hawash. The effect of using saline water for irrigation on the growth and chemical properties of Roselle plants (Hibiscus sabdariffa L.). Z. Acker-und Pflanzenbau 134,251-256. 1971

[12] Tsao and Lo in "Vegetables: Types and Biology". Handbook of Food Science, Technology, and Engineering by Yiu H. Hui CRC Press. ISBN 1574445510\. 2006.

[13]..Doijode, S. D. Seed storage of horticultural crops (pp 157). *Haworth Press*: ISBN 1560229012. 2001.

[14] Expert Group on Health Effects of Electromagnetic Fields. Health Effects of Electromagnetic Fields. Department of Communications, Energy and Natural Resources. An Roinn Cumarsaide Maragus Acmaninni Nadurtha. Dublin 22nd March 2007. www.dcenr.gov.ie/NR/rdonlyres/.../0/ElectromagneticReport.pdf

[15] A. Hameed, T. M. Shah, B. M. Atta, M. A.H. Haq and H. Sayed. Gamma Irradiation effects on seed germination and growth, protein content, peroxdase and protease activity , lipid peroxidation in Desi and Kabuli chickpea. *Pak. J. Bot*., 40(3): 1033-1041, 2008.

[16] Sharif, A., M. R. khan and S. A. Hussain, Effect of gamma radiation on certain characters of *Gossypium hirsutum* L. Pak. J. Agric. Res. 1(2), 114-117.

[17] Urech, M., B. Eicher, J. Siegenthalaer. Effects of microwave and radio frequency electromagnetic fields on lichens, *Bioelectromagnetics*, 1996, 17, 327−334.

[18] Khalafallah, A.A. and S. M. Sallam. Response of maize seedlings to microwaves at 945 MHz. *Romanian Biophys*. J., 19, (1), 49−62, 2009.
[19] Jonas, H., Responses of maize seedlings to microwave irradiations, *Environmental Pollution*. *Series B*. *Chemical and Physical*, 1983, 6, 207−219.
[20] Blackman, R. L. and V. F. Eastrop (1994). Aphids on the World's Trees. An Identification and Information Guide. *Wallingford: CAB International*. ISBN 0-85198-877-6.).
[21] H. Czosnek and H. Laterrot. A worldwide survey of tomato yellow leaf curl viruses. Arch Virol (1997) 142: 1391±1406.
[22] Volkrodt, W. 1988. Electromagnetic pollution of the environment. In Robert Krieps (Ed.): Environment and health: a holistic approach. Luxembourg Ministries of Environment and Health, the Commision of the European Communities and the World Health Organization

Optical response of composite materials: comparison of different approaches

Guillermo Ortiz[1*], Marina Inchaussandague[2], Diana Skigin[2], Ricardo Depine[2], and Luis Mochán[3]

[1]Departamento de Física, Facultad de Ciencias Exactas, Universidad Nacional del Nordeste, Avenida Libertad 5400, Campus-UNNE, W3404AAS Corrientes, Argentina
[2]Grupo de Electromagnetismo Aplicado, Departamento de Física, FCEN, Universidad de Buenos Aires, and IFIBA, CONICET, Argentina
[3]Instituto de Ciencias Físicas, Universidad Nacional Autónoma de México, Apdo. Postal 48-3, 62251 Cuernavaca, Morelos, Mexico
*corresponding author, E-mail: gortiz@exa.unne.edu.ar

Abstract

We consider a composite material comprising periodically distributed metallic spheres in a dielectric host matrix. We investigate the capabilities of the effective non-retarded method (ENR) to reproduce the reflectance/transmittance of an inhomogeneous slab made of such a material. First, the effective dielectric function of the composite medium is obtained using the ENR approach, and it is introduced into the Fresnel coefficients to calculate the reflectance/transmittance of the slab. This response is compared with that obtained with the Korringa-Kohn-Rostoker (KKR) wave calculation method for various thicknesses and for different filling fractions. Within this framework, we calculate the electromagnetic response of a slab of a given thickness for different values of the lattice constant. As this value decreases, the KKR results approach those given by effective medium theories, as is to expect because in this case the long wavelength condition is better fulfilled.

1. Introduction

Research on metamaterial structures undergoes continuous progress due to their unique electromagnetic behavior and the associated application potential [1]. With constant advances in design and fabrication capabilities, metamaterial development appears to be restricted by the properties of naturally available materials used to build metamaterial structures. An interesting route to obtain materials with tailorable dielectric function is the use of metal-dielectric mixtures. Effective medium theories describe the effective dielectric function of such complex systems through the dielectric function of the components and a limited number of parameters, usually the filling fraction of the components only [2, 3]. Therefore, these theories can provide just an approximate description of the effective behavior of complex mixtures and it is questionable to what extent real metal-dielectric composites can be described by simple mixing formulae. For many applications, a more advanced description is necessary for a correct prediction of the observed effective dielectric function.

The effective non-retarded method (ENR) is based on Haydock's recursive scheme [4], which permits to obtain the frequency-dependent complex macroscopic dielectric response of 2D and 3D periodic metamaterials in the long wavelength limit. This method allows calculations for 3D structures with arbitrary geometry, such as interpenetrated inclusions made out of dispersive and dissipative components. The details of the procedure to obtain the total macroscopic dielectric response have been recently published in [5, 6]. The method is based on the use of the long wavelength approximation within the recursive Haydock's method [4], to find a tridiagonal representation of a characteristic function, from which the macroscopic dielectric function of the composite material can be obtained. Since the coefficients that appear in the tridiagonal representation only depend on the geometry and not on the material, once they are obtained for a particular geometry of the scatterers they can be used for different types of materials, saving computation time.

When the interparticle distance and (or) the size of the particles become(s) comparable to the wavelength of the incident radiation, a more accurate description of the electromagnetic response is required. Among the methods suggested for the calculation of the transmission/reflection coefficient of composite periodic structures made of spheres, the so-called on-shell methods appear to be numerically efficient. In the KKR method the electromagnetic interactions between the scatterers arranged in the periodic lattice are calculated by means of the layer-multiple-scattering method for spherical scatterers [7, 8, 9]. In this method, the composite medium is first divided into layers parallel to a given crystallographic plane, each layer containing a two dimensional lattice of identical spheres. Next, a multipole expansion in spherical waves is used to calculate the multiple scattering between spheres in a given layer. Finally, a plane-wave expansion is used to account for the multiple scattering between layers. The computer program MULTEM [8, 9] is the numerical implementation of the vector KKR method and allows the calculation of frequency bands of the infinite crystal and of the transmission/reflection coefficient of light incident on a slab of the composite medium. Recently, simulated reflectance spec-

tra calculated by means of the vector KKR method in high order band frequencies, have shown a clear correlation between theoretical and experimental results [10, 11, 12].

In this work we explore the dependence of the electromagnetic response of a 3D metal-dielectric composite slab on the relevant parameters of the material, and compare the results obtained by the ENR approximation and the KKR method. First, in section 2, we use the ENR approach to estimate the macroscopic dielectric response of a medium comprising a simple cubic lattice of metallic spheres in a dielectric host. In section 3 we consider a slab made of such a material and calculate the reflectance and transmittance using the Fresnel coefficients for normal incidence. We compare the results with those obtained with the KKR method and with the classical effective medium theory (MG). The response of the complex system is analyzed for different filling fractions, starting from the very diluted case with very small spheres, up to the case of almost touching spheres. We analyze the potential and limitations of each method to describe the electromagnetic response of the inhomogeneous slab. Finally, concluding remarks are provided in section 4.

2. Optical resonances of the macroscopic dielectric function

The system comprises a periodic arrangement of metallic spheres of radius r located at the centers of cubic unitary cells with lattice parameter L. The spheres are embedded in a dielectric host material with permittivity $\epsilon_{\rm host}$. A scheme of the composite material is shown in Fig. 1. To model the permittivity of the spheres $\epsilon_{\rm sph}$ as a function of frequency we use the well known Drude formula

$$\epsilon_{\rm sph}(\omega) = 1 - \frac{\omega_p^2}{\omega^2 + i\,\omega\,\Gamma}\,, \qquad (1)$$

where ω_p is the plasma frequency, Γ accounts for the losses due to the absorption in the material and i is the imaginary unit. An important parameter that characterizes the composite medium is the filling fraction (f), which is the fraction of volume in a unit cell that is occupied by spheres. For a structure of spheres arranged in a simple cubic lattice f is given by $(4/3)\,\pi\,(r/L)^3$. Then, the filling fraction is low for dilute systems of spheres and increases as the structure becomes denser. For the limiting case of nearly touching spheres in a simple cubic lattice, f reaches the maximum value of 0.52, approximately.

Effective medium theories such as ENR and Maxwell-Garnett approximation (MG) describe the effective dielectric function of the composite medium (ϵ^M) in terms of the dielectric function of the components and the filling fraction of the structure.

As mentioned above, the ENR method allows calculations for particles of arbitrary geometry. To discretize the structure, the method considers a cubic unit cell of side L with $2M+1$ points per side. When the discretization procedure is applied to particles with curved surfaces such as spheres, their surfaces exhibit a roughness which softens as M is increased. Therefore, the method is especially suitable for treating particles with a planar geometry, such as cubes or parallelepipeds. The roughness can produce modes that appear as small fluctuations in the electromagnetic response, and therefore the minimum value of M necessary to describe adequately the system geometry must be found in each example.

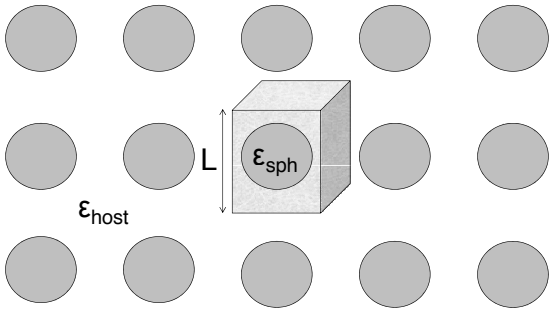


Figure 1: Scheme of the composite medium: a simple cubic structure of metallic spheres with permittivity $\epsilon_{\rm sph}$ immersed in a dielectric host medium with permittivity $\epsilon_{\rm host}$. The cubic unit cell of side L is shown.

To investigate the features of the macroscopic dielectric function calculated with ENR and MG approaches, we show in Figure 2 its real and imaginary part versus the normalized frequency. For the numerical simulations, we consider silver spheres at optical frequencies and use $\hbar\,\Gamma$ = 0.03 eV and $\hbar\,\omega_p$ = 8.5 eV in equation (1). Two different values of r/L are investigated: 0.22 (Figure 2 (a)) and 0.38 (Figure 2 (b)), which correspond to filling fractions 0.045 and 0.23, respectively. The host medium is titanium dioxide with $\epsilon_{\rm host}$ = 7.84. For the simulations with the ENR method we have used M = 120.

If the particles are small (dilute system, r/L = 0.22, f = 0.045), the system behaves as a dielectric system at low frequency. The curve of Im $\{\epsilon^M\}$ exhibits a peak close to 2 eV due to the excitation of a dipole resonance which occurs for $\omega \approx \omega_p/(1+2\,\epsilon_{\rm host})^{1/2}$. The results obtained using both approaches are similar, although it is noted that the peak in Im $\{\epsilon^M\}$ for the ENR method is slightly wider than that predicted by the MG approximation. In the limiting case of a single sphere system ($r/L \to 0$), the relation $\epsilon_{\rm sph} = -2\,\epsilon_{\rm host}$ is verified at the dipole resonance [13, 14].

When the filling fraction increases to 0.23, the dipole resonance shifts to lower frequencies and appears at 1.71 eV, approximately. Also, Im $\{\epsilon^M\}$ presents another peak associated to a multipole resonance at 2.5 eV. In both cases, as expected, Re $\{\epsilon^M\}$ and Im $\{\epsilon^M\}$ verify the Kramers-Kroning relationship.

It should be noted that the MG approach predicts only the dipolar interaction between the scatterers, and therefore it is suitable for treating dilute systems of spheres. For denser systems, interactions of higher multipole order have

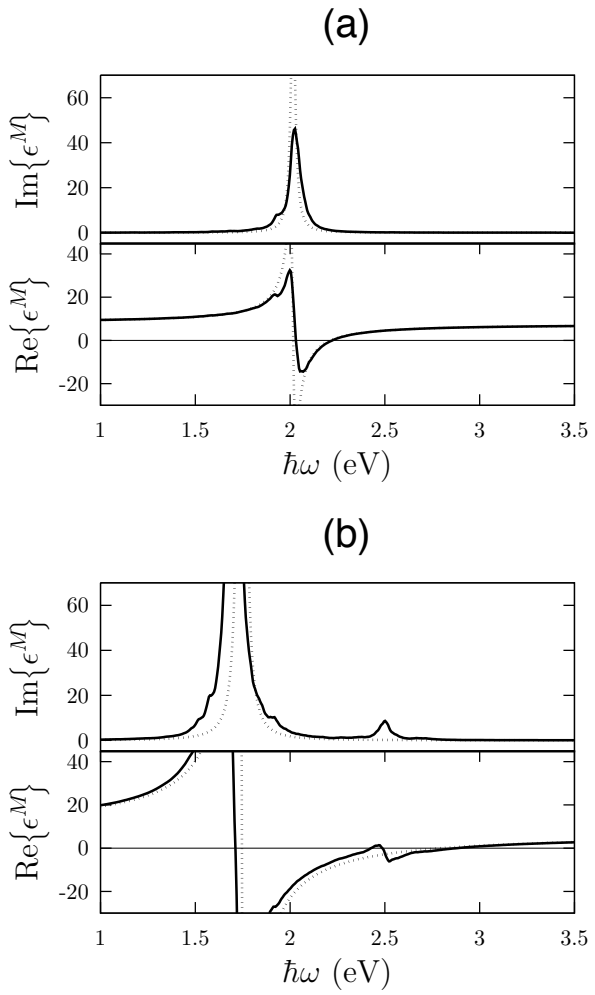


Figure 2: Imaginary and real parts of the macroscopic dielectric function ϵ^M as functions of the normalized frequency for a simple cubic lattice of silver particles in a dielectric host medium with $\epsilon_{\mathrm{host}} = 7.84$. (a) $f = 0.045$ and (b) $f = 0.23$. The dotted line corresponds to the macroscopic dielectric function obtained by the Maxwell-Garnett approach.

a significant impact on the optical properties of thin films of nanomaterials and therefore solutions obtained with more sophisticated theoretical formalisms are required. In the following section we analyze the electromagnetic response of a slab made of a composite material.

3. Optical properties of thin films of nanomaterials

We consider normal incidence on free standing films of thickness 360 nm made of the same composite systems analyzed in the previous figure. In Figure 3 we show the reflectance (Fig. 3(a), (b) and (c)) and transmittance (Fig. 3(d), (e) and (f)) for different values of the filling fraction, $f = 0.045$, 0.151 and 0.23, respectively. We present curves obtained with three different approaches: the KKR method, the ENR method and the MG approximation. For the KKR simulations, we construct the slab with 32 layers of spheres separated a distance $L = 11.25$ nm. It can be observed that the curves corresponding to the ENR approach present small fluctuations in the resonance region due to the modes associated with the surface roughness of the particles, which, as explained before, results from the discretization of the spheres in the numerical implementation. Despite these fluctuations, the method describes very well the optical properties of the film. For all values of the filling fraction considered, the curves exhibit oscillations due to the Fabry-Perot interference in the region of low frequencies. On the other hand, due to the excitation of the dipole resonance, in the frequency range close to 2 eV the reflectance is very high (more than 80% of the incident energy) and no energy is transmitted through the slab. We can note that for $f = 0.045$, the curves corresponding to the KKR and to the MG approaches are in excellent agreement, as expected for a dilute system of spheres. When the filling fraction is increased to 0.151 and 0.23, the reflectance band becomes wider and exhibits a pronounced dip at 2.5 eV approximately, where the reflectance and the transmittance of the slab are negligible for both filling fractions. The splitting of the reflectance band is due to the excitation of multipole resonances of higher orders, which occur at those frequencies at which Im $\{\epsilon^M\}$ presents a peak and Re $\{\epsilon^M\}$ is zero (see Fig. 2 (b)). When Re $\{\epsilon^M\}$ changes from negative to positive, the system's behavior changes dramatically, since the effective medium becomes a transparent material which allows light propagation. This effect has been reported in the literature and is also known by the name of optical extraordinary transmission. These type of anomalies cannot be predicted by the MG approach because it does not take into account multipolar interactions of higher orders. Conversely, since the KKR and the ENR methods consider in their formulations multipolar interactions between the spheres, they describe adequately the splitting of the reflection band at those frequencies at which multipole resonances are excited. Notice that, even for a thin slab (thickness of the order of the wavelength), the ENR approach correctly describes the electromagnetic response of the composite medium.

To investigate the influence of the thickness of the slab on its electromagnetic response, in Fig. 4 we show the reflectance (Fig. 4(a)) and transmittance (Fig. 4(b)) for a slab of thickness 1820 nm and $f = 0.23$. We include curves obtained with the KKR, ENR and MG methods. For the KKR calculations, we consider 64 layers of spheres ($L = 28.44$ nm and $r = 10.8$ nm). As in the previous case, we observe oscillations due to the Fabry-Perot interference in the region of lower frequencies. However, since the slab is thicker than the film considered in the previous figure, in this case the adjacent maxima of these oscillations are closer. As expected, the spectral positions of the resonances are the same as those of the previous figure, since they do not depend on the thickness of the slab. The curves obtained with

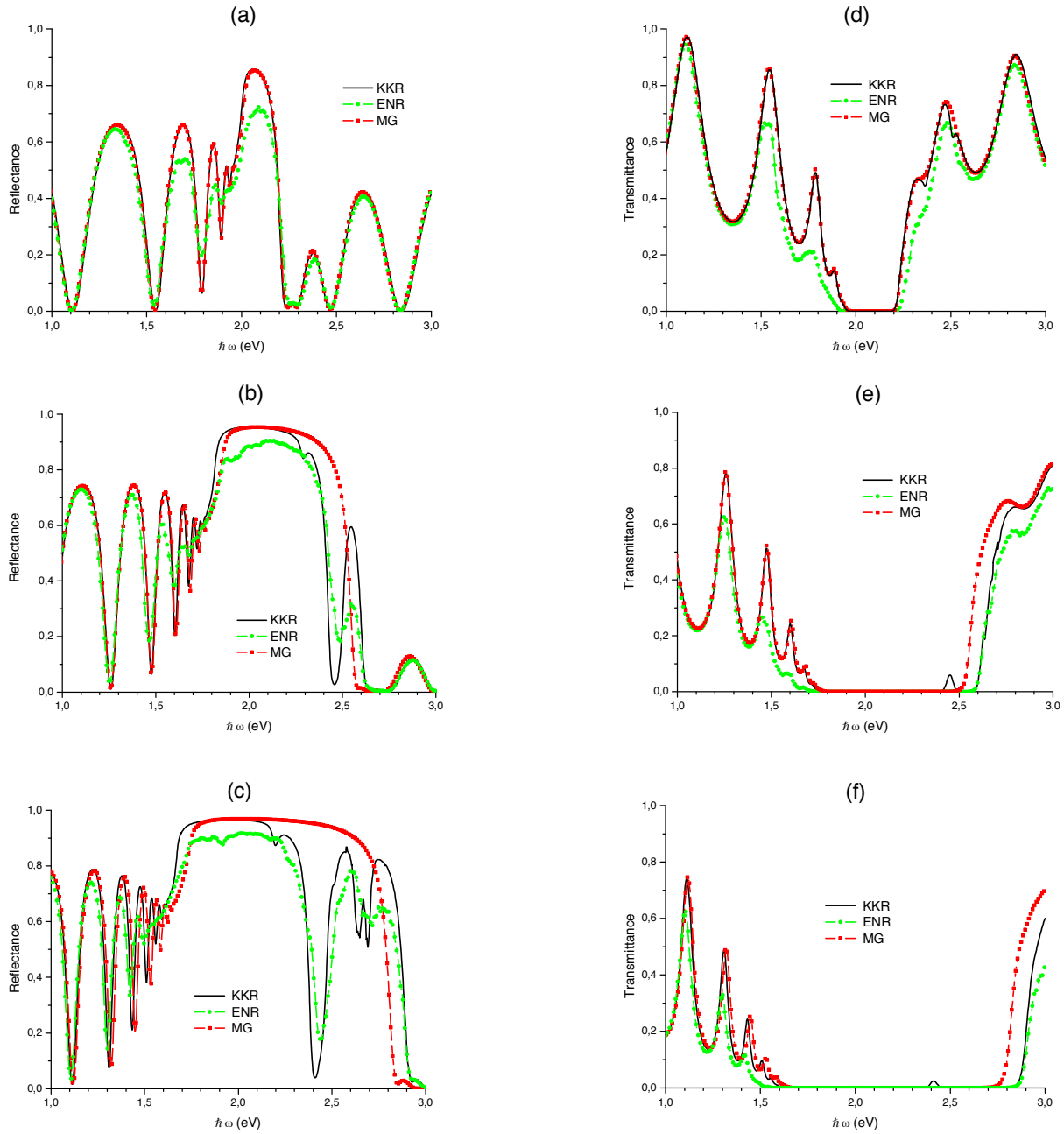


Figure 3: Reflectance and transmittance as functions of the normalized frequency for a slab of thickness 360 nm made of silver spheres immersed in titanium dioxide with $\epsilon_{\text{host}} = 7.84$. The parameters are the same as in Figure 2. (a) and (d) $f = 0.045$, (b) and (e) $f = 0.151$, (c) and (f) $f = 0.23$.

the KKR and the ENR methods are in good agreement and predict the splitting of the reflection band at the multipole resonance.

The macroscopic dielectric response obtained with the ENR method depends on the ratio r/L, contrarily to what occurs in the KKR formulation. The KKR approach requires to specify r and L separately, and this means that for a given thickness of the slab and for a fixed r/L, there are infinite pairs (r, L) that can produce a response comparable to that of the effective theory. For a fixed thickness of the slab, different numbers of layers of spheres (N) represent different lattice parameters L. If N is increased, L decreases and if f is kept fixed, the spheres become smaller. To investigate the influence of N in the results obtained by the KKR method, in Figure 5 we plot the reflectance as a function of the normalized frequency for $f = 0.045$ (Figure 5(a)) and $f = 0.23$ (Figure 5(b)) for varying N (8, 16 and 32), as indicated in the figures. Other parameters are the same as in the previous figure. We observe that as the number of layers increases, the curves converge to the results predicted by the ENR method. For both filling fractions, we have a good agreement between the methods for $N = 32$, which corresponds to a lattice parameter $L = 11.25$ nm. Note that for $f = 0.045$ the radius of the sphere is $r = 2.48$

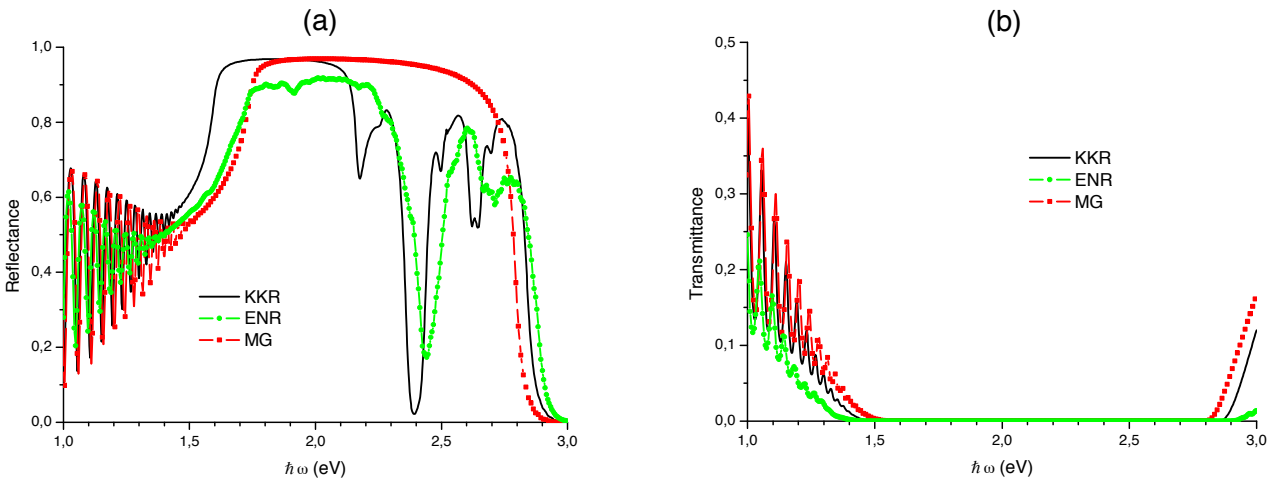


Figure 4: Reflectance (a) and transmittance (b) as functions of the normalized frequency for a slab of thickness 1820 nm made of silver spheres immersed in a dielectric medium with $\epsilon_{\rm host} = 7.84$. The filling fraction is $f = 0.23$. Other parameters are the same as in Figure 3 .

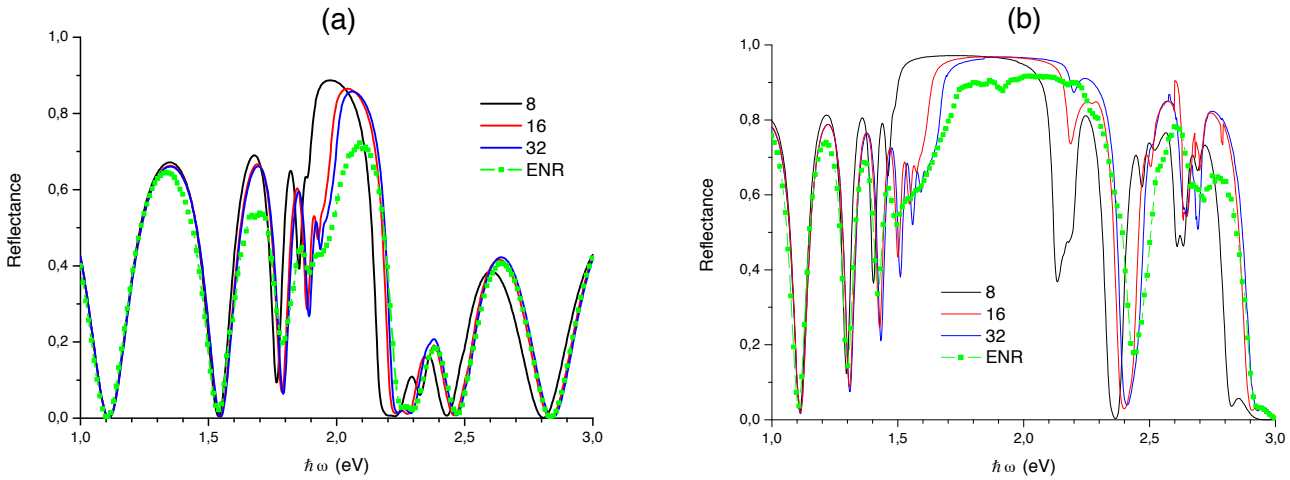


Figure 5: Reflectance as a function of the normalized frequency frequency obtained with the KKR method for a slab of thickness 360 nm made of silver spheres immersed in a dielectric medium with $\epsilon_{\rm host} = 7.84$ for 8, 16 and 32 layers. Other parameters are the same as in Figure 3. (a) $f = 0.045$, (b) $f = 0.23$.

nm whereas for $f = 0.23$ it is $r = 4.28$ nm. If N is further increased, the response of the system is approximately the same as for $N = 32$ (not shown). This is to expect, since as N increases, the long wavelength condition is better fulfilled and the material tends to behave as a homogeneous medium.

4. Conclusions

We have considered a composite material comprising periodically distributed metallic spheres in a dielectric host matrix. The macroscopic response of the composite medium was calculated with the ENR approach. The reflectance and transmittance of a slab made of such a nanomaterial were calculated with the KKR and the ENR approaches for various thicknesses and for different filling fractions. The results were also compared with those obtained with the MG approximation. Comparison between the three approaches are in very good agreement, except at the frequencies of excitation of multipole resonances, at which the reflection band splits. At these frequencies, only the ENR and the KKR method give accurate results since the MG approach does not take into account the multipolar interaction between the spheres. It was shown that the ENR method also provides reliable results for thin films of thicknesses of the order of the incident wavelength. Simulations performed with the KKR method for a thin slab and for varying the

number of layers show that as this number increases, the KKR results converge to the response given by the ENR method. This is to expect since the long wavelength condition is better fulfilled and then the material behaves as a homogeneous medium.

Acknowledgement

G. O. acknowledges ANPCyT-UNNE (PRH-PICT 2008-135), M. I. and D. S. acknowledge partial support from Consejo Nacional de Investigaciones Científicas y Técnicas (CONICET-PIP 112-200801-01880) and Universidad de Buenos Aires (UBA-20020100100533).

References

[1] W. Cai and V. Shalaev, *Optical Metamaterials: Fundamentals and Applications*, Springer, New York, 2009.

[2] D. A. G. Bruggeman, Berechnung verschiedener physikalischer Konstanten von heterogenen Substanzen. I. Dielektrizittskonstanten und Leitfhigkeiten der Mischkrper aus isotropen Substanzen, *Ann. Phys.* 416: 665-679, 1935.

[3] J. C. M. Garnett, Colours in metal glasses and metal films, *Philos. Trans. R. Soc. London A* 203: 385-420, 1904.

[4] R. Haydock, The recursive solution of the Schrödinger equation, *Solid State Physics* 35: 215, 1980.

[5] E. Cortés, W. L. Mochán, B. S. Mendoza and G. P. Ortiz, Optical properties of nanostructured metamaterials, *Phys. Status Solidi B* 247: 2102–2107, 2010.

[6] W. L. Mochán, G. P. Ortiz and B. S. Mendoza, Efficient homogenization procedure for the calculation of optical properties of 3d nanostructured composites, *Opt. Express* 18: 22119–22127, 2010.

[7] A. Modinos, Scattering of electromagnetic waves by a plane of spheres-formalism, *Physica A* 141: 575–588, 1987.

[8] N. Stefanou, V. Yannopapas and A. Modinos, Heterostructures of photonic crystals: frequency bands and transmission coefficients, *Comput. Phys. Commun.* 113: 49–77, 1998.

[9] N. Stefanou, V. Yannopapas and A. Modinos, MULTEM 2: A new version of the program for transmission and band-structure calculations of photonic crystals, *Comput. Phys. Commun.* 132: 189–196, 2000.

[10] L. A. Dorado, R. A. Depine, and H. Míguez, Effect of extinction on the high-energy optical response of photonic crystals, *Phys. Rev. B* 75: 241101 (R), 2007.

[11] L. A. Dorado, and R. A. Depine, Interplay between crystal-size and disorder effects in the high-energy response of photonic crystal slabs, *Phys. Rev. B* 76: 245103, 2007.

[12] L. A. Dorado, R. A. Depine and D. Schinca, Experimental and theoretical analysis of the intensity of beams diffracted by three-dimensional photonic crystals, *Phys. Rev. B* 78: 075102, 2008.

[13] U. Kreibig and M. Vollmer, *Optical Properties of Metal Clusters*, Springer, 1995.

[14] C. F. Bohren and D. R. Huffman, *Absorption and Scattering of light by small particles*, John Wiley and Sons, Inc., 1993.

Comprehensive Study of Compact LHM CSRR and CSSR-Based Design BPWG Filter

Ehab K. I. Hamad[1], Hany A. Atallah[2], and Mohamed A. Hassanien[1]

[1]Electrical Engineering Department, Aswan Faculty of Engineering,
South Valley University, Aswan 81542, Egypt
[2]Electrical Engineering Department, Qena Faculty of Engineering,
South Valley University, Qena 83523, Egypt
*Corresponding author, E-mail: e.hamad@ieee.org

Abstract

In this paper, a compact band pass waveguide metamaterial filter based on complementary split ring resonator (CSRR) and complementary split square resonators (CSSR) using relatively low dielectric constant substrate are presented. The presented waveguide filter combines a conventional band pass filter characteristics and negative refractive index (NRI) metamaterial characteristics. The left handed metamaterial (LHM) is made of CSRR and CSSR, etched on the ground plane. The effective parameters of the CSRR unit cell are extracted using robust retrieval algorithm. The CSRRs can be tuned to pass the signals at slightly different frequencies and thus, give rise to a pass band with a certain bandwidth, which can to some extent be controlled with the geometrical parameters of the CSRR and CSSR. The frequency characteristics of the proposed waveguide filter are successfully optimized using numerical experimentation techniques. The results show that the compactness is achieved by using CSRR compared to use CSSR and other metamaterials structures. Simulations results based on a 3D full wave electromagnetic simulator Ansoft HFSS based on the finite element method are presented.

1. Introduction

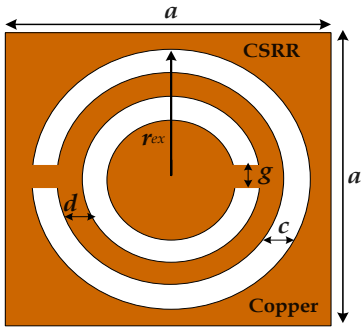
Recently, pioneer research of the complementary split ring resonator (CSRR) has been proposed in many articles [1-2] and can be derived from the SRR structure in a straightforward way by using the concepts of duality and complementariness. This CSRR structure provides negative-ε effective permittivity and negative-μ effective permeability if it used in waveguide transmission line. Because of their small size CSRRs are called sub-lambda structures. CSRR and CSSR are resonant structures that are used widely in electromagnetics [3–4]. For example, these structures are used in periodic configurations to design metamaterial structures [5–6]. Also, because of their resonance behavior SRRs and CSRRs can be used to design slow wave transmission lines, phase shifters, various kinds of microstrip filters, etc. [1-6]. Due to this fact, a super-compact pass band structure can be realized using CSRRs. The CSRRs are etched on the ground plane, and provide a negative index of refraction to the dielectric media [5]. The electromagnetic (EM) behaviors of the CSRRs are similar to those of the electromagnetic bandgap (EBG) structures and/or the defected ground structures (DGS) [7]. However, it is difficult to design and finding the equivalent circuits of EBG and DGS. It may be worth pointing out the attenuation produced by CSRR is better than EBG structures and DGS. Size miniaturization of microwave filters is of much demand in the today's rapid changing communication world. Even those filters size are large at the lower end of microwave frequencies. These components (CSRRs) for metamaterials can design filter with improved filter characteristics and size miniaturization [8]. Little waveguide filter designs have been proposed for size miniaturization and performance enhancement in the past few decades [9] so there are still some areas for improvements when using metamaterials in the filter design.

In this paper, a compact metamaterial structure using CSRR and CSSR are used to design a band pass waveguide filter (BPWGF) are designed and analyzed in waveguide technology by using artificial LHM implemented by means of CSRRs. A detailed parametric study and comprehensive study of CSRR and CSSR are carried out to demonstrate the effects of the geometrical parameters. There are two important factors such as cell dimensions (split ring radius) and split ring gap widths have been discussed in this work. On the other hand the effective parameters are extracted using robust retrieval algorithm illustrating the negative refractive index of the CSRR metamaterial structure. Such techniques give a very good miniaturization and high performance filter. The frequency characteristics of the proposed waveguide filter are successfully optimized using Ansoft HFSS [10]. Also the equivalent circuit model and parameters extraction method for the CSRR structure are presented.

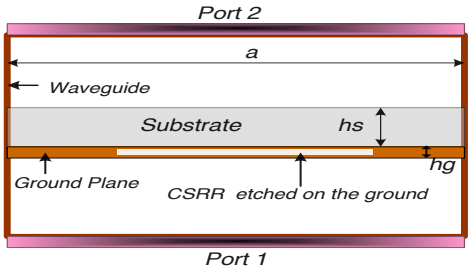
2. Design of CSRR-Based LHM BPWG Filter

The CSRRs are etched on a commercial low loss dielectric substrate; Rogers&Duroid 5870 with relative dielectric permittivity ε_r of 2.33 and height h of 0.508 mm coated with

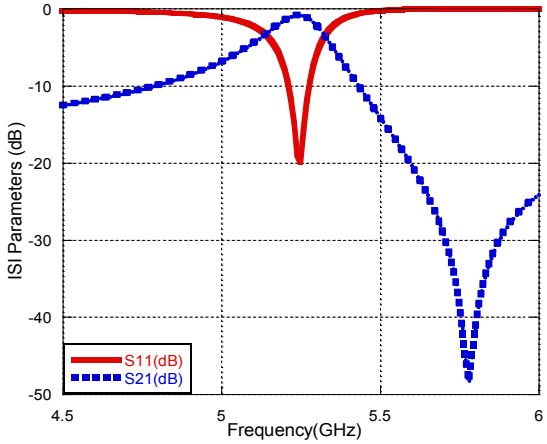
a conductive layer of copper with thickness t of 0.035 mm. The CSRR unit cell is depicted in Figure 1 with r = 3.13 mm and $c = d$ = 0.4 mm, which gives a theoretical resonant frequency of 5.2 GHz according to the theories developed above, which is designed for IEEE802.11a WLAN system at 5.2 GHz band. The transversal periodicity is a = 7.26 mm, which is approximately 1/8 λ_o at resonance in order to achieve the homogeneity property of the LHM medium. The MTM unit cell designed above is used to construct the 2-D MTM periodic structure to employ the LHM flat lens for beam focusing application [5].



(a) CSRR configuration (top view)



(b) CSRR unit cell (side view)



(c) S-parameters

Figure 1: CSRR-based LHM unit cell and simulated S-parameters

2.1. Parametric Studies on CSRR Cell Geometry

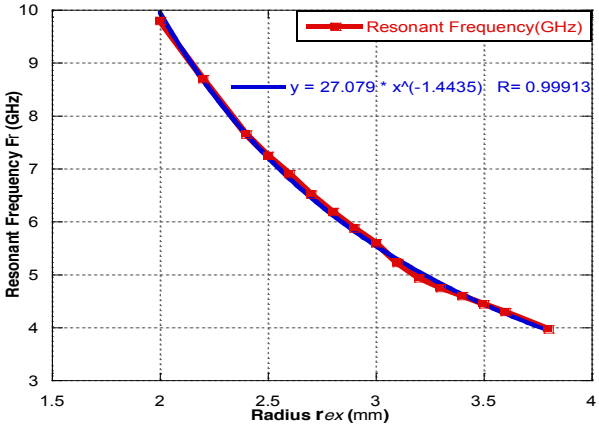
To design and optimize the CSRR structure an intensive study of various cell parameters has been carried out to explore the effects of different parameters on the overall performances of the CSRR structure. It is observed that the gap width and the radius of the split ring affect extremely its resonant frequency and bandwidth. In the following section, the effects of some parameters will be investigated in depth using EM simulator.

2.1.1. Split Ring Radius

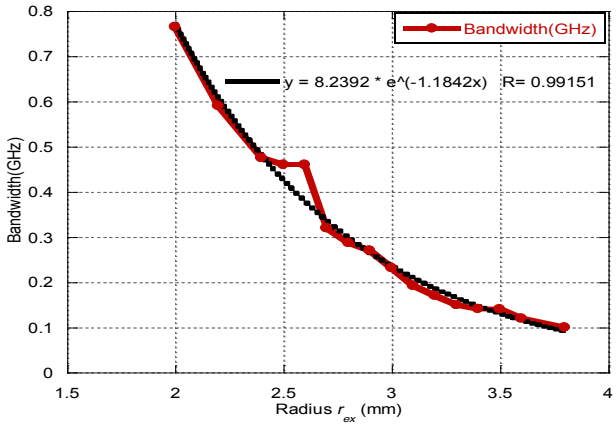
In Fig. 2, the CSRR parameters, resonant frequency and bandwidth are depicted as a function of the split ring radius. Following several optimization simulations shown in Fig. 2(a), one can observe that the split ring radius affects the resonant frequency, which decreases as split ring radius increases. By using curve fitting, the following equation is obtained; the other parameters are keep constant to the optimal values:

$$f_r = 27.079 \times r_{ex}^{-1.4435} \quad (1)$$

where f_r is the resonant frequency in GHz, r_{ex} is the split ring radius in mm and R = 0.99913 is the correlation coefficient calculated from MathCAD.



(a) Effect of ring radius on the resonant frequency



(b) Effect of ring radius on the bandwidth

Figure 2: Effect of ring radius on the resonant frequency and the bandwidth

Figure 2(b) illustrates the effect of split ring radius on the bandwidth, it is found that the split ring radius inversely proportional to the bandwidth of the CSRR.

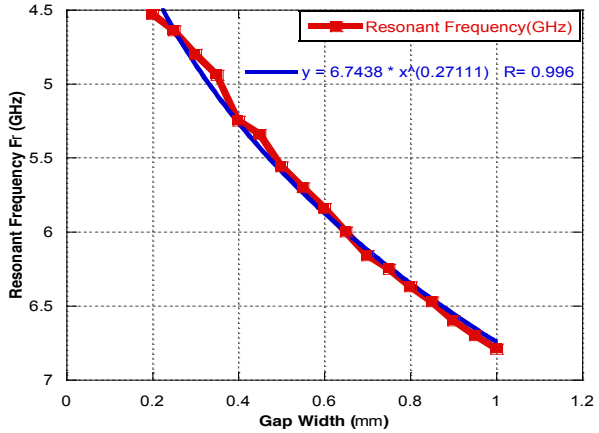
2.1.2. Split Ring Gap Width

In this section, the resonant frequency and bandwidth are investigated as a function of the gap width of the split rings. After intensive simulation, the influence of the gap width on

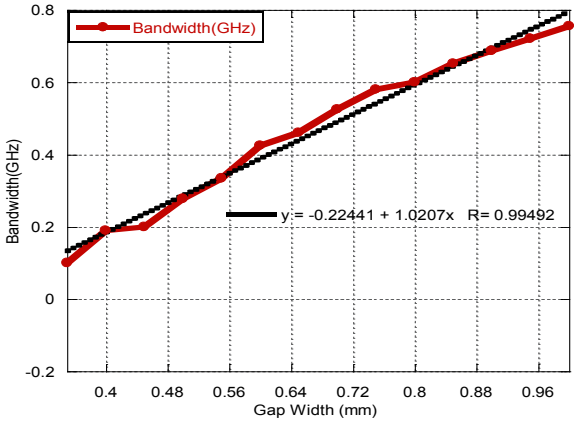
resonant frequency is clarified. The resonant frequency increases as gap width increases and hence the effective capacitance decreases. The following equation is obtained using curve fitting techniques to fit the simulation results of the resonant frequency in term of gap width while the other parameters are kept to the optimal values.

$$f_r = 6.7438 \times g^{0.27111} \quad (2)$$

where f_r is the resonant frequency in GHz, g is the gap width in mm and $R = 0.996$ is the correlation coefficient calculated using MathCAD.



(a) Effect of ring gap width on the resonant frequency



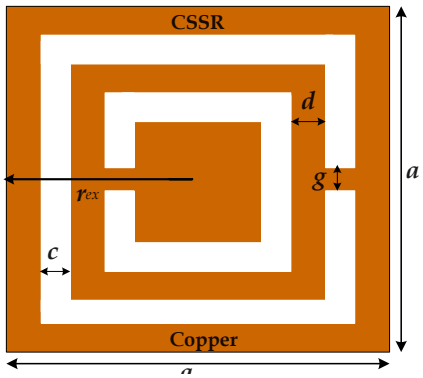
(b) Effect of ring gap width on the bandwidth

Figure 3: Effect of ring radius on resonant frequency and bandwidth

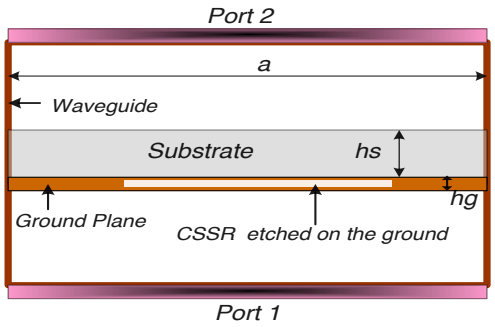
Figure 3(b) gives the CSRR bandwidth for different gap width values. From this study, it is evident that the gap width is linearly proportional to the bandwidth.

3. Design of CSSR BPWG Filter

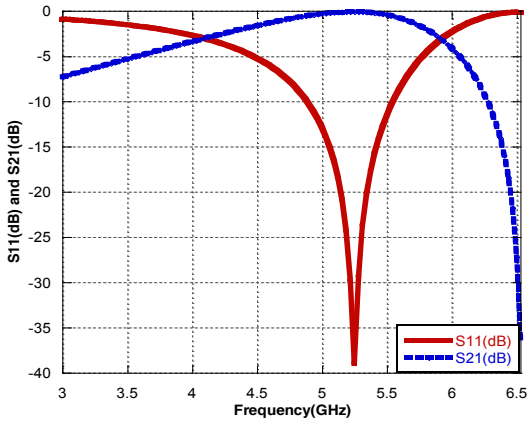
The CSSRs are etched on a commercial low loss dielectric substrate (Rogers&Duroid 5870) with relative dielectric permittivity ε_r of 2.33 and 0.508 mm thick, coated with copper layer of thickness $t = 0.035$ mm. The CSSR unit cell is depicted in Figure 4 with $r_{ex} = 5.3$ mm and $c = d = 0.4$ mm, which gives a theoretical resonant frequency of 5.25 GHz, which is designed for IEEE802.11a WLAN system at 5.25 GHz. The transversal periodicity a is 11.6 mm, which is approximately 1/5 λo at resonance in order to achieve the homogeneity property of the LHM medium.



(a) CSSR configuration (top view)



(b) CSSR unit cell (side view)



(c) CSRR reflection and transmission coefficients

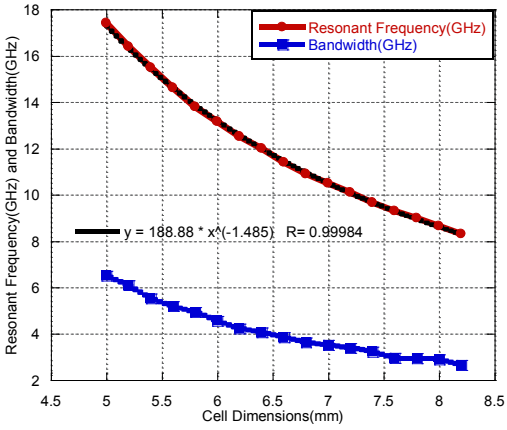
Figure 4: SRR-based LHM unit cell and simulated S-parameters

3.1. Parametric Studies on CSSR: Cell Dimensions

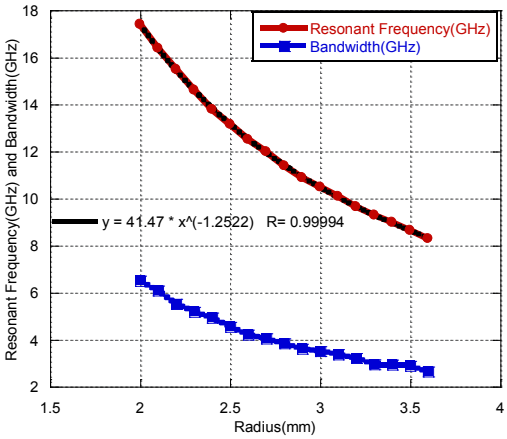
The CSSR parameters, resonant frequency and bandwidth are depicted as a function of the cell dimensions and split radius. Fig. 5(a) illustrates effects of the cell size on the resonant frequency, which decreases as the cell size increases. By using curve fitting techniques to fit the simulation curve, the following equation is obtained:

$$f_r = 188.88 \times a^{-1.485} \quad (3)$$

where f_r is the resonant frequency in GHz, a is the cell dimension in mm and $R = 0.99984$ is the correlation coefficient calculated from MathCAD.



(a) Effect of cell size on the resonant frequency



(b) Effect of split radius on the resonant frequency

Figure 5: Effect of cell dimension and split radius on the resonant frequency and the bandwidth

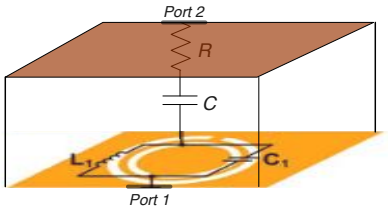
Figure 5(b) gives the CSSR resonant frequency and the bandwidth for different square split radius values. From this Figure, it is clear that the resonant frequency decreases as the split radius increases. To fit the simulation data a curve fitting technique is used and following equation is derived:

$$f_r = 41.47 \times r^{-1.2522} \tag{4}$$

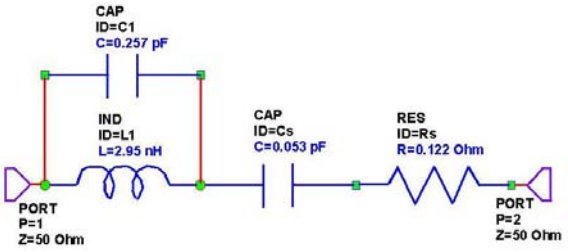
where f_r is the resonant frequency in GHz, r is the split radius in mm and R = 0.99994 is the correlation coefficient calculated from MathCAD.

4. Equivalent Circuit Model of CSRR and Parameter Extraction

In this section an accurate equivalent circuit model for the CSRR and the parameter extraction method are presented. Recently, CSRRs as shown in Figure 6 have been proposed as new constitutive elements for the synthesis of negative permittivity and LHMs in planar configuration [11]. The CSRR unit cell can provide cutoff frequency at certain frequencies without any periodic array. Therefore, the CSRR can be modeled simply as a parallel LC circuit. The etched gap areas correspond to a capacitance and the metallic rings are equivalent to an inductance. A more accurate model of the CSRR would include an extra capacitance to consider the fringing fields around the discontinuity area. A series resistance with the tank circuit to consider the conductive loss is incorporated. In order to extract the values of the equivalent circuit elements, the S-parameters of the CSRR unit are calculated using an EM simulator.



(a) Layout



(b) Equivalent circuit model

Figure 6: Layout and equivalent circuit model of CSRR unit cell

Figure 6 illustrates the typical unit cell layout and its equivalent circuit model for the etched CSRR in the ground plane. The substrate for simulation has a relative dielectric constant of 2.33and a thickness of h = 0.508 mm. The dimensions are r = 3.13 mm and c = d = 0.4 mm, which gives a theoretical resonant frequency of 5.2 GHz. The equivalent circuit model of the CSRR shown in Figure 6 consists of LC tank circuit with capacitive and resistive coupling elements. The LC tank circuit includes a shunt LC resonator (L_1 and C_1) and a capacitance element (Cs) connected in series. Firstly, the performance of the CSRR is obtained by full wave simulation. To determine the element values of the equivalent circuit, three independent equations are required. The first one is given by the resonance condition of the whole tank circuit, which leads to the zeros of S_{11} at f_1. The second one is given by the resonance condition of the series LC circuit (L_1 and C_1), which leads to the zeros S_{21} at f_2. The third one arises from the 3 dB insertion loss at f_3. Finally, the element values in the equivalent circuit of Figure 6 can be expressed by these three special frequency points as follow:

$$C_1 = \frac{Y_o(f_2^2 - f_1^2)}{20\pi f_3(f_3^2 - f_1^2)} \tag{5}$$

$$L_1 = \frac{1}{4\pi^2 f_2^2 C_1} \tag{6}$$

$$C_s = \left(\frac{f_3^2}{f_2^2} - 1\right) C_1 \tag{7}$$

where, Y_o is the characteristic admittance of the ports for S parameters. It is obvious from Eq. (7) that the value of C_s is

negative. The series negative capacitance is undesirable for the design of high-pass and band-stop filters since it forbids the transmission at high frequency band. The equivalent circuit simulation result using the obtained equivalent circuit parameters is shown in Fig. 7 for comparison with the field calculated results. As shown in Fig. 7, the circuit simulation results show excellent agreement with field calculations.

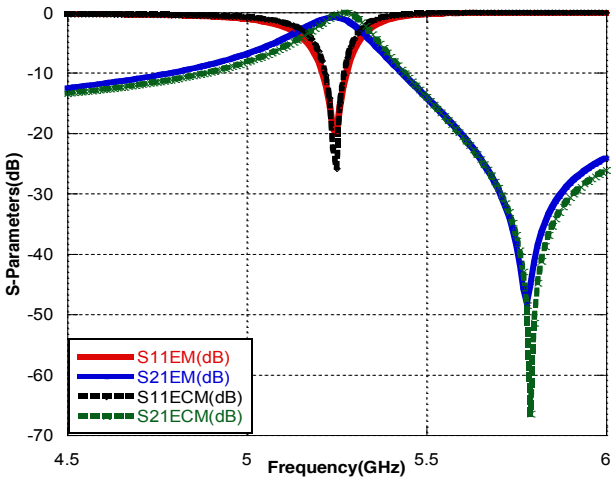


Figure 7: The results of the full wave simulation of EM and the equivalent circuit using AWR.

For the CSRR dimensions that is shown in Figure 7. The extracted circuit parameters are as follows: C_1 = 0.257 pF, L_1 = 2.95 nH, C_s = - 0.053 pF, and R = 1.22 Ω where $f_c = f_3 =$ 5.13 GHz, $f_o = f_1$ = 5.25 GHz, f_2 = 5.75 GHz and Z_o = 50 Ω.

5. Retrieving the Effective Parameter

In order to retrieve the effective permittivity and permeability of thickness d of metamaterial structure, we need to characterize it as an effective homogeneous slab [12] and the effective parameters are extracted from the transmission and reflection characteristics. Continuous material can be characterized by the complex variables S_{11} and S_{21}, The complex normalized wave impedance z and relative index n are retrieved from the S-parameters [13]:

$$z = \pm\sqrt{\frac{(1+S_{11})^2 - S_{21}^2}{(1-S_{11})^2 - S_{21}^2}} \tag{8}$$

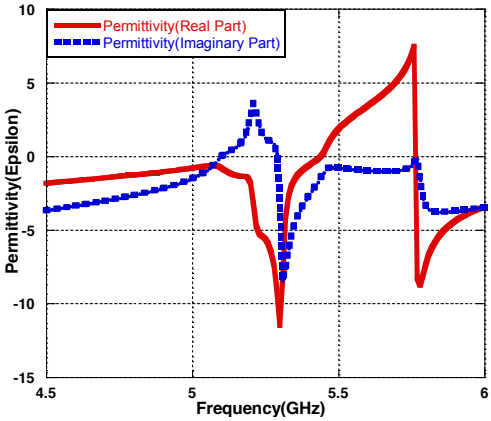
and

$$n = \frac{1}{k_o d}\cos^{-1}\left[\frac{1}{2S_{21}}\left(1 - S_{11}^2 + S_{21}^2\right)\right] \tag{9}$$

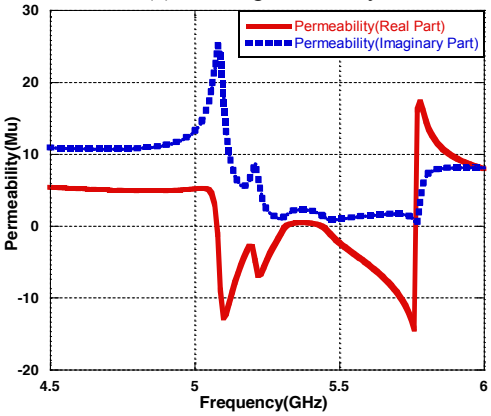
where k_o denotes the wave number of the incident wave in free space. Finally, the effective permittivity and the effective permeability can be calculated in terms of the refractive index n and the intrinsic impedance z from:

$$\varepsilon = n/z \quad \text{and} \quad \mu = nz \tag{10}$$

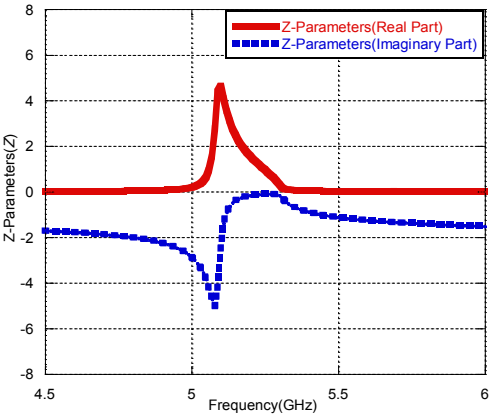
Using the equations discussed above using robust method algorithm to retrieve the constitutive effective parameters of CSRRs LHM structure to extract the permittivity. The permeability and refractive index for the LHM unit cell designed at 5.2 GHz is depicted in Fig. 8. It's obvious that the unit cell has a negative refractive index in the operating frequency band.



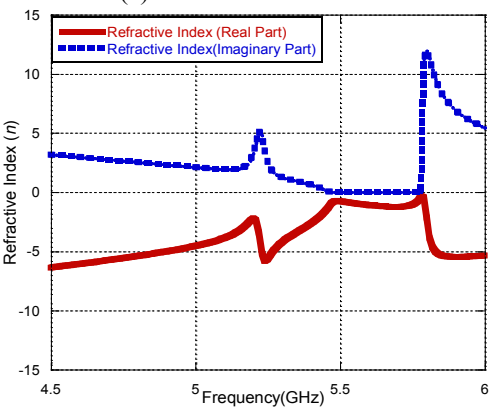
(a) CSRR permittivity



(b) CSRR permeability



(c) CSRR Z-Parameters



(d) CSRR refractive index

Figure 8: CSRR-based LHM unit cell

6. Conclusions

In this paper, a design of a compact metamaterial band pass waveguide filter has been presented by the capabilities of using CSRR and CSSR structures. A parametric investigation for different variables has been presented. Also an accurate equivalent circuit model for the CSRR unit cell and the parameter extraction method are presented. An observed significant compactness is achieved by using CSRR structure compared to CSSR unit cell. In addition, the effective parameters of the CSRR unit cell are extracted using robust retrieval algorithm to verify the LHM characteristics of the structure and the obtained results show a LH characteristic in the operating band. The designed structure is suitable for metamaterial flat lens designs and beam focusing applications.

References

[1] Zhang, X.-C., Z.-Y. Yu, and J. Xu, Novel band-pass Substrate Integrated Waveguide (SIW) filter based on Complementary Split Ring Resonators (CSRRS), *Progress in Electromagnetics Research*, PIER 72, pp. 39–46, 2007.

[2] Bonache, J., F. Mart´ın, F. Falcone, J. D. Baena, T. Lopetegi, J. Garcıa-Garcıa, M. A. G. Laso, I. Gil, A. Marcotegui, R. Marque, and M. Sorolla, "Application of complementary split-ring resonators to the design of compact narrow band pass structure in microstrip technology", *Microwave and Optical Technology Letters*, vol. 46, no. 5, September 2005.

[3] Ehab K. I. Hamad and Hany A. Atallah, "Compact CSRRs-Based Metamaterial Band Stop Filter with Controlled Rejection Band", *IEEE International Conference on New Paradigms in Electronics and Information Technologies* (PEIT011), Alexandria, Egypt, October 2011.

[4] Ortiz, N., J. D. Baena, M. Beruete, F. Falcone, M. A. G. Laso, T. Lopetegi, R. Marque, F. Martın, J. Garcıa-Garcıa, and M. Sorolla, "Complementary split-ring resonator for compact waveguide filter design", *Microwave and Optical Technology Letters*, vol. 46, no. 1, 5 July 2005.

[5] Hany A. Atallah and Ehab K. I. Hamad, "Radiation Pattern Improvement of RDRA Using LHM Flat Lens Composed of CSRR", *IEEE–APS Middle East Conference on Antennas and propagation* (MECAP), Cairo, Egypt, October 2010.

[6] Ehab K. I. Hamad and Adel A. AbdelRaheem, "Patch Antenna Improvement by Beam Focusing Using LHMTM Perfect Lens Composed of CSRRs", *International Metamaterial Conference*, February 2010.

[7] Ehab K. I. Hamad, Hany A. Atallah, and Mohamed A. Hassanien, "New Compact Microstrip Multi-Resonator with G-Shaped Defected Ground Structure", *IEEE-28th National Radio Science Conference* (NRSC), Cairo, Egypt, April 2011.

[8] J.-S. Lim, Y.-T. Lee, C.-S. Kim, D. Ahn and S. Nam, "A vertically periodic defected ground structure and its application in reducing the size of microwave circuits", *IEEE microwave and Wireless Component Letters*, vol. 12, no. 12, pp. 479-481, December 2002.

[9] H. Bahrami, M. Hakkak and A. Pirhadi, "Using Complementary Split Ring Resonators (CSRR) to Design Band pass Waveguide Filters", *Proceedings of Asia-Pacific Microwave Conference IEEE Proceedings*, vol. 7, no. 20, pp 1-4244-0749-4, 2009.

[10] Ansoft HFSS,www.ansoft.com/products/hf/hfss/.

[11] Hrabar, S. and G. Jankovic, "Basic radiation properties of waveguides filled with uniaxial single-negative metamaterials", *Microwave and Optical Technology Letters*, vol. 48, no. 12, December 2006.

[12] D. R. Smith, D. C. Vier, Th. Koschny, and C. M. Soukoulis, "Electromagnetic parameter retrieval from inhomogeneous metamaterials", *Phys. Rev. E*, 71, 036617 2005.

[13] Chen X., T. M. Grzegorczyk, B. Wu, J. Pacheco and J. Kong, "Robust method to Retrieve the Constitutive Effective Parameters of Metamaterials", *Physical Review E. 70*, 016608(1-7), July 2004.

Virtual Singular Scattering of Electromagnetic Waves in Transformation Media Concept

Yurii Barabanenkov[1], Mikhail Barabanenkov[2*], Sergey Nikitov[1]

[1]V.A Kotelnikov Institute of Radioengineering and Electronics, Russian Academy of Sciences, Moscow, Russia
[2]Institute of Microelectronics Technology, Russian Academy of Sciences, Chernogolovka, Moscow, Russia
*corresponding author, E-mail: barab@iptm.ru

Abstract

If a scatterer and an observation point (receive) both approach the so-called near field zone of a source of electromagnetic waves, the scattering process becomes singular one which is mathematically attributed to the spatial singularity of the free space Green function at the origin. Starting from less well known property of left-handed material slab to transfer the singularity of the free space Green function by implementing coordinate transformation, we present a phenomenon of virtual singular scattering of electromagnetic wave on an inhomogeneity located in the volume of left – handed material slab. Virtual singular scattering means that a scatterer is situated only virtually in the near field zone of a source, being, in fact, positioned in the far field zone. Such a situation is realized if a scatterer is embedded into a flat Veselago's lens and approaches the lens's inner focus because a slab of Veselago medium produces virtual sources inside and behind the slab and virtual scatterer (as a source of secondary waves) from both slab sides. Considering a line-like dielectric scatterer we demonstrate that the scattering efficiency is proportional to product of singular quasistatic parts of two empty space Green functions that means a multiplicative quasistatic singularity of the Green function for a slab of inhomogeneous Veselago medium. We calculate a resonance value of the scattering amplitude in the regime similar to the known Mie resonance scattering.

1. Introduction

Newly proposed transformation optics concept [1,2] assumes that the space for electromagnetic (EM) field can be bent in an almost arbitrary way (in the absence of gravity) by filling EM space with spatial transformation media. Transformation media will implement the coordinate transformation, squeezing the originally flat electromagnetic space and guiding light along curved trajectories [3].

We define abovementioned transformation media concept as "newly" because this idea is not new. The origin of the concept one may find in the general relativity as a statement that given a curved space-time with a metric tensor, Maxwell's equation may be written as if they were valid in a flat-time in which there is an optical medium with a constitutive equation [4]. Answering the question with whom did the idea originate that gravitation is equivalent to an optical medium, F. de Felice [4] wrote that perhaps A.Einstein was the first. Later on in 1923 Gordon [5,6] tried to describe dielectric media by an "effective metric" and wanted to use a gravitational field to mimic a dielectric medium. Interestingly, in contrast to Gordon [5], Landau and Lifshitz [7] tried to use dielectric media to simulate a gravitational field.

In connection with mapping of EM fields in physical space to the electromagnetism of empty flat space, note the paper [8] dates back to 1959 where the covariant Maxwell equations [9] in non-inertial reference system were transformed to usual three dimensional vector form for particular problem of EM field study in rotating system of reference. In this case the displacement vector $\vec{D}$ and the magnetic field vector $\vec{B}$ were expressed through the electric field vector $\vec{E}$ and the magnetic flux vector $\vec{H}$ via constitute equations

$$\vec{D} = \vec{E} - (1/c)\vec{v} \times \vec{H} \ ,$$
$$\vec{B} = \vec{H} + (1/c)\vec{v} \times \vec{E}$$

where $\vec{v}$ was a local speed of rotating. The formulas were obtained also related the electric field and the magnetic flux in the non-inertial and the inertial systems of reference. In 1960 Plebanski [10] formulated the EM effect of curved space-time or curved coordinates in concise constitutive equations for general case. The constitutive equations [10] are obtained from abovementioned ones by replacing the first terms in the right hand side of these equations to $\varepsilon\vec{E}$ and $\mu\vec{H}$, respectively, and by replacing the vector $\vec{v}$ to $-\varpi$, where the symmetric matrices $\varepsilon = \mu$ and vector ϖ are written in terms of the space-time metric tensor. Now media with such ε and μ and ϖ are called after Pendry et al [1] the transformation media. The transformation media lead to modern metamaterials that include the so-called left-handed materials (LHMs) and not only demonstrate superlensing effect but are able to avoid objects and flow around them, as it was demonstrated numerically [1] and analytically in terms of bistatic scattering [11]. A flat perfect LHM slab is commonly referred to as Veselago's lens [12]

in which both the permittivity ε and the permeability μ are equal to minus one. The terms optical left and right handedness were introduced by Veselago [12] to distinguish LHMs, in which the wave vector, the electric and magnetic fields vectors of a wave form a left-handed orthogonal set, from conventional right-handed media with the right-handed triple of the same vectors.

Superlensing effect was demonstrated experimentally with a slab of silver [13,14]. Resonantly coupled plasmon polaritons propagating on both surfaces of the silver slab were identified to be responsible for the superlensing effect. The slab volume itself seems to be not so important. Schweizer et al [15] supposed that resonantly coupled frequency selective surfaces, e.g. stacks of multiple meander structures, might also enable subwavelength imaging. Geometrical parameters of the meander structures (corrugation and spacer between metal films) may be changeable to a large degree.

We present in this paper a phenomenon of virtual singular scattering of electromagnetic wave on an inhomogeneity located in the volume of left – handed material slab on the basis of less well known property of left-handed material slab to transfer the singularity of the free space Green function by implementing coordinate transformation.

We use the Green function approach [16], elaborated for line source wave scattering by line dielectric inhomogeneity inside LHM slab. The central point of our method is a transformed integral equation for the Green function of inhomogeneous LHM slab written in terms of the Green function for homogeneous LHM slab and a volume scattering potential accounting for the dielectric inhomogeneity inside the slab. A solution to this transformed integral equation is presented with the aid of a scattering operator (T-matrix), which satisfies a Lippman-Schwinger equation. Solution to the Green function for inhomogeneous LHM slab is expressed by a scattering amplitude in the case of a thin linelike scatterer as compared with the free space wavelength. The scattering amplitude evaluated through an exact solution to the Lippman - Schwinger equation via modeling the scattering potential of the linelike scatterer by non-local separable potential.

2. Scattering operator

Let s-polarized monochromatic EM wave with the frequency ω is incident from the background medium Ω_0 with both permittivity and permeability equal to unity, ε_0 = μ_0 = 1, onto an L thick 2D inhomogeneous LHM slab (region Ω_1 bounded from two sides by the planes z = 0 and z = L of the Cartesian coordinate system x, y, z). The electric field of the wave has the y-component only $E_y(x,z)$ = $(4\pi\omega\mu_0 / ic^2)Gj_y$. Here an operator denotations and the Gaussian systems of units are used; $G(\vec{\rho},\vec{\rho}')$ is a 2D Green function for the LHM slab, j_y stands for the current density of EM field source. The points $\vec{\rho} = (x,z)$ and $\vec{\rho}' = (x',z')$ are placed inside the regions Ω_a and Ω_b, respectively, where indices a,b .= 0,1.

We describe LHM using the dielectric permittivity and the magnetic permeability which are both effective-medium parameters of artificial composite materials. In the case of natural substances, the magnetic permeability ceases to have any physical meaning already at relatively low frequency [17]. However, unlike natural substances, artificial composite materials involving substances with exceedingly large dielectric permittivity may nevertheless show a magnetic response that is incompatible with the Landau-Lifshitz argument [18].

The inhomogeneous LHM slab means spatially regular LHM slab which possesses nonrandom inhomogeneities consisting of right-handed nonmagnetic material. The inhomogeneous slab has an inhomogeneous dielectric permittivity $\varepsilon(x,z)$ = $-1+\delta\varepsilon_0+\delta\varepsilon(x,z)$ and homogeneous magnetic permeability $\mu = \mu' + i\mu''$ whose real part μ' can be close to minus one and $\mu'' \to 0$. The homogeneous deviation $\delta\varepsilon_0$ of the dielectric permittivity and small imaginary part μ'' of magnetic permeability both save the convergence of the Green function $G^{(0)}(\vec{\rho},\vec{\rho}')$ of homogeneous slab for any receive and source plane positions (see section 2.1). The nonrandom part $\delta\varepsilon(x,z)$ accounting for inhomogeneities. Clearly, the limit $\delta\varepsilon(x,z) \to 0$ corresponds to vanishing of inhomogeneities and, hence, a situation of homogeneous LHM slab.

The Green function $G(\vec{\rho},\vec{\rho}')$ is naturally subdivided into four pieces [16] $G_{a,b}(\vec{\rho},\vec{\rho}')$ depending on in which region $\Omega_{a,b}$ is positioned the source $\vec{\rho}'$ and the receiver $\vec{\rho}$ points. Physically G_{00} describes transmitted through and reflected from the slab wave radiation, G_{10} and G_{01} describe incoming into the slab and outgoing from the slab radiation, respectively, and G_{11} describes radiation propagation inside the slab. These four Green functions are linked between them by the standard boundary conditions of the electric and magnetic field tangential component continuity on the slab boundaries.

The extended boundary condition technique [20] allowed [16] to derive a specific radiation conditions on the slab boundaries for the Green function G_{10} of incoming radiation and the integral equation for this Green function with an effective scattering potential followed by a continuous extension of G_{10} from the slab boundaries to outside region of the slab that gives the Green function G_{00}. Similarly, one can derive a specific radiation conditions on the slab boundaries for the Green function G_{11} of propagated radiation and the integral equation for this Green

function with effective scattering potential followed by a continuous extension of G_{11} from the slab boundaries to outside region of the slab that gives the Green function G_{01}.

On the next step we write down the Green function of inhomogeneous LHM slab G_{ab} in terms of the Green function of homogeneous one $G_{ab}^{(0)}$. In particular, we have

$$G_{00} = G_{00}^{(0)} + G_{01}^{(0)}\ T\ G_{10} \qquad (1)$$

where the scattering operator of the inhomogeneity $T(\vec{\rho},\vec{\rho}')$ obeys the Lippman - Schwinger equation

$$T = V_1 + V_1\ G_{11}^{(0)}\ T \qquad (2)$$

Here $V_1(x,z) = -k_0^2[\delta\varepsilon(x,z)]\mu$ is the inhomogeneous component of the effective volume scattering potential $V(x,z) = V_0 + V_1(x,z)$ which also has the homogeneous $V_0 = k_0^2 - k_{01}^2$ part; $k_0 = \omega/c$ and $k_{01} = k_0[(-1+\delta\varepsilon_0)\mu]^{1/2}$ are the wave numbers in the free space and homogeneous LHM slab, respectively. The effective volume scattering potential $V(x,z)$ has the 1D Fourier transform with respect to the x-component of the spatial position vector $\hat{V}(q,q',z) = \hat{V}_0(q,q',z) + V_1(q-q',z)$ with singular potential of homogeneous slab $\hat{V}_0(q,q',z) = V_0 2\pi\delta(q-q') + V_S(q,q',z)$ and regular volume potential $V_1(q-q',z)$ accounting for inhomogeneities. The singular surface part $V_S(q,q',z) = (1-\mu)i\gamma_q[\delta(z-\eta)+\delta(z-L+\eta)]2\pi\delta(q-q')$ describes the effect of magnetic permeability jump on the slab boundaries, $\eta \to 0$; $\gamma_q = (k_0^2 - q^2)^{1/2}$ stands for the longitudinal wave number.

2.1. Green function $G_{ab}^{(0)}$ singularity transfer by homogeneous LHM slab

In the case of homogeneous slab ($\varepsilon = \mu = -1$) the effective potential $\hat{V}(q,q',z)$ consists of surface part $V_S(q,q',z)$ only that simplifies abovementioned integral equations for the Green functions G_{10} and G_{11} to algebraic and easy resolved form. The outgoing radiation Green function G_{01} one can get on the basis of a reciprocity relation [16] $(1/\mu_a)G_{a,b}(\vec{\rho},\vec{\rho}') = (1/\mu_b)G_{b,a}(\vec{\rho}',\vec{\rho})$.

Figure 1 demonstrates that the Green function $G^{(0)}(\vec{\rho},\vec{\rho}')$ of perfect Veselago's lens is simple obtained [2,16] from the empty space Green function $G_0(\vec{\rho}-\vec{\rho}')$ by a spatial coordinate transformation from the physical z-axis to EM (empty) space $\tilde{z}$ coordinate: $\tilde{z} = z$ if $z < 0$, $\tilde{z} = -z$ if $0 < z < L$, and $\tilde{z} = z - 2L$ if $z > L$. However, these relations are valid for only definite

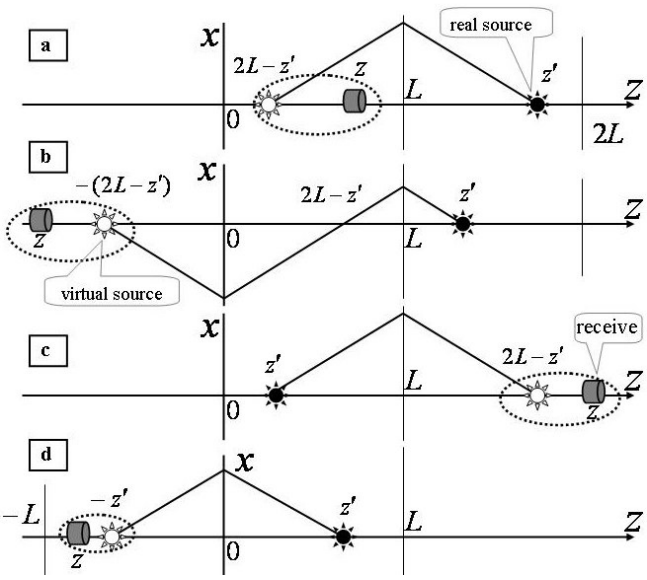


Figure 1: Singularity transfer by homogeneous LHM slab from right outside plane $z = z'$, $L < z' < 2L$, to inside (a) and left outside (b) focal planes $z \to 2L - z'$, $z > 2L - z'$ and $z \to -(2L - z')$, $z < -(2L - z')$, respectively; singularity transfer from inside plane $z = z'$, $0 < z' < L$ to right (c) and left (d) outside focal planes $z = 2L - z'$, $z > 2L - z'$ and $z \to -z'$, $z < -z'$, respectively.

positions of receive and source planes. Otherwise, the Green function $G^{(0)}$ in angular spectrum representation is diverged due to the evanescent wave enhancement effect [19]. Really, Figure 1(a) schematically shows that incoming radiation Green function $G_{10}^{(0)}$ coincides with the empty space Green function $G_{10}^{(0)} = G_0(x-x', z-2L+z') = G_0(x-x', -\tilde{z}+\tilde{z}')$ and has singularity at inside focal plane $z \to 2L - z'$ under conditions $z > 2L - z'$ and $L < z' < 2L$. Other three panels of Figure 1 (b,c,d) illustrate the properties of the transmitted radiation Green function (panel b) $G_{00}^{(0)} = G_0(x-x', -\tilde{z}+\tilde{z}')$ with singularity at left outside focal plane $z \to -(2L - z')$ under conditions $z < -(2L - z')$ and $L < z' < 2L$; the Green function of radiation outgoing from inside to the right outside slab region (panel c) $G_{01}^{(0)} = -G_0(x-x', \tilde{z}-\tilde{z}')$ with singularity at right outside focal plane $z \to 2L - z'$ under condition $z > 2L - z'$; and the Green function of radiation outgoing from inside to the left outside slab region (panel d) $G_{01}^{(0)} = -G_0(x-x', \tilde{z}'-\tilde{z})$ with singularity at left outside focal plane $z \to -z'$ under condition $z < -z'$.

Figure 1(a), for example, may be treated as if source and receive are situated in the positions $2L - z'$ and z,

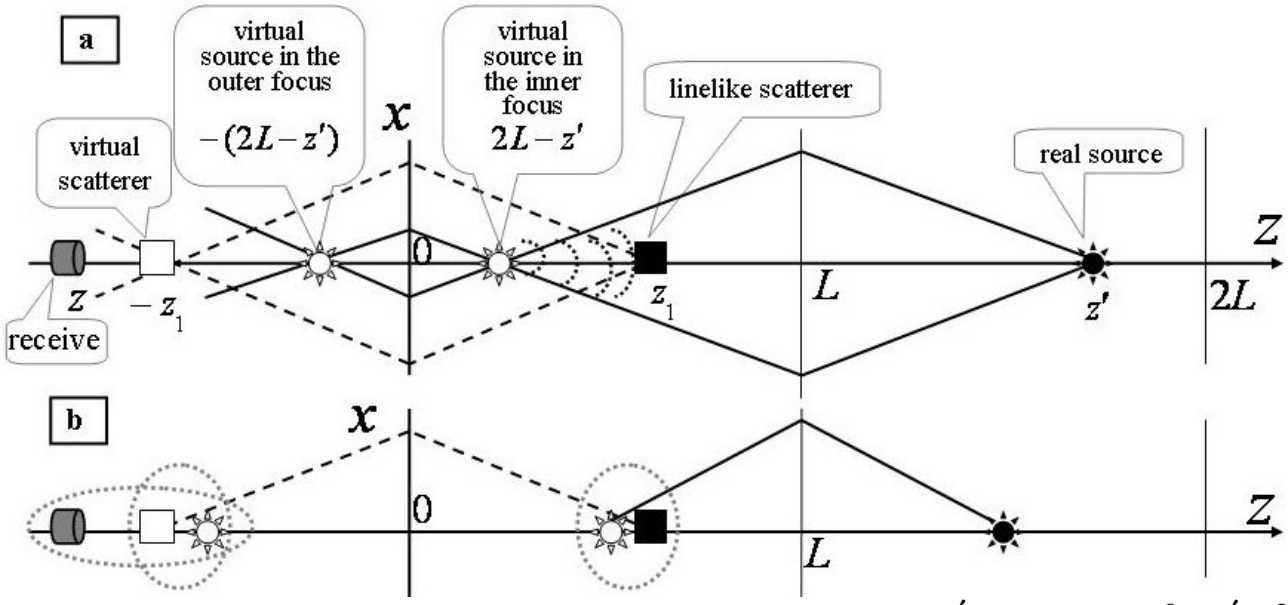


Figure 2: (a) Multiplicative effect in singularity transfer from the right outside plane $z = z'$ at some position $0 < z' < 2L$ to the left outside focal plane, $z = -(2L - z')$, by LHM slab via linelike scatterer z_1. (b) At a definite position of the real source z', the real $z_1 \to 2L - z'$, $z_1 > 2L - z'$ and virtual $z < -z_1 < -(2L - z')$, $z \to -(2L - z')$ scatterers are radiated by singular quasistatic fields of inside $2L - z'$ and outside $-(2L - z')$ virtual sources, respectively, and receive is in the near field region of both outside virtual source and virtual scatterer.

respectively. Besides, it is important to stress that in the two last panels of Figure 1(c,d) one get the inside slab source image on the outside region of the slab.

3. Scattering amplitude

Physically Eq.(1) evidently means that transmitted through or reflected from the inhomogeneous LHM slab radiation, created, for example, by a point source on the right outside region of the slab, is incoming into the slab next can be scattered by a slab volume inhomogeneities and then is outgoing the slab. The further detailed investigation of the outgoing radiation is precluded by the unknown Green function G_{10} for incoming into inhomogeneous slab radiation. Therefore, assuming weak scatterer constant potential $V_1 = k_0^2 \delta\varepsilon$, we replace this unknown Green function G_{10} in Eq.(1) with known one $G_{10}^{(0)}$ in perfect Veselago's lens that gives approximate equation

$$G_{00} \approx G_{00}^{(0)} + G_{01}^{(0)}\, T\, G_{10}^{(0)} \tag{3}$$

For definiteness we consider below the case of small linelike inhomogeneity infinitely extended along the y-axis (see black box in Figure 2) and whose rectangular cross section occupies a region in the xz-plane with centre point x_1, z_1 and linear dimensions $\Delta x, \Delta z$. Assuming these dimensions to be smaller than the wavelength in the free space, $k_0 \Delta x << 1$ and $k_0 \Delta z << 1$, Eq.(3) reads

$$G_{00}(x, z; x', z') \approx G_{00}^{(0)}(x, z; x', z') + \tilde{T} G_{01}^{(0)}(x, z; x_1, z_1) G_{10}^{(0)}(x_1, z_1; x', z') \tag{4}$$

Here $\tilde{T}$ denotes a scattering amplitude that is obtained by integration the scattering operator Eq.(2) over all its four arguments. Physically Eq.(4) represents a multiplicative effect in singularity transfer beyond Born's approximation written in [16] as $G_{00} \approx G_{00}^{(0)} + V_1 G_{01}^{(0)} G_{10}^{(0)}$.

Figure 2(a) schematically demonstrates this effect. Clearly, the real source can be freely moved in the slab outside region $L < z' < 2L$. Current position of the real source defines current positions of the inner and outer slab focuses. At a definite position of the real source, the real and virtual scatterers are radiated by singular quasistatic fields of inside and outside virtual sources, respectively. Besides, a receive is situated in the near field region of both outside virtual source and virtual scatterer (dotted lines in Figure 2(b)).

4. Multiplicative effect in singularity transfer

4.1. Transmission mode

Let us introduce the physically important defocusing parameters δz and $\delta z'$ for positions of receive and source planes, respectively, relatively the position z_1 of linelike scatterer plane defined by $\delta z = -z - z_1$ and $\delta z' = z_1 - 2L + z'$. Supposing these defocusing parameters are much more the linelike scatterer cross

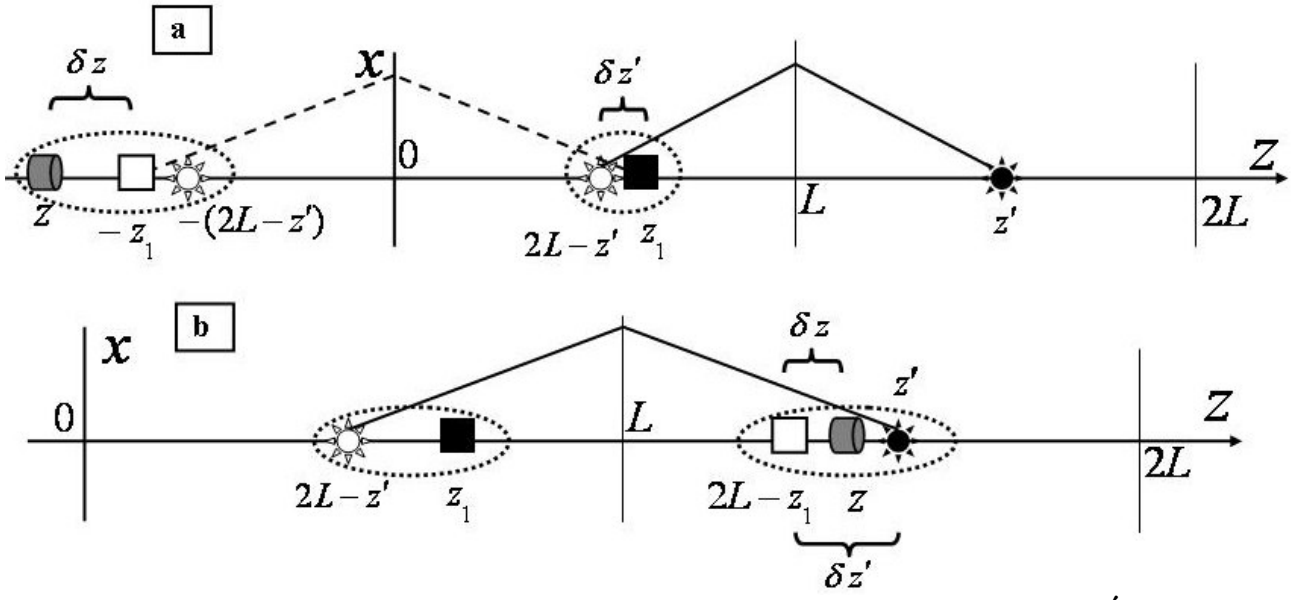


Figure 3: Multiplicative effect in singularity transfer by LHM slab from the right outside plane $z = z'$ to the left (a) and right (b) outside focal planes $z \to -(2L - z')$, $z < -z_1 < -(2L - z')$, and $z \to 2L - z_1$, $z' > z > 2L - z_1$, respectively, via linelike scatterer $z = z_1$ near inside focal plane $z_1 \to 2L - z'$, $z_1 > 2L - z'$.

section dimensions, $\delta z >> \Delta x, \Delta z$ and $\delta z' >> \Delta x, \Delta z$, and supposing an exact focusing with respect to the x axis, $x = x' = x_1$, one can simplify Eq.(4) as follows (Fig.3(a))

$$G_{00}(x, z; x', z') \approx G_{00}^{(0)}(x = 0, -z - 2L + z') - \tilde{T} G_0(x = 0, \delta z) G_0(x = 0, \delta z') \quad (5)$$

4.2. Reflected mode

Simplification for Eq.(4) in the case of slab reflected radiation, with the receive and source planes being placed both in the right $z > L$ and $z' > L$ outside region of the slab, is performed similar to the case of transmitted radiation: the defocusing parameters are now defined by $\delta z = z - 2L + z_1$ and $\delta z' = z' - 2L + z_1$ that gives (Fig.3(b))

$$G_{00}(x, z; x', z') \approx G_{00}^{(0)}(x = 0, z - z') - \tilde{T} G_0(x = 0, \delta z) G_0(x = 0, \delta z') \quad (6)$$

5. Exact scattering amplitude under resonance

Our last step is to demonstrate that small inhomogeneity in the LHM slab can contribute significantly into scattered field in the regime similar to the well known Mie resonance scattering. Let us replace, following [21], the local scattering potential $V_1(x, z)$ in Eq.(2) with an auxiliary non-local separable scattering potential

$$V_1(x, z)\delta(x - x')\delta(z - z') \to f_1 \xi(x, z)\xi(x', z') \quad (7)$$

Here $f_1 = k_0^2 \delta\varepsilon \Delta x \Delta z$ is the Born's scattering amplitude [16] and a function $\xi(x, z)$ is normalized to unit. The Lippman -Schwinger Eq.(2) with separable potential is resolved exactly in accordance with the well known theory of potential scattering [22]. The corresponding solution gives for the scattering amplitude

$$\tilde{T} = \frac{f_1}{1 - f_1 \left(\xi G_{11}^{(0)} \xi \right)} \quad (8)$$

where a bilinear form with scalar product is in the denominator.

The Green function $G_{11}^{(0)}$ of radiation propagated inside the perfect planar LHM slab is presented by the divergent integral [16]. However this Green function has been numerically calculated [23] for a lossy slab with $\varepsilon = -1 + i\delta_\varepsilon$ and $\mu = -1 + i\delta_\mu$ where both δ_ε and δ_μ are small positive real numbers. We perform an analytical estimation of this Green function in the asymptotical limit $\mu' = -1$, $\mu'' \to 0$ and reveal a resonance property of the scattering amplitude (8) with its resonance value

$$\tilde{T} \approx f_1 / i\mu'' \quad (9)$$

under the resonance condition

$$k_0 \Delta z \approx \left(\frac{\Delta z}{L} \right)^2 \left(\ln \frac{1}{|\mu''|} \right)^2 \left(\frac{|\mu''|}{\delta\varepsilon} \right)^{1/2} << 1 \quad (10)$$

where both dimensions of the scatterer cross section are equal $\Delta x = \Delta z$. Fig.4 demonstrates that the resonance value of the scattering amplitude (9) may be not so small for practically interesting dimensions of the inhomogeneity. At the same time, the inset in Fig.4 proves satisfaction of the resonance condition (10), i.e. that the scatterer cross

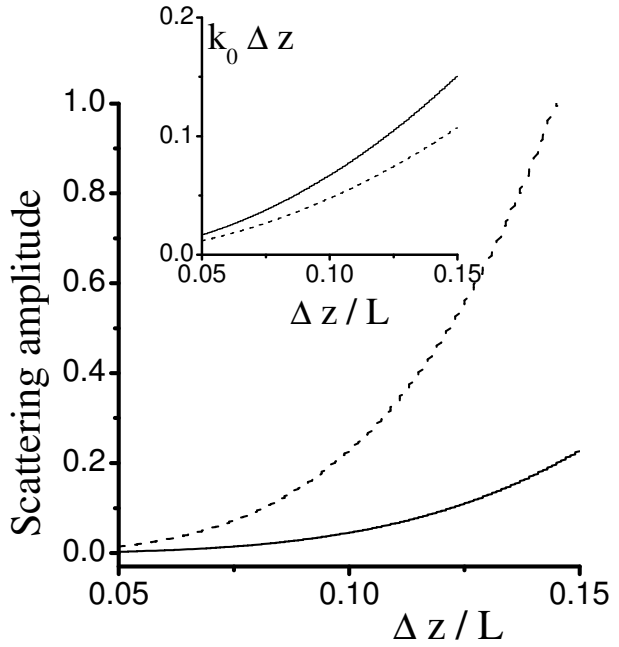


Figure 4: Calculated resonance scattering amplitude (9) versus the normalized dimension of the linelike inhomogeneity with small constant value of the dielectric permittivity $\delta\varepsilon = 0.1$ inside the LHM slab (black box in Figure 2) for the imaginary part of the inhomogeneity magnetic permeability $\mu'' = 10^{-2}$ (solid curves), 10^{-3} (dashed curves) and the magnetic permeability real part equal to $\mu' = -1$. The inset visualizes the inequality (10).

dimension have to be smaller than the free space wavelength.

6. Discussion

Let us discuss a resolution of a linelike scatterer with respect to its depth extension in the LHM slab. Firstly note, the defined in the section 4 defocusing parameters δz and $\delta z'$ are supposed to be much more the linelike scatterer cross dimensions. Nevertheless, these defocusing parameters can be much less the wave number in the background, $k_0\delta z << 1$ and $k_0\delta z' << 1$, until the linelike scatterer cross dimensions are much less the wave number also, $k_0\Delta z << 1$ and $k_0\Delta z' << 1$.

Consider in more details Eq.(6) for the Green function of inhomogeneous slab reflected radiation

$$G_{00}(x,z;x',z') \approx G_{00}^{(0)}(x=0,z-z') + G_{00}^{(R)}(x_1,z;x_1,z') \quad (11)$$

where the term $G_{00}^{(R)} = -\tilde{T}G_0(x=0,\delta z)G_0(x=0,\delta z')$ takes the form

$$G_{00}^{(R)}(x_1,z;x_1,z') \approx -\tilde{T}\frac{1}{(2\pi)^2}\left(\ln\frac{2}{k_0\delta z}\right)\left(\ln\frac{2}{k_0\delta z'}\right) \quad (12)$$

in the quasistatic limit. We remind that the empty space Green function is proportional to the first type Hankel function of the zero order, $G_0(\vec{\rho}) = (1/4i)H_{(0)}^1(k_0\vec{\rho})$, and asymptotically tends to logarithm expression, $(1/2\pi)Ln(2/k_0\vec{\rho})$, in the quasistatic limit, $k_0\vec{\rho} << 1$.

The term $G_{00}^{(R)}$ describes a contribution of linelike scatterer into the Green function of the inhomogeneous LHM slab in the case of reflection from the slab. This term is proportional to scattering amplitude of the scatterer and product of two Green functions' quasistatic singularities, provided the source and receive points being focused on the scatterer with small defocusing parameters.

A resolution of a linelike scatterer with respect to its depth extension is defined by the first logarithm in right hand side of Eq.(12). Fig.5 gives illustration to Eq.(12) presenting the normalized quantity $G_{00}^{(R)}$ as a function of defocusing parameter δz measured in linelike scatterer thickness Δz.

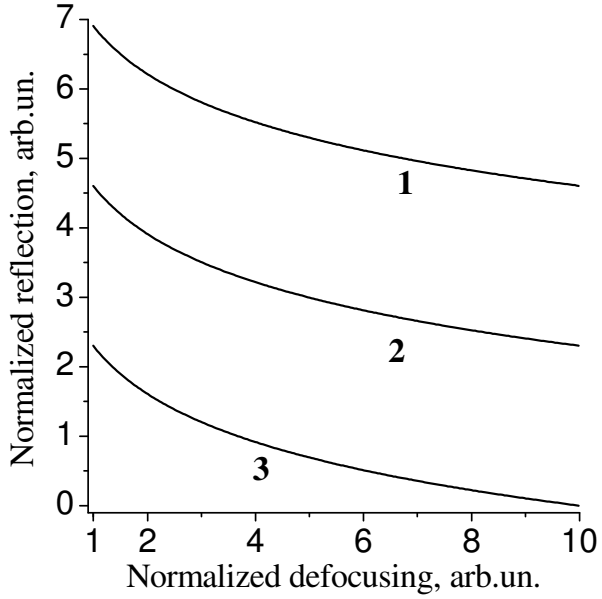


Figure 5: The dependence of the normalized reflection $G_{00}^{(R)}\left[-\tilde{T}(2\pi)^{-2}\ln(2/k_0\delta z')\right]^{-1}$ from linelike scatterer on the normalized defocusing parameter $\delta z/\Delta z$ at different values of the parameter $k_0\Delta z/2 = 10^{-3}$ (curve 1), 0.01 (2), and 0.1 (3).

7. Conclusions

We present a phenomenon of electromagnetic wave virtual singular scattering as if the wave virtual receive and virtual source points were in near zone of a scatterer. Such sort of singular scattering can be realized in the case when the scatterer is positioned inside a left-handed material slab and the real source and real receiver points are placed at definite positions in outside of the slab.

We apply the usual Green function approach and potential scattering theory [22] to s-polarized electric wave field multiple scattering by dielectric inhomogeneity placed inside left handed material slab.

As known [24], light distribution near focus of a right handed material lens is written in terms of Lommel's functions that are regular, not singular ones. In contrary, the wave field near inside focus of perfect Veselago's lens is described by the Green function of empty space, with virtual source point being placed in this inside focus. The similar singular behaviour has the wave field near outside perfect Veselago' s lens focus also, being described by the empty space Green function with virtual source point placed in this outside focus. As a consequence it is obtained the phenomenon of singular wave scattering by a weak and thin dielectric inhomogeneity as a linelike scatterer placed near inside focus of Veselago's lens. In this case the linelike scatterer is radiated by singular quasistatic field near the inner focus of Veselago's lens that enhanced the effect of scattering. Besides, the outgoing from the left-handed material slab scattered radiation is enhanced by similar singular manner near outside focus of Veselago's lens. In result the effect of wave scattering by linelike scatter near inside Veselago's lens focus is appeared to be proportional to product of singular quasistatic parts of two empty space Green functions that means a multiplicative quasistatic singularity of the Green function for inhomogeneous left-handed material slab.

Modelling the linelike scatterer by non-local separable scattering potential reveals a resonance property of the scattering amplitude related to singular behaviour of the Green function for waves propagated inside perfect left-handed material slab.

To the end, note that positions of the inside and outside focuses of a flat slab of homogeneous left handed material (perfect Veselago' s lens) are defined by positions of the real source and the real receive points and the slab thickness. Therefore for given small inhomogeneity inside left-handed material slab one can find such positions of real source and real receive points, which bring visible image for the inhomogeneity due to described phenomenon of singular scattering.

The latter has at least two conclusions. First, it may be proposed a principle of non-contact tunneling near field optical microscopy with some features of tomography using optical singularities produced by Veselago like medium, in a manner as if an optical antenna of near field scanning microscope will be able to penetrate inside tested surface [25]. Really, Veselago like medium allows to display a set of near field images taken from different observation points of the object using any projection rendering system. Due to a phenomenon of electromagnetic wave virtual singular scattering, the brightness of the object image will be as high as if source and receive are both located in the near field zone of the object. Second, in the Introduction we note that left-handed materials are currently considered as media which enable precise control over the flow of electromagnetic waves. Using these artificial materials, the first microwave cloaking has been achieved [26]. However, even an ideal perfect cloak (curved electromagnetic space) may be electromagnetically detected within its working band [27] on the basis of a radiation (some kind of electromagnetic source) generated at propagation of a fast-moving charged particle through the cloak. At the same time, perfect artificial material consisting of huge amount of identical electrotechnical elements is rather illusion in practice. Defects of such materials may function as abovementioned current sources [27]. One sort of such defects, i.e. a dielectric inhomogeneity in left handed material slab, has been considered in this paper.

Acknowledgements

This work was supported in part by the Russian Academy of Sciences projects “Passive multichannel human radio- and acusto-thermotomography in near zone”, “Scientific bases of heterogeneous telecommunication and location systems”.

References

[1] J.B. Pendry, D. Schurig, D.R. Smith, Controlling electromagnetic fields, *Science* 312: 1780- , 2006.

[2] U. Leonardt, T.G. Philbin, General relativity in electrical engineering, *New J. Phys.* 8: 247- , 2006.

[3] U. Leonhardt, Optical conformal mapping, *Science* 312: 1777- 1780 , 2006.

[4] F. de Felice, On the gravitational field acting as an optical medium, *General Relativity and Gravitation* 2: 347-357, 1971.

[5] W. Gordon, Zur lichtfortpflanzung nach der relativitätstheorie, *Ann. Phys. (Leipzig)* 72: 421-456, 1923.

[6] S. Antoci, L. Mihich, A forgotten argument by Gordon uniquely selects Abraham’s tensor as the energy-momentum tensor for the electromagnetic field in homogeneous, isotropic matter, *http://arxiv.org/abs/gr-qc/9704055v1*

[7] L.D. Landau, E.M. Lifshitz, *The Classical Theory of Fields,* Fourth Revised English Edition, Pergamon, Oxford, UK, p. 275, 1975.

[8] Yu.N. Barabanenkov, Maxwell equations in rotating system of reference, *Scientific Reports of Higher School, Phys-Math Sciences* 1: 141 – 145, 1959.

[9] A. Einstein, Die Grundlage der allgemeinen Relativitätstheorie, *Ann. Phys*. 49: 769-822 , 1916; translated without p.769 as The Foundation of the General Theory of Relativity, *The Principle of Relativity*, Dover, New York, pp. 111–164,1952.

[10] J. Plebanski, Electromagnetic waves in gravitational fields, *Phys. Rev.* 118: 1396 – 1408, 1960.

[11] H. Chen, Bae-Ian Wu, B.Zhang, J.A. Kong, Electromagnetic wave interactions with a metamaterial Cloak, *Phys. Rev. Lett.* 99: 063903 (2007)

[12] V.G. Veselago, The electrodynamics of substances with simultaneously negative values of ε and μ, *Sov. Phys. Usp.* 10: 509-514, 1968.

[13] N. Fang, H. Lee, Ch. Sun, X. Zhang, Sub–diffraction-limited optical imaging with a silver superlens, *Science* 308: 534-537, 2005.

[14] S.C. Kehr, Y.M. Liu, L.W. Martin, P. Yu, M. Gajek, S.-Y. Yang, C.-H. Yang, M.T. Wenzel, R. Jacob, H.-G. von Ribbeck, M. Helm, X. Zhang, L.M. Eng, R. Ramesh, Near-field examination of perovskite-based superlenses and superlens-enhanced probe-object coupling, *Nature Communications* 249: 1-9, 2011

[15] P. Schau, K. Frennera, L. Fub, H. Schweizer, H. Giessenb, W. Osten, Rigorous modeling of meander-type metamaterials for sub-lambda imaging, *Proc. SPIE* 8083: 808303, 2011

[16] Yu.N. Barabanenkov, M.Yu. Barabanenkov, S.A. Nikitov, Line source wave scattering by line inhomogeneities inside left-handed material slab: Green function approach, *Proc. PIERS* Cambridge, USA, pp.789-799, 2008.

[17] L.D. Landau, E.M. Lifshitz, *Electrodynamics of Continuous Media,* Pergamon, Oxford, UK, p. 251, 1981.

[18] R. Merlin, Metamaterials and Landau-Lifshitz permeability arguments: large permittivity begets high-frequency magnetism, *PNAS*:106, 1693-1698 , 2009.

[19] .B. Pendry, Negative refraction makes a perfect lens, *Phys. Rev. Lett.* 85: 3966 – 3969, 2000

[20] L. Tsang, J.A. Kong, R. Shin, *Theory of Microwave Remote Sensing*, John Wiley, New York, 1985.

[21] Yu.N. Barabanenkov, M.Yu. Barabanenkov, Radiative transfer theory with time delay for effect of a pulse imprisonment in a resonant random media: general transfer equation and point-like scatterer model, *Waves in Random Media* 7: 607-633 ,1997.

[22] J.R. Taylor, *Scattering Theory: the Quantum Theory of Nonrelativistic Collisions*, John Wiley, New York, 1972.

[23] Pi-G. Luan, H.-Da Chien, Ch.-Ch. Chen, Chi-Sh. Tang, Analysis on the imaging properties of a left-handed material slab, *arXiv:physics/0311122v2 [physics.optics]*

[24] M. Born, E. Wolf. *Principles of Optics*, Pergamon Press, New York, 1964.

[25] M.Yu. Barabanenkov, Yu.N. Barabanenkov, S.A. Nikitov, Near field introscopy of two dimensional nonhomogeneous left-handed material slab, *Proc. SPIE* 8083: 808305, 2011

[26] D. Schuring, J.J. Mock, B.J. Justice, S.A. Cummer, J.B. Pendry, A.F. Starr, D.R. Smith, Metamaterial electromagnetic cloak at microwave frequencies, *Science* 314: 977-980, 2006.

[27] B. Zhang, Bae-Ian Wu, Electromagnetic detection of a perfect invisibility cloak, *Phys. Rev. Lett.*: 103, 243901, 2009.

Dual-Band Coherent Perfect Absorption/Thermal Emission From Ultrathin Bilayers

Simin Feng

Michelson Lab, Physics Division,
Naval Air Warfare Center, China Lake, California, USA
*corresponding author, E-mail: simin.feng@navy.mil

Abstract

Dual-band perfect absorption/thermal emission is shown to be a general property of an ultrathin bilayer consisting of a dielectric and a totally reflective layer if the permittivity of the dielectric can be described by Drude-Lorentz (DL) model. The two bands coexist and reside on opposite sides of the Lorentzian resonant frequency where the material loss is small. However, the perfect absorption mechanism for the two bands is distinguishably different. One band is related to Fabry-Pérot phenomenon and the surge of refractive index near the Lorentzian resonance. This band is polarization insensitive. The other band is associated with excitation of Brewster-type mode at the ϵ-near-zero (ENZ) wavelength and occurs only for p-polarized wave at oblique incidences. This mode has a fast-wave non-radiative character and propagates along the ultrathin ENZ layer superimposed on the highly reflective surface. Both bands exhibit wide-angle high emission with a small shift in their center frequencies which can be tuned by tuning the Lorentzian resonance. The resonance-enhanced dual band absorption occurs in the ultrathin DL layer at the weakly absorbing wavelengths as a consequence of an interaction between the total transmission and the total reflection. We demonstrate this phenomenon in a silicon carbide/copper bilayer. The suggested structure may have applications in biological and chemical sensors, IR sensors, thermal emission controls, thermophotovoltaics, and photodetectors.

1. Introduction

There has been considerable interest in various absorbers and thermal emitters due to high demand applications in thermal sensing and energy harvesting. Thermal emission is often characterized by broadband, incoherent, and quasi-isotropic due to the intrinsic random nature of thermal fluctuations. For renewable energy application, it is desirable to have a narrow-band radiation that matches with electronic transition of photovoltaic cells [1] to maximize energy conversion efficiency. In the past few years, photonic bandgap materials have been investigated for changing absorption spectrum and reducing radiation bandwidth [1]–[5]. On the other hand, the ability of controlling emission spectrum and direction also has important applications such as tailoring radiation [6, 7] and thermal sensing. To increase coherence and modify emission characteristics, there has been increasing attention on patterning surface microstructures, such as subwavelength gratings [8]–[11], microcavities [12]–[15], and metamaterials [16]–[19]. It is of great interest in manipulating light to achieve total absorption at a subwavelength scale. Dual-band absorption [20]–[23] is a desired feature for infrared sensors, thermal emitters, and integrated multifunctional devices. In this paper, we will show that dual-band wide-angle perfect absorption is a general property of ultrathin bilayers composed of a primary dielectric layer and a secondary reflective layer if the permittivity of the dielectric can be described by Drude-Lorentz (DL) model. Coherent enhanced absorption is resulted from an interplay between the total transmission of the primary layer and the total reflection of the secondary layer. In the following, we will analyze this phenomenon with both real metal substrate and perfect electric conducting (PEC) ground and demonstrate this property in a silicon carbide (SiC)/copper (Cu) bilayer structure.

2. Coherent perfect absorption

2.1. Basic theory

Figure 1 shows the geometry of the bilayer structure and the coordinate system used in the simulation. Due to the azimuthal symmetry, the polar angle θ is sufficient to describe the direction of the absorption/thermal emission. Consider transverse magnetic (TM) modes, corresponding to non-zero field components H_y, E_x, and E_z. Assume a harmonic time dependence $\exp(-i\omega t)$ for the electromagnetic field. From Maxwell's equations, the magnetic field H_y satisfies the following wave equation:

$$\frac{\partial^2 H_y}{\partial x^2} + \frac{\partial^2 H_y}{\partial z^2} + k_0^2 \epsilon \mu H_y = 0\,, \tag{1}$$

where $k_0 = \omega/c$; the ϵ and μ are, respectively, the permittivity and permeability of the material. Equation (1) permits solutions of the form $\psi(z)\exp(i\beta x)$. Here the transverse wave number β is determined by the incident wave, and is conserved across the interface,

$$\beta^2 = k_0^2 \epsilon \mu - \alpha^2\,, \tag{2}$$

where α is the wave number in the z direction. The functional form of $\psi(z)$ is either a simple exponential $\exp(i\alpha z)$ for the semi-infinite regions or a superposition of $\cos(\alpha z)$

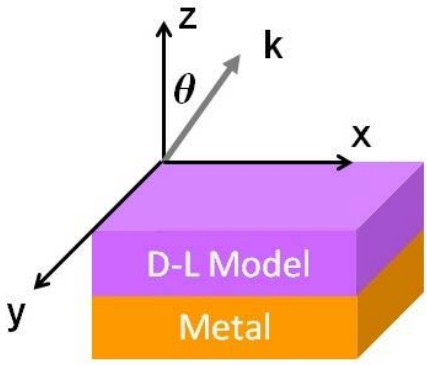


Figure 1: A schematic diagram of a bilayer structure. The permittivity of the primary (top) layer is described by Drude-Lorentz model while the secondary (bottom) layer is highly or totally reflective substrate, such as metal or PEC. The angle θ represents the direction of thermal emission or absorption.

and $\sin(\alpha z)$ terms for the bounded regions along the z direction. The other two components E_x and E_z can be solved from H_y using Maxwell's equations. Only non-magnetic materials are considered. Assume the permittivity of the primary layer in Fig. 1 is described by Drude-Lorentz model, which is given by

$$\epsilon = \epsilon_\infty + \frac{\omega_p^2}{\omega_0^2 - \omega^2 - i\gamma\omega}\,, \tag{3}$$

where the permittivity at the high frequency limit $\epsilon_\infty = 3.8$. The plasma frequency $\omega_p = 0.43\,\mu m^{-1}$; the Lorentzian resonant frequency $\omega_0 = 0.11\,\mu m^{-1}$; and the damping factor $\gamma = 8 \times 10^{-3}\,\mu m^{-1}$. The dispersion in Eq. (3) and the corresponding refractive index are shown in Fig. 2. The Lorentzian resonant wavelength is about $9.1\,\mu$m. For ideal perfect absorption to occur, the substrate should be totally reflective, such as PEC. However, we use copper (Cu) as the highly reflective substrate in our simulation for future potential practical implementation, meanwhile we will use PEC ground to assist our analysis. The complex permittivity of copper can be obtained from Palik [24]. Thus, perfect absorption here is not in a strictly mathematical sense, but rather in a practical sense, meaning close enough to 100%. The complex permittivity of copper and refractive index are provided in Fig. 3 for convenience.

The electromagnetic field can be solved by scattering matrix method and matching boundary conditions at the interface of each layer, i.e. the continuity of H_y and E_x. The transmittance (T) and reflectance (R) of electromagnetic (EM) power can be calculated via the Poynting vector $\boldsymbol{S}$, given by $\boldsymbol{S} = \Re(\boldsymbol{E} \times \boldsymbol{H}^*)$. The fraction of energy absorbed by the structure is described by the absorptance (A), where $A = 1 - T - R$ as required by energy conservation. From the absorption spectrum, the emission spectrum can be obtained from Kirchhoff's law which directly relates the absorptance with the emissivity [25, 26]. For a PEC substrate, there is no transmission and the tangential com-

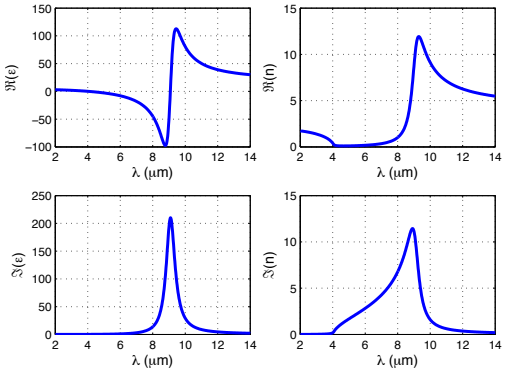


Figure 2: Real (left-top) and imaginary (left-bottom) parts of the permittivity given by Eq. (3), as well as the real (right-top) and imaginary (right-bottom) parts of the corresponding refractive index.

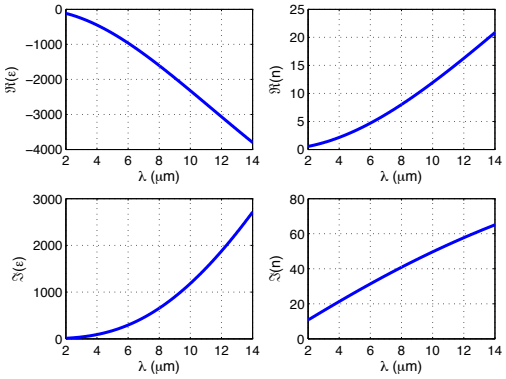


Figure 3: Real (left-top) and imaginary (left-bottom) parts of the permittivity of copper given from Palik [24], as well as the real (right-top) and imaginary (right-bottom) parts of the corresponding refractive index.

ponent of the electric field $E_x = 0$ at the PEC-dielectric interface. Thus, the magnetic field H_y is proportional to the $\cos(\alpha z)$ term if the origin of the z-coordinate is located at the PEC-dielectric interface. By matching boundary conditions at the air-dielectric interface, it is straight forwards to derive the reflection coefficient of the magnetic field as

$$r = \frac{1 + \eta\tan(\alpha_2 d)}{1 - \eta\tan(\alpha_2 d)}\exp(-i2\alpha_1 d)\,, \tag{4}$$

where the subscripts 1 and 2 refer to, respectively, air and the dielectric. The α_j $(j = 1, 2)$ is given from Eq. (2); and the d is the thickness of the dielectric layer; and

$$\eta = i\frac{\mathcal{Z}_2}{\mathcal{Z}_1} = i\frac{\alpha_2\epsilon_1}{\alpha_1\epsilon_2}\,, \tag{5}$$

where $\mathcal{Z}_1$ and $\mathcal{Z}_1$ are the impedance generalized for oblique incidences; the ϵ_1 and ϵ_2 are, respectively, the permittivity of air and the dielectric material. The reflected electric field $E_x = \mathcal{Z}_1 H_y$. From the Poynting vector calculation, the reflectance of the power is given by $R = |r|^2$; and thus the absorptance $A = 1 - R$ can be obtained. Perfect absorption occurs when the reflection coefficient is zero where

the effective impedance ($\mathcal{Z}_e$) of the ENZ-PEC structure is matched to that of free-space. From Eq. (4), we have

$$\mathcal{Z}_e \equiv -i\mathcal{Z}_2 \tan(\alpha_2 d) = \mathcal{Z}_1 \,. \tag{6}$$

For the real metal substrate, it is an open boundary and the numerical simulation is based on scattering matrix method which computes the transmission and reflection coefficients of the magnetic field (H_y). The associated electric field can be derived from the magnetic field by solving Maxwell's equations. Then, the transmittance (T) and reflectance (R) of the electromagnetic power can be calculated via the Poynting vector. Thus, the absorptance $A = 1 - T - R$.

2.2. Simulation and analysis

In the following discussion and figures, we will use the term "emissivity" and "absorptance" interchangeably for convenience. Figure 4 compares the emission characteristics of the DL/Cu and DL/PEC bilayer structures. The results are very similar using the real metal or PEC as the substrate. Two bright bands with broad emission angle are located on opposite sides of Lorentzian resonance where the material loss is small (see Fig. 2). The angle of perfect emission or absorption depends on the wavelength, dielectric constant, and thickness of the layers. The longer wavelength band around $10 \sim 12\,\mu$m is associated with Fabry-Pérot (FP) resonance and Lorentzian enhanced permittivity and refractive index (see top panels in Fig. 2), which allows the Fabry-Pérot resonant condition to be satisfied for the ultrathin layer. This band has a broader bandwidth and also appears for TE polarized wave; and thus it is insensitive to the polarization as long as the material is isotropic. The shorter wavelength band around $4\,\mu$m is due to the ϵ-near-zero (ENZ) effect [27]-[29] and occurs only for p-polarized waves at non-zero angles of incidence where the normal component of the electric field inside the ENZ medium is extremely high due to the continuity of the normal component of electric displacement field. Since the transmission of the bilayer is zero, perfect absorption occurs at an angle where the reflection of the p-polarized wave is zero, corresponding to excitation of Brewster-type mode [30], which is a fast-wave non-radiative mode propagating along the ultrathin ENZ layer [29]. When the resonant transmissions from the DL layer are totally reflected by the substrate, the coherence-enhanced absorption can occur via multi-reflection and repeated absorption. In the Drude-Lorentz/metal bilayer structures, the shorter wavelength band has a Brewster-type total transmission while the longer band has a Fabry-Pérot type total transmission. The strong coupling between the total transmission of the DL slab and the total reflection of the substrate results in the coherent perfect absorption.

Interestingly, the large imaginary part of the permittivity at the Lorentzian ENZ wavelength $\lambda \approx 9\,\mu$m does not introduce strong absorption in the ultrathin slab because the huge dissipation destroys the coherence. Thus, at the Lorentzian ENZ wavelength the optical coherence cannot be built-up inside the DL cavity; and the absorption is small

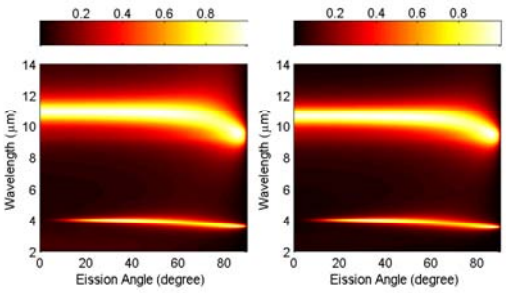


Figure 4: Emissivity of the bilayer in Fig. 1 vs. emission angle (θ) and wavelength. The permittivity of the primary layer is described by Drude-Lorentz model given by Eq. (3). The secondary layer is copper (left) and PEC (right). The thickness of the DL and Cu layers is, respectively, $0.35\,\mu$m and $0.15\,\mu$m. Color bars represent the magnitude of the emissivity. The shorter (longer) wavelength band is located at the left (right) side of the Lorentzian resonance (see left panels in Fig. 2).

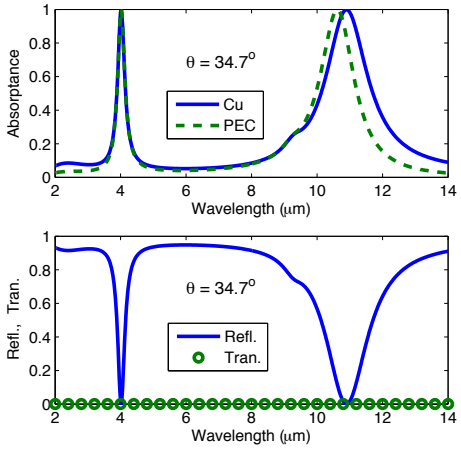


Figure 5: Top panel: absorptance versus wavelength at the perfect absorption angle $\theta = 34.7^\circ$ of the shorter wavelength band when the substrate is Cu (blue-solid) and PEC (green-dashed). Bottom panel: reflectance (blue-solid) and transmittance (green-circles) of the DL/Cu bilayer versus wavelength at the corresponding angle. Simulation parameters are the same as those in Fig. 4.

due to the ultrathin layer. Absorptance versus wavelength at the perfect absorption angle of the shorter wavelength band is illustrated in the top panel of Fig. 5 for both copper and PEC substrates. The bottom panel of Fig. 5 shows the corresponding transmittance and reflectance for the copper substrate. With the zero transmittance, perfect absorption corresponds to the zero reflection. The spectral and angular locations and bandwidths are related to the permittivity and material dispersion. With the advance of metamaterial fabrication, the desired spectral locations of peak absorption or emission and other spectral features can be engineered by properly designing the Lorentzian resonant frequency and the damping factor.

The total round-trip Fabry-Pérot phase (Φ_F) of the DL

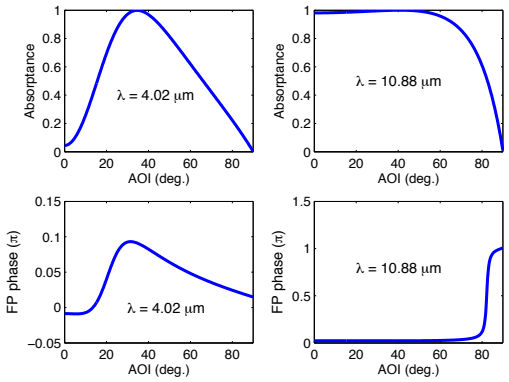


Figure 6: Top panels: absorptance of the DL/Cu bilayer vs. AOI at the perfect absorption wavelength of the shorter band $\lambda = 4.02\,\mu$m (left) and the longer band $\lambda = 10.88\,\mu$m (right). Bottom panels: total round-trip FP phase Φ_F (in the unit of π) vs. AOI at the corresponding wavelength.

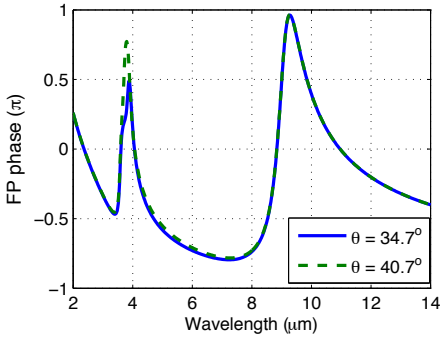


Figure 7: Total round-trip FP phase Φ_F (in the unit of π) vs. wavelength at the perfect absorption angle of the shorter wavelength band ($\theta = 34.7°$, blue-solid) and the longer wavelength band ($\theta = 40.7°$, green-dashed).

cavity is given by

$$\Phi_F = \phi_1 + \phi_2 + \frac{4\pi d}{\lambda}\Re\left(\sqrt{\epsilon}\right)\cos\theta_d\,, \tag{7}$$

where the d is the thickness of the DL cavity. The ϕ_1 and ϕ_2 are the reflection phases from the DL medium to air and to the substrate copper, respectively. The third term in Eq. (7) represents the propagation phase inside the DL cavity. The permittivity ϵ is given by Eq. (3). The refraction angle θ_d inside the DL medium is given by

$$\theta_d = \tan^{-1}\left(\frac{\Re(k_x)}{\Re(k_z)}\right) = \tan^{-1}\left(\frac{\beta}{\Re(\alpha)}\right)\,, \tag{8}$$

where the β is real and determined by the angle of incidence; and α can be obtained from Eq. (2). It is straight forward to calculate the reflection phases ϕ_1 and ϕ_2 from the reflection coefficients at the interface of the two media. In the longer wavelength band in Fig. 4, the blue-shift of the emission frequency as the angle increases can be explained from the cosine factor in Eq. (7). To satisfy the FP resonant condition, as the angle increases, the reduced propagation phase can be compensated by increasing the refractive index (see top-right panel in Fig. 2) through blue-shifting the resonant frequency.

Figure 6 shows the absorptance and the total round-trip Fabry-Pérot phase Φ_F versus angle of incidence (AOI) at the perfect absorption wavelength of the shorter and longer wavelength bands. Figure 7 shows the total FP phase as a function of wavelength at the perfect absorption angle of the shorter and longer wavelength bands. For a single slab, resonant transmission occurs when the total Fabry-Pérot phase is an integer multiple of 2π. As illustrated in Figs. 6 and 7, the near-zero total FP phase at the central wavelength of the longer band is a clear indication of FP resonance-assisted perfect absorption. The shorter band is related to Brewster-induced total transmission and occurs only for p-polarized wave at the oblique incidences (AOI $\neq$ 0). Regardless of different transmission mechanisms, the primary layer forms a resonant cavity whereas the secondary layer provides an optical feedback via reflecting the total transmission from the primary layer, leading to the cavity-enhanced coherent perfect absorption, as a result of the multiple-reflection and repeated absorption.

3. Emission from SiC/Cu bilayer

In this section, we will demonstrate above phenomenon by replacing the ideal Drude-Lorentzian medium with a real material – silicon carbide (SiC). The permittivity of silicon carbide can be obtained from Palik [24]:

$$\epsilon = \epsilon_\infty\left(1 + \frac{\omega_L^2 - \omega_T^2}{\omega_T^2 - \omega^2 - i\gamma\omega}\right)\,, \tag{9}$$

where $\epsilon_\infty = 6.7$ and the damping factor $\gamma = 4.76\,\mathrm{cm}^{-1}$. The frequency $\omega_L = 969\,\mathrm{cm}^{-1}$ is the longitudinal optical phonon frequency whereas the $\omega_T = 793\,\mathrm{cm}^{-1}$ is the transverse optical phonon frequency. Silicon carbide has a Lorentzian resonance in infrared region as shown in Fig. 8.

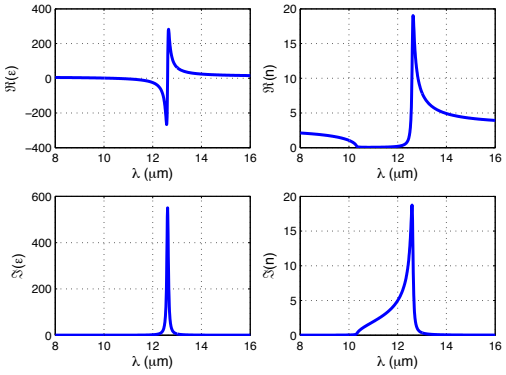


Figure 8: Real (left-top) and imaginary (left-bottom) parts of the permittivity of silicon carbide obtained from Eq. (9), as well as the real (right-top) and imaginary (right-bottom) parts of the corresponding refractive index.

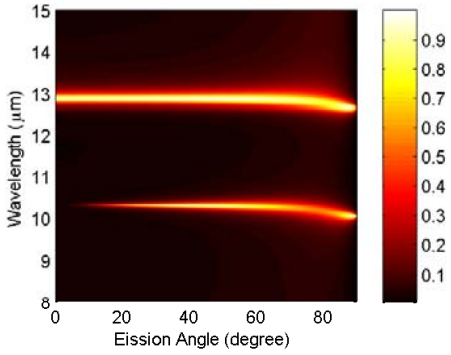


Figure 9: Emissivity of the SiC/Cu bilayer structure vs. emission angle and wavelength. The thickness of the SiC and Cu layer is, respectively, 320 nm and 150 nm. Color bar represents the magnitude of the emissivity. The shorter (longer) wavelength band is located at the left (right) side of Lorentzian resonance (see left panels in Fig. 8).

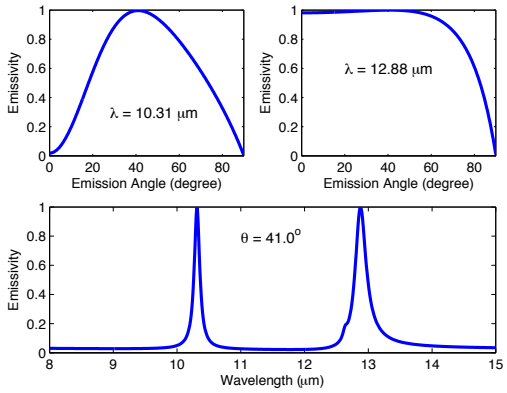


Figure 10: Top panels: emissivity vs. emission angle at the perfect emission wavelength of the shorter wavelength band (left panel, $\lambda = 10.31\ \mu$m) and the longer wavelength band (right panel, $\lambda = 12.88\ \mu$m). Bottom panel: emissivity vs. wavelength at the emission angle $\theta = 41.0°$.

The emissivity of the SiC/Cu bilayer as a function of emission angle and wavelength is provided in Fig. 9. A dual-band wide-angle thermal emission from this bilayer structure can be observed. The two coexisting wavelength bands are located on opposite sides of Lorentzian frequency where the material loss is small. Again, there is no strong absorption at the Lorentzian ENZ wavelength ($\sim 12.5\ \mu$m) since the huge dissipation destroys the coherence of the electromagnetic field inside the ultrathin cavity. Thus, the cavity-enhanced absorption cannot be achieved at this wavelength. Due to the smaller damping factor in the Lorentzian resonance of the silicon carbide, the emission bandwidths are narrower than those in above DL model. Figure 10 illustrates the emissivity versus emission angle at the perfect emission wavelength of the shorter (top-left) and longer (top-right) bands, as well as the emissivity vs. wavelength (bottom) at the emission angle $\theta = 41°$. The separation between the two bands are less than that in the previous model due to the relatively smaller damping factor in the silicon carbide.

4. Conclusions

In conclusions we have demonstrated the cavity-enhanced dual-band wide-angle absorption/thermal emission around Lorentzian resonance in ultrathin bilayer structures. Many engineered materials can often be effectively described by Drude-Lorentz model, thus the proposed bilayer structures is applicable for a broad range of materials. The layered geometry allows easy integration. The dual-band spectrum and wide acceptance angle are desired features for multi-functional devices including thermal emitters, IR sensors, photodetectors, absorbers, and bolometers.

Acknowledgement

The author gratefully acknowledge NAVAIR's Core Science and Technology Electro-Optics Initiative program.

References

[1] S. Y. Lin, J. Moreno, and J. G. Fleming, Three-dimensional photonic-crystal emitter for thermal photovoltaic power generation, *Appl. Phys. Lett.* 83: 380–382, 2003.

[2] D. L. C. Chan, M. Soljačić, and J. D. Joannopoulos, Thermal emission and design in one-dimensional periodic metallic photonic crystal slabs, *Phys. Rev. E* 74: 016609, 2006.

[3] M. Laroche, R. Carminati, and J.-J. Greffet, Coherent Thermal Antenna Using a Photonic Crystal Slab, *Phys. Rev. Lett.* 96: 123903, 2006.

[4] M. Florescu, K. Busch, and J. P. Dowling, Thermal radiation in photonic crystals, *Phys. Rev. B* 75: 201101(R), 2007.

[5] A. Chutinan and S. John, Light trapping and absorption optimization in certain thin-film photonic crystal architectures, *Phys. Rev. A* 78: 023825, 2008.

[6] A. Alù, M. G. Silveirinha, A. Salandrino, and N. Engheta, Epsilon-near-zero metamaterials and electromagnetic sources: Tailoring the radiation phase pattern, *Phys. Rev. B* 75: 155410, 2007.

[7] K. Halterman, S. Feng, and V. C. Nguyen, Controlled leaky wave radiation from anisotropic epsilon near zero metamaterials, *Phys. Rev. B* 84: 075162, 2011.

[8] J.-J. Greffet, R. Carminati, K. Joulain, J.-P. Mulet, S. Mainguy, and Y. Chen, Coherent emission of light by thermal sources, *Nature* 416: 61–64, 2002.

[9] N. Bonod, G. Tayeb, D. Maystre, S. Enoch, and E. Popov, Total absorption of light by lamellar metallic gratings, *Opt. Express* 16: 15431–15438, 2008.

[10] E. Popov, S. Enoch, and N. Bonod, Absorption of light by extremely shallow metallic gratings: metamaterial behavior, *Opt. Express* 17: 6770–6781, 2009.

[11] J. A. Mason, S. Smith, and D. Wassermana, Strong absorption and selective thermal emission from a mid-infrared metamaterial, *Appl. Phys. Lett.* 98: 241105, 2011.

[12] S. Maruyama, T. Kashiwa, H. Yugamia, and M. Esashi, Thermal radiation from two-dimensionally confined modes in microcavities, *Appl. Phys. Lett.* 79: 1393–1395, 2001.

[13] H. Saia and H. Yugami, Thermophotovoltaic generation with selective radiators based on tungsten surface gratings, *Appl. Phys. Lett.* 85: 3399–3401, 2004.

[14] I. Celanovic, D. Perreault, and J. Kassakian, Resonant-cavity enhanced thermal emission, *Phys. Rev. B* 72: 075127, 2005.

[15] J. R. Brown, A. P. Hibbins, M. J. Lockyear, C. R. Lawrence, and J. R. Sambles, Angle-independent microwave absorption by ultrathin microcavity arrays, *J. Appl. Phys.* 104: 043105, 2008.

[16] Y. Avitzour, Y. A. Urzhumov, and G. Shvets, Wide-angle infrared absorber based on a negative-index plasmonic metamaterial, *Phys. Rev. B* 79: 045131, 2009.

[17] X. Liu, T. Starr, A. F. Starr, and W. J. Padilla, Infrared Spatial and Frequency Selective Metamaterial with Near-Unity Absorbance, *Phys. Rev. Lett.* 104: 207403, 2010.

[18] X. Liu, T. Tyler, T. Starr, A. F. Starr, N. M. Jokerst, and W. J. Padilla, Taming the Blackbody with Infrared Metamaterials as Selective Thermal Emitters, *Phys. Rev. Lett.* 107: 045901, 2011.

[19] L. Li, Y. Yang, and C. Liang, A wide-angle polarization-insensitive ultra-thin metamaterial absorber with three resonant modes, *J. Appl Phys.* 110: 063702, 2011.

[20] Y. Ma, Q. Chen, J. Grant, S. C. Saha, A. Khalid, and D. R. S. Cumming, A terahertz polarization insensitive dual band metamaterial absorber, *Opt. Lett.* 36: 945-947, 2011.

[21] G. Kang, I. Vartiainen, B. Bai, and J. Turunen, Enhanced dual-band infrared absorption in a Fabry-Perot cavity with subwavelength metallic grating, *Opt. Express* 19: 770–778, 2011.

[22] B. Zhang, Y. Zhao, Q. Hao, B. Kiraly, I.-C. Khoo, S. Chen, and T. J. Huang, Polarization-independent dual-band infrared perfect absorber based on a metal-dielectric-metal elliptical nanodisk array, *Opt. Express* 19: 15221–15228, 2011.

[23] P. Ding, E. Liang, G. Cai, W. Hu, C. Fan, and Q. Xue, Dual-band perfect absorption and field enhancement by interaction between localized and propagating surface plasmons in optical metamaterials, *J. Opt.* 13: 075005, 2011.

[24] E. D. Palik, *Handbook of Optical Constants of Solids*, Academic, San Diego, 1998.

[25] J.-J. Greffet and M. Nieto-Vesperinas, Field theory for generalized bidirectional reflectivity: derivation of Helmholtzs reciprocity principle and Kirchhoffs law, *J. Opt. Soc. Am. A* 15: 2735–2744, 1998.

[26] C. Luo, A. Narayanaswamy, G. Chen, and J. D. Joannopoulos, Thermal Radiation from Photonic Crystals: A Direct Calculation, *Phys. Rev. Lett.* 93: 213905, 2004.

[27] Yi Jin, Sanshui Xiao, N. Asger Mortensen, and Sailing He, Arbitrarily thin metamaterial structure for perfect absorption and giant magnification, *Opt. Express* 19: 11114–11119, 2011.

[28] S. Feng, Loss-Induced Omnidirectional Bending to the Normal in ϵ-near-Zero Metamaterials, *Submitted to Phys. Rev. Lett.*.

[29] S. Feng and K. Halterman, Perfect absorption in ultra-thin epsilon-near-zero metamaterials induced by fast-wave non-radiative modes, *arXiv:1112.0580v1*.

[30] G. Shkerdin, J. Stiens, and R. Vounckx, "The relationship between reflectivity minima and eigenmodes in multi-layer structures," *J. Opt. A: Pure Appl. Opt.* 5: 386-396, 2003.

Cut wires grating — single longitudinal wire" planar metastructure to achieve microwave magnetic resonance in a single wire

Galina Kraftmakher*, Valery Butylkin

Kotelnikov Institute of Radioengineering & Electronics RAS, Fryazino branch, Russia
E-mail: *gkraft@ms.ire.rssi.ru

Abstract

Here we present metastructures containing cut-wire grating and a single longitudinal cut-wire orthogonal to grating's wires. Experimental investigations at microwaves show these structures can provide strong magnetic resonant response of a single nonmagnetic cut-wire in dependence on configuration and sizes in the case when metastructures are oriented along the direction of wave propagation and cut-wires of grating are parallel to the electric field of a plane electromagnetic wave. It is suggested a concept of magnetic response based on antiparallel resonant currents excited by magnetic field of surface polaritons in many spatial LC-circuits created from cut-wire pairs of a grating and section of longitudinal cut-wire. Three separately observed resonant effects connected with grating, LC-circuits and with longitudinal cut-wire have been identified applying measurements in waveguides, cutoff waveguides and free space. To tune and mark resonance split cut-wires are loaded with varactor diodes.

1. Introduction

We know, at microwaves metamaterals containing chiral inclusions, can possess an effective magnetic permeability, which depends on the orientation of inclusions relative to the magnetic field **h** of the incident electromagnetic wave. Resonance phenomena caused by the excitation of resonance currents by the field **h**. Presently extensive investigations are directed toward the development of magnetic metamaterials containing technologically simple line wires to apply in dispersion engineering [1]. The main attention is devoted to a cut-wire pair that possesses both the electric and magnetic response due to the possibility of parallel current induction by the electric field and antiparallel current, by the magnetic field [2, 3]. Since the magnetic and electric resonance responses are generated practically at the same frequency, it is difficult to separate these signals and evaluate the magnetic contribution.

In paper [4] it is suggested a new way to create separately a strong microwave magnetic response using cut-wires. It was found in waveguides that a line wire of length l_m, which is oriented along waveguide axis parallel to the direction of propagation of an electromagnetic wave (and perpendicularly to its electric field **E**) and arranged asymmetrically near a cut-wire grating forming surface polaritons, can exhibit a resonance response that has a magnetic nature. A giant resonance is observed in longitudinal single cut-wire of a definite (resonance) length in a certain frequency range corresponding to the existence of surface polaritons (below the resonance frequency of the polariton-generating grating of cut-wires parallel to the **E**-field). In this paper we investigate this very interesting phenomenon experimentally in waveguides (WGD), cutoff waveguides (Cut WGD) and free space in dependence on configuration and sizes. We suggest and verify a concept of magnetic response based on possibility of antiparallel resonant currents induction by magnetic field of surface polaritons in many spatial LC-circuits from cut-wire pair of grating and section of longitudinal cut-wire. We demonstrate and identify three separately observed resonant effects. The first resonance is due to parallel currents induction in grating's wires, the second resonance effect is due to excitation of antiparallel currents in LC-circuits and the third resonance is due to contribute of total currents from LC-circuits along longitudinal cut-wire l_m. To tune and mark the resonance varactor-loaded split cut-wire is applied.

2. Investigated metastructures. Concept of the magnetic response

Different metastructures have been investigated at microwaves in dependence on configuration and sizes. Obtained results allow to suggesting a concept of resonance response of a single longitudinal cut-wire that has a magnetic nature. It is investigated "Cut-wire grating -single longitudinal cut-wire (*Gr-LCW*)" metastructure, "Wire pair – longitudinal cut-wire (*Wire pair-LCW*)", "Cut-wire grating -parallel cut-wire (*Gr-PCW*), metastructures with varactor-loaded split *LCW* and *PCW*.

2.1 Measurements methods (waveguides, free space)

We have measured frequency dependence of the transmission coefficient T of electromagnetic wave of metastructures arranged along the axis and oriented parallel to the side wall of a standard waveguide, WGD (48x24 mm) and a below-cutoff rectangular section, Cut WGD (16x24 mm). The measurements were performed in frequency range 3-6 GHz. We have used also a standard waveguide (23x10 mm) and a below-cutoff rectangular section (8x10mm) to measure transmission in frequency range 8-12 GHz. To prepare Cut WGD a fragment of the main WGD (of the length L=25mm) is divided into three sections by metal spacers parallel to the direction of wave propagation. Investigated metastructure is placed into a central cutoff WGD section (fig. 1b).

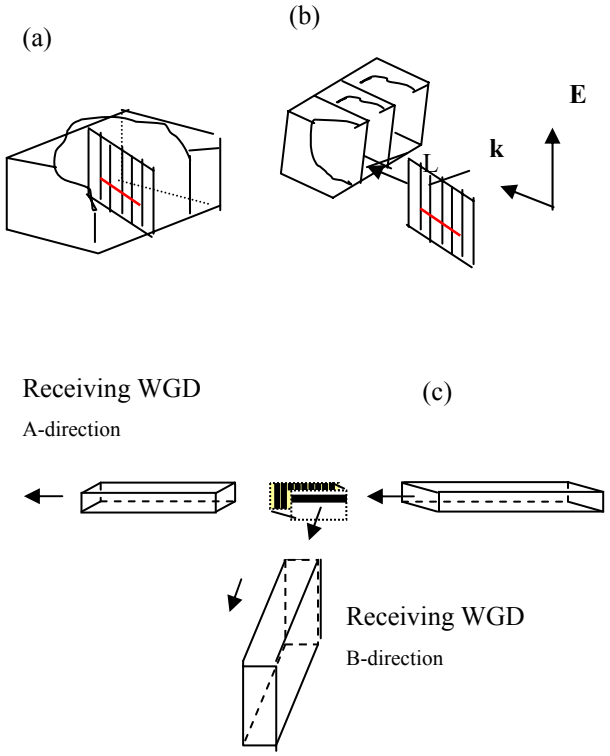


Fig. 1. Metastructure in (a) WGD, (b) Cut WGD section and (c) free space.

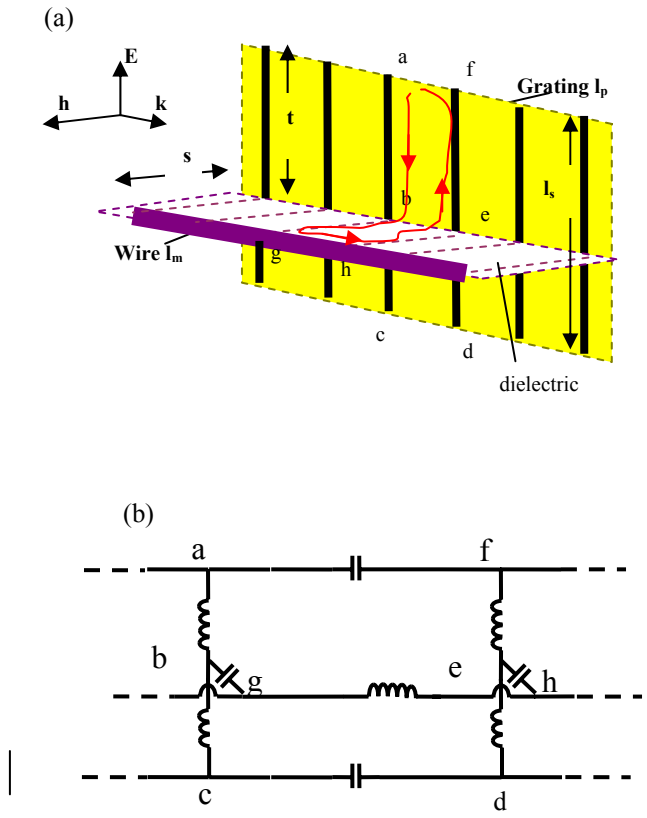


Fig.2. "Gr-LCW" metastructure (a) and its equivalent electric diagram (b).

A comparative analysis of the signal transmission spectra in the main and below-cutoff waveguide section is an important method of identification of the type of excited resonance [5]. For example, in the case of magnetic excitation (magnetic resonance in WGD, **MR**) the transparency band in Cut WGD is observed above the **MR** frequency. In addition, the magnetic excitation is characterized by the presence of superforbidden band below the **MR.** In the case of electric excitation (electric resonance, **ER**), the transparency band in Cut WGD is observed below the **ER** frequency.

We have measured also the frequency dependence of the transmission coefficient *T* of metastructures arranged in free space in the gap between transmitting and receiving waveguides for two cases. In the first case receiving and transmitting WGD are placed along the same axis (A-direction). In the second case receiving WGD is placed along transverse B-direction (fig. 1c).

2.2. Experimental verification

2.2.1. "Gr-LCW" metastructure

Below we present results of investigation of metastructure "cut-wire grating -single longitudinal cut-wire" (**Fig.2a**), like [4], placed along propagation direction of electromagnetic wave and engineered to have magnetic resonance properties using only cut-wires, l_p and l_m are lengths of grating's wire and longitudinal cut-wire *LCW, s* – distance between *Gr* and *LCW*. Grating of wires *lp* parallel to the **E**-field exhibits a resonance response, which is manifested by resonance **I** of the electric type and characterized by a resonance dependence of the transmission coefficient with a minimum at a certain frequency dependent on the wire length. This grating is excited by the **E**-field (induction of parallel currents) and generates surface waves (polaritons) near resonance **I** (below the resonance frequency). Local transverse magnetic field of polaritons inducts electromotive forces and antiparallel currents in many spatial LC-circuits (such as *abghefa* and *cdehgbc* created from cut-wire pairs of a grating and section of LCW) and like-directed currents along *LCW*. Equivalent electric diagram is shown in **Fig. 2b**. Directions of currents which run in many LC-circuits *abghefa* are the same along wire l_m and opposed to currents of circuits *cdehgbc*. In the case of symmetrically located wire l_m (t=l_p/2) these opposed currents along LCW of circuits *abghefa* and *abghefa* are practically quenched. In the case of asymmetrically location, if *LCW* length l_m is resonant the wave of current along wire l_m and the resonance response are very strong. Resonance response of a *LCW* l_m can be detected separately because its resonance frequency depends on length and distance *s* and is different from frequencies of grating and LC-circuits.

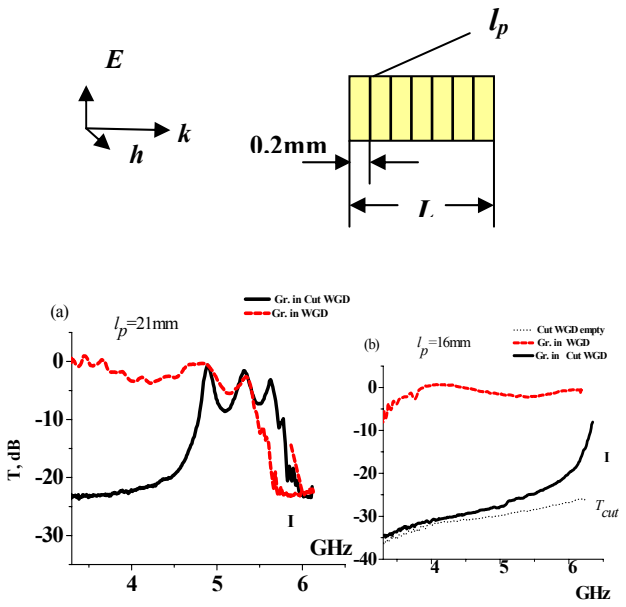
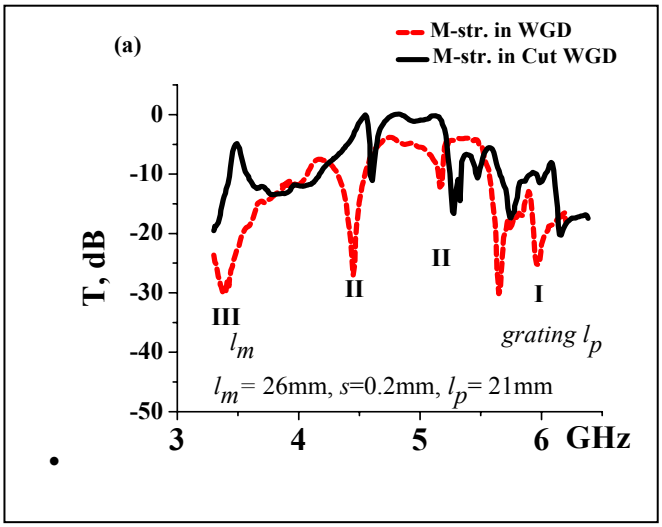


Fig.3. Frequency dependences of T in the WGD (dashed curves) and Cut WGD (solid curves) in the presence of (a) Gr. of l_p=21mm and (b) Gr. of l_p=16mm.

Fig. 3a shows the frequency dependences of transmission T measured in the presence of Gr. of l_p=21mm, for which resonance **I** is observed in the WGD at 6 GHz and pass-band is observed in the Cut WGD section at frequencies below this resonance. **Fig. 3b** shows corresponding frequency dependences of T measured in the presence of Gr. of l_p=16mm, for which resonance **I** and pass-band (below **I**) are observed above 6 GHz in the WGD and Cut WGD. Position of pass-band below the resonance **I** specifies electric excitation and electric-type resonance of grating.



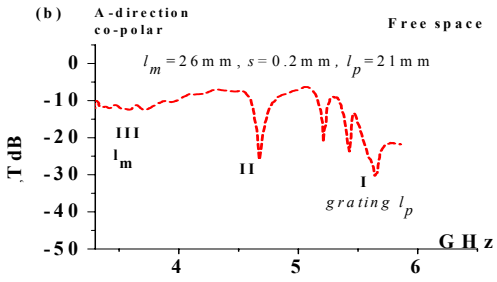
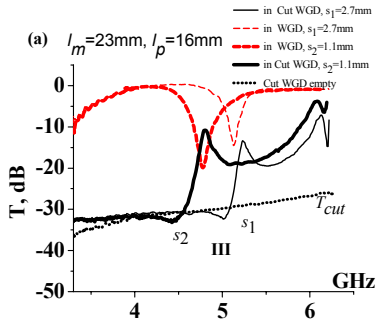
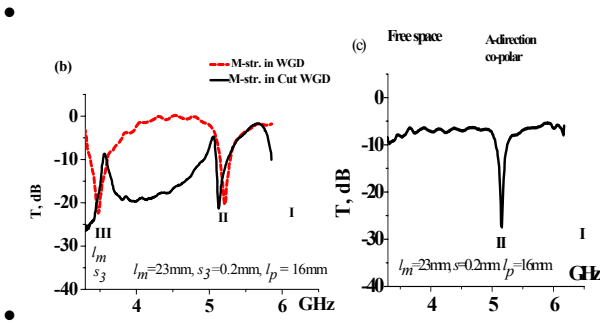


Fig.4. Frequency dependences of T in the presence of "*Gr-LCW*" meta-str.(l_p=21mm, l_m=26mm) in (a) WGD (dashed) and Cut WGD (solid) and (b) free space (A-direction).





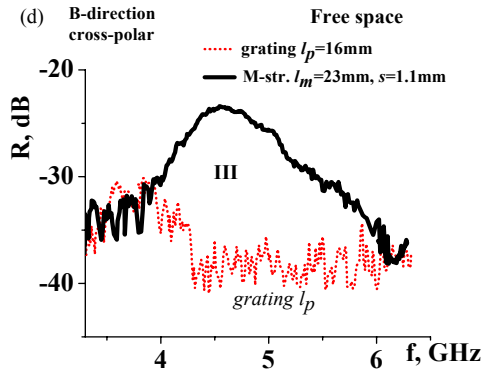


Fig.5. Frequency dependences of T in the presence of "*Gr-LCW*" meta-str.(l_p=16mm, l_m=23mm) in (a,b) WGD (dashed) and Cut WGD (solid) and (c,d) free space (A- and B-directions).

Now let us consider the results of measurements in the presence of metastructure "*Gr-LCW"*

In **fig. 4** we see frequency dependences of transmission *T* measured in WGD and Cut WGD (a) and in free space (b) in the presence of metastructure "*Gr-LCW"* with l_p=21mm, l_m=26mm, *s*=0.2mm, $t = l_p/4$. In this case in addition to resonance **I** of *the Gr.* the metastructure exhibits magnetic resonances **II** (of *LC*-circuits) and **III** (of *LCW*)**.** The below-cutoff section exhibits, besides pass-band due to *Gr.*, a new transparency band that extends from resonances **III** and **II** toward high-frequency region, **fig. 4a**. Such position of pass-bands identifies magnetic excitation and magnetic type of the resonance (**MR**). The resonance **II** is due to antiparallel currents in *LC-circuits* excited by transverse magnetic field of polaritons and resonance **III** is due to contribute of total currents from *LC*-circuits along longitudinal cut-wire l_m. How can we make out the difference between resonances **II** and **III** and mark out the resonance **III** of *LCW* l_m? One can easy do it by measurement of transmission *T* in free space (A-direction). In this case (**fig. 4b**) resonance response of *LCW* l_m in A-direction is practically not entered in contrast to responses of *Gr.* and *LC-circuits.* There is also the way to mark out the resonance response of a cut-wire applying varactor diodes (see part **2.3**).

Fig. 5 shows frequency dependences of transmission *T* measured in WGD and Cut WGD (a,b) and in free space (c,d) in the presence of metastructure "*Gr-LCW"* with l_p=16mm, l_m=23mm and different distance *s*. Value l_p=16mm is selected so as to provide resonance **I** and corresponding pass-band in Cut WGD would shift to the high-frequency edge of the interval of measurements and do not overlap with magnetic resonance **III** related to the l_m wire. Resonance **III** was excited at 5.1 GHz for a distance of *s*=2.7mm and shifted to lower frequencies (4.7 GHz) when *s* was decreased to 1.1mm (**fig. 5a**). When s_3=0.2mm resonance **III** of l_m wire was observed at frequency 3.5 GHz (**fig. 5b).** The below-cutoff section exhibited the corresponding pass-bands (above frequency of the magnetic resonance **III** of l_m wire and supperforbidden bands (below **III**, which occur at about 5 and 4.4 GHz and follow behind the shifting resonance **III**. Resonance **II** related to the *LC-circuits* was depicted at frequency 5.2 GHz in WGD and free space (**fig. 5b,c**).

Resonance **III** of l_m is not depicted in free space in A-direction, but one can observe resonance response in B-direction by measurement of cross-polarized reflected wave from l_m wire , **fig. 5d.**

A strong resonance **III** is observed when the l_m wire is arranged asymmetrically relative to l_p wire grating, its intensity decreases when l_m wire shifts to symmetrically location. In the case of $t=l_p/2$ resonance response **III** is absent.

Strong **MR III** is observed if the l_m value is close to half-wavelength in the frequency region adjoining resonance **I** from the side of lower frequencies, which is the region of existence of surface polaritons generated by wire grating l_p. The position of **MR III** depends on wire length l_m. **MR III** shifts toward higher frequencies with decreasing l_m and pass-band of the below-cutoff section in this case exhibits the corresponding shift as one can see in **Fig. 6a**.

In the case of using two wires with different lengths l_{m1} and $l_{m2,}$ two **MR**s **III** are excited at different frequencies and two pass-bands appear that are characteristic of the magnetic excitation (**fig. 6b**).

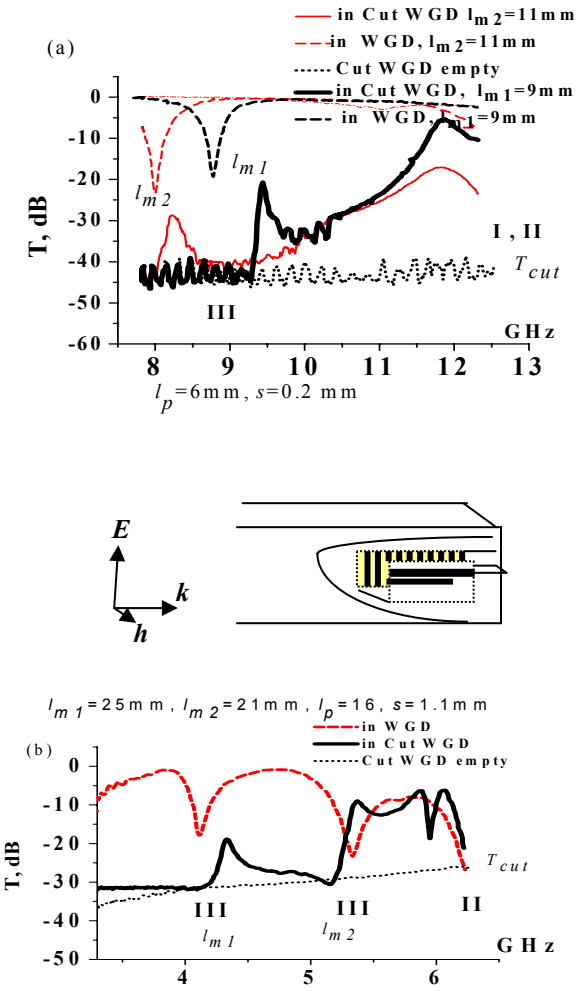


Fig.6. Frequency dependences of T in the WGD (dashed) and Cut WGD (solid) in the presence of (a)"Gr-LCW" meta-str and (b) "Gr-Two LCW, lm1, lm2" metastructure.

2.2.2. "Wire-pair – LCW" metastructure

One can imagine wire grating l_p as composition of many wire-pairs and confirm suggested conception by investigation of metastructure consisting one wire pair and *LCW*. We show that metastructure (see **fig. 7),** created from one pair of cut-wires **AB** in composition with asymmetrically located longitudinal cut-wire **CD** orthogonal to **AB** parallel to the electric field of incident electromagnetic wave, can also possess magnetic resonance response of longitudinal cut-wire **CD** at frequencies different from electric response of cut-wires **AB.** Conditions to achieve magnetic response and resonance properties are like as in the case of metastructure *"Gr–LCW*.

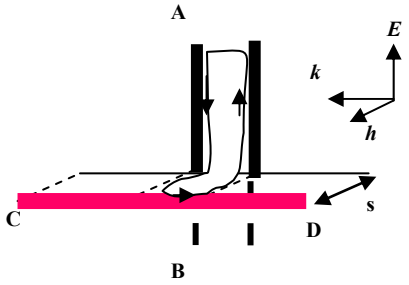


Fig. 7. Metastructure "Cut-wire pair-LCW"

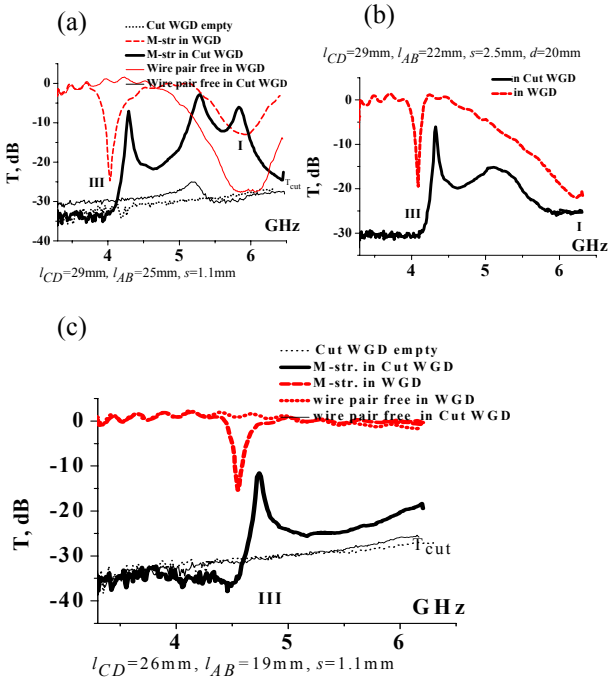


Fig. 8. Frequency dependences of transmission T in the WGD (dashed bold) and Cut WGD (solid bold) in the presence of metastructures *"Cut-wire pair-LCW"*

In **Fig. 8** we see frequency dependences of transmission T measured in WGD and Cut WGD in the presence of metastructures "Cut-wire pair-L*CW",* distance between wires **AB** is 20mm. We observe in WGD electric resonance **I** related to the wire pair **AB** without *LCW* **CD** at 6 GHz and corresponding pass-band in Cut WGD (below resonance **I**). In addition with "Cut-wire-pair-*LCW"* metastructure we observe magnetic resonance **III** related to wire **CD** and corresponding pass-band in Cut WGD (above the magnetic resonance frequency), (**Fig. 8a**). Decreasing the length l_{AB} resonance **I** shifts to the high-frequency edge of the interval of measurements and do not overlap with magnetic resonance **III** related to the **CD** wire (**Fig. 8b,c**).

2.2.3. "Cut-wire grating – PCW" metastructure

Let us consider "Cut-wire grating -single parallel cut-wire (*Gr-PCW*)" metastructure created from grating of wires l_p and a cut-wire (marked l_e*)* located parallel l_p on distance s (**Fig. 9.**)

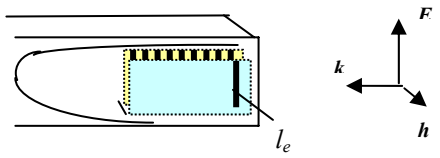


Fig. 9. Metastructure "Cut-wire grating-PCW"

In this case electric-dipole resonance (ER) is excited, which depends on the wire length (l_e) and can be observed both with and without l_p wire grating. The below-cutoff section exhibits a pass-band, which situated below the **ER** frequency and is characteristic of the electric excitation. In the case of strong change of distance s resonance frequency related to l_e wire is not practically shifted (**Fig. 10)** in contrast to **MR** frequency related to l_m wire (**Fig. 5a,b**).

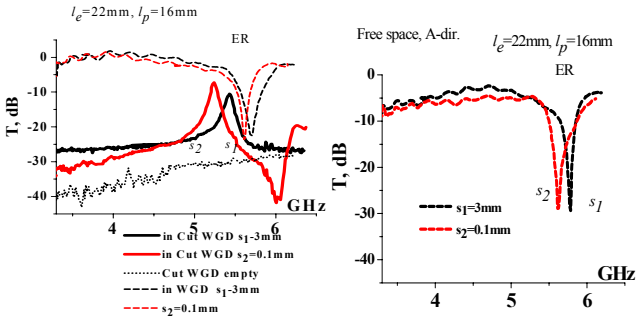


Fig. 10. Frequency dependences of transmission T in the presence of "Gr-PCW" metastructure in (a) the WGD and Cut WGD and (b) free space A-direction

In the case of using two wires with different lengths l_{e1} and l_{e2} two **ER**s (**ER$_1$** and **ER$_2$**) are excited at different frequencies and two pass-bands (in Cut WGD) appear that are characteristic of the electric excitation (**Fig. 11**).

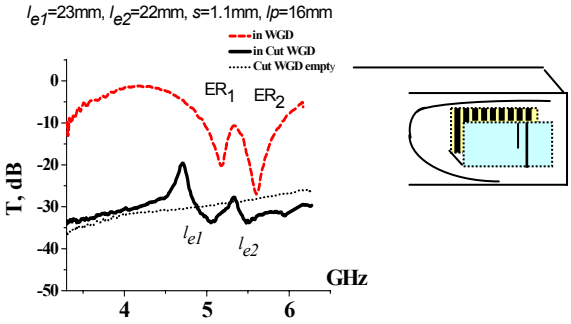


Fig. 11. Frequency dependences of transmission T in the WGD and Cut WGD in the presence of "Gr-two PCW" metastructure.

2.3. Split LCW and PCW loaded with varactor diodes

It is special interest to study a metastructure using varactor diodes. In [6] it has been demonstrated that the resonant frequency of split ring resonators (SRRs) can be tuned using varactor diodes. The resulting particle has been called a varactor-loaded split ring resonator (VLSRR). In this paper we use varactor diodes in metastructures to tune resonance response related to cut-wires and match the resonance minima of transmission T to concrete resonant elements with certainty what is important for multi-resonance system.

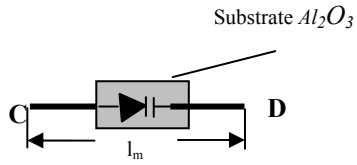


Fig. 12. Split cut-wire loaded with varactor diode

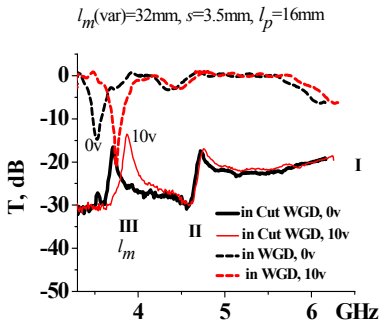


Fig. 13. Frequency dependences of transmission T in the WGD (dashed) and Cut WGD (solid) in the presence of metastructure "*GR-VLSLCW*" under different bias conditions

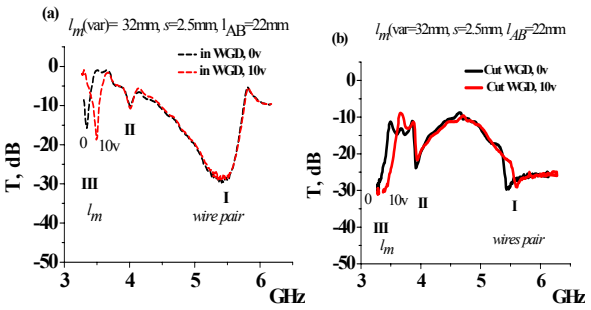


Fig. 14. Frequency dependences of transmission T in the presence of metastructure "*Cut-wire-pair-VLSLCW*" under different bias conditions in (a) WGD and (b) Cut WGD

By analogy with [7] we call resulting cut-wire as varactor loaded split longitudinal cut-wire l_m (VLSLCW) or varactor-loaded split parallel cut-wire l_e (VLSPCW).

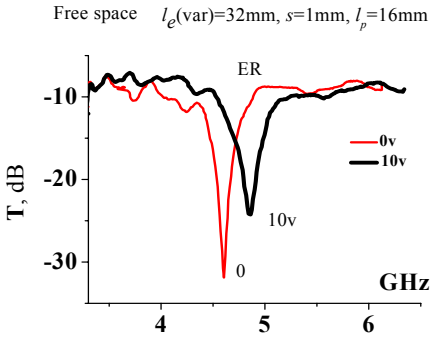


Fig. 15. Frequency dependences of transmission T in the presence of metastructure "*Gr-VLSPCW*" under different bias conditions in free space A-direction.

Split cut-wire is loaded with varactor diode placed on substrate Al_2O_3 in the gap as we see in **Fig. 12**.

Frequency dependences of transmission T in the WGD and Cut WGD in the presence of metastructures "*GR-VLSLCW*" and "*Cut-wire-pair-VLSLCW*" are demonstrated in **Fig. 13**, **14** under different bias conditions. These metastructures show electric resonance response **I** related to grating of wires l_p (or wire pair **AB**), resonance **II** and magnetic resonance **III** related to split longitudinal cut-wire l_m (or split cut-wire **CD**) loaded with varactor diode SMV1234. Resonance **III** of wire *VLSLCW* shifts from 3.53 GHz to 3.74 GHz (**Fig. 13**) and from 3.34 GHz to 3.49 GHz (**Fig. 14**) with the tuning voltage V_{DC} from 0 to 10v. Corresponding pass-band in Cut WGD (above **III)** follows the shifting resonance **III**. Positions of resonances **I** and **II** are practically not changed.

Metastructure "*Gr-VLSPCW*" consisting of wire grating l_p and split cut wire l_e loaded with varactor exhibits electric resonance response **I** related to grating of wires l_p and electric resonance **ER** related to wire *VLSPCW*. **Fig. 15** shows that the resonance **ER** shifts from 4.6 GHz to 4.86 GHz with the tuning voltage V_{DC} from 0 to 10v corresponding to varactor tuning capacitance from 9.63 to 1.47 pF.

3. Discussion

We investigate composite multi-resonance metastructure at microwaves. Using different measurement methods we can match the resonance minima of transmission T to concrete resonant elements of metastructure and identify resonance type (magnetic or electric). We can observe separately three resonances in dependence on design. The emphasis is resonance in longitudinal cut-wire placed near wire grating.

We suggest a concept of magnetic response based on anti-parallel resonant currents excited by magnetic field of surface polaritons in many spatial LC-circuits created from cut-wire pairs of a grating and section of longitudinal cut-wire. Obtained results confirm this conception. Is there any possibility of traditional electric excitation in this case? Theoretically, yes, because near each cut-wire-end of a grating there is opposed longitudinal electric field. This field can induce opposed currents along longitudinal wire, so, total longitudinal current is practically absent. Experimentally we investigated the possibility of using resonance in a single planar double split ring PDSR to study the local polarization characteristics of electric or magnetic fields of surface polaritons supported by wire grating [7]. By moving the PDSR different resonance effects were observed in dependence on excitation by different components of electric or magnetic fields. Resonance effects which could be excited by longitudinal electric field are absent.

4. Conclusions

In this paper it is observed that nonmagnetic single longitudinal cut-wire arranged in necessary planar metastructure can show a magnetic resonance response in dependence on design, when metastructure is disposed along propagation direction of electromagnetic wave. Different composition metasructures "*Cut-wire grating – single longitudinal cut-wire LCW*", *Wire-pair - LCW*" are investigated at microwaves. Obtained results allow to suggesting and verifying a concept of the magnetic resonance excitation based on antiparallel currents in many LC-circuits created from cut-wire pairs of a grating and section of longitudinal cut-wire. Frequency dependences of transmission *T* are measured in waveguide, cutoff waveguide and free space. Three resonance areas **I**, **II** and **III** in transmission are observed. One can match each resonance minimum to concrete resonant elements. The resonance **I** is related to wire grating, while resonances **II** and **III** are related to LC-circuits and the *LCW*. One can also identify resonance type (electric excited by electric field or magnetic excited by magnetic field) by measurements in cutoff waveguides. The resonance **I** is identified as electric type while the resonance **II** and **III** are magnetic resonances excited by magnetic field of surface polaritons. Resonance frequencies **II** and **III** are not the same and different from frequency **I** depending on grating's wire length, *LCW* length and distance *s* between *LCW* and grating.

Present investigation shows a practical way to the excitation of a magnetic resonance in nonmagnetic longitudinal line cut-wire which is arranged perpendicularly to the electric field of incident electromagnetic wave near a grating of cut-wires parallel to the electric field. It is suggested a concept of magnetic resonance response based on antiparallel currents in many *LC-circuits* created from cut-wire pairs of a grating and section of longitudinal cut-wire. The resonance **III** is due to contribute of total like-directed currents from *LC-circuits* along longitudinal cut wire.

Acknowledgements

Acknowledgements. This study was supported by the RFBR, projects nos. 10-08-00018, and 11-02-90403.

References

1. Christophe Caloz, Metamaterial dispersion engineering: A new paradigm in microwave science and technology, pp. 1-2, Proceedings of *Metamaterials'2010*, pp. , Karlsruhe, Germany, Sept. 13-18, 2010.
2. Shalaev, V. M., Kawata S., *Advances in Nano-optics and Nano-photonics*. *Nanophotonics with surface plasmons*, Elsevier, 2007.
3. Dolling, G., Enkrich, C. and Wegener, M., at al., "Cut-wire pairs and plate pairs as magnetic atoms for optical metamaterials," *Optics Letters,* Vol. 30, No. 23, 3198-31200, 2005.
4. Butylkin, V. S., and Kraftmakher G.A., "Magnetic Type Resonance in Nonmagnetic Line Wire Excited by Surface Plasmons in Microwave Range," *Tech. Phys. Letters*, Vol. 37, No. 4, 399–312, 2011; see also in *Proceedings* of *Metamaterials'2010*, Karlsruhe, Germany, 450-452.
5. Kraftmakher, Galina, "New realization and microwave properties of double negative material", *Int. Journal of Applied Electromagnetics and Mechanics*, Vol. 19, Nos. 1-4, 57-61, 2004.
6. I. Gil, J. Garcia-Garcia, J. Bonache, F. Martin, M. Sorolla and R. Marques, "Varactor-loaded splt ring resonators for tunable notch filters at microwave frequencies", *Electronics Letters,* Vol. 40, No. 21, 2004.
7. V.S. Butylkin, G.A. Kraftmakher, S.L. Prosvirnin, "Method of Surface Polariton Field Structure Measurement Using Resonance Excited in a Single Planar Double Split Ring", *Tech. Phys. Letters*, Vol. 38, No. 2, 147–150, 2012.

Optimization for both the size and spacing between two antennas for a 2 * 2 MIMO system using MNG metamaterial

Belgacem AOUADI[1], Mondher LABIDI[1] and Jamel BELHADJ TAHAR[1]

[1]6'Tel Research Unit, Higher School of Communications of Tunis, Sup'Com University of Carthage, Tunisia
b_aouadi@yahoo.fr

Abstract

In this paper, we try to study the behavior of a 2*2 Multi-Input Multi-Output (MIMO) antennas such as the spacing and the isolation between the two radiating elements. In fact, we demonstrate how a negative magnetic permeability Metamaterial (MNG) can enhance the antenna array of a multiple input multiple-output (MIMO) communication system. The MNG is inserted between the ground plane and the substrate to decrease the correlation between the two antennas. Each antenna is designed to operate at about 4.5 GHz. The performance of a patch antenna array using MNG was elucidated relative to a similar array without MNG. Design and simulations are done using Ansoft's HFSS.

1. Introduction

Recent growth in the use of wireless wide-area networks (WWAN) thanks to its advantages like good accessibility and high bit rate has pushed the wireless industry to find the best technique in order to increase its spectrum efficiency and guarantee the best quality of service. Thus, Multiple-input Multiple-output (MIMO) technology remains the most promising in the evolution of wireless broadband access networks [1]. Indeed, MIMO systems promise higher channel capacities compared to single antenna systems by exploiting the spatial characteristics of the multipath wireless propagation channel [2]. Nevertheless, the antenna elements are strongly coupled with each other which affect the performances of a MIMO system [3]. Many studies have been fructified to optimize the isolation characteristic of a MIMO antenna. Some of methods are based on the isolation elements between the radiating elements [4] as well as using a shorting strip [5] or also a corrugated ground plane [6]. Otherwise, we find another recent technique to more enhance the characteristics of a MIMO system based on the use of μ-negative metamaterial (MNG) structures [7], [8]. In [8], MNG structures consists of a concentric combination of Edge-Coupled Split Ring Resonator (EC-SRR) and a Broadside-Coupled Square Ring Resonator (BC-SRR) with dimensions chosen to provide an effective negative permeability for two bands. Moreover, The MNG is inserted between the two antennas (back to back). In this study, we have just used SRR to develop MNG at about 4.5 GHz and it was inserted between the ground plane and the substrate. On the other hand, we have used MNG to reduce the size of each antenna and the spacing between the two elements. In fact, Metamaterials have been extensively applied for antenna applications recently to achieve antenna miniaturization [9] and improved directivity [10].

In this paper, we quantify the performance of a miniaturized patch antenna array for a 2*2 MIMO communications system using MNG for different values of spacing (λ/2, λ/4 λ/8 and λ/10). Then, we set the spacing value = λ/10 and we evaluate the behavior of the proposed system when we change the position of each antenna. Finally, we suggest a perspective by designing a 4*4 MIMO system.

Following this introduction, we discuss the design and the performances of the proposed antenna and MNG in Section 2. The design and the results of simulations of the proposed perspective are presented and discussed in Section 3. Finally, we conclude the paper in Section 4.

2. Antenna Design and Performances

2.1. Antenna Configuration

Before insertion of MNG, the antenna geometry used in this study is a square patch with a recessed microstrip feed line (50 Ω) with dimensions of L_F = 32.5mm and W_F=1mm, backed by a substrate and a perfect conductor ground plane. The size of each radiating element is L_P =W_P = 20mm and it's assumed as a Finite conductivity. Both of the elements and the microstrip line are printed on the same side of a Teflon substrate (L_S = 60mm, W_S= 55 mm), T_S = 1,27mm in thickness and a dielectric constant of 2.2. In this case the two identical antennas were separated by d= λ/2 where λ is the free space wavelength. The structural details of the proposed 2*2 MIMO system are shown in Fig.1

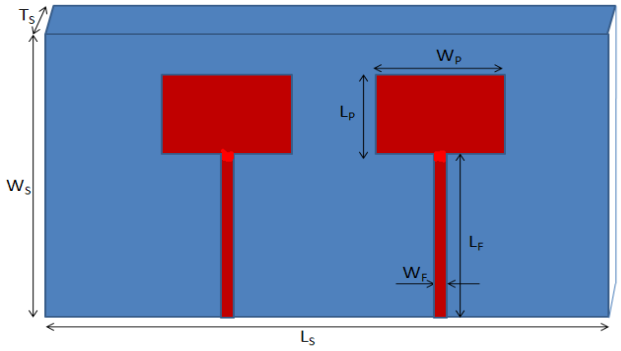


Figure 1: Schematic of the proposed 2*2 MIMO system without MNG

2.2. MNG design and miniature antenna

In this research, the proposed MNG was composed by Split Ring Resonators (SRRs). Indeed, The effective permeability characteristics of the SRR unit cell can be determined using the method described in [11] et [12] and it was -4.931 at 4.5 GHz. Furthermore, we have chosen a group of a = 4 sets of MNG slabs. Each set consists of b=7 unit cells. The optimized separation distance between the MNG slabs is c= 5.31 mm. Based on these conditions, a significant reduction (96%) in the area occupied by the each patch antenna was achieved. In fact, to match the resonance frequency (4,5GHz) and the same spacing (d= λ/2) between the two elements, the dimensions of the 2*2 MIMO system with MNG must be as follow: L_P =W_P =4mm, L_S =50.89mm, W_S = 19.17mm, T_S = 0.5mm, L_F = 6mm and W_F =0.3mm.

The dimensions of the proposed MNG were shown in Fig.2. The Perspective view of the two antennas with MNG and spacing λ/2 is shown in Fig.3.The simulated S-parameters for the proposed antenna system with and without MNG are shown in Fig. 4.

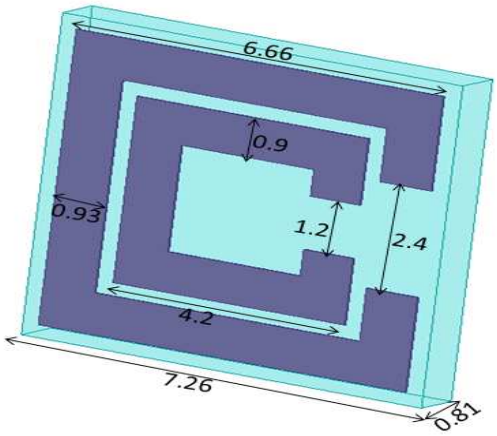


Figure 2: Dimensions (in millimeter) of the proposed MNG

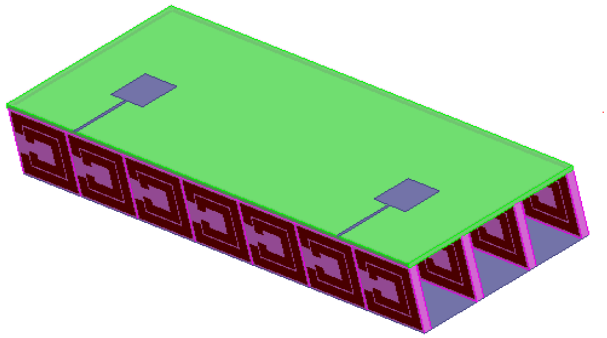


Figure 3: Perspective view of the two antennas with MNG (λ/2)

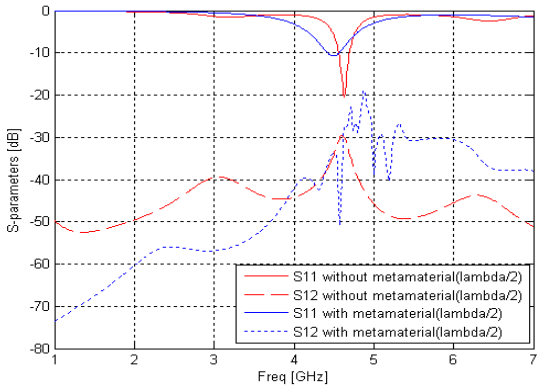


Figure 4: S-Parameters with and without MNG for MIMO system

The antennas (without MNG) resonate at 4.5 GHz with a return loss of -20.52 dB. The mutual coupling measured in terms of S_{12}, is -30dB compared to -40.24 dB for the design with MNG structures. In this situation (MNG and d =λ/2), we haven't achieved the best isolation characteristic and the minimum spacing between the two radiating elements. Therefore, in the next section, we will try to improve further these two requirements of a 2*2 MIMO system.

2.3. Analysis of the spacing and Isolation Characteristics

The dimensions of each patch antenna, the values of T_S, a, W_S, L_F and c were conserved as mentioned in 2.2. However, the others dimensions of MNG, the microstrip line and the substrate were changed as shown in Tab.1. The simulated S-parameters for different values of d are illustrated in Fig. 5.

Table 1: Dimensions of MNG and the substrate for different values of d

	L_S (mm)	W_F (mm)	b
d =λ/2	50.89	0.3	7
d =λ/4	36.3	0.7	5
d =λ/8	29.04	0.7	4
d =λ/10	29.04	0.7	4

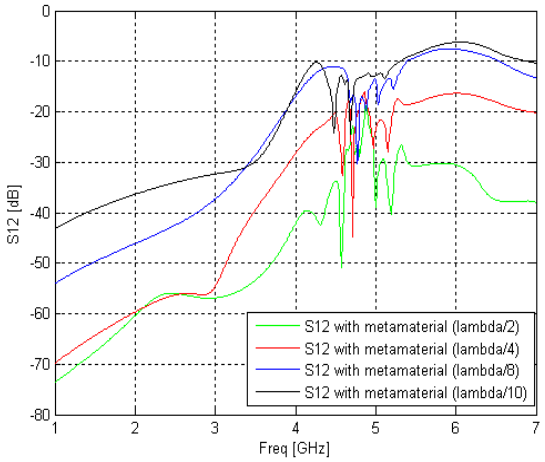


Figure 5: Measured mutual coupling between the antenna elements for different antenna spacing

Fig. 5 shows that it is obvious that the addition of the MNG structure improves the isolation characteristic and also the spacing (d= λ/10) between the two antennas. Moreover, we have the best dimensions of the substrate and the MNG which optimizes significantly the cost of construction of our suggested 2*2MIMO system. Clearly, the transmission coefficient S_{12} is -20dB when d= λ/10 compared to -11.36 when d= λ/8, -22.83dB when d= λ/4 and -40.24dB when d= λ/2.

2.4. Variation of the mutual coupling when the two antennas are opposite and d = λ/10

In this section, we set d = λ/10 as the spacing between the two elements and we assume that the two antennas are opposite to evaluate the performances of the new configuration. As a result, we have conserved the details of each patch antenna, microstrip line and the value of b and T_S as mentioned in 2.3. On the other hand, we have used a new values of a =6, c=3.56, L_S = 29.04mm and W_S = 22.66mm. The Simulated S_{12} characteristics are shown in Fig.7.

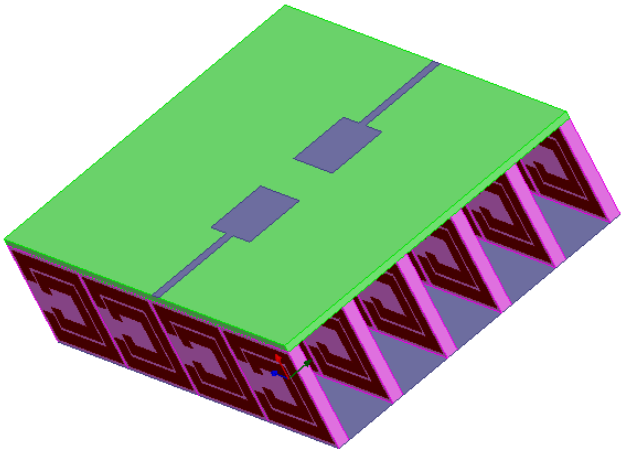


Figure 6: New configuration with opposite antennas

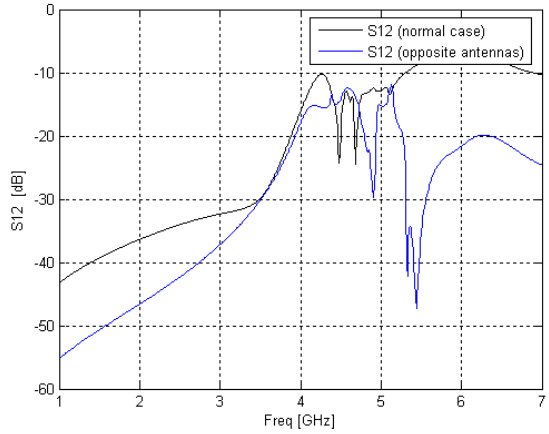


Figure 7: Simulated S12 characteristics for the new configuration

Based on the above results, we can confirm that the orientation of the antennas affect the mutual coupling strengths. In fact, the measured isolation becomes -13.56dB.

2.5. Design and Performances of a 4*4 MIMO system

As we mentioned above, the correlation between any two antennas within a MIMO system should be kept as low as possible in order to improve the performance and capacity of MIMO systems. In this section, we evaluate the behavior of a 4*4 MIMO system as a perspective for our study in this paper. The perspective view of this design is presented in Fig.8.In fact, we have conserved the same dimensions of a 2*2 MIMO system as mentioned in 2.2 when d= λ/10.
The results of simulations are shown in Fig.9.

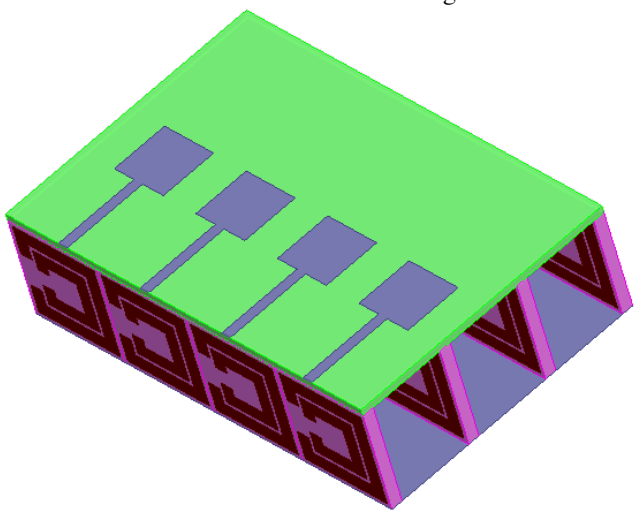


Figure 8: Perspective view of a 4*4 MIMO systems

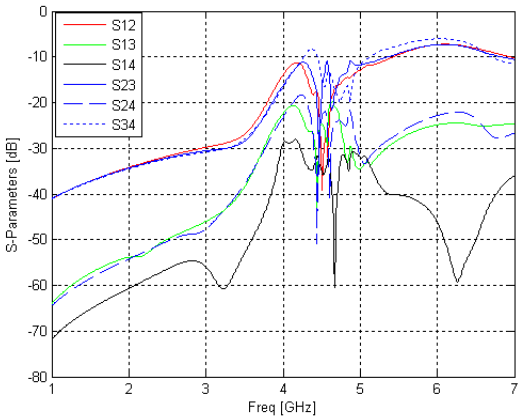


Figure 9: S-Parameters for the proposed perspective

As expected, the isolation between each two antennas seems more or less varied like S_{12} = -37.83dB, S_{13} = -25.64dB, S_{14} = -35.83dB, S_{23} = -18.44dB, S_{24} = -22.46dB and S_{34} = -15.67dB.

3. Conclusion

In this paper, 2*2 MIMO systems for different configurations are discussed. They are shown how it is possible to minimize the volume occupied by the antennas, the spacing between the two elements and the mutual coupling thanks to MNG structure. As a result, we must choose an optimal compromise between the various cases already studied. Additionally, we have proposed another structure (4*4 MIMO systems) that is developed based on the initial design. Measured results show that these arrays have also a good performances and it can be a promising solution for applications in cognitive radio.

References

1. IEEE 802. 11n, Joint Proposal: High Throughput Extension to the 802. 11 Standard: PHY, doc.: IEEE 802. 11-05/ 1102r4.
2. G. J. Foschini and M. J. Gans, “On limits of wireless communications in a fading environment when using multiple antennas,” Wireless Personal Commun., vol. 6, no. 3, pp. 311–335, 1998.
3. David A. Sanchez-Hernandez, Multiband Integrated Antennas for 4G Terminals, Artech House, INC. 2008.
4. Seokjin Hong, Kyungho Chung, Jaewon Lee, Sangwook Jung, Sang-Sun Lee, and Jaehoon Choi, "Design of a Diversity Antenna with Stubs for UWB applications," Microwave and Optical Technology Letters, Vol. 50, No. 5, pp.1352-1356, May 2008.
5. K. L. Wong, C. H. Hua, B. Chen and S. Yang, “Three-antenna MIMO system for WLAN operation in a PDA phone”, Microwave and Opt. Technol. Lett., vol. 48, no. 7, pp. 1238–1242, Jul. 2006.
6. M. Karaboikis, C. Soras, G. Tsachtsiris and V. Makios, “Compact Dual-Printed Inverted-F Antenna Diversity Systems for Portable Wireless Devices”, IEEE Antennas Wireless Propagat. Lett., vol. 3, pp. 9–14, 2004.
7. M. M. Bait-Suwailam, M. S. Boybay, and O. M. Ramahi, “Electromagnetic Coupling Reduction in High-Profile Monopole Antennas Using Single-Negative Magnetic Metamaterials for MIMO Applications,”IEEE Trans. Antennas Propag.,vol. 58, no. 9, pp. 2894–2902, Sep., 2010.
8. Haider R. Khaleel, Hussain M. Al-Rizzo, Daniel G. Rucker , Yasir A. Rahmatallah, and Seshadri Mohan, “Mutual Coupling Reduction of Dual-band Printed Monopoles Using MNG Metamaterial”, IEEE AP-S/URSI 2011, 978-1-4244-9561-0/11/$26.00, 2011
9. A. Sanada, M. Kimura, I. Awai, C. Caloz, and T. Itoh, “A planar zerothorder resonator antenna using a left-handed transmission line,” in Proc. 34th Eur. Microw. Conf., Oct. 2004, vol. 3, pp. 1341–1344.
10. S. Enoch, G. Tayeb, P. Sabouroux, N. Guérin, and P. Vincent, “A metamaterial for directive emission,” Phys. Rev. Lett., vol. 89, no. 21, p. 213902, Nov. 2002.
11. Clifton Carthelle Courtney, "Time-Domain Measurement of the Electromagnetic Properties of Materials," IEEE Transaction on Microwave Theory and Techniques, Vol. 46, No. 5, pp. 517-522, May 1998.
12. Rechard W. Ziolkowski, "Design, fabrication, and testing of double negative metamaterials," IEEE Transaction on Antennas Propagation., vo1.51, No. 7, pp.1516-1529, July 2003

Damping of the opaque band and layer-by-layer transmission through disordered two dimensional photonic crystals

Yurii Barabanenkov[1], Mikhail Barabanenkov[2*]

[1]V.A Kotelnikov Institute of Radioengineering and Electronics, Russian Academy of Sciences, Moscow, Russia
[2]Institute of Microelectronics Technology, Russian Academy of Sciences, Chernogolovka, Moscow, Russia
*corresponding author, E-mail: barab@iptm.ru

Abstract

Assuming that two dimensional photonic crystals with disorder is a good approximation in studying wave transmission through a localizing two dimensional dense random medium slab, a layer-by-layer decay of the incident electromagnetic field energy density through two dimensional photonic crystals composed of dielectric rods and stability of opaque band of a hexagonal packing of cylindrical pores with positional disorder in silicon matrix are investigated by the Riccati equation method.

1. Introduction

The propagation of electromagnetic (EM) waves in randomly inhomogeneous slab of nondissipative medium can in general be described by a normal diffusion process which predicts an inverse linear decrease of the transmission with the slab thickness. The transmission through a medium possessing more higher concentration of scatterers behaves inverse quadratic dependence at the localization transition followed by an exponential decay [1] if scattering becomes strong enough, as in the case of resonance scattering [2]. As it is known [3], the resonance leads to both large scattering amplitude and large scattering delay time. The latter results in inapplicability of a traditional Boltzmann equation method [4]. In the weak scattering limit the transport of EM field in a random medium is described by the radiation transfer equation [5]. Beyond this limit as in the case of dense media consisting of randomly distributed dielectric spheres tuned to the Mie resonant scattering, the propagation of EM waves may be correctly described by the modified radiation transfer equation which predicts a diffusion regime with a decrease of diffusion coefficient due to an accumulation of EM field energy in resonant scatterers. [6]. Nevertheless, the self-consistent theory of localization [7,8] has been adopted as the simplest approach to the problem. This theory provides an implicit equation for the energy diffusion coefficient of EM field [8] which is no longer a local variable but is determined by macroscopic coherent wave interference throughout the entire medium and even depends on the size of entire medium slab in the vicinity of the localization threshold [9]. The self-consistent theory extends the perturbative weak localization treatment of the corrections to classical diffusive behavior of the wave energy. Starting from dilute media in the zero approximation, a numerous corrections are required to describe denser media in which the diffusion coefficient may goes to zero.

An alternative approach from relatively dense random media such as photonic crystals (PCs) with moderate disorder has been proposed by John [9]. PCs feature opaque bands, i.e. frequency ranges for which incident electromagnetic waves are totally reflected because of both microscopic Mie resonant scattering and the Bragg-like multiple scattering [10]. Opaque bands and Anderson localization are closely related. Really, both inhibit wave's propagation due to interference in nondissipative media and can only be obtained for strongly scattering media. One of the ways in the framework of this approach of treating localization of EM waves is to study the EM field intensity transmitted through a slab of 2D PCs with disorder as a function of slab thickness at EM field wavelength taken from opaque band in transmission spectrum of perfect 2D PC. It is anticipated that the localization regime is if average transmitted intensity decreases exponentially with PC slab thickness increase. The 2D geometry precludes possible depolarization effect of EM waves which functions as effective absorption [11,12].

In the currently presented report we investigate by the Riccati equation method a layer-by-layer decay of the incident EM field energy density through 2D photonic crystal and a problem of stability of the opaque band of 2D inverse PCs with positional disorder.

2. Riccati equation and two dimensional opaque band calculation

2D PCs are periodic arrangements of parallel dielectric or air rods. For in-plane propagation, two types of EM modes can be defined according to whether the electric (TE polarization) or magnetic (TH polarization) fields is parallel to the rod axis.

Let a plane EM wave with the wavevector $\vec{k}_0$ be incident from a background dielectric medium ε^{bac}=1 at an angle α on an $L=(N-1)\Lambda_1+2\rho$ thick slab of 2D PC (Figure 1) consisting of $m=1,2,...,N$ layers of rods with

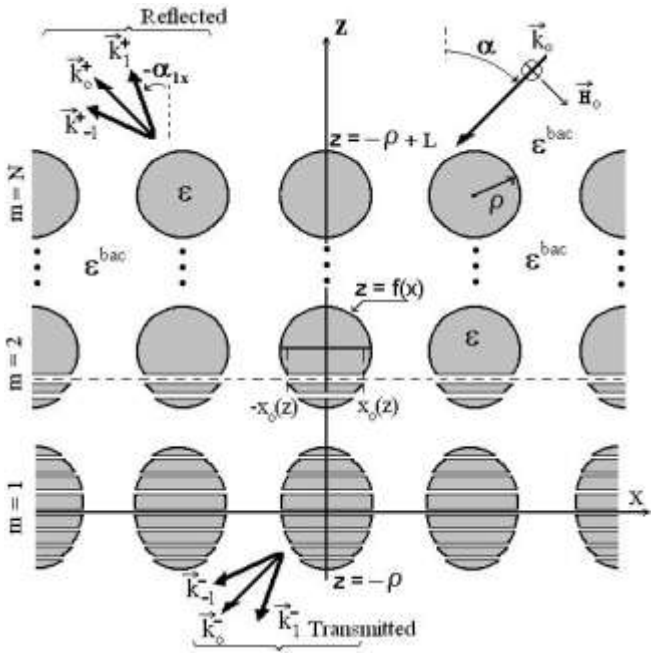


Figure 1: Schematic showing of xz plane of splitting the 2D PC slab into auxiliary slices and splits. The electric field vector $\vec{E}_0$ of a plane wave incident at angle α is parallel to the y axis (TE polarization). The wave vector $\vec{k}_0$ and the magnetic vector $\vec{H}_0$ of the wave lie in the xz plane of incidence. The vector $\vec{H}_0$ is replaced by the vector $\vec{E}_0$ in the case of TH polarization. $\vec{k}_\mu^{\pm}$ are reflected (+) and transmitted (-) spectral modes, respectively, directed at angle $\alpha_{\mu x}$ to the z axis.

radius ρ and dielectric permittivity ε, infinitely extended along the y axis of the rectangular coordinate system xyz. The rods constitute a rectangular lattice with periods Λ_1 and Λ_2 along the z and x axes, respectively. A circumference of a rod in the xz plane is given by the function $z = f(x)$. Following the transfer relations method [15], the slab is divided into a set of slices perpendicular to the z axis and separated from each other by infinitesimal splits. The composition rule of T-matrices leads to a system of exact matrix equations, i.e. transfer relations for the matrix wave reflection and transmission coefficients of a set of slices and the matrix amplitudes of waves in splits between slices. The transfer relations give, in particular, a differential basic Riccati equation for the matrix wave reflection coefficient from a slab, the embedding parameter of these differential equations with given "initial" condition is taken along the z axis. The slicing is, in essence, applied successively to layers of the rods, which are gratings, starting from the bottom layer (m = 1 in Figure 1). The wave field scattered by the first layer is transferred over an interlayer spacer with a corresponding phase shift to the next layer of the rods and so on.

2.1. TE polarization

In the case of TE polarization the Riccati equation is written in the matrix form as follows

$$\frac{dR}{dz} - i(\sigma R + R\sigma) = aF(z) + aF(z)R + RaF(z) + RaF(z)R \tag{1}$$

as $-\rho < z < -\rho + L$ and $R_{\mu,\nu}(k_{0x}) \to 0$ as $z \to -\rho$. Here $R_{\mu,\nu}(k_{0x})$ is the matrix reflection coefficient of an auxiliary interface $\xi = f(x,z)$ truncated by a plane z = const, the indices $\mu,\nu = 0,\pm1,\pm2\ldots$ relating to diffracted and incident spectral orders, respectively. Physically, $R_{\mu,\nu}(k_{0x};-\rho+L)$ means a partial wave reflection coefficient into the μ th Bloch mode from the PC slab. Diagonal matrixes σ and a have elements $\sigma(\mu) \equiv k_{\mu z}^+ = \left[k_0^2 - \left(k_{\mu x}^+\right)^2\right]^{1/2}$ and $2\pi a = -iV_0/\sigma(\mu)$ where $k_{\mu z}^+$ and $k_{\mu x}^+ = k_{0x} + 2\pi\mu/\Lambda$ are the x and the z component of the scattered spectral order wave vector $\vec{k}_\mu^+$, respectively; $V_0 = -k_0^2(\varepsilon - \varepsilon^{bac})/\varepsilon^{bac}$, $k_0 = 2\pi(\varepsilon^{bac})^{1/2}/\lambda_0$, λ_0 is the wavelength in the background, $k_{0x} = -k_0 \sin\alpha$, $k_{0z} = -k_0 \cos\alpha$. The matrix $F_{\mu\nu}(z) \equiv F_{\mu-\nu}(z)$, with the elements

$$f_\mu(z) = \frac{\pi}{\Lambda_1\Lambda_2}\sum_{n=1}^{p}\exp\left(i\frac{2\pi n}{\Lambda_1}z\right) \cdot \iint_G dz'dx' \exp\left[-i\left(\frac{2\pi n}{\Lambda_1}z' + \frac{2\pi\mu}{\Lambda_2}x'\right)\right] \tag{2}$$

is responsible for the spectral order's, propagating or evanescent, mutual transformation due to the multiple scattering on the array of the rods. The integration in Eq.(2) is carried out over the structure unit cell; p is a number of slices at the virtual layering of each array of the rods. In the case of symmetric function $f(x) = f(-x)$, Eq.(2) reads

$$f_\mu(z) = \frac{1}{\mu}\sin\left[\frac{2\pi\mu}{\Lambda_2}x_0(z)\right] \tag{3}$$

where $x_0(z)$ stands for a root of the equation $f(x) = f(-x) = z$ at $0 \le x \le \rho$. In the case of

circular rods, the function $x_0(z)$ has the form $x_0(z) = \left\{\rho^2 - \left[z-(m-1)\Lambda_2\right]^2\right\}^{1/2}$ as $\left|z-(m-1)\Lambda_2\right| < \rho$ and the plane z = const intersects the m th layer of the rods. Otherwise the matrix $F_\mu(z)$ is equal to zero.

The z components, Π_z, of the Poynting's vector for the EM field in the regions of wave reflection from, $\Pi_z(z > -\rho + L)$, and transmission through, $\Pi_z(z < -\rho)$, the L thick slab of 2D PC are given [15] in terms of the tensor coefficients of wave reflection $R_{\mu,0}$ and transmission $T_{\mu,0}$, respectively. Averaging these z components along the planes $z = -\rho + L$ and $z = -\rho$ results in

$$\Pi_z(z = -\rho + L) = k_{0z} + \sum_\mu k^+_{\mu z}\left|R_{\mu 0}(k_{0x}; -\rho + L)\right|^2$$

and

$$\Pi_z(z = -\rho) = \sum_\mu k^-_{\mu z}\left|T_{\mu 0}(k_{0x}; -\rho + L)\right|^2 \qquad (4)$$

where the sums are only taken over the propagating spectral orders with $\left|k^+_{\mu x}\right| \le k_0$. Here $\vec{k}^-_\mu$ is the transmitted spectral order wave vector with components $\vec{k}^-_{\mu x} = \vec{k}^+_{\mu x}$ and $\vec{k}^-_{\mu z} = -\sigma(\mu)$. These two energy fluxes should be identical in accordance with the Poynting theorem in the case of non-absorptive rods, $\Im\varepsilon$ =0.

2.2. TH polarization

In the case of TH polarization of the incident wave the Riccati equation (1) has modified coefficient a

$$\frac{dR}{dz} - i\left(\sigma R + R\sigma\right) = a^- F(z) + a^+ F(z)R + Ra^+ F(z) + Ra^- F(z)R \qquad (5)$$

where matrices $a^\pm$ have elements

$$2\pi a^\pm = -i\frac{V_0}{\sigma(\mu)}\left[\pm\frac{\sigma(\mu)\sigma(\nu)}{k_0^2} + \frac{\varepsilon^{bac}}{\varepsilon}\frac{k^+_{\mu z}\,k^+_{\nu z}}{k_0^2}\right] \qquad (6)$$

The z components Π_z averaged along the abovementioned z planes read

$$\frac{\Pi_z(z = -\rho + L)}{\left|\Pi_{0z}\right|} = -1 + \sum_\mu \frac{k^+_{\mu z}}{\sigma_{k_0}}\left|R_{\mu 0}(k_{0x}; -\rho + L)\right|^2$$

and

$$\frac{\Pi_z(z = -\rho)}{\left|\Pi_{0z}\right|} = \sum_\mu \frac{-k^+_{\mu z}}{\sigma_{k_0}}\left|T_{\mu 0}(k_{0x}; -\rho + L)\right|^2 \qquad (7)$$

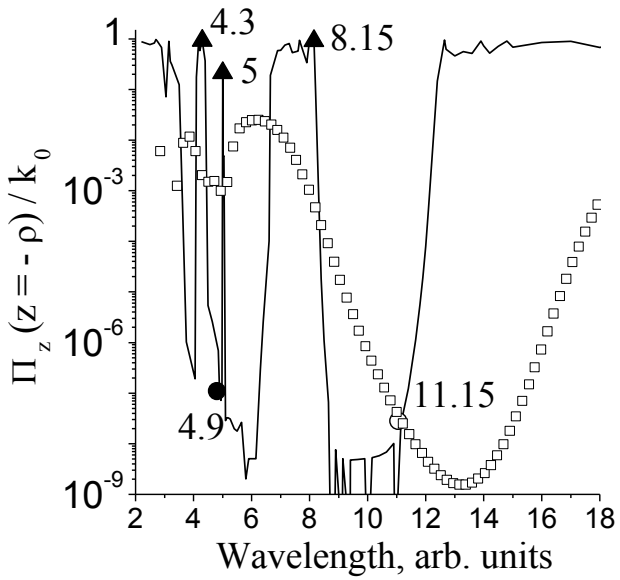


Figure 2: Calculated relative power of EM radiation transmitted through N = 18 arrays of circular rods arranged in a square lattice versus the wavelength of the EM waves assuming wave normal incidence, ε^{bac}=1, ε = 8.41, and arbitrary units for the λ, period $\Lambda_{1,2}$ = 4, and radius ρ = 0.6. The curve with open squares corresponds to the transparency frequency spectrum for a layer of thickness $L = 18\Lambda$ of randomly arranged parallel circular rods with density $n = \Lambda^{-2}$ and the scattering cross section $S(\lambda)$. Solid and open triangles and circles with numbers mark some specific wavelengths.

Where $\Pi_{0z} = -(1/8\pi)(C/\sqrt{\varepsilon^{bac}})\varepsilon^{bac}E_0^2\cos\alpha$ is the z component of the incident TH polarized wave $\vec{E}_0$. Here C is the light velocity in vacuum.

For numerical calculations, the matrix Riccati equations are reduced to 15×15 equations for a matrix reflection coefficients which describes mutual transformation of the 15 first spectral orders. The reduced system is computed by Runge-Kutta routine.

The EM wave field energy flux, $\Pi_z(z = -\rho)$, transmitted through an L thick slab of a 2D PC is evaluated in the case of non-absorptive rods, $\Im\varepsilon$ =0, by solving the Riccati equation (1) or (5) with the aid of the Poynting theorem (4) or (7) in the case of TE or TH polarization, respectively.

3. Layer-by-layer transmission through a stack of dielectric rod arrays

Solid line in Figure 2 represents frequency transmission spectrum (normal incidence of TE polarized wave) through N = 18 arrays of dielectric circular rods arranged in a square lattice. The parameters of the PC were taken from Ref. [16]: ε^{bac} = 1, ε = $(2.9)^2$, $\Lambda_{1,2}$ = 4. Figure 2 shows that the transmission spectrum has two opaque bands

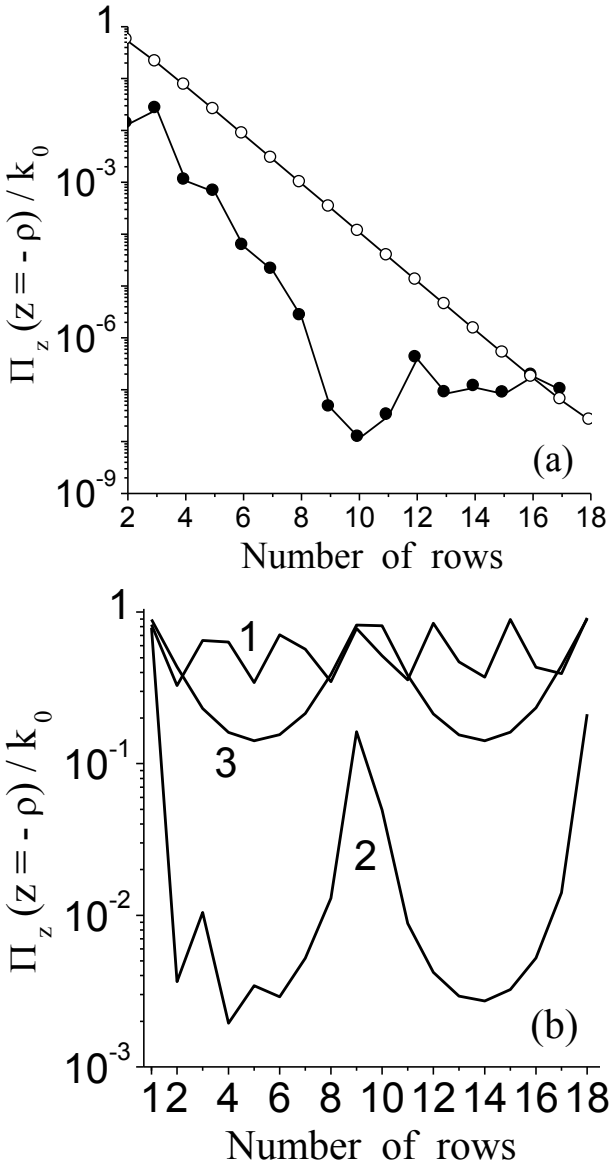


Figure 3: Calculated relative power of EM radiation transmitted through the photonic structure described in Figure 2 versus the number of circular rod arrays for the wavelengths: (a) λ = 4.9 (solid circles), 11.15 (open circles); (b) 4.3 (curve 1), 5 (curve 2), and 8.15 (curve 3).

separated by a transparency window. We denote the wavelength intervals $8.2 \le \lambda \le 12.4$ and $3 \le \lambda \le 6.5$ as the main and additional spectral gaps [10], respectively. Besides, Figure 2 shows (curve with open squares) the exponential power law

$$T_{loc} = \begin{cases} \left(\frac{\ell_e}{N}\right)^2 \exp\left(-\frac{N}{N_0}\right), & if \quad \xi > L, \\ \left(\frac{a}{N}\right)^2 \exp\left(-\frac{N}{N_0}\right), & if \quad \xi < L, \end{cases} \qquad (8)$$

of the scaling theory [17] for wave transmission through a localized dense random medium slab of the same thickness $L = N\Lambda$, with the localization threshold being $\ell_c = \lambda$, the elastic mean free path $\ell_e = 1/nS$, and the localization length ξ. Here $n = \Lambda^{-2}$ is the number density of scatterers with the scattering cross section $S(\lambda)$. The spectral dependence of the parameters ℓ_e, $N_0 \equiv \xi/\Lambda$, and $a = (\ell_c - \ell_e)/\Lambda$ were evaluated according to Ref.[18] with regard to the self-consistent theory of localization.

Plotting the transmission against the penetrated number of the rod arrays, a linear relationship in Figure 3(a) for the wavelength λ = 11.15 (open circles) reveals an exponential decay of the transmission with increasing PC slab thickness L. Exponential decay is preserved for any wavelength taken within the main gap of the spectrum in Fig.2. On the other hand, this is not the case with the wavelengths λ = 4.9 (solid circles in Figure 3(a)). Moreover, three curves in Figure 3(b) demonstrate different modulation periods of transmittance upon the number of rod arrays for the wavelengths corresponding to the transmission peaks within the additional gap (see λ = 4.3 and 5 in Figure 2) and the low wavelength edge of the main gap (λ = 8.15 in Figure 2).

4. Positional disorder and opaque band of two dimensional porous PC

In this section we consider transmission spectra of 2D inverse PCs formed by the hexagonal set of circular cylindrical pores in non-absorbing silicon matrix (Figure 4).

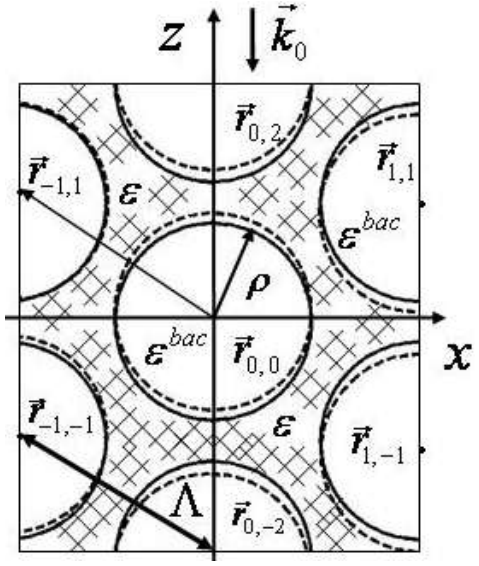


Figure 4: Schematic showing of xz plane of a unit cell of 2D hexagonal porous PC with period Λ. The shaded area corresponds to the matrix. Open areas correspond to the ordered (solid lines) and positionally disordered (dashed lines) cylindrical air pores.

The transmission spectra of 22 arrays of pores were computed by Eqs.(1) and (4) in the case of TE polarized wave incidence and by Eqs.(5) and (7) in the case of TH polarization. The integration in Eq.(2) was carried out over the area G shown in Figure 4 as a shaded part of a unit cell. The spectra for the PC with a disordered unit cell were calculated for each realization of the pore positions with the subsequent averaging of spectra over realization. Spectral positions of the long- and short-wavelength edges of opaque band in each transmission spectrum were determined at a level of 0.1 of the z component $\Pi_z(L)$ of the Poynting's vector for the EM field in the region of wave transmission (the thickness of PC slab L was approximated by 5 unit cells in the z axis direction).

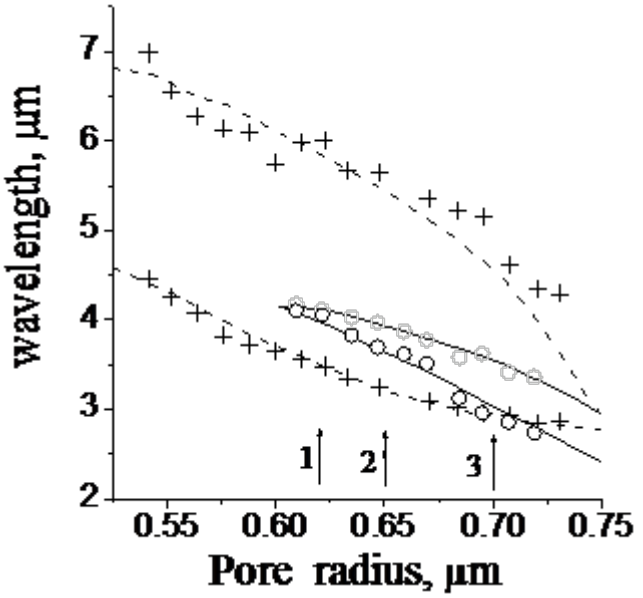


Figure 5: Long-wavelength and short-wavelength edges of an opaque band in the reflection spectrum of the TE (solid curve) and TH (dotted curve) waves incident normally on a silicon matrix with a hexagonal system of circular cylindrical pores as a function of a pore radius. A layer of PCs are formed by 22 arrays of pores with the hexagonal lattice period Λ = 1.5 μm. Symbols (+,○) represent the experimental data [13,20].

Coordinates of the pore centers in the unit cell were defined [19] by the radius vector $\vec{r}_{ij} = \vec{r}_{ij}^{(0)} + \vec{r}_{ij}^{(s)}$ with the components $(x,z)_{ij} = (x,z)_{ij}^{(0)} + (x,z)^{(s)}$, where $(x,z)_{ij}^{(0)}$ are the regular position of the pore centers ($x_{0,0}^{(0)} = x_{0,\pm2}^{(0)} = z_{0,0}^{(0)} = 0$, $x_{1,\pm1}^{(0)} = \sqrt{3}\Lambda/2$, $x_{-1,\pm1}^{(0)} = -\sqrt{3}\Lambda/2$, $z_{0,\pm2}^{(0)} = \pm\Lambda$, $z_{1,\pm1}^{(0)} = \pm\Lambda/2$, $z_{-1,\pm1}^{(0)} = \pm\Lambda/2$), $(x,z)^{(s)}$ is a random displacement of the pore centers in disordered cell $x^{(s)} = (\sqrt{3}\Lambda/2 - 2\rho)\gamma_x$, $z^{(s)} = (\Lambda - 2\rho)\gamma_z$. The quantity $\gamma_{x,z}$ was randomly distributed in the interval from -0.3 up to 0.3.

We compare spectral positions of both edges of opaque bands in transmission spectra of silicon 2D PCs (ε = 11.56) calculated with the same PC period equal to Λ = 1.5 μm but different pore radii with the experimental results corresponding to free-standing bars of porous silicon (see Figures 3 and 5 in Ref.[20]; see, also Ref.[13]). Figure 5 shows a good agreement between the calculated results and the experimental data [13].

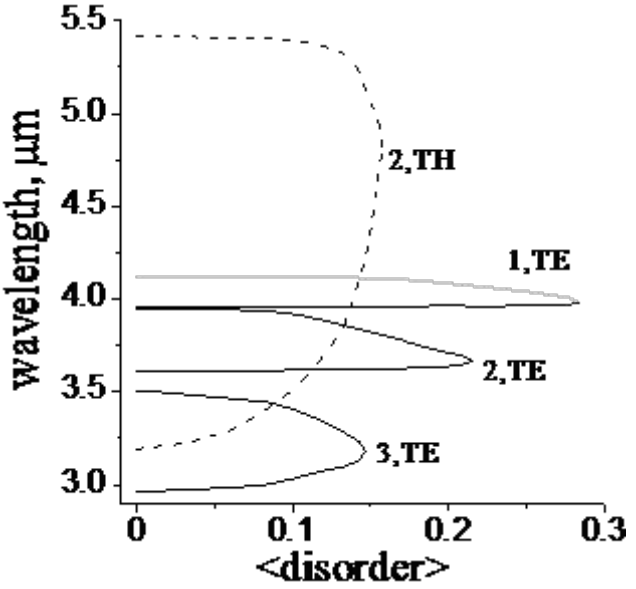


Figure 6: Reflection frequency band edges of the TE and TH polarized radiation from the photonic structure with a period of 1.5 μm and pore radius equal to (*1*) 0.62, (*2*) 0.65, and (*3*) 0.7 m. A random quantity $|\gamma_{x,z}|$ is plotted on the abscissa axis as a measure of pore disordering in PC's unit cell.

Three values of the pore radius (0.62, 0.65, and 0.7 μm), for which the calculations were carried out with random variation of the pore centre positions in the unit cell of PC, are depicted by arrows in Figure 5. The calculation results are presented in Figure 6. Note, the selected pore sizes are approximately equal to the half-period of the hexagonal lattice and comparable to the wavelengths taken within the opaque band of the spectrum of PC with this lattice. The wavelength means the wavelength in the silicon matrix. The specified conditions are optimal for the formation of the most pronounced PC opaque band [21].

Figure 6 shows that the opaque band narrows as the disorder in a pore position in a PC unit cell increases. In the case of TE polarization of incident radiation, the band spectral width in regular structure is 0.16, 0.33, and 0.54 μm at a pore radius of 0.62, 0.65, and 0.7 μm, respectively. In the case of TH polarization, the opaque band is several times

wider (2.22 μm). The opaque band widths reduce by one half at the disorder degree of $\left|\gamma_{x,z}\right|$ = 0.24 (ρ = 0.62 μm); $\left|\gamma_{x,z}\right|$ = 0.17 (TE) and 0.14 (TH) (ρ = 0.65 μm), and $\left|\gamma_{x,z}\right|$ = 0.11 (ρ = 0.7 μm).

5. Discussion and Conclusions

Let us begin discussing our results with a set of dielectric rods. Square lattices of dielectric circular rods (see Figure 1) features two opaque bands in their transmission spectra in the case of TE polarized incident wave. The lowest (main) and high order Mie resonances and the Bragg-like multiple scattering of EM waves were determined [10] as mechanisms of formation and spectral position of these two, main and additional, opaque bands (see Figure 2). The lowest Mie resonance falls into the main band. At the same time, exponential decay of the transmission through an increasing number of rod arrays is calculated for any wavelength taken within this main band. However, we revealed a sufficiently abrupt (exponential-power) decay of the EM wave field versus the PC slab thickness for the wavelength falling in the additional opaque band with transmission spices (see Figure 3(a)). These results allowed one [10] to consider PCs composed of dielectric rods as a good zero approximation in studying wave transmission through a localizing 2D dense random medium slab because (a) the lowest Mie resonance defines the spectral position of the localization window [22] and (b) the band persisted even if a disorder is introduced in a regular set of dielectric rods [14].

As inverse PCs is concerned, we can conclude the following. First, complicated shape of an elementary scatterer practically precludes at least analytical description of resonant scattering process like Mie resonant scattering. Second, the opaque band as a whole is more stable to the disordering in the case of TE polarized incident waves. Third, the opaque band in the spectra of PCs formed by pores with a smaller size is more stable to the positional disordering of pores. At the same time, the smaller are the pores the spectrally narrower is the opaque band. Fourth, the opaque band is more sensitive to the positional disordering of pores in the case of TH polarization.

Acknowledgements

This work was supported in part by the Russian Academy of Sciences projects “Passive multichannel human radio- and acusto-thermotomography in near zone”, “Scientific bases of heterogeneous telecommunication and location systems”.

References

[1] D.S. Wiersma, P.Bartolini, ALagendijk, R. Righini, Localization of light in a disordered medium, *Nature* 390: 671–673, 1997.

[2] M.P.Van Albada, B.A.Van Tiggelen, A. Lagendijk, A. Tip, Speed of propagation of classical waves in strongly scattering media, *Phys.Rev. Lett.* 66: 3132-3135, 1991.

[3] R.G. Newton, *Scattering Theory of Waves and Particles*, McGraw-Hill, New York, 1966

[4] E. Kogan, M. Kaveh, Diffusion constant in a random system near resonance, *Phys. Rev. B* 46: 10636–10640, 1992.

[5] A. Ishimary, *Wave Propagation and Scattering in Random Media,* Academic Press, New York, 1995.

[6] Yu.N. Barabanenkov, L.M. Zurk, M. Yu. Barabanenkov, Poynting's Theorem and Electromagnetic Wave Multiple Scattering in Dense Media Near Resonance. Modified Radiative Transfer Equation, *J. Electromagnetic Waves and Applications* 9: 1393-1420, 1995.

[7] P. Wölfle, D. Vollhardt, *Self-Consistent Theory of Anderson Localization*, in Electronic Phase Transitions, Elsevier Science, Amsterdam, 1992.

[8] B.A.Van Tiggelen, A. Lagendijk, D.S. Wiersma, Reflection and transmission of waves near the localization threshold, *Phys.Rev. Lett.* : 84, 4333-4336, 2000.

[9] S. John, Strong localization of photons in certain disordered dielectric superlattices, *Phys.Rev. Lett.* :58, 2486-2489, 1987.

[10] Yu.N. Barabanenkov, M.Yu.Barabanenkov, Mie resonances and Bragg-like multiple scattering in opacity of two-dimensional photonic crystals, *J. Opt. Soc. Am. A* : 23, 581-585, 2006.

[11] E.E. Gorodriichev, A.I. Kuzovlev, D.B. Rogozkin, Influence of the inhomogeneity properties on the depolarization of multiply scattered light in a turbid medium, *Proc. SPIE* 5829: 74-87, 2005.

[12] M. Xu, R.R. Alfano, Light Depolarization in Turbid Media, *Proc. SPIE* 5693: 88-91, 2005.

[13] A. Birner, A.-P.Lia, F. Müller, U. Gösele, P. Kramper, V. Sandoghdar, J. Mlynek, K. Busch, V. Lehmann, Transmission of a microcavity structure in a two-dimensional photonic crystal based on macroporous silicon, *Materials Science in Semiconductor Processing* 3: 487-491, 2000.

[14] M. Bayindir, E. Cubukcu, I. Bulu, T. Tut, E. Ozbay, C.M. Soukoulis, Photonic band gaps, defect characteristics, and waveguiding in two-dimensional disordered dielectric and metallic photonic crystals, *Phys. Rev. B* 64: 195113-7, 2001.

[15] Yu.N. Barabanenkov, V.L. Kouznetsov, M.Yu. Barabanenkov, Transfer relations for electromagnetic wave scattering from periodic dielectric one-dimensional interface, *Electromagnetic waves, v.24, Progress in Electromagnetic Research* (ed. J.A.Kong) EMW Publishing, Cambridge, Massachusetts USA, 1999, pp.39-75.

[16] E. Centeno, B. Guizal, D. Felbacq, Multiplexing and demultiplexing with photonic crystals, *J. Opt. A.: Pure Appl. Opt.* 1: L10 - L13, 1999.

[17] D. Sornette, Anderson localization and wave absorption, *J. Stat. Phys.* 56: 669 – 680, 1989.

[18] C.A. Condat, T.R. Kirkpatrick, *Localization of acoustic waves, Scattering and Localization of Classical Waves in Random media*, ed. P.Sheng, World Scientific, Singapure, 1990.

[19] Zhi-Y. Li, X. Zhang, Zh.-Q. Zhang, Disordered photonic crystals understood by a perturbation formalism, *Phys. Rev. B* 61: 15738 – 15748, 2000.

[20] A. Birner, R.B. Wehrspohn, U.M. Gösele, K. Busch, Silicon-Based Photonic Crystals, *Adv. Mater.* 13: 377 - 388, 2001.

[21] M. Megens, W.L. Vos, Particle Excursions in Colloidal Crystals, *Phys. Rev. Lett.* 86: 4855-4858, 2001

[22] A.A. Chabanov, A.Z. Genack, Photon Localization in Resonant Media, *Phys. Rev. Lett.* 87: 153901-4, 2001.

On the dynamics of cutting arc plasmas: the role of the power supply ripple

L. Prevosto[1,*], B. Mancinelli[1], and H. Kelly[1,2]

[1]Grupo de Descargas Eléctricas, Departamento Ingeniería Electromecánica
Facultad Regional Venado Tuerto (UTN) Laprida 651 (2600), Venado Tuerto (Santa Fe), Argentina
[2]Instituto de Física del Plasma (CONICET), Departamento de Física
Facultad de Ciencias Exactas y Naturales (UBA)
Ciudad Universitaria Pab. I, (1428) Buenos Aires, Argentina
*corresponding author, E-mail: prevosto@waycom.com.ar

Abstract

The power sources used in cutting arc torches are usually poorly stabilized and have a large ripple factor. The strong oscillatory components in the voltage and arc current produce in turn, large fluctuations in the plasma quantities. Experimental observations on the dynamics of the non-equilibrium plasma inside the nozzle of a 30 A oxygen cutting torch are reported in this work.

1. Introduction

The plasma cutting process is characterized by a transferred electric arc that is established between a cathode, which is a part of the cutting torch, and a work–piece (the metal to be cut) acting as the anode [1]. In order to obtain a high–quality cut, the plasma jet must be as collimated as possible (i.e., it must have high power density). To this end, the transferred arc is constricted by a metallic tube (a nozzle) with a small inner diameter (of the order of one millimeter). A vortex–type high-pressure flow is forced through the nozzle to provide arc stability and to protect its inner wall.

Time fluctuations in thermal plasma direct–current (dc) devices are important for any technological application. A special effort has been made by several researchers (see for instance Ref. [2] to [4]) both from an experimental or a numerical points of view, to understand the dynamics of the plasma flow inside non–transferred arc torches (like spraying torches). In such torches, large plasma jet fluctuations arise either from ripple in the direct–current power supply, or random arc root movement at the anode, or combined effects of gas dynamic and electromagnetic instabilities causing cold gas entrainment. On the other hand, it is implicitly assumed in most of the experimental or numerical works in transferred arc torches (like cutting torches), that the plasma is steady [1]. However, the power sources used in such plasma torches are usually poorly stabilized and have a large ripple factor (with root–mean–square –rms– deviations that vary between ≈ 5 to 10 % of the mean voltage). This is due to the fact that the torch currents are of the order of 100 A, which difficult an effective filtering of the ripple. If a 3–phase transductor type of power supply is used, then the fundamental ripple frequency is 150 Hz and if 3–phase silicon controlled rectifier based power supply is used, then the ripple frequency is 300 Hz. The strong oscillatory components in the voltage and arc current should produce in turn, large fluctuations in the plasma quantities that vary at the ripple frequency.

In this work, experimental observations on the plasma dynamics inside the nozzle of a cutting torch are reported. It is employed a technique previously developed in our laboratory consisting in using the nozzle as a large–sized Langmuir probe [5].

2. Experimental set–up

The experiment was carried out using an oxygen high–energy density cutting torch. It consisted of a cathode centered above an orifice in a converging-straight copper nozzle without liquid cooling. The cathode was made of copper (7 mm in diameter) with a hafnium tip (1.5 mm in diameter) inserted at the cathode center. A flow of oxygen gas cooled the cathode and the nozzle and was also employed as the plasma gas. The gas passed through a swirl ring to provide arc stability. The nozzle consisted in a converging-straight bore (with a bore radius R_N = 0.5 mm and a length L_N = 4.5 mm) in a copper holder surrounding the cathode (with a separation of 0.5 mm between the holder and the cathode surface). To avoid plasma contamination by metal vapors from the anode, a rotating steel disk was used as the anode, with its upper surface located at 6 mm from the nozzle exit. A well–stabilized arc column was obtained, with the arc root sliding on the disk lateral surface. It was found that this surface resulted completely not melted (thus, practically no metal vapors from the anode were present in the arc). More details on the experimental configuration can be found elsewhere [6]. A 3–phase transductor power supply with a voltage ripple level of ≈ 7 % and a fundamental frequency of 150 Hz was used to run the torch. The measured torch operating conditions were: arc current 30 A (rms), gas mass flow rate 0.39 g s^{-1} and torch chamber pressure p_{ch} = 0.6 MPa. For the voltage measurements, the reference electrode was the

anode (grounded) and the cathode voltage resulted in – 145 V (rms).

As previously quoted, the nozzle was used as a large sized Langmuir probe. Note that the necessary condition for a comprehensive use of a Langmuir probe (that is: the plasma should not be perturbed sufficiently far away from the probe surface) is accomplished in this case, since the nozzle–probe behaves as a natural boundary to the arc. The nozzle biasing circuit is shown in Fig. 1. Different nozzle–anode voltage values (V_N) were obtained using a high–impedance rheostat (2 kΩ of total resistance), connected between the cathode and the anode of the arc, while the nozzle current (i_N) was calculated from the voltage drop through a small resistance R_0. In practice, the nozzle was always biased close to the cathode voltage. Both the V_N and i_N waveforms were registered by using a two–channel digital oscilloscope (Tektronix TDS 1002 B) with a sampling rate of 500 MS/s and an analogical bandwidth of 60 MHz.

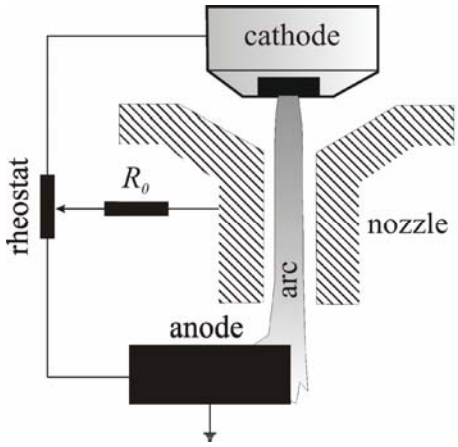


Figure 1: Schematic of the nozzle biasing circuit.

Finally, a set of sweeping electrostatic probes [6] was used to determine the floating potential close to the nozzle exit (at 0.5 mm). The plasma potential value (V_p) at the nozzle exit was then obtained from the floating experimental value taking into account an electric field strength of ≈ 7 V/mm in the external part of the arc [7] and the voltage drop between the plasma and the floating potentials (which is proportional to the plasma electron temperature). In the case we are considering, we will show later that the electron temperature is relatively low (about 5000–6000 K at the arc border) and hence such difference results of only about 5 V [8].

3. Results and discussion

A typical ion current (i_N) waveform for a rms nozzle voltage value close to the cathode one is shown in Fig. 2. The result of performing Fourier analysis on the ion current signal is also shown. The rms value of the oscillatory component reaches ≈ 52 % of the mean value with a fundamental frequency (f) of 150 Hz (i.e., the ripple frequency). A marked spike of short duration (of the order of 100 μs) which actually presents a complex fine structure associated with the non–destructive double–arcing phenomenon is clearly recognized in this figure [9].

From the floating potential measurement close to the nozzle exit, a plasma potential mean value of ≈ –20 V (with a rms deviation of 7 %) was obtained for the given arc operating conditions.

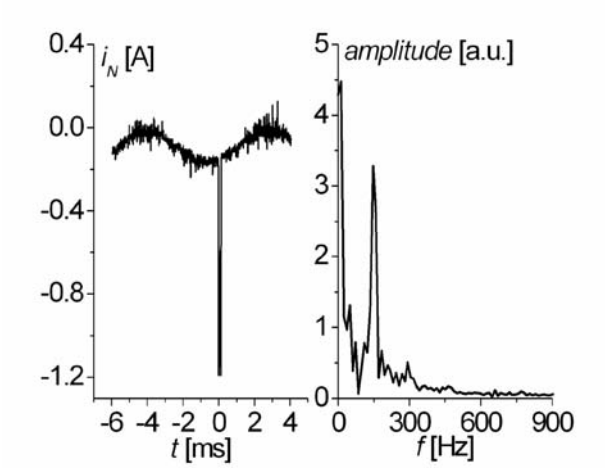


Figure 2: Typical ion current waveform. The FFT analysis is also shown.

In what follows, it will be presented a physical interpretation of the ion current signal taking into account the ripple component. This interpretation is based on the use of a physical model for the space-charge layer between the arc plasma and the nozzle wall. Since the temporal variations introduced by the ripple are very slow as compared with the characteristic times in the layer (electron plasma frequency, transit time of sound perturbations along the layer, etc.), a previously developed steady model [5,10] will be adopted, with the additional assumption that the plasma quantities follows instantaneously the arc current and arc voltage variations.

At the vicinities of the nozzle wall the electron temperature (T_e) is well decoupled from the gas temperature (close to the temperature of the nozzle wall T_h ≈ 1000 K). The composition of this non–equilibrium plasma was calculated by using the generalized Saha–equation [11]

$$\frac{n^2}{n_n} = 2\frac{Q_i}{Q_0}\left(\frac{2\pi m k T_e}{h^2}\right)^{3/2} \exp\left(-\frac{E_I}{k T_e}\right) \qquad (1)$$

plus the equation of state

$$\frac{p}{k} = T_e\, n + T_h\,(n + n_n) \qquad (2)$$

(where n is the plasma density, n_n is the neutral particle density, Q_i and Q_o are the statistical weights of oxygen ions and atoms, m is the electron mass, k is the Boltzmann's constant, h is the Planck's constant, E_I is the ionization energy of the oxygen atoms, and p is the pressure).

The ion current collected by the nozzle was calculated by integrating the ion flux evaluated at the edge of the plasma–layer boundary

$$i_N = 2\pi R_N \, e \int_{z=0}^{z=L_N} \Gamma_+ \Big)_s \, dz \qquad (3)$$

where $\Gamma_+ \Big)_s = n_s \, v_{+s}$ (z is the coordinate directed along the nozzle wall). Due to the colisional regime of the layer [5,10] the ion entrance velocity v_{+s} is lower than the Bohm velocity in a factor of $\left(\lambda_+ / \lambda_{Ds} \right)^{1/2}$ [12]. (Here λ_+ is the colisional ion mean free path and λ_{Ds} is the electron Debye length at the layer entrance)

The thickness of such a space–charge layer was approximated as [13]

$$D \approx 2.2 \times 10^4 \, \Delta V^{3/5} \, n^{-1/2} \, T_e^{-1/10} \qquad (4)$$

where all the physical variables are given in MKS units ($\Delta V \equiv V_N - V_p$). Eq. (4) allows to determine D at the nozzle exit, since at this position V_p is known from the floating potential measurements.

The formulation also includes the following assumptions: (i) a linear variation of the pressure (p) along the nozzle (where $p(0) = p_{ch}$ and $p(L_N) = 0.1$ MPa); (ii) at the adjacency of the nozzle wall T_e only depends on the radial coordinate; and (iii) a constant value of the layer thickness along the nozzle. Assumptions (i) and (ii) have been shown to be valid in cutting torches (e.g., [14]). Concerning the assumption (iii), it has been shown to be valid in cutting torches operated at low gas flow rates [5]. With all these considerations, Eqs. (1), (2), and (3) constituted a closed system that allowed to obtain n_n, n, and T_e at the plasma–layer boundary for given values of $p(z)$ and i_N. In particular, the integral of Eq. (3) was approximated by a nine–term polynomial using the well–known Chebyshev formula. Finally, the D value was obtained from the decoupled Eq. (4) in terms of the previously obtained plasma quantities.

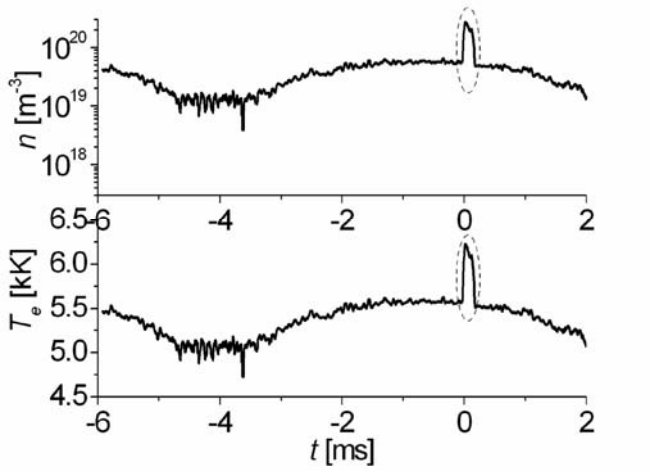


Figure 3: The electron temperature and the plasma density calculated from the experimental results showed in Fig. 2.

Fig. 3 shows the oscillations of T_e and the plasma density n corresponding to the experimental results showed in Fig. 2. Note that the T_e and n values during the spike development cannot be taken with confidence since the assumptions employed to perform the inversion could not be valid (especially Eq. (4), which assumes that the particle creation or destruction processes can be ignored) at these times. The observed electron temperature (mean value ≈ 5 400 K) shows a rms deviation ≈ 5 % (± 300 K), which is of the order of the arc voltage ripple level. A considerable different situation occurs with n. In this case the rms deviation was ≈ 75 %, much greater than that of T_e. This is expected because in this scenario Eq. (1) approximately gives $n \propto T_e^{\alpha}$ (with $\alpha \approx 15$).

4. Conclusions

The non–equilibrium plasma inside the nozzle is far from the steady state in time, in contrast to what is frequently assumed. The ripple of the power source was identified as the main oscillation source. Arc electric oscillations due to the power source ripple exert strong influence on the characteristics of the plasma inside the nozzle of a cutting torch. In particular, the most sensitive quantity is the plasma density which shows a rms deviation ≈ 75 %, much greater than that of the electron temperature of the order of the arc voltage ripple level ≈ 7 %. This is expected because the plasma density grows strongly with the electron temperature for relatively low values ≈ 5000–6000 K.

Acknowledgements

This work was supported by grants from CONICET (PIP 5378) and Universidad Tecnológica Nacional (PID 1389). L P and H K are members of the CONICET.

References

[1] V. A. Nemchinsky and W. S. Severance, What we know and what we do not know about plasma arc cutting, *J. Phys. D*: *Appl. Phys.* 39: R423–438, 2006.

[2] V. Rat and J. F. Coudert, Pressure and arc voltage coupling in dc plasma torches: Identification and extraction of oscillation modes, *J. Appl. Phys.* 108: 043304, 2010.

[3] J. F. Coudert and V. Rat, Influence of configuration and operating conditions on the electric arc instabilities of a plasma spray torch: role of acoustic resonance, *J. Phys. D: Appl. Phys.* 41: 205208, 2008.

[4] S. Ghorui and A. K. Das, Origin of fluctuations in atmospheric pressure arc plasma devices, *Phys. Rev. E* 69: 026408, 2004.

[5] L. Prevosto, H. Kelly and B. Mancinelli, On the physical origin of the nozzle characteristic and its connection with the double-arcing phenomenon in a cutting torch, *J. Appl. Phys*. 105: 013309, 2009.

[6] L. Prevosto, H. Kelly and B. Mancinelli, On the Use of Sweeping Langmuir Probes in Cutting Arc Plasmas – Part I: Experimental Results, *IEEE Trans. Plasma Sci*. 36: 263–270, 2008.

[7] L. Prevosto, H. Kelly and F. O. Minotti, On the Use of Sweeping Langmuir Probes in Cutting Arc Plasmas –

Part II: Interpretation of the Results, *IEEE Trans. Plasma Sci.* 36: 271–277, 2008.
[8] Y. P. Raizer, *Gas Discharge Physics*, Berlin, Germany: Springer, 1991.
[9] L. Prevosto, H. Kelly and B. Mancinelli, On the dynamics of the space-charge layer inside the nozzle of a cutting torch and its relation with the "non-destructive" double-arcing phenomenon, *J. Appl. Phys.* 110: 083302, 2011.
[10] L. Prevosto, H. Kelly and B. Mancinelli, On the space-charge boundary layer inside the nozzle of a cutting torch, *J. Appl. Phys.* 105: 123303, 2009.
[11] M. C. M. van de Sanden, P. P. J. M. Schram. A. G. Peeters, J. A. M. van der Mullen, and G. M. W. Kroesen, Thermodynamic generalization of the Saha equation for a two-temperature plasma, *Phys. Rev. A* 40: 5273–5276,1989.
[12] R. N. Franklin, You cannot patch active plasma and collisionless sheath, *IEEE Trans. Plasma Sci.* 30: 352–356, 2002.
[13] T. E. Sheridan and J. Goree, Colisional plasma sheath model, *Phys. Fluids B* 3: 2796–2804, 1991.
[14] S. Ghorui, J. V. R. Heberlein and E. Pfender, Non equilibrium modelling of an oxygen-plasma cutting torch, *J. Phys. D: Appl. Phys.* 40: 1966–1976, 2007.

Magnetic Shape Memory Alloys as smart materials for micro-positioning devices

A. Hubert[1*], N. Calchand[1], Y. Le Gorrec[1], J.-Y. Gauthier[2]

[1]Institut Femto-ST UMR 6174, UFC/ENSMM/UTBM/CNRS,
24 rue Alain Savary, 25000 Besançon, France
[2]Laboratoire Ampère UMR 5005, Université de Lyon/CNRS,
INSA Lyon, bâtiment A. de Saint-Exupéry, Avenue Jean Capelle,
69621 Villeurbanne cedex, France
*corresponding author, E-mail: arnaud.hubert@femto-st.fr

Abstract

In the field of microrobotics, actuators based on smart materials are predominant because of very good precision, integration capabilities and high compactness. This paper presents the main characteristics of Magnetic Shape Memory Alloys as new candidates for the design of micromechatronic devices. The thermo-magneto-mechanical energy conversion process is first presented followed by the adequate modeling procedure required to design actuators. Finally, some actuators prototypes realized at the Femto-ST institute are presented, including a push-pull bidirectional actuator. Some results on the control and performances of these devices conclude the paper.

1. Introduction

Electromagnetic devices have become promising contenders in the area of ultra-high precision manufacturing, manipulation and sensing. Most of these promising new technologies uses active/adaptive materials as a base for actuation principles because of compactness, integrations and smart use capabilities [1, 2]. This paper reports recent results obtained using a new type of smart material called Magnetic Shape Memory Alloy (MSMA) which is an alloy of Ni-Mn-Ga.

Currently, most of the high-precision devices use piezoelectric materials such as PZT because of their high-dynamic bandwidth and their nearly linear behaviour. Piezoelectric materials are used to design micropositioning devices by using *classical* mode of working [3, 4] or by using *stick and slip* mode of working [5, 6]. In the field of magnetic active materials, the main applications use magnetostrictive materials [7, 8] especially Terfenol-D. This material is the most used because of the important progress in its performances since its first use in 1950 by the Naval Ordnance Laboratory in the USA and its high magneto-mechanical coupling compared to the other magnetostrictive materials. Examples of actuators and positioning devices using magnetostrictive materials can be found in [9, 10, 11].

Piezoelectric and magnetostrictive materials are the most used adaptive materials for positioning application. Nevertheless, alternative solutions exist and MSMAs are a class of active materials which typically generate 6% strain in response to externally applied magnetic fields [12]. In contrast to conventional heat driven shape memory alloys (SMAs), the magnetically driven MSMAs exhibit higher operating frequency, making them attractive for actuation applications. Most of the work on characterization and modeling of MSMAs has been focused on quasistatic actuation, i.e., strain dependence on magnetic field. Very few studies take into account the dynamical behaviour and even fewer propose MSMA based actuator prototypes. The purpose of this paper is to present a modeling procedure taking into account the complex magneto-mechanical behaviors of MSMA and the dynamical characteristics of actuators at the same time, to design new micropositioning devices.

Among all the offer concerning magnetic active materials, Magnetic Shape Memory Alloy is a relatively new candidate. It was first experimented in 1995/1996 at the MIT for the Ni-Mn-Ga alloy [13] and at the University of Minnesota for the Fe-Pd alloy [14]. Since these first works, lots of researchs have been conducted all around the world (see [15, 16] for reviews) but very few concrete applications exist today due to the complex dynamic behaviour of MSMA and due to the difficulties to improve its manufacturing process. Currently, only single crystal samples present significant magneto-mechanical coupling characteristics and even if a lot of studies are conducted concerning thin films deposition and polycrystal samples [17, 18], these types of structures are presently less adequate for actuation applications because of a lower magneto-mechanical coupling.

MSMA can be seen as a mixture of a classical shape memory alloy (SMA) and a magnetostrictive material. In a way, its microscopic behaviour is similar to SMAs but strain is not only due to a martensite/austenite phase transformation but is also due to a martensite reorientation under magnetic fields. In this second mode of working – martensite rearrangement –, MSMA can be compared with standard magnetostrictive materials but with a much more important magneto-mechanical coupling (6 % of maximal strain for Ni-Mn-Ga instead of 0.16 % for Terfenol-D).

This paper first explains the working principle of this active material and gives some tools for static and dynamic behaviour modeling. Then, some design rules will be presented to propose efficient actuators. These modeling works will be used as guidelines to design a new micro-positioning stage. It will be based on two antagonist MSMA-based actuators to perform a one-degree-of-freedom linear axis stage with a full-range motion of the order of millimeters and a micrometers precision. Measurements conducted on the prototype will be presented and commented.

2. Basis on MSMA modeling and behaviour

2.1. MSMA Properties and Characteristics

As seen before, the working principle of MSMA is quite similar to the working of SMA but its actuation can also result from magnetic field application. This second mode of working allows to increase significantly the dynamical bandwidth of the device because it uses a magneto-mechanical energy conversion process instead of a thermo-mechanical. Since fifteen years, these materials knew some improvements concerning mainly the working temperature range and the maximum available strain. When actuated by magnetic fields, a large strain (6 to 10 %) is obtained with a response-time in the range of milliseconds (to compare with tenth of seconds or even seconds for SMA). The MSMA used in this paper is a non-stoechiometric Ni-Mn-Ga monocrystal corresponding to the most currently used MSMA materials. In this alloy, the martensite phase appears in three different *variants* corresponding to the three possible crystallographic directions in the sample (see Fig. 1 (a)).

The martensitic reorientation principle is presented in Fig. 1 (b): at high temperature, the MSMA sample is in austenitic phase (A). After a cooling process, the austenite phase is transformed into a martensite phase without any favoured variants. Therefore the resulting sample contains martensite variants into three equal portions (M1, M2 and M3). If a mechanical stress is applied in a specific direction, then the fraction of variant with its short axis in this direction grows. If this stress is high enough then the sample will only contain this variant (for example M2 in Fig. 1 (b)). If the stress decreases, the volume fraction of the M2 variant also decrease but in an irreversible behaviour (large hysteresis). In a same way, if a magnetic field is applied, the variant with its easy magnetization axis in the field direction, is favoured. For MSMA, the easy magnetization direction is the same as the short axis of the M1 variant. In this case, this variant fraction increases as shown in Fig. 1 (b) by the application of a magnetic field perpendicular to the stress field. The balance between magnetic field and mechanical stress allows a control of the macroscopic strain. With a pre-stress, one can therefore obtain an actuator driven by the magnetic field only. Austenite phase can also be recovered by heating.

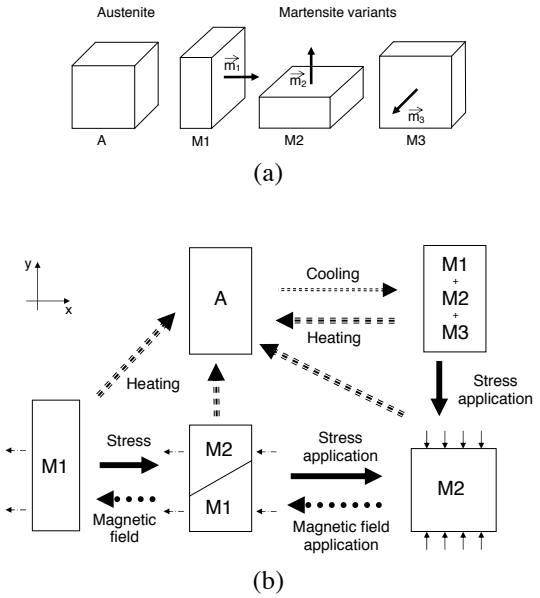


Figure 1: MSMA behaviour: (a) austenite phase and the three martensite variants and (b) martensitic reorientation: effects of mechanical stress, magnetic field and temperature.

Besides these interesting properties, the material also has some important drawbacks. They are the brittleness of the single-crystal, the high required magnetic field (400 kA/m), the large dependence of the material parameters on temperature changes, a small blocking stress (2-3 MPa) and a large hysteretical thermo-magneto-mechanical behaviour. More details about the structural properties of this material can be found in [15].

2.2. Quasi-Static Modeling of MSMA

Two theories can be used to model the behaviour of MSMA:

- The first one is based on *microscopic* properties and physics of solid. The following papers are representative of the works done on MSMA materials with this approach [19, 20, 21, 22].

- The second one is based on *macroscopic* properties and thermodynamics. In [23, 24, 25], such models are proposed whereas in [26, 27, 28], a more mechatronics-based approach is taken. They explicitly take into account the salient features (dynamics of system) required to make actuators.

While the first theory is prefered by physicists, the second one is prefered by engineers and is best-suited to design actuators and micropositioning applications. This paper will focus mainly on actuator design and only few details will be given concerning our modelling works (recent results could

be found in [29]). To simplify the mathematical expressions, only isothermal actuation in the xy plan is considered in this paper with a control of position along the x axis. In such a configuration, only M1 and M2 variants are relevant.

To model quasi-static behaviour of MSMA using the thermodynamic approach, it is first necessary to propose an expression for the internal energy $\mathcal{U}$ or a similar thermodynamic potentiel using Legendre Transform (for exemple, Gibbs free energy $\mathcal{G}$ or Helmholtz free energy $\mathcal{F}$). This potential must take into account all physical phenomena that are necessary to capture the experimental behaviour [30] namely:

- chemical energy,
- thermal energy,
- mechanical energy,
- magnetic energy.

In the case of MSMA, an irreversible behaviour takes place when phase rearrangement or transformation appears. This one is associated with a dissipation function and a Clausius-Duhem inequality is able to take into account the irreversibility and the increase of the total entropy of the system. In our work, thermodynamics of irreversible processes with internal variables is used. These internal variables are quantities used as additionnal *internal state variables*. This additional knowledge from the micro-physical material behaviour permits to compute explicitely the available work in the case of irreversible processes.

The complete thermodynamic expressions of MSMA used by authors are fully described in [28] and the internal variables are linked to a micro/macro approach. The Fig. 2 displays a Representative Elementary Volume of the MSMA, i.e. a mean – macroscopic – representation of the microscopic structure of this material. This one allows to express different internal variables:

- z_o: austenite volume fraction,
- z_k: volume fraction of martensite variant k ($k \in \{1; n\}$), i.e. the martensite presents n different variants. Let $\sum_{k=1}^{n} z_k = (1 - z_o)$ be the global fraction of martensite,
- α and $(1 - \alpha)$ the proportions of the Weiss domains inside a variant representing the Representative Elementary Volume,
- θ the rotation angle of the magnetization vector associated to the two Weiss domains of variant M_2. Indeed, under the magnetic field $\vec{H}$, this magnetization rotates in order to become parallel to the magnetic field. As the field $\vec{H}$ is parallel to $\vec{x}$, there is no rotation of Weiss domains of variant M_1.

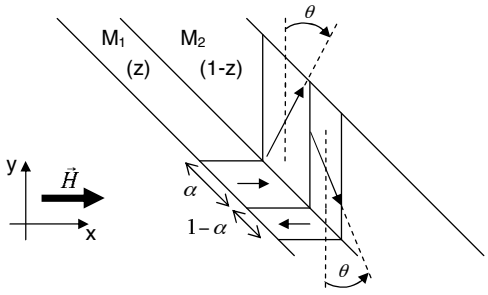


Figure 2: Representative Elementary Volume when the MSM sample is only composed of two martensite variants M_1 and M_2 ($z = z_1$ and $1 - z = z_2$).

In [28], we proposed the following expression for the Gibbs free energy :

$$\begin{aligned}\rho G(\sigma, H, T, z, \alpha,\theta\,) &= C_p\left[(T - T_o) - T \cdot \log\frac{T}{T_o}\right] \\ &- \sigma\gamma z - \frac{\sigma^2}{2E} + K_{12} z(1 - z) \\ &- \mu_o M_S\left(z\left((2\alpha - 1)H - \frac{M_S}{2\chi_a}(2\alpha - 1)^2\right)\right. \\ &\left. + (1 - z)\left((\sin\theta)H - \frac{M_S}{2\chi_t}(\sin\theta)^2\right)\right)\end{aligned} \tag{1}$$

where σ, H and T are the stress, the applied magnetic field and the temperature of the MSMA sample, respectively. All other variables are material parameters and can be experimentally identified (see [31]). In this expression, the magneto-thermo-mechanical coupling is expressed by the choice of the internal variable z. The total strain ε can therefore be deduced as:

$$\varepsilon = -\frac{\partial(\rho G)}{\partial\sigma} = \frac{\sigma}{E} + \gamma z = \varepsilon^e + \varepsilon^{dtw} \tag{2}$$

with ε^e the elastic strain and ε^{dtw} the strain resulting from a rearrangement between M1 and M2 variants ($\gamma = 0.06$ is the maximal strain due to a complete martensitic rearrangement). The magnetization M can also be computed as:

$$\mu_o M = -\frac{\partial(\rho G)}{\partial H} \tag{3}$$

$$= \mu_o M_S\left((2\alpha - 1)z + \sin\theta(1 - z)\right) \tag{4}$$

With this modelling procedure, a thermodynamical force π^z associated with the z fraction of martensite is also deduced as:

$$\begin{aligned}\pi^z = -\frac{\partial\rho G}{\partial z} &= \sigma\gamma - K_{12}(1 - 2z) \\ &+ \mu_o M_S\left[(2\alpha - 1)H - \frac{M_S}{2\chi_a}(2\alpha - 1)^2\right. \\ &\left. - H\sin\theta + \frac{M_S}{2\chi_t}\sin^2\theta\right]\end{aligned} \tag{5}$$

This term can be used explicitly in the Clausius-Duhem inequality to compute the dissipation dD, i.e. the irreversibility of the processes, associated with a phase rearrangement

processes.

$$dD = \pi^z dz \geq 0 \tag{6}$$

This explicit expression can therefore be used to integrate the available work $\int d\mathcal{W}$ resulting from the energy conversion process. This quasistatic modeling based on thermodynamics of irreversible processes can be used to predict accuratelly the stress/strain behaviour of MSMA samples as a function of the applied magnetic field and applied external stress. A comparison between simulation and experimental results are plotted in Fig. 3 (see [28]).

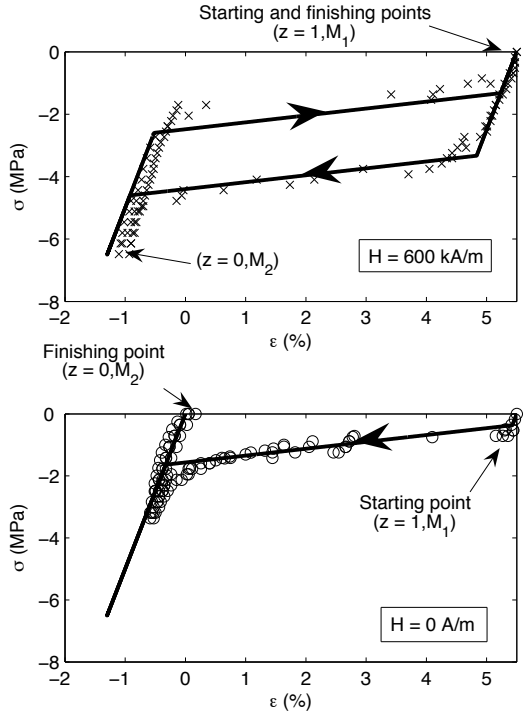


Figure 3: Strain *vs* stress plots for two different magnetic fields: model prediction (solid line) and experiments (crosses or circles) [28].

2.3. Dynamic modeling of MSMA based actuators

At this point, it should be emphasized that an actuator is not only a smart material but a more complex mechatronics device which includes a smart material, a mechanical structure, a power supply, a load, its associated control system and a few other components. To model the dynamic behaviour of such a device, the authors proposed in [31] to associate thermodynamics of irreversible processes with an Hamiltonian modeling. The irreversible behaviour associated with the MSMA non-linearity can be captured with internal variables and the behaviour of other components can be capture with generalized coordinates $\mathbf{q}$ and generalized momenta $\mathbf{p}$. This association allows to extend the "classical" Hamiltonian formalism to the non-conservative case (open and dissipative) with geometric or kinematic constraints. The Hamiltonian formalism uses an energy function – a thermodynamic potential – corresponding to the total energy of the system, the *Hamiltonian* function $\mathcal{H}(\mathbf{q}, \mathbf{p})$ [32, 33].

For a conservative system – a thermodynamically close and non-dissipative system –, we simply have: $\mathcal{H}(\mathbf{q}, \mathbf{p}) = \mathcal{T}(\mathbf{p}) + \mathcal{V}(\mathbf{q})$ with $\mathcal{T}$ and $\mathcal{V}$ the kinetic and potential/internal energy of the system. But an *open* system as our actuator means that it exchanges some energy with external environment. This is the case, for example, when the system is controlled with an external generalized force $\mathbf{f}_{ext}$ depending explicitly on the time t (we then speak about *non-autonomous* systems). For our system, the external generalized force is the current or the voltage – depending on the type of control – supplied by the electronic power converter. Furthermore, a *dissipative* system means that some part of the inner energy is non-available after *any motion* of the system as claimed by irreversibility and the Clausius-Duhem inequality. This could be computed using dissipated energy during any motion. Finally, system with *constraints* means that there is some topologic constraints on the admissible motion of this system. These geometric or kinematic constraints can be taken into account in the dynamical equations using a Lagrange multiplier technique. To include all these phenomena, we make use of an *extented Hamiltonian function* $\mathcal{H}'$ with these features:

- The external generalized forces $\mathbf{f}_{ext}(\mathbf{q}, t)$ are taking into account in the variation of $\mathcal{H}'$ by adding the influence of their virtual works $\delta\mathcal{W}_{ext} = \mathbf{f}_{ext}(\mathbf{q}, t) \cdot \delta\mathbf{q}$.
- Dissipations by static and viscous frictions are taking into account by adding their dissipated energies variations $\delta\mathcal{Q}_s(\mathbf{q})$ and $\delta\mathcal{Q}_v(\dot{\mathbf{q}})$. The dissipation by viscous friction $\mathcal{Q}_v(\dot{\mathbf{q}})$ is computed with a Rayleigh dissipation function $\mathcal{R}(\dot{\mathbf{q}})$ like $\mathcal{Q}_v(\dot{\mathbf{q}}) = \int_{t_1}^{t_2} \mathcal{R}(\dot{\mathbf{q}})\, dt$.
- The *holonomic* kinematic constraints $\mathbf{c}(\mathbf{q}) = 0$ are taking into account with a Lagrange multipliers technique by adding the term $\lambda \cdot \delta\mathbf{c}(\mathbf{q})$ to the variation $\delta\mathcal{H}'$.

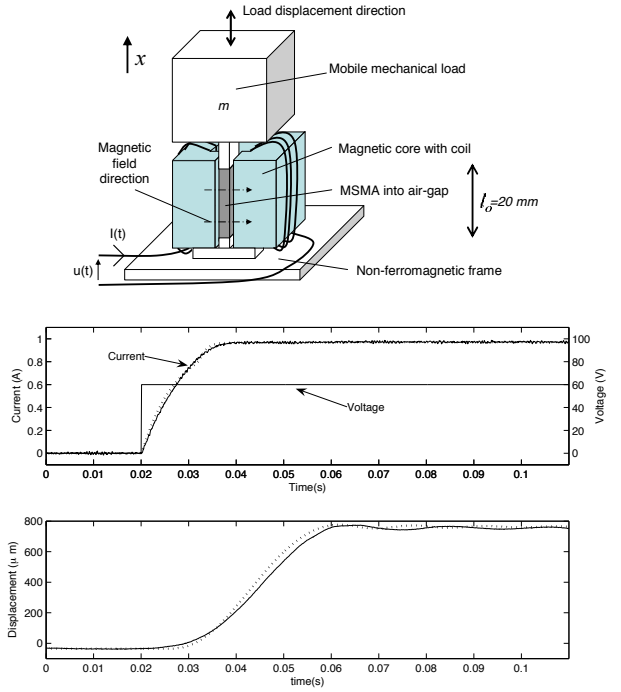
Finally, we have:

$$\delta\mathcal{H}' = \delta\mathcal{H} - \mathbf{f}_{ext} \cdot \delta\mathbf{q} - \delta\mathcal{Q}_s - \delta\mathcal{Q}_v + \lambda \cdot \delta\mathbf{c} \tag{7}$$

The Hamilton principle using $\delta\mathcal{H}'$ gives the following Hamilton equations:

$$\begin{cases} \dot{q}_i = \dfrac{\partial \mathcal{H}}{\partial p_i} \\ \dot{p}_i = -\dfrac{\partial \mathcal{H}}{\partial q_i} - \dfrac{\partial \mathcal{R}}{\partial \dot{q}_i} + \dfrac{\partial \mathcal{Q}_s}{\partial q_i} + f_{ext,i} - \lambda_i \cdot \dfrac{\partial c_i}{\partial q_i} \end{cases} \tag{8}$$

These equations were used to model the dynamic behaviour of a simple actuator using MSMA and described in [31] and in the Fig. 4 (a). The comparison between theoretical and experimental dynamical response for an open loop control (voltage step) are reported in the Fig. 4 (b) and shows that the predictions given by this modelling procedure are quite accurate (see [31] for more details).



(b)

Figure 4: (a) description of a simple MSMA actuator, (b) dynamic behaviour of the system: voltage, current and displacement *vs* time (simulation: dotted line and experimental results: solid line) [31].

3. MSMA as an active material for actuator design

3.1. General design considerations

Very few prototypes of actuators using MSMA are reported in the literature. The majority use the simple principle described previously in Fig. 4 (a), [34, 35, 36] and some few others use in addition the *Inchworm* or *stick and slip* principles [37, 38]. The descriptions and models presented in authors previous papers and summed up in the previous sections give a better understanding of MSMA behaviour. This knowledge can therefore be used to design new actuators and to improve the performances of these devices. One of our latest version of actuators will be described in the following. Its characteristics and performances will be discussed.

3.2. Push-Pull Configuration

The study of the simple actuator described previously and in [31] shows that some advantages and disavantages of MSMA must be exploited to design competitive actuators compared to actuators using other active materials. First, it should be stressed that MSMA is not, at the moment, competitive for applications where other active materials are well-established. In particular for very high precision positioning (better than one micrometer) or for very small displacements (in the nanometer range), piezoelectric materials are far more competitive. In addition, if very low bandwidth and high forces are required, thermal or classical SMA materials are better-suited. The field of applications for MSMA must be found as niches where its specific characteristics can be exploited and its main drawbacks hidden. The following technical specifications were proposed to design a second version of MSMA based micro-actuator:

- The actuator must be as fast as possible (fast dynamics). This property mainly depends on the current establishment time, therefore, the coil design and the power electronics have to be improved and optimized.
- The mechanical structure must be designed to avoid backslash (for precision considerations) and friction (for efficiency considerations).
- Temperature of the device must be kept below 40 ^{o}C to avoid austenitic transformation.
- A position sensor has to be included in the final device to allow a position feedback control. The overall dimension must be kept as small as possible.

Several keynotes must be stressed for a good design with MSMA. These active materials present a strong hysteretical behaviour that must be exploited as a consequence. For example, this hysteresis should be used to keep a stable position without external supply. This allows a low energy consumption for embedded applications in space or in microrobotic fields. Authors proposed in [39] to achieve this by using a push-pull configuration as described in Figure 5. This configuration allows to replace efficiently the mechanical pre-stress device of MSMA simpler actuators. The working of this device follows these steps (see Figure 5):

- a linear simple MSMA actuator A is used to displace the positionning stage in the $+x$ direction: a magnetic field in the A airgap reorients martensite M1 of the A MSMA sample into martensite M2. This pushes the positioning stage in $+x$ direction,
- this motion stresses the linear simple actuator B and transforms its M2 martensite into M1 martensite,
- if no field is applied, the static position of the stage is kept thanks to the strong hysteresis of the stress/strain characteristic of MSMA (nevertheless, external load must be kept under a blocking stress, see Figure 3),
- the linear MSMA acturator B is used to displace the positioning stage in the $-x$ direction. The principle is the same as for the actuator A except for the direction.

A new prototype is designed according to the previous requirements. The coils are fully-optimized using both analytical and finite elements methods. The actual coil structure creates a magnetic field of 1 T with a current of 2 A

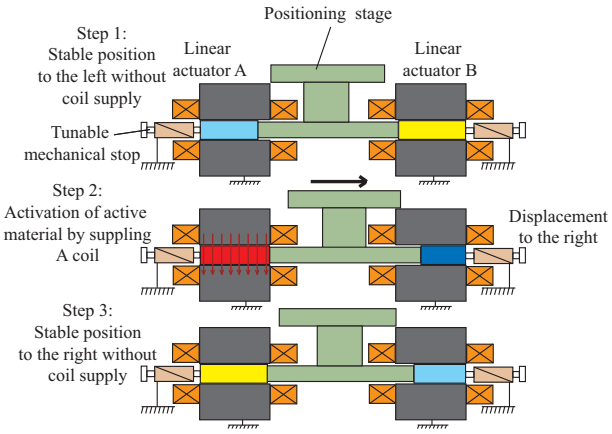
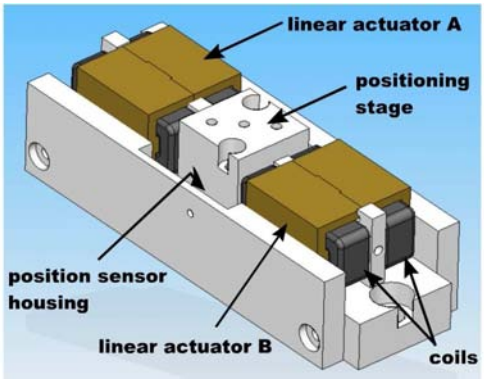
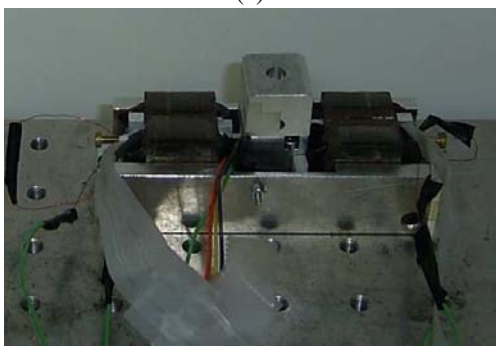


Figure 5: Description of the push-pull configuration of an actuator using two antagonist MSMA samples.

for a size of $19 \times 25 \times 25$ mm^3. The power electronics is designed to feed the two coils using Pulse Width Modulation (PWM) techniques and a displacement sensor is now included in the final prototype. Electronics includes a feedback control of the current, a PWM generator, a displacement feedback control and a temperature control (using micro-thermocouples). Figure 6 shows the CAD model of this device and a picture of the final prototype. The overall dimensions of this actuator are $110 \times 40 \times 30$ mm^3.



(a)



(b)

Figure 6: Push-pull actuator using two antagonist MSMA samples: (a) CAD model, (b) picture of the final prototype.

Another drawback of MSMA is its very low efficiency. It is also the case for SMA but it is amplified in this case by the magnetic actuation because of the requirement of a relatively high magnetic field density (around 1 T) inside the MSMA sample to activate martensite reorientation. To reach these levels, high current are required into the coils and this leads to significant Joule effect losses. Due to heat diffusion, these losses could increase the temperature inside the MSMA and, as a consequence, cancel out the working principle of this actuator because of a martensite/austenite transformation above a temperature threshold.

To by-pass these problems, it is be possible to fed these coils by current pulses.

3.3. Characteristics and performances

With this new device, some measurements were conducted to extract the performances of this new MSMA-based actuator. Theses performances are summarized in the sequel:

- Displacement range: a total displacement range of approximately 1 mm is now possible. The range is different at high and low velocities as it was proved in [40]. These differences result mainly of different balances between energy transfer (available work) and dissipation at low and high velocities. Some results are reported in Fig. 7 for a low and a high speed motion. Without external load, the time constant of the position control is in the order of 10 milliseconds. The maximal blocking force is between 2 and 3 MPa.

- Efficiency and control by current pulses: as previously noticed, a control by current pulses is possible (see Fig. 8). This mode of working gives two mains advantages. First, the actuator keeps a position at rest without feeding: this limits the energy requirements and gives the device a high efficiency in static mode. Secondly, the actuator can be supplied by current pulses to change a position: this allows a high reduction of the mean value current and therefore a major decrease of the joule effect heating. The maximum current in the coil can be easily increased for a short time, without any austenitic transformation (only magnetic fields intensity significantly activate martensite reorientation). As this field is proportional (without saturation) to the current times the turns number of the coil, we can increase the current as well as the number of turns to increase this field. In current pulse mode, heating phenomena are lowered even if the current density is significantly increased beyond the standard levels met in classical electromagnetic devices. From the design point of view, it is also relevant to reduce the section of wires and to increase the number of turns for the coils. This allows to reduce the size of the device and to boost significantly the magnetic fields, and therefore the overall performances of the device.

- Resolution and precision: the resolution was measured with a train of pulse (see Fig. 9), the maximal precision is about 1 micrometer and it seems, at the moment, difficult to improve this accuracy. This limit is mainly due to the complexity of the dynamic thermo-magneto-mechanical behaviour and the difficulty to achieve an accurate control (non-linear and non-invariant system, manufacturing process defect,...). Therefore, at this time, MSMA-based actuator are hardly relevant for the high resolution actuator when the precision must be far better than micrometer. Nevertheless, for precision in the range of micrometers, MSMA is a valid alternative to other active materials.

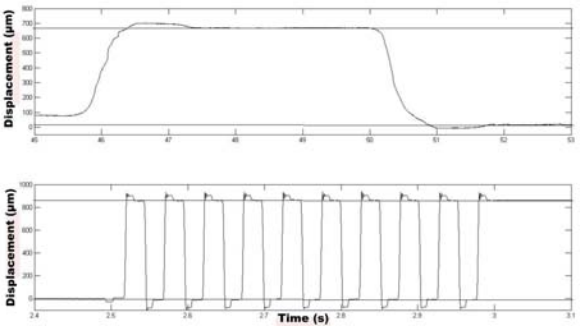


Figure 7: Displacement measurements of the MSMA-based actuator (low and high velocity modes of working).

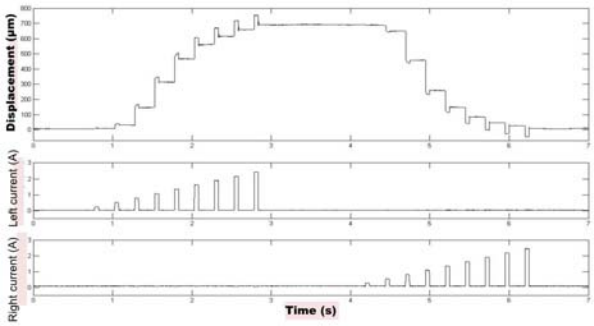


Figure 8: Current pulses control of the MSMA-based actuator.

3.4. Control strategies

To increase the precision and robustness, this actuator was also feedback-controlled using position and current measurements. The current sensor is a Hall-effect sensor (LTS 25 NP from the LEM company) and the integrated position sensor is a low-cost photoelectric infrared reflexion sensor (HOA 1404-002 from the Honeywell company). This latter has a measurement range of 2 mm with a precision of a few micrometers depending on the analog signal processing and on the quantization of the analog to digital converter connected to the digital controller. Figure 10 represents the

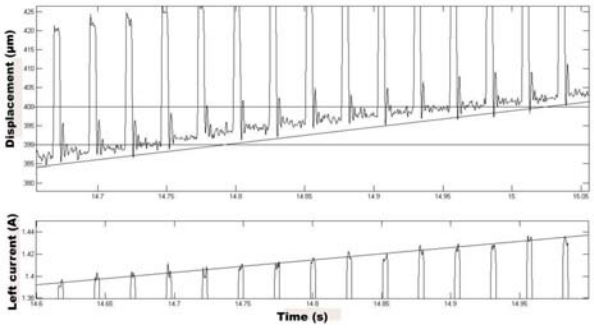


Figure 9: Resolution of the MSMA-based actuator.

block-diagram of the feedback control with a “linear” current control (without current pulse control). This feedback control is enough to give a positioning precision of a few micrometers.

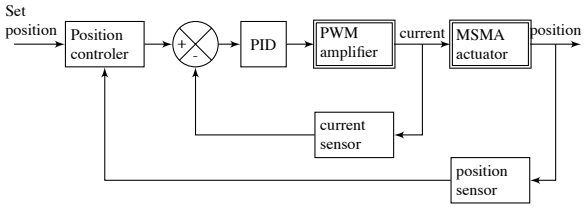


Figure 10: Block-diagram of the feedback control of MSMA-based actuator with a “linear” current control.

One of the main advantages of active materials is the possibility to use them as actuator as well as sensor. This seems also possible with MSMA materials as reported in [41]. This paper uses the change of the inductance value at low magnetic field as an indirect measurement of the stage position. This indirect measurement was also noticeable on our device and we are currently studying the self-sensing potential to remove the integrated position sensor. Nevertheless, perturbations due to the saturation of magnetic cores at high current level and to the electromagnetic radiation of the PWM power converter lead to an important signal processing treatments and to real-time problem of computation. These estimation difficulties reduce significantly the precision of the self-sensing indirect measurements in the device. Nowadays, the precision of this actuator with an integrated position sensor is far better than the precision using a self-sensing estimation principle. It will certainly be improved in the near future.

Some works are actually conducted by the authors concerning the improvement of the non-linear control of the device using port-Hamiltonian control techniques [42]. These advanced control strategies [43, 44, 45] are fully-compatible with the thermodynamics/Hamiltonian modeling presented in this paper.

4. Conclusion

In this paper, the working principle of Magnetic Shape Memory Alloys was explained. An extented thermodynamics/Hamiltonian formalism was presented to model the complex non-linear magneto-thermo-mechanical behaviour of this relatively new active material. Based on this model, an application of a push-pull actuator was proposed, designed and experimented. Some measurements are reported showing a precision of a few micrometers for a displacement range of 1 mm with a time constant of about 10 milliseconds with no load. The control of this actuator can be achieved with a pulse current feedforward control or with a current/position feedback control. Typical applications of such kind of actuators are in the micro-robotic or spatial fields with requirements between these of piezoelectric active materials and these of SMA active materials. The maximal strain of MSMA is one or two orders greater than that of piezoelectric or magnetostrictive materials and the response-time of MSMA is one or two orders smaller than that of classical SMA. For larger motions, the displacement range of this actuator can be amplified with compliant mechanical structures as is the case for actuators based on other active materials (see [46] for a amplified piezoelectric structure and [47] for an amplified magnetostrictive actuator).

Self-sensing potentials can also be pursued but currently technological improvements must be reached to replace efficiently integrated position sensor. Authors are actually focused on the control problem to improve the performance of this device using port-Hamiltonian control techniques. These ones are fully-suitable for the thermodynamics/Hamiltonian modeling presented in this paper and they can take into account the strong non-linear hysteretical behaviour of these active materials. Nevertheless, the dynamic magneto-thermo-mechanical behaviour of this material is so complex and so strongly non-linear that even today, due to a major control difficulties, the diffusion of this promising technology is dramatically reduced.

Acknowledgement

Authors would like to thank Yoann Loirat and David Guibert (Femto-ST Institute, Besançon, France) for the help during the actuator design and improvements. Authors would also thank Prof. C. Lexcellent from the Femto-ST Institute for discussions and collaborations concerning the modeling of SMA and MSMA. This work was partially supported by the project "*Conception et réalisation d'actionneurs haute résolution utilisant des matériaux actifs de type alliage à mémoire de forme magnétiques*" funded by the OSEO-ANVAR French agency (*Aide aux jeunes pour l'innovation, june 2008*) and by the ANR project Hamecmopsys "Hamiltonian Methods for the Control of Multidomain Distributed Parameter Systems", Agence Nationale de la Recherche, France.

References

[1] H. Janocha, Ed., *Adaptronics and Smart Structures. Basics, materials, Design, and Applications*. Springer-Verlag, 1999.

[2] J. L. Pons, *Emerging Actuator Technologies: A Micromechatronic Approach*. John Wiley and Sons, 2005.

[3] S. Bashash and N. Jalili, "Robust adaptative control of coupled parallel piezo-flexural nanopositioning stages," *IEEE/ASME Transactions on Mechatronics*, vol. 14(1), pp. 11–20, February 2009.

[4] S. Polit and N. J. Dong, "Development of a high-bandwidth xy nanopositioning stage for high-rate micro-/nanomanufacturing," *IEEE/ASME Transactions on Mechatronics*, vol. 99, pp. 1–10, June 2010.

[5] J. Y. Peng and B. Chen, "Modeling of piezoelectric-driven stick-slip actuators," *IEEE/ASME Transactions on Mechatronics*, vol. 16(2), pp. 394–399, April 2011.

[6] R. Merry, N. de Kleijn, N. van de Molengraft, and M. Steinbuch, "Using a walking piezo actuator to drive and control a high-precision stage," *IEEE/ASME Transactions on Mechatronics*, vol. 14(1), pp. 21–31, February 2009.

[7] E. du Tremolet de Lacheisserie, *Magnetostriction: Theory and Applications of Magnetoelasticity*. CRC Press, 1993.

[8] O. Söderberg, A. Sozinov, Y. Ge, S.-P. Hannula, and V. K. Lindroos, *Handbook of Magnetic Materials, vol. 16 (Giant Magnetostrictive materials)*, K. H. J. Buschow, Ed. Elsevier, 2005.

[9] D. Davino, A. Giustiniani, and C. Visone, "Design and test of a stress-dependant compensator for magnetostrictive actuators," *IEEE Transactions on Magnetics*, vol. 46(2), pp. 646–649, January 2010.

[10] Y. Sato and K. Shinohara, "Power-saving drive in 2-position control of giant-magnetostrictive actuator," *IEEE Transactions on Magnetics*, vol. 45(10), pp. 4554–4557, September 2009.

[11] W.-J. Kim and A. Sadighi, "A novel low-power linear magnetostrictive actuator with local three-phase excitation," *IEEE/ASME Transactions on Mechatronics*, vol. 15(2), pp. 299–307, March 2010.

[12] S. J. Murray, M. Marioni, S. M. Allen, R. C. O'Handley, and T. A. Lograsso, "6 percent magnetic-field-induced strain by twin-boundary motion in ferromagnetic Ni-Mn-Ga," *Applied Physical Letters*, vol. 77, pp. 886–8, 2000.

[13] K. Ullakko, J. K. Huang, C. Kantner, R. C. O'Handley, and V. V. Kokorin, "Large magnetic-field-induced strains in Ni2MnGa single crystals," in *Applied Physics Letters*, vol. 69, no. 13, 1996, pp. 1966–1968.

[14] R. D. James and M. Wuttig, "Magnetostriction of martensite," in *Philosophical Magazine A*, vol. 77, no. 5, 1998, pp. 1273 – 1299.

[15] O. Söderberg, Y. Ge, A. Sozinov, S.-P. Hannula, and V. K. Lindroos, "Recent breakthrough development of the magnetic shape memory effect in Ni-Mn-Ga alloys," *IOP Smart Materials and Structures*, vol. 14, pp. 223–335, 2005.

[16] J. Pons, E. Cesari, C. Seguì, F. Masdeu, and R. Santamarta, "Ferromagnetic shape memory alloys: Alternatives to Ni-Mn-Ga," *Materials Science and Engineering A*, vol. 481-482, pp. 57–65, 2008.

[17] M. Kohl, D. Brugger, and B. Krevet, "Ferromagnetic shape memory actuator for large 2d optical scanning," in *19th IEEE International Conference on Micro Electro Mechanical Systems, Istanbul, Turkey*, 2006.

[18] M. Kohl, D. Brugger, M. Ohtsuka, and B. Krevet, "A ferromagnetic shape memory actuator designed for large 2d optical scanning," *Sensors and Actuators A*, vol. 135, pp. 92–98, 2007.

[19] R. Tickle and R. D. James, "Magnetic and magnetomechanical properties of Ni_2MnGa," *Journal of Magnetism and Magnetic Materials*, vol. 195, pp. 627–638, juin 1999.

[20] A. DeSimone and R. D. James, "A constrained theory of magnetoelasticity," *Journal of the Mechanics and Physics of Solids*, vol. 50, no. 2, pp. 283–320, 2002.

[21] P. Müllner, V. Chernenko, and G. Kostorz, "A microscopic approach to the magnetic-field-induced deformation of martensite (magnetoplasticity)," *Journal of Magnetism and Magnetic Materials*, vol. 267, pp. 325–334, 2003.

[22] R. Ahluwalia, T. Lookman, and A. Saxena, "Dynamic strain loading of cubic to tetragonal martensites," *Acta materialia*, vol. 54, pp. 2109–2120, 2006.

[23] O. Heczko, "Determination of ordinary magnetostriction in Ni-Mn-Ga magnetic shape memory alloy," *Journal of Magnetism and Magnetic Materials*, vol. 290-291, pp. 846–849, 2005.

[24] B. Kiefer and D. C. Lagoudas, "Magnetic field-induced martensitic variant reorientation in magnetic shape memory alloys," *Philosophical Magazine Special Issue: Recent Advances in Theoretical Mechanics, in Honor of SES 2003 A.C. Eringen Medalist G.A. Maugin*, vol. 85(33-35), pp. 4289–4329, 2005.

[25] R. N. Couch and I. Chopra, "A quasi-static model for NiMnGa magnetic shape memory alloy," *Smart Materials and Structures*, vol. 16, pp. S11–S21, 2007.

[26] R. C. Smith, M. J. Dapino, T. R. Braun, and A. P. Mortensen, "A homogenized energy framework for ferromagnetic hysteresis," *IEEE Transactions on Magnetics*, vol. 42(7), pp. 1747–1769, 2006.

[27] N. N. Sarawate and M. J. Dapino, "A continuum thermodynamics model for the sensing effect in ferromagnetic shape memory Ni-Mn-Ga," *Journal of applied physics*, vol. 101, pp. 123 522–1–123 522–11, 2007.

[28] J. Y. Gauthier, C. Lexcellent, A. Hubert, J. Abadie, and N. Chaillet, "Modeling rearrangement process of martensite platelets in a magnetic shape memory alloy Ni_2MnGa single crystal under magnetic field and (or) stress action," *Journal of Intelligent Material Systems and Structures*, vol. 18, no. 3, pp. 289–299, 2007.

[29] ——, "Magneto-thermo-mechanical modeling of a magnetic shape memory alloy Ni-Mn-Ga single crystal," *Annals of Solid and Structural Mechanics*, vol. 2, no. 1, pp. 19–31, 2011.

[30] H. B. Callen, *Thermodynamics and an introduction to thermostatistics, 2^{nde} edition*. John Wiley and Sons, 1985.

[31] J. Y. Gauthier, A. Hubert, J. Abadie, N. Chaillet, and C. Lexcellent, "Nonlinear hamiltonian modelling of magnetic shape memory alloy based actuators," *Sensors & Actuators A*, vol. 141, pp. 536–547, 2008.

[32] C. Lanczos, *The Variational Principe of Mechanics, Fourth edition*. Dovers Publications, Reprint of 1970 University of Toronto Press, 1986.

[33] H. Goldstein, *Classical Mechanics, second edition*. Addison Wesley, 1980.

[34] I. Suorsa, J. Tellinen, E. Pagounis, I. Aaltio, and K. Ullakko, "Applications of magnetic shape memory actuators," in *8th international conference ACTUATOR 2002*, Bremen (Germany), 2002.

[35] I. Suorsa, J. Tellinen, I. Aaltio, E. Pagounis, and K. Ullakko, "Design of active element for MSM-actuator," in *ACTUATOR 2004 / 9th International Conference on New Actuators*, Bremen (Germany), juin 2004.

[36] I. Suorsa, E. Pagounis, and K. Ullakko, "Magnetic shape memory actuator performance," *Journal of Magnetism and Magnetic Materials*, vol. 272-276, pp. 2029–2030, 2004.

[37] F.-X. Wang, W.-J. Li, Q.-X. Zhang, X.-J. Wu, and C. Ge, "Design and control of linear actuators made by magnetically controlled shape memory alloy," in *IEEE International Conference on Mechatronics*, July 10-12 2005, pp. 583–586.

[38] Q.-X. Zhang and F.-X. Wang, "A novel linear actuator and its controlling system," in *IEEE International Conference on Automation and Logistics*, August 18-21 2007, pp. 979–984.

[39] J. Y. Gauthier, A. Hubert, J. Abadie, C. Lexcellent, and N. Chaillet, "Multistable actuator based on magnetic shape memory alloy," in *ACTUATOR 2006, 10th International Conference on New Actuators, Bremen, Germany*, 2006, pp. 787–790.

[40] ——, "Original hybrid control for robotic structures using magnetic shape memory alloys actuators," in *IEEE/RSJ International Conference on Intelligent Robots and Systems*, 2007, pp. 787–790.

[41] I. Suorsa, E. Pagounis, and K. Ullakko, "Position dependent inductance based on magnetic shape memory materials," *Sensors and Actuators A*, vol. 121, pp. 136–141, 2005.

[42] N. Calchand, A. Hubert, Y. Le Gorrec, and B. Mashke, "From canonical hamiltonian to port-hamiltonian modeling. Application to magnetic shape memory alloys actuators," in *ASME 2011 Dynamic Systems and Control Conference (DSCC'2011)*, Airlington, Virginia, USA, 31 oct.-01 nov. 2011.

[43] A. J. van der Schaft, *L_2-Gain and Passivity Techniques in Nonlinear Control*. Springer-Verlag, 2000.

[44] A. Astolfi and A. J. van der Schaft, Eds., *Lagrangian and Hamiltonian Methods for Nonlinear Control*, ser. Special Issue of European Journal of Control, Volume 10, Number 5. Hermes, 2004.

[45] B. Brogliato, R. Lozano, B. Maschke, and O. Egeland, *Dissipative Systems Analysis and Control. Theory and applications, 2^{nde} edition*. Springer-Verlag, 2007.

[46] M. Grossard, M. Boukallel, N. Chaillet, and C. Rotinat-Libersa, "Modeling and robust control strategy for a control-optimized piezoelectric microgripper," *IEEE/ASME Transactions on Mechatronics*, vol. 99, pp. 1–10, June 2010.

[47] F. Claeyssen, N. Lhermet, F. Barillot, and R. L. Letty, "Giant dynamic strains in magnetostrictive actuators and transducers," in *ISAGMM*, Guiyang, China, October 9-12 2006.

Surface impedance of $BaFe_{2-x}Ni_xAs_2$ in the radio frequency range

A. Abbassi[1], M. Saint-Paul[2], R. Dkiouak[1], M. R. Britel[3], Zhao-Sheng Wan[2,4], Huinqian Luo[4], Xiagye Lu[4], Cong Ren[4], and Hai-Hu Wen[4,5]

[1] Faculté des Sciences et Techniques de Tanger, BP 416 Tanger, Université Abdelmalek Essaâdi, Morocco.
[2] Institut Néel, CNRS, Université Joseph Fourier, BP 166, Bât E, F 38042 Grenoble Cedex 9, France.
[3] Laboratoire des Technologies Innovantes, ENSAT , Université Abdelmalek Essaâdi UAE, BP 1818 Tanger, Morocco.
[4] Institute of Physics and National Laboratory for Condensed Matter Physics, Chinese Academy of Sciences, P.O Box 603, Beijing 100190, People's Republic of China.
[5] National Laboratory for solid State Microstructures, Department of Physics, Nanjing University, 210093 Nanjing, People's Republic of China.
*corresponding author, E-mail:abdellatif1966@hotmail.com

Abstract

We report measurements of the temperature dependence of the surface impedance in superconducting $BaFe_{1.93}Ni_{0.07}As_2$ crystals using the radiofrequency reflection technique in the 5<T<30K temperature range. An LC resonant circuit with a phase sensitive detection was used at 92MHz. A measurement assembly with point contacts was used at 30MHz. The recent discovery of iron based arsenide superconductors $BaFe_{2-x}Ni_xAs_2$ has attracted much interest. For a Ni doping level of 7% the superconducting phase transition is found around 20K. The temperature dependence of the superconducting penetration depth was determined.

1. Introduction

The recent discovery of iron based arsenide superconductors $BaFe_{2-x}Ni_xAs_2$ has attracted much interest [1-3].

The measurements of the surface impedance $Z_S = R_S + iX_S$ probe the complex conductivity [4-7]. The real part of the surface impedance is proportional to the loss of the radio frequency power and caused by the normal carriers. The imaginary part is determined by the response of the superconducting carriers and characterized the non dissipating energy stored in the superconducting surface layer λ which is the magnetic penetration depth. When the sample is superconducting magnetic field is fully shielded from the sample's interior, the magnetic field is limited to the superconducting depth λ, which is approximately 1 μm. After the sample passes from the superconducting to the normal sate, the magnetic field penetrates into the sample a much larger distance equal to the normal skin depth δ. For our samples, this distance is of the order of 70 μm at 100 MHz.

The second probe for the superconducting carriers is the use of ultrasonic measurements. When a sound wave propagates through a metal the microscopic electric field due to the displacement of the ions can impart energy to electrons removing energy from the wave. In a superconductor well below the superconducting transition T_C attenuation of sound waves are markedly lower than in a normal metal.

2. EXPERIMENT

We report measurements of the surface impedance in the (ab) plane of superconducting $BaFe_{1.93}Ni_{0.07}As_2$ crystals.

2.1. Experimental set up

The crystals were grown using an Fe/Ni-As self flux method, details are given [3]. Typical crystals have dimensions of 7x5x0.2 mm^3. The crystallographic c-axis is perpendicular to the plane of plate-like crystals along the smallest dimension.

To determine change in the surface impedance, the sample is placed inside a coil which is part of resonant series LC (capacitor) circuit, resonant frequency of 92 MHz having a quality factor Q of 80. The sample is mounted on the end of sapphire plate with a small amount of silicon grease. RF magnetic field is applied parallel to the (ab) plane. In this geometry screening currents flow around the crystal in both a, b and c axes directions. The dimension along the c-axis is very small it results that the c-axis contribution is small in comparison to the contribution given by the (ab) plane. Measurements were done at 92 MHz by monitoring the reflected RF power at resonance. The reflected power is measured using a phase sensitive detector. A balanced mixer multiplies the reflected RF voltage v_r with the forward RF voltage v_i . After removing the ac components by a low pass filter, the dc component V_0 is proportional to

the reflected RF voltage v_r. V_0 is expressed with the amplitudes and the phase shift between v_R and v_I.

$$V_0 = |v_I| * |v_R| * \cos(\theta) \qquad (1)$$

The sample was mounted in a non resonant circuit with spring contact connectors at the end of a coaxial line. Two spring contacts were pressed to the surface of the sample.

The sample circuit block was fixed at the end of a semi-rigid coaxial cable in a liquid helium cryostat. Temperature was controlled with a calibrated germanium resistance thermometer.

Ultrasonic waves were generated and detected at 15 and 45 MHz with LiNbO3 transducers bounded to the crystal.

2.2. RESULTS

The temperature dependences of the voltage V_0 of the LC circuit with $BaFe_{1.93}Ni_{0.07}As_2$ crystal and $BaFe_{1.85}Ni_{0.15}As_2$ crystal, are reported in Fig 1. Measurements without sample are also shown.

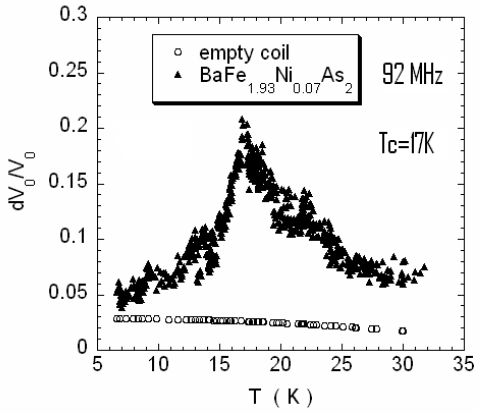


Figure 1: Temperature dependence of the relative change dV_0/V_0, LC circuit measured at 92 MHz with $BaFe_{1.93}Ni_{0.07}As_2$ crystal dimensions 7x5x0.2 mm^3, superconducting phase transition T_C = 17 K and the empty coil.

It is found that V_0 drops precipitously as the temperature is lowered through T_C in the $BaFe_{1.93}Ni_{0.07}As_2$ crystal Fig1.

A very sharp behaviour is observed at T_C =13K for the $BaFe_{1.85}Ni_{0.15}As_2$ crystal Fig 2. The effects observed with this second crystal are one order of magnitude smaller.

In reflection measurements reflected RF voltage v_R depends on the transmission line impedance Z and the characteristic line impedance Z_0, Z_0=50Ω .

$$\frac{v_R}{v_I} = \frac{Z - Z_0}{Z + Z_0} \quad \text{with} \quad \frac{Z}{Z_0} = \left[\frac{Z_L + jZ_0 \tan(\beta l)}{Z_0 + jZ_L \tan(\beta l)}\right] \qquad (2)$$

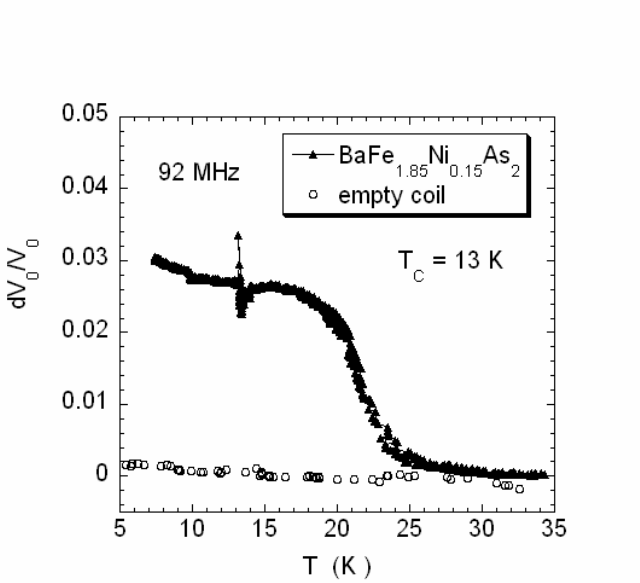


Figure 2: Temperature dependence of the relative change dV_0/V_0 , LC circuit measured with $BaFe_{1.85}Ni_{0.15}As_2$ crystal dimensions 7x5x0.2 mm^3, superconducting phase transition T_C = 13 K and the empty coil

Z_L is the impedance of the resonant LC circuit or the non resonant circuit, β is the electric wave vector and l is the coaxial line length. In our case an angle βl of 3.3π was estimated.

For the non resonant circuit we have plotted in Fig3 the reflected voltage normalized to its value just above Tc which is equivalent to the impedance normalized at its value in the normal state. This approximation is justified by the fact that small changes of Z_L induce a linear variation of the reflected voltage in equation (2). We plotted in Fig3 the normalized voltage V_0 to its value at Tc for the resonant circuit. The effect of the empty coil has been subtracted. The normalized reflected voltage is proportional to the superconducting penetration depth [6]:

$$\frac{v_R}{v_R^N} \approx \frac{\lambda}{\delta_N} \qquad (3)$$

δ_N being the skin depth in the normal sate.

The experimental data obtained with the non resonant circuit at 30 MHz and resonant circuit at 92 MHz with the $BaFe_{1.93}Ni_{0.07}As_2$ crystal follow the temperature dependence given by the two fluid model [4]

$$\lambda \approx \lambda(0)\left[1 - \left(T/T_C\right)^4\right]^{-1/2} \qquad (4)$$

The most striking feature of the data is the drastic change of the electric impedance concomitant with the sharp decrease of the ultrasonic attenuation at 15 and 45 MHz around Tc. This confirms that $BaFe_{1.93}Ni_{0.07}As_2$ crystal follows an unconventional superconducting behaviour. According to the BCS theory, ultrasonic attenuation drops after the carriers condensate below Tc, the exponential temperature decrease below Tc is related to the superconducting energy gap [9].

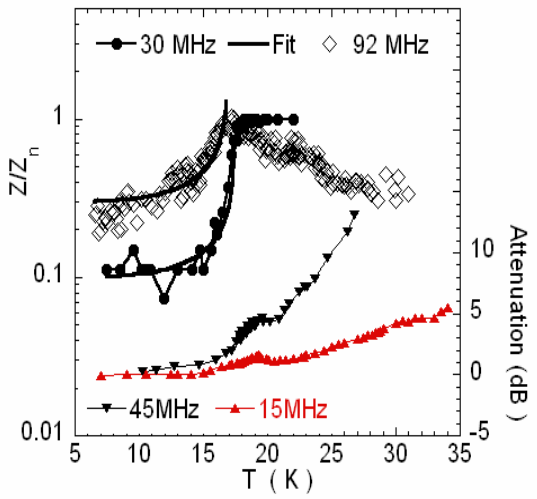


Fig 3 $BaFe_{1.93}Ni_{0.07}As_2$ crystal .Temperature dependence of the normalized impedance Z/Zn, non resonant circuit at 30 MHz, resonant circuit at 92MHz. The solid lines (Fit) are calculated with equation (4) with Tc= 17.5K, and Tc=18K.Temperature dependence of the ultrasonic attenuation at 15 and 45 MHz.

A penetration depth at 0K $\lambda(0) \sim 7\mu m$ is estimated with equation (3). This value is larger than the value expected for this material [5]. Surface roughness should lead to an exaggerate λ value via an underestimate of the effective sample area. The standard equivalent circuit model, ideal transformer, for the coupled system of coil and sample leads to the complex impedance:

$$Z_L = R_1 + R_2 \frac{M^2\omega^2}{R_2^2 + L_2^2\omega^2} + j\left[L_1 - L_2 \frac{M^2\omega^2}{R_2^2 + L_2^2\omega^2}\right]\omega \qquad (5)$$

Where R_1 and L_1 are the resistance and the inductance of the empty coil. M is the mutual inductance between coil and sample, k is the effective filling factor.

$M^2 = kL_1L_2$

R_2 and L_2 are the resistance and inductance related to the sample. This model works well for the normal conductors but for superconductors it is difficult to extract the intrinsic surface resistance and reactance of the sample.

Behavior of V_0 around the superconducting transition of the $BaFe_{1.85}Ni_{0.15}As_2$ crystal can be related to the sharp drop in inductance at Tc and a peak in RF losses just above Tc. Such a peak in RF losses can be attributed to weakly connected loops consisting of weak-link Josephson junctions created at the contacts between the microcrystals [7].

3. Conclusions

We have reported measurements of the temperature dependence of the penetration depth in the iron based superconductors $BaFe_{1.93}Ni_{0.07}As_2$ in the radio frequency range. Smaller RF effects were observed for the high Ni concentration x=0.15. The mechanism of superconductivity in the iron based superconductors is not well understood. It has been proposed that superconductivity depends on spin and orbitals fluctuations [8]. This can explain the unconventional behavior of the ultrasonic attenuation observed in the $BaFe_{2-x}Ni_xAs_2$ samples [4].

References

[1] H. Hosono , *J. Phys.Soc.Jpn, 77*, 1–8, (2008).

[2] K. Ahilan, F.L. Balasubramanian, T. Ning, A. Imai, A.S. Sefat, M.A. Jin, B.C. McGuire, B.C. Sales, and D. Mandrus, *J.Phys.Condens. Matter*, **20**, 472201, (2008).

[3] Chen Yanchao, Xingye Lu, Meng Wang, Huiqan Luo and Shiliang Li, *Supercond. Sci. Techno.*, **24**, 065004, (2011).

[4] G. Goll, Unconventional Superconductors *Springer Tracks in Modern Physics Springer-Verlag* Berlin (2006).

[5] J. S. Bobowski, J. C. Baglo, James Day, P. Dosanjh, Rinat Ofer, B. J. Ramshaw, Ruixing liang, D.A. Bonn, W. N Hardy, Huiqian Luo, Zhao-Sheng Wang, Lei Fang, and Hai-HU Weng, *Phys. Rev. B*, **52**, 094520, (2010).

[6] A. Gould, E.M. Jackson, K. Renouard, R. Crittenden, S.M. Bhatat, N.D.Spencer, L.E. Dolhert, and R.F. Wormsbecher, Physica C **156**, 55-558, (1988).

[7] V.A. Gasparov, R. Huguenin D. Pavuna, and J. Van der Maas, *Solid State Com.*, **69** 1147-1151, (1989).

[8] Hiroshi Kontani and Seiichiro Onari, *Phys Rev Lett.*, **104**, 157001, (2010).

[9] M. Saint-Paul, A. Abbassi, Zhao-Sheng Wan, Huinqian Luo, Xiagye Lu, Cong Ren, and Hai-Hu Wen (submitted to be published).

An Electromagnetic Suspension Platform for Position and Tracking Control Verification

Chin E. Lin* **Wei-Cheng Huang**

Department of Aeronautics and Astronautics, National Cheng Kung University, Tainan, Taiwan
* e-mail: chinelin@mail.ncku.edu.tw

Abstract

A hybrid electromagnetic suspension platform using four actuators is built for ball and plate demonstration. Position and tracking control by applying an improved Fuzzy Logic Control is implemented in the proposed system. The hybrid electromagnetic suspension (EMS) actuator is designed with a permanent magnet and an electromagnetic (EM) coil with iron core. Their interaction between permanent magnet and PWM current controlled EM constructs the 2D motion performance of plate to a ball. In this paper, the mathematical model of the ball and plate system is derived through the Euler-Lagrange equation. An improved Fuzzy Logic Control (FLC) law is developed following a human experience-based on the traditional FLC law and a directed control law. This enhanced FLC law can significantly reduce overshoot and settling time than traditional FLC. The control circuit is designed and fabricated on a microprocessor as the control kernel using a commercial touch panel for position feedback. A microprocessor closed loop circuit outputs PWM signal through the enhanced Fuzzy logic control and settles the plate to the required performance. In this paper, the position and tracking control of a ball on the plate is tested through four hybrid EMS actuators. System performance is demonstrated with excellent results.

Keywords: Hybrid Electromagnetic Suspension (EMS) Actuator, Ball and Plate System, Fuzzy Logic Control, Sensor Feedback.

1. Introduction

New advanced and well-developed system technologies dominate world industry into a modern trend. Mechanical equipment is still relatively fundamental to most industries but requires higher precision and better performance. The traditional precision machines are cooperated with other mechanisms to reach the anticipated system performance quality. Several practical problems confronted with machine, such as friction, vibration, noise, heat, and etc. To overcome the above mentioned problems, the system can be improved by its machining precision, or applying lubricant to reduce friction, and introducing control force to less vibration. The magnetic suspension (MS) technology is a feasible solution to improve the traditional mechanical system defeats in studies. The MS system prevents the mechanical system from heat damage resulting from contact, friction, vibration and extends the machine lifecycle, to release mechanism size problem, but improve its precision substantially.

In MS application, hybrid electromagnetic suspension (EMS) actuators are designed using permanent magnetic and electromagnetic coil to achieve operation flexibility (Chinese Patent I-228574, 20050301). Some detail design feature is accomplished to construct actuators in applications.

The ball and plate system is a nonlinear dynamic problem typically. The ball and plate system is commonly created for control system modeling [1, 2, 3], design, implementation, and verification [4, 5] as a training tool for science and engineering practices in many applications. Constructing from EMS actuators into a ball and plate system, Lin and Ker used Back-stepping Controller to control the ball position successfully [6]. It is an unprecedented literature about applying the MS system in balance and stable control in the ball and plate system. However there were some defeats found in further studies. By some design improvement and applying different control strategy, this paper presents some important results of the ball and plate control using the improved MS actuator with modified modeling and system formulation.

2. Ball and Plate System

In the ball and plate system, Newton's Second Law can be used for derivation. In order to avoid an incomplete consideration of force, the Euler-Lagrange method is actually used to derive the dynamic behavior of the ball and plate system. Euler-Lagrange is processing by calculating energy, and can effectively deal with more complex conditions. After finishing system modeling, the stability verification can be simulated by using MATLAB/Simulink.

2.1. Ball and plate system modeling

The mathematical model of proposed system as illustrated in Figure1. To derive the motion equation for the proposed system, assuming the ball rolling on the plate without slippage, spin and friction [7]. Assume the plate is geometrically symmetry.

The proposed system state variables are defined by the acceleration of gravity as g, the plate length as $2d$, choosing the plate angle from X-axis and Y-axis as α and β, respectively, the ball position as (x_b, y_b), the radius of ball as r_b, the mass of plate as M, moment of inertia of

plate in the X-axis and Y-axis are both I_P because of symmetry, the mass and moment of inertia of the ball as m and I_b, respectively. F_{M_X} is the magnetic force of X-axis, and F_{M_Y} is the magnetic force of Y-axis.

By applying the Euler-Lagrange's equation, the mathematical model for the proposed system is given by:

$$\frac{d}{dt}\frac{\partial T}{\partial \dot{q}_i}-\frac{\partial T}{\partial q_i}+\frac{\partial V}{\partial q_i}=Q_i,\ i=1,2,3,4 \tag{1}$$

$$q_1=x, q_2=y, q_3=\alpha, q_4=\beta \tag{2}$$

where T is kinetic energy, V is potential energy and Q is external force.

$$T=T_b+T_P \tag{3}$$

$$T_b=\frac{1}{2}m_b\left(\dot{x}_b^2+\dot{y}_b^2\right)+\frac{1}{2}I_b\left(\omega_x^2+\omega_y^2\right)$$

$$=\frac{1}{2}\left(m_b+\frac{I_b}{r_b^2}\right)\left(\dot{x}_b^2+\dot{y}_b^2\right) \tag{4}$$

$$T_P=\frac{1}{2}\left(I_P+I_b\right)\left(\dot{\alpha}^2+\dot{\beta}^2\right)+\frac{1}{2}m_b\left(x_b\dot{\alpha}+y_b\dot{\beta}\right)^2$$

$$=\frac{1}{2}\left(I_P+I_b\right)\left(\dot{\alpha}^2+\dot{\beta}^2\right)+\frac{1}{2}m_b\left(x_b^2\dot{\alpha}^2+y_b^2\dot{\beta}^2+2x_by_b\dot{\alpha}\dot{\beta}\right) \tag{5}$$

where T_b is kinetic energy of ball and T_p is kinetic energy of plate.

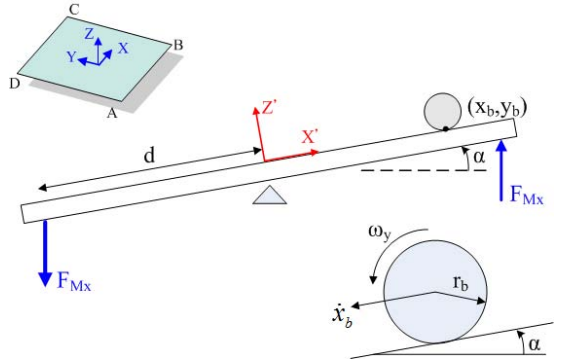


Figure 1: Mathematical model of proposed ball and plate system.

$$V=V_b=m_bg\left(x_b\sin\alpha+y_b\sin\beta\right) \tag{6}$$

$$Q_3=2F_{M_X}d\cos\alpha \tag{7}$$

$$Q_4=2F_{M_Y}d\cos\beta \tag{8}$$

Finally, the Euler-Lagrange's equations of ball and plate system are

$$\left(m_b+\frac{I_b}{r_b^2}\right)\ddot{x}_b-m_b\left(\dot{\alpha}\dot{\beta}y_b+\dot{\alpha}^2x_b\right)+m_bg\sin\alpha=0 \tag{9}$$

$$\left(m_b+\frac{I_b}{r_b^2}\right)\ddot{y}_b-m_b\left(\dot{\alpha}\dot{\beta}x_b+\dot{\beta}^2y_b\right)+m_bg\sin\beta=0 \tag{10}$$

$$m_b\left(\ddot{\beta}x_by_b+\dot{\beta}\dot{x}_by_b+\dot{\beta}x_b\dot{y}_b+2\dot{\alpha}\dot{x}_bx_b\right)+\left(I_P+I_b+m_bx_b^2\right)\ddot{\alpha}$$
$$+m_bgx_b\cos\alpha=F_{M_X}d\cos\alpha \tag{11}$$

$$m_b\left(\ddot{\alpha}x_by_b+\dot{\alpha}\dot{x}_by_b+\dot{\alpha}x_b\dot{y}_b+2\dot{\beta}\dot{y}_by_b\right)+\left(I_P+I_b+m_by_b^2\right)\ddot{\beta}$$
$$+m_bgy_b\cos\beta=F_{M_Y}d\cos\beta \tag{12}$$

Let $x_1=x_b, x_2=\dot{x}_b, x_3=\alpha, x_4=\dot{\alpha}, x_5=y_b, x_6=\dot{y}_b, x_7=\beta, x_8=\dot{\beta}$

$$\begin{bmatrix}\dot{x}_1\\ \dot{x}_2\\ \dot{x}_3\\ \dot{x}_4\\ \dot{x}_5\\ \dot{x}_6\\ \dot{x}_7\\ \dot{x}_8\end{bmatrix}=\begin{bmatrix}x_2\\ A\left[m_b\left(x_4x_5x_8+x_4^2x_1\right)-m_bg\sin x_3\right]\\ x_4\\ 0\\ x_6\\ A\left[m_b\left(x_1x_4x_8+x_8^2x_5\right)-m_bg\sin x_7\right]\\ x_8\\ 0\end{bmatrix}+$$

$$\begin{bmatrix}0&0&0&1&0&0&0&0\\ 0&0&0&0&0&0&0&1\end{bmatrix}^T\begin{bmatrix}u_1\\ u_2\end{bmatrix} \tag{13}$$

where $A=\dfrac{1}{m_b+\dfrac{I_b}{r_b^2}}$,

$$u_1=\frac{K_1\left(I_p+I_b+m_bx_5^2\right)\quad K_2\left(m_bx_1x_5\right)}{\left(I_p+I_b+m_bx_1^2\right)\left(I_p+I_b+m_bx_5^2\right)\quad\left(m_bx_1x_5\right)^2}$$

$$u_2=\frac{K_1\left(m_bx_1x_5\right)-K_2\left(I_p+I_b+m_bx_1^2\right)}{\left(m_bx_1x_5\right)^2-\left(I_p+I_b+m_bx_1^2\right)\left(I_p+I_b+m_bx_5^2\right)}$$

$$K_1=2F_{M_X}d\cos x_3-m_bgx_1\cos x_3-m_b\left(x_2x_5x_8+x_1x_6x_8+2x_1x_2x_4\right)$$

$$K_2=F_{M_y}d\cos x_7-m_bgx_5\cos x_7-m_b\left(x_2x_4y_5+x_1x_4x_6+2x_5x_6x_8\right)$$

2.2. Simulation

A normal simulated interface of the ball and plate system is established using MATLAB/Simulink. From this software, the complicated state space equation like as Eq. (13) can easily be simulated with different kind of initial conditions. The simulation result about position tracking from an initial position to a target position can be achieved smoothly. It verifies the X and Y trajectory diagram being controllable and reliable.

3. System Architecture

3.1. The Proposed System Architecture

An EMS actuator ball and plate system is constructed for study. It is divided into five parts as shown in Figure 2. Microcontroller MSP-430 CPU is used as a control kernel. The ball and plate structure includes a steel ball, a touch panel as a position sensor, a plate pedestal and four MS actuators. The ball diameter is 25.4 mm and its surface resistance is nearly zero; the MCU gets ball position from

touch panel sensor through UART1 interface. The function of the plate pedestal is to support the steel ball and the touch panel sensor. The magnetic force can move the plate pedestal and adjust its angle to change the ball position. Two power supplies are used to offer actuator drive and microprocessor controller to separate ground to avoid interference from analog circuit to digital circuit. The balancing control procedure is reading the signal of ball position from the touch panel sensor. Next step, the microcontroller calculates the control signal strength using the control law. The control signal sends to the drive circuit by Pulse Width Modulation (PWM); then, the control current conveys to MS actuator from drive circuit. The process is repeating until the ball reaches at the target position. At the same time, MCU transmits the ball position to terminal through UART0 for recording. Figure 3 is the basic block diagram of control loop.

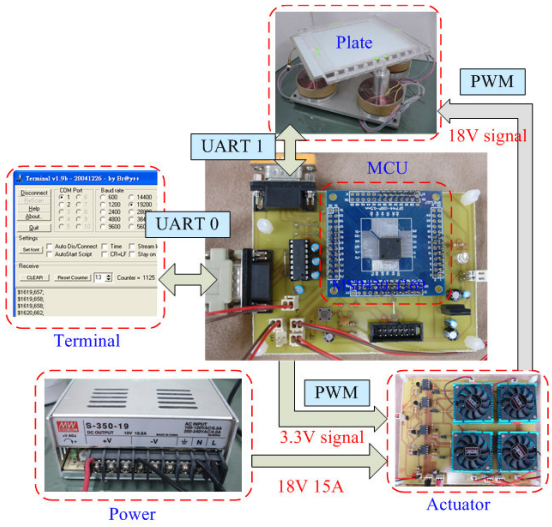


Figure 2: The proposed system architecture.

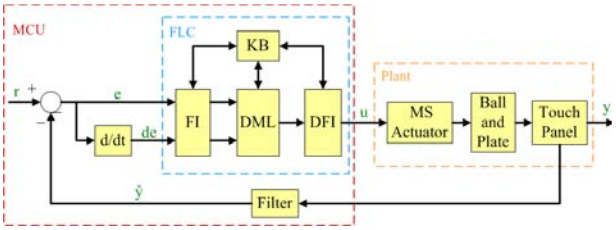


Figure 3: The basic block diagram of control loop.

3.2. MCU MSP430F169

MSP430F169 is a TI MSP430 family product [Texas Instruments products, on web: http://ti.com/ available in August 2009] for signal processing. It is adopted to build control function among sensors to main computer. The MSP430F169 series are microcontroller configurations with a fast 12-bit ADC, two built-in 16-bit timers, two USART, and 48 I/O pins. The ADC12 module is a high-performance 12-bit analog-to-digital converter.

3.3. Actuator (Photo coupler and MOSFET)

In the ball and plate system, when the MCU receives the ball position, then transmits four PWM signals to control magnetic suspension actuators. However, the current carried by PWM signals which come from the MCU are too small to drive the actuators. Therefore, the small PWM signal comes from the MCU will be magnify through MOSFET (IRFZ44) via photo coupler (PC923).

The maximum voltage and current of IRFZ44 are 60V and 55A, respectively. The photo coupler PC923 can isolate two different voltage, and the maximum isolated voltage can be 15~30V. Figure 7 is the circuit of actuator.

3.4. Magnetic Suspension Actuator

The main function of MS actuator is to perform as a filter to generate reverse force to absorb external vibration force. The general actuator used spring and damping to suppress the vibration. Here, permanent magnets substitute for the damping device. Permanent magnet is the principle of magnetic fields interacting on repulsive or attractive force between N or S polarities. Then, the magnetic suspension system design adopts two different design types from attractive force and repulsive force in system structures. Most studies verified that the repulsion-type magnetic suspension is a naturally unstable system as a result it is very difficult to control. To overcome the repulsive interaction, Fig.8 shows the magnetic suspension actuator structure (Chinese Patent I-228574) [6], including the pedestal, the holding tube, the motion support, the iron core, the permanent magnet and coils. The design details are shown in Table 1 with system parameters in consideration.

Considering an EMS actuator, assume the EM coil has n turns in a unit length to make the total coil of nh turns in the solenoid around the iron core. The magnetic force can be derived as:

$$F_{mag} = \frac{1}{2}\mu_0 N^2 A_{gap}\left(\frac{i_c}{x}\right)^2 \qquad (14)$$

where μ_0 is the permeability of free space, A_{gap} is the cross-section area of the face of air gap, $N = nh$.

3.5. Touch Panel

The touchkit provides controllers to communicate with host devices with RS232, USB, PS2, and I2C interface. In this paper, the MCU use RS232 to connect with touch panel through UART1. After connecting with touch panel, the touchkit controllers report touched/untouched point with the packet format list. Each point packet has 5 bytes in length and contains the resolution of the touch point, 11 bits of 1st axis coordination data and 11 bits of 2nd axis coordination data. Figure 4 is the point packet transformation. The numbers shown on the left received from the touch panel will transfer to the X and Y position of the ball on the right.

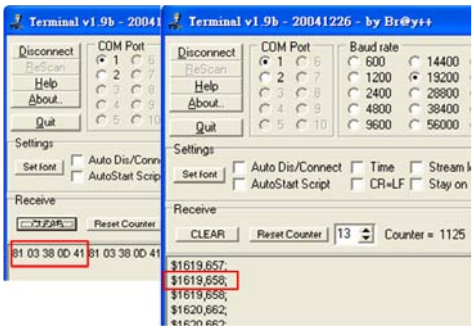


Figure 4: The point packet transformation.

4. Application of Control Law in the Ball and Plate System

After L. A. Zadeh created the fuzzy set theory in 1965 , the fuzzy set theory has been widely used in systems engineering, signal process, control engineering and other fields. Fuzzy logic control law let the control law express a set of qualitative conditional statements and inaccurate decision rules, and quantify it by fuzzy mathematics.

4.1. Method of position tracking

Figure 5 is the sketch of position tracking. As ball starts to roll, these four MS actuators will drive the ball to roll into the balance boundary [9]. Figure 6 shows the flowchart of position tracking. First of all, the UART1_RX of MSP430 waits for receiving the data of ball's position from the touch panel. When the data are received cumulatively to 5 bytes, MCU calculates the ball position error and error differential using Eqs.(15)-(16).

$$e(k) = r(k) - y(k) \tag{15}$$

$$\dot{e}(k) = e(k) - e(k-1) \tag{16}$$

After calculating, the controller will proceed to forecasted fuzzy control. Subsequently, the crisp_x and crisp_y are output. Because the four MS actuators must drive at the same time, the MCU needs to determine which MS actuator needs drive. As a result, the crisp_x and crisp_y will be parameters to decide which rule will be used to drive the four MS actuators.

The partitions and the shapes of the membership function for ball position error, error differential and control input are shown in Figure 7. Method of circular trajectory tracking

Figure 8 is the circular trajectory tracking. For ball starts to roll, these four MS actuators will drive the ball to roll along the circular trajectory. Figure 9 shows the flowchart of circular trajectory tracking. First of all, the UART1_RX of MSP430 waits for receiving the first data of ball's position from the touch panel. When the first data are received cumulatively to 5 bytes, MCU calculates and finds out the nearest position from the 12 locations on the circular trajectory shown on the Figure 8. Each location is separated from 30 degree. To find out the nearest location means to find out the initial tracking degree θ_0 .

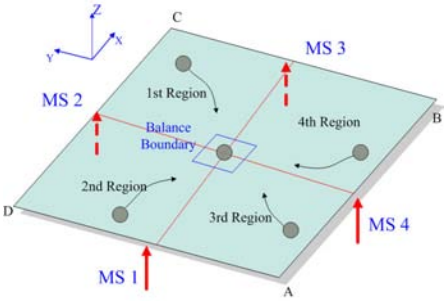


Figure 5: Sketch of position tracking.

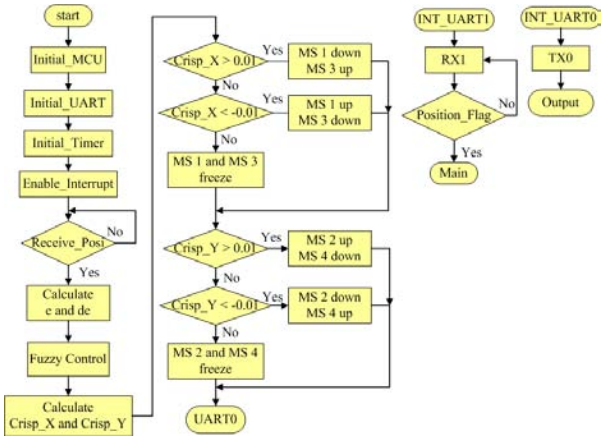


Figure 6: Control flowcharts of position tracking.

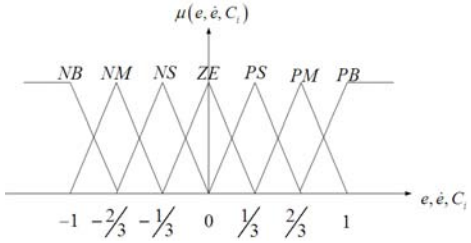


Figure 7: Membership functions.

After finding the initial tracking degree θ_0 , MCU calculates the ball position error and error differential using Eqs.(17)-(21)

$$\theta_0 = 2\pi \times \frac{i}{12} \tag{17}$$

where i is the nearest position of the 12 locations.

$$e_x(k) = (O_x + R\cos(\theta_0 + \frac{2\pi n}{T})) - x(k) \quad n = 1, 2, 3, ... \tag{18}$$

$$e_y(k) = (O_y + R\sin(\theta_0 + \frac{2\pi n}{T})) - y(k) \quad n = 1, 2, 3, ... \tag{19}$$

where (O_x, O_y) is the center of circle, R is the radius and T is the sampling times of one period

$$\dot{e}_x(k) = e_x(k) - e_x(k-1) \tag{20}$$

$$\dot{e}_y(k) = e_y(k) - e_y(k-1) \tag{21}$$

After calculating, the controller will proceed to forecasted fuzzy control. Subsequently, the crisp_x and crisp_y are output. Because the four MS actuators must drive at the

same time, the MCU needs to determine which MS actuator needs drive. As a result, the crisp_x and crisp_y will be parameters to decide which rule will be used to drive the four MS actuators.

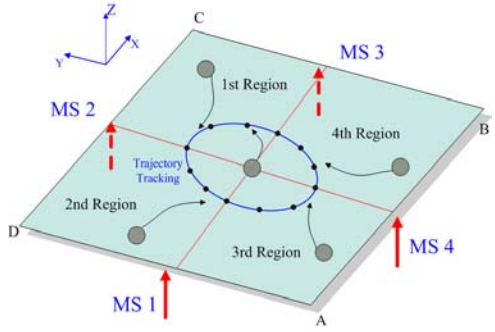


Figure 8: Sketch of circular trajectory tracking.

The partitions and the shapes of the membership function for ball position error, error differential and control input can be observed.

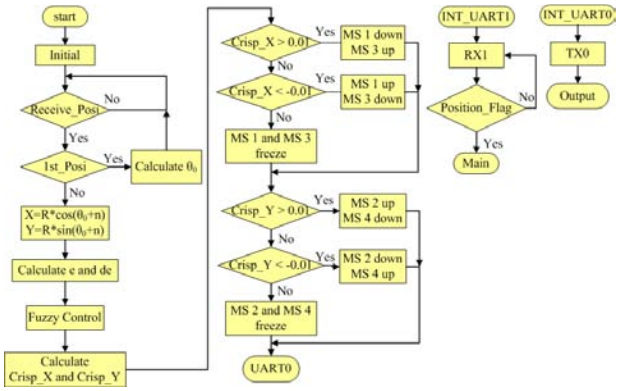


Figure 9: Control flowcharts of circular trajectory tracking.

4.2. Rule table

In this ball and plate controlling system, the rule table [10] is completed by the operator's experience and anticipation. It simulates the human ability of decision-making is the kernel of the fuzzy controller. The control force is decided by the input variables e and $\dot{e}$

Traditionally, for common fuzzy logic rule when the current state is far from the set point, the system will be given a large control force to stable the beam. However, when the current state is near to the sliding surface, the system will oscillate around the set point. Therefore, the system must be coordinated with rule table or forecast table as Table 1.

In Table 2, the forecast table predicts the next step and let the control force occur in advance to improve the stability control system. In this way, it can stop before the state reaches to the equilibrium position, so that the speed of the ball will drop zero and the overshoot will be also decreased.

Table 1 Forecast of fuzzy-rules.

	PB	**PM**	**PS**	**ZE**	**NS**	**NM**	**NB**
PB	NB	NB	NB	NB	NB	NM	NS
PM	NB	NM	NM	NM	NM	NS	ZE
PS	NB	NS	NM	NS	ZE	ZE	PS
ZE	NM	NM	NS	ZE	PS	PM	PM
NS	NS	ZE	ZE	PS	PM	PS	PB
NM	ZE	PS	PM	PM	PM	PM	PB
NB	PS	PM	PB	PB	PB	PB	PB

5. Implementation and Test

After unit function tests, the overall system is integrated for verification tests, as shown in Figure 2.

5.1. Sampling Period and Accuracy in the Ball and Plate System

The process times was read out from the digital oscilloscope. The operation frequency is roughly about 25~30Hz, depend on the velocity of ball. When the ball speed become fast, the touchkit controller will output ball position slowly. The accuracy of the ball position is calculated from its speed and the output frequency of touchkit. As the speed of ball faster, the accuracy of the ball position is worse.

5.2. Position tracking tests

The forecasted fuzzy logic controller is chosen to evaluate the performance of the ball and plate in nonlinear control system applications, two kinds of set points are carried out in different initial conditions to check the system equilibrium and stable capability. The first set point is (0, 0), and the balance zone sets on ±1cm from set point. When the ball rolls into the balance zone, the MCU will stop control. The test results meet the desired performance with settling time from 3~6 *seconds*.

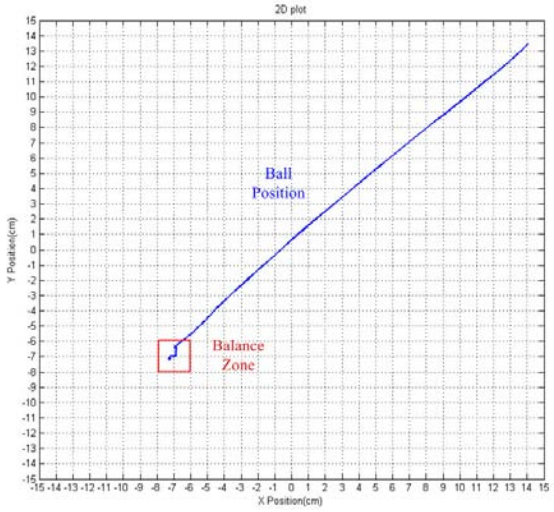


Figure 10: 2D ball position from (14, 13.5) to (-7, -7).

The second set point is (-7, -7), and the balance zone sets on ±1cm from set point. When the ball rolls into the balance zone, the MCU will stop control. The test results also show very good agreement with the desired performance as typical characteristics in Figure 10 and Figure 11, with settling time from 3~7 *seconds*.

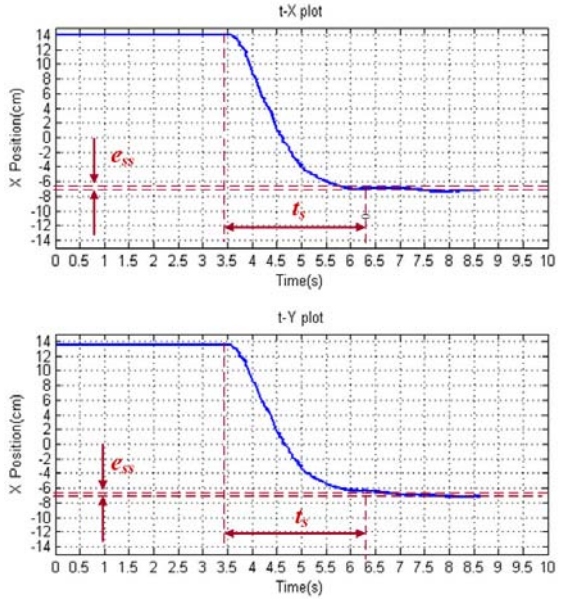


Figure 11: t-X plot and t-Y plot from (14, 13.5) to (-7, -7)

5.3. Trajectory tracking tests

The forecasted fuzzy logic controller is chosen to evaluate the performance of the ball and plate in nonlinear control system applications, several tests are carried out in different initial conditions to check the system trajectory tracking capability. The trajectory is designed as a circle with center of circle O (0, 0), and radius $R = 5$. The test results appear very excellent performance with the circular tracking and trajectory following as shown with a typical case in Figure 12 and Figure 13.

6. Conclusion

This paper presents the dynamic model derivative of ball and plate system for control practice. After using Euler-Lagrange method, this nonlinear problem can be represented as a state space equation. Besides, the MATLAB/Simulink is used to verify this dynamic model and simulate the system control performance.

System hardware and software including MS actuator, drive circuit, touch panel sensor, microcontroller and control law, are accomplished in mechatronics of hybrid EMS actuator with a new version.

In order to test the performance of the position and trajectory tracking, four EMS actuators are built into the ball and plate system. The ball and plate system controls the ball to stop at any position on the plate. From above results, the settling time, percentage overshoot and steady state error of improved FLC are better than traditional FLC. Furthermore, the controller controls the ball into the balance zone successfully. On the other hand, this paper also presents the circular trajectory tracking and the algorithm about how to approach the nearest location in order to start tracking.

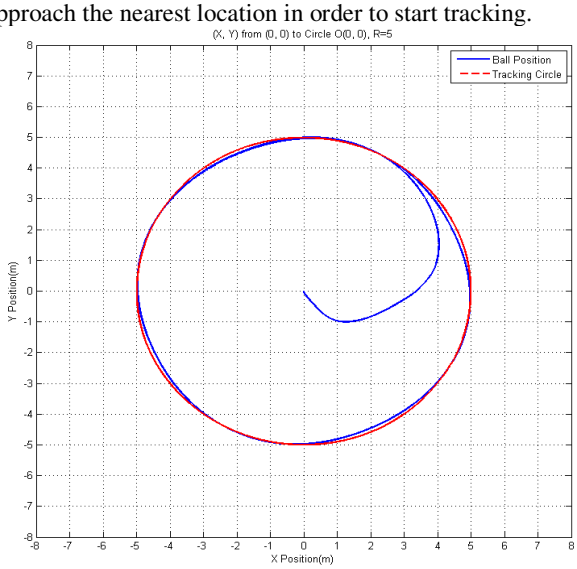


Figure 12: 2D plot of ball position from (0, 0) to circular trajectory of O(0, 0) and R=5.

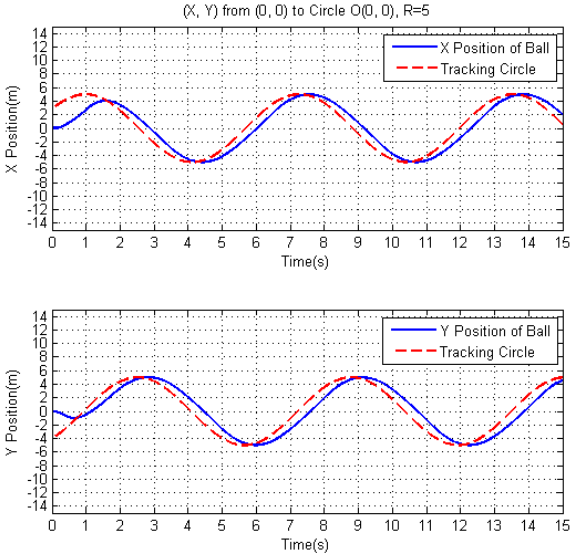


Figure 13: t-X plot and t-Y plot from (0, 0) to circular trajectory of O(0, 0) and R=5.

Acknowledgement: This work is supported from National Science Council under contract: NSC99-2218-E006-239.

References

[1] Moreno-Armendariz, M. A., Perez-Olvera, C. A., Rodriguez, F. and Rubio, E., "Indirect hierarchical FCMAC control for the ball and plate system," *Neurocomputing*, Vol. 73, No. 13-15, 2454–2463, 2010.

[2] Casagrande, D., Astolfi, A. and Parisini, T., "Switching-Driving Lyapunov Function and the Stabilization of the

Ball-and-Plate System," *IEEE Transactions on Automatic Control*, Vol. 54, No. 8, 1881–1886, 2009.
[3] Sinaga, E. F., Manurung, E. B., Chee, V. A. and Djajadi, A. "Building and controlling a ball and plate system," in *Proceedings of the 2nd International Conference on Advances in Communication, Network, and Computing*, Bangalore, India, March 2011, 600–608.
[4] Yuan, D. and Zhang, Z., "Modelling and control scheme of the ball-plate trajectory-tracking pneumatic system with a touch screen and a rotary cylinder," *IET Control Theory and Applications*, Vol. 4, No. 4, 573–589, 2010.
[5] Dong, X. C., Zhang, Z. and Chen, C. "Applying genetic algorithm to on-line updated PID neural network controllers for ball and plate system," in *Proceedings of the 4th International Conference on Innovative Computing, Information and Control*, Kaohsiung City, Taiwan, December 2009, 751–755.
[6] Lin, Chin E. and Ker, C. C., "Control implementation of a magnetic actuating ball and plate system," *International Journal of Applied Electromagnetics and Mechanics*, Vol. 27, No. 1-2, 133–151, 2008.
[7] Cendra, H., Etchechoury, M. and Ferraro, SJ., "Impulsive control of a symmetric ball rolling without sliding or spinning," *Journal of Geometric Mechanics*, Vol. 2, No. 4, 321–342, 2010.
[8] Lin, Chin E. and Jou, H. L., "Force model identification for magnetic suspension systems via magnetic-field measurement," *IEEE Transactions on Instrumentation and Measurement*, Vol. 42, No. 3, 767–771, 1993.
[9] Bai, M., Tian, Y. T. and Su, J. T., "Position control of ball and plate system based on ANFIS," *Dynamics of Continuous Discrete and Impulsive System-Series B-Applications & Algorithms*, Vol. 13, 165–168, 2006.
[10] Rad, A. B. and Chan, P. T. and Lo, W. L., "An online learning fuzzy controller," *IEEE Transactions on Industrial Electronics*, Vol. 50, No. 5, 1016–1021, 2003.

Investigation of Ionized Fields Due to Bipolar DC Transmission Lines

M. Aissou, AK. Laifaoui, H. Aitsaid.
Laboratory of Electrical Engineering
University of Bejaia
Bejaia, Algeria
aissoumas@yahoo.fr

H. Nouri[2], Y. Zebboudj[1]
[1]Laboratory of Electrical Engineering
University of Bejaia
[2]Department of Electrical Engineering,
University of M'sila.

Abstract— **This paper is aimed at the analysis of bipolar corona associated with the ionized field around high voltage bipolar direct current (HVDC) transmission line conductor. The finite element method (FEM) is used to solve the Poisson's equation and a modified method of characteristics is used to satisfy the current continuity condition. The two methods are repeated iteratively to get a self consistent solution of the describing equations. The effectiveness of this approach is tested by comparing the computed results with previously experimental and calculated values. The agreement with experimental results is found to be satisfactory.**

I. INTRODUCTION

Analysis of bipolar ionized field in different geometric configurations, such as high-voltage direct current (HVDC) transmission, electrostatic precipitators, and spray chargers receives the attention of many investigators in the last few decades. The prospects for the widespread use of HVDC transmission underlie the great interest in the evaluation of corona power loss on bipolar transmission lines. In electrostatic precipitators, the major difficulty is the "back corona" which results in a bipolar ionized field that seriously affects the precipitator operation. In addition, bipolar spray charging, as opposed to monopolar charging, was implemented to eliminate corona discharges active at the leaf tips of the sprayed crops [1].

II. DESCRIPTION OF THE PROBLEM

A. Mathematical Formulation

The equations that constitute the mathematical description of the ionized field in air are:

$$\nabla.\vec{E} = \frac{(\rho_+ - \rho_-)}{\varepsilon_0} \quad (1)$$

$$\nabla.\vec{J}_+ = \frac{-R_i \cdot \rho_+ \cdot \rho_-}{q_e} \quad (2)$$

$$\nabla.\vec{J}_- = \frac{R_i \cdot \rho_+ \cdot \rho_-}{q_e} \quad (3)$$

$$\vec{J}_+ = \rho_+.\mu_+.\vec{E} - D_+ \cdot \nabla \cdot \rho_+ \quad (4)$$

$$\vec{J}_- = \rho_-.\mu_-.\vec{E} + D_- \cdot \nabla \cdot \rho_- \quad (5)$$

Equation (1)-(5) are respectively the Poisson's equation, the continuity condition of $\vec{J}$, the total current density vector $\vec{J}$, the positive and negative current density vectors $\vec{J_\pm}$ and the continuity condition of $\vec{J_\pm}$. K_+ and K_- are the mobilities of positive and negative ions, ρ_+ and ρ_- are the positive and negative space charge density values. R_i is the ion recombination coefficient in air, and q_e is the electron charge

B. Simplifying Assumption

In reality it is extremely difficult to find an exact solution to these equations due to their nonlinear nature. All attempts for solving these differential equations were based on some simplifying assumptions the most common ones are [1-5]:

- The space is full of charges of both polarities. The thickness of the ionization region around the inner electrode is so small to be disregarded with respect to the interelectrode spacing.
- The entire electrode spacing is characterized mainly by the transport of ions at the passive electrode.
- The space charge affects only the magnitude and not the direction of the electric field, which is known as the first Deutsh's assumption [6].
- Diffusion of ion is neglected.
- The surface field of the coronating conductors remains constant at the onset values E_{crit+} and E_{crit-} irrespective of the corona intensity. This is known as Kaptzov's assumption and before as Peek's assumption.

III. PROPOSED METHOD OF ANALYSIS

The bipolar configuration investigated consists of two conductors stressed by voltage $+v$ and $-v$, each with a

radius R located at a height H above the ground and separated by a distance D. Figure1

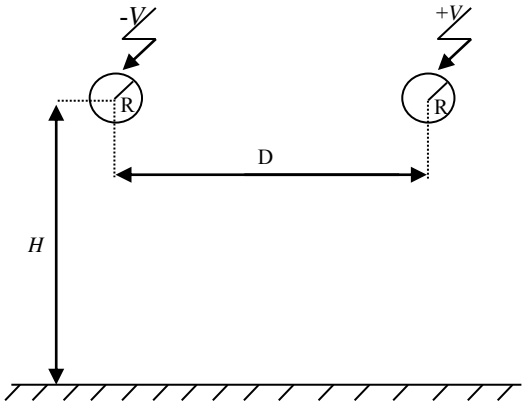


Figure I . Bipolar transmission line configuration

The details of each step of the proposed method are explained in the hereafter.

A. Field Mapping

The FET is applied to determine the potential and field values and to map the field lines equipotential contours. Initially, the space-charge density values are not known and, therefore, they are assigned zero. The electrostatic grid is generated by mapping the space-charge-free-field around the bipolar transmission line conductors. Under the applied voltage $\pm V$, the conductor's surface charges are simulated by line charges $\pm q$, located at the centers of the conductors and their images with respect to the ground plane.

As the transmission line conductors are assumed infinitely long, the investigated configuration is considered to be a two dimensional problem in the $X - Y$ plane. Symmetry about the Y axis equal corona onset voltages, which represents one half of the area of interest for the analysis. The field lines emanate from N nodes selected on the circumference of the conductor Figure II.

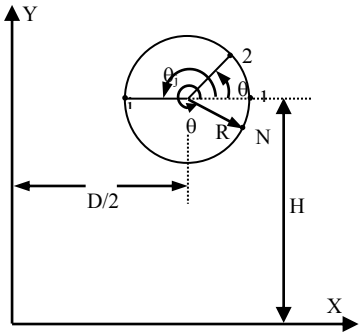


Figure II. Regions were the field lines and equipotential are mapped

The point of intersection between the j^{th} field line and i^{th} equipotential contour represents the node (i, j) of the grid.

B. The Space Charge Density

The space charge density values at the grid nodes are estimated using a modified MOC applied to the flux tubes surrounding the field lines. This is achieved by satisfying the positive and negative current continuity conditions along the axis of the flux tubes. Therefore (6) and (7) are simultaneously integrated by the Euler modified method to give the first estimate of the space-charge density values at the nodes along the axis of the flux tubes in the bipolar ionized region.

$$\frac{\partial \rho_{+i,j}}{\partial \ell} = -\frac{\rho_{+i,j}}{E}\left[R_i \frac{\rho_{-i,j}}{ek_+} + \frac{\left(\rho_{+i,j} - \rho_{-i,j}\right)}{\varepsilon_0}\right] \quad (6)$$

$$\frac{\partial \rho_{-i,j}}{\partial \ell} = \frac{\rho_{-i,j}}{E}\left[R_i \frac{\rho_{+i,j}}{ek_-} - \frac{\left(\rho_{+i,j} - \rho_{-i,j}\right)}{\varepsilon_0}\right] \quad (7)$$

Where ℓ is the length measured along the axis of the flux-tube starting from the conductor surface and E is the electric field at the node (i, j).

C. Finite Element Solution of Poisson's Equation

Poisson's equation is solved by minimizing energy functional with respect to each nodal potential value, were the potential ϕ within each element is approximated as a linear function of coordinates, namely:

$$\phi = \phi^e w^e = \phi_p w_p + \phi_s w_s + \phi_t w_t$$

With p, s and t represent the nodes of the element e and w is the corresponding shape function.
This minimization leads to a set of simultaneous equations for values of ϕ at nodes. The array of nodal potentials is denoted by $\phi^{(m)}$.

D. Correction of The space Charge Density

If the maximum mismatch between the two last estimate of the potential at the $(i, j)^{th}$ node, $\phi_{i,j}^m$ and $\phi_{i,j}^{m+1}$ is less than a prespecified error δ_1, stop, make a new guess for $\rho_{0\pm}$.

$$e = \left|\phi_{i,j}^m - \phi_{i,j}^{m+1}\right| \Big/ \phi_{av}$$

C. Estimation of Discrete Space Charge at Grid Nodes

The distributed space-charges are represented by discrete line charge extending parallel to the coronating conductor and located at the grid nodes. Hence, the charge permit length at node (i, j) is

$$Q_{i,j} = \left(\rho_{+i,j} - \rho_{-i,j}\right) V_{i,j}$$

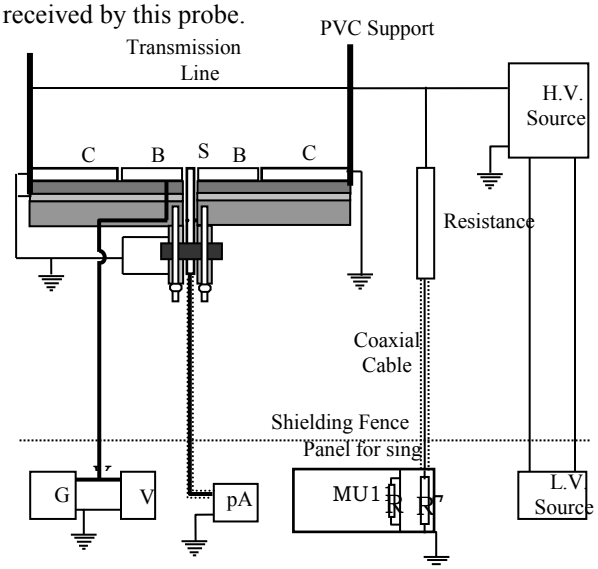
Where $V_{i,j}$ is the volume surrounding the node (i,j) per unit length.

E. Grid Updating

In the next grid generation, the traced field lines and equipotential contours are not only due to the applied voltage, but also due to the space-charges estimated at the grid nodes in step (5).Also the recent space-charge density values around the periphery of the coronating conductor. $\rho_{\pm i,j}$ are used as initial values when integrating (6) and (7). Steps are repeated until the maximum mismatch in the nodal space-charge density values between two successive grid generations is than a prespecified error δ_2.

IV. EXPERIMENTAL SETUP AND PROCEDURE

To investigate the effectiveness of the present method of analysis, an experimental setup was built at the Research Laboratory, University of Bejaia, Algeria. It consists of two wires-plane system, each with a radius R = 0.2mm, two ground planes 150x800 mm^2 and electrode plate 200x800 mm^2 in dimensions, was made of stainless steel, 1mm in thickness. To maintain the stainless steel plate horizontally, it was fixed to a wooden plate of the same size Figure III. In order to measure the current density distribution underneath the transmission line conductors, the aluminium probe (S) is incorporated at a same surface level and in centre of the electrode plate. The circular probe of radius r_s so that the probe (S) lies flash with the surface of on electrode to form an annular gap of width $g = r_e - r_s$. The probe is ground through the Pico-ammeter to measure the corona current received by this probe.



S: circular probe
B: electrode plane
C: ground plates.

V: voltmeter
G: low voltage source

Figure III. View of the experimental setup

V. RESULTS AND DISCUSSION

The bipolar transmission line configurations were tested in the laboratory. Smooth conductors $(\eta = 1)$ with radii $R = 0{,}2mm$, were tested of $H = 50mm$ above the ground plane and spacing of $D = 120mm$. The recombination coefficient R_i was taken as $2\text{x}10^{-12}\ m^3/s$, the positive and negative ion mobilities are according to the applied voltage. A sample of the finite element grid that covers the area of interest around the positive and the negative conductors, for this configuration is shown in Figure IV.

Fig V shows a comparison of characteristic lines with and without the calculated space charge distribution. It is clear that space charge has a very significant effect in concentrating the characteristic lines under the conductor to a larger extent than in the space charge free solution. For one of the bipolar transmission line configuration tested in the laboratory, the measured and calculated ground plane current-density and electric field profiles are shown in figure (VI-VII). It is clear that the agreement between the measured and calculated

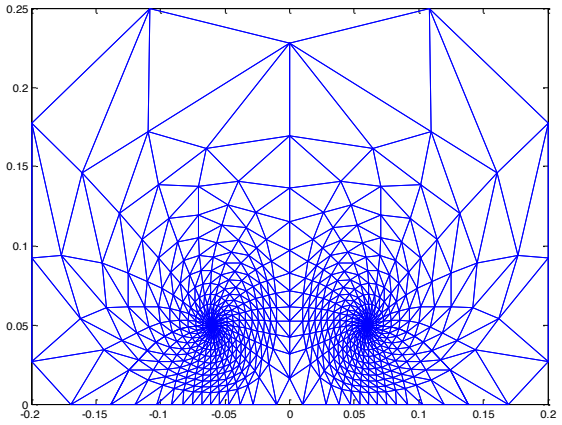


Figure IV. Generated grid for a bipolar transmission line

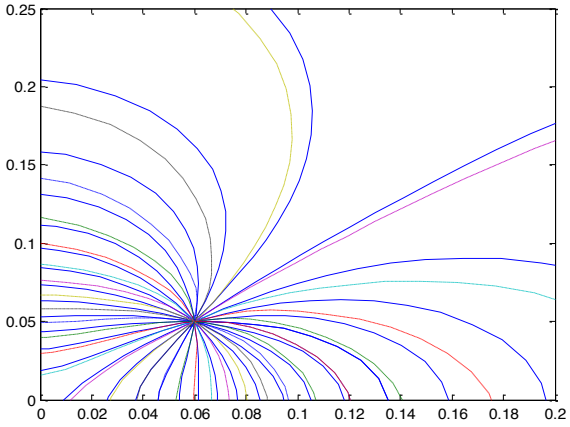


Figure V. Field lines with (solid lines) and (dashed lines) the presence of the space charges density.

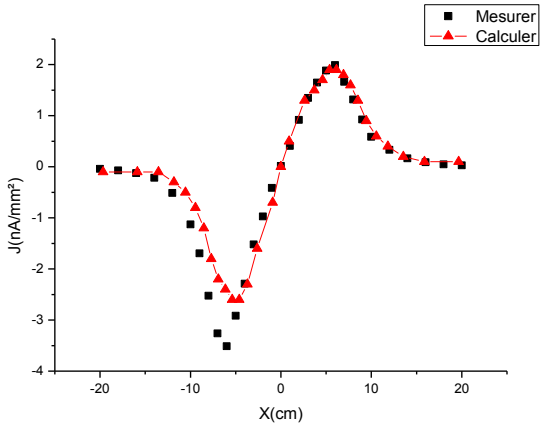


Figure VI. Current density profiles at the ground plane.

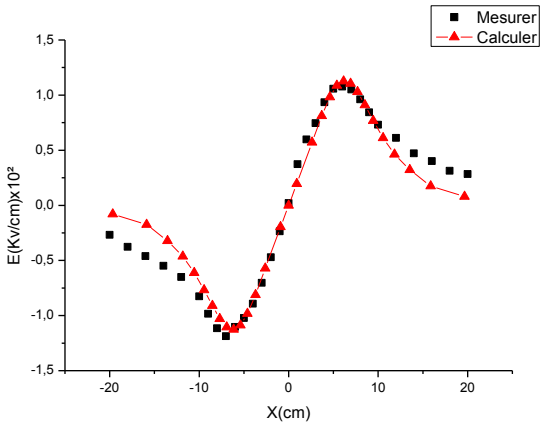


Figure VII. Electric field profiles at the ground plane.

VI. CONCLUSION

A computational algorithm was presented for the calculation of corona discharge, electric field, and current density profiles associated with bipolar HVDC transmission lines. The algorithm is based on the FEM and the MOC where the former solves Poisson's equation and the latter solves the current continuity equation. A new iterative finite-element method is developed for the analysis of the bipolar ionized fields without resort to Deutsch's assumption.

To investigate the effectiveness of the proposed method of analysis, a laboratory model was built. The agreement between the measured and theoretical findings is satisfactory.

REFERENCES

[1] Z.M.Al-hamouz,"Adaptive finite-element ballooning analysis of bipolar ionized fields", IEEE Trans.Ind.Appl.1995.

[2] K.Adamiak,"Adaptive approach to finite element modelling of corona fields", IEEE Trans.Ind.App.Vol.30, No.2, March/April 1994.

[3] M.Abdel-salam and Z.Al-hamouz,"Afinite element analysis of the bipolar ionized field", IEEE Trans.Ind.App, Vol.31, May/June 1995.

[4] W.Janischewsky and G.Gela,"Finite element solution for electric fields of discharging DC transmission lines", IEEE Trans.Power.App.Syst, Vol.PAS-98, pp 1000-1012, may/June 1979.

[5] Z.M.Al-hamouz, M.Abdel-salam and A. Mufti", Improved calculation of finite element analysis of bipolar corona including ion diffusion", IEEE Trans.Ind.App, Vol.34, No.2, March/April 1998.

[6] W.Deutsch, Uber die dichteverteilung unipolar ionenstrome, Ann-Phys.Vol.5, 588-612, 1933.

[7] U.Corbellini and P.Pelachi,"Corona losses in HVDC bipolar lines", IEEE Trans.Power delivery, Vol.11, No.3, July 1996.

[8] Z.M.Al-hamouz,"Corona power loss computation in bundled bipolar conductors", IEEE Trans.Ind.App, 2000.

[9] Z.M.Al-hamouz,"Finite element analysis of corona in wire-duct electrostatic precipitators", IEEE Trans

Analytical model for the TeraHertz noise in $In_{0.53}Ga_{0.47}As$ n^+nn^+ diodes

Fatima Zohra Mahi[1], Luca Varani[2], Paval Shiktorov[3] and Evgenij Starikov[3], Viktor Gruzhinskis[3]

[1]Physics of Semiconductor Devices Laboratory LPDS, University of Bechar, Algeria,
[2]Institute of Electronics of the South, University of Montpellier II, France,
[3]Semiconductor Physics Institute, Vilnius, Lithuania.
*corresponding author, E-mail: fati_zo_mahi2002@yahoo.fr

Abstract

In this contribution we present an analytical approach for the calculation of terahertz frequency noise spectrum in n^+nn^+ structure based on $In_{0.53}Ga_{0.47}As$ material by using the analytical model of Heterostructure Barrier Varactor (HBV) proposed in Ref. [1]. The model enables to interpret the different resonances appearing in the current and voltage spectral densities. In particular, we discuss the effect of geometrical parameters such as the total length of device and the free carriers concentration on the noise resonance. The results can be usuful to optimizing the device parameters for the generation of high frequency resonances noise.

1. Introduction

The noise analysis in n^+nn^+ diodes, in the space-inhomogeneous and hot-carriers conditions resolution, has recently attracted much attention. At low frequencies, the noise spectra properties in n^+nn^+ diodes is calculated by an analytical approach proposed in Ref. [2] and by a Monte Carlo simulator presented in Ref. [3]. In the terahertz frequency some basic questions concerning the discussion of the noise spectrum in n^+nn^+ structure have not yet explained. For this reason we propose an analytical model for the high-frequency noise calculation in n^+nn^+ diodes for InAlAs material. The model is an extension of the analytical approach of Heterostructure Barrier diodes proposed in article [1], it provides an accurate description of the resonances appearing in the high frequency region. Moreover, our analytical model takes into account the fluctuations of the free carriers, the returning carriers and the plasma resonance at n^+n homojunctions for the spectral current density calculation. Under these considerations the conduction current may be neglected and we consider the drift-current fluctuations in our calculation. The results of current noise describe, on the one hand, the contribution of the n^+ and n regions by the position dependence of noise spectra and, on the other hand, the noise on various device parameters by the discussion of the total length and free carriers concentration. The discussion of the appearance of the resonances noise is useful to optimize the geometrical parameter of device for the extraction of the high-order harmonics. To extract the high-frequency signal, the diode is embedded into a parallel output resonant circuit when a large-amplitude microwave voltage is applied.

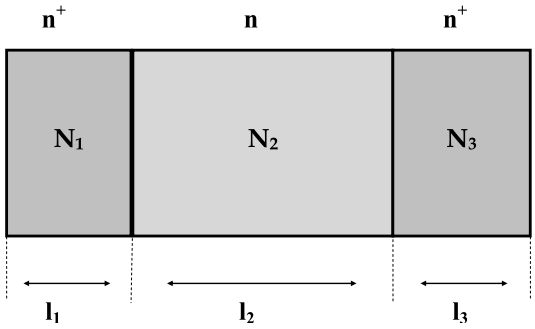


Figure 1: Schematic view of the n^+nn^+ diodes with: l_1 and l_3 the lengths of the n^+ regions, l_2 the length of n regions.

The effectiveness of this model, for the calculation of fluctuations spectrum, has been verified for the nanometric structures such as Schottky barrier diodes (SBD) in article [4] and Heterostructure Barrier diodes (HBV) in article [1].

2. Analytical Model

We are interested in the first step to the evolution of the spectral current density in inhomogeneous n^+nn^+ $In_{0.53}Ga_{0.47}As$ structure. For this case we consider the fluctuations of the drift current δj in terahertz frequency region and the thermal current fluctuations in gigahertz frequency. Then, in the second step, the spectrum of voltage fluctuations is calculated between the terminals of the n^+nn^+ diode embedded into an external RLC resonant circuit. For the spectrum noise calculation, we consider an n^+nn^+ diode similar to the Heterostructure Barrier Varactor n^+n-barrier$-nn^+$ structure with absence of depletion region ($l_d = 0$) studied in Ref [1].

The n^+nn^+ structure shown in figure 1, where l_i is the length of the i-regions (i =1, 2, 3), N_1, N_3 the dopings of the first and second n^+ regions respectively and N_2 the doping of the n region.

2.1. Low frequency current noise model in n^+nn^+ diodes

In the low frequency the noise dominant is the thermal noise, science the n^+nn^+ structure presents an Ohmic current voltage (I-V) characteristic. The evaluation of the thermal current fluctuations corresponding to the Lorenzian form as:

$$S_{R_i}(\omega) = \frac{4kT}{R_i}\frac{1}{1+(\omega\tau)^2} \tag{1}$$

where R_i is the resistance of $i-$region, τ is average time between two collisions defined as $\tau = \frac{\mu_n m^*}{e}$ and μ_n is the mobility. The resistance of i-region can be written as:

$$R_i = \rho_i \frac{l_i}{A_i} \tag{2}$$

where ρ_i is the electrical resistivity and A_i is the cross section of $i-$region. The electrical resistivity calculated at moderate temperature (300 K) and is given by:

$$\rho_i = \frac{1}{eN_i\mu_n} \tag{3}$$

According to the equation (1), the spectral density exhibits it's high value corresponding to the analytical form $\frac{4kT}{R_i}$ when $\omega \to 0$.

2.2. High frequency current noise model in n^+nn^+ diodes

The low frequency current noise calculation has been recently performed by the high frequency analytical model proposed in this contribution. It should be note that the current fluctuations model in terahertz frequency region ($f \geq$ 1 THz) takes into account only the fluctuations of free carriers when the drift component of the current is considered.

The analytical expressions, which describe the current noise characteristics of n^+nn^+ diodes, are derived to the analytical model of Heterostructure barrier varactor [1]. Moreover, for the high frequency region, the current noise behavior to a n^+nn^+ diode is evaluated at room temperature under a constant voltage applied between its terminals. In accordance with Ref. [1] the current spectral density can be represented as:

$$S_{jj}(\omega) = \left(\omega\frac{eA}{L}\right)^2 \sum_{j=1}^{3}\left|\sum_{i=1}^{3} N_i l_i b_{i,j}\right|^2 S_{ff}^j \tag{4}$$

where $S_{ff}^i = 4kT\frac{1}{Am^*}\frac{\nu_i}{N_i l_i}$ is the spectral density of the thermal Langevin force normalized to the free carrier number in $i-$region, m^* is the effective masse of materials, ν_i the momentum relaxation, $L = \sum_{i=1}^{3} l_i$ is the total length of diode and the $b_{i,j}$ elements of the inverse matrix developed in [1] and expressed as: $a_{11} = -\omega^2 + i\omega\nu_1 + \omega_1^2(1-r_1), a_{32} = a_{12} = -r_2\omega_2^2, a_{22} = -\omega^2 + i\omega\nu_2 + \omega_2^2(1-r_2)$, $a_{31} = a_{21} = -r_1\omega_1^2$, $a_{23} = a_{13} = -r_3\omega_3^2$, $a_{33} = -\omega^2 + i\omega\nu_1 + \omega_3^2(1-r_3), r_i = \frac{l_i}{L}$ are the relative lengths and $\omega_i^2 = (e^2/\epsilon\epsilon_0 m^*)N_i$ is the plasma frequency of the $i-$regions. The equation (4) presents the model of current noise spectrum in high frequency, it's available in the terahertz frequency region ($f \geq$1 THz) but it can not be applied in the low frequency region less then 1 THz.

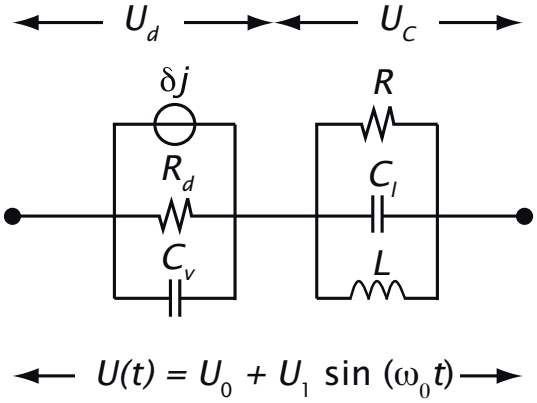


Figure 2: The series connection of the n^+nn^+ diode with a RLC parallel resonant circuit.

The total spectral current density at low and high frequency in n^+nn^+ structure is calculated by coupling the equations (4) and (1):

$$S_{ii}(\omega) = S_{R_i}(\omega) + S_{jj}(\omega) \tag{5}$$

The equation (5) describes the full spectrum of current fluctuations and includes both the low (S_{R_i}) and the high frequencies (S_{jj}) noise components.

2.3. Voltage noise spectrum at n^+nn^+ terminals

Here we shall consider the n^+nn^+ diode embedded into a particular parallel resonant circuit when a microwave voltages $U(t) = U_0 + U_1 sin(\omega_0 t)$ is applied to the whole circuit. The corresponding equivalent scheme is presented in Fig. 2.

The diode is simplified to the resistance $R_d(U_d)$, the capacitance $C_v(U_d)$ which depend on the voltage drop U_d between the diode terminals and the drift-current fluctuations described by the spectral density $S_{jj}(\omega)$. The resonant circuit is characterized by the inductance L, the capacitance C_l and the noiseless resistance R. The voltage fluctuations drop between the diode terminals, δU_d, is obtained by the analytical model detailed in article [5]. The first iteration of spectrum voltage fluctuations obtains as:

$$S_{U_dU_d}^1(\omega) = |Z(\omega)|^2 \left[S_{jj}(\omega) + S_{jj}^v(\omega)\right] \tag{6}$$

where $Z(\omega)$ is the linear impedance of the diode + circuit and S_{jj}^v is the spectrum of extra current fluctuations given as:

$$S_{jj}^v(\omega) = (\omega C_v^0)^2 \sum_{n\neq 0}^{\pm\infty} |\gamma_n|^2 \, |Z(\omega-\omega_n)|^2 \, S_{jj}(\omega-\omega_n) \tag{7}$$

The terms of equation (7) is detailed in articles [5] and [6], where C_v^0 is the constant component capacity of diode and

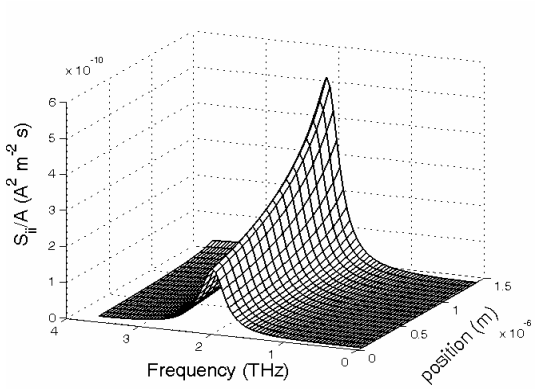


Figure 3: Spectra density of current fluctuations in $In_{0.53}Ga_{0.47}As$ n^+nn^+ diode calculated at frequencies $f <$ 4 THz. With l_1 =0.3 μm, l_2 =1 μm, l_3 =0.3 μm, $N_{1,3} = N_+ = 5\times10^{18}$ cm^{-3} and $N_2 = N_- = 10^{17}$ cm^{-3}.

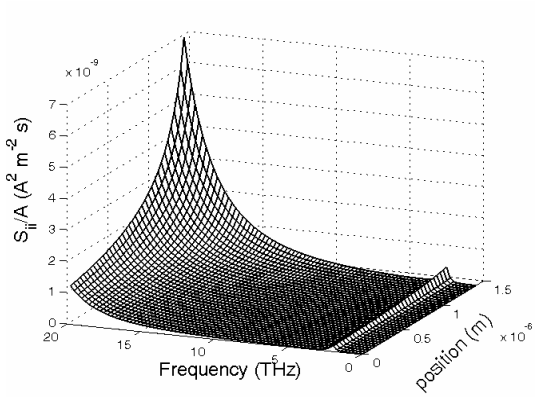


Figure 4: Spectra density of current fluctuations of $In_{0.53}Ga_{0.47}As$ n^+nn^+ diode calculated at high terahertz frequency $0 < f < 25$ THz in the same conditions as figure 3.

γ_n is the relative contribution of the varying part of the n^+nn^+ diode capacitance at the frequency of the n^{th} harmonic of the pumping voltage ω_n =nω_0.

3. Results and discussion

The spectral current density of $In_{0.53}Ga_{0.47}As$ n^+nn^+ structure is calculated for the low terahertz frequency region ($f \leq$4 THz) in figure 3 and for the high terahertz frequency region ($f \leq$20 THz) in figure 4. The mobility and thermal collision time values for $In_{0.53}Ga_{0.47}As$ material are defined in the doctorate these [7].

In figure 3, we remark the appearance of a resonance peak at 2 THz compared to the results of figure 4 where the importance noise peak appears near 20 THz witch can produce the high order harmonics. This means that the $In_{0.53}Ga_{0.47}As$ is useful material for the generation of the high terahertz frequency by n^+nn^+ structures. Moreover, we can increase the limited value for the extraction of harmonics in $In_{0.53}Ga_{0.47}As$ n^+nn^+ structure by the discussion of the lengths effect on the current spectral density (see figure 5).

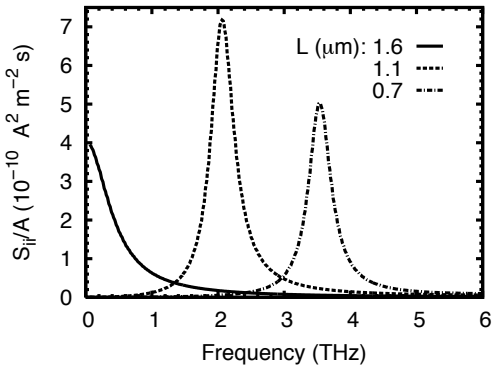


Figure 5: Spectra density of current fluctuations in $In_{0.53}Ga_{0.47}As$ n^+nn^+ structure as a function of length of device. Curve 1: L =1.6 μm, Curve 2: L =1.1 μm and Curve 3: the total length L =0.7 μm.

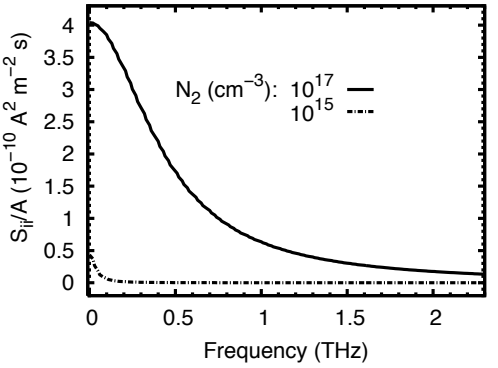


Figure 6: Spectra density of current fluctuations in a $In_{0.53}Ga_{0.47}As$ n^+nn^+ structure as a function of free carrier concentration of n region.

In figure 5, we remark that the frequency position of the resonance peak increases when the total length decreases. Therefore the resonance frequency position increases significantly. According to the results of figure 5, the length value witch gives the higher frequency resonance noise is 0.7 μm.

The figure 6 presents the effect of carriers concentration on the current spectral density. We observe that the current spectral density value increases when the free carrier concentration increases from 10^{15} cm^{-3} to 10^{17} cm^{-3} (see figure 6). The 10^{17} cm^{-3} value of free carrier concentration can produces the high resonance noise.

The dependence of voltage noise spectrum to the length of device is calculated in figure 7 by using Eq. (6) when the length values are 1.6 μm, 1.1 μm and 0.7 μm. The figure 7 includes the extra part of the spectrum of displacement-current fluctuations (second term of equation (6)) when the resonant of circuit condition (n^+nn^+ structure + circuit RLC) is tuned to the frequency of the third harmonics ω_{res}=3ω_0 of the pumping signal at frequency ν_0=200

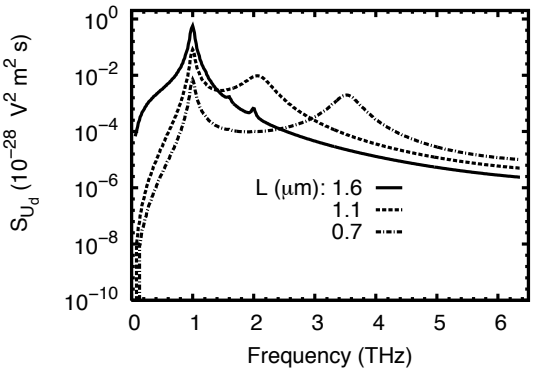


Figure 7: Spectral density of voltage fluctuations between the $In_{0.53}Ga_{0.47}As$ n^+nn^+ structure as a function of the length of device. With $R = 9.5 \times 10^{-10}\Omega m^2$, $L = 1.02 \times 10^{-23}$ Hm^2, C_l=2.7×10^{-4} Fm^{-2}, R_d^0=3.7 ×10^{-5} Ωm^2, C_v^0=2.2×10^{-3} Fm^{-2}.

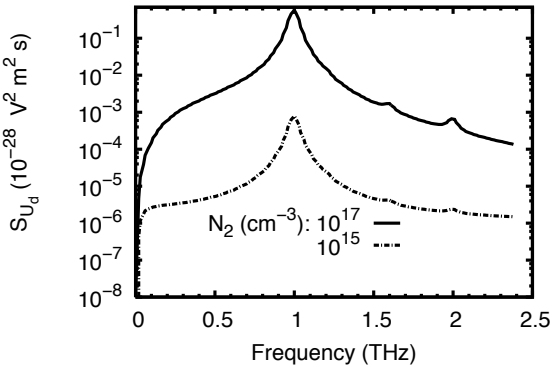


Figure 8: Spectral density of voltage fluctuations between the $In_{0.53}Ga_{0.47}As$ n^+nn^+ structure as a function of free carrier concentration of n region. With $R = 9.5 \times 10^{-10}$ Ωm^2, $L = 1.02 \times 10^{-23}$ Hm^2, C_l=2.7×10^{-4} Fm^{-2}, $R_d^0 = 3.7 \times 10^{-5}$ Ωm^2, C_v^0=2.2×10^{-3} Fm^{-2}.

GHz and the amplitude is U_0=0.45 V. The first resonance peak generated by the n^+nn^+ structure is at 1 THz for different length values. Moreover, we observe the presence of an additional resonance peak at 2 THz and 4 THz corresponding to 1.1 μm and 0.7 μm respectively associated to the decreasing of the total length.

The figure 8 shows the appearance of voltage resonances noise for different free carrier concentration. We observe that the voltage spectrum increases when the free carrier concentration increases and leads to the appearance of an additional resonance peaks at 1.5 THz and 2 THz for the concentration 10^{17} cm^{-3} (see figure 8).

By using this analytical model we can extract n harmonics generated between the resonances peaks appearing at the frequencies 1 THz and 4 THz in figure 7. The results of figure 9 calculated in accordance with Eq. (6) and by changing the parameters of the resonant circuit compared to the condition of figure 7 (changing the resistance R, inductance L and the capacitance C values). We remark the

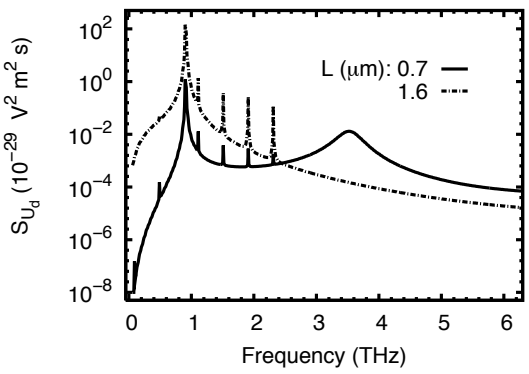


Figure 9: Spectral density of voltage fluctuations between the $In_{0.53}Ga_{0.47}As$ n^+nn^+ terminals calculated for 1.6 μm and 0.7 μm (dashed and solid lines, respectively). With $R = 10^{-8}$ Ωm^2, $L = 1.02 \times 10^{-23}$ Hm^2, C_l=0.8×10^{-3} Fm^{-2}, R_d^0=3.7 ×10^{-5} Ωm^2, C_v^0=2.2×10^{-3} Fm^{-2}.

appearance of resonances peaks in frequencies $\omega_{res} \pm n\omega_0$ when the most important resonance noise is at the frequencies 1 THz and at 4 THz for the total length 0.7 μm.

4. Conclusions

The analytical model proposed in this contribution describes the high frequency part of noise spectral densities in n^+nn^+ structure of $In_{0.53}Ga_{0.47}As$ material.

The evaluation of the current noise of $In_{0.53}Ga_{0.47}As$ n^+nn^+ structure produce a resonance noise appears in high terahertz frequency near 17 THz due to the high mobility of free carriers. The results of the current noise can be useful to calculate the voltage noise when the n^+nn^+ diode is embedded into an external resonant circuit for the extraction of the high-order harmonics. The resonance peaks of the voltage noise spectrum appear in freqiencies $\omega_{res} \pm n\omega_0$ from 1 THz to 4 THz for the device parameters L =0.7 μm and N_2 =10^{17} cm^{-3}.

The discussion of the total length and free carrier concentration dependence on spectrum densities is useful for optimizing the device parameters for the extraction of the high-order harmonics and for the generation of the terahertz frequency.

Acknowledgement

This work is partly supported by the Algerian ministry of higher education and research through contract N. D03820100006, by grant N. MIP-87/2010 of Lithuanian Science Council and by TeraLab-Montpellier.

References

[1] F. Z. Mahi, A. Helmaoui, L. Varani, P. Shiktorov, E. Starikov and V. Gruzhinskis, *Journal of Physics: Conference Series* 193 012067, IOP Publishing, 2009.

[2] O. M. Bulashenko, P. Gaubert, L. Varani, J. C. Vaissière and J. P. Nougier, *Journal of Applied Physics* 88, 2000.

[3] L. Varani and L. Reggiani, *La Rivista Del Nuovo Cimento*, 17 pp. 68-77, 1999.

[4] F. Z. Mahi, A. Helmaoui, L. Varani, P. Shiktorov, E. Starikov and V. Gruzhinskis, *Physica B* 403: pp. 3765–3768, 2008.

[5] F. Z. Mahi, A. Helmaoui, L. Varani, C. Palermo, P. Shiktorov, E. Starikov and V. Gruzhinskis, *Fluctuation and Noise Letters* 10: pp. 121–131, 2011.

[6] F. Z. Mahi, A. Helmaoui, L. Varani, P. Shiktorov, E. Starikov and V. Gruzhinskis, *IEEE proce* 978-1-4577-0191, 2011.

[7] Giulio Sabatini, Etude Monte Carlo de matériaux et composants électroniques à haute mobilité pour les applications TeraHertz, *thèse de doctorat de l'université de Montpellier II*, Soutenue 7 Décembre 2009.

Pspice Modeling of Nonlinear Transmission Lines Analog To Digital Conversion

Hala J. El-Khozondara[1], Rifa J. El-Khozondar[2], Ibtesam Abu Ariban[3], B. Z. Essimbi[4]

[1]Department of Electrical Engineering, IUG, P. O. Box 108, Gaza, Palestine
[2]Physics Department, Al-Aqsa University, P.O. box 4051, Gaza, Palestine
[3]Physics Department, IUG, Gaza, Palestine
[4]ZHO, Optoelectronics, University Duisburg-Essen, D-47048 Duisburg, Germany
[5]Department of Physics, Faculty of Science, University of Yaounde I, P. O. Box 812, Yaounde, Cameroon
*corresponding author, E-mail: hkhozondar@iugaza.edu.ps.

Abstract

Nonlinear transmission lines (NLTL) that consist of coplanar waveguide periodically loaded with resonant tunnel diode (RTD) are capable of shaping signal waveforms during transmission. Such system is the basis of very interesting microwave signal generation circuits and it has a lot of applications in electronics. Pspice is used to model analog to digital converter by generating short electrical pulses on a nonlinear transmission line. Nonlinear transmission line realized as electrical lattice with *N* electrical cells coupled by inductor and resistor in series. Each cell consists of a resonant tunnel diode in parallel with both resistor and capacitor. Attenuation represented by the resistor is cancelled by nonlinear effect. This cancellation produces the desired effect.

1. Introduction

The high speed performance of most digital system is limited by distributed transmission line effects of packaging and interconnects, and not by switching speed of semiconductor devices. In many cases, the quest of higher performance is centering on layout and topological considerations. System performance can be improved by studying transmission line effects [1].

The nonlinear transmission line (NLTL) has three fundamental and quantifiable characteristics just as any nonideal transmission line. These are nonlinearity, dispersion, and dissipation. Along with some other characteristics (e.g. impedance, length, etc.), they define a transmission line's behavior with arbitrary simulation. What distinguishes one class of line from another is the degree to which these characteristics occur and interact. Resonant tunneling diodes have demonstrated maximum frequency of oscillation as high as 1.2 THz. Having the highest frequency among active devices, RTD's have been employed in oscillator, mixer, and switching applications [2-4].

NLTLs consisting of coplanar waveguide (CPW) periodically loaded with resonant tunneling diodes (RTD) provide nonlinearity due to the N-shaped of current-voltage characteristic of the RTD, dispersion due to the periodicity, and dissipation due to the finite conductivity of the CPW conductor and parallel resistance of the diodes [5].

These NLTL is capable of generating picosecond electrical pulses [6]. An important related application is pulse sharpening for the more traditional non-return-to-zero (NRZ) data transmission in digital circuits by improving the rise and fall times of the pulses. Improving the transitions by shrinking the rise and fall times of pulses can be useful in other applications, such as high speed sampling and timing systems [7].

It has shown by previous studies that pulse reshaping is closely related to the N-shaped current-voltage characteristic of RTD [8]. Essimbi and Jäger [9] have performed a study of generating short electrical pulses using a schottky transmission line periodically loaded with RTD. They have been able to break down single wide pulse into multiple pulses.

The focus of this work is on the properties of microwave transmission lines periodically loaded by RTD. Section 2 presents the model of NLTL. Section 3 is dedicated to Pspice simulation results and their significance. conclusion is followed in section 4.

2. Model Description

The equivalent circuit of the nonlinear transmission line (NLTL) used in our simulation is represented in Fig. 1. The equivalent circuit consists of N repeated cells of resonant tunneling diode (RTD) in parallel with capacitor (c) and parallel resistor (Rp). Each cell connected in series with inductor (L) and resistor (R). Using Kirchhoff laws we can write the equations which govern the processes of the nonlinear waves in this equivalent circuit.

$$c\frac{dV_n}{dt} = I_n - I_{n+1} - J_n - \frac{V_n}{R_p} \tag{1}$$

$$L\frac{dI_n}{dt} = V_{n-1} - V_n - RI_n, \tag{2}$$

where V_n and I_n are respectively the voltage at the n^{th} node and current entering the n^{th} node, and J_n is the current through the RTD defined by

$$J_n = BV_n(V_n - U_1)(V_n - U_2), \tag{3}$$

where U_1 and U_2 are constants, and B is the factor which is determined by the slope at V=0. Equation (3) shows that the

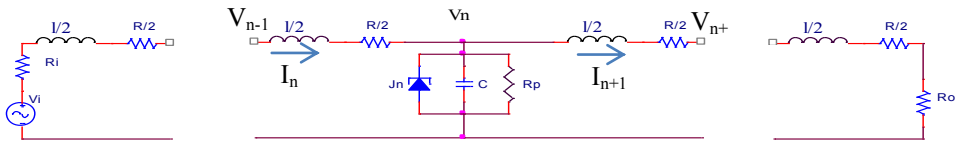


Figure 1. Equivalent circuit of RTD-NLTL

RTD current-voltage characteristic obeys the cubic relation. The RTD current-voltage characteristic curve expressed by equation (3) for different values of U_1 and U_2 are plotted in Fig. (2. a) shows the RTD characteristic curve at U_1 = 0.1 V and U_2 = 0.2 V. In this case, the area S_1 that is above the zero current line equal the area S_2 under the zero current line.While Fig. (2. b) displays the characteristic curve at U_1 = 0.1 V and U_2 = 0.3 V. Considering $S_1 < S_2$. The RTD characteristic curve at U_1 = 0.2 V and U_2 = 0.3 V is plotted in Fig. (2.c) where $S_1 > S_2$.

3. Circuit Parameters and numerical results

The experimental electric circuit is composed of N=80 elements, where the values of the parameters are as follows: R=0.25 Ω, c =53.1 fF, l=37.3 pH, and R_p=10 KΩ. The input resistor R_1 =50 Ω is introduced at the input port of the circuit to an input voltage and the output is set free. Equation (1) and (2) are solved numerically using Pspice simulation program.

The input voltage is defined to be a sinusoidal signal with amplitude 0.5 V and frequency 2GHz. The output at n=30, 40, and 50 for U_1=0.1V and U_2=0.2V, S_1=S_2, is shown in

Fig. 3. The output signal has a kink and antikink structure with constant pulse width. Repeating the measurement with U_1=0.1V and U_2=0.3V where S_1< S_2, we get Fig. 4. In this case, we notice that the pulse suffers from dispersion where the pulse width widens as it propagates. However, when U_1=0.2V and U_2=0.3V where S_1> S_2, the pulse will propagate while its width decrease as exhibited in Fig. 5.

4. Conclusion

Nonlinear transmission lines (NLTL) modeled as N electrical cells consist of RTD in parallel with capacitor and resistor coupled by inductor and resistor in series are capable of shaping signal waveform during transmission. Such system is the basis of very interesting microwave signal generation circuits and it has a lot of digital applications. Pspice is used to model analog to digital converter by generating short electrical pulses on a nonlinear transmission line.

Attenuation represented by the resistor is cancelled by nonlinear effect. This cancellation produces kink and antiknik pulses which has a fast rise time is an indication of the usefulness of the system in converting analog to digital signal.

References

[1] D. Winklestein, M. B. Steer, R. Pomerleau, Simulation of arbitrary transmission line networks and nonlinear transmissions, IEEE T Circuits Syst. 38: 418- 422 , 1991.

[2] R. K. Hoffmann, Handbook of Microwave Integrated Circuits, Artech House, Inc., Norwood, 1987.

[3] H. C. Liu, D. D. Coon, Heterojunction Double-Barrier Diodes for Logic Applications, Appl. Phys. Lett. 50: 1246-1248, 1987.

[4] E. Özbay, D. M. Bloom, D. H. Chowand, J. N. Schulman, 1.7 ps, Microwave, Integrated-Circuit-Compatible InAs/AlSb Resonant Tunneling Diodes, IEEE Electr Device L. 14: 400 – 402, 1993.

[5] E. R. Brown, J. R. Soderstrom, C. D. Parker, L. J. Mahoney, K. M. Molvar, and T. C. McGill, Oscillations Up To 712 GHz in InAs/AlSb Resonant-Tunneling Diodes, Appl. Phys. Lett. 58: 400-402, 1991.

[6] D. Jäger, Characteristics of travelling waves along nonlinear transmission lines for monolithic integrated circuits, A review, int. J. Electron. 58: 649-669, 1985.

[7] E. Afshari, A. Hajimiri, Non-linear transmission lines for pulse shaping in silicon, IEEE solid state circuits, 40: 744-752, 2005.

[8] Y. I. Vorontsov, Certain properties of delay lines containing tunnel diodes, Radiotekhnika I electron. 9: 478-483, 1964.

[9] B. Z. Essimbi, D. Jäger, Generation of electrical short pulses using a schottky transmission line periodically loaded with tunneling diodes, phys. Scr. 81:1-4, 2010.

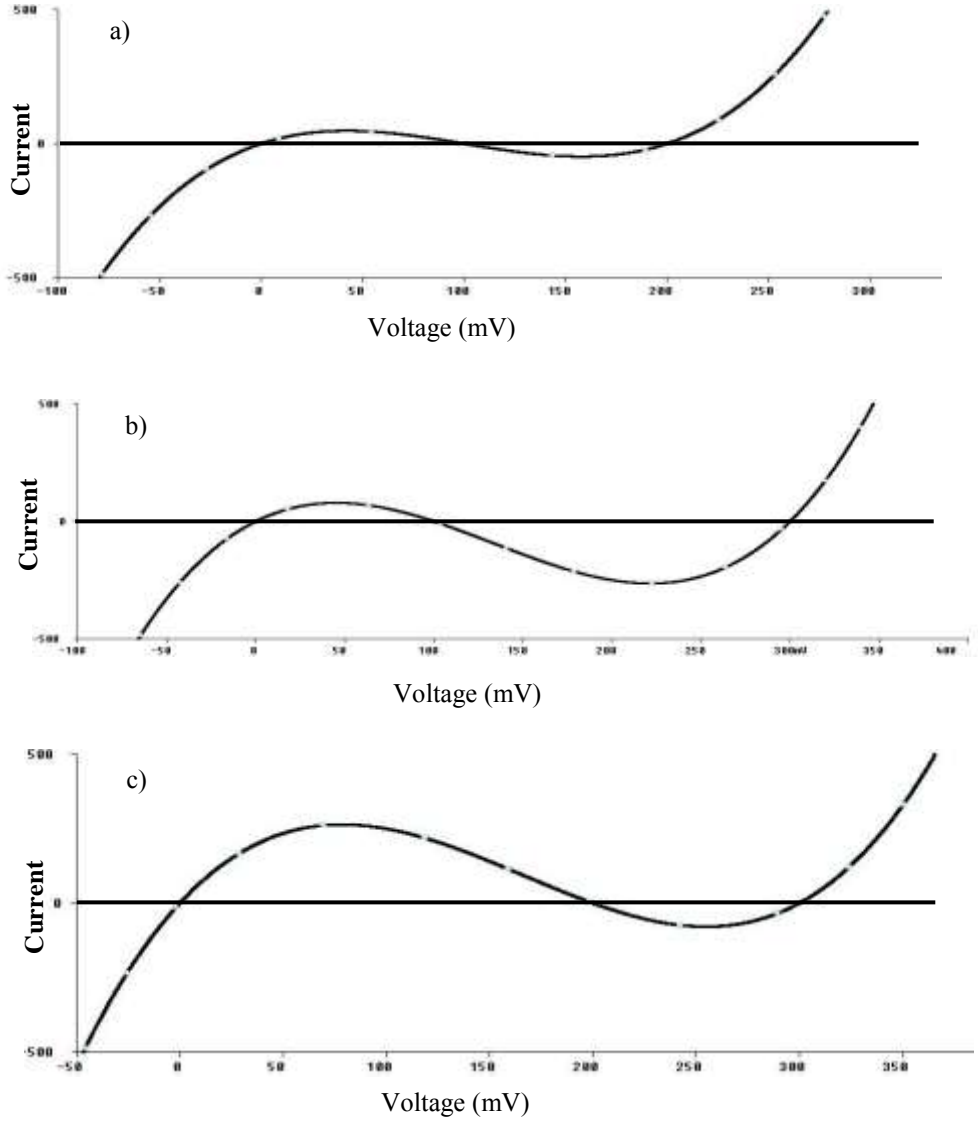


Figure 2. The characteristic curve of the RTD for a) U_1=0.1 V and U_2=0.2 V; b) U_1=0.1 V and U_2=0.3 V; c) U_1=0.2 V and U_2=0.3 V.

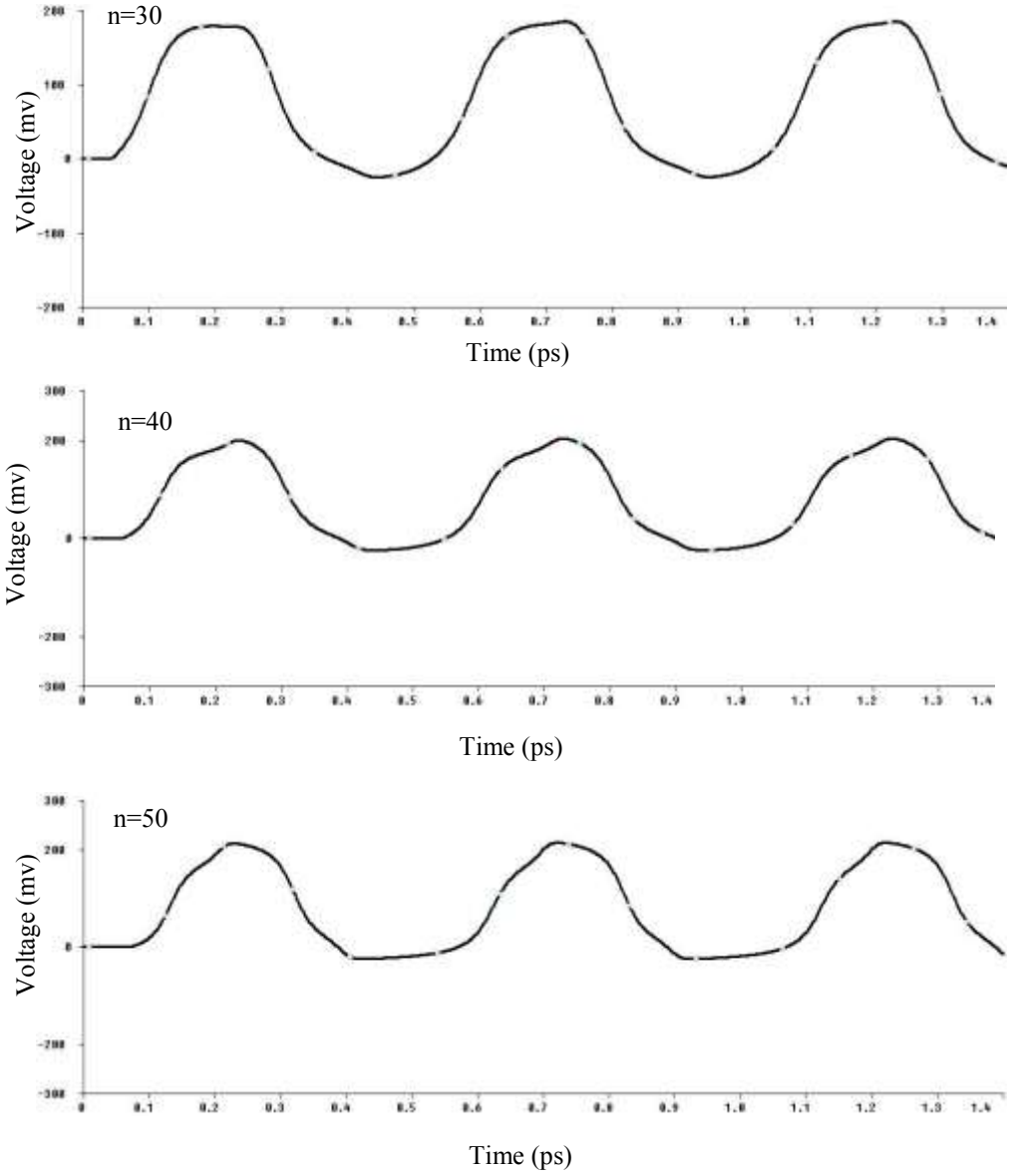


Figure 3. Pulse profile versus normalized time at n=30, 40, 50, U_1=0.1 and U_2=0.2.

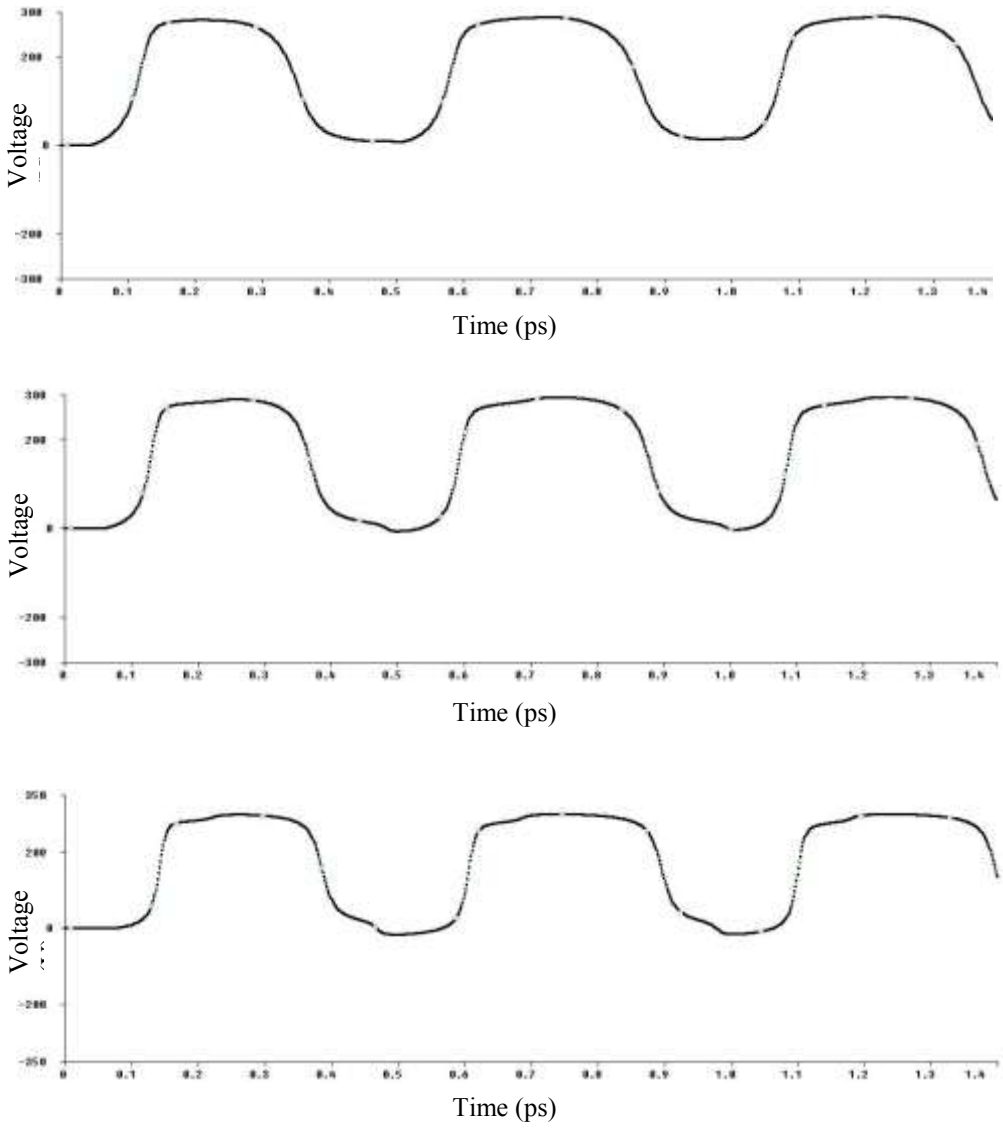


Figure 4. Pulse profile versus normalized time at n=30, 40, 50, U_1=0.1 and U_2=0.3.

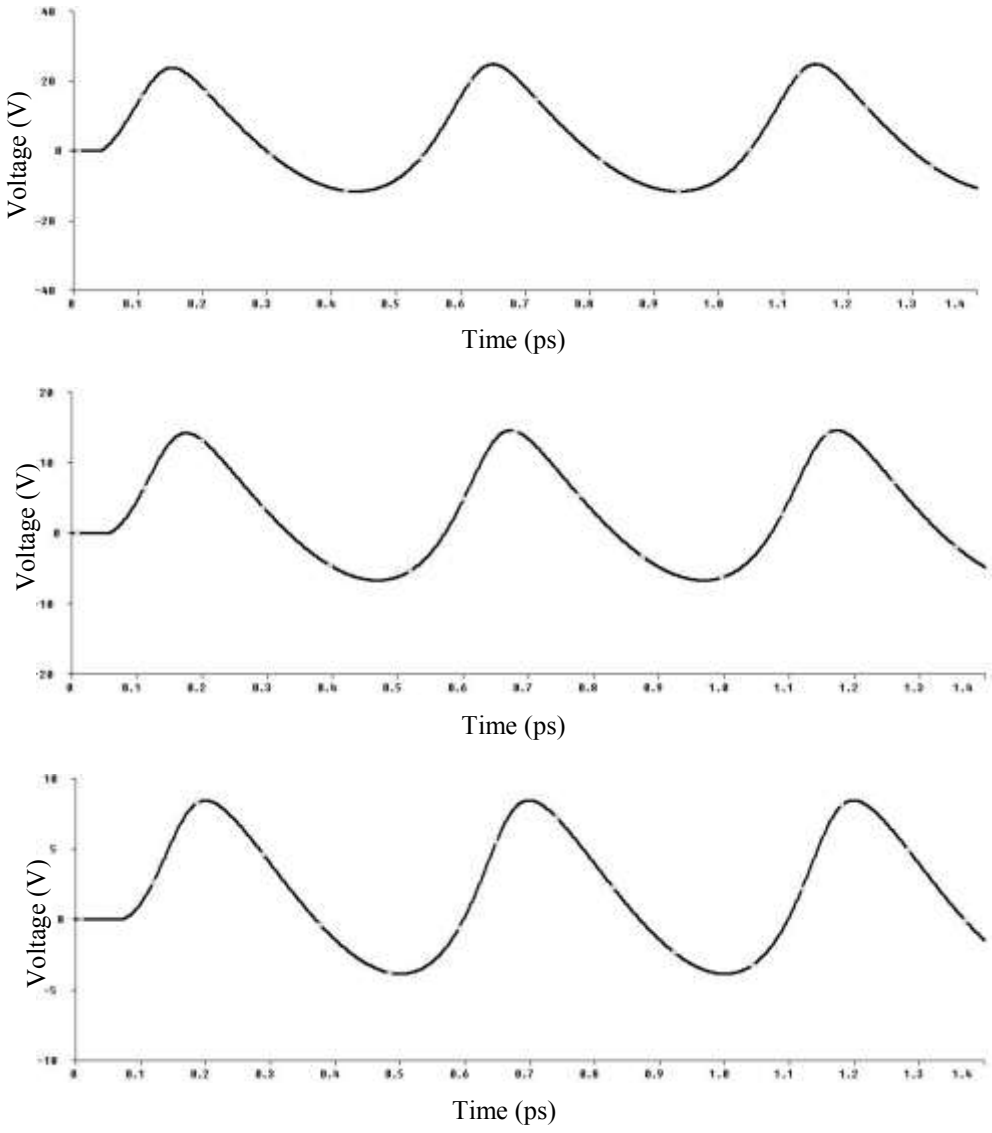


Figure 5. Pulse profile versus normalized time at n=30, 40, 50, U_1=0.2 and U_2=0.3.

Compact Active Integrated Antenna by Using an Interdigital Coupling Strip for WiMAX Applications

Mohammad Ojaroudi[1], Jalil Mazloum[1], Ali Jalali[1], and Nasser. Ojaroudi[2]

[1]Faculty of Electrical and Computer Engineering, Shahid Beheshti University, Tehran, Iran.
[2]Faculty of Electrical & Computer Engineering, Shahid Rajaee Teacher Training University, Tehran, Iran
*corresponding author, E-mail: m.ojaroudi@sbu.ac.ir

Abstract

A novel active feedback antenna for WiMAX applications is presented. By using an interdigital coupling strip in the active feedback antenna two new resonances can be achieved. Also the proposed interdigital radiating patch has a major advantage in providing tighter capacitive coupling to the line in comparison to known radiating patch. In order to generate DC isolation in the RF path, we use a pair of gap distances in the microstrip loop. Simulated and experimental results obtained for this antenna show that the proposed Active Integrated Antenna (AIA) has a good return loss and radiation behavior within the WiMAX frequency range

1. Introduction

In the last few years, there have been rapid developments in worldwide interoperability for microwave access (WiMAX) applications. The 2.5/3.5/5.5 GHz (2.500–2690/3400–369/5250 5850 MHz) bands are demanded in practical WiMAX applications,. During the last years, there are various antenna designs, which enable antennas with low profile, lightweight, flush mounted, and WiMAX devices. These antennas include the planar inverted-F antennas (PIFAs) [1], printed dipole antenna [2], the chip antennas [3], and the planar monopole antennas [4]. However, up to now, a printed antenna that has T-shaped notch configuration has not been reported.

In WiMAX communication systems, one of key issues is the design of a compact active antenna while providing wideband characteristic over the whole operating band. It is a well-known fact that active feedback presents really appealing physical features, such as simple structure, small size, and low cost. Because of all these interesting characteristics, active feedback are extremely attractive to be used in WiMAX applications, and growing research activity is being focused on them [5-8].

In this study, based on Electromagnetic Coupling (EC), an interdigital coupling strip in the microstrip transmission line is used to perturbs two resonance frequencies at 3.5 GHz (WiMAX) and 4.2 GHz (C-band). The proposed interdigital radiating patch is shown in Figure 1 (a). This structure has a major advantage in providing tighter capacitive coupling to the line in comparison to known radiating patch [9]. In the proposed configuration a pair of gap distances are playing an important role in the radiating characteristics of this antenna, because it can adjust the electromagnetic coupling effects between the interdigital radiating patch and the microstrip transmission line [7].

2. Antenna Design and Configuration

The proposed passive antenna fed by a 50-Ω feed line is shown in Figure 1, which is printed on a FR4 substrate of thickness 0.8 mm, and permittivity 4.4. The numerical and experimental results of the input impedance and radiation characteristics are presented and discussed. The Ansoft simulation software high-frequency structure simulator (HFSS) [10] is used to optimize the design and agreement between the simulation and measurement is obtained.

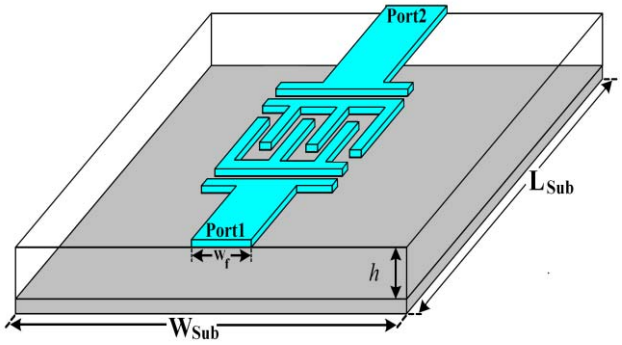


Figure 1: The proposed antenna by using an interdigital coupling strip.

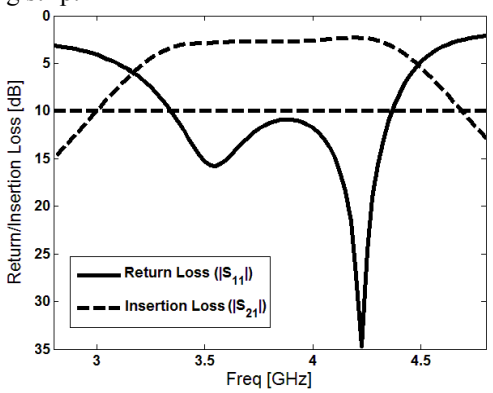


Figure 2: Measured return loss and insertion loss characteristics for the passive microstrip antenna.

Figure 2 shows the measured return loss and insertion loss characteristics of the proposed antenna as shown in Figure 1. The fabricated antenna has the frequency band of 3.27 to over 4.38 GHz with two resonance frequencies around 3.53 and 4.23 GHz.

3. Active Integrated Antenna Design

The presented active feedback antenna is shown in Fig. 3, which is printed on an FR4 substrate of thickness 1.6 mm, permittivity 4.4, and loss tangent 0.018. The proposed active feedback antenna structure consists of an interdigital coupling strip for radiating element, a microstrip loop, and a amplifier with DC bias circuit and matching circuit for active part. The width of the 50-Ω microstrip line is fixed at 3.2 mm, as shown in Figure 1. The matching circuit to the left and right of the device controls the degree of feedback. On the other side of the substrate, a conducting ground plane is placed. In addition, to satisfy the oscillation-phase requirement, the microstrip loop is fixed to a suitable electrical length, taking the measured phases of the amplifier and passive antenna into consideration [8]. The proposed antenna is connected to a 50-Ω SMA connector for signal transmission.

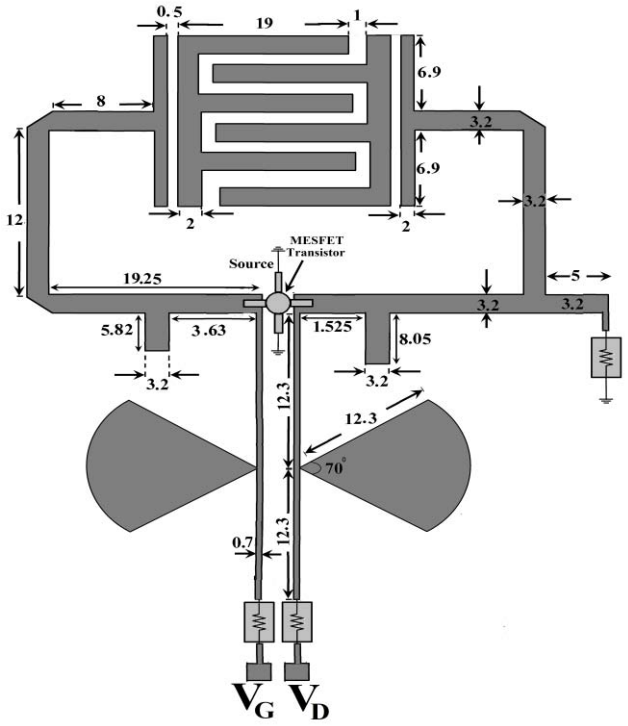


Figure 3: Configuration of the proposed active integrated antenna with GaAs MESFET.

The simulated radiation patterns including the co-polarization and cross-polarization for the E-plane (y-z plane) and H-plane (x-z plane) at the resonance frequencies are shown in Figure 2 (b). The simulated radiation patterns are calculated by using the gap-source technique with the commercial EM simulator HFSS, considering the complete active feedback antenna, which has same layout, except with an active transistor [3]. The received cross-polarizations in the E-plane and H-plane of the AIA are approximately 17 and 14 dB lower than the maximum co-polarized radiation, respectively. As seen in Figure 3, the radiation pattern in the H-plane is asymmetrical due to the asymmetrical presence of the distributed oscillator-feedback circuitry. The obtained gain by the amplifier is of 11.2dB. The designed feedback-antenna oscillator has stable oscillation and a clear spectrum at the frequency of 3.54 GHz, which is only a 0.2% deviation from the design frequency.

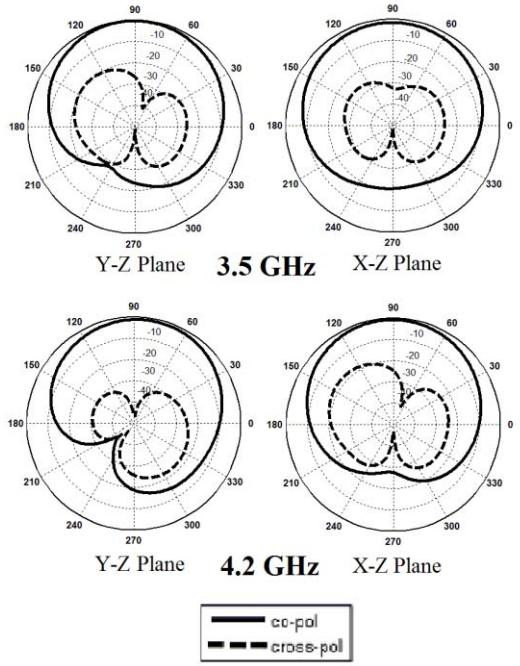


Figure 4: simulated radiation patterns of the proposed antenna.

4. Conclusions

As presented above, the AIA is an interesting subject for WiMAX applications. In this paper, an active integrated antenna using a interdigital coupling strip antenna, are presented. In the proposed structure, based on Electromagnetic Coupling (EC), an interdigital coupling strip in the microstrip transmission line is used to perturbs two resonance frequencies at 3.5 GHz (WiMAX) and 4.2 GHz (C-band). The amplifier design based on the AIA concept has been shown to provide an efficient and successful method for designing high efficiency and compact systems. The obtained gain by the amplifier is of 11.2dB. The designed feedback-antenna oscillator has stable oscillation and a clear spectrum at the frequency of 3.54 GHz, which is only a 0.2% deviation from the design frequency.

Acknowledgements

The authors are thankful to Microwave Technology Company staff for their beneficial and professional help. (www.microwave-technology.com).

References

[1] F.R. Hsiao and K.L. Wong, Compact planar inverted-F patch antenna for triple-frequency operation, Microwave Opt Technol Lett 33 (2002), 459–462.

[2] V. Stoiljkovic, S. Suganthan, and M. Benhaddou, A novel dualband center-fed printed dipole antenna, in Proc IEEE Antennas Propag Soc Int Symp 2 (2003), 938–941.

[3] Y. Dakeya, T. Suesada, K. Asakura, N. Nakajima, and H. Mandai, Chip multiplayer antenna for 2.45GHz-band application using LTCC technology, Int IEEE MTT-S Microwave Symp Dig 3 (2000), 1693–1696.

[4] P. Chein-Yuan, H. Tzyy-Sheng, C. Wen-Shen, and H. Chien-Hsiang, Dual wideband printed monopole antenna for WLAN/WiMAX application, IEEE Antennas Wirel Propag Lett 6 (2007), 149–151.

[5] Kai Chang, "Active Integrated Antennas," Proc. IEEE, VOL. 50, NO. 3, MARCH 2002.

[6] Hall,P.S., Gardner.,P., and Ma, G., "Active Integrated Antenna", *IEICE Trans*. *Commun*., 2002, E85-B, (9),pp. 1661-1666.

[7] J.C.Liu, C. S. Cheng, H. C. Chen and P., C, Chen, "Active Integration RingAntenna/phase shifter for direct conversions", *IEE Proc*.- *Microw*. *Antennas Propag*., Vol. 151, No 4, pp 357-361,August 2004

[8] G.Yun, "Compact oscillator-type active antenna for UHF RFID reader", *Electronic Letters*, Vol. 43, No.6, March 2007.

[9] M. Ojaroudi, Sh. Yzdanifard, N. Ojaroudi, and M. Nasser-Moghaddasi, "Small Square Monopole Antenna with Enhanced by Using Inverted T-Shaped Slot and Conductor-Backed Plane ", IEEE Transactions on Antenna and Propagation, VOL. 59, No. 2, pp. 670-674, February 2011.

[10] Ansoft High Frequency Structure Simulation (HFSS), Ver. 13, Ansoft Corporation, 2010.

A 20 – 40 GHz Balun in 0.13 μm GaAs pHEMT Technology

Antoine Khy, and Bernard Huyart

Département de Communications et Electronique (COMELEC), Institut TELECOM – TELECOM ParisTech – LTCI CNRS, Paris, France
*Antoine Khy, E-mail: antoine.khy@telecom-paristech.fr

Abstract

This paper presents the design of a millimeter-wave Marchand balun realized in 0.13 µm GaAs pHEMT technology. The balun uses two Lange couplers as quarter-wavelength λ/4 line elements with short- and open-circuit terminations. The theoretical principle is based on coupling and reflections of RF signals that occur within the device in order to achieve a wide operational bandwidth. Although the design of this kind of architecture usually involves full-wave electromagnetic (EM) simulations, the proposed balun was designed with the help of components models made available by the foundry process. The realized balun shows return loss below – 6dB, insertion loss better than 6 dB, as well as amplitude and phase mismatch not exceeding 0.4 dB and 7°, respectively. Measurements results compared to simulations highlight the accuracy limits of the components models.

1. Introduction

Baluns are three port networks that can be considered as 3 dB power dividers with two outputs 180° out of phase. These components are used in circuits such as balanced mixers [1] – [7], frequency doublers [8] and triplers [9] in order to perform single-ended to differential conversion of the signal. The performance of these circuits is heavily impacted by the baluns quality. In integrated circuits technology, there are basically two categories of baluns: lumped elements and distributed baluns. Lumped elements baluns [10],[11] usually consist of high/low-pass filters combinations. These structures are not usable at millimeter-wave frequencies since inductors and capacitors have low resonant frequency. On the other hand, distributed baluns cannot be used in practice below approximately 20 GHz since they are made of quarter-wavelength λ/4 elements that occupy much chip area. However, at millimeter-wave frequencies they become very attractive due to their compactness and wideband characteristics. Indeed, distributed baluns have operational bandwidths that can exceed an octave. The various distributed architectures reported so far are Marchand-type baluns [12] that primarily differ in the quarter-wavelength λ/4 line that is used to realize the desired coupling. Spiral transformers [3],[4],[7], broadside coupled lines [5],[6] and Lange couplers [1],[2] are commonly used in distributed baluns. In the presented Marchand balun, Lange couplers have been chosen because components models were made available in the design kit of the OMMIC D01PH foundry process (0.13 µm GaAs pHEMT technology). The aim of this work is to assess the validity of the components models of the design kit as frequency increases towards millimeter-waves.

In the following, we present the theoretical analysis of the Marchand balun, the design procedure and a comparison between measurement and simulation results.

2. Analysis and Design of the Marchand balun

Fig. 1 presents the diagram of the Marchand balun as well as an individual Lange coupler with ports naming convention shown. The balun consists of the combination of two quarter-wavelength λ/4 Lange couplers whose coupled ports are connected to a via-hole that acts as short-circuit (S/C) while direct ports are tied together. The input port of the upper Lange coupler is the balun input (port 1) whereas the input port of the lower one is left unconnected as open-circuit (O/C). The 180° out of phase outputs (ports 2 and 3) are taken from each of the isolated ports of the Lange couplers.

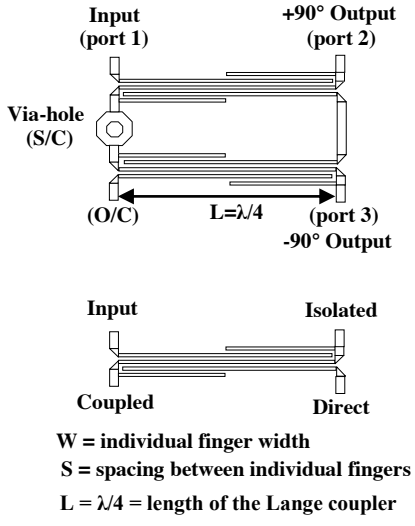


Figure 1: Diagram of the Marchand balun and individual Lange coupler with ports naming convention

If we assume ideal couplers, i.e. lossless, with infinite directivity, coupling coefficient C and transmission coefficient $T = -j\sqrt{1-C^2}$, the corresponding scattering matrix $[S]_{coupler}$ of an individual coupler is given by

$$[S]_{coupler} = \begin{bmatrix} 0 & C & -j\sqrt{1-C^2} & 0 \\ C & 0 & 0 & -j\sqrt{1-C^2} \\ -j\sqrt{1-C^2} & 0 & 0 & C \\ 0 & -j\sqrt{1-C^2} & C & 0 \end{bmatrix} \quad (1)$$

The [S] parameters of the balun are derived from coupling and transmission properties of the couplers as well as reflection from short- and open-circuit terminations. As an example, the successive steps to derive the total transmission coefficient from port 1 to port 2, namely S21 are illustrated in Fig. 2. In Fig. 2 a), the most straightforward path for an incident signal between input port 1 and output port 2 is depicted. The resulting S21 is – CT with negative sign due to short-circuit (S/C) 180° phase shift. Fig. 2 b) shows a little more complicated situation since the signal is transmitted from the upper Lange coupler to the lower one, then transmitted to the open-circuit (O/C) termination where total reflection occurs, transmitted back to the upper coupler and finally coupled to the output. Thus, the resulting S21 is T^3C. Fig. 2 c) is identical to Fig. 2b) until the signal is coupled to the (S/C) after being reflected by the (O/C) instead of being transmitted back to the upper coupler. The (S/C) introduces 180° phase shift, then the signal is coupled back to the (O/C), totally reflected, transmitted to the upper coupler and coupled to the output. In this case, S21 is equal to $T^3C\times(-C^2)$. From the situation depicted in Fig. 2 c), the signal repeatedly goes back and forth between the (O/C) and (S/C) et is finally coupled to the output, so the successive contributions to total S21 are $T^3C\times(-C^2)\times(-C^2)$, then $T^3C\times(-C^2)\times(-C^2)\times(-C^2)$ and so on. The total transmission coefficient from port 1 to port 2 is the sum of all of these terms and can be written as

$$S21 = -CT + \frac{T^3C}{1+C^2} = j\frac{2C\sqrt{1-C^2}}{1+C^2} \quad (2)$$

A similar analysis allows the derivation of the other [S] parameters. It can be shown that the scattering matrix $[S]_{balun}$ is as follows:

$$[S]_{balun} = \begin{bmatrix} -C^2 + \frac{T^4}{1+C^2} & -CT + \frac{T^3C}{1+C^2} & CT - \frac{T^3C}{1+C^2} \\ -CT + \frac{T^3C}{1+C^2} & -T^2 + \frac{T^2C^2}{1+C^2} & C^2 - \frac{T^2C^2}{1+C^2} \\ CT - \frac{T^3C}{1+C^2} & C^2 - \frac{T^2C^2}{1+C^2} & -T^2 + \frac{T^2C^2}{1+C^2} \end{bmatrix} \quad (3)$$

$$[S]_{balun} = \begin{bmatrix} \frac{1-3C^2}{1+C^2} & j\frac{2C\sqrt{1-C^2}}{1+C^2} & -j\frac{2C\sqrt{1-C^2}}{1+C^2} \\ j\frac{2C\sqrt{1-C^2}}{1+C^2} & \frac{1-C^2}{1+C^2} & \frac{2C^2}{1+C^2} \\ -j\frac{2C\sqrt{1-C^2}}{1+C^2} & \frac{2C^2}{1+C^2} & \frac{1-C^2}{1+C^2} \end{bmatrix} \quad (4)$$

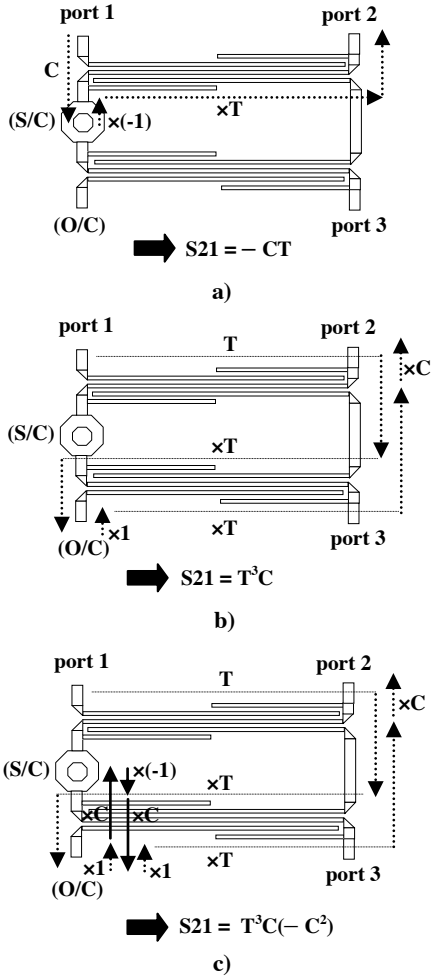


Figure 2: Procedure followed for total transmission coefficient (S21) derivation

From (4), it is clear that S21 = – S31 which means that the two outputs have equal power and are 180° out of phase. Also, the [S] parameters of the balun depend only on the coupling coefficient C. Fig. 3 shows the magnitude of S11 and S21 (or S31) as a function of C. For optimal coupling coefficient value of 0.577 or – 4.8 dB, the magnitude of S11 is null and S21 has a peak value of 0.707 or – 3 dB. This result shows that the Lange couplers have to be under-coupled for optimal performance of the balun. Furthermore, for operation centered at 30 GHz, $\lambda/4$ = 696 µm with dielectric constant ε_r=12.9 for GaAs substrate. These guidelines allow to set initial dimensions W, S and L for the Lange couplers, where W is an individual finger width, S is the spacing between the fingers and L = $\lambda/4$ is the length of the couplers.

Table 1: Performance comparison with previously reported baluns of various types

Ref.	[2]	[4]	[5]	[6]	[7]	This Work
Technology	0.25 µm GaAs	0.15 µm GaAs	0.18 µm CMOS	0.18 µm CMOS	0.18 µm CMOS	0.13 µm GaAs
Balun Type	Lange	Transformers	Asymmetric Broadside	Symmetric Broadside	Transformers	Lange
RF freq. (GHz)	20 – 40	25 – 52	20 – 67	28 – 67	17 – 36	21 – 35
Bandwidth (%)	67	70	108	82	72	50
Return Loss (dB)	–	–	< –10	< –10	< –10	< –10
Insertion Loss (dB)	< 6	< 10	< 8	< 6	< 7	< 6
Amplitude/Phase Mismatch (dB/deg.)	0.5 / 10	1 / 12	1 / 8	0.9 / 4	1 / 10	0.5 / 6
Size (mm^2)	1.12*	0.08	0.06	0.07	0.07	0.22

* including RF testing pads. Effective chip size is approximately the same as for the presented balun, i.e. 0.2 mm^2

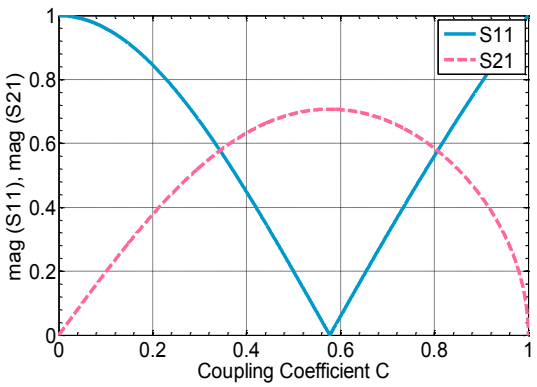


Figure 3: Magnitude of S11 and S21 function of coupling coefficient C

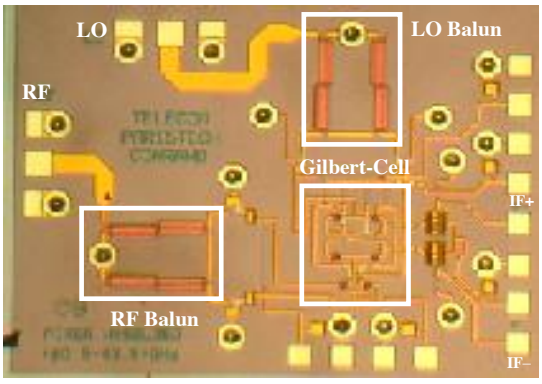


Figure 4: Millimeter-wave Gilbert-cell mixer integrating two Marchand baluns at LO and RF ports

The design of the Marchand balun was performed with the Advanced Design System (ADS) software from Agilent Technologies. After simulation and optimization realized with the help of components models (Lange couplers, via-holes and transmission lines), we find W = 5 µm, S = 14 µm and L = 690 µm. Fig. 4 is an example of application of the balun that we designed. It shows a millimeter-wave Gilbert-cell mixer [1] in which the balun is used to provide single-ended to differential conversion of RF and LO signals.

3. Measurements Results

The balun was fabricated and characterized by on-wafer measurements between 10 GHz and 50 GHz. Input return loss S11 and insertion loss (S21 and S31) are plotted in Fig. 5 while amplitude mismatch (S21 – S31) and phase mismatch (offset from 180° ideal value) between port 2 and port 3 are depicted in Fig. 6. S11 is better than -6 dB and both S21 and S31 are above -6 dB over an octave bandwidth between 20 GHz and 40 GHz. From Fig. 6, measured amplitude and phase mismatch do not exceed 0.4 dB and 7°, respectively. Despite the lack of full-wave electromagnetic (EM) simulations, the realized balun exhibit good performance.

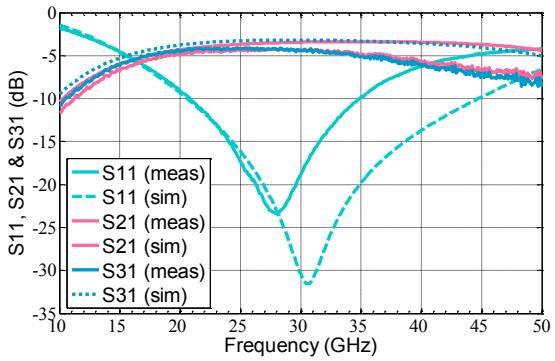


Figure 5: Input return loss (S11) and insertion loss (S21, S31)

Measurements results are consistent with simulations based on components models when considering mismatch between the two outputs. However, losses are clearly underestimated in simulations for frequencies above 25 GHz, making evidence of the limits of the components models.

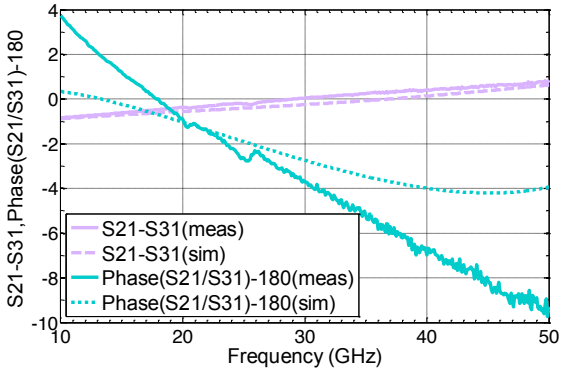


Figure 6: Amplitude (dB) and phase (deg.) mismatch

Table 1 shown on top of the previous page presents performance comparison of the presented balun with other reported millimeter-wave baluns of various types. Devices using broadside coupled lines [5],[6] show higher potential for wideband applications (bandwidth over 100 %). This is due to the use of sophisticated 3D structures in which a larger number of parameters can be optimized to obtain the desired results. On the other hand, baluns made of Lange couplers are only able to operate in narrower bandwidth. The 67 % bandwidth in [2] is probably overestimated since no return loss measurement was published. It is our guess that the actual bandwidth is closer to 50 – 60 %, which is of same order than the balun presented in this paper. As for spiral transformers baluns [4],[7], they show bandwidth values around 70 – 75 %. Broadside coupled lines- and transformers-based baluns occupy intrinsically less chip area because of spiral shape of transformers and coupled lines made of superimposed metal layers for broadside coupling. These architectures are designed using extensive full-wave electromagnetic (EM) simulations since no models are available for these components. This results in rather good consistency between measured and simulated results, especially for losses estimation.

4. Conclusions

This work has presented the design of a millimeter-wave Marchand balun based on components models simulations. Measurements show good agreement with simulations except for losses that are not completely taken into account by the components models at high frequencies. Additional efforts are required to extend the frequency range of operation in order to reach a full octave bandwidth.

References

[1] A. Khy and B. Huyart, A (35 – 45) GHz low power direct-conversion Gilbert-cell mixer in 0.13 µm GaAs pHEMT technology, *European Microw. Conf. 2010 (EuMC)*, Paris, pp. 1058 – 1061, 2010

[2] K. S. Ang and I. D. Robertson, A monolithic double-balanced upconverter for millimeter-wave point-to-multipoint distribution systems, *IEEE Gallium Arsenide Applications Symposium Proceedings*, pp. 439 – 442, 2000

[3] P.-S. Wu, C.-H. Wang, T.-W. Huang and H. Wang, Compact and broadband millimeter-wave monolithic transformer balanced mixers, *IEEE Trans. Microwave. Theory. & Tech.*, vol. 53, no. 10, pp. 3106 - 3114, Oct. 2005

[4] C.-C. Kuo, C.-L. Kuo, C.-J. Kuo, S. Maas and H. Wang, Novel miniature and broadband millimeter-wave monolithic star mixers, *IEEE Trans. Microwave Theory & Tech.*, vol. 56, no. 4, pp. 793 - 802, Apr. 2008

[5] H.-K. Chiou and T.-Y. Yang, Low-loss and broadband asymmetric broadside-coupled balun for mixer design in 0.18 µm CMOS technology, *IEEE Trans. Microwave Theory & Tech.*, vol. 56, no. 4, pp. 835 - 848, Apr. 2008

[6] H.-K. Chiou and J.-Y Lin, Symmetric offset stack balun in standard 0.13 µm CMOS technology for three broadband and low-loss balanced passive mixer designs, *IEEE Trans. Microwave Theory & Techn.*, vol. 59, no. 6, pp. 1529 - 1538, Jun. 2011

[7] H.-Y. Yu, S.-S. Choi, S.-H. Kim and Y.-H. Kim, K-band balun with slot pattern ground for wide operation using 0.18 µm CMOS technology, *Electronics Letters*, vol. 43, no. 5, Mar. 2007

[8] Y.-A. Lai, C.-N. Chen and Y.-H. Wang, Compact doubler with simple harmonic suppression and gain-compensation functions, *IEEE Microwave & Wireless Components Letters*, vol. 21, no. 7, pp. 371 – 373, Jul. 2011

[9] S.-W. Lin, H.-C. Chiu and J. S. Fu, High-efficiency Ka band microwave monolithic integrated circuit frequency tripler using lumped-element balun, *IET Microwaves, Antennas and Propagation*, vol. 5, iss. 1, pp. 30 – 37, 2011

[10] H. K. Chiou, H. H. Lin and C. Y. Chang, Lumped-element compensated high/low-pass balun design for MMIC double-balanced mixer, *IEEE Microwave Guided Wave Letters*, vol.7, no. 8, pp. 248-250, Aug. 1997

[11] D. Kuylenstierna and P. Linner, Design of broadband lumped-element baluns with inherent impedance transformation, *IEEE Trans. Microwave Theory & Techn.*, vol. 52, no. 12, pp. 2739 - 2745, Dec. 2004

[12] N. Marchand, Transmission line conversion transformers, *Electronics*, vol. 17, no. 12, pp. 142 – 145, Dec. 1944

Microstrip Low-Pass Filters by using Novel Defected Ground Structure Slot with a pair of Protruded T-Shaped Strips inside the Slot

Mohammad Ojaroudi[1], Nasser Ojaroudi[2], Reza Habibi[3] , and Homauon Ebrahimian[4]

[1]Young Research Club, Ardabil Branch, Islamic Azad University, Ardabil, Iran.
[2]Faculty of Electrical & Computer Engineering, Shahid Rajaee Teacher Training University, Tehran, Iran
[3]West Azarbijan Power Distribution Company, Urmia, Iran
[4]Depertment of Electrical Engineering, Ardabil Branch, Islamic Azad University, Ardabil, Iran.
*corresponding author, E-mail: m.ojaroudi@iauardabil.ac.ir

Abstract

In this paper, two novel low-pass filters using Defected Ground Structure (DGS) slot with a pair of protruded T-shaped strips inside the slot are presented. The resonant frequency of the slot can be easily controlled by changing the protruded T-shaped strips dimensions, without changing the area taken by the structure. Using this DGS slot, two quasi-elliptic low-pass filters were designed, fabricated and tested. The experimental results show good agreement with simulation results and demonstrate that excellent stop-band performance could be obtained through the proposed low-pass filter. The filters have a cut-off frequency of about 2.4 GHz.

1. Introduction

Conventionally the microwave low-pass filter (LPF) is implemented either by all shunt stubs or by series connected high-low stepped-impedance microstrip line sections. However, generally these are not easily available in microwave band caused by the high impedance microstrip line and the spurious pass-bands. To remove these disadvantages, Defected Ground Structures (DGS) for microstrip lines have been presented in recent years. They have been presented in a number of different shapes for filter applications [1-5]. This technique is suitable for periodic structures, and for both low-pass and band-pass filters, e.g., [6]–[8]. The DGS applied to a microstrip line causes a resonant character of the structure transmission with a resonant frequency controllable by changing the shape and size of the slot.

This paper introduces a DGS with folded T-shaped arms. The resonant frequency of the structure with this slot can be controlled by adjusting the distance between the T-shaped arms without changing the area occupied by the slot or the aperture. Two quasi-elliptic low-pass filters based on this slot were designed and fabricated on a RO4003c substrate with 1.524 mm in thickness and with a relative dielectric constant of 3.38. The resonant behavior of the DGS used here introduces transmission zeroes to the filter response and consequently improves its stop-band performance.

2. Low-Pass Filter with DGS

The basic configuration a fifth-order low-pass filter (LPF) with apertures under the high-impedance transmission lines is shown in Figure 1 (a). In general, the cut-off frequency of the microwave low-pass filter (LPF) can be adjusted by setting proper values of the lumped elements of the filter [9]. In addition, the transmission line lengths of the filter elements, assumed to be much shorter than the wavelength, can be calculated from where, indices and correspond to stubs with capacitive and inductive character, respectively. Therefore, the length of microstrip line can be reduced and the line width can be increased, which avoid the high impedance in conventional filters. To realize the desired capacitive and inductive values of the filter elements by the stubs of the high/low impedance transmission lines, the characteristic impedance and effective dielectric constant of these transmission lines have to be determined. The low-pass filter in Figure 1 (a) was designed on a RO4003c substrate with 1.524 mm in thickness and with a relative dielectric constant of 3.38.

Defected Ground Structure (DGS) evolved from Photonic Band Gap (PBG) is realized by etching defected pattern and slot in the ground plane. The etched defect in ground plane disturbs the shield current distribution in the ground plane. This disturbance can increase the effective capacitance and inductance of a transmission line respectively. Thus, an LC equivalent circuit can represent the proposed unit DGS circuit [1-3]. The proposed DGS slot is shown in Figure 1 (b). The slot is etched in the ground metallization under the microstrip line. This slot has a major advantage in providing tighter capacitive coupling to the line in comparison to known microstrip DGS. Moreover, the resonant frequency of the structure can be controlled by changing the distance between the folded T-shaped arms. The resonant frequency of the slot can be modified by changing the overall slot size which shifts the cut-off frequency of the filter down. To shift the frequency up instead of frequency back, it is necessary to reduce the inductance of the narrow stripline that is located over the slot. This can easily be done by increasing the width of the strip [10]-[11].

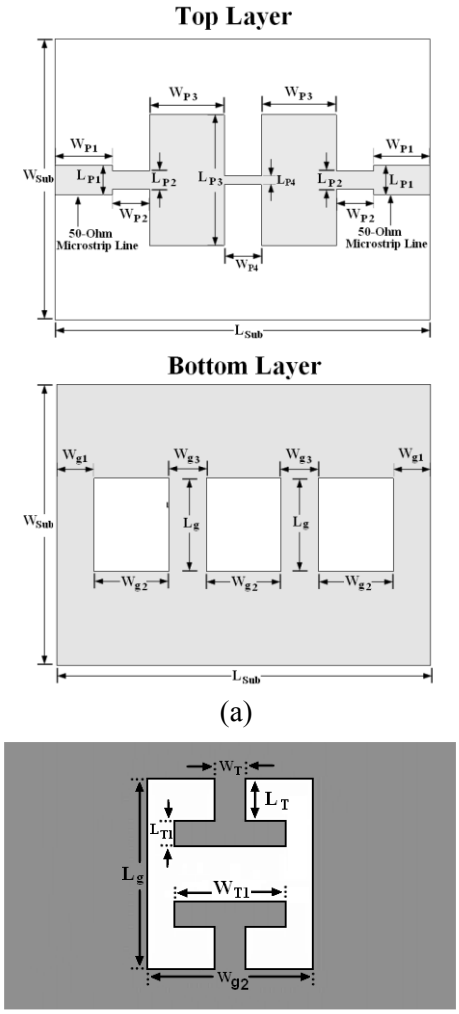


Figure 1. (a) Top and bottom layouts of a fifth-order low-pass filter with apertures under the high-impedance transmission lines, (b) Bottom side layout of the DGS with folded T-shaped arms.

The optimal dimensions of the designed microstrip filters are as follows: $W_{sub} = 30mm$, $L_{sub} = 40mm$, $W_{P1} = 3.2mm$, $L_{P1} = 6mm$, $W_{P2} = 4mm$, $L_{P2} = 2mm$, $W_{P3} = 8mm$, $L_{P3} = 14mm$, $W_{P4} = 4mm$, $L_{P4} = 1mm$, $L_g = 10mm$, $W_{g1} = 6mm$, $W_{g2} = 8mm$, $W_{g3} = 4mm$, $W_T = 2mm$, $L_T = 2mm$, $W_{T1} = 6mm$ and $L_{T1} = 2mm$.

3. Low-Pass Filter with Additional Transmission Zeros

The microstrip low-pass filter, Fig. 1 (a), was designed on both substrate sides by opening apertures in the ground metallization under the high-impedance transmission line. Replacing some of the apertures by the proposed folded T-shaped arms structure introduces transmission zeroes. The number of transmission zeroes is equal to the number of apertures with folded T-shaped arms. One transmission zero is introduced into the filter response by replacing the central aperture by the proposed folded T-shaped arms structure. This slot, however, shifts the cut-off frequency of the filter down. To shift the cut-off frequency back, it is necessary to reduce the inductance of the narrow stripline that is located over the slot [10]. For the input/output connections 50-Ohm microstrip lines are used. The simulated results are obtained using the Ansoft simulation software high-frequency structure simulator (HFSS) [12].

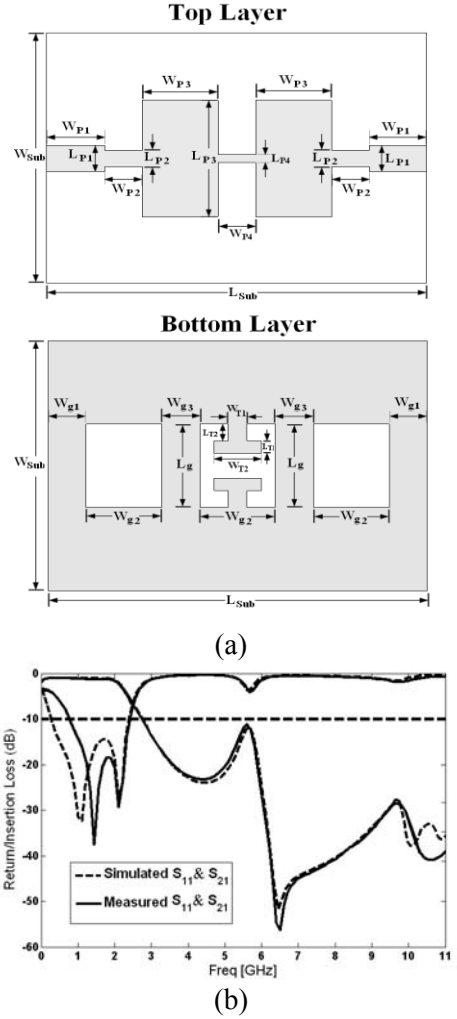


Figure 2. (a) Top and bottom layouts of a fifth-order low-pass filter with one DGS slot with folded T-shaped arms, (b) Return and insertion loss of a fifth-order low-pass filter with one transmission zero.

Figure 2 (a) shows the top and bottom layouts of the designed filter with central aperture replaced by the proposed folded T-shaped arms structure, and Figure 2 (b) shows the measured and simulated return and insertion loss of the filter. As shown in Figure 2 (b), a transmission zero, which improves behavior of the filter stop band, is observed at 6.42 GHz.

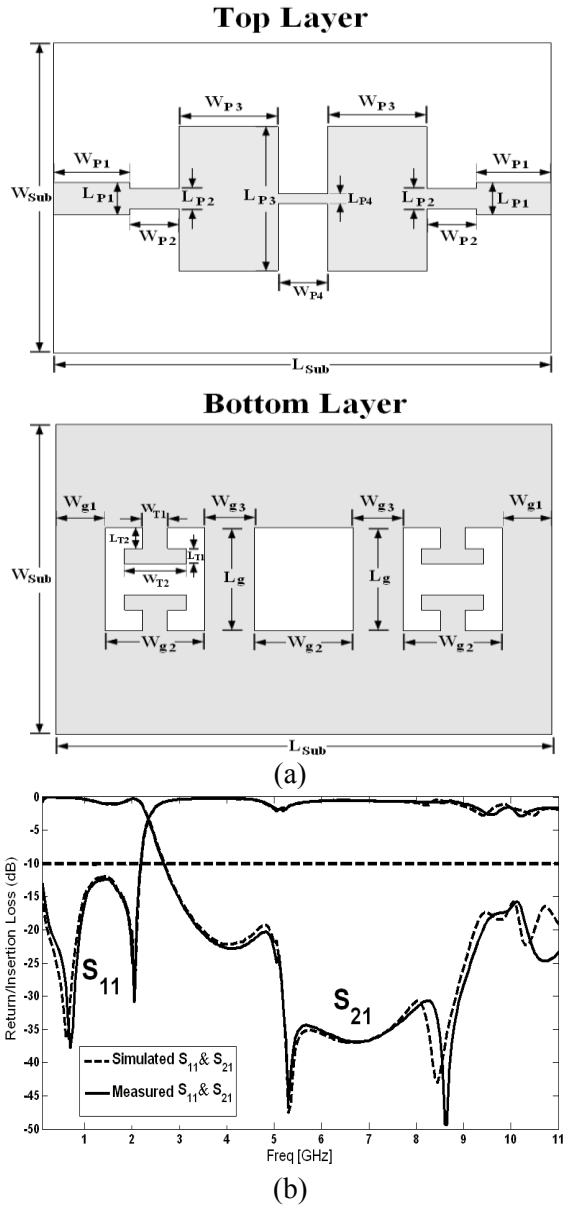


Figure 3. (a) Top and bottom layouts of a fifth-order low-pass filter with two DGS slots with folded T-shaped arms, (b) Return and insertion loss of a fifth-order low-pass filter with two transmission zeroes.

In order to improve the stop-band behavior of filter responses two rectangular slots with T-shaped arms inserted in the positions of the two apertures, as shown in Fig. 3 (1). The proposed filter with optimal design was built and tested in the Antenna Measurement Laboratory at Iran Telecommunication Research Center (ITRC). Figure 3 (b) shows the simulated and measured insertion and return loss of the filter. As shown in Figure 3 (b), two transmission zeros are introduced to the filter response at about 5.28 and 8.72 GHz. Consequently a wide stop-band was achieved. Additionally, the proposed DGS lowpass filter also has characteristics of wider and deeper stopband than those of conventional lowpass filters.

4. Conclusions

In this paper, two compact quasi-elliptic low-pass filters by using novel DGS slot with folded T-shaped arms are designed and fabricated. The main advantages of the proposed DGS are its compact size and the fact that the parallel resonant frequency can be controlled without changing the overall slot area of the DGS. The transmission zeros introduced to the filter responses improves their stop-band behavior. Simulation results using 3-D HFSS shows good consistency with experimental results. It is also of potential to be used in microwave and millimeter wave ICs.

Acknowledgements

The authors are thankful to Microwave Technology Company staff for their beneficial and professional help. (www.microwave-technology.com).

References

[1] D. Ahn, J.-S. Seok, C.-S. Kim, J. Kim, Y. Qian, and I. Itoh, "A design of low-pass filter using the novel microstrip defected ground structure,"*IEEE Trans*. *Microw*. *Theory Tech*., vol. 49, no. 1, pp. 86–93, Jan. 2001.

[2] C.-S. Lim, C.-S. Kim, D. Ahn, Y.-C. Jeong, and S. Nam, "Design of the low-pass filters using defected ground structure," *IEEE Trans*. *Microw*. *Theory Tech*., vol. 53, no. 8, pp. 2539–2545, Aug. 2005.

[3] J. S. Yun, G. Y. Kim, J. S. Park, D. Ahn, K. W. Kang, and J. B. Lim, "A design of the novel coupled line bandpass filter using defected ground structure," in *IEEE MTT-S Int*. *Dig*., Boston, MA, Jun. 2000, pp. 327–330.

[4] J. S. Park, J. S. Yun, and D. Ahn, "A design of the novel coupledline bandpass filter using defected ground structure with wide stopband performance," *IEEE Trans*. *Microw*. *Theory Tech*., vol. 50, no. 9, pp. 2037–2043, Sep. 2002.

[5] Jong-Sik Lim, Chul-Soo Kim, Young-Taek Lee, Dal Ahn and Sangwook Nam, "Design of lowpass filters using defected ground structure and compensated microstrip line",*ELECTRONICS LETTERS 24th* October 2002, Vol.38, No.22.

[6] A. B. Abdel-Rahman, A. K. Verma, A. Boutejdar, and A. S. Omar, "Control of bandstop response of Hi-Lo microstrip low-pass filter using slot in ground plane," *IEEE Trans*. *Microw*. *Theory Tech*., vol. 52, no. 3, pp. 1008–1013, Mar. 2004.

[7] H.-W. Liu, Z.-F. Li, W. Sun, and J.-F. Mao, "An improved 1-D periodic defected ground structure for microstrip line," *IEEE Microw*. *Wireless Compon*. *Lett*., vol. 14, no. 4, pp. 180–182, Apr. 2004.

[8] C.-S. Kim, J.-S Lim, J.-H. Kim, and D. Ahn, "A design of a miniaturized 2-pole bandpass filter by using slot and hair-pin line," in *IEEE MTT-S Int*. *Dig*., Fort Worth, TX, Jun. 2006, pp. 1983–1986.

[9] A. R. Ali, A. Abdel-Rahman, A. Amari, and A. S. Omar, "Direct and cross-coupled resonator filters using defected ground structure (DGS) resonators," in *Proc*. *35th Eur*. *Microw*. *Conf*., Paris, France, Oct. 2005, pp. 1275–1278.

[10] A. Abdel-Rahman, A. K. Verma, A. Boutejdar, and A. S. Omar, "Compact stub type microstrip bandpass filter using defected ground plane," *IEEE Microw*.*Wireless Compon*. *Lett*., vol. 14, no. 4, pp. 136 138, Apr. 2004.

[11] S.-W. Ting, K.-W. Tam, and R. P. Martins, "Compact microstrip quasi-elliptic bandpass filter using open-loop dumbbell shaped defected ground structure," in *IEEE MTT-S Int*. *Dig*., San Francisco, CA, Jun. 2006, pp. 527–530.

[12] Ansoft High Frequency Structure Simulation (HFSS), Ver. 13, Ansoft Corporation, 2010.

Facet Phase's Influence on Adiabatic Chirp and Transmission Penalty for Index-Coupled Distributed-Feedback Lasers

Kechaou Khalil[1,3], Thedrez Bruno[1], Grillot Frédéric[1,2], Erasme Didier[1], Aubin Guy[3] Kazmierski Christophe[4]

[1]Institut TELECOM, TELECOM ParisTech, CNRS LTCI, 46 Rue Barrault, 75634 Paris,France
[2]European University of Bretagne, INSA, CNRS FOTON, 20 av. des Buttes de Coësmes, 35043 Rennes, France
[3]Laboratory for Photonics and Nanostructures, CNRS, Route de Nozay, 91460 Marcoussis, France
[4] III-V Lab, Common laboratory of Alcatel-Lucent Bell Labs France', 'Thales Research and Technology' and 'CEA Leti', 91460 Marcoussis, France

khalil.kechaou@telecom-paristech.fr

Abstract

A study of the adiabatic chirp for antireflection/high reflection coated index-coupled distributed feedback laser (AR/HR IC-DFB) is presented theoretically and confirmed experimentally. The variation of HR facet phase can lead to either blue or unexpectedly to red adiabatic chirp which affects the high-speed transmission performance. This represents an important criterion for laser selection in mid-range transmission applications.

1. Introduction

AR/HR IC-DFB lasers are good candidates for telecommunication applications due to their high AR facet efficiency and their good single-mode yield. However, their modulation performances are often reduced by the shift of their emission wavelength during direct current modulation. The resulting increase of the laser linewidth accounts for a few GHz [1] with a negative impact on the transmission quality. Due to gain compression, it is known that conventional Fabry-Perot (FP) semiconductor laser suffers from blue chirp. We demonstrate in this paper that in the case of an IC-DFB laser, the adiabatic chirp can be surprisingly turned to red in some cases. We study the occurrence of such phenomena with respect to the facet phase (relative position of the HR facet cleavage plane with respect to the grating) and show the strong impact of this parameter on the transmission penalty.

2. Theory and numerical results

2.1. Model

It is known that the power distribution inside the IC-DFB laser shifts from uniform at threshold to non uniform at higher output power, leading to intra-cavity Spatial Hole Burning (SHB) [2]. The resulting spatial index variation *n(z)* locally affects the grating which becomes slightly non-uniform. This reacts on the cavity resonant wavelength and leads to a lasing wavelength shift while the power is increased. The effects of these non-linearities on the AR/HR IC-DFB behavior have been modeled using a transfer matrix method (TMM) [3, 4]. The aim is to calculate the DFB laser performance at threshold and to predict its static behaviour above-threshold. The method is applicable to any laser design.

To tackle the distribution non-uniformity of carrier and photon density, the DFB laser structure is split into *N* cascaded sections consisting of many grating periods in which all physical parameters, like the injection current, the material gain the photon density, the carrier density and the refractive index are assumed to be homogeneous. The laser is modelled by assimilating the Bragg grating to a rectangular network. The transfer matrix for one corrugation period is defined by:

$$\overline{M_{Period}} = \begin{bmatrix} \frac{n_1+n_2}{2n_1} & \frac{n_1-n_2}{2n_1} \\ \frac{n_1-n_2}{2n_1} & \frac{n_1+n_2}{2n_1} \end{bmatrix} \times \begin{bmatrix} e^{k_2 l} & 0 \\ 0 & e^{-k_2 l} \end{bmatrix} \times \begin{bmatrix} \frac{n_1+n_2}{2n_2} & \frac{n_2-n_1}{2n_2} \\ \frac{n_2-n_1}{2n_2} & \frac{n_1+n_2}{2n_2} \end{bmatrix} \times \begin{bmatrix} e^{k_1 l} & 0 \\ 0 & e^{-k_1 l} \end{bmatrix} \quad (1)$$

where n_1 and n_2 are the refractive indices, and k_1 and k_2 are the complex propagation constants in the two refractive index regions. The real part of the propagation constant is determined by the net gain, which is non-uniform along the device for the case of index-coupled DFB laser. The imaginary part depends on refractive index, which affects the frequency shift of the laser. The transfer matrix throughout the Bragg grating in sections is calculated from the *m* power of the transfer matrix for one corrugation period. To describe completely a DFB laser with cleaved facets, the transfer matrix can be written as:

$$\overline{M} = \overline{R_1} \times \overline{\phi_1} \times \left(\overline{M_{Period}}\right)^{m_N} \ldots \left(\overline{M_{Period}}\right)^{m_i} \ldots \left(\overline{M_{Period}}\right)^{m_2} \ldots \left(\overline{M_{Period}}\right)^{m_1} \times \overline{\phi_2} \times \overline{R_2} \quad (2)$$

where m_i is the number of period in the ith section, $\overline{R_1}$ and $\overline{R_2}$ are the reflectivity matrix at the left and right side, $\overline{\phi_1}$ and $\overline{\phi_2}$ are the partial propagation matrix corresponding to incomplete corrugation period at left and right facets:

$$\overline{R_1} = \frac{1}{\sqrt{1-R_1^2}} \begin{bmatrix} 1 & -R_1 \\ -R_1 & 1 \end{bmatrix} \quad (3)$$

$$\overline{R_2} = \frac{1}{\sqrt{1-R_2^2}} \begin{bmatrix} 1 & R_2 \\ R_2 & 1 \end{bmatrix} \quad (4)$$

$$\overline{\phi_{1,2}} = \begin{bmatrix} e^{j\phi_{1,2}} & 0 \\ 0 & e^{j\phi_{1,2}} \end{bmatrix} \quad (5)$$

The nonlinear field gain can be well approximated by a logarithmic formula including the gain compression effect in the vicinity of the emission frequency:

$$g(N(z),P(z)) = \frac{g_0 \cdot \ln\left(\frac{ed_{qw}B_{rad}N(z)^2}{J_0}\right)}{1+\varepsilon P(z)} \quad (6)$$

In this approximation, g_0, e, d_{qw}, B_{rad}, J_0, ε, N and P are respectively the empirical gain coefficient, the electron charge, the thickness of one quantum well, the radiative recombination coefficient, the transparency current density, the gain compression coefficient, the carrier density and the photon density. At threshold, the net gain must offset the losses:

$$\int g.dz = \alpha_{tot} = (\alpha_{\text{int}} + 2\alpha_{DFB})L \quad (7)$$

In equation (4) α_{DFB} represents the cavity loss, L the cavity length and α_{int} is the internal losses which depend on the carrier density N including losses caused by the diffraction on technological inhomogeneities, light propagation and absorption losses in InP layers and differential losses in wells. For TMM, the oscillation condition at threshold is computed by using:

$$\overline{M}_{11}(\alpha_{DFB}, \lambda) = 0 \quad (8)$$

where λ is the lasing wavelength. Assuming that n_1 and n_2 are uniform along the cavity, a prediction-correction method has been used to calculate the lasing mode represented by (α_{th}, λ_{th}). In fact, the initial guesses (α_i, λ_i) of solutions correspond to Fabry-Perot modes. After calculating the value of $\overline{M}_{11}$ for (α_i, λ_i), (α_i+dα, λ_i) and (α_i, λ_i+dλ), we compute the relative variations allowing the correction of the values of α and λ. This procedure is iteratively repeated until a relative variation less than 10^{-9} is reached. Above threshold, the photon density distribution is calculated using elementary transmission matrices while that of the carrier density is computed using the steady-state carrier rate equation:

$$\frac{I}{eV} = N(z)\left(A_{nrad} + B_{rad}N(z) + C_{aug}N(z)^2\right) + v_g\, g(z)P(z) \quad (9)$$

where I, V, A_{nrad}, C_{aug} and v_g are respectively the injected current, the cavity volume, the non-radiative recombination coefficient, the Auger recombination coefficient and the group velocity of light. The resulting index variation is given by:

$$n(z) = n^{th} + \Gamma \frac{dn}{dN}\left(N(z) - N_{th}\right) \quad (10)$$

where n^{th} is the refractive index at threshold, Γ is the confinement factor, N_{th} is the carrier density at threshold and dn / dN is the slope of the refractive index with respect to the carrier density. The above-threshold resolution method was described in reference [4]. Indeed, for uniform-injected current, an iterative procedure is adopted. It consists on the resolution of the oscillation condition (8) using the new photon and carrier density distribution calculated by the equations system (7) and (9) based on the previous index distribution at lower injected current. The new obtained solution (α, λ) leads to another distribution of photon and carrier. Therefore, we re-solve (8). All steps are repeated until reaching an unchanged (α, λ).

2.2. HR facet phase effect

A very important point specific to DFB lasers is the effect of *n(z)* induced by *N(z)* on the grating. As a result, their threshold conditions and lasing wavelengths are modified continuously after lasing causing adiabatic chirp. This phenomenon is strongly related to SHB due to the electron-photon coupling inside the cavity. The SHB is strongly dependent on the HR facet phase, which drives the interference between the grating and the HR facet.

The HR facet phase effect on SHB leads to a modification of the threshold condition and so of the lasing mode, which causes different chirp behavior. As depicted in figure 1, the normalized threshold cavity loss αL versus the normalized detuning coefficient δL defined as the normalized deviation of the lasing wavelength from Bragg wavelength has a parabolic distribution with respect to the HR facet phase:

$$\delta L = < n > \left(\frac{2\pi}{\lambda} - \frac{2\pi}{\lambda_B}\right)L \quad (11)$$

with

$$\lambda_B = 2 < n > \Lambda \qquad (12)$$

Where $<n>$ is the mean value of the longitudinal distribution of the effective index, λ_B is the Bragg wavelength and Λ is the corrugation period length.

The minimum threshold cavity loss is obtained at Bragg wavelength (δL=0) for φ_{HR}= π. In that case, the lasing wavelength is located within the laser stop-band. Lasers emit at short wavelengths (δL>0) for φ_{HR} between 0 and π and at long wavelength otherwise (Fig.1.(b) and 1.(c)). When φ_{HR} approaches 0 and 2π, the laser is not single-mode anymore. These two families of lasers exhibit different adiabatic chirp behaviors as shown on figure 2. The effective refractive index distribution inside the laser is presented in figure 3 for several injected currents with fixed HR facet phase in order to highlight the SHB effect on adiabatic chirp. One can see that the index distribution $n(z)$ is flat at threshold and becomes non-uniform while the power is increased.

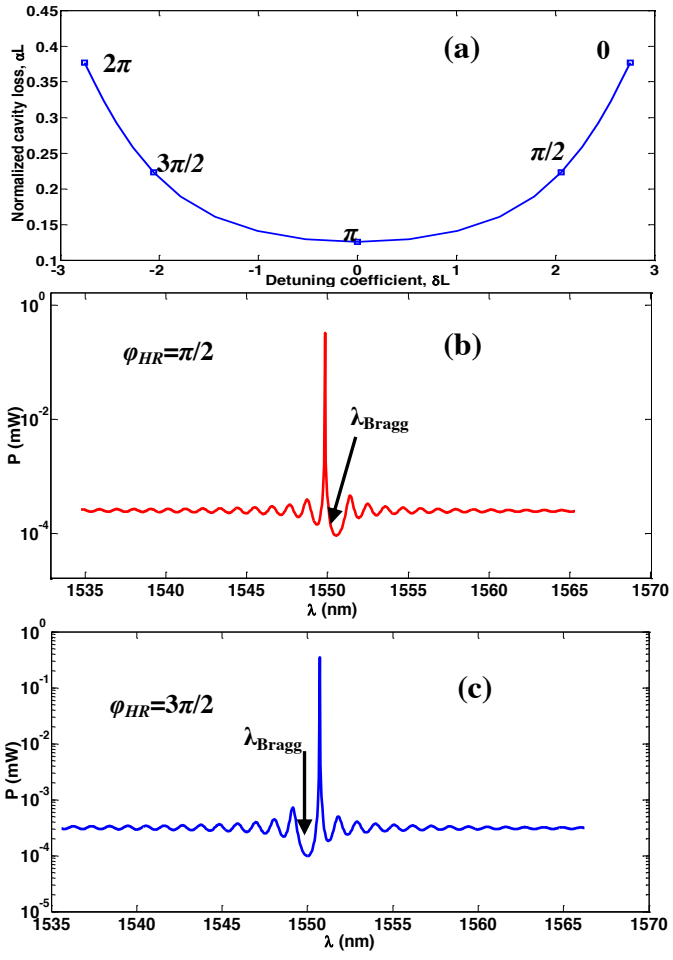


Figure 1: (a) Calculated threshold cavity loss variation versus the normalized detuning coefficient for an AR(0.1%)/HR 300-μm-long IC-DFB laser for several cases of HR facet phase φ_{HR} from 0 to 2π, κL = 1.6 (b) Laser spectrum for φ_{HR} = π/2 (c) Laser spectrum for φ_{HR} = 3π/2

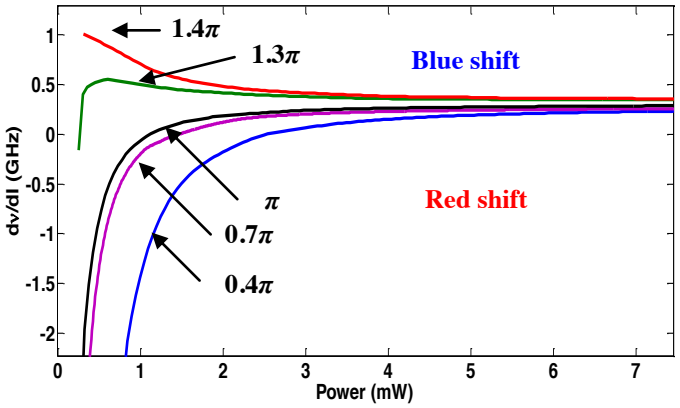


Figure 2: Calculated frequency shift coefficient versus power for an AR (0.1%)/HR 300-μm-long IC-DFB laser for several cases of HR facet phase, κL = 1.6

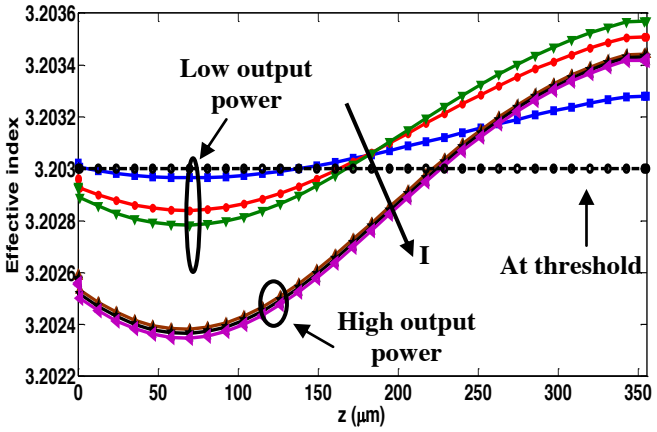


Figure 3: Longitudinal distribution of the effective index for an AR (0.1%)/HR 300-µm-long IC-DFB laser for several injected current values, φ_{HR}= 0.4π, κL = 1.6, AR facet localized at z=0

At low output power, $n(z)$ presents significant variations, leading to a strong derivative of the frequency with respect to current, as seen in figure 2. At high output power, the non-uniform index distribution gets stabilized and does not affect the Bragg resonance anymore. The frequency shift converges independently of HR facet phase to the same positive value (i.e. blue shift) as that of a FP laser (figure 3) at high output power because of the carrier density increase needed to compensate for gain compression (figure 2). In the SHB predominance region (figure 2), the chirp is strongly power dependent, and can be either positive or negative according to the value of the HR facet phase. The lasing wavelength shifts towards the blue for φ_{HR} between 0 and π (δL>0) and towards red for φ_{HR} between π and 2π (δL<0). Hence, the lasing wavelength detuning plays a critical role in predicting the chirp behavior and in distinguishing the red and blue chirp.

The HR facet phase value defines the cleavage plane position. The cleavage plane is positioned at the low index

area of the Bragg grating for φ_{HR} between 0 and π and at the high index area for φ_{HR} between π and 2π (figure 4.(a) and (b)).

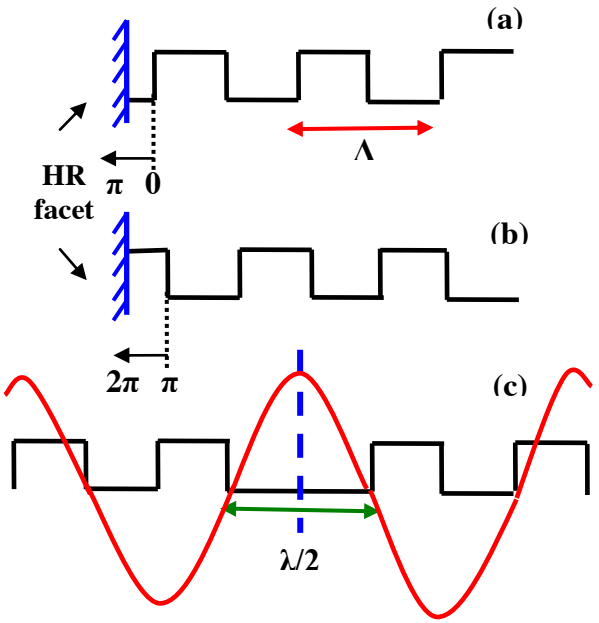


Figure 4: Cleavage plane position with depending on HR facet phase (a) $0 < \varphi_{HR} \leq \pi$, (b) $\pi < \varphi_{HR} \leq 2\pi$, (c) Optical field in the laser cavity unfolded around the HR facet for $\varphi_{HR} = \pi$.

Figure 4.(c) shows the Bragg grating with its facet mirror image for $\varphi_{HR} = \pi$. In that specific case, the laser behaves similarly as a $\lambda_B/2$ cavity surrounded by two perfectly tuned Bragg grating. In this optimal configuration the lasing wavelength is equal to λ_B and the photon density $P(z)$ is strongly localized at the HR facet. For other facet phases, the situation is more complex.

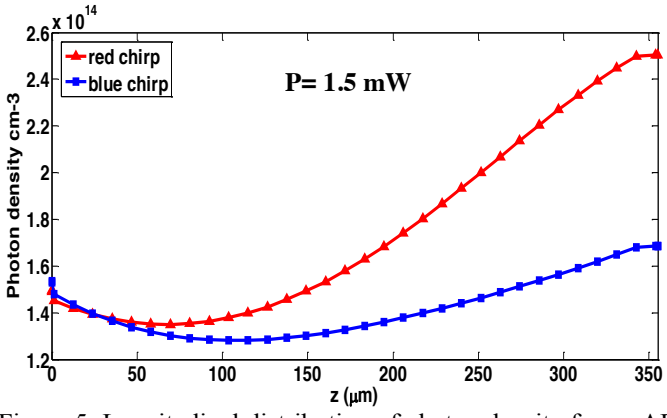


Figure 5: Longitudinal distribution of photon density for an AR (0.1%)/HR 300-μm-long IC-DFB laser for φ_{HR}= 0.4π (red chirp) and φ_{HR}= 1.4π (blue chirp), κL = 1.6 and P= 1.5 mW AR facet localized at z=0

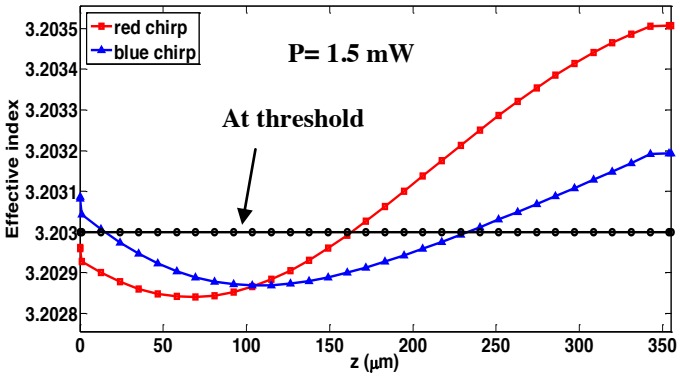


Figure 6: Longitudinal distribution of the effective index for an AR (0.1%)/HR 300-μm-long IC-DFB laser for φ_{HR}= 0.4π (red chirp) and φ_{HR}= 1.4π (blue chirp), κL = 1.6 and P=1.5 mW AR facet localized at z=0.

Figure 5 illustrates two photon density distributions associated to two values of φ_{HR}. As can be seen, the photon density distribution is indeed strongly dependent on φ_{HR}. This results in different profiles for the intracavity index variation. Figure 6 shows in black line the index value at threshold. dv/dI is negative (red chirp) when the average difference between the effective index along z and the value at threshold is positive since in that case, the Bragg wavelength increases (red case). In the opposite case (blue line), the Bragg wavelength decreases, and the Bragg frequency shifts towards the blue.

3. Experimental results

The frequency shifts coefficients (dv/dI) measured on IC-DFB laser through small-signal modulation in figure 7 clearly confirm the theoretical predictions. The modulation frequency is larger than 30 MHz in order to avoid thermal effects and is chosen to be far smaller than the laser resonance frequency. The experimental setup is described in reference [5]. The measurement is done with a Mach-Zehnder interferometer allowing the recording of the amplitude and the phase of the chirp.

Lasers with red and blue chirp lead to different transmission penalties in 300 km standard-dispersion fiber for Non-Return-to-Zero (NRZ) 2.5 Gb/s signals with respect to Back-to-Back measurement (Figure.7).

Adiabatic chirp is related to the steady state wavelength difference between high and low modulated levels producing a frequency shift proportional to the instantaneous optical output power:

$$\Delta\nu = \int \frac{d\nu}{dI} dI \qquad (13)$$

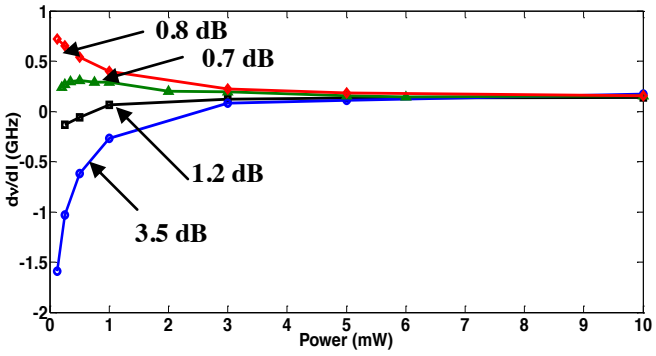


Figure 7: Measured frequency shift coefficient versus power for an AR (0.1%)/HR 300-µm-long IC-DFB laser, κL = 1.6. Penalty values at 10^{-9} Bit Error Rate (BER) are given for a 300 km transmission at 2.5 Gb/s

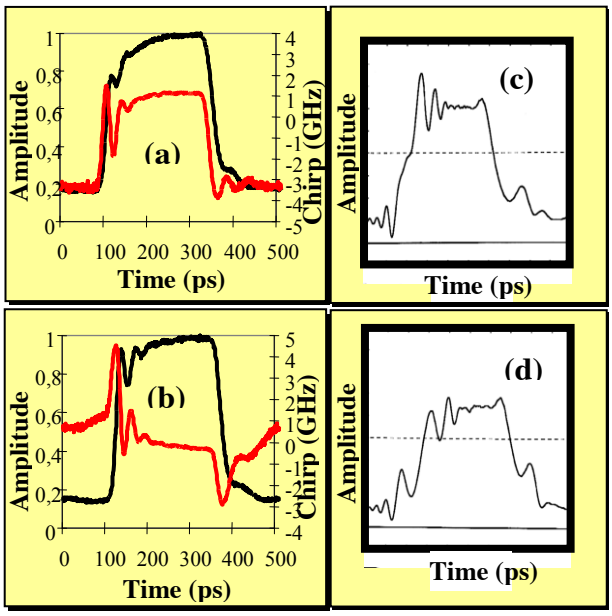


Figure 8: Measured chirp and amplitude time profile for large signal modulation between 0 and 10 mW for lasers with blue chirp (a) and red chirp (b) , Calculated amplitude time profile after 200 km transmission long for lasers with blue chirp (c) and red chirp (d)

Figure 8.(a) and 8.(b) show that lasers with red chirp ($\Delta\nu \sim 0$) and blue chirp (($\Delta\nu > 0$) have not the same amplitude time profile after 200 km transmission long at 2,5 Gb/s as shown in figure 8.(c) and 8.(d). The penalty at 10^{-9} BER appears to be lower when the adiabatic chirp approaches Binder and Kohn's condition [6] given by $\Delta\nu = m.(B/2)$ where m is the intensity modulation depth and B is the signal bit rate. The green curve (blue chirp) in figure 7 appears to be the one, which better fits this requirement compared to other corresponding to red chirp.

4. Conclusion

We have presented, theoretically and experimentally, the HR facet phase's impact on chirp behavior of IC-DFB lasers. The red and blue chirp was observed for lasers with negative and positive detuning coefficients respectively. We have demonstrated the importance of this effect on transmission using BER measurements showing high transmission performance for lasers with blue chirp which flexibly access to Binder and Kohn's condition. These results are of first importance for mid-range transmission applications.

Acknowledgements

The authors are grateful to the "MODULE" project from the French national initiative "ANR-VERSO" program and Systematic Paris-region.

References

[1] Agrawal, G.P and Dutta, N.K, Long Wavelength Semiconductor Lasers, Springer, 1986

[2] Rabinovich,W.S and Feldman, B.J, "Spatial Hole Burning Effects in Distributed Feedback Lasers", IEEE journal of Quantum electronics, vol. 25, No.1, 1989

[3] Bjork, K and Nilsson, O., "A new exact and efficient numerical matrix theory of complicated laser structures: properties of asymmetric phase-shifted DFB lasers", IEEE J. Lightwave Technol., LT-5, 140-146(1987).

[4] Orfanos, I and Sphicopoulos, T, "A tractable above-threshold model for the design of DFB and phase-shifted DFB lasers", IEEE Quantum electronics, 27(4), 1991

[5] Provost J.G , Grillot, F "Measuring the chirp and the linewidth enhancement factor of optoelectronic devices with a Mach-Zehnder interferometer", IEEE photonics journal, vol 3, No 3, 2011

[6] Binder, J and Kohn, U: "10 Gbits/s-Dispersion Optimized Transmission at 1,55 µm Wavelength on Standard Single Mode Fiber", IEEE photonics technology letters, Vol.6, No.4 (1994).

Some Features of Magnetometric and Sensor Devices Based on the Field Effect Hall Sensor

M.L. Baranochnikov[1], A.V. Leonov[1], V.N. Mordkovich[1], D.M. Pazhin[1] and M. M. Filatov[2]*,

[1] Institute of Microelectronics Technology and High Purity Materials, Russia
[2] All-Russia Research Institute of Automatics, Russia
*corresponding author: filatov@vniia.ru

Abstract

The features of properties of the field-effect Hall sensor (FEHS) in which the capabilities of the conventional Hall element and field-effect transistor are integrated with the metal-insulator-semiconductor-insulator-metal (MISIM) control system are considered. The FEHS exhibits very high electrical characteristics and the functionability under hard radiation and temperature conditions. In this case, the MISIM system makes it possible to control the FEHS characteristics, and to use circuit solutions providing the development of original devices based on FEHS.

1. Introduction

Some time ago, we have proposed the field-effect Hall sensor (FEHS) combining the properties of the conventional Hall sensor and the field-effect transistor with an embedded channel and a two-gate control system such as the metal-insulator-semiconductor-insulator-metal (MISIM) [1,2]. FEHSs are fabricated based on the "silicon-on-insulator" (SOI) technology, which allows the use of the silicon substrate and insulating layer embedded therein as one of the field-effect control systems. The other control system consists of a metal gate on the insulator film on the outer surface of the thin silicon layer separated from the substrate by a buried insulator (Fig. 1).

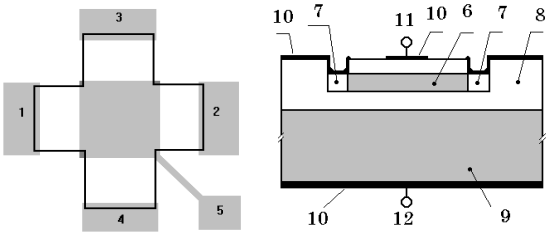


Figure 1: SOI FEHS design: (**left**) top view: (1,2) current electrodes, (3,4) Hall electrodes, (5) top gate electrode; (**right**) cross section: (6) active layer (n-Si), (7) ohmic contacts (n^+-Si), (8) SiO_2, (9) substrate (n-Si), (10) Al film, (11) top gate, (12) bottom gate.

2. Properties of the field-effect Hall sensor

It is known that the "silicon-on-insulator" technology was proposed, first of all, as a method for increasing the radiation resistance of microelectronic devices to pulsed ionizing radiations and to broaden the range of their operating temperatures [3]. Physically, these advantages of SOI devices are caused by the small thickness of the cut silicon layer and buried insulator preventing the transfer of carriers generated by radiation or/and temperature in the silicon substrate to the silicon device layer. Since the FEHS is a SOI device, the stability to pulsed irradiation and functionability at temperatures exceeding the operating temperature of silicon Hall sensors by 200-250°C are also inherent to it [1,4]. Moreover, the choice of the sign and potential of control gates during irradiation makes it possible to increase the FEHS stability to stationary ionizing irradiation (Fig. 2),

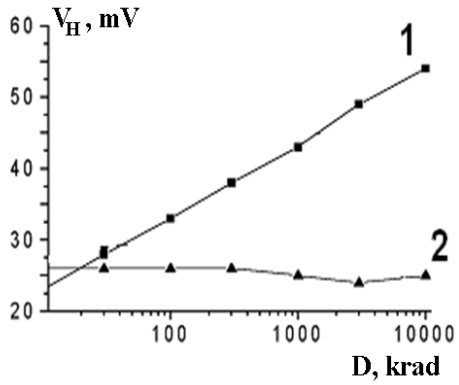


Figure 2: Experimental dependences of the Hall emf on the gamma irradiation dose at various electrical conditions of the FEHS during irradiation: (1) all FEHS electrodes are short-circuited, voltage is absent; (2) voltage is applied to power supply electrodes and control gates, the FEHS channel is completely closed and is opened only for measurement time.

and the feature of the formation of radiation defects in the thin silicon layer of the SOI structure causes the device stability to neutron irradiation [5-7]. Furthermore, due to the

n^+-n-n^+ structure of the conducting channel, the FEHS functions at low temperatures as well, including the liquid-helium temperature [8].

Figure 3 shows the typical current-voltage, gate-drain, and hall-gate characteristics of FEHSs. All these characteristics (what is especially important, including the hall-gate one) are transistor-type ones, and particular curves depend on the sign and value of gate potentials and on that whether the potential is applied to one of gates or to both gates simultaneously.

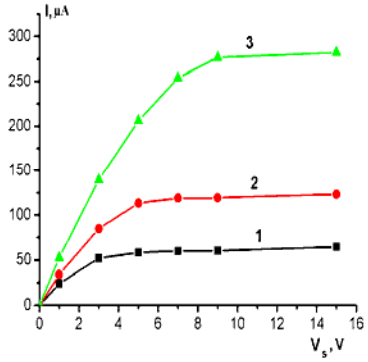


Figure 3a: Typical (a) current-voltage, (b) gate-drain, and (c) hall-gate characteristics of the FEHS. (a) Gate voltages V_g = (1) 3, (2) 5, and (3) 9 V; (b,c) supply voltages V_s = (1) 3, (2) 5, and (3) 9 V.

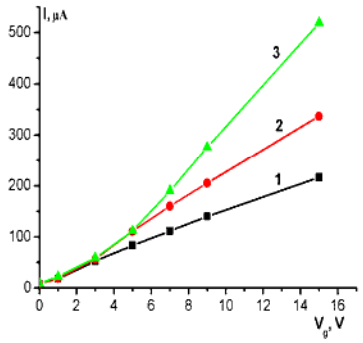


Figure 3b: Typical (a) current-voltage, (b) gate-drain, and (c) hall-gate characteristics of the FEHS. (a) Gate voltages V_g = (1) 3, (2) 5, and (3) 9 V; (b,c) supply voltages V_s = (1) 3, (2) 5, and (3) 9 V.

We also note that various FEHS characteristics, e.g., the temperature coefficient of magnetic sensitivity can be controlled by varying the gate potential (Fig. 4).

As is known [9], the Hall emf is inversely proportional to the thickness of the silicon region where electric current flows. The FEHS channel thickness was 0.15-0.2 μm which is at least ten times smaller than in ordinary Si Hall sensors. Therefore, the FEHS threshold sensitivity is significantly higher than that of silicon analogues and is ~0.5 mV/mT at the channel width of 0.5 mm. Due to the small channel thickness, the typical FEHS operating current is 0.2 … 0.4 mA which is much lower than that of Si analogues. Such an operating current causes a very high specific magnetic sensitivity of the FEHS, which can exceed 10000 V/A·T in comparison with 10^2 … 10^3 V/A·T characteristic of conventional semiconductor Hall sensors [9].

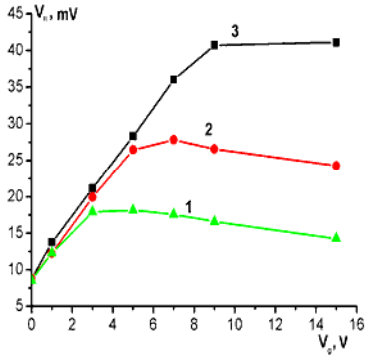


Figure 3c: Typical (a) current-voltage, (b) gate-drain, and (c) hall-gate characteristics of the FEHS. (a) Gate voltages V_g = (1) 3, (2) 5, and (3) 9 V; (b,c) supply voltages V_s = (1) 3, (2) 5, and (3) 9 V.

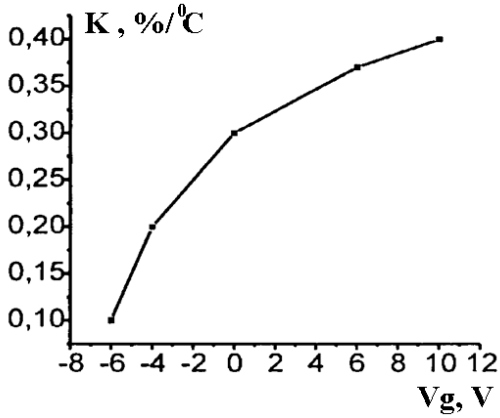


Figure 4: Coefficient of the temperature dependence of the FEHS magnetic sensitivity.

It is important that the MISIM system allows modulation of the channel current, hence, Hall signal measurement at the modulation frequency. As an example, Fig. 5 shows the measurement scheme of magnetic fields, in which synchronous detection of the net signal [10] is used. Figure 6 shows the frequency dependence of the FEHS intrinsic noise. We can see that the FEHS noise decreases approximately by 1.5 orders of magnitude at a frequency of ~10 kHz. This makes it possible to increase the signal-to-noise ratio with increasing modulation frequency. In this case, an appreciably lower threshold magnetic induction is detected using the FEHS than the Earth's magnetic field. An additional advantage of the use of field gates for current modulation is suppression of switching interferences

inherent to commonly used circuits in which the Hall signal is subjected to synchronous detection [11].

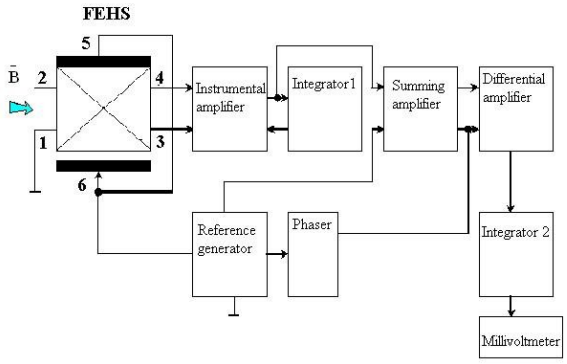


Figure 5: Block diagram of magnetic field measurements based on synchronous detection of the SOI FEHS signal. (1,2) Current electrodes, (3,4) Hall electrodes, (5,6) top and bottom gate electrodes.

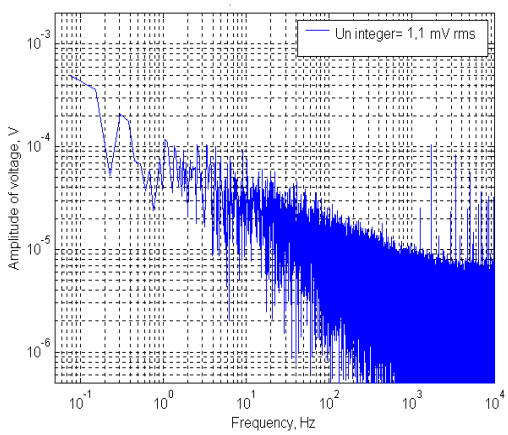


Figure 6: Frequency dependence of intrinsic noises of the SOI FEHS.

3. Field-effect control system of the FEHS as a feedback element

The MISIM field-effect control system provides the circuit possibility of organizing the feedback using the magnetically induced signal. This makes it possible to alternatively perform both magnetic induction measurements and to propose new sensor devices.

In general, in magnetometric devices using the Hall senor, the output signal is presented as voltage or current [9]. The FEHS allows easy transform of the magnetic induction effect to measurements of the measuring device frequency [12]. In this case, the FEHS represents an element incorporated in a self-excited oscillator whose output signal varies in proportion to the magnetic field induction, which results in a change in the generation frequency (Fig. 7).

The difference of this induction-frequency converter from conventional ones [13] consists in the FEHS nature in which capacitances of both MIS systems can be varied by potentials applied to gates and (or) by supply voltage. Therefore, the operation frequency range of the induction-frequency converter based on the FEHS can be widely enough varied independently of magnetic influence. Figs. 8-10 illustrate the properties of the induction-frequency converter based on the FEHS.

Another example of the use of the feedback through the MISIM FEHS system is the device capable of stabilizing the FEHS channel current (Fig. 11, Table 1) [14]. It is based on that the Hall signal (magnetically induced or caused by residual voltage) in the FEHS varies with current, and the gate potential is varied via the feedback circuit so that to restore a required channel current. The table demonstrates the efficiency of such a stabilizer by the example of microcurrents. By varying the load resistance R_L in the stabilized current circuit, a situation was created in the experiment, which should lead to a similar change in the current flowing through the circuit. Since the Hall signal depends on the product of the channel current and the magnetic field induction [9], the high degree of stabilization in the experiment with microcurrents was provided using a permanent magnet with induction B = 1 mT, placed on the FEHS housing cover.

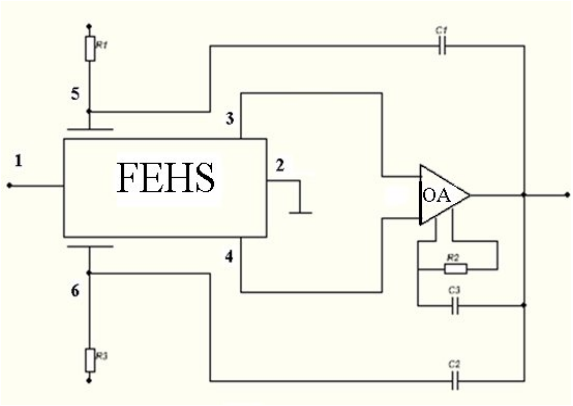


Figure 7: Primary magnetic field induction-frequency converter based on the SOI FEHS: (1,2) current electrodes, (3,4) Hall electrodes, (5,6) top and bottom gate electrodes.

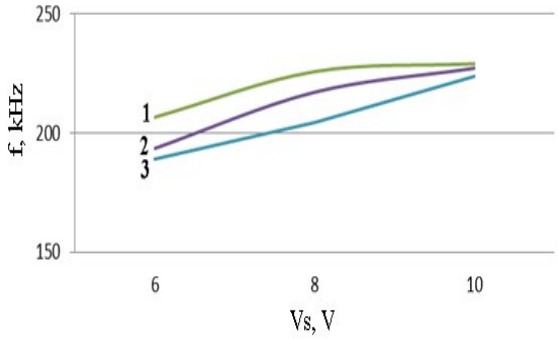


Figure 8: Dependence of the autogeneration frequency of the induction-frequency converter on the SOI FEHS supply voltage. The corresponding dependences are measured at the SOI FEHS top gate voltage of 8 V and bottom gate voltages of (1) 6, (2) 8, and (3) 10 V.

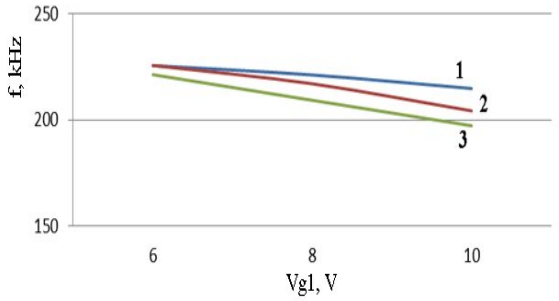


Figure 9: Dependence of the autogeneration frequency of the induction-frequency converter on the SOI FEHS top gate voltage at the bottom gate voltages of (1) 6, (2) 8, and (3) 10 V.

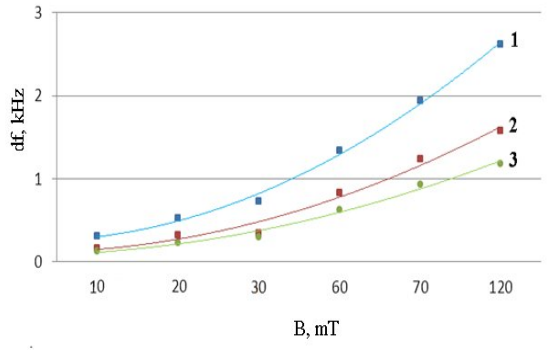


Figure 10: Dependence of the autogeneration frequency of the induction-frequency converter on the external magnetic field strength. The corresponding dependences are measured at the SOI FEHS supply voltage of 8 V, top gate voltage of 8 V, and bottom gate voltages of (1) 6, (2) 8, and (3) 10 V.

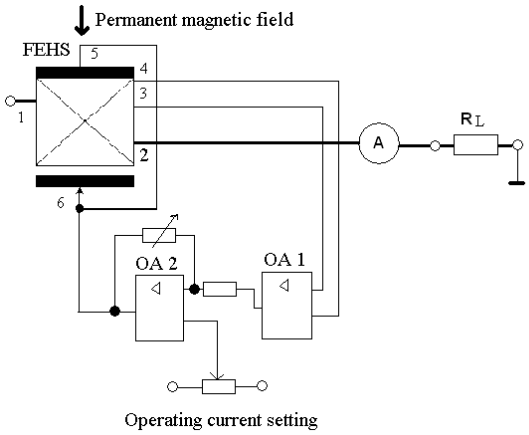


Figure 11: Stabilization circuit of the electric current flowing in the SOI FEHS channel. (1,2) current electrodes, (3,4) Hall electrodes, (5,6) top and bottom gate electrodes.

Table 1: Dependence of the stabilized current on the load resistance

Stabilized current, μA	Load resistance, Ω
100	15000
101	7500
102	0,5

4. Conclusions

The FEHS has the properties of the ordinary Hall element and field-effect transistor with MISIM control system. The use of the "silicon-on-insulator" technology results in that the capability of the FEHS as a magnetic field detector and its functionability under hard radiation and temperature conditions significantly exceeds not only the capability of silicon analogues, but also, in many cases, properties of Hall elements based on semiconductor compounds such as GaAs and InSb. The MISIM field-effect system provides additional possibilities of improving the FEHS characteristics (e.g., improving the threshold magnetic sensitivity by orders of magnitude) and controlling its characteristics (e.g., the temperature coefficient of magnetic sensitivity). The MISIM design of the FEHS makes it possible to propose new circuit solutions for processing the magnetically induced signal. The attraction of such solutions was demonstrated by the examples of FEHS applications in magnetic induction-frequency converters and in non-contact electric current stabilizers.

References

[1] M.L. Baranochnikov, A.D. Mokrushin, V.N. Mordkovich , D.M. Pazhin, N.M. Omelianovskaya, Field Effect Hall Sensor - new type of magnetic field primary transformer, *Sensors and Systems, (in russian)*, № 7 (50), p. 33-38, 2003.

[2] M.L. Baranochnikov, A.D. Mokrushin, V.N. Mordkovich, D.M. Pazhin, N.M. Omelianovskaya, V.V. Tarasov, NOVEL SILICON-ON-INSULATOR CONTROLLABLE HALL ELEMENT in *Abstr. Of European Magnetic Sensor and Actuators Conference EMSA*, Caen (France), M.41, 30 June – 2 July, 2008.

[3] Silicon-on-insulator technology: *materials to VLSI/ by Colinge J.P.- 2nd edition.* Kluwer Academic publishers. Boston/Dordrect/London, 267, 1997.

[4] A.D. Mokrushin, N.M. Omeljanovskaja, A.V. Leonov, V.N. Mordkovich, D.M. Pazhin Radiation effects in SOI magnetic sensitive elements under different radiation conditions. *Progress in semiconductor –on-insulator structures and devices operating at extreme conditions;* Edited by F. Balestra, A. Nazarov and V.S. Lysenko. Dordrecht/Boston/London: Kluwer Academic Publishers, Vol. 58. 221–227, 2002.

[5] A.D. Mokrushin, N.M. Omeljanovskaja, A.V. Leonov, V.N. Mordkovich, D.M. Pazhin Radiation effects in SOI magnetic sensitive elements under different radiation conditions. *Progress in semiconductor –on-insulator structures and devices operating at extreme conditions;* Edited by F. Balestra, A. Nazarov and V.S. Lysenko. Dordrecht/Boston/London: Kluwer Academic Publishers, Vol. 58. 221–227, 2002.

[6] K.D. Shcherbachev, V.T. Bublik, V.N. Mordkovich, D.M. Pazhin, Features of radiation defects formation in a silicon layer «silicon on insulator» structures. *Semiconductors,* v.45, № 6, 2011.

[7] A.D. Mokrushin, N.M. Omeljanovskaja, A.V. Leonov, V.N. Mordkovich, D.M. Pazhin Radiation effects in SOI magnetic sensitive elements under different radiation conditions: *Conference abstracts. / NATO Advanced Research Workshop "Progress in semiconductor –on-insulator structures and devices operating at extreme conditions"* – Kiyv, p. 44–45, 2000.

[8] A.V. Leonov, A.D. Mokrushin, N.M. Omeljanovskaja, The peculiarity of electrons mobility in thin Si layer of dielectric-Si-dielectric structure. *Semiconductors*, v. 46, № 4, (in press), 2012.

[9] R.S. Popovich, *Hall Effect Devices* / *Second Edition.* – Bristol: IOP Publishing Ltd, 419 p., 2004.

[10] Magnetosensitive IC. *Patent of Russian Federation* №2328014, 2008.

[11] A. Cooper, I. Bringnell, A magnetic field transducer with frequency modulated output. *J. Phys., E: Sci. Instr.,* v.17. 627-630, 1984.

[12] Magnetosensitive IC. *Patent pending.* Priority from 13.04.2011.

[13] O.N. Negodenko, Yu.P. Mardamshin, Microelectronics sensors with frequency input based on negatron analogues. *Technology and design of electronics apparatus,* №5-6, p.19-22, 2000.

[14] Magnetosensitive IC for electrical current stabilization. *Patent of Russian Federation.* Decision to grant a patent from 29.09.2011.

A simple ferromagnetic hysteresis model for current transformer simulation

Tiago Staudt*, Mauricio Rigoni, Walter P. Carpes Jr., Nelson Jhoe Batistela

Department of Electrical Engineering,
Federal University of Santa Catarina (UFSC-GRUCAD), Florianopolis, Brazil
*corresponding author, E-mail: staudt@grucad.ufsc.br

Abstract

Current transformers (CT) are commonly used in instrumentation to measure AC electric currents. This work presents a simple procedure to model ferromagnetic hysteresis in order to simulate nearly all effects in quasi-static systems for a non-saturated CT operating in steady state. The main goal is to provide a simple model based on an actual magnetic core to analyze CT behavior during design stages. It relies on core magnetic characterization, whose results are used to set the values of input parameters such as permeability and core losses. A simulation algorithm that allows the calculation of most CT electrical quantities is also presented. Reliable estimation of amplitude and phase errors can be obtained for a wide range of operating points. Experimental results show that the proposed approach represents adequately CT behavior by using a measured anhysteretic curve to determine the magnetic permeability and a resistance to model core losses.

1. Introduction

Current transformers (CT's) are devices used to change current levels and to provide galvanic insulation between two distinct interconnected electric circuits. This paper focus on CT's used in low-frequency current sensing applications. To correctly simulate CT behavior, it is imperative to appropriately consider the core magnetic properties. Reference [1] utilizes the Preisach model to describe hysteresis, while in [2] the authors consider the Jiles-Atherton model for the same purpose. These approaches normally deal with the CT behavior during transients. It is important to simulate CT operation in this condition because equipments such as electronic relays and circuit breakers may not operate correctly due to a failure in the current measurement caused by CT saturation [3]. Equally relevant is the CT performance under normal operation conditions (i.e. in steady state and with a non-saturated magnetic core). However, there are few papers in the literature dealing with the optimization of CT performance in these situations. The CT behavior under normal operation conditions is very important in design stages to determine if the chosen design parameters lead to a CT that fits the application measurement precision requirements.

For industry applications, reliable and easy to implement simulation algorithms are usually preferred. This paper proposes a simpler model for consideration of the ferromagnetic hysteresis that is particularly well suited for CT operation under normal conditions. So that all the project requirements are accomplished, CT designs may take several iterations. The use of the proposed model during the initial stages tends to avoid several trial and error iterations to reach an optimized solution, potentially reducing project costs. Different configurations (core materials, number of turns, cross section area, and so on) can be simulated during design phase to find the solution that best fits the requirements for a specific application.

This work is basically divided in three parts: (i) description of the CT calculation algorithm, (ii) utilization of the proposed ferromagnetic hysteresis model to accurately simulate CT behavior and (iii) final model validation through experimental results. As stated before, the ferromagnetic hysteresis model depends on the magnetic characterization of the core material. This means that, prior to simulation, input parameters such as permeability model and core losses constants shall be obtained experimentally for each magnetic material utilized in CT cores. A simple way to obtain these parameters will also be presented.

2. Current Transformer Electric Model

In order to develop the CT calculation algorithm (presented in section 4), it is required to find analytical equations that describe the CT electromagnetic behavior. The model utilized in this paper is based on concentrated electric parameters. This approach is well known in the literature and the main contribution of this work is in the simple methodology to estimate the parameter's values. The equivalent electric circuit used in the simulation is based on the procedure described in [4].

Fig. 1 shows a simplified CT electromagnetic circuit used as a base for the model development, where v_x, i_x, r_x, e_x, N_x, ϕ_{mx} and ϕ_{Llx} are, respectively, voltage, current, wire resistance, induced voltage, number of turns, magnetic flux and leakage magnetic flux. The index x can assume values "1" and "2", representing primary side or secondary side, respectively. R_{burden} is the CT load connected at the secondary side, R_i, R_e and R_{med} are the internal, external and medium radius, respectively, which define the CT toroidal geometry and h is the core height.

The model development starts from Maxwell's equations. The main equations are Ampere's Law (1), which relates the primary current with the magnetic field, and Faraday's Law (2), which relates the magnetic flux with the induced electric voltage in the core.

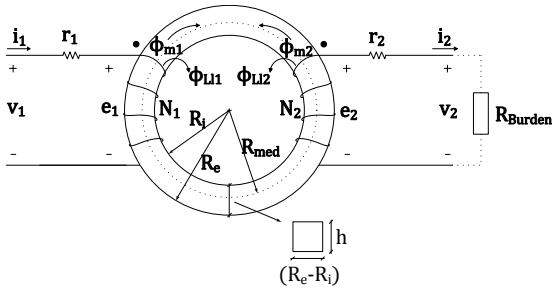


Figure 1: Simplified electromagnetic circuit of a CT.

$$\oint_L \overrightarrow{H_1} \cdot \overrightarrow{dl} = N_1 i_1, \tag{1}$$

$$e_2 = -\frac{d(N_2\phi)}{dt}, \tag{2}$$

where $\overrightarrow{H_1}$ is the instantaneous total magnetic field delivered to the electromagnetic system and ϕ is the effective flux in the core.

The voltage equations in each winding are written as follows:

$$v_1 = r_1 i_1 + \frac{d\lambda_{m1}}{dt}, \tag{3}$$

$$v_2 = -r_2 i_2 + \frac{d\lambda_{m2}}{dt}, \tag{4}$$

where λ_{mx} are the linkage fluxes in the core, defined as:

$$\lambda_{m1} = N_1\phi = N_1[\phi_{m1} + \phi_{Ll1} - \phi_{m2}], \tag{5}$$

$$\lambda_{m2} = N_2\phi = N_2[\phi_{m1} - \phi_{Ll2} - \phi_{m2}], \tag{6}$$

Voltage equations are re-written in terms of the inductances. One may notice that the inductance has been considered constant in the time derivative. As will be shown in section 4, its value is updated at each time step during the simulation and, under this condition, this is a valid approach. Thus, both linear and non-linear analysis may be performed with this algorithm. The primary quantities are also referred to the secondary using the ideal transformer equations to make it easier to analyze the CT behavior. Primed variables ($\prime$) indicate primary quantities referred to the secondary side.

$$v_1\prime = r_1\prime i_1\prime + L_{m2}\frac{di_1\prime}{dt} + L_{Ll1}\prime\frac{di_1\prime}{dt} - L_{m2}\frac{di_2}{dt} \tag{7}$$

$$v_2 = -r_2 i_2 - L_{m2}\frac{di_2}{dt} - L_{Ll2}\frac{di_2}{dt} + L_{m2}\frac{di_1\prime}{dt} \tag{8}$$

Equations (7) and (8) may be represented as an equivalent electric circuit as shown in Fig. 2. In this figure, the

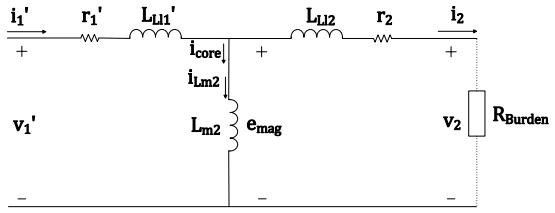


Figure 2: Equivalent electric circuit of a CT without considering losses.

variable e_{mag} is the same as e_2 because all electrical quantities are referred to the secondary side.

The differential equation system defined by (7) and (8) are written in matrix form as (9) and the solution is given by (10).

$$\mathbf{Y} = \mathbf{A}x + \mathbf{M}\frac{dx}{dt}, \tag{9}$$

$$\frac{dx}{dt} = \mathbf{M}^{-1}(\mathbf{Y} - \mathbf{A}x), \tag{10}$$

where $\mathbf{Y} = \begin{bmatrix} v_1\prime \\ v_2 \end{bmatrix}$, $\mathbf{A} = \begin{bmatrix} r_1\prime & 0 \\ 0 & -r_2 \end{bmatrix}$, $x = \begin{bmatrix} i_1\prime \\ i_2 \end{bmatrix}$, $\mathbf{M} = \begin{bmatrix} L_{m2} + L_{Ll1}\prime & -L_{m2} \\ L_{m2} & -(L_{m2} + L_{Ll2}) \end{bmatrix}$.

Inductance L_{m2} is associated to the core magnetization and its value is related to the instantaneous core permeability. In this paper, it is calculated using:

$$L_{m2} = \frac{N_2^2}{\Re}, \tag{11}$$

where $\Re$ is the reluctance of the magnetic circuit, which is a function of physical parameters and core permeability. In an actual core, this quantity is non-linear and a core ferromagnetic hysteresis model provides ways to take this into account.

Experimental core characterization provides data for the permeability model used to calculate inductance L_{m2}. Three different permeability models have been tested (see section 6). Leakage inductances $L_{Ll1}\prime$ and L_{Ll2} are typically negligible quantities for CTs with high permeability cores operating under quasi-static systems. As other assumptions in the model would potentially generate higher errors than the precise leakage inductances determination, a very small value for $L_{Ll1}\prime$ and L_{Ll2} has been assigned just to guarantee the calculation of the inverse matrix $\mathbf{M}^{-1}$ (see equation (10)) without significantly influencing the results. If necessary, these leakage inductances can be estimated either experimentally or through analytic calculations.

3. A comprehensive ferromagnetic hysteresis model

The model presented so far considers nearly all parameters of a practical CT for quasi-static systems, except the core

losses. To obtain more precise and reliable results, it is crucial to take into account these parameters in the model. Fig. 3 shows how the CT core has been modeled for the simulation.

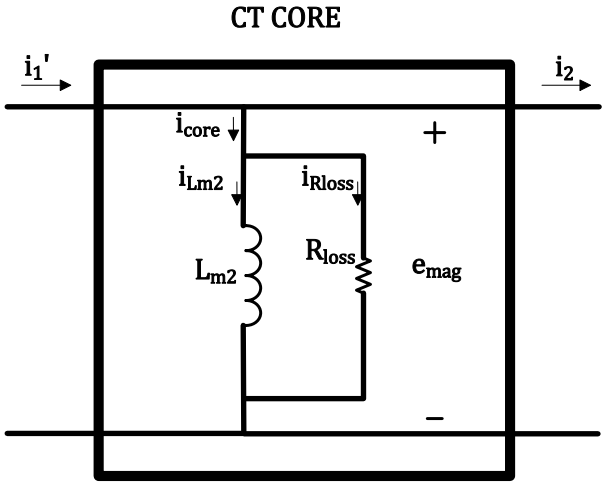


Figure 3: Core equivalent electric circuit.

A non-linear inductance (L_{m2}) represents the core BH magnetization characteristic while a parallel resistance (R_{loss}) take the magnetic losses into consideration. The resulting equivalent electric circuit used in simulation is represented in Fig. 4.

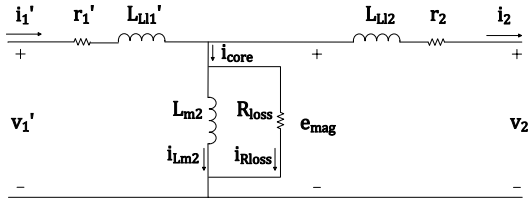


Figure 4: CT equivalent electric circuit considering losses.

The correct solution of the resulting differential equation system (10) requires an accurate electric parameter's determination. As the system is solved iteratively, the parameters shall be determined in each step so that better results can be achieved. To do this, it is necessary to find an analytical equation for permeability and core losses in function of induction (refer to section 5 for further information on this topic). The permeability is used to determine magnetic field and consequently the induced current over the inductive component. Three kinds of permeability models have been tested: (i) linear ($\mu_r Cte$), (ii) obtained by the magnetization curve ($\mu_r MagIni$) and (iii) by using an anhysteretic curve ($\mu_r ah$) [5]. For the resistance, the state of the art about magnetic losses theory separates the core total loss as a sum of three parts: hysteresis, induced current and excess losses. In this work, the representation of the losses in terms of the total loss or in terms of the three components is equivalent, because the resistance used to model the core loss is connected in parallel with the inductance of the core. To guarantee reliable simulation results, it is imperative to measure only the total loss. Based in Steinmetz empirical equation, (12) is satisfactorily used to represent the total loss in function of maximum induction for each operating point in the following way:

$$P = k_{loss}\, m\, f\, B_m^{\beta_{loss}} \tag{12}$$

where P is the loss (W), m, f and B_m are respectively the core mass (kg), operation frequency (Hz) and the maximum induction (T) and k_{loss} and β_{loss} are constants obtained experimentally (see section 5). To calculate the equivalent loss resistance, the following equation is used:

$$R_{loss} = \frac{e_{mag}^2}{P} = \frac{e_{mag}^2}{k_{loss}\, m\, f\, B_m^{\beta_{loss}}} \qquad [\Omega] \tag{13}$$

The electric quantity e_{mag} represents the internally induced voltage in the CT core (see figure 4). It is calculated by solving the aforementioned differential equation system. All other electric circuit parameters are obtained directly from the physical prototype. An algorithm to solve the differential equations has been developed and then all the electric and magnetic quantities are calculated during the iterative process.

4. Simulation algorithm

At this point, a ferromagnetic hysteresis model has been incorporated to a current transformer analytical model. This section presents a simulation algorithm that has been used to simulate CT behavior using the development presented in sections 2 and 3.

The simulation starts generating the current $i_1\prime$, which is the excitation for the CT, a known value. The calculation of voltage $v_1\prime$ is done based in (10) as follows:

$$v_1\prime = \frac{1}{M_{11}^{-1}}[\frac{di_1\prime}{dt} + M_{11}^{-1} r_1\prime i_1\prime - M_{12}^{-1}(v_2 + r_2 i_2)], \tag{14}$$

where M_{11}^{-1} and M_{12}^{-1} are the coefficients of the first line of the inverse 2×2 matrix $\mathbf{M}^{-1}$. The coefficients of matrix $\mathbf{M}$, particulary L_{m2}, shall be updated at each time step with the values from previous iteration using (11).

The induced voltage e_{mag} is obtained directly from the circuit of Fig. 4.

$$e_{mag} = v_1\prime - r_1\prime i_1\prime - L_{Ll1}\prime \frac{di_1\prime}{dt}, \tag{15}$$

The magnetic induction is calculated using (2) and (15).

$$B = \frac{1}{N_2 S} \int e_{mag} dt \tag{16}$$

where S is the core effective cross-section area.

The effective magnetic field in the core H_{core} is obtained from the relationship between magnetic reluctivity ν and induction:

$$H_{core} = \nu B \tag{17}$$

The current over the inductive element in the core is given by:

$$i_{Lm2} = \frac{H_{core} l_m}{N_2} \tag{18}$$

The loss resistance can then be calculated by using (13) and the currents flowing through it is given by:

$$i_{Rloss} = \frac{e_{mag}}{R_{loss}} \tag{19}$$

Current i_2 and voltage v_2 can finally be calculated:

$$i_2 = i_1\prime - i_{Lm2} - i_{Rloss}, \tag{20}$$

$$v_2 = i_2 R_{burden}, \tag{21}$$

Equations (14) to (21) define a current transformer model that considers nearly all non-linearities of a practical current transformer for quasi-static systems. Next section shows how the permeability and loss models can be obtained from experimental results.

5. A simple procedure to obtain permeability and loss constants

As stated before, the ferromagnetic hysteresis model described in section 3 relies on the experimental core characterization to determine the permeability relationship with magnetic induction and the constants used to calculate equivalent resistance R_{loss}. These data can be obtained using information provided by the manufacturer or by measuring the core loss through standardized methods [6]. In this work, it was used the equipment MPG 100D from Brockhaus Messtechnik [7] to characterize the core. This equipment provides all data necessary to determine the simulation parameters.

5.1. Permeability models

The permeability dependence on the induction will be considered using three different models: constant ($\mu_r Cte$); obtained from initial magnetization curve ($\mu_r MagIni$) and obtained from the anhysteretic curve ($\mu_r ah$). The constant permeability model $\mu_r Cte$ is obtained by simply measuring permeability at frequency and induction values corresponding to the operating point that is desired to simulate the CT. For the sample utilized in this validation, the measured value was $\mu_r Cte = 16823$ (relative permeability) for a maximum induction of $1\ T$ at $60\ Hz$. The permeability model $\mu_r MagIni$ is obtained by measuring the initial magnetization curve for several induction and magnetic field values. A trend equation in the form $y = Ax^{\eta}$ is calculated when a graph of permeability versus induction is plotted as shown in Fig. 5. Constants A and η are determined using curve fitting and the trend equation is used as the relationship between permeability and induction in the algorithm.

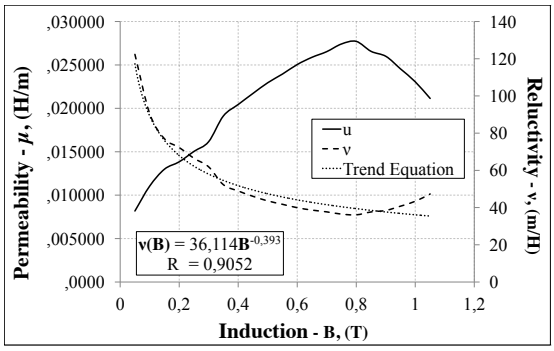


Figure 5: Permeability model obtained from initial magnetization curve.

To obtain the permeability model $\mu_r ah$, it is necessary to find the anhysteretic curve of the material [5]. This is a theoretical curve and it corresponds to the magnetization without energy consumption, an ideal phenomenon that does not exists in practice. There are some ways to obtain this curve experimentally, but the procedure is complicated and demand special equipments. To keep the hysteresis model and its parameter determination as simple as possible, the anhysteretic curve has been approximated from the BH loop, measured at $10\ Hz$, by calculating its medium curve as shown in Fig. 6. This measurement frequency has been chosen to minimize the core loss influence on the anhysteretic curve determination. The following equations have been used:

$$B_{ah} = f(H_{ah}), \tag{22}$$

$$B_{ah} = \frac{B_1 + B_2}{2}, \tag{23}$$

$$H_{ah} = \frac{H_1 + H_2}{2}, \tag{24}$$

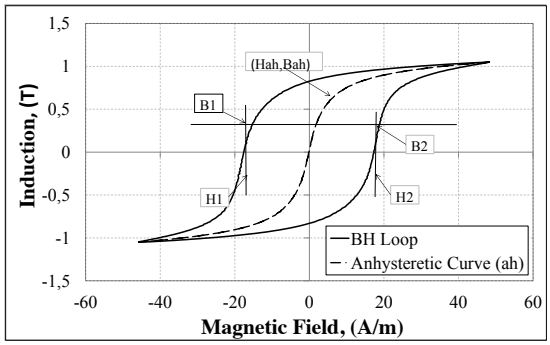


Figure 6: Simplified method to calculate the anhysteretic curve.

After obtaining the $B_{ah} = f(H_{ah})$ curve, it is necessary to find the reluctivity (ν) versus induction (B) relationship to be inserted as an analytical equation in the model. The polinomial trend equation used in the simulation presented in the next section is shown in Fig. 7, which was measured at $10\,Hz$ and at $B = 1.05\,T$. It has been assumed that this procedure to obtain such a curve does to not affect significantly the model accuracy and this assumption has been confirmed based on the validation results. If different operating points (induction levels) than the one used to calculate this curve are supposed to be simulated, it may be necessary to determine the anhysteretic curve for the new induction level to have more precise and reliable results. This is necessary because the anhysteretic curve obtained by this method is an approximation of the real curve. The experimentally derived analytical equation parameters may slightly change for distinct induction level provoking additional errors in the simulation results.

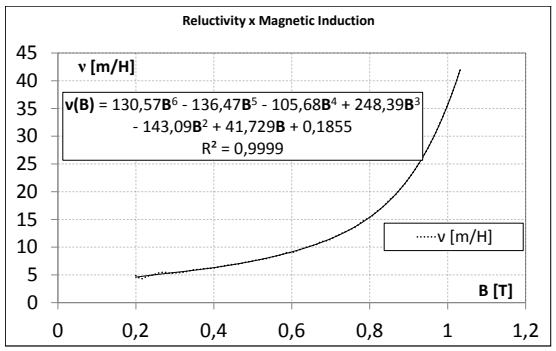


Figure 7: Polinomial trend equation for $\mu_r ah$ model.

The inductance L_{m2} is calculated using (11) according to the chosen permeability model.

5.2. Loss constants

The parameters k_{loss} and β_{loss} of equation (12) shall be obtained from the measured total core loss. A curve of total loss versus induction at constant frequency shall be plotted. Then, a trend curve is calculated in the form $P = k\,B^{exp}$. Based in this trend curve, the constants k_{loss} and β_{loss} are determined. This procedure is similar to the one indicated in section 5.1 to calculate the $\mu_r MagIni$ trend equation. With this information, it is possible to calculate the resistance representing the loss through equation (13).

The remaining input parameters necessary to simulation depend on the physical construction of the CT. With all input data defined, it is possible to present the simulation results.

6. Validation of the proposed model with experimental data and simulation

The simulation results will be compared with experimental data obtained from a prototype that has a grain-oriented silicon-iron alloy as the core magnetic material. Table 1 summarize the most important prototype physical characteristics.

Table 1: Prototype physical characteristics.

Parameter	Value
mass	$262.35\ g$
mean magnetic length	$172.37\ mm$
Effective Area	$195.29\ mm^2$
i_1	$70.254\ A$
N_1	1
N_2	500
N_{aux}	100
r_1	$0.2\ \Omega$
r_2	$1.6\ \Omega$
R_{burden}	$202.8\ \Omega$

The winding designated by N_{aux} is an auxiliary one used to measure indirectly the magnetic flux in the core through the induced voltage while it is in operation. A picture of the prototype used in the validation is shown in Fig. 8.

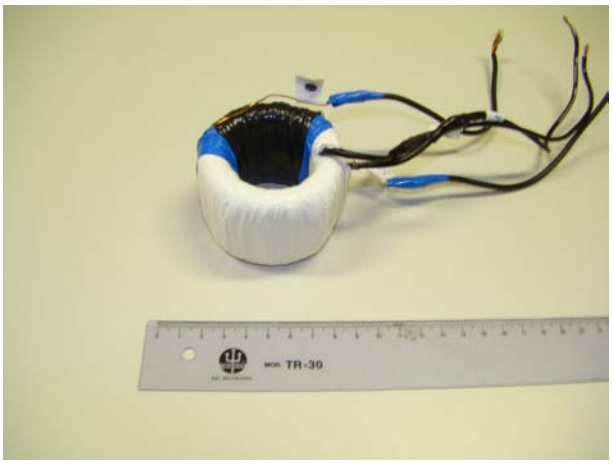


Figure 8: Prototype utilized in the validation.

The operating point used to validate the model was set at an induction level of $B = 1.0\,T$ and at a system frequency of $60\,Hz$. It corresponds to the magnetic induction obtained within the current transformer when it is excited with the current level indicated in table 1. Fifty electric cycles were simulated to guarantee that the CT had reached the steady state condition and the simulation waveforms were synchronized with the experimental results. To better evaluate the algorithm performance, some variations of the input parameters will be presented. The three permeability models will be considered with and without inserting

losses in the simulation. Fig. 9 shows a comparison between the simulation results without considering losses and the measured waveform for the secondary current, i_2. The difference between the experimental result and simulation is not clear in this figure. Fig. 10 shows a zoom of the region selected in Fig. 9 to better evaluate the curves.

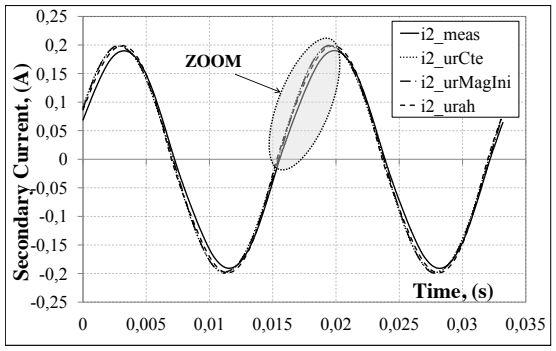


Figure 9: Secondary current without considering losses in the model.

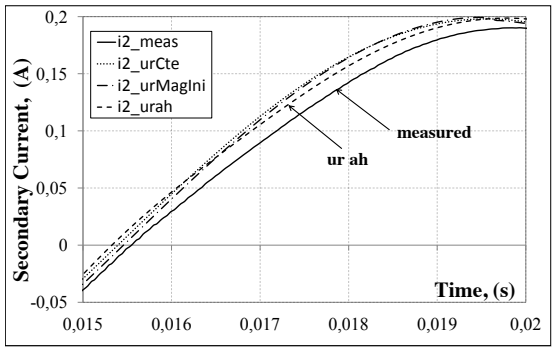


Figure 10: Closer view in secondary current without considering losses in the model.

Fig. 11 shows the simulation result considering losses for the secondary current, i_2, in the same zoomed region as shown in Fig. 9. As Fig. 10 and Fig. 11 are in the same scale, it is possible to see that the insertion of losses in the simulation increases the accuracy. When the permeability model obtained from anhysteretic curve is used, the results are closer to the measured waveform.

The theoretical current flowing through the core, i_{core}, defined in the electric equivalent circuit of Fig. 4, is also shown for comparison. This current was obtained from the magnetic field measured in the sample, as they are proportional. Fig. 12 shows a simulation of i_{core} without considering losses, i.e. the core is represented only by the inductance L_{m2} (see Fig. 2). Fig. 13 considers the complete equivalent circuit of Fig. 4, with losses included. From Fig.

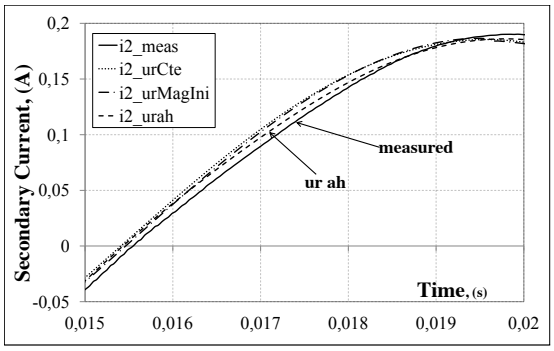


Figure 11: Closer view in secondary current with loss consideration in the model.

13, it is possible to conclude that the permeability model obtained from the anhysteretic curve is the best choice to represent the practical case. Also, the loss insertion highly improved simulation accuracy.

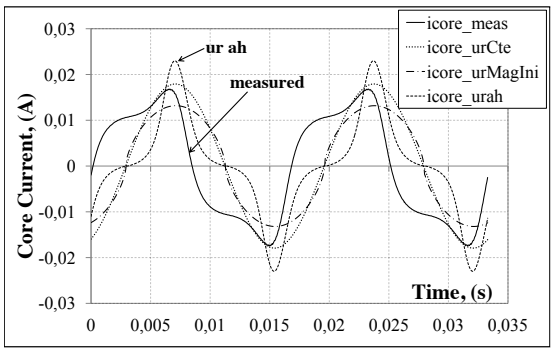


Figure 12: Comparison between the three permeability models and the experimental result for the total current flowing through the core (i_{core}) without considering losses.

Other two magnetic quantities, induction and field, are also analyzed. Fig. 14 and Fig. 15 show a comparison between simulated and measured BH loops. Fig. 14 does not include losses in the simulation. As can be seen in this figure, the simulated BH loops are just a line for the three permeability model and they do not represent correctly the measured loop. On the other hand, the results shown in Fig. 15 include losses in the model. Again, it can be noticed that the permeability model best representing the practical case is that obtained from the anhysteretic curve with loss inclusion.

7. Discussion

The validation results presented in previous section have shown that the procedure described to simulated CT behavior under normal operational conditions is effective. In

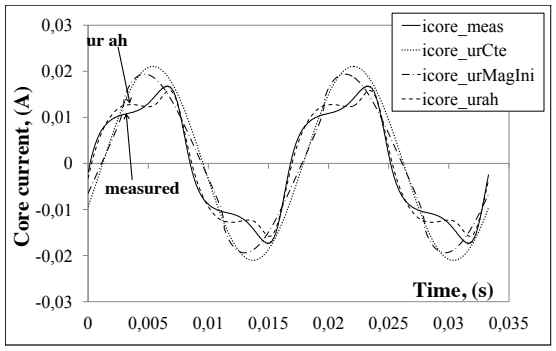


Figure 13: Comparison between the three permeability models and the experimental result for the total current flowing through the core (i_{core}) considering losses.

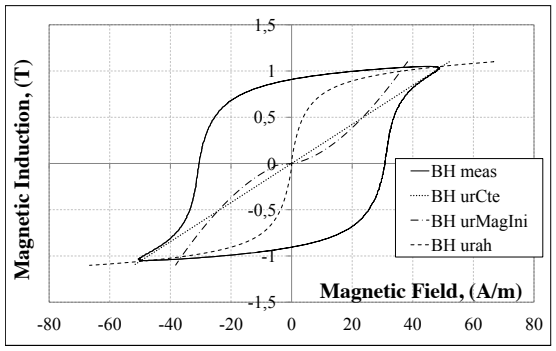


Figure 14: Comparison between the three permeability models and the experimental result for the BH loop in the core without considering losses.

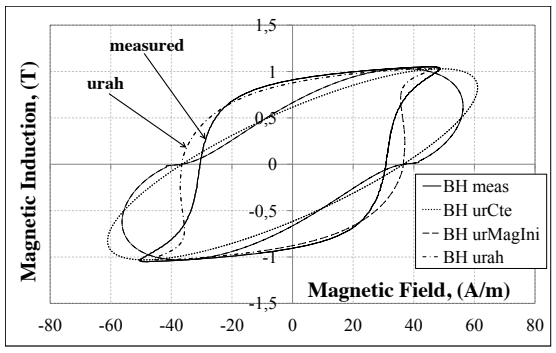


Figure 15: Comparison between the three permeability models and the experimental result for the BH loop in the core with losses considered.

order to compare different approaches that can normally be used to model the non-linear behavior of the magnetic material utilized in the core, three permeability models have been tested. The model based on the anhysteretic curve has produced very accurate results. Additionally, the results have shown that the loss insertion in model is crucial to obtain reliable results.

The results regarding the secondary current have been shown in Fig. 10 and Fig. 11. As the utilized prototype has a high permeability magnetic material, the core current (i_{core}) derived from the magnetic field has a small magnitude. This has lead to a small difference between the experimental and simulated curves for the secondary current (i_2) even if all distinct simulations are considered. From these curves, it is hard to conclude about the model accuracy, even though it also confirms that hysteresis model is more precise. On the other hand, it is possible to notice from figures 12, 13, 14 and 15 that the permeability model and the losses consideration in the model are hugely significant to model the ferromagnetic hysteresis in CT core correctly.

Even if high permeability cores are generally utilized in precision current sensors, it is crucial for the CT designers to analyze all effects that may introduce amplitude and phase erros in the measurement. The relatively simple procedure described in this paper offers support for engineers to better understand CT electromagnetic behavior under different physical configurations.

8. Conclusions

This paper has presented an intuitive way to consider nearly all aspects on CT operation in the cited conditions by using a simple procedure to model ferromagnetic hysteresis. It has been presented a simulation algorithm as a tool to analyze the electromagnetic behavior of current transformers during design stage. Several variations of project parameters, such as different magnetic materials, number of turns, core size, burden resistance, and so on can be simulated to obtain an optimized solution for any specific application. The model is based in the CT electric equivalent circuit and the equations are derived from the electromagnetic theory. To make it simpler to implement in industry, the input parameters are based on experimental data that can be obtained either from the manufacturer datasheet or by standardized magnetic material characterization techniques. Accurate calculations of core quantities are crucial to precisely estimate amplitude and phase errors in the CT. Six different simulations have been presented considering three models to represent the magnetic permeability and the influence of the losses in the calculation. The results have been compared with experimental data obtained from a real CT. It has been found that the input parameter variation best representing CT performance considers the permeability obtained from the anhysteretic curve and the loss inclusion in the model.

Acknowledgement

The authors gratefully acknowledge N. Sadowski, M. V. F. da Luz and P. A. da Silva Jr. for their contribution in this work.

References

[1] Rezaei-Zare, A.; Iravani, R.; Sanaye-Pasand, M.; Mohseni, H.; Farhangi, S.; , "An Accurate Current Transformer Model Based on Preisach Theory for the Analysis of Electromagnetic Transients," *Power Delivery, IEEE Transactions on*, vol.23, no.1, pp.233-242, Jan. 2008

[2] Annakkage, U.D.; McLaren, P.G.; Dirks, E.; Jayasinghe, R.P.; Parker, A.D.; , "A current transformer model based on the Jiles-Atherton theory of ferromagnetic hysteresis," *Power Delivery, IEEE Transactions on* , vol.15, no.1, pp.57-61, Jan 2000

[3] Guerra, F. C. F., "Current Transformer Model," *Power Delivery, IEEE Transactions on*, Vol. 22, No. 1, 187-194, Jan. 2007.

[4] Krause, P. C. Wasynczuk, O., Sudhoff, S. D., *Analysis of Electric Machinery and Drive Systems*, IEEE Press, New Jersey, 2002.

[5] Pearson, J.; Squire, P. T.; Atkinson, D. *Which anhysteretic magnetization curve?*, IEEE Transactions on Magnetics, v. 33, n. 5, p. 3970-3972, 1997.

[6] IEC 404-2. *Magnetic Materials*. 3rd. edition, 1996.

[7] Brockhaus Messtechnik. Electrical Steel Tester (MPG 100D) *Available at: http://www.brockhaus.com*.

Thermal Reduction in Portable Systems Using DVS Technique

Diary R. SULAIMAN

Electrical Engineering Department, Engineering College, Salahaddin University-Hawler
Erbil, IRAQ
E-mail: diariy@gmail.com

Abstract

With the continuous increases in switching frequency and power density, the low power and high performance VLSI systems have become the most significant consideration in the design of mobile and portable systems. Minimization of energy consumption in the battery powered portable applications is always a challenging task in the scaled down CMOS technologies. Power and thermal management challenges are highly related. Higher power consumption results in higher temperature, which enhances many physical failure mechanisms. Modern processors employ thermal management mechanisms that reduce power consumption when the temperature exceeds a threshold value. In this paper, the dynamic thermal management (DTM) technique has been presented to monitor the operation temperature of the chip at runtime, and regulate on-chip temperature for high-performance portable microprocessors. Simulation is used to confirm both of the theoretical background in a successful manner.

1. Introduction

The increasing popularity of mobile applications, like cellular phones, and personal digital assistance (PDA), forces system designers into the low power domain to extend the operational time, this make temperature to be an important design constraint for portable microprocessors. This can be done by lowering the clock frequency for a fixed duration whenever the thermal sensors indicate that the thermal limit is exceeded.

A digital CMOS microprocessor and integrated circuit (IC) operates charging and discharging capacitors, which producing dissipation of power. The main CMOS IC dissipated power is the dynamic power, Equation (1) shows that, reducing supply voltage (V_{dd}) will reduce dynamic power P_D in a quadratic manner.

$$P_D = \alpha(\frac{1}{2} C_L V_{dd}^{\ 2} f_{CLK}) \quad (1)$$

Where P_D is the dynamic power, α is the probability of the transition in the clock period, C_L is the load switching capacitance, and f_{CLK} is the clock frequency. Dynamic voltage scaling (DVS) is a technique of power and thermal reduction in microprocessors including portable systems by scaling down both the supply voltage and operating frequency during idle periods of execution. The maximum execution time of the task is equal to its deadline. Therefore, E/4 is the minimum possible energy consumption of the task under timing constraint. Any further decrease in V_{dd} would violate the task deadline. In order to provide required system performance, V_{dd} should be scaled as low as possible to minimize energy consumption. Processors with DVS normally adapt effectively with its workload variations by adjusting the V_{dd} and the desired f_{CLK}. Figure (1) shows the actual execution time of a task when the voltage is scaled down (Dynamic Voltage Scaling – DVS). The maximum execution time of the task is equal to its deadline.

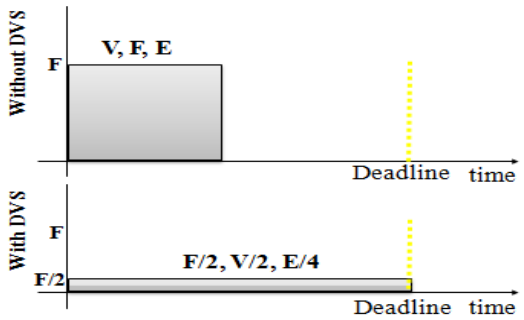


Figure 1: Real time task with and without DVS

The normalized power, frequency and supply voltage are plotted in Figure (2).

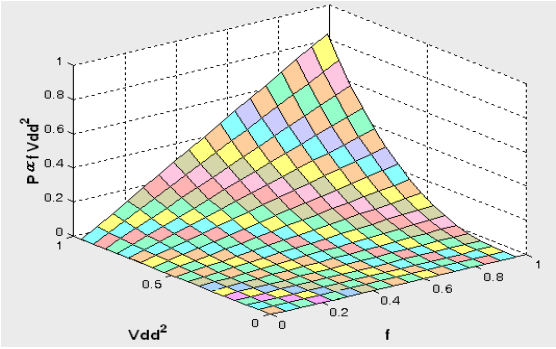


Figure 2: The normalized power, frequency and supply voltage

The processor is currently operating with a mid-range voltage level; sensor data indicate that, the temperature is

within an acceptable range and that the performance is less than the goal. The controller directs the voltage regulator to step up the supply voltage and monitors the temperature rise and performance counters, and continues to raise the frequency and voltage until achieving the desired performance target. If software application behavior causes a thermal spike, the manager takes immediate action to coordinate a response between the voltage, frequency, and the temperature. The controller can adapt to the system and push the operating conditions to the acceptable limits.

The energy-temperature efficient design for portable processor is required to maximize the useful lifetime of the battery source, which is accomplished by adjusting both the supply and clock frequency depending on the workload variation and thermal monitoring and control, which was studied throughout this paper.

2. Dynamic Voltage Scaling (DVS)

It is known that, for any computer system, the processor core consumes a large amount of energy and is about 20-58% according to the applications, this is shown in Figure (3):

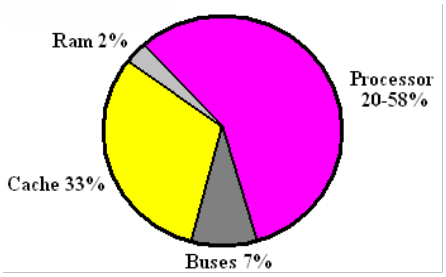


Figure 3: Power consumption rates of a computer system

Dynamic voltage frequency scaling (DVS) is a technique to reduce power and energy consumption of processors and computer systems, by lowering the supply voltage and operating frequency at runtime. Figure (4) shows the time line plot of device technology with respect to power dissipation, it is clear that the power dissipation is increasing, so the DVS technique becomes effective for the current and future processor technologies.

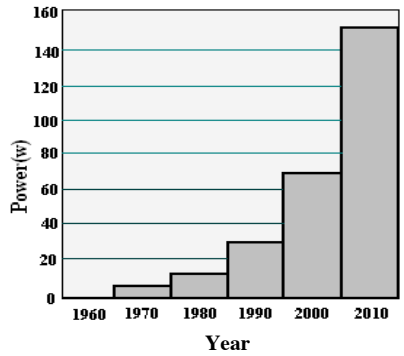


Figure 4: The device technology with respect to power dissipation

There are three key components for synchronizing a processor with a DVS technique [17]:

- A processor that can operate over a range of voltages.
- A regulation loop that can generate the required voltage for specific frequencies.
- An operating system that can vary the processor speed, it predict and set the desired clock frequency to be used by the regulation loop to adjust the processor clock frequency with the corresponding voltage level.

Figure (5) shows the block diagram of DVS control circuit applied to a microprocessor. The regulation loop that can generate the minimum voltage required for the desired speed, the voltage controlled oscillation (VCO), and the control loop are the main and essential components of DVS system. Operating systems that can intelligently vary the processor speed with a microprocessor can operate over a wide voltage range are also another required components for implementing such systems.

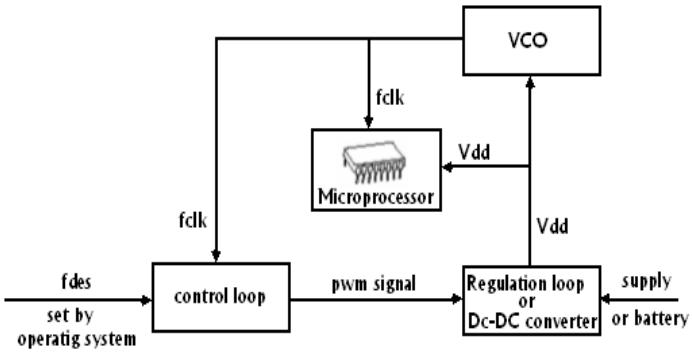


Figure 4: The DVS controller Block diagram

3. Dynamic Thermal Management

Microprocessors with variable workloads require initialize some electrical circuits to control both the supply voltage and operating frequency (DVS), and then controlling the thermal management system. Increasing the operating voltage will increase the thermal energy within the processor and it is proportional to the required clock frequency. Figure (5) shows the block diagram of CPU closed loop for both of power and thermal management.

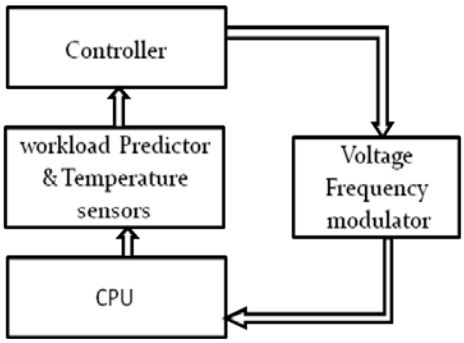


Figure 5: The block diagram of CPU Power & thermal management

To keep the temperature below the maximum, the power-thermal controller mechanism is required in modern processors to reduce the energy consumption, this is

achieved by adjusting the supply voltage and operating frequency whenever temperature reaches maximum, which is known as thermal management technique, during the off or idle period of time, dynamic energy consumption is greatly reduced. In order to estimate working temperature through thermal sensors for portable systems, two thermal sensors in association with its thermal monitor are required; the software can be used to provide the CPU temperature to the operating system. The sensor is working as a thermal comparator to determine the processor temperature. The temperature controller circuit determines when to initialize thermal management system. For practical designs, the controller will detect the best choice between measured values.

4. Simulation Results

The optimal frequency for executing a program is the frequency that satisfies both power and temperature limits based on the supply voltage and the processor clock speed control companion with the voltage-frequency lookup table, and according to the processor workload prediction & temperature monitoring. The temperature of the processor depends on the CPU activity or workload variation. Figure (6) shows the variation of the temperature over time with the average workload of a machine.

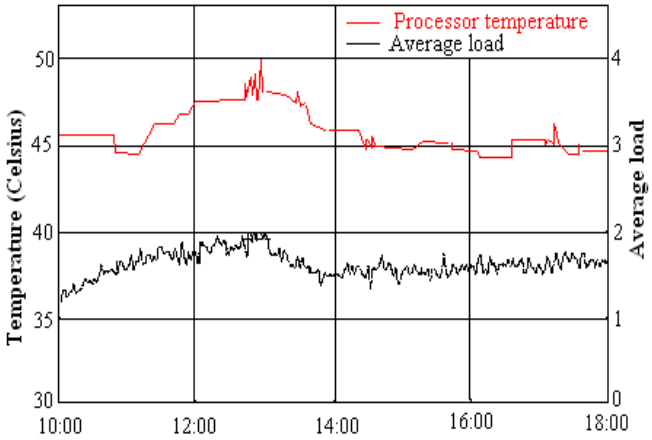


Figure 6: The Variation of the processor temperature vs. workload

High performance portable processors have high CPU utilization, and are typically designed to meet a safe design of temperature to maintain the processor below its maximum operating temperature within a minimum power dissipation range.

The general block diagram of CPU Power & thermal management was shown in Figure (5) and it consists of controller, voltage-frequency modulator, workload predictor and temperature sensors. To Obtain a real temperature readings directly from the processor, temperature sensors would be ideal. These sensors are based on analog CMOS circuit designs, and placed in one of the hot spots of the processor chip (register File). The thermal sensor TC1047A is the preferred sensor in this study. It develop an output voltage proportional to temperature with a nominal temperature coefficient of 6.25mV/°C and 10mV/°C respectively. Both temperature to voltage converters can sense a -40°C to +125°C temperature range while operating from a single 2.5V supply. The devices feature an offset without the need for a negative supply voltage. The extremely low operating current minimizes self-heating and maximizes battery life. High accuracy, low operating current and small packages make this sensor ideal for a variety of applications such as high speed processors, cellular phones, consumer electronics, printers, industrial control appliances, and office equipments.

Different SPEC CPU2000 benchmarks are used (gzip, vpr, gcc, mcf, crafty, parser, eon, perlbmk, gap , votex, bzip2, twolf) to ensure the circuit operation and obtain the expected and desired results. The used benchmarks are run for separate instances; these benchmarks are able to distinguish the way a hardware device temperature is increasing with workload and the way its temperature decrease when the workload is finished. The simulation results of thermal and Power reduction (%) is shown in Figure (7).

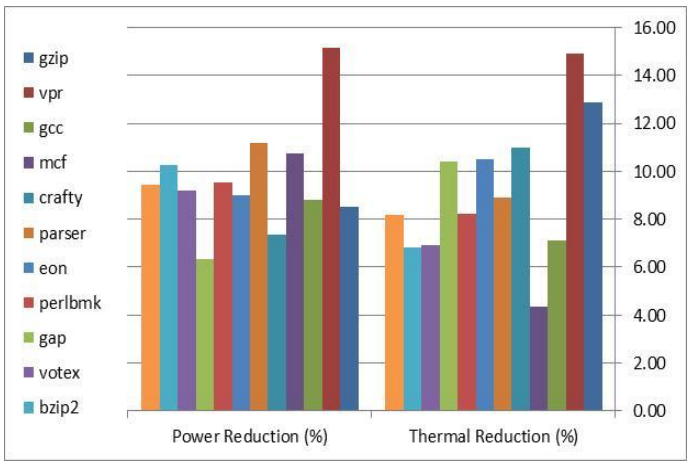


Figure 7: The simulation results of thermal and Power reduction (%)

The simulation results show that, the processor temperature reduction is high as 8.93%, and power savings is high as 9.62 % for the used benchmarks. Therefore, the thermal management technique, which is presented throughout this paper, can significantly improve processor temperature and power efficiency especially for portable microprocessors.

5. Conclusions

Processor speeds double approximately every eighteen months, while improving microprocessor's power and temperature have been the primary consideration in digital VLSI design, thermal reduction technique has emerged as an effective way to achieve minimizing in energy consumption as well as low temperature designs. In this study, the DVS technique was tested with different simulation benchmarks, the simulation results show strict limitation of both power and temperature. This study has a

potential saving of thermal reduction (8.93%) and power dissipation reduction of (9.62%) for the used benchmarks. Therefore, the DVS technique confirms superiority on power dissipation reduction as well as temperature reduction mechanisms, and it shows the greatest promise in processor's thermal-energy optimization effectively.

References

[1] N. Mehta, and B. Amrutur, "Dynamic Supply and Threshold Voltage Scaling for CMOS Digital Circuits Using In-Situ Power Monitor" IEEE Transactions on Very Large Scale Integration (VLSI) Systems", Vol.PP, Issue 99, 2011.

[2] R. Cochran, and S. Reda, "Consistent Runtime Thermal Prediction and Control Through Workload Phase Detection", The 2010 Design Automation Conference (DAC'10), Pp 62-69, USA, June 2010.

[3] F. Zanini, D. Atienza, C. N. Jones, G. D. Micheli, "Temperature Sensor Placement in Thermal Management Systems for MPSoCs", The IEEE International Symposium on Circuits and Systems (ISCAS'2010), Paris, France, 2010.

[4] J. Donald, and M. Martonosi, "Techniques for Multicore Thermal Management: Classification and New Exploration", Proceedings of the 33rd International Symposium on Computer Architecture (ISCA'06), Boston, USA, 2006.

[5] G. M. Almeida, R. Busseuil, E. A. Carara, N. H´ebert, S. Varyani,G. Sassatelli, P. Benoit, L. Torres, and F. G. Moraes, Predictive Dynamic Frequency Scaling for Multi-Processor Systems-on-Chip, IEEE International Symposium of Circuits and Systems (ISCAS'2011), Rio de Janeiro, Brazil, 2011.

[6] M.P. Gupta, C. Minki, S. Mukhopadhyay, S. Kumar, "Thermal management of multicore processors using power multiplexing", 12th IEEE Intersociety Conference on Thermal and Thermomechanical Phenomena in Electronic Systems (ITherm2010), Las Vegas, USA, 2010.

[7] C. H. Lin, C. L. Yang, and K. J. King, "joint performance/power/thermal management of DRAM memory for multi-core systems", Proceedings of the 14th ACM/IEEE international symposium on Low power electronics and design, August, 2009.

[8] K. Kim, and V. D. Agrawal, "Minimum Energy CMOS Design with Dual Subthreshold Supply and Multiple Logic-Level Gates", 12th International Symposium on Quality Electronic Design, USA, March 2011.

[9] N. Mehta, G. Naik, and B. Amrutur, " In-situ power monitoring scheme and its application in dynamic voltage and threshold scaling for digital CMOS integrated circuits", ACM/IEEE International Symposium (ISLPED'2010), USA, October 2010.

[10] R. K. Megalingam, N. Krishnan, V. A. Ashok, and M. Arunkumar: Highly power efficient, uncompromised performance cache design using dual-edged clock, 2nd IEEE International Conference on Computer Science and Information Technology, August, 2009.

[11] S. Zhen, B. Zhang, P. Luo, K. Yang, X, Zhu, and J. Li, A high efficiency synchronous buck converter with adaptive dead time control for dynamic voltage scaling applications, IEEE/IFIP 19th International Conference on VLSI and System-on-Chip (VLSI-SoC), Hong Kong, China, 2011.

[12] Intel Application Note, April 2004.
http://int.xscalefreak.com/XSDoc/PXA27X/28001201.pdf

Design, Manufacturing and characterization of integrated inductors with magnetic layers for DC-DC converter

Dagal Yaya[1], Désiré Allassem[1], Mahamoud Youssouf[2], Ali Siblini[1]*, Jean Pierre Chatelon[1] and Jean Jacques Rousseau[1]

[1]Université de Lyon, F-42023, Saint Etienne, France; Université de Saint Etienne, Jean Monnet, F-42023, Saint Etienne, France; LT2C, F-42023, Saint Etienne, France.
[2]IUSTA BP 6033 N'Djamena TCHAD
*corresponding author: siblini@univ-st-etienne.fr

Abstract

This paper presents the conception, fabrication and characterization of integrated inductors containing magnetic layers. We require different steps of micro-technologies: preparation of glass and ferrite substrates, RF sputtering, photolithography, etching and finally electroplating techniques for copper and gold films. The geometrical magnitudes are determined by using HFSS simulator software. The measurements performed at low and high frequencies (up to 1 GHz) permit to verify the correlation between experiment and simulation results. The inductance of the manufactured spiral inductor is about 200 nH and it is constant from low frequency up to 0.9 GHz.

1. Introduction

Considerable research has been recently devoted to the miniaturization of electronic components for the fabrication of high consumption portable devices (cellular phones, computers, cameras, avionics, motoring…) [1-3]. For example, in a typical amplifier MMIC (Monolithic Microwave Integrated Circuits), up to 80 % of the area is occupied by chip inductors [4-6]. Thus, to reach this purpose, we have to conceive outstanding miniaturized components capable to work at higher and higher frequencies. The integrated inductors have been widely used in RF circuits such as voltage controlled oscillators [7], low-noise amplifiers [8], power amplifiers and matching circuits, etc…

For this reason, our laboratory is committed to the development of high frequency passive components in order to reduce their size and to increase their performance by using appropriate magnetic materials. A massive Yttrium Iron Garnet: $Y_3Fe_5O_{12}$ (YIG) is used as magnetic material and copper as conductive layer. Our purpose is to manufacture integrated inductors based on thick magnetic layers for power converters applications. To conceive these inductors, a High Frequency Structure Simulation software (HFSS) has been used. The micro-manufacturing steps (Micro-machining, RF sputtering, photolithography …) will be described. And finally a comparison between the simulation and measurement results as a function of frequency and thickness of the magnetic core will be presented.

2. Design of the spiral inductor

We have used HFSS software for the conception and the simulation of the integrated spiral inductor. Figure 1 shows the design used for the simulation. The simulated structure consists of a glass substrate of thickness E_{sub}, a magnetic thick layer of thickness E_{YIG}, and a spiral copper film of thickness e forming a coil of N turns encountered by its ground shielding. The cross section of this simulated inductor is presented in the figure 2. Figure 3 shows the pattern of the square spiral coil with its ground shielding. After studying different spiral shape of the coil (square, circular and octagonal) and different number of turns, the design of figure 3 has given the better results.

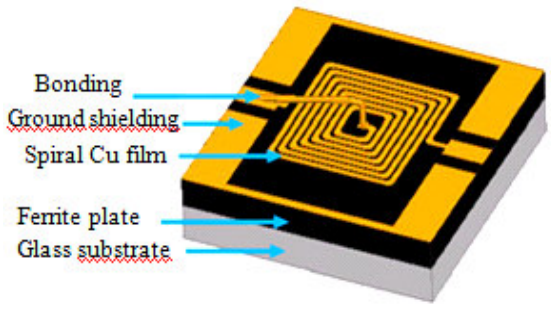


Figure 1: The spiral inductor structure with its magnetic core

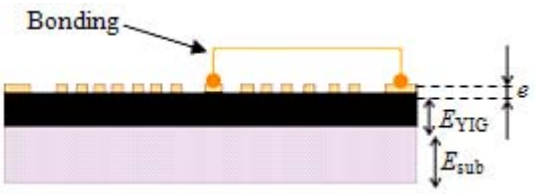


Figure 2: Cross section of the spiral inductor structure.

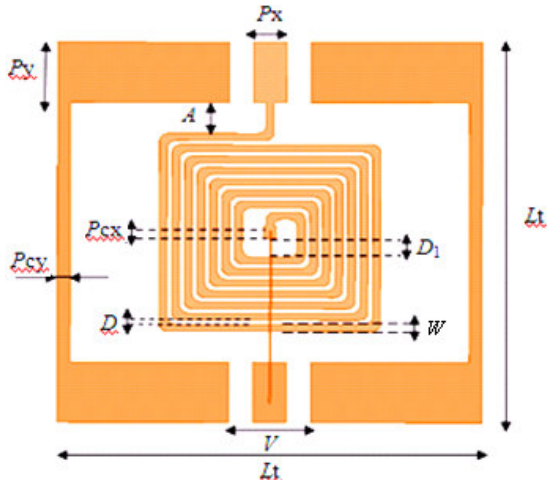


Figure 3: Pattern of the copper spiral coil with its ground shielding.

The geometrical magnitudes with their symbols are defined as follows:

- *W* is the width of the spiral coil ribbon,
- *D* is the distance between two successive turns,
- *D*1 is the distance between the central terminal and the first turn,
- *P*x is the width of the external terminal,
- *P*y is the length of the external terminal and the width of the ground shielding horizontal side,
- *P*cx is the side of the central end of the spiral coil,
- *P*cy is the width of the ground shielding vertical side,
- *V* is the distance between the two parts of the ground shielding,
- *Lt* is the side of the ground shielding,
- *A* is the distance between the external turn and the ground shielding horizontal side,
- *S* is the area occupied by the spiral coil (without the ground shielding).

The values of all these geometrical magnitudes and those of figure 2 are summarized in the table 1.

Table 1. Values of the geometrical parameters of the spiral inductor structure

Symbol	Size (µm)
W	125
D	60
*D*1	400
*P*x	500
*P*y	1000
*P*cx	200
*P*cy	200
V	1200
Lt	6270
A	500
S	3000x3000
N	7
e	10
E_{YIG}	0-1000
E_{sub}	1000

3. Technological steps of the spiral inductor fabrication

The spiral inductor has been manufactured with the following technological steps (figure 4):

a) Preparation of the glass-ferrite substrate: The YIG wafer of 1 mm thickness is sawed at the same size of the glass substrate; it is then stuck on it to have the desired thickness. This plate is grinded by micro-machining and it is then polished to obtain the required roughness measured by a profilometer.

b) Copper deposition: A film of copper (5 µm thick) is deposited by RF sputtering technique on the whole YIG surface.

c) Deposition of a photo-resistive resin on the copper film by spin coating.

d) Insolation of the photoresist by using a mask having the same pattern of figure 3.

e) Revelation of the exposed resin area.

f) Wet etching of the copper film.

g) Dissolution of the residual photoresist.

These micro-technological steps are followed by the deposition of a gold thin film (less than 1 µm) by electro-deposition on the obtained copper coil to protect it from the oxidation. Finally a bonding to connect the central end of the spiral layer to the second external terminal is performed. This bonding is made of a gold wire having a diameter equals to 18 µm or 25 µm. The photograph of the final manufactured inductor is showed in figure 5.

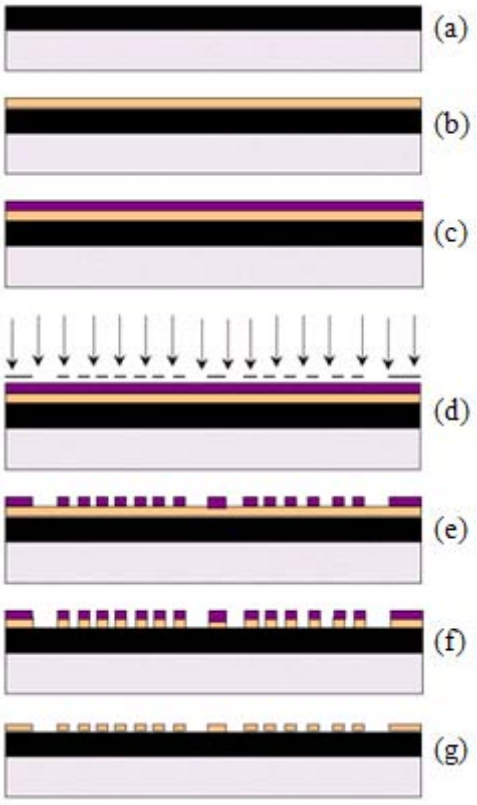


Figure 4: Manufacturing steps of the spiral inductor

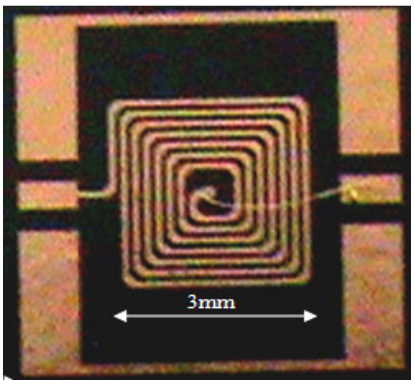


Figure 5: Photograph of the manufactured spiral inductor with its YIG core.

4. Experimental and simulation results

We present, firstly, the simulation results concerning the influence of the magnetic material on the inductance value of the spiral inductor prototype for different thicknesses. Secondly, a comparison between simulation and experimental frequency behaviors of the inductance *L* and the series resistance R of the inductor will be presented.

4.1. Influence of the magnetic material thickness

The purpose of this section is to study the influence of the magnetic core on the inductance value of the integrated inductor. For this reason, we have done several simulations by varying the thickness of the magnetic material (E_{YIG}) from 0 (inductor without magnetic material) to 400 µm. At 100 MHz, the simulated inductance, obtained without magnetic material (L_{air}) is about 100 nH. Figure 6 shows the evolution of the inductance with the thickness of the magnetic core. We can see easily the fast rise of the inductance in the thickness range from 0 to 100 µm. For E_{YIG} equals to 100 µm, the inductance *L* becomes practically1.7 times L_{air}. But from this thickness, *L* varies slowly to reach 1.85 times L_{air} for E_{YIG} equals to 400 µm and 1.95 (approximately twice L_{air}) for 1000 µm.

The variation of the inductance with the thickness of the YIG layer can be explained by the distribution of the field lines around the spiral coil. This distribution is usually more concentrated near the coil and it will be more concentrated in the presence of a magnetic material in the vicinity of this structure and the field lines that are far from the coil will be less concentrated. This is why the value of inductance is not proportional to the thickness of the YIG wafer; it is not also proportional to its magnetic permeability. But for higher permeability, the inductance value may be doubled for a smaller thickness. The proximity effects could be also the mechanism responsible for lowering the quality factor [9, 10]. To reach values more than twice Lair, we think introduce, in perspective, two magnetic wafers.

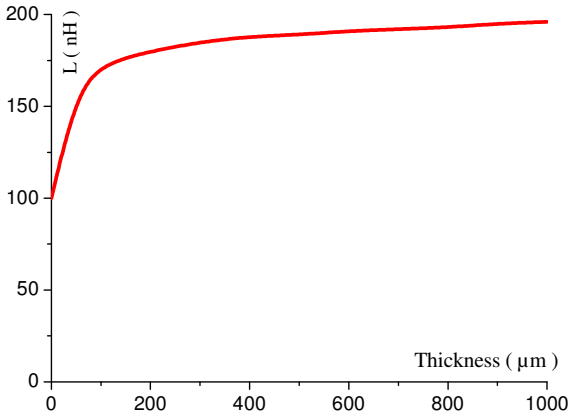


Figure 6: Variation of the inductance as a function of the magnetic material thickness.

4.2. Frequency characterization of the spiral inductor

The aim of this second section is to study the behavior of the inductor as a function of frequency. The measurements are performed using the vector network analyzer ZVA 67 for the frequency range from 10 MHz up to 1.2 GHz. We have used the simulator ANSYS HFSS v.13 in order to compare the experimental results with the simulation one. In both cases, the thickness of the YIG wafer is E_{YIG} = 500µm. For the simulation, we have chosen the following parameters for the YIG wafer: μ_r = 40 for the relative permeability and ε_r = 15 for the relative permittivity (manufacturer's values). In the measurement as in simulation, we have used the results as *S* parameters (S_{ij}). These parameters are then transformed into admittance parameters (Y_{ij}). The most suitable model is that of the figure 7. In this model, C_{fb} is the coupling capacitance between the windings. By using this LRC model and the admittance parameters, we can extract the different elements of this model as follows [11]:

$$Y = -Y_{12} = \frac{1}{R + jL\omega} + jC_{fb}\omega \,, \tag{1}$$

$$R = \frac{-\mathrm{Re}(Y_{12})}{\mathrm{Re}(Y_{12})^2 + (\mathrm{Im}(Y_{12}) + C_{fb}\omega)^2} \,, \tag{2}$$

$$L\omega = \frac{\mathrm{Im}(Y_{12}) + C_{fb}\omega}{\mathrm{Re}(Y_{12})^2 + (\mathrm{Im}(Y_{12}) + C_{fb}\omega)^2} \,, \tag{3}$$

$$Q = \frac{\mathrm{Im}(Y_{12}) + C_{fb}\omega}{\mathrm{Re}(Y_{12})} \,, \tag{4}$$

$$C_{fb} = \frac{1}{(2f_0.\pi)^2 L_0} \,, \tag{5}$$

L_0 is the inductance value at low frequency (initial inductance) and **f_0 is** the resonance frequency, obtained by plotting the imaginary part of Y_{12}. It corresponds to the frequency at which the curve of $\mathrm{Im}(Y_{12})$ passes through zero.

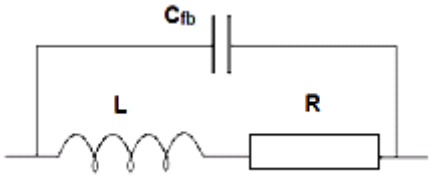


Figure 7: Series model of the integrated inductor with the coupling capacitance between windings.

4.2.1. *Frequency behavior of the inductance*

Figure 8 illustrates the simulated and the measured inductance as a function of frequency for E_{YIG} = 500µm. The curve corresponding to the experimental values shows that the inductance decreases with the increase of the frequency. This decrease is expected because in reality, the permeability of magnetic material decreases when the frequency increases. But the simulated inductance remains practically constant versus frequency up to 0.9 GHz. Because during the simulation, the value of the relative permeability is fixed to μ_r = 40 for all frequencies from 10 MHz up to 1.2 GHz. The gap between the two curves may be due to the calibration of the network analyzer, or to the fixed value of the magnetic permeability (μ_r = 40) during the simulation which is may be less than the real value. One can observe also, for the 2 curves, the sharp drop of the inductance at about 1 GHz. This frequency corresponds to the resonance of the structure.

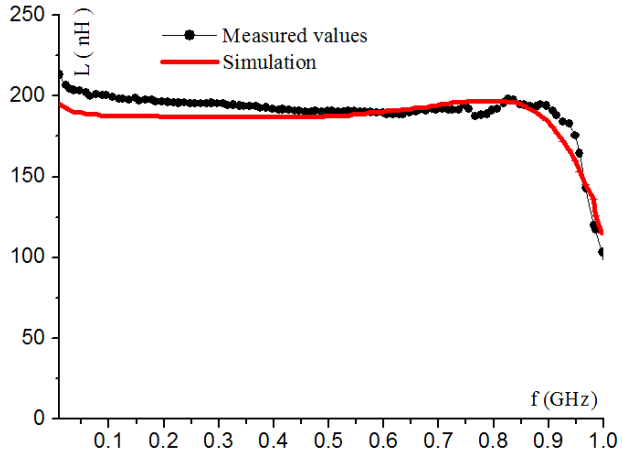


Figure 8: Evolution of the inductance versus frequency

4.2.2. *Frequency behavior of the resistance*

To study the evolution of the series resistance *R* as a function of frequency, we have used HFSS software for the simulation, the LCR-meter HP 4284A working from 20 Hz to 1 MHz for low frequency measurements and the vector network analyzer ZVA 67 (10 MHz - 67 GHz) for high frequency.

The low frequency characterization was performed at 3 frequencies (100 kHz, 500 kHz and 1 MHz). Table 2 shows the experimental results obtained for the series resistance of the manufactured prototype with a magnetic wafer of thickness E_{YIG} = 500µm. The simulation results correspond to the inductor of same dimensions.

Table 2: Resistance the spiral inductor as a function of frequency

Frequency	Simulation	Measure
100 kHz	1.67 Ω	1.97 Ω
500 kHz	1.67 Ω	2.3 Ω
1 MHz	1.67 Ω	2.4 Ω

At low frequency the simulated resistance of the spiral inductor is constant as showed in table 2. This resistance is independent of the frequency and of the magnetic core. It equals to the resistance of the copper spiral coil of figures 3 or 5. The calculated DC value of this resistance is R_{DC} = 1.66 Ω, practically the same by comparing it with the simulated one (1.67 Ω). However, the measured resistance is higher than the simulated one. This could be explained by the fact that the thickness *e* and the width *W* of the copper ribbon are given constant for the simulation, but in reality these 2 magnitudes are not uniform because of the irregularity of the wet etching time. We can also say that the large experimental values of the resistance may be due to the oxidation of the copper ribbon surface.

The same manufactured inductor has been characterized at high frequency. In this range the coupling capacitance C_{fb} does not have any influence and the series resistance can be defined by the following equation:

$$R = \frac{-\mathrm{Re}(Y_{12})}{\mathrm{Re}(Y_{12})^2 + \mathrm{Im}(Y_{12})^2}, \qquad (6)$$

The curves in Figure 9 illustrate the evolution of the simulated and measured series resistance of the integrated inductor as a function of frequency.

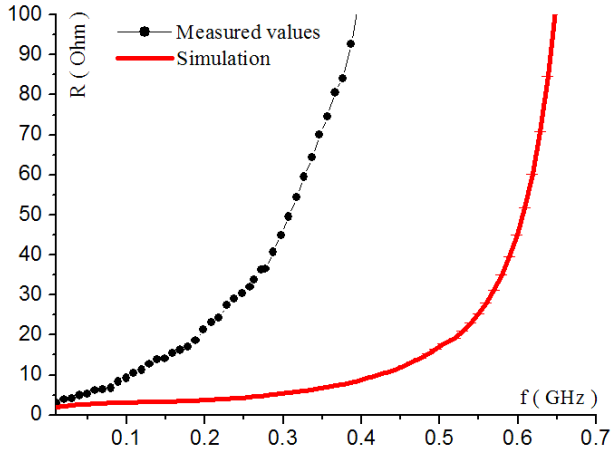


Figure 9: Resistance of the spiral inductor versus frequency

At 10 MHz, the resistance (3 Ω) measured by the vector network analyzer is very close to that measured by the LCR-meter at 1 MHz. At these frequencies the skin and proximity effects are negligible. However, from 100 MHz, we notice that the measured resistance begins to increase

rapidly due to the skin and the proximity effects [12-13]. These effects become important at high frequency. For example at 400 MHz, the resistance is multiplied by a factor of 21 by comparison with the measured value at 10 MHz.
However, there is a slow increasing of the simulated resistance up to 400 MHz (*R* equals to 1.9 Ω at 10MHz and 8.6Ω at 400MHz that corresponds to a ratio less than 5). But from 500 MHz, we observe a fast increase of the simulated resistance. The presence of the magnetic material, which helps to concentrate the field lines, permits to increase the magnetic field and consequently the inductance of the spiral inductor. However, the presence of thick magnetic core increase both magnetic filed and the proximity effects. When the thickness of the magnetic layer increases; the effects of induced currents in the copper spiral coil is greater. These effects cause the increase of the series resistance and consequently the decrease of quality factor.

5. Conclusions

To design of the integrated inductor with magnetic core we have used HFSS simulator. By changing the shape, the geometrical parameters and the number of turns, we have chosen the best configuration (square spiral inductor). To manufacture this inductor we have used different technique (micro-machining, RF sputtering, photolithography, electroplating, bonding …). And to perform morphological and electromagnetic characterizations, we have used preferment equipment and software. We have found that the inductance increases by adding a magnetic layer to the spiral inductor; it could be doubled by increasing the thickness of the ferrite plate but this increase is limited by the proximity effects and the eddy currents at high frequency. The experimental results concerning the frequency dependence of the inductance and the series resistance of the manufactured integrated inductor are confirmed by HFSS simulations. In perspective, we will try to fabricate inductors with two magnetic layers to increase the performance of these components. The main purpose is to fabricate miniature integrated inductors for DC-DC converters.

References

[1] Gyoung-Bum Kim, Seung-Yong Cha, Eun-Kyung Hyun,Young-Chai Jung, Yoon-Suk Choi, Jae-Sung Rieh, Seong-Rae Lee, and Sung-Woo Hwang, Integrated planar spiral inductors with CoFe and NiFe ferromagnetic layer, *Microwave and optical technology letters*, vol.50, No.3, 2008.

[2] C. Yang, F. Liu, T. Ren, L. Liu, H. Feng , A. Z. Wang , H. Long , Fully integrated ferrite-based inductors for RF ICs, *Sensors and Actuators A* 130–131, 365–370, 2006.

[3] Ren Tianling, Yang Chen, Liu Litian , Wang A Z, and Zhang Xiao, Equivalent circuit analysis of an RF Integrated Inductor with Ferrite Thin- Film, *Chinese Journal of Semiconductors*, vol.27, No.3, 2006.

[4] R. Melati, et *al*., Design of a new electrical model of a ferromagnetic planar inductor for its integration in a micro-converter, *Mathematical and Computer* 2011, doi:10.1016/jmcm.2011.06.014.

[5] J. Y. C. chang et *al.*, *IEEE Electron Device Lett.*14, 246, 1993.

[6] J. N. Burghartz et *al*., *IEEE Electron Device Lett.*17, 428, 1996.

[7] J. Craninckx, M. S. Steyaert, A, 1.8 GHz low-phase-noise CMOS VCO using optimized hollow spiral inductor, *IEEE J. Solid State Circ.*32, 5, 736-744, 1997.

[8] D.K.Schaeffer, T .H. Lee, A 1.5V 1.5GHz CMOS low noise amplifier, *IEEE J. Solid State Circ.* 32, 5, 745-759, 1997.

[9] Viala B., Royet A-S, and Couderc S. Investigation of Anomalous Losses in Thick Cu Ferromagnetic Spiral Inductors. *IEEE Transactions on Magnetics,* Vol. 41, No. 4, 3583-3585, 2005.

[10] Royet A-S., Viala B., Couderc S., and Orlando B. Investigation of proximity effects in ferromagnetic inductors with different topologies: modeling and solutions. *Transactions of Magnetics Society of Japan,* Vol.5, No.4, 144-145, 2005.

[11] Yu Cao et *al*. Frequency –Independent Equivalent-circuit Model for on –chip spiral inductors, IEEE Journal of solid state circuits, Vol. 38, No.3, 2003.

[12] Ivan C. H. Lai and Minoru Fujishima*, A New On-Chip Substrate-Coupled Inductor Model Implemented With Scalable Expressions*'' IEEE Journal of solid state circuits, Vol. 41, No. 11, 2491-2499, 2006.

[13] Nam-Jin Oh and Sang-Gug Lee, A simple model parameter extraction methodology for on-chip spiral inductor, *ETRI Journal,* vol. 28, No. 1, 115-118, 2006.

Study and fabrication of a planar integrated magnetic transformer

F. Kahlouche*, Khamis Youssouf, Mahamoud Youssouf, A. Siblini, S. Capraro, J. P. Chatelon and J. J. Rousseau

Université de Lyon, F-42023, Saint Etienne, France; Université de Saint Etienne, Jean Monnet, F-42023, Saint Etienne, France; LT2C, F-42023, Saint Etienne, France.
*corresponding author: faouzi.kahlouche@univ-st-etienne.fr

Abstract

This paper presents the design and the fabrication of a planar integrated transformer with magnetic core. Yttrium Iron Garnet (YIG) was chosen for its high frequency behavior that permits the applications of this material in the microwaves and the magneto-optical domains. The choice of the transformer structure and the fabrication of the primary and secondary circuits are presented. HFSS software is used for the conception and the simulation of primary and secondary circuits that are both identical spiral inductors. To perform the pattern of these inductors we have used the photolithography technique. We have also introduced the use of negative photoresist SU-8 for the fabrication of an air bridge to connect the central end of the spiral coil to the external terminal.

1. Introduction

The use of magnetic cores to increase the performances of spiral inductors is being an active area of research in the development of the integrated circuits. In addition, these studies focus to increase the inductance L and the quality factor Q and also to reduce the size and the cost of manufacturing [1]. Our work is based on previous studies of inductors with magnetic core, to design and manufacture planar integrated transformers with new designs and techniques of fabrication. The face-to-face integrated transformer has been designed by using High Frequency Structure Simulation (HFSS) taking into account the coupling capacitances and magnetizing inductance. The frequency behavior of this structure was studied at low and high frequencies using a LCR-meter and a Vector network analyzer. To manufacture the designed integrated transformer, various techniques have been performed: micro-machining, RF magnetron sputtering, gold electro-deposition, photolithography in a clean room and finally, we have implemented an air bridge to connect the central end of the spiral inductors to the external terminal instead of the classical bonding.

2. Structure of the magnetic transformer

Many papers are devoted to integrated transformers with and without magnetic core for applications in the field of high frequencies [2] [3] [4]. Applications concern both signal transformers or low power transformers for power electronics applications such as DC-DC converters [5] [6].
Most part of studies are related to transformers on silicon wafers without any magnetic core, operating frequencies range from some MHz until some GHz. Transformers with magnetic core provide many advantages depite the increase of the manufacturing complexity. Both coupling factor and primary inductance can be increased by using a magnetic core. Moreover specific structures behave like an electromagnetic shielding and contribute to strongly decrease the electromagnetic radiations.

Several works concern the structure of coils, various approaches are commonly used to perform windings: interleaved windings, stacked winding arrangement, center tapped interleaved transformers …. [7] [8].

Figure 1.a illustrates an interleaved transformer, this structure presents moderate coupling factor (k~ 0.7) with a reduced self-inductance.
Figure 1.b shows the stacked transformer. In contrast to the interleaved transformer, the use of multi-layer metal and the presence of both vertical and lateral magnetic coupling, provide a high self-inductance and a coupling factor k~0.9).

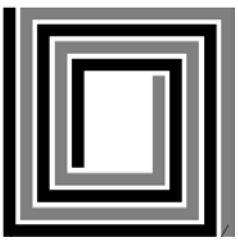


Figure 1.a

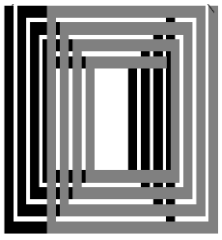


Figure 1.b

Figure 1: Interleaved and stacked transformer

This paper presents a face-to-face integrated transformer structure composed of two identical planar inductors with magnetic material (YIG) separated by an insulating layer (Figure 2). The right hand design of Figure 2 is obtained using the HFSS simulator software. This structure would promote inductance value, coupling factor and reduce chip area occupied by the transformer.

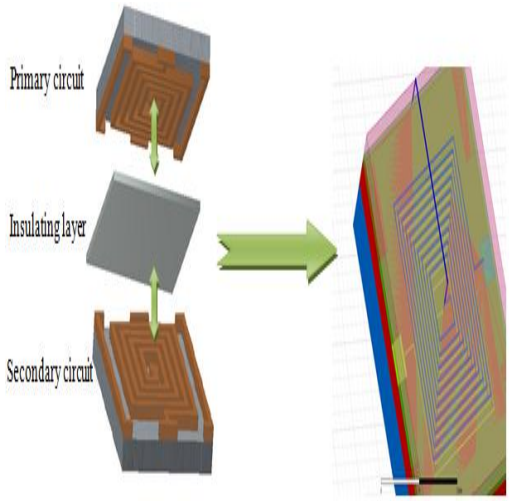


Figure 2: Face-to-face transformer structure.

2.1. Modeling and HFSS Simulation of the transformer

HFSS simulator is a 3-D electromagnetic solver marketed by Ansoft [9], it simulates the electromagnetic behavior of the structure basing on the modeling finite-element method. The face-to-face transformer model used in our simulation is presented in figure 3.

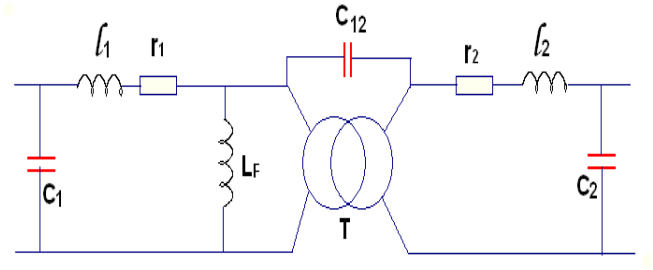


Figure 3: High frequency transformer model.

The different parameters or this face-to-face transformer model are:

- ℒ1, ℒ2 and L_F represent the leakage inductances of primary, secondary windings and the magnetizing inductance respectively.
- r1 and r2 are the series resistances of the primary and secondary windings respectively.
- C1 and C2 represent the coupling capacitances of the primary and secondary coils. C12 is the coupling capacitance between the primary and secondary windings.

Figure 4 shows the frequency behavior of the simulated magnetizing inductance. In this figure, we observe that the magnetizing inductance is almost constant up to several hundreds MHz (180 MHz). Beyond this frequency, there is a decrease in the inductance when the frequency increases. One can see that the inductance is practically constant versus frequency up to 200 MHz, this explains the good behavior of the integrated face-to-face transformer structure.

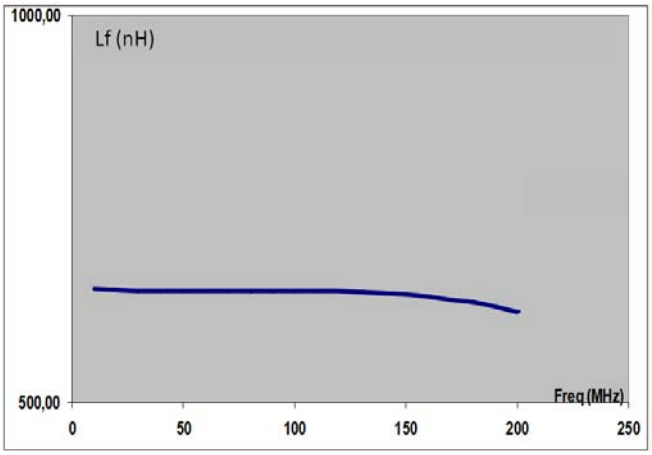


Figure 4: Frequency behavior of the magnetizing inductance.

2.2. Primary or secondary circuit fabrication

Figure 5 shows the different steps of fabrication of the spiral inductor with air bridge connection, the magnetic core used in our fabrication is a commercial YIG (Yttrium Iron Garnet). For adherence reasons, the surface of YIG is prepared, for the copper film deposition, by polishing. The dimensions of the YIG wafer are (25mm×50mm×0,5mm).

a) The copper film of 5 µm thickness deposited by RF magnetron sputtering on the YIG substrate, this deposition technique have the advantage that the deposited film has the same composition of the target bulk material, also it has the advantage of Molecular Beam Epitaxy (MBE) because of its speed. Only pure copper film is deposited.
b) A 100 nm SPR 505A photoresist (PR) layer is then spun on the deposited Cu film.
(c) The PR layer is photo-patterned with UV insolation;
(d) The chemical etching is performed with ferric chloride to obtain the square spiral inductor of 7 turns, 3270 µm side, 125 µm line width, and 60 µm line spacing (figure 6).
(e) A very thin layer of gold is deposited by electroplating on the conducting spiral coil.
(f) For the air bridge fabrication, a thick layer of negative photoresist SU-8 is spun.
(g) To uncover the two contacts that will be connected by the air bridge, the SU-8 is photo-patterned and backed to be solidified [10].
(h) A second copper film is sputtered on the obtained pattern.
(i) Deposition of PR and finally.
(j) UV insolation to obtain the air bridge.

The gold layer was electroplated to prevent Cu from the oxidation during the backing of the SU-8 layer.

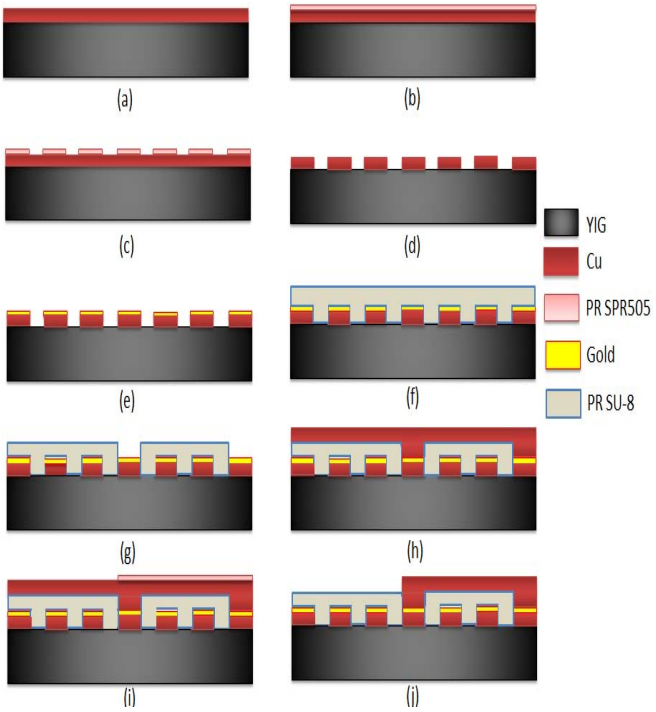


Figure 5: The different steps for primary or secondary Integrated inductor fabrication.

Figure 6 below shows the photography of the manufactured primary or secondary inductor with the YIG wafer; deposited on alumina substrate (Al_2O_3). Copper bridges of 125µm and 500µm were performed.

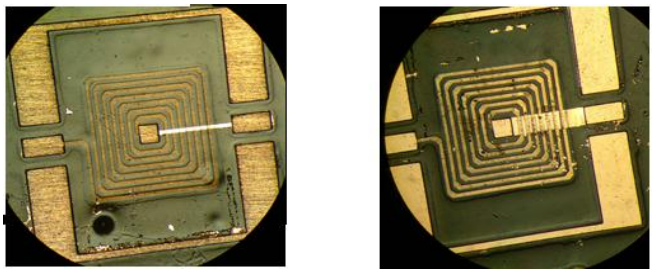


Figure 6: Photography of the manufactured primary and secondary inductors.

3. Conclusions

A primary circuit for planar integrated magnetic transformer has been designed by using HFSS simulator and then manufactured. To fabricate this spiral inductor we have applied a strict protocol (in a clean room) to obtain good adhesion of copper and gold films and to have the desired pattern of the spiral coil with its ground shielding. Instead of the classical bonding to connect the central end of the spiral coil to the external terminal, we have performed an air bridge by using the photolithography technique. the electromagnetic characterizations was performed using a precision LCR-meter HP 4284A for low frequency up to 1 MHz and a vector network analyzer ZVA 69 for high frequency up to 1 GHz. The simulated magnetizing inductance is practically constant as a function of frequency up to 200 MHz; this explains the good behavior of the integrated face-to-face transformer structure. In perspective we will try to fabricate the secondary circuit of the magnetic transformer and to assemble the two parts of the transformer. At the first time the characterization will be performed at room temperature after that a characterization at high temperature (200°C) will be performed.

References

[1] C. Y. Yue and S. S.Wong, "*On-chip spiral inductors with patterned ground shields for Si-based RF IC's,"* IEEE J. Solid-State Circuits, vol. 33, no. 5, pp. 743–753, 1998.

[2] Josep Cabanillas Costa ''*Analysis of integrated transformers and its applications to RFIC design"*. Thèse de doctorat de l'université de Barcelona. Octobre 2002.

[3] Jae Y.Park and Mark G.Allen ''*High Current Integrated Micro inductors and Micro transformers using Low Temperature Fabrication Processes*'' School of electrical and Computer Engineering Georgia Institute of Technology Atlanta, GA 30332-0269.

[4] Jinglin Shi, Wen Yan Yin, Kai Kang and Jun Fa Mao Le Wei ''*Frequency-Thermal Characterization of On-Chip Transformers with Patterned Ground Shields*'' IEEE Transactions on Microwave Theory and Techniques, Vol 55, No 1, Janvier 2007

[5] J. R. Long, "*Monolithic transformers for silicon RF IC design*" IEEE J. Solid-State Circuits, vol. 35, pp. 1382, Sept. 2000.

[6] M.Mino, T.Yachi, A.Tago, K.Yanagisawa and K.Skakibara ''Micro transformer with Monolithically Integrated Rectifier Diodes for Switching Converters'' PESC, pp 503-508, June 1993.

[7] S.S Mohan '' *The Design, Modeling and Optimization of on Chip Inductor and Transformer Circuits*'' These de doctorat de l'Université de Stanford, December 1999.

[8] Shu Jung Pan,Wen Wan Win and Le Wei Li *''Comparative Investigation on Various On Chip Center Tapped Interleaved Transformers*'' Int J RF and Microwave CAE 14;424-432,2004.

[9] A. Corporation *Ansoft HFSS*, 2011.

[10] Ru Feng and Richard J Farris, *"Influence of processing conditions on the thermal and mechanical properties of SU8 negative photoresist coatings",* J. Micromech. Microeng, vol. 13, no 1, pp. 80-88, 2003.

New Advances in Monitoring the Aging of Electric Cables in Nuclear Power Plants

Maud Franchet[1], Nicolas Ravot[1], Nicolas Grégis[1], Josy Cohen[1] and Odile Picon[2]

[1]CEA, LIST, Embedded Systems Reliability Laboratory
Saclay Nano-Innov, Institut CARNOT CEA LIST
Point courier 172, 91191 Gif-sur-Yvette CEDEX
*corresponding author, E-mail: maud.franchet@cea.fr
[2]Université Paris-Est, ESYCOM

Abstract

Monitoring the aging of electric cables used in nuclear power plants is a crucial issue for nuclear industrials, whose objective is to extend the lifetime of their plant while ensuring its security. For cost and efficiency reasons, reflectometry, which is a non-destructive method, is well-adapted to this problem. Unfortunately, it may be not sensitive enough to small changes of the cable. To overcome this difficulty this article proposes to use time-frequency tools (the Wigner Ville transform and a normalized time-frequency cross-correlation function) in addition to time domain reflectometry. This method has been applied on two RG-59B coaxial cables (one new and the other one aged) cables commonly used in nuclear power plants.

1. Introduction

The safety and the extension of lifetime of nuclear power plants (NPPs) are two major issue nuclear industrials are faced with. This puts the focus on monitoring their condition. As kilometers of cables run across NPPs, they are among the crucial elements to watch over. The challenge here is to predict when a cable has to be changed before it is too much worn out and damaged, in order to limit risks. This is one purpose of the Advance project, a FP7 European program. Indeed important defects, such as open or short circuits (hard faults), can put the safety of the plant at stake (one may imagine the tragic consequences that a fire caused by a short-circuit may have). Thus this is crucial to prevent them from occurring.

Among all the existing methods for monitoring cables, many are destructive (e.g.: Elongation at Brake, cf.[1]) or not able to predict their remaining lifetime (e.g.: Partial Discharge). Because it is not efficient enough, far too long and problematic in an environment where the time to exposure has to be reduced to its bare minimum, visual inspection is difficult too. For all these reasons, reflectometry, which is a non-destructive method, appears to be well suited to study cable aging in NPPs. It is based on the injection of a signal e(t) into the wire network and the analysis of the reflected signal r(t) measured at the injection point. Several reflectometry methods exist depending on the studied domain and the type of signal used. In time domain reflectometry (TDR) [2], [3], [4], a step or a pulse is injected, whereas in frequency domain reflectometry (FDR) [5] a set of stepped-frequency sine waves is used. In the following, the chosen method is TDR.

Studying cable aging involves to be able to detect minor modifications. This is the same challenge as detecting soft faults (incipient defects), which translate into reflected signals of very low amplitudes. Indeed only slight changes due to aging will affect the reflectograms obtained by TDR. To detect them, TDR can't be used alone, as it is highlighted in [6]. Another tool is needed. In this article, we propose to apply a time-frequency transform, called the Wigner Ville transform (WVt), on TDR results and compute a normalized time-frequency cross-correlation function (TFC). This is part of a method called Joint Time-Frequency Domain Reflectometry (JTFDR) proposed by [7]. This has shown promising results for soft faults (cf. [8]). However the WVt is a quadratic transform. Then unwanted cross-terms can affect the results. To overcome this problem the Pseudo Wigner Ville transform (PWVt) can be used instead of the WVt (cf.[9]). JTFDR has already been used by [10] to study local aging of cables used in NPPs. This is comparable to detecting soft faults. Nevertheless the aging process may affect the entire length of the cable. So the efficiency of such a method has to be tested for global aging too and a tool to decide if a cable has to be replaced or not has to be defined.

This is the purpose of this study, where two RG-59B coaxial cables, usually used in NPPs are compared. One is in mint condition whereas the other was thermally aged. TDR measurements have been made on both. Two kinds of injected signals have been used, in order to study the impact of the width of the injected signals. Then the TFC is applied on these results. The reflectometry measurements are exposed in part II. In part III, the signal processing step is explained and applied to the considered example. A method to determine if a cable is aged or not is finally proposed.

2. TDR MEASUREMENTS

2.1. The device under test (DUT)

For this study, two RG-59B coaxial cables, commonly used in NPPs, are considered. Their characteristic impedance is $Z_c = 75\Omega$. One is in mint condition and will be called the unused cable whereas the other has been uniformly heated over its length, during 500 hours at 162°C. The heating was made in a heat chamber. This simulates a fast and brutal aging, which uniformly affects the cable over its length. The aged cable will be called the used cable.

2.2. Experimental setup

TDR measurements were made on both cables. The experimental setup is pictured in Fig.1. A vector network analyzer (VNA Agilent E5071c 9kHz-4.5GHz) was used to inject a Gaussian pulse into the device under test and measure the result. This wave propagates all along the line and is reflected at the end of the line, which is left open-ended at its far-end, and travels back to the injection point. This reflected wave is then measured in the frequency domain and transposed in the time domain thanks to an IFFT (Inverse Fast Fourier Transform), in order to obtain a reflectogram. Two Gaussian pulses of different width at half-height ($1ns$ and $5ns$) are tested. In the following, e_1 refers to the pulse of $1ns$ width and e_5 to the one of $5ns$ width.

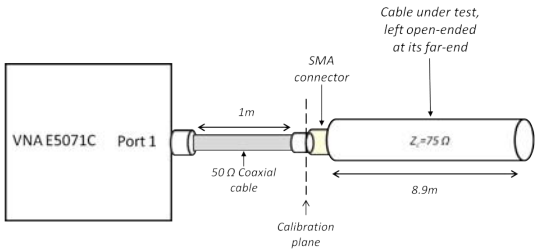


Figure 1: Experimental Setup (VNA : Vector Network Analyzer)

2.3. TDR results

Fig. 2 displays the reflectograms obtained with e_1 and Fig. 3 the ones obtained with e_5.

On each reflectogram two reflected pulses are visible. The first one at $t_1 = 9ns$ is due to a mismatch between the injection setup and the cable under test. The second one at around $t_2 = 100ns$ corresponds to the pulse reflected at the end of the line, which was left open-ended. For both injections, the differences between the reflectogram of the healthy and the aged cables are quite small. The most evidential one is a slight time-shift ($\Delta t = 1.13ns$ if e_1 is used and $\Delta t = 1.12ns$ if e_2 is used) of the pulse reflected at the end of the line. Thus the aging of the cable leads to an increase in its propagating velocity, which lets us think

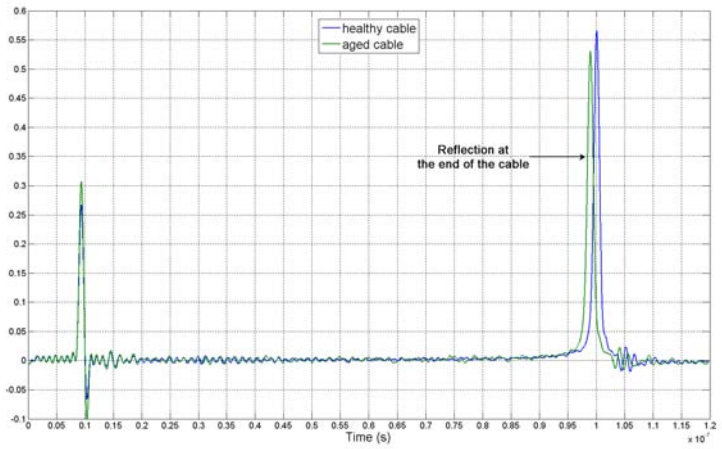


Figure 2: Reflectograms obtained after injecting a Gaussian pulse of 1ns width at half-height

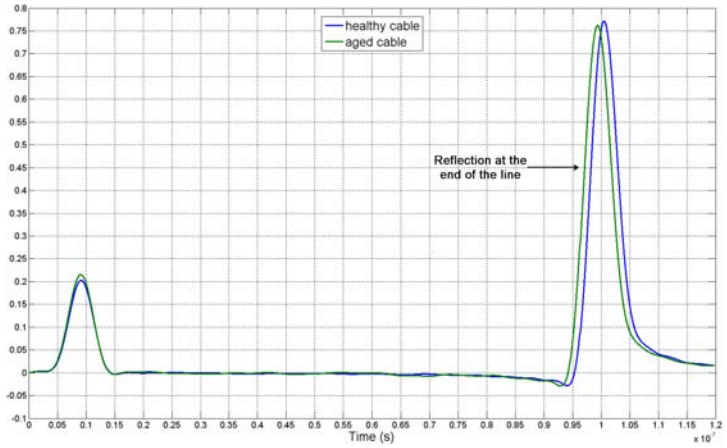


Figure 3: Reflectograms obtained after injecting a Gaussian pulse of 5ns width at half-height

that the dielectric coating has been impacted by the process. Besides, a greater number of tiny differences between the cables are revealed when a thiner probe signal is used. These variations can be due to the small imperfections of the cable or the measurement noise.
However to make the differences between the healthy and the aged cables more probant another tool is needed. For doing so, a Time-Frequency Cross-correlation (TFC) is applied on TDR results.

3. Signal Processing Step

The goal of this signal processing step is to make the small differences between the two cables more relevant.
It is based on the use of the Wigner Ville transform (WVt) and a normalized Time-Frequency Cross-correlation function (TFC). This tool was first introduced by [7] and used, as part of the JTFDR process, to amplify the reflected pulses on soft faults (cf.[8]). Indeed it has been designed to enhance signals of very low amplitudes. It has also been used to study a local aging of cables present in NPPs (the cable was locally heated at different temperatures, cf.[10]) but never to study a global aging of cables.

3.1. Theoretical background

The WVt of a signal $x(t)$ is defined in (1), where ω is the pulsation ($rad.s^{-1}$). This time-frequency transform belongs to the Cohen class. Equation (2) gives the WVt of a delayed Gaussian pulse $r(t) = (\frac{\alpha}{pi})^{\frac{1}{4}} \cdot A \cdot \mathrm{e}^{-\alpha(t-t_d)^2/2}$(where t_d is the time delay, α the scale factor and A the amplitude of the signal).

$$W_x(t,\omega) = \frac{1}{2\pi}\int_{-\infty}^{+\infty} x^*(t-\frac{\tau}{2}) \cdot x(t+\frac{\tau}{2})\mathrm{e}^{-j\omega\tau}d\tau \quad (1)$$

$$W_r(t,\omega) = \frac{1}{\pi}A^2 \cdot \mathrm{e}^{-\alpha(t-t_d)^2-\omega^2/2} \quad (2)$$

The WVt can perfectly locate linear frequency chirps but suffers from a severe drawback when applied to multi-component signals, such as the ones measured in TDR. Due to its quadratic nature, unwanted crossterms emerge between the real components. These terms pollute the result. To mitigate this problem, [9] proposes to use the Pseudo Wigner Ville transform (PWVt) instead of the WVt. The PWVt, defined in (3) is a windowed version of the WVt, where $w(t)$ is the chosen window.

$$PW_x(t,\omega) = \frac{1}{2\pi}\int_{-\infty}^{+\infty} w(\frac{\tau}{2}) \cdot w^*(-\frac{\tau}{2}) \cdot x^*(t-\frac{\tau}{2}) \cdot x(t+\frac{\tau}{2})\mathrm{e}^{-j\tau\omega}d\tau \quad (3)$$

Let's denote $s(t)$ the injected signal and $r(t)$ the reflected one measured at the last step. In order to make the components of weak magnitudes more relevant, a normalized time-frequency cross-correlation (TFC) $C_{sr}(t)$ between $PW_s(t,\omega)$ and $PW_r(t,\omega)$ is computed (cf.eq. (4)), where T_s is the time duration of the reference signal $s(t)$. As the injected signal is a Gaussian pulse, a Gaussian window of same width has been chosen for $w(t)$. The peaks of the TFC are used to detect points of discontinuities in the cables. $E_r(t)$ and E_s are normalization terms. Thanks to the dependency of $E_r(t)$ to time t, the weakest components of $r(t)$ appear with the same range of magnitude as the larger ones.

$$C_{sr}(t) = \frac{2\pi}{E_r(t)\cdot E_s}\cdot\int_{t'=t-T_s}^{t'=t+T_s}\int_{-\infty}^{+\infty} PW_r(t',\omega) \int_{-\infty}^{+\infty} PW_r(t',\omega)\cdot PW_s(t'-t,\omega)d\omega dt' \quad (4)$$

$$E_r(t) = \int_{t'=t-T_s}^{t'=t+T_s}\int_{-\infty}^{+\infty} PW_r(t',\omega)d\omega dt' \quad (5)$$

$$E_s = \int_{-\infty}^{+\infty}\int_{-\infty}^{+\infty} PW_s(t',\omega)d\omega dt' \quad (6)$$

3.2. TFC results

Fig. 4 and Fig. 5 show the results obtained when a Gaussian pulse of $5ns$ and $1ns$ width are injected in the cables under test (cf.Fig. 3 and Fig. 2) and the PWVt is used to compute the TFC.

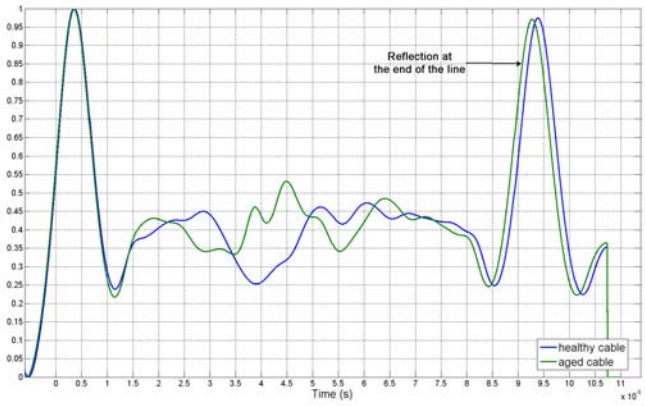


Figure 4: TFC obtained with the PWVt, when the injected signal is a Gaussian pulse of $5ns$ width at half-height

On both results we can remark a notable difference between the healthy and the aged cables. Indeed like on TDR results, we can observe a small time-shift of the peaks of the aged cable. Besides, the amplitudes of these peaks differ between the aged and the healthy cable, especially when a pulse of 1ns width at half-heigt is injected. Thus a greater number of variations can be seen when a thiner injected pulse is used. Finally as no local defect seems to really emerge, we deduce that the aging process has affected the cable on its entire length.
The last step is now to determine an automatic criteria

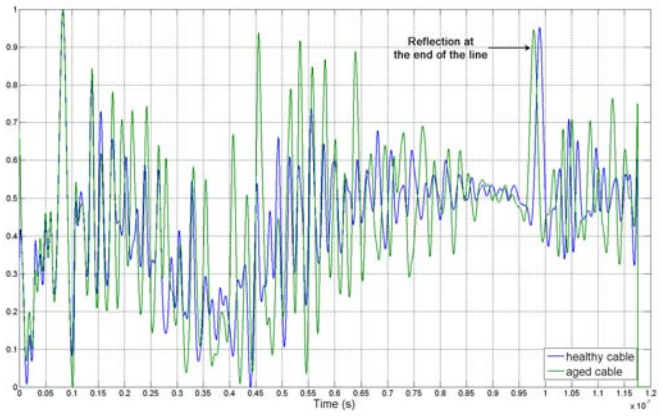


Figure 5: TFC obtained with the PWVt, when the injected signal is a Gaussian pulse of $1ns$ width at half-height

telling if a cable is aged or not. This is the purpose of the next paragraph.

3.3. The correlation coefficients: a tool to distinguish a healthy cable from an aged one

Thanks to the TFC the small changes due to the aging process have been amplified. However a criteria has now to be chosen in order to determine if a cable is aged or not. In statistics, the correlation coefficients between two results are commonly used to assess if they are alike. This the tool chosen in this study to decide if a cable is aged or not. As a consequence, a reference to which TFC results can be compared is required. For this study, the results obtained with the cable considered as healthy are taken as references. Table 1 gives the results obtained, for both kinds of injection, when the TFC is computed with the WVt and the PWVt.

Table 1: Correlation Coefficient.

Width of the injected pulse	Correlation coefficient obtained with the WVt	Correlation coefficient obtained with the PWVt
$1ns$	0.57	0.65
$5ns$	0.96	0.94

Generally, two results are considered as dissimilar when their correlation coefficient is lower than 0.98. Considering this threshold, we may conclude that, whatever the kind of time-frequency transform used (the PWVt or the WVt), our tested cable is aged. Then the coefficients obtained with an injected signal of 1ns width are significantly lower than the one obtained with a pulse of 5ns width. As a conclusion, using a thiner injected signal makes it easier to determine if a cable has been aged or not. Indeed a better temporal resolution can be achieved. However this also means an increase in the frequency bandwidth, which leads to more attenuation due to the frequency losses in the cable.

4. Conclusions

Monitoring the state of nuclear power plants is a crucial and topical issue. As transmission lines are critical components that have to be watched over, the impact of aging on cables has to be studied and a way to determine if a cable is aged or not has to be found. Indeed thanks to this tool a cable could be replaced before it becomes a threat to the safety of the plant.
To tackle this challenge, we propose to perform Time Domain Reflectometry (TDR) measurements on these cables. This has the advantage of being a non destructive method. As aging is a slow process, a time-frequency tool called TFC (Time-Frequency Cross-correlation) is then applied on these reflectograms in order to bring out the slight changes. To simulate aging, a cable was uniformly heated over its length. According to our results, this aging has a global impact on the line and one of the most affected factors is its propagating velocity. This means that dielectric coating of the cables has been damaged. Moreover, a greater number of variations due to aging can be observed when a thinner injected pulse is used for TDR measurements.
Besides, in order to determine if a cable is aged or not, we propose a 3-steps process:

1. Perform TDR measurements on the cables.
2. Compute the time-frequency cross-correlation (TFC) of these reflectograms.
3. Compute the correlation coefficients between these TFC results and a reference. If the coefficients are lower than a certain threshold, the cable is considered as aged.

This method performs well on the studied example. However this study has to be deepened in order to see if this is able to discriminate different level of aging. This is the object of current and future work made within the framework of Advance project, a FP7 European program.

Acknowledgement

The authors would like to thank Dr. Vit Placek from the Nuclear Research Institute Rez (Czech Republic) who lent us the tested cables. This work has been made within the framework of Advance project, a FP7 European program. For more details about this project, please visit the website `http://www.advance-fp7.eu`.

References

[1] J. Kim, "Evaluation of cable aging degradation based on plant operating condition," *Journal of Nuclear Science and Technology*, vol. 42, no. 8, pp. 745–753, 2005.

[2] T.-W. Pan, C.-W. Hsue, and J.-F. Huang, "Time-domain reflectometry using arbitrary incident waveforms," *Microwave Theory and Techniques, IEEE*

Transactions on, vol. 50, no. 11, pp. 2558 – 2563, nov 2002.

[3] N. Ravot, "Analyse et diagnostic de rseaux filaires complexes par rflectomtrie," Ph.D. dissertation, Universit Paris-Sud XI, 2007.

[4] F. Auzanneau, M. Olivas, and R. Ravot, "A simple and accurate model for wire diagnosis using reflectometry," in *PIERS Proceedings, August 2007*, 2007.

[5] H. Vanhamme, "High resolution frequency-domain reflectometry," *Instrumentation and Measurement, IEEE Transactions on*, vol. 39, no. 2, pp. 369 –375, apr 1990.

[6] L. A. Griffiths, R. Parakh, C. Furse, and B. Baker, "The invisible fray: a critical analysis of the use of reflectometry for fray location," *IEEE Sensors J.*, vol. 6, no. 3, pp. 697–706, 2006.

[7] Y. J. Shin, "Theory and application of time-frequency analysis to transient phenomena in electric power and other physical systems," Ph.D. dissertation, University of Texas, 2004.

[8] J. Wang, P. Crapse, J. Abrams, Y. J. Shin, and R. Dougal, "Diagnostics and prognostics of wiring integrity via joint time-frequency domain reflectometry," in *10th Joint FAA/DoD/NASA Conference on Aging Aircraft*, April 2007.

[9] M. Franchet, N. Ravot, and O. Picon, "The use of the pseudo wigner ville transform for detecting soft defects in electric cables," in *IEEE/ASME International Conference on Advanced Intelligent Mechatronics, Budapest, Hungary, 3-7 jul, 2011*, 2011.

[10] J. Wang, P. Crapse, Y. J. Shin, and R. Dougal, "Diagnostics and prognostics of electric cables in nuclear power plants via joint time-frequency domain reflectometry," in *Electrical Insulation, 2008. ISEI 2008. Conference Record of the 2008 IEEE International Symposium on*, 9-12 2008, pp. 24 –27.

A Simple Electromagnetic Analysis of Magnetic NDE Using a Double Rectangular Coil an a Hall Effect Sensor

Laroussi Bettaieb, Hamid Kokabi, and Michel PoloujadoffF

Université Pierre et Marie Curie (UPMC), Laboratoire d'Électronique et Électromagnétisme (L2E),
Aile 65/66 – 2ème étage - 4, Place Jussieu 75252 Paris Cedex 05.
laroussi.bettaieb@supelec.fr; hamid.kokabi@upmc.fr; michel.poloujadoff@upmc.fr

Abstract

In this paper a simple analysis and measurement in eddy current NDE are presented. A Hall probe is associated to a double Printed Circuit Board PCB. The configurations examined involve the coil in air and the coil above aluminum plates, either with or without cracks of various depths. The agreement between experimental and theoretical results is very good, showing that a very simple model accurately describes the electromagnetic fields.

Keywords: Hall Effect probe, eddy current testing, simplified analytical analysis of eddy currents, magnetic field measurement, rectangular double coil.

1. Introduction

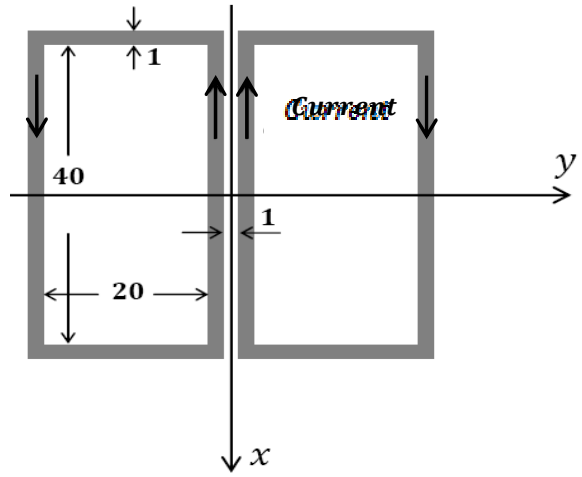
The early apparatus for Electromagnetic Non Destructive Evaluation (E-NDE or E-NDT) consisted of a circular probe coil whose impedance was measured all over the surface of the metal sheets to be examined. Variations of impedance indicated the presence of flaws [1 to 6]. This method is still very popular, but many efforts are under development to increase its sensitivity. One suggestion has been to replace the impedance value by the resulting magnetic field as the basic signal.

Since the SQUID is a very attractive sensor of magnetic field intensity, it has been attempted to introduce it in the vicinity of the probe coil [7 to 13]. But, since it is subject to saturation, investigators replaced the circular coil by a double D. In an excellent paper, Poulakis and Theodoulidis [14] have simplified the equipment by using a double rectangular printed circuit board coil and a SQUID. They have presented such a system, and given a series expansion analysis which is reported in [15].

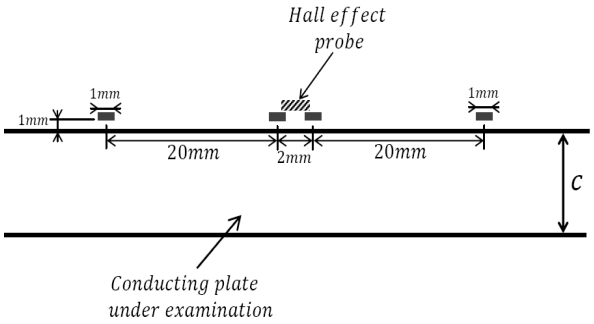
In what follows, we present an experimental set up including a double rectangular coil where the SQUID is replaced by a Hall probe which is less sensitive, but may be installed very close to the area to be examined. And we give a simplified analytical model which is simpler than the above quoted one, without loss of accuracy.

2. Analysis of the coil field

The set up is described in figure 1. In figure 1.a, a double rectangular coil printed circuit is shown. In figure 1.b, we show a conducting plate of thickness c, and the printed circuit above it; a Hall probe is attached as shown.



(A)



(B)

Figure 1: (A) Top view of the rectangular double printed coil; (B) Side view of this coil above an aluminum plate.

We first analyze the electromagnetic field created, in free space, by a current of $1.7A$ flowing in the double D coil.

This may be done by integrating the Biot and Savart formula (figure 2.a)

$$d\vec{B} = \frac{\mu_0 I}{2\pi} \frac{\vec{dl} \wedge \vec{PM}}{\|\vec{PM}\|^3} \quad (1)$$

at a point M, where P is varied along the two rectangles. As for M, for the purpose of this paper, it will be varied in the plane normal to figure 2.b and including Oy. We considered that, if $(\frac{L}{l} \geq 2)$, it is enough to evaluate the field as if L was infinite (in [16], the authors make an analogous remark, but adopt $\frac{L}{l} \geq 4$).

Therefore, the calculation of the coil field is reduced to a fourfold application of the **Biot** and **Savart** law for infinitely long conductors [17 to 19].

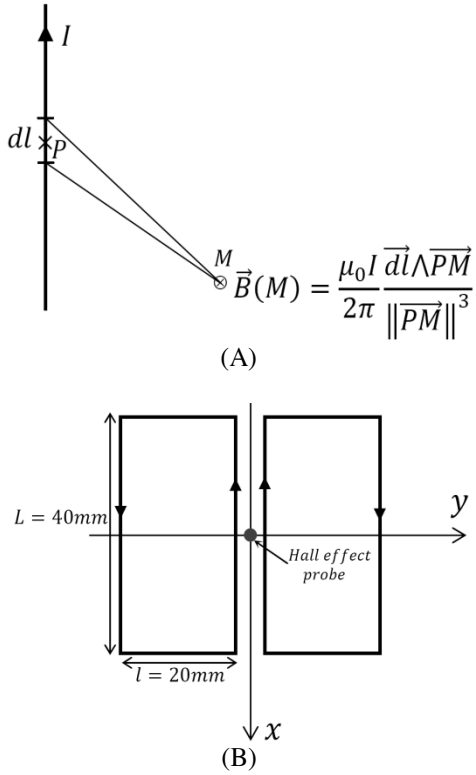


Figure 2: (A) Differential element for application of Biot and Savart law; (B) location of the Hall effect probe.

Those approximations have been carefully checked. In figure 3, the value of the normal component of the double rectangular coil field, is described for three values ($2, 8, 22mm$) of the vertical distance from the double rectangular plane (current intensity being $1.72A$). There is no significant difference between experimental and theoretical values.

3. Analysis of the currents induced in flawless plate and of the resulting B_z field

Assume now that the plate in figure 1.b has a resistivity equal to $5.82 * 10^{-8}\ \Omega.m$ (Aluminum $AG3$ at $20°C$); its dimensions in the directions Ox, Oy, Oz are $110, 100$, and $5mm$. The current in the double rectangular coil is $1.72A$ (as above) and its frequency is $180Hz$. The corresponding skin depth is $9.1mm$, much larger than the plate thickness.

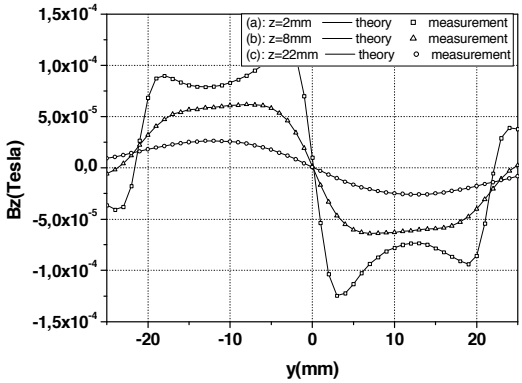


Figure 3: Magnetic field evaluation and measurement for the excitation coil in air for different values of altitude z.

Clearly, this means that the magnetic field of the currents induced in the plate is totally negligible in comparison to the exciting field. Therefore, the plate can be viewed as shown in figure 4.

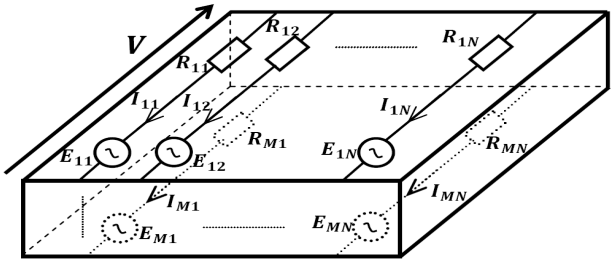
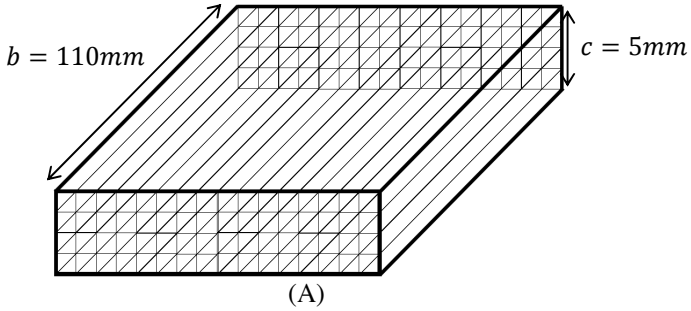
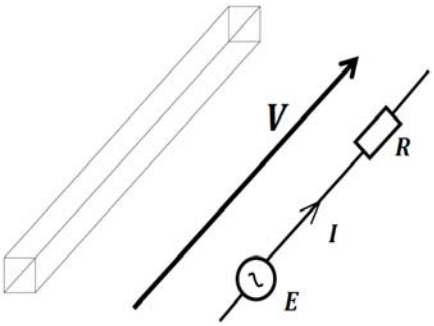


Figure 4: Model for the evaluation of emf and currents induced inside the sane conducting plate.

The vector potential is parallel to Ox; its origin may be chosen arbitrarily; if we take this origin inside the plate, just below the geometrical center of the double rectangular coil, the emf's shown in figure 4 will be clearly defined as in figure 5, where the plate is divided into $M \times N$ small elements; each one has a resistance R_{ij} which is easy to evaluate; the potential difference between the two sides of the plate will be called V; an emf $E_{ij} = -\frac{dA_{ij}}{dt}$ is created along element (i, j), A_{ij} being the potential vector created by the double rectangular coil along this element.





(B)

Figure 5: (A) Division of a sane plate into elements; (B) electrical model of one element.

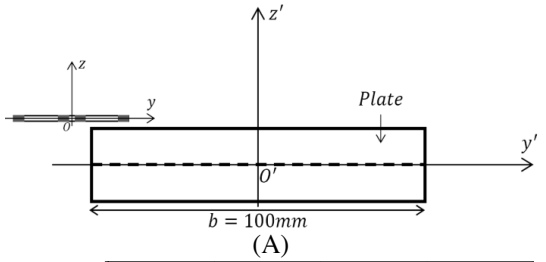
The sum of the currents in the individual conductors must be zero; therefore, if the current in element (i, j) is I_{ij}, we have $M * N + 1$ equations:

$$E_{ij} - R_{ij} * I_{ij} = V \quad (2)$$

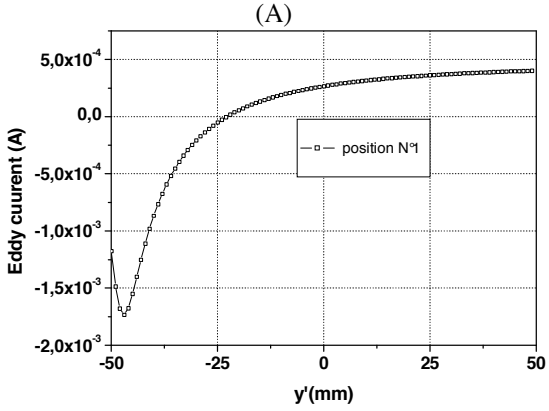
$$\sum_{i,j} I_{ij} = 0 \quad (3)$$

which determine V and the I_{ij}'s.

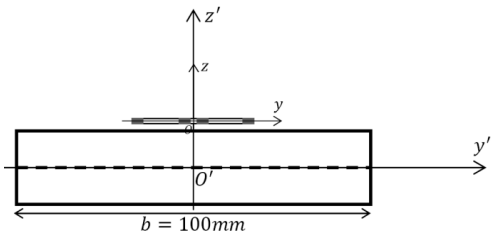
In figure 6, the result of this analysis is shown for three positions of the double rectangular coil (which is $1mm$ above the plate). Note that, in the present application, E_{ij} does not significantly depends on j.



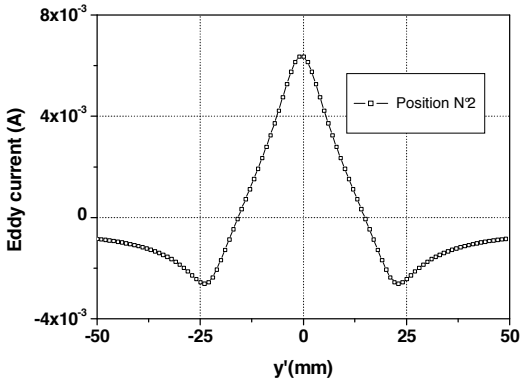
(A)



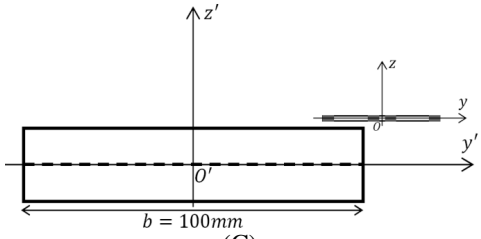
(A)



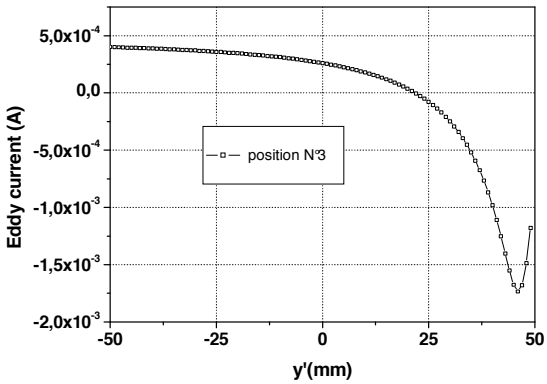
(B)



(B)



(C)



(C)

Figure 6: Induced currents for three positions of the exciting coil ((A), (B), and (C). Note that the currents do not depend on z′.

The corresponding component of B_z at the center of the double rectangular coil is given in figure 7.

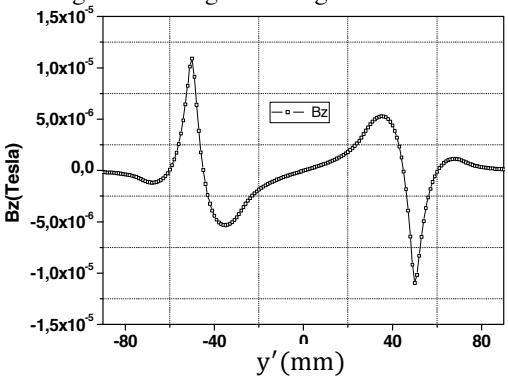


Figure 7: Computed values of B_z for a sane plate for $y = 0$.

4. Analysis of plate with a calibrated flaw

Consider now two plates similar to the above one, but with a calibrated crack (figure 8). The width of the crack is $w = 1mm$, and the depths are $depth = 0.5$ and $1mm$ respectively. The induced currents are described as explained in figure 8.a and 8.b.

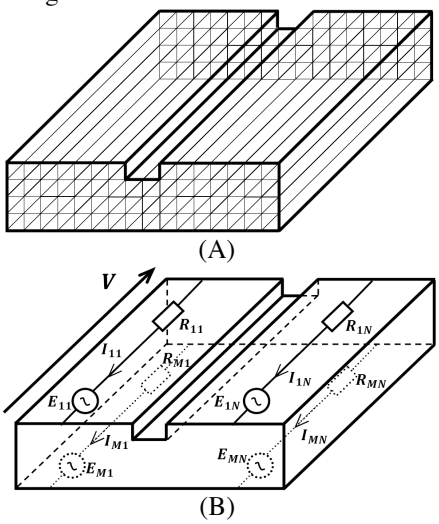


Figure 8: Same view as in figure 5, but there is a calibrated crack.

The distribution of the output signal (B_z field) is shown in figure 9.

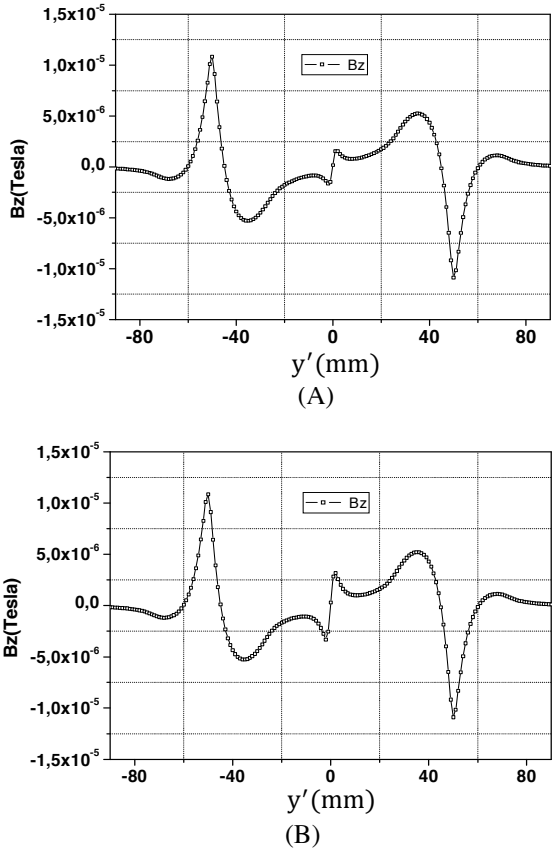


Figure 9: Same as figure 7, but with a crack width equal to 1mm; (a) depth = 0.5mm; (b) depth = 1mm.

5. Experimental results

The double rectangular coil shown in figure 1.a was laid upon a glass epoxy substrate with $0.5mm$ thickness. The copper layer thickness is $35\mu m$; its width is $1mm$. The permissible rms value of the current is $1.72A$ and its frequency is $180Hz$; the total resistance is 1Ω.

The Hall effect probe has been made by "ITRAN, France". Its surface is a few mm^2, its volume is $0.001mm^3$. The white magnetic field noise is $10pT/\sqrt{Hz}$. A synchronous detection is used, in order to distinguish the very small signal created by the eddy currents from the much larger excitation field. Its sensitivity is $5mV/\mu T$ [20]. Its sensitivity is much smaller than the SQUID sensitivity, but it can operate very near the center of the double rectangular coil (the active part of a SQUID must be distant of more than $1cm$ of the same point).

At the center of the sane plate, the theoretical and experimental values are given in figure 10.

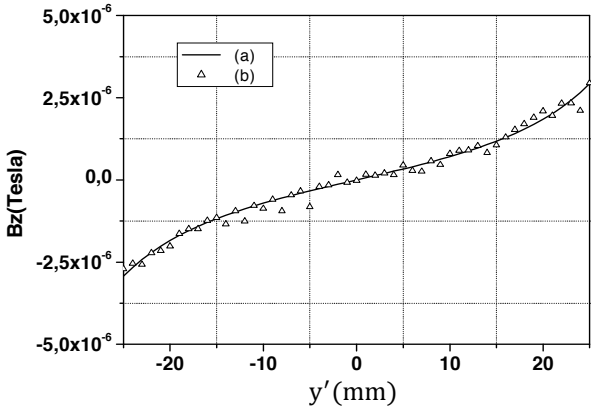
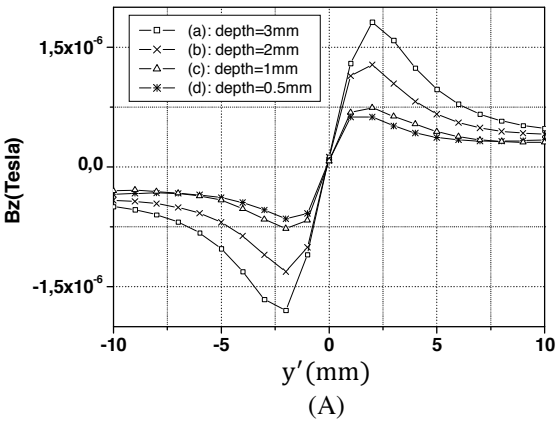
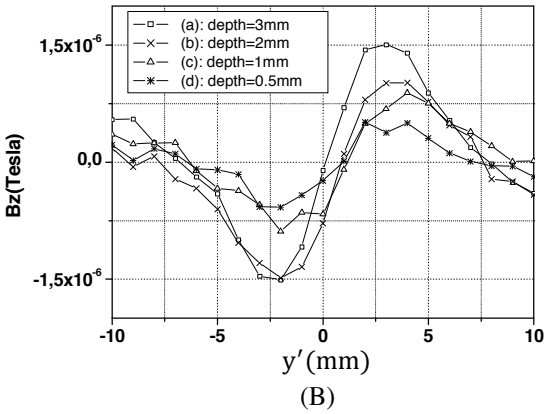


Figure 10. Comparison of theory and measurement in the center of a sane plate.

When there is a calibrated crack at the center of the plate, the predicted field B_z is described in figure 11 (A) for a width $w = 1mm$ and for four different depths ($depth = 0.5, 1, 2$ and $3mm$). The corresponding measured values are described in figure 11 (B).





(B)

Figure 11: Comparison of theory (A) and measurement (B) in the case of a crack in the center, for four different values of the crack depth.

6. Conclusion

In this paper, we describe the development of a simple, but accurate, theoretical treatment of eddy current analysis of planar samples with and without flaws. We have carefully tested the computation technique by eddy current scanning experiments using a Hall probe. The agreement between experimental and theoretical results is very good, showing that our novel model-based calculations describe well the signals obtained when using a double rectangular excitation coil and a Hall Effect probe.

7. References

[1] C. V. Dodd, W. E. Deeds, Analytical solutions to eddy-current probe-coil problems, Journal of Applied Physics, vol. 39, n° 6, pp. 2829-2838, 1968.

[2] C. V. Dodd, W. E. Deeds, Integral solutions to some eddy current problems, International Journal of Nondestructive Testing, vol. 1, pp. 29-90, 1969.

[3] S. M. Nair, J. H. Rose, Electromagnetic induction (eddy currents) in a conducting half-space in the absence of in homogeneities: a new formalism, Journal of Applied Physics, vol. 68, n° 12, pp. 5995-6009, 1990.

[4] J. O. Fava, and M. C. Ruch, Calculation and simulation of impedance diagrams of planar rectangular spiral coils for eddy current testing, NDT&E International, vol. 39, pp. 414-424, 2006.

[5] T. P. Theodoulidis, and E. E. Kriezis, Impedance evaluation of rectangular coils for eddy current testing of planar media, NDT&E International, vol. 35, pp. 407-414, 2002.

[6] J. R. Bowler, and T. P. Theodoulidis, Coil impedance variation due to induced current at the edge of a conductive plate, Journal of physics D: Applied Physics, vol. 39, pp. 2862-2868, 2006.

[7] H. Weinstock and M. Nisenoff, Non-destructive evaluation of metallic structures using a SQUID gradiometer, SQUID '85, Proc. 3rd International Conference on Superconducting Quantum Devices, Hahlbohm H.D. and Lubbig H., Eds., 843--847, de Gruyter, Berlin, 1985.

[8] H. Weinstock, SQUID Sensors: fundamentals, fabrications and applications, NATO ASI series E: Applied Science, Kluwer Academic Publishers, 1996.

[9] J. Clarke, SQUIDS, Scientific American, pp. 46-53, 1994.

[10] G. B. Donaldson, SQUID sensors, Kluwer, Dordrecht, NL, pp. 599-628, 1996.

[11] J. P. Wikswo, SQUID magnetometers for biomagnetism and nondestructive testing: important questions and initial answers, IEEE Trans. Appl. Supercond, vol. 5, n° 2, pp. 74-120, 1995.

[12] J. Clarke, A. I. Braginski, The SQUID Handbook: Fundamentals and Technology of SQUIDs and SQUID Systems, Volume I, Wiley-VCH Verlag GmbH&Co, KGaA, Weinheim, 2004 et 2006.

[13] W. G. Jenks, S. S. H. Sadeghi and J. P. Wiskswo, SQUIDS for NDE, J. Phys. D 30, pp. 293-323, 1997.

[14] Poulakis,Theodoulidis,www.ndt.net/article/hsndt2007/files/Poulakis_Theodoulidis.pdf

[15] J. R. Bowler and T. Theodoulidis, Coil impedance variation due to induced current at the edge of a conductive plate, Journal of Physics D: Applied Physics, 39:2862--2868, 2006.

[16] M. Ya. Antimirov, A. A. Kolyshkin, and R. Vaillancourt, Application of a perturbation to the solution of eddy current testing problems, IEEE Trans. on Mag., vol. 30, no. 3, pp. 1247-1252, 1994.

[17] N. Tsopelas, N. J. Siakavellas, Performance of circular and square coils in electromagnetic-thermal non-destructive inspection, NDT&E International vol. 40, pp. 12-28, 2007.

[18] A. I. Rusinov, High precision computation of solenoid magnetic fields by Garrett's methods, IEEE, Trans. on Mag., vol.30, n° 4, 2004.

[19] J. T. Conway, Exact solutions for the magnetic fields of axisymmetric solenoids and current distributions, IEEE Trans. on Mag., vol. 37, n° 4, 2001.

[20] P. Leroy, C. Coillot, V. Mosser, A. Roux and G. Chanteur, Use of magnetic concentrator to highly improve the sensitivity of Hall effect sensors, Sensor Letters, vol. 5, n° 1, pp. 162-166, 2007.

Reconsidering Ampere's Double Layer Representation for Magnetic Field Evaluation in a NDE Application

Michel Poloujadoff, Laroussi Bettaieb, and Hamid Kokabi

Université Pierre et Marie Curie (UPMC), Laboratoire d'Électronique et Électromagnétisme (L2E),
Aile 65/66 – 2ème étage - 4, Place Jussieu 75252 Paris Cedex 05.
laroussi.bettaieb@lgep.supelec.fr; hamid.kokabi@upmc.fr; michel.poloujadoff@upmc.fr

Abstract

The paper has two different objectives. The first one is to show that Ampere's double layer method, which is equivalent to one of the Maxwell equations, leads to the integration of a simple closed form expression, thus avoiding the need to solve complicated partial differential equations. The second aim is to study the case of a zero volume defect in a NDE problem by a perturbation method and the introduction of a double layer. The combination of these two techniques leads to a very fast solution of the problem. A practical example including an experimental check is given.

Keywords: Ampere's double layer, eddy currents, magnetic field evaluation, NDE, zero volume crack.

1. Introduction

Maxwell's equations forms are the basis of all studies in the field of electromagnetic non-destructive evaluation (NDE) [1 to 12]. Ampere's theorem has been established through this definition of magnetic masses and of "double layers" which allow the computation of the field of a given current loop through closed form expressions, not through partial differential equations [13 to 22], thus simplifying the solution process.

The object of the present paper is to apply that property in the case of a particular problem of non destructive evaluation. We shall limit ourselves to this example.

2. Presentation of an example

Non Destructive Evaluation (NDE) can be considered as a method which allows to detect a flaw (here: a crack) in a metallic conducting plate. More specifically, if we create an alternating magnetic field in a metallic object, this leads to the creation of eddy currents, which in turn create a magnetic reaction field. Conducting this experiment first with a flawless reference object, then with another object, seemingly identical to the first one, differences between the reaction fields may reveal internal differences, essentially flaws.

In the present paper, we consider a flawless aluminum plate whose dimensions are ($100\ mm \times 110\ mm \times 5\ mm$), and resistivity $\rho = 5.82 * 10^{-8}\Omega.m$ (AG3 alloy at 20°C). We create a uniform alternating field $\vec{B}_{exc} = B_m \cos(\omega t)\overrightarrow{Ox}$

(amplitude $B_m = 6.74 * 10^{-4}T$, frequency $f = 180Hz$) (see figure 1.a), and we evaluate the field of the eddy currents.

The question to be answered is: what would be the difference if we consider another plate of same dimensions and resistivity, but with a crack as shown in figure 1.b?

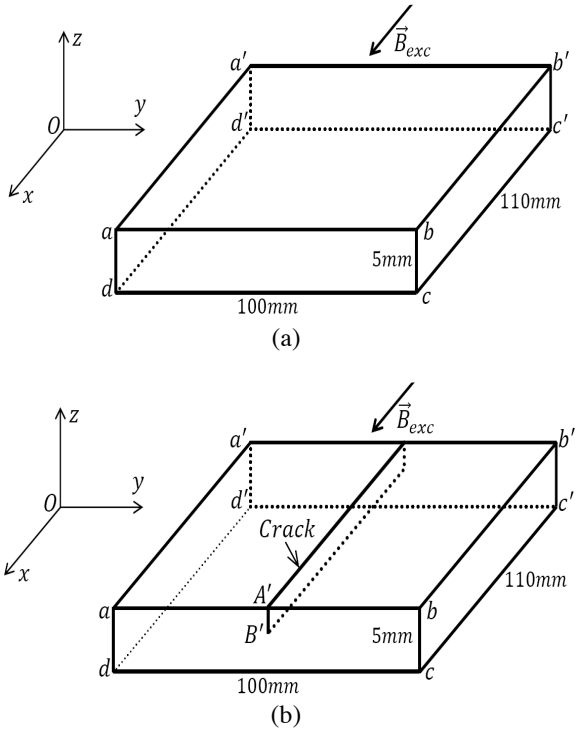


Figure 1: Description of a flawless plate (a) and a defective one (b).

3. Method analysis

3.1. Flawless plate

The first step is to analyze the case of the flawless plate, and this is rather simple. Indeed, in the present case, the standard penetration depth in the plate at $180Hz$ is $9.11mm$, which means that skin effect is negligible, so the induced currents are

just proportional to the time derivative of the vector potential of the exciting field (see appendix 1).

3.2. First approach to the analysis of a defective plate: Introduction of a perturbation method

The second step is to determine the currents in the defective plate. Two possibilities exist. Indeed, we may either directly evaluate the currents, or directly evaluate the difference between the currents in the flawless and in the defective plates. In both cases, we shall have the choice between using a double Fourier series expansion or a finite element (or finite difference) method. We have chosen to evaluate directly the perturbation introduced by the crack in the induced currents. And we shall see that any finite difference or finite element method leads directly to the characterization of Ampere's layer and to an evaluation of the crack effect.

If the current density in the flawless plate is shown in figures 2.a and 2.b, one can consider that the existence of the crack $A'B'$ is equivalent to a fictitious source of currents (see figure 2.c) whose values are the opposite of the values of the currents existing at the same place in the flawless plate [23 and 24]. This method belongs to the set of so called "perturbation methods", as the well known methods of Thevenin or Babinet.

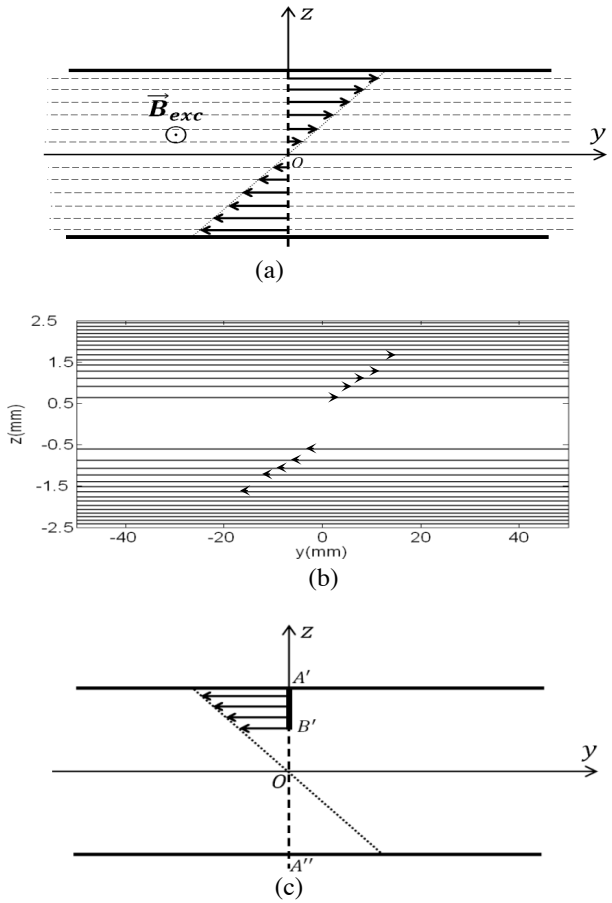


Figure 2: Description of the eddy currents in the abcd plane, in the case of a flawless plate (a) and (b). Fictitious source of current equivalent to the crack (c).

3.3. Introduction of a numerical determination of the perturbation currents

The currents densities described in figure 2.b are governed by the equations:

$$\partial j_y/\partial y + \partial j_z/\partial z = 0 \ (div\vec{j} = 0) \quad (1)$$
$$\partial j_y/\partial z - \partial j_z \partial y/= 0 \ (curl\vec{j} = 0) \quad (2)$$

Both being satisfied if there exists a function Q (called: current function) such that:

$$\begin{cases} j_y = -\partial Q/\partial z \\ j_z = \partial Q/\partial y \end{cases} \quad (3)$$

with

$$\partial^2 Q/\partial y^2 + \partial^2 Q/\partial z^2 = 0. \quad (4)$$

The boundary conditions are specified in figure 2.c, with $\partial Q/\partial y = 0$ (symmetry with respect to Oz (i.e. $j_z \equiv 0$)) and also Q is a parabolic function of z between A' and B' for $y = 0$.

Also $Q \equiv 0$ along the two limits $z = \pm c/2$. These data and conditions suffice to determine the values of $Q(y,z)$ all over the plane by use of any numerical method (series development, finite elements or finite differences methods).

When $Q(y,z)$ is known by any of these well known numerical methods, the lines
$Q(y,z) = cte$ are the current lines, as shown in figure 3.

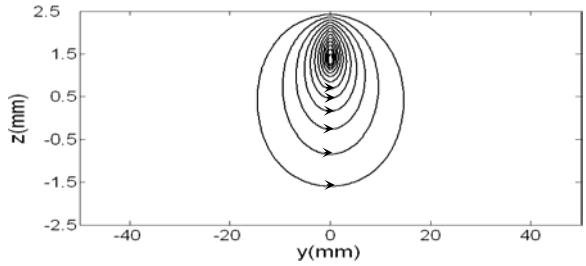


Figure 3: Currents lines generated by the fictitious source.

The combination of the current lines of the unperturbed plate (cf. figure 2.a) and of the fictitious source (cf. figure 3) yields the resultant current lines in the defective plate (figure 4).

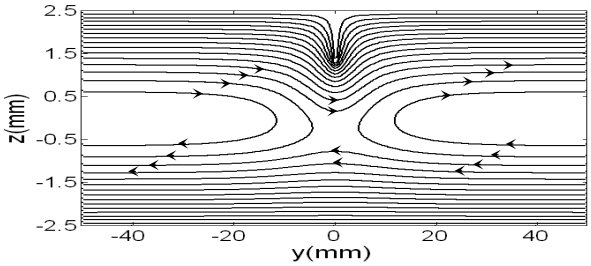


Figure 4: Currents in the defective plate, deduced from figures (2b) and (3).

It seems that, from this point, it is easy to evaluate the field created by the induced currents. In fact, this is not so, because of the complicated shape of the current lines. This is why recourse to Ampere's double layer of magnetic masses has been made [25].

3.4. Introduction of Ampere's magnetic masses

The basis of Ampere's magnetic field theory is that a small current loop whose intensity is I, is equivalent to two magnetic masses $\pm dm$, separated by a distance δ, in such a way that $\delta dm = IdS$, I being the loop current, dS the loop surface, δ the distance between the two masses (see figure 5.a). It is customary to call $P = \delta.[dm/dS]$ the "power" of the double layer. Therefore the "power" of the double layer is equal to the loop current. The scalar magnetic potential created by a magnetic mass dm at distance r being $dm/4\pi r$, the scalar magnetic potential created by the magnetic dipole (figure 5.b), or by the current loop is equal to:

$$V = \delta.[dm/4\pi].[sin\theta/r^2] = [IdS/4\pi].[sin\theta/r^2]. \quad (5)$$

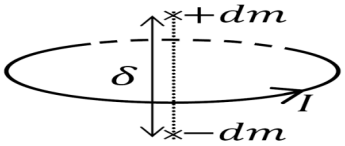
The radial magnetic field is:

$$B_r = -\delta.[dm/2\pi].[sin\theta/r^3] = -[IdS/4\pi].[sin\theta/r^3], \quad (6)$$

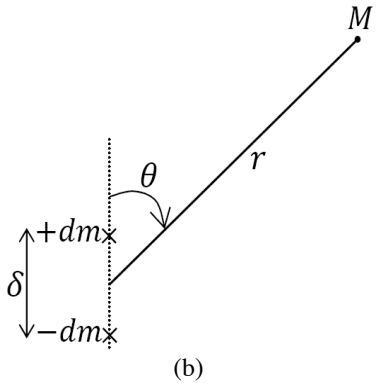
and the tangential magnetic field it is:

$$B_t = \delta.[dm/4\pi].[cos\theta/r^2] = [IdS/4\pi].[cos\theta/r^2]. \quad (7)$$

Therefore, the magnetic field of the eddy current is extremely easy to evaluate by the repetition of a closed form formula.



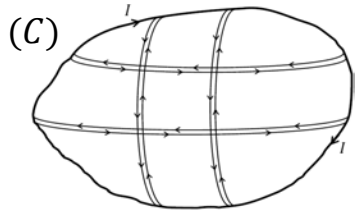
(a)



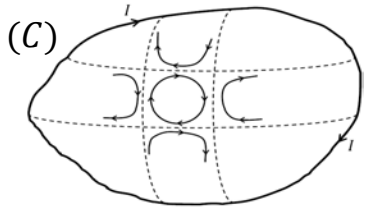
(b)

Figure 5: Definition of Ampere's equivalent magnetic masses.

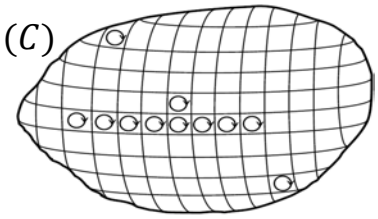
Now, consider a current loop (C), as sketched in figure 6.a. We do not modify the system by adding additional lines carrying simultaneously two opposite currents $+I$ and $-I$. This system of currents is equivalent to the set of small current loops depicted in figure 6.b and 6.c, with all the currents in the loops being equal to I. Thus, outside the double layer, the magnetic field is the same as the field of the double layer of magnetic masses if its density is equal to $\pm I/\delta$. Ampere has experimentally demonstrated that relationship, which is equivalent to the expression $\vec{I} = rot\vec{H}$, introduced by Maxwell, who called it "Ampere's theorem" as a token of admiration to his predecessor (see appendix 3).



(a)



(b)



(c)

Figure 6: Set of small current loops equivalent to a large one.

3.5. Relationship between Q and the loop currents

In the present case, an important remark is that function Q, defined above, is precisely proportional to the magnetic mass density because the following relation holds (see figure 7)

$$\int_A^B \vec{j}.\overrightarrow{dl} = \sum_A^B (j_1 - j_1 + j_2 - j_2 + j_3 - j_3) + j_4 = j_4 = QB - QA = QB \text{ with } QA = 0. \quad (8)$$

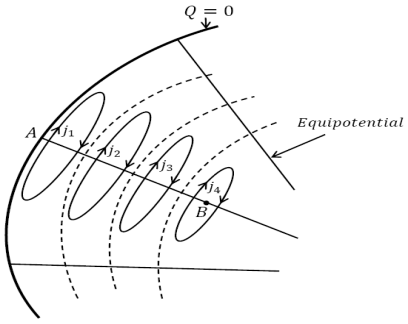


Figure 7: Equivalence of function Q and small loop currents.

3.6. Field created by the currents described in figure 3

We can now come back to figures 1 and 3. Figure 3 shows the lines of currents in any plane parallel to $abcd$ of figure 1.b. Therefore, the current loops in figure 3 represent, in fact, small solenoids parallel to the crack (figure 8.a). Each one has to be divided into elementary loops parallel to plane $abcd$. Each loop is equivalent to two layers of opposite signs, so that every layer is cancelled by the next one, except the two extreme ones (see figure 8.b).

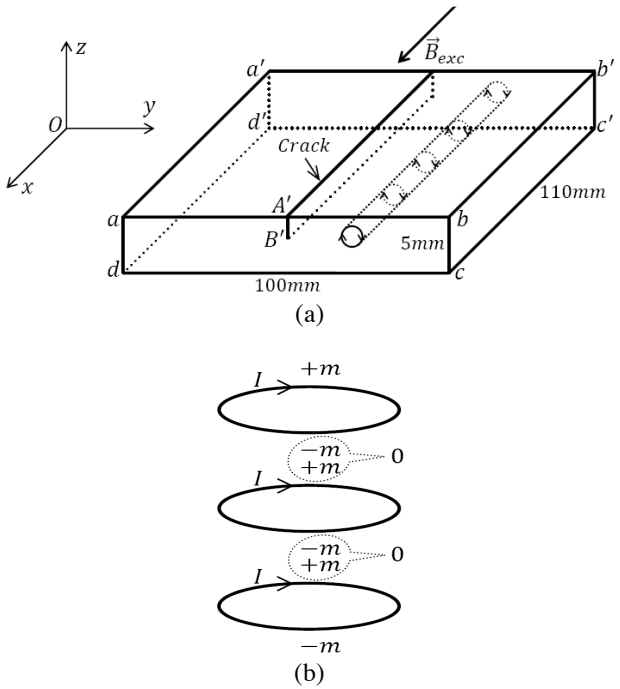


Figure 8: Reduction of the currents to two layers of magnetic masses at faces $abcd$ and $a'b'c'd'$.

Therefore, the field of the currents is equivalent to the field of magnetic masses laying on the two planes $abcd$ and $a'b'c'd'$. At each point, magnetic mass density and Q are equal:

$$I = Q \tag{9}$$

The field of magnetic masses, being Newtonian, is rather easy to evaluate as explained above.

3.7. Experimental check

The theoretical formulation given above has been checked experimentally, with the data given in the introduction. The depth of the crack was $depth = A'B' = 2mm$. The z component of the magnetic field of both the flawless plate and the cracked one are zero at the center of the plate ($x = 0$). For the case $x = 45mm$, the magnetic field is represented by figure 9. The difference of experimental (see appendix 2) and theoretical values is very small (2%), as shown in figure 9.

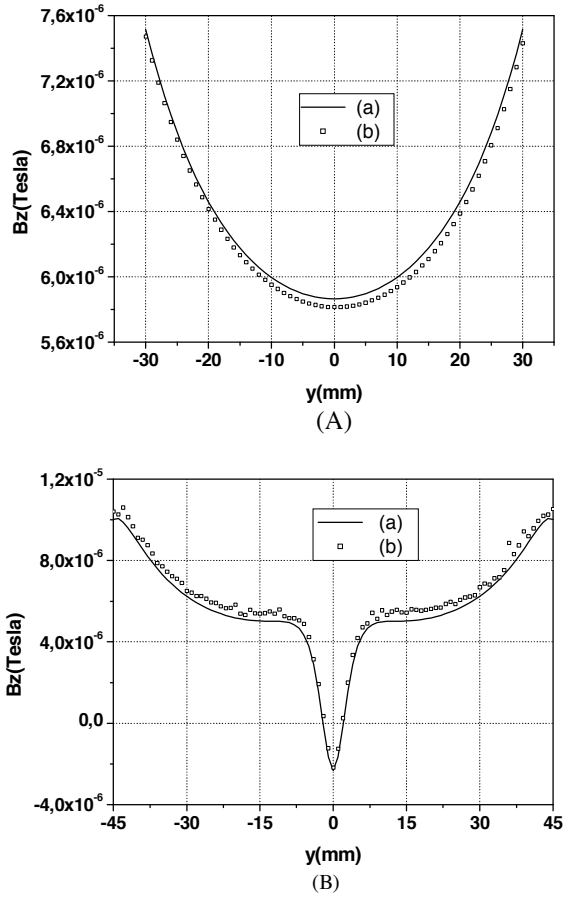


Figure9**:** Theoretical (a) and experimental (b) values of B_z in the case of the flawless plate (A), and of the defective (B) one for $x = 45mm$.

4. Conclusion

In this paper, we have examined the expression of the magnetic field of induced currents under two different forms. The first is Maxwell's formulation which is a partial differential equation which has to be solved. The second one is Ampere's expression which consists of closed form differential elements which just have to be added up. The latter formulation considerably simplifies the computation process and reduces the computing time.

We have also pointed out that the magnetic masses are easily defined by a current function Q whose spatial derivatives are the current densities.

We have also given an example of a zero volume crack which can be easily represented by an equivalent fictitious sources of currents, following the well known Thevenin's or Babinet's principle.

The results have been carefully checked with our experimental set up. Good agreement between theory and experiment has been found.

APPENDIX 1: INDUCED CURRENTS IN THE FLAWLESS PLATE

For figure 1.a and figure 1.b, we choose a direct reference frame Oxyz with Ox parallel to the induced field and Oz denoting the vertical direction. Thus the potential vector, created by the excitation field inside the plate, at point $M(M_y, M_z)$, is directed in the Oy direction and its value is:

$$A(M_y, M_z) = B * M_z .$$

Since the skin depth of aluminum at $180Hz$ is twice as large as the plate thickness, the corresponding current density is:

$$j_y(M_y, M_z) = \frac{1}{\rho}\frac{\partial A(p_y, p_z)}{\partial t} = \frac{\omega}{\rho} B_m M_z \sin(\omega t),$$

which means that the current lines are parallel to Oy [26 to 30].

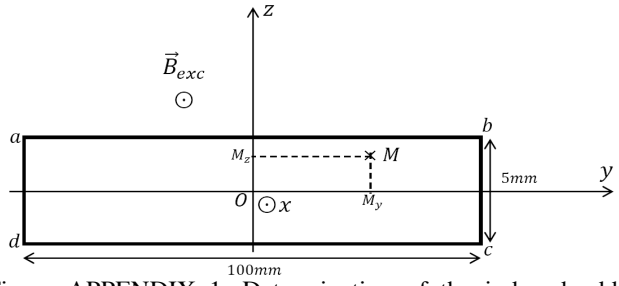


Figure APPENDIX 1: Determination of the induced eddy currents density j_y.

APPENDIX 2: SHORT DESCRIPTION OF THE EXPERIMENTAL SET UP

The excitation field is created by a Helmholtz coil pair H, with a cross section of $12\ mm \times 15\ mm$ each, an external diameter of $240mm$ and with a spacing of $120mm$. The aluminum plate P is mounted on a horizontal stage, thus allowing movement along the x and y directions. The vertical component of the induction field is measured by a sensor S which, in the present case, is a Hall effect micro-sensor [31], associated with a lock-in amplifier which allows a synchronous detection.

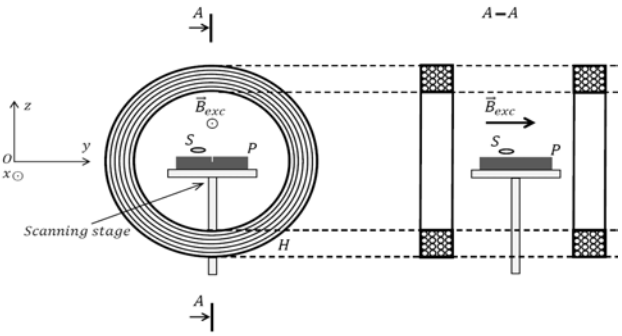


Figure APPENDIX 2: Instrumental set-up.

APPENDIX 3: EQUIVALENCE BETWEEN THE AMPERE'S AND MAXWELL'S STATEMENTS

Consider a current loop I, equivalent to a double layer made of positive and negative charges. The absolute value of the charge density is $\frac{dm}{dS} = \frac{I}{\delta}$. Consider a closed circuit divided in $\widehat{AB}$ and $\widehat{BA}$, where the distance between A and B may become infinitesimally small (figure Appendix 3). According to Poisson's theorem,

$$\oint_{(C)} \vec{H}\vec{dl} = \int_A^B \vec{H}_e\vec{dl} + \int_B^A \vec{H}_i\vec{dl} = 0.$$

Now, $H_i = \frac{dm}{dS}$ is oriented form A to B, and $\int_B^A \vec{H}_i\vec{dl} = -\frac{dm}{dS}\delta$, so that $\int_A^B \vec{H}_e\vec{dl} = -\int_B^A \vec{H}_i\vec{dl} = +\frac{dm}{dS}\delta = I$, which is Maxwell's expression $\oint_{(C)} \vec{H}\vec{dl} = I$, if the distance between A and B is becoming infinitesimally small.

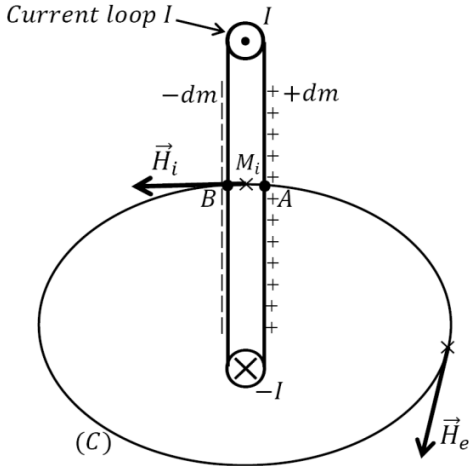


Figure APPENDIX 3: Equivalence between Ampere's and Maxwell's expressions of the Ampere's theorem.

Acknowledgment

The authors would like to thank very warmly Dr. Hans-Joachim Krause, researcher and "SQUID applications" Group leader at Forschungszentrum Jülich, for all his advises and the pre reviewing of this paper.

References

[1] Y. Gotoh, A. Kiya, N. Takahashi, Electromagnetic Inspection of Outer Side Defect on Steel Tube With Steel Support Using 3-D Nonlinear FEM Considering Non-Uniform Permeability and Conductivity, IEEE Transaction on Magnetics, vol. 46, no. 8, pp. 3145 - 3148, 2010.

[2] R. Hamia, C. Cordier, S. Saez, C. Dolabdjian, Eddy-Current Nondestructive Testing Using an Improved GMR Magnetometer and a Single Wire as Inducer: A FEM

Performance Analysis, IEEE Trans. Magn., vol. 46, no. 10, pp. 3731–3737, 2010.

[3] C. V. Dodd, W. E. Deeds, Analytical solutions to eddy-current probe-coil problems, Journal of Applied Physics, vol. 39, no. 6, pp. 2829-2838, 1968.

[4] C. V. Dodd, W. E. Deeds, Integral solutions to some eddy current problems, International Journal of Nondestructive Testing, vol. 1, pp. 29-90, 1969.

[5] L. Bettaieb, H. Kokabi, M. Ploujadoff, A. Sentz and A. Tcharkhtchi, Fatigue and/or crack detection in NDE, Nondestructive Testing and Evaluation, vol. 24, no. 4, pp. 1-12, 2009.

[6] Y. Cha, K. H. Kim, J. Shon, Y. H. Kim, and J. Kim, Surface flaws detection using AC magnetic field sensing by a thin film inductive microsensor," IEEE Trans. Magn., vol. 44, no. 11, pp. 4022–4025, 2008.

[7] C. Cordier, S. Saez, S. Lebargy, and C. Dolabdjian, Accurate steel tube axis alignment in nondestructive evaluation probe, IEEE Trans. Magn., vol. 44, no. 10, pp. 2409–2413, 2008.

[8] Y. Hatsukade, S. Okumo, K. Mori, and S. Tanaka, Eddy-current-based SQUID-NDE for detection of surface flaws on copper tubes, IEEE Trans. Appl. Supercond., vol. 17, no. 2, pp. 780–783, 2007.

[9] S. Hirano, Y. Inada, E. Matsumoto, A. Saito, K. Aizawa, M. Matsuda, S. Kuriki, and S. Ohshima, SQUID nondestructive testing system with vibrating normal pick-up coil, IEEE Trans. Appl. Supercond., vol. 17, no. 2, pp. 788–791, 2007.

[10] K. Tsukada, T. Kiwa, T. Kawata, and Y. Ishihara, Low-frequency eddy current imaging using MR sensor detecting tangential magnetic field components for nondestructive evaluation, IEEE Trans. Magn., vol. 42, no. 10, pp. 3315–3317, 2006.

[11] K. Chomsuwan, S. Yamada, M. Iwahara, H. Wakiwaka, and S. Shoji, "Application of eddy current testing technique for high-density doublelayer printed circuit board inspection," IEEE Trans. Magn., vol. 41, no. 10, pp. 3619–3321, 2005.

[12] N. V. Nair, V. R. Melapudi, H. R. Jimenez, X. Liu, Y. Deng, Z. Zeng, L. Udpa, T. J. Moran, and S. S. Udpa, A GMR-based eddy current system for NDE of aircraft structures, IEEE Trans. Magn., vol. 42, no. 10, pp. 3312–3314, 2006.

[13] W. S. Dunbar, The volume integral method of eddy current modeling, Journal of Nondestructive Evaluation, vol. 5, no. 1, pp. 9-14, 1985.

[14] S. M. Nair, J. H. Rose, Electromagnetic induction (eddy currents) in a conducting half-space in the absence of in homogeneities: a new formalism, Journal of Applied Physics, vol. 68, no. 12, pp. 5995-6009, 1990

[15] Z. Zeng, L. Udpa, S. S. Udpa, and M. S. C. Chan, Reduced magnetic vector potential formulation in the finite element analysis of eddy current nondestructive testing, IEEE Trans. Magn., vol. 45, no. 3, pp. 964–967, 2009.

[16] J. H. McWhirter, J. J. Oravec, and R. W. Haack, Computation of magnetic fields in three-dimensions based on Fredholm integral equations, IEEE Transaction on Magnetics, vol. 18, n° 2, pp. 373-377, 1982.

[17] T. Morisue, A new formulation of the magnetic vector potential method in 3-D multiply connected regions, IEEE Trans. Magn., vol. 24, no. 1, pp. 90–93, 1988.

[18] O. Biro, K. Preis, and W. Renhart, Finite element analysis of 3D multiply connected eddy current problems, IEEE Trans. Magn., vol. 25, no. 5, pp. 4009–4011, 1989.

[19] G. Rubinacci, A. Tamburrino, and S. Ventre, An efficient numerical model for a magnetic core eddy-current probe, IEEE Trans. Magn., vol. 44, no. 6, pp. 1306–1309, 2008.

[20] Y. Le Bihan, J. Pavo and C. Marchand, Calculation of ECT signal of a minute crack by FEMBIM hybrid method, Eur. Phys. J. Appl. Phys., vol. 28, pp. 355-360, 2004.

[21] A. Ruosi, M. Valentino, G. Pepe, V. Monebhurrn, and D. Lesselier, High T_c SQUIDs and eddy-current NDE/: a comprehensive investigation from real data to modeling, Meas. Sci. Techno. vol. 11, pp. 1639-1648, 2000.

[22] J. Bird, T. A. Lipo, A 3-D magnetic charge finite-element model of an electrodynamic wheel, IEEE Transaction on Magnetics, vol. 44, n° 2, pp. 253-265, 2008.

[23] L. Codecasa, P. Dular, R. Specogna, F. Trevisan, A Perturbation Method for the $T-\Omega$ Geometric Eddy-Current Formulation, IEEE Transaction on Magnetics, vol. 46, no. 8, pp. 3045 - 3048, 2010.

[24] M. Ya. Antimorov, A. A. Kolyshkin, R. Vaillancourt, Application of a perturbation method to the solution of eddy current testing problems, IEEE Transaction on Magnetics, vol. 30, no. 3, pp. 1247-1250, 1994.

[25] I. El Nahas, B. Szabados, M. Poloujadoff, R. Findlay, and X. Wu, A three-dimensional electromagnetic field analysis technique utilizing the magnetic charge concept,

IEEE Transaction on Magnetics, vol. 23, no. 5, pp. 3853-3859, 1987.

[26] R. L. Stoll, The analysis of eddy currents, Oxford: Clarendon press, 1974.

[27] L. Bettaieb, H. Kokabi, M. Poloujadoff, A. Sentz, and H. J. Krause, Analysis of Some Non Destructive Evaluation Experiments Using Eddy Currents, Research in Nondestructive Evaluation, vol. 20, no. 3, pp. 159-177, 2009.

[28] L. Bettaieb, H. Kokabi, M. Poloujadoff, A. Sentz, V. Moser, and C. Coillot, Comparison Of The Use Of SQUID an Hall Effect Sensors In NDE, Materials Evaluation, vol. 68, no. 5, pp. 535-541, 2010.

[29] J. A. Tegopoulos and E. E. Kriezis, Eddy currents in linear conducting media, studies in electrical and electronics engineering, vol. 16, Amsterdam: Elsevier, 1985.

[30] C. V. Dodd, The use of computer-modeling for eddy current testing, research techniques in nondestructive testing, vol. III, edited by R. S. Sharpe (ed.). London: Academic Press, pp. 429-479, 1977.

[31] P. Leroy, C. Coillot, V. Mosser, A. Roux and G. Chanteur, Use of magnetic concentrator to highly improve the sensitivity of Hall effect sensors, Sensor Letters, vol. 5, no. 1, pp. 162-166, 2007.

Time- and Frequency-Domain Evaluation of Stochastic Parameters on Signal Lines

Paolo Manfredi, Igor S. Stievano, Flavio G. Canavero*

Dipartimento di Elettronica,
Politecnico di Torino, 10129 Torino, Italy
*corresponding author, E-mail: flavio.canavero@polito.it

Abstract

This paper focuses on the derivation of enhanced transmission-line models allowing to describe, in time and frequency domain, a realistic interconnect with the inclusion of external uncertainties, like process variations or routing and layout uncertainties. The proposed method, that is based on the expansion of the well-known telegraph equations in terms of orthogonal polynomials, turns out to be accurate and more efficient than alternative solutions like Monte Carlo method in determining the transmission-line response sensitivity to parameters variability. Moreover, an implementation into standard circuit analysis tools such as SPICE is possible. Two application examples based on PCB structures of common use in commercial packages conclude the paper.

1. Introduction

Nowadays, the numerical simulation of interconnect structures is a fundamental step in the design phase due to the urging necessity to perform right-the-first-time designs. In this regard, several tools are available, although they are usually deterministic and this represents a strong limitation whenever manufacturing tolerances or uncertainties on design parameters cannot be neglected. In this framework, the stochastic analysis is a tool that is extremely useful in the early design phase for the prediction of the system performance and for setting realistic design margins. Relevant examples are provided by the process-induced variability or routing decisions that unavoidably impact on the performance of PCB lines.

The typical resource allowing to collect quantitative information on the statistical behavior of the circuit response is based on the application of the brute-force Monte Carlo (MC) method, or possible complementary methods based on the optimal selection of the subset of model parameters in the whole design space. Such methods, however, are computationally expensive, and this fact prevents us from their application to the analysis of complex realistic structures.

Recently, an effective solution that overcomes the previous limitation has been proposed. This methodology is based on the polynomial chaos (PC) theory and on the representation of the stochastic solution of a dynamical circuit in terms of orthogonal polynomials [1]. PC technique enjoys applications in several domains of Physics; we limit ourselves to mention that the authors of this contribution proposed an extension of PC theory to distributed structures described by transmission-line equations [2]. Furthermore, a SPICE implementation of this methodology and its extension to lumped circuit elements has been recently provided [3].

This paper extends the PC theory to the stochastic simulation of a realistic interconnected structure consisting of a cascade connection of distributed multiconductor interconnects and lumped multiport circuits. Both frequency- and time-domain results are presented, being the latter obtained through either harmonic superposition or SPICE simulation. In addition, an extension in the formulation allowing to account for variability in the interconnect length will be presented. The feasibility and strength of the proposed approach are then further validated by means of the stochastic simulation of two realistic structures, for which the effects of uncertainties in the system parameters are predicted and analyzed.

2. Polynomial Chaos Primer

This Section provides a brief overview of the PC method. The idea underlying this technique is the spectral expansion of a stochastic function (intended as a given function of a random variable) in terms of a truncated series of orthogonal polynomials. Within this framework, any function H, carrying the effects of variability, can be approximated by means of the following truncated series [4]

$$H(\ldots,\xi) = \sum_{k=0}^{P} H_k(\ldots)\cdot\phi_k(\xi), \qquad (1)$$

where $\{\phi_k\}$ are suitable orthogonal polynomials expressed in terms of the random variable ξ. The above expression is defined by the class of the orthogonal bases, by the number of terms $P+1$ (limited to the range from 2 to 20 for practical applications, depending also on the number of random variables considered) and by the expansion coefficients H_k. The choice of the orthogonal basis relies on the distribution of the random variables. Uncertainties arising from fabrication tolerances turn out to be properly characterized in terms of Gaussian variability. Hence, the most appropriate orthogonal functions for the expansion (1) are the Hermite polynomials, the first three being $\phi_0 = 1$, $\phi_1 = \xi$

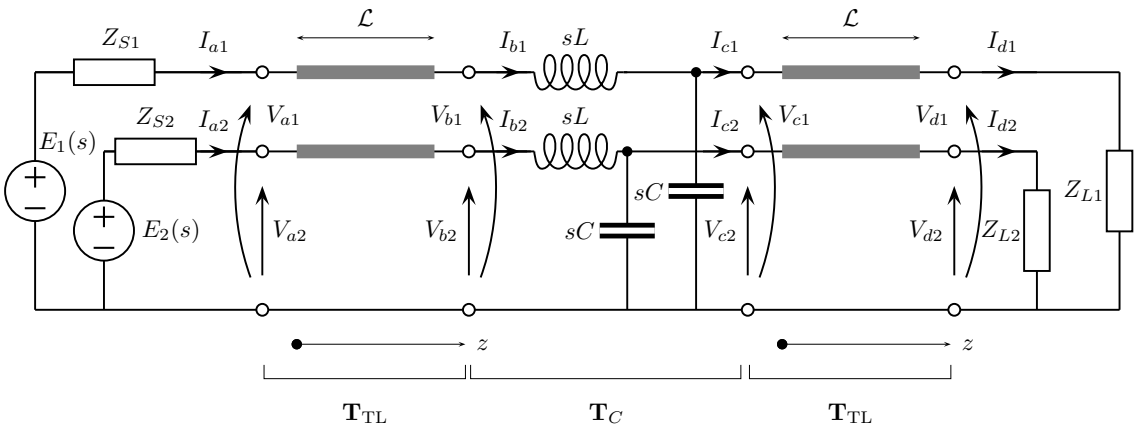


Figure 1: Test structure used to demonstrate the proposed approach.

and $\phi_2 = \xi^2 - 1$, where ξ is the standard normal random variable with zero mean and unit variance. It is relevant to remark that any random parameter in the system, e.g., the substrate permittivity ε_r, can be related to ξ as follows

$$\varepsilon_r = \bar{\varepsilon}_r + \sigma_\varepsilon \xi, \tag{2}$$

where $\bar{\varepsilon}_r$ and σ_ε are the mean value and standard deviation, respectively. The orthogonality property of Hermite polynomials is expressed by

$$< \phi_k, \phi_j > = < \phi_k, \phi_k > \delta_{kj}, \tag{3}$$

where δ_{kj} is the Kronecker delta and $< \cdot, \cdot >$ denotes the inner product in the Hilbert space of the variable ξ with Gaussian weighting function, i.e.,

$$< \phi_k, \phi_j > = \frac{1}{\sqrt{2\pi}} \int_{-\infty}^{\infty} \phi_k(\xi)\phi_j(\xi)\exp(-\xi^2/2)d\xi. \tag{4}$$

When the variability is more properly characterized in terms of uniform distribution, Legendre polynomials $\phi_0 = 1$, $\phi_1 = \xi$, $\phi_2 = \frac{3}{2}\xi^2 - \frac{1}{2}$, etc., can be used. In this case, ξ in uniform in the range $[-1, 1]$ and the inner product is defined as

$$< \phi_k, \phi_j > = \frac{1}{2} \int_{-1}^{1} \phi_k(\xi)\phi_j(\xi)d\xi. \tag{5}$$

With the above definitions, the expansion coefficients H_k of (1) are computed via the projection of H onto the orthogonal components ϕ_k. It is worth noting that relation (1), which is a known nonlinear function of the random variable ξ, can be used to predict the probability density function (PDF) of $H(\xi)$ via numerical simulation or analytical formulae [5].

The basic results of PC theory outlined above can be extended to the case of multiple independent random variables. However, for the sake of brevity, the formal development (consisting in the application of orthogonality relations to build higher dimensional polynomials as the product combination of polynomials in one variable) is omitted here and readers are referred to [2].

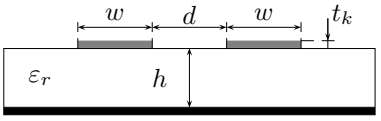


Figure 2: Microstrip cross-section for the interconnects in Fig. 1.

3. Stochastic Simulation of Interconnected Structures

This Section summarizes the proposed procedure for the stochastic simulation of a complex interconnected structure like the one shown in Fig. 1. The depicted scheme provides an exemplification of a typical high-speed data link composed by two transmitters (represented by the Thévenin sources on the left) driving a distributed – possibly multiconductor – interconnect terminated by digital receivers (here assumed linear and simply described by their $Z_{L1,2}$ input impedances). The interconnect is supposed to be composed by two identical sections linked by a connector represented by a simple LC equivalent.

The proposed strategy is the following: (i) generate extended stochastic models for the different parts composing the cascaded structure. The extended models are obtained by expanding the characteristics of the different circuit elements involved in the scheme of Fig. 1 according to (1); (ii) simulate the entire structure in the frequency domain by suitably concatenating these models. If a time-domain calculation is desired, in principle this can be accomplished through harmonic superposition.

3.1. Stochastic Model for Distributed Lines

For the sake of simplicity, the discussion is based on a lossless three-conductor line, as the coupled microstrip structure shown in Fig. 2, in presence of a single random parameter. Futhermore, Gaussian variability is assumed. The wave propagation on the distributed parts of the structure is governed by the telegraphers equation in the Laplace do-

main [6]

$$\frac{d}{dz}\begin{bmatrix}\mathbf{V}(z,s)\\ \mathbf{I}(z,s)\end{bmatrix} = -s\begin{bmatrix}0 & \mathbf{L}\\ \mathbf{C} & 0\end{bmatrix}\begin{bmatrix}\mathbf{V}(z,s)\\ \mathbf{I}(z,s)\end{bmatrix}. \quad (6)$$

In the above equation, s is the Laplace variable, $\mathbf{V} = [V_1(z,s), V_2(z,s)]^T$ and $\mathbf{I} = [I_1(z,s), I_2(z,s)]^T$ are vectors collecting the voltage and current variables along the multiconductor line (z coordinate) and $\mathbf{C}$ and $\mathbf{L}$ are the p.u.l. capacitance and inductance matrices, depending on the geometrical and material properties of the structure.

The solution of a transmission-line equation like (6) is given by the combination of its chain parameter matrix (CPM), that writes

$$\mathbf{T}_{\mathrm{TL}}(\mathcal{L}, s) = \mathrm{expm}\left(-s\begin{bmatrix}0 & \mathbf{L}\\ \mathbf{C} & 0\end{bmatrix}\mathcal{L}\right), \quad (7)$$

where expm denotes the matrix exponential, with the boundary conditions defined by the port electrical relations of the terminal elements defining the source and the load. The CPM relates voltages and currents at the two extremities of the block, i.e.,

$$\begin{bmatrix}\mathbf{V}(\mathcal{L},s)\\ \mathbf{I}(\mathcal{L},s)\end{bmatrix} = \begin{bmatrix}\mathbf{T}_{\mathrm{TL},11}(\mathcal{L},s) & \mathbf{T}_{\mathrm{TL},12}(\mathcal{L},s)\\ \mathbf{T}_{\mathrm{TL},21}(\mathcal{L},s) & \mathbf{T}_{\mathrm{TL},22}(\mathcal{L},s)\end{bmatrix}\begin{bmatrix}\mathbf{V}(0,s)\\ \mathbf{I}(0,s)\end{bmatrix}. \quad (8)$$

In Fig. 1, $z = 0$ corresponds to the sections indicated with either a or c, whereas $z = \mathcal{L}$ corresponds to the section b or d. By defining for notation convenience $\mathbf{X}_{a,b}(s) = [\mathbf{V}_{a,b}(s), \mathbf{I}_{a,b}(s)]^T$, (8) can be rewritten as

$$\mathbf{X}_b(s) = \mathbf{T}_{\mathrm{TL}}(\mathcal{L}, s)\mathbf{X}_a(s) \quad (9)$$

and a similar relation holds between sections c and d.

When the problem becomes stochastic, in order to account for the uncertainties affecting the guiding structure, we must consider the p.u.l. parameters as random quantities, with entries depending on the random variable ξ. In turn, (6) becomes a stochastic differential equation, leading to randomly-varying voltages and currents along the line. Therefore, they also depend on ξ.

The expansion (1) of the p.u.l parameters and of the unknown voltage and current variables in terms of Hermite polynomials, yields a modified version of (6), whose second row becomes

$$\begin{aligned}&\tfrac{d}{dz}(\mathbf{I}_0(z,s)\phi_0(\xi) + \mathbf{I}_1(z,s)\phi_1(\xi) + \mathbf{I}_2(z,s)\phi_2(\xi)) =\\ &-s(\mathbf{C}_0\phi_0(\xi) + \mathbf{C}_1\phi_1(\xi) + \mathbf{C}_2\phi_2(\xi))(\mathbf{V}_0(z,s)\phi_0(\xi) +\\ &+\mathbf{V}_1(z,s)\phi_1(\xi) + \mathbf{V}_2(z,s)\phi_2(\xi)),\end{aligned} \quad (10)$$

where a second-order expansion (i.e., $P = 2$) is assumed; the expansion coefficients of electrical variables and of p.u.l. parameters are readily identifiable in the above equation.

Projection of (10) and of the companion relation arising from the first row of (6) on the first three Hermite polynomials leads to the following augmented system, where the random variable ξ does not appear explicitly, due to the integral projection form given in (4):

$$\frac{d}{dz}\begin{bmatrix}\tilde{\mathbf{V}}(z,s)\\ \tilde{\mathbf{I}}(z,s)\end{bmatrix} = -s\begin{bmatrix}0 & \tilde{\mathbf{L}}\\ \tilde{\mathbf{C}} & 0\end{bmatrix}\begin{bmatrix}\tilde{\mathbf{V}}(z,s)\\ \tilde{\mathbf{I}}(z,s)\end{bmatrix}. \quad (11)$$

In the previous equation, vectors $\tilde{\mathbf{V}} = [\mathbf{V}_0, \mathbf{V}_1, \mathbf{V}_2]^T$ and $\tilde{\mathbf{I}} = [\mathbf{I}_0, \mathbf{I}_1, \mathbf{I}_2]^T$ collect the different coefficients of the polynomial chaos expansion of the voltage and current variables. The new p.u.l. matrix $\tilde{\mathbf{C}}$ turns out to be

$$\tilde{\mathbf{C}} = \begin{bmatrix}\mathbf{C}_0 & \mathbf{C}_1 & 2\mathbf{C}_2\\ \mathbf{C}_1 & (\mathbf{C}_0 + 2\mathbf{C}_2) & 2\mathbf{C}_1\\ \mathbf{C}_2 & \mathbf{C}_1 & (\mathbf{C}_0 + 4\mathbf{C}_2)\end{bmatrix} \quad (12)$$

and a similar relation holds for matrix $\tilde{\mathbf{L}}$.

It is worth noting that (11) is analogous to (6) and plays the role of the set of equations of a multiconductor transmission line with a number of conductors that is $(P + 1)$ times larger than those of the original line. It should be also remarked that the increment of the equation number is not detrimental for the method, since for small values of P (as typically occurs in practice), the additional overhead in handling the augmented equations is much less than the time required to run a large number of MC simulations.

As far as the solution of the stochastic problem is concerned, the augmented equation (11) is used in place of (6), as well as the corresponding CPM, that becomes

$$\tilde{\mathbf{T}}_{\mathrm{TL}}(\mathcal{L}, s) = \mathrm{expm}\left(-s\begin{bmatrix}0 & \tilde{\mathbf{L}}\\ \tilde{\mathbf{C}} & 0\end{bmatrix}\mathcal{L}\right). \quad (13)$$

The augmented CPM relates the coefficients of the voltage and current variables (i.e., $\tilde{\mathbf{X}}_{a,b}(s) = [\tilde{\mathbf{V}}_{a,b}(s), \tilde{\mathbf{I}}_{a,b}(s)]^T$) at the line extremities.

Readers are referred to [2] for additional details on the formulation for multiple random variables. Moreover, extension of the procedure to the general case of lossy transmission lines is straightforward, and amounts to including the resistance and conductance matrices in (6) and the corresponding augmented matrices – resulting from their expansion – in (11) and (13).

3.2. Stochastic Model for Lumped Blocks

Again, the discussion is referred to Fig. 1. The multiport equation for the LC block writes

$$\mathbf{X}_c(s) = \mathbf{T}_C(s)\mathbf{X}_b(s), \quad (14)$$

where $\mathbf{X}_c(s) = [\mathbf{V}_c(s), \mathbf{I}_c(s)]^T$ and

$$\begin{aligned}\mathbf{T}_C(s) &= \begin{bmatrix}\mathbf{T}_{C,11}(s) & \mathbf{T}_{C,12}(s)\\ \mathbf{T}_{C,21}(s) & \mathbf{T}_{C,22}(s)\end{bmatrix}\\ &= \left[\begin{array}{cc|cc}1 & 0 & -sL & 0\\ 0 & 1 & 0 & -sL\\ \hline -sC & 0 & 1+s^2LC & 0\\ 0 & -sC & 0 & 1+s^2LC\end{array}\right].\end{aligned} \quad (15)$$

When we intend to include the variability of the connector parameters, we must consider the LC elements as random quantities and expand the circuit equations in terms of Hermite orthogonal polynomials, as already done for the case of distributed interconnects. By introducing a new random variable η, possibly different from the variable ξ that affects the distributed part, the second-order expansion of (14) yields

$$\begin{aligned}&\mathbf{X}_{c,0}\phi_0(\eta)+\mathbf{X}_{c,1}\phi_1(\eta)+\mathbf{X}_{c,2}\phi_2(\eta)=\\&(\mathbf{T}_{C,0}\phi_0(\eta)+\mathbf{T}_{C,1}\phi_1(\eta)+\mathbf{T}_{C,2}\phi_2(\eta))(\mathbf{X}_{b,0}\phi_0(\eta)\\&+\mathbf{X}_{b,1}\phi_1(\eta)+\mathbf{X}_{b,2}\phi_2(\eta)).\end{aligned} \tag{16}$$

Again, projection onto the first three Hermite polynomials leads to the following deterministic augmented system

$$\tilde{\mathbf{X}}_c(s)=\tilde{\mathbf{T}}_C(s)\tilde{\mathbf{X}}_b(s), \tag{17}$$

where $\tilde{\mathbf{X}}_c(s)=[\tilde{\mathbf{V}}_c(s),\tilde{\mathbf{I}}_c(s)]^T$ collects the coefficients of the PC expansion of the voltage and current variables at section c. The four blocks of $\tilde{\mathbf{T}}_C$ turn out to be

$$\tilde{\mathbf{T}}_{C,ij}=\begin{bmatrix}\mathbf{T}_{C,ij,0} & \mathbf{T}_{C,ij,1} & 2\mathbf{T}_{C,ij,2}\\ \mathbf{T}_{C,ij,1} & (\mathbf{T}_{C,ij,0}+2\mathbf{T}_{C,ij,2}) & 2\mathbf{T}_{C,ij,1}\\ \mathbf{T}_{C,ij,2} & \mathbf{T}_{C,ij,1} & (\mathbf{T}_{C,ij,0}+4\mathbf{T}_{C,ij,2})\end{bmatrix}, \tag{18}$$

with $i,j=1,2$. Also in this case, the augmented equations belong to the same class as the initial ones, and the system matrices have the same structure as in (12). The extension to multiple random variables is in principle obtainable as for the case of distributed structures.

3.3. Incorporation of the Boundary Conditions

The simulation of a structure like the one of Fig. 1 amounts to combining the port electrical relations of the two terminal elements defining sources (transmitters) and loads (receivers) with the overall CPM, resulting from the cascaded connection of the two transmission-line sections and the lumped network. According to the properties of the CPM, the overall matrix is given by the product of the matrices of the individual blocks. For the stochastic case, this leads to:

$$\tilde{\mathbf{T}}=\tilde{\mathbf{T}}_{\mathrm{TL}}\tilde{\mathbf{T}}_C\tilde{\mathbf{T}}_{\mathrm{TL}}. \tag{19}$$

It should be noted that in general the generation of each extended model in (19) must be carried out including all the random variables in the problem (ξ and η, in this case), whether they affect all blocks or only a part of them, in order to have a consistent representation of all blocks for the concatenation.

When dealing with augmented models, also the port relations – although here no variability is assumed on the terminations – must be written in an extended form, in order to allow their combination across sections a and d, similarly to what is done in (19) for the continuity across sections b and c. This will represent the last step in the development of the presented methodology.

For the example of Fig. 1, the port equations at the terminations become

$$\begin{cases}\mathbf{V}_a(s,\xi,\eta) &= \mathbf{V}_S(s)-\mathbf{Z}_S(s)\mathbf{I}_a(s,\xi,\eta)\\ \mathbf{V}_d(s,\xi,\eta) &= \mathbf{Z}_L(s)\mathbf{I}_d(s,\xi,\eta),\end{cases} \tag{20}$$

with $\mathbf{V}_S(s)=[E_1(s),E_2(s)]^T$ and $\mathbf{Z}_{S,L}=\mathrm{diag}([Z_{S1,L1},Z_{S2,L2}])$. These deterministic terms can be considered as a zero-order expansion, thus proportional to ϕ_0. Expansion of (20) and the subsequent projection onto Hermite polynomials leads to

$$\begin{cases}\tilde{\mathbf{V}}_a(s) &= \tilde{\mathbf{V}}_S(s)-\tilde{\mathbf{Z}}_S(s)\tilde{\mathbf{I}}_a(s)\\ \tilde{\mathbf{V}}_d(s) &= \tilde{\mathbf{Z}}_L(s)\tilde{\mathbf{I}}_d(s),\end{cases} \tag{21}$$

where in this specific case $\tilde{\mathbf{V}}_S(s)=[\mathbf{V}_S(s),0\dots0]^T$, while $\tilde{\mathbf{Z}}_S(s)$ and $\tilde{\mathbf{Z}}_L(s)$ are diagonal, due to the absence of variability on the termination networks. If needed, the above equations can be suitably modified to account for variability in the characteristics of the source and load elements.

The solution of the stochastic system is achieved via the standard procedure used for combining the boundary conditions with the equations given by the CPM [6]. As an example, the source and load currents can be computed as

$$\begin{cases}\tilde{\mathbf{I}}_a=\mathbf{A}^{-1}\mathbf{b}\\ \tilde{\mathbf{I}}_d=\tilde{\mathbf{T}}_{21}\tilde{\mathbf{V}}_S+(\tilde{\mathbf{T}}_{22}-\tilde{\mathbf{T}}_{21}\tilde{\mathbf{Z}}_S)\tilde{\mathbf{I}}_a,\end{cases} \tag{22}$$

where

$$\begin{cases}\mathbf{A}=\tilde{\mathbf{T}}_{11}\tilde{\mathbf{Z}}_S+\tilde{\mathbf{Z}}_L\tilde{\mathbf{T}}_{22}-\tilde{\mathbf{T}}_{12}-\tilde{\mathbf{Z}}_L\tilde{\mathbf{T}}_{21}\tilde{\mathbf{Z}}_S\\ \mathbf{b}=(\tilde{\mathbf{T}}_{11}-\tilde{\mathbf{Z}}_L\tilde{\mathbf{T}}_{21})\tilde{\mathbf{V}}_S,\end{cases} \tag{23}$$

whereas the voltages are obtained from (21).

3.4. Frequency-Domain Stochastic Analysis

Once the unknown voltages and currents are computed, the quantitative information on the spreading of circuit responses can be readily obtained from the analytical expression of the unknowns. As an example, the frequency-domain solution of the terminal voltage V_{d2}, arising from (21) and (22) with a single random variable ξ and $P=2$, is

$$\begin{aligned}V_{d2}(j\omega,\xi)=V_{d2,0}(j\omega)+V_{d2,1}(j\omega)\xi+\\+V_{d2,2}(j\omega)(\xi^2-1),\end{aligned} \tag{24}$$

where the first numerical index denotes the conductor and the second one denotes the expansion term. The above relation can be used for instance to compute the PDF of $|V_{d2}(j\omega,\xi)|$.

4. Time-Domain Stochastic Analysis

Several techniques can be adopted to apply PC modeling also to time-domain simulation, depending on the waveform and circuit characteristics.

4.1. Harmonic Superposition

The time-domain response can be readily obtained from the frequency-domain solution by considering a periodic input source and expressing it in terms of a truncated Fourier series

$$e(t) \simeq c_0 + \sum_{n=1}^{N} c_n \mathrm{e}^{j2\pi f_n t} + c_n^* \mathrm{e}^{-j2\pi f_n t}, \qquad (25)$$

where c_0 is the signal average over one period and c_n is the complex Fourier coefficient for the n-th harmonic at frequency f_n. Being the system of Fig. 1 linear, its time-domain behaviour is in principle obtainable by the superposition of the analyses carried out for all signal harmonics. For the individual solution at frequency f_n, the voltage sources of Fig. 1, appearing also in (20), are replaced by their n-th harmonic components, i.e., $E_{1,2}(s_n) = E_{1,2}(j2\pi f_n) = c_{n,1,2}$. The time-domain expression of the output voltage $v_{d2}(t,\xi)$ is then obtained as a linear superposition of harmonics:

$$\begin{aligned} v_{d2}(t,\xi) = v_0 + \textstyle\sum_{n=1}^{N} \big[& V_{d2}(j2\pi f_n, \xi)\mathrm{e}^{j2\pi f_n t} + \\ & V_{d2}^*(j2\pi f_n, \xi)\mathrm{e}^{-j2\pi f_n t} \big], \end{aligned} \qquad (26)$$

where v_0 is the DC term, obtained from a DC calculation, and the output coefficients $V_{d2}(j2\pi f_n, \xi)$ are computed according to (24). The linearity of Fourier decomposition assures that the PC structure is preserved also for the time-domain expression of the output:

$$v_{d2}(t,\xi) = v_0 + v_{d2,0}(t) + v_{d2,1}(t)\xi + v_{d2,2}(t)(\xi^2 - 1), \qquad (27)$$

where

$$v_{d2,j}(t) = \sum_{n=1}^{N} V_{d2,j}(j2\pi f_n)\mathrm{e}^{j2\pi f_n t} + V_{d2,j}^*(j2\pi f_n)\mathrm{e}^{-j2\pi f_n t} \qquad (28)$$

with $j = 0, 1, 2$.

4.2. SPICE Implementation

An alternative solution, suitable for lossless lines with non-periodic inputs, is the implementation of the augmented transmission-line equations (11) into standard analysis tools such as SPICE [3]. This can be easily achieved by means of the generalized Branin's equivalent for multinconductor transmission lines [6], that is suitable for handling also non-symmetric p.u.l. matrices, as typically occurs in the generated augmented systems (cf. (12)). Of course, the created model is also suited to carry out frequency-domain simulations.

Besides new p.u.l. parameters, also new boundary conditions (i.e., line terminations) must be defined in order to solve (11). As shown in Sec. 3.3, when considering linear lumped terminations in the form of Thévenin or Norton equivalents and when no variability is attributed to them (as considered in this contribution), this simply amounts to replicating the original termination impedances on the additional conductors. On the other hand, no replication is required for independent sources. Readers are referred to [3] for the derivation of SPICE stochastic models for linear lumped elements.

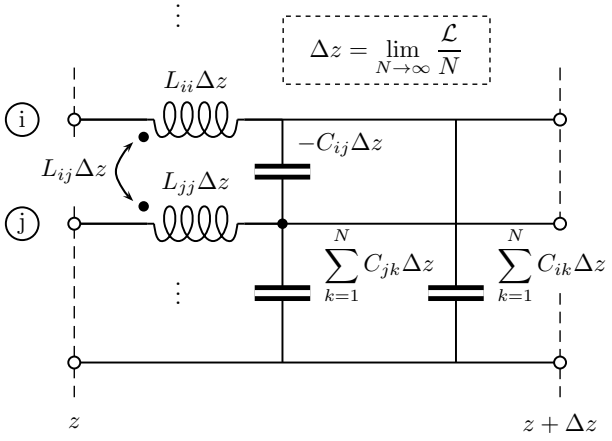


Figure 3: Per-unit-length equivalent circuit for multiconductor transmission lines.

5. Uncertainty in the Interconnect Length

The advocated stochastic models can take into consideration any variation in the p.u.l. parameters, i.e., in the interconnect cross-section. Nonetheless, they can be adapted to account also for uncertainties in the interconnect length, whose inclusion is of paramount importance when the routing decisions are not a priori known [7].

Figure 3 shows the p.u.l. equivalent circuit describing telegraph equations, whose solution is bound to the computation of the chain-parameter matrix (7). From both Fig. 3 and (7), it is clear that in principle nothing changes if $\mathbf{L}$, $\mathbf{C}$ and $\mathcal{L}$ are replaced by $\mathbf{L}' = \mathbf{L} \cdot \mathcal{L}$, $\mathbf{C}' = \mathbf{C} \cdot \mathcal{L}$ and $\mathcal{L}' = 1$ m, respectively. Yet, thanks to this definition, variations of the length $\mathcal{L}$ can be associated to $\mathbf{L}'$ and $\mathbf{C}'$, that act as the p.u.l. parameters of an equivalent line of length 1 m.

As an example, if the random interconnect length can be expressed by means of the following series

$$\mathcal{L} = \mathcal{L}_0\phi_0(\xi) + \mathcal{L}_1\phi_1(\xi) + \ldots, \qquad (29)$$

it is possible to study the equivalent line whose random p.u.l. parameters are given by

$$\begin{aligned} \mathbf{L}' &= (\mathbf{L}\mathcal{L}_0)\phi_0(\xi) + (\mathbf{L}\mathcal{L}_1)\phi_1(\xi) + \ldots \\ \mathbf{C}' &= (\mathbf{C}\mathcal{L}_0)\phi_0(\xi) + (\mathbf{C}\mathcal{L}_1)\phi_1(\xi) + \ldots \end{aligned} \qquad (30)$$

which are analogous to (1). Therefore, the same procedure described in Section 3 can be used.

In the general case, i.e., when the p.u.l. parameters are random themselves and also expressed according to (1), the following relations can be used to determine the expansion coefficients of the equivalent p.u.l. parameters $\mathbf{L}'$ and $\mathbf{C}'$:

$$\begin{aligned} [\ldots, \mathbf{L}'_k, \ldots]^T &= \tilde{\mathbf{L}}[\ldots, \mathcal{L}_k \cdot \underline{\underline{\mathbf{I}}}, \ldots]^T \\ [\ldots, \mathbf{C}'_k, \ldots]^T &= \tilde{\mathbf{C}}[\ldots, \mathcal{L}_k \cdot \underline{\underline{\mathbf{I}}}, \ldots]^T, \end{aligned} \qquad (31)$$

where $\underline{\underline{\mathbf{I}}}$ denotes the identity matrix, while $\tilde{\mathbf{L}}$ and $\tilde{\mathbf{C}}$ are the augmented parameters associated to the original line.

6. Applications and numerical results

In this section, the proposed technique is applied to the analysis of two different PCB structures. Both frequency-domain and time-domain simulations are presented, carried out by means of both MATLAB and SPICE.

6.1. Structure #1

In this section, the proposed technique is applied to the analysis of the structure of Fig. 1, where the transmission lines are 5-cm long and have the cross-section of Fig. 2 with the following nominal parameters: $w = 100\,\mu$m, $d = 80\,\mu$m, $h = 60\,\mu$m, $t_k = 35\,\mu$m, $\varepsilon_r = 3.7$. The values of the connector parameters are $L = 3$ nH and $C = 0.4$ pF. The line is excited by ideal linear drivers (one active and one off), whose equivalent series impedances are $Z_{S1} = Z_{S2} = 25\Omega$ and $Z_{L1} = Z_{L2} = sC_L$, being $C_L = 10$ pF.

The randomness is provided by the substrate parameters, i.e., h and ε_r, that are considered to be the same for both the transmission lines, as well as by the lumped capacitance C. These parameters are considered as three independent Gaussian random variables with a relative standard deviation of 10%. The total number of terms $P + 1$ (corresponding also to the magnification of the size with respect to the original system) is given by

$$P + 1 = \frac{(p + n)!}{p!n!}, \tag{32}$$

where n is the number of random variables and p is the order of accuracy, that represents the maximum degree of the polynomials used for the expansion.

The approximate relations given in [8] were used to numerically compute the PC expansion of the p.u.l. parameters of the coupled microstrips, whereas the expansion of the CPM for the lumped block is analytically obtained from (15).

In the first example the structure is analyzed in frequency domain. Figure 4 shows the transfer functions between the voltage source and the two right-end terminations. The black thick lines represent the response of the structure for the nominal values of its parameters, while the thinner black lines indicate the limits of the $\pm 3\sigma$ bound (σ being the standard deviation) determined from the results of the proposed technique. Finally, a qualitative set of 100 MC simulations is plotted using gray lines. Clearly, the parameter variations lead to a spread in the transfer function, that is well predicted by the estimated 3σ limits.

Often the knowledge of the standard deviation represents a limited information, since the quantitative information about how the values are distributed is missing. Nonetheless, from the analytical PC model we can also obtain the probability density function of the system responses. Figure 5 compares the PDFs of $|V_{d2}/E_1|$ computed at three different frequencies by means of the PC technique with those generated after 40,000 MC simulations. The frequencies correspond to the dashed vertical lines shown in Fig. 4.

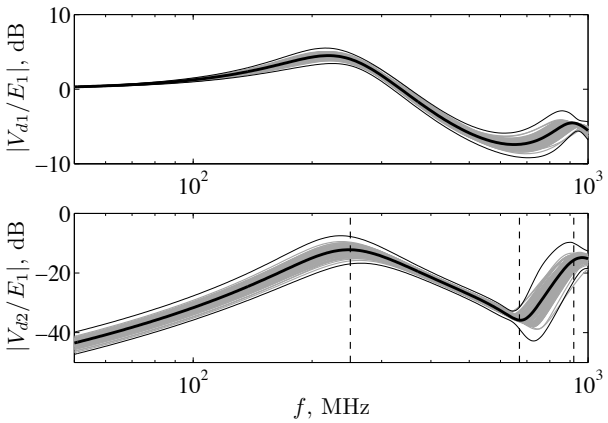


Figure 4: Magnitudes of $|V_{d1}(j\omega)/E_1(j\omega)|$ and $|V_{d2}(j\omega)/E_1(j\omega)|$ for the variability of substrate parameters and connector capacitance. Solid black thick line: deterministic response; solid black thin line: $\pm 3\sigma$ limits of the third-order PC expansion; gray lines: a sample of responses obtained by means of the MC method (limited to 100 curves, for graph readability).

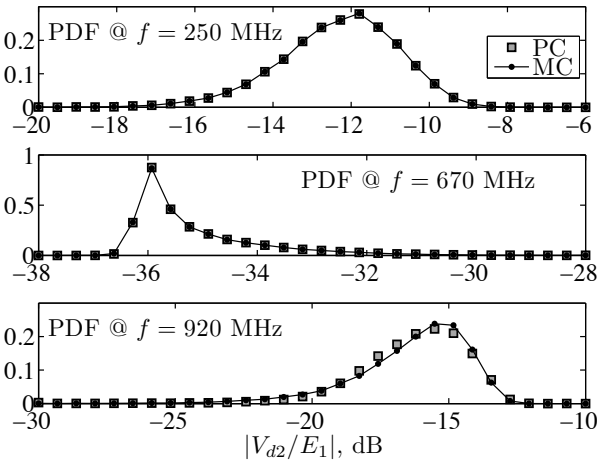


Figure 5: Probability density function of $|V_{d2}(j\omega)/E_1(j\omega)|$ computed at different frequencies. The distributions marked MC refer to 40,000 MC simulations, whereas those marked PC refer to the response obtained via a third-order PC expansion.

The good agreement between the actual and the predicted PDFs and, in particular, the accuracy in reproducing the tails and the large variability of non-Gaussian shapes of the reference distributions, confirm the potential of the proposed method. For this example, it is also clear that a PC expansion with order 3 (i.e., $P + 1 = 20$) is already accurate enough to capture the dominant statistical information of the system response.

Figure 6 shows the results for a time-domain analysis

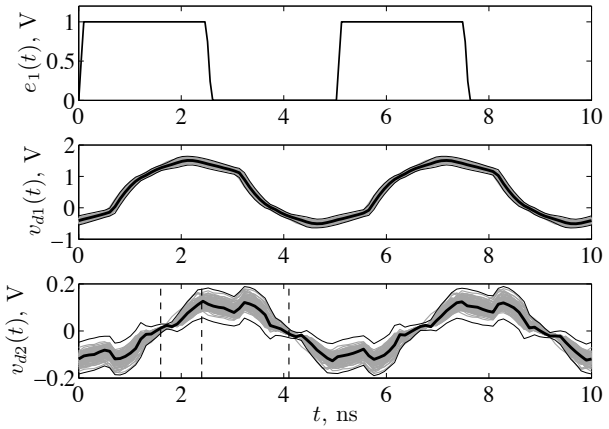


Figure 6: $v_{d1}(t)$ and $v_{d2}(t)$. Solid black thick line: deterministic response; solid black thin line: $\pm 3\sigma$ limits of the third-order PC expansion; gray lines: a sample of responses obtained by means of the MC method (limited to 100 curves, for graph readability).

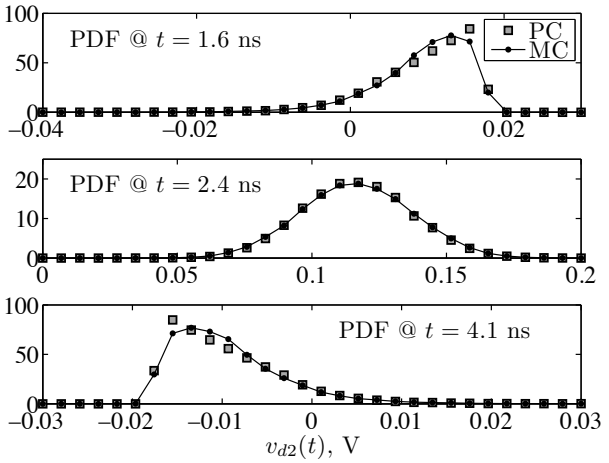


Figure 7: Probability density function of $v_{d2}(t)$ computed at different time points. The distributions marked MC refer to 40,000 MC simulations, whereas those marked PC refer to the response obtained via a third-order PC expansion.

on the same structure. In this case the time-domain voltage source $e_1(t)$ is a trapezoidal wave with an amplitude of 1 V, rise and fall times of 100 ps, duty cycle 50% and total period of 5 ns. Harmonic superposition with $N = 30$ harmonics is considered for the calculations. Figure 7 shows the PDFs computed at three time points, analogously to what was done for the frequency-domain analysis. Again, a PC expansion with 20 terms is accurate enough.

Finally, Tab. 1 collects the main figures regarding the efficiency of PC method. The reported times are referred to the quantitative stochastic simulation of the structure of Fig. 1, which is performed within MATLAB both in time and frequency domain. For fairness, the table includes also the overhead introduced by PC due to the building of the augmented matrices. Nevertheless, the speed-up observed is over two orders of magnitude.

Table 1: CPU time required by the stochastic simulation of the structure of Fig. 1 by means of the MC and of the proposed PC-based method.

Method	Order	Simulation time	Speed-up
Time domain			
MC	–	2 h 15 min	–
PC	3	11.9 s	680×
PC	4	24.9	325×
Frequency domain			
MC	–	14 min	–
PC	3	5.9 s	140×
PC	4	7.5	110×

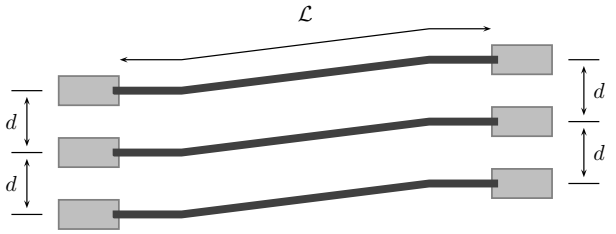


Figure 8: Interconnect geometry for the proposed application #2.

6.2. Structure #2

Layout and routing uncertainties may significantly affect signal integrity in interconnects at the package and board level as well [7]. Let us consider the geometry in Fig. 8, that represents the wiring between two components on the same substrate. The cross-section of this microstrip interconnect is shown in Fig. 9. Several sources of uncertainty may be present. First, routing decisions as well as the displacement between the two components impact on the interconnect length. For high-speed applications, the general trend is to minimize the path in order to avoid degradations. Therefore, a variation in the range 5 ± 0.5 cm is a reasonable assumption. In the example of Fig. 8, a second source of uncertainty is provided by the pad pitch for the two components, that in fact defines the trace separation. In this application, it is supposed to vary in the range 2.5 ± 1 mm. Finally, a fine control of the substrate properties is sometimes prohibitive, depending on the process technology. For instance, variations of the permittivity in the range 4.5 ± 0.25 are likely to be expected. These three sources of variation represent an example of the most influential that can be expected in a problem like the one sketched in Fig. 8. All the remaining parameters are considered to assume fixed values, i.e., $w = 1$ mm, $h = 0.2$ mm and $t_k = 0.03$ mm.

In order to validate the flexibility of the proposed approach, a SPICE polynomial chaos model for the interconnect in Fig. 8 is created that accounts for the aforementioned variations, which are all considered as uniform. As such, Legendre polynomials represent the optimal choice

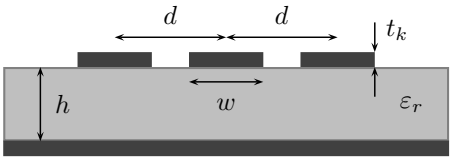


Figure 9: Microstrip cross-section for the interconnect in Fig. 8.

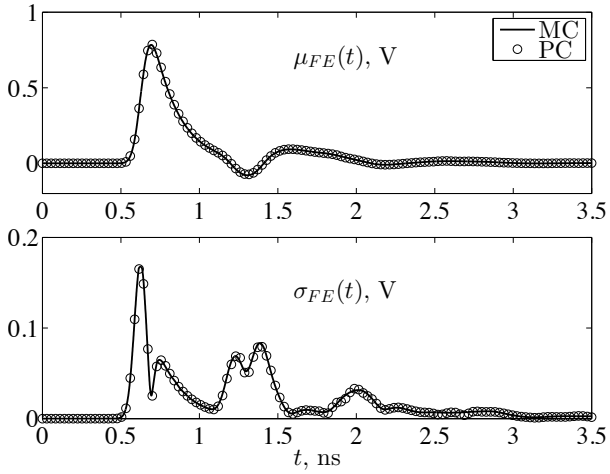


Figure 10: Mean value (top panel) and standard deviation (bottom panel) of the voltage transmitted at the far end of the middle trace, computed with both MC and PC.

for the basis $\{\phi_k\}$. First, a transient simulation is performed. The center trace is driven at the near-end side with a current source in shunt connection with a 50-ohm resistance. The source waveform is a Gaussian pulse of peak amplitude of 0.1 A, occurring at about $t = 320$ ps, and 3 dB width of about 60 ps. All the other terminations are RC loads with a 50-ohm resistance and a capacitance of 10 pF. Figure 10 shows the mean value and the standard deviation for the signal propagated at the far-end side $v_{FE}(t)$, computed with HSPICE both from the PC model and by means of 10,000 simulations carried out with the available MC feature. Figure 11 shows the PDF of the far-end crosstalk $v_{FEXT}(t)$ computed at $t = 650$ ps instead. Of the two PC curves, the one marked (ii) is computed by increasing the expansion order from 2 to 3 w.r.t. the one marked (i), thus showing that the number of terms can be effectively increased to achieve a better accuracy.

A frequency sweep is also performed for the structure under consideration. In this case, the transient current source is replaced by a phasor with amplitude 1 A and phase zero. All the other parameters are left unchanged. The interconnect system is simulated up to 5 GHz. Mean value and $\pm 3\sigma$ estimations are reported in Fig. 12 for the far-end crosstalk. A set of MC responses is included as well, thus confirming that the 3σ bound provides a valuable information about the spread of the response. Figure 13 shows a PDF of the signal propagated on the driven trace instead.

Finally, Tab. 2 collects the computational times and the

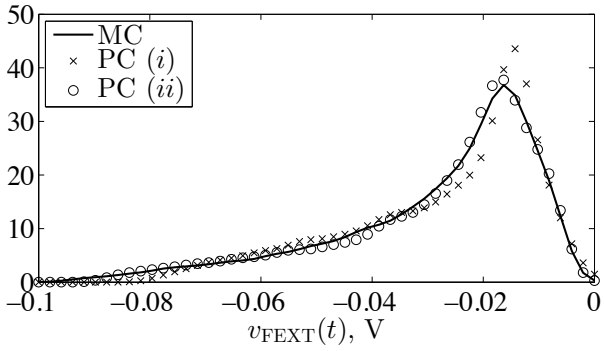


Figure 11: PDF of far-end crosstalk at $t = 650$ ps, computed with both MC and PC. In the latter case, two models with different accuracy were used.

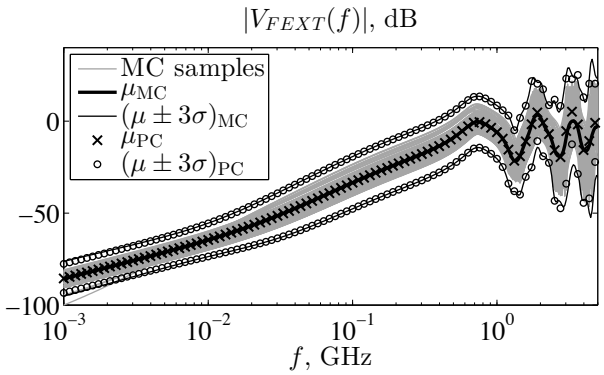


Figure 12: Far-end crosstalk. Solid black lines: mean value (thicker one) and $\pm 3\sigma$ limits (thinner ones) computed with MC; crosses and circles: mean value and $\pm 3\sigma$ limits obtained from the PC model; gray lines: a sample of responses obtained by means of MC method (limited to 100 curves for graph readability).

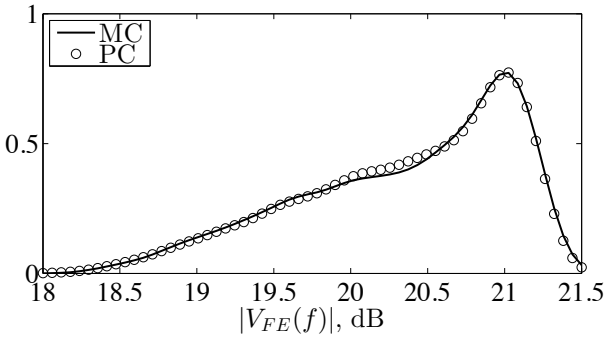


Figure 13: PDF of the far-end transmission (on the middle trace) at $f = 2.5$ GHz, computed with both MC and PC.

memory required by the simulations. From these results it is clear that PC allows to obtain the same information as MC, with comparable accuracy but a great efficiency improvement.

7. Conclusions

This paper addresses the uncertainty-aware analysis for the design of realistic board-level interconnections. The proposed approach is based on the expansion of the governing equations onto a basis of orthogonal polynomials. The result is a modified model that inherently takes possible random variations of the interconnect parameters into account. Nonetheless, the generated stochastic models can be implemented and solved into standard circuit analysis tools such as SPICE. The method offers comparable accuracy and improved efficiency with respect to alternate methods like Monte Carlo simulations. Two realistic application examples involving high-speed PCB links are used to demonstrate the feasibility and strength of the approach.

Table 2: CPU time and memory required by the HSPICE simulations by means of the MC feature or the proposed PC-based method.

Method	Simulation time	Memory usage	Speed-up
Time domain			
MC	16 min	8554 kb	–
PC (i)	5 s	1947 kb	190×
PC (ii)	50 s	8155 kb	19×
Frequency domain			
MC	10 min 48 s	163 kb	–
PC	3 s	8146 kb	210×

References

[1] D. Xiu, G. E. Karniadakis, The Wiener-Askey Polynomial Chaos for Stochastic Differential Equations, *SIAM Journal of Sci. Computation* 24(2): 619–622, 2002.

[2] I.S. Stievano, P. Manfredi, F.G. Canavero, Parameters Variability Effects on Multiconductor Interconnects via Hermite Polynomial Chaos, *IEEE Trans. Comp. Pack. & Man. Tech.* 1(8): 1234–1239, 2011.

[3] P. Manfredi, I.S. Stievano, F.G. Canavero, Alternative SPICE Implementation of Circuit Uncertainties Based on Orthogonal Polynomials, *Proc. 19th IEEE Conf. Electri. Perfor. Electron. Pack. Sys.*, San Jose, CA, U.S.A., pp. 41–44, 2011.

[4] R.G. Ghanem, P.D. Spanos, *Stochastic Finite Elements. A Spectral Approach*, Springer-Verlag, New York, 1991.

[5] A. Papoulis, *Probability, Random Variables and Stochastic Processes*, McGraw-Hill, New York, 1965.

[6] C.R. Paul, *Analysis of Multiconductor Transmission Lines*, Wiley, New York, 1994.

[7] A. Rong, A.C. Cangellaris, Interconnect Transient Simulation in the Presence of Layout and Routing Uncertainty, *Proc. 19th IEEE Conf. Electri. Perfor. Electron. Pack. Sys.*, San Jose, CA, U.S.A., pp. 157–160, 2011.

[8] B.C. Wadell, *Transmission Line Design Handbook*, Artech House, Boston, 1991.

Statistical Uncertainty Budget in a Reverberation Chamber

Philippe Besnier, Christophe Lemoine, Abdou Khadir Fall

Université Européenne de Bretagne, INSA, IETR, UMR CNRS 6164,
20 avenue des buttes de Coësmes F-35708 RENNES, France
*corresponding author, E-mail: philippe.besnier@insa-rennes.fr

Abstract

This communication deals with the a priori estimation of the statistical uncertainty budget in a reverberation chamber. Under the assumption of an ideal random field, given a sample of N independent measurements, the theoretical performance of a stirring process is defined from the starting point of the acquisition identically and independent measurement data . However, in a real reverberation chamber, there is no proof for independence of individual measurements although we may check for correlation within data. A direct method may consist in quantifying the empirical uncertainty of the statistical first moment. According to the central limit theorem, this follows a gaussian probability density function. In fact, given an appropriate estimation of the standard deviation of the estimation of the moment of the parent distribution, thus uncertainty budget may be evaluated. This paper discusses some experiment results that deals with either frequency stirring or mechanical stirring procedures. These measurements tends to prove that frequency stirring is an easier way to provide as many independent measurements as anticipated from correlation analysis between consecutive realizations (frequency steps) . However, mechanical stirring may not operate with the same efficiency.

1. Introduction

Reverberation chambers are nowadays used for many applications ranging from EMC measurements (immunity testing) to Radio Frequencies applications. A reverberation chamber operates as an oversized electromagnetic cavity where some modifications of the boundary ce onditions and/or excitation are able to drastically modify the field distribution in a quasi-random way [1][2] . Finally, a reverberation chamber measurement is based on the post-processing of a set of currents, voltages measured in one or different places in the working volume of the chamber. Post-processing techniques consist in providing a statistic of this sample which is mainly obtained through a selected stirring procedure. The stirring process must be good enough to provide a stochastic sequence of measured values. Thus, in principle, if one gets a sample of size N_{iid} made up of statistically independent measurements the theoretical uncertainty budget may be determined. As far as the first moment estimation is concerned, it follows the central limit theorem [3]. As predicted from the plane wave spectrum theory, the underlying probability density functions (pdfs), at least in a well-oversized cavity, is either gaussian or that of a combination of normal (Gaussian) independent variables depending on the physical parameter under investigation. Numerous experimental results confirm this prediction of the plane wave spectrum theory. For example, a rectangular projection of the electric field follows a Rayleigh distribution. Therefore, the estimation of the first moment of this projection would be given by :

$$\widehat{E} \sim p_{Norm}(\mu, \frac{\sigma}{\sqrt{N_{iid}}}) \tag{1}$$

where μ and σ are, respectively, the moment and the standard deviation of the underlying Rayleigh distribution , in this case related to each other as $\sigma \approx 0,52\mu$ and p_{Norm} is the pdf of a Gaussian distribution.

Therefore, in a well oversized reverberation chamber the statistical uncertainty budget would be only dependent on the size sample, N_{iid}. This sample may be obtained through any stirring process (mechanical stirrer, frequency hopping or receiver/transmitter stirring) or a combination of these. The common method for choosing an adequate stirring process is to check that measurements are uncorrelated. In practice, given a reasonable estimation of the correlation among individual measurements, one checks that correlation is not detected [4]. However, even a very residual correlation has been proved to break the rule given by (1) [5]. Last but not least, in case we could claim that correlation observed through a given correlation operator does not exist, it is only a necessary condition for independence, but it does not prove independence. In the case of a mechanical stirrer, we may suspect that a correlation operator would not be sensitive to some types of correlation that may appear between non adjacent positions of the stirrer [6]. The limited density of propagating modes may support this hypothesis. This paper discusses two correlation models and then introduces a discussion about some experimental results aiming at determining the uncertainty budget of the ensemble average estimation.

2. Correlation models and effective sample size

Analysis of the correlation between individual realizations of a given sample is not by far en easy process. The relationship between correlation and the various physical parameters of a reverberation chamber is not well known. Various hypothesis may be considered. The stirring process

suggests that there are at least two types of correlations. A well known factor for correlation is due to an unsufficient modification of the boundary conditions of the electromagnetic field between consecutive stirrer positions, frequencies of operation, or movement of a transmitter/receiver in the RC. Correlation for these various stirring processes may be studied through a model of correlation that supposes that equal changes induce equal correlations. It's obviously a rough approximation that may be not always consistent for example with any mechanical stirrer geometry and shape. Once the consecutive correlation between realizations is made negligible, the question of correlation is bound to the fact that the random properties of the RC are related to the number of modes involved in the stirring process. Then, a set of realizations yield to partially correlated data. This suggests a simple hypothesis of a residual and maybe uniform or average correlation.

The following subsections provide a quick analysis of these two correlation models, i.e., the uniform residual correlation and the persistent correlation between consecutive realizations. Note that these models do not exclude each other.

2.1. Variance of the average estimation of independent data

We start with $X = (X_1, X_{2,}..., X_{n-1}, X_N)$ a sample of size N individual measurements in a reverberation chamber. In the following development, one is interested to estimate the variance of $\hat{\mu}$ w hich is the estimation of the first moment. The variance of this estimator is indeed an indication of the statistical uncertainty budget in the reverberation chamber according to (1).

The variance of this set of data is given by :

$$var(\sum_{i=1}^{N} X_i) = \sum_{i=1}^{N} var(X_i) + 2 \sum_{i \leq 1 < j \leq N}^{N} cov(X_i, X_j) \tag{2}$$

If data are supposed independent, they are therefore uncorrelated. Thus, the variance of the estimation of the first moment, $\hat{\mu}$ is given by :

$$var(\hat{\mu}) = var(\frac{1}{N} \sum_{i=1}^{N} X_i) = \frac{1}{N^2} N\sigma^2 = \frac{\sigma^2}{N} \tag{3}$$

where $\sigma^2$is the variance of the random variable X. This is the best performance one might expect from a set of N measurements is a reverberation chamber.

2.2. Variance of the average estimation. Uniformly correlated data

In case of uniformly correlated data, we define the autocorrelation function ρ_u as :

$$\rho_u = \frac{cov(X_{i,}X_j)}{\sigma^2} \; \forall i, j \; i \neq j \tag{4}$$

In that case, the variance of the estimation of the first moment becomes :

$$var(\hat{\mu}) = \frac{\sigma^2}{N}(1 + (N-1)\rho_u) \tag{5}$$

Thus, for a large value of N, i.e. $N \gg \frac{1}{\rho_u}$, one gets :

$$var(\hat{\mu}) \to \sigma^2 \varrho_u \tag{6}$$

Even a low residual correlation causes a limit in the reduction of the uncertainty budget of the estimation of $\hat{\mu}$. This result was mentionned in a recent communication [5] as a possible cause of unexpected uncertainties in reverberation chamber measurements depending on the stirring process under investigation.

2.3. Variance of the average estimation. Persistent correlation between consecutive realizations

This correlation model applies only if the sample is collected and ordered in such a way that the consecutive realizations are performed with small changes in the boundary conditions in the reverberation chamber. Its means the collection consists of a set of consecutive mechanical stirrer positions or consecutive frequencies (electronic stirring). This may applied to detect the maximum performance of the stirring process and provides an indication of the minimum change of angle or frequency that has to be made, at a given central frequency of operation of the chamber. It suggests also that the correlation between consecutive data is somewhat uniform within the sample.

Suppose that the correlation is reduced to the first order autoregression model below :

$$X_i = \rho_c X_{i-1} + \epsilon_t \tag{7}$$

In this expression ρ_c is the correlation coefficient between two consecutive data and ϵ_t is an independant and identically distributed random variable called the innovation . This innovation follows the following stationarity condition and therefore, $var(X_i) = \sigma^2$ still holds.

$$var(\epsilon_t) = (1 - \rho_c^2)\sigma^2 \tag{8}$$

From equation (7)The covariance $cov(X_i, X_{i-1})$ is given by :

$$cov(X_{i,}X_{i-1}) = cov(\rho_c X_{i-1} + \epsilon_t, X_{i-1}) = \varrho_c \sigma^2 \tag{9}$$

Moreover, the first order autoregression model also yield to the following relation between data at a distance p from each other :

$$cov(X_{i,}X_{i-p}) = \varrho_c^p \sigma^2 \tag{10}$$

From equation (2) and given the relationships (9) and (10) we obtain :

$$var(\sum_{i=1}^{n} X_i) = N\sigma^2 + 2N\sigma^2 \sum_{p=1}^{N-1} \varrho_c^p \tag{11}$$

If we suppose $\varrho \ll 1$ we find :

$$var(\hat{\mu}) = \frac{\sigma^2}{N}\frac{(1+\rho_c)}{(1-\rho_c)} \tag{12}$$

We can eventually define an effective sample size such as :

$$N_{ESS} = N\frac{1-\rho_c}{1+\rho_c} \tag{13}$$

This relationship of the effective sample size in equation (13) was previously established on the only basis of the properties of the autoregression model hypothesis and was also proposed for the second order autoregression model for higher values of correlation [4].

3. Statistical uncertainty evaluation from measurements.

From the previous developments a main question arises. Is it possible to check for the effective sample size of the sample that was measured given a stirring process ? As already mentionned, a measurement in a reverberation chamber is the result of an estimation, that of the first moment for example. And this estimation behaves as in equation (1). Given of sufficient number of M samples of size N_{iid} (either its real size in the optimum case or its equivalent size) the estimation of the standard deviation $\hat{\sigma}_\mu$ among the M estimation of $\hat{\mu}$ should result to a value close to $\sigma/\sqrt{N_{iid}}$. Therefore, we would find :

$$\hat{N}_{iid} = \frac{\sigma^2}{(\hat{\sigma_\mu})^2} \tag{14}$$

In principle, it's therefore possible to get an empirical estimation of the effective sample size from a sufficienlty accurate estimation of standard deviation of the moment estimation (ensemble average). It requires however that the number M of samples reach at least a hundreed to get a rough estimation and more than a thousand to get an estimation of $\hat{N}_{iid}$ within a few percents. An observation of the cdf obtained from a hundreed estimation of $\hat{\mu}$ enables to get a picture of the result as well.

The following experiments aim at providing some examples of results obtained for two types of stirring methods. The first experiment investigates the efficiency of the frequency strirring method while the second experiment investigates the efficiency of the mechanical stirring method.

Both experiments were carried out within the IETR reverberation chamber (8.7 m x 3.7m x 2.9 m) at a central frequency of operation of 700 MHz, well above the lowest usable frequency of the chamber. A exponential distribution for the magnitude for the measured power at the terminal of a receiving antenna.

3.1. Measurements in frequency stirring mode

3.1.1. Principle

The frequency stirring procedure is applied over a 20 MHz bandwidth, using N equally spaced frequencies of operation. Therefore, we would like to check that the set of N realizations (or its equivalent sample size N_{ESS} given for example by equation (13)) forming a sample of these measurements at these different frequencies of excitation corresponds to i.i.d.realizations. An individual measurement consists of the power received at the terminal of a receiving log-periodic antenna. The power received at an antenna follows a exponential distribution function for which $\sigma = \mu$.

To get a sufficient amount of samples we make use of M=100 hundreed positions of the stirrer and P=15 receiving antenna positions to estimate $\hat{\sigma_\mu}$ such as :

$$\hat{\sigma}_\mu = \frac{1}{P}\sum_{p=1}^{P}\hat{\sigma}_{\mu,p} \tag{15}$$

with,

$$\hat{\sigma}_{\mu,p} = \frac{1}{M}\sum_{m=1}^{M}\left(\sqrt{\mu_{p,m,}^2 - \left(\frac{1}{M}\sum_{m=1}^{M}\mu_{p,m}\right)^2}\right) \tag{16}$$

and

$$\mu_{p,m} = \frac{1}{N}\sum_{n=1}^{N}X_{p,m,n} \tag{17}$$

$\hat{\sigma}_{\mu,p}$ corresponds to a standard deviation estimated for the antenna position p. This standard deviation is calculated within a sample of M data (stirrer positions) : $\mu_{p,m}$. Each of these $\mu_{p,m}$ represents the ensemble average at the antenna position p and stirrer position m of a set of measurements $X_{p,m,1}, ..., X_{p,m,n}, ..., X_{p,m,N}$ at N equally spaced frequencies within the 20 MHz bandwidth.

3.1.2. Example of results and analysis

As an exemple, we choose first of all $N = 100$ stirring frequencies. The step frequency between two measurements is therefore about 200 kHz. A preliminary analysis of the realizations suggested that the persistent correlation between consecutive realizations is inexistent (i.e. ρ_c is assumed to be null). The effective sample size within this frequency band was also estimated to be 100.

We focus first on an arbitraty position of the antenna, say $p = 1$. Fig. 1 shows the cumulative distribution function of the ensemble averages performed for the M=100 different stirrer positions for this antenna position. The normalized standard deviation to the mean of this sample is calculated to be 0.1088. Applying equation (14) for an exponential distribution leads to estimate $N_{iid} = 84$. Fig.1 compares the theoretical distributions for $N_{iid} = 84$ and $N_{iid} = 100$ with the experimental distribution. We see a slight departure from the N=100 curve in this case.

Looking at another arbitrary position 2 of the antenna, we get a different picture from Fig.2

The corresponding estimation of N_{iid} corresponds to 67 and the departure from N=100 is now much sensitive.

These variations may have two different causes at least. First of all, from an antenna position to another, the random

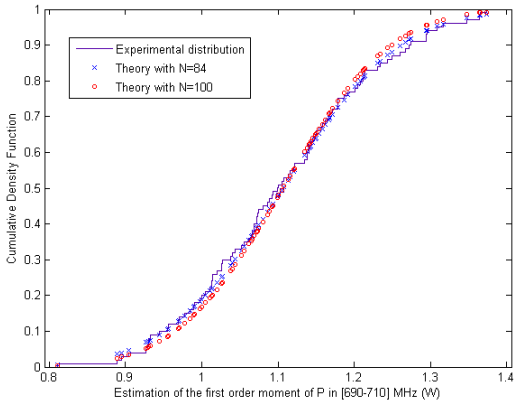


FIGURE 1 – Distribution of the ensemble average sample over M=100 stirrer positions for a frequency stirring performed over N=100 frequencies as observed for antenna position p=1.

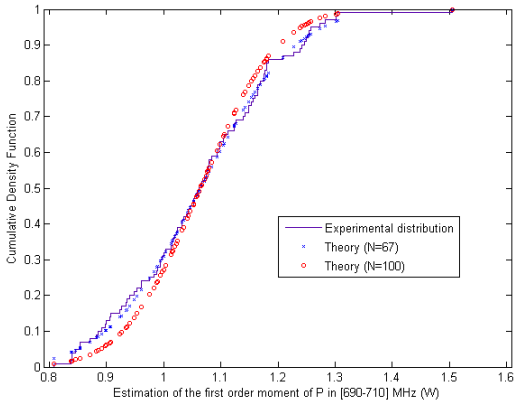


FIGURE 2 – Distribution of the ensemble average sample in the same conditions as in Fig.1 for antenna position p=2.

Antenna position	1	2	3	4	5	6	7	8
N_{iid} from $\hat{\sigma}_{\mu,p}$	84	67	96	108	78	89	89	89
Antenna position	9	10	11	12	13	14	15	$\hat{\sigma}_\mu$
N_{iid} from $\hat{\sigma}_{\mu,p}$	74	80	82	82	81	99	79	84

TABLE 1 – Estimation of the size Niid from the estimation of the standard deviation of the ensembe average for the different positions of the receiving antenna. N=100 stirring frequencies

Antenna position	1	2	3	4	5	6	7	8
N_{iid} from $\hat{\sigma}_{\mu,p}$	95	90	107	114	100	100	127	109
Antenna position	9	10	11	12	13	14	15	$\hat{\sigma}_\mu$
N_{iid} from $\hat{\sigma}_{\mu,p}$	88	89	97	100	115	122	102	104

TABLE 2 – Estimation of the size Niid from the estimation of the standard deviation of the ensembe average for the different positions of the receiving antenna. N=200 stirring frequencies

nature of the electromagnetic field may be slightly different. However, such a factor may not contribute at all, if we consider that electronic stiring provides a very large amount of natural modes within the chamber. Another factor to be considered is the quality of the standard deviation estimation. Tab. 1 gathers the results of all the 15 antenna positions. The average over the 15 positions $\hat{\sigma}_\mu$ yields to the final estimation of $N_{iid} = 84$.

According to this final estimation, it seems that the sample of 100 stirring frequencies thus gives a slightly reduced sample size. Therefore, the sequence of equally spaced frequencies may not offer the optimum choice. Indeed, the effective sample size was estimated with a much larger sample of N=400 frequencies within the same 20 MHz frequency band, using a second order autoregressive model.

In order to check this hypothesis, we choose to double the number of frequencies, N=200. In this situation correlation between consecutive frequencies occurs. The same procedure is then applied and results are reported in Tab. 2. The ensemble of different estimated size for the sample, from an antenna position to another still varies to some extent since the estimation of variance suffers from the still limited size of the samples. However, values are significantly higher than in the case of N=100 stirring frequencies. And the average over the 15 positions $\hat{\sigma}_\mu$ yields to the final estimation of $N_{iid} = 104$. This is now close to the effective sample size as determined from the model of persistent correlation between consecutive frequencies. Further analysis shows that the numbers of table 2 are not significantly modified when choosing higher values for N. As far as frequency stirring operation is concerned, it can be concluded that the effective sample size as determined from this correlation model is consistent enough with measurements.

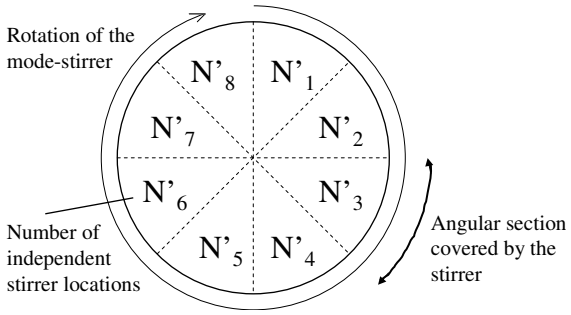


FIGURE 3 – Subdivision of the stirrer in 8 sectors and corresponding independent N_i' realizations estimated from experiments

Sector of the stirrer	Estimation of the sample size
1	14
2	14
3	15
4	14
5	13
6	15
7	16
8	13
Total	114

TABLE 3 – Size of the equivalent iid sample for each each of 8 sections of the stirrer

3.2. Mechanical stirring mode

As far as mechanical stirring is concerned the same set of data is used. Frequencies and stirrer positions play each other role. N is now the number of stirrer positions, and the purpose of the analysis is to check that the stirrer provides an effective sample size as close as possible to the one calculated from equation (13). The estimation of the effective sample size was $N_{ESS} = 130$.

Here we call N the number of independent samples given by the central limit theorem, among the N = 400 locations of the mode-stirrer. We have estimated using autoregressive models that, at 700 MHz, there are 130 uncorrelated positions of the mode stirrer over 360.

Estimation of $\hat{\sigma}_\mu$ requires a different approach, the standard deviation of the estimated average over the stirrer positions has to be performed on the antenna positions first. Then the normalized average standard deviation is averaged over all frequencies.

After these operations, we find that the equivalent size of the sample equals 80. Therefore, $N_{iid} = 80$ equivalent independent realizations instead of the expected size $N_{ESS} = 130$ corresponds to a significant shift of the standard deviation to mean ratio. Therefore, for mechanical stirring, having uncorrelated consecutive realizations may not necessarily imply that these realizations are strictly independent.

In order to deepen this assumption, we propose to make the same analysis, but dividing the complete rotation of the mode stirrer into several angular subsections as shown in Fig. 3.

The procedure is then repeated independently for each of these 8 sectors. Tab. 3 provides the estimation of the equivalent sample size for each one. Two conclusions may be established. First of all, the hypothesis of a somewhat uniform spreading of the independant positions over the entire rotation of the stirrer seems to be a reasonable assumption. This conclusion holds only for this specific stirrer and may also be expected since the chamber is well overmoded.

However, the most important observation to be made, is that the sum of each sector of the stirrer provides a higher total (114), than the effective sample size provided by analysis of the full rotation of the stirrer (80). This result indicates that a residual correlation may exist among stirrer positions. If such a residual correlation follows a uniform correlation model, equation (6) states that the effective sample size reaches a floor value. Analysing 1/8th revolution of the stirrer provides a far less number of independent realizations not yet hidden by the residual correlation. These results seem therefore to be well in line with some recent works [5].

A further simple analysis may confort this idea. Supposing that the effective sample size for the complete stirrer position is the one provided by a residual correlation according to equation (6) . Let's recall that our estimation for this effective sample size was $N_{ESS} = 130$. This sample size may be considered as a set of measurement without consecutive correlation. We may therefore estimate this residual correlation from the difference between the theoretical sample size $N_{th} = 130$ and the estimated sample size $N_{est} = 80$ using equation (5) :

$$N_{est} = \frac{N_{th}}{1 + (N_{th} - 1)\varrho_u} \tag{18}$$

This yields to $\rho_u = 0.005$. Giving a 1/8th sector of the stirrer rotation, the new theoretical value for N_{th} is 130/8. Applying a second time equation (18), the new estimated N_{est} for one sector of the stirrer becomes 15. This value is found to be coherent with the results of Table3 .

4. Conclusions

The statistical uncertainty budget must be controled in day to day operation of reverberation chambers. The moment estimation is a key parameter for a lot of ensemble average based measurements such as EMI measurements or antenna measurements (efficiency, total radiated power...). Starting from a presupposed maximum available uncorrelated data, one may look for the maximum performance in terms of statistical uncertainty.

This communication presented some possible ways of assessing this performance from a set of many measurements. The empirical uncertainty thus observed is analysed with respect to the theoretical sample size as determined from correlation analysis between individual realizations.

The above results seem to acknowledge that performances of a mechanical stirring and of a frequency stirring in a reverberation chamber may appear as different. In particular, the mechanical stirrer may be not efficient enough to provide as many as independent measurements as expected from an estimation of the effective sample size, if it is calculated from the observation of correlation between consecutive realizations. On the contrary, the performance of a frequency stirring is in line with what is expected from the determination of the effective sample size calculated in the same conditions. A possible explanation of this result is obviously the completely different mode of operation of the chamber. Frequency stirring operation is able to generate numerous propagation modes in a well overmoded chamber and modifies drastically the fields in the chamber. There will be unlikely a stationnary wave not affected by this stirring process. The mechanical stirrer is may be not able to do so, due to possible symetries in his shape and/or the limited number of modes that are sufficiently involved by the stirrer.

References

[1] D.A .Hill, *Electromagnectic fields in cavities. Deterministic an statistical theories*,IEEE press, Series on Electromagnetic Wave Theory,Wiley, 2009.

[2] P. Besnier, B. Démoulin, *Electromagnectic reverberation chambers*, ISTE/Wyley&Sons, August 2011

[3] A. Papoulis, *Probability, Random Variables and Stochastic Processes*,*New York : Mac Graw Hill* 4th edition , 2002.

[4] C. Lemoine, P. Besnier, M. Drissi, *Estimating the effective sample size to select independent measurements in reverberation chamber*, *IEEE trans. EMC*, Vol. 50, No. 2, 227-236, 2008

[5] A. Cozza, *A skeptic's view of unstirred components*, *EMC Europe,* Proc. int. symp. on, 2011.

[6] C. Lemoine, P. Besnier, M. Drissi, *" Evaluation of frequency and mechanical stirring efficiency in a reverberation chamber*, *EMC Europe,* Proc. int. symp. on, 2008.

Sensitivity analysis to compute advanced stochastic problems in uncertain and complex electromagnetic environments

Sébastien Lalléchère[1,2], Basile Jannet[1,2,3], Pierre Bonnet[1,2], Sébastien Girard[1,2], and Françoise Paladian[1,2]

[1]Clermont University, Blaise Pascal University, Pascal Institute, Clermont-Ferrand, 63000, France
[2]CNRS, UMR 6602, Pascal Institute, Aubière, 63177, France
[3]CEA, DAM, Gramat, F-46500 Gramat, France
*corresponding author, E-mail: sebastien.lallechere@univ-bpclermont.fr

Abstract

This paper deals with the advanced integration of uncertainties in electromagnetic interferences (EMI) and electromagnetic compatibility (EMC) problems. In this context, the Monte Carlo formalism may provide a reliable reference to proceed to statistical assessments. After all, other less expensive and efficient techniques have been implemented more recently (the unscented transform and stochastic collocation methods for instance) and will be illustrated through uncertain EMC problems. Finally, we will present how the use of sensitivity analysis techniques may offer an efficient complement to rough statistical or stochastic studies.

1. Introduction

A large set of electromagnetic (EM) problems are currently treated with a very high level of accuracy from numerical and/or experimental devices. Their deterministic design may reveal quite convenient if input data are precisely controlled. Due to the disturbed EM environment where most of the radio systems evolves, the electromagnetic compatibility (EMC) issues are rarely entirely known: from the number of parameters impinging both the sources, victims and/or coupling paths, the deterministic design of the problem appears utopian. In this context, a crucial point relies on our ability to estimate the impact of different Random Variables (RV) on given outputs.

1.1. Stochastic context

The Monte Carlo (MC) formalism remains one of the most spread statistical technique to handle with stochastic treatments. As explained in [1], the MC method needs few requirements on the chosen random output. In an integration approach, this technique is well suited for singular (irregular) kernels and it is not compulsory to access analytic information on their statistical form. The "classical" MC reveals independent of the problem dimension and can be used for many stochastic issues involving a high numbers of RV. Nevertheless, as pointed out in [2], the main disadvantage of MC remains its slow convergence rate. Thus, it may appear computationally prohibitive (even for high-dimensional problems) but is still interesting to access a "reference" result. Finally, the difficulty remains to set the threshold defining the MC convergence level.

Different stochastic techniques have been successfully computed since 2002 in order to give a more realistic view of EM simulations including uncertainties. We may for instance cite the unscented transform (UT) [3, 4, 5] or the "Lagrange" stochastic collocation (SC) [6, 7, 8, 9, 10] methods, the kriging technique [11], the polynomial chaos expansion [12, 13, 14], and the experimental design [15]. Far from appearing as an exhaustive review of stochastic and statistical methods in electromagnetism, the previous quoted techniques were mainly applied to numerical simulations including various EM domains: shielding effectiveness [3, 4, 5, 9], scattering and propagation [6, 9], susceptibility [9, 10, 11, 15] and/or (bio-)EMC/EMI [7, 8, 12, 13, 14] problems.

1.2. Aims and motivations

From domains as environmental modeling, mechanics, safety and reliability, the sensitivity analysis (SA) methods are widely spread from twenty years. We may commonly define the SA for a given physical model as a method used to determine how various values of an independent variable will impact a particular dependent variable under a given set of assumptions. This is typically a deterministic view regarding a mathematical expression as a function of "inputs" that produce "outputs"; deterministic means that the same set of "input" variables gives always the same "output" values. For a considered "output" quantity, the goal is to determine the contributions from "input" and their interactions with the model.

Various objectives are expected from SA: modelling complex and combined phenomena, calibrating "input" parameters, simplifying a model (decreasing the number of variables), organizing the "input" parameters both from qualitative and quantitative points of view. Obviously, this treatment may lead to a better understanding of the studied system, to simplify it and to check its reliability.

Different techniques are available, and we may mention, without exhaustiveness the screening techniques (to access to the most influential inputs among a large number

from coarse sorting), and the variance based sensitivity indices (measures of importance). Thus, both qualitative and quantitative treatments are allowed chosing one of the previous techniques. Another way to present SA methods may be to consider if the sensitivity needs require a local or a global analysis. This is equivalent to consider respectively the linearity hypothesis between "inputs" or to study the interactions between parameters. In the following, we will focus on global analysis.

2. Theoretical principles

This section is dedicated to the theoretical details of the stochastic and SA methods used in this work.

2.1. Notations and approaches

In our models, a stochastic parameter Z will be given from a RV $\hat{u}$ as follows:

$$Z = Z^0 + \hat{u}, \tag{1}$$

where Z^0 is called the initial value (mean) and $\hat{u}$ is characterized by a given statistical distribution law (zero-mean with a certain variance). In the following, the random value Z may represent different kind of parameters: geometrical details, material values , and/or source characteristics.

In this paper, we will consider a model for which an "output" F is a deterministic function of k "inputs" denoted by $u_1, u_2, \dots u_k$. We may sum up the k "inputs" in a row vector $\mathbf{u}$

$$\mathbf{u} = (u_1, u_2, \dots, u_k), \tag{2}$$

and write $F(\mathbf{u})$ the global effect of k "inputs" a priori considered as RV for a computational (analytical and/or numerical) model F.

The aim of this study is to focus on two efficient methods: the UT [3] and the SC [9] techniques. These two previous approaches rely on the same philosophy with the simplicity of MC but faster convergence rates. Their main advantage remains their high precision.

A sensitivity analysis technique widely spread in models of large dimension is the screening design proposed in [16]. It deals efficiently with models containing a lot of input factors and may lead to quick qualitative assessment since the number of model evaluations is linear in the number of model factors. Obviously other techniques may be used with different degrees of accuracy and efficiency to rank RV by influence.

2.2. Stochastic methods fundations

In the following, we will detail theoretical principles considering 1-RV formalism. We may extend it to multi-RV cases without any loss of generality.

2.2.1. UT basis

As explained in [3], the use of the UT method is similar to the MC technique. The main difference relies on the number of realizations needed to obtain the statistical moments of a given output. Thus, instead of several thousands of repetitions, only a few selected ones are necessary.

Some conditions are required to compute UT for a single RV: we may know both the moments of the RV $\hat{u}$ and the nonlinear mapping of the random output ($I(\hat{u})$). Its nth order moment may be expressed as follows

$$\mathbb{E}\{I(\hat{u})^n\} = \int I(u)^n pdf(u) du, \tag{3}$$

where pdf(u) is the probability density function of the RV $\hat{u}$. A discrete equivalent of the relation (3) is used for the integration

$$\int I(u)^n pdf(u) du \approx \sum_i \omega_i I(S_i)^n, \tag{4}$$

where S_i are the so-called sigma points (for the integration). If the nonlinear mapping $I(\hat{u})$ is well behaved, it could be expressed from Taylor polynomial series (g_j coefficients) as

$$\int I(u)^n pdf(u) du = \sum_{j=0}^{\infty} g_j \int u^j pdf(u) du. \tag{5}$$

From the discrete sum (4), each integration term of (5) may be expressed from $k+1$ ($k = 0, 1, 2, \dots$) equations as

$$\int u^k pdf(u) du \approx \sum_i \omega_i S_i^k = \mathbb{E}\{\hat{u}^k\}. \tag{6}$$

The nonlinear system depicted in (6) allows the computation of the sigma points S_i and weights ω_i from the moments of the RV $\hat{u}$. As detailed in [3], the minimum number of S_i points for a given order of the UT technique may be derived using the Gauss quadrature schemes. Indeed, considering (6), the solution is not unique and different sets of (S_i, ω_i) may be obtained as illustrated in the following.

2.2.2. SC foundations

The idea of the technique is to choose a polynomial approximation of a given output I depending on a random parameter Z (1). In a first time, the function $S \rightarrow I(Z^0; S)$ is expanded in Lagrangian basis functions of order n

$$I(Z^0; S) \approx \sum_{i=0}^{n} I_i(Z^0) L_i(S), \tag{7}$$

with $L_i(S) = \prod_{\substack{j=0 \\ j \neq i}}^{n} \frac{S - S_j}{S_i - S_j}$. One of the most interesting properties of the Lagrangian basis relies on its reducing characteristic: $L_i(S_j) = \delta_{ij}$ (Kronecker δ) and we may write $I_i(Z^0) = I(Z^0; S_i)$. Then, the integration computation is

based upon the Gauss quadrature with identical points S_i than the ones previously needed by the SC method

$$\int_D pdf(u)f(u)du \approx \sum_{i=0}^{n} \omega_i f(S_i), \tag{8}$$

where pdf is the probability density function introduced in the previous section. Similarly to the UT case, the real numbers ω_i are called integration weights. From (7), we may detail I with its polynomial approximation

$$\mathbb{E}\left\{I(Z^0;S)\right\} = \sum_{i=0}^{n} I_i(Z^0) \int_D L_i(s)pdf(s)ds \tag{9}$$

From (9), we may straightforward compute weights following

$$\omega_i = \int_D L_i(s)pdf(s)ds. \tag{10}$$

We will detail in the following the statistical moments computation enabled by the pair $(S_i;\omega_i)$.

2.2.3. Computing the sigma points/weights and the statistical moments

Although the UT and SC appear very similar considering the computation of their respective sigma points/weights, they differ from their basis. From the different solutions proposed for the one-variable case, the minimum number of pairs (S_i,ω_i), for a given order n, is straightforward available by the Gauss quadrature scheme (identical to the SC case). Therefore, the expression of the integration points/weights is similar for the UT [3] and SC [8], and the results will be identical.

The collocation technique gives the collocation points (S_i) and weights (ω_i) necessary to compute, for instance, the 1st and 2nd-order statistical moments of the random parameter Z (1).

Table 1: UT/SC computation of statistical moments (1st and 2nd) for the 1-RV case.

Stat. moment	Computation
Mean	$mean(Z) = \sum_{i=0}^{n} \omega_i Z_i$
Variance	$var(Z) = \sum_{i=0}^{n} \omega_i Z_i^2 - [mean(Z)]^2$

From previous notations ($\mathbb{E}(Z)$ for instance), in order to simplify the discussion, the $\langle Z\rangle$ and σ_Z^2 symbols will stand respectively for the mean and variance of the Z output.

The formalism detailled in Tab. 1 is common to the UT and SC methods for single RV. The computation of the sigma points and weights (multi-RV) may be found respectively in [5, 8]. In the following, we will present the numerical differences existing between the UT and SC multivariate results.

2.3. Sensitivity analysis

In early 90's, an approach was proposed by Morris [16] to discriminate the "inputs" of a given modelling (for instance a determined computational relation F). This work aimed to determine which "inputs" had important effects on a given "output". This model is widely used since it is easy to compute and may reveal particularly efficient with models containing hundreds of "inputs". Thus, among the numerous methods available to conduct SA, we use in this paper the method introduced by Morris [16] (see [17, 18] for a review of SA techniques).

The main idea from [16] was, among a large variety of "inputs", to reasonably compute which may be considered negligible, additive and linear, non-linear and/or in interactions with other "inputs". With this objective, a "discretized" approach was originally proposed by Morris. Indeed, the factorial sampling plan proposed in [16] is composed of individual randomizations named "one factor-at-a-time". The elementary influence of the ith "input" is computed for a discrete number of values called "level" (given by the ith factor varying range). Let $\mathbf{u}$ be a given RV vector containing k random "inputs" as depicted in the relation (2). We may set a varying range depicted by their minima and maxima values for each RV respectively u_1^{min}, u_1^{max}, $\ldots$, u_k^{min}, u_k^{max} defining the definition domain Ω. Originally, the sensitivity approach requires to sample p levels for each ith RV through a given δ_i parameter. From [16], the k "inputs" were given over $[0;1]$ range. In this work, we propose an elementary influence criterion c_i, for a given $\mathbf{u}$ value, with δ a predetermined multiple of δ_i

$$c_i(\mathbf{u}) = \frac{F(u_1 \ldots u_{i-1}, u_i + \delta, u_{i+1} \ldots u_k) - F(\mathbf{u})}{\delta} \times \chi_i, \tag{11}$$

where χ_i is a given normalization coefficient depending on the $[u_i^{min};u_i^{max}]$ range. In the following, D_i will stand for the finite distribution of elementary influence criterion c_i ($i = 1,\ldots,k$) obtained from randomly sampling a number n of different $\mathbf{u}$ vectors.

Obvisouly, the choice of δ_i may influence the quantitative results proposed by [16]. Indeed, the number of discrete "levels" $p+1$ given directly represents the sampling sharpness ($\delta_i = \frac{u_i^{max}-u_i^{min}}{p}$). The principle used in [19] requires to uniformly sample the k-dimensional parallelepiped standing for the $\mathbf{u}$ potential values from Ω. Given a number n of starting points, we may define n $\mathbf{u}$-vectors following the simple rule "one-factor-at-time". This means moving from $\mathbf{u} = u_1, u_2, \ldots, u_k$ to $\mathbf{u} + \delta\mathbf{e}_i$, where $\mathbf{e}_i$ is a zero vector with a unit as its ith component. We may ensure that the "translated" point $\mathbf{u} + \delta\mathbf{e}_i$ is still in the definition domain. From an iterative process, we may obtain the discrete D_i distribution from the relation (11).

As explained in [19], each RV is evaluated regarding two distinct measures: μ_i and σ_i, being respectively the estimated mean and standard deviation of D_i. From a practical point of view, it should be better to compute a measure enabling to integrate the potential non-monotonic model

behaviour by defining a rougher criterion. Thus, let μ_i^* stands for the mean of the distribution E_i of the absolute values of c_i parameter. μ_i^* will be more restrictive than μ since D_i may contain elements contrary signed. They may vanished from the influence estimate and lead to erroneously considered corresponding parameters as negligible. Thus, we may write

$$\mu_i = \frac{1}{n}\sum_{i=1}^{n} c_i, \tag{12}$$

$$\mu_i^* = \frac{1}{n}\sum_{i=1}^{n} |c_i|, \tag{13}$$

$$\sigma_i = \sqrt{\frac{1}{n}\sum_{i=1}^{n} (c_i - \mu_i)^2}. \tag{14}$$

Practically, the "Morris" screening design enables to rank RV from a quantitative point of view. It aims to represent the random parameters from a $\{\mu_i$ (or $\mu_i^*)$ / $\sigma_i\}$ representation. A high value of "μ_i" reprents an "input" with a high overall impact. A high value of "σ_i" stands for a parameter highly involved in interaction with other factors. In the following, we will detail results from the μ_i^* criterion. Obviously, different parameters from this screening design technique may impact the reliability and efficiency of treatments. Thus, the sampling sharpness may be a crucial point since the grid used to quantify RV elementary effects may be too coarse. In most cases, the discretization grid is set to $p = 100$ or 1000 levels. In order to improve the reliability of results, the relations (12; 13) are evaluated several times in order to produce a cloud of N points. From a computing efficiency point of view, the "Morris technique" requires $n \times (k+1) \times N$ calls to the computational relation F in order to entirely compute results.

The Morris analysis may be presented throughout an analytical test function f depending on $\mathbf{u} = (u_1, \ldots, u_{11})$

$$f(\mathbf{u}) = u_1 u_2 + \frac{5}{u_3\,(u_{11} + 0.5) + \cos(u_4) + 0.1} + 4u_5^3 + 4u_6 - u_7 + u_8 \exp(u_9) + 0.2u_{10}, \tag{15}$$

with u_i, $i = 1 \ldots 11 \in [0; 1]$. In this case, the initial "Morris" parameters are set following: $n = 10, p = 1000$ and $N = 100$. Thus, the whole process requires $12,000$ calls to analytical function f from the relation (15).

As expected comparing relation (15) and Fig. 1, the u_6, u_7 and u_{10} parameters appear as linear ones and may be set apart. Contrary to other values, u_i $(i = 3, 4, 5)$ ones may not be neglected (inner interactions inside model). Obviously, their characterization only offer a qualitative approach and it is necessary to proceed to a precise and effective quantitative computation to obtain influence orders.

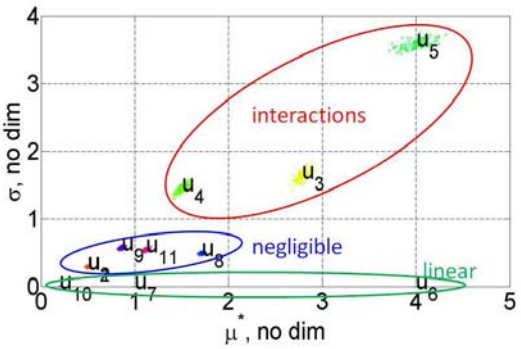


Figure 1: RV ranking from screening design.

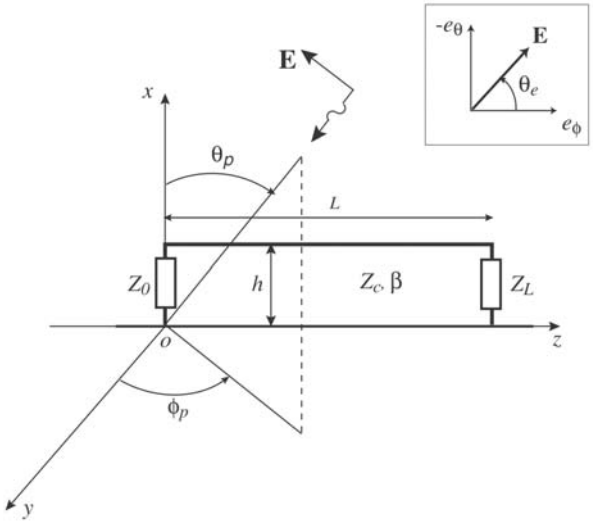


Figure 2: Transmission line illuminated by a plane wave [11].

3. The stochastic EMC issue

3.1. Setup and initial parameters

In this work, the case of a transmission line illuminated by a plane wave with multiple random parameters is used from [11]: attenuation constant α, diameter d, frequency f, length L, height h above an infinite ground plane. The excitation source is a plane wave linearly polarized (Fig. 2). An analytical formulation can be obtained for the current I at load $Z_L = 1k\Omega$ (Z_0 is set to 50Ω), and we may write

$$I = I(L, h, d, Z_L, E_0, \alpha\,, Z_0, f, \theta_p, \theta_e, \phi_p) + I_p, \tag{16}$$

with I_p a randomly distributed disturbing current adding to the formula proposed in [11].

The purpose of adding in (16) the current I_p is to input a linear RV into the global model. Even if the problem appears relatively simple, the complexity, here, comes from the number of RV and there is no use facing straightforward this issue considering MC. Obviously, some sparse

Table 2: Initial sets of parameters for the stochastic study.

Value	L(m)	h(mm)	d(mm)	$Z_L(\Omega)$	E_0(V/m)	α
Min	1.2	8	0.6	996	996	0.
Max	4.5	32	1.4	1004	1004	0.01
Value	$Z_0(\Omega)$	f(MHz)	θ_p(rad)	θ_e(rad)	ϕ_p(rad)	I_p(A)
Min	46	1	-0.3	-0.3	-0.3	0.15
Max	54	50	$+0.3$	$+0.3$	$+0.3$	0.25

grid techniques [12, 20] may improve considerably the efficiency of stochastic techniques but this may reveal quite restricted if, independently, each RV needs not less than 4 or 5 collocation points. The aim of this study is to propose a two-steps work. First, based upon a qualitative analysis, our aim is to rank the RV from their relative effect and to reduce their total number by setting the least influential parameters to deterministic values. Then, the use of stochastic techniques fits well with a quantitative analysis of the parameters sensitivity.

3.2. Stochastic techniques accuracy and efficiency

Since the Taylor polynomial expansion is still usable for two random variables, the UT technique may be used to achieve multivariate stochastic problem. Moreover, as illustrated in [8], the single-variable SC method may be generalized to multi-RV problems. As explained previously, by choosing sigma points from the Gauss quadrature, the UT and SC techniques might appear quite similar with identical integration points and weights. Based upon their distinct foundations, for multivariate case, the different two RV (S_i, ω_i) sets jointly with the different moments computation involve variations around the numerical results.

In this section, we have arbitrarily chosen the line length L and the source frequency f to achieve a stochastic processing of the EMC problem (Fig. 2). The L and f parameters will be both given by two independent RV (respectively $\hat{u}_1$ and $\hat{u}_2$) following a zero-mean normal distribution respectively with variances $\sigma^2_{\hat{u}_1} = 2.083.10^{-4}$ and $\sigma^2_{\hat{u}_2} = 2.083.10^{10}$. From the expression (1), the two random parameters may be written

$$\begin{aligned} L &= L^0 + \hat{u}_1 \\ f &= f^0 + \hat{u}_2, \end{aligned} \tag{17}$$

with L^0 and f^0 the length and frequency means. The Fig. 3 shows how straightforward the current variance may be obtained for a large set of points. The previous random variations are applied to each element of the set ($L^0_i \in D_L = [1.2m; 4.5m]$; $f^0_j \in D_f = [1MHz; 50MHz]$). The SC convergence and the sensitivity of the model are first showed in Fig. 3. The results depicted in Fig. 3 show the convergence of the SC method (from the I variance). Considering the SC accuracy for 3^2 and 5^2 points (respectively SC3 and SC5), the two data sets almost overlap.

In Fig. 4, the results from UT fit very well with the "converged" data from SC. Thus, Fig. 4(a) shows the agreement for $\langle I \rangle$ between SC3 and the approximation from the UT

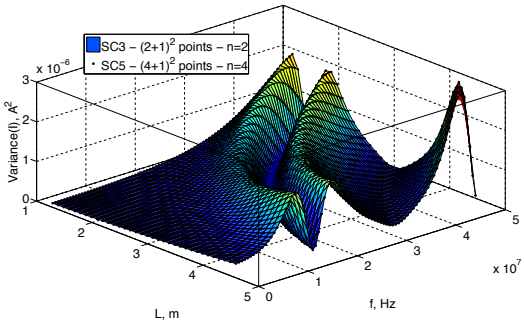


Figure 3: Variance(I) from SC3 and SC5.

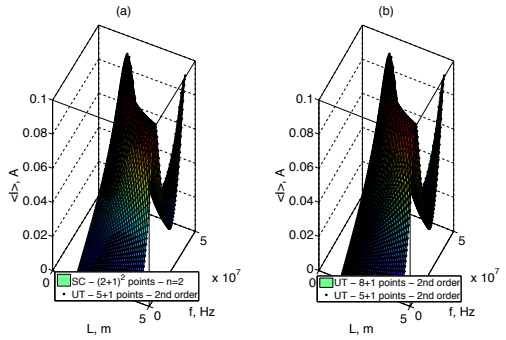


Figure 4: Mean(I) from SC3, UT5 and UT8.

(2nd order) involving $5 + 1$ points (UT5). A great agreement appears also from Fig. 4(b) considering the slight differences existing between a same UT accuracy (2nd order) involving $5 + 1$ or $8 + 1$ points (respectively UT5 or UT8). The UT5 and UT8 differences rely on the non-uniqueness of the solution as detailled in [5].

The accuracy of each stochastic formalism (UT/SC) is defined from MC simulations reference. First, it is necessary to determine a reference set of $\langle I \rangle$ values: empirically, the MC convergence appears for 10^5 realizations. Then, in order to compute the error due to stochastic treatments, a criterion is defined standing for this relative error

$$err_{i,j} = 100 \times \frac{\left| u^{SC/UT/MC}_{i,j} - u^{MCref}_{i,j} \right|}{\left| u^{MCref}_{i,j} \right|}, \tag{18}$$

considering $err_{i,j}$ stands for the relative error for each pair $(L_i, f_j) \in D_L \times D_f$. The reference MC values are given for 10^6 simulations and are depicted previsouly by $u^{MCref}_{i,j}$. $u^{SC/UT/MC}_{i,j}$ represents the elementary (i,j)-value obtained respectively from SC, UT and MC (10^5 realizations).

The Fig. 5 shows the relative error given for the set of points (L_k, f_k) ($k = 1, \ldots, Np$ with Np the total number of length/frequency points). The MC convergence may be considered for 10^5 simulations since the error level remains almost everywhere lower than 0.04% from 10^6 MC realizations. Obviously, the UT/SC time and memory saves ap-

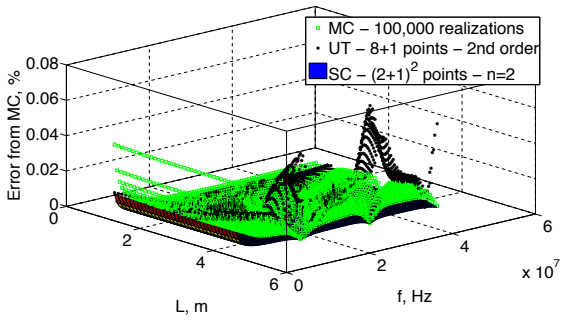


Figure 5: Mean(I) error from reference MC data (10^6 simulations) for MC (10^5 realizations), UT8 and SC3.

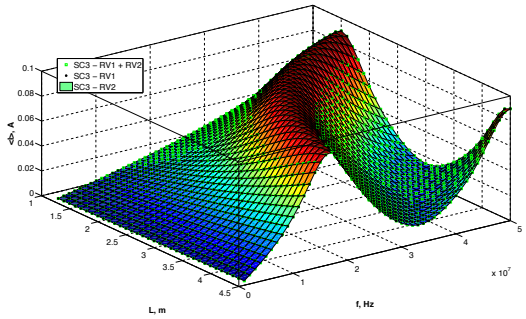


Figure 6: $\langle I \rangle$ from RV_1 and/or RV_2.

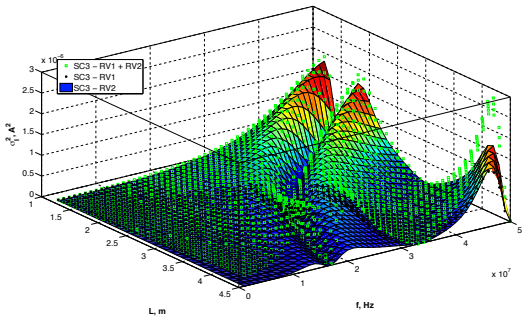


Figure 7: σ_I^2 from RV_1 and/or RV_2.

pear clearly from previous example since the stochastic formalisms need less than 10 realizations compared to the MC technique which requires about 100,000 simulations. In comparison with those MC simulations, the UT/SC curves fit very well and sometimes better precisions are obtained. This perfectly justifies viewing UT/SC as a smart way to proceed to MC. Moreover, for a comparative number of simulations (SC3/UT8 need exactly 9 realizations), the SC method reveals more accurrate than the UT model. Of course, it is possible to improve the UT efficiency by a good choice of the sigma points and weights (and reducing this example to only 6 simulations). The precision levels remain comparable betwen UT and SC but some subdomains show a better accuracy (more than 30 times). The major advantage of SC techniques (high level of accuracy) is clearly illustrated in the Fig. 5.

Furthermore, it would be possible to improve the SC efficiency using techniques from [21] to reduce the number of SC realizations needed, it could be particularly interesting for multivariate stochastic problems involving $4, 5, \ldots$ RV where the SC tensor products lead to some numerical limitations [13]. A numerical problem (and especially a stochastic EMC one) with several RV may appear complex to solve due to the large number of variables. Nevertheless, a solution may be to reduce the number of variables to a minimum regarding their relative influence. Based upon [3], the comparison of results (mean, variance, ...) from one RV simulation with those involving a set of RV provides information on the significant parameters and a view of the model sensitivity.

3.3. Preliminary sensitivity analysis

In this part, we will put the focus on the use of the SC method in order to lead preliminary sensitivity analysis. From previous definition of the multi-RV issue, we may wonder if the straightforward computing of first statistical moments provides information about the relative sensitivity of RV. Thus, arbitrarily choosing L and f parameters, the Fig. 6 shows that $\langle I \rangle$ including RV1 and/or RV2 as random parameters may not allow to distinguish the most influential parameter from the previous 2RV-set. Indeed, very few differences appear between stochastic treatments involving independently RV1, RV2 and combining L and f parameters.

Obviously, similarly to [3], the variance computing from Tab. 1 may provide more reliable results to distinguish properly the most influential parameters. Indeed, regarding the Fig. 7, differences exist between the three characteristic random treatments involving respectively RV1, RV2 and RV1+RV2. Obviously, it is possible to better quantify the influence of each parameter from "relative" error criteria considering the 2-RV problem as a reference. However one issue remains particularly constraining since this work is based upon a rough hypothesis assuming the most relevant parameters are well known. That is the reason why, we will detail, in the following paragraph, how the "classical" SA Morris method may offer a reliable and efficient solution.

3.4. Most influential subset of RV from SA

From previous theoretical aspects and relation (19), the "Morris" influence criterion C_i may be derived from various expressions since the χ_i normalization coefficient has not been defined yet. In the following, we will put the focus on χ_i equivalent to the ith range length

$$\chi_i = u_i^{max} - u_i^{min}, \tag{19}$$

where $[u_i^{min}; u_i^{max}]$ stands for the range of ith RV.

Considering the relation (16), a screening design model [16] enables us to arrange the set of parameters (Fig. 8) by influence. The model parameters are set to $p = 100$

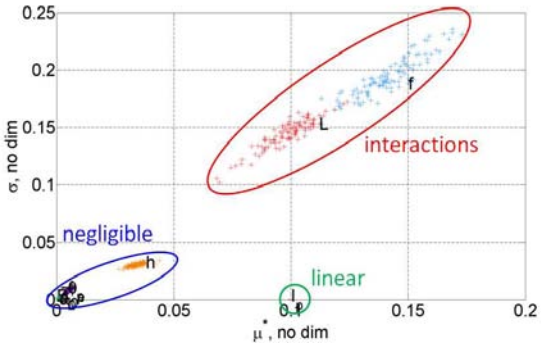


Figure 8: RV ranging from screening design.

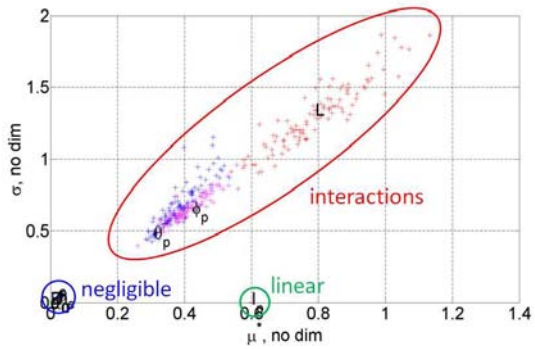


Figure 9: RV ranging from screening design based upon Tab. 3.

sampling levels, $n = 100$ starting points (i.e. 100 **u**-vectors) and $N = 100$ pairs (μ_i, σ_i) in influence clouds ($i = 1, \ldots, k$; $k = 12$ RV). Thus, the impact of the f and L parameters appear quite similar (relatively most influential ones) and some dependency exists between them (physically understandable). Their effect should not be neglected, contrary to most parameters which appear negligible. As expected from (16), the linear "coupling" current I_p may behave linearly to other variables and we may set it apart.

From the Fig. 8, we may conclude that our numerical problem with several random parameters may be characterized by a smaller subset of 2 RV: stimulation frequency f and line length L.

The SA technique required $n \times (k+1) \times N = 130,000$ calls to the analytical formula (16). The global stochastic collocation cost may be evaluated ensuring the convergence of the method (SC3 and SC5), and $50 = (3^2+3*2)+(5^2+5*2)$ calls were necessary. Those $130,050$ realizations may be compared to the 10^6 MC simulations needed considering the two previous RV f and L. A straightforward SC approach would have reavealed useless since 3^12+5^12 calls to the relation (16) would be far less efficient than MC approach. Moreover, the sensitivity study proposed enables lightening the post-treatments since the most influential variables are highlighted as explained in the following.

The SA technique is based upon the initial problem defined. Thus, a different definition of initial RV ranges of variation leads to a distinct issue and involves different results. In this context, we may wonder the quantitative influence effects due to moving initial values from Tab. 2 to Tab. 3.

Table 3: A different set of initial ranges for RV (Fig. 9).

Value	L(m)	h(mm)	d(mm)	$Z_L(\Omega)$	E_0(V/m)	α
Min	2.0	8	0.6	900	996	0.
Max	4.0	32	1.4	1100	1004	0.01
Value	$Z_0(\Omega)$	f(MHz)	θ_p(rad)	θ_e(rad)	ϕ_p(rad)	I_p(A)
Min	46	890	0.0	0.0	0.0	0.2
Max	54	910	1.5	1.5	1.5	0.8

As depicted in Fig. 9, a distinct set of initial parameters ranges will lead to different conlusions from screening design (most influential parameters: incidence direction trough θ_p and ϕ_p angles, and length L). Thus, the definition domain of the **u** random vector appears as a crucial point.

3.5. Quantitative impact of RV

This part illustrates the SC ability to achieve a reliable sensitivity analysis in a random EMC problem. Among all the variables depicted in Fig. 2, we will focus on the line length and frequency excitation. Relying on previous SA, the L and f RV need to be included in the stochastic model (other variables may be set to determinsitic mean values). We may rely on the stochastic techniques (SC and/or UT) to lead a entire sensitivity analysis to quantify the impact of one parameter to another.

An influence criterion was defined in [3] to characterize the sensibility of one RV. Based upon the SC results, a similar parameter is

$$In_{Z_i} = -\log\left(\left|1 - \frac{var\left(I(Z_i)\right)}{var\left(I(Z_1, Z_2, \ldots, Z_k)\right)}\right|\right), \quad (20)$$

with $var\left(I(Z_i)\right)$ and $var\left(I(Z_1, Z_2, \ldots, Z_k)\right)$ the variances of the current I given respectively from one RV Z_i ($i = 1, \ldots, k$) and k RV. As depicted previously, the two random outputs are given considering two RV, respectively $RV1$ for L and $RV2$ for f.

The influence of each parameter is shown in Fig. 10 and Fig. 11. As expected, the relative behaviour of each parameter appears similar since the two parameters are dependent on a physical point of view. The computation of the influence from (20) lays emphasis on the dominant effect of length at low frequency (influence levels greater than 1dB). In comparison with f-influence (Fig. 11), the maximum levels are greater regarding L-effect ($In < 1.4$dB for the frequency).

In order to better understand the relative effect of each parameter, we may define a relative influence criterion from previous In_{Z_1} and In_{Z_2} parameters (respectively for L-$RV1$ and f-$RV2$) following

$$\tilde{In}_{Z_i} = \frac{In_{Z_i}}{\sum_{j=1}^{k} In_{Z_j}}. \quad (21)$$

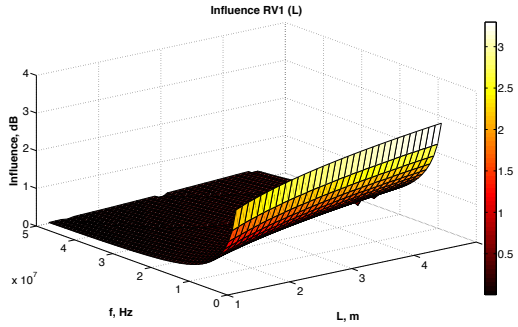


Figure 10: Influence of L parameter (RV1).

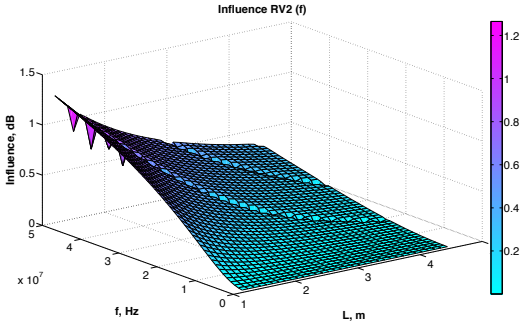


Figure 11: Influence of f parameter (RV2).

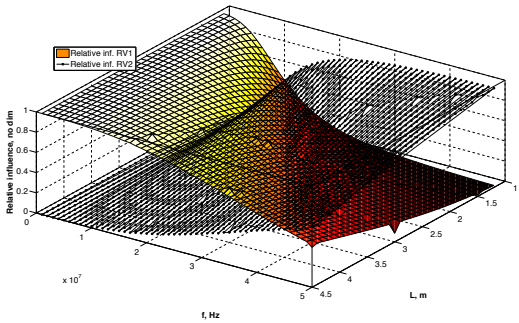


Figure 12: Relative influence of L/f parameter from one to another.

The Fig. 12 gives an overview of the relative influence of parameters L and f following the relation (21). As expected, the physical dependence between the two random parameters involves a well-balanced distribution between L and f. Indeed, based upon the given domain sampling, a quick counting distinguishing major effects of length or frequency shows an influence rate respectively of 55.64% and 44.36% for L and f. Obviously, this last remark might have been expected from Fig. 8 since the two parameters representation (interaction clouds) were closed. Nevertheless, no quantitative information might be extracted since the "Morris" SA only provides "qualitative" results. The major interest of the previous analysis relies on the ability given to precisely extract influence rates for large working domains.

4. Conclusion and prospects

In this contribution, a sensitivity analysis technique jointly with stochastic methods were presented to solve EMC problems. The use of unscented transform (UT) and stochastic collocation (SC) have been fully justified from their high simplicity and accuracy. Uncertainties involving source parameters (frequency) and geometry of a transmission line (length) have been defined considering various random variables (RV) UT/SC efficiency and precision were detailled regarding this stochastic EMC issue in multi-RV case. Since the UT and SC methods are similar to well chosen MC simulations, their efficiency appears to be an important advantage compared with Monte Carlo (MC): minimizing computing time more than 20,000 times. Moreover, one of their main advantages relies on their non-intrusive characteristic: similarly to MC, the techniques only need to achieve numerical measurements for particular input parameter values (without causing deep alteration in electromagnetic codes). Unfortunately, the efficiency may drastically decrease when the number of RV increases. That's the reason why we proposed a sensitivity analysis (SA) method to determine what are the most important variables. Based upon SA results, only significant parameters were studied to quantitatively compute their influence domains. This may be particullarly interesting to optimize EMI/EMC tests and to improve EMC equipments design. The whole process may perfectly apply oneself to other electromagnetic simulation/experimental tools.

References

[1] W.H. Press, S.A. Teukolsky, W.T. Vetterling, B.P. Flannery, *Numerical Recipes*, Cambridge University Press, 2nd edition, 1992.

[2] N. Mishra, N. Gupta, Quasi Monte Carlo Integration Technique for Method of Moments Solution of EFIE in Radiation Problems, *ACES Journal*, vol. 24, no. 3, pp. 306–311, June 2009.

[3] L. De Menezes, D. Thomas, C. Christopoulos, Accounting for uncertainty in EMC studies, *Proc. 2009 Int. Symp. on EMC*, Kyoto, Japan, 2009.

[4] L. De Menezes, D. Thomas, C. Christopoulos, A. Ajayi, P. Sewell, The use of unscented transforms for statistical analysis in EM, *Proc. EMC Europe 2008*, Hamburg, Germany, 2008.

[5] L. De Menezes, A. Ajayi, C. Christopoulos, P. Sewell, G.A. Borges, Efficient computation of stochastic electromagnetic problems using unscented transforms, *IET Sci. Meas. Technol.*, vol. 2(2), pp. 88–95, 2008.

[6] C. Chauvière, J.S. Hestaven, L.C. Wilcox, Efficient Computation of RCS from Scatterers of Uncertain Shapes, *IEEE Trans. On Ant. And Prop.*, vol. 55, no. 5, pp. 1437-1448, May 2007.

[7] P. Bonnet, F. Diouf, C. Chauvière, S. Lalléchère, M. Fogli, F. Paladian, Numerical simulation of a Reverberation Chamber with a stochastic collocation method, *Compte Rendu de l'Académie des Sciences, Physique*, vol. 10, pp. 54-64, 2009.

[8] P. Bonnet, C. Chauvière, S. Lalléchère, F. Paladian, B. Pecqueux, Recherche de configurations critiques pour un problème de C.E.M. stochastique, *Proc. 15th Int. Symp. on EMC*, Limoges, France, April 2010.

[9] F. Paladian, P. Bonnet, S. Lalléchère, Modeling complex systems for EMC applications by considering uncertainties, *Proc. XXXth URSI GA 2011*, Istambul, Turkey, August 2011.

[10] F. Diouf, F. Canavero, Crosstalk statistics via collocation method, *Proc. IEEE Int. Symp. on Electromagnetic Compatibility*, Austin TX, USA, Aug. 2009.

[11] V. Rannou, F. Brouaye, M. Hélier, W. Tabbara, Kriging the quantile: application to a simple transmission line model, *Inst. of Ph. Publish., Inverse problems 18*, pp. 37-48, PII: S0266-5611(02)20767-4.

[12] A. El Habachi, Propagation de la variabilité de la morphologie humaine sur le Débit d'Absorption Spécifique en dosimétrie numérique, *PhD Thesis Supélec*, Paris, France, 2011.

[13] H. Bagci, A.C. Yucel, J.S. Hesthaven, E. Michielssen, A fast stroud-based collocation method for statistically characterizing EMI/EMC phenomena on complex platforms, *IEEE Trans. on EMC*, vol. 51, no. 2, pp. 301-311, 2009.

[14] P.S. Sumant, H. Wu, A.C. Cangellaris, N.R. Aluru, A sparse grid based collocation method for model order reduction of finite element approximations of passive electromagnetic devices under uncertainty, *Proc. 2010 IEEE MTT-S International*, Anaheim, CA, USA, pp. 1652-1655, May 2010.

[15] I. Tarhini, C. Guiffaut, A. Reineix, S. Karam, B. Pécqueux, J.C. Joly, Etude paramétrique de la susceptibilité des cartes électroniques par les plans d'expériences numériques, *Proc. Int. Symp. On EMC*, Paris, France, May 2008.

[16] M.D. Morris, Factorial sampling plans for preliminary computational experiments, *Technometrics*, Vol. 33, No. 2, pp. 161–174, 1991.

[17] A. Saltelli, M. Ratto, S. Tarantola, F. Campolongo, Sensitivity analysis practices. Strategies for model-based inference, *Reliability Engineering and System Safety*, vol. 91, pp. 1109-1125, 2006.

[18] B. Iooss, Revue sur l'analyse de sensibilité globale de modèles numériques, *Journal de la Société Française de Statistiques*, vol. 152, no. 1, pp. 3–25, 2011.

[19] F. Campolongo, J. Cariboni, A. Saltelli, V. Schoutens, Enhancing the Morris method, *Sensitivity Analysis of Model Output*, Los Alamos National Laboratory, 2005.

[20] D. Xiu, J.S. Hesthaven, High order collocation methods for differential equations with random inputs, *SIAM J. Sci. Comput.*, Vol. 27, No. 3, pp. 1118–1139, 2005.

[21] A.H. Stroud, Remarks on the disposition of points in numerical integration formulas, *Math. Tables Other Aids Comput.*, vol. 11, no. 3, pp. 1118–1139, Oct. 1957.

Study of a reverberation chamber shape inspired from chaotic cavities

K. Selemani[1]*, E. Richalot[1], O. Legrand[2], F. Mortessagne[2]

[1]Université Paris-Est, ESYCOM, Marne-la-Vallée, Cité Descartes, 77 454 Marne-la-Vallée, France
[2]LPMC, Université de Nice-Sophia Antipolis, Parc Valrose, 06108 Nice cedex 2, France
*corresponding author, E-mail: selemani@univ-mlv.fr

Abstract

Using the knowledge gained from the wave chaos theory, we present a simple modification of the shape of a reverberation chamber (RC) consisting in inserting a metallic hemisphere on a cavity wall. The presented simulation results show a significant improvement of the field statistical properties, and this without resorting to a mode stirrer.

1. Introduction

The reverberation chambers, widely used for electromagnetic compatibility studies or antenna characterisation [1], are resonant cavities, usually of rectangular shape and equipped with a stirrer in motion having a complex shape. They are used beyond a minimum frequency from which the fields are statistically isotropic and uniform on a stirrer rotation [2]. As it appears that these statistical requirements correspond to the properties of most modes of a chaotic cavity [3], we propose the use of a chaotic cavity as a reverberation chamber cavity. Indeed, in a chaotic cavity, generic modes (also called *ergodic* modes, see e.g. [4]) display Gaussian statistics for each component. This statistical behavior can be met at relatively low frequency, thereby leading to statistically isotropic fields and random polarizations even for an unstirred cavity field. Thus, the statistical behavior of each individual ergodic mode might constitute the keystone of an effective reduction of the *lowest* usable frequency (LUF) in chaotic RCs [5].

The application of the wave chaos theory to electromagnetic systems comes from the analogy between the Schrödinger's and Helmholtz's equations in the case of a flat cavity [3]. The Schrödinger equation being scalar, the small cavity height allows the problem reduction to a 2D system with a single field component, so that most studies of chaotic electromagnetic cavities were carried out in 2D [6]. However, a few studies of 3D cavities showed similar properties [7].

Drawing inspiration from a 2D chaotic cavity, we studied a parallelepipedic cavity provided with a metal half-sphere on one wall (fig.1). Its dimensions are: W = 0.785m along (Ox), L = 0.985m along (Oy) and H = 0.995m along (Oz). The hemisphere centred at (31W/42, 3L/4, H) has a radius of R = 0.15m. To evaluate how well the cavity is operating, the distributions of the six field components are examined and compared to those obtained with the cavity without hemisphere.

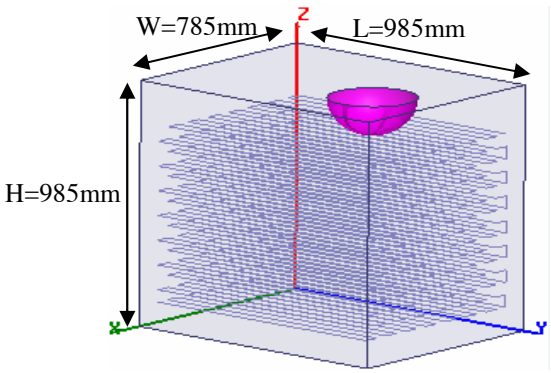


Figure 1: Cavity with hemisphere and 3D grid for field values extraction.

The simulations are performed using HFSS software, by searching for eigenmodes. The first 232 modes of the empty parallelelipedic cavity as well as the first 232 modes of the cavity loaded by a hemisphere are studied here. Their resonant frequencies vary between 214MHz and 1GHz. To study the field distributions, the values of the three electric field components are recorded for each mode at 1001 points within the cavity volume. These points are taken on a 3D grid included in the cavity (Fig. 1). The distance between two adjacent lines as well as between the 3D grid and the cavity walls is of 50mm. The fields associated to each eigenmode are normalized so that the mean of the square electric field amplitude on the grid points is unitary.

Using simulation results, we first of all focus on the distribution of each field component and determine if a Gaussian law is followed. We then examine the isotropy of the fields associated to the cavity resonances while considering the difference between the standard deviations of each component. Besides, the invariance of the field statistical properties through a rotation of the orthonormal basis is used as a test of the field isotropy.

2. Field distribution

We first examine the distribution of the three field components for each eigenmode. The orthonormal basis is defined according to the cavity edges as reported in Fig. 1. In a well-operating reverberation chamber, as for the ergodic modes of a chaotic cavity, a normal distribution is expected for each field component.

We focus, as an example, on the mode at 995MHz, but similar results are obtained with other modes. The mapping of electric field (Fig.2) indicates that the disturbance associated with the hemisphere is global, as the distribution is no longer regular as in the empty cavity (Fig.3). From the 1001 values of the electric field components, we plot the associated histograms as well as the closest normal distributions (for E_x in Figs.2-3). Visually there is a good agreement between theoretical and empirical laws after the insertion of the hemisphere. The Kolmogorov-Smirnov (KS) at 95% confidence is used to determine whether the two laws are close enough. The answer is 0 if they match and 1 otherwise. In the presented case of Fig. 2, the answer is 0, whereas it is 1 in Fig. 3.

Besides the normal distribution of its components, the field is also required to be isotropic in a well-operating reverberation chamber. We recall that an *ergodic* field is also isotropic. The field isotropy will be studied in more details in the second part of this paper, but we will first of all eliminate the null components because of the strong degradation of the field isotropy they imply. Whereas the field components that vanish are analytically known for the empty cavity, they have to be determined numerically in the modified cavity. As the field values issued from simulations are never strictly null, a criterion is necessary to decide if a component can be considered or not as null. The criterion of Eq. 1 to consider a field component E_i as null has been determined by examining the empty cavity simulation results, where the null components are analytically known:

$$\frac{\mu(|E_i|)}{\max\{\mu(|E_x|),\mu(|E_y|),\mu(|E_z|)\}} \le 0.06 \qquad (1)$$

where $\mu(x)$ indicates the mean value of x.
This special treatment of the null field components is particularly important, as it appears from the simulations of the parallelelipedic cavity, that the KS test answer is 0 for the numerical noise associated to these null components. The latter would indeed appear as being Gaussian distributed if they were not eliminated before applying the KS test. To avoid this problem and show the presence of these modes degrading the field isotropy, the response of the KS test has been modified by associating the value -1 to null components.

The nullity and KS tests were performed with the first 232 eigenmodes of both cavities. The results obtained for the E_x components of the eigenmodes are given in Fig. 4 for the empty cavity and in Fig. 5 in the presence of the hemisphere. The increase of the number of zero-answers due to the hemisphere insertion clearly appears. Moreover, the Gaussian character of the field improves with increasing frequency in the modified cavity whereas it seems almost completely absent in the empty cavity. The same tests performed on E_y and E_z components of the modes confirm these remarks.

The results obtained for the three electric field components are summarized in Table I. It can firstly be noticed that, whereas each field component is null for about 28.4% of the modes within the empty cavity, it almost never occurs within the modified cavity. The normal law is widely followed by the field components in the presence of the hemisphere, with a success ratio of the KS test above 72%, whereas the test response is predominantly 1 without the hemisphere.

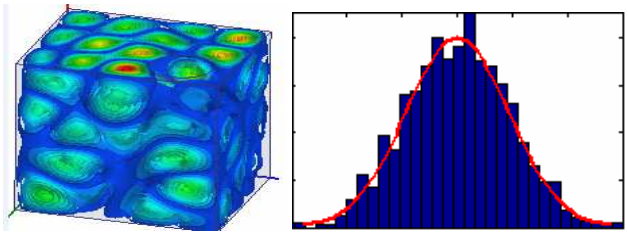


Figure 2: Electric field amplitude and associated distribution of E_x component at 995MHz (230th mode) for the cavity with an hemisphere

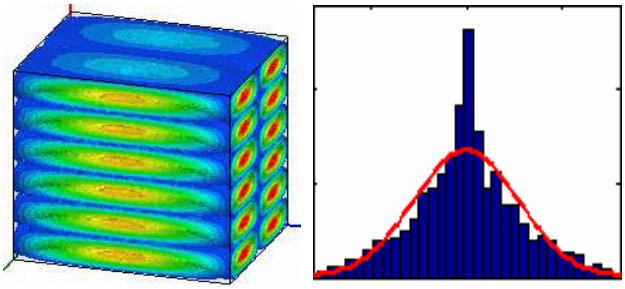


Figure 3: Electric field amplitude and associated distribution of E_x component at 993MHz (230th mode) for the empty cavity.

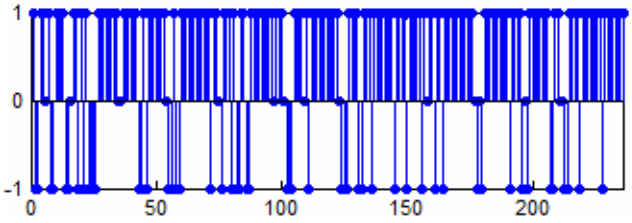


Figure 4: KS test for E_x components of the empty cavity modes.



Figure 5: KS test for E_x components of the modes obtained with a hemisphere.

Table 1: Results (%) of the KS test performed on the distribution of the three field components for the 232 resonant modes of the empty and modified cavities.

		Null (-1)	KS_95%= 1	KS_95% = 0
Empty cavity	E_x	23.71	69.4	6.9
	E_y	25.43	48.71	25.86
	E_z	30.6	38.79	30.6
With ½ sphere	E_x	2.59	23.28	74.14
	E_y	1.72	20.26	78.02
	E_z	2.59	24.57	72.84

As for an ergodic mode the three field components are normally distributed, we now define a global homogeneity indicator of the three field properties. It takes the value of -1 if at least one component is null, 0 if each component is non-null and follows a normal distribution, and 1 if no component is null and at least one of the components does not follow a normal distribution

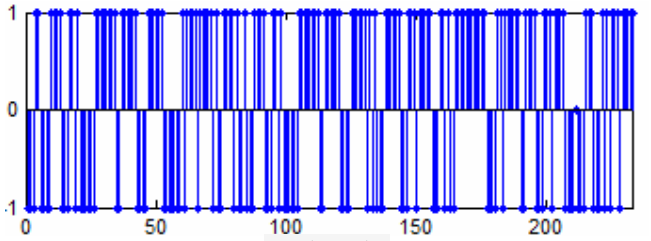


Figure 6: Global homogeneity test of all modes, empty cavity

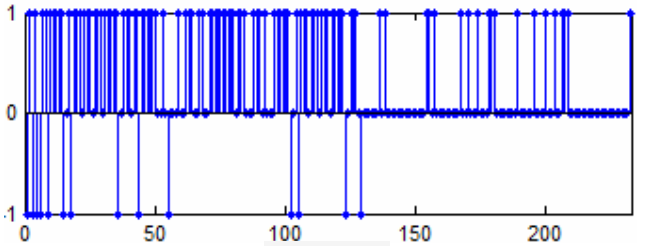


Figure 7: Global homogeneity test of all modes, cavity with ½ sphere

In the empty cavity, many components are either null or do not follow a normal distribution (Fig.6). In the cavity with a hemisphere null components get extremely rare with increasing frequency; many of them follow a normal distribution (Fig. 7). Table 2 summarizes the results of this global test for all the modes in both cavities. It clearly indicates that the insertion of the hemisphere drastically decreases the number of modes having a null component and increases the number of modes with three normally distributed components.

Table 2: Results (%) of the global homogeneity test performed on the modes

Modes	0	1	-1
Empty cavity	0.42	58.9	40.68
c. with ½ sphere	50	43.97	6.03

If the field is isotropic then it presents the same distribution regardless of the chosen orthonormal coordinate system. To verify this property, we modify the first chosen coordinate system of Fig. 1 by performing a rotation of θ_r=30° about the Ox axis, of φ_r=20° about the Oy axis and of ψ_r=60° about the Oz axis. The already presented tests are then applied, for each eigenmode of both cavities, to the three components related to this new basis. The results obtained for the global homogeneity indicator of the modified cavity are presented in Fig. 8.

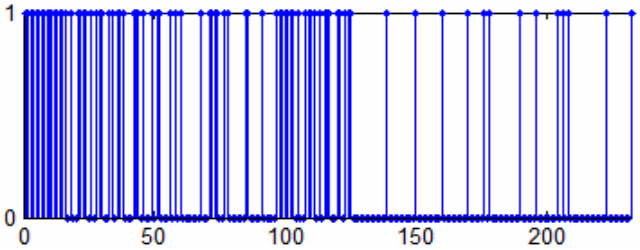


Figure 8: Global homogeneity test for the modified cavity, after basis rotation.

The coordinate system rotation eliminates the null components; similarly, the analytical field expressions in the empty cavity indicate that no null component remains in this case. The variation of the number of zero answers from 50% in the initial coordinate system to 63.8% after basis rotation indicates that some modes associated to a zero answer are not ergodic as their field distributions are sensitive to the chosen projection basis.

The modes whose three components are non-null and normally distributed in both coordinate systems, as expected for Gaussian ergodic modes, are presented in Fig. 9. For each mode, if the global homogeneity test takes the value 0 in both coordinate systems, then 0 is indicated, else 1 is associated to this mode. The zero answer is obtained for 38.8% of the modes. As already noticed, the field statistical properties improve with increasing frequency. From the 130th mode, the zero value appears for 73.5% of the modes.

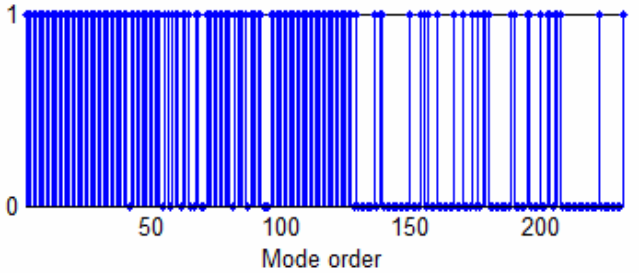


Figure 9: Global homogeneity test for the modified cavity, in both bases.

To further investigate the field isotropy, the standard deviations of the three field components will now be examined.

3. Standard deviation and field isotropy

The field isotropy implies an equality of the standard deviations of each field component. Therefore, we examine here the standard deviations of the three electric field components for each eigenmode, and use the difference between them as an indicator of the field istropy. The orthonormal basis as defined in Fig. 1 is chosen.

The standard deviations are calculated from the components values at the 1001 points of the cavities. Their frequential variations are given in Figs. 10-11.

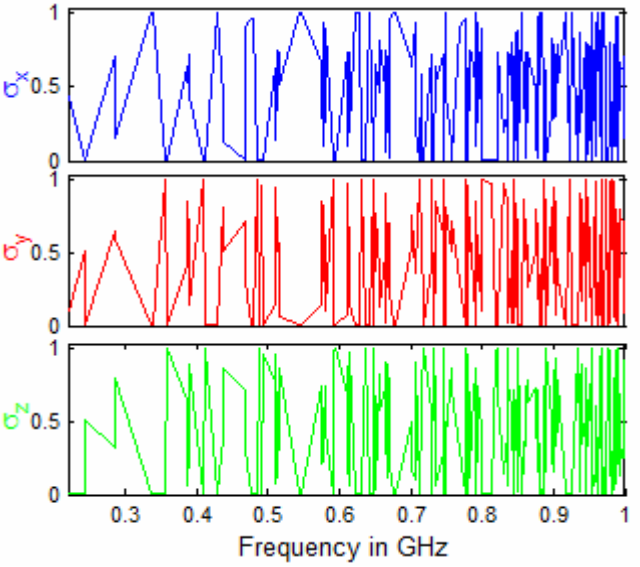


Figure 10: Standard deviation of E_x, E_y and E_z for the empty cavity.

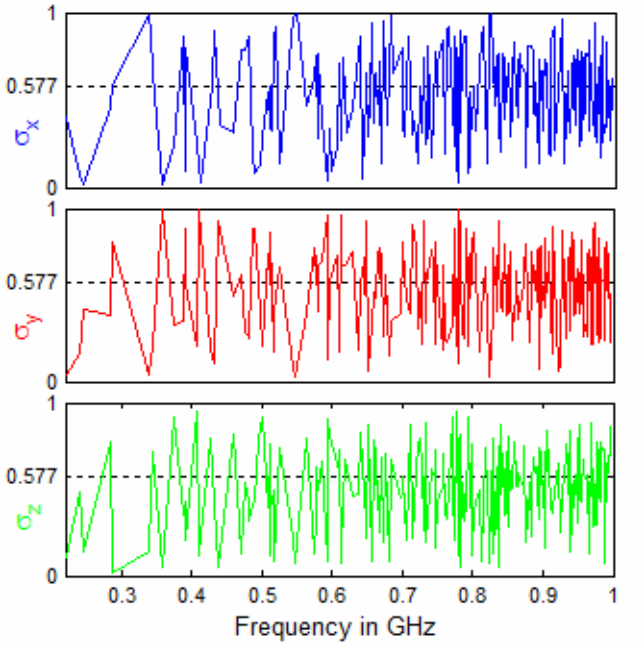


Figure 11: Standard deviation of E_x, E_y and E_z for the cavity with an hemisphere.

We notice a decrease of the standard deviations excursion with increasing frequency in the case of the cavity with a hemisphere, whereas no noticeable evolution appears in the empty cavity. In the latter case, a large number of very small standard deviations are obtained, that correspond to the vanishing of the related field components. These very small values are fewer with the hemisphere. The corresponding null components, very detrimental to the field isotropy, have already be pointed out in Section 2.

The value of 0.577 indicated in Fig. 11 corresponds to an ideal mode whose three components have a zero mean and identical standard deviations. It is expected in a chaotic cavity that the standard deviations fluctuate around this value. Between 700MHz (corresponding to the 76th mode) and 1GHz, the mean values of the standard variations are of 0.54 for E_x, 0.53 for E_y and 0.52 for E_z.

Thus, in the ideal case of an istropic field, the standard deviations of the three electric field components are equal. To evaluate the istropy of the modes, we propose the indicator $\Delta\sigma$ defined in Eq. 2. Its value, comprised between 0 and 1, decreases when the three standard deviations become similar. $\Delta\sigma$ is equal to 1 when one field component vanishes whereas, in the ideal isotropic case, it is vanishing.

$$\Delta\sigma = \frac{\max(\sigma_x,\sigma_y,\sigma_z) - \min(\sigma_x,\sigma_y,\sigma_z)}{\max(\sigma_x,\sigma_y,\sigma_z) + \min(\sigma_x,\sigma_y,\sigma_z)} \qquad (2)$$

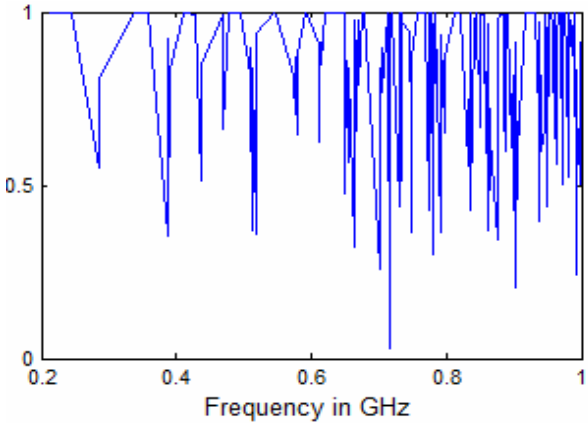


Figure 12: Δσ versus frequency for the empty cavity

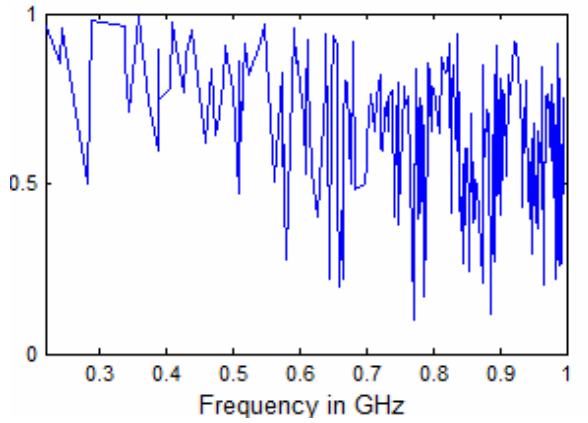


Figure 13: Δσ versus frequency for the modified cavity

Figure 12 indicates that in the empty parallelelipedic cavity, the variation domain of Δσ remains globally similar while the frequency increases. On the other hand, Δσ globally decreases with the frequency in the modified cavity (Fig. 13). The difference between the parameters of both cavities clearly appears after 700MHz: whereas the mean value of Δσ between 700MHz and 1GHz is of 0.7985 for the empty cavity, it is of 0.5964 in the modified cavity. This is an indication of the improvement of the field isotropy due to the insertion of the hemisphere.

4. Conclusion

Drawing inspiration from studies developped in the field of wave chaos, a simple modification of the parallelipedic cavity has been proposed with the aim of obtaining homogeneous and isotropic fields. Through simulation results, it has been shown that the ratio of field components following a normal distribution drastically increases after this geometric modification, and that this ratio grows with increasing frequency. The field isotropy has also been discussed from three different points of view. First the modes presenting null components, which are very detrimental to the field isotropy, have been counted, and the reduction of their number in the modified cavity geometry is clearly demonstrated. Then, the invariance of the field statistical properties with respect to the orthonormal basis has been tested. Finally, the analysis of the standard deviations of the three components and, for each mode, of their dispersion, confirms the same trend.

According to the presented results, the very simple cavity modification we propose permits a considerable improvement of the field statistical properties. The adaptation of this geometrical modification to reverberation chambers could be performed in two ways. The first one consists of inserting a metallic hemisphere within classical reverberation chambers equipped with a stirrer. In the second approach, the hemisphere is considered as a mode-stirrer and moves on the cavity wall. In both approaches, it is expected that the spectral overlap of homogeneous and isotropic modes will lead to better statistical field properties than when the modes do not individually meet the required statistical properties. It would result in the improvement of the reverberation chambers operation and very likely in the decrease of their LUF.

Aknowledgment

The authors thank the french National Research Agency (ANR) for financially supporting the project CAOREV of which this work is a part.

References

[1] P.-S. Kildal, K. Rosengren, J. Byun, J. Lee, "Definition of effective diversity gain and how to measure it in a reverberation chamber", *Microwave and Optical Technology Letters*, Vol. 34, No. 1, July 5 2002, pp. 56-59.

[2] M. O. Hatfield, M. B. Slocum, E. A. Godfrey, and G. J. Freyer, "Investigations to extend the lower frequency limit of reverberation chamber," in *Proc. IEEE Int. Symp. Electromagn. Compat.*, Denver, CO, 1998, vol. 1, pp. 20–23.

[3] H.–J. Stöckman, *Quantum Chaos: an introduction*, Cambridge University Press (1999).

[4] M.V. Berry, *Semiclassical mechanics of Regular and Irregular Motion*, in Chaotic Behaviour of Deterministic Systems, edited by R.H.G. Helleman and G. Ioss, Les Houches 82, Session XXXVI (North-Holland, Amsterdam, 1983).

[5] L. R. Arnaut, "Operation of electromagnetic reverberation chambers with wave diffractors at relatively low frequencies," *IEEE Trans. Electromagn. Compat.*, vol. 43, no. 4, pp. 635–653, Nov. 2001.

[6] J. Barthélemy, O. Legrand, F. Mortessagne, "Complete S-matrix in a microwave cavity at room temperature", Phys. Rev E, 71, 016205 (2005).

[7] U. Dörr, H. J. Stöckmann, M. Barth, and U. Kuhl, "Scarred and chaotic field distributions in a three-dimensional Sinai-microwave resonator", *Phys. Rev. Lett.*, vol. 80, no. 5, pp. 1030–1033, Feb. 1998.

Multivariate uncertainty analysis of scattered electric field from building facades in urban environment

Shermila Mostarshedi[1*], Bruno Sudret[2], Elodie Richalot[1], Joe Wiart[3], and Odile Picon[1]

[1]Université Paris-Est, Laboratoire ESYCOM, France
[2]Université Paris-Est, Laboratoire Navier (Ecole des Ponts ParisTech, IFSTTAR, CNRS), France
[3]Orange Labs, France
* shermila.mostarshedi@univ-mlv.fr

Abstract

In the context of wave propagation in urban environment, the importance of the random variation of different facade parameters (ex. material permittivity, architectural details dimensions and distribution) on the reflected electric field from the building has been studied. Two approaches for a multivariate sensitivity analysis are proposed. Taylor series expansion is used to introduce the variance decomposition. The sensitivity indices are obtained in different diffraction zones of the building. A Monte Carlo simulation is used to verify the validity of the perturbation approach in all zones and to calculate different statistical moments. Correlation coefficients are introduced and highlight the influential facade parameters.

1. Introduction

Wireless communications, particularly mobile networks, experienced a great expansion recently worldwide. These networks are very dense in urban areas and the electromagnetic field distribution is highly dependent on city structures. It is essential to have predictive tools to assess as accurately as possible the distribution of electromagnetic fields in order to enable optimized implementation of base stations. Prediction of electromagnetic fields levels in a complex environment is meaningful when presented with an acceptable amount of uncertainty. Although statistical models for the radio wave propagation in urban environment have been used since a long time [1]–[3], wave propagation site-specific simulators do not usually accept variable parameters for building architectural details and seldom report extra information concerning the uncertainty of the results. While sources of uncertainty on the scattered field are abundant in urban environment, in this study they are restricted to those arising from building faces. Some of these architectural parameters are: permittivity of concrete and glass, type of glazing, dimensions and distribution of windows. In a previous study [4], we have investigated the influence of some building parameters on the scattered field and we have quantified the importance of each parameter in a single-variate analysis. In this paper, we propose a multivariate sensitivity analysis and uncertainty propagation using the perturbation method and the Monte Carlo simulation.

2. Building properties

The sources of uncertainty in the reflection/scattering mechanism in urban environment are numerous. If we restrict the study to those related to the building facades, several parameters related to the architecture of buildings can be identified. The random variation of these parameters can influence the scattered field and thus create an uncertainty on the calculated field. Some of these architectural parameters are: permittivity of concrete and glass, type of windows (thickness of glass, number of slabs), dimensions and distribution of windows. The influence of these variables may vary according to different conditions such as wave polarization, incident angle and observation distance.

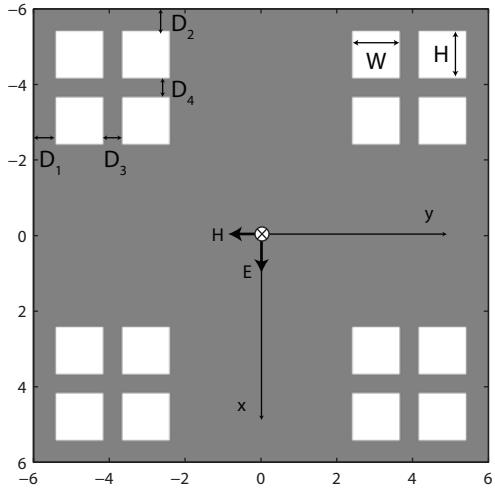


Figure 1. Generic concrete-glass building facade presented for the mean values of geometrical parameters

In this study, we have chosen 8 random variables among all possible architectural variations. These parameters are

defined for the generic 12m×12m concrete-glass building illustrated in Figure 1. In order to cover all possible values for different input parameters, no special hypothesis has been taken for the statistical distribution and all parameters are supposed to have a uniform variation over the authorized interval. The parameters are :

- Concrete relative permittivity: $U\varepsilon_C = [5, 9]$
- Glass relative permittivity: $U\varepsilon_G = [2, 5]$
- Width of windows: $U_W = [0.5, 2]$
- Height of windows: $U_H = [0.5, 2]$
- Horizontal distance of windows from the vertical edge of building: $U_{D1} = [0.2, 1]$
- Vertical distance of windows from the horizontal edge of building: $U_{D2} = [0.2, 1]$
- Horizontal distance between windows in each bloc: $U_{D3} = [0, 1]$
- Vertical distance between windows in each bloc: $U_{D4} = [0, 1]$

The facade is illuminated by a TE polarized plane wave in normal (θ_i=0°) incidence and the reflected electric field is calculated in specular direction and in different diffraction zones of the building facade. The calculation method, presented in [5] allows a fast and accurate calculation of the reflected field from building facades in different diffraction zones. In this method, a wave illuminating the surface of an object can be replaced, with respect to the induction theorem, by electric and magnetic equivalent currents at the interface between the air and the object. The total radiation of these fictive currents gives the reflected field from the object. In order to calculate the radiation of surface currents, we use the Green's functions associated with the interface between two semi-infinite media which have the advantage of being without singularities.

The choice of different observation distances is made according to the definition of standard diffraction zones of a radiating object. Figure 2 summarizes some of the most important existing definitions [6]–[9] where D represents the largest dimension of the building and λ the free-space wavelength.

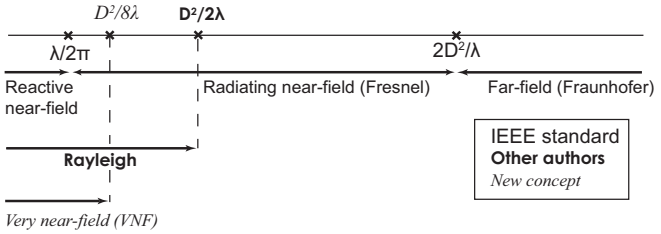


Figure 2. Standard radiation zones from a radiating object of size D

In order to show the nature of field variations in different regions, the building facade of Figure 1 is illuminated by a TE polarized plane wave in normal incidence. The amplitude of the reflected electric field is presented in Figure 3 as a function of the distance from the building and along the z axis. The mean values of the parameters are chosen for facade geometrical properties and the working frequency is fixed to 900 MHz. As shown in this figure, the amplitude of the electric field goes through a very fluctuating zone until attaining its maximum value before the end of the Rayleigh zone. The amplitude decreases monotonously with the distance after this peak.

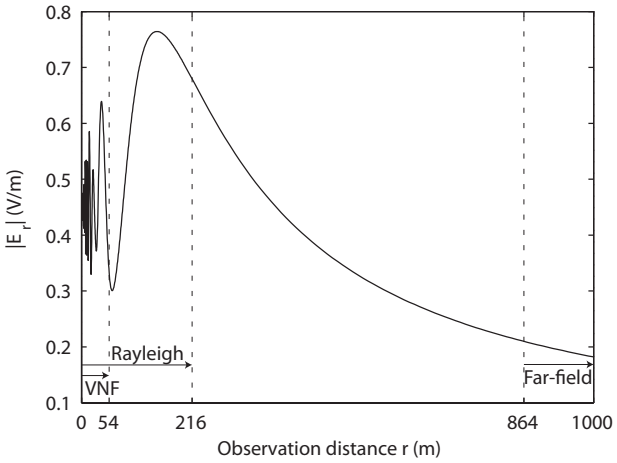


Figure 3. Evolution of the amplitude of the reflected electric field as a function of the observation distance

3. Statistical studies

The influence of each random variable on the total reflected electric field is highlighted using two different approaches. As a first approach we use the perturbation method which gives a quick insight to the sensitivity of the output variable to each input variable. The results are obtained assuming that the Taylor series expansion of the output expression is valid around the mean value of each parameter. In order to verify the validity of the first approach and knowing that a sample simulation time using the Green's functions method is reasonably short, we propose a Monte Carlo simulation with a small number of samples.

3.1. Perturbation method

The perturbation method is based on the Taylor series expansion of the response function around the mean value of the input parameters. The input is represented as a random vector $\boldsymbol{X} = [X_1, X_2, \ldots, X_M]$ and the output is a function of the input random vector $Y = f(\boldsymbol{X})$. The approximation remains valid if the variations of the input parameters (X_i) around their mean values are small. The mean and the variance of the response can be estimated as follows [10].

The Taylor series expansion of $f(\boldsymbol{X})$ around the mean value of the input parameters is given by:

$$f(X) = f(\mu_X) + \sum_{i=1}^{M} \left.\frac{\partial f}{\partial x_i}\right|_{x=\mu_X} (X_i - \mu_i) + \frac{1}{2}\sum_{i=1}^{M}\sum_{j=1}^{M} \left.\frac{\partial^2 f}{\partial x_i \partial x_j}\right|_{x=\mu_X} (X_i - \mu_i)(X_j - \mu_j) + o\left(\left\|(X - \mu_X)\right\|^2\right) \quad (1)$$

Taking the expectation from both sides of (1):

$$E\left[f(X)\right] \approx f(\mu_X) + \sum_{i=1}^{M} \left.\frac{\partial f}{\partial x_i}\right|_{x=\mu_X} E\left[(X_i - \mu_i)\right] + \frac{1}{2}\sum_{i=1}^{M}\sum_{j=1}^{M} \left.\frac{\partial^2 f}{\partial x_i \partial x_j}\right|_{x=\mu_X} E\left[(X_i - \mu_i)(X_j - \mu_j)\right] \quad (2)$$

By definition $E\left[(X_i - \mu_i)\right] = 0$, so the first order approximation of the mean value is:

$$E\left[f(X)\right] \approx f(\mu_X) \quad (3)$$

The first order approximation of the variance is thus:

$$\begin{aligned} \mathrm{Var}\left[f(X)\right] &= \mathrm{E}\left[\left(f(X) - \mathrm{E}\left[f(X)\right]\right)^2\right] \\ &\approx \mathrm{E}\left[\left(f(X) - f(\mu_X)\right)^2\right] \\ &\approx \mathrm{E}\left[\left(\sum_{i=1}^{M} \left.\frac{\partial f}{\partial x_i}\right|_{x=\mu_X} (X_i - \mu_i)\right)^2\right] \end{aligned} \quad (4)$$

If the input parameters are independent, the response variance becomes:

$$\mathrm{Var}\left[f(X)\right] = \sigma_Y^2 \approx \sum_{i=1}^{M} \left(\left.\frac{\partial f}{\partial x_i}\right|_{x=\mu_X}\right)^2 \sigma_i^2 \quad (5)$$

The variance is thus decomposed into the contribution of each single input parameter. Finally the importance factors or the sensitivity indices can be defined as follows:

$$S_i = \left(\left.\frac{\partial f}{\partial x_i}\right|_{x=\mu_X}\right)^2 \left(\frac{\sigma_i}{\sigma_Y}\right)^2 \quad (6)$$

The sensitivity index S_i quantifies the uncertainty brought to the total variance Var[$f(X)$] by the i-th input variable. The sensitivity indices naturally sum up to unity.

For the building facade in Figure 1 and the input variables defined in Section 2, the sensitivity indices as well as the estimated output mean and standard deviation are calculated for a normally incident TE polarized plane wave at a few observation distances in specular direction along z axis and are presented in Table 1. We note that the building discretization size is chosen to be 5 mm. The same calculations have been conducted with a 3 mm precision and the results are almost identical. We observe for all zones, starting from the Rayleigh zone, that the concrete relative permittivity is the most important parameter. This parameter is followed by either the dimensions (width and height) of windows in the Rayleigh zone or both the dimension and the relative permittivity of glass in far zones of the building. The influence of the distribution of windows is almost negligible. We need to emphasize on the fact that results obtained for r = 20 m do not satisfy the physical expectations; the near-field of the building cannot be independent from the relative permittivity of concrete. It seems that the Taylor decomposition of the response, in its current form, is not a valid approach for this particular observation zone. The Monte Carlo simulations presented in the next sub-section will clarify this hypothesis.

3.2. Monte Carlo simulation

Monte Carlo simulation is the basic approach to estimate the whole probability density function $f_Y(y)$ provided that the sample set is large enough. The mean, the variance and other statistical moments can thus be extracted from the simulation results. The sensitivity analysis in this case is achieved by using the correlation between the output and each input parameter. The Pearson's correlation coefficient characterizes the importance of input parameters on the output response subject to a linear relation between them while the Spearman's correlation coefficient measures the importance assuming a monotonous relationship between the input and the output. The empirical Pearson's correlation coefficient is given by:

$$\rho_{P\,xy} = \frac{1}{n} \frac{\sum_{i=1}^{n} (x^{(i)} - \bar{x})(y^{(i)} - \bar{y})}{\hat{\sigma}_x \hat{\sigma}_y} \quad (7)$$

where $\bar{x}$ and $\hat{\sigma}$ are the empirical mean and standard deviation of each sample set.

Table 1. Sensitivity indices of the input parameters for $\theta_i = \theta_r = 0°$ in different diffraction zones of the building (discretization = 5mm)

	Very near-field	**Rayleigh**	**End of Rayleigh**	**Fresnel**	**Start of far-field**	**Far-field**
	r = 20 m	**r = 100 m**	**r = 216 m**	**r = 400 m**	**r= 864 m**	**r = 1000 m**
S_{ε_C}	0.0590	0.5237	0.6992	0.7313	0.7411	0.7418
S_{ε_G}	0.0950	0.0327	0.0976	0.0971	0.0963	0.0962
S_W	0.1898	0.1813	0.1005	0.0857	0.0813	0.0810
S_H	0.1898	0.1813	0.1005	0.0857	0.0813	0.0810
S_{D1}	0.1292	0.0367	0.0011	7.9525e-005	3.4675e-006	1.9252e-006
S_{D2}	0.1292	0.0367	0.0011	7.9525e-005	3.4675e-006	1.9252e-006
S_{D3}	0.1040	0.0038	1.8869e-005	9.4571e-007	3.6345e-008	2.0002e-008
S_{D4}	0.1040	0.0038	1.8869e-005	9.4571e-007	3.6345e-008	2.0002e-008
μ_E	0.3886	0.6249	0.6796	0.4308	0.2099	0.1820
σ_E	0.0777	0.0572	0.0516	0.0321	0.0155	0.0135

If we define the rank of each sample as its ordinal number while the set is sorted in ascending order, the Spearman's correlation coefficient is the linear correlation of the rank sets :

$$\rho_{S\,xy} = 1 - \frac{6}{n}\frac{\sum_{i=1}^{n}(rx^{(i)} - ry^{(i)})^2}{n^2 - 1} \qquad (8)$$

where *rx* and *ry* are the rank sets.

For the previous problem, 1000 samples of the 8 input random variables are generated according to the uniform distribution using the Latin Hypercube sampling technique. The amplitude of the reflected electric field is observed in the same conditions as previously. The empirical correlation coefficients along with the mean and the standard deviation are presented in Table 2. We remind that the discretization of the building is kept to 5 mm, the same Monte Carlo simulation with 1000 samples has been conducted with 3 mm precision and the results are quite identical. According to the correlation coefficients in Table 2, the same conclusions are drawn regarding the importance of the parameters in each zone, except for the very near-field. We note that the relative permittivities of concrete and glass affect the very near field of the building contrarily to the results obtained by the linearization technique. The Monte Carlo simulation is universal and independent of the nature of variation of the field in the region, we will thus explore the results at r = 20 m in order to verify if the Monte Carlo simulation has converged. Otherwise, we note a very good agreement between the values of the mean and the standard deviation obtained with the two approaches.

The accuracy of Monte Carlo moment estimator as a function of the number of samples is presented in Figure 4. We observe that in near regions especially at r=20m of the building the accuracy of the estimator with 1000 samples is less than in the other diffracting regions of the building. The sensitivity studies in the fluctuating near-field region of the building is not only inappropriate for the series expansion techniques but also needs to be provided with more important number of samples in order to guarantee the same precision as the other regions. Another Monte Carlo simulation is conducted at 20 m and 100 m using 5000 samples for input parameters, the results confirm those obtained in Table 2 with a slight difference.

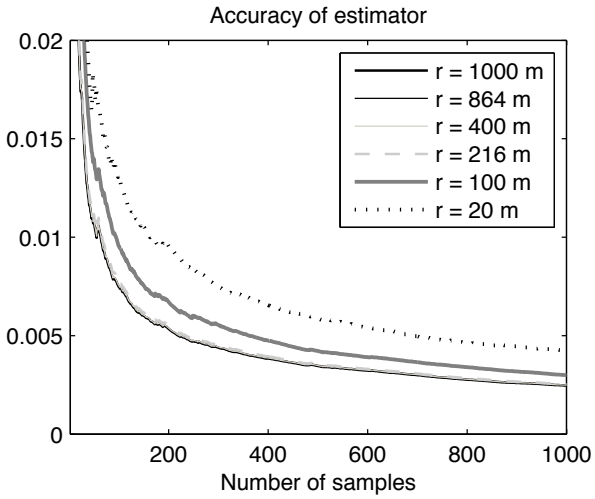


Figure 4. Accuracy of Monte Carlo Simulation mean estimator as a function of number of samples in different zones

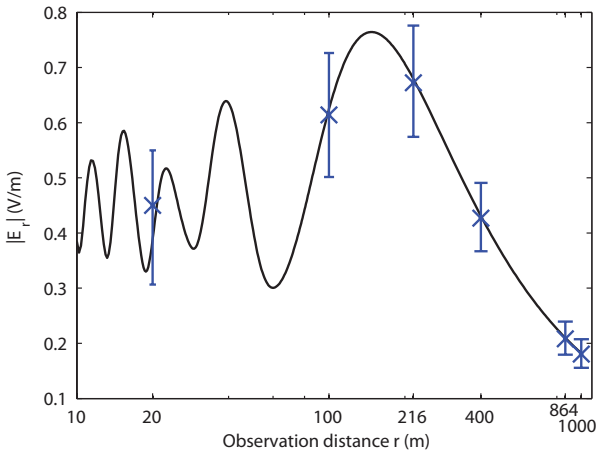


Figure 5. Median, 0.025 and 0.095 quantiles of the reflected electric field using 1000 samples in different diffraction zones

Table 2. Pearson's and Spearman's correlation coefficients of the input parameters for $\theta_i = \theta_r = 0°$ in different diffraction zones of the building (discretization = 5mm)

	Very near-field		**Rayleigh**		**End of Rayleigh**		**Fresnel**		**Start of far-field**		**Far-field**	
	r = 20 m		**r = 100 m**		**r = 216 m**		**r = 400 m**		**r= 864 m**		**r = 1000 m**	
$\rho_{P\varepsilon C}$ $\rho_{S\varepsilon C}$	0.5442	0.5796	0.7140	0.7250	0.8099	0.8191	0.8276	0.8363	0.8329	0.8420	0.8333	0.8424
$\rho_{P\varepsilon G}$ $\rho_{S\varepsilon G}$	-0.1411	-0.1176	0.1736	0.1577	0.2738	0.2498	0.2725	0.2482	0.2713	0.2464	0.2712	0.2463
ρ_{PW} ρ_{SW}	0.0589	0.0510	-0.4052	-0.3976	-0.3436	-0.3342	-0.3264	-0.3175	-0.3209	-0.3120	-0.3205	-0.3115
ρ_{PH} ρ_{SH}	0.0732	0.0528	-0.3867	-0.3727	-0.3124	-0.2928	-0.2943	-0.2756	-0.2886	-0.2697	-0.2882	-0.2693
ρ_{PD1} ρ_{SD1}	0.0321	0.0324	-0.1704	-0.1523	-0.0269	-0.0208	-0.0049	-0.0019	0.0016	0.0037	0.0020	0.0042
ρ_{PD2} ρ_{SD2}	-0.0677	-0.0762	-0.1761	-0.1678	-0.0473	-0.0457	-0.0267	-0.0267	-0.0206	-0.0209	-0.0202	-0.0205
ρ_{PD3} ρ_{SD3}	0.0608	0.0262	-0.0818	-0.0775	-0.0413	-0.0432	-0.0388	-0.0414	-0.0382	-0.0408	-0.0382	-0.0409
ρ_{PD4} ρ_{SD4}	0.0738	0.0473	-0.0445	-0.0330	-0.0064	0.0011	-0.0048	0.0022	-0.0045	0.0027	-0.0044	0.0026
$\hat{\mu}$	0.4556		0.6175		0.6729		0.4264		0.2078		0.1801	
$\hat{\sigma}$	0.0613		0.0589		0.0542		0.0337		0.0163		0.0142	

Figure 5 shows the variation of the reflected electric field as a function of the distance in logarithmic scale. Using the results of the Monte Carlo simulation with 1000 samples, the median and the 0.025 and 0.975 quantiles are given for each nominal distance. As presented in Table 3, the closer the observation distance gets, the larger the range of variations becomes. The Coefficient of Variation (CV) which is a measure of dispersion is also calculated at each observation distance.

Table 3. Quantile ranges and Coefficients of Variation for different observation distances

	$Q_{0.975} - Q_{0.025}$	$CV = \sigma/\mu$
r = 20 m	0.2432	0.1345
r = 100 m	0.2247	0.0953
r = 216 m	0.2016	0.0806
r = 400 m	0.1239	0.0791
r = 864 m	0.0598	0.0786
r = 100 m	0.0518	0.0786

4. Conclusions

Two sets of sensitivity parameters have been presented in different diffraction zones of a building whose varying parameters contain the material as well as geometrical properties of the facade. The first set based on variance decomposition is only valid when the Taylor series expansion of the reflected electric field is possible. In the very near-field of the building this hypothesis is no longer valid and a Monte Carlo simulation has to be employed. The second set contains the correlation coefficients which can be accurate in all diffraction zones subject to a sufficiently large number of samples. Both studies agree on the fact that the concrete permittivity is the most important parameter in all diffraction zones, while the glass permittivity and the dimensions of windows can be secondly important if we are far or close to the building facade, respectively. In a very near field, again the material properties are more influential than the geometrical parameters because the distance is too small and lets only the very local variations be visible. Basically, while keeping the same windows distribution in blocs, the relative distance from the building edges is not important. Both studies have been conducted with two different degrees of precision (5 mm and 3 mm) for the definition of the building and for a normally incident plane wave; the smaller precision gives reasonably accurate results. The conditions of validity and the importance of different parameters may vary in an oblique incidence condition or with a different wave polarization. We also remind that in this study the glazing type of windows is not taken into account.

References

[1] H. Suzuki, A statistical model for urban radio propagation, *IEEE Trans. Communications*, 25: 673–680, 1977.

[2] M.F. Iskander, Z. Yun, Propagation prediction models for wireless communication systems, *IEEE Trans. Microwave Theory and Techniques*, 50:662–673, 2002.

[3] T.K. Sarkar, J. Zhong, K. Kyungjung, A. Medouri, M. Salazar-Palma, A survey of various propagation models for mobile communication, *IEEE Antennas Propagat. Mag.*, 45: 51–82, 2003.

[4] S. Mostarshedi, E. Richalot, M.-F. Wong, J. Wiart, O. Picon, Statistical study of the influence of building architectural properties on scattered fields in urban environment, *Ann. Telecommun.*, 66: 483–490, 2011.

[5] S. Mostarshedi, E. Richalot, J.-M. Laheurte, M.-F. Wong, J. Wiart, O. Picon, Fast and accurate calculation of scattered electromagnetic fields from building faces using Green's functions of semi-infinite medium, *IET Microwaves, Antennas & Propagation*, 4:72–82, 2010.

[6] IEEE standard definitions of terms for antennas, *IEEE Trans. Antennas Propagat.*, 17: 262–269, 1969.

[7] A. Yaghjian, An overview of near-field antenna measurements, *IEEE Trans. Antennas Propagat.*, 34: 30–45, 1986.

[8] S. Laybros, P. F. Combes, H. J. Mametsa, The very-near-field region of equiphase radiating apertures, *IEEE Antennas and Propagat. Magazine*, 47: 50–66, 2005.

[9] S. Laybros, P. F. Combes, On radiating-zone boundaries of short λ/2, and λ dipoles, *IEEE Antennas and Propagat. Magazine*, 46: 53–64, 2004.

[10] B. Sudret, Uncertainty propagation and sensitivity analysis in mechanical models - Contributions to structural reliability and stochastic spectral methods, Habilitation à diriger des recherches, Université Blaise Pascal, Clermont-Ferrand, France, 2007.

Statistical models for antennas

A. Sibille[1,2*], C. Roblin[1,2], M.A. Yousuf[1,2], M. Sacko[1,2], Z. Mhanna[1,2], and E. De Mur[2]

[1]Telecom ParisTech, France
[2]ENSTA ParisTech, France
*corresponding author, E-mail: alain.sibille@telecom-paristech.fr

Abstract

This paper addresses the pros & cons for developing statistical models intended to provide a representative description of antenna behavior in their use context. The analysis is made both from the point of view of the relevance and that of the difficulties in developing such models. Statistical antenna modeling is applied to a few cases in the field of wireless communications, addressing the statistical variations of the antennas themselves, of their immediate environment and of the local propagation context.

1. Introduction

Antennas are assumed to be deterministic objects, by the vast majority of antenna designers and researchers of this scientific community. This stems from two major considerations:

- Maxwell equations are deterministic, there is no universal source of randomness
- An antenna can be fabricated with a good reproducibility and similarly be measured reliably.

Unfortunately this deterministic assumption cannot be entirely retained, for the following reasons:

- The control of antenna characteristics, whether they were mechanical or structural (material parameters), cannot be perfectly guaranteed, either because the requirements on the antenna properties are very high (e.g. space antennas) or because the fabrication and materials tolerances are large (e.g. for cost constraints)
- Antennas are rarely used in isolated environments. Most of the time they are placed in more or less close objects or supporting parts, which will tend to modify the performance [1]. In that case, characterizing an antenna in the ideal environment of an anechoic chamber may be illusory
- Degradations may happen in the course of the antenna lifetime [[2]] or because it is deformed in its normal use conditions

While all these disturbances are still deterministic in their physical nature, their highly changing and uncontrolled character makes them more amenable to statistical approaches than to deterministic modeling.

Although these considerations are not new and they might have been addressed decades ago, the inclusion of statistical methods in antenna design or modeling is very little spread [3]. In our opinion, there are reasons that currently tend to promote it:

- Software tools and the associated computing machines are now powerful enough to carry out full wave electromagnetic simulation of antennas in a short computation time, which opens the door to the incorporation of surrounding objects and to the inclusion of stochastic variations on the parameters.
- System modeling in general tends to be as close as possible to reality, which means to critically address the above considerations. In particular, statistical models can be introduced into standards, as already done in a number of cases, in order to make sure that all users of these standards do use the same stochastic data

In the present work, we address statistical antenna modeling and try to highlight, in addition to the general benefit of these approaches, also the intrinsic difficulties and some routes for progress.

2. Main issues in antenna statistical modeling

The statistical antenna modeling problem is schematically represented in Fig. 1. It is defined by the selection of a set of random input parameters (antenna structural parameters, environmental parameters…), which constitute the input stochastic space, and by a set of output quantities of interest. The problem we address is the construction of the input-output relation and the obtention of the statistical distribution of the output quantities. This is, generally speaking, a formidable task. Indeed:

- Depending on the problem considered, the number of input parameters may be extremely large, especially if one considers wide variations on the environment characteristics and on the antenna architecture. Further, defining multivariate distribution of these parameters, which may not be independent, is far from obvious
- Unless of small input parameters, the input-output relation will generally be highly non linear
- The output quantities may reduce to a single scalar, but in general we will be interested in a vector or a higher

order tensor in order to precisely represent the electromagnetic properties of the environed antennas. The dependencies between entries of this tensor need to be accounted for.



Figure 1: Input-output relation between random antenna parameters and the quantities of interest.

Given the fundamental difficulty ahead, we need to reduce the problem to something tractable. In this respect, some main ways can be considered, such as:

- identify and classify random variations in the input parameters. One major difficulty in modeling the output quantity occurs when the database from which is constructed a statistical model exhibits inconsistent variations. Typically this occurs if the antennas are of too different types, resulting in broad variations with little consistency. A simple and classical way to reduce the degree of randomness and to provide more regularity is to classify the samples into categories, for each of which a specific model is developed.
- apply suitable transformations on the input or output parameters, in order to smooth statistical distributions, reduce correlations and improve linearity
- sample the stochastic space in a smart manner in order to learn the main dependencies and reduce the errors in converging towards stable distributions

In the next sections, a few examples of these approaches to the context of wireless communications are shown.

3. Application to wireless communications

3.1. Antenna design and optimization

Proper design is probably the major issue for antennas. Over the past century and beyond, antenna design has been based on a combination of comprehensive engineering and of empirical knowledge, complemented by trials and errors using fabrication and measurements or electromagnetic simulations of test antennas. Indeed, although the laws of classical electromagnetism are perfectly known since Maxwell, the understanding of their effects in the case of real objects is often uneasy and non intuitive, unless of simple ones or presenting major symmetries. In this context, one possible way to guide the antenna designer is to extract some if not all of the main dependencies of the antenna characteristics on its structure and parameters. Obviously, this can only be done in a limited volume and sub-space of the stochastic space, whose dimension is essentially infinite. However, in many cases there are constraints that very much limit the possibilities in terms of antenna type, such as the obligation of planarity. Another way to reduce the exploration of the stochastic space is just to take into account the referenced body of existing design types, when the literature is documented enough.

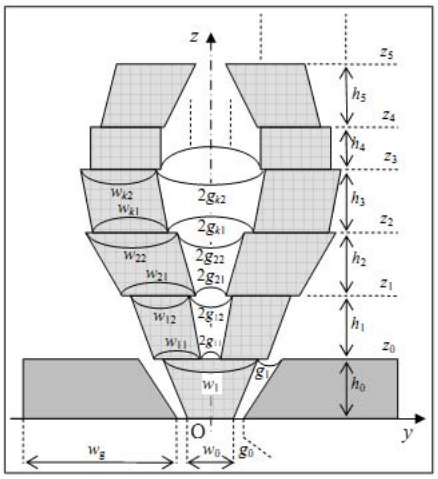


Figure 2: Input-output relation between random antenna parameters and the quantities of interest (from [5]).

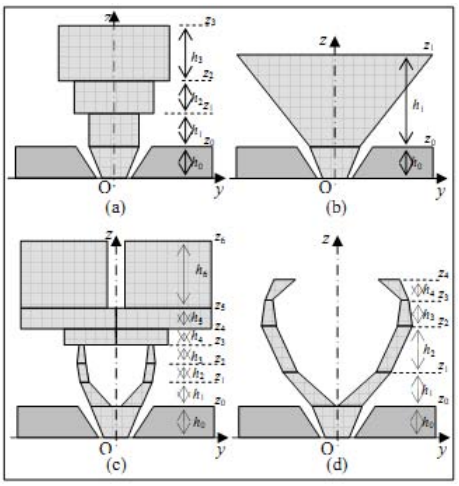


Figure 3: Various particular designs: (a) Staircase Monopole, (b) Triangular Monopole, (c) Dual Feed Monopole, and (d) Shaped (hollow) Monocone (from [5]).

Such an approach was followed in the PhD thesis of M.A. Yousuf [4], a systematic investigation of the effect of design parameters variations on antenna parameters has been conducted, for a series of planar ultra wide band (UWB) antennas (see also [5]). The "generic" design shown in Fig. 2 is sufficiently flexible to cover a wide set of antenna architectures fed by a coplanar waveguide (CPW), as demonstrated in Fig. 3 showing a few differing antenna architectures. For a given type of design (e.g. a dual feed monopole), a moderate variation of the various geometrical parameters around their mean value allows to determine up to what extent the antenna characteristics are impacted, and what statistical distributions are obtained. For this purpose, certain constraints should be enforced. Indeed the geometrical parameter variations may not be unphysical or

inconsistent, e.g. resulting in overlapping conductors or grossly incorrect line widths, to give just obvious examples. In [4], various designs have been optimized through conventional multi-objective optimization using a genetic algorithm and statistics of the antenna output parameters have also been obtained for the sets of designs respecting basic performance goals, such as a reasonable impedance matching in the band of interest. Given the Monte-Carlo design generation method employed, checking proper matching can only be done subsequently to electromagnetic simulation, meaning that the antennas too far away from this goal are just rejected and not taken into account in the antenna parameters statistics.

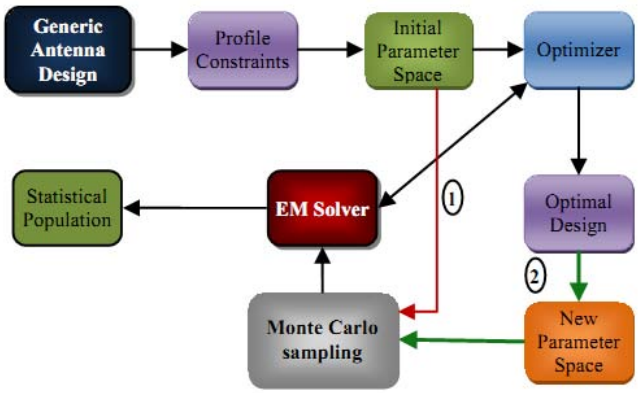


Figure 4: schematic methodology for simultaneous optimization of an antenna design and generation of output parameters statistical distributions around the optimum.

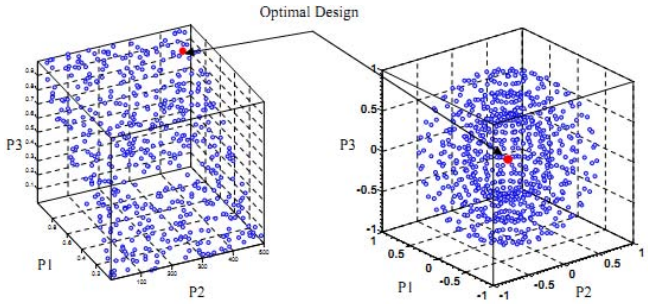


Figure 5: initial exploration of a threefold input parameters stochastic space (left), followed by a refined exploration around a certain optimum (right).

The main issue is, as implied by the expression "multi-objective optimization", that the final design depends whether the optimization favors the impedance matching, or the antenna gain, or any other relevant antenna parameter. Obviously, it may be interesting to see how the other antenna parameters are impacted, around a given "optimal" design. This may help the designer by informing him about the easiness or difficulty in reaching good performance on this or that parameter. This is the reason why, as visualized in the methodology of Fig. 4, both the optimization and the construction of statistical distributions are carried out simultaneously. In a second step, a refinement of the design parameters space exploration around a given optimal one yields the statistical distributions of the various antenna parameters interest around the optimal point (Fig. 5). Naturally, depending how this optimal point is selected, the distributions will be impacted accordingly. As an example, the Pareto front for the mean realized gain (MRG) and the mean matching efficiency (MME), as defined in [4], as well as the cumulative distribution function (CDF) of the MRG around the chosen optimal point are shown in Fig. 6.

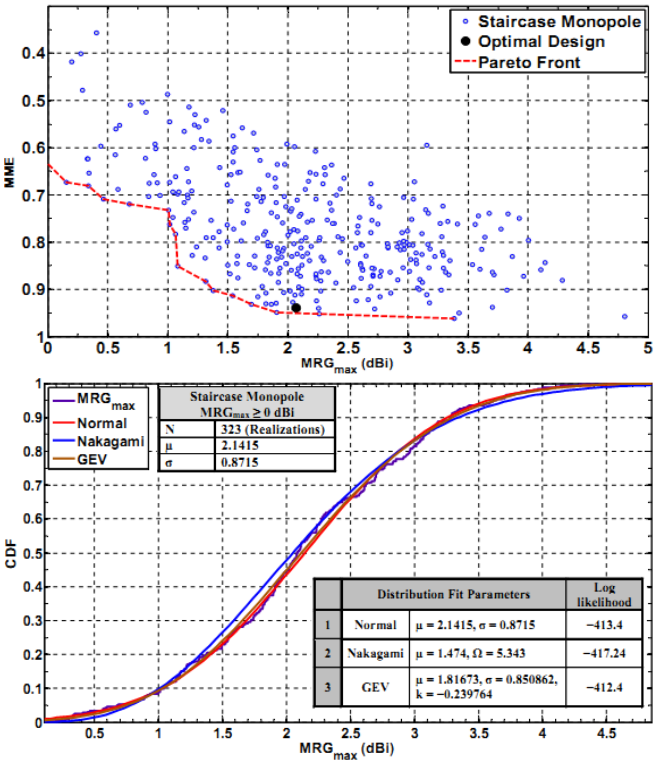


Figure 6: Multi-objective optimization and Pareto front for a staircase monopole design (up) and CDF of the MRG (down), extracted from [4].

3.2. Description of antenna randomness

In this section, we address the following goal: to provide a representative statistical description of the variations of antenna characteristics encountered for a given use case.
The objective here is to provide the wireless communication system designer with a realistic model of the transceivers radioelectric performance, at least that related to the antenna characteristics. As opposed to the previous section, the goal is not to design these antennas optimally but to express what the characteristics are in practice. Naturally, the main difficulty is in assessing the variety of antenna types that can be found in real life. Obviously it is impossible to buy an example of all commercialized antennas worldwide, but the problem also presents two more major difficulties:

- the need for such antenna statistical models is maximum at the moment when a future communication standard is being studied, which means that antennas and radio terminals are not yet available. Even worse, the use cases are not solidly established
- the greatest uncertainty in terms of antenna performance is found for the massively used

transceivers, such as wireless handsets or even femtocells or access points, whose generalization at large is on the way. Such devices are often used in unfavorable electromagnetic conditions, with strong disturbances by close objects.

From these considerations we conclude that establishing statistical models for wireless devices antenna performance is all but simple. However, given that these devices and their possibly poor performance directly impact the quality of the radio link and subsequently affect the whole system design optimization, these difficulties should not be seen as dissuasive. Below, we show two examples of the statistical performance of wireless terminals antennas in differing use contexts.

3.2.1. UWB RFID tag antennas

In this section, we address the performance of UWB tag antennas, intended to be used in a wireless system where the objects to which the tags are attached can both be identified and located, with a sub-meter accuracy. UWB is well known to potentially provide this accuracy but for most existing systems, the tags are "active", i.e. equipped with a full transceiver. Aside from cost, this solution consumes local power, which can only be achieved over long periods of time (several years) with rather bulky batteries. The main goal of the SELECT project (supported by the european commission under grant agreement 257544) is to provide a system based on modulated backscattering by the tag, which consumes much less tag local power. The main disadvantage is a roughly doubled path loss, since the signal emitted by the radiated suffers two way propagation without amplification. Therefore the link range may be very limited, unless of a very efficient system design and optimized signal processing. In this context, the tag performance should be carefully investigated, especially as the object to which it is attached is expected to be detrimental to the antenna radioelectric behavior.

A preliminary measurement campaign and analysis of a variety of "tag-like" antennas in the absence or presence of generic objects, such as plates of various materials, has been conducted and presented in [6] (see also [7]). Pictures and details on the type and dimensions (in mm) of these antennas are presented in Fig. 7. The complex radiation pattern of each antenna has been fully characterized over 4π sr in both linear polarizations in an anechoich chamber, over the 3-5 GHz band relevant for SELECT. In addition, a selection of material plates, of varying thickness, permittivity and distance to the antenna have been placed in close proximity to the antenna, and again the radiation patterns have been measured. Overall, this resulted in a database of 96 isolated or disturbed tag antenna characteristics.

The statistics of the "effective figure of merit (FoM)" for modulated backscattering based tags is depicted in Fig. 8, in both horizontal and vertical polarization and for either isolated (full lines) or disturbed antennas (dashed lines). We see that the statistical distribution is quite broad, typically showing backscattering FoM varying over more than 50 dB. Obviously it is paramount to have a good idea of the real tag performance before designing the full system. However these "bare" values of the FoM just tell part of the story, and including them into a multipath channel is necessary to get the full picture. This is highlighted below, in section 3.3.

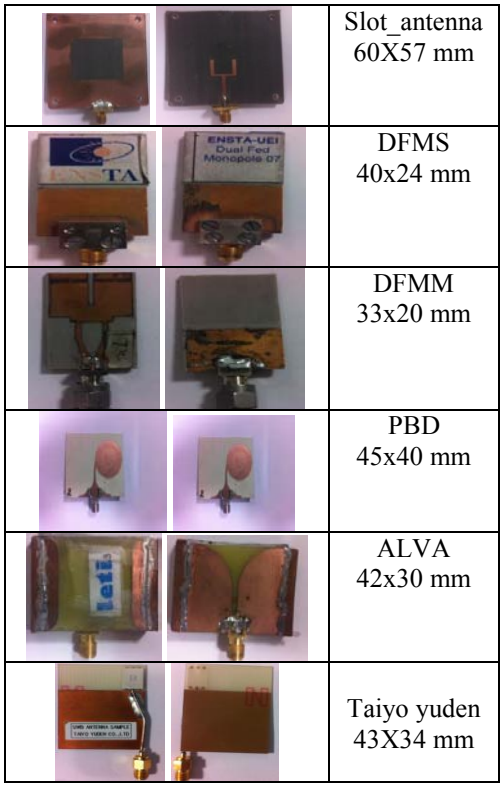


Figure 7: photographs on both sides of UWB-RFID tag antennas for the SELECT project (from [7])..

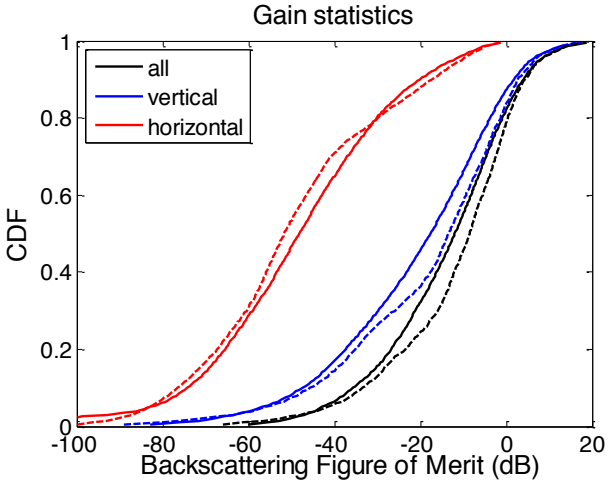


Figure 8: CDF of the figure of merit for modulated backscattering RFID UWB tag antennas (from [7]).

3.2.2. antenna near a wall

In many use cases, an antenna is placed close to a wall (e.g. for below rooftop base station antennas). It is very clear that

in the general case, the wall can bring a strong disturbance to the antenna radiation pattern, owing to the numerous refraction and reflection phenomena of which it is the place. This disturbance is commonly disregarded, although it may impact the radiation pattern very much and consequently affect the cell coverage. An extremely simple model highlights the problem crudely. Let us consider horizontal plane ray propagation between an omnidirectional vertically polarized radiator and an infinite homogeneous wall. From Descartes's laws and Fresnel coefficients, it is very easy to compute the complex radiation wave amplitude in any direction, by summing all original and reflected or transmitted waves, taking into account multiple reflections at the wall-air interfaces. In Fig. 9, we see an example of such a power radiation pattern, both for the omnidirectional antenna and for the antenna in presence of a wall. In the latter case, there is a strong deviation to omnidirectionality, with a strong fading for some directions. If the antenna is close to the wall, such a pattern can be seen as the "effective gain pattern", and treated as such for incorporation into a radio link performance calculation. In other words, the wall need not be considered as a part of the propagation channel, rather as a part of the antenna.

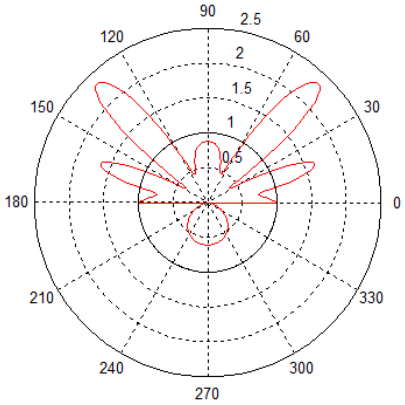


Figure 9: radiation pattern for an isolated omnidirectional antenna (black) and in presence of a wall (red).

Depending on the frequency and on the wall parameters (permittivity, thickness, distance to the antenna), the pattern will be differently impacted. It is interesting to have an idea of the statistics of the deviation between the isolated antenna pattern (often considered to be a relevant pattern for further analysis) and the disturbed one. In Fig. 10, this is shown after aggregating the power gain patterns computed over the various directions and various statistical realizations. In this example, 3 frequencies have been chosen (1.9, 2 and 2.1 GHz), the permittivity has been regularly varied from 3 to 6 every integer value, the thickness from 100 mm to 300 mm every 50 mm and the distance from 100 mm to 300 mm every 50 mm, overall resulting in 300 realizations, multiplied by the number of directions with 1° resolution. Two assumptions have been considered, either taking into account only radiation in the antenna half space (180°) or in the full space (360°).
The distribution exhibits a low gain tail, with values worse than -10 dB below the original antenna gain in 0.35 % of the cases (half space radiation). This is not bad, actually due to the fact that the wall acts as a reflector and improving the situation in many cases. However, if we consider also through the wall radiation the situation is much worse, due to the reflection at the wall-air interfaces.
Such cases are being investigated more seriously through full wave electromagnetic modeling, including the elevation dependence.

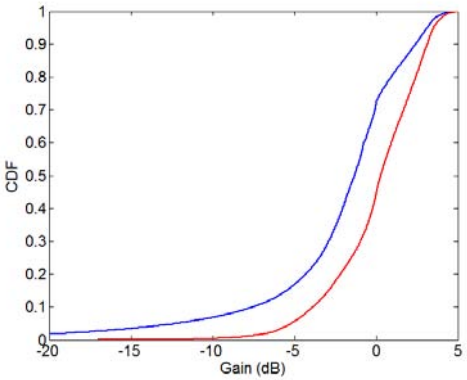


Figure 10: Statistical distribution of the antenna gain over 360° (blue) and over 180° (red).

3.3. Joint antenna/radio channel stochastic modeling

In the previous sections, we addressed the problem of developing statistical models for antenna characteristics. One of the main difficulties is that these characteristics embody a large amount of information data, typically radiation patterns over a certain band of frequencies. Even though there are techniques to reduce this amount through data compression techniques [8], the number of data values often remain high. Now, one the questions to ask is the following: can we reduce this number drastically by taking into account the way an antenna is used, in order to model the "final" quantities of interest rather than a full radiation pattern ? In other words, we are in general not interested in the detailed characteristic of an antenna but in the way it behaves. Said differently, a global "user level" performance is often the result of an integration of the fine characteristics, given certain weighting functions.
As an example, let us consider a radio link where the link quality is governed by the individual characteristics of both Tx and Rx antennas but also of the propagation channel. All three effects obviously involve plenty of complexity, however we are interested in only very simple link quality criteria, such as the path loss in the simplest case. Is it possible to combine all fine physical phenomena into a single stochastic problem, for instance described by the sole path loss statistical distribution ? Such a distribution will "hide" the inherent complexities, but this is exactly what we want, provided the parameters defining the distribution can be determined with the adequate level of knowledge.

3.3.1. Mobile communications example

Some examples of this approach can be found in [6], [9]-[11]. The idea there was to compute an "antenna effective gain", taking into account both the antenna radiation patterns

and the radio propagation channel through a simple model. The effective gain is a generalization of the "mean effective gain" (MEG) [12], which has been proposed two decades ago in an attempt to average an antenna gain over the possible directions, polarizations and powers of the multipaths. Here, the stochastic character was three-fold and due to:

- the variations in multipath angles, powers and cross-polarization levels
- the variations in the distance and orientation of the terminal antenna vs. the main electromagnetic disturber (e.g. the head for a handset in voice call mode)
- the variability of antenna characteristics themselves, through the involvement of a selection of different antenna types

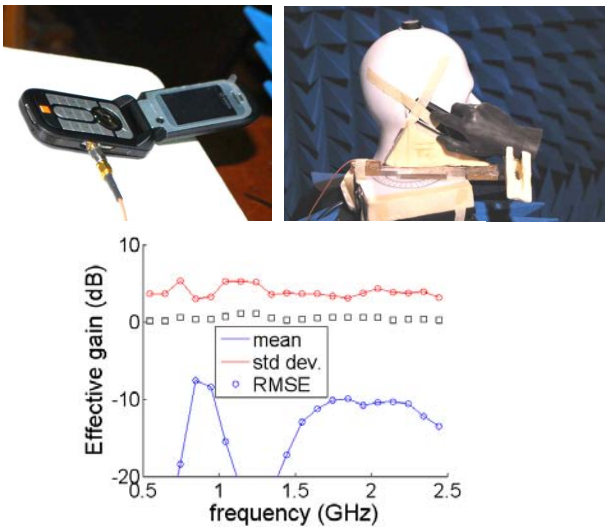


Figure 11: view of a SAGEM 901c handset and its placement on a phantom head, together with the main statistical parameters of the effective gain (from [9]).

In Fig. 9 is shown a picture of SAGEM 901c handset, where the internal antenna is accessed through a coaxial cable, which has been used in a series of full radiation patterns measurements when placed in proximity with a head phantom and a hand phantom, simulating a user during a phone conversation. By varying the phone placement parameters and by using a model of the propagation channel, it was possible to extract statistics of the antenna effective gain, as explained in [9]. Naturally, the MEG exhibits a frequency dependence highlighting the dual GSM band character of the phone, but the results also show that, in this case, a lognormal distribution of the effective gain is adequate within well less than 1 dB in most cases.

3.3.2. UWB RFID example

Through the same approach as in the previous section, the database of RFID UWB tags described 3.2.1 in has been combined with the simplified propagation model as described in 3.3.1 (detailed in [9]), specialized to the case of an indoor environment. The statistics of the backscattering effective gain (BEG, equal to 0 dBi in the case of an ideal isotropic RFID) are shown in Fig. 12, with the right set of curves standing for vertical antennas (with a vertically polarized reader) and the left set standing for tag antennas randomly rotated in all directions (see more details in [6]). This shows that very low values of the BEG can occur in poor situations. Obviously it is important to account for these realities in the design of the multi-readers system, in order to dimension it properly.

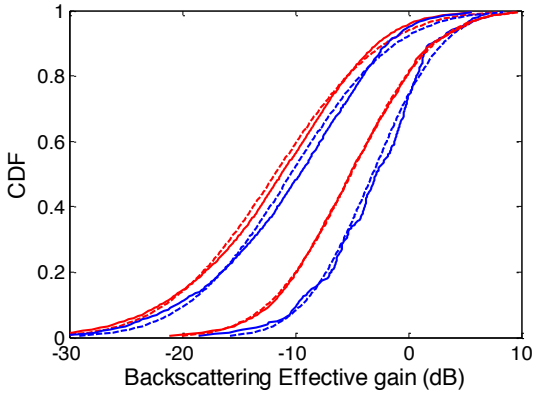


Figure 12: blue: isolated tags ; red: disturbed tags - dash: Gaussian fitting

4. Discussion

4.1. Various issues on statistical antenna modeling

The few selected examples above show the richness and variety of cases where a statistical approach may be interesting in order to model a situation where a variability, or uncertainty, will benefit in being properly described. Such potential benefits are the following:

- To provide tools that can help a system designer to evaluate performance in a realistic representation of the reality
- To standardize models that can be used as a reference for researchers/engineers around the world. Beyond a few discrete model examples (such as commonly done in standardized channel models), the benefit is to cover a much larger number of cases and to include the important variability of the antennas in their use context
- To exploit statistical models beyond the sole extraction of the mean and the variance, i.e. towards the full statistical distribution, which is able to provide important information of higher order on the system performance (e.g. link outage statistics).

In many cases, we will be happy if the Gaussian distribution is found to be adequate, on account of its well known extreme simplicity. In such a case, the stochastic generation of random variables is quite easy, even for correlated multiple variables ; Unfortunately, although the Gaussian distribution often occurs in nature due to the central limit theorem, most observed distributions are *not* Gaussian. We will have to resort to tricks in order to recover a Gaussian distributed variable from one that is not. One such trick is to through transform the variables. The lognormal distribution is the simplest example of this technique, where the initial variable (received power) is not Gaussian distributed while

its logarithm is. Another trick is by mapping-demapping between an original distribution and a best-fit one, where it is possible to compute and exploit correlations in the Gaussian domain. This e.g. done in [13] and applied to the modeling of UWB RFID antenna characteristics in both the angular and delay domains. Obviously, this is practicable only when the distributions do not deviate too much from the Gaussian.

Of particular importance are the tail distributions, where tail here means a particularly low valued (or high valued) output parameter, such as a gain. When such tails occur, even though they express a low probability for these low valued parameters, they may have dramatic effects, such a link outage. It is probably more important to correctly model these dramatic events than those which are very favorable and pose no problems, just providing particularly good performance. There are many possible (physical) causes for the appearance of tails. In [11], radiation blocking by a major obstruction has been identified to cause tails in the antenna effective gain, and modeled as a mixture of distributions.

4.2. How to construct statistical distributions ?

As pointed out above, the effort to obtain a statistical distribution is important, since we need to control the many parameters involved in its elaboration and the impact of these parameters on the distribution. Basically, statistical distributions are intimately dependent on the choice of the input parameters, and choosing them and their range is all but a simple task. Some of the big questions are:

- How can we choose the input parameters ? In the example of the handset for instance, how can we chose the distance, orientation & tilt parameters of the handset with respect to the head ? Some assumptions can be made, while another much "heavier" approach is to make enquiries on a representative set of the user population.
- An even more challenging question is: how can we choose the handset types used to build a distribution ? There are hundreds of handset models, even worse they change every few years according to the technology and use case evolutions (e.g. from pure telephones to handsets, from clamshell type to flat bar type). The size and shape of the head are obviously not unique, even the electromagnetic properties of the biological tissues change from one person to another. Finally the way to hold the phone by the hand and all the characteristics of the hand itself are important.

This frustrating complexity should not lead us to give up a lost fight, but rather to identify the level of accuracy we expect from the statistical distributions, the degree of representativeness we wish for them, according to the way the modeled distributions will be used, and the effort we are ready to pay.

Given these considerations, one possible way out is to limit the level of ambition, e.g. in terms of model universality. By reducing the number of modeled use cases, we diminish the size of the input stochastic space to explore.

A second way is to identify the main dependencies, and explore in a more refined manner the corresponding directions of the input stochastic space. For instance, in the handset case, the distance to head parameter is certainly more important than the orientation vs. the vertical axis, due to the power absorption by the head. Such dependencies can be discovered in the course of the building of the distributions. Techniques such as importance sampling do this by using a precise methodology [14].

5. Conclusion

In this work, we have attempted to highlight reasons why the statistical modeling of antennas may be seen as a relevant and useful objective, the goal being to provide a better representation of reality and uncertainty than what we have by just considering average or "typical" antenna models. The stochastic character of antennas comes from the antennas themselves or from their environment. The statistical description is thus able to take into account use conditions in a realistic manner. Some examples supporting these views have been shown in the paper, taken from the field of wireless communications.

It is anticipated that, in the future, such approaches will gain recognition and will be more often used, just as they will be for electromagnetic problems in general.

Acknowledgements

The research leading to these results has received funding from the European Union Seventh Framework Programme FP7/2007-2013 under grant agreement n° 257544.

References

[1] Mellah, M. A.; Sibille, A.; Roblin, C.; Nedil, M.; Denidni, T. A., "Statistical Modeling of the Antenna – Head Interaction", *Antennas and Wireless Propagation Letters*, Vol. 10, 454–457, 2011

[2] Olsson, T. and Koptioug, A.I, "Statistical Analysis of Antenna Robustness", *IEEE Transactions on antennas and propagation*, AP-53, 1, pp. 566 - 570, 2005.

[3] Shifrin, Y.S., *Statistical antenna theory*, The Golem Press, Boulder, Colorado, 1971.

[4] M.A. Yousuf, "Parametric Modeling of Small Terminals and Multiband or UWB Antennas", PhD thesis, Ecole Polytechnique, Sept. 29, 2011

[5] C. Roblin & M.A. Yousuf, A Generic Design of Planar UWB Antennas for Parametric or Statistical Analysis *Proc. 3rd European Conference on Antennas and Propagation EuCAP*, March 23-27, 2009, Berlin, Germany.

[6] A. Sibille, M. Sacko, Z. Mhanna, F. Guidi, and C. Roblin, Joint antenna-channel statistical modelling of UWB backscattering RFID, *ICUWB 2011*, Bologna, September 14-16, 2011

[7] R. D'Errico, V. Heiries, J. Keignart, D. Dardari, N. Decarli, C. Roblin, A. Sibille, F. Guidi, M. Sacko, Z. Mhanna, SELECT FP7 project n°257544, Backscatter

propagation modelling: Interim report, 31/07/2011, http://www.selectwireless.eu/

[8] C. Roblin, Ultra compressed parametric modelling of UWB antenna measurements, *Proc. 1st European Conference on Antennas and Propagation EuCAP*, 6-10 Nov. 2006, Nice, France

[9] A. Sibille and M. A. Mellah, A Statistical Model of Handsets Effective Gain Accounting For User Influence And Local Propagation, *Proc. 4th European Conference on Antennas and Propagation EuCAP*, 12-16 Apr. 2010, Barcelona, Spain

[10] A. Sibille, C. Roblin, S. Bories, & and A. C. Lepage, "A Channel-Based Statistical Approach to Antenna Performance in UWB Communications", *IEEE Transactions on Antennas and Propagation*, vol. 54, n° 11. November 2006, pp. 3207-3215

[11] A. Sibille, J. Guterman, A. Moreira and C. Peixeiro, "Performance evaluation of 2.4 GHz laptop antennas using a joint antenna-channel statistical model", TD(09)930, *COST 2100 Management Committee Meeting*, Vienna, Austria, September 28-30, 2009

[12] T. Taga, Analysis for mean effective gain of mobile antennas in land mobile radio environments, *IEEE Transactions on Vehicular Technology*, **39**, 2, May 1990, pp. 117-131

[13] M.Sacko, A. Sibille and C.Roblin, Statistical analysis of UWB tag antenna backscattering, AES 2012, Paris, France, April 16-19, 2012

[14] R Sinivasan, Importance Sampling: Applications in Communications and Detection, Springer, 2009

Dielectric relaxations due to electrons in oxides

Jean-Claude Badot*

Laboratoire de Chimie de la Matière Condensée de Paris, Chimie-ParisTech, UPMC, CNRS, Paris, France
*corresponding author, E-mail: jc-badot@chimie-paristech.fr

Abstract

This report deals with the fundamental aspect of the dielectric relaxations due to electrons in conducting oxides (powders, thin films, composites). It is shown that is possible to evidence conductivity, resistivity and permittivity relaxations due to electrons: small-polarons, bipolaron hopping at high frequency and interfacial polarizations (e.g. grain boundaries) at lower frequencies. The importance of all these phenomena is discussed in relation with their possible interventions in dielectric spectra.

1. Introduction

The electrical response of a material is due to charge density fluctuations, when it is submitted to a time-dependent electric field. This response can be described by the time dependent current density j(t) or dipole moment μ(t). In the frequency domain, these fluctuations are either expressed by the frequency-dependent complex permittivity ε, conductivity σ or resistivity ρ. The time scale (or relaxation time) of the fluctuations depends on the scale at which they occur. According to H. Fröhlich [1] and A.J. Bosman and A.H. van Daal [2], the Debye dielectric relaxation can only occur with small-polaron formation in semiconducting oxides (mixed valence compounds). As the dielectric relaxation is the result of an electric dipole reorientation, we have to consider only local (confined) hopping of small-polarons around an immobile ion or long-range hopping between two trapping centers [3]. The dielectric relaxation time corresponds to the hopping time of the charge and is generally thermally activated [4].

However, the study of electrical transport properties becomes complicated since the compounds of the above type are generally made under form of powders or thin films. Different dielectric relaxations are evidenced, resulting from the polarizations at the different scales of the architecture (Figure1): (a) interatomic (polaron hopping), (b) clusters (agglomerates) of particles (grains), (b) particles (grains), (c) sample/current collector interface [5, 6]. Strongly frequency dependence of the permittivity in low frequency region was noted in several oxides powders which consist of semiconducting particles and/or clusters separated by quasi-insulating grain-boundary layers. In this scheme, the particles and the clusters are polarized by the accumulation of charge carriers on their boundaries, under the action of an electric field.

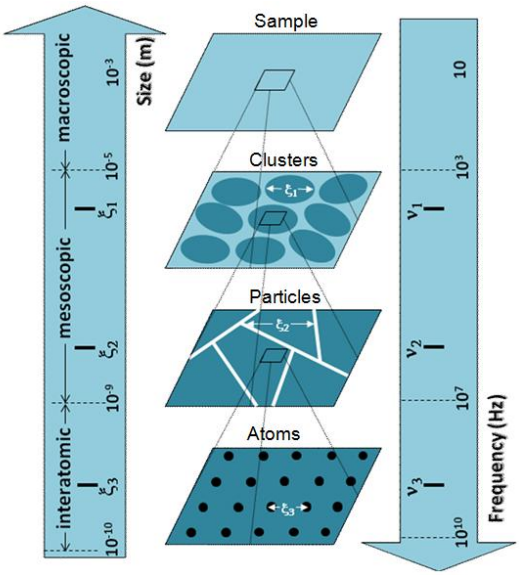


Figure 1: Schematic description of a hierarchical architecture at different scales of a powdered material: different sources of polarizations vs. frequency and size.

The particles and the clusters can be assimilated to "giant dipoles" giving rise to dielectric relaxations, whose relaxation frequencies are decreasing functions of their sizes size and the resistivities. In this case, the relaxation times correspond to the transit times of the charge carriers within the particles and the clusters. These phenomena were previously evidenced in conducting oxides [2, 5-12].

Dielectric and conductivity data covering a broad frequency range from low-frequency to microwaves are presented for three types of conducting oxides: a) $WO_3.H_2O$ (powder) [10], b) Li_xMoO_3 (powder, nanobelts) [11], c) $Li_xV_2O_5$ (thin films) [12]. Particle size effects have been evidenced when the particles become nanometric giving rise to some modifications of electronic transfers [10-12].

2. Experimental devices

The experimental devices (Fig. 2), described in previous papers [5- 12], consist of a coaxial cell (APC7 standard) in

which the cylindrically shaped sample (powder pellet or thin film on metallic substrate) fills the gap between the inner conductor and a short circuit. The sample admittance Y_s is computed from measurements of the complex reflection coefficient of the device. The complex (relative) permittivity of the sample $\varepsilon = \varepsilon' - i\varepsilon''$ (real part ε' and imaginary part ε'') is computed from the admittance $Y = G + iB$. The knowledge of the complex permittivity ε allows the determination of complex conductivity σ and resistivity ρ

$$\sigma(\omega) = \rho(\omega)^{-1} = i\,\omega\,\varepsilon_0\,\varepsilon(\omega) \qquad (1)$$

where ε_0 is the vacuum permittivity ($\varepsilon_0 = 8.84\text{x}10^{-12}$ F.m^{-1}).

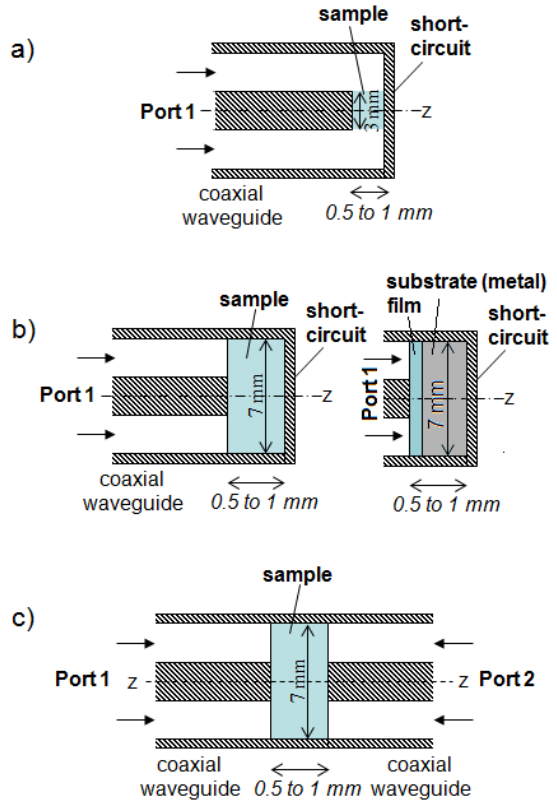


Figure 2. Coaxial cells used to measure frequency dependent permittivity (ε', ε'') and conductivity (σ) for: a) powders pellets of diameter 3 mm (SuperPol); b) powders pellets and thin films of diameter 7mm (SuperMit and SuperBic); c) anisotropic samples (nanobelts) of diameter = 7 mm (SuperPolar) [11].

When the sample is anisotropic (e.g. nanobelts), the experimental device (Fig. 2c) consists of a coaxial cell loaded to the two ports (1 and 2) of the network analyzer (HP 8510 from $4.5\text{x}10^7$ to 10^{10} Hz). The samples (NB) having uniaxial anisotropy fills the gap between the two inner conductors connected to the ports 1 and 2. This device permits to measure simultaneously the reflection and transmission coefficients, and thus the components $\varepsilon_\perp$ (i.e. perpendicular to sample axis) and $\varepsilon_{//}$ (i.e. parallel to sample axis) of the permittivity (uniaxial) tensor.

3. Some examples

3.1. An electro active compound: $WO_3.H_2O$ [10]

The interest in studying the electrical properties of $WO_3.H_2O$ powders is necessary because their electrochromic and infrared modulation properties are depending on their morphologies and electronic populations. The role of the powder morphology has been investigated on two types of compounds: the first one being constituted by nanoparticles (Fig. 3a) and the second by micrometric particles (Fig. 3b).

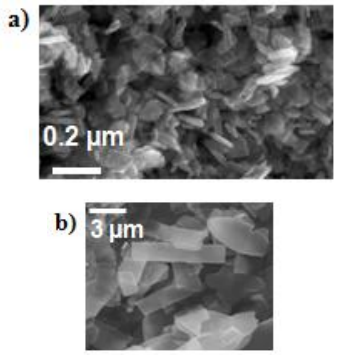


Figure 3: SEM micrographs of $WO_3.H_2O$ powders: (a) nanoparticles and (b) micronic particles [10].

Dielectric and resistivity spectra of $WO_3.H_2O$ powders were recorded in a frequency range 40 - 10^{10} Hz at temperatures varying between 200 and 300 K. Complex resistivity and permittivity diagrams have permitted to obtain thermal behaviours of both dc-conductivity and permittivity of the powder particles. Particle size effect has been evidenced, giving rise to stronger electron (small polaron) localization on the particle surface and higher activation energy for the nanometric particles.

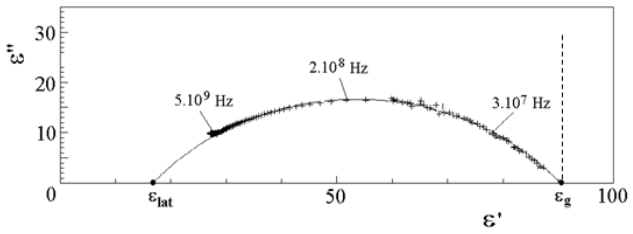


Figure 4. Cole-Cole plot of the imaginary $\varepsilon_G''(\omega)$ vs. the real part $\varepsilon_G'(\omega)$ of the complex permittivity $\varepsilon_G(\omega)$ at T = 283 K for microscale particles. The contributions of the dc-conductivity and the interfacial (grain boundaries and Ag/sample interfaces) polarizations have been subtracted [10].

In the higher frequency range ($\approx 10^8$ Hz), a dielectric relaxation (Fig. 4) was evidenced and attributed to structural water motions. These rotational motions are also influenced by the size effect. Figure 5 shows the relaxation frequency ν_w observed in microparticles with a constant value $\nu_{w0} = 2\text{x}10^8$ Hz whatever the temperature. Since the activation energy is equal to zero, the water molecules rotate without breaking hydrogen-bonds. We may thus suspect that they

perform oscillations similar to co-operative "windscreen wiper" motions. The relaxation frequency of water motion in nanoparticles is thermally activated, following an Arrhenius law, $\nu_w = \nu_0 \exp(-E_w/kT)$, with an activation energy $E_w \approx 0.03$ eV. The prefactor ν_0 has the same value as the water relaxation frequency in microparticles, i.e. $\nu_0 = \nu_{w0} = 2x10^8$ Hz. The activation energy $E_w \approx kT$ corresponds to the "ion- mobile dipole" interaction.

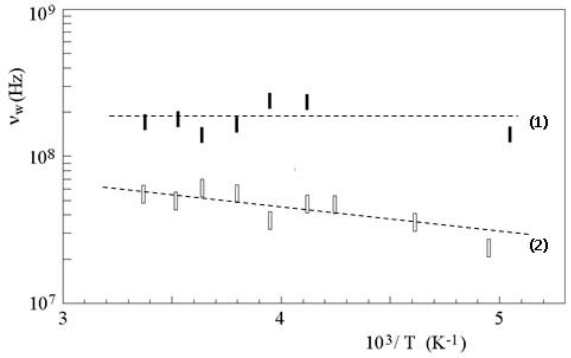


Figure 5. Inverse temperature dependence of the relaxation frequency of structural water motion in micrometric (■) and nanometric (□) particles of $WO_3.H_2O$ [10].

Accordingly, the existence of an electrostatic field created by a charge-space in the nanometric particles, has induced a slowing-down of the water molecules motions. We have evidenced a strong interaction between moving small-polarons and water molecules in a hydrate. The size effect acts on the electronic transport in $WO_3.H_2O$, because its high permittivity $\varepsilon_g \approx 100$ is the result of an antiferroelectric order of the H_2O dipoles. We may anticipate that lithium ions will tend to segregate on the nanoparticles surface. Consequently, insertion and de-insertion of lithium ions would be faster, since diffusion on the particle surface requires lower energy than in the particle bulk. This hypothesis agrees with experimental evidence of a better reversibility of Li insertion-deinsertion for the nanometric powder after several electrochemical cycles.

3.2. A compound for lithium batteries: MoO_3 [11]

Studying the electronic transport in Li_xMoO_3 powders is of the utmost interest due to the strong influence of the grain size and morphology on their electrochemical cycling properties.

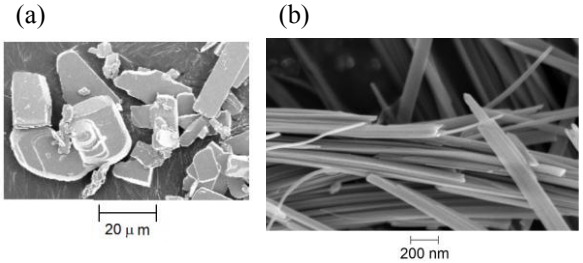


Figure 6. SEM picture of αMoO_3: (a) classical powder (CP) and (b) nanobelts (NB) [11].

Original synthesis method permitted to obtain nanobelts of αMoO_3 with a slightly better reversibility of Li insertion-deinsertion and a higher efficiency of lithium insertion process. The role of the morphology and size effect has been investigated by comparing the electron transport properties of micronic powder and nanobelts (Fig. 6).
The broadband dielectric spectroscopy technique from 40 to 10^{10} Hz was applied to Li_xMoO_3 micronic powder (Fig. 7a) and nanobelts (Fig. 7b) between 200 and 400 K. High resolution TEM observations confirmed that the nanobelts are single crystals. Dielectric relaxations were found, by using a decomposition procedure of the Cole-Cole plots [11].

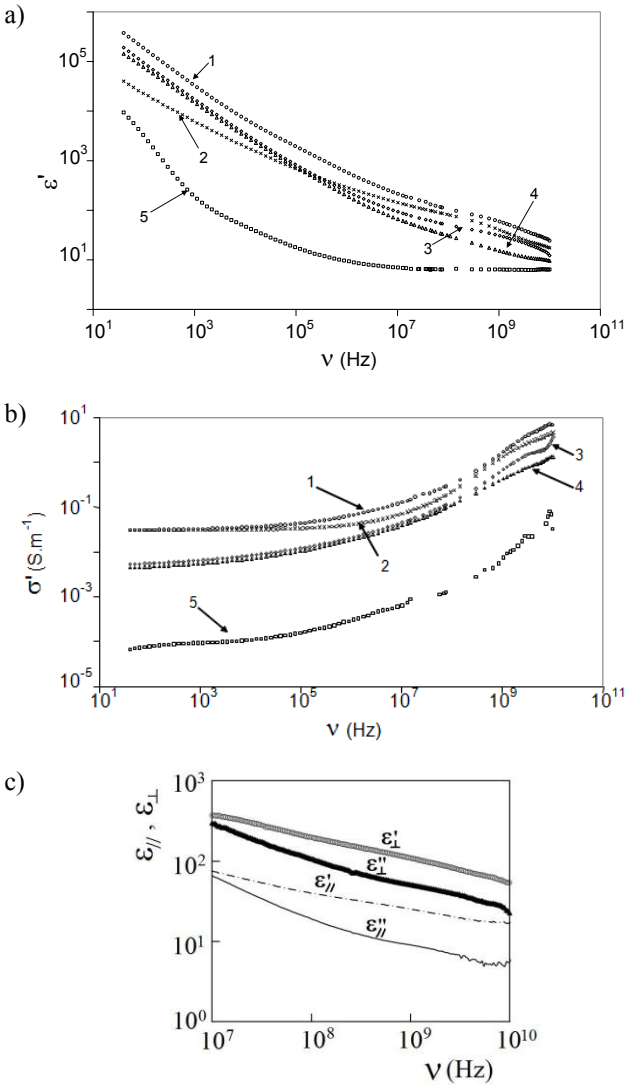


Figure 7. Real parts of: a) the permittivity ε' and b) the conductivity σ vs. frequency for different lithium contents x in MoO_3 classical powder (CP) (1: x=0.45; 2: x=0.31; 4: x=0.11; 5: x=0.01) and nanobelts (NB) (3: x=0.28) at 300 K. c) Real ($\varepsilon'_{\perp}$, $\varepsilon'_{//}$) and imaginary ($\varepsilon''_{\perp}$, $\varepsilon''_{//}$) parts of the components $\varepsilon_{\perp}$ and $\varepsilon_{//}$ of the complex permittivity tensor for $Li_{0.28}MoO_3$ (NB) vs. frequency at 300 K [11].

In summary, different electrical relaxations were shown on Li_xMoO_3, resulting from the polarizations at the different scales of the samples: i) polaron and bipolaron motions along chains parallel to c axis (Fig. 8), ii) grains (crystallites), iii) aggregates of grains. For micronic particles (classical powder), the change from polaronic to bipolaronic conduction has been evidenced with the increase of the lithium content x. On the other way, this conduction change was not observed in the case of nanobelts owing to morphology and size effects. This phenomenon was attributed to a stronger surface effect for nanobelts giving rise to a different conduction mechanism. Moreover, the influence of the permittivity was reported on its action on the electronic transport in Li_xMoO_3.

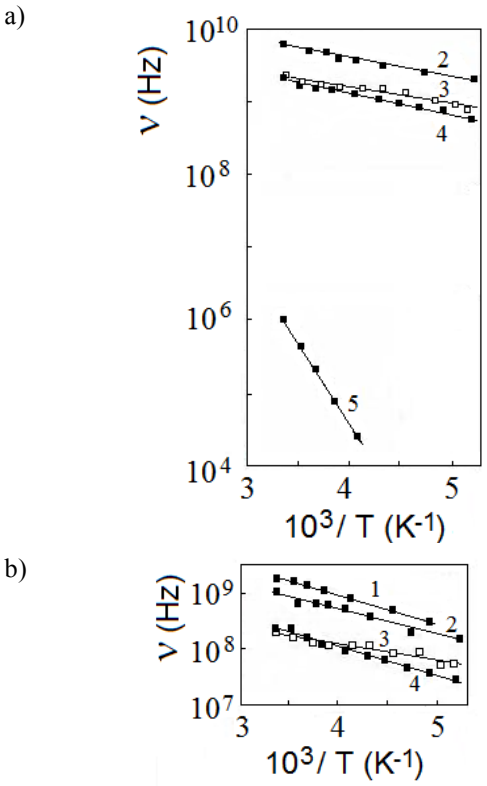


Figure 8. a) Relaxation frequencies of polaron motion as function of inverse temperature T^{-1} ($\log \nu$ vs. T^{-1}) in Li_xMoO_3 classical powder (CP) (2: x = 0.31; 4: x = 0.11; 5: x = 0.01) and nanobelts (3: x = 0.28); (b) Relaxation frequencies of bipolaron motion as function of inverse temperature T^{-1} ($\log \nu$ vs. T^{-1}) in (CP) (1: x = 0.45; 2: x = 0.31; 4: x = 0.11) and (NB) (x = 0.28) [11].

Particle size effect is evidenced giving rise to different thermal behaviors between the two types of powders. The influence of the permittivity was reported on its action on the electronic transport in Li_xMoO_3. The crystal permittivity has a supplementary contribution of the [Li^+-electron] dipoles in addition to that of electronic transitions and lattice.

This work opens up new prospects for a more fundamental understanding of the electronic transport in relation to the electrochemical properties of αMoO_3.

3.3. $Li_{0.2}V_2O_5$ thin films obtained by ALD [12]

The V_2O_5 thin film (thickness 260 nm) was deposited on titanium substrate by Atomic Layer Deposition (ALD). An annealing process at 500°C in air was required to obtain crystallized V_2O_5. Thin film thickness of about 260 nm has been measured by profilometry. Scanning electron micrographs have shown that the films consist of particles with mean size d_p = 450 nm. X-Ray diffraction linewidths of V_2O_5 have permitted to determine the mean coherence length, ξ = 40 nm, of the diffracting domains, as previously reported. Since $\xi < d_p$, the particles can be thus considered as small polycrystals (or aggregates) constituted by some single crystalline domains or grains (i.e., diffracting domains). $Li_{0.2}V_2O_5$ is prepared by electrochemical lithiation of the V_2O_5 thin film: the lithium insertion is compensated by excess electrons, reducing V^{5+} into V^{4+} and contributing to the electronic conductivity by small-polaron hopping. The frequency dependence of the real and imaginary parts ε' and ε" of $Li_{0.2}V_2O_5$ thin film permittivity ε are respectively shown in Fig. 9a and 9b.

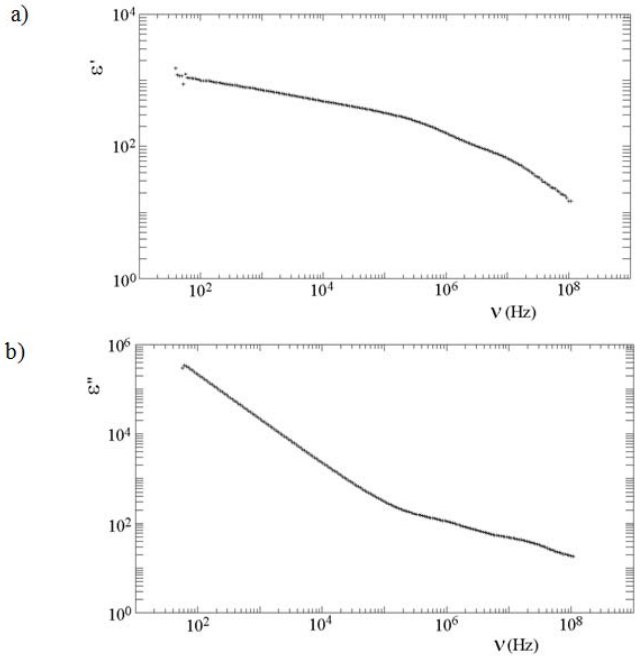


Figure 9. Dielectric spectra of $Li_{0.2}V_2O_5$ thin film deposited on titanium substrate (thickness = 260 nm). (a) real part ε', (b) imaginary part ε" of the permittivity vs. frequency ν at 213 K [12].

All the data are presented in the form of complex resistivity and permittivity diagrams which have been analyzed in relation to characterizations with scanning electron microscopy (SEM) and X-ray diffraction (XRD).

Dc-conductivity of the $Li_xV_2O_5$ films determined with complex resistivity plots (Fig. 10) is due to surface diffusion of small-polarons on particles or grains. This phenomenon originates from the small size of the particles (submicronic) and grains (nanoscopic), which facilitates the lithium ions segregation (with the excess electrons) on their surfaces.

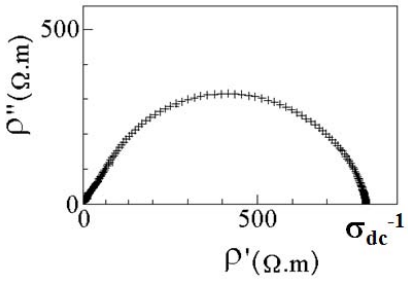


Figure 10. Plot of imaginary part ρ"(ν) vs. real part ρ'(ν) of the complex resistivity at 213 K for a $Li_{0.2}V_2O_5$ thin film deposited on titanium substrate (thickness = 260 nm) [12].

The temperature dependence of the dc-conductivity is ruled by two Arrhenius regimes (Fig. 11). For the low-temperature regime (T < 260 K), the activation energy is E_{LT} = 0.05 eV. For the high-temperature regime (T > 260 K), the activation energy E_{HT} is higher and equal to 0.10 eV.

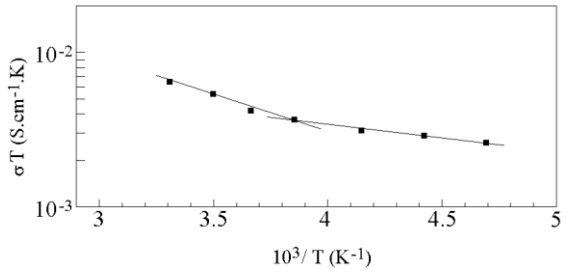


Figure 11. Dc-conductivity σ_{dc} as a function of inverse temperature T^{-1} ($\sigma_{dc}T$ vs. T^{-1}) for the $Li_{0.2}V_2O_5$ thin film deposited on titanium substrate (thickness = 260 nm) [12].

Complex permittivity plots (Fig. 12) shown four dielectric relaxations (P2, P3, P4 and P5) which are easily evidenced and represented by circular arcs, i.e. well fitted by the Cole-Cole function.

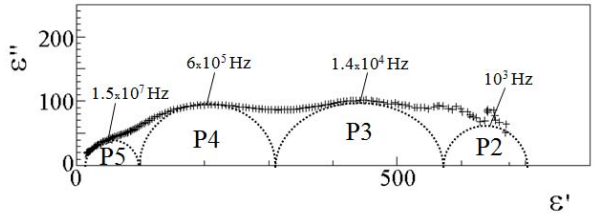


Figure 12. Cole-Cole plots of imaginary part ε"(ν) vs. real part ε'(ν) of the complex permittivity at 213 K for a $Li_{0.2}V_2O_5$ thin film deposited on titanium substrate (thickness = 260 nm). Plot obtained upon subtracting the film dc-conductivity contribution (evidence of four dielectric relaxations) [12].

The lower frequency relaxation domain P2 is attributed to the interface substrate/film which has a negligible effect on the complex resistivity (Fig. 10). The higher frequency relaxation domain P5 corresponds to the small-polaron hopping within the grain (crystallite) as previously shown [7]. The relaxations P3 and P4 are attributed to polarons motions on the grain and particle surface, respectively. Their corresponding activation energies E_3 = 0.05 eV and E_4 = 0.10 eV are respectively equal to E_{LT} and E_{HT}. Since the surface diffusion of the charges is easy around the particles and the grains, these later being polarized under the action of an electric field. The relaxation frequency ν_r of P3 or P4 is related to the polaron diffusion coefficient from the expression $D \propto \nu_r a^2$, where a (diffusion length) is the mean size of the particle ($a = d_p$) or the grain ($a = \xi$). From the Einstein relation, the diffusion coefficient D is connected to the conductivity via $D \propto \sigma_{dc}T$. It is thus possible to establish a phenomenological relationship:

$$a \propto \left(\frac{\sigma_{dc} T}{\nu_r} \right)^{1/2} \qquad (3)$$

Since the ratio d_p/ξ = 11 confirms well the relationship $(\sigma_{LT}\nu_4 / \sigma_{HT}\nu_3)^{1/2}$ obtained from (3), we can attribute the relaxation P3 and P4 to the polarization reversals of the particles and grains (crystallites) respectively. In conclusion, the high temperature (T > 260 K) regime of the film dc-conductivity is due to charges diffusion along the grains surface (*nanostructure*), whereas its low-temperature regime is due to charge diffusion along the particles surface (*sub microstructure*).

4. Conclusions

The three examples show that the broadband dielectric spectroscopy is well adapted to study electronic conductors, such as mixed valence oxides. Dielectric relaxations can be evidenced due to electrons hopping (polarons, bipolarons). Main part of compounds under form of powders constitutes complex hierarchical architectures whose responses are due to multiscale electrical polarizations, i.e. from interatomic to macroscopic scales (Fig. 1).

Acknowledgements

The author is thankful to Dr. Olivier Dubrunfaut (LGEP, Gif-sur-Yvette).

References

[1] H. Fröhlich, S. Machlup, T.K. Mitra, Low mobility materials and Debije loss due to electrons, *Phys. Kondens. Mater*. 1: 359-366, 1963.

[2] A.J. Bosman, H. J. van Daal, Small-polaron versus band conduction in some transition metal oxides, *Adv. Phys*. 19: 1-117, 1970.

[3] G.L. Sewell, Model of Thermally Activated Hopping Motion in Solids, *Phys. Rev*.129: 597-608, 1963.

[4] A.S. Alexandrov, N. Mott, *Polaron and Bipolarons*, World Scientific, Singapore, 1998.

[5] J.C. Badot, E. Ligneel, O. Dubrunfaut, D. Guyomard, B Lestriez, Multi-scale description of the electronic transport within the hierarchical architecture of a composite electrode for lithium battery, *Adv. Funct. Mater*. 19: 2749-2758, 2009.

[6] K.A. Seid, J.C. Badot, O. Dubrunfaut, S. Levasseur, D. Guyomard, B. Lestriez, Multiscale electronic transport mechanism and true conductivities in amorphous carbon-$LiFePO_4$ nanocomposites, *J. Mater. Chem*. DOI: 10.1039/c2jm13429b, 2012.

[7] B. Pecquenard, J.C. Badot, N. Baffier, N.E. Belhadj-Tahar, Electronic transport properties in α and ε phases of $Li_xV_2O_5$ bronzes: radio-and microwave frequency dielectric studies, *Phys. Stat. Sol. (a)* 159: 469-484, 1997.

[8] J.C. Badot, O. Dubrunfaut, Evidence for transition from polaron to bipolaron conduction in electroactive $Li_xCr_{0.11}V_2O_{5.16}$ powders: a dynamic study from 10 to 10^{10} Hz, *J. Solid State Chem*. 184: 3208-3215, 2011.

[9] J.C. Badot, V. Bianchi, N. Baffier, N.E. Belhadj-Tahar, Dielectric and conductivity spectroscopy of $Li_{1-x}Ni_{1+x}O_2$ in the range of 10 to 10^{10} Hz: polaron hopping, *J. Phys.: Condensed Matter*, 14: 6917-6930, 2002.

[10] L. Beluze, J.C. Badot, R. Weil, V. Lucas, Broadband dielectric and resistivity spectroscopy of $WO_3.H_2O$ in the range of $10^3 – 10^{10}$ Hz: particle size effect, *J. Phys. Chem. B* 110: 7304-7308, 2006.

[11] S. Berthumeyrie, J.C. Badot, J.P. Pereira-Ramos, O. Dubrunfaut, S. Bach, Ph. Vermaut, Influence of the lithium insertion on the electronic transport in electroactive MoO_3 nanobelts and classical powders: morphological and particle size effects, *J. Phys. Chem. C*, Vol. 114, 19803-19814, 2010.

[12] J.C. Badot, A. Mantoux, N. Baffier, O. Dubrunfaut, D. Lincot, Submicro- and nanostructural effects on the electrical properties of $Li_{0.2}V_2O_5$ thin films obtained by atomic layer deposition (ALD), *J. Phys. Chem. Sol*. 67: 1270-1274, 2006.

Design and evaluation of two coaxial transmission lines to characterize electromagnetism properties of hard clays (non crushed) and concrete

T. Bore[1]*, D. Placko[2], D. Coelho[1], S. Delepine-Lesoille[1], C. Gatabin[5], P. Sabouroux[3] G. Six[4] and F. Taillade[4]

[1]Andra, 1-7 rue Jean Monet, 92298 Chatenay-Malabry France
[2] SATIE, ENS Cachan, CNRS, 61 avenue du président Wilson
94 235 Cachan Cedex France
[3] Université Aix Marseille, Institut Fresnel - UMR CNRS 6133 - 13013 Marseille, France
[4] Université Paris Est, IFSTTAR, MACS, F-75015, Paris, France.
[5] CEA, Saclay, DEN/DANS/DPC/SECR/LECBA, 91191 Gif-sur-Yvette, France
*corresponding author: thierry.bore@andra.fr

Abstract

The use of electrostatic and electromagnetic sensors such as Time Domain Reflectometry (TDR) probes has gained increasing importance for water content measurements since several years, for long term monitoring of structures, among which radioactive waste repositories.. Prior to perform in-situ experiments with TDR probes, it is mandatory to have an accurate knowledge of the electromagnetic properties of materials under interest as a function of their water content. As in-situ calibration is invasive, calibration was performed on samples. For that purpose, a new experimental setup consisting in two coaxial transmission line fixtures was designed and used on clay and concrete samples. Clayrock samples are cm sized. Since fractures and compaction have major influence, this laboratory system allows measurements on non crushed clayrock samples. It results that dielectric properties are highly dependent of frequency. Crushed argillite sample presents smaller permittivity than intact samples. Concrete transmission line was designed so as to respect large representative elementary volume. Concrete curing on the induce decrease of permittivity. Measurements are limited by Waxwell-Wagner.phenomena, to be studied further.

1. Introduction

The French National Radioactive Waste Management Agency (Andra) is in charge of long-term management of radioactive waste produced in France. Andra operates two surface repositories to manage respectively low- and intermediate-level short-lived radioactive waste and very-low-level radioactive wastes. Andra also manages a surface repository, which has entered its post-closure monitoring phase since 2003. After having concluded in 2005 to the feasibility of deep geological disposal for high-level and long-lived radioactive waste, Andra was charged by the French 2006 planning act to design and create an industrial center for a geological repository called CIGEO. The underground installations of the CIGEO repository will be built progressively and operated over a period on the order of a century. In the framework of this project, monitoring of the environment and repository structures, which in Andra's project is called "Observation and Surveillance", should provide requested information for its operation and its reversible management.

Water content is a key parameter to monitor in nuclear waste repositories since it drives radioactivity confinement. More precisely, monitoring water content in clay structures (crushed clay of cover structures on the one hand, hard clay host rock of the underground repository one the other hand) contributes to assess safety, enables to confirm and precise long-term radionucleide transfer models.

Concrete water content monitoring is also required since it drives long-term evolution of structures (structural heath). For intermediate-level long-lived wastes, the envisioned disposal cells would be few hundred meter long tunnels, with thick concrete liners, placed inside a clay host rock located 500 m deep from the surface. French law imposes reversibility and retrievability of the wastes for at least a century. To ensure this challenge, on top of careful design, structural health monitoring will be mandatory. Water content in concrete liners will be influenced by (i) concrete pouring (ii) ventilation (iii) heat transfers from wastes (iv) host rock hydraulic evolution. Such expected (modelised) phenomenology is to be compared with in situ measurements. Sensors and related acquisition chains must perform accurate measurements within decades without any maintenance. Indeed, the cells will not be accessible as soon as the first waste package is placed inside the cell.

Unlike mechanical and thermal processes for which vibrating wire sensors and platinum probes have proved their efficiency for more than half a century on dam monitoring, for water content monitoring, very few

technologies allow accurate and long-term monitoring without maintenance.

Andra initiated tests on water content sensing chains in 1994, when a one-to-one scale mock-up of a cover structure, made of crushed clay, was instrumented with four water content sensor types. Capacitive sensors, Time Domain Reflectometry (TDR) sensors, tensiometric suction probes and neutronic probes were implemented. TDR resulted to be the only efficient technology: it survived and provides accurate measurements. Nowadays, more than 80 TDR sensors still provide accurate water content measurements.

More recently, in collaboration with EDF, Andra evaluated various technologies for concrete water content measurements [1]. TDR design was adapted to fit concrete structure specificities (size, metallic bars…) and preliminary results are interesting.

However, despite interesting measurements, TDR probes actually provide indirect measurement of water content. A major difficulty to face is the link between the performed permittivity measurements with host material water content to sense. Various empirical models are used for soil ([2][3][4]). Yet it is well known they are not valid for clays, neither for concrete. Another solution is to rely on laboratory calibrations. However, it encounters opposite specifications (i) need for large samples to place the TDR probes and respect interaction field (ii) duration of water content forced variations. This calls for the dielectric characterization of concrete and clay, as a function of their water content.

Concerning the clay rock, Andra has performed a huge number of physical and chemical measurements in its underground laboratory located at Bure (eastern Paris Basin, France) ([5][6][7]). The electromagnetic properties and especially the electrical permittivity, remain poorly known. A campaign of characterization has been reported on the clay from the Mont Terri (Switzerland) site with a coaxial transmission line. For ease of manipulation, the study only considered crushed and altered clay. Samples were crushed down to 2mm grains and re-compacted. Such a preparation modifies initial clay porosity. Thus, we wonder about the representativeness of permittivity measurements obtained on crushed clay compared to the unaltered rock. Electromagnetic properties of Bure clay rock were also measured with two different methods: at a low frequency range (from 100 kHz to 10 MHz) using impedance measurement and at higher frequency range (from 500 MHz to 10 GHz) with a coaxial probe [8]. A large part of the useful dielectric spectrum is missing: standard TDR sensing lines (such as Campbell TDR100) make use of a step electric pulse, the frequency content of the measured TDR wave form extends from about 20 kHz to roughly 1.5 GHz [9]. A large part of the useful dielectric spectrum is missing.

Concerning concrete, literature is abundant. Nevertheless, the variety of concrete, the dispersion of the results and the specificities of our concrete called for the development of our own transmission line for this material.

This paper reports on the development of two transmission line fixtures to measure the complex electrical permittivity of Bure clay rock and concrete over the 50 MHz – 1 GHz frequency range. The first section deals with the different aspect of the measurement chain: the design of the cells and the software used to obtain the electromagnetic properties from the scattering matrix. Section 3 focuses on the obtained electromagnetic characterization of clay rock. The procedure to prepare sample and the hydrical characterization is also approached. Section 4 concerns the electromagnetic characterization of concrete.

2. Method for electromagnetic characterization

2.1. Experimental procedure

Among the various possibilities to perform electromagnetic characterization, two categories can be distinguished, resonant versus non-resonant methods. The first type is used to get accurate knowledge of dielectric properties at several discrete frequencies, whereas the second category allows knowledge of dielectric properties over a large frequency range. As previsouly explained, TDR application requires characterization over a very large frequency range. We thus focused on non resonant method. Among those techniques we selected transmission/reflection methods.

This method requires devices able to direct the electromagnetic energy toward a material and to collect what is reflected or transmitted through the material.Since the goal is to characterized non-crushed clay, a unique sample must provide characterization on the whole frequency range. Rectangular and circular guides do not fit this requirement. This is why we selected coaxial transmission lines. What is more, with such a design, we benefit from previous tests performed with a similar line used to measure the complex permittivity of cement exudation products [10].

Feasibility of clay shaping is an intrinsic limitation for this choice. For concrete, the lines must be designed so as to fit the material heterogeneity, to respect the criteria of the representative elementary volume (REV). This is why two transmission lines were developed dedicated either to clay rock (small size to ease shaping) or to concrete (large size cells to perform representative measurement).

The coaxial line is connected to a calibrated vector network analyser (VNA) with two ports which sends a monochromatic electromagnetic wave and records the interaction of the sample through S-parameters. The calibration was performed using a classical SOLT (Short – Open – Load – Though) calibration method procedure. The VNA is connected to a PC through a GIP-USB connection.

Nicholson - Ross [11] and Weir [12] formalized electromagnetic characterization of materials using transmission/reflection method in a wave guide. This procedure, commonly called NWR process allows the reconstruction of the complex permittivity and complex

permeability of materials using the measured scattering parameters. This NWR procedure assumes a fundamental TEM propagation in the line. The upper frequency limit of the line is so given by the frequency of the first higher order mode (the TE_{01} mode) [13]:

$$f_c^{TE_{01}} = \frac{c}{\pi(b+a)\sqrt{\varepsilon_r \mu_r}}, \quad (1)$$

with c = 299792458 $m.s^{-1}$, a and b respectively the inner and outer radii of the coaxial conductors (see Figure 2), ε_r and μ_r the relative permittivity and permeability of the filling material.

2.2. From S parameters to electromagnetic characteristics: Epsimu® software

EpsiMu® [14] software provides in real time the electromagnetic properties from the measured scattering matrix and information on the geometry of the coaxial lines. It combines two-ports de-embedding [15] and the NRW procedure. It limits the required number of calibration steps, which ease manipulations and enables non-expert workers to make large number of measurements.

As depicted in Figure 1, the de-embedding operation consists in obtaining the scattering matrix of the sample [S_{sample}] from the scattering matrix measured at the reference plane [S_{cell}] and the transition matrixes [S_A] and [S_B]. The transition matrixes can be expressed with the electrical distances d_1 and d_2 and the attenuation coefficient α. These three parameters constitute the identity card (IC) of the line. As detailed in [16], IC determination requires a single measurement of the S-parameters of the cell, filled with an electrical short.

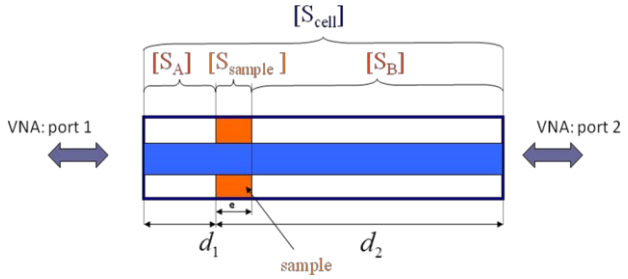


Figure 1: Principle of de-embedding operation.

The determination of d_1 and d_2 is sensitive and can induce uncertainties To overcome this difficulty, a calibration procedure based on various well-known materials like air and Teflon was developed to find the optimized determination of d_1 and d_2 [17].

2.3. Transmission line

2.3.1. Design

The cell can be divided in three sections: two conical transition units and a specimen holder (Figure 2). The inner dimensions of the cell are determined in order to match the impedance of the source (50 Ω) yielding a condition over the value of the ratio of the rayon: b/a=2.302 [18]. This condition has to be respected for the whole transmission line so as to avoid impedance gap.

For clay and concrete, both cells were made of brass, for its electric properties, its price and ease of shaping.

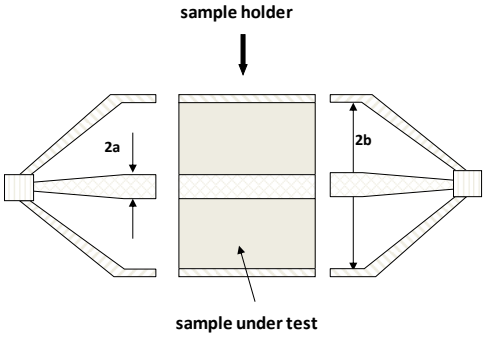


Figure 2: Scheme of the coaxial cell.

For clay, cell dimensions were reduced to ease shaping and to enable the realization of various samples from the same core. The cell is characterized by inner radii a=6.52 mm and outer radii b=15 mm. When air filled the cut-off frequency of the TE01 mode is 4.4 GHz, whereas when filled with water, the cut-off frequency is closed to 500 MHz. The specimen holder has a length of 20 mm; the coaxial cell length is finally 152 mm. The figure 3 is a picture of the coaxial cell connected to the VNA.

With such dimensions, it has been previously observed that the experimental bench is actually limited to 50 MHz-1 GHz range (in air) [9], because of NWR procedure.

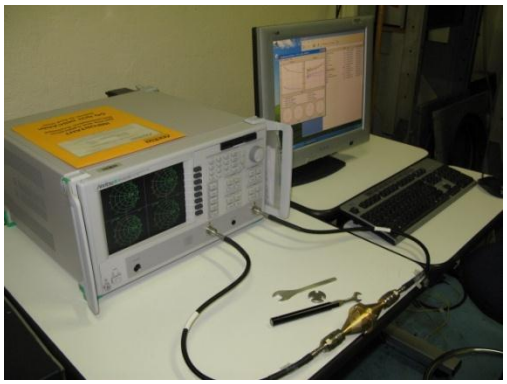


Figure 3: Photography of the coaxial cell connected to the VNA.

Concrete is a mixture of mineral aggregates in a specific binder formulation. In our case, the size of the aggregate ranges from 4 to 8 mm (see 4.1 for the detailed composition of concrete). In order to access representative electromagnetic properties, [19] and [20] showed that material sample needs to be at least three times greater than the bigger aggregate. That means all dimensions of the holder must be larger than 24 mm, which reduces in turn the higher frequency limit. The proposed coaxial cell is defined by inner radii a=50 mm and outer radii b=21.75 mm, the sample holder is 60 mm length. As illustrated in Figure 4, the coaxial cell length is finally closed to 600 mm. When air-filled, the cut-off frequency of the TE01 mode is

1.33 GHz. The figure 6 is photography of the whole transmission line.

Concrete was directly poured into a volume of the coaxial cell bounded by 2 thin dielectric walls to confine the liquid material, as already tested in [21]. It is then possible to monitor the evolution of electromagnetic characteristics during concrete drying. The volume in interest for the concrete samples is 250 cm^3.



Figure 4: Photography of the transmission line for concrete.

It is worth noting that various designs for coaxial transmission line were reported for concrete dielectric characterization [22] [23], [24], [25]. Chosen dimensions result quite different, as listed in Table 1.

Table 1: Different coaxial cell used for concrete dielectric properties characterization

Ref.	a (mm)	b (mm)	Aggregate max size (mm)	Impedance (Ω)	f (GHz)
[22]	12.7	75	38	107.5	1.07
[23]	22	50.5	10	49.9	1.31
[24]	24.6	80	30	50	0.91
[25]	7.7	25	mortar	70	2.92
Andra	21.75	50	8	50	1.33

Although the size of our cell is really close to the cell developed by [24], comparison of dielectric properties will be restricted by concrete type.

2.3.2. *Modeling of the cell*

Modeling of the transmission line has been realized using the commercial 3D finite elements software Comsol, Radio Frequency module [26]. The main objective was to evaluate the quality of the de-embedding process.

The whole cell was modeled (see Figure 5) which provides the S parameters [S_{cell}]. Then the same de-embedding equations used by EpsiMu and detailed in [15] are applied; [S_{sample}] is obtained.

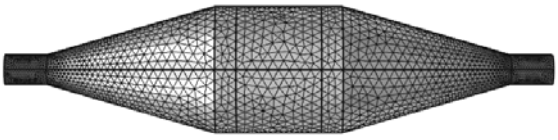


Figure 5: Picture of the meshed cell.

The cell was meshed with an adaptative mesh allowing a λ/5 resolution. The small cell was modeled, filled with bi-distilled water. We have considered constant dielectric properties over the frequency range with a permittivity equals to ε_r =80. Notice that when the cell is filled with bi-distilled water, the cut-off frequency is close to 500 MHz. Data were calculated and measured over the 50 MHz – 500 MHz frequency range.

Comparison between experimental data and modeling are illustrated in Figure 6 and Figure 7 for $S_{11sample}$ and $S_{21sample}$ respectively.

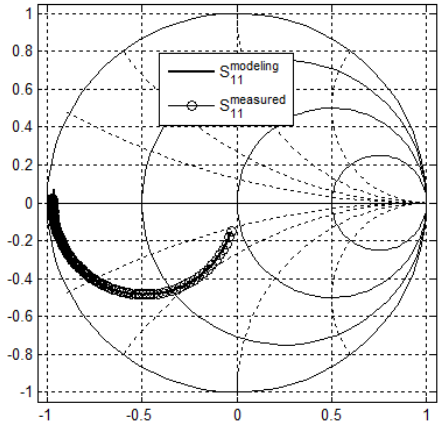


Figure 6: Comparison of $S_{11sample}$ when water filled.

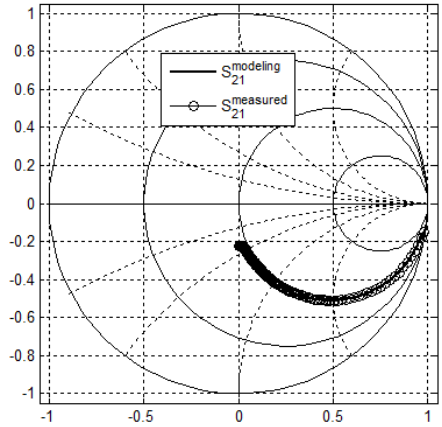


Figure 7: Comparison between $S_{21sample}$ when water filled.

The comparisons between measured and calculated $S_{saùple}$ are very good. These examples illustrate the quality of the de-embedding step.

In further study, such a model could be use in an inversion procedure. It would then provide access to electromagnetic properties on a larger frequency range, above 1 GHz and

beyond 50 MHz (presently limited by NRW procedure), as proposed by [27] and [28].

3. Electromagnetic Characterization of clay rock

3.1. Sample preparation

Clay samples under interest, called COX argillite, are clay-rich rocks that contain up to 50% clay (illite and illite/smectites), carbonates and tectosilicates (quartz). Their void fraction ranges from 15 to 20%, with very small pore dimensions, mostly ranging from 2 to 100 nm. Clay platelets exhibit an electric charge, resulting in interaction with solute cations and water. These properties provide clayrocks with some resistance to dehydration, unless they are fractured.

The use of coaxial line requires that the material under test is carefully drilled and machined to precisely fit in between the inner and outer conductors. The first goal was to check feasibility and to evaluate representativeness of the shaped samples, variability induced by shaping procedure.

To prepare the samples, a large clay core from Andra underground laboratory conserved in sealed bag to avoid any contact with air, is over-cored in order to obtain rough specimen with diameter larger than finished specimen. Rough specimens are then shaped in order to obtain a perfect cylinder with the same dimensions as the sample holder (radii equal to 15 mm and height equal to 20 mm).

Three specimens were produced by this way. One sample is dedicated to serve as a "witness" (reference); its apparent density (geometrical measurement using a caliper,ρ in Table 2) is measured. The other two samples (no1 and 2 in the following) were drilled to form a central hole to insert the inner conductor (see Figure 8 for illustration of the sample preparation). The electromagnetic characterization can be performed on the two samples. Finally, water mass content, porosity and degree of saturation are measured on the three samples. Water content is measured by loss of water using an oven held at 105°C. Porosity is determined according to the dry density and a grain density equal to 2.7023 g/cm3 [29] and the saturation degree (SW_{105}) is accurately deduced from these parameters.

In order to evaluate the effect of crushing on the electric permittivity, the two samples were manufactured to form a remoulted specimen. Since this procedure induced loss of material, a piece of the initial core was added. These samples were crushed using a mini plagues crusher (IKA-WERKE MF10), settled with following parameters: 5500 rpm, 1.25 mm sieve. All the grains lower than 1.25 mm were recovered, all the material was crushed. The powder thus obtained was stabilized in a climatic chamber regulated at 20°C in order to get a water content mass similar to the initial samples. The powder was then compacted to 160 MPa using an isostatic press (CIP). The result was a new small carrot which it is advisable to machine for introducing into the sample holder.

A lot of difficulties were encountered during the preparation of the samples. In addition to cracking caused by the mechanical release after coring, associated with the laminated structure of the COX argillite, the presence of small pyrite grains which rapidly oxidize in contact with air and sometime fossils also contributes to brittle the material. In order to obtain an acceptable 8 to 12 cm length rough specimen, 3 to 5 cores were eliminated.

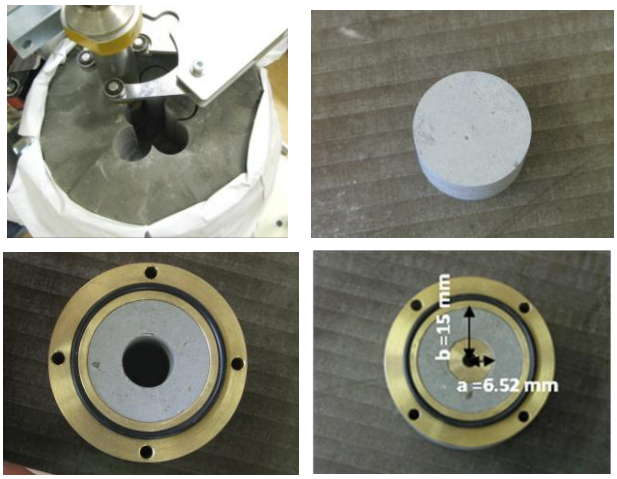


Figure 8: Illustration of the shaping process.

3.2. Experimental results

The Figure 9 and Figure 10 represent the electric permittivity for the three characterized sample. Table 2 reminds the hydraulic characterization made on the 3 samples.

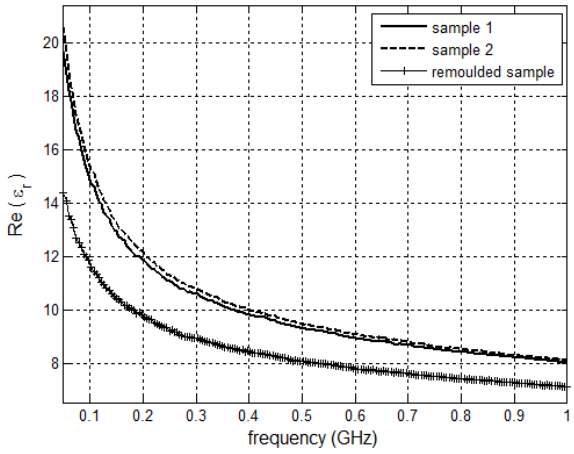


Figure 9: Real part of the electric permittivity for sample 1, sample 2 and the remoulted sample.

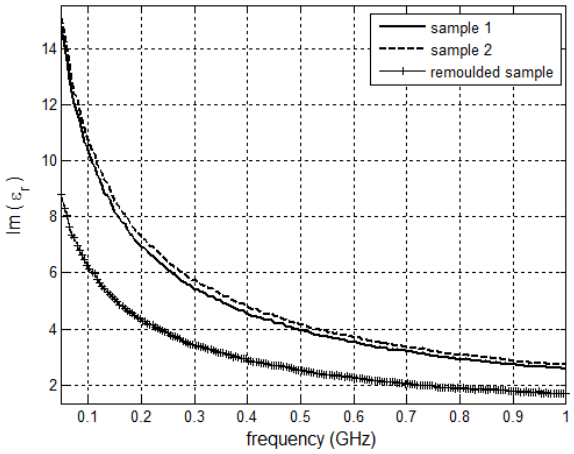


Figure 10: Imaginary part of the electric permittivity for sample1, sample 2 and the remoulted sample.

Table 2: Hydrical characterization of clay samples

Sample	RH (%)	Porosity (%)	$W_{105°}$ (%)	ρ (g/m^3)	$S_{W105°}$ (%)
1	Ambient	15.77	2.67	2.276	38.54
2	Ambient	16.41	3.00	2.259	41.30
remoulted	Ambiant	17.14	2.86	2.239	37.35

3.3. Discussions and perspectives

Strong dependence on frequency is observed on the three samples. Figures show a large value at low frequency: at 50 MHz, $Re(\varepsilon_r)$ equals 19.60 for sample 1, 20.58 for sample 2 and 14.30 for the remoulted sample. They also indicate that both real and imaginary parts of permittivity decrease with increasing frequency: at 1 GHz $Re(\varepsilon_r)$ equals 8.07 for sample 1, 8.14 for sample 2 and 7.12 for the remoulted sample. This kind of behavior is common with porous complex materials.

The comparison between sample 1 and 2 gives dielectric really similar properties (for real and imaginary part). The hydraulic properties for sample 1 and 2 are also close. Indeed, the water content equals 2.67% for sample 1 whereas it equals 3.00 % for sample 2. Previous study [30] on Bure clayrock has shown a variation range for water content between approximately 1% and 9%. A variation of 0.37 % of water content is not significant, the sample 1 and 2 can be considered as similar. This comparison validates the reproducibility of the measurement and the proposed shaping procedure.

The dielectric properties can be calculated in two directions. For example, it can be deduced from the couple $S_{11sample}$ and $S_{21sample}$ (called direct characterization) or from the couple $S_{22sample}$ and $S_{12sample}$. (called indirect characterization).The comparison between direct and indirect characterization have not shown significant difference (this result is not illustrated). This result confirms, for this frequency range, the homogeneity of the three characterized samples.

The last information is linked with the comparison between the intact samples and the remoulded sample. The dielectric properties are quite different, meanwhile the hydrical properties of the three samples are almost similar. The difference observed on the dielectric properties could be explained by the change in the porosity induced by the crushing. Indeed, the pore size distribution varies from the micro/meso-pore size range for the intact rock to the meso/macro-pores for the remoulded sample. This hypothesis will be confirmed in a near future by mercury Intrusion Porosimetry (MIP) measurements for instance.

Concerning the study made on the clay from the Mont Terri, the frequency range of inspection was from 1 MHz to 500 MHz at maximum. The clayrock from Mont-Terri is not the same but is physically closed to Bure clayrock. As mentioned before, this study was focusing on crushed clayrock. The study reports value between 9.32 and 12.55 for $Re(\varepsilon_r)$ at 50 MHz for clayrock with a water content between 2.71 % and 3.28% and density between 1.41 g/m^3 and 1.60 g/m^3. The order of magnitude is close to our value. The study reports the same effect of the frequency. The other study [8] reports order of magnitude closed to our value, but a precise comparison has to be performed.

It is important to link the characterizations with electromagnetic sensors. For TDR application, where electronic device averages dielectric properties over a large frequency range, the observed frequency dependence could be a major issue. Moreover, the observed difference between the dielectric properties of intact and crushed clayrock may also induce water content measurement undertainties. In some case, TDR probes are inserted into a small core made of crushed clayrock before being installed on field. This core is then put on field by digging a hole and inserting the instrumented core. In such configuration, the measurement may be biased.

The presented characterization pertains to a larger study on electromagnetic characterization on clayrock. Next step is to measure water content influence. Samples are presently placed in climatic chambers with different relative humidity. Water content stabilization is checked by daily weighing. The hydraulic characterizations will be completed with a water content measurement at 150°C in nitrogen atmosphere due to clay-water interaction, as some water remains between smectite platelets after drying at 105°C.

The other part of this study will focus on the effect of crushing on the dielectric properties, the aim is to reproduce the presented result to evaluate the reproducibility.

4. Electromagnetic characterization of concrete

4.1. Removal of concrete during casting

Concrete was directly inserted into the central part of the coaxial line during the realization of a concrete liner in the Andra underground laboratory (see figure 14) in December 2012. Two samples were realized so as to evaluate homogeneity of concrete, variability of measurements.



Figure 11: Casting of concrete during the realization of the gallery at the underground laboratory.

The table 3 gives the composition of the high performance concrete.

Table 3: Concrete formulation

Premix composition (kg/t)	CEM I 52.5 N PMES	200
	Sand 0/4	430
	Aggregate 4/8	369.4
Added in the mixer (kg/premix ton)	Water	78
	Superplasticizer	2.4

The slump test gives a result of 210 mm. Compressive strength at 28 days performed on cylinder sample (16 mm x 32 mm) was measured to be 69 MPa.

4.2. Experimentals results

The Figure 12 and Figure 13 represent the dielectric properties of sample 1 and sample 2. The values obtained in the direct and indirect characterization are compared.

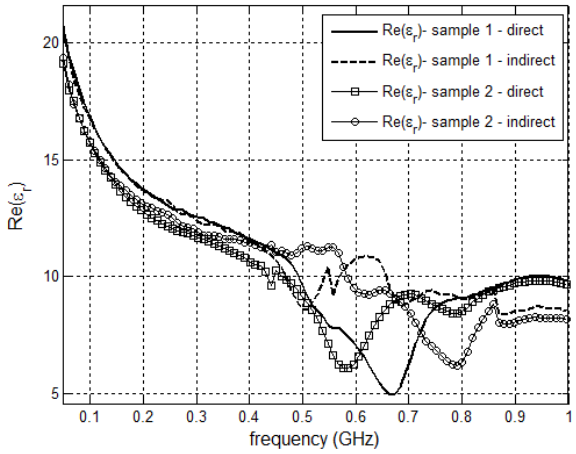


Figure 12: Real part of the electric permittivity for sample 1, and sample 2 obtained with both couple of S parameters.

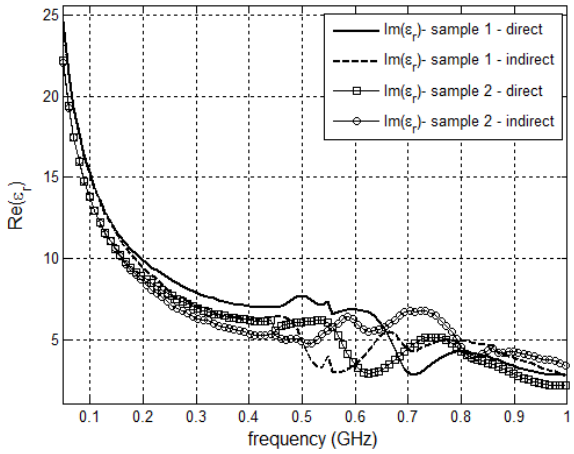


Figure 13: Imaginary part of the electric permittivity for sample 1, and sample 2 obtained with both couple of S parameters.

The Figure 14 and Figure 15 represent the effect on curing on the dielectric properties for sample 1. For the time being we dispose of measurement on 50 days. For those pictures, we selected the direct data characterization.

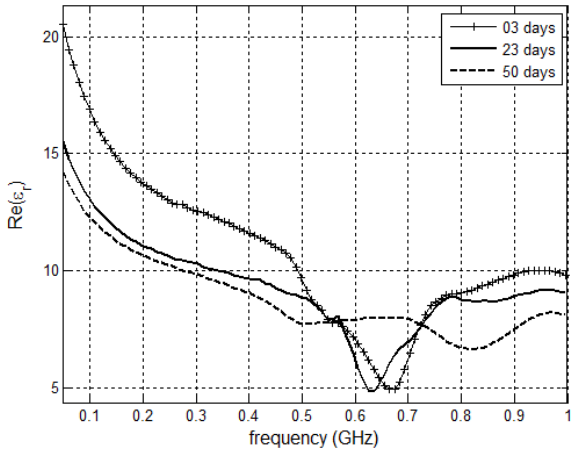


Figure 14: Curing effect on the real part of the electric permittivity for sample 1.

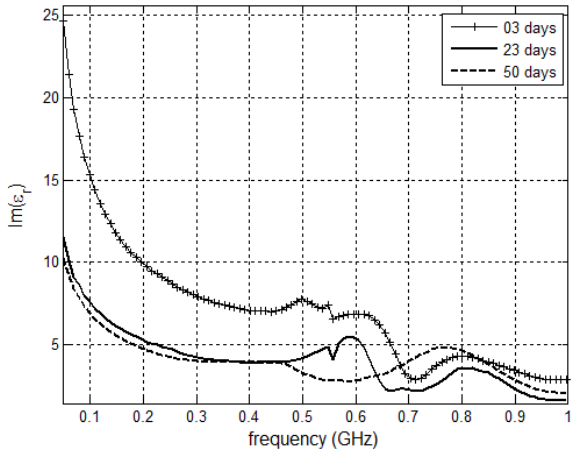


Figure 15: Curing effect on the imaginary part of the electric permittivity for sample 1.

4.3. Discussions

We can observe the same behavior than in clayrock: both real and imaginary parts of permittivity significantly decrease with increasing frequency. This well-known behavior ([22],[23],[24]) can be observed regardless the curing state (see Figure 14 and Figure 15).

Figure 12 and Figure 13 confirm the two samples are similar. However, they also reveal local heterogeneities. On these figures data from the direct and indirect characterizations of the two samples are represented. The dielectric properties of the two samples, taken from both sides, are really similar on the 50 MHz - 400 MHz frequency range, but begin to shift around 500 MHz. Since it evoluates with curing and depends on the characterization direction, we attribute such unstable phenomena to Maxwell Wagner relaxation. It was expected for concrete samples [22]. Permittivity measurements of concrete presented in [23] and [24] did not encountered this kind of phenomena. As a consequence, reliable permittivity values must be taken above 500 MHz. It could be interested in a further study to evaluate the influence of the geometry of the sample on such effects.

The effect of curing on the dielectric properties is presented in Figure 14 and Figure 15. Real and imaginary parts of permittivity decrease with curing. This decreasing may be interpreted with the physical and chemical state of concrete. When concrete is mixed, a release of a large amount of $Ca^{2+}$and OH^- happens. The presence of these ions resulted in the concrete paste becoming highly polarizable and conductive. This induces a high value of the real part of the permittivity and a very high value for the imaginary part. However as hydratation progress the free water starts changing to absorbed water and irrotationnally bound. As the cement hardened, the polar molecules find it harder to move resulting in less polarization and a decrease in the dielectric properties.

Concerning comparison with literature, the values are at the order of magnitude. For example, [24] after three days of curing finds a value close to 11 for $Re(\varepsilon_r)$ and close to 4 for $Im(\varepsilon_r)$ at 400 MHz. **Erreur ! Source du renvoi introuvable.** finds values close to 12 for $Re(\varepsilon_r)$ and 5 for $Im(\varepsilon_r)$. Our values for the sample 1 and the direct characterization are 11.59 for $Re(\varepsilon_r)$ and 7.05 for $Im(\varepsilon_r)$.

5. Conclusions

As a part of an ongoing research, two coaxial fixtures have been developed to characterize clay rock (intact or crushed) and concrete in the frequency range of 50 MHz to 1 GHz. A small cell was designed for clay centimeter size sample, whereas a bigger cell was designed for decimeter size concrete sample so as to respect large representative elementary volume.

The dielectric properties were obtained from the scattering matrix using EpsiMu® software. A 3D Finite Elements modeling of the small coaxial cell was also performed, in order to improve the inversion algorithms. The purpose is to assess the electromagnetic characterization in a wider band of frequencies.

Three clayrock samples characterization were presented. Strong dependence of dielectric properties versus frequency is observed on the three samples. Two samples, realized with the same core and considered with identical hydrical properties, have validated the reproducibility of the measurement and the shaping procedure. The remoulted sample, which was realized with the other sample, has shown the effect of crushing on dielectric properties. The change in porosity is supposed to be responsible of this variation. This hypothesis will be soon checked with mercury Intrusion Porosimetry (MIP) measurements. The next step of our study is to evaluate water content influence. Otherwise, precise comparison with other study made on clay rock from Bure underground laboratory will be performed [8].

Concerning concrete, two sample holders were directly filled during the casting of concrete in the underground laboratory. The characterizations have shown a strong frequency dependence on the dielectric properties. Both real and imaginary part decrease with curing effect. The measurements were perturbed above 400 MHz. We attribute such phenomena to Maxwell Wagner relaxation. Despite the specificity of concrete, comparison with literature has shown value at this same order of magnitude.

We presented here the first part of a large electromagnetic material characterization campaign. Sub soil surface are concerned too. All the dielectric properties are currently used in our works about TDR modeling, as input data. Our aim is to develop an instrumentation system around the TDR probe, in order to achieve a reliable estimation of the dielectric parameters, and then the water content within waste repository structures. In that way, the study of characterization is fundamental.

References

[1] G. Moreau, J.-P. Dubois F. Agostini, F. Skoczylas, B. Masson, J. Salin "Survey of the future concrete structures lifetime measuring the water content: four types of embedded sensor under checking" Fontevraud 7, Sept. 26-30 2010

[2] G.C. Topp, J.L. Davis and P. Annan "Electromagnetic determination of soil water content : Measurement in coaxial transmission lines" Water Resour. Res, 16:574-582; 1980

[3] D.A Robinson, C.M.K. Gardner and J.D Cooper, "Measurement of relative permittivity in sandy soils using TDR, capacitance and theta probes : comparison including the effects of bulk soil electrical conductivity", J. Hydrol. (Amsterdam) , 223:198-211, 1999 .

[4] M.C. Dobson, F.T. Ulaby, M.T.Hallikainen and M.A. El Rayes, "Microwave dielectric behavior of wet soil, Part II : Dielectric mixing models", IEEE Trans. Geosci. Remote Sens., 23 :35-46, 1985

[5] S. Sammartino, A. Bouchet, D. Prêt., J.C Parneix and E. Tevissen, "Spatial distribution of porosity and minerals in clay rocks from the Callovo-Oxfordian formation (Meuse / Haute Marne, Eastern France) implications on ionic species diffusion and rock sorption capability", Applied Clay Science 23, p. 157-166, 2003.

[6] E. Gaucher, C. Robelin, J.M. Matray, G. Négrel, Y. Gros, J.F. Heitz, A. Vinsot, H. Rebours, A. Cassagnabère, A. Bouchet, (2004) ANDRA underground research laboratory interpretation of the mineralogical and geochemical data acquired in the Callovo-Oxfordian formation by investigative drilling, Physics and Chemistry of the Earth A/B/C 29, p. 55-77

[7] D. Jougnot, A. Revil, N. Lu and A. Wayllace,"Transport properties of the Callovo – Oxfordien clay rock under partially saturated conditions", Water Resources Research, 46, xx – xx, 2010.

[8] L. Comparon, Etudes expérimentales des propriétés électriques et diélectriques des matériaux argileux consolidés, Phd Thesis, Institut de Physique du Globe de Paris, 2005.

[9] T.J. Heimowaara, W. Bouten and J.M. Verstraten, "Frequency domain analysis of time domain reflectometry waveforms. A four component complex dielectric mixing model for soils", Water Resources Research, **30**, 201-209, 1994

[10] T. Bore, Amélioration du diagnostic de l'endommagement des gaines de précontraintes extérieures par sonde capacitive, Phd Thesis, Conservatoire National des Arts et Métiers, Paris, 2011.

[11] A. M. Nicolson, and G. F. Ross, Measurement of the intrinsic materials by time domain techniques, IEEE Transactions on Microwave Theory and Techniques, 19(4), 377-382, (1970).

[12] W. Weir, Automatic measurement of complex dielectric constant and permeability at microwave frequencies, Proceedings of the IEEE, 62, pp. 33-36, (1974).

[13] D. Pozar, *Microwave Engineering*, Wiley, pp 128 – 129 1998.

[14] www.epsimu.fr

[15] Agilent - Application note n°1364-1 : De-embedding and embedding S-parameter network using a Vector Network Analyzer

[16] Sabouroux P. et Boschi P, Simplification de la procédure de mesure de caractéristiques électromagnétiques de matériaux en temps réel., Revue de l'Electricité et de l'Electronique (REE) – No.8, pp 84-89, novembre 2005

[17] D. Ba, and P. Sabouroux , EpsiMu a tool for permittivity and permeability measurement in microwave domain at real time of all materials. application to solid and semi-solid materials, Microwave and Optical Technology Letters, 52 (12), 2643 - 2648, 2010.

[18] L.F. Chen, C.K. Ong, C.P Neo, V.V. Varadan, V.K. Varadan, *Microwave Electronics, Measurement and Materials Characterization*, Wiley, pp 56 – 57, 2004.

[19] A. Robert, Recherche de méthodes d'interprétation des mesures géoradar et de thermographie infrarouge appliquées au contrôle non destructif et à l'auscultation in situ des matériaux de construction, Phd Thesis, EPFL, Lausanne, 1997

[20] M. Adous, Coaxial/cylindrical transition line for broadband permittivity measurement of civil engineering materials, Measurement Science and Technology, **17** ,(2006), 2241 – 2246.

[21] P.Sabouroux and D. Ba, "Epsimu, a Tool for Dielectric Properties Measurement of Porous Media: Application in Wet Granular Materials Characterization", Progress In Electromagnetics Research B, Vol. 29, 191-207, 2011.

[22] I.L. Al Qadi, S. Riad, R. Mostaf and W. Su, "Design and evaluation of a coaxial transmission line fixture to characterize Portland cement concrete", Construction and Building Materials, **11**, 163 – 173, 1997

[23] J.H. Bungey, M.R. Shaw, S.G. Millard, M.N. Soutsos and B.A. Austin, "The influence of concrete composition upon radar test results", Proceeding of the NDT-CE, NDT in Civil Engineering Conference, 1997.

[24] A. Robert, "Dielectric permittivity of concrete between 50 MHz and 1 GHz and GPR measurement for building materials evaluation", Journal of Applied Geophysics, **40**, 89 – 94, 1998.

[25] W. Chew, J. Kenneth and G. Otto, "Design and calibration of a large broadband dielectric measurement cell", IEEE Transaction on Geoscience and Remote Sensing, 29, 42 – 47, 1991.

[26] www.comsol.com.

[27] J. Barker Jarvis, E.J. Vanzure and W.A. Kissick, 'Improved technique for determining complex permittivity with the transmission/reflection method", IEEE Transactions on Microwave Theory and Techniques, **38**(8), 1096-1103, 1990

[28] A.H. Boughriet, C. Legrand and A. Chapton, "Noniterative stable transmission/reflection method for low loss material complex permittivity determination", IEEE Transactions on Microwave Theory and Techniques, **45**(1), 52-57, 1997

[29] S. Savoye, J. Page, C. Puente, C. Imbert and D. Coelho, New experimental Approach for studying diffusion through an intact and unsaturated medium : a case study with Callovo-Oxfordian Argilite, Environmental Science and Technology, Vol **44**, N°10, 3698 – 3704, 2010.

[30] Boulin, Expérimentation et Modélisation du Transfert d'hydrogène à travers des argiles de centre de stockage de déchets radioactifs, Phd Thesis, Institut Polytechnique de Grenoble, 2008

Multiscale electronic transport mechanism and true conductivities in amorphous carbon–LiFePO4 nanocomposites

K. A. Seid,[1] B. Lestriez[1], J.-C. Badot,[2] O. Dubrunfaut,[3] D. Guyomard[1] and S. Levasseur,[4]

[1]Institut des Mat_eriaux Jean Rouxel (IMN), Universit_e de Nantes, CNRS, France.
[2]Laboratoire de Chimie de la Mati_ere Condens_ee de Paris, Chimie ParisTech (ENSCP), CNRS, UPMC Univ Paris 06, France
[3]Laboratoire de G_enie Electrique de Paris, SUPELEC, UPMC Univ Paris 06, Univ Paris-Sud, CNRS, France
[4]UMICORE Cobalt & Specialty Materials, Belgium
E-mail: kalid-Ahmed.seid@lgep.supelec.fr
Kalido96@yahoo.com

Abstract

Composite and nanostructured materials have hierarchical architecture with different levels: (a) macroscopic (substructure of porous clusters); (b) mesostructural (particles constituting the clusters);and (c) microscopic and nanometric (coatings, bulk of the particles). The identification of the key parameters that affect the electronic transport across all observed size scales is required, but is not possible using conventional dc-conductivity measurements. The broadband dielectric spectroscopy (BDS) from low-frequencies (few Hz) to microwaves (few GHz) is applied to one of the most important composite materials for lithium batteries. LiFePO4 is wrapped in a carbon coating whose electrical properties, although critical for battery performance, have never been measured due to its nanometre-size and the powdery nature of the material.

1. Introduction

A lithium-ion battery also known as Li-ion battery or LiB is a family of rechargeable battery types using no lithium metal at the negative electrode in which lithium ions move from the negative electrode to the positive electrode during discharge, and back when charging (Figure 1). Chemistry, performance, cost, and safety characteristics vary across LiB types. Unlike lithium primary batteries (which are disposable), lithium-ion electrochemical cells use an intercalation lithium compound as the electrode material instead of metallic lithium. Lithium-ion batteries are common in consumer electronics. They are one of the most popular types of rechargeable batteries for portable electronics, with one of the best energy densities, no memory effect, and a slow loss of charge when not in use. Beyond consumer electronics, LiBs are also growing in popularity for military, electric vehicle, and aerospace applications. Research is yielding a stream of improvements to traditional LiB technology, focusing on energy density, durability, cost, and intrinsic safety.

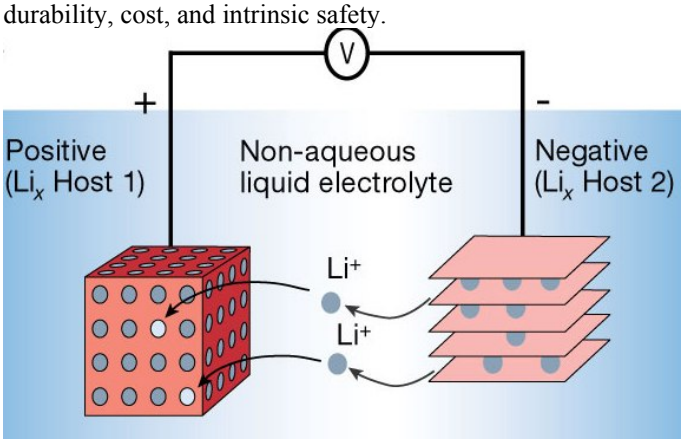


Figure 1. The operating principle of a lithium ion battery [1]

Positive and negative electrodes are however composite electrodes. The composite electrode is a very complex medium obtained by mixing together the active material (AM) grains with non-electro active additives such as a conducting agent (C) and a polymeric binder (B) For high rate performance this medium needs to bring very efficiently the ions and the electrons to the surface of the active material (AM) particles. The composition and architecture of the composite electrode should be able to allow an efficient electrical conductivity which enables sufficient cycle life for the battery especially for high rate applications.

The resulting hierarchal architecture induces polarizations which are generally visible by the BDS because they involve changes in local charge density. at the micro structural scale, a conducting polycrystalline material (compact powders, ceramics) presents interfacial polarizations. The interfaces are generally grain (particles) boundaries or more often, the contact area between the grains. If the grains (particles) are assembled into clusters

(i.e. agglomerates), there exists a different interface between clusters.

In addition, an interface exists between the sample and the electrodes contact (e.g., gold, silver) used for the measurement. These types of polarization are visible only at low frequencies. The characteristic frequencies of the different phenomena observed in dielectric spectroscopy are classifiable according to the characteristic scale at which they are observed. Furthermore, the larger characteristic size the smaller the characteristic frequency is (Figure 2).

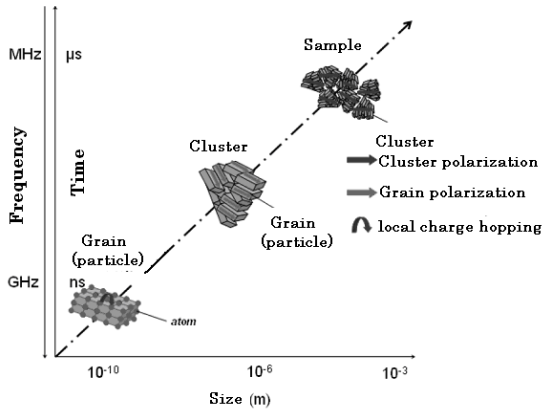


Figure 2. Multi-scale analysis of electric polarization in a conducting material

2. Experimental method

A Transverse Electromagnetic (TEM) wave is emitted using a network or impedance analyzer through a coaxial output. This TEM wave is propagated in the coaxial waveguide. The interaction is followed by the study of the reflection coefficient of the TEM wave when the sample is placed at the end of a coaxial line terminated by a short circuit. Figure 3 below shows the measuring cell for determining the electrical parameters of a sample versus frequency.

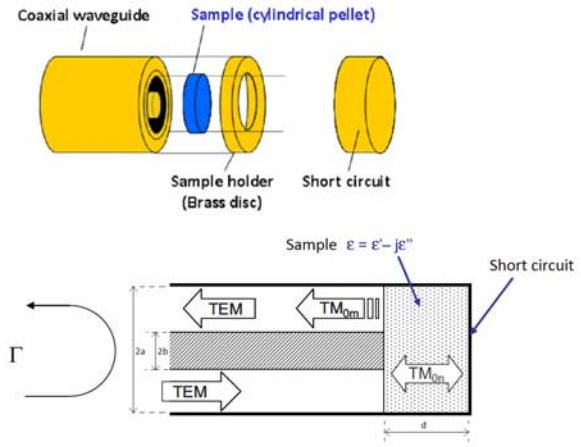


Figure 3.Schemes 3D and 2D of the measuring cell in a reflection mode. TM0m or n are transverse magnetic waves.

The measurements of the reflection coefficient versus frequency are made with impedance or network analyzers. In order to achieve dielectric spectra over a wide frequency band, it is necessary to use several measuring devices (Figure 4). Each one is independent. An alternator enables to use successively these analyzers without dismantling the cell, which is very important during measurements versus temperature. In our case, we used three devices: a HP 8510 (and then an Agilent PNA network analyser E8364B used between (10 MHz – 10 GHz), an Agilent 4291 impedance analyzer (1 MHz - 1.8 GHz) and an Agilent 4294 impedance analyzer (40 Hz - 110 MHz).

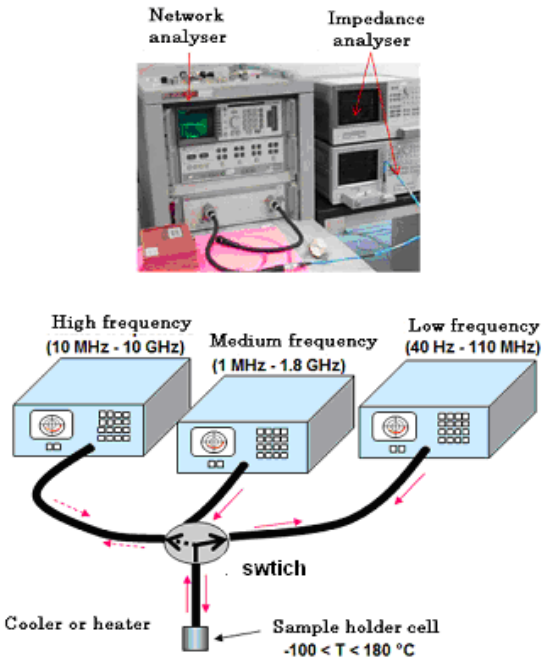


Figure 4. Experimental setup with 3 machines in case of a cell in reflection setup.

3. Discussion

The broadband dielectric spectroscopy (BDS) is well-known for ionic conductors and polymers but much less used for electronic conductors. We have applied this technique to the study of nanocomposites prepared from the most important active material for lithium batteries, cluster of $LiFePO_4$ particles, coated in a core shell morphology with an amorphous carbon coating of few nanometres thick. Our objective was to extract the electronic conductivity of this nacomposite at all the scales of its architecture (from inter atomic distances to macroscopic lengths), with the aim of identifying the limiting parameters and move on to systematic and rational manufacturing, Processing and engineering practices for the better.

Binary systems ($LiFePO_4$ with its carbon coating) were studied to establish the fundamental know-how on the electrical properties of the different scales and the existing correlation between the scales of a compacted powder.

The results obtained in this work demonstrate that the BDS can distinguish the different types of electronic transfers involved at the different scales of the material architecture. These phenomena occur from interatomic to macroscopic sizes with the influence of the morphology of the different constituents at these scales. Considering a composite material composed of an active material (e.g. $LiFePO_4$) and a conductive agent (e.g. carbon coating), when the frequency increases, different kinds of polarizations, giving rise to dielectric relaxations, appear in following order: a) Space-charge polarization (low-frequency range) due to the interface between the sample and the conductive metallic layer deposited on it; b) Polarization of C-$LiFePO_4$ clusters (micronic and/or submicronic scales) due to the existence of resistive junctions between them; c) Electron hopping between sp^2 domains (nanometric scale) within the carbon coating around the $LiFePO_4$ particles.

The frequency dependence of the real parts of the conductivity and of the permittivity for $LiFePO_4$ (LFP) at room temperature is shown in Figu**Erreur ! Source du renvoi introuvable.**re 5a and b respectively. The lowest measured value is about $10^{-7}S.m^{-1}$ at 40Hz and the lack of dc-conductivity plateau shows that our set-up does not allow accessing to the very low value of the dc-conductivity

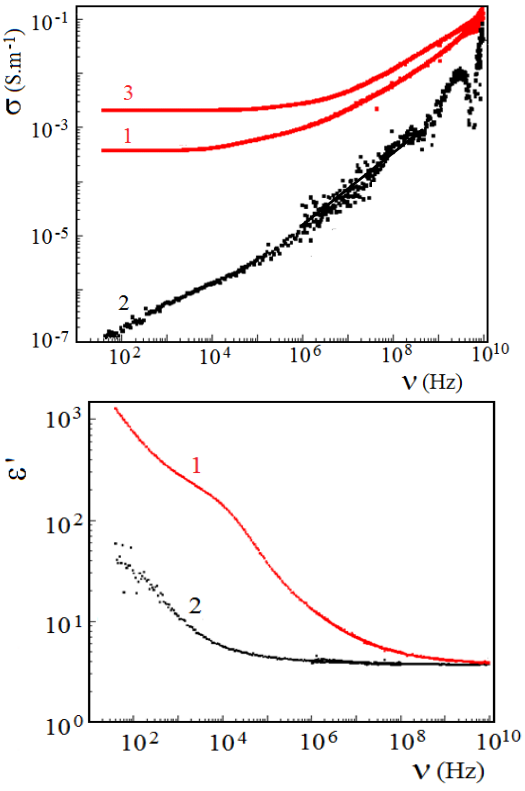


Figure 5. Real parts of the conductivity (a) and of the permittivity (b) as a function of the frequency for both carbon-coated and uncoated samples, i.e. CLFP3 (curve 1) and LFP (curve 2), at 298K. In (a) the real part of the conductivity is also given at 398K for CLFP3 (curve 3).

Figure 5b shows also the existence of a dielectric relaxation around 10^2 Hz at room temperature because ε' value is decreasing from 40 to a constant value equal to 4 at higher frequencies (i.e. above 10^6 Hz). This relaxation would be due to cluster boundary or to silver/sample interface. Above 10^5 Hz, the frequency dependence of $LiFePO_4$ conductivity follows a power law:

$$\sigma = A\omega^s \qquad (1)$$

where A and s are fitting parameters. The value of the exponent s is equal to 0.75 and thus describes a variable range hopping (VRH) conduction mechanism [2]. This describes electrical conduction in disordered systems with localized sites randomly distributed in the crystal network. [3] In this case, the hopping probability depends on the spatial separation of the sites.

The carbon coating in C-$LiFePO_4$ drastically increases the electrical conductivity in the whole frequency range (Figures 5a). At 298K, the dc-conductivity σ_S of the sample has a value of more than 10^{-4} $S.m^{-1}$ below 10^5 Hz and the high frequency conductivity reaches almost 10^{-1} $S.m^{-1}$ in the GHz region. This type of frequency dependence shows that in the composite C-$LiFePO_4$ the carbon-coating constitutes continuous conducting paths spanning throughout the sample.[4] this situation can be realized with a small volume fraction of conductor owing to the core-shell morphology of the carbon-coated $LiFePO_4$ material.[5] The disappearance of the power law evolution in the CLFP3 sample confirms the dominant role of the coating with the existence of one or more relaxation domains above 0.1MHz (Fig. 5a). Figure 5b shows the existence of a low frequency relaxation around 10^4 Hz for CLFP3, which is due to its higher conductivity σ_S correlated to the presence of the carbon-coating. At the higher frequencies, C-$LiFePO_4$ and $LiFePO_4$ permittivities converge to a frequency independent residual permittivity ε_∞ corresponding to the effective (bulk) permittivity of $LiFePO_4$ (LFP). Indeed, in CLFP3, the volume fraction of the carbon coating is too small in the sample to play significantly on the residual permittivity(ε_∞).

The entire Nyquist (Cole-Cole) plot, i.e. ε" vs. ε' of CLFP3 (in the low-frequency part of the dielectric spectrum at 300 K is presented figure 6 below. The first dispersion domain (D1) is fitted T with a good precision by a straight line, which correspond to a υ^{n-1} frequency response of the complex permittivity with an exponent n of about 0.14 whatever the sample and the temperature. Upon subtracting this low frequency contribution, a second dispersion domain D2 (figure 6b) is evidenced and well fitted by a circular arc corresponding to dielectric relaxations described by the CC-function.The relaxation domain D3 (Figure c) is unambiguously defined after subtracting the contributions D2 and is also described by the CC-function. By the same procedure, the relaxations D4 (Figure d) is obtained.

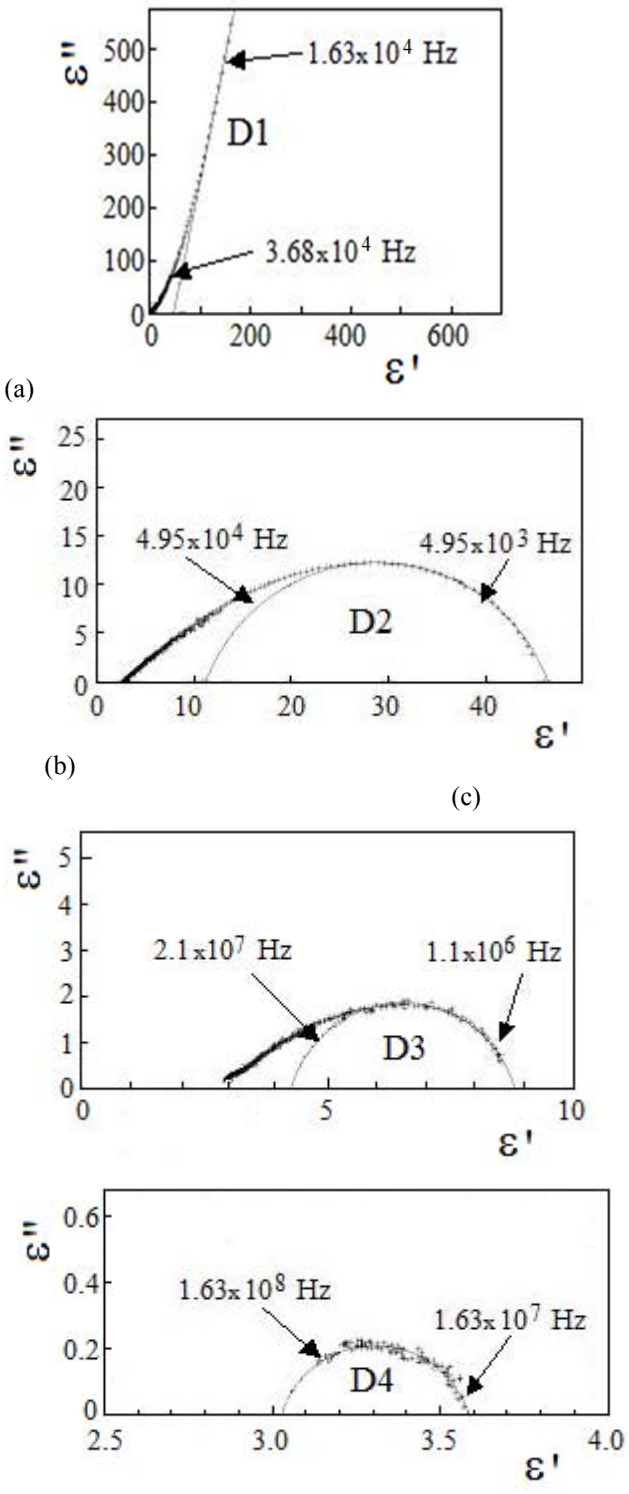


Figure 6. (a) to (d) Cole–Cole plots of the imaginary part ε"(ν) vs. the real part ε'(ν) of the complex permittivity at 298 K for CLFP3:

All the relaxation frequencies ν_i (i = 2, 3 and 4) have thermally activated behaviors, and can be described by Arrhenius behavior.

$$\nu_i = \nu_{0i} \exp\left(-\frac{E_i}{kT}\right) \qquad (2)$$

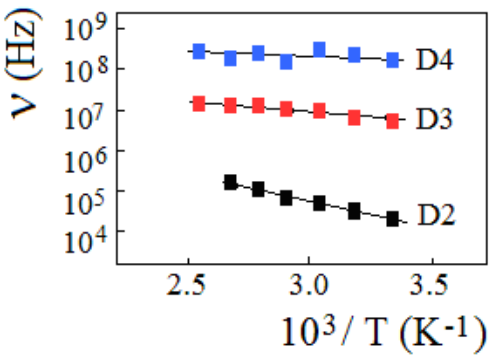
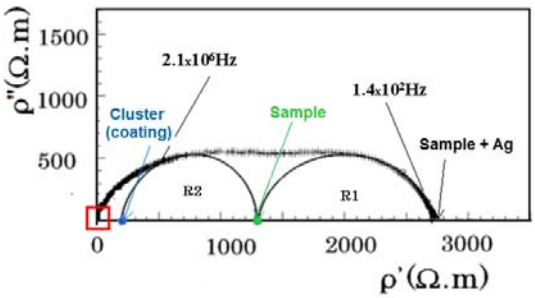
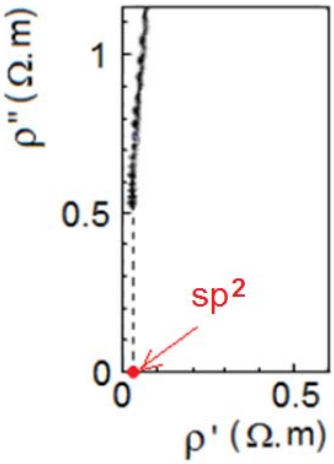


Figure 7. (a) Relaxation frequencies of the different relaxations (D2, D3 and D4) as functions of inverse temperature in CLFP3.

On the other hand the entire resistivity Nyquist plot (ρ" vs. ρ') of CLFP3 at 300 K is depicted in figure 8. To provide evidence for the different resistivity relaxations, we used decomposition procedure of the Nyquist plots similar to the complex permittivity diagrams. The first dispersion domain R1 is well fitted by a circular arc in the low-frequency part of the plot and thus described by the complex CC-function. R1 crosses the real axis ρ′ at ρ_{SM} (low-frequency limit) and at ρ_S (high-frequency limit). After subtraction of the domain R1, the higher frequency contribution R2 is evidenced (Figure 8a) and also fitted by a circular arc. R2 crosses the real axis at ρ_S (low-frequency limit) and at ρ_{CLe} (high-frequency limit). The incremental resistivities $\Delta\rho_1$ and $\Delta\rho_2$ of R1 and R2 correspond to the sample/Ag interface and to the clusters junction resistances, respectively. ρ_S and ρ_{CLe} correspond to the sample and cluster resistivities, respectively. We can consider that the cluster conductivity σ_{CLe} is governed by the coating conductivity σ_{co} because the coating constitutes continuous pathways in the clusters. Hence, their electrical behaviors can be similar, the cluster conductivity corresponding to the effective value of the coating conductivity. Moreover, the zoom of the high frequency part of the complex resistivity plot permits to determine the effective resistivity of the sp^2 domains ρ_{sp2e} (Figure 8b).





(b)

Figure 8. (a) Nyquist plot of the imaginary part ρ"(ν) vs. the real part ρ'(ν) of the complex resistivity at 298 K for CLFP3 (c-LiFePO4); (b) zoom of the high frequency part of the plot (determination of sp2 effective conductivity).

In summary, the hierarchy of the conduction pathways from the nanosize scale (i.e. coherent length of sp^2 domains) to the macroscopic one is described in Figure 9.

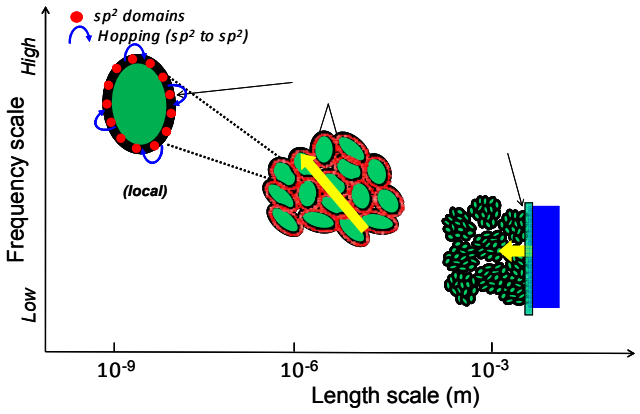


Figure 9. Schematic description of the hierarchical.

The conductivity and permittivity of the composites measured are effective parameters since they are functions of the relative concentration of the different phases. Using the Brick Layer Model and the General Effective Medium theory, it was possible to provide some orders of magnitude for the true values of the conductivity at the different scales of the material (Figure 10), i.e. cluster, coating and sp^2 domain levels.

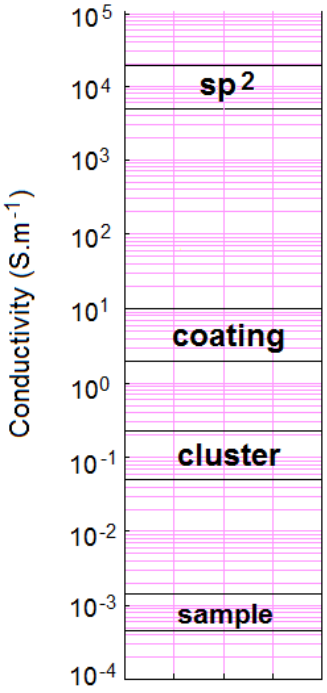


Figure 10. Schematic description of the hierarchical architecture within the samples giving rise to different sources of polarizations.

We have thus established an empirical expression to describe the sample conductivity with respect to that of the smaller level (coherence length of sp^2 domains) that allows to identify and quantify all the limitations.

According to our work, the major drop in conductivity is due to the presence of sp^3 discontinuities in the coating that result in a loss of ~10^3 when going from the sp^2 domains to the coating scale. Although the carbon volume in the C-$LiFePO_4$ cluster **is** very low (less than 5v%), the loss is only a factor of ~10 when going from the coating to the cluster scale. Inter-cluster junctions result in another conductivity loss of ~10. The high activation energy for electrons transport associated with the sp^3 discontinuities result in a large decrease of the conductivity with decreasing temperature, which is a drawback or limitation of the C-$LiFePO_4$ material.

4. Conclusions

This work provided a new approach towards a fundamental understanding of the electrical properties of composites for lithium ion batteries. It also gave a new perspective on the quantitative relationships existing between the different scales. This relationships offer the opportunity to pin point the limiting scales and conductivity mechanisms. Which in turn will be instrumental to make

adjustments on the whole process of the electrode material synthesis, processing, manufacturing and engineering.

Acknowledgements

Financial funding from CNRS, Universitè de Nantes, UMICORE, and the ANR program no. ANR-09-STOCK-E-02-01 is acknowledged.

References

[1] J.-M. Tarascon & M. Armand, *Issues and challenges facing rechargeable lithium batteries*, Nature,(2001) 414, 359-367

[2] N.F. Mott, Phil. Mag. 19 (1969) 835

[3] N. F. Mott and E. A. Davis, *Electronic Processes in Non-Crystalline Materials*, 2nd Ed. (Oxford University Press, Oxford, UK, 1979).

[4] R. Pelster, G. Nimtz, B. Wessling, *Fully protonated polyaniline: Hoping transport on a mesoscopic scale*, Phys. Rev. B , 49 (1994) 12718

[5] C. Chiteme and D.S. McLachlan, *Measurement of universal and non-universal percolation exponents in macroscopically similar systems*, Physical B 279 (2000) 69

Signs, curls, and time variations: learning to appreciate Faraday's law

A. Sihvola[1], **J. Leppävirta**[1], **and H. Kettunen**[1]

[1]Aalto University, School of Electrical Engineering, Department of Radio Science and Engineering, Finland
ari.sihvola@aalto.fi

Abstract— This talk presents the analysis of a study on the development of conceptual understanding of dynamic electromagnetic fields of electrical engineering students in Finland. The focus of the study was Faraday's law. A coil with two light-emitting diodes and a strong permanent magnet was used with which the induced electromotive force could be made visible. However, the field and flux directions, temporal changes, and topological constellations within this setting determine in a subtle manner the character of the resulting electric effect. The demonstration was used on electromagnetic field theory classes at Aalto University, Finland, to assess the conceptual understanding of the students. Drawing from the Peer Instruction principle, the students were asked to fill in a questionnaire concerning this experiment, first on their own, and secondly after discussing with their neighbors in the classroom. They were asked about the direction of the electric force and the confidence of their answer. The results show that the answer is not very obvious: students tend to vote for the wrong answer. The Peer Instruction discussion greatly improves the situation. Also, the confidence of the students increases thanks to the discussion period with neighbors. The results, however, seem to be somewhat sensitive to the exact constellation and the administration of the experiment.

1. INTRODUCTION

In the curriculum of electrical engineering, one of the most challenging topics is the set of Maxwell equations, both for the student and also for the teacher. The divergence relations can certainly be approached from the intuitive understanding of field lines that emanate from a charge. The Gaussian view of total electric flux through a closed surface being equal to the enclosed net charge leads to Coulomb's law, which again, as an analogy to the forces of Newtonian gravitation, strengthens the conceptual framework of physical understanding in the students' minds. Along with this picture, it is easy to connect the vanishing divergence of the magnetic flux density with the non-existence of magnetic monopoles: the magnetic field lines have neither sources nor sinks, they always form closed loops.

More challenging is to bring the student to grasp the meaning of the Maxwell curl equations: Ampère's law supplemented with the displacement current term, and Faraday's law. To acquire a mental picture of the "rotor" operation, or curl, of a vector field requires spatial imagination. In addition, when the curl equations also involve temporal differentiations, the resulting combination of symbols and operators is not instantly digestible for a freshman student.

In this presentation, we focus on Faraday's law and our experiences in teaching to find the most effective ways to help students to develop conceptual understanding of the manner how a varying magnetic field brings forth an electric force.

2. FARADAY'S LAW: DIFFERENTIAL AND MACROSCOPIC FORMS

In the language of vectors, Faraday's law reads

$$\nabla \times \mathbf{E}(\mathbf{r}, t) = -\frac{\partial \mathbf{B}(\mathbf{r}, t)}{\partial t} \tag{1}$$

where $\mathbf{E}$ is the electric field vector and $\mathbf{B}$ is the magnetic flux density, depending on the space $\mathbf{r}$ and time t. This relation is a (partial) differential equation, in other words it is satisfied pointwise: at any point in any time instant, the time variation of the magnetic field dictates the curl of the electric field. Furthermore, the law gives an exact quantitative connection for the relation.

However, the conceptual understanding of this relation requires thinking in not pointwise and differential but rather integrated terms. Use of Stokes's theorem gives the following relation. Given

an open surface, the time variation of the total magnetic flux Φ through it gives the electromotive force over the closed line that forms the boundary of this surface:

$$\mathtt{emf} = -\frac{\mathrm{d}\Phi}{\mathrm{d}t} \tag{2}$$

This relation – many students would agree – is considerably more intuitive than the differential form of Faraday's law (1).

However, even if relation (2) is simple in form and straightforward to use in quantitative enumeration of the voltage that is created by changing magnetism, there are still several possibilities to get the direction (the sign) of the electromotive force wrong. For the first, it is the time derivative of the flux rather than the flux itself which matters for the induced force. In addition, the right-hand-rule convention between the flux direction and the direction of the bounding contour has to be correctly accounted for, and thirdly, the additional minus sign does not make it easier to decipher the final direction of the electromotive force. However, Lenz's law gives useful advice in determining the direction of the induced electromotive force.

In electromagnetics textbooks, there are several different approaches to cover Faraday's law. Certain books introduce outright the Maxwell equations in their full glory with all curls and divergences [2, 3, 4, 5]. Others reach towards the full-wave electromagnetics in a stepwise manner: first teaching the principles of static fields (electrostatics, steady currents, and magnetostatics), and only then focus on Faraday's law, first in the integral form (Equation (2)), from which, by exploiting Stokes' theorem, arrive in the differential form (1) [6, 7, 8, 9]. An even softer path is to move from statics to dynamics through slowly-varying fields. In connection of such fields, Faraday's law is embraced but not yet the displacement current term in the Ampère–Maxwell law [10, 11, 12].

3. SIMPLE DEMONSTRATION OF THE ELECTROMOTIVE EFFECT

Fortunately, it is rather easy to demonstrate the message carried by Faraday's law. The ends of a copper wire, coiled into a large number of turns, are connected by an LED, light-emitting diode. There is no battery in the circuit, and hence the LED does not emit light. However, when a bar magnet is moved into the coil or drawn away from the coil, a voltage is excited and the LED emits a light pulse, depending on the direction of the north pole of the magnet and the speed with which the magnet is moved.

In fact, the most effective way is to solder two LED diodes (with different colors) on the wire ends, such that the polarities are opposites (see Figure 1). Then they serve as indicators for a (sufficiently speedy) increase or decrease of the magnetic flux through the coil.

4. PEER INSTRUCTION AND FARADAY'S LAW DEMONSTRATION

The device shown in Figure 1 has been used to demonstrate Faraday's law in electromagnetics courses at the Aalto University in Finland. To study the students' true understanding of the connections between the magnetic field change and the induced electromotive force, a quantitative study was conducted during the same lecture when Faraday's law was covered on the mathematical and physical contexts. The coil experiment was applied and the students were asked to predict the direction of the induced current (= the color of the LED that would flash) and explain their reasoning. The study was performed in connection with the course "Dynamic Field Theory" in the Department of Electrical and Communications Engineering at the Helsinki University of Technology (presently Aalto University) in 2005 and in 2011. The number of students participating in the study was 78 in 2005 and 99 in 2011.

In particular, the Peer Instruction (PI) method developed by Mazur (1997) [1] was used in order to engage students in active participation. In PI, students first consider the given problem alone. After the first guesses, the students are asked to discuss the problem with their close neighbors in the classroom and then reconsider their responses.

In more detail, the study was administered in the following manner.

4.1. Faraday' law in the classical manner

The lecture starts with the introduction of Maxwell equations. Then the focus moves into one of these, the Faraday's law. The teacher presents the law, both in its differential (1) and macroscopic (2) forms, and explains and interprets its physical meaning.

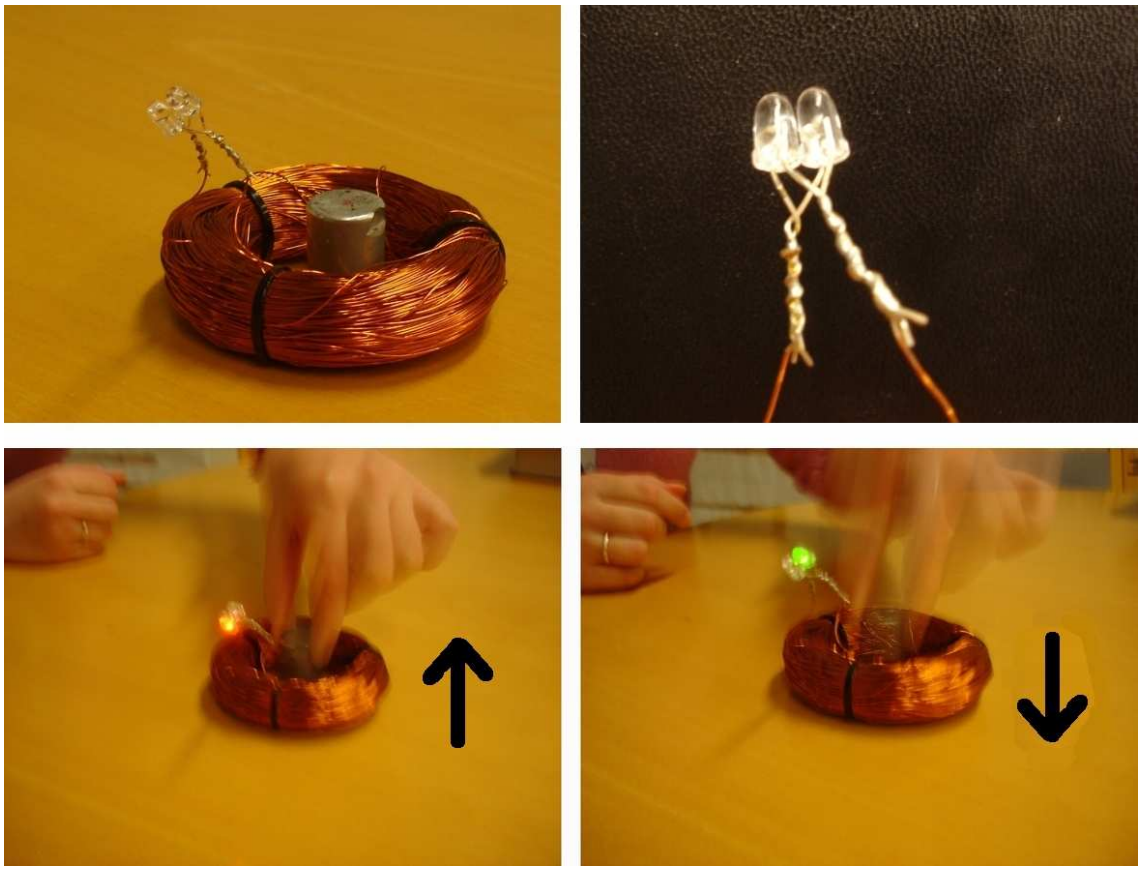


Figure 1: The device (top left panel) consists of copper wire coiled into a large number of turns, with ends soldered to light-emitting diodes (top right panel), one red, one green, with opposite polarity connections. A bar magnet is drawn off or put back into the center of the coil (bottom panels). The direction of the movement and the orientation of the magnet determines which of the LEDs (red or green) flashes.

4.2. Demonstration of the effect

Next, the teacher puts the coil on the table in front of the classroom and explains that he will start changing the magnetic field by moving the magnet inside the coil and out of it. First, by putting the magnet very gently on the table in the center on the coil, nothing happens, and also taking it away very slowly, no LED will flash. However, taking it quick enough, the red light flashes (the color of course depends on whether the north pole or south pole is on top—the same movement with the bar magnet upside down would switch the color). And reversely, putting the magnet back fast, the result is a flash of green light (note that this reverse action is more difficult to manage because the magnet easily hits the table surface, and a sufficiently speedy movement is necessary to produce a clear flash).

4.3. Preparation for the questionnaire

The teacher repeats the demonstrations a couple of times, always explaining the effect and emphasizing the connection of the speed of the movement to the time derivative in the Faraday's law. Then the teacher says that he would ask the students to respond to the question what would happen if he left the *magnet* sitting in the center of the coil and would lift the *coil* up, of course swiftly enough. Would there be LED light? And if yes, what color? The teacher repeats once more the lifting of the magnet (red) and setting it back (green).

4.4. Pre-discussion responses

The students are given a questionnaire where they fill in their prediction what happens (red light / green light / no light) when the coil will be lifted and the magnet remains stationary. In addition, they are supposed to mark their confidence about their answer (whether they are definitely sure or probably sure about it, or just guessing). Furthermore, they are asked to explain their reasoning leading to this answer.

4.5. Data fusion

After having filled in their answers, the students are asked to discuss the phenomenon with their neighbors for around five minutes. They are asked to find their way closer to the correct solution by arguing for their own explanations and learning from the others.

4.6. Post-discussion responses

After the discussion period, the students give their answers again and also rate their confidence level on this new answer, which, of course, may or may not be the same as their pre-discussion answer and confidence.

4.7. Mother Nature gives the correct answer

Finally, the teacher does the experiment and lifts the coil, the magnet remaining on the table. And, nonintuitively, the red light flashes. The students are asked to write down their thoughts about learning the correct answer to the question.

5. RESULTS

The data consisted of two sets of filled questionnaires, one from the year 2005 (78 replies) and the other from 2011 (99 replies). The results are collected in Table 1.

Table 1. The distribution of students' answers and self-rated confidence levels before and after the discussion.

		2005	2011		2005	2011
	Answer	*f* (%)		My answer is	*f* (%)	
Before discussion	Red light[a]	32 (41)	33 (33)	Definitely correct	18 (23)	37 (37)
	Green light	46 (59)	63 (64)	Probably correct	45 (58)	49 (50)
	Neither	-	3 (3)	Just a guess	15 (19)	11 (11)
	No answer	-	-	No answer	-	2 (2)
After discussion	Red light	43 (55)	37 (37)	Definitely correct	27 (35)	38 (38)
	Green light	29 (37)	44 (44)	Probably correct	30 (39)	29 (29)
	Neither	-	2 (2)	Just a guess	9 (12)	8 (8)
	No answer	6 (8)	16 (16)	No answer	12 (15)	24 (24)

Note. 2005 n=78, 2011 n=99
[a]The correct answer

In graphical form, the results are shown in Figure 2. Here both years' responses are collected together.

From the results, the following observations can be made. Firstly, as is easy to believe, extremely few students expected that there is no flash when the coil is lifted. However, there is an interesting split between the red light answers (correct) and green light ones. Indeed, when the students replied on their own (pre-discussion answer), the majority of them chose the wrong answer (we can see about twice as many greens as reds). This is in some sense understandable: if one reasons logically from the point of view of relative movement of the magnet and the coil, one would expect that since green is affiliated with downward movement of the magnet (with stationary coil), then also the upward movement of the coil (with stationary magnet) would produce green light.

However, the essence in the emergence of the induced electromotive effect is the manner how the total magnetic flux through the coil changes. Hence it does not matter whether the magnet is drawn away from the coil (red light) or the coil is taken away from the magnet (also red light).

Fortunately, the post-discussion responses by the students showed a shift towards the correct answer (for the total count, the red–green opinions divided roughly evenly).

As to the confidence of the students, it seems that the majority were definitely sure or probably sure of their answers, and this confidence increased after the discussion: only 15% said that their answer is just a guess (pre-discussion), and the corresponding figure for post-discussion was 12%. The number of students who were definitely sure that their answer was right increased considerably after the discussion: from 31% to 46%. Of course, even after discussion there were students who were definitely convinced about the correctness of their wrong answer.

As a final note, the quantitative results in Table 1 and Figure 2 are averages over the two lectures given six years apart in time. The position of the Dynamic Field Theory course in the second-year

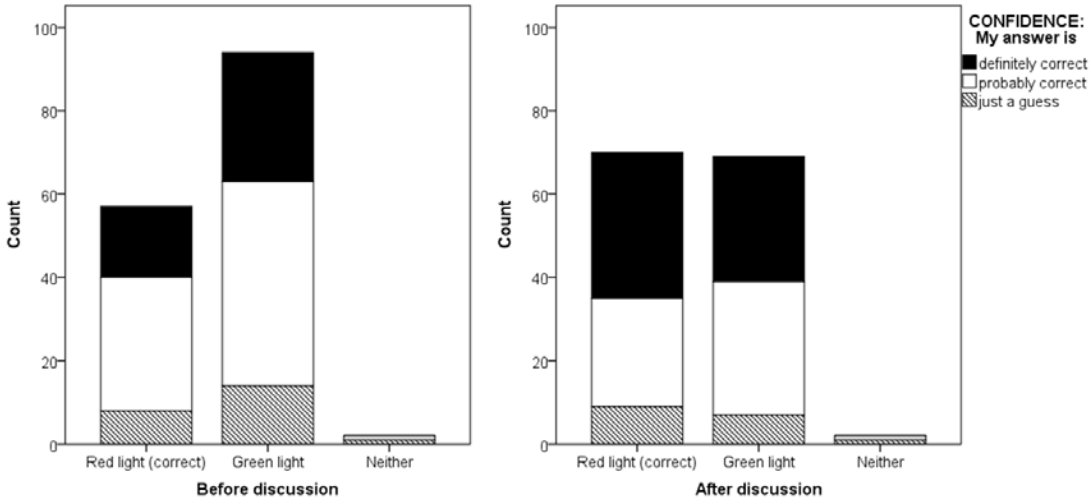


Figure 2: The distribution of students' answers and confidence levels before and after the discussion. The 2005 and 2011 data are combined. Data of those participants who gave no answer for the post-discussion questions were removed from the data set. The remaining sample size was 155.

schedule of the Electrical Engineering curriculum, as well as the teacher, have remained the same. Also the course material and the structure of the Faraday's law lecture has been very similar in these two years. Of course, the individual students and hence the population have been different. Indeed, when the results were separated into the two classes, there were clear differences in the outcomes. The positive effect of the discussion in increasing the share of right answers was clearly larger in 2005 compared to 2011, as can be seen from Table 1. This is, however, not necessarily a consequence of a decrease of students' capabilities. A more likely explanation is the nature of the coil–magnet problem itself. The relativity of the movement and temporal change of the absolute flux through the coil are two equally plausible logical ways of approaching the situation. These two different attractors are competing in a student's mind to determine her/his prediction for the correct color that will flash. In this kind of situation, the exact wording of the teacher during the preparation phase and the amount of time given for the students to make up their minds can have a strong influence on the general outcome of the responses.

REFERENCES

1. E. Mazur, *Peer Instruction: A user's manual*, Series in Educational Innovation, Prentice Hall, Upper Saddle River, NJ, 1997.
2. J. A. Kong, *Electromagnetic Wave Theory*, Wiley, 1986.
3. R. E. Collin, *Field Theory of Guided Waves*, Second Edition, IEEE Press, 1990.
4. H. A. Haus, J. Melcher, *R. Electromagnetic Fields and Energy*, Prentice Hall, 1989.
5. D. S. Jones, *The Theory of Electromagnetism*, Pergamon Press, 1964.
6. D. K. Cheng, *Field and Wave Electromagnetics*, Addison Wesley, 1989.
7. G. L. Pollack, D. R. Stump, *Electromagnetism*, Addison Wesley, 2002.
8. J. D. Kraus, *Electromagnetics*, Fourth Edition, McGraw-Hill, 1992.
9. J. D. Jackson, *Classical Electrodynamics*, Third Edition, John Wiley, 1999.
10. B. M. Notaroš, *Electromagnetics*, Pearson, 2011.
11. J. R. Reitz, F. J. Milford, R. W. Christy, *Foundations of Electromagnetic Field Theory*, Addison Wesley, 1993.
12. Z. Popović, B. D. Popović, *Introductory Electromagnetics*, Prentice Hall, 1999.

Difficulties in teaching electromagnetism: an eight year experience at Pierre and Marie Curie University

H. Roussel, M. Hélier

L2E, Laboratoire d'Électronique et Électromagnétisme
UPMC Univ Paris 6, UR2, L2E, BC 252, 4 place Jussieu F-75005 Paris, France
*corresponding author, E-mail: helene.roussel@upmc.fr

Abstract

We will begin by outlining the details of how electromagnetics are taught in the electrical engineering program offered at Pierre and Marie Curie University (a French example) from the undergraduate to the Masters degree levels. We will also discuss how our methods are and should be adapted to teach waves propagation without discouraging students.

1. Introduction

Teaching electromagnetics in France is an increasingly challenging task. There are several reasons for that. First, many students are tempted to choose Shannon over Maxwell due to the perception that they have of digital devices, ignoring the fact that high data rate systems are electromagnetic ones. Secondly, students feel that electromagnetics is a difficult and demanding subject, as opposed to digital systems design, for instance, which is believed to be easier to grasp and more rewarding. Finally, because of a recent phenomenon of de-industrialization in Europe as well as the social downgrading of technical jobs in companies compared with the importance given to positions related to leading projects or financial management; some students still tempted by an academic career in sciences, prefer to turn to system level activities and are concerned about becoming too specialized as RF engineers. This disinterest is paradoxical as our society deeply depends on electromagnetic systems (mobile phone networks, communication networks, computer system operating now in the microwave band, transportation, even the controversial high frequency trading of the market...). Nevertheless, in other countries, especially in Asia, electromagnetics studies are still appealing to students [1] and when they study in France, their enthusiasm does not wane and they are not discouraged by the level of mathematical skills required. Moreover, many of these students are certain to have the chance in the future to take part in the design and production of RF devices on an industrial scale due to the expansion of many Asian countries and the high international demand for such products. A good summary of the teaching methods of electromagnetism around the world can be found in [2]. This interesting article, published in 1990, shows that electromagnetic courses offered during the Electronic Engineering (EE) Undergraduate program are comparable in each country and that students' interest in ElectroMagnetism (EM) is continuously declining. During the second year, students are first introduced to static and magnetic fields during a basic EM course; the course on electromagnetic fields (Maxwell's equations) is often given in the third year. Furthermore in all countries, teaching electromagnetism should be combined with teaching mathematics, such as linear algebra, vector calculus, integral calculus and the study of complex variable functions. We believe that this is the main reason why students drop out of courses related to electromagnetism: there is a conflict with mathematics, especially vector calculus and three dimensional representations that can not be ignored. Another reason is the growing interest for new technologies mostly in the digital domain which are not identified as being linked to electromagnetism courses.

Many initiatives however have been implemented to counter this decline. Some are based on technology (virtual experiments [3] or real ones [4]), some are based more on pedagogy [5] and some on a mixed approach [6]. One of the common goals of these approaches is to allow students to visualize and and give concrete expression to the abstract concepts of electromagnetics. A well known example is the Center of Excellence for Multimedia Education and Technology (CAEME) initiative started in 1991 at the University of Utah under the supervision of Professor Magdy Iskander [7]. This initiative was based on dedicated multimedia software packages that allowed students to learn interactively and perform simulations of electromagnetic experiments. Another interesting program is the Technology Enabled Active Learning (TEAL) approach developed at MIT since 2000 [8]. The idea is here to replace passive learning (traditional lectures) among large classes (500-600 students) by active learning and the use of educational technology applied to smaller groups of students (120 students). Students following the program could carry out desktop experiments, visualize and simulate several electromagnetic phenomena and have Web access to assignments. The interesting and original part of this, is that the effectiveness of such an approach has been carefully assessed in terms of what students retain by comparing the results obtained through pre-tests, post-tests and surveys with two groups of students: the experimental group enrolled in the TEAL pro-

gram and the control group attending traditional lectures. The experimental group retained significantly more and improved their conceptual understanding of electromagnetics. Even if an enhanced perception of abstract concepts using hands-on activities, visual effects and simulation software is not enough to improve learning, it seems to help students when associated with a well-structured course. Moreover, in terms of this experience, it should be noted that the TEAL approach was applied to smaller classes than the traditional one, and seems to also benefit from better student monitoring.

2. Courses related to EM in EE Undergraduate and master programs at the University Pierre and Marie Curie (UPMC)

During the Undergraduate cycle [9], two EM courses are mandatory for students registered in the EE program. The first, Electrostatics and Magnetism: Fundamentals and Applications, is offered during the fourth semester for twelve weeks with two hours of lectures and tutorials per week and twelve hours of experimenting. This gives a total of sixty hours. This first contact with electrostatics is often the most difficult because it involves new mathematical concepts such as vector operators. Every year we change the course to improve this essential step. This is done by trying to make it more concrete and more accessible by facilitating the understanding of physical phenomena through simple examples. To ensure that these concepts are property acquired by our students, we are proposing this year to set up a project for the second semester. This project consists of a questionnaire similar to the Brief Electricity and Magnetism Assessment (BEMA) done by students at the beginning of the semester and end of the semester to measure their initial and final grasp of concepts. This is a standard procedure in many countries, particularly the United States [10]. This project involves the maximum number of students to include students from different tracks at UPMC, general physics, applied physics and EE at the same level (second year).

The second course takes place during the last semester of the EE undergraduate program and is called, Radiation and Propagation, it follows the same framework as the former course. Using a more punchy course title: Application, Radiation and Propagation helped students see the immediate relevance and applicability of these courses. Following a poll to determine what the students learned and where their interests lie, we found that they continue to express regret about not having enough practical courses. Indeed, given the cost of equipment used to develop practical work on electromagnetism and the time needed to learn how to use this material, we limited this teaching in a four-hour session. This session combines measurements of small dipoles with or without reflector/ one or more director and simulations of wire antennas with the free Numerical Electromagnetic Code (NEC-4) based on the method of moment solution. During this session, students compare measurements with simulations and analytical solutions given in classroom.

The postgraduate program [11] is easier to put together. Indeed, when students get to the first level of the Masters degree they can choose among five specialities. Two of these concern EM: the Communication Systems program and, to a lesser extent, the Sensors, Measurements and Instrumentation program. Teaching electromagnetism at this level is easier because students have opted to pursue this field of study and are more receptive to electromagnetic waves; nonetheless the topic remains theoretical and complex for most students. Several courses are offered to the students. The first is called Mathematics for Communication Systems and takes place during the first semester of the first year (M1). It provides the students with all of the mathematical tools (generalized functions, Green's functions, Hilbert's spaces, probabilities) required to understand theory and recent concepts in electromagnetics. The next courses are provided during the second semester of the first year and deal with Electromagnetic Compatibility (an introduction), Antennas, Transmissions Lines and Guiding Structures.

During the first semester of the second year (M2) of the Communication Systems program, complementary courses allow students to deepen their knowledge in electromagnetics, depending on the program they have chosen. Students registered in the Electronic On-Board Systems program follow an Advanced Electromagnetic Compatibility course with a final exam requiring the analysis and synthesis of a paper. This course is boosted by several talks given by experts from the transportation industry (Dassault Aviation, Eurostar and Renault) who give practical examples of on-board systems and explain electromagnetic compatibility issues with regard to industrial equipment. Students registered in the RF and Microwaves System program will attend an Advanced Antennas course and an Advanced Microwave Devices course as well. The students in both programs take courses on Mobile Communication Systems. The second semester of the second year is devoted to a six-month internship in a company or laboratory. Some of these companies, like Thales, Orange, Bouygues Telecom, Ericsson are involved in the design or use of microwave systems, others like PSA Peugeot Citroën, Renault, Safran or Alstom develop, produce and market vehicles (cars, trains) or engines for airplanes in which high frequency devices are integrated or in which high frequency phenomena may be encountered (lightning for instance).

3. Some proposals to increase the attractiveness of electromagnetism

In order to encourage students to choose Maxwell instead of Shannon, one solution would be to decouple physical understanding from mathematics by using numerical packages such as Matlab, Maple and Mathematica, as suggested in [12] and [13]. In our department we combine the use

of these computer algebra systems with continuous development of new practical courses (antenna measurements combined with complex computation done using EM tools, EMC measurements, guided waves measurements, Radar simulation, etc.) as well as new applicable tutorials. Confucius said "I see, I forget. I hear, I remember. I do, I understand." This saying is particularly pertinent in terms of abstract teaching. The best way to understand the mechanisms involved in the interaction of a wave with its environment is to perform EM measurements for various configurations rather than to develop the equations which govern the propagation in the medium considered.

We give you two examples of practical courses offered at UPMC during EE graduate program. The first concerns EMC measurements. In our department we have designed a metallic box (copper) with or without a small opening on one side. The dimensions of the box are determined so that several resonance frequencies appear in measurements frequency band (300 MHz - 1 GHz). The experiment is carried out in a Faraday cage (see figure 1). In the box we introduce a field sensor for measuring illumination at different frequencies and configurations of the box. These measurements allow us to highlight the effects of leakage through the side slots of the copper box.



Figure 1: EMC measurements

For the course entitled "Radar and Location", we benefit from the Learning and Teaching version of the software MOCEM (MOCEM LT), an "all in one" tool to simulate SAR image for different configurations (see figure 2). MOCEM LT has been offered by DGA MI to UMPC for teaching purposes on radar and SAR imagery. The LT version of MOCEM is a limited version with less functionality than the original software MOCEM V3 developed by Alyotech under contract and specifications of the DGA (French Defense Agency) [14] . MOCEM principles are based on GO-PO principes but with a kind of shorcut in the computation using a estimation the EM level that results of the SAR intregration process. Two phenomena are considered, the diffuse effect resulting from many incoherent scatterers in the image resolution cell and the coherent response coming from reflective surfaces (ground and dielectric or metallic plates). The advantage of this software is that we can easily illustrate many courses (radar, EM propagation) by analyzing the effects observed in the 3D view of the main mechanisms (figure 3) or by observing the synthetic image for different radar configurations (figure 4).

These experiments are very popular with students but obviously go hand-in-hand with lectures that will reinforce the observations made during the experiments.

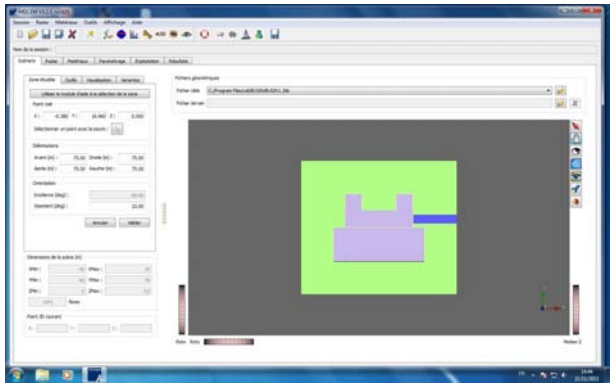


Figure 2: One of the proposed configuration in MOCEMLT: industrial building

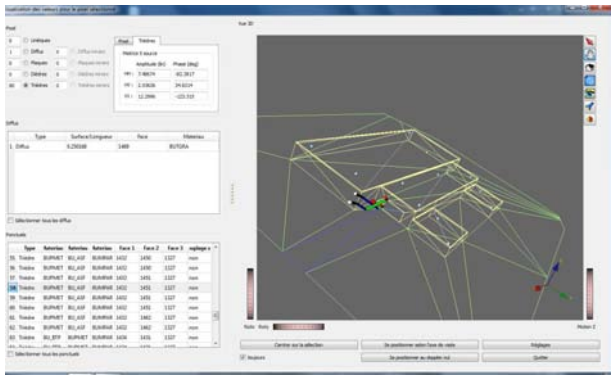


Figure 3: 3D view of the main mechanisms

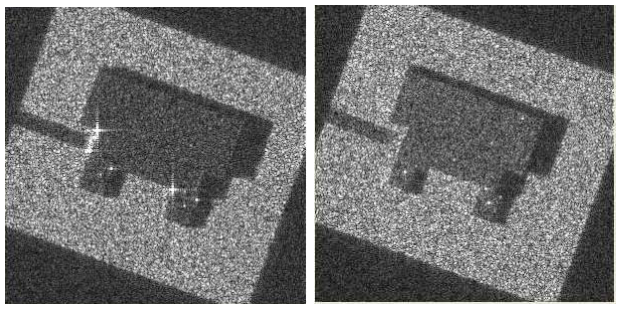


Figure 4: synthetic image for two incident angles: 60° and 40°

4. Conclusion

The teaching of electromagnetism in electrical engineering courses must be tailored to an audience which is more and more reluctant to adhere to abstract disciplines. In our opinion, the best solution for making EM courses more attractive is to offer as early as the first year, practical applications and intensively use of mathematical computer-aided teaching tools to overcome, at the beginning, the difficulties linked to mathematics. Finally, after the first two years of the Undergraduate program, it is necessary to return to these mathematical concepts through further EM courses in the first year of the Master program.

Acknowledgement

The authors would like to thank all their colleagues teaching electromagnetics at Pierre and Marie Curie University, involved in the undergraduate program (bachelor), their colleagues teaching in the "Communication Systems" program (master, postgraduate program) and DGA for its contribution.

References

[1] X. M. Zhang, S. L. Zheng, Y. Du, X. F. Ye and K. S. Chen, Perspective of Electromagnetics Education, *Progress in Electromagnetics Research Symposium Proceedings*, Xi'an, China, March 22-26, 2010.

[2] F.-J. Rosenbaum, Teaching Electromagnetics Around the World : A Survey, *IEEE Trans. on Education*, Vol. 33: 22–34, 1990.

[3] L. Sevgi, A New Electromagnetic Engineering Program and Teaching Via Virtual Tools, *Progress In Electromagnetics Research B*, Vol. 6, 205-224, 2008.

[4] M. Lumori, E. Kim, Engaging Students in Applied Electromagnetics at the University of San Diego, *IEEE Transactions on Education*, Vol. 53, No.3, August 2010.

[5] J. Leppävirta, H. Kettunen, A. Sihvola, Complex Problem Exercices in Developing Engineering Student's Conceptual and Procedural Knowledge of Electromagnetics, *IEEE Transactions on Education*, Vol. 54, No.1, February 2011.

[6] J. Bunting, R. Cheville, VECTOR: A Hands-On Approach That Makes Electromagnetics Relevant to Students, *IEEE Transactions on Education*, Vol. 52, No.3, August 2009.

[7] O. de los Santos Vidal, R. Jameson, M. Iskander, Interaction and Simulation-Based Multimedia Modules for Electromagnetics Education, *FIE '96 Proceedings*, 1996.

[8] Y.-J. Dori, E. Hult, L. Breslow and J. Belcher, How Much Have They Retained? Making Unseen Concepts Seen in a Freshman Electromagnetism Course at MIT, *Journal of Science Education and Technology*, Vol. 16, No. 4, August 2007.

[9] http://www.licence.elec.upmc.fr.

[10] L. Ding, R. Chabay, B. Sherwood, R. Beichner, Evaluating an electricity and magnetism assessment tool: Brief electricity and magnetism assessment, *Physical review special Topics- Physics education research 2*, 2006.

[11] http://www.upmc.fr/fr/formations/departements.html.

[12] D. Ioan, I. Munteanu, Symbolic computation with Maple V for undergraduate electromagnetics education, *IEEE Trans. on Education*, Vol. 44:217, 2001.

[13] A. Norman, M. Mani, A new approach in teaching electromagnetism: how to teach EM to all levels from freshman to graduate and advanced-level students, *Proc. American Society for engineering education annual Conference*, 2003.

[14] C. Cochin, P. Pouliguen, B. Delahaye, D. Le Hellard, P. Gosselin, F. Aubineau, MOCEM -An 'all in one' tool to simulate SAR image, *Synthetic Aperture Radar (EUSAR)*, 2008.

Waves are not vectors, and fields are not waves either

Alain Bossavit

Laboratoire de Génie Électrique de Paris,
CNRS & Univ. Paris-Sud, Orsay, France
*corresponding author, E-mail: bossavit@lgep.supelec.fr

Abstract

This is an apology for the introduction, in advanced electromagnetics courses, of some basic differential geometric notions: covectors, differential forms, Hodge operators. The main advantages of this evolution should be felt in computational electromagnetism.

1. Introduction

At a time when physicists talk about scalar or vector bosons, pseudovector mesons, and so forth, to say nothing of vector potential or Poynting "vector", it's a good idea to challenge this habit to confuse words and things. Not that the confusion is terribly damaging, of course. We know, don't we, what we are talking about, it's only the taxpaying common person who risks being confused – should they try to understand a bit of the science we pretend to possess and to teach. And it's inevitable to represent physical entities we wish to understand by mathematical objects, since only the latter can be handled within a logic-based formal discourse. What is at stake is the *choice* of these mathematical objects.

For choice there is: Several formalisms exist, within which classical electrodynamics can be described: A quaternionic one was popular before Heaviside's reformulation in use nowadays, based on vector fields. Some authors prefer tensors. Others favor Clifford algebras. Here, I will use differential forms, and try to explain why this is the best choice.

2. Differential forms as field descriptors

The criterion in this respect is the time-honored one of parsinomy: Introduce abstract entities only when adequate to the physical entities one wants to deal with, and only when it becomes necessary. Therefore, a well structured theory will start with weak mathematical structures and enrich them on demand, as the theory grows, as if painting layer over layer of the desired theoretical framework. Rather than unwrapping this metaphor, let's have an example.

Consider the case of the electric field $E(x)$ at a point x where it is well defined (i.e., not at a material interface). This vector tells about the force exerted by the field over a unit electric charge placed at x. This force itself is known, to first order, via the virtual work $E(x) \cdot v$ involved in moving the charge from x to $x + v$, where vector v stands for the virtual displacement. The mapping $v \to v \cdot E(x)$ being linear and continuous on the space V of three-dimensional vectors, it is – by the very definition of a dual – some element $e(x)$ of the dual V^* of V. Such elements are called *covectors* and the pairing between a vector v and a covector ω is denoted by $\langle v\ ;\ \omega\rangle$. So we have here $v \cdot E(x) = \langle v\ ;\ e(x)\rangle$, showing that the electric field, as a physical entity, is totally described by the field (in the mathematical sense) $x \to e(x)$, a field of *co*vectors. (We denote this field by e in what follows. It's called a *differential form* of degree one, or *1-form*. Cf., e.g., [1, 2].) Comparing now the two sides of the equality $v \cdot E(x) = \langle v\ ;\ e(x)\rangle$, we see two possible mathematical representations of the electric field: (1°) The one on the left, which uses the vector field E *in association with* the metric structure conferred on space by the dot product " $\cdot$ ", (2°) The one on the right, which uses the 1-form e *plus nothing else*. Parsimony mandates (2°) as the best choice: E appears as an auxiliary entity, that plays the role of *proxy* for the real thing, e.

To show how the 1-form e (taken at some instant of time, of course) gives complete information on the electric field, let's work out the electromotive force (e.m.f.) along some oriented curve c. For this, chop c into a sequence of segments $\{x_{i-1}, x_i\}$, with x_0 at the start-point of c and x_n at the end-point, call v_i the vector from x_{i-1} to x_i, and form the sum $\sum_i \langle v_i\ ;\ e(x_{i-1})\rangle$. As the subdivision of c is properly refined, with n going to infinity, this Riemann sum tends to a number, that we shall denote either by $\int_c e$ (the integral of e along c), or $\langle c\ ; e\rangle$, to emphasize the duality pairing between the integration domain c and the integrandum e. This limit number is the e.m.f. along c: It's what a voltmeter, whose connecting threads would follow the path c, would display. Since c can be any (smooth enough) oriented curve, the 1-form e does indeed know all what is physically meaningful about the electric field.

Note that $\langle c\ ; e\rangle$ is also the number that would be obtained by evaluating the so-called *circulation* of the proxy field E, that is to say, the integral $\int_c \tau(x) \cdot E(x)\, \mathrm{d}x$, where $\tau(x)$ is the tangent vector of length 1 at point x of curve c, oriented in the forward direction along c, and $\mathrm{d}x$ the measure of lengths. Comparing these two expressions of the e.m.f., one sees that the *metric* of space provided by the dot-product " $\cdot$ " is not essential to the physical description of the field: One could change this metric for a different

one, with dot product " $\cdot'$ ", say, and then, one would have to describe the field by a different proxy vector-field E', and to equip the curve c with a different set τ' of tangent vectors and a different lineal measure $\mathrm{d}'x$, in order to preserve the equality $\int_c \tau(x) \cdot E(x)\,\mathrm{d}x = \int_c \tau'(x) \cdot E'(x)\,\mathrm{d}'x$ between these two different expressions for the same e.m.f. $\langle c\,;e\rangle$. *Fields are not vectors,* therefore: A vector field like E is not the mandatory representation of the electric field, as a physical entity. The 1-form e does the job much better.

Similar considerations apply to the magnetic induction. Knowledge of it is total if one knows, for any oriented surface S, the induction flux $\langle S\,;b\rangle$ it embraces. Faraday's law then connects the rate of variation of this flux with the e.m.f $\langle \partial S\,;e\rangle$ along the boundary ∂S of S:

$$\mathrm{d}_t\langle S\,;b\rangle + \langle \partial S\,;e\rangle = 0. \tag{1}$$

(Beware that S must *not* change in time for this to hold, so that one has $\mathrm{d}_t\langle S\,;b\rangle = \langle S\,;\partial_t b\rangle$.) Orienting the surface means providing it with a gyratory sense (clockwise or counterclockwise), and orientations of S and its boundary should "match", that is, the forward direction along ∂S should respect the gyratory sense assigned to S.

[Some technical details are required to analyze the meaning of this compact expression $\langle S\,;b\rangle$. First, a bivector (or 2-vector) $u \vee v$ (the "join" of vectors u and v, both anchored at the same point of space) is the algebraic object represented by the parallelogram spanned by u and v, with orientation (i.e., gyratory sense) provided by the rule "go along u first, then turn to direction v". Bivectors at a point form a vector space, whose dual elements are called *bicovectors*, or 2-covectors. Starting from two covectors ω and η, one may form a 2-covector $\omega \wedge \eta$ by the rule $\langle u \vee v\,;\omega \wedge \eta\rangle = \langle u\,;\omega\rangle\ \langle v\,;\eta\rangle - \langle v\,;\omega\rangle\ \langle u\,;\eta\rangle$. A differential form of order 2, or 2-form, is a smooth field of 2-covectors. To understand $\langle S\,;b\rangle$, where b is such a 2-form, imagine surface S chopped into small patches $u_i \vee v_i$, each based at point x_i of S, and form the Riemann sum $\sum_i \pm\langle u_i \vee v_i\,;b(x_i)\rangle$, where the sign in front of $u_i \vee v_i$ is + if this patch has the same orientation as S itself, – otherwise. The limit of that is, by definition, $\langle S\,;b\rangle$.]

Although such cumbersome details are needed in the theory, one can easily bypass them: Just think of e and b as *mappings* from oriented curves or surfaces to reals, the value being interpreted as an e.m.f. or a flux. These maps are linear (and also continuous, in some rather involved sense). Linearity means that, for instance, $\langle c_1\,;e\rangle + \langle c_2\,;e\rangle = \langle c_1 + c_2\,;e\rangle$, where c is the curve obtained by chaining c_1 and c_2: This linearity reflects the fact that, in case the end-point of c_1 is the start-point of c_2, a voltmeter would measure for this chain the sum of the e.m.f.'s measured along c_1 and c_2 separately. Hence the concept of *chain*: a weighted sum, with real coefficients, of oriented submanifolds of common dimension p ($p = 1$, in our example, with both coefficients equal to +1) and of *cochain*: a p-cochain is an element of the dual of the space of p-chains. Examples are the 1-cochain e and the 2-cochain b. Zero-cochains are just functions (such as the scalar electric potential ψ). The expressions "p-form" and "p-cochain" can be taken as synonyms.

Thanks to the linear structure thus conferred to chains, one may consider the boundary operator ∂ as a linear map, from p-chains to $(p-1)$-chains, which can be useful: For instance, the boundary of curve c joining point p to point q, considered as a 1-chain, is the 0-chain $\partial c = q - p$. If surface S is a cylinder bounded by two closed curves c_1 and c_2, then ∂S is a chain based on c_1 and c_2, like e.g. $c_2 - c_1$, depending on how S, c_1 and c_2 are oriented. (The orientation of ∂S, which must match that of S, is thus determined, but it may not match with the orientations of the various components of the chain ∂S. Hence the minus signs.) Also, in finite element practice, one will often deal with surfaces made of triangular facets of the mesh. As mesh elements are independently oriented, such surfaces will be 2-chains based on mesh facets, with weights ± 1 (or 0, for facets lying outside), and their boundaries will be edge-based 1-chains, also with weights ± 1 or 0.

3. Exterior derivative, Maxwell's equations

But the main advantage of this linearity is perceived in what follows: Define a new operator denoted d, called *exterior derivative*, from $(p-1)$-cochains to p-cochains, by the clause

$$\langle S\,;\mathrm{d}e\rangle = \langle \partial S\,;e\rangle \ \text{ for all } p\text{-chains } S, \tag{2}$$

that is to say, define d as the *dual* of ∂. (This is the general form of the Stokes theorem.) Turning to (1), where S was but a dummy variable, we can get rid of it, and transform (1), using d, into the following local expression of Faraday's law:

$$\partial_t b + \mathrm{d}e = 0, \tag{3}$$

which is as simple as possible. In particular, no metric element is used in it, contrary to what happens in the standard expression $\partial_t B + \mathrm{rot}\,E = 0$.

There, B plays proxy in a way similar to what we already described about E. The flux $\langle S\,;b\rangle$ embraced by S can be written as $\int_S n(x) \cdot B(x)\,\mathrm{d}x$, where $\mathrm{d}x$ is the areal measure and n one of the two fields of unit-length vectors normal to S. This normal field has to be chosen in such a way that (applying the right-hand rule), the gyratory sense indicated by counter-clockwise rotation around n coincides with the orientation of S. Then, the equality $\int_S n \cdot \mathrm{rot}\,E = \int_{\partial S} \tau \cdot E$ comes from the elementary version of the Stokes theorem, and (1) is seen to result in $\partial_t B + \mathrm{rot}\,E = 0$. All the objects we are dealing with here, E, B, τ, n, the curl operator rot, are metric-dependent, but these dependencies appear to cancel each other, resulting in the completely metric-free expression (3)!

The behavior of B, as a proxy field for b, is more complex than that of E: Not only B will have to change if the metric is changed, in order to keep the flux $\langle S\,;b\rangle$ invariant, but with unchanged metric the sign of B will still depend on which orientation convention (right-hand or left-hand) is adopted. Orientation of the ambient three-dimensional

space (that is, the choice of which species of screws, snails, stairs, etc., are deemed right-handed or left-handed) is a convention which has no necessary connection with the choice of metric and/or Cartesian axes, but quite often—by choice of the analyst, not by physical necessity—all these elements go together: The basis of vectors w_1, w_2, w_3 one selects is supposed to determine the scalar product (by the rule $u \cdot v = \sum_i u^i v^i$, if $u = \sum_i u^i w_i$ and $v = \sum_i v^i w_i$), and is supposed to be right-handed. Changes of basis—which cannot have any physical import—then wreak havoc in the relations between mathematical entities, hence these arcane notions of "axial" (vs "polar") vectors, of right-handed vs left-handed cross products, etc., that make the teaching of Electromagnetism so taxing. As (1) demonstrates, all these things can be discarded.

By analogy, one can guess that Ampère's law, $-\partial_t D + \mathrm{rot}\, H = J$ in standard terms, must be replaced by

$$-\partial_t d + \mathrm{d}h = j, \tag{4}$$

where h is a 1-form and d and j are 2-forms. There is however an important difference. For j to properly represent current density, its integral $\int_\Sigma j$, or $\langle \Sigma \,;\, j \rangle$ in the alternate notation, over a surface Σ, should represent an intensity going *through* Σ, which implies a crossing direction with respect to Σ, not the same thing at all as the gyratory sense that was necessary on S for $\langle S \,;\, b \rangle$ to make sense. Of course, if the ambient space is oriented, the two kinds of orientation are related by the right-hand rule, but why should one impose this conventional, human created, feature—an orientation of the space we inhabit—in background of a physical theory, if it can be avoided?

It can, as follows: Let's distinguish *outer* orientation, characterized in the case of surfaces by a crossing direction, from *inner* orientation, characterized by a gyratory sense. Two-chains based on outer-oriented surfaces will be called *twisted* 2-chains [3], those based on inner-oriented ones being known from now on as *straight* 2-chains, for due contrast. A similar distinction holds for 1-chains: An outer orientation, for a curve γ, is a way to turn around it (instead of going along it) in a definite sense, that is to say, a consistent system of inner orientations of closed loops encircling γ. Twisted 1-chains are those based on such outer-oriented curves. Now if γ is the boundary $\partial\Sigma$, the outer orientations of Σ and $\partial\Sigma$ "match" when the forward direction along such an encircling loop coincides with the crossing direction assigned to Σ. Finally, twisted cochains are defined as mappings from twisted chains to reals, the d being again the dual of ∂, and eq. (4) can be interpreted as a relation between the $\sim$1-form h (note the use of $\sim$ as a shorthand for "twisted") and the $\sim$2-forms d and j.

The real number $\langle \gamma \,;\, h \rangle$ is the magnetomotive force (m.m.f.), not "along" γ, like an e.m.f., but "around" it, so to speak, which makes sense when one thinks that an m.m.f. is created by Ampère turns, i.e., current flows, that do "turn around" γ in a clearly defined way. Symmetrically, the induction flux $\langle S \,;\, b \rangle$ is not "through" S, contrary to what its standard representation $\int_S n \cdot B$ tends to suggest, with this n that looks like a crossing direction. The meaningful direction is instead the forward one along the boundary ∂S, which abstractly represents the way one arranges along ∂S the threads of the voltmeter that records—thanks to Faraday's law—the rate of change of the magnetic flux. Hence the word "embraced" to correct, as much as possible, the wrong suggestion that magnetic flux would be, like intensity, the flux of some kind of "stuff" across a surface. This, on the other hand, is all right with j, for $\langle \Sigma \,;\, j \rangle$ is the quantity of electric charge that crosses Σ, per unit of time. Electric charge q, by the way, is a twisted 3-form, the integral $\langle \Omega \,;\, q \rangle$ of which over a volume Ω represents the total charge inside Ω. A straightforward application of the Stokes theorem shows then that

$$\partial_t q + \mathrm{d}j = 0 \tag{5}$$

expresses *conservation of electric charge*. Charge density q, here, rather than being a new entity in the theory, is defined from d by $q = \mathrm{d}\, d$, so one can see, by applying d to both sides of (4), that (5) derives from (4), thanks to the relation $\mathrm{d} \circ \mathrm{d} = 0$, which itself is a consequence, by duality, of the obvious property $\partial \circ \partial = 0$, "the boundary of a boundary is zero" [4].

Magnetic charge, if such a thing existed, would similarly be represented by the (straight, this time) 3-form $m = \mathrm{d}b$. The fact that $\mathrm{d}b = 0$ is, again, seen to be a consequence of Faraday's law by letting d act on both sides of (3), under the natural assumption that b has been null until some instant t, for instance $t = 0$. We have all reasons to believe that $m = 0$ indeed [5], but if experience said otherwise some day, adapting Maxwell's theory to that would be easy: Just put, on the right-hand side of (3), a term $-k$, where k is a (straight) 2-form, interpreted as the current of magnetic charge [6]. Then, magnetic charge would be conserved, $\partial_t m + \mathrm{d}k = 0$, as a consequence of (4).

A last remark on the straight-vs-twisted opposition: straight and twisted forms appear in other fields of physics. In Thermodynamics, for instance, temperature is a 0-form, its gradient is (the proxy of) a 1-form, heat flux is a twisted 2-form, and volumic enthalpy is a $\sim$3-form. Entropy has the same status. One can observe on this that so-called "intensive variables" always correspond to straight forms, while "extensive" ones are twisted forms. This is no accident, and straight [resp. twisted] p-forms are proper generalizations of the concept of intensive [resp. extensive] variables.

4. Constitutive laws

The metric structure thus appears as superfluous, so far. Worse, using it when stating Maxwell's equations hides some important things, such as the difference in nature just evoked between intensive and extensive quantities. Yet, the metric thus expelled comes back, in an interesting way, in the constitutive laws.

We expect, of course, two relations such as $h = \nu b$ and $d = \epsilon e$ to complete (3) and (4). But ν and ϵ there

can no longer be mere numbers, since they connect objects of different types. They must be, accordingly, *operators*: What we have, at each point x of space, is a map $\nu(x)$ from straight 2-covectors to twisted covectors, and a map $\epsilon(x)$ from straight covectors to twisted 2-covectors. These maps encode the behavior of matter (or of vacuum) at point x. (Ohm's law, similarly, would be $j = \sigma e + j^s$, where j^s is the "source" current, the one that generates the field. But let's ignore this issue and consider j in (4) as given.) These maps, considered locally, at point x, or globally, as in $h = \nu b$ and $d = \epsilon e$, are called , when they are linear—which we assume here for brevity—"Hodge operators". As it appears, they encode the metric structure of space-time (they determine the light cone, in particular). So at this stage one has a neat separation between the so-called *pre-metric* part of Maxwell's theory (essentially (3) and (4), both conservation laws of sorts, plus derived relations such as (5) and dd = 0), and its metric aspects—constitutive laws—that characterize the medium in which the electromagnetic field develops, and thus appear as less fundamental than the two main equations.

Such a separation is more difficult in the classical theory: In $B = \mu H$, for instance, we have most often a scalar μ, but also, sometimes, a symmetric tensor μ_{ij}, so that components of B are given by $B^i = \sum_j \mu_{ij} H^j$. A mere change of basis being enough to pass from a scalar to such a tensor, this casts in doubt the notion of *isotropy*: Isotropy cannot be understood as the presence of off-diagonal components in matrix μ, since that could be achieved by a change of basis which is, physically, irrelevant. A more refined notion of anisotropy comes from restricting changes of basis to *orthonormal* ones, so that eigenvalues of μ acquire an invariant character. It then seems to make sense to identify isotropy with the equality of these three principal values. But this amounts to endow the chosen metric (in which the proxies of b and h are B and H) with a physical character that it may not possess. The usual Euclidean metric has such a character as far as the vacuum is concerned, because our geodesy is based on the very existence of light rays, so that the metric we favor is adapted to Maxwell's equations in the void (hence the scalar character of ϵ_0 and μ_0 in the laws $D = \epsilon_0 E$ and $B = \mu_0 H$). But this is not necessarily the case in crystals, be it natural ones or artificial ones such as metamaterials.

5. Anisotropy

Hodge operators help understand this question better. As a rule, they are symmetric and positive definite, which means that the ∼3-forms $e(x) \wedge \epsilon e(x)$ and $b(x) \wedge \nu b(x)$ don't vanish for $e(x) \neq 0$ and $b(x) \neq 0$, and that (let's drop the x, understood, from now on) $e \wedge \epsilon e' = e' \wedge \epsilon e$ and $b \wedge \nu b' = b' \wedge \nu b$ whatever e, e', b, b'. By setting $|b|_\nu = \lambda(b(x) \wedge \nu b)^{1/2}$, where λ is a suitable constant [7], one obtains a norm on the vector space of 2-covectors, from which a Euclidean norm $|\ |_\nu$ on vectors is easily derived. Hence a metric, "ν-adapted" in the sense that, if B and H are the proxies of b and h for *this* metric, then $B = H$.

Now let's turn towards ϵ. By the same process, one can form an ϵ-adapted metric $|\ |_\epsilon$, which quite often will be the same as $|\ |_\nu$, up to a multiplicative constant. This is what happens for the vacuum, for which this constant is to do with its impedance. It also happens for most kinds of transparent matter, where the constant is affected by another multiplicative factor, called the *refractive index* of the material. In both cases, there is isotropy in a physically meaningful sense, for light rays, it can be proven, propagate at the same velocity in all directions and whatever the polarization, even though a choice of metric non-adapted to either ϵ or ν could mask this fact.

So what about genuine anisotropy? This holds when, having chosen one of the hodges (usually, ν) to make a metric with, the eigenvalues of the matrix ϵ that links the proxies D and E of d and e by $D = \epsilon E$, happen to be distinct. (Proxies D and E are, of course, those relative to the ν-metric.) Then the velocity of light (as measured by using the ν-metric) depends on direction, and the very notion of light cone can even collapse if the three principal values differ two by two, to be replaced by a more complex geometrical object, the Fresnel surface [6]. Propagation velocity of a plane wave then also depends on its polarization, hence the spectacular phenomenon of *birefringence* [8].

6. Conclusion and prospects

This geometric view of the Maxwell equations we have sketched here is almost a century old [3, 9, 10, 11] and has not been adopted yet in mainstream treatises. It should be. It's the best way to present modern numerical techniques, be they based on the Galerkin method with edge elements, on finite volume ideas, or on so-called "mimetic" heuristics. The above viewpoint leads naturally to such methods, which can be presented under the common header "Generalized Finite Differences" [12]. The salient points are (1°) By attaching degrees of freedom to elements of the mesh (not only and exclusively nodes, but also edges, facets, volumes), one is led, almost compulsorily, to a discrete expression of the conservation laws (3) and (4), which in a sense introduces no approximation error, (2°) The Hodge operators ϵ and ν must be approximated by square matrices (indexed over edges and facets, respectively), and it's in this process that approximation errors appear. So the central task of the theory, from the numerical point of view, consists in *approximating Hodge operators in a consistent way*, and this is where different techniques may compete. This is also where geometric objects introduced for purely mathematical purposes long ago, such as *Whitney forms* [13], become useful.

Some benefits can be drawn from this also when dealing with waves, and in metamaterial studies. A plane wave is a time-varying field of covectors of the form $e(t, x)$ = Re[E $\exp(i(\omega t - \langle x\ ;\ \kappa \rangle))$], where both E and κ are covectors, and a similar expression for h. Again, no metric element there, contrary to what happens in the standard formalism where $x \cdot \kappa$, with κ a vector, would replace $\langle x\ ;\ \kappa \rangle$. Treating κ as a covector shifts emphasis from the direction of propaga-

tion of the wave (which is along the *vector* κ in the standard treatment) to the planes of equal phase (those parallel to the kernel of the *covector* κ). This small difference eases up the treatment of wave propagation in anisotropic media, including the study of dispersion relations. In particular, a streamlined treatment of the Fresnel surface is obtained. It's even more true with *Bloch waves* when studying crystal-like media (replace E above by a cell-periodic covector field $\mathrm{E}(x)$ borne by a Bravais cell). The difference between Bravais cells (parts of V) and Brillouin zones (parts of V^*) is better marked and metric properties are not in the way.

Fields, to sum up, are physical entities, and there exist mathematical entities with the same name that can represent them. The latter are our creation, and should be chosen with care. Differential forms, aka cochains, i.e., fields of covectors (*bi*-covectors in some cases, as has been explained) are the recommended choice. Other mathematical entities, namely fields of special form called "waves" (plane waves, spherical waves, Bloch waves ...) also are useful (when taken as wave *packets*) to represent physical fields, but just that. Fields are not waves, waves are not vectors, not even vector fields, vector fields "are" not the physical fields they stand proxy for. One should not reify vector fields (or differential forms, for that matter) and believe in their existence as physical objects.

References

[1] W.L. Burke, *Applied Differential Geometry,* Cambridge University Press, Cambridge (U.K.), 1985.

[2] Th. Frankel, *The Geometry of Physics, An Introduction,* Cambridge U.P., Cambridge (U.K.), 1997.

[3] W.L. Burke, "Manifestly parity invariant electromagnetic theory and twisted tensors", *J. Math. Phys., 24,* 1 (1983), pp. 65-9.

[4] C.W. Misner, K.S. Thorne, J.W. Wheeler, *Gravitation*, Freeman, New York, 1973.

[5] A.S. Goldhaber, W.P. Trower, "Resource Letter MM-1: Magnetic monopoles", *Am. J. Phys., 58,* 5 (1990), pp. 429-39.

[6] F.W. Hehl, Y.N. Obukhov, "Electric/magnetic reciprocity in premetric electrodynamics with and without magnetic charge, and the complex electromagnetic field", *Phys. Lett. A, 323* (2004), pp. 169-75.

[7] A. Bossavit, "On the notion of anisotropy in constitutive laws: some implications of the 'Hodge implies metric' result", *COMPEL, 20,* 1 (2001), pp. 233-9.

[8] A. Fresnel, "Mmoire sur la double réfraction", *Mémoires de l'Acad. de l'Institut de France, 7* (1827), pp. 45-176.

[9] F. Kottler, "Maxwell'sche Gleichungen und Metrik", *Sitzungber. Akad. Wien IIa, 131* (1922), pp. 119-46.

[10] E.J. Post, "Kottler-Cartan-van Dantzig (KCD) and Noninertial Systems", *Found. Phys., 9,* 7/8 (1979), pp. 619-40.

[11] M.J.A. Schouten, D. Van Dantzig, "On ordinary quantities and W-quantities", *Comp. Math., 7* (1939), pp. 447-73.

[12] A. Bossavit, "Discretization of Electromagnetic Problems: The 'Generalized Finite Differences Approach' ", in W.H.A. Schilders, E.J.W. Ter Maten (Eds): *Numerical Methods in Electromagnetism* (Handbook of Numerical Analysis, Vol. 13), Elsevier (Amsterdam), 2005, pp. 105-97. (Available at http://butler.cc.tut.fi/∼bossavit/BackupICM/DEP.pdf.)

[13] H. Whitney, *Geometric Integration Theory*, Princeton U.P. (Princeton), 1957.

Fractional-order Rectangular Waveguides

R. Ismail[1], A. G. Radwan[2]

[1]Mathematics Department, German University in Cairo (GUC), Cairo, Egypt
[2]Engineering Mathematics Department, Faculty of Engineering, Cairo University, 12613, Egypt

Abstract

Recently, rectangular waveguides have been considered as a mean of transmitting power or information through electromagnetic propagation. The general way to study the waveguide behavior is by solving the conventional Maxwell's equations. During the last four decades, the dynamical modeling of many physical phenomena has been restudied using the concept of fractional-calculus which increases the degree of freedom over conventional modeling. In this paper we will focus on restudying the effect of fractional-order derivatives with respect to time on the conventional Maxwell's equations that control the behavior of electromagnetic fields. The generalized analysis and analytical forms of the fractional-order rectangular waveguide will be introduced as an example. Through this example, we will show the effect of the fractional-order parameters on the waveguide properties. In addition, we will verify that the analysis of the conventional rectangular waveguide is a special case from the fractional-order study when the fractional-orders equal "1".

1. Introduction

Fractional calculus is a branch of mathematical analysis that studies non-integer differentiation and integration. Although the root of fractional-calculus has been related to the same time-interval of the conventional calculus, its real revolution started five decades ago [1-2]. One of the main reasons for this delay is the absence of real applications that can prove its usefulness and also due to its complexity relative to the integer-order calculus. After 1960, many papers focused on the approximation and realization of the fractional-element and its advantages [3-5].

In particular, the basic definitions of the fractional integral (J^{α}) and fractional derivative (D^{α}) of a function f(t) are given by [1-2]

$$J^{\alpha}f(t) = \frac{1}{\Gamma(\alpha)}\int_0^t (t-\tau)^{\alpha-1} f(\tau)d\tau, \quad (1)$$

$$D^{\alpha}f(t) \equiv \frac{d^{\alpha}}{dt^{\alpha}} f(t) = D^{m}\left(J^{m-\alpha}f(t)\right), \quad (2)$$

By applying the above definition in particular on the natural exponential function [6] we see

$$D^{\alpha}e^{ax} = a^{\alpha}e^{ax} \quad (3)$$

In this paper we discuss the time domain fractional order case of rectangular wave guides. We study Maxwell's equation in the fractional-order sense and illustrate that the integer-order case is considered as a special case of such an equation. We apply on an example of a rectangular waveguide showing how imposing fractional parameters affects some of its properties.

2. Fractional order Maxwell's Equations

Maxwell's equations constitute formalism for the development of modes describing electro-magnetic phenomena. The four Maxwell laws have been adopted successfully in many applications and involve only the integer order derivatives. Recently, a closer look for the cases of transmission lines, electrical motors and transformers, that reveal the so called skin effect, motivated a new perspective towards the replacement of conventional models by fractional ones.

In this section we restudy the equations of Maxwell in the fractional sense. According to Faraday's law, assuming general order derivative α:

$$\nabla \times E = -\frac{\partial^{\alpha}}{\partial t^{\alpha}} B = -\mu \frac{\partial^{\alpha}}{\partial t^{\alpha}} H \quad (4)$$

For some general derivative β, the 2nd Maxwell curl equation is written as

$$\nabla \times H = \varepsilon \frac{\partial^{\beta}}{\partial t^{\beta}} E \quad (5)$$

Using phasor representation for the electromagnetic fields $H = Re(\boldsymbol{H_s}e^{\gamma t})$, $E = Re(\boldsymbol{E_s}e^{\gamma t})$ and with the aid of (3), the fractional wave equations are:

$$\nabla^2 E_s - k_{\alpha,\beta} E_s = 0 \quad (6)$$

$$\nabla^2 H_s - k_{\alpha,\beta} H_s = 0 \quad (7)$$

with $k_{\alpha,\beta} = \mu\epsilon\gamma^{\alpha+\beta} = \mu\epsilon\gamma^2$ when $\alpha + \beta = 2$, which as the conventional case is retrieved. Now, it's more convenient to have a practical example from the conventional case to see the effect of the fractional derivatives on its performance as shown in the next section.

4. Fractional Rectangular Waveguides

Consider a rectangular waveguide with cross section *a and b*. We shall assume that the waveguide is filled with a source-free lossless dielectric material and its walls are perfectly conducting. Let $\gamma = j\omega$ and put $E_s =< E_{xs}, E_{ys}, E_{zs} >$. Consider the TM mode for the case $\alpha + \beta = 2$, Applying (6) and (7) with the boundary conditions $(E_z = 0\ at\ y = 0, y = b, x = 0\ and\ x = a)$ this yields to the following fields

$$E_{zs} = E_0 sin\left(\frac{m\pi}{a}x\right) sin\left(\frac{n\pi}{b}y\right) e^{-k_z z} = E_{zsc} \quad (8a)$$

$$E_{xs} = \left(\frac{-k_z}{h^2}\frac{m\pi}{a}E_0\right) cos\left(\frac{m\pi}{a}x\right) sin\left(\frac{n\pi}{b}y\right) e^{-k_z z} = E_{xsc} \quad (8b)$$

$$E_{ys} = \left(\frac{-k_z}{h^2}\frac{n\pi}{b}E_0\right) sin\left(\frac{m\pi}{a}x\right) cos\left(\frac{n\pi}{b}y\right) e^{-k_z z} = E_{ysc} \quad (8c)$$

$$H_{xs} = \frac{j^{2-\alpha}\epsilon\omega^{2-\alpha}}{h^2}\frac{n\pi E_0}{b} sin\left(\frac{m\pi x}{a}\right) cos\left(\frac{n\pi y}{b}\right) e^{-k_z z} = (j\omega)^{1-\alpha} H_{xsc} \quad (8d)$$

$$H_{ys} = \frac{-j^{2-\alpha}\epsilon\omega^{2-\alpha}}{h^2}\frac{m\pi E_0}{a} cos\left(\frac{m\pi x}{a}\right) sin\left(\frac{n\pi y}{b}\right) e^{-k_z z} = (j\omega)^{1-\alpha} H_{ysc} \quad (8e)$$

where $h^2 = \mu\epsilon w^2 + k_z^2$, and the set $\{E_{zsc}, E_{xsc}, E_{ysc}, H_{xsc}, H_{ysc}\}$ is the solution in the conventional case [7] when $\alpha = 1$. The ratio between the magnetic fields H_{xs} and H_{ys} with respect to their conventional case is $(j\omega)^{1-\alpha}$ as illustrated by (8d) and (8e) respectively. Therefore, the fractional order affects the magnetic fields by two ways simultaneously:

- adding an extra phase equal to $(1-\alpha)\pi/2$
- Scaling the magnitude by the factor $\omega^{1-\alpha}$ which is a nonlinear function of the frequency. Then if $\alpha < 1$ this ratio will increase as the frequency increases. However, if $\alpha > 1$, so the power of ω will be negative, which shrinks the effect of H as frequency increases.

Fig. 1 illustrates the real and imaginary part of this ratio versus the fractional-order α for three different frequencies $\omega = \{10^7, 10^9, 10^{11}\} Rad/Sec$. It is clear that the real part increases by huge factor for small α passing by "1" in the conventional case, and decaying exponentially for higher α. The imaginary part equals zero in the conventional case and has a different sign once $\alpha > 1$. Similarly, Fig. 2 shows the absolute value of the real and imaginary parts of this ration versus the frequency for four different values of the fractional order $\alpha = \{0.4, 0.8, 1.2, 1.6\}$.

5. Conclusions

This paper introduced the Maxwell's equations in the time-domain fractional-order case. The fractional-order waveguide analysis in the case of TM mode under the condition $\alpha + \beta = 2$ is discussed. It is proved that, the conventional case is a special case where $\alpha = \beta = 1$ from the introduced fractional case. The effect of the fractional-order parameter on the magnetic fields is studied from both phase and magnitude prospective where an extra phase is added and the magnitude is multiplied by a nonlinear function of frequency. This function increases (decreases) exponentially as α decreases (increases). We can study the general case for both α and β showing how imposing fractional derivatives are in the operation of the rectangular waveguide giving us a wide degree of freedom to control its characteristics like the intrinsic impedance and cutoff frequency.

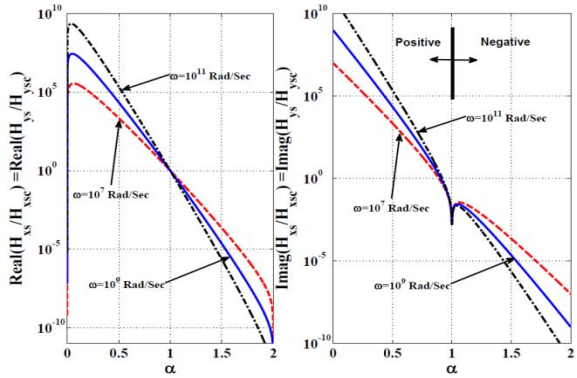


Fig. 1 The ratio of the fractional-order magnetic field to the conventional one versus the fractional order

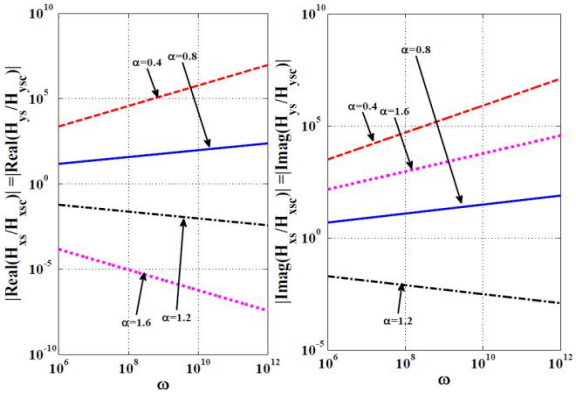


Fig. 2 The ratio of the fractional-order magnetic field to the conventional one versus the frequency

References

[1] S. G. Samko, A. A. Kilbas and O. I. Marichev, *Fractional integrals and derivatives: theory and application*, Gordon & Breach, 1987.

[2] J. Sabatier, O.P. Agrawal and J.A. Tenreiro Machado, *Advances in fractional calculus; theoretical developments and applications in physics and engineering*, Springer, 2007.

[3] G. Carlson, and C. Halijak, "Approximation of fractional capacitors $(1/s)^{1/n}$ by a regular Newton process, " *IEEE Trans*. *Circuits &Syst*, 11, 210-213, 1964.

[4] M. Nakagawa, and K. Sorimachi, "Basic characteristics of a fractance device," *IEICE Trans*. *Fundam*. *Electron*. *Commun*. *Comput*. *Sci*., vol. E75, no.12, pp. 1814-1819, 1992.

[5] T. C. Haba, G. L. Loum, G. Ablart, "An analytical expression for the input impedance of a fractal tree obtained by a microelectronical process and experimental measurements of its non-integral dimension," *Chaos, Solitons and Fractals*, 33, 364–373, 2007.

[6] Kostadin Trenˇcevski, ˇZivorad Tomovski, "On fractional derivatives of some functions of exponential type", Univ. Beograd. Publ. Elektrotehn. Fak., Ser. at. 13 (2002), 77–84.

[7] M.N.O. Sadiku, "Elements of Electromagnetics", 5th edition, Oxford University Press, 2010.

Experimental Demonstration of Two Kinds of Carpet Cloak

Di Bao, **Khalid Z Rajab** , **Yang Hao**

School of Electronic Engineering and Computer Science
Queen Mary, University of London, London E1 4NS, UK
Email: yang.hao@elec.qmul.ac.uk

Abstract— In this paper, two kinds of all dielectric carpet cloak are reported with detailed simulation and experiment results. The first structure is made of a high-ϵ dielectric-loaded foam mixture and the second is realized by dielectric disk matrix (DDM) with varied periods. Both cloaks are demonstrated to work for all incident angles over a wide range of microwave frequencies. The performance of these two cloaks are compared in the end.

1. INTRODUCTION

The theory of transformation optics has been proposed to design novel and complicated electromagnetic and optical devices by controlling the path of wave propagation [1, 2]. One of the most famous example, the invisibility cloak, has been realized and attracted intensive attention in the past few years. The first experimental verification was carried out at microwave frequencies [3], but earlier designs of free-space cloaks suffered from inherent limitations of metamaterials such as high loss and narrow bandwidth because the inclusion of material with extreme-values properties ($\epsilon, \mu < 1$). Li et al. proposed the ground-plane cloak design [4], which makes broadband cloaking feasible. The idea has been experimentally verified at both microwave and optical frequencies [5, 6, 7, 8, 9], which require high index background materials or contain a very large number of metamaterial cells, so they are heavy and complex to fabricate. In 2009, the idea of the quasi-cloak, which consists of a few carefully designed all-dielectric blocks was proposed in [10], and it completely removes the constrains of metamaterials without significantly sacrificing its performance. Thus it enables certain practical applications from microwave to optical frequency band. The idea has been demonstrated in microwave region with I-shaped metal structures printed on PCBs with F4B substrates [8].

In this paper, we report on two different realizing methods of all dielectric carpet cloak: a high ϵ dielectric loaded foam mixture and dielectric disk matrix (DDM) with varied density [12, 13]. In the foam mixture, polyurethane foam mixed with different ratios of barium titanate is used to produce the required range of permittivities, while in DDM, varied density of the cylinders can generate different permittivities. These two cloaks are then tested in a near-field scanner system in X-band frequencies, and both demonstrated to work from all incident angle.

2. MEASUREMENT OF THE CYLINDERS

Periodic arrays of high-index dielectric cylinders has been used at microwave frequencies operating off-resonance in order to achieve low loss, broadband materials with gradient refractive indices, and have been examined with both parameter retrieval and Fourier Transform methods based on finite element method simulations (Ansoft HFSS)[14]. Carpet cloaks are then realized by manipulating the height or density of the cylinders [13, 15]. In this section, the properties of dielectric cylinders are studies through both simulation and experiment results.

In the experiment realization of DDM carpet cloak, we would need to characterize the dielectric properties of the dielectric disks first. Now considering ten cylinders with heights of 2.1 mm, radius of 1.5 mm, and dielectric constant of 36. Since the cylinders are electrically very small and it is very difficult to measure with normal method, we use the method of measuring the phase shift when they are put in a waveguide periodically. X-band waveguide is used here to test the transmission parameters. There are two kinds of arrangement. The first is one-layered configuration as shown in Fig. 1(a), sample 1. Here, ten cylinders are placed periodically with the period of 10 mm between each cylindrs in the waveguide, where the left and right sides are the ports and other four sides are the metallic walls. The second is a two-layered configuration, also with the period of 10 mm as shown in Fig. 1(b), sample 2. The measurement of these two samples are similar. We will present the analysis of sample 1 as an example.

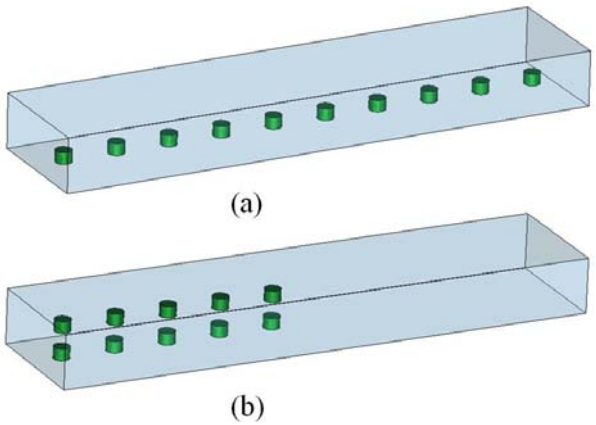


Figure 1: cylinders placed periodically in wave guide (a) one layer (b) two layers

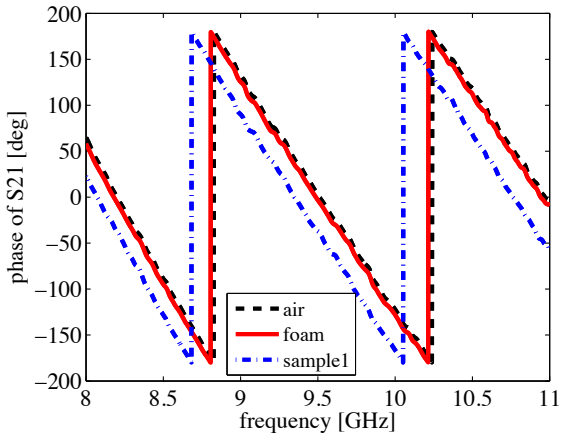


Figure 2: Measured phase of air, foam, and one layer cylinders in the waveguide.

An X band waveguide (WG) with the size of 22.86 mm by 10.16 mm and working frequency ranging from 8.2 GHz to 12.4 GHz is used to carry the samples. With a network analyzer(PNA 5230), the transmission parameters of the empty waveguide, waveguide with sample 1 placed on one layer of 1 mm thick foam, and waveguide with just the foam are measured independently. The phases of $S21$ are shown in Fig. 2. The $S21$ phase of the WG loaded with air is almost the same with the one loaded with foam, which means that the electric properties of the foam are close enough to those of air, so it is reasonable to support the cylinders with the foam and ignore it in the data processing.

The waveguide loaded with sample 1 can be assumed to be loaded with a piece of material with the dielectric constant of ϵ_r and dimension of 22.86 mm by 10.16 mm by 100 mm. So, the phase shift can be expressed as:

$$\phi_0 = j\beta_0 d \tag{1}$$

$$\phi_s = j\beta_s d \tag{2}$$

Here, d is the length of the sample, ϕ_0 and ϕ_s are the phase shift in air and sample, β_0 and β_s are the propagation constant in air and sample,which can also be expressed as:

$$\beta_0 = \sqrt{k_c^2 - k^2} \tag{3}$$

$$\beta_s = \sqrt{k_c^2 - \epsilon_r k^2} \tag{4}$$

Here, k_c is the cutoff frequency of the waveguide. So, we can get:

$$\phi_s - \phi_0 = j(\beta_s - \beta_0)d = j(\sqrt{k_c^2 - \epsilon_r k^2} - \sqrt{k_c^2 - k^2})d \tag{5}$$

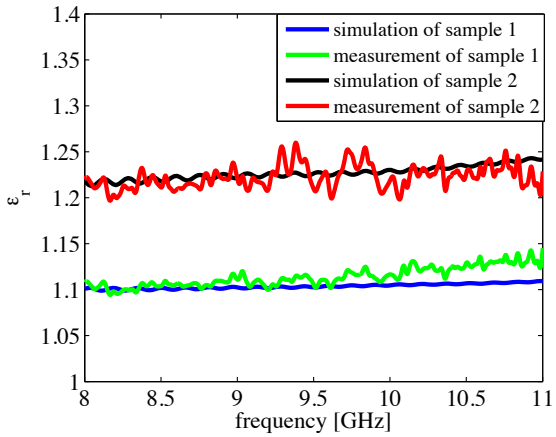


Figure 3: Calculated ϵ value of the periodic cylinders from measurement and simulated data

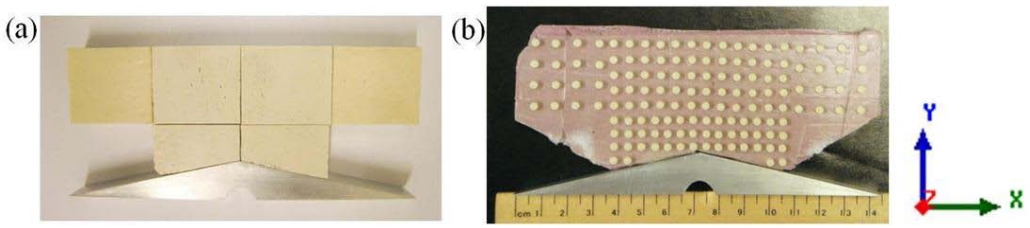


Figure 4: Photoes of the perturbation bounded by the cloaks. The perturbation is an aluminium triangle of height 16mm and base 144 mm. At the base of the triangle is a metal boundary. (a) $BaTiO_3$-loaded polyurethane foam cloak (b) DDM cloak

The solution is:

$$\epsilon_r = \frac{k_c^2 - (\frac{\phi_s - \phi_0}{jd} + \beta_0)^2}{k^2} \tag{6}$$

With Eq.(6) and the measured data, the effective dielectric constant can be calculated for sample 1. A model is setup in CST 2009 to compare the results.

Following the same procedure, sample 2 is also processed. The results of both sample 1 and 2 are shown in Fig. 3. The simulation and measurement are in good agreement. So, we reach the conclusion that the dielectric constant of the sample is 36, and we shall use them in the following work to physically build the carpet cloak.

3. CLOAK DESIGN AND FABRICATION

It has already been shown [10] that the spatially dispersive dielectrics can be simplified to relatively few dielectric blocks, while still maintaining the overall performance characteristics in minimizing the scattering signature of the object. Based on this simplified cloaking design, a cover structure is designed to reduce scattering from a triangular-shaped perturbation with its base placed on the ground plane. The perturbation has a height of 16 mm, base of 144 mm, and thickness of 15 mm. The carpet cloak is composed of down-sampled selection of six dielectric blocks, with relative permittivities of 1.17, 1.30 and 1.46 as in paper [12].

In the fabrication of the loaded foam mixture cloak, polyurethane foam mixed with different ratios of high ϵ barium titanate ($BaTiO_3$) is used to produce the required range of permittivities. Polyurethane is used to create a low-ϵ foam matrix, and $BaTiO_3$ can be used to load the foam in order to increase the effective permittivity while not greatly altering the mechanical properties of the structure. The density of $BaTiO_3$ powder is low, and the small particle size is advantageous when used in a dispersion system and is less likely to affect the polymer matrix structure. This results in less damage to the mechanical properties of the composite material. Both substances exhibit low loss and low dispersion at microwave frequencies, and are thus suitable for our requirements. The detailed description can be found in [12]. For the DDM cloak, dielectric disk matrices with

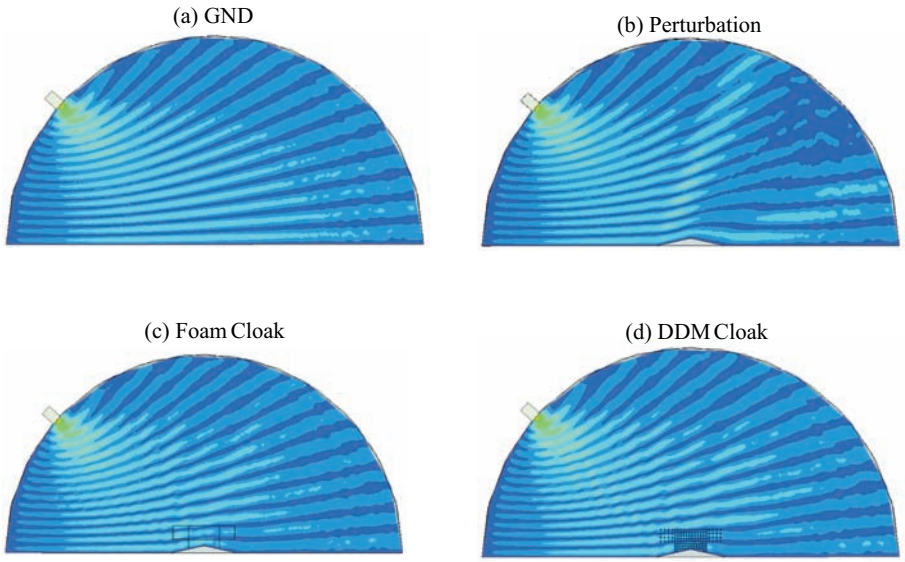


Figure 5: Simulated field distributions of (a) the ground plane (b) the ground with the perturbation (c) foam cloaked perturbation (d) DDM cloaked perturbation.

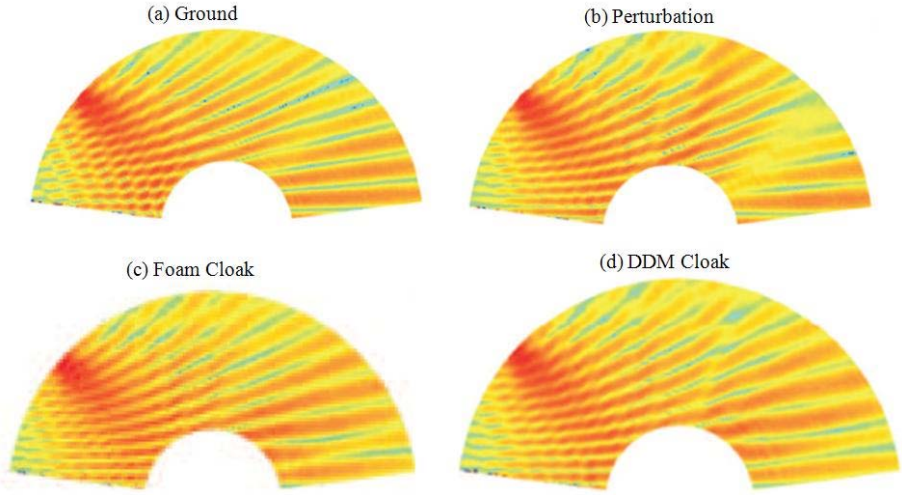


Figure 6: Measured field distributions of (a) the ground plane (b) the ground with the perturbation (c) foam cloaked perturbation (d) DDM cloaked perturbation.

varied period have different effective permittivities. With the dielectric disks discussed in previous section, three layers of dielectric disks are placed around the perturbation along z axis separated by foam with dielectric properties close to that of air, with the period of 5 mm for each layer. The periods in x and y axes are selected to be 8,6,5 mm, corresponding to the effective permittivities of 1.17, 1.30 and 1.46. The photographes of both cloaks are shown in Fig. 4.

4. RESULTS AND DISCUSSIONS

A near-field scanner system is designed and built to test all incident angles performance of the carpet cloaks in X-band as described in [12]. Both simulation and experiment are carried out to test the performance of the two cloaks with the field distribution at 8 GHz shown in Fig. 5 and Fig. 6. The simulation is based on the Finite element method (Ansoft HFSS). The simulated field distribution of ground plane in Fig. 5(a) is in an evenly distributed quasi-standing wave manner. In Fig. 5(b), when the perturbation is place on the ground plane, the scattering leads to at least two separate paths of the reflected waves with one strong shadow in the reflection region. In Fig. 5(c,d), both cloaks work successfully to 'hide' the perturbation by reconstructing the scattered waves: the two separate scattered beams are no longer visible, and the wavefront profile appears very similar to that of the ground plane. The experiment results in Fig. 6 are in good agreement with simulation

results. However, there is still a small gap in the DDM cloak field around about 100 degree. Also, while the foam cloak has been demonstrated to work up to 12 GHz, the DDM cloak can only work up to 9 GHz [13].

5. CONCLUSION

In this paper, two carpet cloaks are designed and tested: the high-ϵ dielectric-loaded foam mixture cloak and the dielectric disk matrix (DDM) with varied periods. The properties of dielectric disk are studies in detailed. Both cloaks are demonstrated to work for all incident angles over a wide range of microwave frequencies. The foam cloak has better bandwidth performance than the DDM cloak.

REFERENCES

1. J. Pendry, D. Schurig, and D. Smith, "Controlling electromagnetic fields," *Science*, vol. 312, no. 5781, p. 1780, 2006.
2. U. Leonhardt, "Optical conformal mapping," *Science*, vol. 312, no. 5781, p. 1777, 2006.
3. D. Schurig, J. J. Mock, B. J. Justice, S. A. Cummer, J. B. Pendry, A. F. Starr, and D. R. Smith, "Metamaterial electromagnetic cloak at microwave frequencies," *Science*, vol. 314, p. 977980, 2006.
4. J. Li and J. Pendry, "Hiding under the carpet: A new strategy for cloaking," *Physical Review Letters*, vol. 101, no. 20, p. 203901, 2008.
5. R. Liu, C. Ji, J. J. Mock, J. Y. Chin, T. J. Cui, and D. R. Smith, "Broadband ground-plane cloak," *Science*, vol. 323, no. 5912, pp. 366–369, 2009.
6. T. Z. G. B. Jason Valentine, Jensen Li and X. Zhang, "An optical cloak made of dielectrics," *Nat. Mater.*, vol. 8, no. 568, 2009.
7. L. Gabrielli, J. Cardenas, C. Poitras, and M. Lipson, "Silicon nanostructure cloak operating at optical frequencies," *Nature Photonics*, vol. 3, no. 8, pp. 461–463, 2009.
8. H. Ma, W. Jiang, X. Yang, X. Zhou, and T. Cui, "Compact-sized and broadband carpet cloak and free-space cloak," *Optics Express*, vol. 17, no. 22, pp. 19 947–19 959, 2009.
9. T. Ergin, N. Stenger, P. Brenner, J. Pendry, and M. Wegener, "Three-dimensional invisibility cloak at optical wavelengths," *Science*, vol. 328, no. 5976, p. 337, 2010.
10. E. Kallos, C. Argyropoulos, and Y. Hao, "Ground-plane quasicloaking for free space," *Phys. Rev. A*, vol. 79, no. 6, p. 63825, 2009.
11. J. Lee, J. Blair, V. Tamma, Q. Wu, S. Rhee, C. Summers, and W. Park, "Direct visualization of optical frequency invisibility cloak based on silicon nanorod array," *Optics Express*, vol. 17, no. 15, pp. 12 922–12 928, 2009.
12. D. Bao, K. Rajab, Y. Hao, E. Kallos, W. Tang, C. Argyropoulos, Y. Piao, and S. Yang, "All-dielectric invisibility cloaks made of batio3-loaded polyurethane foam," *New Journal of Physics*, vol. 13, p. 103023, 2011.
13. D. Bao, W. Tang, C. Argyropoulos, E. Kallos, and Y. Hao, "Experimental verification of carpet cloak realized with dielectric cylinders," in *Antennas and Propagation (APSURSI), 2011 IEEE International Symposium on*. IEEE, 2011, pp. 2861–2864.
14. D. Bao, C. Argyropoulos, E. Kallos, and Y. Hao, "Properties and applications of periodic dielectric particles as tunable-index materials," in *Antennas & Propagation Conference, 2009. LAPC 2009. Loughborough*. IEEE, 2009, pp. 549–552.
15. D. Bao, E. Kallos, W. Tang, C. Argyropoulos, Y. Hao, and T. Cui, "A broadband simplified free space cloak realized by nonmagnetic dielectric cylinders," *Frontiers of Physics in China*, pp. 1–5, 2010.

Comparison of Piezoelectric Switching Shunt Circuits for Vibration Suppression

Yuan-Ping Liu[1,2], Dejan Vasic[1,3,*] and François Costa[1,4]

[1]Lab. SATIE, UniverSud, Ecole Normale Supérieure de Cachan, Cachan, France
[2]Department of Engineering Science and Ocean Engineering, National Taiwan University
[3]Université de Cergy-Pontoise, Neuville/Oise, France
[4]IUFM, Université Paris Est Créteil (UPEC), Place du 8 mai 1945, 93000 St Denis, France
*corresponding author, E-mail: vasic@satie.ens-cachan.fr

Abstract

In past decade, there were several piezoelectric switching shunt techniques proposed for the vibration suppression. The piezoelectric switching shunt techniques were popular recently because they are the semi-active/passive control systems, which can be adaptive to the environmental variation and reduce the power requirement in the active control system. However, the performance of these shunt techniques are not compared in detail yet. The purpose of this paper is to review these switching shunt techniques and to compare the performance and point out their inherent problems.

1. Introduction

One of popular applications of piezoelectric materials is to use the piezoelectric transducer for the structure vibration suppression. In this application, the piezoelectric element is attached on the host structure and a shunt circuit is connected to the piezoelectric elements. The piezoelectric elements convert the vibration energy of the host structure into electrical energy and then the generated electrical energy dissipates in the shunt circuit. In other words, the vibration energy is dissipated in the shunt circuit, so the vibration of the host structure can be suppressed. The piezoelectric shunt techniques mentioned above were widely used due to their simple configurations and compact size. Moreover, it does not require heavy amplification as active vibration control.

Since the piezoelectric element has larger intrinsic capacitor, an impedance matching shunt circuit is required to maximize the generated power. Although the shunt circuit can be optimized by a passive network but it cannot be adaptive to the environmental variation. To overcome this drawback, the switching shunt circuit was proposed and popularly used in recent years. In the switching shunt circuits, the switches are operated synchronously with the vibration of the host structure to optimize the power flow. Moreover, an external voltage supply can be also connected to the piezoelectric material to increase the performance of the vibration suppression.

Several switching shunt circuit topologies and corresponding switching laws were proposed. The two most efficient switching shunt-damping techniques are SSDV (Synchronized Switching Damping on a Voltage source) technique [1] and VSD (Velocity-controlled Switching Damping) technique [2]. In SSDV technique, the switching shunt circuit only turns "ON" at the extreme of the displacement to shift the phase of the voltage across the piezoelectric element. In VSD, the switching shunt circuit turns ON or OFF according to the polarity of the vibration velocity of the host structure. An external voltage source is connected to enlarge the voltage amplitude across the piezoelectric element and to optimize the dissipated power in both shunt circuit techniques. In theory, the vibration can be cancelled totally if the external voltage is set properly in both SSDV and VSD techniques.

Although SSDV and VSD techniques can have good performance, they both require a dynamic voltage source to ensure the stability of the control system. However, it is not easy to implement a fast dynamic voltage source in practice. In addition, a lot of audible re-injected noises may generate in SSDV and VSD systems. To decrease these noises, Lallart et al. proposed the blind switch damping (BSD) technique [3]. The BSD adopts a periodic switching law and modulates the voltage across the piezoelectric element into high frequency. With the modulation, the BSD technique can decrease the re-injected harmonic noise. However, the performance of BSD is related to the carrier switching frequency. Specifically, the BSD has poor damping performance with high switching frequency, so the BSD is difficult to set the switching frequency in the ultrasonic frequency range. Liu et al. applied PWM (pulse width modulation) in the shunt switching law [4]. The PWM shunt technique not only can decrease the audible noises more efficiently but also ensure the stability of the control system with a constant voltage source. However, PWM shunt technique has the problem of switching noises.

There were several innovative piezoelectric switching shunt circuits in past decade, but their performances were not yet compared and discussed. In this paper, the performances, drawbacks and system requirements of tree piezoelectric

switching shunt techniques, shown in figure 1, will be discussed. According to the comparison, we found that the voltage waveform across the piezoelectric element is the key parameter to design the piezoelectric switching shunt circuits. We can optimize the piezoelectric switching shunt circuit based on the piezoelectric voltage.

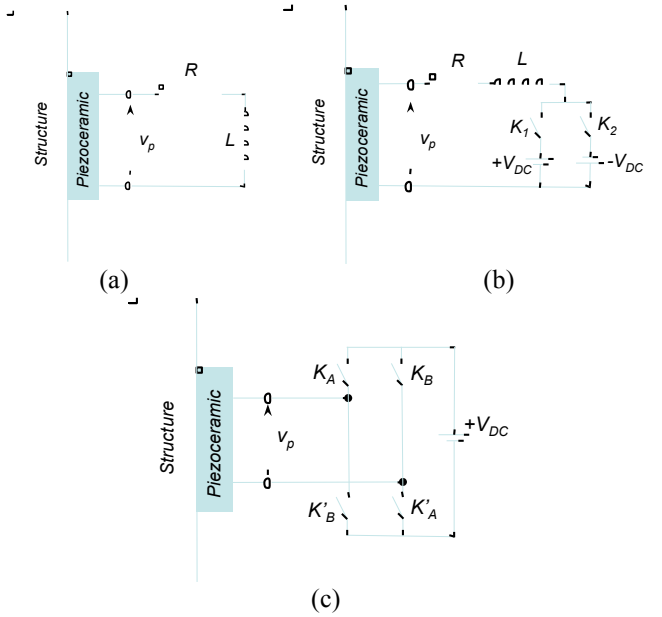


Figure 1: (a) Inductive-resistive shunt (b) SSDV (Synchronized Switching Damping on a Voltage source) (c) VSD (Velocity Controlled Switching Damping).

2. Electromechanical model

The system consists of a piezoelectric patches bounded on a host structure. The governing equation of piezoelectric elements can be represented as equations (1) and (2).

$$F_P = K_P^E u + \alpha v_P \tag{1}$$

$$I = \alpha \dot{u} + C_P \dot{v_P} \tag{2}$$

where F_P is external force exerted on the piezoelectric element, I is outgoing current generated from the piezoelectric element, K_P^E is short circuit stiffness, α is force-voltage coupling factor, C_P is static capacitance of the piezoelectric element and u is displacement of the system.

A mechanical model based on a spring–mass system gives a good description of the vibration behavior near the resonance of the host structure. Therefore, for simplicity, this system can be modeled as a one degree-of-freedom system of a mass M, a spring K and a damper D. According to dynamics equation, the differential governing equation of this electromechanical system can be expressed as equations (3) and (4):

$$M\ddot{u} + D\dot{u} + Ku + \alpha v_P = f \tag{3}$$

$$I = \alpha \dot{u} + C_P \dot{v}_P \tag{4}$$

Equations (3) and (4) are linear equations. However, the semi-active control is a nonlinear control method essentially, and it is not easy to analyze. To make the analysis more intuitive, the work cycle (or energy cycle) is adopted here to analyze the non-linear shunt circuit. The work cycle is the trace on piezoelectric displacement-voltage plane. The observing point of interest is the power generated from the mechanical part. At this point, the average power out of the piezoelectric element in a period can be expressed as:

$$P_r = \frac{1}{T}\int_0^T \alpha\, \dot{u} v_P dt \tag{5}$$

where T represents the period of the vibration, i.e. $T=2\pi/\omega$. Accordingly, the energy flowing out of the piezoelectric in one vibration cycle can be expressed as:

$$E_r = \alpha \int_0^{u(T)} v_P du \tag{6}$$

The integration in equation (6) also stands for the area in the displacement-voltage plane, representing the energy flowing out of the piezoelectric element. The real energy, which flows out of the piezoelectric element, is the key issue in damping design. The energy flows out of the piezoelectric element is larger when the vibrating energy loss in the shunt circuit in each cycle is larger.

On the other hand, the phase difference between the velocity and the piezoelectric voltage is one of the key to design the shunt damping. With phase difference, a portion of the power generated from the piezoelectric elements and flowing into the shunt circuit will flow back to the piezoelectric element. Therefore, the phase difference in the displacement-voltage plane is a key parameter of interest. However, equation (6) has only the information on the real power but no information on the apparent power. To obtain the apparent power P_a, the velocity and the piezoelectric voltage are put in phase:

$$P_a = \frac{1}{T}\int_0^T \alpha\, \dot{u} v_P(t+t_0) dt \tag{7}$$

where t_0 is the time difference between the piezoelectric voltage and the velocity at the fundamental frequency. The area of the work cycle, *i.e.* the corresponding energy form, can be written as:

$$E_r = \alpha \int_0^{u(T)} v_P(t+t_0) du \tag{8}$$

According to the definition of the power factor F_p,

$$F_P = \frac{P_r}{P_a} = \frac{E_r}{E_a} \tag{9}$$

In summary, there are two work cycles in the displacement-voltage plane. One cycle tracks for the real power and the other cycle tracks for the apparent power. The areas of the work cycles represent the corresponding energy flows in one vibration period and the area ratio between the two work cycles represents the power factor.

3. Switching control strategy

The equivalent circuit of the host structure with the shunt circuit can be illustrated in Figure 2. In figure 2, $\dot{u}$ represents the velocity of the host structure at a particular location of the structure, which also can be viewed as the current in the equivalent circuit. The voltage v_p is the

voltage across the piezoelectric element. In this following, v_p is directly named piezoelectric voltage for simplicity.

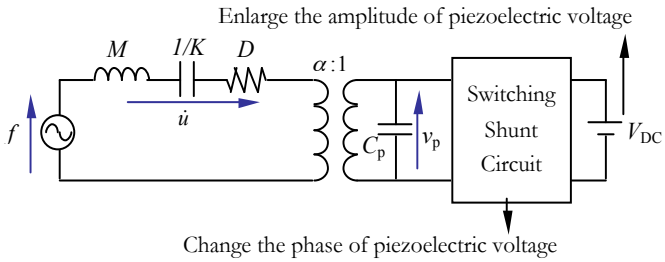


Figure 2: Equivalent electric circuit of the single-mode piezoelectric switching shunt damping technique

The force f comes from the external disturbance and the vibration velocity $\dot{u}$ is a result of the parameter of piezoelectric element and the shunt damping by the way of voltage v_p. The voltage v_p is equivalent to a damping mechanical force. Therefore, the purpose of the switching circuit is to change the waveforms of piezoelectric voltage v_p to enlarge the dissipated energy [5-10]. According to Equation (6), to have the best damping performance, the piezoelectric voltage v_p should be in phase with velocity $\dot{u}$ and the voltage amplitude should be large enough to cancel the vibration as well. The first circuit study here is the passive inductive-resistive technique (figure 1-(a)). It can put in phase velocity $\dot{u}$ and voltage v_p near the resonance of the host structure. The second circuit study is the SSDV technique (figure 1-(b)). It has both characteristics (change phase and increase the voltage), so it can be one of most efficient switching damping technique. The third circuit study is the VSD technique (figure 1-(c)). It can provide a square wave piezoelectric voltage v_p in phase with velocity and high voltage amplitude like SSDV technique (figure 3-(c)). However, the square voltage waveform has large harmonics. These harmonics may leak into structure again to generate the noise. In addition, to keep the stability, the voltage level in piezoelectric voltage required being adaptive to the vibration amplitude. A dynamic DC voltage is typical adopted to control the piezoelectric voltage amplitude to ensure the stability. When the piezoelectric voltage is set too large, the given piezoelectric voltage may excite the vibration of the structure but not dissipate the vibration energy. In such a condition, the velocity $\dot{u}$ is flowing in the opposite direction and the control system enters into an instability state. To ensure the stability, the piezoelectric voltage requires to be set at zero voltage or to be adaptive to the vibration amplitude. Therefore, a dynamic DC voltage was often adopted to control the piezoelectric voltage amplitude.

To overcome the drawbacks mentioned above, we introduce a new damping technique by applying the Pulse Width Modulation (PWM) on the piezoelectric voltage. The proposed damping technique is so called "pulse width modulation damping" (PWMD). The PWM voltage waveform (figure 3-(d)) is a pulse chain with different pulse widths, but the structure is the same than VSD. Similarly as synchronized damping techniques, the PWM voltage follows the phase of the velocity in order to enlarge the dissipated power in the switching circuit as well as to increase the damping effect of the host structure. More specifically, piezoelectric voltage and velocity have equal polarities. Moreover, the pulse widths of the voltage are based on the amplitude of the sampling velocity or absolute value of the displacement. When the sampling velocity is small (large displacement), small pulse width is applied. When the sampling velocity becomes large (small displacement), larger pulse width is applied. Accordingly, the average voltage across the piezoelectric element is adaptive to the velocity and the displacement. As a result, we do not need an adaptive voltage source to ensure the stability, but only a constant voltage source.

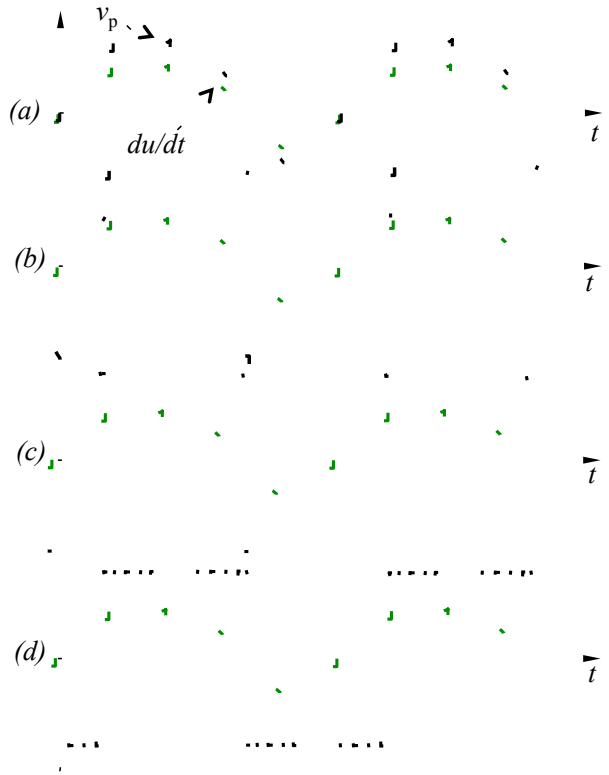


Figure 3: The ideal waveform of v_p and $\dot{u}$: (a) Inductive-resistive shunt (b) SSDV shunt (c) VSD shunt, full wave (d) VSD shunt, PWMD technique

4. Inductive-resistive shunt network

The typical inductive-resistive shunt network shown in Figure 1-(a) is examined by the work cycle and amplitude attenuation. It is known that the inductive-resistive shunt network has good performances only when the LC_p electrical resonant frequency matches with the mechanical resonant frequency of the structure. The calculations for the optimal resistance and inductance in a series resonant shunt are well known and will only be briefly presented here for completeness. For resonant shunt vibration control, the resistor and the inductor in the shunt circuit must be tuned to achieve maximum energy dissipation from the mode of interest. Therefore, the optimal resistance and inductance for a series resonant shunt circuit can be calculated by:

$$R_{opt} = \frac{1}{(C_P\omega)^2\alpha^2 D} \quad (10)$$

$$L_{opt} = \frac{1}{C_P\omega^2} \quad (11)$$

When the mechanical and electrical resonant frequencies are mismatch, the work cycles are shown in Figure 4. We can see that the power factor in this case is poor. However, when the mechanical frequency and the electrical resonant frequency are close to each other, the area of the apparent work cycle and the real work cycle are almost equal (Figure 5). Specifically, good power factor leads to good performances, this is due to the power does not flow back to the piezoelectric element. Typical inductive-resistive shunt network uses the inductor to compensate the contribution of the piezoelectric intrinsic capacitance, but only at the resonant frequency. This is the underlying reason why the inductive-resistive shunt network only has good performances with small bandwidth. Most importantly, the work cycle observation is really an effective way to examine the damping performances.

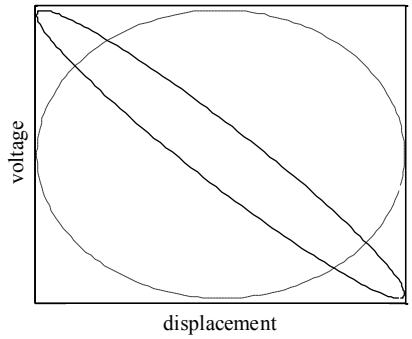


Figure 4: The work cycle of the inductive-resistive shunt network: the resonant frequencies mismatches

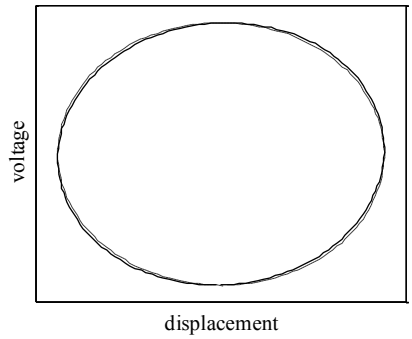


Figure 5: The work cycle of the inductive-resistive shunt network: the resonant frequencies matches

There are three conclusions that we can get from the work cycles observation to evaluate the performances of a damping circuit.

1. The optimum damping situation corresponding to the area ratio of two work cycles is equal to 1, and the corresponding power factor should also be 1.
2. In the whole controllable bandwidth, the power factor should be always equal to 1.
3. The maximum power transfer out of the piezoelectric element can be described as maximum area of the real work cycle, which is actually rectangular shape in the charge-voltage plane in the case of same external voltage.

Analytic calculation of the displacement amplitude at resonance can be made from previously expressed equations, assuming that the mechanical displacement u and the excitation force f are purely sinusoidal.

First, for reference we establish the maximum displacement in the case of short circuit state, *i.e.* $v_p = 0$. Substituting equations (4) into equation (3), the dynamic of the structure can be expressed in frequency domain:

$$\left.\frac{u}{f}\right|_{sh} = \frac{1}{K - M\omega^2 + jD\omega} \quad (12)$$

$$\omega_r^{sh} = \sqrt{\frac{K}{M}} \quad (13)$$

$$u_{max}^{sh} = \frac{F_M}{D\omega} \quad (14)$$

where ω_r is the resonant angular frequency. F_M and u_{max} represent the maximum amplitude of the external force and the maximum amplitude of the displacement at resonant frequency respectively. Superscript "*sh*" represents the short circuit state.

The expression of the mechanical displacement u_{max} for the inductive-resistive technique as a function of force amplitude F_M and circuit parameters:

$$u_{max}^{LR} = \frac{F_M}{\omega\sqrt{(2D)^2 + \left(\frac{1}{\alpha^2 C_P\omega}\right)^2}} \quad (15)$$

The expression of the vibration attenuation A (dB) at the resonance frequency when the damping system is turned on is given in Equations (14) and (15).

$$A_{LR} = 20log_{10}\frac{D}{\sqrt{(2D)^2 + \left(\frac{1}{\alpha^2 C_P\omega}\right)^2}} \quad (16)$$

5. SSDV technique

The electrical circuit of the semi-passive damping technique called SSDV (Synchronized Switching Damping on a Voltage source) is represented in Figure 1-(b). The difference between this circuit and the previously is that the piezoelectric element is now switched on a positive or a negative voltage source across the *LR* shunt circuit. It has been shown that the dissipated energy depends on the voltage amplitude across the piezoelectric elements. The role of these additional constant voltage sources, having respectively a $+V_{DC}$ and a $-V_{DC}$ value, is to increase the voltage amplitude of v_P and thus to increase the damping effect. The switch K_1 is turned ON when a maximum of displacement u occurs and the voltage v_p starts to oscillate, until K_1 is turned OFF. The switching ON period is equal to a half of the resonant period of the LC_P circuit. Assuming that the electrical resonant period is very small compared to the mechanical vibration period, the voltage v_P can make the inversion in this short period. The same function can be obtained by turning switch K_2 ON at the minimum displacement. Theoretical waveforms of the velocity $\dot{u}$ and

the voltage v_P are presented in Figure 3-(b). The amplitude of the voltage v_P is limited by the loss of energy during the inversion process. The work cycle is shown in figure 6. The expression of the maximum of piezoelectric voltage V_{P1} and V_{P2} is given in [1].

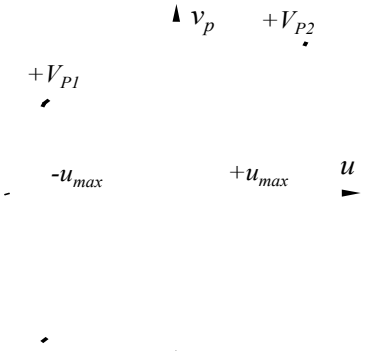


Figure 6: The work cycle of the SSDV technique

Analytic calculation of the displacement amplitude at resonance can be made from previously expressed equations. The expression of the mechanical displacement u_{max} as a function of force amplitude F_M, voltage sources parameter V_{DC} and the quality factor of the resonant circuit Q_I is given in Equation (17),

$$u_{max}^{SSDV} = \frac{\pi F_M\left(1-e^{-\pi/2Q_i}\right)-4\alpha V_{DC}\left(1+e^{-\pi/2Q_i}\right)}{\pi D\omega\left(1-e^{-\pi/2Q_i}\right)+\left(4\alpha^2/C_P\right)\left(1+e^{-\pi/2Q_i}\right)} \quad (17)$$

The expression of the vibration attenuation A (dB) at the resonance frequency can obtain by comparing with Equations (14) and (17).

$$A_{SSDV} = 20log_{10}\left(\frac{\left(1-e^{-\pi/2Q_i}\right)-(4/\pi)(\alpha V_{DC}/F_M)\left(1+e^{-\pi/2Q_i}\right)}{\left(1-e^{-\pi/2Q_i}\right)+(4/\pi)(\alpha^2/C_P D\omega)\left(1+e^{-\pi/2Q_i}\right)}\right) \quad (18)$$

According to equation (18), it can be noticed that the vibration is possibly cancelled out totally if the DC sink V_{DC} is set properly. However, when the V_{DC} is set too large, equation (18) is no longer correct. The limitation of the DC sink voltage is:

$$V_{DC} \leq \frac{\pi}{4\alpha} F_M \frac{\left(1-e^{-\pi/2Q_i}\right)}{\left(1+e^{-\pi/2Q_i}\right)} \quad (19)$$

6. VSD technique

The switching circuit of the VSD system is shown in Figure 1-(c) and Figure 7. To put the velocity $\dot{u}$ and the piezoelectric voltage v_p in phase, four switches are used to control the phase of the piezoelectric output voltage. When the velocity is positive, the switches K_A and K'_A are ON and the switches K_B and K'_B are OFF. The piezoelectric voltage is thus positive in this stage. When the velocity is negative, the switches K_B and K'_B are ON and the switches K_A and K'_A are OFF. The piezoelectric voltage is thus negative in this stage. Accordingly, the velocity and the piezoelectric voltage become in phase. The ideal waveforms are shown in Figure 3-(c). It should be noted that this methodology is not only for the specific frequency but working for a wide frequency range. Actually, the wider bandwidth is the key advantage of the semi-active control compared to the passive shunt circuit.

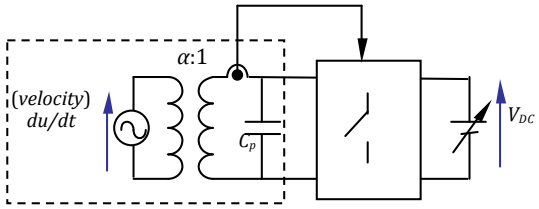


Figure 7: The basic thinking of the velocity-controlled switching damping

On the other hand, according to the operation law of the VSD, the switching period of the VSD is the vibration period. The VSD have a large switching period, this fact implies that the VSD can use smaller speed switch or use in the higher frequency range compared to SSDV. The bandwidth of the VSD is mainly depended on the sensing observability of the sensor and the sensing signal conditioner themselves. In practice, we can get the phase of the mechanical current by detecting: 1) zero-crossing of the velocity or 2) the local extreme displacement. However, the velocity is the derivative of the displacement, the high frequency noise easily leak into the system in the velocity signal.

The VSD technique can fit all requirements for good performances of a damping system. The ideal work cycle of the VSD technique is shown in Figure 8. The work cycle is rectangular because of the waveforms of the velocity and the voltage are sinusoidal and square respectively. The rectangular work cycle will have the maximum area under the same physical limitations. Furthermore, the power factor of the VSD is equal to 1 in all observable frequencies due to the piezoelectric voltage always follow the phase of the velocity. The work cycles of the apparent power and the real power are both rectangular and overlapping well even though the frequency may vary. In other words, the VSD system has the optimal energy cycle, and is the best semi-active damping method. From the viewpoint of power electronics, VSD is actually a power factor correction circuit to force the power factor to be one.

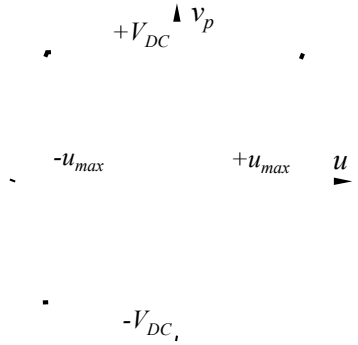


Figure 8: The work cycle of the SSDV technique

For the analytic calculation of the amplitude attenuation, first, we establish the expression of the piezoelectric voltage, which is determined by the switching. More specifically, the piezoelectric voltage is closed to squared waveform and the

amplitude is based on the connected DC voltage. According to Fourier theory, the first harmonic of the waveform in VSD is:

$$v_P = \frac{4}{\pi} V_{DC} \sin(\pi d)\, signe(\dot{u}) e^{j\omega t} \quad (20)$$

where d is the duty cycle of the VSD switches. In the ideal case, $d = 0.5$. However, in practice, to avoid the short circuit of the switch in the switching transition, it exists a very short period that the four switches are turned off, which is called dead time. The ideally duty cycle of 0.5 is impossible in practice and thus we introduced it here as a parameter. It should be noted that the piezoelectric voltage follows the velocity, so the term $\boldsymbol{signe(\dot{u})}$ is added in equation (20). Substituting equation (20) into equation (3) and writing it in the frequency domain leads:

$$(K - M\omega^2)u + jD\omega u = f - j\alpha \frac{4}{\pi} V_{DC} \sin(\pi d) \quad (21)$$

At resonant frequency, the maximum amplitude of displacement of VSD is:

$$u_{max}^{VSD} = \frac{F_M - \alpha \frac{4}{\pi} V_{DC} \sin(\pi d)}{D\omega} \quad (22)$$

where superscript "*VSD*" represents that the piezoelectric element connects to the VSD circuit. Compared with equations (14), the theoretical attenuation of the displacement can be obtained:

$$A_{VSD} = 20log_{10}\left(1 - \alpha \frac{4}{\pi} \frac{V_{DC}}{F_M} \sin(\pi d)\right) \quad (23)$$

According to equation (23), it can be noticed that the vibration is possibly cancelled out totally if the DC sink V_{DC} is set properly. However, when the V_{DC} is set too large, equation (23) is no longer correct. The limitation of the DC sink voltage is:

$$V_{DC} \leq \frac{\pi}{4\alpha} \frac{F_M}{\sin(\pi d)} \quad (24)$$

Under this maximum DC voltage limitation, the DC voltage works like a sink to dissipate the energy. However, once the DC voltage is set above the maximum value, it works like a source. The voltage source will excite the vibration of the structure. In other words, the piezoelectric element becomes an actuator but no longer a damper.

7. PWMD technique

To overcome the drawbacks of the VSD and SSDV techniques (high frequency excitation and audible noise), we introduce a new damping technique by applying the pulse width modulation (PWM) technique on the piezoelectric voltage. In this technique, the average voltage across the piezoelectric element is adaptive to the velocity and the displacement. As a result, we do not need an adaptive voltage source to ensure the stability, but only a constant voltage source.

In addition, the PWM signal has fewer harmonics compared to the square signal. Figure 9 illustrates the theoretical spectrums of square signal and PWM signal. In the square signal, there are several harmonics closed to the fundamental frequency. However, in PWM signal, the harmonic next to the fundamental frequency is the switching frequency, *i.e.* the fundamental frequency of the pulse signal. As long as the switching frequency is set high enough, the PWM signal can decrease the harmonics contents in the square signal effectively. This characteristic leads that the PWM piezoelectric voltage can improve the re-injected noise in the host structure. If the switching frequency is set in an ultrasonic frequency range, we can even eliminate most audible noises. It should be mentioned that the PWM signal can be easily demodulated by a low-pass filter, but it is not necessary to reconstruct the modulating signal in the damping application. The most important is that the piezoelectric voltage and the velocity should have equal polarity. The host structure can be a low-pass filter itself. However, we can still add an inductor between the switching circuit and the host structure to filter out the switching noises, but the inductor may introduce the extra phase delay to influence the control performance. On the other hands, in figure 9, PWM signal has smaller fundamental component because the PWM signal has zero voltage in some switching periods. The PWMD requires higher DC voltage to have equal damping performance as the square-voltage based switching shunt circuit.

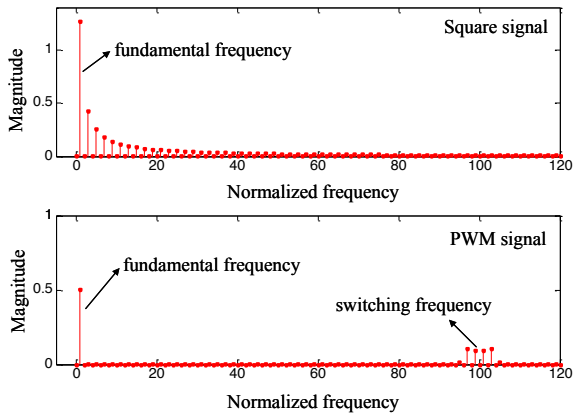


Figure 9: Spectrums of square signal and proposed PWM signal.

In practice, PWM technique is typical based on comparison between a modulating signal (at low frequency) and a triangle carrier (at high frequency). A sinusoidal modulating signal S and a triangle wave T are shown in figure 10-(a) and their resulting signal A after comparison is shown in figure 10-(b). Signal A is a two-level PWM signal (0 and 1), which is different from the voltage waveform in figure 3-(d) (three levels: -1, 0 and 1). To accomplish a three-level PWM signal, the circuit presented in figure 11 is adopted [11]. Except signal A, the inverse modulating signal ($-S$) is compared with triangle signal T to get signal B shown in figure 10-(c). Then, the differential signal between signals A and B, *i.e.* (A-B), is the three levels PWM signal of interest (Figure 10-(d)). In figure 1-(c), the left leg of the full-bridge switches is controlled by signal A and the right leg of the full-bridge switches is controlled by signal B. Then, a constant voltage source V_{DC} is connected after the full-

bridge switching circuit. As a result, piezoelectric voltage v_p can be a PWM signal and its amplitude is V_{DC}. It should be noted that the switching frequency f_{sw} is twice the carrier triangle frequency f_c, *i.e.* f_{sw} =2f_c [11]. Therefore, to cancel out the re-injected audible noise, we can set the carrier frequency above 10 kHz to obtain ultrasonic switching frequency (>20 kHz).

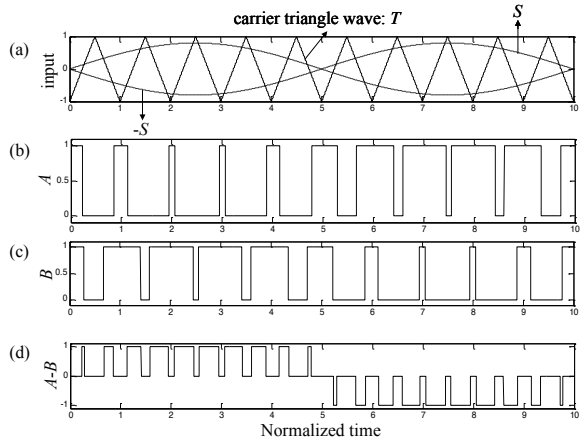


Figure 10: Signal processing of three-level PWM signal.

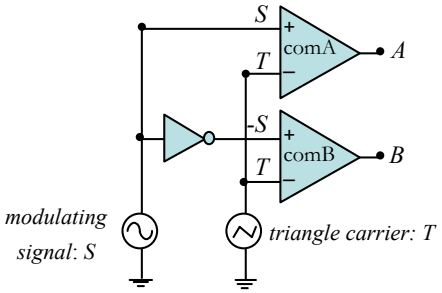


Figure 11: Implementation of three-level PWM signal.

For the analytic calculation of the amplitude attenuation of the PWMD technique, we consider the first harmonic of PWM signal. The fundamental harmonic of voltage v_p can be expressed as [13]:

$$v_P = \beta V_{DC} signe(\dot{u}) e^{j\omega t} \tag{25}$$

where the function $\boldsymbol{signe}(\dot{\boldsymbol{u}})$ implies that the piezoelectric voltage follows the phase of velocity and β is the modulation index, which represents the amplitude ratio between the sensing signal and the carrier signal, *i.e.*

$$\beta = \frac{\kappa u_{max}}{V_C} \tag{26}$$

where V_c , κ and u_{max} are the amplitudes of carrier signal, sensor gain and the amplitude of the displacement. Equation (26) implies that the piezoelectric voltage is adaptive to the displacement. In other words, the pulse width variation in PWM signal can be equivalent to an adaptive voltage. As a result, there is no requirement about the external dynamic voltage source in the PWMD technique and the loop can be stable with a constant voltage source. This is one of most important advantage about PWMD technique.

Substituting equation (25) and equation (26) into equation (3) and transforming it into frequency domains in steady state. The steady-state displacement u_{max} controlled by PWMD can be obtained:

$$u_{max}^{PWMD} = \frac{F_M}{\sqrt{(K-M\omega^2)^2+\left(D\omega+\frac{\alpha\kappa}{V_C}V_{DC}\right)^2}} \tag{27}$$

According to equation (27), the displacement decreases with increasing voltage. The displacement becomes very small as the voltage V_{DC} approach infinite, but never achieves zero or negative value. This characteristic is different from the other switching shunt circuits with an external constant voltage. For example, the resulting displacement in the typical SSDV is negative value in theory with infinite external voltage. A negative displacement means that the host structure is excited again after the vibration suppression. It also means the control system enters into an instability state. In other words, equation (27) proves that the PWMD control system is possible to stay in the stable region with a constant voltage.

Therefore, the theoretical attenuation of the displacement at resonance frequency can be derived from equations (27) and the short circuit reference (14):

$$A_{PWMD} = 20log_{10}\left(\frac{D\omega}{D\omega+\frac{\alpha\kappa}{V_C}V_{DC}}\right) \tag{28}$$

It should be noticed that the expression within the logarithmic expression of equation (28) must be positive. This fact implies that the PWMD system never enters into the instability state. When the sensor gain or DC voltage is zero, there is no attenuation. As the V_{DC} is approaching infinite, the attenuation is infinite and the displacement can be cancelled totally in theory.

8. Experimental results

The experimental structure is a cantilever steel beam with two 31-type PZT layers, which is shown in figure 12. The dimensions of the beam and the piezoelectric element are shown in table 1 and the experimental setup is shown in figure 13. The beam was excited at the fixed end by an electromagnetic shaker. A CCD laser displacement sensor (Keyence LK-G32) was set to measure the displacement at 16 mm from the free end of the beam. The laser displacement sensor was connected to the sensing interface circuit to get the velocity signal. Then, by the logic circuit proposed in figure 11, the velocity signal was compared with a bipolar linear triangle signal generated from the functional generator to obtain the PWM driving signals for the four switches. The switching shunt circuit was made by two IR2104 gate drivers and four IRF840 MOSFETs.

The model identification has followed the method proposed in [12]. Table 2 arranges the model parameters obtained by the measurements near the first resonance directly. These measured data were calculated to obtain the other parameters of the model given in table 3. The detailed

relationships between the measured data and the corresponding model parameters are arranged in the last column of table 3.



Figure 12: Experimental beam structure.

Table 1. The piezoelectric layer and Steel Beam.

	steel beam	piezoelectric element
length	189mm	38mm
width	34.8mm	16mm*2 layers
thickness	0.8mm	0.5mm
location	None	29 mm from fixed end

Table 2. Model parameters obtained by measurement.

	values	definitions
κ/V_c	1000 V^{-1}	the ratio between sensor gain and triangle voltage
f_{short}	16.37 Hz	short-circuit resonant frequency
f_{open}	16.4 Hz	open-circuit resonant frequency
ζ	0.0105	open-circuit mechanical damping coefficient
C_p	45 nF	piezoelectric inherent capacitance
λ	1220 Vm^{-1}	The ratio between the measured displacement and open circuit voltage

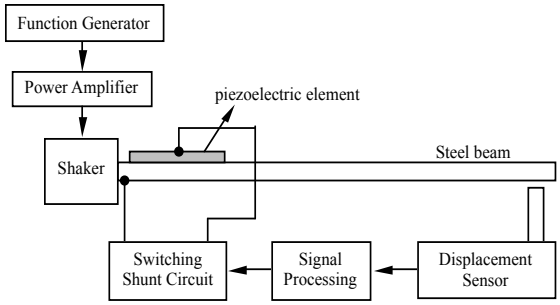


Figure 13: Experimental setup.

Table 3. Model parameters calculated by measured data

	values	definitions
k^2	0.0037	$k^2 = \frac{f_{open}^2 - f_{short}^2}{f_{short}^2}$
α	0.0000549 NV^{-1}	$\alpha = \lambda C_P$
K	18.29 Nm^{-1}	$K = \frac{n\lambda}{k^2}$
M	0.0017 kg	$M = \frac{K}{4\pi^2 f_{short}^2}$
D	0.004 $Nm^{-1}s^{-1}$	$D = 4\pi\zeta M f_{open}$

8.1. VSD technique

The beam is driven around the first resonant frequency. The DC voltages of the VSD testing system were set at 0V, 3V, 6V, 9V and 12V. The last DC voltage was set at 12V because the experimental maximum voltage is around 12.5V. Once the DC voltage was set exceeding 12.5V, the VSD system enters into unstable state. The displacement amplitude rises again after the maximum voltage reached. The experimental frequency responses are shown in figure 14. It can be seen that when the voltage increases, the attenuation increases as well. The displacement can be cancelled effectively in the case of 12V DC voltage sink from 2.18mm to 0.16mm at 16.4Hz. The residual displacement at resonant frequency is closed to the vibration in the non-resonant state, which is similar to the SSDV technique.

Furthermore, according to equation (23) and model parameters in table 3, the attenuation of the vibration at short-circuit resonant frequency was calculated and plotted in figure 15. In this figure, the experimental points match the theoretical curve well. The minimum point of attenuation in figure 15 represents the zero displacement and the corresponding DC voltage represents the stability limit. The DC voltage limit is around 12.5V in our experiment and the theoretical value is 12.8V in our theoretical model.

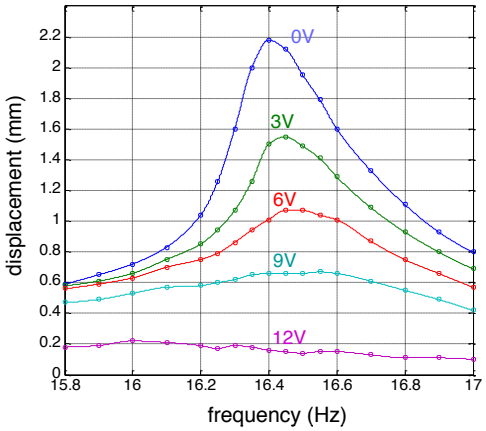


Figure 14: The frequency response the VSD system.

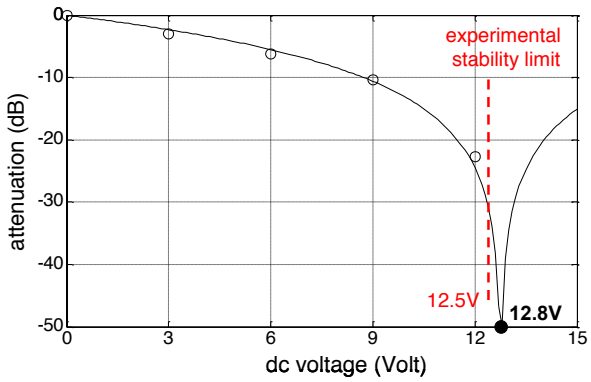


Figure 15: The experimental results (points) and the theoretical prediction (line) of the maximum DC voltage.

8.2. PWMD technique

With the same testing beam, we implement now the PWMD technique. The beam was driven near the first resonant frequency. Triangle carrier frequency was set at 20 kHz. The experimental waveforms of the PWMD are shown in figure 16. Compared to the ideal waveform in figure 3-(d), there were some switching noises. These switching noises came from the switching action on the piezoelectric inherent capacitance and led the electromagnetic interference (EMI). Specifically, the switching noise influenced electronic signals by the electromagnetic radiation, so we can see the noises in the displacement and the velocity.

The DC voltages V_{DC} were set at 0V (short circuit), 10V, 20V and 30V to observe the frequency response of the host structure. The experimental frequency responses are shown in figure 17. It can be seen that the displacement decrease with the increasing voltage. The displacement can be cancelled effectively in the case of 30V DC voltage sink from 1.95 mm to 0.38 mm at 16.35 Hz (-14dB). The residual displacement at resonance frequency is close to the vibration in the non-resonant state, which is similar to the SSDV technique or VSD technique.

We varied the external DC voltage to test the stability of the control system at small displacements. First, we applied $V_{DC} = 60$ V on our PZT patches. The system could keep stable, but the EMI noise became larger. When we applied $V_{DC} = 90$ V on our PZT patches. The system still stayed in stable state, but the amplitude of the EMI noise became larger than the resulting displacement in the measurement. In fact, too large EMI noises in the measured velocity caused the comparators could not output correct switching signals and thus the shunt circuit could not switch at the correct points. Consequently, the maximum piezoelectric voltage was determined by the EMI noise in our experiment. Next, we stopped the vibration directly to check the stability again. Similarly as the steady state testing, the beam structure connected the PWMD circuit with different external DC voltage values. Considering time response, when the vibration became smaller gradually, the host structure could stop at zero displacement with different DC voltage values. In such a condition, the typical SSDV may enter into the instable state. The displacement excited by the external voltage again in SSDV when the displacement is too small. This testing is to ensure that the PWMD control system can stay in the stable state in general.

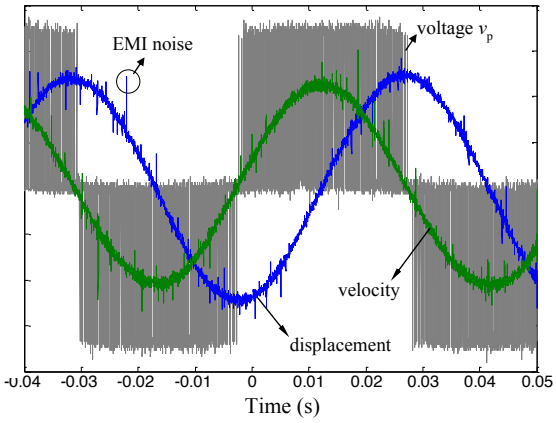


Figure 16: PWMD, experimental waveforms.

On the other hand, we varied the carrier frequencies (2 kHz, 10 kHz and 20 kHz) with a constant voltage $V_{DC} = 10$ V to see the relationship between the performance and the carrier frequencies. The damping performance was independent of the carrier frequencies at a constant voltage. Moreover, in our experiment, we could hear a lot of audible noise at 2 kHz carrier frequency (4 kHz switching frequency), but the host beam was silent at 10 kHz and 20 kHz carrier frequencies. This result implied that we could set the switching frequency above audible vibration modes to reject the acoustic noise into the structure effectively. In practice, the carrier frequency bandwidth is mainly limited by two factors. Firstly, a higher switching speed induces a larger switching noise. It was mentioned that the switching noise might cause the PWMD circuit works incorrectly. Therefore, the switching frequency should be sufficiently low to limit the electromagnetic perturbations as result of the switching noise. On the other hand, the carrier frequency must be much larger than the controlled resonance frequency of the structure to avoid the inter-modulation. Most importantly, the PWMD can set the carrier frequency above 10 kHz (the switching frequency is 20 kHz) to reject the audible noise and to suppress the vibration simultaneously.

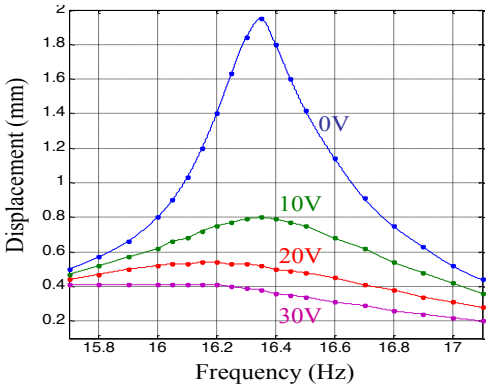


Figure 17: PWMD, Experimental frequency response.

9. Conclusions

This paper compared two novel piezoelectric damping techniques (VSD and PWMD) to the traditional resonant shunt damping technique and SSDV technique. First, the expressions of the vibration attenuation A (dB) at the resonance frequency for each technique were derived. Then, in the SSDV and VSD techniques, it was noticed that the vibration is possibly cancelled out totally if the DC sink V_{DC} is set correctly. However, when the V_{DC} is set too large, the DC link works like a source. The voltage source will excite the vibration of the structure. In other words, the piezoelectric element becomes an actuator but no longer a damper. This is a drawback of these techniques. To overcome the drawbacks of the VSD and SSDV techniques (high frequency excitation and audible noise), we propose a new damping technique by applying the pulse width modulation (PWM) technique on the piezoelectric voltage. In PWMD technique, the piezoelectric voltage has two significant characteristics. First, the piezoelectric voltage is modulated in a high frequency range to obtain a smooth spectrum between the carrier frequency and the modulating frequency, so the PWMD can reject the acoustic harmonic noises. Secondly, the piezoelectric voltage is adaptive to the vibration displacement by the pulse widths variation, so the PWMD can stay in stable state with a constant voltage source. Most importantly, the PWMD can still provide a very good performance with these advantages. The control strategy and corresponding switching circuit were implemented. We observed some limitations of the PWMD experimentally. First, although the applied voltage decreases the vibration displacement, but larger piezoelectric voltage also generated larger EMI noises. Secondly, the carrier frequency was limited by the inter-modulation at low frequency and by the EMI noises at high frequency.

Acknowledgements

The authors are grateful to Eleceram Technology Co., Ltd and for providing us with different types of piezoelectric layers used in the research work. The funding of this project, from ANR (Agence Nationale de la Recherche), France under EVA project, is gratefully acknowledged. Funding from National Science Council, Taiwan under project NSC 100-2917-I-564-020 is also gratefully acknowledged.

References

1. Lefeuvre E., Badel A., Petit, L, Richard C. and Guyomar D. “Semi-passive piezoelectric structural damping by synchronized switching on voltage sources,” *Journal of Intelligent Material Systems and Structures*, Vol. 17, pp. 653-660, 2006
2. Liu Y. P., Vasic D., Costa F., Wu W. J. and Lee C. K., “Velocity-controlled Switching Piezoelectric Damping Based on Maximum Power Factor Tracking and Work Cycle Observation,” *Presented at ICAST 2008*, No. 40, Ascona, Switzerland, October 6-9, 2008.
3. Lallart M., Harari S., Petit L., Guyomar D., Richard T., Richard C. and Gaudiller L., “Blind switch damping (BSD): A self-adaptive semi-active damping technique,” *Journal of Sound and vibration*, Vol. 328, pp. 29-41, 2009.
4. Liu Y. P., Vasic D. and Costa F., “Piezoelectric Structural Damping based on the Pulse Width Modulation Switching Circuit”, *Presented at ICAST 2011*, No. 48, Corfu, Greece, October 10-12, 2011.
5. Richard C, Guyomar D, Audigier D and Ching G 1999 Semi-passive damping using continuous switching of a piezoelectric device *Smart Structures and Materials 1999: Conf.*; *Proc. SPIE* **3989** 288-99
6. Hagood N W and von Flotow A 1991 Damping of Structural Vibrations with Piezoelectric Materials and Passive Electrical Networks *Journal of Sound and Vibration* **146** 243-68
7. David C L and Lesieutre G A 2000 An Actively Tuned Solid-State Vibration Absorber Using Capacitive Shunting of Piezoelectric Stiffness *Journal of Sound and vibration* **232** 601-17
8. Clark W W 2000 Vibration control with state-switched piezoelectric materials *Journal of Intelligent Material Systems and Structures* **11** 263-71
9. Cunefare K A, De Rosa S, Sadegh N and Larson G 2000 State-switched absorber for semi-active structural control *Journal of Intelligent Material Systems and Structures* **11** 300-10.
10. Richard C, Guyomar D, Audigier D and Bassaler H 2000 Enhanced semi-passive damping using continuous switching of a piezoelectric device on an inductor *Conf.*; *Proc. SPIE* **3989** 288-99
11. Anderskouv N, Nielsen K and Andersen M High-Fidelity 1996 Pulse-Width Modulation Amplifiers Based on Novel Double-Loop Feedback Techniques *Presented at the 100th AES convention* 4258
12. Lefeuvre E, Badel A, Richard C and Guyomar D 2005 Piezoelectric energy harvesting device optimization by synchronous electric charge extraction *Journal of Intelligent Material Systems and Structures* **16** 865-76

Electromagnetic controllable surfaces based on trapped-mode effect

V. Dmitriev[1], S. Prosvirnin[2,3], V. Tuz[2,3], and M. N. Kawakatsu[1*]

[1]Department of Electrical Engineering, Federal University of Para, Belem, Para, Brazil
[2,3]Institute of Radioastronomy of National Academy of Sciences of Ukraine
[2,3]School of Radio Physics, Karazin Kharkiv National University, Ukraine
*corresponding author, E-mail: mnkawakatsu@yahoo.com.br

Abstract

In this report we present some recent results of our theoretical investigations of electromagnetically controllable surfaces designed on the basis of periodic arrays made of metallic inclusions of special form which are placed on a thin substrate of active material (magnetized ferrite or optically active semiconductor). The main peculiarity of the studied structures is their capability to support the trapped-mode resonance which is a result of the antiphase current oscillations in the elements of a periodic cell. Several effects, namely: tuning the position of passband and the linear and nonlinear (bistable) transmission switching are considered when an external static magnetic field or optical excitation are applied. Our numerical calculations are fulfilled in both microwave and optical regions.

1. Introduction

The development of smart materials in microwave and optic regions can be realized by involving the plasmonic and metamaterial technologies. Here the promising way is to combine known optically active materials with special artificial inclusions which are the key elements of the metamaterial constructions [1,2,3,4]. As an example, the metamaterial array can be placed on the magnetic (ferrite, antiferromagnetic) or semiconductor substrate. In this case the tuning of optical properties can be realized with using an external static magnetic field (ESMF). Also the conception of controlling the light propagation with light which is based on the nonlinear effect of optical bistability or multistability can be employed in the optical band. The devices based on these principles can have numerous applications in optical switching, differential amplification, optical transistor, power limiting, pulse shaping, and optical digital data processing functions.

The goal of this report is to present the peculiarity of linear and nonlinear optical switching in a planar metamaterial which bears the trapped-mode resonances. For this reason we consider a planar metamaterial made of an array of double-ring (DR) elements placed on a thin magnetic or semiconductor substrate (Fig. 1). Such configuration is chosen to construct the metamaterial due to the fact that DR elements are polarization insensitive at the normal incidence of the exciting wave which can enlarges the area of potential applications.

Thus, we demonstrate that by using a magnetized ferrite substrate in this array it is possible to tune the trapped-mode frequency with external magnetic field. Our calculations show that in the microwave region, as the ESMF is applied, the shift can reach about 20% of the resonant frequency. The orientation of ESMF can be different, namely normal to the plane (Faraday geometry) of the substrate or in-plane (Voigt geometry). Note that in the latter case the system becomes polarization dependent.

Switching of the transmission band with the ESMF can be achieved in the array placed on a magnetized ferrite substrate in the case when the frequency of the trapped-mode resonance is tuned nearly the frequency of the ferromagnetic resonance. We show that for the magnetization applied in the Faraday geometry, a good electromagnetic switching can be realized.

Another possibility of controlling electromagnetic radiation is to use a semiconductor substrate. We show the possibility to almost completely switch off the array transmission band by optically activating its silicon substrate. For low plasma density no effect is produced on the array responses, however, increasing it above a certain value the structure becomes almost totally reflective as a consequence of the significant increase of the real and imaginary parts of the refraction index.

Still another possibility of controlling the electromagnetic wave propagation is based on the effect of optical bistability. Typically the devices realized on the optical bistability principle consist of a resonant cavity containing a material which refraction index or/and absorption coefficient are depended on the field intensity of incident light. A perspective way to reduce the size of these devices and the input field intensity required for optical bistable switching lies in using planar metamaterials which can support the trapped-mode resonances.

The strong field confinement and nonlinear effects enhancement is achieved in the investigated arrays placed on a nonlinear substrate made of an antiferromagnetic film. The system is considered to be under ESMF applied in the Faraday geometry. In the structures of such kind it is possible to obtain the sufficient field localization in the thin nonlinear substrate which leads to the realization of all-

optical switching. In particular we show that the switching can be achieved between different levels of transmission nearly the frequency of the trapped-mode excitation.

2. Problem statement

The square unit cell ($d = d_x = d_y$) of the structure under study consists of one double-ring (DR) (Fig. 1). The radii of the outer and inner rings are a_1 and a_2, respectively. The width of both the metal rings is $2w$. The array is placed on a dielectric substrate with thickness h.

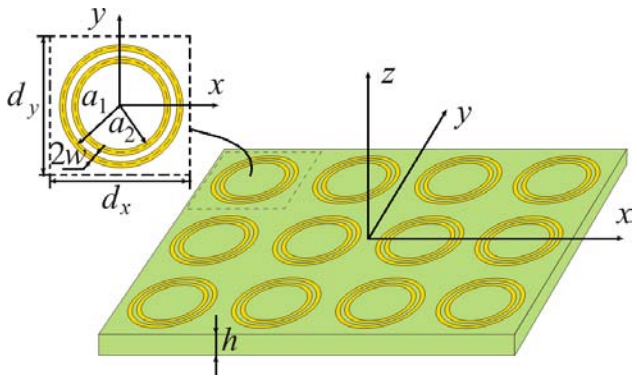


Figure 1. Array of two concentric metal rings on a substrate made of active material.

As the excitation field a normally incident linearly polarized plane monochromatic wave of frequency ω and amplitude A is selected.

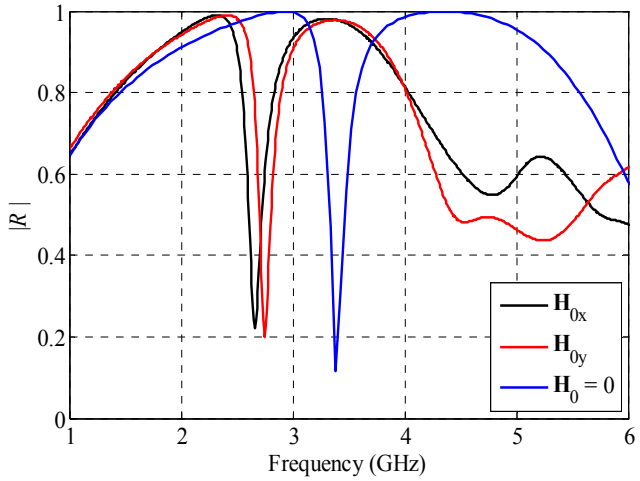
To provide the numerical calculations we use both our own algorithms and software, and commercial one. The first technique is based on the Method of Moments [5,6]. It involves solving an integral equation for surface currents induced in the metallic pattern by the incident electromagnetic wave and calculating the scattered fields produced by currents as a superposition of partial spatial waves. The Method of Moment is paired with a special algorithm which allows solving the nonlinear problem [2,3]. As commercial software we use Computer Simulation Technology (CST) Studio [7].

3. Numerical results

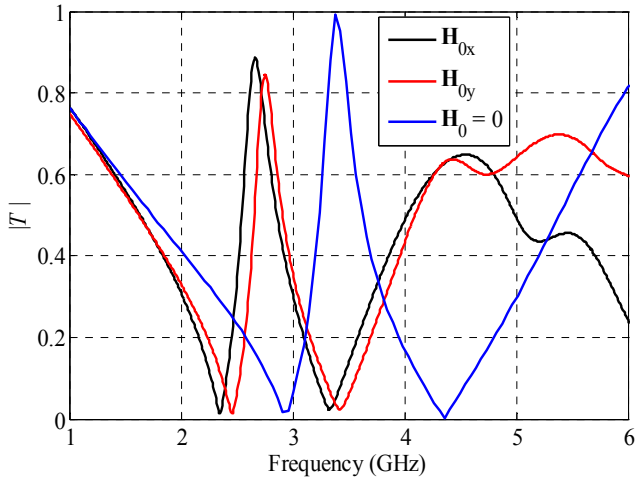
In [2] a parametric study of the DR array placed on a dielectric substrate was made in order to optimize the geometrical parameters of system to obtain a high quality factor (Q-factor) trapped-mode resonant conditions. In this array the trapped-mode corresponds to a narrow transmission resonance which exists between two broad reflection resonances, corresponding to the rings individual resonance. When the substrate has non-negligible loss, it was observed a compromise between high Q-factor and the maximum transmittance at the trapped-mode resonance, about 12 and 70%, respectively. A high Q-factor was observed for smaller differences between the rings radius, however the maximum transmittance is reduced, since the loss is increased due to a higher field confinement between the rings. In order to obtain a high Q-factor and a high transmittance at the trapped-mode resonance, we considered the following values for the geometrical parameters of the DR array (see Fig. 1): $d_x = d_y = 13$, $a_1 = 6$, $a_2 = 5$, $2w = 0.2$ and $h = 1.6$ (all dimensions are in millimeters).

For the array placed on a ferrite substrate we consider the mathematical model of a magnetized ferrite substrate described in [8]. In the following we show the possibility to shift the trapped-mode resonant frequency with magnetization of the ferrite substrate. The ferrite material is TTI-3000 [8], considering a ferromagnetic resonant frequency of $\omega_0/2\pi = 3{,}5$ GHz, which can be controlled by the ESMF $\mathbf{H}_0$.

The reflection and transmission spectra of this structure are shown in Fig. 2 for magnetization in x- and y-directions, and in Fig. 3 for z-direction. For comparison purpose, in these figures are also shown the structure responses for a non-magnetized ferrite substrate.

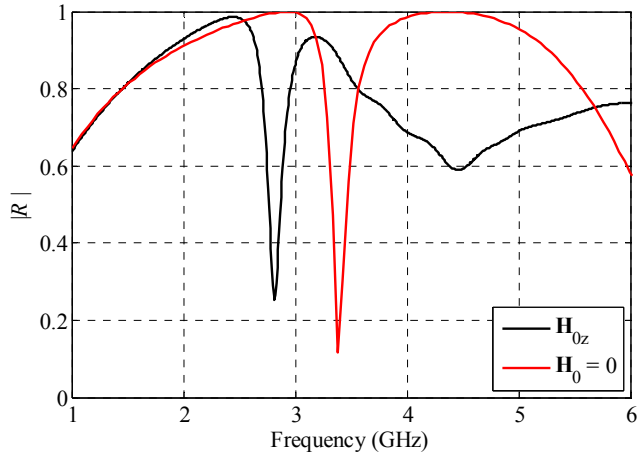


(a)

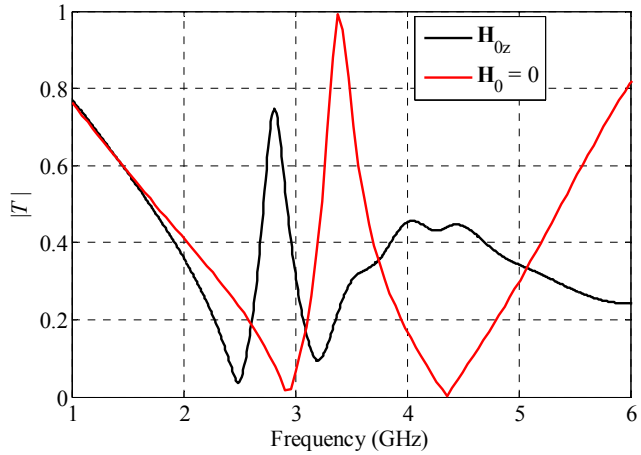


(b)

Figure 2. Reflection (a) and transmission (b) spectra of the array placed on a ferrite substrate magnetized in x- and y-directions, and for a non-magnetized one; $\omega_0/2\pi = 3{,}5$ GHz.



(a)



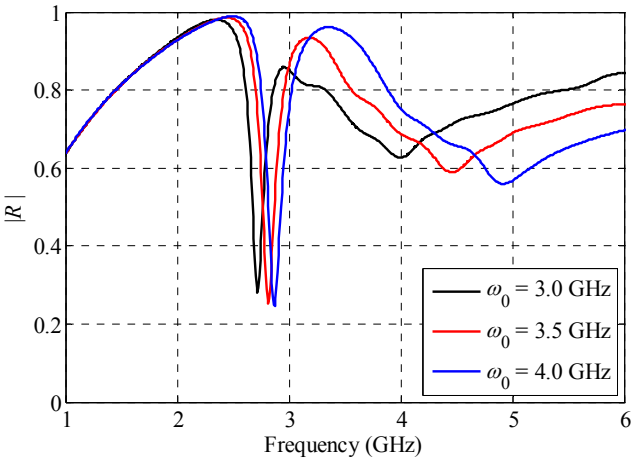
(b)

Figure 3. Reflection (a) and transmission (b) spectra of the array placed on a ferrite substrate magnetized in z-direction and for a non-magnetized one; $\omega_0/2\pi = 3{,}5$ GHz.

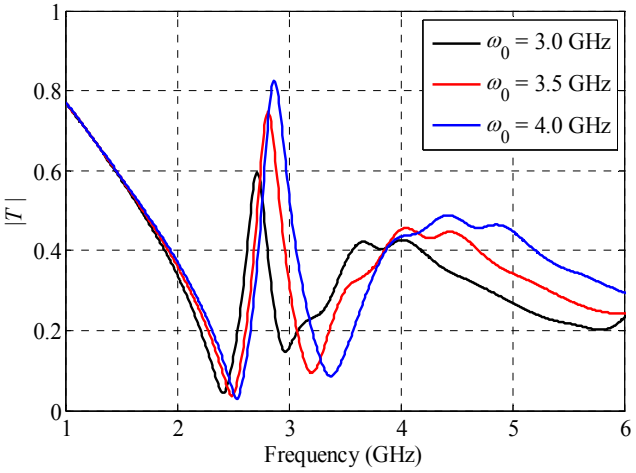
As can be seen in Figs. 2 and 3, a similar resonant frequency shift is achieved for different orientation of the magnetization, around 20% of the resonant frequency. However for normal magnetization the attenuation on the maximum transmittance is larger than for parallel one. Note that for parallel magnetization the structure is polarization dependent, while for normal one it is polarization independent (as explained in [2]), but the dependence on polarization is small in the trapped-mode region, as can be observed in Fig. 2, where we consider the cases of magnetization applied in parallel ($\mathbf{H}_{0x}$) and orthogonal ($\mathbf{H}_{0y}$) to the incident wave polarization.

To analyze the effect of the ferromangetic resonant frequency ω_0 on the trapped-mode band, we shown in Fig. 4 the structure responses for magnetization in z-direction and different ω_0. One can see, that near the frequency of ferromagnetic resonance, the trapped-mode resonance shift is increased, however the attenuation in the maximum of transmittance is also increased. This is an obvious consequence of the ferromagnetic resonant characteristics, i.e. near the resonance the values of both the real and imaginary parts of the permeability tensor parameters are larger and their variation is higher [1].

When the magnetization is along z-direction, the Faraday and Kerr effects take a place in the ferrite substrate. The polarization state of the electromagnetic waves reflected from and transmitted through the structure can be analyzed using the azimuth θ and ellipticity η angles, as illustrated in the inset of Fig. 5b, [1]. These angles were calculated for $\omega_0/2\pi = 3{,}5$ GHz and are shown in Fig. 5. As can be seen, in the trapped-mode band the Faraday rotation enhancement provided by the structure is about 2 times in comparison with the ferrite substrate without metallization.



(a)

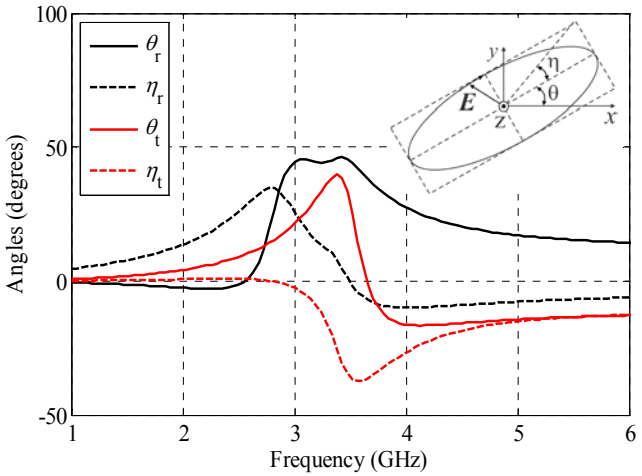


(b)

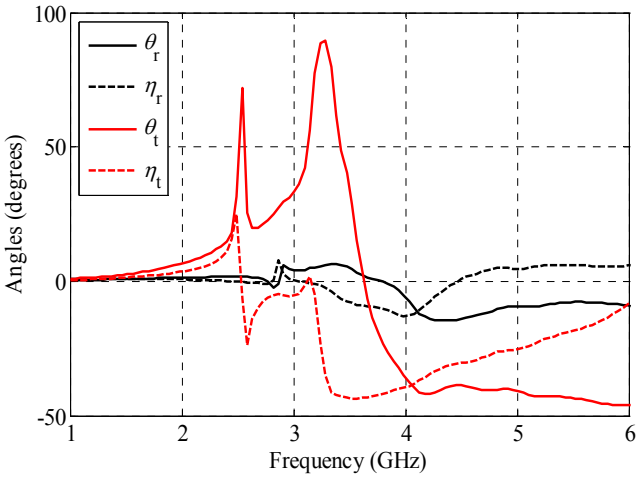
Figure 4. Reflection (a) and transmission (b) spectra of the array placed on a ferrite substrate magnetized in z-direction for different ω_0.

Since in the vicinity of the ferromagnetic resonance the magnetic loss is very large, we investigate the possibility of designing an array with switch on and off functionality of the trapped-mode transmission band by adjusting the ferromagnetic resonant frequency. For showing this functionality, we considered the substrate made of ferrite TT2-125 with $\omega_0/2\pi = 3{,}5$ GHz. In Fig. 6 the responses of

the structure are shown for a magnetized ferrite substrate and for a non-magnetized one. As can be seen, the transmission coefficient can be switched from 1 to 0.3 at the trapped-mode resonance. We think that with applying appropriate optimization of the geometrical and/or physical parameters it is possible to achieve a more complete transmission band switching.

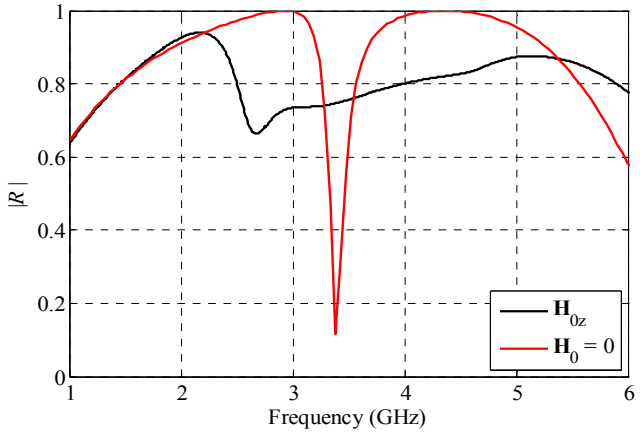


(a)

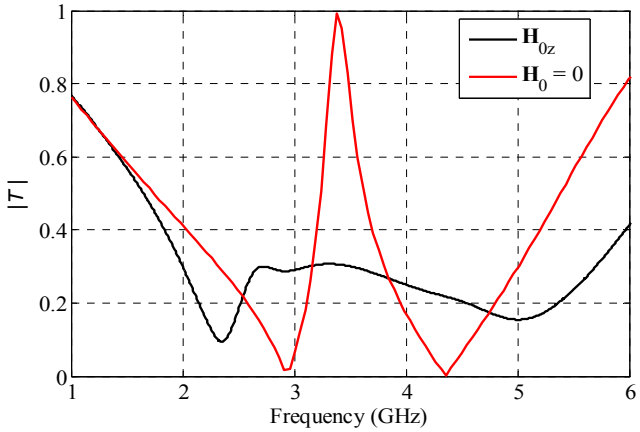


(b)

Figure 5. Azimuth θ and ellipticity η angles of waves reflected from and transmitted through a ferrite substrate without metalization (a) and through the structure with magnetization along z-direction; $\omega_0/2\pi = 3{,}5$ GHz.



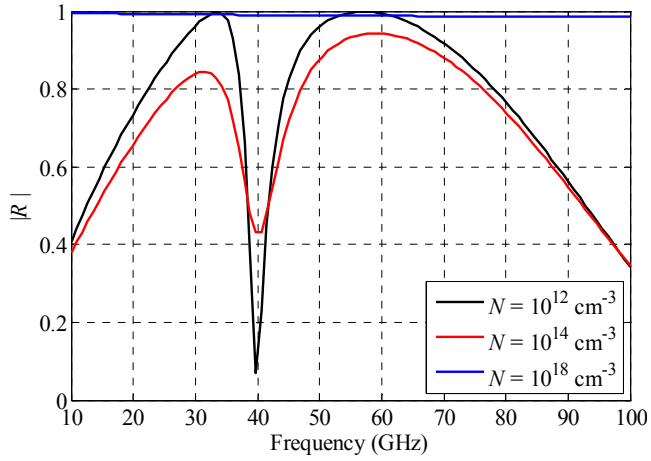
(a)



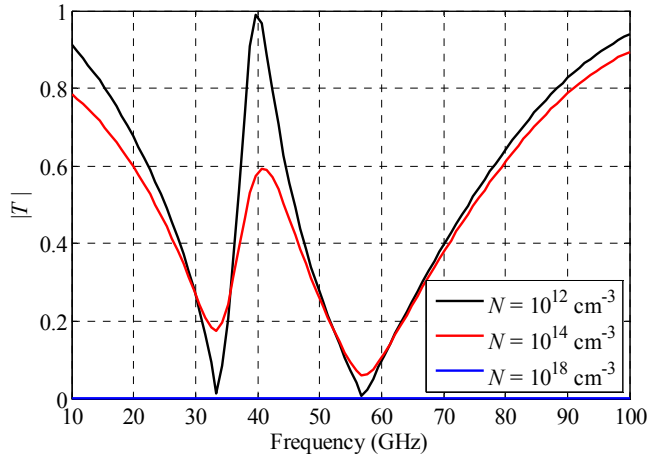
(b)

Figure 6. Reflection (a) and transmission (b) spectra of the array placed on a ferrite substrate magnetized in z-direction, and for a nonmagnetized one. The ferrite material is TT2-125 with $\omega_0/2\pi = 3{,}5$ GHz.

For the array placed on a silicon substrate we consider the mathematical model of an optically activated silicon substrate described in [9]. In Fig. 7 the array responses for different values of N are shown. For $N = 10^{12}$ cm^{-3}, the influence of induced plasma on the refraction index of the silicon substrate is negligible and a high Q-factor transmission resonance exists with almost total transmission at 40 GHz. Increasing N to 10^{18} cm^{-3}, one comes to the regime of almost complete reflection of the incident wave due to the significant increase of the real and imaginary parts of the silicon refraction index.



(a)



(b)

Figure 7. Reflection (a) and transmission (b) spectra of the array placed on an optically activated silicon substrate for different values of the plasma density N.

Finally, we consider a situation when the DR array is placed on a substrate made of antiferromagnetic film (AF). The metamaterial parameters are $d_x = d_y = 0.3$, $a_1 = 0.11$, $a_2 = 0.09$, $2w = 0.004$ and $h = 0.05$ (all dimensions are in millimeters). As a convenient material for the substrate, MnF_2 antiferromagnetic film is considered [10,11]. The ESMF is applied to the system in the Faraday geometry. The physical parameters of the AF film are $\varepsilon_r = 5.5$, $H_e = 450$ kG, $H_a = 7.87$ kG and $M_0 = 0.6$ kG. The gyromagnetic ratio is $\gamma = 1.97\times10^{10}$ rad.s^{-1}.kG^{-1} and the damping coefficient is fixed at $\tau = 4.25\times10^{-4}$, which is the origin of the absorption. For one fixed external magnetic field, $H_0 = 1.0$ kG, in the dispersion curves of permeability tensor components there are two resonant frequencies, $æ_1 \approx 0.262$ ($f \approx 0.2618$ THz) and $æ_2 \approx 0.268$ ($f \approx 0.2678$ THz) which are shown in Fig. 8. Here $\mu_1 = 1 + \chi_1$ and $\mu_2 = \chi_2$ are diagonal and nondiagonal elements of the permeability tensor, and the expressions of magnetic susceptibility $\chi_1 = \chi_{xx}^{(1)} = \chi_{yy}^{(1)}$ and $i\chi_2 = \chi_{xy}^{(1)} = -\chi_{yx}^{(1)}$ can be found in [10,11]. Under the action of intense light the dynamical magnetization in AF media nonlinearly couple with the wave magnetic field which leads to the magnetic optical nonlinearity. In this case the magnetic susceptibility can be presented as below

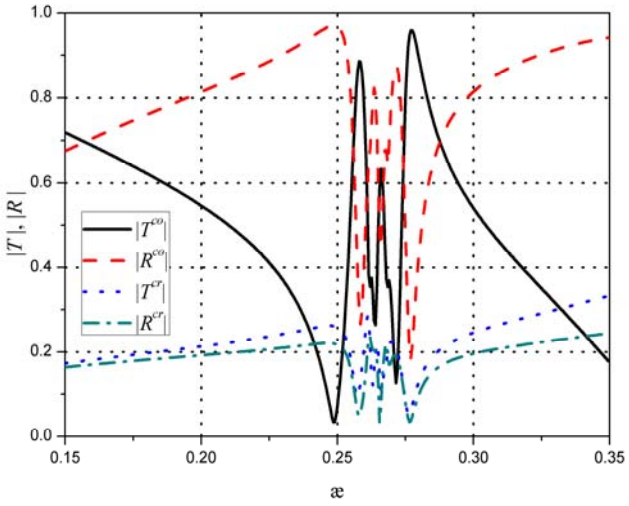
$$\chi_{ik}^{(1)}(\mathbf{H}) = \chi_{ik}^{(1)} + \sum_{j=1}^{3}\chi_{ikj}^{(2)}H_j + \sum_{j=1}^{3}\sum_{m=1}^{3}\chi_{ikjm}^{(3)}H_jH_m \qquad (1)$$

where the expressions and typical dispersion curves of the second- and third-order susceptibility are given in [10,11]. From these papers the conclusion is that in the vicinity of each resonant frequency, the real and imaginary parts of these susceptibility components are of the order 10^{-8} and negligible small outside the vicinity, and they are symmetrical and antisymmetrical with respect to the resonant frequencies, respectively.

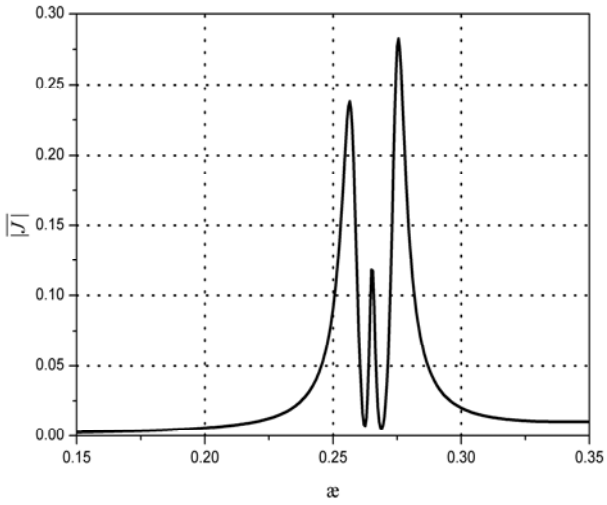
Remarkably, when the magnetic field strength inside the AF film increases both the real and imaginary parts of magnetic permeability undergo changes which, under a certain threshold level of the input light intensity, can lead to dispersion-absorption bistable behavior of the system. Here the way to obtain large magnitude of the magnetic field strength in the AF film lies in the choice of the parameters of the DR array of metamaterial to tune the frequency of the trapped-mode excitation to the frequency of antiferromagnetic resonance. Just such a situation is given in Fig. 9 where the optical response of the metamaterial in the case when the intensity of input light is small (linear regime) is presented. The behavior of the dispersion characteristics of the AF permeability leads to appearing alternate bands of high transmission and absorption in the spectra of metamaterial. One can see that in the frequency band of the trapped-mode excitation there is a peak of current magnitude, but its frequency dependence has a form of alternating maxima and minima due to the strong absorption in the substrate in the vicinity of the AF resonances nearly $æ_1 \approx 0.262$ and $æ_2 \approx 0.268$. However, since the magnetic field strength is proportional to the current and the current magnitude obviously increases when the intensity of the incident field rises, under a certain intensity of the incident field the magnetic properties of substrate can change.

To study such nonlinear response of metamaterial we use the technique proposed in our previous publications [3,4]. According to this method, at the first stage, the current distribution J along the strips, the reflection R and transmission T coefficients are determined under an assumption that the intensity of input light S is small (linear regime). For these calculations the Method of Moments is used. At the second stage, the transmission line theory is applied to estimate the inner magnetic field strength which is directly proportional to the current magnitude averaged over a metal pattern extent. It gives us a nonlinear equation related to the average current magnitude in the metal strips. In this equation the input field intensity is a parameter and, at a fixed frequency ω, its solution is the average current magnitude which depends on the intensity of the incident field. On the basis of the found current the inner magnetic field strength is estimated, and then the actual parameters of

permeability tensor, reflection and transmission coefficients are calculated as functions of the frequency and intensity of the incident field.



(a)

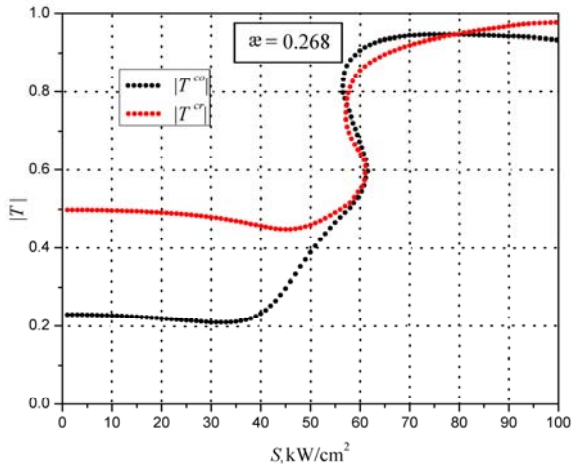


(b)

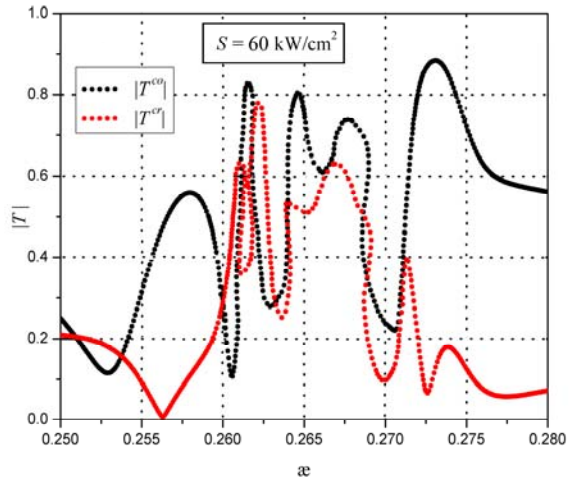
Figure 9. Reflection, transmission spectra (a) and average current magnitude (b) of the array placed on an antiferromagnetic substrate. Linear regime.

Our calculations show that in the case of the nonlinear permeability of substrate, dependences of the transmission coefficient magnitude versus the incident field intensity have a form of hysteresis (Fig. 10a). Such form of curves of the transmission coefficient magnitudes is studied quite well and is explained by the nonlinear phase-shift and nonlinear attenuation which appear in the nonlinear system. As the incident field intensity increases, the nonlinear phase shift rapidly raises and the attenuation decreases that guarantee the presence of obvious bistable switching.

The frequency dependences of the transmission coefficient magnitudes also manifest discontinuous switching with frequency changing. Since the dispersion curves of nonlinear susceptibility have the bands of grow and decay, the real and imaginary parts of the permeability tensor coefficients also increase and decrease with frequency. The bistable transmission occurs exactly in these frequency bands and is manifested in the ambiguity of the transmission coefficient magnitudes at the leading and trailing edges of the resonance.



(a)



(b)

Figure 10. Transmission spectrum versus incident field intencity (a) and frequency (b) of the array placed on an antiferromagnetic substrate. Nonlinear regime.

4. Conclusions

We present electromagnetically controllable surfaces designed on the basis of periodic DR metallization arrays which are placed on a thin substrate of optically active material. The DR metallization array has the interesting peculiarity of supporting the trapped-mode resonance with polarization insensitivity feature for a normally incident electromagnetic plane wave. Using a magnetized ferrite substrate as controlling element, we showed the possibility

to shift the trapped-mode resonant frequency in about 20%, without significant degradation of the transmission band.

An enhancement of Faraday effect was observed in the studied structure. Also by tuning the ferromagnetic resonant frequency to be near the trapped-mode frequency, it is possible to design a switch off and on functionality. In the presented configuration the maximum transmittance has a switch off and on ratio of about 0.3, but we think that with future optimization of the geometrical and/or physical parameters it is possible to achieve a more complete switching. By using an optically activated silicon substrate as controlling element, we demonstrated the possibility to have an almost total switching functionality of the transmission band.

We show that in the DR array placed on an antiferromagnetic substrate the all-optical switching can be realized. It is possible due to the capability of studied metamaterial provides the sufficient field localization inside the thin nonlinear substrate at the frequency of the trapped-mode excitation.

In conclusion, a planar DR metamaterial, which bears a high-quality-factor trapped-mode resonance, is a promising object for realization of a polarization-insensitive, controllable switching.

Acknowledgements

We would like to acknowledge the Brazilian agencies CAPES and CNPq.

References

[1] S. Prosvirnin and V. Dmitriev, Electromagnetic wave diffraction by array of complex-shaped metal elements placed on ferromagnetic substrate, *European Physical Journal Applied Physics*, vol. 49, 2010.

[2] M. Kawakatsu, V. Dmitriev, and S. Prosvirnin, Microwave Frequency Selective Surfaces with High Q-Factor Resonance and Polarization Insensitivity, *Journal of Electromagnetic Waves and Applications*, vol. 24, no. 2–3, pp. 261–270, 2010.

[3] V. Tuz, S. Prosvirnin, and L. Kochetova, Optical bistability involving planar metamaterials with broken structural symmetry, *Phyical. Review B,* vol. 82, P.233402, 2010.

[4] V. Tuz, S. Prosvirnin, All-optical switching in metamaterial with high structural symmetry - Bistable response of nonlinear double-ring planar metamaterial, *European Physical Journal Applied Physics*, vol. 56, 30401, 2011.

[5] R. Mittra, C. H. Chan and T. Cwik, Techniques for analyzing frequency selective surfaces – A Review, *Proceedings of the IEEE*, pp. 1593–1615, 1988.

[6] B. Lin, S. Liu and N. Yuan, Electrically and magnetically anisotropic substrates, *IEEE Transactions on Antennas and Propagation*, vol. 54, 2006.

[7] The programs web page is www.cst.com.

[8] D. M. Pozar, Microwave Engineering, John Wiley and Sons, New York, 1998.

[9] C. H. Lee, P. S. Mak, and A. P. De Fonzo, Optical control of millimeter-wave propagation in dielectric waveguides, *IEEE Journal of Quantum Electronics*, vol. 16, 1980.

[10] S.-C. Lim, J. Osman and D. Tilley, Calculation of nonlinear magnetic susceptibility tensors for a uniaxial antiferromagnet, *Journal of Physics D: Applied Physics*, vol. 33, 2899-2910, 2000.

[11] Y. Zhao, S.-F. Fu, H. Li, and X.-Z. Wang, Bistable transmission of antiferromagnetic Fabri-Perot resonator, *Journal of Applied Physics*, vol. 110, 023512, 2011.

Preliminary electrical characterization of piezoelectric transformer for plasma glow discharge generator

F. Pigache[1]*, C. Nadal[1] and Y. Lefevre[1]

[1]Université de Toulouse; INP, UPS; Laboratoire Plasma et Conversion d'Energie (LAPLACE); Ecole Nationale Supérieure d'Electrotechnique, d'Electronique, d'Informatique, d'Hydraulique et des Télécommunications (ENSEEIHT), F-31071 Toulouse cedex 7, France, and CNRS; LAPLACE; F-31071 Toulouse, France
*françois.pigache@laplace.univ-tlse.fr

Abstract

This paper deals with the preliminary electrical characterization of piezoelectric transformer used as a plasma glow discharge generator. This unusual application of piezoelectric transformer leads to a specific nonlinear electrical behavior. It is essential to identify the concerned physical mechanisms for a better understanding of the operational energy conversions.

1. Introduction

The piezoelectric transformers (PTs) have been developed for several ten years because of their noteworthy properties of insulation, compactness and high efficiency. Some structures are particularly dedicated to high step-up voltage such as the Rosen type transformer. These transformers are commonly used as a two-port network electronic component as a voltage converter or impedance adapter. It has also been used as a spark generator, comparable to the principle in the gas lighter which has been discovered and patented in 60's. Since these years, many strides have been made in piezoelectric material synthesis, leading to strongly improve their electromechanical conversion properties. Consequently, for few years, other kinds of applications with piezoelectric transformers have appeared, by taking advantage of their permittivity as well as their dynamic polarization for plasma discharge devices.

A remarkable demonstration is the atmospheric pressure argon plasma jet using a cylindrical piezoelectric transformer realized by Kim *et al*. [1]. The cylindrical transformer used in this device is a variant of the Rosen type transformer [2]. The obtained plasma discharge is a DBD (Dielectric Barrier Discharge), leading to the formation of plasma bullets in the argon flow passing through the transformer. The resulting plasma formation is issued from the high electrical potential on the electrode of the secondary part of the transformer. This high step-up voltage property can be achieved only by supplying the transformer at a frequency close to one of its mechanical resonance frequencies.

Note that this is not the only way to use the piezoelectric transformer for plasma discharge generation. Indeed, considering that the high electrical potential is developed all along the surface of secondary part of the PT, the resulting electrical field may be sufficient to promote glow discharges in the surrounding gas. In this configuration, the secondary electrode can be simply removed and the PT considered like in open circuit condition (no load). The resulting architecture of a Rosen type transformer and parameters are shown on figure 1.

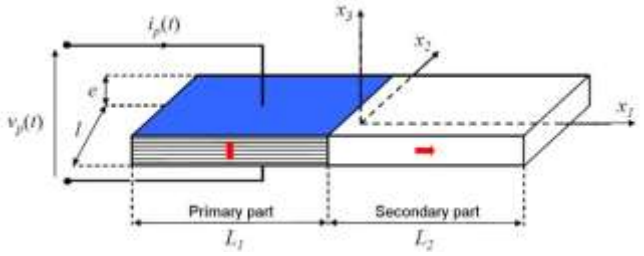


Figure 1: Rosen type transformer architecture.

The figure 2 shows the theoretical electrical potential surrounding a Rosen type transformer (cross view) when it is supplied at different frequencies, corresponding to its longitudinal resonant modes [3].

As a consequence, depending on specific environment conditions (such as a convenient low pressure) and the PT supplied by voltage source close to one of the transformer resonant frequencies, the resulting surface electrical potential leads to the glow discharge in the surrounding gas. Obviously, the spatial-temporal patterns of the plasma discharges are strongly dependent on this voltage amplitude, the vibratory mode, the gas nature and pressure. Figure 3 illustrates the experimental glow discharges (front view) obtained for the first three longitudinal vibratory modes in different gas pressure conditions. The first significant observation about this glow discharge experience is the low input voltage required (1.8V). Commonly, several hundred volts are necessary to promote a glow discharge even in so low pressure environment. This remarkable capability is issued from the high step-up voltage ratio of the Rosen PT,

especially when it is in open circuit condition. However, this open circuit condition must be carefully considered because the presence of glow discharge constitutes an equivalent nonlinear load. The open circuit condition can be reasonably considered before the ignition of the discharge.

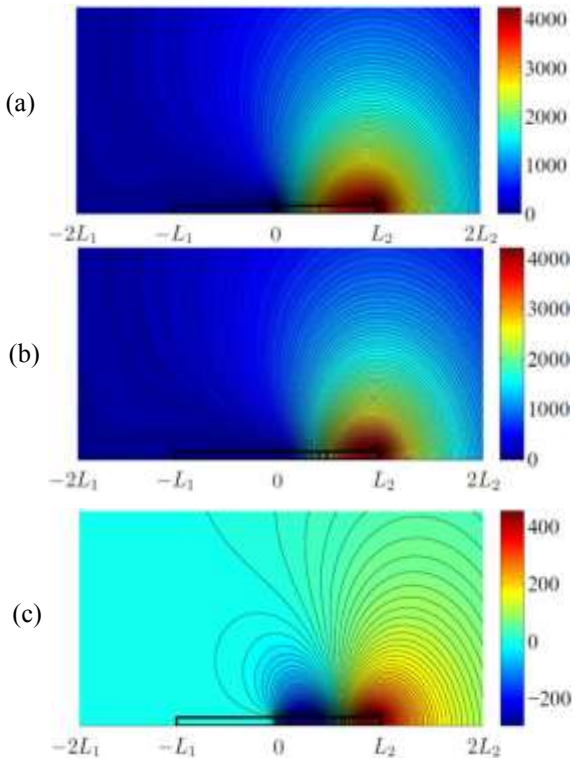


Figure 2: Electrical potential surrounding Rosen PT in λ/2 resonant mode (a), λ mode (b) and 3λ/2 mode (c)[3].

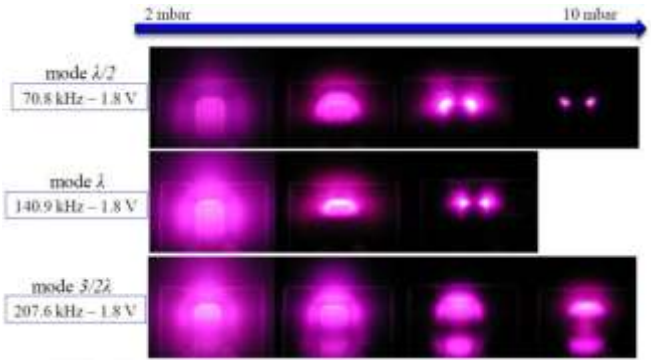


Figure 3 - Patterns of plasma glow discharges in function of the air pressure (front view).

The glow discharges only occur in a specific range of pressure depending on the generator characteristics. Beyond an upper pressure limit, the electric field is insufficient to provide enough energy to the gas to ignite a discharge. Moreover, there is a lower limit below which there is not a sufficient free charge density to promote collisions and therefore to maintain a discharge. In the present experimental conditions, the lower and upper limits are respectively about 2 mbar and 40 mbar.

Several characterizations of the plasma discharges have been investigated in order to reach a better understanding of the physical properties of this latter [3][4]. Meanwhile, few studies have been dedicated to the electrical behavior of the device during plasma discharge operation. Consequently, the following sections are dedicated to the electrical characterization of the Rosen PT used as a glow discharge generator. Firstly, experimental investigations are detailed, leading to discuss about the specific behaviors observed. Then, an electrical equivalent model is used to provide new elements of understanding of the voltage conditions necessary to ignite the glow discharges.

2. Experimental investigations

Because of the plasma glow discharge is distributed on the half surface of the transformer and the lack of the secondary electrode, no electrical measurements are available on the secondary side. Consequently, the electrical measurements can only be made on the primary side. The piezoelectric generator is supplied by high speed bipolar amplifier HSA4052 at frequency around 70kHz, corresponding to the first resonant frequency (λ/2 resonance mode). The electrical quantities measured are the primary voltage v_p and the primary current i_p. The device is placed inside a vacuum chamber and the pressure is fully controlled beyond the upper and lower limits of plasma discharge ignition. Additionally, it can be reasonably admitted that the influence of the acoustic impedance of surrounding gas is negligible whatever the pressure condition.

First of all, the generator is supplied under pressure condition below the lower limit in order to evaluate its electrical behavior without plasma discharge. Thus, transfer functions of the input admittance are obtained and given on figure 4. Measurements are made around the resonant frequency with different input voltage values. In spite of the lack of plasma discharge, the electrical characteristics clearly demonstrate a nonlinear tendency, depending on the voltage amplitude.

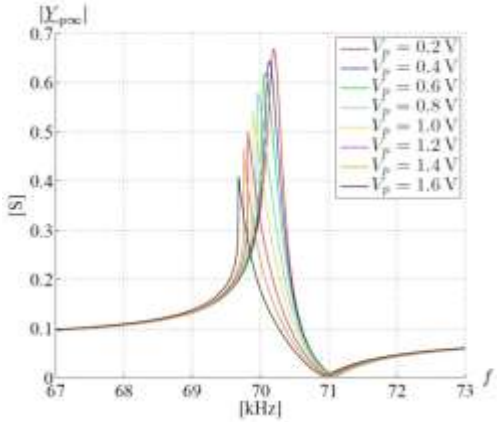


Figure 4 - Admittance transfer functions obtained at 0.5 mbar.

It may be noted that the transfer function only describes the frequency evolution of the fundamental part of the input

admittance $|Y_{p\infty}|$. Consequently, the harmonic part of the admittance is consciously omitted in the study.

Based on the observations of figure 4, it appears a drift of the resonant frequency toward the lower frequencies, an abrupt transition and an amplitude decreasing with the increase of input voltage amplitude. The common linear admittance characteristic is only obtained for the lowest input voltage amplitude. Additionally, the anti-resonant frequency is not affected by the voltage variation. Finally, the transfer function in up- and down- frequency sweep demonstrates a hysteretic behavior (not depicted here).

Actually, this behavior is well known and it is especially obvious in device with low vibration damping [5]. In the present case, the no output load condition and the weak mechanical damping coefficient promote this nonlinear behavior. In [6-7], it is attributed to the high mechanical vibration amplitude and modeled by considering additional square and cubic terms in the piezoelectric constitutive relations.

Now that the reference admittance profile is described, the influence of the plasma glow discharge can be discussed. A campaign of admittance measurements is undertaken under different air pressure conditions and voltage amplitude. Some selected curves are shown on figure 5, figure 6 and figure 7.

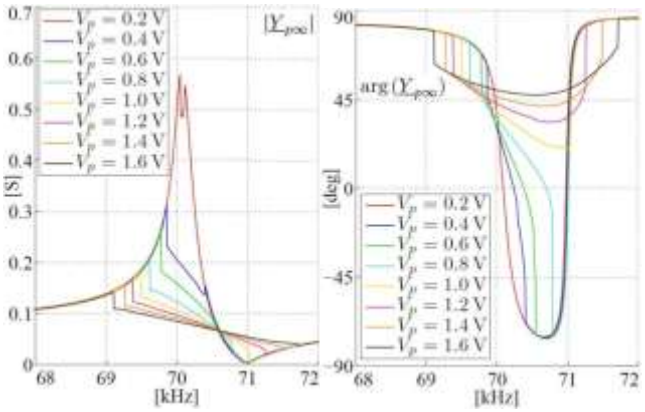


Figure 5: Admittance measurements at 5.6mBar air pressure.

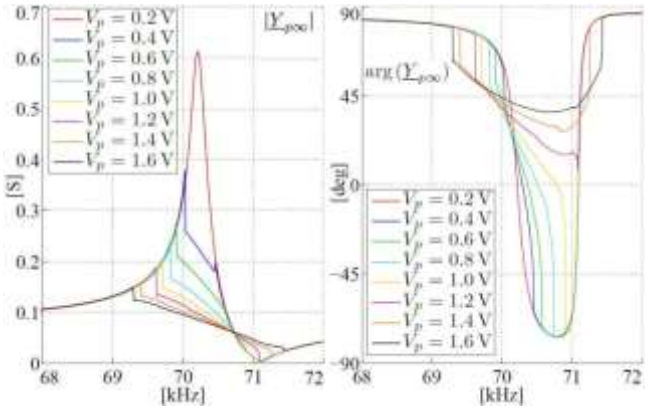


Figure 6: Admittance measurements at 10mBar air pressure.

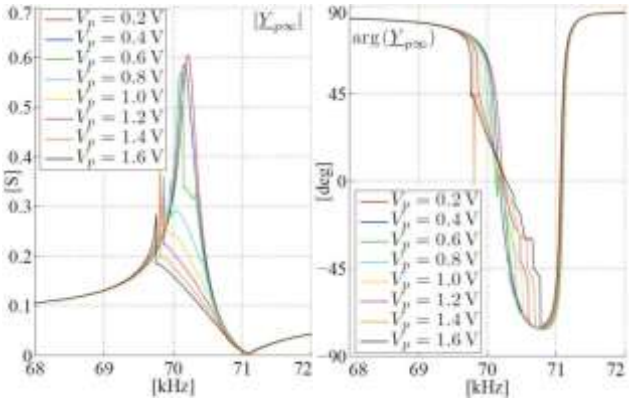


Figure 7: Admittance measurements at 40mBar air pressure.

The different observations about the admittance measurements are itemized as follow:

- An additional nonlinear appearance is obvious close to the resonant frequency,
- The discontinuity of the transfer function coincides with the discharge appearance,
- The phase diagram is also strongly affected by the discharge,
- The higher the voltage amplitude, the wider the frequency range of the discontinuity is,
- For the lowest voltage amplitudes and beyond a pressure value, the admittance characteristics become identical to those on figure 4, corresponding to the discharge extinction.

Because the electrical behaviors appearing during the plasma glow discharge are non-linear and complex, no interpretation is possible between the ignition and extinction frequencies, in any case based on this admittance characterization method. However, according to these observations, it can be considered that the glow discharge manifestation is bounded by two singular frequencies; the ignition frequency f_{ignit} and the extinction frequency f_{ext}. These singular values depend on the voltage amplitude, the gas pressure and most likely on the gas nature. When the convenient voltage and pressure conditions are not met to generate a plasma discharge, the transfer function is not affected and identical to the reference one presented in figure 4.

The ignition and extinction frequencies are finally collected in function of the voltage amplitude on figure 8, figure 9 and figure 10 for the different pressure conditions. Moreover, the measurements are done in up- (SU) and down- (SD) frequency sweep and lead to following comments:

- Firstly, it is obvious that the frequency evolution is quite linear with the voltage amplitude,
- The presence of glow discharge is delimited by a triangular area in these frequency-voltage frames, centered on the resonance frequency,
- It clearly appears that this area is reduced with the pressure increasing,

- Moreover, the area is truncated with the pressure increasing, meaning that the voltage amplitude is insufficient to meet the ignition condition,
- The ignition frequency is different according to the up- and down- frequency sweep, and it does not correspond to the extinction frequency.
- Intuitively, we can consider that these frequency values coincide with the condition of a sufficient electrical potential to ignite the plasma discharge.

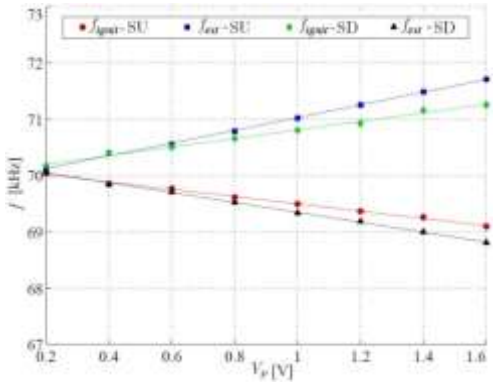


Figure 8: Ignition and extinction frequencies in function of input voltage at 5.6mbar air pressure.

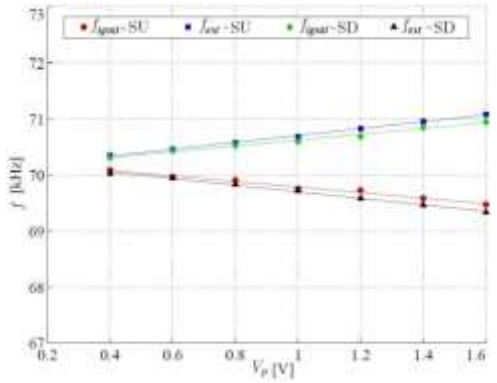


Figure 9: Ignition and extinction frequencies in function of input voltage at 20mbar air pressure.

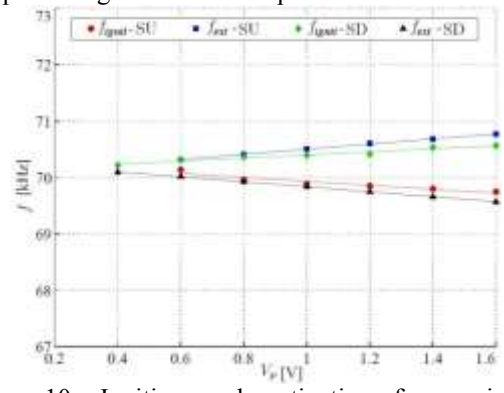


Figure 10: Ignition and extinction frequencies in function of input voltage at 40mbar air pressure.

By considering the characteristics on figure 5, it appears that the presence of the glow discharge conceals the nonlinear behavior observed on figure 4. Indeed, this remark relies on the superposition of admittance curves below and beyond to the discharge frequency range, contrary to the observation on figure 7.

From this acknowledgment, it can be considered as acceptable to use the classical linear modeling of piezoelectric transformer in convenient pressure condition.

3. Modeling approach

The objective is to verify if the ignition and extinction frequencies coincide with a specific value of the electrical potential. To this goal, the electrical equivalent circuit is used. Basically, the electrical behavior of the Rosen type PT is approximated by an electrical equivalent circuit when it is used in convenient linear operating conditions. As seen above, it is not the present case due to the simultaneous nonlinear influences of the low vibration damping and the plasma discharge. Nevertheless, this linear approximation can be acceptable in convenient experimental conditions i.e. between 5mbar to 40mbar air pressure condition.

The simplified electrical equivalent circuit is shown on figure 11. It is composed of parallel components on the primary side, a serial RLC branch corresponding to the mechanical resonant equivalent behavior and an ideal conversion ratio Ψ. The superscript $^{(1)}$ indicates that the elements correspond to the first longitudinal vibratory mode.

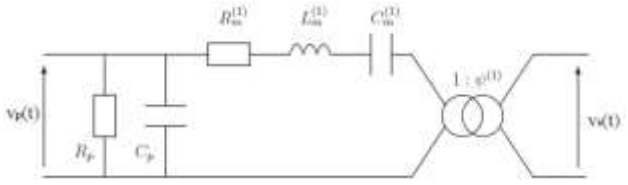


Figure 11 – Electrical equivalent circuit of a piezoelectric transformer.

Note that the equivalent components on the secondary part are not considered as usually. Indeed, the lack of secondary electrode and the high length of the secondary part allow to neglect its electrical influence. Moreover, consequently to the lack of secondary electrode, it is inappropriate to consider the existence of an output voltage $v_S(t)$. It can be considered as a fictive quantity describing the maximal electrical potential on the secondary part.
Because the interesting points are the ignition and extinction frequencies which mark out the validity of the linear assumption, it is necessary to express the output voltage in function of frequency. The voltage gain |G| is expressed in (1).

$$|G| = \frac{|v_S|}{|v_P|} = \frac{\psi}{\sqrt{\left[1-\delta\left(\frac{\omega^2}{\omega_S^2}-1-\frac{Q}{Q_m}\right)\right]^2+\left[\frac{\delta}{Q_m}\frac{\omega}{\omega_S}+\delta Q\left(\frac{\omega}{\omega_S}-\frac{\omega_S}{\omega}\right)\right]^2}} \quad (1)$$

where $\delta = \frac{C_m}{C_p}$ $\omega_S = \frac{1}{\sqrt{L_m C_m}}$

ω_S, Q, Q_m are the serial resonance pulsation, the electrical quality factor and the mechanical quality factor respectively.

Considering the infinite impedance of the secondary part, the electrical quality factor Q is null. Equation (1) is simplified, leading to the expression (2) according to the reduced pulsation x.

$$\delta^2 x^4 + \left[\frac{\delta^2}{Q_m^2} - 2\delta(\delta+1)\right]x^2 + (\delta+1)^2 = \frac{\psi^2}{|G|^2} \tag{2}$$

The solution of equation (2) gives:

$$x^2 = \frac{\omega^2}{\omega_S^2} = 1 + \frac{1}{\delta} - \frac{1}{2Q_m^2} \pm \frac{1}{\delta}\sqrt{\left(\frac{\delta}{2Q_m^2}\right)^2 - \frac{\delta^2}{Q_m^2}(\delta+1) + \frac{\psi^2}{|G|^2}} \tag{3}$$

If the mechanical quality factor Q_m is high (low vibration damping), the equation (3) can be simplified as follows:

$$\omega = \omega_S\sqrt{1+\frac{1}{\delta}}\sqrt{1 \pm \frac{|\psi|}{|G|.(\delta+1)}} = \omega_P\sqrt{1 \pm \frac{|\psi|}{|G|.(\delta+1)}} \tag{4}$$

where ω_P is the parallel resonant frequency.

Finally, if the fraction in the root square is small compared to unity, the frequency relation in function of the output voltage can be approximated as follows;

$$f(v_P) \approx \frac{\omega_P}{2\pi}(1 \pm \theta.|v_P|) \quad \text{with} \quad \theta = \frac{|\psi|}{|v_S|(\delta+1)} \tag{5}$$

It comes a proportional relation to the primary voltage amplitude v_P and inversely proportional to the fictive secondary voltage amplitude v_S. Because it is intuitive to consider that the glow discharge is ignited for a peculiar value of the electrical potential (at least for a given pressure and gas), then the ignition value of v_S can be considered as a constant. In this case and according to (5), the ignition frequency varies linearly with the primary voltage amplitude. This demonstration is in accordance with the frequency-voltage frames shown on figures 8, 9 and 10. The same argument is valid for the extinction frequency.

Another way of discussion is to simulate the fictive output voltage in function of the frequency and the input voltage. These simulations are obtained from the linear electrical equivalent circuit previously presented in figure 11. The parameter values are obtained by a conventional experimental identification method (impedance analyzer). The ignition and extinction frequencies are drawn on the voltage characteristics on figures 12, 13 and 14 and lead to obtain the output voltage values. The mean voltage values are also represented. Note that the characteristics drawn between the ignition and extinction voltage values are absolutely not insured because it is beyond the validity of the linear assumption.

It clearly appears that the ignition and extinction output voltages are constant, especially on figure 12 and 13. It is more questionable on figure 14. It can be reasonably attributed to the influence of the non linear behavior observed in figure 7 and it also demonstrates the limit of validity of this simplified approach.

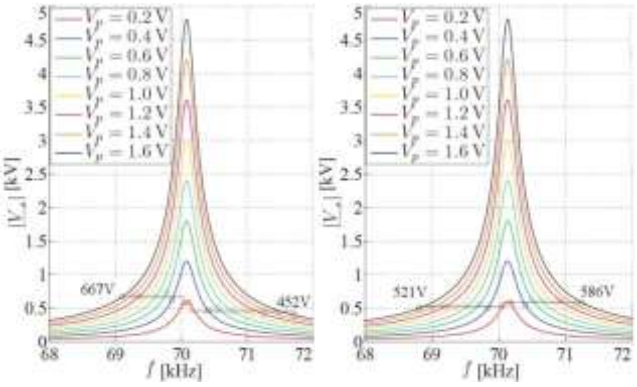


Figure 12: Ignition and extinction output voltages at 5.6mBar air pressure in up- (left) and down- (right) frequency sweep.

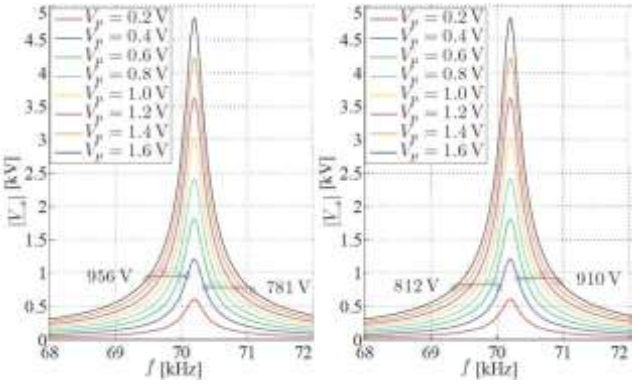


Figure 13: Ignition and extinction output voltages at 20mBar air pressure in up- (left) and down- (right) frequency sweep.

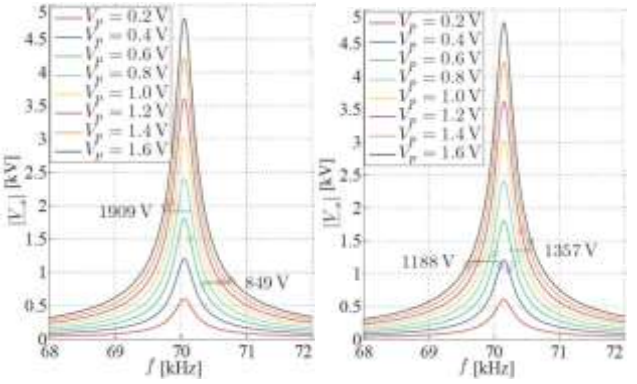


Figure 14: Ignition and extinction output voltages at 40mBar air pressure in up- (left) and down- (right) frequency sweep.

It clearly appears that whatever the frequency sweep, the ignition voltage is still higher than the extinction voltage. It coincides with the required conditions for a plasma ignition of any gas. It is noticeable that for crescent pressure condition, the voltage amplitude must be much higher and for the lowest input voltage configurations, the maximum output voltage cannot meet the ignition condition.

4. Conclusions

This paper was about the preliminary electrical characterization of a piezoelectric plasma discharge generator. The Rosen type transformer was placed in low pressure environment condition, relieved of the secondary electrode and supplied around a resonant frequency. It has led to the generation of a glow plasma discharge distributed along the secondary part of the transformer.

The preliminary experimental campaign has relied on the admittance measurements with frequency sweep, highlighting the different origins of nonlinear behaviors. In spite of the simplicity of this approach, several observations have been done and have led to use the electrical equivalent circuit up to its limit of validity. By the way, it has been demonstrated that the plasma ignition is due to a sufficient electrical potential distributed on the secondary piezoelectric element. If this preliminary study has demonstrated the behavior in frontier of the plasma discharge condition, future works must be dedicated to the dynamic behavior during the plasma discharge.

References

[1] H. Kim, A. Brockhaus and J. Engemann, "Atmospheric pressure argon, plasma jet using a cylindrical piezoelectric transformer", *Applied Physics Letters*, vol. 95, no. 21, 211501-211501, 2009.

[2] J. Engemann, M. Teschke, "Device for producing an atmospheric pressure plasma", US patent n° 2009/0122941, may 14, 2009.

[3] C. Nadal, F. Pigache and Y. Lefevre, "Analytical Modeling of Electrical Potential Repartition on Piezoelectric Transformer", *IEEE IFC Symposium*, 602-607, Newport Beach, CA, 2010.

[4] H. Itoh, K. Teranishi and S. Suzuki, "Discharge plasmas generated by piezoelectric transformers and their applications", *Plasma Sources Science and Technology*, vol. 15, no. 2, 51-61, 2006.

[5] J. Yang, "Weakly nonlinear behavior of a plate thickness-mode piezoelectric transformer," IEEE Trans. Ultrason. Ferroelectr. Freq. Control, vol. 54, no. 4, 877‐881, Apr. 2007.

[6] K. Ishii, N. Akimoto, S. Tashirio, and H. Igarashi, "Influence of load resistance on higher harmonic voltages generated in a piezoelectric transformer," Jpn. J. Appl. Phys., vol. 37, no. 9B, pp. 5330‐5333, 1998.

[7] F. Pigache, C. Nadal, "Modeling and identification of Rosen-type transformer in nonlinear behavior", Transactions on Ultrasonics, Ferroelectrics and Frequency Control, vol.58, no.12, 2011.

Analysis of Coupling between Electric Cables and Multi-Dimensional-Dipoles Near-Field Radiation

E. R. Rajkumar, M. Bensetti, B. Ravelo and M. Kadi

IRSEEM (Institut de Recherche en Systèmes Electroniques Embarqués), EA 4353,
At the graduate school of engineering ESIGELEC,
Avenue Galilée, 76801 Saint Etienne du Rouvray, France.
*corresponding author, E-mail: e.rajkumar@esigelec.fr

Abstract

In this paper the investigation of couplings between metallic cables facing to the electromagnetic (EM) near-field (NF) radiated by 2D/3D configurations of elementary EM dipoles is presented. A sincere attempt has been made to evaluate the 3D equivalent component models as of 2D models. The NF coupling voltages across the cables is obtained by considering the 2D and 3D dipoles radiation with a hybrid method. This 2D/3D dipoles concept is particularly important for the modeling of electronic circuit emissions at high frequencies. To validate the hybrid method, few configurations are tested and validated. Here two configurations are presented. First one is with a metallic wire having cm-length above the ground plane disturbed by the EM-near-waves from the electronic circuits in proximity. For that, we model the EM radiation of the disturbing electronic circuits and then, apply the hybrid method to evaluate the coupling voltages induced through the wires. By considering the radiations around hundreds MHz, we demonstrate that the hybrid method proposed enables us to generate voltages in good agreement with the simulations performed with the commercial tools. In the second, analyses made with a 3D-model coil self for the wide band from 0.1 GHz to 0.5 GHz generates once again a good correlation between the terminal voltages of the wire using hybrid method. The results are in good accordance in each other in the proposed method; hence this hybrid method with equivalent 3D dipole can be utilized for the study of radiated coupling.

Keywords: Near-field (NF) coupling, multi-dimensional dipoles, electromagnetic (EM) radiation, EM compatibility (EMC), hybrid method.

1. Introduction

The complex integrity of electronic cards that are included in embedded systems is increasing particularly in the automotive and aeronautical domain. Due to high level of integration, systems integrate electronic components and cables together in the proximity. Hence the analysis of electromagnetic compatibility (EMC) and electromagnetic interference (EMI) issues is gained limelight of recent researchers in the field. This study has become of part of the design stage itself [1-7]. The radiation of electronic components and its effect on the cables have been discussed in the recent literature [8-15]. In the study of radiation of components, cables of a board IRSEEM laboratory developed a near field test bench [16-18], to estimate the fields; radiated electromagnetic measurements can be performed with a near field bench. Near field measurements are used to locate the region of high or low fields radiated by a board and to evaluate the shielding efficiency locating faults in a metallic cable. Also and also an inverse-method modeling method based on the optimization of equivalent sources constituted by EM elementary of dipoles capable reproducing the same radiation as the disturbing elements [19-24].

To investigate the EMC effect on such systems, the electronic team of IRSEEM laboratory proposes various methods for conducted and radiated emission, and also immunity [25-27]. A part of research conducted in IRSEEM involved radiated emission and radiated immunity, separately. The study of radiated emission and radiated immunity in both education and research is extensive.

Due to this, an examination of metallic wires susceptibility is conducted vis-à-vis the EM radiation in the RF frequency range is described.

From the literatures it is understood that the existing works on this EMC radiated susceptibility subject were mainly based either on the radiated far-field interaction on the wires [28-32] or the coupling between EM NF caused by the elementary dipoles [33-37]. Hence there is a need of a new methodology capable of capable of calculating radiated coupling. In the following sections we describe our proposed methodology in dealing with complex structure of metallic cables and electronic component.

This paper is organized in three main sections. In the First section cable immunity study with 2D and 3D dipoles along with the ground plane setup is discussed. It is based on the association of the emission model and also the coupling model induced on the metallic wires by using the analytical formulae established in [28]. Second section investigates the complex structure of metallic wire with the ground plane and the induced voltages are calculated at the terminals as

introduced in [43]. The third section is discussing the electronic structure in the calculation of radiated coupling. The last section is the conclusion.

2. Metallic cable immunity facing to the 2D/3D-dipoles radiation NF radiation and style

It is necessary to investigate the conducting coupling for the immunity of the power electrical system [38-41]. As a general application of this proposed hybrid method, we also investigated some comparisons with the PEEC method. For that, it seems necessary to consider multi-dimensional elementary dipoles as it represents more realistic structures for example in three dimensions. Hence, it becomes essential to validate the hybrid method with the radiating structures as 2D or 3D dipoles. To do this, we realized analysis of 2D and 3D dipole radiations.

2.1. Analysis of 2D and 3D dipole radiations

With 2D configuration, the radiating dipole elements cannot be integrated in PEEC model. For this reason, we established the equivalent 2D and 3D models as depicted in Figure 2 generating the same EM NF radiations.



Figure 2: Representation of 2D and 3D dipoles [39].

2.1.1. Comparison and validation of 3D dipoles in the radiated coupling

To understand the radiation of the 2D and 3D dipoles, we have considered these elements as radiating source placed above a ground plane. In order to validate the equivalent design setup of 3D-dipole, the following cases are studied and the EM field generated by 2D and 3D dipoles placed over a ground plane is analyzed and tabulated. The objective is to find a 3D equivalent structure which radiates the same field of 2D dipole. The results have been validated for 2D-dipole [42-47]. The studied structures are given as follows. In this section, the simulation parameters are kept constant throughout the studies for which the current source amplitude was varied between 0.1 A and 0.4 A, the operating frequency is between 100 MHz and 2 GHz.

2.1.2. Representation of 3D dipole

To realize 3D dipoles, three cases of configurations were considered.

- Case 1: Figure 3 represents the configuration considered. Dipole made of copper, with only one face excited and other faces are constituted by copper.

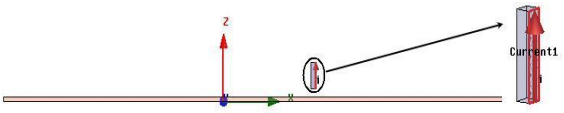


Figure 3: Design of 3D dipole in HFSS. The dipole is placed at 1 mm above the ground plane

Case 2: Figure 4 illustrates the top view of case 2 of the 3D dipoles configuration. Here, the dipole made of copper, with only one face excited but other 3 faces are current sources.

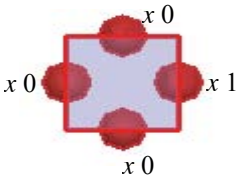


Figure 4: Top view of the 3D dipole. The four red circles show the faces excited with currents. Only one face is excited (x 1) and others do not act as sources**.**

Case 3: Figure 5 represents the top of view of the case 3 of the 3D dipole investigated. The dipole made of copper, with all faces excited.

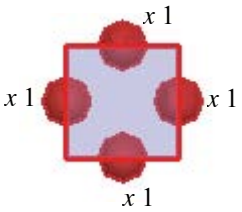


Figure 5: Top view of the 3D dipole. The four red circles show the faces excited with currents. All the faces are excited (x 1).

2.2. Analysis with 3D full wave simulation

The design structure shown in Figure 5 was simulated with the 3D EM standard software HFSS on changing only the dipole for various cases (Case 1 – Case 3). Figure 6 shows the comparison of the Electric field simulated from the 2D dipole and Case 1 and Case 2 of 3D dipole.

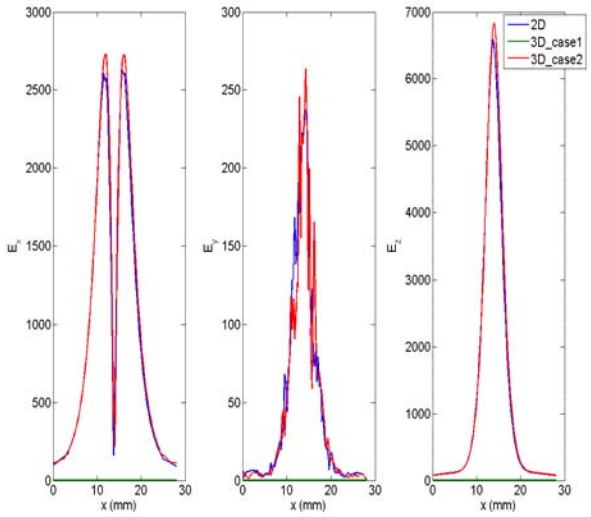


Figure 6: Comparison between 2D and Cases 1 and 2 of 3D dipole.

From the results and comparison between these three types of configuration, it is observed that 3D dipole Case 2 components are almost equivalent to the 2D dipole configuration. The E_x field component lies around 2.7 kV for both 2D and 3D dipole of Case 2 and E_y falls around 0.26 kV and E_z falls around 6.9 kV. With the results obtained, we understand the 3D dipole made of copper with ports in all faces is a compatible model. As illustrated in Figure 6, we see that all the field components of the 3D dipole are approximated 4 times that of the 2D dipole. It is also observed that we have excited 4 faces and scaling down the 3D dipole by a scaling factor of 4, we observe that the system equal to 3D dipole Case 2 and the results are matched with 2D dipole.

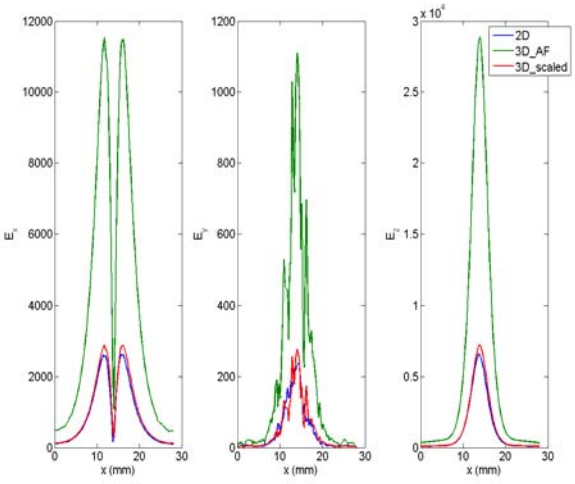


Figure 7: Comparison between 2D and 3D dipoles (Case 3). The 3D-scaled plot is the same as the 3D_AF (Case 3), but scaled by a factor of 4.

2.3. Study of different configurations of elementary dipoles and the metallic wire

In this study we observed that 3D dipole made up of copper with current ports excited on one face is a compatible of 2D dipole and this model can be used for further study.

Case 1: Dipole placed at the centre of the cable

The objective of this study is to find $V(0)$ and $V(L)$ using the 2D dipole and 3D dipole equivalent model. Figures 8 represent the simulation with the 2D dipole. The cable of length 8 mm, radius 0.1 mm is places 2 mm above the ground plane and the dipole is placed at the centre of the cable and above the ground plane, in the z direction.

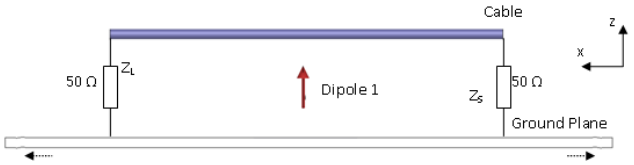


Figure 8: Case of one 2D dipole placed in the centre of the cable.

The centre of the dipole is situated at 1 mm above the ground plane. The cable is terminated with 50 Ω at the source and load ends. The comparison of simulations results of the coupling effect between the 3D dipole and the cable is shown in Figure 9. From the figure we understand that 2D dipole and 3D dipole results are in good accordance with each other. As 2D dipole $V(0)$ starts from 1.59 V and $V(L)$ also starts from 1.59 V and ends both at 1.62 V. Similarly for the 3D dipole, $V(0)$ starts from 1.63V and $V(L)$ 1.69V. The relative errors between the two results are plotted in Figure 10. As the error on 2D and 3D lies between 4% and 6% which is in tolerable level, it is understood that the equivalent 3D dipole can be used for PEEC and related other studies.

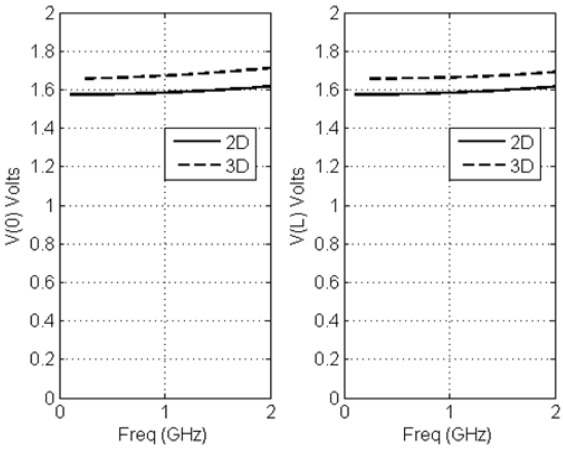


Figure 9: Comparison between 2D and 3D dipole placed at the centre of the cable.

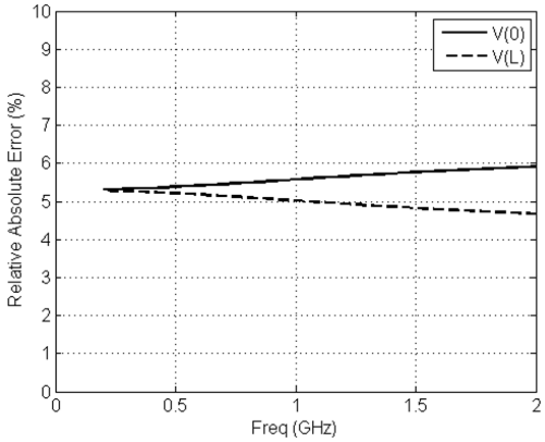


Figure 10: Relative absolute error (%) between 2D and 3D dipole.

Case 2: Two dipoles placed symmetric to each other with respect to the *x*-axis

The above setup is used to analyze the symmetrical between the two 2D and two 3D dipoles and which is placed above the ground plane and terminated with 50 Ω at the ends. Figure 11 shows the two 2D dipoles above the ground plane and at an angle of 45 degree on both sides towards the centre and both are excited with the same current. Similarly, Figure 12 shows the 3D dipole setup on the same setup of 2D dipole.

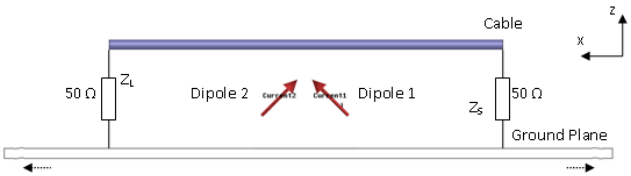


Figure 11: Two symmetric 2D dipoles used as the source of excitation.

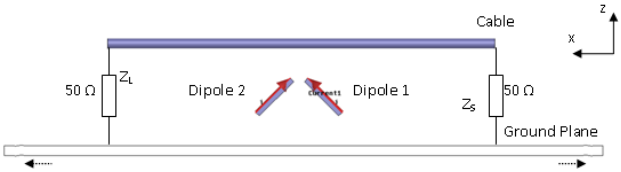


Figure 12: Two symmetric 3D dipoles used as the source of excitation.

The following figure displays the comparison results of the coupling voltage generated from the 2D and 3D dipoles. From the results it is evident that $V(0)$ and $V(L)$ of both 2D and 3D dipoles are in accordance with each other and the relative error rate also calculated and tabulated which is less than 6% as illustrated .

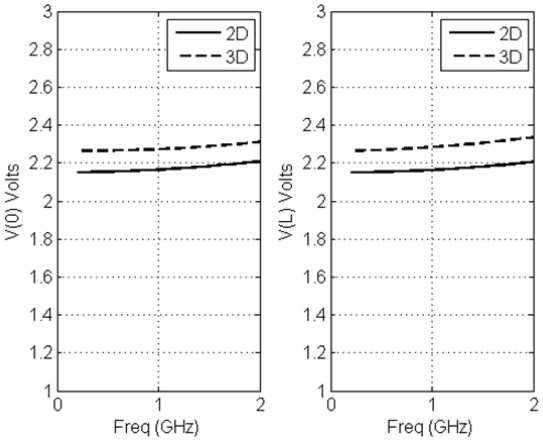


Figure 13: Comparison between the source and load voltages between 2D dipoles and 3D dipoles.

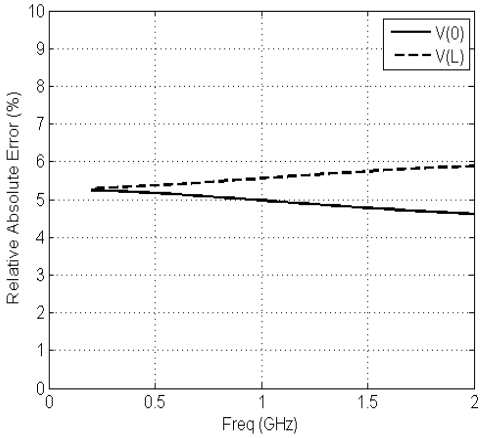


Figure 14: Relative absolute error (%) between 2D and 3D dipoles.

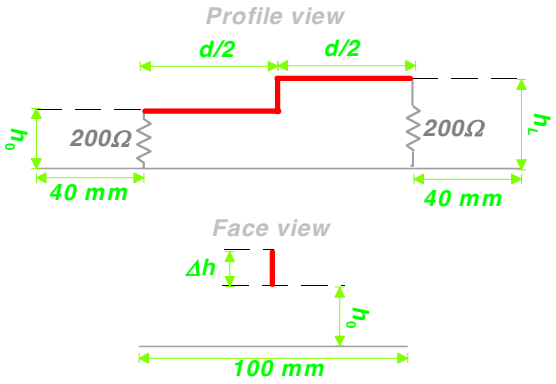
3. Validation of the proposed Hybrid Method with complex structures of cables

The hybrid method presented in this paper was also validated with realistic concrete structure. The following subsections present the results obtained. Here the complexity of the electric cable form is also taken into account.

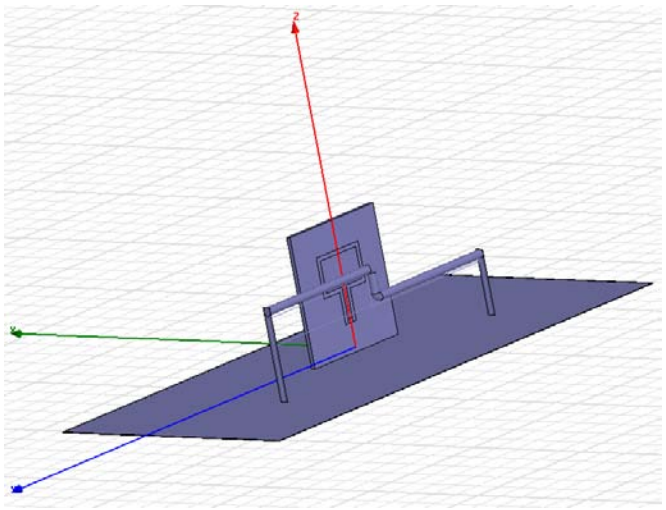
3.1. Complex structure metallic wire in the projected L shape

To demonstrate the field of validity of the hybrid method understudy, a complex configuration is considered. For that we modified the wire shape as explained in Figure 15. We recall that in this case the physical characteristic of the wire are kept the same as previously. Whereas the geometrical parameters (d = 100 mm, h_0 =20 mm, h_L =30 mm, Δh =10 mm) are changed as illustrated in Figure 15(a).

With this structure, we once again proceed with the hybrid method based on the modeling of the NF radiation associated with the analytical method for evaluating the coupling voltages. Therefore, we realize the results established with the hybrid method summed up in Table 1 which are compared with those generated from full-wave simulations. We can see that a good similarity between the two results is found with this case of complex configuration.



(a)



(b)

Figure 15: Profile and face views (a) and HFSS design (b) illustrating the configuration considered with complex form wire [43].

x_p	$V_{HFSS}(0)$	$V_{HFSS}(L)$	$V_{hybrid}(0)$	$V_{hybrid}(L)$
13 mm	208 mV	220 mV	180 mV	268 mV
14 mm	210 mV	225 mV	181 mV	275 mV
15 mm	214 mV	231 mV	183 mV	283 mV
16 mm	217 mV	237 mV	205 mV	289 mV
17 mm	219 mV	243 mV	223 mV	297 mV

Table 1: Comparison between the coupling voltages generated at the extremities of the wires obtained with full wave computation and the hybrid method proposed for the configuration shown in Figure15 [43].

4. Validation of the proposed Hybrid Method with complex structures of cables

In this subsection, we considered a radiating device constituted by the self-coil described in Figure 16. This latter is comprised of a self coil structure with core material having permittivity and permeability equal to unity. This radiating device is placed at the proximity of the metallic wire as illustrated by the HFSS design shown in Figure 16. In this case, the terminal loads are equal to $Z(0) = Z(L) = 200\ \Omega$. Figure 17 indicates the geometrical parameters of the whole structure (a = 25 mm, b = 9.3 mm, r = 1.5 mm, d = 100 mm, x_p =19 mm). The different views explain how the radiating device was placed according to the reference axes.

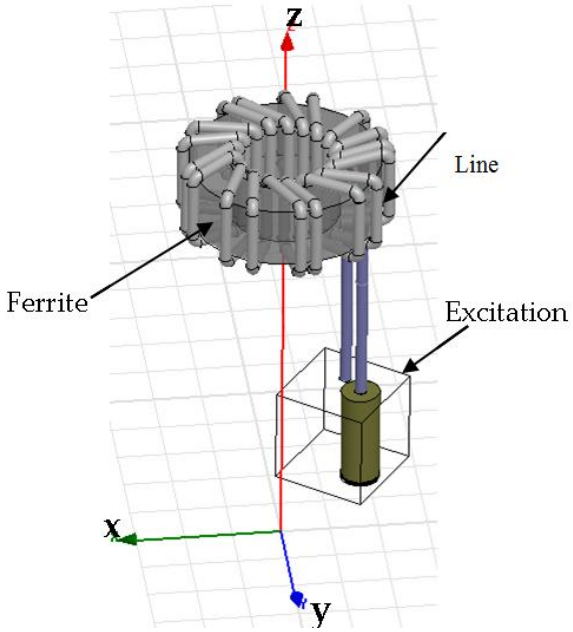


Figure 16: 3D design of the considered radiating circuit [43].

By exciting the radiating coil structure with a sine wave signal with power P_{in} = 1 W and with frequencies varied from f_1 = 100 MHz to f_2 = 500 MHz, we determine the coupling voltages at the terminations of the wire in the same way as in previous cases with the hybrid method developed. To do this, we first compute the electric-NF horizontal component and the magnetic-NF component of the EM-field radiated in the area delimited by the wire surface and the vertical axis on its extremities. Then, the Taylor's formulations were used to predict the coupling voltages desired. As results, we obtain the graphs depicted in Figure 17. It indicates the comparison of full-wave HFSS simulations and the results from the hybrid method.

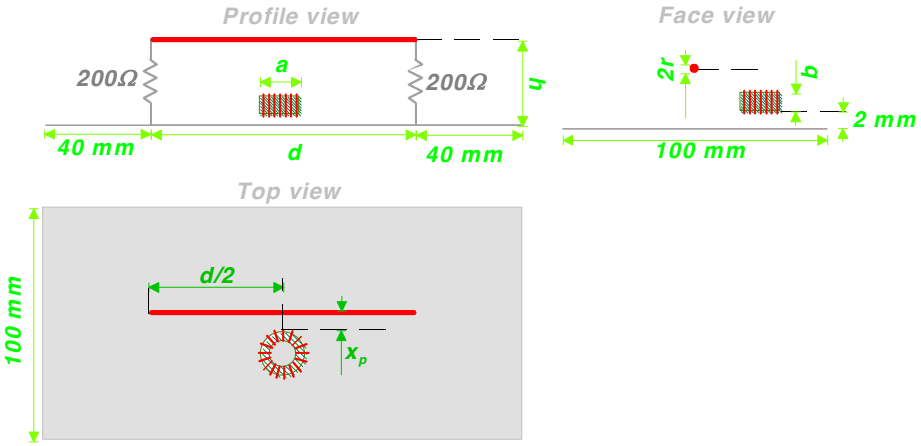


Figure 17: Geometrical description of the configuration based on the wire associated with a 3D-radiating element formed by a coil self.

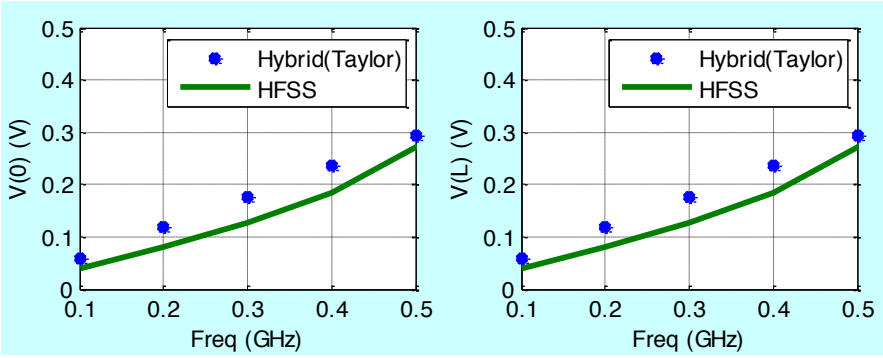


Figure 18: Comparison of coupling voltages induced with the hybrid method proposed and from HFSS [43].

5. Conclusions

This paper demonstrated the possibility of utilization of 2D and 3D dipoles as perturbation sources in the calculation of radiated coupling. A synthetic methodology based on the combination of the EM-NF radiation model and the analytical susceptibility formulation is introduced. Analytical methods are only valid if the radiating source is situated above the wires and not for the case of the radiating source placed below the wire which can be found in most of real applications. Moreover, it is very difficult also to estimate the coupling with purely analytical approach when the perturbation sources are placed close to the cable.

To address these limitations, the proposed hybrid method is being dealt with different configurations and the first section explains the advantage of investigating with complex structures of cables which is important in the real time applications. It has been investigated with the configuration shown in section 3.1 and the results obtained are in good accordance with full wave simulation and the proposed hybrid method. In the section the self coil is investigated in the MHz range and the results obtained from hybrid method and with full wave simulation and the results are in less than 10%. Hence the proposed method is capable of addressing cable immunity related to automobile applications successfully. Further it can be integrated with the PEEC method which is being developed in IRSEEM and can be validated along with measurement setup [48-50].

Acknowledgements

These research works is within the frame of the "Time Domain Electromagnetic Characterization and Simulation for EMC" (TECS) project which is part-funded by the Haute-Normandie Region (FRANCE) and the ERDF via the Franco-British INTERREG IVA European programme No 4081.

References

[1] T. Ostermann and B. Deutschmann, "TEM-cell and surface scan to identify the electromagnetic emission of integrated circuits," *in Proc. of 13th ACM Great Lakes Symp. VLSI*, Washington, DC, USA, pp. 76–79, 2003.

[2] K. Aunchaleevarapan, K. Paithoonwatanakij, W. Khan-ngern, and S. Nitta, "Novel method for predicting PCB configurations for near-field and far-field radiated EMI using a neural network," *IEICE Trans. Commun.*, Vol. E86-B, No. 4, pp. 1364–1376, Apr. 2003.

[3] F. de Daran, J. Chollet-Ricard, F. Lafon and O. Maurice, "Prediction of the field radiated at one meter from PCB's and microprocessors from near EM field cartography," *in Proc. of IEEE Int. Symp. EMC*, Istanbul, Turkey, May 2003, pp. 479–482.

[4] B. Archambeault, C. Brench and S. Connor, "Review of printed-circuit-board level EMI/EMC issues and tools," *IEEE Trans. EMC*, Vol. 52, No. 2, May 2010, pp. 455-461.

[5] T. Yang, Y. Bayram and J. L. Volakis, "Hybrid analysis of electromagnetic interference effects on microwave active circuits within cavity enclosures," *IEEE Trans. EMC*, Vol. 52, No. 3, Aug. 2010, pp. 745-748.

[6] D. Vye, "EMI by the dashboard light," *Microwave Journal*, Vol. 54, No. 7, pp. 20-23, Jul. 2011.

[7] T. Hubing, "Ensuring the Electromagnetic Compatibility of Safety Critical Automotive Systems," *Invited Plenary Speaker at the 2011 APEMC*, Jeju, South-Korea, May 2011.

[8] S. Chen, T. W. Nehl, J.-S. Lai, X. Huang, E. Pepa, R. De Doncker and I. Voss, "Towards EMI prediction of a PM motor drive for automotive applications," *in Prof of 18th Annual IEEE Applied Power Electronics Conference and Exposition*, *APEC'03*, Orlando, FL, USA, Vol. 1, pp. 14-22, 9-13 Feb. 2003.

[9] M. Wiles, "An overview of automotive EMC testing facilities," *Automotive EMC Conference 2003*, Milton Keynes, UK, Nov. 6, 2003.

[10] J. Shin, "Automotive EMC standards and testing," *Tutorial Workshop Digests on "Introduction to Automotive EMC Testing at the 2011 APEMC*, Jeju, S. Korea, May 2011.

[11] K. Liu, "An update on automotive EMC testing," *Microwave Journal*, Vol. 54, No. 7, pp. 40-46, Jul. 2011.

[12] . B. Revol, J. Roudet, J. L. Schanen and P. Loizelet, "EMI study of a three phase inverter-fed motor drives," *in Proc. of the IEEE IAS Annual Meeting 2004*, Vol. 4, pp. 2657-2664, 3-7 Oct. 2004.

[13] J. Benecke and S. Dickmann, "Analytical HF model of a low voltage DC motor armature including parasitic properties," *In Proc. of 18th Int. Symp. EMC 2007*, Honolulu, HI, 9-13 Jul. 2007.

[14] B. Mirafzal, G.L. Skibinski, R.M. Tallam, D.W. Schlegel and R.A. Lukaszewski, "Universal induction motor model with low-to-high frequency-response characteristics," *IEEE Trans. Ind. Appl.*, Vol. 43, No. 5, pp. 1233-1246, Sep. 2007.

[15] D. Baudry, A. Louis, and B. Mazari, "Characterization of the open ended coaxial probe used for near field measurements in EMC applications," *Progress in Electromagnetics Research*, *PIER*, Vol. 60, pp. 311–333, 2006.

[16] D. Baudry, L. Bouchelouk, A. Louis, and B. Mazari, "Near-field test bench for complete characterization of components radiated emission," *in Proc. of EMC Compo 2004 Conference*, Angers, France, April 2004, pp. 85-89.

[17] D. Baudry, F. Bicrel, L. Bouchelouk, A. Louis, B. Mazari, and P. Eudeline, "Near-field techniques for detecting EMI sources," *in Proc. of IEEE Int. Symp. on EMC*, Santa Clara, CA, USA, Vol. 1, pp. 11-13, Aug. 2004.

[18] Y. Vives-Gilabert, C. Arcambal, A. Louis, F. Daran, P. Eudeline and B. Mazari, "Modelling Magnetic

Radiations of Electronic Circuits using Near-Field Scanning Method," *IEEE Trans. EMC*, Vol. 49, No. 2, May 2007, pp. 391-400.

[19] Y. Vives-Gilabert, C. Arcambal, A. Louis, P. Eudeline and B. Mazari, "Modelling Magnetic Emissions Combining Image Processing and an Optimization Algorithm," *IEEE Trans. EMC*, Vol. 51, No. 4, Nov. 2009, pp. 909-918.

[20] P. Fernandez Lopez, A. Ramanujan, Y. Vives Gilabert, C. Arcambal, A. Louis, and B. Mazari, "A radiated emission model compatible to a commercial electromagnetic simulation tool," *in Proc. of 20th Int. EMC Zurich Symp.*, pp. 369-372, Zurich, Switzerland, Jan. 2009.

[21] P. Fernandez-Lopez, C. Arcambal, D. Baudry, S. Verdeyme and B. Mazari, "Radiation Modelling and Electromagnetic Simulation of an Active Circuit," *in Proc. of EMC COMPO 09*, Toulouse, France, Nov. 17-19 2009.

[22] P. Fernandez-Lopez, C. Arcambal, D. Baudry, S. Verdeyme, and B. Mazari, "Simple Electromagnetic Modelling Procedure: From Near-Field Measurements to Commercial Electromagnetic Simulation Tool," *IEEE Trans. Instrum. Meas.*, Vol. 59, No. 12, Dec. 2010, pp. 3111-3120.

[23] Antonni G., et al., ''PEEC modeling of automotive electromagnetic problems,'' *ACES Newsletter*, Vol. 23, No. 1, pp. 39-50.

[24] Agrawal, A. K. et al., "Transient response of multiconductor transmission lines excited by a no uniforme field," *Mission Research Corporation*, Albuquerque, NM 87108.

[25] Sattewhite R. S et al., "The response of a terminated two-wire transmission line excited by a nonuniform electromagnetic field," IEEE Trans. Ant. Propag., Vol. E, pp. 987-989, 1965.

[26] Rachidi. F, "Formulation of the field to transmission line coupling equations in terms of magnetic excitation field," IEEE Trans. EMC, Vol. 35, No. 3, pp. 404-407, 1993.

[27] Leseigneur, C., et al., ''Near field coupling model between electronic systems and transmission line,'' IEEE Int.Symp. EMC, Ft.Laudredale, USA, 22-27 Jul. 25-30 2010.

[28] J. J. Laurin, Z. Ouardhiri, and J. Colinas, "Near-field imaging of radiated emission sources on printed-circuit boards," *in Proc. of IEEE Int. Symp. EMC*, Aug. 2001, Vol. 1, pp. 368–373.

[29] A. Ramanujan, Z. Riah, A. Louis, and B. Mazari, "Computational Optimizations Towards an Accurate and Rapid Electromagnetic Emission Modelling," *Progress In Electromagnetics Research B*, Vol. 27, pp. 365-384, 2011.

[30] C.-N. Chiu and C.-C. Yang, "A solution for increasing immunity against the influence of ground variations on a board integrated GPS antenna", *Progress In Electromagnetics Research C*, Vol. 15, pp. 211-218, 2010.

[31] H. Xie, J. Wang, R. Fan, and Y. Liu, "Spice models for radiated and conducted susceptibility analyses of multiconductor shielded cables," *Progress In Electromagnetics Research*, *PIER 103*, pp. 241-257, 2010.

[32] L. Paletta, J. P. Parmantier, F. Issac, P. Dumas, and J. C. Alliot, "Susceptibility analysis of wiring in a complex system combining a 3-D solver and a transmission-line network simulation," *IEEE Trans. EMC,* Vol. 44, No. 2, pp. 309-317, May 2002.

[33] C. D. Taylor, R. S. Sattewhite, and C. W. Harrison, "The response of a terminated two-wire transmission line excited by a nonuniform electromagnetic field," *IEEE Trans. Ant. Prop.*, Vol. 13, No. 6, pp. 987-989, Nov. 1965.

[34] A. K. Agrawal, and H. J. Price, "Transient response of multiconductor transmission lines excited by a non uniform electromagnetic field," *IEEE Trans. Ant. Prop.*, Vol. 18, pp. 432- 435, Jun. 1980.

[35] F. Rachidi, "Formulation of the field to transmission line coupling equations in terms of magnetic excitation field," *IEEE Trans. EMC*, Vol. 35, no. 3, pp. 404-407, Aug. 1993.

[36] S. Atrous, D. Baudry, E. Gaboriaud, A. Louis, B. Mazari, and D. Blavette, "Near-field investigation of the radiated susceptibility of printed circuit boards," *in Proc. of 2008 Int. Symp. on EMC Europe*, Hamburg, Germany, 8-12 Sep. 2008.

[37] S. Atrous, "Mise en place d'une méthodologie de caractérisation en immunité champ proche de dispositifs électroniques," *PhD. Thesis, Université de Rouen*, 2009.

[38] C. Leseigneur, P. Fernandez-Lopez, C. Arcambal, D. Baudry and A. Louis, "Near-field coupling model between electronic systems and transmission line," *in Proc. of IEEE Int. Symp. EMC*, Fort Lauderdale, FL, USA, pp. 22-27, 25-30 Jul. 2010.

[39] E. R. Rajkumar, A. Ramanujan, M. Bensetti and A. Louis, "Modelling of Radiated Coupling due to Electromagnetic Field Components using Hybrid Models," *Proceedings of workshop 2emc 2010*, Rouen, France, 18-19 November 2010.

[40] E. R. Rajkumar, A. Ramanujan, M. Bensetti, and A. Louis, "On Modeling the Near-Field Coupling between an Electronic Device and a Transmission Line in the Presence of a Ground Plane," *Proceedings of Progress In Electromagnetics Research Symposium (PIERS)*, Marrakesh, Morocco, 20-23 March, 2011.

[41] E. R. Rajkumar, A. Ramanujan, M. Bensetti, B. Ravelo and A.Louis, "Comparison between Hybrid Methods in the Optimization of Radiated Coupling Calculation," *Proceedings of the 5th International Conference on electromagnetic Near-field Characterization and Imaging* (*ICONIC*) 2011, Rouen, France, 30 November– 2 December, 2011.

[42] E.R.Rajkumar, M. Bensetti, B. Ravelo A. Ramanujan, and M.Kadi, "A hybrid technique for radiated coupling exposed to near- and far-fields", (*accepted*) *Proceedings of the 16ème Colloque international sur la compatibilité électromagnétique* (*CEM*), 2012, Rouen, France, 25-27 April 2012.

[43] E. R. Rajkumar, B. Ravelo, M. Bensetti, and P. Fernandez-Lopez, "Application of a hybrid model for the susceptibility of arbitrary shape metallic wires disturbed by EM near-field radiated by electronic structures," *Progress In Electromagnetics Journal (PIER) B* 37, pp. 143-169, 2012.

[44] E. R. Rajkumar, A. Ramanujan, M. Bensetti, and A. Louis, "A Comparison and validation of Two and Three Dimensional Dipoles in the calculation of radiated coupling," *Proceedings of Progress In Electromagnetics Research Symposium (PIERS)*, Suzhou, China, 12-16 September 2011.

[45] E. R. Rajkumar, M. Bensetti, B. Ravelo and M.Kadi, "Cable immunity analysis with 2D/3D-dipoles near-field radiation", *Submitted for communication to Advanced Electromagnetics Symposium* (*AES*) *2012*, Paris, France, 16-19 April 2012.

[46] E. R. Rajkumar, M. Bensetti, B. Ravelo and M.Kadi, "Improvised PEEC method in the modeling of the near-field coupling with electrical cable", *Proceedings of Progress In Electromagnetics Research Symposium (PIERS)*, Kuala Lumpur, Malaysia, 27-30 March 2012.

[47] F. Costa and G. Rojat, "Sources de perturbations, couplages, SEM , CEM en électronique de puissance, " *D3290*, *Technique de l'ingenieur* 1999.

[48] F. Duval, A. Louis, B. Mazari, L. Pichon, K. Henry, A. Nazif, and F. De Daran, "Using hybridization between Partial Element Equivalent Circuit and Multiconductor Transmission Line to improve EMC on rear battery car," *SAE World Congress*, April 14-17, 2008, Detroit, Michigan, USA

[49] I. Yahi, F. Duval, A. Louis, and B. Mazari, "A new capacitive coupling consideration in the PEEC method," *Proc. of Workshop 2emc'07*, Oct. 18-19 2007, Rouen, France.

[50] F. Duval, "Gestion du câblage des masses électriques dans véhicule automobile – Application CEM," (in French) *Ph.D Thesis, Université de Paris XI*, 2007.

Near-field Map Radiated by Structures Disturbed by Arbitrary Transient Signals

Yang Liu and Blaise Ravelo

IRSEEM, (Institut de Recherche en Systèmes Electroniques Embarqués), EA 4353,
At the graduate school of engineering ESIGELEC,
Av. Galilée, BP 10024, 76801 Saint Etienne du Rouvray, France.
Tel.: +33 (0)2 32 91 59 71
Fax: +33 (0)2 32 91 58 59
E-mail: yang.liu@esigelec.fr, blaise.ravelo@esigelec.fr

Abstract

This paper presents a calculation method of time-domain electromagnetic (EM) near-field (NF) maps from the frequency dependent data. The method established enables to establish the time-dependent NF emitted by electronic structures excited by arbitrary wave form transient perturbations and frequency NF map data. The mechanism of the methodology is explained in details. This method is based on the combination of the fast Fourier transform and inverse fast Fourier transform (FFT/IFFT) with the 2D space domain data. For the validation process, the proposed method routine was performed with Matlab programming. Then, comparison of the ultra-short duration transient magnetic NF radiated by a planar microstrip device is made owing to the ultra-short current with time duration lower than 20 ns. The magnetic NF radiated by a planar-microstrip device simulated with a standard 3D EM simulator was analyzed. As expected, the computation results with the method proposed is well correlated to the simulations. This method developed in this paper is useful for predicting the transient EM radiations emitted by electrical/electronic systems due to the electromagnetic interference (EMI) perturbations in the power electronic and RF/digital circuits.

Keywords: Near-field (NF) emission, transient perturbations, electromagnetic compatibility (EMC), FFT, time-frequency method.

1. Introduction

Due to the complexity increase, the electromagnetic compatibility (EMC) and electromagnetic interference (EMI) characterization cannot be neglected during the design process of modern high-speed electronic equipment architectures [1-2]. This characterization seems necessarily to be more deeply deepened in particular for investigating the near-field (NF) radiations [3-7]. The NF modeling constitutes one of crucial steps of the reliability and the safety of the new electronic products. Accurate modeling method of the electromagnetic (EM) emission in near-field zone becomes one of electronic engineer designer and researcher most concerns [6-9]. To avoid the doubtful issues related to the EM coupling, this analysis seems indispensable for the modern RF/digital electronic boards vis-à-vis the increase of the integration density and the operating numerical data-speed which achieves nowadays several Gbit/s [1][9]. In this scope, the influence of time-domain EM-radiations at high RF-/microwave-frequencies especially, in near-field remains an open question for numerous electronic engineer designers. In fact, the current and voltage commutations in the non-linear electronic devices such as diodes, MOSFETs and also the amplifiers can create critical undesired transient perturbations [10-11]. Such electrical perturbations are susceptible to generate transient EM-field radiations which need to be modeled by the electronic design and manufacture engineers.

In practice, only the frequency-modeling of EM-radiation is not sufficient for the representation of certain EM-transient phenomena notably when the source of perturbation behaves as short duration flash pulse-wave. In fact, it is not enable to precise the eventual instant time and the intensity peak of the EM-pulse. That is why the time-domain representation is particularly essential for the infrequent and ultra-short duration wave emission analysis.

In order to investigate more concretely these unwanted time-domain perturbations, different modeling and measurement techniques dedicated to the characterization of EM-near-field were recently introduced and published in the literature [11-22]. Furthermore, there are several EM-solvers integrated in the commercial simulation tools for the determination of the EM-field radiations by the RF/microwave devices especially in frequency domain [23-28]. In fact, the computation method of the EM-field becomes systematically more and more complicated when considering the electronic device operates with UWB base band signals. Despite the recent investigations conducted on the FDTD method [12][14], the accuracy of the

computation results with these time-domain commercial tools remains difficult to use for the case ultra-short duration transient near-field analyses. In addition, more practical techniques [15-17] have been also introduced in particular for the measurement of the EMI in the electric- and electronic- systems. But compared to the existing frequency measurement techniques, they are not practically sufficient because the limitations either in terms of space-resolution or electro-sensitivity or simply the calibration process. So, the reconstruction of the accurate cartographies of time-dependent EM-waves in near-field is still an open challenge.

As aforementioned and discussed in [9-10], the EM-transient analysis is particularly important for the immunity prediction of mixed or analogue-digital components constituting the high-speed electronic boards regarding the eventual radiations of high power electrical circuitry as the case of neighboring hybrid electric vehicle propulsion systems.

To assess such an EMC effect, as reported in [29], the electronic circuit designers working on analogue/mixed signal (AMS) subsystems have preferred software tools such as SPICE, while those working on RF/microwave front-end components have tended to manipulate S-parameters frequency-domain design and simulation tools. By cons, currently, one needs the fusion of the both approaches as AMS engineers are required to make further analysis on the critical components by using the adequate EM simulation tools. This constitutes one of improvement techniques in the area of EMC applications. In this optic, the modeling of mixed component EM-near-field emission becomes one of the crucial steps before the implementation process. Therefore, the major issue can be caused both in frequency- and time-domains should be forecasted. For this reason, the purpose of this paper is focused on the time-domain EM-near-field calculation from the frequency-dependent data.

To cope with this limitation, one proposes in this paper, an efficient computation method based on the transform of wide bandwidth and base band frequency-dependent data for the determination of the transient EM-near-field mapping. Of course, in order to take into account the transient radiation specific to the expected use cases, an adequate excitation signal should be considered. This excitation is usually defined according to certain technical parameters (amplitude, temporal width, variation speed, time-duration…) which qualifies the undesired disturbing signal susceptible to propagate in the emitting circuits. Then, the fast Fourier transform (*fft*) mathematical treatment of the assumed disturbing signal synchronized with the given discrete frequency-dependent data in the adequate frequency range enables to determine the transient wave radiation mapping.

2. Description of the time-frequency computation method understudy

The methodology of the investigated time-frequency computation method is illustrated in detail in this section. To do this, the theoretical approach including the routine algorithm is presented.

The Fourier transform is well known as a relation enabling to transform the data sampled in time-domain into frequency-domain. With numerical computation, the Fourier transform is usually implemented as an instruction defined by fast Fourier transform (FFT). Its inverse calculation process is performed by the function called inverse fast Fourier transform (IFFT). In this paper, we will extend these functions to reconstitute the time-dependent magnetic NF maps $H_{x,y,z}(t)$ radiated by an electronic device from the frequency components $H_{x,y,z}(f)$ according to any excitation undesired currents or voltages for the EMC applications [30].

2.1. Theoretical approach of the investigated time-frequency computation method

For the beginning, let us consider the time-dependent plot of the arbitrary wave form signal $x(t)$ represented in Figure 1. This signal is considered as the excitation of the electronic structure tested. As indicated in this figure, the sampled data corresponding to this test signal is supposed and discretized from the starting time t_{min} to the stop time t_{max} with time step equal to Δt.

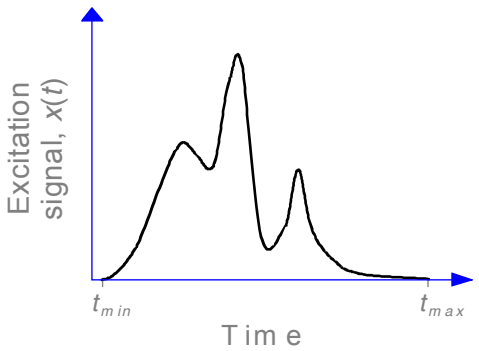


Figure 1: Example of time-dependent plot of transient excitation signal.

It means that the number of time-dependent samples noted as n is equal to:

$$n=\text{int}\left(\frac{t_{\max}-t_{\min}}{\Delta t}\right), \qquad (1)$$

with the function **int**(α) generates the lowest integer number greater than the real number α.

By definition, we can determine mathematically the frequency-dependent spectrum of *i(t)* as a complex number denoted as:

$$I(f_k) = fft\left[i(t_k)\right], \tag{2}$$

where $t_k = k \cdot \Delta t$ and $k = \{1 \cdots n\}$ .In this expression, the variable f_k represents the sampling frequency of the spectrum data. These frequencies can be extracted from the sampling time parameters by the following expression.

$$f_k = k \cdot \Delta f \,, \tag{3}$$

with $k = \{1 \cdots n\}$ and Δf is the step frequency which is determined by the relation below.

$$\Delta f = \frac{1}{t_{\max} - t_{\min}}, \tag{4}$$

In order to operate with arbitrary transient excitation signal, the frequency spectrum magnitude needs to be normalized as a complex coefficient. For this reason, $\underline{I}_0$ is assumed as a harmonic component sinusoidal current necessary for generating the electric or magnetic field spectrum $\underline{H}_0(f)$, the harmonics of the input current can be normalized with the following complex coefficients in function of the frequency:

$$\underline{c}_k = \frac{\underline{I}(f_k)}{\underline{I}_0}, \tag{5}$$

This normalization is illustrated by spectrum representation in Figure 2 [30].

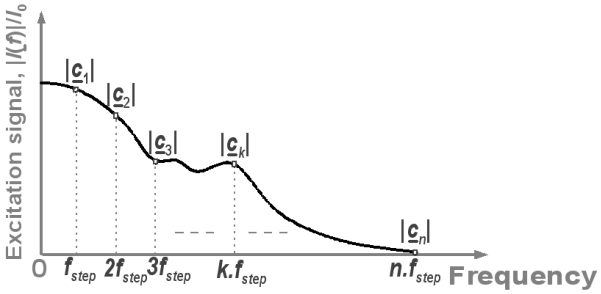


Figure 2: Extraction of the frequency spectrum coefficients from the excitation signal spectrum.

For the base band applications, it is interesting to note that the starting frequency f_{min} must be equal to the frequency step Δf. In this scope, the spectrum value can be extrapolated linearly to generate the DC-component of the excitation signal. According to the signal processing theory, the DC-component of the ultra-short transient signal is negligible at very low frequency band. So, the extrapolation operating will not change the calculation results. The upper frequency f_{max} must belong in the frequency bandwidth containing higher than 95% spectrum energy of the excitation signal.

Once, the frequency spectrum coefficients are defined, the time-dependent NF data corresponding to the transient current signal can be carried out by convoluting the frequency coefficients $\underline{c}_k$ and the frequency-domain field data. The routine process will be presented in detail in the next subsection.

2.2. Computational process of the proposed method

The computation method proposed in this paper can be generally summarized in two steps. After extracting the frequency spectrum coefficient $\underline{c}_k$ from the transient excitation signal *i*(*t*) as explained in the previous subsection, we will focus on the convolution between frequency spectrum coefficient and the frequency electric and magnetic field data.

Let us denote $\underline{H}(x, y, z_0, f)$ the frequency dependent magnetic field recorded in the plane $z = z_0$ above the considered radiating electronic device as highlighted by Figure 3.

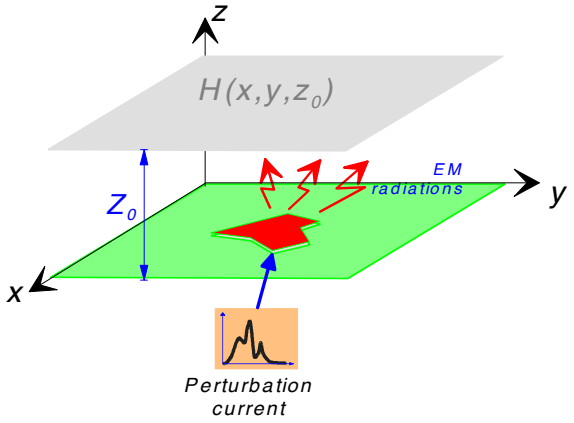


Figure 3: Representation of the magnetic NF scanned in the plane placed at height z_0 above the radiating device.

The frequency EM field data $\underline{H}(x, y, z_0, f)$ can be obtained by measurement scans or numerical computation by simulations. In this case, it is very important to emphasize that the frequency EM field data $\underline{H}(x, y, z_0, f)$ needs to be synchronized with the specific frequency interval $[f_{\min}, f_{\max}]$ of the transient excitation signal *i*(*t*) and the frequency step Δf . As presented in Figure 3, the magnetic NF time-dependent data $\underline{H}(x, y, z_0, t)$ is generated by the device under test excited by the current *i*(*t*). As argued above, the magnetic NF data $\underline{H}(x, y, z_0, t)$ can be determined with the IFFT with the convolution product of

the frequency coefficient $\underline{c}_k$ and the frequency dependent NF data $\underline{H}(x, y, z_0, f)$ via the following equation:

$$\underline{H}(x, y, z_0, t) = ifft\left[\underline{c}_k \cdot \underline{H}(x, y, z_0, f)\right], \qquad (6)$$

To reconstitute the time-domain results, the imaginary part of the data $\underline{H}(x, y, z_0, t)$ is not necessary. Therefore, the desired time-domain results are obtained with the expression:

$$H(x, y, z_0, t) = \Re eal\left[\underline{H}(x, y, z_0, t)\right], \qquad (7)$$

where the function ***Real***(α) represents the real part of the complex number α. The routine process of the proposed computation method is presented in Figure 4 [30]. This working flow is performed with different operations in order to provide the time-domain EM NF radiated by the device under test with arbitrary transient excitation signal $i(t)$.

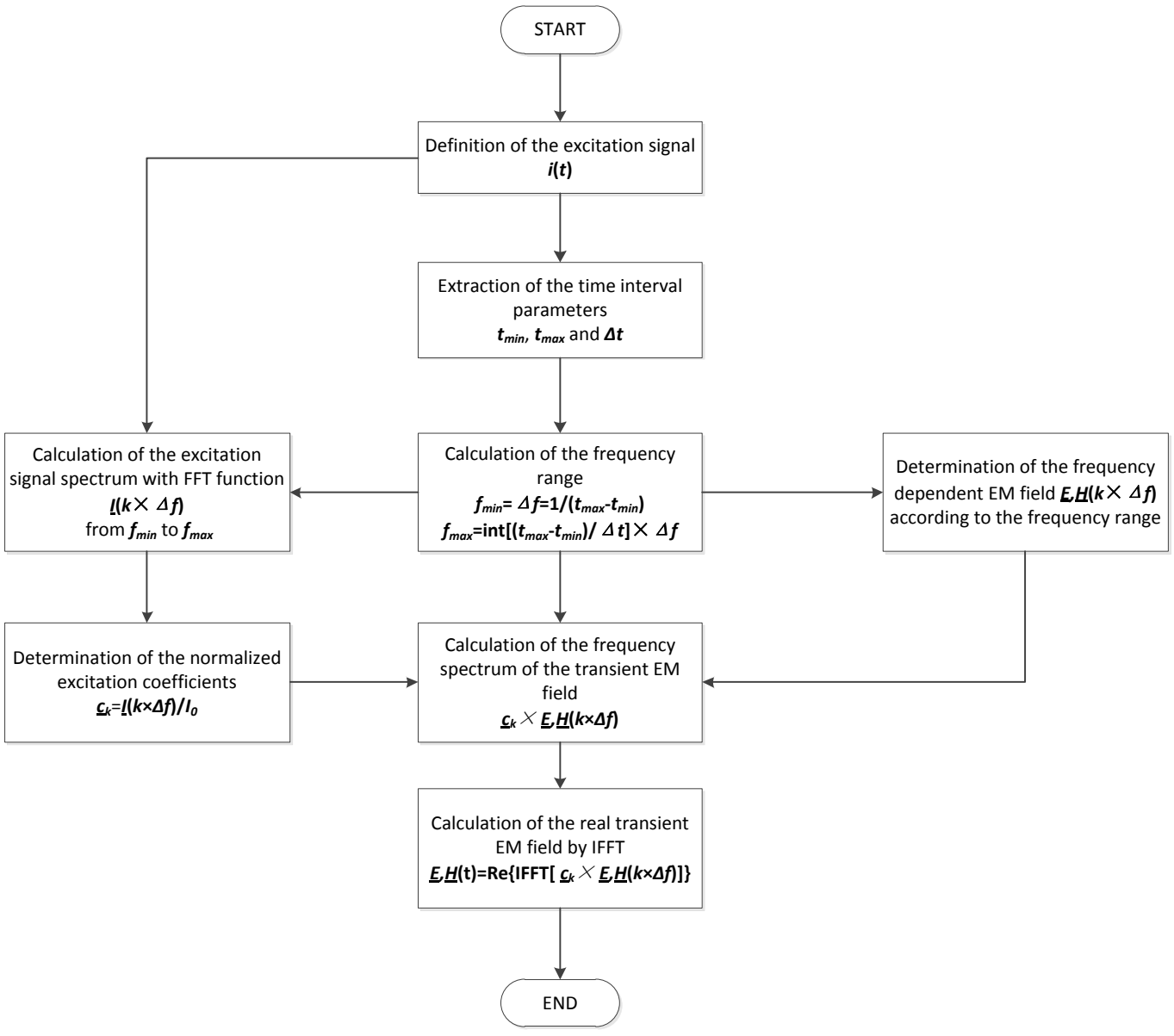


Figure 4: Routine process of the time-frequency computation method proposed.

To validate the investigated method, a Matlab program has been implemented according to the algorithm described in Figure 4.

3. Validation results

To get further insight about the feasibility of the computation method proposed, the analysis of transient EM NF wave emitted by an example of microwave device were carried out. The proof of concept was designed with the standard 3-D EM tools HFSS from ANSYS™ for generating the frequency-dependent data used for the determination of transient magnetic NF. Then, the standard computational tool CST MWS was employed to generate the reference magnetic NF mappings in time-domain.

3.1. Description of the perturbation signal considered

In order to highlight the influence of the wave form and the transient variation of the currents supposed propagating on the electronic structure under test, the considered short-duration pulse excitation current $i(t)$ is assumed as a bi-exponential form analytically defined as:

$$i(t) = I_M (e^{-\frac{t}{\tau_1}} - e^{-\frac{t}{\tau_2}}), \qquad (8)$$

with the parameters τ_1 and τ_2 are real time-constants. The numerical application was made by taking the current amplitude I_M = 1A and the time-constants $\tau_1 = \tau_2/2$ = 2 ns. In this case, we evaluate the bandwidth of the perturbation signals as $\omega_{95\%} \approx 3.07$ Giga-rad.s^{-1}.

Figure 5 displays the transient plot of this excitation current. We can see that the time interval range was defined from t_{min} = 0 ns to t_{max} = 20 ns. The sampling current $i(t_k)$ was made with the time step Δt = 0.2 ns.

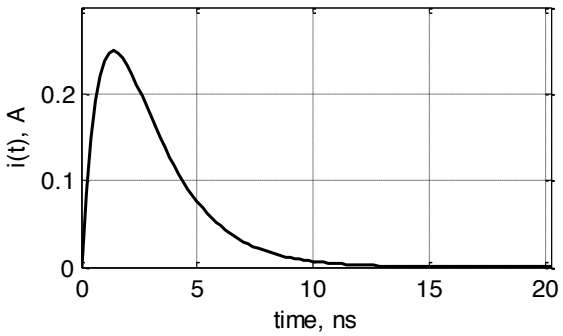


Figure 5: Transient plot of the considered excitation current $i(t)$.

Figures 6 represent the variations of the perturbation current frequency spectrum.

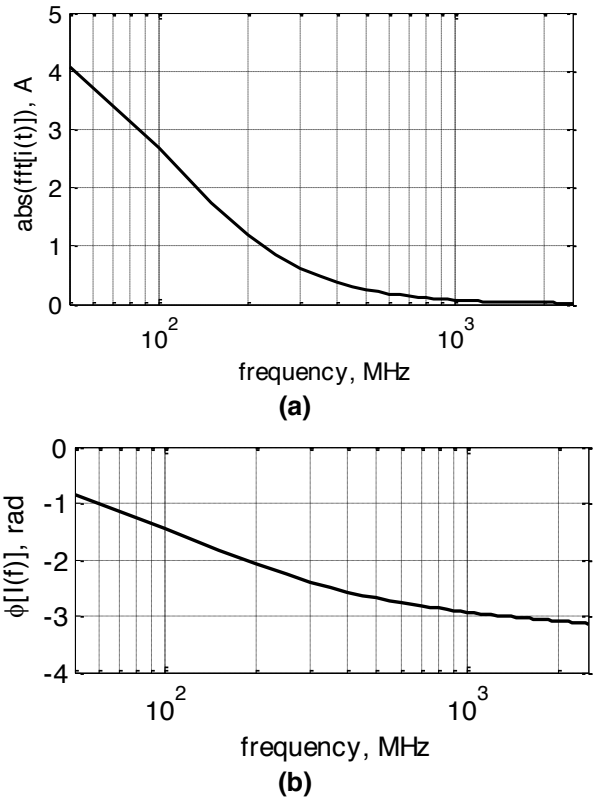
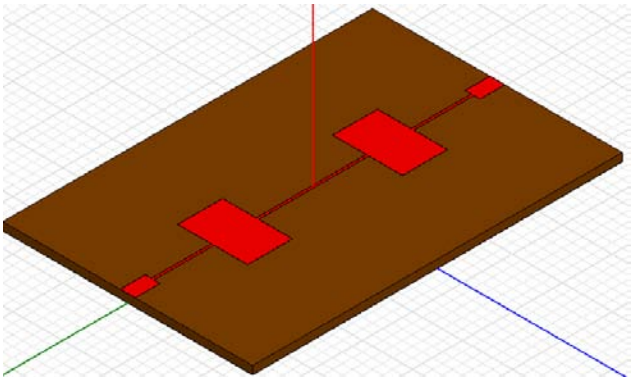


Figure 6: Frequency spectrum of $i(t)$: (a) magnitude and (b) phase.

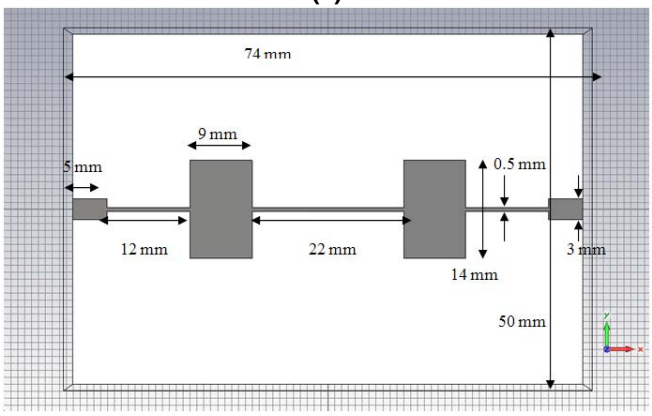
As illustrated in Figure 6(a), this base band signal presents a frequency bandwidth of about f_{max} = 2 GHz. In this frequency band belongs more than 95% of the spectrum excitation signal energy. The calculated data $\underline{I}(f) = fft[i(t)]$ implies the frequency coefficient values of $i(t)$ according to the definition expressed in (5) as described earlier in subsection 2.1.

3.2. Design of the structure under test

As a concrete proof of concept, a low-pass Tchebychev filter implemented in planar microstrip technology presented in Figures 7 was designed. This electronic structure presents geometrical dimensions L_x = 74 mm and L_y = 50 mm. The 3D representation is displayed in Figfure 7(a). Its layout top view including the geometrical dimensions is represented in Figure 7(b).



(a)



(b)

Figure 7: (a) 3D design with HFSS and (b) top view of the CST design of the low-pass microstrip filter under test.

This prototype device was printed on the FR4-epoxy substrate having relativity permittivity $\varepsilon_r = 4.4$, thickness $h =$ 1.6 mm and etched Cu-metal thickness $t = 35$ µm.

After simulations of this Tchebychev filter, the results of the next subsections are obtained.

3.3. Validation results

This subsection is divided in two paragraphs. The first one presents the reference results of the time-domain magnetic NF data simulated from the EM 3D software CST MWS with the pulse current presented in Figure 5. The last one is the results of the computational method applied to the frequency dependent data obtained from HFSS by considering the same excitation signal plotted in Figure 5.

3.3.1. Time dependent simulation results from CST MWS

By simulating this low-pass filter excited by the current shown in Figure 5 with CST MWS in the time interval range delimited by $t_{min} = 0$ ns and $t_{max} = 20$ ns step $\Delta t = 0.2$ ns, one gets the magnetic-field plots shown in Figures 8. These results correspond to the magnetic NF emission in the horizontal surface plane placed at the height $z_0 = 6$ mm above the metallic plane of the circuit under test and taken at the arbitrary instant time $t_0 = 2$ ns. It results the cartographies of the magnetic field components displayed in Figures 8. These magnetic NF components were mapped in the horizontal plane delimited by -38mm < x < 38mm with step $\Delta x = 2$ mm and -24mm < y < 24mm with physical space step $\Delta y = 2$ mm.

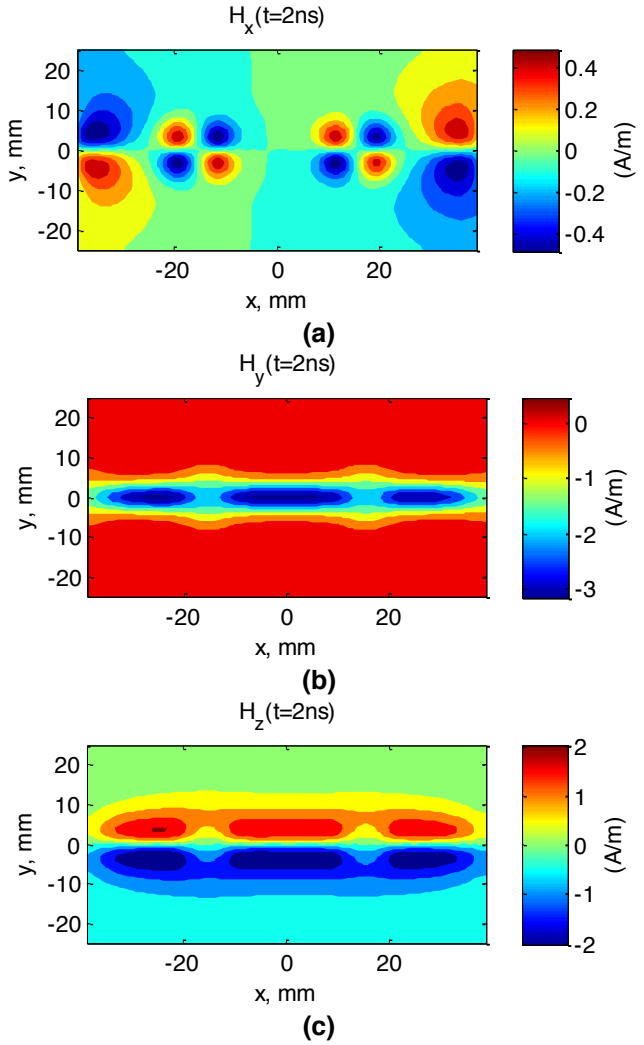


Figure 8: Cartographies of transient magnetic field components radiated by the circuit shown in Figure 5: (a) H_x, (b) H_y and (c) H_z computed from CST mapped in the horizontal plane equated by $z_0 = 6$ mm..

3.3.2. Time-dependent results from the calculation method understudy

After simulation performed with HFSS in the frequency range starting from $f_{min} = 0.05$ GHz to $f_{max} = 2.5$ GHz with step $\Delta f = 0.05$ GHz, one gets the cartographies of magnetic field component magnitudes displayed in Figures 9. These maps correspond to the numerical data mapped in the same horizontal plan as previously ($z_0 = 6$ mm). These maps were taken at the frequency $f = 1$ GHz. These HFSS computation frequency-dependent data $H_x(f)$, $H_y(f)$ and $H_z(f)$ were employed for the determination of the time dependent data

$H_x(t)$, $H_y(t)$ and $H_z(t)$ regarding the transient input current plotted in Figure 5. So that by application of the computation algorithm summarized earlier in Figure 4 of subsection 2.2, one gets the cartographies of the magnetic NF, depicted in Figure 10 at the arbitrary instant time $t_0 = 2$ ns. Despite the slight difference between the $H_z(y)$-plots from the proposed method and the CST-computation, one remarks that once again, a very good correlation between the magnetic field components computed from the standard EM-tool CST and those obtained with the developed method in the vertical cut-plan equated by $x = -5$mm is demonstrated in Figure 10.

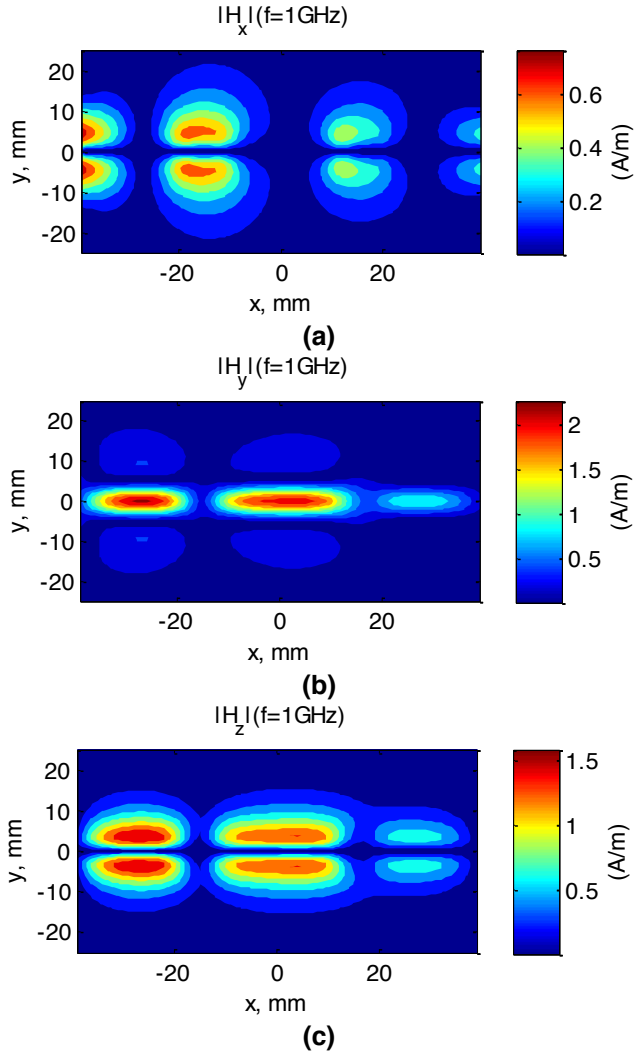


Figure 9: Cartographies of frequency-dependent magnetic NF components radiated by the circuit shown in Figure 5: (a) H_x, (b) H_y and (c) H_z computed from HFSS at $f = 1$ GHz.

The presented computation results reveal the efficiency and the utility of the proposed method for the case of elementary magnetic dipoles and also by considering the EM-radiation of realistic use case electronic devices.

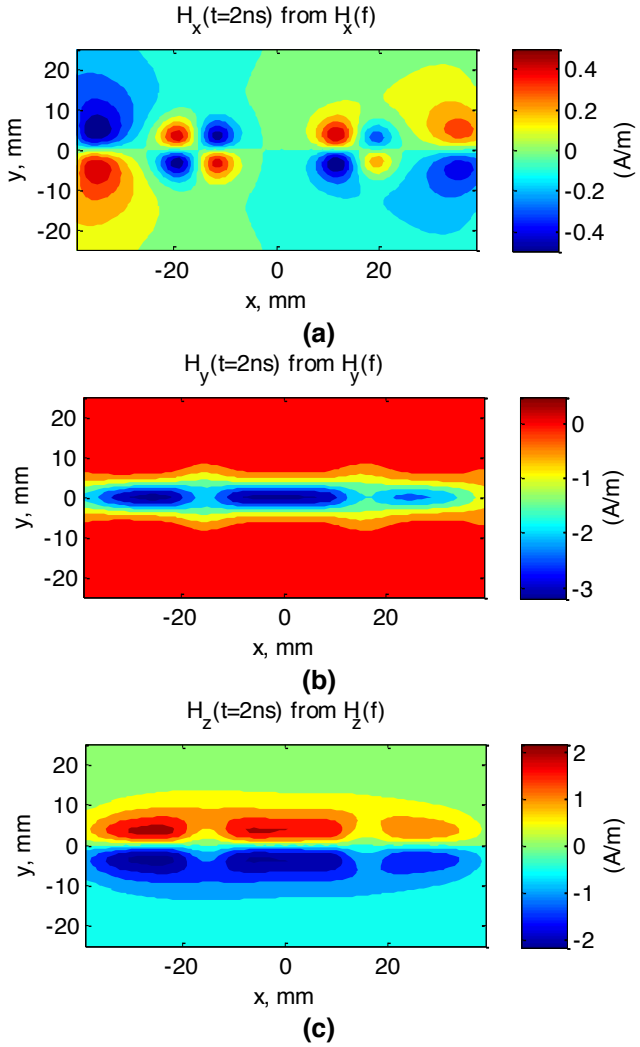


Figure 10: Cartographies of magnetic NF components obtained from the proposed method and regarding the simulated frequency-dependent data from HFSS: (a) H_x, (b) H_y and (c) H_z.

4. Conclusions

A computation method of the time-dependent magnetic NF radiated by electronic devices perturbed by ultra-short duration transient currents is successfully presented in this paper. It is based on the exploitation of the frequency-dependent mapped magnetic NF data regarding the perturbation pulse current operated with *fft*-calculations [30]. The methodological analysis was made by taking into account an arbitrary form of the transient pulse signal exciting the considered emitting radiation source. It was explained how the frequency-bandwidth of the frequency-dependent base band EM-field must be chosen according to the considered excitation current.

In order to demonstrate the relevance of the developed method, it was implemented into Matlab and applied to the

treatment of the magnetic NF radiated by concrete electronic structures. So, the feasibility of the method was demonstrated through the determination of transient magnetic NF from the frequency-dependent one emitted by the low-pass planar microstrip filter. The excitation current was assumed as an ultra-short transient pulse having half-bandwidth lower than 5 ns which presents a base band frequency spectrum with bandwidth of about 2 GHz. As results, very good agreements between the transient magnetic NF component cartographies obtained from the proposed method and those directly calculated from the referential formulations was found out.

The introduced time-domain near-field computation method is beneficial in terms of:

- ☞ Simplicity of the determination of EM NF maps according to the ultra-short duration transient excitation. So it offers a new process of time domain treatment of near-field data.
- ☞ It is flexible for various types of excitation signal which can be expressed analytically and also from the realistic use case of disturbing signal.
- ☞ It can be adapted also to different forms of electronic structures.
- ☞ With base band measured data in ultra wide bandwidth, one can achieve significant EM-field measurement in very short time duration.

However, its main drawback is the limitation in terms of time step which depends on the frequency range of the considered initial frequency-data.

In the next step of this work, we envisage to use this method to transpose in time-domain the modeling of EM-radiation with the optimized association of elementary dipoles developed in [4][5][7] for investigating the microelectronic structure NF emissions.

Acknowledgements

Acknowledgement is made to European Union (EU) and Upper Normandy region (FRANCE) for the support of this research through the European INTERREG IVA project No 4081 entitled "Time-Domain Electromagnetic Characterization and Simulation (TECS)".

References

[1] B. Archambeault, C. Brench and S. Connor, "Review of Printed-Circuit-Board Level EMI/EMC Issues and Tools," *IEEE Trans. EMC*, Vol. 52, No. 2, pp. 455-461, May 2010.

[2] T. Yang, Y. Bayram and J. L. Volakis, "Hybrid Analysis of Electromagnetic Interference Effects on Microwave Active Circuits Within Cavity Enclosures," *IEEE Trans. EMC*, Vol. 52, No. 3, pp. 745-748, Aug. 2010.

[3] J. Shi, M. A. Cracraft, J. Zhang and R. E. DuBroff, "Using Near-Field Scanning to Predict Radiated Fields," *Proc. IEEE Ant. Prop. Int. Symp.*, San Jose, CA (USA), Vol. 3, pp. 1477-1480, 1989.

[4] Y. Vives-Gilabert, C. Arcambal, A. Louis, F. Daran, P. Eudeline and B. Mazari, "Modeling Magnetic Radiations of Electronic Circuits using Near-Field Scanning Method," *IEEE Tran. EMC*, Vol. 49, No. 2, pp. 391-400, May 2007.

[5] P. Fernández-López, C. Arcambal, D. Baudry, S. Verdeyme and B. Mazari, "Radiation Modeling and Electromagnetic Simulation of an Active Circuit," *Proc. EMC Compo'09*, Toulouse, France, Nov. 17-19 2009.

[6] Z. Song, S. Donglin, F. Duval, A. Louis and D. Fei, "A Novel Electromagnetic Radiated Emission Source Identification Methodology," *Proc Asia-Pacific Symposium on EMC* (*APEMC*), Pekin, China, April 12-16 2010.

[7] Y. Vives-Gilabert, C. Arcambal, A. Louis, P. Eudeline and B. Mazari, "Modeling Magnetic Emissions Combining Image Processing and an Optimization Algorithm," *IEEE Tran. EMC*, Vol. 51, No. 4, pp. 909-918, Nov. 2009.

[8] D. Baudry, C. Arcambal, A. Louis, B. Mazari and P. Eudeline, "Applications of the Near-Field Techniques in EMC Investigations," *IEEE Trans. EMC,* Vol. 49, No. 3, pp. 485-493, Aug. 2007.

[9] P.-A. Barriere, J.-J. Laurin and Y. Goussard, "Mapping of Equivalent Currents on High-Speed Digital Printed Circuit Boards Based on Near-Field Measurements," *IEEE Trans. EMC*, Vol. 51, No. 3, pp. 649 - 658, Aug. 2009.

[10] R. Jauregui, M. Pous, M. Fernández and F. Silva "Transient Perturbation Analysis in Digital Radio," *Proc. IEEE Int. Symp. EMC*, Fort Lauderdale, Florida, USA, pp. 263-268, Jul. 25-30 2010.

[11] Y. Liu, B. Ravelo, and P. Fernandez-Lopez, "Modeling of Magnetic Near-Field Radiated by Electronic Devices Disturbed by Complex Transient Signals", *Applied Physics Research* (*APR*), Vol. 4, No. 1, pp. 3-18, Feb. 2012.

[12] R. S. Edwards, A. C. Marvin and S. J. Porter, "Uncertainty Analyses in the Finite-Difference Time-Domain Method," *IEEE Trans. EMC*, Vol. 52, No. 1, pp. 155-163, Feb. 2010.

[13] L. Liu; X. Cui and L. Qi; "Simulation of Electromagnetic Transients of the Bus Bar in Substation by the Time-Domain Finite-Element Method," IEEE Trans. EMC, Vol. 51, No. 4, Nov. 2009, pp. 1017-1025.

[14] R. Jauregui, P. I. Riu and F. Silva "Transient FDTD Simulation Validation," *Proc IEEE Int. Symp. EMC*, Fort Lauderdale, Florida, USA, pp. 257-262, Jul. 25-30 2010.

[15] Y. Liu and B. Ravelo, “Transformation champ proche temporel avec la méthode de SOP”, (in French) *Accepted for communication to Proc. 16ème Colloque international sur la compatibilité électromagnétique* (*CEM*) *2012*, Rouen, France, 25-27 Avril 2012.

[16] Y. Liu, B. Ravelo, A. K. Jastrzebski, and J. Ben Hadj Slama, “Calculation of the Time Domain z-Component of the EM-Near-Field from the x- and y-Components”, *Proc. the 41st European Microwave Conferenc*e (*EuMC*) 2011, Manchester, UK, pp. 317-320, Oct. 9-14 2011.

[17] B. Ravelo, “E-Field Extraction from H-Near-Field in Time-Domain by using PWS Method,” *Progress In Electromagnetics Research* (*PIER*) B, Vol. 25, 2010, pp. 171-189.

[18] W. Winter and M. Herbrig, “Time Domain Measurement in Automotive Applications,” *Proc. IEEE Int. Symp. EMC*, Austin, Texas, USA, pp. 109-115, Aug. 17-21 2009.

[19] T. Ordas, M. Lisart, E. Sicard, P. Maurine and L. Torres, “ Near-Field Mapping System to Scan in Time Domain the Magnetic Emissions of Integrated Circuits,” *Proc. PATMOS’ 08: Int. Workshop on Power and Timing Modeling Optimization and Simulation*, Ver. 1-11, 2009.

[20] R. Cicchetti, “Transient Analysis of Radiated Field from Electric Dipoles and Microstrip Lines,” *IEEE Trans. Ant. Prop.*, Vol. 39, No. 7, pp. 910-918, Jul. 1991.

[21] S. Braun, E. Gülten, A. Frech and P. Russer, “Automated Measurement of Intermittent Signals using a Time-Domain EMI Measurement System,” *Proc. IEEE Int. Symp. EMC*, Austin, Texas (USA), pp. 232-235, Aug. 17-21 2009.

[22] J. Rioult, D. Seetharamdoo and M. Heddebaut, “Novel Electromagnetic Field Measuring Instrument with Real-Time Visualization,” *Proc IEEE Int. Symp. EMC*, Austin, Texas (USA), pp. 133-138, Aug. 17-21 2009.

[23] M. Adada, “High-Frequency Simulation Technologies-Focused on Specific High-Frequency Design Applications,” *Microwave Engineering Europe*, pp. 16-17, Jun. 2007.

[24] Agilent EEsof EDA, “Overview: Electromagnetic Design System (EMDS),” (2008, Sep.) [Online]. Available: http://www.agilent.com/find/eesof-emds

[25] Ansoft corporation, “Simulation Software: High-performance Signal and Power Integrity,” Internal Report, 2006.

[26] ANSYS, “Unparalleled Advancements in Signal- and Power-Integrity, Electromagnetic Compatibility Testing,” (2009, Jun. 16) [Online]. Available: http://investors.ansys.com/

[27] North East Systems Associates (NESA), “RJ45 Interconnect Signal Integrity,” (2010 CST Computer Simulation Technology AG.) [Online]. Available: http://www.cst.com/Content/Applications/Article/Article.aspx?id=243

[28] M. Adada, “High-Frequency Simulation Technologies-Focused on Specific High-Frequency Design Applications,” *Microwave Engineering Europe*, pp. 16-17, Jun. 2007.

[29] R. Rammal, M. Lalande, E. Martinod, N. Feix, M. Jouvet, J. Andrieu and B. Jecko, “Far Field Reconstruction from Transient Near-Field Measurement Using Cylindrical Modal Development”, *Int. J. Ant. Prop., Hindawi*, Article ID 798473, 7 pages, Vol. 2009.

[30] B. Ravelo and Y. Liu, “Extraction of transient near-fields radiated by electronic devices from frequency data”, To be published in Intech Book chapter under the working title "*Fourier Transform / Book 1*", ISBN 979-953-307-537-1, Ed. By S. Salih, Feb. 2012.

On the Time-Domain Near-Field Radiation with PWS Method

Yang Liu[1], Blaise Ravelo[2] and Jaleleddine Ben Hadj Slama[2]

[1]IRSEEM, EA 4353, ESIGELEC,
Av. Galilée, BP 10024,
76801 Saint Etienne du Rouvray, France
Phone : +33 (0)2 32 91 59 71 / Fax : +33 (0)2 32 91 58 59
[2]LSE – National Institute of Applied Sciences and Technology, BP 676,
1080 Tunis Cedex, Tunisia
E-mail: yang.liu@esigelec.fr, blaise.ravelo@esigelec.fr, bhslama@yahoo.fr

Abstract

This article develops a computational method of electromagnetic (EM) near-field/near-field (NF/NF) transform in the time-domain for investigating the emissions of electronic structures perturbed by arbitrary form transient signals. The method proposed is aimed to the determination of the transient NF radiation at certain distances away from a given 2D NF map by using the plane wave spectrum (PWS) transform. The routine methodology of the computational method proposed is explained in details. To validate the NF/NF computational method proposed, a proof of concept based on a microstrip planar circuit was designed and simulated with a commercial EM tool. By considering a transient pulse current with some ns width, the EM NF maps at some mm above the simulated circuits were generated. Then, comparisons between results obtained with the method proposed and simulations are performed. A very good correlation between the behaviors of the EM NF from the NF/NF method and simulations is confirmed. This method is useful for the prediction transient EM emitted by complex structures for the EMC application.

Keywords: Near-field/near-field (NF/NF) transform, computational method, electromagnetic compatibility (EMC), transient EM radiation, plane wave spectrum (PWS).

1. Introduction

Facing to the unceasing development of electronic technology, the modern systems integrate more and more different hybrid functions in a confine space. For this reason, the electromagnetic interference (EMI) becomes an important malfunctioning source of various types of electrical and electronic equipments [1-8]. In this scope, the electromagnetic compatibility (EMC) characterization according to the standard requirements needs to be taken into account during the design process [9-13]. Up until now, one of the most complicated EMC problems is caused by the undesired near-field (NF) coupling effects [1][14-23]. In addition, the determination of EM NF map is one of efficient ways to predict the EMI source in order to assure the reliability and safety of new electronic products [20-22]. So, measurements techniques and modeling methods of the NF emitted by electronic systems were developed [15-23]. To investigate the influence of these unintentional NF emissions, susceptibility and immunity analyses were also realized [24-32].

Nevertheless, most of EMC NF characterizations are usually carried out in frequency-domain [1][14-23]. However, as the operating data speed achieves currently several Gbits/s with millions of transistors switch simultaneously, the frequency-domain radiating EMC characterization seems to be insufficient. In this case, the time-domain EMC analysis and modeling can be necessary to identify EMI perturbations. Till now, in our knowledge, few investigations have been done for the time-domain modeling of the EM radiated emissions [33-45]. Furthermore less research works have been made on the NF analyses in time-domain.

That is why we are motivated to propose the present method of the NF/NF transform. This method was proposed first in frequency-domain [46] and then applied in time-domain for the case of the EM elementary dipoles [47]. Theories on the transient radiation of dipoles are presented in [48-54]. The principle of this method is mainly based on the plane wave spectrum (PWS) transform associated with the fast Fourier transform as introduced in [55-60].

This article focus on a space-time computation method enabling to map the EM NF in a plane situated at a certain distance of the given 2D NF data in time-domain as proposed recently in [61-64]. The calculation is based on the plane wave spectrum (PWS) theory combined with the FFT. First, we will introduce the methodology. Then, validation results will be given to demonstrate the feasibility of the technique with a concrete device.

2. Presentation of the near- field / near-field transform in time domain

The near-field extraction method proposed in this article is based on the PWS theory combined with the plane wave propagation properties and the time-frequency transform. The methodology of the investigated computation method is detailed in this section. The theoretical approach is illustrated in the first subsection. Then, the calculation routine is represented by the working flow chart in the second subsection. Finally, validation results are presented in the next section.

2.1. Theoretical principle of the NF/NF extraction method proposed

In this section, the theoretical principle of the time-domain NF extraction method is introduced in detail. To do this, let us begin with some recall on the PWS theory.

2.1.1. Recall on the PWS theory

The PWS theory is known as an efficient method to decompose any field as a sum of plane waves propagating in different directions. It is widely used for predicting the electromagnetic radiation for EMC application.

By definition, any electric or magnetic fields in the rectangular coordinate system *(Oxyz)*, the EM field vectors $\vec{E}(x,y,z_0)$ and $\vec{H}(x,y,z_0)$ can be decomposed as a sum of its PWS components, which are respectively given mathematically by the following formulas.

$$\begin{cases} \overrightarrow{P_e}(k_x,k_y) = \int_{-\infty}^{\infty}\int_{-\infty}^{\infty} \vec{E}(x,y,z_0)\, e^{j(k_x\cdot x + k_y\cdot y)} dx\cdot dy \\ \overrightarrow{P_h}(k_x,k_y) = \int_{-\infty}^{\infty}\int_{-\infty}^{\infty} \vec{H}(x,y,z_0)\, e^{j(k_x\cdot x + k_y\cdot y)} dx\cdot dy \end{cases}. \quad (1)$$

As we can see, the PWS transform is very similar to the 2D Fourier transform. It can be implemented easily by the function of the 2D fast Fourier transform (FFT2) and the inverse 2D fast Fourier transform (IFFT2) in Matlab. So that, the inverse PWS (IPWS) transform is given by the formulas below.

$$\begin{cases} \vec{E}(x,y,z_0) = \dfrac{1}{4\pi^2}\int_{-\infty}^{\infty}\int_{-\infty}^{\infty} \overrightarrow{P_e}(k_x,k_y) e^{-j(k_x\cdot x + k_y\cdot y)} dk_x\cdot dk_y \\ \vec{H}(x,y,z_0) = \dfrac{1}{4\pi^2}\int_{-\infty}^{\infty}\int_{-\infty}^{\infty} \overrightarrow{P_h}(k_x,k_y) e^{-j(k_x\cdot x + k_y\cdot y)} dk_x\cdot dk_y \end{cases}. \quad (2)$$

In the considered coordinate system *Oxyz*, the wave vector can be decomposed with the unit vector $\left(\overrightarrow{u_x},\overrightarrow{u_y},\overrightarrow{u_z}\right)$ as the following expression.

$$\vec{k}(f) = k_x(f)\overrightarrow{u_x} + k_y(f)\overrightarrow{u_y} + k_z(f)\overrightarrow{u_x}, \quad (3)$$

In the frequency-domain, the module of the wave vector which is also called the wave number can be written as the equation below.

$$k(f) = \sqrt{k_x^2(f) + k_y^2(f) + k_z^2(f)} = \frac{2\pi}{\lambda(f)}, \quad (4)$$

with $\lambda(f) = \dfrac{c}{f}$, the propagating wavelength at the frequency f , where c is the light speed in the certain medium.

The PWS operation consists in the decomposition of the planar EM-field in its 2-D spectrum similar to fast Fourier transform known with the instruction ***fft2*** of the Matlab language. Thus, the properties of the plane wave propagation can be applied to the 2D EM field after the PWS transform. The extraction technique proposed in this article is based on the combination of the plane wave property with the PWS transform.

Let us denote that $\vec{E}(x,y,z_d)$ and $\vec{H}(x,y,z_d)$ the electric and magnetic field the height $z = z_d$ above the radiation source. Therefore, their PWS can be finally written as follows:

$$\begin{cases} \overrightarrow{p_e}_{z=z_d}\left(k_x,k_y\right) = \overrightarrow{p_e}_{z=z_0}\left(k_x,k_y\right)\cdot e^{-jk_z(z_d-z_0)} \\ \overrightarrow{p_h}_{z=z_d}\left(k_x,k_y\right) = \overrightarrow{p_h}_{z=z_0}\left(k_x,k_y\right)\cdot e^{-jk_z(z_d-z_0)} \end{cases}, \quad (5)$$

and the electric or magnetic field can be carried out by using the inverse PWS transform:

$$\begin{cases} \vec{E}(x,y,z_d) = IPWS\left[\overrightarrow{p_e}_{z=z_d}\left(k_x,k_y\right)\right] \\ \vec{H}(x,y,z_d) = IPWS\left[\overrightarrow{p_h}_{z=z_d}\left(k_x,k_y\right)\right] \end{cases}, \quad (6)$$

The principle of this NF/NF transform by using the PWS theory is also illustrated by Figure 1.

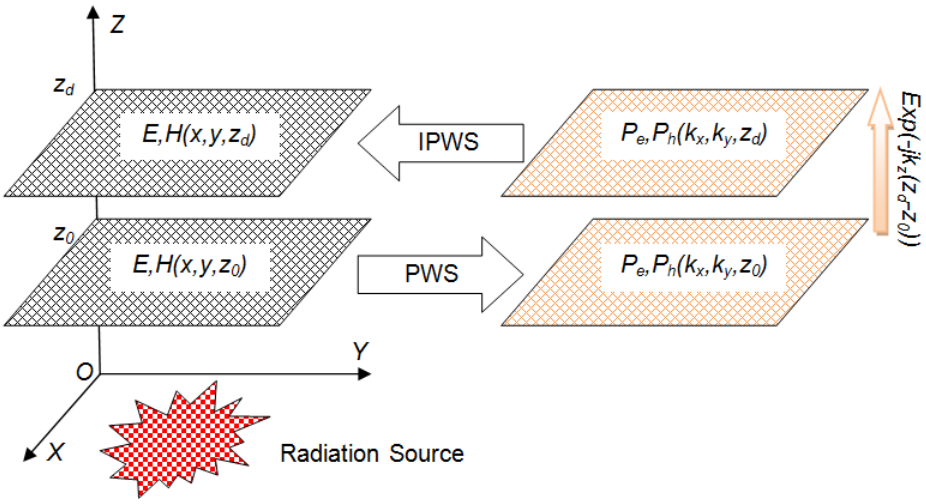


Figure 1: Principle of the NF/NF transform proposed.

2.1.2. Routine algorithm of the time-frequency computation method

It is important to note that the PWS theory can be applied only in the frequency-domain. In this article, the electric and magnetic field recorded in time-domain must be transported into the frequency-domain. The classic transform between the time- and frequency- domain is the Fourier transform.

So, first, we need calculate the frequency-domain field data from the given time-domain field data by using the function FFT in Matlab program. Then, after the NF/NF PWS transform, we apply the inverse Fourier transform to the obtained frequency-domain field data in order to achieve the time-domain field at the different height.

Figure 2 explains the different steps of the transform understudy.

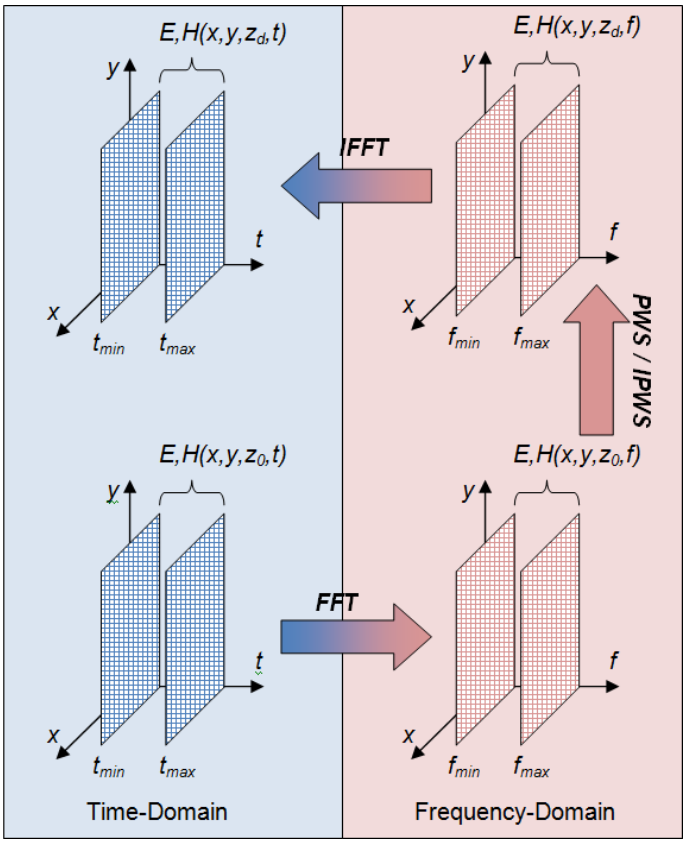


Figure 2: Different steps for extracting the EM field at different heights.

2.2. Flow method of the NF/NF transform technique

The theoretical approach is clearly introduced in the previous section. In order to implement the investigated computation method, the working flow chart summarizes the proposed method to several steps, shown by Figure 3.

For further study, a Matlab program was realized with the algorithm in Figure 3 in order to validate our proposed extraction method.

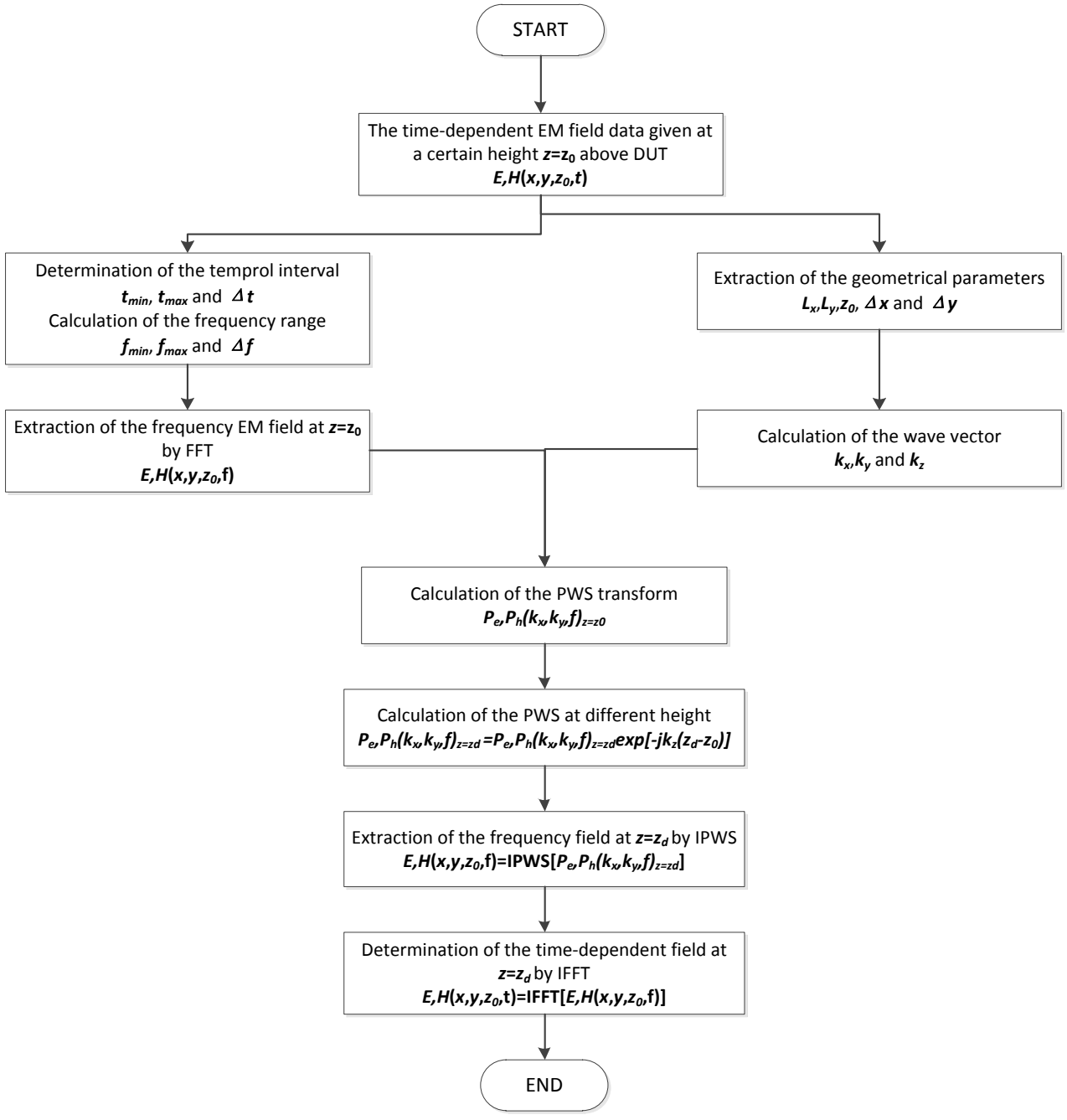


Figure 3: Routine process of the near-field/near-field transform in time-domain.

3. Validation results

This section is depicted on the application of the routine process established in Figure 3. For that, we considered the EM NF field emitted by an arbitrary shape microstrip device. We point out that the study is based on the simulations performed with the standard commercial 3D simulation solver CST Microwave Studio and the Matlab program.

3.1. Description of the device under test

First, a microstrip circular resonator displayed in Figure 4 is designed as the device under test in order to verify the feasibility of the method understudy. The resonator is based on an Alumine substrate with relative permittivity $\varepsilon_r = 10$.

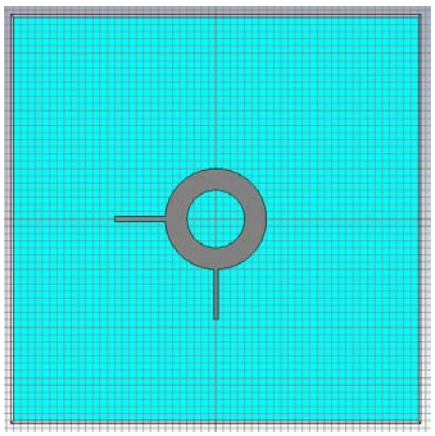


Figure 4: Overview of the microstrip circular resonator.

This circular resonator is fed by the via port with the transient current presented in Figure 5. This excitation transient current $i(t)$ as a Gaussian signal modulated 1.25 GHz sine carrier.

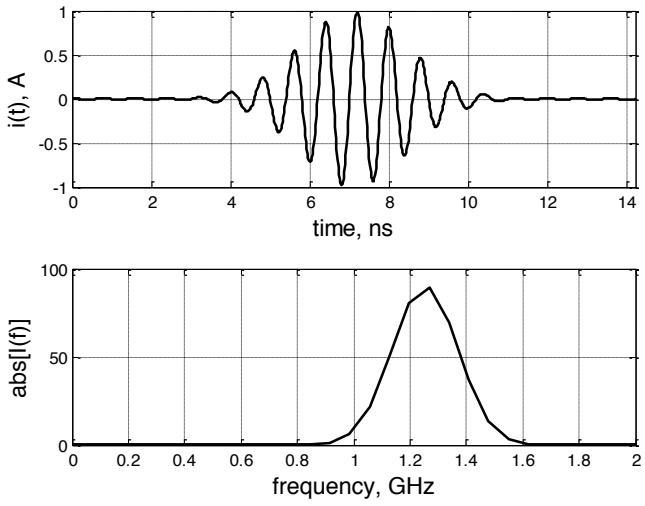


Figure 5: Transient plot of the considered excitation current $i(t)$ and the frequency spectrum $I(f)$.

To validate the method proposed in this article, comparisons of different results were made between the CST Microwave simulation and the computation method proposed.

3.2. Comparisons between different results

The comparisons of different EM field components are illustrated by the following figures.

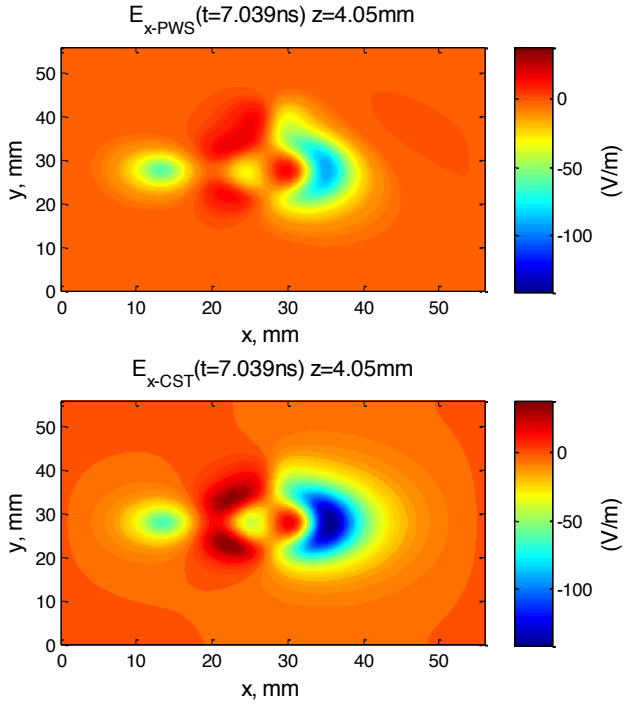


Figure 6: Comparison of E_x at z = 4.05 mm obtained by CST simulation and the proposed computation method.

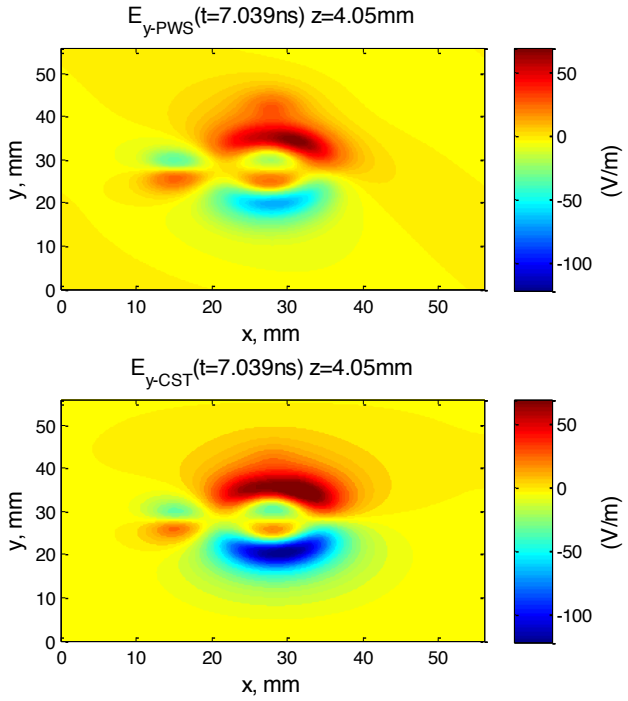


Figure 7: Comparison of E_y at z = 4.05 mm obtained by CST simulation and the proposed computation method.

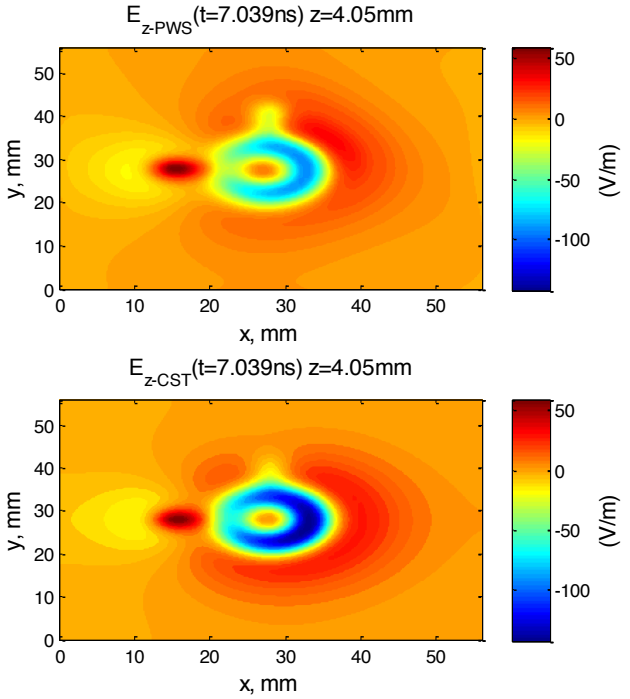


Figure 8: Comparison of E_z at z = 4.05 mm obtained by CST simulation and the proposed computation method.

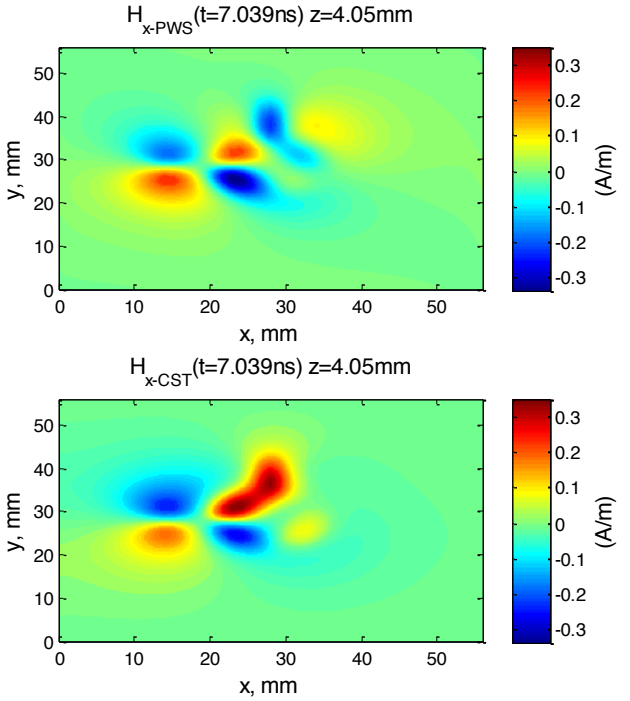


Figure 9: Comparison of H_x at z = 4.05 mm obtained by CST simulation and the proposed computation method.

From these figures, one can see the almost very good agreement can be found between the cartography of the different time-domain electric or magnetic field components achieved by the CST simulation and our proposed PWS method.

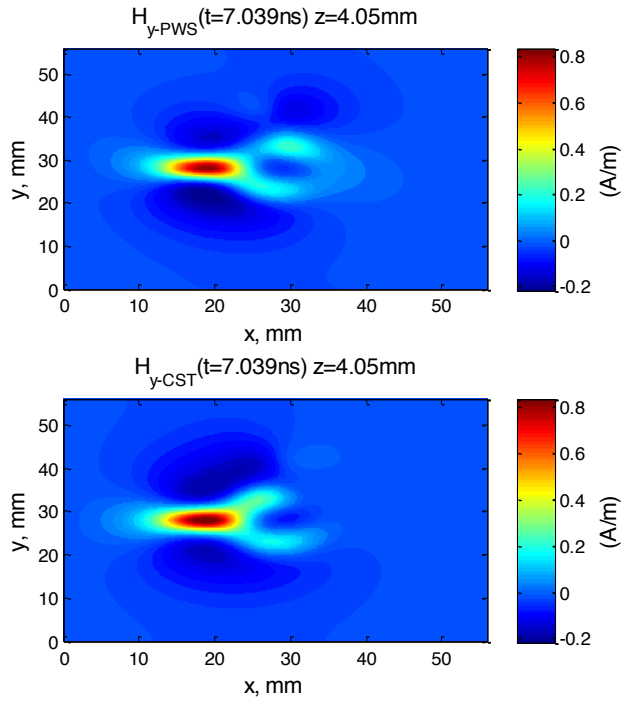


Figure 10: Comparison of H_y at z = 4.05 mm obtained by CST simulation and the proposed computation method.

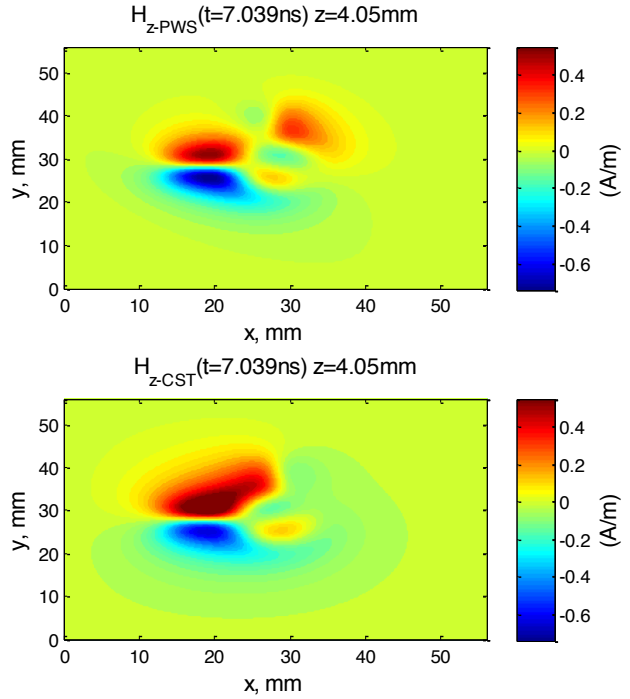


Figure 11: Comparison of H_z at z = 4.05 mm obtained by CST simulation and the proposed computation method.

However, some difference can be figured out, they might be caused by the numerical errors during the calculating process.

For further study, the profile comparisons along a line in the plane are displayed by the figures below. Once again, the good correlation can be easily found.

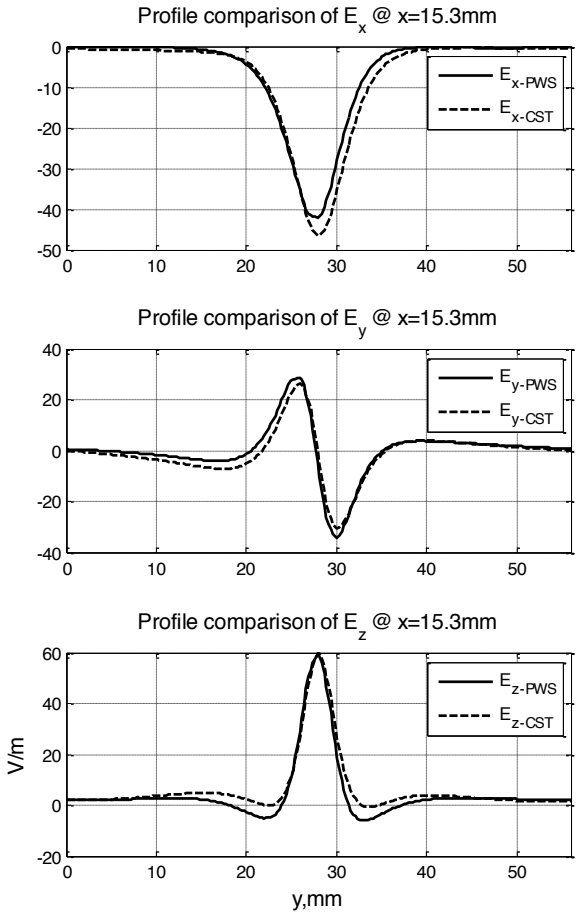


Figure 12: Comparisons of the eclectic field components profiles obtained from the proposed PWS computation method and the CST simulation, detected in the vertical cut-plan x = 15.3mm.

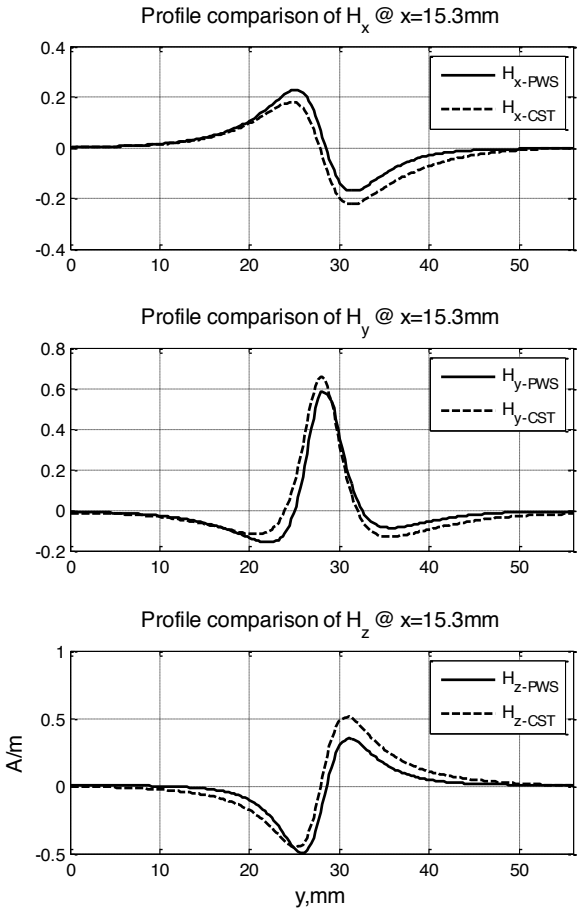


Figure 13: Comparisons of the magnetic field components profiles obtained from the proposed PWS computation method and the CST simulation, detected in the vertical cut-plan x = 15.3mm.

4. Conclusion

A computational method of the NF/NF transform in time-domain is presented in this article by using the PWS theory associated with the FFT. The fundamental principle of the method is established. The proposed method was validated by studying the EM NF radiated by a microstrip device.

First, the theoretical approach of the investigated method is given. This method is based on the combination of the PWS theory associated to the plane wave propagation property. To apply these principles to the time-dependent field data, the time-frequency transform is obviously necessary and realized by the fast Fourier transform. Then, the methodology of this NF/NF transform was illustrated and summarized in several steps by the working flow chart. The algorithm of the proposed method was implemented by a Matlab program. At the end, to get further insight of the feasibility of this method, the transient near-field radiation of a microstrip circular resonator was studied by using the 3D simulation software. The validation of the method

proposed was carried out by comparing the electric and magnetic field components obtained from the simulation and the NF/NF transform proposed. As expected, the good correlation between them was found.

The time-domain NF/NF transform method developed in this article is useful for predicting the NF radiation at a certain position. One can apparently apply this method to simplify the near-field emission modeling or measurement in time. Thus, in the prospects, we plan to extend this method for the EMC applications as introduced in [65] based on the time-frequency NF calculation algorithm developed in [66].

Acknowledgements

Acknowledgement is made to European Union (EU) and Upper Normandy region (FRANCE) for the support of this research through the European INTERREG IVA project No 4081 entitled "Time-Domain Electromagnetic Characterization and Simulation (TECS)".

References

[1] K. Aunchaleevarapan, K. Paithoonwatanakij, W. Khan-ngern and S. Nitta, "Novel method for predicting PCB configurations for near-field and far-field radiated EMI using a neural network," *IEICE Trans. Commun.*, Vol. E86-B, No. 4, pp. 1364–1376, Apr. 2003.

[2] F. de Daran, J. Chollet-Ricard, F. Lafon and O. Maurice, "Prediction of the field radiated at one meter from PCB's and microprocessors from near EM field cartography," Proc. IEEE Int. Symp. EMC, Istanbul, Turkey, pp. 479–482, May 2003.

[3] C.-N. Chiu and C.-C. Yang, "A solution for increasing immunity against the influence of ground variations on a board integrated GPS antenna", Progress In Electromagnetics Research C, Vol. 15, pp. 211-218, 2010.

[4] B. Archambeault, C. Brench and S. Connor, "Review of printed-circuit-board level EMI/EMC issues and tools," IEEE Trans. EMC, Vol. 52, No. 2, pp. 455-461, May 2010.

[5] T. Yang, Y. Bayram and J. L. Volakis, "Hybrid analysis of electromagnetic interference effects on microwave active circuits within cavity enclosures," IEEE Trans. EMC, Vol. 52, No. 3, pp. 745-748, Aug. 2010.

[6] D. Vye, "EMI by the dashboard light," Microwave Journal, Vol. 54, No. 7, pp. 20-23, Jul. 2011.

[7] T. Hubing, "Ensuring the Electromagnetic Compatibility of Safety Critical Automotive Systems," Invited Plenary Speaker at the 2011 APEMC, Jeju, S. Korea, May 2011.

[8] S. Chen, T. W. Nehl, J.-S. Lai, X. Huang, E. Pepa, R. De Doncker and I. Voss, "Towards EMI prediction of a PM motor drive for automotive applications," in Prof of 18th Annual IEEE Applied Power Electronics Conference and Exposition, APEC'03, Orlando, FL, USA, Vol. 1, pp. 14-22, 9-13 Feb. 2003.

[9] M. Wiles, "An overview of automotive EMC testing facilities," Automotive EMC Conference 2003, Milton Keynes, UK, Nov. 6, 2003.

[10] J. Shin, "Automotive EMC standards and testing," Tutorial Workshop Digests on "Introduction to Automotive EMC Testing" at the 2011 APEMC, Jeju, S. Korea, May 2011.

[11] K. Liu, "An update on automotive EMC testing," Microwave Journal, Vol. 54, No. 7, pp. 40-46, Jul. 2011.

[12] B. Revol, J. Roudet, J.L. Schanen and P. Loizelet, "EMI study of a three phase inverter-fed motor drives," in Proc. of the IEEE IAS Annual Meeting 2004, Vol. 4, pp. 2657-2664, 3-7 Oct. 2004.

[13] J. Benecke and S. Dickmann, "Analytical HF model of a low voltage DC motor armature including parasitic properties," In Proc. of 18th Int. Symp. EMC 2007, Honolulu, HI, 9-13 Jul. 2007.

[14] J. J. Laurin, Z. Ouardhiri and J. Colinas, "Near-field imaging of radiated emission sources on printed-circuit boards," *Proc. IEEE Int. Symp. EMC*, Vol. 1, pp. 368–373, Aug. 2001.

[15] T. Ostermann and B. Deutschmann, "TEM-cell and surface scan to identify the electromagnetic emission of integrated circuits," *Proc. of 13th ACM Great Lakes Symp. VLSI*, Washington, DC, USA, pp. 76–79, 2003.

[16] D. Baudry, A. Louis, and B. Mazari, "Characterization of the open ended coaxial probe used for near field measurements in EMC applications," Progress in Electromagnetics Research, PIER, Vol. 60, pp. 311–333, 2006.

[17] D. Baudry, L. Bouchelouk, A. Louis, and B. Mazari, "Near-field test bench for complete characterization of components radiated emission," Proc. EMC Compo 2004 conference, Angers, France, pp. 85-89, Apr. 2004.

[18] D. Baudry, F. Bicrel, L. Bouchelouk, A. Louis, B. Mazari, and P. Eudeline, "Near-field techniques for detecting EMI sources," Proc. IEEE Int. Symp. on EMC, Santa Clara, CA, USA, Vol. 1, pp. 11-13, Aug. 2004.

[19] Y. Vives-Gilabert, C. Arcambal, A. Louis, F. Daran, P. Eudeline and B. Mazari, "Modeling Magnetic Radiations of Electronic Circuits using Near-Field Scanning Method," IEEE Trans. EMC, Vol. 49, No. 2, pp. 391-400, May 2007.

[20] Y. Vives-Gilabert, C. Arcambal, A. Louis, P. Eudeline and B. Mazari, "Modeling Magnetic Emissions Combining Image Processing and an Optimization Algorithm," IEEE Trans. EMC, Vol. 51, No. 4, pp. 909-918, Nov. 2009.

[21] P. Fernandez Lopez, A. Ramanujan, Y. Vives Gilabert, C. Arcambal, A. Louis, and B. Mazari, "A radiated emission model compatible to a commercial electromagnetic simulation tool," in Proc. of 20th Int.

EMC Zurich Symp., pp. 369-372, Zurich, Switzerland, Jan. 2009.

[22] P. Fernandez-Lopez, C. Arcambal, D. Baudry, S. Verdeyme, and B. Mazari, "Simple Electromagnetic Modeling Procedure: From Near-Field Measurements to Commercial Electromagnetic Simulation Tool," IEEE Trans. Instrum. Meas., Vol. 59, No. 12, pp. 3111-3120, Dec. 2010.

[23] Z. Song, S. Donglin, F. Duval, A. Louis and D. Fei, "A novel electromagnetic radiated emission Source identification methodology," Asia-Pacific Symp. EMC, Pekin, China, Apr. 12-16 2010.

[24] H. Xie, J. Wang, R. Fan, and Y. Liu, "Spice models for radiated and conducted susceptibility analyses of multiconductor shielded cables," Progress In Electromagnetics Research, PIER 103, pp. 241-257, 2010.

[25] L. Paletta, J. P. Parmantier, F. Issac, P. Dumas and J. C. Alliot, "Susceptibility analysis of wiring in a complex system combining a 3-D solver and a transmission-line network simulation," IEEE Trans. EMC, Vol. 44, No. 2, pp. 309-317, May 2002.

[26] C. D. Taylor, R. S. Sattewhite and C. W. Harrison, "The response of a terminated two-wire transmission line excited by a nonuniform electromagnetic field," IEEE Trans. Ant. Prop., Vol. 13, No. 6, pp. 987-989, Nov. 1965.

[27] A. K. Agrawal and H. J. Price, "Transient response of multiconductor transmission lines excited by a non uniform electromagnetic field," IEEE Trans. Ant. Prop., Vol. 18, pp. 432- 435, Jun. 1980.

[28] F. Rachidi, "Formulation of the field to transmission line coupling equations in terms of magnetic excitation field," IEEE Trans. EMC, Vol. 35, no. 3, pp. 404-407, Aug. 1993.

[29] S. Atrous, D. Baudry, E. Gaboriaud, A. Louis, B. Mazari and D. Blavette, "Near-field investigation of the radiated susceptibility of printed circuit boards," in Proc. of 2008 Int. Symp. on EMC Europe, Hamburg, Germany, 8-12 Sep. 2008.

[30] C. Leseigneur, P. Fernandez-Lopez, C. Arcambal, D. Baudry and A. Louis, "Near-field coupling model between electronic systems and transmission line," in Proc. of IEEE Int. Symp. EMC, Fort Lauderdale, FL, USA, pp. 22-27, 25-30 Jul. 2010.

[31] E. R. Rajkumar, B. Ravelo, M. Bensetti, and P. Fernandez-Lopez, "Application of a hybrid model for the susceptibility of arbitrary shape metallic wires disturbed by EM near-field radiated by electronic structures," Progress In Electromagnetics Journal (PIER) B 37, pp. 143-169, 2012.

[32] E. R. Rajkumar, B. Ravelo, M. Bensetti, Y. Liu, P. Fernandez-Lopez, F. Duval and M. Kadi, "Experimental study of a computational hybrid method for the radiated coupling modelling between electronic circuits and electric cable", *To be published in International Journal of Advances in Engineering & Technology* (*IJAET*), Vol. 3, No. 1, Paper ID: IJAET0703711, Mar. 2012.

[33] W. Winter and M. Herbrig, "Time domain measurement in automotive applications," IEEE Int. Symp. EMC, Austin, Texas, USA, pp. 109-115, Aug. 17-21 2009.

[34] S. Braun, E. Gülten, A. Frech and P. Russer, "Automated measurement of intermittent signals using a time-domain EMI measurement system," IEEE Int. Symp. EMC, Austin, Texas, USA, pp. 232-235, Aug. 17-21 2009.

[35] J. Rioult, D. Seetharamdoo and M. Heddebaut, "Novel electromagnetic field measuring instrument with realtime visualization," IEEE Int. Symp. EMC, Austin, Texas, USA, pp. 133-138, Aug. 17-21 2009.

[36] R. S. Edwards, A. C. Marvin and S. J.Porter, "Uncertainty analyses in the finite-difference time-domain method," IEEE Trans. EMC, Vol. 52, No. 1, pp. 155-163, Feb. 2010.

[37] L. Liu, X. Cui and L. Qi, "Simulation of Electromagnetic Transients of the Bus Bar in Substation by the Time-Domain Finite-Element Method," IEEE Trans. EMC, Vol. 51, No. 4, pp. 1017-1025, Nov. 2009.

[38] R. Jauregui, P. I. Riu and F. Silva, "Transient FDTD Simulation Validation," IEEE Int. Symp. EMC, Fort Lauderdale, Florida, USA, pp. 257-262, Jul. 25-30 2010.

[39] R. Cicchetti, "Transient analysis of radiated field from electric dipoles and microstrip lines," IEEE Trans. Ant. Prop., Vol. 39, No. 7, pp. 910-918, Jul. 1991.

[40] J. Song and K.-M. Chen, "Propagation of EM pulses excited by an electric dipole in a conducting medium," IEEE Tran. Ant. Prop., Vol. 41, No. 10, pp. 1414-1421, 1993.

[41] A. Lakhtakiaa, V. K. Varadana and V. V. Varadana, "Time-harmonic and time-dependent radiation by bifractal dipole arrays," Int. J. Electronics, Vol. 63, No. 6, pp. 819-824, Dec. 1987.

[42] H. G. Schantz, "Electromagnetic energy around hertzian dipoles," IEEE Tran. Ant. Prop. Magazine, Vol. 43, No. 2, pp. 50-62, Apr. 2001.

[43] W. Jun-Hong, J. Lang and J. Shui-Sheng, "Optimization of the dipole shapes for maximum peak values of the radiating pulse," IEEE Tran. Ant. Prop. Society Int. Symp., Vol. 1, pp. 526-529, 1997.

[44] J. C.-E. Sten and A. Hujanen, "Aspects on the phase delay and phase velocity in the electromagnetic nearfield," Progress In Electromagnetics Research, Vol. 56, pp. 67-80, 2006.

[45] B. Shanker, M. A. Lu, A. Ergin and E. Michielssen, "Plane-wave time-domain accelerated radiation boundary kernels for FDTD analysis of 3D electromagnetic phenomena," IEEE Trans. Ant. Prop., Vol. 53, No. 11, pp. 3704-3716, Nov. 2005.

[46] Y. Liu, B. Ravelo, P. Fernandez-Lopez, D. Baudry and J. Ben Hadj Slama, "Near-field/near-field transform in frequency domain with PWS method", *Proc*. *5th*

International Conference on Electromagnetic Near-Field Characterization and Imaging (*ICONIC*) *2011*, Rouen, France, Nov. 30 – Dec. 2 2011.

[47] B. Ravelo, Y. Liu and J. B. H. Slama, "Time-Domain Planar Near-Field/Near-Field Transforms with PWS Method", Eur. Phys. J. Appl. Phys. (EPJAP), Vol. 53, No. 1, Feb. 2011, 30701-pp. 1-8.

[48] H. R. Hertz, "Untersuchungen ueber die Ausbreitung der elektrischen Kraft," (in German) Johann Ambrosius Barth, Leipzig, 1892.

[49] V. I. Selin, "Asymptotics of the electromagnetic field generated by a point source in a layered medium," Computational mathematics and mathematical physics, Vol. 41, No. 6, pp. 915-939, 2001.

[50] I. P. Kozlov, "Electromagnetic fields in planar-layered media close to a zero of the permittivity," J. Comm. Technol. Electron., Vol. 45, No. 5, pp. 496-502, 2000.

[51] D. D. Ebenezer and P. R. Stepanishen, "A wave-vector-time-domain technique to determine the transient acoustic radiation loading on cylindrical vibrators in an inviscid fluid with axial flow," The Journal of the Acoustical Society of America, Vol. 89, No. 1, pp. 39-51, 1991.

[52] M. Birsan, "Low-frequency transient (time domain) electromagnetic fields propagating in a marine environment," Int. J. Numerical Modelling, Devices and Fields, Vol. 17, No. 3, pp. 325-333, Apr. 2004.

[53] W. C. Chew and J. A. Kong, "Electromagnetic field of a dipole on a two-layer earth," Geophysics, Vol. 46, No. 3, pp. 309-315, Mar. 1981.

[54] S. I. Smagin and V. N. Mazalov, "Calculation of the electromagnetic fields of dipole sources in layered media," *Doklady Physics*, Vol. 50, No. 4, pp. 178-183, Apr. 2005.

[55] C. A. Balanis, *Antenna theory: Analysis and design*, 3rd ed., Wiley, New York (USA), 2005.

[56] D. T. Paris, W. M. Leach and E. B. Joy, "Basic theory of probe-compensated near-field measurements," IEEE Tran. Ant. Prop., Vol. 26, No. 3, pp. 373-379, May 1978.

[57] J. J. H. Wang, "An examination of the theory and practices of planar near-field measurement," *IEEE Tran. Ant. Prop.*, Vol. 36, No. 6, pp. 746-753, Jun. 1988.

[58] P. S. H. Leather and J. D. Parsons, "Plane wave spectra test-zone fields and simulation of antenna pattern measurements," *Electronic Letters*, Vol. 39, No. 25, pp. 1780-1782, Dec. 2003.

[59] J. Shi, M.A. Cracraft, J. Zhang, R.E. DuBroff, "Using Near-Field Scanning to Predict Radiated Fields," *IEEE Ant. Prop. Int. Symp. 1989*, San Jose, CA, USA, Vol. 3, pp. 1477-1480.

[60] J. Higashiyama, Y. Tarusawa, "Method for measuring radiated electric field excited by linear array antenna using near field to far field transformation," *Proc. 18th Int. Zurich Symp. EMC*, Munich, Germany, Sep. 24-28 2007, pp. 417-420.

[61] Y. Liu and B. Ravelo, "Calculation of Electrical Field from Magnetic Near-Field with PWS Method in Time-Domain", (Accepted for communication) *Proc. 16ème Colloque international sur la compatibilité électromagnétique* (*CEM*) *2012*, 25-27 Avril 2012, Rouen, France.

[62] Y. Liu, B. Ravelo, A. K. Jastrzebski, and J. Ben Hadj Slama, "Computational Method of Extraction of the 3D E-Field from the 2D H-Near-Field using PWS Transform", *Proc. 10th Int. Symposium on Electromagnetic Compatibility (EMC) Europe 2011*, York, UK, Sep. 26-30 2011, pp. 555-560, ISBN: 978-0-9541146-3-3.

[63] Y. Liu, B. Ravelo, A. K. Jastrzebski, and J. Ben Hadj Slama, "Calculation of the Time Domain z-Component of the EM-Near-Field from the x- and y-Components", *Proc. 41st European Microwave Conference (EuMC) 2011*, Manchester, UK, Oct. 9-14 2011, pp. 317-320.

[64] B. Ravelo, "E-field extraction from H-near-field in time-domain by using PWS method," *Progress In Electromagnetics Research B Journal*, Vol. 25, pp. 171-189, 2010.

[65] Y. Liu, B. Ravelo, and P. Fernandez-Lopez, "Modeling of Magnetic Near-Field Radiated by Electronic Devices Disturbed by Complex Transient Signals", *Applied Physics Research* (*APR*), Vol. 4, No. 1, Feb. 2012, pp. 3-18.

[66] B. Ravelo and Y. Liu, "Extraction of transient near-fields radiated by electronic devices from frequency data", To be published in Intech Book chapter under the working title "*Fourier Transform / Book 1*", ISBN 979-953-307-537-1, Ed. By S. Salih, Feb. 2012.

Experimental Reconstructions of Dielectric Targets with Metallic Inclusions by Microwave Imaging

Ricardo Monleone[1], Andrea Randazzo[2], Matteo Pastorino[2*], and Andrea Salvadè[1]

[1]University of Applied Sciences of Southern Switzerland, Manno, Switzerland
[2]University of Genoa, Genova, Italy
*corresponding author, E-mail: matteo.pastorino@unige.it

Abstract

Nondestructive imaging of dielectric targets with metallic inclusions is discussed in this paper. The proposed approach is based on the solution, by means of the distorted-wave Born approximation, of the integral equations of the inverse scattering problem. Preliminary experimental results are reported. They have been obtained by applying the developed reconstruction procedure to scattering data provided by a prototype of an imaging system working at microwave frequencies with a tomographic arrangement.

1. Introduction

This paper deals with nondestructive testing (NDT) techniques for inspecting dielectric materials. In the last years, nondestructive and noninvasive methods and systems have acquired an ever growing importance in a lot of applications, including industrial, civil, medical, and military fields. As it is well known, several techniques, based on different basic principles (e.g., ultrasounds, X-rays, and so on) have been successfully applied and continuously improved and ameliorated by research groups working in several different countries around the world.

In this scenario, a very promising approach is represented by the use of electromagnetic techniques, especially those based on microwaves [1]-[41]. In fact, microwave signals are potentially able to directly retrieve the distributions of physical parameters of the structure under test (SUT), e.g., the distributions of the dielectric permittivity and electric conductivity, starting from measures of the electromagnetic field collected outside the inspected body. Such measurements can be usually achieved by probes which are not in direct contact with the SUT.

Moreover, quite cheap imaging systems can be developed at microwave frequencies, since the required apparatuses are similar to those usually employed in telecommunication networks. Finally, they also allow for safe diagnoses, since microwaves are non-ionizing radiations and low-level powers are usually sufficient for accurate inspections of penetrable materials.

However, despite the potential significant advantages over other more consolidated techniques, most microwave NDT approaches exhibit some limitations that still prevent a wide application and commercial diffusion. In particular, the relationship relating the dielectric properties of the materials composing the SUT to the measured samples of the scattered electromagnetic field is difficult to *invert* since it is a nonlinear and usually strongly ill posed [42].

Consequently, complex and computationally expensive approaches must be devised in order to obtain accurate and reliable reconstructions in real environments. Significant computational times are also serious limiting factors for applications requiring a real or quasi-real time processing.

In this paper, an inverse scattering method based on the numerical solution of the integral equations (in their nonlinear form) relating the scattering target to the measured values of the electric field [1] is proposed.

The nonlinearity of the problem is addressed by iteratively linearizing the scattering equations by means of the distorted-wave Born approximation [43], whereas the ill-posedness of the considered inverse problem is dealt with by using an efficient regularization method based on the truncated Landweber method [44].

The electric field data are collected by using a prototype of an illuminating/measuring system working at microwave frequencies, which has been developed in [45]. This imaging system allows inspecting a SUT positioned on a rotating platform made by a weakly scattering material. The apparatus can collect multi-illumination multiview data at different heights by means of a couple of transmitting and receiving antennas. These antennas can be moved all around the SUT. The transmitted wave and the samples of the scattered electric field are obtained by using a vector network analyzer (VNA).

This paper reports examples of reconstruction results concerning the nondestructive inspection of dielectric targets with metallic inclusions. To retrieve the positions and shapes of the inclusions inside the SUT, the reconstruction of the distribution of the electric conductivity is necessary. As it is well known, retrieving the electric conductivity distribution of an inhomogeneous target is usually considered much more difficult than retrieving the distribution of the dielectric permittivity [1].

However, the possibility of locating metallic inclusions inside dielectric objects is quite appealing in several industrial applications, e.g., in the wood industry [46], where undesired metallic objects can compromise the

industrial process and may also damage the machinery used in that application.

The paper is organized as follows. Section 2 provides a description of the adopted imaging configuration. Moreover, in the same section, the reconstruction procedure is outlined, too. The prototype of the microwave tomograph is briefly described in Section 3, whereas Section 4 reports some preliminary experimental results concerning quite complex targets containing metallic inclusions. Finally, some conclusions are drawn in Section 5.

2. Imaging configuration

The developed imaging system is able to reconstruct the distributions of the dielectric properties of horizontal slices of the SUT. Essentially, it works under tomographic imaging conditions. The related configuration can be thus schematized as shown in Figure 1.

A transmitting (TX) antenna is successively positioned in S different locations $\mathbf{r}_s^{TX}$, $s = 1, \dots, S$. The TX antenna generates a set of known z-polarized incident waves, whose electric field vectors can be expressed as

$$\mathbf{e}_s^{TX}(\mathbf{r}, \omega) = e_s^{TX}(x, y, \omega)\hat{\mathbf{z}} \tag{1}$$

where ω is the working frequency. It should be noted that the proposed approach do not require plane wave illumination of the SUT.

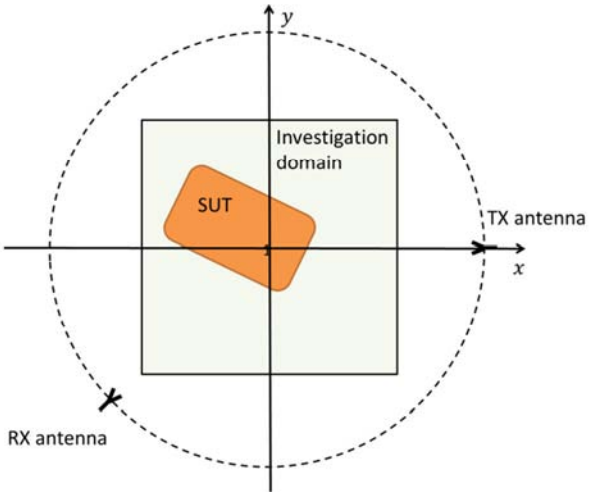


Figure 1: Schematic representation of the imaging configuration (top view).

The SUT interacts with the impinging electric field. We also assume that the SUT has a cylindrical geometry, with the cylindrical axis directed along a direction parallel to the electric field vectors of the incident electric field (i.e., the z axis).

Moreover, the dielectric properties are assumed to be independent from the z coordinate, i.e.,

$$\begin{aligned} \epsilon(\mathbf{r}) &= \epsilon(x, y) \\ \sigma(\mathbf{r}) &= \sigma(x, y) \end{aligned} \tag{2}$$

being ϵ and σ the dielectric permittivity and the electric conductivity, respectively.

From the above hypotheses it result that the resulting total electric field is z-polarized, too, and it can be written as

$$\begin{aligned} \mathbf{e}_s^{RX}(\mathbf{r}, \omega) &= e_s^{RX}(x, y, \omega)\hat{\mathbf{z}} \\ &= e_s^{scatt}(x, y, \omega)\hat{\mathbf{z}} + e_s^{TX}(x, y, \omega)\hat{\mathbf{z}} \end{aligned} \tag{3}$$

In equation (3), $e_s^{scatt}(x, y, \omega)$ is the *scattered* electric field, which is a mathematical quantity taking into account the effects of the interactions between the incident electric field and the SUT.

In the considered approach, the total electric field resulting from such interactions is measured, for any location of the transmitting antenna, by a receiving (RX) antenna successively positioned at M points, which are indicated by $\mathbf{r}_{s,m}^{RX}$, $s = 1, \dots, S$, $m = 1, \dots, M$.

From a mathematical point of view, the relationship between the measured total electric field and the dielectric properties of the SUT can be modeled by using a Lippmann-Schwinger equation, i.e.,

$$\begin{aligned} &e_s^{RX}(x, y, \omega) \\ &= e_s^{TX}(x, y, \omega) \\ &+ j\frac{k_0^2}{4}\int_D \tau(x', y')\, e_s^{RX}(x', y', \omega) H_0^{(2)}(k_0\rho) dx' dy' \end{aligned} \tag{4}$$

where $k_0 = \omega\sqrt{\epsilon_0\mu_0}$ is the free-space wavenumber (being ϵ_0 and μ_0 are the dielectric permittivity and the magnetic permeability of the vacuum, respectively). In equation (4), the *contrast function* is defined as

$$\tau(x, y) = \epsilon(x, y) - \frac{j\sigma(x, y)}{\omega\epsilon_0} - 1 \tag{5}$$

where $H_0^{(2)}$ is the Hankel function of zero-th order, and second kind, and $\rho = \sqrt{(x - x')^2 + (y - y')^2}$.

The imaging procedure is aimed at retrieving, starting from the measured samples of the total electric field collected in $S \times M$ measurement locations, the contrast function, which contains the information about the unknown distributions of the dielectric properties. Consequently, equation (4) is discretized (by using pulse basis function to represent the unknowns) and computed at the measurement positions, leading to the following discrete equation

$$\mathbf{e}^{scatt} = \mathbf{H}\mathrm{diag}(\boldsymbol{\tau})\mathbf{e}^{RX} \tag{6}$$

where

$$\mathbf{e}^{scatt} = \begin{bmatrix} e_1^{scatt}\left(x_{1,1}^{RX}, y_{1,1}^{RX}, \omega\right) \\ \vdots \\ e_S^{scatt}\left(x_{S,M}^{RX}, y_{S,M}^{RX}, \omega\right) \end{bmatrix} \tag{7}$$

is an array containing the samples of the scattered electric field at the $M \times S$ measurement points. Moreover, in equation (6), the other arrays are defined as

$$\boldsymbol{\tau} = \begin{bmatrix} \tau(x_1^D, y_1^D) \\ \vdots \\ \tau(x_N^D, y_N^D) \end{bmatrix} \tag{8}$$

and

$$\mathbf{e}^{RX} = \begin{bmatrix} e_1^{RX}(x_1^D, y_1^D, \omega) \\ \vdots \\ e_S^{RX}(x_N^D, y_N^D, \omega) \end{bmatrix} \tag{9}$$

They contain the coefficients of the pulse basis functions in the N subdomains D_n in which the investigation domain is subdivided and the values of the total electric field inside them, respectively. Finally, matrix $\mathbf{H}$ is given by

$$\mathbf{H} = j\frac{k_0^2}{4}\begin{bmatrix} h_{1,1,1} & \cdots & h_{1,1,N} \\ \vdots & \ddots & \vdots \\ h_{S,M,1} & \cdots & h_{S,M,N} \end{bmatrix} \tag{10}$$

where its elements are provided by the following relation

$$h_{s,m,n} = \int_{D_n} \tau(x', y')\, e_s^{RX}(x', y', \omega) H_0^{(2)}\left(k_0 \rho_{s,m}\right) dx' dy' \tag{11}$$

with $\rho_{s,m} = \sqrt{\left(x_{s,m}^{RX} - x'\right)^2 + \left(y_{s,m}^{RX} - y'\right)^2}$.

It is worth noting that in equation (6) the array $\mathbf{e}^{RX}$ is unknown. Consequently, a second equation is needed to solve the inverse problem. Such equation is obtained by applying (4) to points inside the investigation area. By using the same discretization adopted to discretize equation (6), one obtains the following matrix relation

$$\mathbf{e}^{TX} = \mathbf{e}^{RX} - \mathbf{G}\mathrm{diag}(\boldsymbol{\tau})\mathbf{e}^{RX} \tag{12}$$

where

$$\mathbf{e}^{TX} = \begin{bmatrix} e_1^{TX}(x_1^D, y_1^D, \omega) \\ \vdots \\ e_S^{TX}(x_N^D, y_N^D, \omega) \end{bmatrix} \tag{13}$$

is an array containing the values of the incident electric field inside the N subdomains D_n. Moreover

$$\mathbf{G}_{int} = j\frac{k_0^2}{4}\begin{bmatrix} g_{1,1} & \cdots & g_{1,N} \\ \vdots & \ddots & \vdots \\ g_{N,1} & \cdots & g_{N,N} \end{bmatrix} \tag{14}$$

is a matrix whose elements are given by

$$g_{m,n} = \int_{D_n} \tau(x', y')\, e_s^{RX}(x', y', \omega) H_0^{(2)}(k_0 \rho_m) dx' dy' \tag{15}$$

with $\rho_m = \sqrt{(x_n^D - x')^2 + (y_n^D - y')^2}$.

Equations (6) and (12) are combined together in order to obtain the following nonlinear problem

$$\mathbf{e}^{scatt} = \mathbf{H}\mathrm{diag}(\boldsymbol{\tau})\left(\mathbf{I} - \mathbf{G}\mathrm{diag}(\boldsymbol{\tau})\right)\mathbf{e}^{TX} \tag{16}$$

which needs to be solved in order to retrieve the contrast function $\boldsymbol{\tau}$. Once the contrast function has been obtained, the distributions of the dielectric parameters can be calculated by using equation (5).

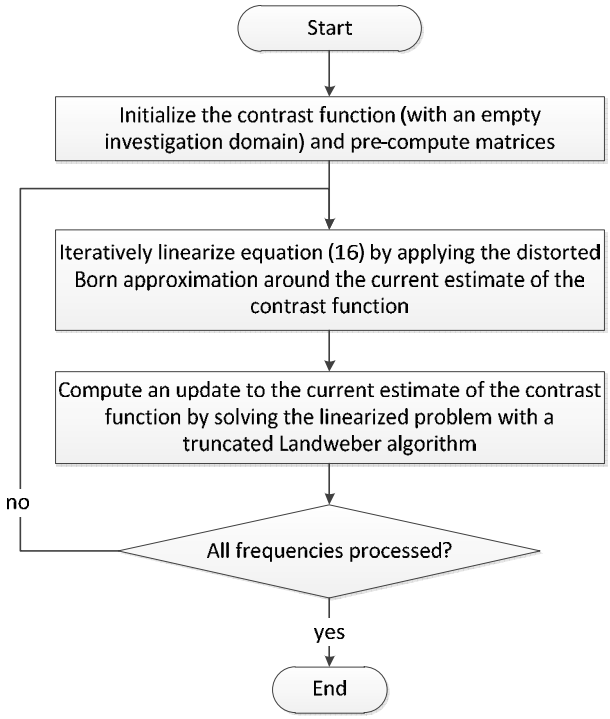


Figure 2: Flow chart of the inversion procedure.

As previously mentioned, the above inverse problem is strongly ill posed. As a consequence, a regularization method must be applied to solve equation (16).

In the developed system, in order to obtain more information from the available imaging configuration, a frequency hopping scheme [23] is also adopted, i.e., the inverse problem (16) is iteratively solved for several frequencies $\omega_1 < \omega_2 < \cdots < \omega_F$ and, at each frequency step, the solution obtained at the previous frequency is used as starting guess for the new inversion performed at the new (higher) frequency.

For any frequency, the inversion is performed by means of an iterative procedure based on a Newton-type approach. In particular, equation (16) is linearized by computing the distorted-wave Born approximation (which coincides with the Frechét derivative of the non-linear operator in (16)) and an update to the current solution is obtained by solving, in a regularized way, the obtained linear equation. In the developed approach, the linearized equation is efficiently solved by means of a truncated Landweber algorithm. For completeness, a schematic representation of the inversion procedure is reported in Figure 2.

3. Measurement system

The samples of the scattered electric field are collected by a prototype of an illuminating/measuring system working at microwave frequencies [1-6 GHz] (Figure 3). The SUT is positioned on a platform made by a weakly scattering material, which includes the investigation area.

Foam microwave absorbers surround the investigation area in order to minimize reflections due to the platform itself and to the motorized antenna actuators located underneath.

This is quite an important point and the effects of possible interfering signals have been accurately considered in [47].
The system can collect multi-illumination multi-view data at different heights by means of a pair of antennas, one transmitting and one receiving. In this application which employs a frequency stepping procedure, wideband log-periodic antennas with 8.5 dBi gain are used (Figure 4). Each antenna can independently be moved to the different illuminating/receiving positions and an additional degree of freedom is provided by the sample holder table, which can rotate around its own axis. All these movements are operated by servo-actuators.

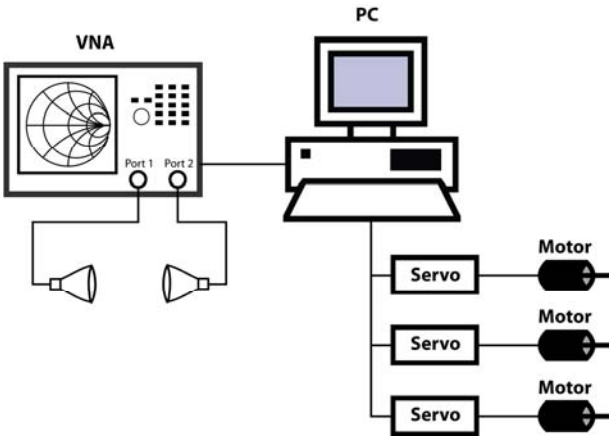


Figure 3: System block diagram of the prototype of microwave tomograph.

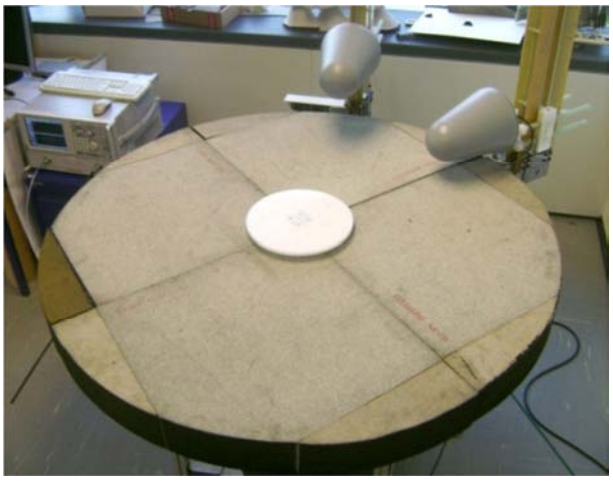


Figure 4: Prototype of microwave tomograph [45]. Investigation area and transmitting and receiving antennas.

The whole system is controlled by a PC running the custom software developed by the authors which is in charge of controlling the servos, the microwave hardware and obtaining the tomographic images.
The microwave hardware consists of a vector network analyzer (VNA) operated in transmission mode, therefore providing the microwave source for the illuminating antenna and the signal processing chain for the scattered electric field picked up by the receiving antenna. In order to increase the system's immunity against external in-band noise sources, the VNA uses a digital IF input filter configured at 300 Hz. This experimental apparatus has been previously described in [45].

4. Experimental results

An example of the results obtained by using the developed system is reported in the present Section. $S = 16$ incident waves, generated by positioning the TX antenna at

$$x_s^{TX} = R_{TX} \cos 2\pi \frac{s}{S}$$
$$y_s^{TX} = R_{TX} \sin 2\pi \frac{s}{S} \quad (17)$$

with $R_{TX} = 730\ mm$, are used to illuminate the test area. $F = 25$ frequencies uniformly distributed in the range 1-5 GHz are considered. For any view, the scattered electric field is collected in $M = 91$ measurement points, uniformly located along a circular arc with an aperture of 270 degrees and a of radius $R_{RX} = 730\ mm$, i.e.,

$$x_{s,m}^{RX} = R_{RX} \cos\left(2\pi \frac{s}{S} + \frac{\pi}{4} + \frac{3}{2}\pi \frac{m}{M-1}\right)$$
$$y_{s,m}^{RX} = R_{RX} \sin\left(2\pi \frac{s}{S} + \frac{\pi}{4} + \frac{3}{2}\pi \frac{m}{M-1}\right) \quad (18)$$

The investigation area is a square domain of side $L = 0.248\ m$, which has been discretized into $N = 63 \times 63$ square cells of side $d = 0.004\ m$.
The SUT is composed by a hollow wood beam with a rectangular cross section of $11.5\ cm \times 7.5\ cm$ and an height of $50\ cm$. A rectangular hole of size $5.5\ cm \times 3.5\ cm$ is present. Moreover, and a plastic object of section $11\ cm \times 9\ cm$ and with the same height is also present. It is located in an adjacent position with respect to the wood slab. The plastic element has a rectangular hole of size $5.3\ cm \times 3.0\ cm$) and filled with sand. The cross section of the resulting "complex" target is shown in Figure 5.
Furthermore, a cylindrical metallic inclusion with circular cross section is located inside the hole of the wood beam. The dielectric properties of the various parts composing the SUT are reported in Table 1. The conductivities of the dielectric materials have low values as compared with the one of the metallic inclusion, and thus are supposed to be negligible.
The distributions of the dielectric properties reconstructed by the developed approach are shown in Figure 6 and Figure 7.
In particular, Figure 6 provide the map of the relative dielectric permittivity of the investigation area, whereas Figure 7 shows the electric conductivity.
In both cases, the reported results are those at the end of frequency hopping loop (i.e., for $5\ GHz$). As can be seen, the reconstruction is fairly good. In particular, the image of the retrieved electric conductivity distribution allows us to locate and shape with rather good accuracy the metallic inclusion inside the hollow wood slab.
As an example of the results that are obtained by using a smaller frequency range, Figure 8 and Figure 9 report the

distributions of the dielectric properties obtained when stopping the frequency loop at 2 GHz. In the present case, although some information about the SUT can be obtained from the permittivity image (Figure 8), the retrieved conductivity profile (Figure 9) is not sufficient to provide meaningful reconstruction about the metallic inclusion.

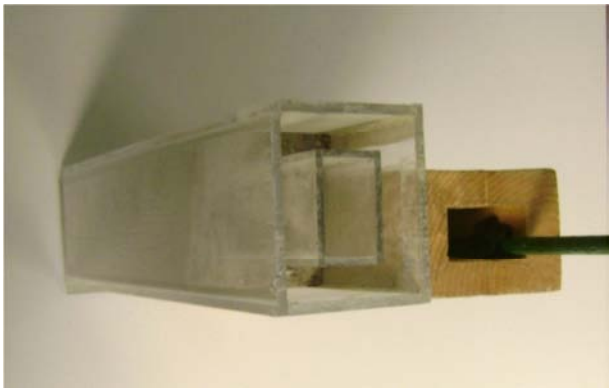


Figure 5: The cylindrical sample under test. Wood, plastic and sand (with two holes and a metallic inclusion).

Table 1: Objects' dielectric properties.

Object	size [cm]	Dielectric permittivity
Hollow wood beam	11.5 × 7.5 × 50 (hole: 5.5 × 3.5 × 50)	2.24
Hollow sand box	11 × 9 cm × 50 (hole: 5.3 × 3.0 × 50)	2.72 (plastic) 3.36 (sand)
Circular cylinder	11 mm (diameter)	Metallic

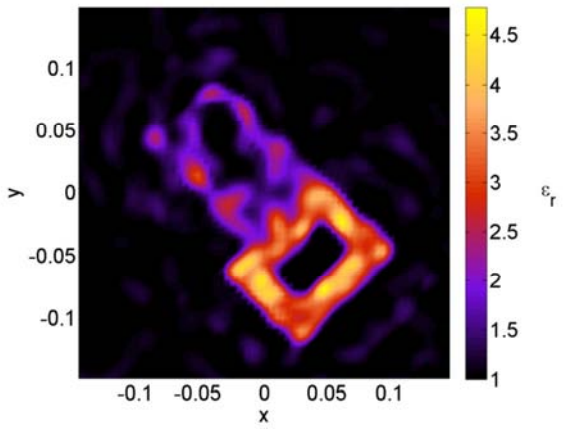


Figure 6: Reconstructed distribution of the relative dielectric permittivity. $f = 5\ GHz$.

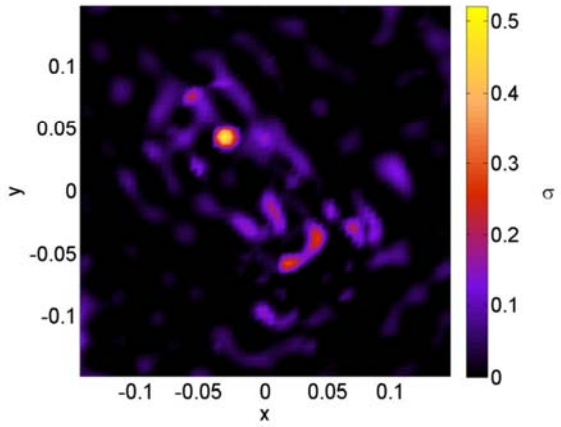


Figure 7: Reconstructed distribution of the electric conductivity. $f = 5\ GHz$.

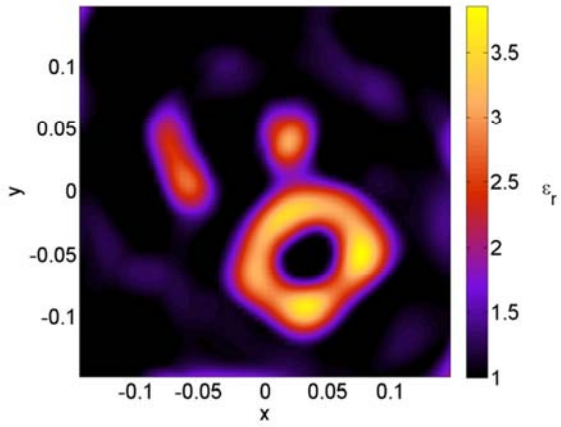


Figure 8: Reconstructed distribution of the relative dielectric permittivity. $f = 2\ GHz$.

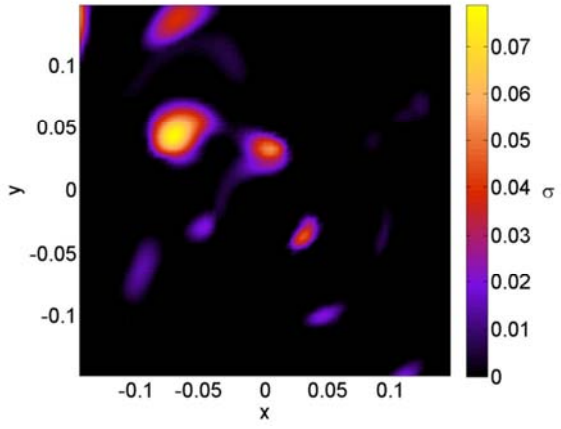


Figure 9: Reconstructed distribution of the electric conductivity. $f = 2\ GHz$.

5. Conclusions

A tomographic system for nondestructive testing of complex dielectric structures, especially developed for the inspection of wood slabs, has been considered in this paper. The system is essentially a prototype of microwave tomograph, which is able to collect multiview multi-frequency scattered field data. The acquired data have been inverted by applying a reconstruction procedure based on the distorted-Born approximation and on an efficient regularization method.

Some results concerning the reconstruction of dielectric objects with metallic inclusions have been presented. They show that the proposed approach, with a proper choice of the working frequency band, is able to provide quite accurate information about the presence of metallic inclusions. Moreover, their shapes and dimensions can retrieved quite accurately.

References

[1] M. Pastorino, *Microwave imaging*. Hoboken N.J.: John Wiley, 2010.

[2] D. Lesselier and J. Bowler, Special issue on "Electromagnetic and ultrasonic nondestructive evaluation," *Inverse Probl.,* vol. 18, 2002.

[3] P. M. van Den Berg and A. Abubakar, "Contrast source inversion method: state of the art," *Prog. Electromag. Res.*, vol. 34, pp. 189-218, 2001.

[4] S. Kharkovsky and R. Zoughi, "Microwave and millimeter wave nondestructive testing and evaluation - Overview and recent advances," *IEEE Instrum. Meas. Mag*., vol. 10, pp. 26-38, 2007.

[5] C.-C. Chen, J. T. Johnson, M. Sato, and A. G. Yarovoy, Special issue on "Subsurface sensing using ground-penetrating radar," *IEEE Trans. Geosci. Remote Sens.,* vol. 45, 2007.

[6] O. Dorn and D. Lesselier, Special issue on "Electromagnetic inverse problems: emerging methods and novel applications," *Inverse Probl.,* vol. 26, 2010.

[7] A. Baussard, E. L. Miller, and D. Lesselier, "Adaptive muliscale reconstruction of buried objects," *Inverse Probl*., vol. 20, pp. S1-S15, 2004.

[8] B. Ravelo, Y. Liu and J. Ben Hadj Slama, "Time-domain near-field/near-field transform with PWS operations," *The European Physical Journal Applied Physics*, vol. 53, 2011.

[9] Y. Liu, B. Ravelo, A. K. Jastrzebski, and J. Ben Hadj Slama, "Computational method of extraction of the 3D E-field from the 2D H-near-field using PWS transform," *Proc. 10th Int. Symposium on Electromagnetic Compatibility (EMC Europe 2011)*, York, UK, 26-30 Sept. 2011, pp. 555–560.

[10] M. El-Shenawee, O. Dorn, and M. Moscoso, "An adjoint-field technique for shape reconstruction of 3-D penetrable object immersed in lossy medium," *IEEE Trans. Antennas Propag*., vol. 57, pp. 520-534, 2009.

[11] P. M. Meaney, M. W. Fanning, D. Li, S. P. Poplack, and K. D. Paulsen, "A clinical prototype for active microwave imaging of the breast," *IEEE Trans. Microwave Theory Tech.,* vol. 48, pp. 1841-1853, 2000.

[12] C.-H. Kuo and M. Moghaddam, "Electromagnetic scattering from a buried cylinder in layered media with rough interfaces," *IEEE Trans Antennas Propag*., vol. 54, pp. 2392-2401, 2006.

[13] Z. Q. Zhang and Q. H. Liu, "Three-dimensional nonlinear image reconstruction for microwave biomedical imaging," *IEEE Trans. Biomed. Eng*., vol. 51, pp. 544-548, 2004.

[14] J. E. Johnson, T. Takenaka, K. Ping, S. Honda, and T. Tanaka, "Advances in the 3-D forward-backward time-stepping (FBTS) inverse scattering technique for breast cancer detection," *IEEE Trans. Biomed. Eng*., vol. 56, pp. 2232-2243, 2009.

[15] G. Bozza, M. Brignone, and M. Pastorino, "Application of the no-sampling linear sampling method to breast cancer detection," *IEEE Trans. Biomed. Eng*., vol. 57, no. 10, Oct. 2010.

[16] J. D. Shea, P. Kosmas, B. D. Van Veen, and S. C. Hagness, "Contrast-enhanced microwave imaging of breast tumors: a computational study using 3D realistic numerical phantoms," *Inverse Probl*., vol. 26, pp. 1-22, 2010.

[17] G. Bellizzi, O. Bucci, and I. Catapano, "Microwave cancer imaging exploiting magnetic nanoparticles as contrast agent," *IEEE Trans. Biomed. Eng*., vol. 58, pp. 2528-2536, 2011.

[18] H. Harada, D. J. N.Wall, T. Takenaka, and T. Tanaka, "Conjugate gradient method applied to inverse scattering problems," *IEEE Trans. Antennas Propag*., vol. 43, pp. 784-792, 1995.

[19] T. M. Habashy and A. Abubakar, "A general framework for constraint minimization for the inversion of electromagnetic measurements," *Prog. Electromag. Res.,* vol. 46, pp. 265-312, 2004.

[20] M. Pastorino, "Stochastic optimizationmethods applied tomicrowave imaging: A review," *IEEE Trans. Antennas Propag*., vol. 55, pp. 538-548, 2007.

[21] I. T. Rekanos, "Shape reconstruction of a perfectly conducting scatterer using differential evolution and particle swarm optimization," *IEEE Trans. Geosci. Remote Sens*., vol. 46, pp. 1967-1974, 2008.

[22] A. Litman, D. Lesselier, and F. Santosa, "Reconstruction of a two-dimensional binaryobstacle by controlled evolution of a level-set," *Inverse Probl*., vol. 14, pp. 685-706, 1998.

[23] R. Ferraye, J. Y. Dauvignac, and Ch. Pichot, "An inverse scattering method based on contour deformations by means of a level set method using frequency hopping technique," *IEEE Trans. Antennas Propag*., vol. 51, pp. 1100-1113, 2003.

[24] D. Colton, H. Haddar, and M. Piana, "The linear sampling method in inverse electromagnetic scattering theory", *Inverse Probl*., vol. 19, pp. 105-137, 2003.

[25] I. Catapano, L. Crocco, and T. Isernia, "On simple methods for shape reconstruction of unknown scatterers", *IEEE Trans. Antennas Propag*., vol. 55, pp. 1431-1436, 2007.

[26] A. Franchois and C. Pichot, "Microwave imaging-complex permittivity reconstruction with a Levenberg-Marquardt method," *IEEE Trans. Antennas Propag*., vol. 45, pp. 203-215, 1997.

[27] X. Chen, "Signal-subspace method approach to the intensity-only electromagnetic inverse scattering problem," *J. Opt. Soc. Am. A,* vol. 25, pp. 2018-2024, 2008.

[28] C. Gilmore, P. Mojabi, and J. LoVetri, "Comparison of an enhanced distorted Born iterative method and the multiplicative-regularized contrast source inversion method," *IEEE Trans. Antennas Propag*., vol. 57, pp. 2341-2351, 2009.

[29] P. Lobel, L. Blanc-Feraud, C. Pichot, and M. Barlaud, "A new regularization scheme for inverse scattering," *Inverse Probl*., vol. 13, pp. 403-410, 1997.

[30] P. Mojabi and J. LoVetri, "Overview and classification of some regularization techniques for the Gauss-Newton inversion method applied to inverse scattering problems," *IEEE Trans. Antennas Propag*., vol. 57, pp. 2658-2665, 2009.

[31] A. Randazzo, M. A. Abou-Khousa, M. Pastorino, R. Zoughi, "Direction of arrival estimation based on Support Vector Regression: Experimental validation and comparison with MUSIC," *IEEE Antennas Wireless Propagat. Lett.*, vol. 6, pp. 379-382, 2007.

[32] G. Oliveri, A. Randazzo, M. Pastorino, A. Massa, "Imaging of separate scatterers by means of a multiscaling multiregion Inexact-Newton approach," *Prog. Electromag. Res.*, vol. 18, pp. 247-257, 2011.

[33] J. T. Case, A. Randazzo, M. Pastorino, R. Zoughi, "Evaluation of reconstruction error in microwave holographic imaging with reduced data sets," *Proceeding of the European Microwave Association* (EuMA), vol. 4, no. 1, pp. 3-10, 2008.

[34] W. Yang, G. Giakos, K. Nikita, M. Pastorino, D. Karras, "Imaging systems and techniques (Editorial)," *Meas. Sci. Technol.*, vol. 20, p. 100101, 2009.

[35] M. Pastorino, "Numerical and experimental reconstructions in microwave imaging of dielectric targets by an Inexact-Newton method: A review," *Proc. Assemblée Générale du GDR Ondes: "Interferences d'ondes"*, Nice, France, 24- 26 Oct. 2011.

[36] M. Pastorino, C. Estatico, A. Randazzo, "A novel regularization scheme for electromagnetic inverse problems," *Proc. European Geosciences Union General Assembly*, Wien, Austria, April 3-8, 2011.

[37] M. Maffongelli, A. Salvadè, R. D. Monleone, S. Poretti, M. Pastorino, A. Randazzo, "Microwave axial tomograph for medical applications: Preliminary set-up configuration," *Proc. IEEE 6th International Symposium on Medical Measurement and Applications (MeMeA 2011)*, Bari, Italy, 30-31 May, pp. 176-181, 2011.

[38] M. Maffongelli, R. Monleone, M. Pastorino, S. Poretti A. Randazzo, A. Salvadè, "Nondestructive inspection of wood materials by a microwave imaging approach - Experimental results", *Proc. 5th International Conference on electromagnetic Near-field (NF) Characterization and Imaging (ICONIC 2011)*, Rouen, France, Nov. 30-Dec. 2, paper 2C, 2011.

[39] A. Randazzo, M. Pastorino, "Microwave detection of unknown targets by using Support Vector Machines," *Proc. 2009 IEEE International Workshop on Imaging Systems and Techniques (IEEE IST09)*, Shenzhen, China, May 11-12, pp. 141-146, 2009.

[40] M. Pastorino, A. Salvadé, R. Monleone, T. Bartesaghi, G. Bozza, and A. Randazzo, "A numerical evaluation of an optimal setup for a microwave axial tomograph aimed at the inspection of wood," *Proc. 2007 IEEE International Workshop on Imaging Systems and Techniques (IEEE IST07)*, Krakow, Poland, May 4-5, 2007.

[41] R. Zoughi, *Microwave non-destructive testing and evaluation*. Dordrecht: Kluwer Academic Publishers, 2000.

[42] D. L. Colton and R. Kress, *Inverse acoustic and electromagnetic scattering theory*. New York: Springer, 1998.

[43] A. G. Tijhuis, K. Belkebir, A. C. S. Litman, and B. P. de Hon, "Multiple-frequency distorted-wave Born approach to 2D inverse profiling," *Inv. Probl.*, vol. 17, no. 6, pp. 1635-1644, Dec. 2001.

[44] C. Estatico, M. Pastorino, and A. Randazzo, "An inexact-Newton method for short-range microwave imaging within the second-order Born approximation," *IEEE Trans. Geosci. Remote Sens.*, vol. 43, no. 11, pp. 2593-2605, Nov. 2005.

[45] A. Salvade, M. Pastorino, R. Monleone, G. Bozza, and A. Randazzo, "A New Microwave Axial Tomograph for the Inspection of Dielectric Materials," *IEEE Trans. Instrum. Meas.*, vol. 58, no. 7, pp. 2072-2079, Jul. 2009.

[46] V. Bucur, *Nondestructive characterization and imaging of wood*. Berlin: Springer, 2003.

[47] R. Monleone, M. Pastorino, J. Fortuny-Guasch, A. Salvadè, T. Bartesaghi, G. Bozza, M. Maffongelli, A. Massimini, and A. Randazzo, "Impact of background noise on dielectric reconstructions obtained by a prototype of microwave axial tomograph," *IEEE Trans. Instrum.Meas.*, vol. 61, no. 1, pp. 140-148, Jan. 2012.

Experimental characterization of tuneable metamaterials based on ferromagnetic microwires

J. Carbonell[*], H. García-Miquel, and J. Sánchez-Dehesa
Departamento de Ingeniería Electrónica, Universitat Politecnica de Valencia
Camino de Vera, s/n, 46022 Valencia (SPAIN)
[*] jorcarol@upvnet.upv.es

Abstract - Ferromagnetic microwires are investigated as fundamental components to generate metamaterials with double negative parameters. Electric and magnetic responses are, respectively, based on the finite conductivity and ferromagnetic resonance of the wires that in turn depend on their chemical composition. Tuning properties of several samples are investigated in terms of the composition of the alloy, the applied magnetic field and DC currents flowing through the microwires. The samples are measured and simulated in a waveguide environment and in a large microwave frequency range.

During almost a decade, a huge amount of research has been devoted to the possibilities of controlling electromagnetic wave propagation in microstructured media, typically made from subwavelength inclusions. This broad area of research covering the whole spectrum from microwaves to optics has fueled the development and synthesis of the so-called metamaterials. More recently, attention has been paid to the use of magnetic materials taking advantage of their magnetic activity to design double negative media. In this case, solutions were initially based on the combined use of ferrites and metallic wire arrays. In this context, it has been recently confirmed that an array of conducting ferromagnetic microwires can provide a double negative response, [1, 2], with experimental evidence of left-handed or backward wave propagation in the microstructure. The ferromagnetic resonance (FMR) phenomenon in microwires, typically occurring at microwave frequencies, was previously studied in terms of material characterization, extraction of resonant permeability models or experimental investigation of resonating configurations.

We have experimentally assessed a double negative propagation behavior in different prototypes made of single and multiple ferromagnetic microwires operating in different microwave bands from 8 to 18 GHz. The route using ferromagnetic inclusions permits one to increase the design capabilities with the use of the natural and tuneable magnetic response of a ferromagnetic material. Tuneability, a salient feature of this approach, is therefore addressed in from three points of view. It is showed that very large tuning bandwidths are achievable by properly polarizing the samples with an external magnetic field, also by varying the material composition of the wires forming the array, and finally by applying a DC current flowing through the microwires.

In order to have a controlled measurement environment, and to avoid unwanted reflections, a waveguide mount has been preferred over a free space configuration. A hollow metallic waveguide is loaded with a number of wires in a row, centered with respect to the lateral walls and vertically oriented. Figure 1(a) shows a scanning electron microscope view of a sample microwire (glass coat partially removed). Different configurations with one and three wires have been analyzed in an experimental setup which is schematized in Fig. 1(b).

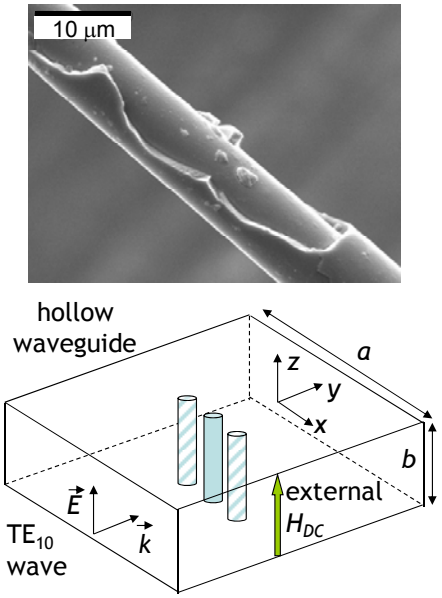


FIG. 1. SEM image of a glass-coated microwire (top) and scheme of the measurement setup employed with vertically oriented microwires (bottom).

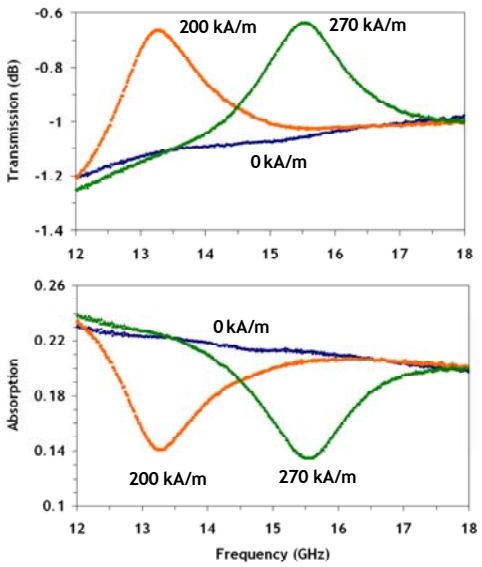


FIG. 2. Transmission and absorption coefficients measured for a single wire sample with composition $Co_{72.5}Si_{12.5}B_{15}$.

Figure 2 shows the measured parameters for a single wire structure with composition $Co_{72.5}Si_{12.5}B_{15}$ varying the applied external static field H_{dc}. From the measured transmission (S_{21}) and reflection (S_{11}), the measured coefficient of power absorption P_{abs} is calculated as:

$$P_{abs} = 1 - |S_{11}|^2 - |S_{21}|^2 \qquad (1)$$

Additionally, a DC current can be applied to the microwires by perforating the waveguide mount (see Fig. 1). We have analyzed that small DC currents circulating through the wires can be used as a tuning parameter, [3]. The DC current allows shifting the frequency at which the enhancement of the transmission response is found under external magnetic fields. Experimental results demonstrate that this tuning parameter generates an effective field along the wire axis that partially cancels and even quenches the externally applied static magnetic field. The tuning features of the studied structures are of great relevance in the metamaterial context, owing to the possibility of extending the operational bandwidths.

Acknowledgements: Work partially supported by MICINN of Spain under contracts with Refs. TEC 2010-19751 and Consolider CSD2008-00066.

REFERENCES

1. H. García-Miquel, J. Carbonell, V. E. Boria, and J. Sánchez-Dehesa, "Experimental evidence of left handed transmission through arrays of ferromagnetic microwires," *Applied Physics Letters*, Vol. 94, 054103, 2009.
2. J. Carbonell, H. García-Miquel, and J. Sánchez-Dehesa, "Double negative metamaterials based on ferromagnetic microwires," *Physical Review B*, Vol. 81, 024401, 2010.
3. H. García-Miquel, J. Carbonell, and J. Sánchez-Dehesa, "Left handed material based on amorphous ferromagnetic microwires tunable by dc current," *Applied Physics Letters*, Vol. 97, 094102, 2010.

Equivalence Between Low Field Microwave Absorption and Giant Magnetoimpedance Through the Poynting Vector

Raúl Valenzuela

Departamento de Materiales Metálicos y Cerámicos, Instituto de Investigaciones en Materiales,
Universidad Nacional Autónoma de México, 04510, México

Abstract

Low field microwave absorption (LFMA) has recently attracted attention as a sensitive method to characterize ferro- and ferrimagnetic materials. LFMA takes place at low fields (comparable to the total anisotropy field of the material) and it is clearly a non-resonant absorption process. It has been established that LFMA is directly associated with the magnetization from the unmagnetized state up to the saturation. In this paper, we present a brief analysis of LFMA and its equivalence with giant magnetoimpedance (GMI), by using the Poynting vector. LFMA is therefore a kind of GMI in the microwave frequency range, albeit in different measuring conditions. We present also LFMA applications in a variety of materials and phenomena in ferromagnetic glasses, such as the effects of stress on the magnetoelastic contribution to total anisotropy in glass-covered microwires; in ferrites, we review the effects of the Verwey transition in magnetite, the Yafet-Kittel triangular arrangement in Ni-Zn spinels, and the effects on some nanostructured Ni-Zn ferrites.

1. Introduction

Low field microwave absorption (LFMA) has been reported in many materials, such as silicate glasses [1], high-temperature superconductors [2], and in magnetically ordered phases as glassy ferromagnets [3], and ferrimagnetic oxides [4]. LFMA is the result of the interaction between magnetic/electric dipoles with the high frequency electromagnetic radiation.

In magnetic materials, it is centered on zero magnetic field, exhibits hysteresis, and occurs at applied magnetic fields well below the resonance conditions, which makes it clearly different from typical ferro-/paramagnetic resonance.

It has been found that LFMA is directly related with the magnetization processes [4,5]; LFMA appears at the onset of magnetic ordering in many materials exhibiting a transition toward spin ordering, such as manganites [6,7] and small band gap insulators [8]. In this paper, we present a brief review of LFMA results and its relationship with giant magnetoimpedance (GMI) phenomenon. GMI is defined as the change in impedance in a magnetic conductor carrying a small AC electric current, when it is subjected to a constant magnetic field.

2. Low Field Microwave Absorption and Giant Magnetoimpedance

In order to establish a sound comparison between LFMA and GMI, the Poynting vector has been used [9]. The pointing vector, in its Abraham form can be written as [10]:

$$\mathbf{P} = \mathbf{E} \times \mathbf{H} \tag{1}$$

where **E** and **H** are the electrical and magnetic field vectors, respectively. **P** represents the directional energy flux density (the rate of energy transfer per unit area). In the case of a sinusoidal electromagnetic field, the time average power flow, P, is obtained through the real part of (1):

$$P = \tfrac{1}{2}\, \mathscr{Re}(\mathbf{E} \times \mathbf{H}^*) \tag{2}$$

$\mathscr{Re}$ is the real part of the operator and **H*** is the complex conjugate of the magnetic field. Since the impedance is defined as the ratio of electrical to magnetic field,

$$Z = E / H \tag{3}$$

and therefore,

$$P = \tfrac{1}{2}\, H^2\, \mathscr{Re}(Z) \tag{4}$$

For the case of very high frequencies (microwaves) where the skin effect is significant, the field, H_s, and the impedance, Z_s, in the surface should be considered:

$$P_s = \tfrac{1}{2}\, H_s^2\, \mathscr{Re}(Z_s) \tag{5}$$

The power derivative, that is the microwave absorption can therefore be expressed in terms of the surface impedance as:

$$\mathrm{d}P_s/\mathrm{d}H = (H_s^2/2)\, \mathrm{d}\, \mathscr{Re}\,(Z_s)/\mathrm{d}H \tag{6}$$

A direct comparison between LFMA can thus be made by taking the field derivative of impedance from GMI measurements, and comparing this results with LFMA measurements of the same sample (at the same temperature). This was performed for a Co-rich Fe alloy [9], as reproduced in Fig. 1, for GMI measurements at 60 MHz and 3 GHz, and LFMA measurements at 9.45 GHz. The

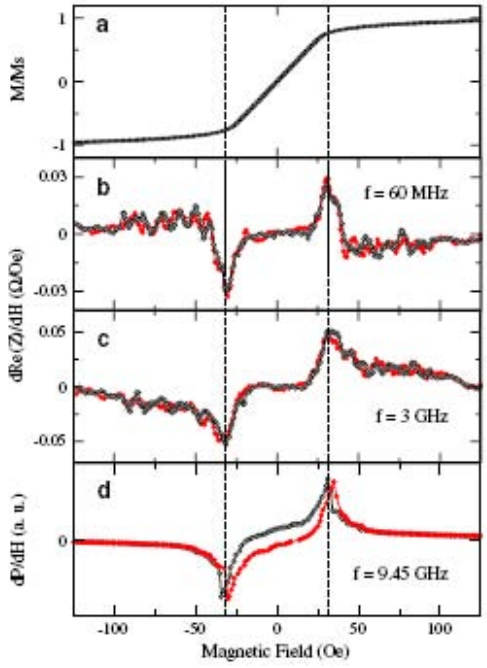


Fig. 1. Measurements in an amorphous ribbon of nominal composition $(Co_{0.94}Fe_{0.06})_{75}B_{10}Si_{15}$. a) longitudinal hysteresis loop at DC field, (b) and (c) numerical derivative of impedance measurements at 60 MHz and 3 GHz, and (d) LFMA signal at 9.45 GHz [9].

magnetic DC hysteresis of the sample was added in order to confirm that the critical points in coincide in all plots. The derivatives of GMI measurements were obtained numerically.

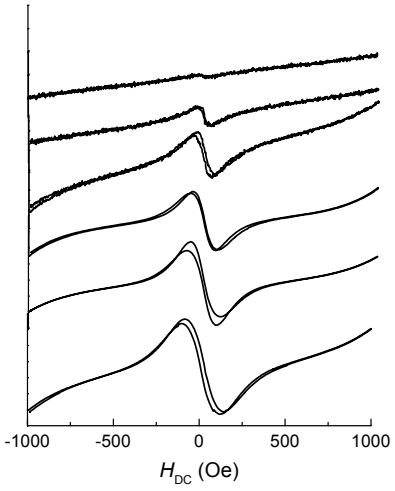


Fig. 2. LFMA as a function of temperature for $Ni_{0.35}Zn_{0.65}Fe_2O_4$ ferrites [11]

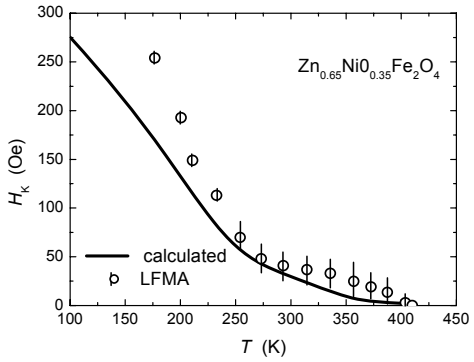


Fig. 3. Comparison of the calculated magnetocrystalline anisotropy from K_1 data in a single ferrite crystal [12] with LFMA measurements in a ferrite with virtually the same composition, as determined from Fig. 2.

Measurements of LFMA as a function of temperature in $Ni_{0.35}Zn_{0.65}Fe_2O_4$ ferrites are shown in Fig. 2 [11]. Note that the signal vanishes at 430 K (Curie point occurs at this temperature), and that the separation between maximum (left) and minimum (right) of the signal, which we call ΔH_{LFMA}, decreases with temperature. In Fig. 3, it is shown a plot of ½ ΔH_{LFMA}. On the other hand, by using measurements of the magnetocrystalline anisotropy constant, K_1, carried out on a single crystal in the temperature range 5 - 450K [12] it was possible to calculate the magnetocrystalline anisotropy as a function of temperature, also plotted on Fig. 3. The agreement is very good, especially if we consider that the calculation from K_1 data involves only an estimation of magnetocrystalline anisotropy, while LFMA measurements are expected to depend on the total anisotropy of the sample.

The direct mechanism of absorption in LFMA, to our knowledge, is not fully understood. In general terms, it is expected that the main absorption process depends on spin rotation under the influence of the microwave field h_{AC}. Domain wall movements could not be expected to contribute directly to the microwave absorption, since their dynamics, as can be observed by the typical dispersion frequencies, are in the kHz range for metals, and in the tens of MHz for ferrites. We think however, that in bulk materials with large domains, domain wall displacements (under the influence of the DC magnetic field) are very important for LFMA since they modify the orientation of large spin volumes in the sample, thereby changing the absorption conditions.

To our knowledge, the sign of LFMA signal has not been analyzed in detail. In most insulator cases, as in ferrites, it seems that it shows a maximum for negative fields and a minimum for the positive field section of the dP/dH vs. H plots, as in Fig. 2. This is the contrary for metals; as in Fig. 1 (d), a minimum appears for negative fields, and a maximum for the other side of the field axis. Some recent results in ferrites seem to indicate that more than the electrical conductivity, it is the spin arrangement which can influence the morphology of the LFMA signal.

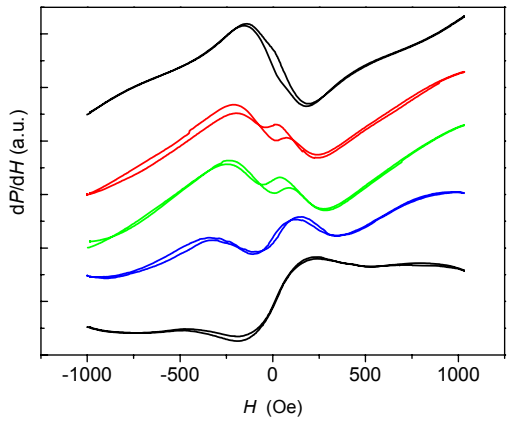


Fig. 4. LFMA measurement on the same ferrite than Fig. 2, at lower temperatures [11].

When LFMA measurements in the same ferrite of Fig. 2 are carried out at lower temperatures, a change in the sign of the LFMA behavior occurs; with a clearly opposite signal (minimum at negative magnetic fields, maximum at positive fields). At these temperatures, this ferrite has shown a change in the spin arrangement: as a consequence of the differences the thermal dependence in the superexchange interactions, the spins in the octahedral sublattice becomes comparable to interactions between tetrahedral and octahedral sublattice, and the antiparallel arrangement changes toward a triangular structure, first proposed by Yafet and Kittel [13].

As LFMA depends on the total anisotropy of the sample, it is also affected by the its magnetoetlastic component. In the case of glass-covered microwires, GMI and LFMA measurements have exhibited a very good agreement to represent the strain state in such microwires as a function of the ratio of glass radius to total (glass + metal) diameter

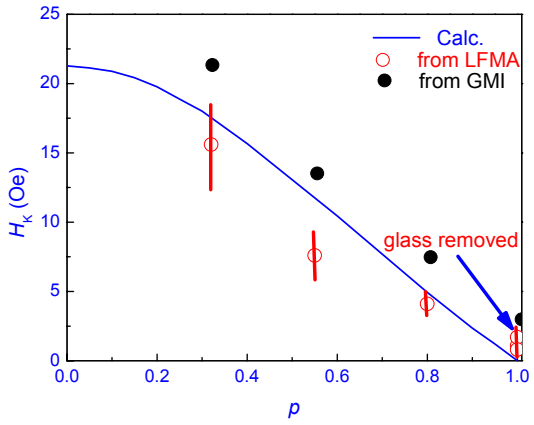


Fig. 5. Anisotropy field as calculated from the effects of stresses on the magnetoelastic part of the anisotropy (continuous line), and deduced from LFMA (red open dots), and GMI (black full dots).

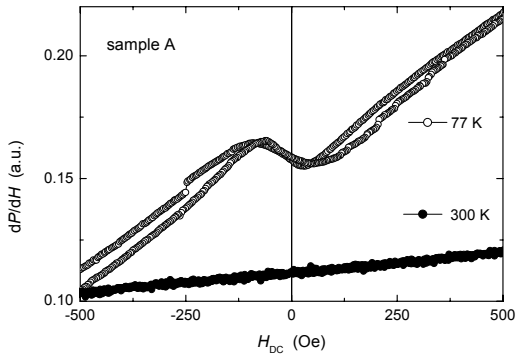


Fig. 6. LFMA in monodisperse NPs of Ni-Zn ferrite, at 77 and 298 K [17]

[14,15]. These strains arise because of the differences in dilatation coefficient between glass and metal. During their fabrication, the metal microwires are covered by molten glass; as temperature decreases toward room temperature, the metal section should undergo a larger contraction than the glass cover. As the latter prevents the metal to contract, it becomes strained by a tensile stress. Such stresses can be calculated [14], in very good agreement with both GMI and LFMA results.

We finally review some recent results of LFMA measurements on ferrite nanoparticles, (NPs) in different aggregation states. Ni-Zn NPs in the 5-8 nm range can be prepared by the forced hydrolysis in a poliol method [16]. By playing with synthesis parameters, they can be prepared as monodisperse NPs, or in the form of clusters containing some tens to hundreds of NPs in the same size range [17]. LFMA on these samples showed clear differences. At room temperature, Fig. 6, monodisperse NPs exhibited a flat LFMA since they are superparamagnetic, and their behavior is closer to that of a magnetically disordered phase. Aggregated NPs, in contrast, showed a clear LFMA

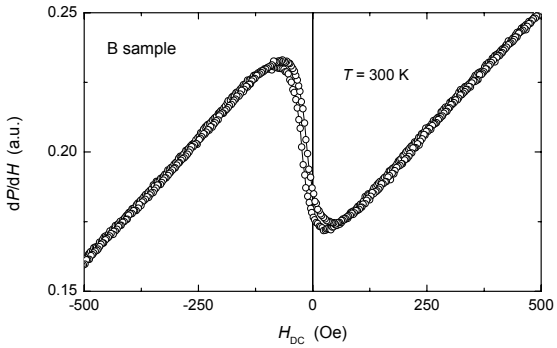


Fig. 7. LFMA from clusters formed by 5-8 NPs of Ni-Zn ferrite, at room temperature [17].

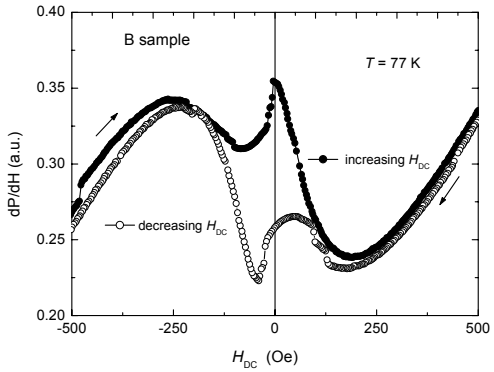


Fig. 8. LFMA measurements in same sample as Fig. 7, at 77 K [17]..

corresponding to a ferrimagnetically ordered phase, as seen in Fig. 7.. At low temperatures (77 K), Fig. monodispersed NPs appeared as an ordered phase, as their blocking temperature (as measured by a fast varying experiment as microwave absorption) is above 77 K. Aggregated NPs at low temperature, Fig. 8, even shows some features which can be adscribed to the onset of the Yafet-Kittel triangular arrangement.

3. Conclusions

The basic mechanism underpinning LFMA is not yet fully understood, but at present, LFMA appears therefore as a powerful research and characterization tool, providing interesting results in a variety of materials and conditions.

Acknowledgements

Author acknowledges support from UNAM, through DGAPA PAPIIT IN 101412

References

[1] R.R. Rakhimov, H.R. Ries, D.E. Jones, L.B. Glebov, L.N. Glebova. Microwave response near zero magnetic field in transition –metal-doped silicate glasses. *Appl. Phys. Lett.*: 76, 751-753, 2000.

[2] G.K. Padam, S.N. Ekbote, M.R. Tripathy, G.P. Srivastava, B.K. Das. Non-resonant microwave absorption studies in $Bi_{1.6}Pb_{0.4}Sr_2Ca_2Cu_3O_{10+x}$. *Physica C*: 315, 45-58, 1999.

[3] H. Montiel, G. Alvarez, I. Betancourt, R. Zamorano, R. Valenzuela. Correlation between low-field microwave absorption and magnetoimpedance in Co-based amorphous ribbons. *Appl. Phys. Lett*. :86, 072503, 2005.

[4] R. Valenzuela, G. Alvarez, H. Montiel, M.P. Gutierrez, M.E. Mata-Zamora, F. Barron, A.Y. Sanchez and R. Zamorano. Characterization of magnetic materials by low field microwave absorption. *J. Magn. Magn. Mater.*: 320, 1961-1965, 2008.

[5] M. Rivoire and G. Suran. Magnetization in thin films with in-plane uniaxial anisotropy studied by microwave absorption. *J. Appl. Phys*.: 78, 1899-1907, 1995.

[6] F.J. Owens. DC magnetic field dependent microwave absorption in CMR material $La_{0.7}Sr_{0.3}MnO_3$. *J. Phys. Chem Solids*: 58, 1311-1314, 1997.

[7] V.V. Srinivasu, S.E. Lofland, S.M. Bhagat, K. Gosh and S.D. Tyagi. Temperature and field dependence of microwave losses in manganite powders. *J. Appl. Phys*.: 86, 1067-1072, 1999.

[8] H. Gavi, B.D. Ngom, A.C. Beye, A.M. Strydom, V.V. Srinivasu, M. Chaker and N. Manyala. Low-field microwave absorption in pulse laser deposited FeSi thin film. *J. Magn. Magn. Mater*.: 324, 1172-1176, 2012.

[9] G. Alvarez, H. Montiel, D. de Cos, R. Zamorano, A. Garcia-Arribas, J.M. barandiaran and R. Valenzuela. Experimental and theoretical correlation between low-field power absorption and magnetoimpedance in amorphous materials. *J. NonCryst. Solids*: 353, 902-904, 2007.

[10] J.D. Jackson, Classical Electrodynamics, 2nd Edition, John Wiley, N.Y., 1975. ISBN: 047130932X.

[11] Broese van Groenou A, Schulkes J A and Annis D A. 1967 *J. Appl. Phys*. **38** 1133-4

[12] G. Alvarez, H. Montiel, J.F. Barron, M.P. Gutierrez, R. Zamorano. Yafet-Kittel type of magnetic ordering in $Ni_{0.35}Zn_{0.65}Fe_2O_4$ ferrites detected by magnetosensitive microwave absorption measurements. *J. Magn. Magn. Mater*.: 322, 348-352, 2009.

[13] Y. Yafet and C. Kittel. Antiferromagnetic arrangements in ferrites. *Phys. Rev*.: 87, 290- 294, 1952.

[14] R. Valenzuela, A. Fessant, J. Gieraltowski and C. Tannous. Effect of the metal-to-wire ratio on the high-frequency magnetoimpedance of glass-coated CoFeBSi amorphous microwires. *Sensors and Actuators A*: 142, 533-537, (2008).

[15] H. Montiel, G. Alvarez, M.P. Gutiérrez, R. Zamorano and R. Valenzuela. The effect of metal-to-glass ratio on the low-field microwave absorption at 9.4 GHz of glass-coated CoFeBSi microwires. *IEEE Trans. Mag.*:42, 532-537, 2008.

[16] Z. Beji, T. Ben Chaabane, L.S. Smiri, S. Ammar, F. Fievet, N. Jouini and J.M. Greneche. Synthesis of nickel-zinc ferrite nanoparticles in polyol: morphological, structural and magnetic studies. *Phys. Stat Solidi A:* 203, 504-512, 2996.

[17] R. Valenzuela, S. Ammar, F. Herbst, and R. Ortega-Zempoalteca. *Nanosc. Nanotech. Lett*.:3, 598-602, 2011.

To the theory of nonreciprocal microwave transmission along a bianisotropic-dielectric-ferrite metasandwich

V.S. Butylkin, G.A. Kraftmakher, and V.P. Mal'tsev

Kotelnikov Institute of Radioengineering and Electronics RAS (Fryazino Branch),
Fryazino, Moscow region, Russia
vasebut@ms.ire.rssi.ru

Abstract

Nonreciprocal transmission of microwaves along metasandwiches "bianisotropic layer – dielectric layer – ferrite plate" under conditions of ferromagnetic resonance excitation in ferrite plate is investigated theoretically and numerically. Obtained results confirm experimentally observed resonant nonreciprocal effects in metasandwiches with grating of double split rings.

1. Introduction

It was observed interesting effect of nonreciprocal transmission of electromagnetic waves along "ferrite plate-grating of resonant elements" metasandwiches spaced in waveguides [1, 2] *(hundredfold increase of nonreciprocity has been obtained as compared with the case of the grating absence)* and in free space [2] *where without a grating nonreciprocity is not quite observed*. It was assumed that the observed effect is caused by the difference in the ferrite absorption of surface microwaves with different rotating senses of magnetic field, the microwaves being formed by the grating. In [3] the polarization of the magnetic field and dispersive characteristics of the surface waves formed by the bianisotropic layer were studied. Unlike [3] in this presentation we include a finite thickness ferrite plate in the system under consideration (Fig. 1). We investigate theoretically the transmission nonreciprocity taking into account the ferrite influence onto the surface waves and their dispersive properties. Similarly [3] we simulate a grating of resonant elements possessing magneto-electric interaction (e.g., split ring resonators (**SRR**) [4-6]) by a bianisotropic layer (**BL**). It is supposed that a bianisotropic layer matter possesses diagonal tensors of effective permittivity $\hat{\varepsilon}$ and permeability $\hat{\mu}$ with unequal components $\varepsilon_{jj}=\varepsilon_j$ and $\mu_{jj}=\mu_j$ as well chirality's tensors with nonzero components $\kappa_{yz}=\kappa_{zy}^{T}=\kappa$. A dielectric permittivity ε_d and a ferrite permittivity ε_f are isotropic, and ferrite`s tensor permeability elements are μ and $\pm i\mu_a$, as usually [7]. To allow for dissipation of electromagnetic energy by a ferrite, let's assume that μ and μ_a are complex number.

2. Surface waves and dispersion equation

Consider harmonic waves propagating along the ***X***-direction:

$$\begin{aligned} &= \boldsymbol{E}\exp\left[i\left(\omega t-k_0 n_x x\right)\right]+\text{c.c.},\\ &= \boldsymbol{H}\exp\left[i\left(\omega t-k_0 n_x x\right)\right]+\text{c.c.}\end{aligned} \qquad (1)$$

Here ω is a wave frequency, $k_0=\omega\sqrt{\varepsilon_0\mu_0}$, $n_x=n'-in''$ is coefficient of slowing-down. Electric field is polarized in the ***Y***-direction just as a magnetostatic field in nonreciprocity experiments.

Using Maxwell equations and zero conditions for wave fields at infinity one can find dependences of wave amplitudes on transverse coordinate *z*:

- in vacuum (or in air) at $z<-b$

$$\begin{aligned} H_x &= -ip\mu_0^{-1/2}A^{+}\exp\left(k_0 pz\right),\\ H_z &= n_x\mu_0^{-1/2}A^{+}\exp\left(k_0 pz\right),\\ E_y &= A^{+}\varepsilon_0^{-1/2}\exp\left(k_0 pz\right);\end{aligned} \qquad (2)$$

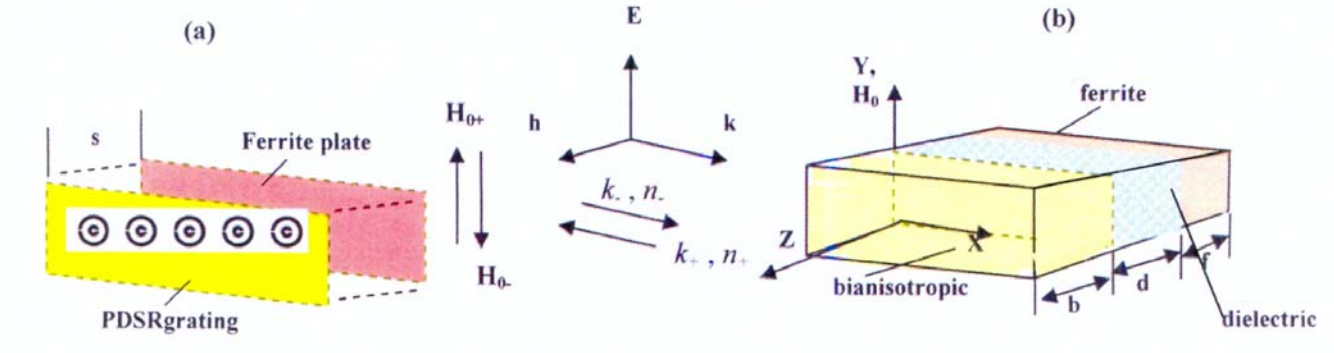


Figure 1. Metasandwiches investigated experimentally (**a**) and theoretically (**b**)

- in bianisotropic layer at $-b < z < 0$

$$H_x = iq\mu_0^{-1/2}\mu_x^{-1}\left(A_c^{\mathrm{b}}\sin(k_0qz) - A_s^{\mathrm{b}}\cos(k_0qz)\right),$$
$$H_z = \left(n_x - i\kappa\right)\mu_0^{-1/2}\mu_z^{-1}\left(A_c^{\mathrm{b}}\cos(k_0qz) + A_s^{\mathrm{b}}\sin(k_0qz)\right), \quad (3)$$
$$E_y = \varepsilon_0^{-1/2}\left(A_c^{\mathrm{b}}\cos(k_0qz) + A_s^{\mathrm{b}}\sin(k_0qz)\right);$$

- in dielectric layer at $0 < z < d$

$$H_x = -is\mu_0^{-1/2}\left[A_{ch}^{\mathrm{d}}\,\mathrm{sh}(k_0sz) + A_{sh}^{\mathrm{d}}\,\mathrm{ch}(k_0sz)\right],$$
$$H_z = n_x\mu_0^{-1/2}\left[A_{ch}^{\mathrm{d}}\,\mathrm{ch}(k_0sz) + A_{sh}^{\mathrm{d}}\,\mathrm{sh}(k_0sz)\right], \quad (4)$$
$$E_y = \varepsilon_0^{-1/2}\left[A_{ch}^{\mathrm{d}}\,\mathrm{ch}(k_0sz) + A_{sh}^{\mathrm{d}}\,\mathrm{sh}(k_0sz)\right];$$

- in ferrite layer at $d < z < d + f$

$$H_x = i\mu_0^{-1/2}\left(\mu^2 - \mu_{\mathrm{a}}^2\right)^{-1}\left[\left(\mu_{\mathrm{a}}n_xA_c^{\mathrm{f}} - \mu rA_s^{\mathrm{f}}\right)\cos(k_0rz)\right.$$
$$\left.+\left(\mu_{\mathrm{a}}n_xA_s^{\mathrm{f}} + \mu rA_c^{\mathrm{f}}\right)\sin(k_0rz)\right],$$
$$H_z = \mu_0^{-1/2}\left(\mu^2 - \mu_{\mathrm{a}}^2\right)^{-1}\left[\left(\mu n_xA_c^{\mathrm{f}} - \mu_{\mathrm{a}}rA_s^{\mathrm{f}}\right)\cos(k_0rz)\right. \quad (5)$$
$$\left.+\left(\mu n_xA_s^{\mathrm{f}} + \mu_{\mathrm{a}}rA_c^{\mathrm{f}}\right)\sin(k_0rz)\right],$$
$$E_y = \varepsilon_0^{-1/2}\left(A_c^{\mathrm{f}}\cos(k_0rz) + A_s^{\mathrm{f}}\sin(k_0rz)\right);$$

- in vacuum at $z > d + f$

$$H_x = ip\mu_0^{-1/2}A^-\exp\left(-k_0pz\right),$$
$$H_z = n_x\mu_0^{-1/2}A^-\exp\left(-k_0pz\right), \quad (6)$$
$$E_y = A^-\varepsilon_0^{-1/2}\exp\left(-k_0pz\right).$$

In (2) - (6) we have introduced parameters

$$p = \sqrt{n_x^2 - 1},\ q = \sqrt{\left(n_{\mathrm{b}}^2 - n_x^2\right)\mu_x\mu_z^{-1}},$$
$$r = \sqrt{\varepsilon_{\mathrm{f}}\mu_\perp - n_x^2},\ s = \sqrt{n_x^2 - \varepsilon_{\mathrm{d}}} \quad (7)$$

for vacuum, bianisotropic medium, ferrite, and dielectric, respectively. In (7) it is denoted

$$n_{\mathrm{b}}^2 = \varepsilon_y\mu_z - \kappa^2,\ \ \mu_\perp = \mu - \mu_{\mathrm{a}}^2/\mu\,. \quad (8)$$

Accounting for conditions of continuity of electric and magnetic field's tangent components at the borders of vacuum-bianisotropic medium (at $z = -b$), bianisotropic medium-dielectric (at z=0), dielectric-ferrite (at $z = d$), and ferrite-vacuum (at $z = d + f$) one can find set of equations for amplitudes $A^{\pm}$, $A_{c,s}^{\mathrm{b,f}}$, $A_{ch,sh}^{\mathrm{d}}$.

From requirement of consistency of these equations the dispersion equation $D(\omega) = 0$ follows. In the simplest case when there are not an air gap and any dielectric spacer the determination $D(\omega)$ is of sixth order and its nonzero elements are

$$d_{11} = 1,\ d_{12} = \cos\left(k_0qb\right),\ d_{13} = \sin\left(k_0qb\right),$$
$$d_{21} = p\mu_x,\ d_{22} = q\sin\left(k_0qb\right),\ d_{23} = -q\cos\left(k_0qb\right),$$
$$d_{32} = 1,\ d_{34} = 1,$$
$$d_{43} = q(\mu^2 - \mu_a^2),\ d_{44} = \mu_x\mu_an_x,\ d_{45} = -\mu_x\mu r, \quad (9)$$
$$d_{54} = \cos\left(k_0rf\right),\ d_{55} = \sin\left(k_0rf\right),\ d_{56} = 1,$$
$$d_{64} = \mu_an_x\cos\left(k_0rf\right) + \mu r\sin\left(k_0rf\right),$$
$$d_{65} = \mu_an_x\sin\left(k_0rf\right) - \mu r\cos\left(k_0rf\right),$$
$$d_{66} = p(\mu^2 - \mu_a^2).$$

Using (2) – (6) one can find that the wave's energy attenuates as $\exp(\mp 2k_0n_{\pm}''L)$ where upper and lower signs relate to waves with energies transferred along and against the ***X***–axis, respectively. Here L is the metasandwich length. The attenuation nonreciprocity per unit length can be defined as $\delta = 2k_0\left(n_+'' + n_-''\right)$.

Transposition of the ferrite and the bianisotropic layer is represented by inversion of signs before of quantities *b, d,* and *f*. As it follows from (9) the solution n_x of the dispersion equation changes sign in this case. As a result the wave transition nonreciprocity has to change sign under transference of the ferrite to opposite side of the bianisotropic layer (grating of resonant elements in experiments).

3. Dispersive characteristics

It is seen that dispersive characteristics of the metasandwich are determined by ferrite's and **SRR**'s dispersion properties. Let's take up the metasandwich containing the bianisotropic layer simulated a grating with like-oriented split ring resonators. As follows from (7) influence of **BL** depends on dispersive behavior of the quantities n_{b}^2 , μ_x , and μ_z. Frequency dependences of these quantities are determined by the **SRR**'s resonant frequency ω_0, the low-frequency limit of permittivity $\varepsilon_y(0) = n_0^2$, and by the frequencies ω_n , ω_μ where the refractive index n_{b} and permeability μ_{z} of the **BL** reverse their signs by passing through zero, as well by the frequency ω_{b} of the break-point of n_{b} and μ_{z} [8]:

$$n_{\mathrm{b}}^2 = n_0^2\left(1 - \omega^2/\omega_n^2\right)/\left(1 - \omega^2/\omega_{\mathrm{b}}^2\right) \quad (10)$$

$$\mu_z = \left(1 - \omega^2/\omega_\mu^2\right)/\left(1 - \omega^2/\omega_{\mathrm{b}}^2\right),\ \ \mu_x = 1 \quad (11)$$

Frequency dependences of the tensor's components of ferrite permeability are determined by the ferromagnetic resonance (**FMR**) frequency $\omega_H = \gamma\left|H_0\right|$, by ferrite saturation

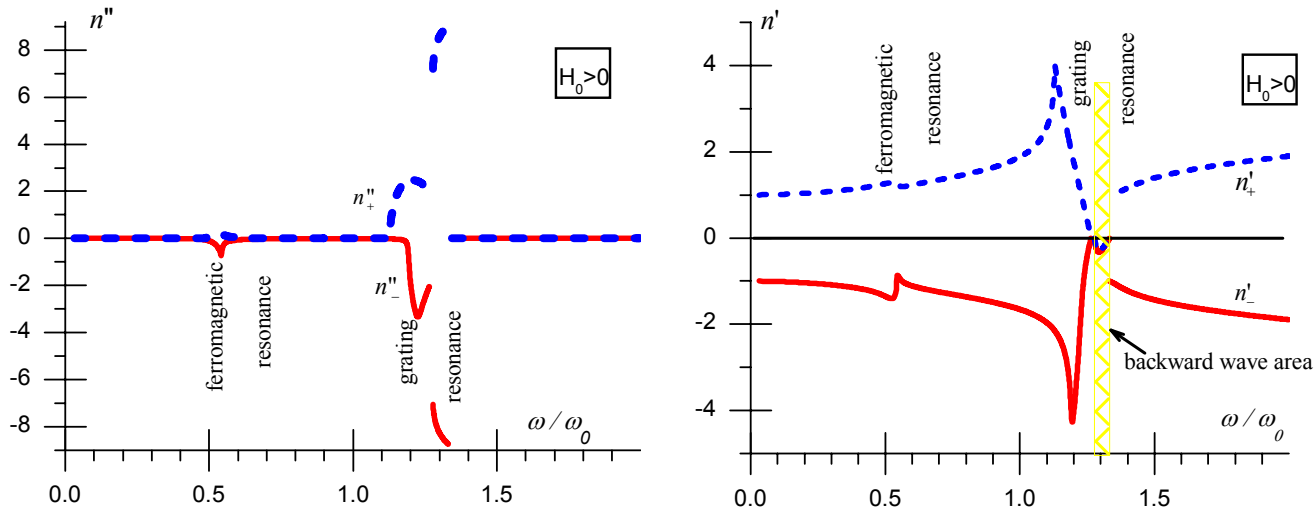


Fig. 2: Frequency dependences of $n_+^{'}$ $n_+^{"}$ (blue dashed curve) and $n_-^{'}$ $n_-^{"}$ (red solid curve) for the waves with energies transferred along and against the ***X***–axis, respectively. The magnetostatic field is positive and corresponds to $\omega_H/\omega_0 = 0.3$.

magnetization $M_0 = \omega_M/4\pi\gamma$, and by transverse relaxation time T (γ is the gyromagnetic ratio) [7]:

$$\mu = \mu^{'} - i\mu^{"} = 1 + \frac{\omega_H\omega_M T^2\left((\omega_H^2-\omega^2)T^2+1\right) - i\omega_M T\left((\omega_H^2+\omega^2)T^2+1\right)}{\left((\omega_H^2-\omega^2)T^2-1\right)^2 + 4\omega_H^2 T^2} \quad (12)$$

$$\mu_a = \mu_a^{'} - i\mu_a^{"} = \frac{\omega\omega_M T^2\left[\left((\omega_H^2-\omega^2)T^2-1\right) - 2i\,\omega_H T\right]}{\left((\omega_H^2-\omega^2)T^2-1\right)^2 + 4\omega_H^2 T^2}\,\mathrm{sign}\,H_0 \quad (13)$$

The analysis based on the dispersion equation (7) has been numerically performed using frequency dependencies of the ferrite and **BL** parameters from [7, 8]. Dispersive characteristics of different metasandwiches have been found and investigated in dependence on the value and sign of the magnetostatic field. Some results are presented in Figs. 2 - 7.

The parameters are b=0.24 mm, f=1 mm, $\omega_0/2\pi = 6$ GHz, $\omega_n = 1.52\omega_0$, $\omega_\mu = 1.27\omega_0$, $\omega_b = 0.74\omega_0$, $n_0^2 = 26$, $T^{-1} = 0.026\omega_0$, $\omega_M = 0.7\omega_0$, $\varepsilon_f = 16$. Curves of Figs. 2 - 7 relate to the lowest mode possessing the least value of the parameter $\mathrm{Re}\,p$ and the most transverse size. Such modes have usually the better matching with the incident wave.

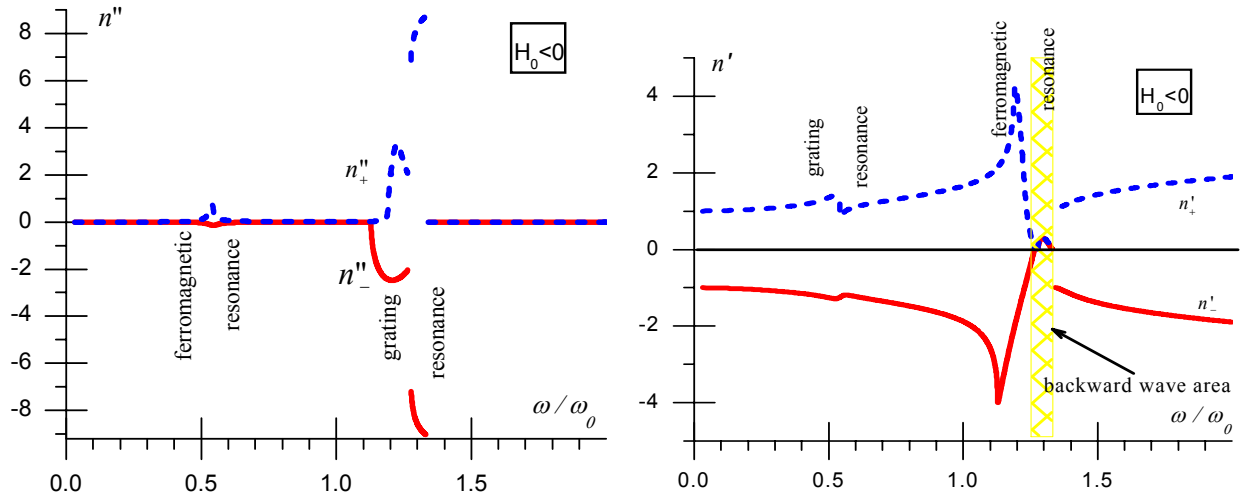


Fig. 3: Frequency dependences of $n_+^{'}$ $n_+^{"}$ (blue dashed curve) and $n_-^{'}$ $n_-^{"}$ (red solid curve) for the waves with energies transferred along and against the ***X***–axis, respectively. The magnetostatic field is negative and corresponds to $\omega_H/\omega_0 = 0.3$.

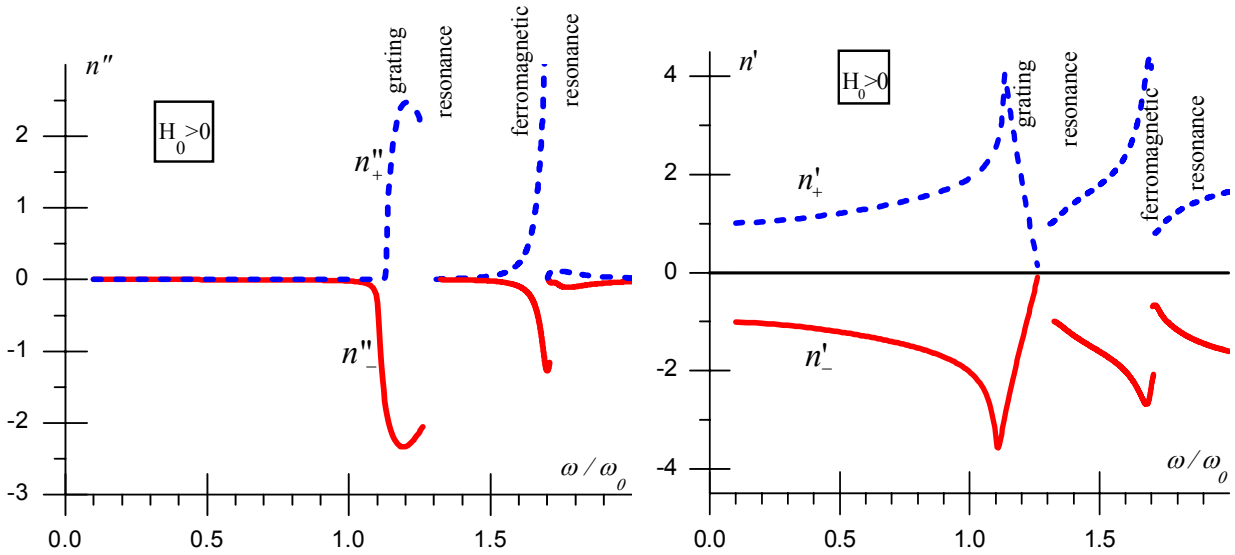


Fig. 4: Frequency dependences of $n_+^{'}$ $n_+^{''}$ (blue dashed curve) and $n_-^{'}$ $n_-^{''}$ (red solid curve) for the waves with energies transferred along and against the ***X***–axis, respectively. The magnetostatic field is positive and corresponds to $\omega_H/\omega_0 = 1.4$.

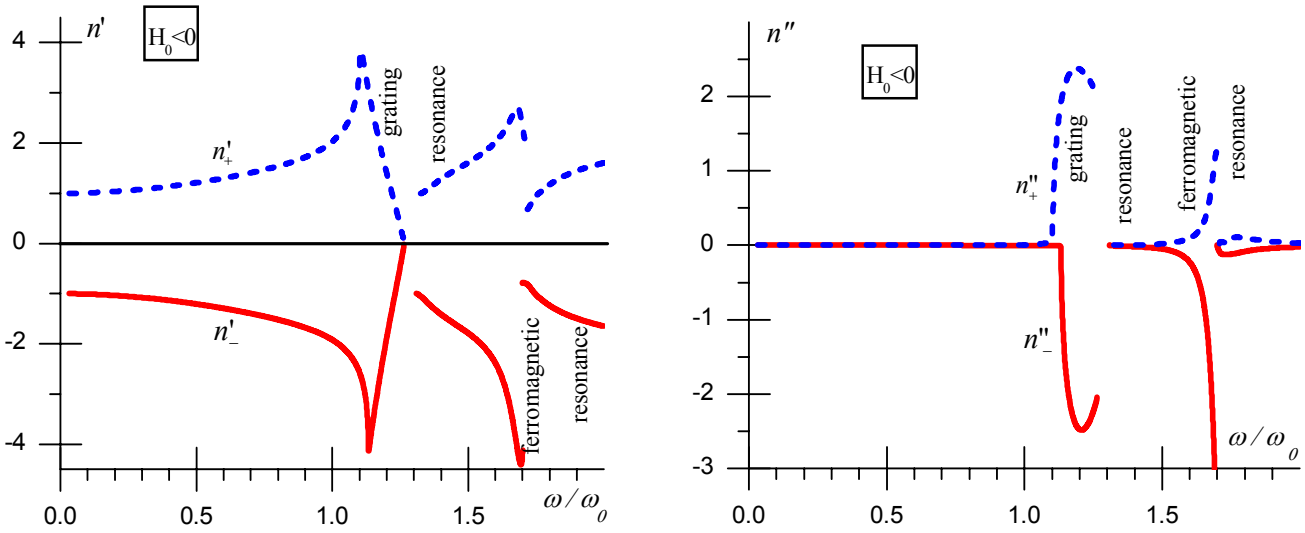


Fig. 5: Frequency dependences of $n_+^{'}$ $n_+^{''}$ (blue dashed curve) and $n_-^{'}$ $n_-^{''}$ (red solid curve) for the waves with energies transferred along and against the ***X***–axis, respectively. The magnetostatic field is negative and corresponds to $\omega_H/\omega_0 = 1.4$.

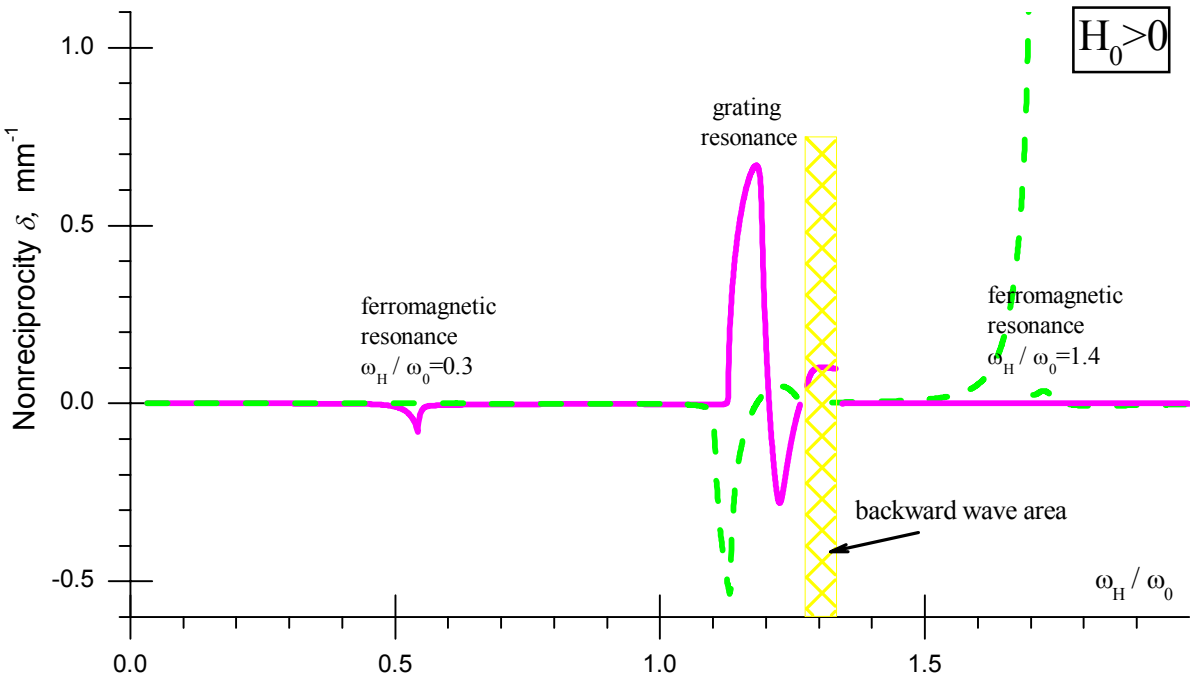


Fig. 6: Frequency dependence of the nonreciprocity per unit length $\delta = 2k_0\left(n_+^{"} + n_-^{"}\right)$ under positive magnetostatic fields corresponding to $\omega_H/\omega_0 = 0.3$ (magenta solid curve) and to $\omega_H/\omega_0 = 1.4$ (green dashed curve).

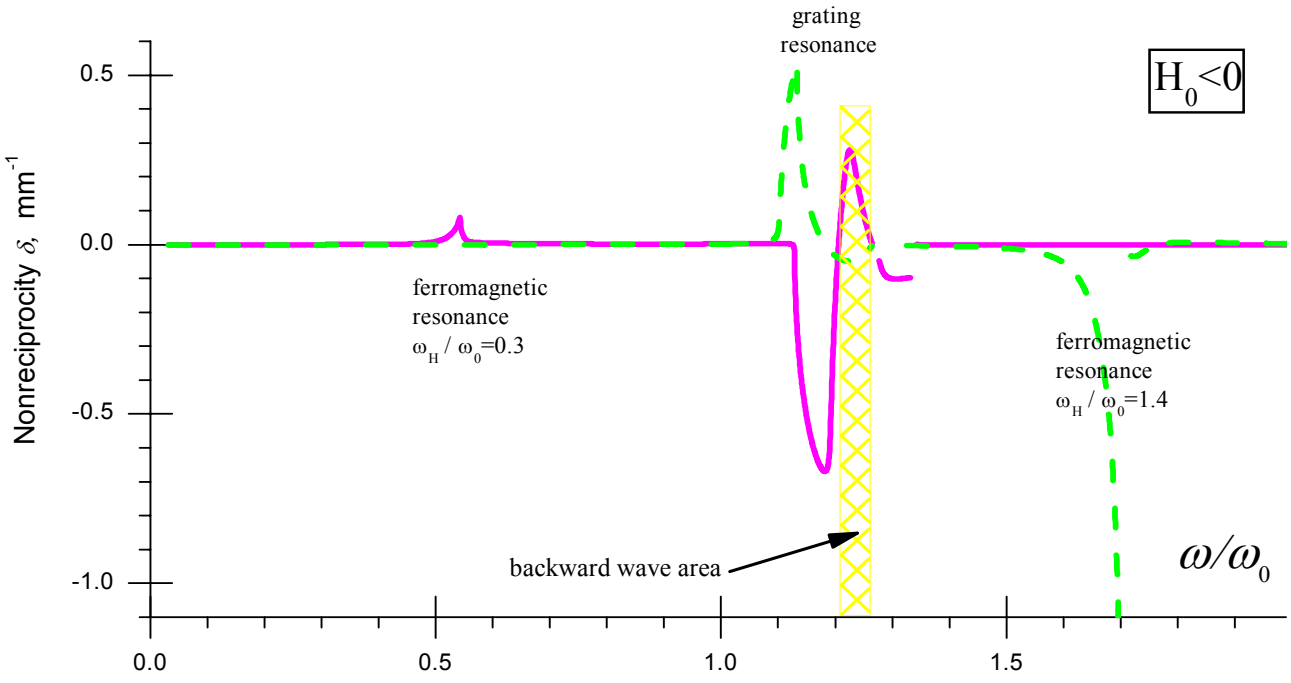


Fig. 7: Frequency dependence of the nonreciprocity per unit length $\delta = 2k_0\left(n_+^{"} + n_-^{"}\right)$ under negative magnetostatic fields corresponding to $\omega_H/\omega_0 = 0.3$ (magenta solid curve) and to $\omega_H/\omega_0 = 1.4$ (green dashed curve).

4. Conclusions

Some basic transmission laws for the waves in the metasandwiches "ferrite plate – dielectric – bianisotropic layer" have been revealed. These laws include the nonreciprocity of microwaves' transmission along the metasandwich placed in free space, the manifestation of the transmission nonreciprocity near the resonance in the grating elements, the change of the nonreciprocity sign by transference of the ferrite plate to opposite side of the **BL**, dependence of the nonreciprocity sign on the relative positions of the ferromagnetic resonance and the resonance in the **BL** elements. All these peculiarities were experimentally observed in [1-3].

Acknowledgements

This study was supported by Russian Foundation for Basic Researches, projects nos. 10-02-00053 and 11-02-90403.

References

[1] V.S. Butylkin and G.A. Kraftmakher, Giant Nonreciprocal Effect under Conditions of Mutual Influence of Ferromagnetic and Chiral Resonances, *Technical Physics Letters*, vol. 32, no. 9, pp. 775-778, 2006.

[2] V.S. Butylkin and G.A. Kraftmakher, Nonreciprocal Microwave Transmission in Metastructures with Transversely Magnetized Ferrite Plate and a Grating of Resonant Elements, *Technical Physics Letters*, vol. 33, no. 10, pp. 856-860, 2007.

[3] V. S. Butylkin, G. A. Kraftmakher, and V. P. Mal'tsev, Surface Waves Guided by a Plate Made from a Bianisotropic Resonance Metamaterial, *Journal of Communications Technology and Electronics,* vol. 54, no. 10, pp. 1124–1135, 2009

[4] Sergei A. Tretyakov, Frederic Mariotte, Constantin R. Simovski, Tatiana G. Kharina, and Jean-Philippe Heliot, Analytical Antenna Model for Chiral Skatterers: Comparison with Numerical and Experimental Data, *IEEE Trans. On Antennas and Propagation*, vol. 44, no. 7, pp. 1006-1014, 1996.

[5] J.B. Pendry, A.J. Holden, D.J. Robbins, and W.J. Stewart, Magnetism from Conductors and Enhanced Nonlinear Phenomena, *IEEE Trans. Microw. Theory Tech*., vol.47, no.11, pp. 2075-2084, 1999.

[6] R. Marques, F. Medina, R. Rafii-El-Idrissi, Role of bianisotropy in negative permeability and left-handed metamaterials, *Physical Review B*, vol. 65, no. 14, pp. 144440- 1-6, 2002.

[7] Benjamin Lax, and Kenneth J. Button. *Microwave ferrites and ferrimagnetics*, McGraw-Hill Book Company, INC. New York – San Francisco – Toronto – London, 1962.

[8] V. S. Butylkin and G. A. Kraftmakher, Passbands of Bianisotropic and Waveguide Bianisotropic Metamaterials Based on Planar Double Split Rings, *Journal of Communications Technology and Electronics*, vol. 53, no. 1, pp. 1–14, 2008.

Giant magnetoimpedance in thin wires: manipulation of magnetic anisotropy

Valentina Zhukova[1], Mihail Ipatov[1], Arcady Zhukov[1,2]

[1]Dpto. de Fís. Mater., UPV/EHU San Sebastián 20018, Spain
[2] IKERBASQUE, Basque Foundation for Science, 48011 Bilbao, Spain
*corresponding author, E-mail: arkadi.joukov@ehu.es

Abstract

In this paper we present the results on Giant magneto-impedance effect (GMI) effect in thin microwires at frequencies till 4 GHz paying special attention to tailoring the GMI effect and achievement of low hysteretic GMI behavior. Correlation between magnetoelastic anisotropy and magnetic field dependences of diagonal and off-diagonal impedance components are observed. We found, that if the surface anisotropy is not circumferential, then the magnetization and, consequently, the magnetic field dependence of impendence present hysteresis. Low field GMI hysteresis, explained in terms of magnetoelastic anisotropy of microwires, has been suppressed by the bias current.

1. Introduction

Among recently introduced soft magnetic materials magnetically soft thin wires (with typical diameters from5 till 120 μm) gained considerable interest owing to their unusual magnetic propertie such as magnetic bistability and giant magneto-impedance, GMI, effect [1-3]. Latest development of industrial applications required miniaturization of the magnetic sensors. Therefore reduction of diameters of magnetically soft wires is one of the prioritary tasks in the field of applied magnetism. Therefore, families of soft magnetic wires with reduced dimensionality and outstanding magnetic characteristics, such as melt extracted wires (typically with diameters of 40-50 μm) [4,5] and glass-coated microwires with even thinner diameters (between 1-40 μm) [6,7] recently gained much attention. The advantage of the Taylor- Ulitovski method allowing the fabrication of glass-coated metallic microwires consists of controllable fabrication of long (up to few km long continuous microwire) and homogeneous thin composite wires.

Recently, certain progress on achievement of excellent soft magnetic properties and high GMI effect of glass coated microwires has been reported at the laboratory level [7]. This gives rise to development of industrial applications for low magnetic field detection in various industrial sectors [6, 8].

GMI effect, consisting of large sensitivity of the impedance of magnetically soft conductor on applied magnetic field, attracted great attention in the field of applied magnetism [9,10] basically due to excellent magnetic field sensitivity suitable for low magnetic field detection. Cylindrical shape and high circumferential permeability observed in amorphous wires is quite suitable for achievement of high GMI effect [4, 7, 8]. It is worth mentioning, that the cylindrical shape is quite suitable for achieving of high GMI effect [6-10].

From the point of view of industrial applications low hysteretic GMI effect with linear magnetic field dependence of the output signal are desirable [6,8]. Anti-symmetrical magnetic field dependence of the output voltage with linear region has been obtained for pulsed GMI effect based on detection of the off-diagonal GMI component of amorphous wires[6, 8, 11]. Such pulsed scheme for GMI measurements resulted quite useful for real GMI sensors development [8]. It must be mentioned, that the shape of magnetic field dependence of the GMI effect (including off-diagonal components) are intrinsically related with the magnetic anisotropy and peculiar surface domain structure of amorphous wires [9,10, 12, 13]. Magnetic anisotropy of amorphous microwires in the absence of magnetocrystalline anisotropy is determined mostly by the manetoelastic term [12-16]. Therefore the magnetic anisotropy can be tailored by thermal treatment [12,17]. On the other hand recently considerable GMI hysteresis has been observed and analyzed in microwires [18]. This GMI hystereeis has been explained through the helical magnetic anisotropy [18].

Consequently in this paper we studied the GMI effect (GMI ratio, $\Delta Z/Z$, diagonal Z_{zz} and off-diagonal impedance tensor $\zeta_{\phi z}$ components) and hysteretic magnetic properties in ultra-thin amorphous glass-coated microwires with vanishing magnetostriction constant and report results on correlation of GMI effect with magnetic anisotropy and possibilities to tailor magnetic field dependence of GMI effect.

2. Experimental details

We have measured dependences of the diagonal Z_{zz} and off-diagonal $Z_{\varphi z}$ impedance components on external axial magnetic field H in Co-rich microwires, as described elsewhere [18]. The microwires with nominal compositions $Co_{67.1}Fe_{3.8}Ni_{1.4}Si_{14.5}B_{11.5}Mo_{1.7}$ and $Co_{66}Cr_{3.5}Fe_{3.5}B_{16}Si_{11}$ different diameters of metallic nucleus, d, total diameters, D, and consequently different ρ - ratios (ρ=d/D) have been fabricated by the Taylor-Ulitovsky method [6,7,12].

The microwires were placed in a specially designed microstrip cell. One wire end was connected to the inner conductor of a coaxial line through a matched microstrip line while the other was connected to the ground plane. The components Z_{zz} and $Z_{\varphi z}$ were measured simultaneously using vector network analyzer. The diagonal impedance of the sample $Zw = Zzzl$, where l is the wire length, was obtained from reflection coefficient S_{11} and the off-diagonal impedance $Z_{\varphi z}$ was measured as transmission coefficient S_{21} as a voltage induced in a 2-mm long pick-up coil wounded over the wire. The static bias field H_B was created by the dc current I_B applied to sample through the bias-tee element. The other experimental details are given in Ref. 18. The frequency range for the off-diagonal component $Z_{\varphi z}$ was 10 – 300 MHz, while diagonal impedance component has been measured till 7 GHz.

As mentioned above, for practical sensor the pulse excitation is preferred over sinusoidal because of simple electronic design and low power consumption, therefore we used also pulsed excitation scheme, as described elsewhere [6,11,12].

Hysteresis loops have been measured by the induction method, as described elsewhere [6].

3. Results and discussion

3.1. High frequency GMI effect

Magnetic field, H, dependence of real part, Z_1 of the longitudinal wire impedance Z_{zz} ($Z_{zz} = Z_1+iZ_2$), measured till 4 GHz in $Co_{66}Cr_{3.5}Fe_{3.5}B_{16}Si_{11}$ and $Co_{67}Fe_{3.85}Ni_{1.45}B_{11.5}Si_{14.5}Mo_{1.7}$ microwires are shown in Fig.1. General features of these dependences is that the magnetic field of maximum shifts to the higher field region increasing the f. High enough magnetic field sensitivity, i.e. GMI effect till GHz- range frequencies should be also underlined.

Off-diagonal and low field diagonal components of GMI, measured in $Co_{67}Fe_{3.85}Ni_{1.45}B_{11.5}Si_{14.5}Mo_{1.7}$ microwire are shown in Fig.2. As can be appreciated from Fig.2, considerable hysteresis for both off-diagonal and longitudinal impedance is observed for studied microwires. Increasing the frequency the GMI hysteresis persists (Fig.2b).

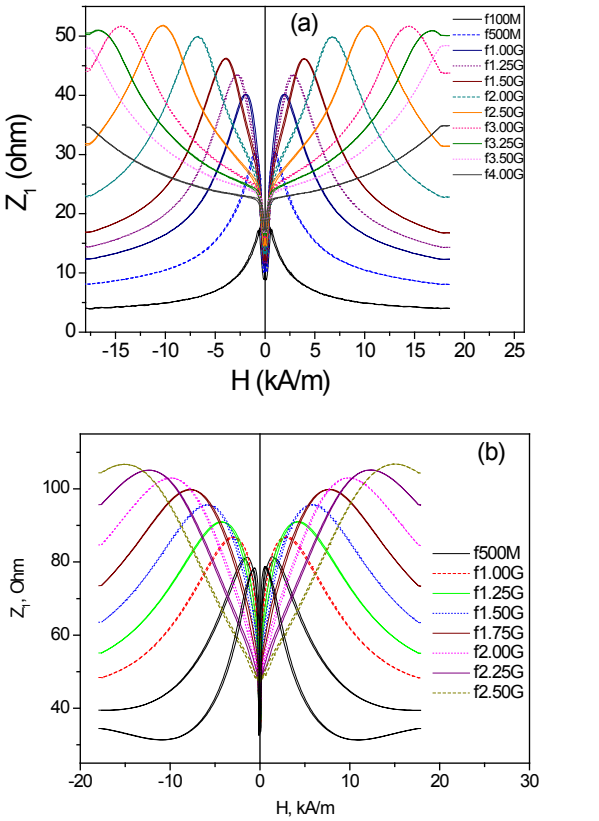


Fig.1. Z(H) dependence of $Co_{66}Cr_{3.5}Fe_{3.5}B_{16}Si_{11}$ (a) and $Co_{67}Fe_{3.85}Ni_{1.45}B_{11.5}Si_{14.5}Mo_{1.7}$ (b) microwires measured at different frequencies

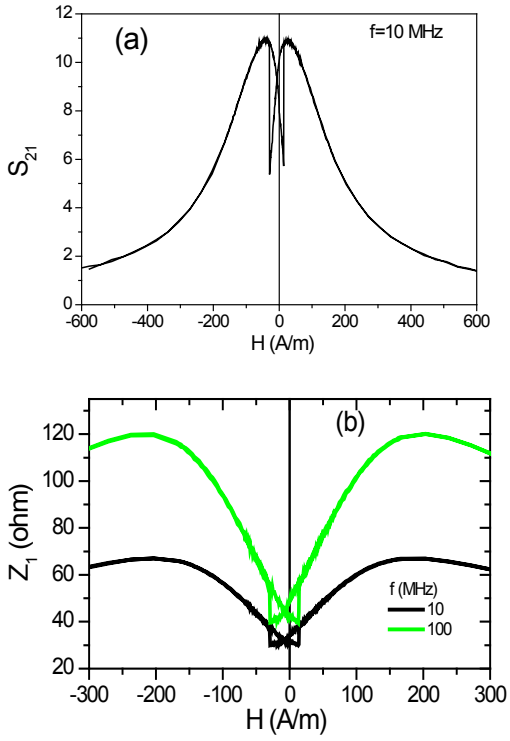


Fig. 2. Magnetic field dependences of the coefficient S_{21} at 10 MHz (a) and Z_1(H) dependences at different frequencies (b) measured in $Co_{66}Cr_{3.5}Fe_{3.5}B_{16}Si_{11}$ microwire.

3.2. Pulsed GMI effect

Fig. 3 shows field dependence of the off-diagonal voltage response, V_{out} measured using pulsed scheme, described elsewhere [3, 9, 12, 13] in $Co_{67.1}Fe_{3.8}Ni_{1.4}Si_{14.5}B_{11.5}Mo_{1.7}$ ($\lambda_s \approx 3 \cdot 10^{-7}$) microwire with different geometry: metallic nucleus diameter and total diameter with glass coating are 6.0/10.2 (ρ≈0,59), 7.0/11.0 (ρ≈0,64) and 8.2/13.7 μm (ρ≈0,6). The off-diagonal components exhibit anti-symmetrical magnetic field dependence, suitable for determination the magnetic field direction in real

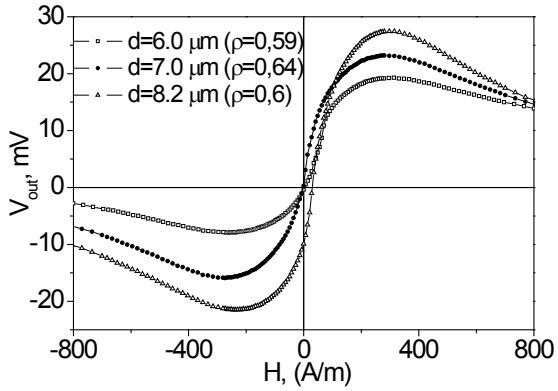


Fig.3. $V_{out}(H)$ response of $Co_{67.1}Fe_{3.8}Ni_{1.4}$ $Si_{14.5}B_{11.5}Mo_{1.7}$ microwires with different diameters, d, and ρ-ratios.

sensor devices [6, 11]. It should be noted from Fig.3 that the $V_{out}(H)$ curves exhibit nearly linear growth within the field range from $-H_m$ to H_m. The H_m limits the working range of MI sensor to 240 A/m and should be associated with the anisotropy field.

3.3. Effect of magnetoelastic anisotropy and GMI hysteresis

The effect of the ρ– ratio on V_{out} (H) (Fig.3) should be attributed to the magnetoelastic anisotropy related with the internal stresses.

It must be underlined, that all studied samples exhibited excellent magnetically soft properties with inclined hysteresis hoops and extremely low coercivities (between 4 and 10A/m). Magnetic anisotropy field, H_k, is found to be determined by the ρ–ratio, decreasing with ρ (Fig.4), as also has been reported earlier [6,12].

On the other hand, it is well established, that strength of internal stresses, σ_i, arising during simultaneous rapid quenching of metallic nucleus surrounding by the glass coating can be controlled by the ρ–ratio: strength of internal stresses increases decreasing ρ–ratio (i.e. increases with increasing of the glass volume) [14-16].

The magnetoelastic energy contribution is given by [6,11]

$$K_{me} \approx 3/2\, \lambda_s \sigma_i, \qquad (1)$$

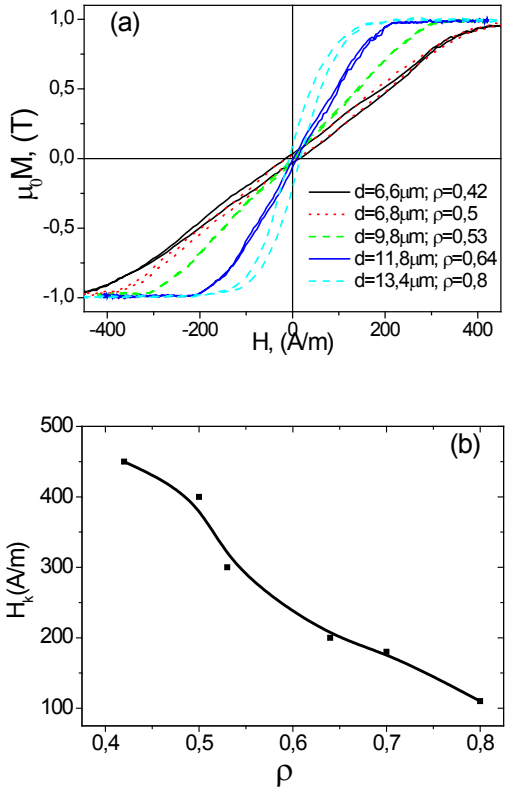


Fig.4. Hysteresis loops of $Co_{67.1}Fe_{3.8}Ni_{1.4}$ $Si_{14.5}$ $B_{11.5}$ $Mo_{1.7}$ microwires with different geometry (a) and dependence of H_k on ρ–ratio (b).

where λ_s is the saturation magnetostriction and σ_i is the internal stress.

The magnetostriction constant is mostly determined by the chemical composition and achieves almost nearly-zero values in amorphous alloys based on Fe-Co with Co/Fe ≈70/5 $\lambda_s \approx 0$ [6, 12,19]. On the other hand, the estimated values of the internal stresses in these glass coated microwires arising from the difference in the thermal expansion coefficients of simultaneously solidifying metallic nucleus and glass coating are of the order of 100-1000 MPa, depending strongly on the ratio between the glass coating thickness and metallic core diameter [6, 14-16], increasing with decreasing ρ–ratio. Consequently, magnetoelastic anisotropy of glass-coated microwires can be controlled by the geometrical ratio ρ through the strength of internal stresses.

Consequently magnetic field dependences of both Z_{zz} and $Z_{\varphi z}$ can be controlled by the magnetoelastic anisotropy through the ρ–ratio.

Similarly the nature of observed low field hysteresis on Z_1(H) and $Z_{\varphi z}$(H) (Figs2a and 2b) is directly related with deviation of the anisotropy easy axis from transversal direction [18]. Therefore, application of circular bias magnetic field H_B produced by DC current I_B running through the wire affects the hysteresis and asymmetry of the MI dependence, suppressing this hysteresis when I_B is high enough (see Fig.5, where effect of bias voltage on diagonal

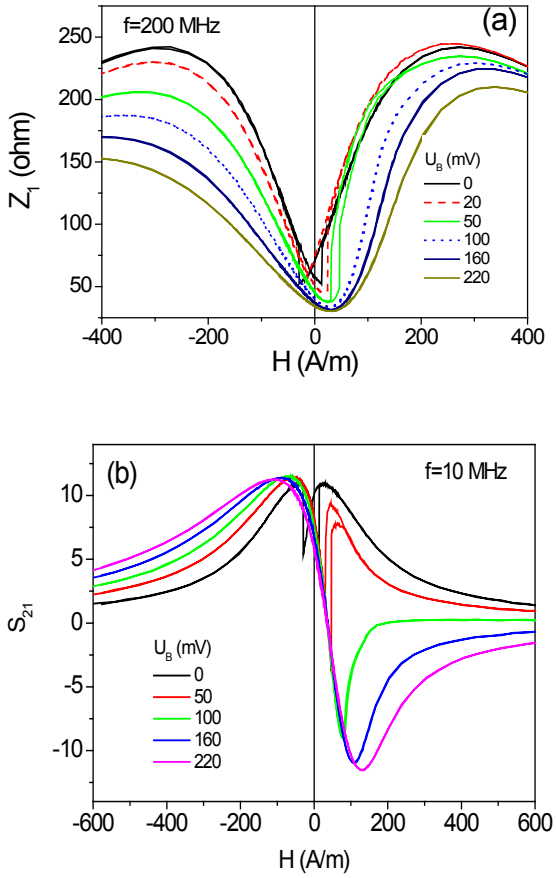


Fig.5. Effect of bias voltage U_B on magnetic field dependence of diagonal impedance (a) and S_{21} parameter (b) of $Co_{67}Fe_{3.85}Ni_{1.45}B_{11.5}Si_{14.5}Mo_{1.7}$ microwire

impedance, Z_1, and on S_{21} parameter, proportional to off-diagonal GMI component is shown). In fact in pulsed exciting scheme when the sharp pulses with pulse edge time about 5 ns are produced by passing square wave multi-vibrator pulses through the differentiating circuit, overall pulsed current contains a DC component that produces bias circular magnetic field [6, 11]. In this way low field hysteresis can be surpassed selecting adequate pulse amplitude.

3.4. Tailoring of GMI effect and magnetic properties by heat treatments

Traditional way to tailor magnetoelastic anisotropy issue of thermal treatment. The influence of Joule heating on off-diagonal field characteristic of nearly zero magnetostriction $Co_{67.1}Fe_{3.8}Ni_{1.4}Si_{14.5}B_{11.5}Mo_{1.7}$ microwire with diameters 9.4/17.0 μm (ρ≈0,55) is shown in Fig. 6. One can see that the thermal annealing with 50 mA DC current reduces the H_m from 480 A/m in as-cast state to 240 A/m after 5 min annealing.

Similarly, current annealing (due to Joule heating) has introduced changes in GMI effect (Fig.6b). This effect should be mostly attributed to the stress relaxation (although electrical current also induce circular magnetic field).

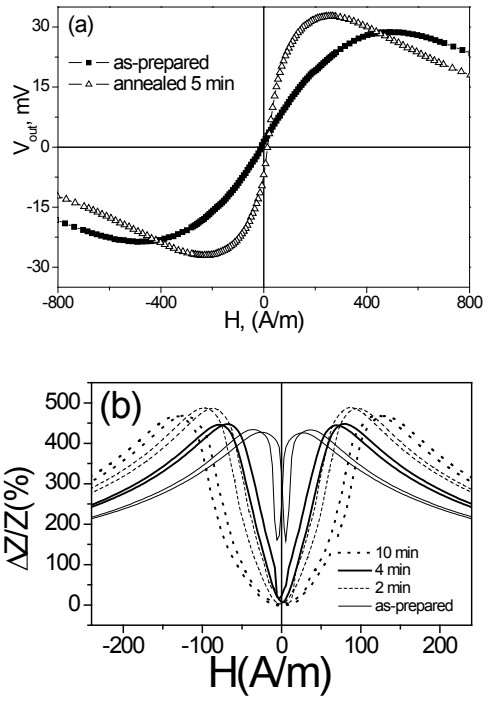


Fig.6. $V_{out}(H)$ of as –prepared and Joule-heated $Co_{67}Fe_{3.85}Ni_{1.45}B_{11.5}Si_{14.5}Mo_{1.7}$ microwire (current annealing with 50 mA current intensity) (a) and $\Delta Z/Z(H)$ dependences of heated $Co_{67}Fe_{3.85}Ni_{1.45}B_{11.5}Si_{14.5}Mo_{1.7}$ microwire measured at f=30 MHz and I=1 mA in microwire subjected to CA annealing at 40 mA for different time (b).

Application of stress and/or magnetic field during annealing of microwires allows inducing considerable magnetic anisotropy. It should be considered, that existence of internal stresses can reinforce effect of magnetic field applied during magnetic field annealing, as previously reported [20]. In some cases this results in drastic changes of hysteretic magnetic properties and GMI behavior [12, 17]. As an example, application of axial magnetic field during annealing induces axial magnetic anisotropy in Co-rich microwires (Fig.7). Here hysteresis loops of $Co_{67}Fe_{3.85}Ni_{1.45}B_{11.5}Si_{14.5}Mo_{1.7}$ microwires (d=22.4 μm, D=22.8 μm) annealed by Joule heating without (CA) and

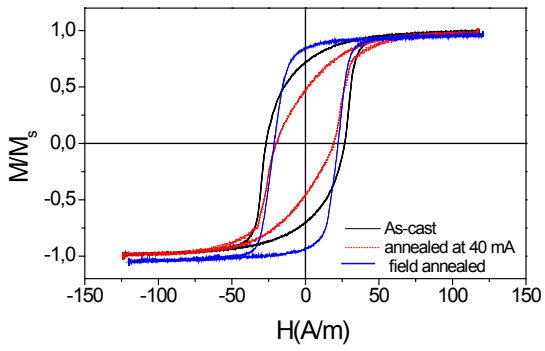


Fig.7 Effect of CA and FCA on bulk hysteresis loops of $Co_{67}Fe_{3.85}Ni_{1.45}B_{11.5}Si_{14.5}Mo_{1.7}$ microwires (d=22.4 μm, D=22.8 μm).

under application of axial magnetic field (FCA) are shown. As can be appreciated, application of magnetic field during annealing completely resulted in the opposite tendency inchanging of magnetic properties induced by annealing: increasing of remanent magnetization and decreasing of coercivity after FCA is observed, while CA treatment induced decreasing of the remanence and of the coercivity.

Most significant changes of both hysteresis loop and GMI behaviour have been observed in Fe-rich microwires subjected to the annealing in the presence of tensuile stresses (Fig.8).

Stress annealing of $Fe_{74}B_{13}Si_{11}C_2$ microwires resulted in induction of considerable stress induced anisotropy [18]. The shape of hysteresis loop completely changes. Additionally the degree of induced changes depends on time

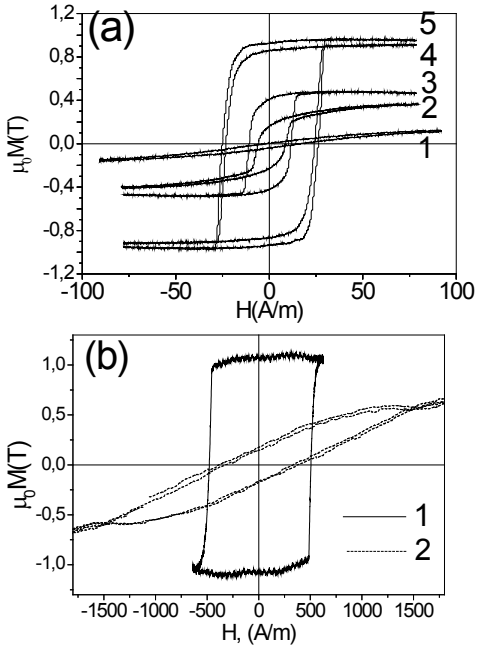


Fig.8 Hysteresis loops of $Fe_{74}B_{13}Si_{11}C_2$ microwire annealed under applied stress of 500 MPa (a) at (1) – 300 ºC 3 hours, (2) – 280 ºC 40 min, (3)- 265 ºC 40 min, (4) 235 ºC 40 min and (5)- 215 ºC 40 min and (b) stress induced changes of hysteresis loops of the same microwires (1- measured under applied stress, 2- measured without stress).

and temperature of annealing (Fig.8a). In this case the easy axis of magnetic anisotropy has been changed from axial to transversal [18]. Additionally, application of stress during measurements of stress-annealed microwires with well-defined transverse anisotropy results in drastic change of the hysteresis loop (Fig.8b).

Origin of such stress-induced anisotropy is related with so-called "Back stresses" originated from the composite origin of glass-coated microwires annealed under tensile stress: compressive stresses compensate axial stress component and under these conditions transversal stress components are predominant [18].

Consequently, these stress annealed samples exhibit stress-impedance effect, i.e. impedance change ($\Delta Z/Z$) under applied stress, σ, observed in samples with stress induced transversal anisotropy (see Fig.9) [18].

It should be assumed that the internal stresses relaxation after heat treatment should drastically change both the soft magnetic behavior and *ΔZ/Z(H)* dependence due to stress relaxation, induced magnetic anisotropy and change of magnetostriction constant under annealing.

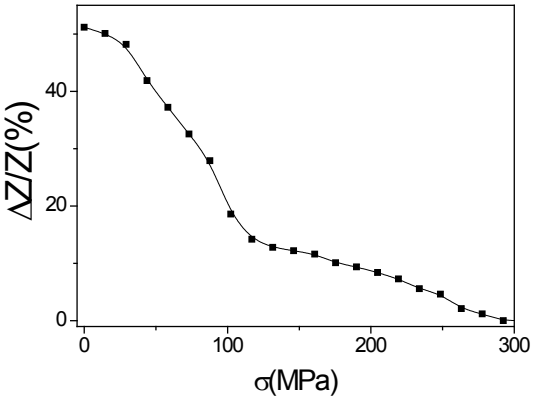


Fig.9 Stress impedance effect of stress annealed $Fe_{74}B_{13}Si_{11}C_2$ glass-coated microwire under stress (468 MPa) at 275ºC for 0.5h measured at frequency, f=10 MHz for the driving current amplitude of 2 mA

Summarizing, GMI magnetic field dependence can be tailored either controlling magnetoelastic anisotropy of as-prepared microwires or by heat treatment. We observed a number of interesting phenomena , such as stress-impedance effect and stress sensibility of overall hysteresis loop shape. Composite character of such microwires results in appearance of additional magnetoelastic anisotropy. Heat treatment is the efficient method of tailoring of magnetic properties and GMI effect of such microwires. Selection of proper chemical composition, geometry and adequate conditions of annealing allows achieving of high GMI effect.

4. Conclusions

In thin amorphous wires, produced by the Taylor-Ulitovski technique, magnetic softness and magnetic field dependence of GMI effect (both longitudinal and off-diagonal) and GMI hysteresis are determined the magnetoelastic anisotropy. This magnetoelastic anisotropy can be tailored by the sample geometry and adequate annealing. There are a number of interesting effects, such as induction of the transversal anisotropy in Fe-rich microwires allowing observation of the stress-impedance effect and stress sensibility of overall hysteresis loop shape. Observed low-field GMI hysteresis can be suppressed by the bias electrical current.

Studies of diagonal and off-diagonal MI tensor components of glass-coated microwires have shown the great potential of these materials for microminiaturized magnetic field sensor application. Their main advantages are high sensitive low-hysteresis field dependence. By varying the alloys composition and applying post fabrication processing it is possible to control the sensor's operating range. Low field

GMI hysteresis has been observed and explained in terms of helical magnetic anisotropy of microwires.

Acknowledgements

This work was supported by EU ERA-NET programme under projects "DEVMAGMIWIRTEC" (MANUNET-2007-Basque-3) and "SoMaMicSens" (MANUNET-2010-Basque-3), by EU under FP7 "EM-safety" project, by Spanish Ministry of Science and Innovation, MICINN under Project MAT2010-18914 and by the Basque Government under Saiotek 10 MIMAGURA project (S-PE11UN087).

.

References

[1] D.C. Jiles, "Recent advances and future directions in magnetic materials", *Acta Materialia* 51: 5907-5939, 2003.

[2] K. Mohri, F.B. Humphrey, K. Kawashima, K. Kimura and M. Muzutani, *IEEE Trans.Magn.,* Mag-26: 1789-1793, 1990.

[3] A.P. Zhukov, The remagnetization process of bistable amorphous alloys, Materials and Design, 14: 299-305, 1993.

[4] V. Zhukova, A. Zhukov, V. Kraposhin, A. Prokoshin and J. Gonzalez, Sensors and Actuators (A) 106: 225-229, 2003.

[5] P. Ciureanu, G. Rudkowska, L. Clime, A. Sklyuyev, A. Yelon, "Anisotropy optimization of giant magnetoimpedance sensors", J. Optoelectronics and Advanced Materials, 6: 905-910, 2004.

[6] V. Zhukova, M. Ipatov and A Zhukov, "Thin Magnetically Soft Wires for Magnetic Microsensors", *Sensors* 9: 9216-9240, 2009.

[7] M. Vazquez, H. Chiriac, A. Zhukov, L. Panina and T. Uchiyama, "On the state-of-the-art in magnetic microwires and expected trends for scientific and technological studies" Phys. Status Solidi A, A 208: 493–501,(2011.

[8] Y. Honkura, "Development of amorphous wire type MI sensors for automobile use", *J. Magn. Magn. Mater*., 249: 375-381, 2002.

[9] L.V. Panina and K. Mohri," "Magneto-impedance effect in amorphous wires"" *Appl. Phys. Lett*. 65: 1189-1191, 1994.

[10] R. Beach and A. Berkowitz, "Giant magnwetic field dependent impedance of amorphous FeCoSiB wire", *Appl. Phys. Lett*. 64: 3652-3654, 1994.

[11] S. I. Sandacci, D. P. Makhnovskiy, L. V. Panina, K. Mohri, and Y. Honkura, "Off-Diagonal Impedance in Amorphous Wires and Its Application to Linear Magnetic Sensors", IEEE Trans Magn., 35: 3505-3510, 2004.

[12] A.Zhukov and V. Zhukova, "Magnetic properties and applications of ferromagnetic microwires with amorphous and nanocrystalline structure", Nova Science Publishers, Inc. 400 Oser Avenue, Suite 1600 Hauppauge, NY 11788, 2009, 162 p. ISBN: 978-1-60741-770-5.

[13] V. Zhukova, N.A. Usov, A. Zhukov and J. Gonzalez, Length effect in Co-rich amorphous wire, Phys. Rev B, 65: 134407-1-7, 2002.

[14] H. Chiriac, T. A. Ovari, and Gh. Pop, "Internal stress distribution in glass-covered amorphous magnetic wires", Phys. Rev. B, **42:** 10105-10113, 1995.

[15] A S Antonov, V T Borisov, O V Borisov, A F Prokoshin and N A Usov, "Residual quenching stresses in glass-coated amorphous ferromagnetic microwires",J. Phys. D: Appl. Phys. **33**; 1161-1168, 2000.

[16] H. Chiriac, T.-A- Ovari and A. Zhukov, "Magnetoelastic anisotropy of amorphous microwires ", J. Magn. Magn. Mater. **254-255**: 469-471, 2003.

[17] A. Zhukov, "Design of magnetic properties of Fe-rich glass – coated magnetic microwires for technical applications", Adv. Func. Mat., 16: 675-680, 2006.

[18] M. Ipatov, V. Zhukova, A. Zhukov, J. Gonzalez, and A. Zvezdin, "Low-field hysteresis in the magnetoimpedance of amorphous microwires", Phys. Rev. B 81: 134421, 2010.

[19] Y. Konno and K. Mohri, "Magnetostriction measurements for amorphous wires", IEEE Trans. Magn., 25, No.5: 3623-3625, 1989.

[20] A. Zhukov, Glass – coated magnetic microwires for technical applications, J. Magn and Magn. Mater 242-245: 216-223, 2002.

Magnons in samples with exchange and dipolar long ranged interactions: Spin wave resonance intensities and Brillouin spectral linewidths

Jean-Claude S. Levy

Matériaux et Phénomènes Quantiques UMR 7162 CNRS, Université Paris 7 Denis Diderot,
10 rue A. Domon et L. Suquet, 75013 Paris,
E-mail: Jean-Claude.Levy@univ-paris-diderot.fr

Abstract

In magnetic materials dipolar interactions which are long ranged compete with exchange local interactions. This has several consequences on spin wave propagation and eigen modes in a finite sample within linear approximation. First the static dipolar field is non uniform over the sample. It acts on the main diagonal term of the dynamical matrix. Moreover even in the case of a 1D sample, dipolar interactions are responsible for a complete magnetic dynamical matrix without any zero. This second point, i.e. the spin wave resolution, is solved here analytically in the case of a simple 1D model with three general consequences. First the spin wave dispersion relation $E(k)$ is shown to be not always monotonous. Then for spin wave resonance the frequency is fixed and eigen modes are shown to include spatial interferences between sine-like waves and damped waves of wavelength corresponding to the same frequency. This specificity leads to several kinds of localization. Finally for Brillouin light scattering where the mode wavelength is fixed from selection rule, the different modes of the sample are shown to exhibit different linewidths. Generalization to other excitations such as electronic levels or phonons in presence of long ranged interactions is also proposed.

1. Introduction

Long ranged magnetic interactions are quite commonly observed in materials and nanomaterials. This is quite obviously the case of dipole-dipole interactions, also called dipolar interactions since they are unavoidable when samples exhibit localized magnetism. These dipolar interactions are responsible for the well known magnetic organization in domains, walls and other singularities such as magnetic vortices [1-3]. Of course among potential long ranged interactions, there are also electric dipole-dipole interactions which are quite similarly long ranged ones and lead to organization in ferroelectric domains, walls and other singularities [4]. So there is a quite large class of materials involved in such a study. It must be added that exchange contributions from next nearest neighbors and further neighbors can arise in magnetic materials with the famous case of superexchange in oxides [5]. As a consequence of this quantum overlapping intermediate range of coupling occurs in numerous materials.

There are many properties which are due to the long range character of magnetic dipolar interactions such as the demagnetizing field and the associated shape anisotropy as well as an effective non linear effect as observed in a local Landau-like Hamiltonian [6]. Here we want to focus on dynamic properties which are influenced by dipolar interactions and more generally by any long ranged interaction. These dynamic properties of magnetic samples can be observed by resonance techniques which are now coupled with surface techniques and thus allow experimentalists to look at the excitations even in nanometric materials, and by Brillouin light scattering techniques which also share a very narrow spatial resolution. When considering these spin waves also called magnons, the well known non uniformity of the static dipolar field, i.e. of the dipolar field created by the static part of the spins [2, 7] was already noticed by many authors as a non uniform contribution to the main diagonal term of the dynamical matrix. But it is not the only change due to long range coupling. Here we want to focus on the general properties of the dynamical matrix which is obtained after linearization of the equations of motion in the ground state. For the sake of simplicity we will consider a 1D sample or an effective 1D layered sample as often considered for various geometries [8-11]. So a first point consists in deriving the full dynamical matrix as deduced either from a Landau- Lifshitz-Gilbert approach when neglecting Gilbert damping or from the quantum equation of motion for local spin when using Tyablikov decoupling in order to look at low order terms. With this dynamical matrix the dispersion relation of spin waves is easily derived, and we will show its general non monotonous character. Approximate dynamical matrices are proved to be invertible analytically, and corrections to these approximate matrices can be introduced and finally solved in a Green function approach. So we will see the consequences of this calculation for stationary modes. Moreover better approximations of this dynamical matrix can be inverted by means of numerical computations and we will see that the comparison between numerical results and analytical predictions reinforce the validity of these predictions. Other mathematical techniques such as the transfer matrix method lead to the same result. A main effect is the occurrence of numerous properties of localization even without any defect except the sample finiteness. This strong localization effect is well in agreement with the existence of magnetic walls, lines, i.e. vortices and other topological defects in the ground state

arrangement of magnetic samples as quite generally observed in the absence of an external field [2,3]. Of course these local magnetic structures, wells, vortices and other topological defects disappear in presence of a convenient saturating extra magnetic field. So such magnetic structures can be deduced as soft spin wave modes when looking close to these transition fields [12] and these soft modes are thus necessarily strongly localized.

While this work on resonance modes necessarily focus on selected frequency because of selection rules which are involved in such experiments, selection rules of Brillouin light scattering fix the spin wave wavelength. We will see that this statement has strong consequences on the effective linewidths of modes observed in Brillouin light scattering.

The extension of the present work to other excitation modes such as elastic modes or electron modes, when long range interactions are involved in the samples, is also discussed with the evidence of special localization properties without any defect. These remarks define .the organization of this paper.

2. The Hamiltonian and the effective 1D dynamical matrix

2.1. The spin Hamiltonian

The spin Hamiltonian is made of three additive parts: the exchange Hamiltonian H_{ex}, the dipolar Hamiltonian H_d. and the Zeeman part H_Z which is due to the external field. These Hamiltonians are defined respectively by

$$H_{ex} = -\frac{1}{2}\sum_{i,j\in V_{ij}} J_{ij}\vec{S}_i * \vec{S}_j \quad (1)$$

Here the summation occurs over all the spins $\vec{S}_i$ and their neighbors weighted by the exchange integral J_{ij} . The dipolar Hamiltonian reads up to a numerical factor:

$$H_d = \sum_{i\neq j}\frac{\vec{S_i}*\vec{S_i}}{r_{ij}^3} - 3\sum_{i\neq j}\frac{(\vec{S_i}*\vec{r_{ij}})(\vec{S_i}*\vec{r_{ij}})}{r_{ij}^5} \quad (2)$$

Finally the Zeeman part reads:

$$H_{ex} = -\sum_i \vec{H}*\vec{S}_i \quad (3)$$

Here the gyrotropic constant times the magnetization has been considered as unity.

2.2. The ground state

Of course the material structure must be defined. It can be a line as in a molecular magnet, a part of a plane lattice in an ultra thin film or a part of a three dimensional lattice in a thin film or a more complex structure in a layered sample. We will retain here the 1D structure which is a common factor. Then the spin structure in the ground state can be obtained from energy minimization such as Monte-Carlo computation [3], Langevin spin dynamics at low temperature [13] or direct computation if possible. If the external field intensity is strong enough, there is a saturation effect: all spins are parallel to the external magnetic field. This is the case we are considering here for the sake of simplicity: a 1D sample made of spins which are parallel in the ground state.

2.3. The equations of motion

With the saturating field all spin deviations are normal to the external field, so they all lie within a plane normal to this field and their amplitude can be represented for the site n of our 1 D sample by a complex number u_n in this plane. Within that picture the general spin deviation equation of motion reads within the linear approximation involved with small spin deviations at a frequency characterized by the energy E either from a Tyablikov decoupling method or from Landau-Lifshitz spin equation of motion:

$$(a-E)u_n - b(u_{n+1}+u_{n-1}) - c(u_{n+2}+u_{n-2}) - d(u_{n+3}+u_{n-3}) + \ldots = 0 \quad (4)$$

Strictly speaking the coefficients $a,b,c,d,..$ depend on the spin location n as already noticed about the amplitude of the demagnetizing field [7]. This detail can be treated in a second step by the introduction of corrective layer dependent terms. Another point also linked with the finiteness of our sample starting from site 1 and finishing at site N is the lack of some terms in this equation, the ones which correspond to non realistic sites. This symmetry breaking appears also when considering the N equations of motion of our system as a function of the N complex spin deviations u_n . This calculation provides the magnetic dynamical matrix.

2.4. The magnetic dynamical matrix

Rewriting the successive equations (4) gives the set of equations from which the dynamical matrix $\mathbf{A}$ of our sample is deduced:

$$(a-E)u_n - b(u_{n+1}+u_{n-1}) - c(u_{n+2}+u_{n-2}) - d(u_{n+3}+u_{n-3}) + \ldots = 0$$

$$(a-E)u_{n+1} - b(u_{n+2}+u_n) - c(u_{n+3}+u_{n-1}) - d(u_{n+4}+u_{n-2}) + \ldots = 0$$

$$(a-E)u_{n+2} - b(u_{n+3}+u_{n+1}) - c(u_{n+4}+u_n) - d(u_{n+5}+u_{n-1}) + \ldots = 0$$

…

And so on. Here it must be recalled that unphysical sites cannot appear, so some terms are missing for a finite sample. In a matrix form, it reads, here written in the case of 8x8 dynamical matrix $\mathbf{A}$ with a linear equation on the spin deviations which will be solved by Green function techniques, i.e. here inversion of the matrix $\mathbf{A}$:

$$\begin{pmatrix} a-E & -b & -c & -d & -e & . & . & . \\ -b & a-E & -b & -c & -d & -e & . & . \\ -c & -b & a-E & -b & -c & -d & -e & . \\ -d & -c & -b & a-E & -b & -c & -d & -e \\ -e & -d & -c & -b & a-E & -b & -c & -d \\ . & -e & -d & -c & -b & a-E & -b & -c \\ . & . & -e & -d & -c & -b & a-E & -b \\ . & . & . & -e & -d & -c & -b & a-E \end{pmatrix}$$

$$\begin{pmatrix} u_1 \\ u_2 \\ u_3 \\ u_4 \\ u_5 \\ u_6 \\ u_7 \\ u_8 \end{pmatrix} = \mathbf{A} * \mathbf{u} = \begin{pmatrix} 0 \\ 0 \\ 0 \\ 0 \\ 0 \\ 0 \\ 0 \\ 0 \end{pmatrix}$$

(5)

Before solving this matrix equation by means of Green functions, let us consider the so defined dispersion relation for ingoing spin waves.

2.5. The dispersion relation for ingoing spin waves

The dispersion relation between pulsation ϖ and wavevector k for ingoing spin waves of spin amplitude $u_n = C\exp[ikna_0 - i\varpi t]$ on layer n where a_0 is the interlayer distance or inter-site distance, is straightforwardly deduced from the expression of the equation of motion (4) for this wave. For such modes the equation of motion reads as a one dimensional dispersion relation $E(k)$ between the spin wave energy E or pulsation ϖ and wavevector k:

$$E = a - 2b\cos(ka_0) - 2c\cos(2ka_0) - 2d\cos(3ka_0) - 2e\cos(4ka_0) - ... \quad (6)$$

This formula is also useful to consider the effect of different interaction ranges. Quite obviously with just nearest neighbor coupling, i.e. $c = d = e = .. = 0$ this dispersion relation is monotonous, with the typical result shown in Figure 1. In that case the dispersion relation is monotonous and there is a one to one correspondence between energy, i.e. frequency, and wave vector, i.e. wavelength. If more extended coupling occurs this is no more the case: for a given wavevector there is still a single energy of ingoing wave, but for a given energy or frequency, several wave vectors or wavelengths can occur at the same time and so these waves are interfering or beating together, some of these interfering waves can be complex. This interference effect for medium ranged or long ranged interactions is responsible for a high level of complexity in such stationary modes [14, 15]. In the case of exchange and dipolar interaction the complexity is high. So for a given frequency one can observe wavefunctions or wave packets with special localization properties. This is specially the case for stationary solutions..

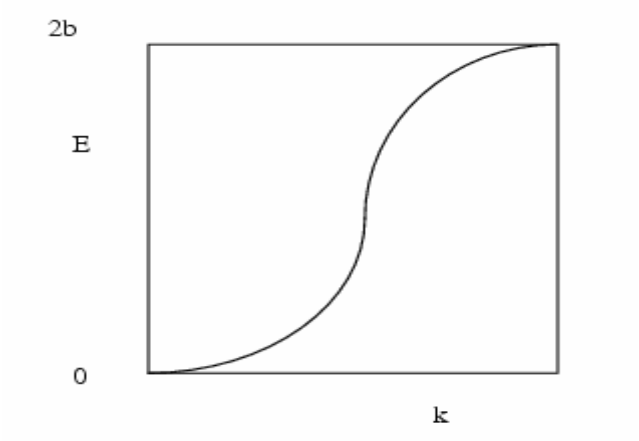


Figure 1: The spin wave spectrum for coupling restricted to the nearest layers (a=0). The magnon bandwidth is 2b.

3. Spin waves resonance with long ranged interactions

3.1. The mathematical resolution of stationary spin waves by Green function approach

The resolution of the set of equations (5) comes from a mathematical trick [16] based upon the matrix algebra. When considering the powers of the matrix **d** corresponding to just nearest neighbor coupling, i.e. with the main diagonal and two symmetric smaller diagonals, one obtains more and more extended diagonals and corrections close to the boundaries. This is shown here by considering the following powers of matrix **δ.**

$$\boldsymbol{\delta} = \begin{pmatrix} 0 & 1 & 0 & 0 & 0 & 0 & 0 & 0 \\ 1 & 0 & 1 & 0 & 0 & 0 & 0 & 0 \\ 0 & 1 & 0 & 1 & 0 & 0 & 0 & 0 \\ 0 & 0 & 1 & 0 & 1 & 0 & 0 & 0 \\ 0 & 0 & 0 & 1 & 0 & 1 & 0 & 0 \\ 0 & 0 & 0 & 0 & 1 & 0 & 1 & 0 \\ 0 & 0 & 0 & 0 & 0 & 1 & 0 & 1 \\ 0 & 0 & 0 & 0 & 0 & 0 & 1 & 0 \end{pmatrix} \quad (7)$$

They are up to extra lines and rows:

$$\boldsymbol{\delta}^2 = \begin{pmatrix} 1 & 0 & 1 & 0 & . \\ 0 & 2 & 0 & 1 & . \\ 1 & 0 & 2 & 0 & . \\ 0 & 1 & 0 & 2 & . \\ . & . & . & . & . \end{pmatrix} \quad \boldsymbol{\delta}^3 = \begin{pmatrix} 0 & 2 & 0 & 1 & . \\ 2 & 0 & 3 & 0 & . \\ 0 & 3 & 0 & 3 & . \\ 1 & 0 & 3 & 0 & . \\ . & . & . & . & . \end{pmatrix}$$

$$\boldsymbol{\delta}^4 = \begin{pmatrix} 2 & 0 & 3 & 0 & 1 & . \\ 0 & 5 & 0 & 4 & 0 & . \\ 3 & 0 & 6 & 0 & 4 & . \\ 0 & 4 & 0 & 6 & 0 & . \\ 1 & 0 & 4 & 0 & 6 & . \\ . & . & . & . & . & . \end{pmatrix}$$

$$\boldsymbol{\delta}^5 = \begin{pmatrix} 0 & 5 & 0 & 4 & 0 & 1 & . \\ 5 & 0 & 9 & 0 & 5 & 0 & . \\ 0 & 9 & 0 & 10 & 0 & 5 & . \\ 4 & 0 & 10 & 0 & 10 & 0 & . \\ 0 & 5 & 0 & 10 & 0 & 10 & . \\ 1 & 0 & 5 & 0 & 10 & 0 & . \\ . & . & . & . & . & . & . \end{pmatrix} \quad (7a)$$

So any set of equations (5) as the dynamical matrix itself can be understood as an algebraic equation over the matrix **d**, with the extra condition:

$$\begin{aligned} A &= P(\mathrm{d}) \\ \mathrm{detA} &= 0 \end{aligned} \quad (7b)$$

Here P(x) is a polynomial form.
This algebraic equation is solved with roots λ_i . So the complete dynamical matrix reads:

$$\prod_i (d - \lambda_i I) = 0 \quad (8)$$

Of course all these matrices commute together, so standard algebraic methods can be used and the dynamical matrix ***A*** itself can be inverted [16]. The inverted matrix expresses itself as a sum of simple elements:

$$A^{-1} = \sum_i c_i (d - \lambda_i I)^{-1} \quad (9)$$

In that equation A^{-1} is the Green function matrix associated with the dynamical matrix ***A***. This result enables us to find the stationary modes as usual, i.e. without long ranged interactions [16].
Of course a lot of corrections must be added in order to balance the extra terms induced by the powers of the initial matrix as seen on equations (7a). Other corrections are also needed to account for the non uniformity of coefficients a, b, c, and so on. As noticed in references 16 and 17, such corrections can be analytically but heavily solved. Theses corrections make the effective characteristic equation (7b) more and more complex to solve, but they do not change its basic structure. So let us just retain the concept of wave beating for these stationary modes when introducing realistic boundary conditions, i.e. corrections. These interference effects will be dealt more easily by introducing local transfer matrix calculations which are a little bit simpler than the direct Green function approach. Of course this local approach looses the global character of the Green function approach.

3.2. Transfer matrix approach of stationary spin waves

The generic equation of motion (4) can be written in the form which breaks the symmetry by specifying the result of the excitation of previous sites:

$$u_{n+N} = -\frac{a_{N-1}}{a_N} u_{n+N-1} - \frac{a_{N-2}}{a_N} u_{n+N-2} - \ldots + \frac{a_0 - E}{a_N} u_n - \ldots - \frac{a_{N-2}}{a_N} u_{n-N+2} - \frac{a_{N-1}}{a_N} u_{n-N+1} - u_{n-N} \quad (10)$$

Then we consider the obvious equations for the already involved previous sites:

$$\begin{aligned} u_{n+N-1} &= u_{n+N-1} \quad (10) \\ &\ldots \\ u_{n-N+1} &= u_{n-N+1} \end{aligned}$$

So finally the set of equations of motion can be translated as a series of local transfer matrix equations, i.e. the result for neighboring sites of the excitation of previous sites. This local transfer matrix approach is an evolution method which has been largely used in mechanics starting from Poincaré [18] and which is also used in electronics where it is useful to follow the signal progression during its treatment.
These basic equations are written in a matrix style:

$$\begin{pmatrix} u_{n+N} \\ u_{n+N-1} \\ . \\ u_{n-N+2} \\ u_{n-N+1} \end{pmatrix} = \begin{pmatrix} -\frac{a_{N-1}}{a_N} & \frac{a_{N-2}}{a_N} & . & \frac{a_{N-1}}{a_N} & -1 \\ 1 & 0 & 0 & 0 & 0 \\ . & . & . & . & . \\ 0 & 0 & . & 0 & 0 \\ 0 & 0 & 0 & 1 & 0 \end{pmatrix} * \begin{pmatrix} u_{n+N-1} \\ u_{n+N-2} \\ . \\ u_{n-N+1} \\ u_{n-N} \end{pmatrix} \quad (11)$$

i.e. in a matrix notation:

$$\mathbf{u}_{n+N} = \mathbf{T} * \mathbf{u}_{n+N-1} \quad (11a)$$

The order of this transfer matrix 2*N* is defined by the range *N* of the interaction. In the case of a limited range of interaction, this transfer matrix is quite smaller than the dynamical matrix. A simple calculation shows that this transfer matrix $\mathbf{T}$ shown in equation (11) is unitary as expected for transfer matrices. The final transfer matrix equation includes the boundary conditions and is deduced from the product of all the local transfer matrices [19]. This final transfer matrix equation reads when magnetic parameters are the same throughout the sample, i.e. when all local transfer matrices are identical, the same condition on parameters *a, b, c,..,* as before:

$$P(\mathbf{T}) = 0 \quad (12)$$

Where $P(x)$ is a polynomial of the variable *x*. The polynomial order is the number *P* of film layers. Now the local transfer matrix diagonalization gives:

$$\mathbf{T} = \mathbf{M}\mathbf{D}\mathbf{M}^{-1} \quad (13)$$

Where $\mathbf{D}$ is a diagonal 2*N*x2*N* matrix with *N* root pairs when 2*N* is the number of layers involved in the interaction range. These root pairs are either: a complex root and its complex conjugate – in that case this defines a bulk wave-, or a real root and its inverse – in that case this defines a surface mode-. This pairing is due to the symmetric property of the transfer matrix $\mathbf{T}$ for ingoing and outgoing waves. Matrix $\mathbf{M}$ is a unitary 2*Nx2N* matrix as usual. In the case of dipolar interactions as for other infinitely ranged interactions, *P* is equal to *N*.
From this diagonalization equation, the evolution equation (11a) can be finally rewritten as:

$$\mathbf{u}_{n+N} = \mathbf{T}^{N+n} * \mathbf{u}_0 = \mathbf{M}\mathbf{D}^{N+n}\mathbf{M}^{-1} * \mathbf{u}_0 \qquad (14)$$

Developing this equation shows that the eigen mode profiles result from the superposition of *N* surface waves and sinusoidal waves since because of symmetry the bulk transfer matrix has for eigen values s and s^{-1} or $s*$ for a complex value.
In other words the transfer matrix method enables us to solve the dynamical matrix equation in a way which is shorter than the Green function approach but obviously leads to the same result of stationary waves made up of numerous beating sine-like waves. This agreement was successfully checked in several cases of intermediate range coupling [15]. So it is now convenient to look at realistic numerical resolution of cases where dipolar interaction and exchange compete [10,20].

3.3. Numerical resolution of stationary spin waves

In order to give evidence for both the interference effect and the localization effect, we report a few classical calculations. The first one shown in Figure 2 gives the numerical profiles of the four lowest lying eigen modes of a finite chain of twelve atoms with a constant nearest neighbor coupling and a constant next nearest neighbor coupling of opposite sign [15]. These results were obtained from transfer matrix approach and their symmetry proves the accuracy of these calculations. Quite obviously these results cannot be explained by a single sine-like behavior.

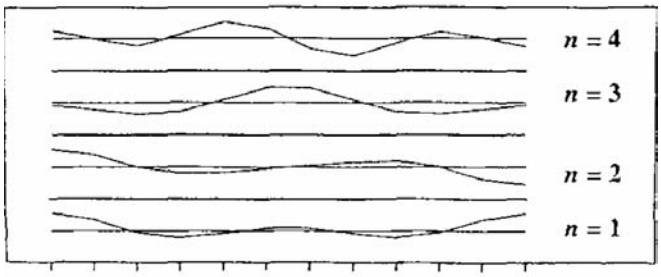


Figure 2: The 4 first spin wave profiles for coupling restricted to the nearest layers and the next nearest neighbors in a twelve atoms chain [15].

In the case of a cube of side 41 considered as a layered sample consisting of 41 layers, we report in Figure 3 the result obtained in reference 9 about the 41 modes of a pure magnetostatic sample. The magnitudes of amplitudes are reported for each site and modes are classified according to increasing energy. In Figure 3 even and odd symmetry are parted in two columns. Quite obviously there are two surface localized modes as usual about spin waves (n=1 and n=2). But there are also many "non central bulk-localized modes" (n=3 –n=23) with no amplitude in the central part and an amplitude peak well inside the sample. These modes are well localized even if for the highest modes this localization is extended over several layers (n=19 – n=23). Then there are "center localized modes" (n=23 – n=39) with no amplitude at the extreme layers and in their vicinity, while there is a non zero amplitude in the central part. These modes as well as the previous ones cannot be understood as pure sine-like modes. Quite numerous nodes can be noticed and they are not arranged in a regular way. These modes exhibit strong interference effects as predicted in the two previous mathematical analyses of simplest cases. Finally the last two modes (n=40 and n=41) appear as more classical bulk modes even if they are not also pure sine-like.
When exchange compete with dipolar interactions [10,11] similar localization effects occur in numerical simulations. Such localization effects not only at the extreme surface are also obvious in the calculation of magnetization reversal in nanoparticles [21].

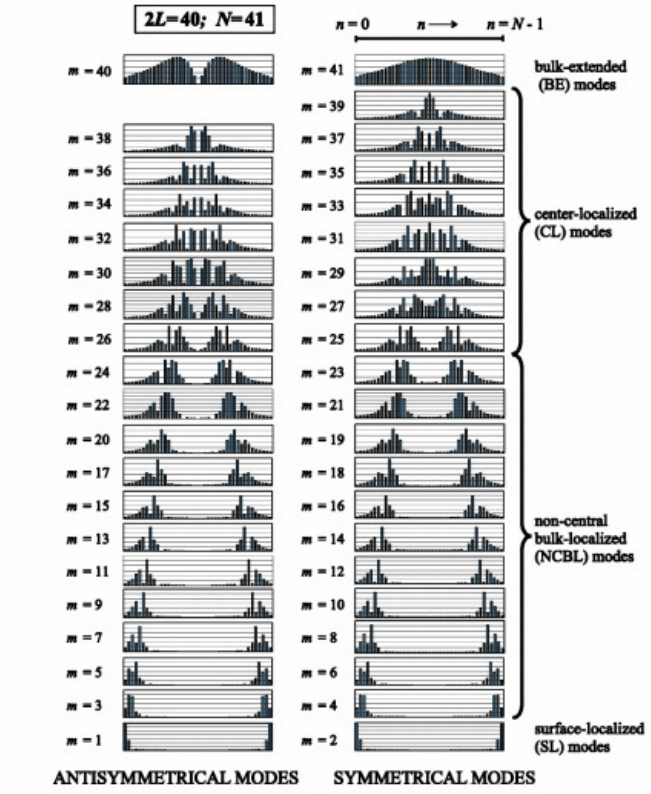


Figure 3: The 41 spin wave profiles for a saturated cubic grain of 41*41*41 spins coupled only by magnetostatic interaction. The sample is considered as layered [9].

These localization effects are now quite obvious when long range interactions such as dipolar ones occur in magnetic materials. We will now see the consequences of these long ranged interactions for Brillouin light scattering experiments.

4. Consequences of long range interactions on Brillouin light scattering

In Brillouin light scattering, the incident light determines the spin wave wavevector k in agreement with the sample size. This selection rule completely changes our writing of the spin deviation equation of motion by introducing the writing of such ingoing waves

$$u_n = C\exp[ikna_0 - i\omega t]$$

Then the equations of motion must consider a complex energy or frequency in order to deal with the symmetry break due to the finiteness of the sample. This leads to the new writing for the real and imaginary part of the *N* eigen frequencies:

$$\mathrm{Re}(E_1) = a - b\cos k - c\cos(2k)) - ... - a_{N-1}\cos((N-1)k)$$
$$\mathrm{Re}(E_2) = a - 2b\cos k - c\cos(2k)) - ... - a_{N-2}\cos((N-2)k)$$
$$\mathrm{Re}(E_1) = a - 2b\cos k - 2c\cos(2k)) - ... - a_{N-3}\cos((N-3)k)$$
..
(15)

And so on. And similarly for the imaginary part:

$$\mathrm{Im}(E_1) = -b\sin k - c\sin(2k)) - ... - a_{N-1}\sin((N-1)k)$$
$$\mathrm{Im}(E_2) = -c\sin(2k)) - ... - a_{N-2}\sin((N-2)k)$$
$$\mathrm{Im}(E_3) - d\sin(3k)) - ... - a_{N-3}\sin((N-3)k)$$
..
(15a)

Here the extension of the previous notation (*a, b, c, d*, ..) is obvious. From equations (15a) it is clear that the imaginary part of the frequency, i.e. its linewidth is large for the first mode defined by the superficial layer and decreases, generally speaking for inside modes. This non uniformity of Brillouin light scattering linewidths was already observed [22].

5. Conclusions

.

During this paper the evidence for localization of modes in spin wave resonance when long ranged interactions such as dipolar ones occur has been shown in different ways. It was also shown that for Brillouin light scattering these long ranged interactions lead to a distribution of linewidths, with generally speaking large linewidths for modes associated with the extreme layers.

Since long ranged interactions occur in numerous materials such as ferroelectrics or multiferroic materials, similar properties of localization or linewidth distribution are expected to occur for resonance or Brillouin light scattering in these materials.

There is also a large class of physical problems with similar mathematical requirements as characterized by full dynamical matrices or large transfer matrices. An obvious analog is the case of elastic modes when long ranged interactions occur. There is a classical approach of phonons and magnons, so even if calculations of elastic properties have a more complex geometry, similar properties of localization or distributed linewidths are expected for long ranged interactions for phonons too. Another analog problem is the one of electronic states when considering local interactions in a tight binding model. When the electron-electron coupling is extended similar properties of localization must be observed.

Finally, usual random walk has for basis the hopping on a neighboring site and so it corresponds to magnon, phonon problems with short range interactions. If one considers random walk with several hopping ranges at the same time, i.e. at the next step the walker can reach a place with a hopping distance n with probability P_n, then a problem similar to the present problem is defined. In that case diffusion is more complex than in the classical approach and leads to complex profiles.

As a conclusion this discrete approach of basic phenomena with extended interaction such as excitation modes are could be quite fruitful in the near future.

References

[1] L.D. Landau and E.M. Lifshitz, *The classical theory of fields*, 2nd ed. Pergamon Press, Oxford, 1962, p.119.

[2] A. Hubert and R. Schäfer, *Magnetic Domains: the analysis of magnetic microstructures*, Springer, Berlin, 1998.

[3] E.Y. Vedmedenko, A. Ghazali and J.-C.S. Levy, Magnetic vortices in ultra thin films, Phys. Rev. B **59**, pp 3329-3332, 1999.

[4] A. Schilling, S. Prosandeev, R.G.P. McQuaid, L. Bellaiche, J.F. Scott and J.M. Gregg, Shape-induced phase transition of domain patterns in ferroelectric platelets, Phys. Rev. B **84**, pp 064110, i-5, 2011.

[5] N.W. Ashcroft and N.D. Mermin, *Solid State Physics*, HRW International Editions, Hong Kong, p.681, 1987.

[6] J.-C.S. Levy, Dipolar induced magnetic anisotropy and magnetic topological defects in ultra thin films, Phys. Rev. B **63**, pp. 104409,1-8, 2001.

[7] H.J.G. Draaisma and W.J.M. de Jonge, Surface and volume anisotropy from dipole-dipole interactions in ultrathin ferromagnetic films, J. Appl. Phys. **64** 3610-3613, 1988.

[8] Rivkin, A. Heifetz, P. R. Sievert, and J. B. Ketterson, Resonant modes of dipole-coupled lattices, Phys. Rev. B **70**, pp. 184410,1-4, 2004.

[9] H. Puszkarski, J.-C.S. Levy and M. Krawczyk, Localization properties of pure magnetostatic modes in a cubic nanograin, Phys. Rev. B **71**, pp. 14421-14432, 2005.

[10] H. Puszkarski, M. Krawczyk and J.-C.S. Levy, Purely dipolar versus exchange dipolar modes in cylindrical nanorods, J. Appl. Phys. **101**, 02436-02446, 2007.

[11] K. Rivkin, W. Saslow, L.E. De Long, and J.B. Ketterson, Dynamic magnetic response of infinite arrays of ferromagnetic particles, Phys. Rev. B **75**, pp. 174408-1-8, 2005.

[12] S. Mamica, J -C. S Levy, Ph. Depondt, and M Krawczyk, The effect of the single-spin defect on the stability of the in-plane vortex state in 2D magnetic nanodots, J. Nanopart. Res. **13** 6075-6083 2011.

[13] Ph. Depondt, J.-C.S. Levy and F.G. Mertens, Vortex polarity in 2-D magnetic plots by Langevin dynamics simulations, Physics Letters A **375**, 628-632, 2011.

[14] H. Puszkarski, J.-C.S. Levy and S. Mamica, Does the generation of surface spin-waves hinge critically on the range of neighbour interaction? Phys. Lett. A **246**, 347-352 1998.

[15] J.-C.S. Levy, Magnon spectra in layered samples: from NN exchange to dipolar coupling, in *Nanostructures and their magnetic properties*, pp 303-328, Ed. J.-C.S. Levy, Research Signpost, Trivandrum Kerala 2009.

[16] J.-C.S. Levy, Surface and interface magnons, Surf. Sci. Reports, **1**, 39-120, 1981.

[17] J.-C.S. Levy, E. Gallais and J.L. Motchane, Thin ferromagnetic films: Spin waves and magnetization, J. Phys. C7, 761-778, 1974.

[18] H. Poincaré, Sur le probléme des trois corps et les équations de la dynamique, Acta. Math. **13** A3-A270 1890.

[19] D. Mercier, J. C. S. Levy, M. L. Watson, J. S. S. Whiting, and A. Chambers, Spin wave modes in layered magnetic sandwich structures, Phys. Rev. B **43**, 3311-3317, 1991.

[20] M. Krawczyk and H. Puszkarski, Theory of comb and bulk-dead magnetostatic modes in elongated nanorods, , in *Nanostructures and their magnetic properties*, pp 257-302, Ed. J.-C.S. Levy, Research Signpost, Trivandrum Kerala 2009.

[21] P.A. Rikvold, G. Brown, S.J. Mitchell and M.A. Novotny, Dynamics of magnetization reversal in models of magnetic nanoparticles and ultrathin films, *Nanostructured magnetic materials and their Applications,* Ed. D. Shi et al., Springer Berlin, pp 164-182, 2002.

[22] G. Gubbiotti, S. Tacchi, M.Madami, G. Carlotti, A.O. Adeyeye and M. Kostylev, Brillouin light scattering studies of planar metallic magnonic crystals, J. Phys. D: Appl. Phys. **43** 264003-264012, 2010.

Application of electromagnetic waves for the degradation mechanisms of painted wooden cultural properties

M.-J.KIM[1*], Y.Kohdzuma[1,2], and K.Fukunaga[3]

Kyoto University, Kyoto, Japan

2Nara National Research Institute for Cultural Properties, Nara, Japan

3National Institute of Information and Communications Technology, Tokyo, Japan

*culstory @ nabunken.go.jp

Abstract

The deterioration processes of the coloring are different by materials, coloring technique and environment. In order to understand a phenomenon of coloring deterioration, it is necessary to consider the different causes. In this study, some causes of coloring deterioration were known from materials analyses and visualization technique with using terahertz wave. Application of terahertz wave to painted wooden cultural properties might contribute to diagnosis of coloring deterioration.

1. Introduction

Painted wooden cultural properties consist of wood, preparation layer such as gypsum, whitewash and lead white, binder such as animal glue and *funori*, and different pigments. As the physical properties of these materials are different from each other, the painted wooden cultural properties show various degradation manners for a long time. Consequently, appearance of historical wooden buildings often shows old-colored surface on wood. On the other hand, some buildings are painted newly after removal of old paintings in the restoration works. The original paintings and the technique have been lost. It is necessary to find out a restoration method of original paintings on wooden cultural properties to hand down the techniques and the materials to future generation.

It is difficult to diagnose the degradation condition of coloring on wooden cultural properties by non-destructive way. Recently, terahertz (THz) wave and millimeter wave have been applied to visualize invisible area, e.g. inner structure of plaster layer as a preparation layer[1.2]. The application of THz imaging to art conservation has been proposed in 2007[3] and to wood cultural heritage related materials in 2008[4]. THz radiation can be used to analyze the materials slightly below the layers of the paint, such as preparation layers[5].Using the THz radiation it is then possible to see through dielectric layers, to discover hidden paintings or preparatory drawings. It can be used to perform subsurface non destructive analysis on paintings and wooden artworks[6]. For the conservation purpose, the most important part of paintings is the preparation layer. THz imaging can provide tomogram non-destructively, which helps conservators to understand the techniques and repainted layer in the previous conservation.

The wooden painting is composed of wood, preparation layer and pigment layer from the bottom. The THz image is taken about 1mm above the surface of the wood[7]. It is possible to see through the painting layer with use of THz wave. Moreover it is possible to use this feature to investigate the dielectric properties of different materials.

Tanzan Jinjya shrine in *Sakurai* city, *Nara*, was built in 678. Many paintings are on the wooden columns and beams of the main hall, so-called *Honden* reconstructed in 1850. The three Japanese traditional painting methods, i.e. *Urushi* painting, painting with use of animal glue and *Chan* painting[8.9], were described in restoration record of *Tanzan Jinjya* shrine in 1850. Some pattern samples which were made for the restoration in 1850 also have been kept in this shrine. The materials and the structures of the patterns samples and the same pattern on *Honden* were analyzed by some electromagnetic waves including THz wave. In this paper, tomograms obtained from THz imaging by time-domain spectrometry, so-called THz-TDS method were compared with actual structure from observation by microscope.

2. Materials and Methods

2.1. Materials

The pattern samples and the *Urushi* painting samples, which were prepared for restoration work 160 years ago, have been kept in *Tanzan Jinjya* shrine. From restoration document record, it is found that the *Urushi* painting samples have been prepared by 9 processes.

The pattern samples are shown in Fig.1. The same pattern from four directions, i.e. north, east, south and west, of *Honden* were measured. As sampling from all the paintings was not allowed, the analyses were done by non-destructive methods only on the surface.

2.2. Investigation Methods

X-ray fluorescence spectrometry (XRF) was applied to elements analysis of pigments. X-ray fluorescence spectrometer (Thermo Scientific, Niton) was used. This

spectrometer is mobile type, and so it is possible to analyze the objects by non-destructive method on site. Analytical conditions are followed; Tube voltage: 40 kV, Tube current: 50 μA, Duration time: 20 sec, Irradiation diameter: 8 mm, under air pressure.

Terahertz spectroscopy and imaging were applied to the pattern samples to visualize the inner structure of the painting and layers. The THz spectrometer was used Picometrix, T-Ray 4000. The irradiated frequency was 0.2 to 1.4 THz. The focus distance was three inches. Imaging was constructed by 0.30000 mm per 1 pixel. Scanning rate was 10 mm/sec. Measuring areas were shown in Fig. 1. From the terahertz spectroscopy and imaging data, the tomogram image was obtained by Time-Domain-Spectroscopy (THz-TDS).



Figure 1: Pattern samples kept in *Tanzan Jinjya* shrine for 160 years.

3. Results and Discussion

3.1. THz spectrum imaging of the pattern samples

The THz images are shown in Fig. 2. These images are constructed by all signals without limiting of the power integration value of frequency domain and the time domain. The color and elements are cited in Table 1.

From the observation of THz image of sample 1, crack and flaking off of pigment were hardly found. The thickness of painting layer is about 0.05 to 2 mm. In the tomogram image, the gold foil and some defects were indicated as the disturbed lines. In this THz image, especially, a flower pattern of right side was absorbed not to image. Though cupper and mercury were detected by X-ray fluorescence spectrometry, it is necessary to investigate cause of this phenomenon in detail.

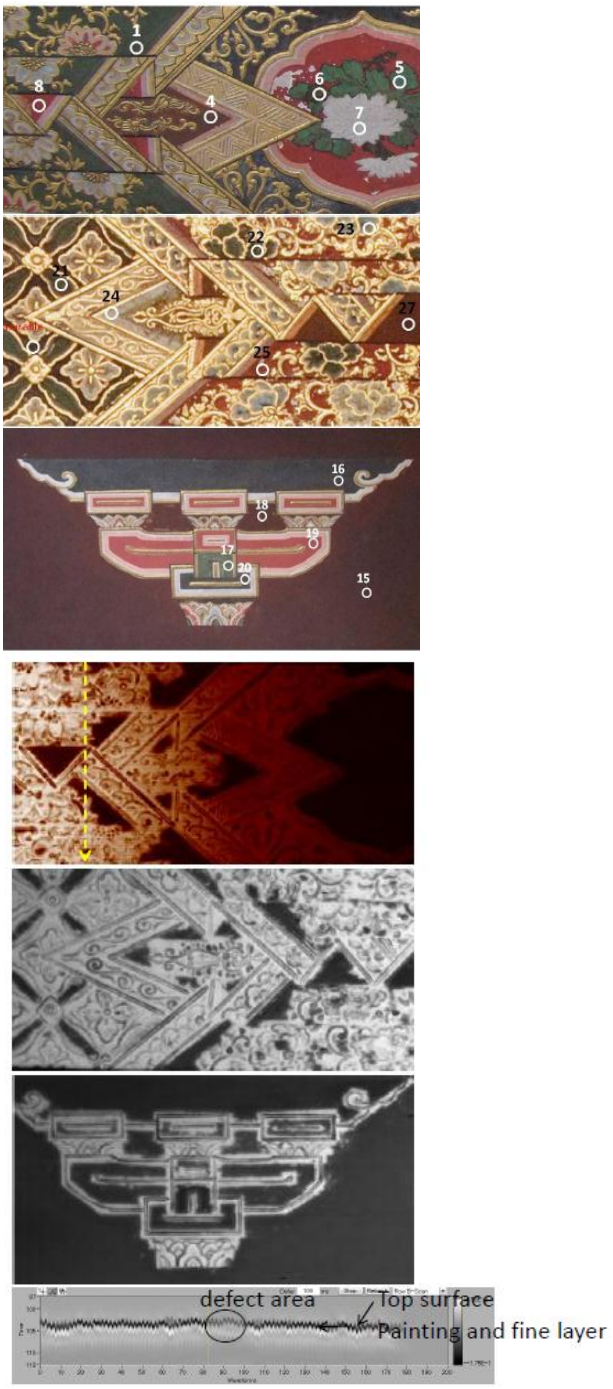


Figure 2:
visible and reflection images and non-invasive cross section image

From the THz image, it was found that wide gold foil ribbon was put over the preparation layer firstly, and then fine patterns were painted on it. Since such information is from inner structure, it is possible to find out it by THz imaging not by surface observation.

The tomogram of sample No.2 is a section located 7.5 mm distance in X-axis direction from the measurement origin. From this tomogram, defected areas of painting layer were found from 6 to 7.6 mm and 39 to 45 mm in X-axis direction. However, this defects were not exfoliation and crack.

Table 1: results of XRF

NO.	color						
1	green 1	Ca	Fe	Cu	Zn	As	Sr
2	green 2	Ca	Fe	Cu	Au	Pb	
3	red 1	Ca	Fe	Hg	Pb		
4	red 3	Ca	Fe	Cu	Zn	As	Pb
5	green 3	Ca	Fe	Cu	Zn	As	Pb
6	green 4	Ca	Fe	Cu	Hg	Pb	
7	white 1	Ca	Fe	As	Sr		
8	red 4	Ca	Fe	Hg	Pb		
9	green 5	Ca	Fe	Cu	Zn	Au	Pb
10	green 5/6	Ca	Fe	Cu	Hg	Pb	
11	blue 1	Ca	Fe	Cu	Pb	Sr	
12	brown 2	Ca	Fe	Cu	As	Pb	
13	green 2	Ca	Fe	Cu	Zn	Au	Pb
14	BKG white	Ca	Fe	Cu	Zn	Hg	Pb
15	BKG	Fe					
16	green 1	Ca	Fe	Cu	Pb		
17	green 2	Ca	Fe	Cu	Zn	As	Pb
18	brown 2	Ca	Fe	Au	Pb		
19	red 1	Ca	Fe	Hg	Pb		
20	blue 1	Ca	Fe	Cu	Au	Pb	
21	green 1	Ca	Fe	Cu	Zn	As	Pb
22	green 2	Ca	Fe	Cu	Au	Pb	
23	blue 2	Ca	Cu	Au	Pb		
24	white/purple 1	Ca	Fe	Au	Pb		
25	red 1	Ca	Fe	Cu	Hg	Pb	
26	brown 1	Ca	Fe	Cu	Zn	As	Pb
27	brown 2	Ca	Fe	Sr			

3.2 Observation of multi-layers structure

In THz imaging of multi-layers structure, an interaction between THz wave and materials contained in each layer should be taken into consideration. THz imaging was applied to *Urushi* painting samples with multi-layers structure.

It is known that THz wave is able to pass through *Urushi* and is strongly reflected by cinnabar[http://www.irug.or http://.thz-spectra.com]. If different materials are contained to *Urushi*, the dependence of frequency on dielectric and refractive indexes of *Urushi* layer is different. In order to estimate the influence of materials contained into *Urushi* on THz imaging, signals obtained from THz-TDS of the 8 different *Urushi* painting samples, which have been kept in *Tanzan Jinjya* shrine since a restoration 160 years ago, were compared.

THz-TDS tomograms of 8 *Urushi* painting samples are shown in Fig. 3. The brighter tone means the stronger reflection in this figure. It is possible to obtain the tomograms of *Urushi* painting by THz-TDS method non-destructively. Each tomogram shows the characteristic structure derived from the individual painting technique. Fig. 4. is THz pulse signals detected from the *Urushi* painting samples NO.1. It is seen that 8 layers are recognized in each *Urushi* painting samples. Existence of 8 different layers is consistent with a restoration document record 160 years ago. The *Urushi* painting sample has nine individual layers from eight processes. Fig. (A) is a THz tomogram obtained from the *Urushi* painting sample. Fig. (B) is a tomogram by THz-TDS for the same *Urushi* painting sample. The latter shows eight signals which are collected with THz-TDS at 10 mm intervals.

In the tomogram, information from some layers overlapped. When a pigment which has very strong reflectivity such as cinnabar is painted on the surface, it is impossible to take information from lower layers. It is only possible to distinguish with four layers, to know the existence of lower layer, and to calculate the film thickness. On the other hand, it is clear that the number of processes is eight from analysis of the signals by TDS. This is consistent with the restoration document 160 years ago. It suggests that inner structure of *Urushi* painting with multi-layers can be visualized by THz-TDS method.

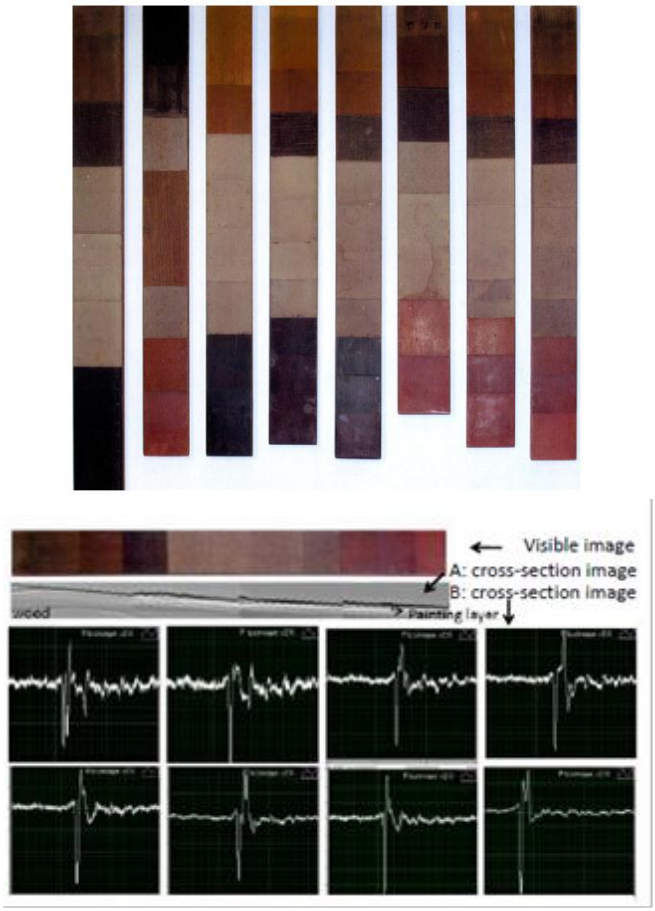


Figure 3: *Urushi* painting samples and THz image

4. Conclusions

As for the painted wooden cultural properties, the painting layer discolors and fades by natural deterioration, and often flakes off from the wood support. In restoration, generally, the deterioration features are often judged only by observation on the surface of the objects, because it is difficult to know the structure of coloring layers and exfoliation area by non-destructive and non-contact ways. In this study, to detect discoloration, fading and exfoliation of coloring and preparation layers, THz spectroscopy and imaging as non-destructive method was applied for painted wooden cultural properties.

The results obtained from color measurement, XRF and THz spectroscopy showed existence of 6 colors and 12 pigments. From the THz imaging, it became possible to detect area exfoliated from wood support and different materials under the coloring layers [11]. For THz imaging of *Urushi* painting, which is composed of one base layer such as cloth, and several *Urushi* layers which sometimes include different materials, ex. clay and pigments, it was possible to distinguish the surface between the base layer and *Urushi* layers. However, it was impossible to distinguish with each *Urushi* layer without materials separately. It is seemed that this phenomenon is caused by difference of refractive index between each material.

X-ray can transmit a substance, on the other hand, infrared and ultraviolet rays reflect on the surface. It is difficult to visualize pigment and preparation layers with these lights. Terahertz wave can penetrate into penetration layer and wood support, and give some information of the inner structure. The mechanisms of deterioration of wooden painting cultural properties, such as flaking off, discoloring, fading and so on have not been clarified yet. Terahertz spectroscopy and imaging is expected to play a large part in restoration of painted wooden cultural properties.

Acknowledgements

The Author thanks Nara Prefecture`s Cultural Asset Building Preservation Society and *Danzan Jinja* shrine, for the supply of precious painted wooden samples. At the same time, the author would like to express deep appreciation to the Kamenori Foundation for their support to this research program by providing a generous scholarship.

References

[1] K.Fukunaga, Innovative terahertz spectroscopy and imaging technique for art conservation science, *e-Cons.Mag*.no.10, 30-42, 2009.

[2] M.-j.KIM, Y.Kohozuma, K.Fukunaga, Y.Fujiwara, Y.Fujii, Application of electromagnetic waves for the degradation mechanisms of wooden paintings(2), *The 28th Annual Meeting of the Japan Society for Scientific Studies on cultural property*, Vol.28, 248-249, 2011.

[3] K.Fukunaga, Y.Ogawa, S.Hayashi, I.Hosako, terahertz spectroscopy for art conservation, *IEICE Electronic Express*, 4, pp.258-263, 2007

[4] J.M.manceau, A.Nevin, C.Fotakis, and S.Tzortzakis, Terahertz time domain spectroscopy for the analysis of cultural heritage related materials, *Applied physics B*, vol.90, no.3-4, pp.365-368, 2008

[5] K.Fukunaga, I.Hosako, Y.Kohdzyma, T.koesuka, M.-j.KIM, T.Ikari, X.Du, Terahertz analysis of ana east asian historical mural painting, journal of the European potical society –Rapid publications 5, 10024, 2010.

[6] I.Hosako, K.Fukunaga, Non destructive observation of defects in dielectric materials and for diagnostics of infrastructure and cultural heritage, 2011

[7] K.Fukunaga, terahertz spectroscopy for non-invasive analysis of cultural properties, Journal of the National Institute of Information and Communications Technology 55, 2008

[8] H.Watanabe., Y.Kohozuma, M.Akada, M.-j.KIM, M.Sato, T.Tachi, J.Obayshi, J.Furihata, S.Wakiya, T.Tamura , analysis of painted materials on historical buildings(2) application of Pyrolysis Gas Chromatography to painted materials on Tanzan-Jinja shrine, *The 28th Annual Meeting of the Japan Society for Scientific Studies on cultural property*, Vol.28, 78-79, 2011.

[9] M.Akada, M.-j.KIM, M.Sato, Y.Kohozuma, Studies on the Degraded state of Oil based Coating Material, *The 28th Annual Meeting of the Japan Society for Scientific Studies on cultural property*, Vol.28, 198-199, 2011.

[10] R.Fukazawa, *Journal of Japan Coating Technology Association*, Vol.143, No11, pp378-388,2008.

[11] G.P.gallerano, A.Doria. E.Giovenalre, G.Messina, A.Petralia. I.Spassovsky, K.Fukunaga, I.Hosako, A.C.More, M.Seracini, Bruno Bisceglia, THz applications in art conservation at enea, contribution to the `Italy in Japan 2011`initiative science, thechnology and innovation

Feasibility of imaging technology using micro- and millimeter wave for nondestructive inspection of wooden buildings

Yuko Fujiwara1[1], Yoshihisa Fujii[1], Soichi Tanaka[1], Shogo Okumura[1]
Hiroyoshi Togo[2], Shoji Mochizuki[3], T. Kojima[2] and NaoyaKukutsu[2]

[1]Graduate School of Agriculture, Kyoto University, Kyoto Japan
[2]NTT Microsystem Integration Laboratories, Atsugi, Japan
[3] Concrete Structure Group Civil Engineering Project, NTT As Labs, Tsukuba, Japan
*corresponding author, E-mail: fujiwara@ h3news1.kais.kyoto-u.ac.jp

Abstract

The feasibility of imaging technology using micro- and millimeter wave for the non-destructive evaluation of wooden constructions involving wooden historical buildings was discussed in this paper. Subsurface structure of a painted wood containing inner defects was estimated by a scanning reflection image analyzer using experimental monostatic system of millimeter wave at 100GHz. The obtained image was compared with the accumulated gray-scale images taken by a micro-focus X-ray CT analyzer. The influence of the anisotropic dielectric properties of wood as well as wood grain on the image was clarified. The distribution of the obtained the inner defects underneath the overlaying painting could be recognized by the imaging. The performance of some different types of antennas and digital image processing to get higher spatial resolution was also evaluated. The experimental system was suitable for the evaluation of subsurface structure up to about 20mm depth from the surface of air-dried wood. We are also developing a novel scanning image analyzing system using micro-wave technology. It is specially designed for the non-destructive evaluation of wooden wall structures. The basic performance of the system will be also discussed in this paper.

1. Introduction

Wood is one of the popular material in many countries, used for instruments, furniture, houses and other facilities. It is consisted of plant cells showing micro honeycomb structure (Figure 1). The main component of the cell wall is cellulose crystalline oriented in the longitudinal direction of cellular structure. Wood cellular structure is porous and light, however, the crystalline is very strong in comparison with its lower density and this is the reason why the wood is strong enough to be used for posts and beams. At the same time the highly oriented crystalline structure brings the anisotropy of dielectric or other physical properties of wood. Wood is an interesting and major dielectric material that the nature affords us for our life.

Wood is the material from natural site and shows larger variance in quality in comparison with other industrial materials. In addition, it deteriorates by biological agents, such as insects and fungi (bio-degradation). In the process of quality control of wood and wooden structures in production and in service, an effective system to evaluate wood quality nondestructively is indispensable.

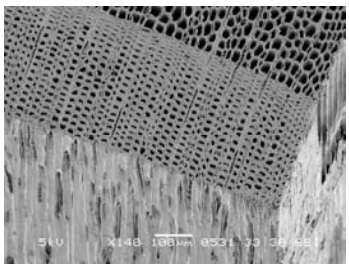


Figure1 Cellular structure of wood (Japanese cypress) observed by electron microscopy (by T. Awano, Kyoto Univ.)

2. Experiments

2.1 Experimental set up

In order to clarify the feasibility of millimeter wave technology as a tool of NDT for wood, we have conducted several basic experiments on dielectric property of wood by a reflection imaging using monostatic system of millimeter wave of 94 or 100GHz (Figure 2) and by a transmission imaging using bistatic system, respectively.

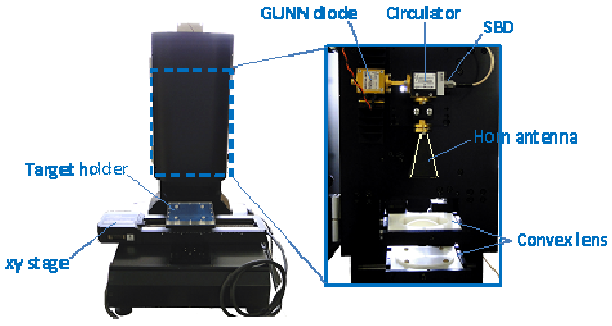


Figure 2 Experimental set up for reflection imaging

2.2 Detection of artificial defect in wood

A small clear specimen from solid wood (Figure3) were prepared from five wood species, Japanese cypress (*Chamaecyparis obtuse*), Japanese cedar *(Criptomeria japonica*) , Pine (*Pinus luchuensis*), Chest nut (C*astanea crenata*) and Zelkva wood (*Zelkova serrate*), respectively. They are all in air-dry condition and cut into two trigonal parts. The two parts are set in the following three conditions; a sheet of thin aluminum foil is inserted between two parts, a gap of 1mm is set between them, or they are in contact together (0mm gap), respectively. Top surface of the pair of specimen was scanned with the apparatus.

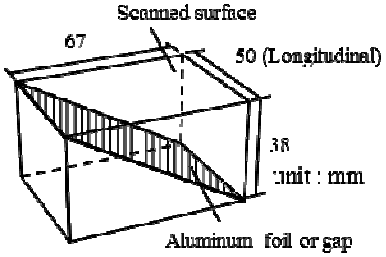


Figure 3 Preparation of wood specimen

Figure 4 shows an example of the relationships between the location of the foil or gaps and the intensity of the detected millimeter wave. The intensity of the reflection from the aluminum foil is larger than others, however it fluctuates in accordance with the depth. This can be attributed to the interference of the millimeter wave decided by the relations between wave length and optical path in the detection system. The intensity of the detected wave in the case of the gaps was of about one third of the one for the aluminum foil. The figure suggests, the gaps located under the depth of several millimeters are not detectable.

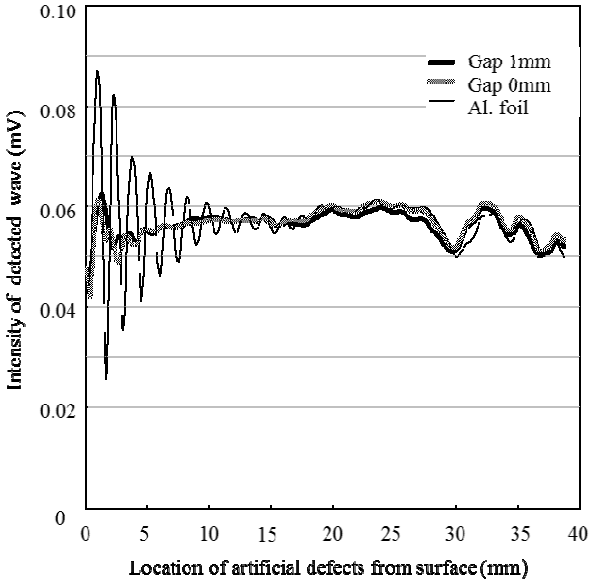


Figure 4 Changes in reflection intensity associated with location of artificial defects

2.3 Imaging of wood with inner defects

Based on the former results, imaging of surface and subsurface of finished wood was conducted. Figure 5 shows an example of image taken by scanning of wood block using reflection imaging by a monostatic system. In the scanning of wood surface finished with Japanese lacquer (Fig.5.a), it was revealed, the pattern of wood grain orientation under the lacquer layer was clearly recognized (Fig. 5.b). To clarify the penetration depth of mm-wave into wood specimen, another test was conducted to detect the layer of aluminum foil inserted between a pair of cut wood blocks (Fig. 5.c) . In the reflection image taken in the same manner as Fig. 3.a, characteristic stripe pattern is recognized near the left side of the image (Fig.5.d). This was caused by the change in the amplitude of the wave that is radiated to the wood, penetrated into the wood and reflected at the foil. The stripe pattern can be attributed to the interference of the penetrating wave with the reflected one. The existence of the inserted foil can be recognized at the depth of about 15 to 18mm at the deepest case for the tested 5 wood species.

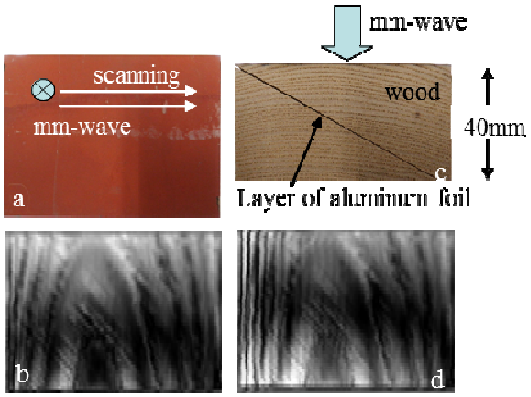


Figure 5 Reflection images of wood sample
a: surface of Zelkova wood sample finished with Japanese lacquer, b: reflection image of sample “a”, c: cross-section of a wood sample cut apart into two triangular prisms, a layer of aluminum foil is inserted between them, d: reflection image of sample “c” of Zelkova wood.

2.4 Comaprison of MMW imaging with X-ray imaging

Figure 6 right shows an example of reflection image of a small wood specimen taken from a post in a Buddhism temple(left). It is attacked by beetles and contains several holes in it. Some visible defects are also seen on the surface (left). The surface of the block was scanned by mm-wave apparatus. On the reflection mm-wave image several characteristic shaded areas (dot line circles) are seen and they suggest the existence of inner defects.

The distribution of inner defects was also evaluated by microfocus X-ray CT apparatus (SMX-160CT-SV3-S, SHIMADZU Corp.). The X-ray image (Fig.7 left) was obtained by accumulating of density distribution in a subsurface tomograms over the areas form the specimen surface up to the depth of 20mm. This was compared with

the mmw-image (right). Characteristic changes can be seen in the X-ray image (left) corresponding to the shaded areas (dot line circles marked as A to F) suggested as inner defects in the mmw-image(right) . However, some other unique shaded areas can be also seen in the X-ray image. They can be attributed to the holes and galleries made by beetles at deeper positions, and they could not detected by the mm-wave imaging.

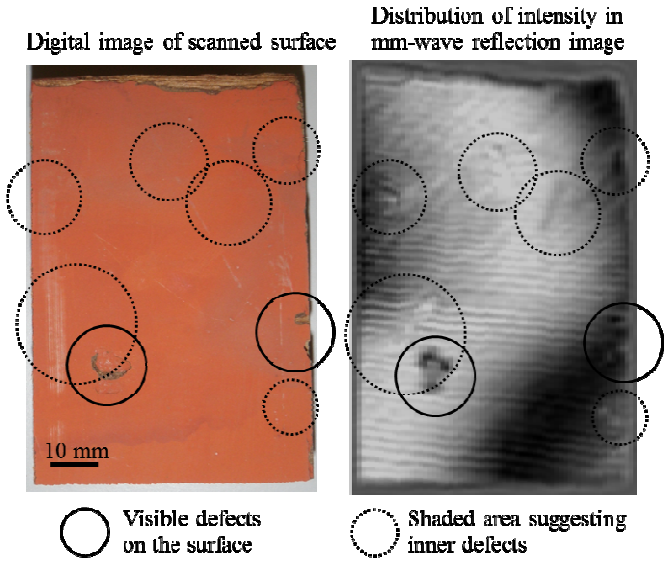


Figure 6 An example of photo (left) and mm-wave reflection image (right) of a surface finished wood block.

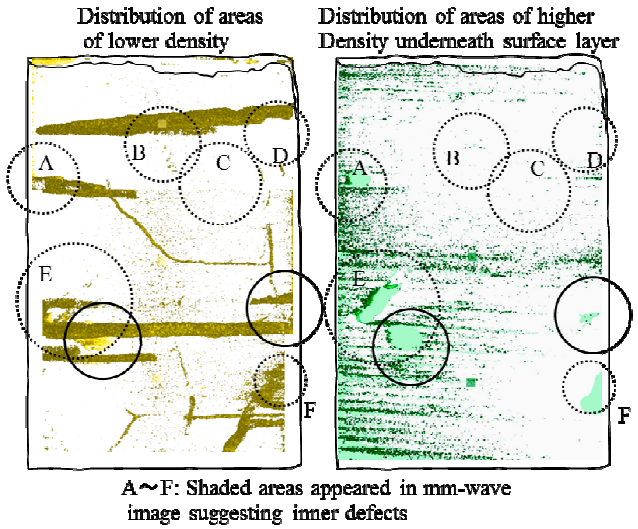


Figure 7 Two density distributions derived from X-ray CT tomograms overlapped on the shaded areas appeared in mm-wave image

3. Closing remarks

We have partly clarified the possibility of the mm-wave reflection imaging for the non-destructive inspection of wood. However, we have been also confronting some limit of the technique. In order to improve the performance of the system, we are now developing another types of imaging apparatus by shifting wave frequency down to microwave frequency ranges.

References

[1] Y. Fujii, Y. Fujiwara, Y. Yanase, S. Okumura, K. Narahara, T. Nagatsuma, T. Yoshimura and Y. Imamura: Nondestructive detection of termites using a millimeter-wave imaging technique. Forest Products J., 57(10) ,75-79, 2007.

[2] S.Tanaka, Y. Fujiwara, Y. Fujii, S. Okumura and H. Togo, et al.Effect of grain direction on transmittance of 100-GHz millimeter wave for hinoki (*Chamaecyparis obtusa*). Journal of Wood Science, 57(3), 189-194, 2011

A framework to design temporal basis functions used in boundary element methods for transient electromagnetic scattering

Elwin van 't Wout[1,2*], Duncan R. van der Heul[2], Harmen van der Ven[1], and Cornelis Vuik[2]

[1]National Aerospace Laboratory NLR, Amsterdam, Netherlands
[2]Delft University of Technology, Delft, Netherlands
*corresponding author, E-mail: Elwin.van.t.Wout@nlr.nl

Abstract

Time domain boundary element methods can be used to model transient electromagnetic scattering from complex structures that may have a nonlinear response. So far no consensus has been reached for the important choice of temporal basis function used in these computational methods. Based on a thorough analysis we will present a framework for the design of temporal basis functions with predefined accuracy and smoothness properties. Besides the customary shifted Lagrange basis functions, also spline basis functions will be derived that have equal interpolation accuracy and the added advantage of being smooth. Computational results show a remarkably higher order of global accuracy in time for the spline basis functions compared to the shifted Lagrange basis functions with equal support.

1. Introduction

Electromagnetic scattering phenomena occur in many fields of engineering science, for example in the modification of the radar signature of an aircraft. Computational methods are widely used for the analysis and design of scatterers. Progress in the construction of materials necessitates the use of sophisticated computational algorithms. For instance, standard methods formulated in frequency domain are unsuitable for modelling scatterers made of chiral and ferromagnetic materials whereas the nonlinear response can be modelled with modern time domain methods.

Boundary element methods are a natural choice to model scattering phenomena because the radiation condition is automatically imposed and only surfaces need to be discretised. Moreover, the use of an absorbing boundary condition to enclose the domain is not needed. The Time Domain Integral Equation (TDIE) method has been introduced as an attractive alternative to numerical schemes that need discretisation of electromagnetic fields [1].

Many developments in the TDIE method are inspired by its frequency domain counterpart, the Method of Moments. However, the temporal basis functions used in the TDIE method evidently have no frequency domain analogue. Various temporal basis functions have been introduced in literature, with the shifted Lagrange polynomials the most popular choice [2, 3, 4, 5, 6]. The choice of temporal basis function has a profound impact on computational properties such as efficiency, accuracy, and stability [2, 3, 7, 8].

For computational methods to be widely applicable to the analysis of engineering problems, it is necessary to know the characteristics of the underlying numerical scheme. The implications of the various choices within the mathematical framework on the computational performance have to be clear.

The influence of different properties of temporal basis functions, such as smoothness and local order of approximation, on the accuracy in time of TDIE methods is not yet fully understood. We will analyse the accuracy by isolating the temporal components and considering the numerical scheme as a finite element method. An important feature of basis functions in finite element methods is their projection from an infinite dimensional solution space onto a finite dimensional function space [9]. Within this finite element space, the basis functions provide a natural way to interpolate the discrete solution within discrete time levels.

In this paper, focus will be on the error originating from the interpolation procedure only. Bounds on the interpolation error can be derived resulting in clear accuracy conditions for temporal basis functions. In this way, a framework is obtained for the design of temporal basis function with predefined interpolation accuracy. The framework leaves enough freedom for other design criteria, for instance smoothness. The influence of the interpolation accuracy on the global accuracy in time will be analysed experimentally.

2. Methodology

In this section the model equations of the TDIE method and important design criteria for temporal basis functions will be summarised.

2.1. Boundary element formulation

Electromagnetic scattering phenomena can be modelled with Maxwell's equations together with interface conditions on the surface of the object. A perfect electric conductor (PEC) will be considered that is surrounded by free space. An incident electromagnetic field will induce an electric current distribution on the scatterer which will result in a backscattered electromagnetic field. Idea be-

hind boundary element methods is to rewrite all three-dimensional volume variables and equations into equivalent formulations on the two-dimensional surface of the scatterer. This can be done with the famous Stratton-Chu formulations that provide expressions for the scattered electromagnetic field in terms of the electric surface current density distribution.

Substitution of the formulation of the scattered field into the interface conditions results in the Electric Field Integral Equation (EFIE) and Magnetic Field Integral Equation (MFIE). The differentiated versions read

$$-\mathbf{n}\times\mathbf{n}\times\iint_\Gamma\left(\mu\frac{\ddot{\mathbf{J}}(\mathbf{r}',\tau)}{4\pi R}-\frac{1}{\epsilon}\nabla\frac{\nabla'\cdot\mathbf{J}(\mathbf{r}',\tau)}{4\pi R}\right)d\mathbf{r}' = -\mathbf{n}\times\mathbf{n}\times\dot{\mathbf{E}}^i(\mathbf{r},t), \quad (1)$$

$$\mathbf{n}\times\mathbf{n}\times\iint_\Gamma\left(\frac{\dot{\mathbf{J}}(\mathbf{r}',\tau)}{4\pi R}+\frac{\ddot{\mathbf{J}}(\mathbf{r}',\tau)}{4\pi c}\right)\times\frac{\mathbf{R}}{R^2}\,d\mathbf{r}' - \mathbf{n}\times\frac{1}{2}\dot{\mathbf{J}}(\mathbf{r},t) = -\mathbf{n}\times\mathbf{n}\times\dot{\mathbf{H}}^i(\mathbf{r},t) \quad (2)$$

where $\mathbf{n}$ denotes the outward pointing unit normal on the surface Γ, $\mathbf{E}^i$ and $\mathbf{H}^i$ the incident electric and magnetic field, $\mathbf{J}$ the induced electric surface current density and $\dot{\mathbf{J}}$ its time derivative, $R=|\mathbf{R}|=|\mathbf{r}-\mathbf{r}'|$,

$$\tau = t-\frac{R}{c} \quad (3)$$

the retarded time, and ∇ and ∇' the nabla operator with respect to $\mathbf{r}$ and $\mathbf{r}'$, respectively. The speed of light is given by $c=(\epsilon\mu)^{-\frac{1}{2}}$ with ϵ and μ the permittivity and permeability of free space, respectively. A linear combination of the EFIE and MFIE results in the Combined Field Integral Equation (CFIE), which will be used in the present analysis.

The boundary element method that will be used as numerical discretisation is a special case of the finite element method. In space, all test and basis functions have to be defined on a surface mesh. The standard Rao-Wilton-Glisson (RWG) functions are used on planar triangular elements [10]. Time is uniformly partitioned in discrete time levels $t_k=k\Delta t$ for $k=0,1,2,\ldots$ with Δt the time step size. Discretisation in time follows a collocation procedure, that is, the CFIE is evaluated in discrete time levels t_k.

The electric surface current density $\mathbf{J}(\tau)$ has to be evaluated in retarded time levels that are in general distinct from t_k. Therefore, the solution has to be interpolated from values on discrete time levels. This is an important feature of the temporal basis functions that are defined as

$$T_j(t)=\begin{cases}F_0(t), & t_{j-1}<t\le t_j,\\ F_1(t), & t_j<t\le t_{j+1},\\ \vdots & \vdots\\ F_d(t), & t_{j+d-1}<t\le t_{j+d},\\ 0, & \text{else},\end{cases} \quad (4)$$

for $j=0,1,2,\ldots,N$ and $F_0,F_1,\ldots,F_d$ polynomials of degree d.

2.2. Temporal basis functions

The choice of temporal basis functions has a profound impact on the numerical properties of TDIE methods, including accuracy, stability and efficiency. Newly constructed temporal basis functions have to meet user-defined design criteria on accuracy, efficiency, smoothness and bandlimitedness, which may conflict with each other [6]. The importance of each criterion depends on the application [2].

Efficiency of computational methods is essential for its application to large-scale problems of industrial interest. The present analysis will therefore restrict to temporal basis functions that result in a fast algorithm. The amount of computational work is strongly related to the size of support of the temporal basis function [3, 7]. For this reason, temporal basis function (4) are used with small values of d, typically 2 or 3. Notice that the temporal basis function T_j is zero for $t\le t_{j-1}$. This is necessary to satisfy the marching condition that results in a fast marching procedure in which solutions at a certain time level can be computed with past, known solutions only [2]. For this reason, the numerical scheme is often called the marching-on-in-time (MOT) scheme.

Accuracy and smoothness will be our main guidelines for the design of temporal basis functions. Smoothness is desired because smooth surface currents are expected from physical principles, and the accuracy of the Gaussian quadrature scheme, used to evaluate the spatial integrals, is likely to improve as well. The discretisation errors of the boundary element method can be subdivided into a spatial and temporal part. Although the errors are coupled, focus will be on the accuracy in time only. The discretisation in time follows the finite element method for which the order of interpolation accuracy can be derived. A high order of accuracy is advantageous because less stringent requirements need to be imposed on the time step size.

3. Design

For polynomial basis functions the truncation error from the interpolation procedure can be derived. The requirement of maximum order of accuracy for a given degree of interpolant results in a certain family of temporal basis functions. The degrees of freedom within this framework can then be chosen such that smooth basis functions are obtained.

3.1. Accuracy

Intrinsic to finite element methods is the restriction of the problem to a finite dimensional subspace [9]. The map of the solution onto this function space of finite dimension is determined by the choice of basis functions. The discrete solution is then represented by a series expansion in basis functions. So with a finite number of solution coefficients, the discrete solution still results in approximated values of the surface current density on the whole time axis. It can therefore be interpreted as an interpolation procedure. For piecewise polynomial basis functions (4), bounds on the

truncation error for interpolation in time can be derived.

Notice that the CFIE contains the unknown $\mathbf{J}$ and its time derivatives $\dot{\mathbf{J}}$ and $\ddot{\mathbf{J}}$. Therefore, polynomial interpolants of degree d have a maximum order of accuracy of $d-1$. To achieve this maximum order of interpolation accuracy, the polynomials have to satisfy several conditions, as derived in [11]. An instructive example is the unit sum condition, i.e.,

$$\sum_{n=0}^{d} F_n(t+n\Delta t) = 1. \tag{5}$$

With the accuracy conditions, a general definition of the temporal basis functions can be derived. For instance, quadratic basis functions, so $d=2$, that are given by

$$T_j(t) = \begin{cases} \frac{1}{2}\tilde{t}^2 + (\frac{3}{2}-\alpha)\tilde{t} + \alpha^2 - \frac{3}{2}\alpha + 1, & t_{j-1} < t \le t_j, \\ -\tilde{t}^2 + 2\alpha\tilde{t} - 2\alpha^2 + 1, & t_j < t \le t_{j+1}, \\ \frac{1}{2}\tilde{t}^2 - (\frac{3}{2}+\alpha)\tilde{t} + \alpha^2 + \frac{3}{2}\alpha + 1, & t_{j+1} < t \le t_{j+2}, \\ 0, & \text{else} \end{cases} \tag{6}$$

have an interpolation accuracy of $\mathcal{O}(\Delta t)$ for any constant α, where $\tilde{t} = \left(\frac{t-t_j}{\Delta t}\right)$.

3.2. Smoothness

The accuracy analysis results in a general representation (6) for quadratic basis functions that satisfy the maximum order of interpolation accuracy $\mathcal{O}(\Delta t)$. The parameter α can be chosen freely. This degree of freedom will be used to require smoothness of basis functions additionally. Continuity of the basis function is obtained if

$$\alpha\left(\alpha - \frac{1}{2}\right) = 0. \tag{7}$$

Moreover, if

$$\alpha - \frac{1}{2} = 0 \tag{8}$$

the time derivative is continuous as well. So for $\alpha = 0$ a $\mathcal{C}^0(\mathbb{R})$ continuous basis function will be obtained and for $\alpha = \frac{1}{2}$ a $\mathcal{C}^1(\mathbb{R})$ continuous basis function. The choice $\alpha = 0$ results in

$$T_j(t) = \begin{cases} \frac{1}{2}\tilde{t}^2 + \frac{3}{2}\tilde{t} + 1, & t_{j-1} < t \le t_j, \\ -\tilde{t}^2 + 1, & t_j < t \le t_{j+1}, \\ \frac{1}{2}\tilde{t}^2 - \frac{3}{2}\tilde{t} + 1, & t_{j+1} < t \le t_{j+2}, \\ 0, & \text{else} \end{cases} \tag{9}$$

which is the *quadratic Lagrange basis function*. The choice $\alpha = \frac{1}{2}$ results in

$$T_j(t) = \begin{cases} \frac{1}{2}\tilde{t}^2 + \tilde{t} + \frac{1}{2}, & t_{j-1} < t \le t_j, \\ -\tilde{t}^2 + \tilde{t} + \frac{1}{2}, & t_j < t \le t_{j+1}, \\ \frac{1}{2}\tilde{t}^2 - 2\tilde{t} + 2, & t_{j+1} < t \le t_{j+2}, \\ 0, & \text{else} \end{cases} \tag{10}$$

which is the *quadratic spline basis function*.

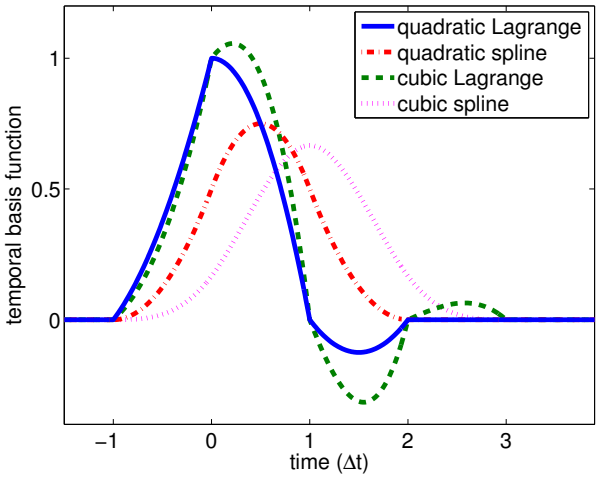


Figure 1: Temporal basis functions.

Cubic polynomial basis functions, so $d=3$ in Eq. (4), have a larger support which may result in more degrees of freedom. With the presented framework, cubic basis functions can be designed that have a maximum order of interpolation accuracy, which is $\mathcal{O}(\Delta t^2)$. For quadratic basis functions a one-parameter family of functions (6) has been obtained for maximum accuracy. In the case of cubic basis functions, a two-parameter family of functions will be obtained. So we have two degrees of freedom in the definition of cubic basis functions that satisfy a maximum order of interpolation accuracy.

Again, the degrees of freedom will be used to require smoothness of the basis functions. For a specific choice of parameters a $\mathcal{C}^2(\mathbb{R})$ continuous basis function can be designed. This temporal basis function is called the *cubic spline basis function* and is defined as

$$T_j(t) = \begin{cases} \frac{1}{6}\tilde{t}^3 + \frac{1}{2}\tilde{t}^2 + \frac{1}{2}\tilde{t} + \frac{1}{6}, & t_{j-1} < t \le t_j, \\ -\frac{1}{2}\tilde{t}^3 + \frac{1}{2}\tilde{t}^2 + \frac{1}{2}\tilde{t} + \frac{1}{6}, & t_j < t \le t_{j+1}, \\ \frac{1}{2}\tilde{t}^3 - \frac{5}{2}\tilde{t}^2 + \frac{7}{2}\tilde{t} - \frac{5}{6}, & t_{j+1} < t \le t_{j+2}, \\ -\frac{1}{6}\tilde{t}^3 + \frac{3}{2}\tilde{t}^2 - \frac{9}{2}\tilde{t} + \frac{9}{2}, & t_{j+2} < t \le t_{j+3}, \\ 0, & \text{else.} \end{cases} \tag{11}$$

Another choice of parameters leads to the well-known *cubic Lagrange basis function* given by

$$T_j(t) = \begin{cases} \frac{1}{6}\tilde{t}^3 + \tilde{t}^2 + \frac{11}{6}\tilde{t} + 1, & t_{j-1} < t \le t_j, \\ -\frac{1}{2}\tilde{t}^3 - \tilde{t}^2 + \frac{1}{2}\tilde{t} + 1, & t_j < t \le t_{j+1}, \\ \frac{1}{2}\tilde{t}^3 - \tilde{t}^2 - \frac{1}{2}\tilde{t} + 1, & t_{j+1} < t \le t_{j+2}, \\ -\frac{1}{6}\tilde{t}^3 + \tilde{t}^2 - \frac{11}{6}\tilde{t} + 1, & t_{j+2} < t \le t_{j+3}, \\ 0, & \text{else,} \end{cases} \tag{12}$$

The various temporal basis functions are depicted in Figure 1 and their numerical characteristics on accuracy and smoothness are listed in Table 1.

Table 1: Derived order of interpolation accuracy for the CFIE and the smoothness of the considered temporal basis functions.

basis function	accuracy	smoothness
quadratic Lagrange	$\mathcal{O}(\Delta t)$	$\mathcal{C}^0(\mathbb{R})$
quadratic spline	$\mathcal{O}(\Delta t)$	$\mathcal{C}^1(\mathbb{R})$
cubic Lagrange	$\mathcal{O}(\Delta t^2)$	$\mathcal{C}^0(\mathbb{R})$
cubic spline	$\mathcal{O}(\Delta t^2)$	$\mathcal{C}^2(\mathbb{R})$

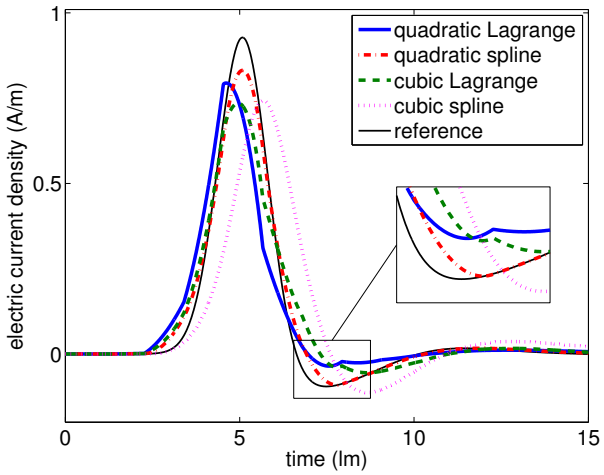


Figure 2: Electric surface current density on the top face of a sphere.

4. Experiments

The TDIE method has been applied to two different test objects, namely a sphere of radius 1 m and a cube with edges of 1 m. The mesh on the surface of the sphere and cube consists of 238 and 480 triangular patches, respectively. The incident field is given by a Gaussian shaped plane wave field.

4.1. Smoothness

The spline basis functions have better smoothness characteristics compared to the shifted Lagrange basis functions. The discrete surface current distribution calculated with the TDIE method is therefore expected to be smooth as well, for spline basis functions. In Fig. 2 and Fig. 3 the results are shown for a large time step size of $\Delta t = 1.13\,\text{lm}$ and $\Delta t = 0.71\,\text{lm}$ for the sphere and cube, respectively. As reference, an experiment with a small time step size has been depicted as well. The figures clearly show that the smoothness properties of basis functions are propagated in the discrete surface current density.

4.2. Accuracy

The accuracy in time of TDIE methods has been analysed by deriving bounds on the interpolation accuracy. Isolating the interpolation procedure results in a concise framework for the design of temporal basis functions. However, the de-

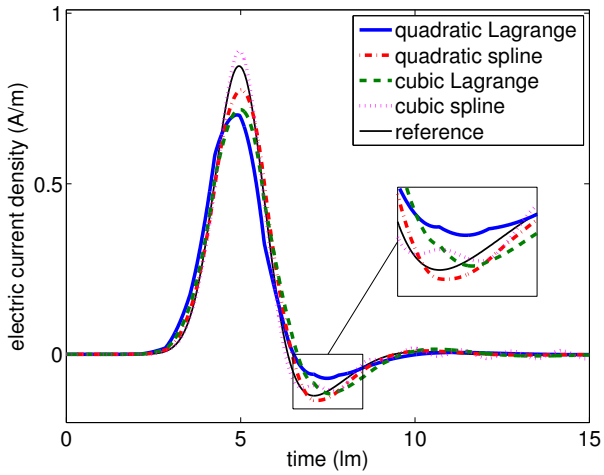


Figure 3: Electric surface current density on the top face of a cube.

rived interpolation accuracy does not have to be of the same order as the global accuracy in time. Analysing the global accuracy of a numerical scheme can be very difficult, even impossible in most cases. But with Richardson's algorithm the order of global accuracy in time can be investigated experimentally. To this end, three cases of the TDIE method will be computed, resulting in discrete surface current densities $J_1(t)$, $J_2(t)$, and $J_4(t)$. They are calculated on the same surface mesh and with exactly the same parameters, except for the time step size, which is Δt, $2\Delta t$, and $4\Delta t$, respectively. The order of global accuracy can be computed as $\log_2\left(\frac{||J_4-J_2||}{||J_2-J_1||}\right)$ where the L^2 norm has been used for $0 \leq t \leq 14\,\text{lm}$.

For the shifted Lagrange basis functions the order of global accuracy equals the interpolation accuracy, as shown in Table 2 and 3. Remarkably, application of the spline basis functions results in a higher order of global accuracy compared to the interpolation accuracy. Apparently, isolating the interpolation from the discretisation scheme in the accuracy analysis yields a smaller order of accuracy for the spline basis functions. The reason of the differences in global accuracy are not yet clear. Of course, a striking difference between shifted Lagrange and spline basis functions is the smoothness of the function, but it is not evident that this is the actual cause of the extra orders of accuracy. A careful explanation of this surprisingly better accuracy for the spline basis functions is a topic for further research.

Table 2: Global order of accuracy, experimentally computed on a sphere with the smallest time step size listed.

basis function	0.014 lm	0.028 lm	0.043 lm	0.057 lm
quadr. Lagrange	1.039	1.085	1.129	1.166
quadr. spline	1.982	2.017	2.005	1.992
cubic Lagrange	2.044	2.093	2.135	2.159
cubic spline	4.079	4.229	4.028	4.016

Table 3: Global order of accuracy, experimentally computed on a cube with the smallest time step size listed.

basis function	$0.012\,\mathrm{lm}$	$0.023\,\mathrm{lm}$	$0.035\,\mathrm{lm}$	$0.047\,\mathrm{lm}$
quadr. Lagrange	1.004	1.014	1.018	1.030
quadr. spline	1.996	2.004	1.989	2.044
cubic Lagrange	2.011	2.027	2.035	2.038
cubic spline	4.133	3.611	4.047	4.551

5. Conclusions

The practical implication of this work is the introduction of a framework for the design of temporal basis functions used in TDIE methods. With this framework a clever choice of temporal basis functions can be made for user-defined requirements on accuracy, efficiency and smoothness. All temporal basis functions in the framework can readily be used in existing codes of MOT schemes, thus improving the flexibility of the TDIE method. As demonstration of the applicability, we have derived spline basis functions that have

1. better smoothness properties,
2. the same order of interpolation accuracy, and
3. a higher order of global accuracy

compared to the shifted Lagrange basis functions with equal support.

References

[1] W. C. Chew, J.-M. Jin, E. Michielssen, and J. Song, *Fast and efficient algorithms in computational electromagnetics*. Boston: Artech House, 2001.

[2] D. S. Weile, G. Pisharody, N.-W. Chen, B. Shanker, and E. Michielssen, "A novel scheme for the solution of the time-domain integral equations of electromagnetics," *IEEE Trans. Antennas Propag.*, vol. 52, no. 1, pp. 283–295, 2004.

[3] B. H. Jung, Z. Ji, T. K. Sarkar, M. Salazar-Palma, and M. Yuan, "A comparison of marching-on in time method with marching-on in degree method for the TDIE solver," *PIER*, vol. 70, pp. 281–296, 2007.

[4] B. Shanker, M. Lu, J. Yuan, and E. Michielssen, "Time domain integral equation analysis of scattering from composite bodies via exact evaluation of radiation fields," *IEEE Trans. Antennas Propag.*, vol. 57, no. 5, pp. 1506–1520, 2009.

[5] A. Geranmayeh, W. Ackermann, and T. Weiland, "Temporal discretization choices for stable boundary element methods in electromagnetic scattering problems," *Appl. Numer. Math.*, vol. 59, pp. 2751–2773, 2009.

[6] E. van 't Wout, H. van der Ven, D. R. van der Heul, and C. Vuik, "The accuracy of temporal basis functions used in the TDIE method," in *Proc. 2011 IEEE Int. Symp. Antennas Propag.*, Spokane, WA, 2011, pp. 2708–2711.

[7] G. Kaur and A. E. Yilmaz, "Accuracy-efficiency tradeoff of temporal basis functions for time-marching solvers," *Microw. Opt. Technol. Lett.*, vol. 53, no. 6, pp. 1343–1348, 2011.

[8] Y. Shi, M.-Y. Xia, R.-S. Chen, E. Michielssen, and M. Lu, "Stable electric field TDIE solvers via quasi-exact evaluation of MOT matrix elements," *IEEE Trans. Antennas Propag.*, vol. 59, no. 2, pp. 574–585, 2011.

[9] S. C. Brenner and L. R. Scott, *The Mathematical Theory of Finite Element Methods*, 3rd ed. New York: Springer, 2008.

[10] S. M. Rao, D. R. Wilton, and A. W. Glisson, "Electromagnetic scattering by surfaces of arbitrary shape," *IEEE Trans. Antennas Propag.*, vol. 30, no. 3, pp. 409–418, 1982.

[11] E. van 't Wout, H. van der Ven, D. R. van der Heul, and C. Vuik, "The accuracy of temporal basis functions used in the time domain integral equation method," National Aerospace Laboratory NLR, Tech. Rep. NLR-TP-2011-042, 2011.

Accurate and Efficient Quadratures for Transient Electromagnetic Potentials

Anatoliy Boryssenko

A&E Partnership, Belchertown, MA
E-mail: anatoliy@ae-paertnership.com

Abstract

Accurate and efficient mixed analytical-numerical quadratures are developed for the transient electromagnetic potentials arising for surface current approximations with the RWG spatial basis in 3D. A source triangle is split into sub-triangles and their partial potentials are formally expressed as double integrals in local polar coordinates. The inner integrals are analytically solved with accurate cancellation of *1/R* singularity. The outer integrals are computed versus the angular variable through a Gauss quadrature to a given accuracy including machine precision. As a result, accuracy is greatly improved and total computational cost is substantially minimized compared to other reported approaches.

1. Introduction

The numerical TDIE-MOT algorithm [1-5] represents a promising branch of computational electromagnetics but a lack of late-time stability still prevents it from use for general purpose simulations. The problem is caused by inaccurate computation of the space-time electromagnetic potential integrals [2-5]. The integration for the RWG spatial basis is often performed in local polar coordinates to cancel preciously the 1/R kernel singularity [4]. While stepping in time, however, intersections of source triangle edges with a causal sphere of the radii *ct* centered at the observation points need to be adequately processed. Such supplementary computations must be performed at each time instant for all possible intersections classified in [2,3] that might be computationally too expensive. Another method [5] moves out the convolution operator from the integrands to exploit filtering properties of delta functions in the simplified transient kernels. But to the end, this method calls for quite complex formal manipulations to incorporate back the convolution operator into final expressions for the EM fields.

In this study, an alternative, accurate and efficient algorithm is developed to compute transient potential integrals arising for 3D PEC structures approximated with the RWG spatial bases. This algorithm departs from prior numerical solutions in the frequency domain [6,7] adopted here in the time domain. In particular, each master source triangle is split up to three subtriangles and their corresponding potential integrals are solved in local polar coordinates as further shown.

The rest of the paper is organized as follows. The relevant theory is summarized in Section 2 and used in Sections 3 to develop the algorithm for mixed analytical and numerical quadratures. Section 4 demonstrates several numerical case studies. Some conclusions are drawn to the end in Section 5. Section 6 includes Appendix to systemize descriptive geometrical information.

2. Problem Formulation

For TDIE-MOT numerical schemes with the RWG spatial base, the surface current and charge are approximated by separable space-time functions [1]

$$\vec{J}(\vec{r},t)=\vec{F}_J(\vec{r})\dot{S}(t)\quad \vec{F}_J(\vec{r})=\begin{cases}\dfrac{l\left(\vec{r}-\vec{r}_0^{\pm}\right)}{2A^{\pm}}, & \vec{r}\in T^{\pm}\\ 0, & \vec{r}\notin T^{\pm}\end{cases} \tag{1}$$

$$\rho(\vec{r},t)=F_\rho(\vec{r})S(t)\quad F_\rho(\vec{r})=\begin{cases}\dfrac{\pm l}{A^{\pm}}, & \vec{r}\in T^{\pm}\\ 0, & \vec{r}\notin T^{\pm}\end{cases} \tag{2}$$

defined over two adjacent triangles $T^{\pm}$ with areas $A^{\pm}$ and the length l of the shared edge. The vectors $\vec{r}$ and $\vec{r}_0^{\pm}$ denote, respectively, the spatial observation point and fixed reference vertex for a particular RWG mode. To facilitate the proposed quadratures, the temporal basis function *S(t)* and its integral primitives $\bar{S}(t)$ are assumed analytically available. Many reported temporal bases meet this requirement including spline, Lagrange interpolating polynomials and others constructed upon a piecewise exponent term t^n ($n \geq 0$).

The magnetic vector and scalar electric potentials generated by the source triangle $T^{\pm}$ [1,4] are eventually expressed as a signed sum of partitioned integrals over the subtriangles by adopting the frequency-domain approaches [6,7]:

$$\begin{aligned}\vec{A}(\vec{r},t)&=\frac{\mu_o}{4\pi}\frac{l}{2A^{\pm}}\int_{T^{\pm}}\partial\vec{r}'\,\frac{\left(\vec{r}'-\vec{r}_0^{\pm}\right)\dot{S}\left(t-R/c\right)}{R}\\&=\frac{\mu_o}{4\pi}\frac{l}{2A^{\pm}}\sum_{i=1}^{M}s_i\cdot\left[\dot{\vec{I}}_i^{V}(\vec{r},t)-\left(\vec{r}_0^{\pm}-\vec{r}_0\right)\dot{I}_i^{S}(\vec{r},t)\right]\end{aligned} \tag{3}$$

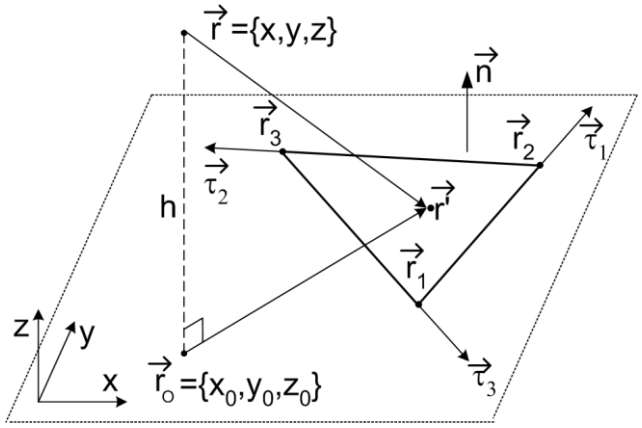


Figure 1: The source subtriangle with internal integration point $\vec{r}'$ and observation point $\vec{r}$ projected to the triangle plane at $\vec{r}_0$.

$$\Phi(\vec{r},t) = \frac{-1}{4\pi\varepsilon_o}\frac{l}{A^{\pm}}\int_{T^{\pm}}\partial\vec{r}'\,\frac{S(t-R/c)}{R} = \frac{-1}{4\pi\varepsilon_0}\frac{l}{A^{\pm}}\sum_{i=1}^{M} s_i \cdot I_i^S(\vec{r},t) \tag{4}$$

where μ_o and ε_o are, respectively, the magnetic and electric constants; R = $|\vec{r}\,-\vec{r}\,'|$ is the distance function; primes stand for geometrical quantities in the source triangle; $\vec{\rho} = \vec{r}\,' - \vec{r}_0$ is the vector in the triangle plane specified by the observation point project $\vec{r}_0$ and integration point $\vec{r}\,'$ (Fig. 1); *i=1..M* is a subtriangle index; M≤3 defines the number of subtriangles and depends on the position of the observation point projection [7]; s_i is a sign factor (A10); the scalar (S) and vector (V) integral components are defined over the i-th source subtriangle Δi as follows

$$I_i^S(\vec{r},t) = \int_{\Delta i}\partial\vec{r}'\,\frac{S(t-R/c)}{R} \tag{5}$$

$$\vec{I}_i^V(\vec{r},t) = \int_{\Delta i}\partial\vec{r}'\,\frac{\vec{\rho}\,S(t-R/c)}{R} \tag{6}$$

3. Mixed Analytical-Numerical Quadratures

3.1. Evaluation of Scalar Integral Component in Eq. (5)

Eq. (5) transformed to the local polar coordinates becomes

$$I^S(\vec{r},t) = \int_{\varphi_A}^{\varphi_B}\partial\varphi\int_0^{\rho(\varphi)}\partial\rho\,\frac{\rho\,S(t-R/c)}{R} \tag{7}$$

where the subtriangle index *i* is omitted hereafter sake of notational simplicity. The angular limits for the outer integral are (A8-A9) and the upper limit for the inner integral is

$$\rho(\varphi) = d\sec(\varphi) \tag{8}$$

Carrying out the change of the variables from ρ to R in the inner integral (7) through the use of the Jacobian [6]

$$dR\cdot R = d\rho\cdot\rho \tag{9}$$

cancels accurately the 1/R singular term and leads to

$$I^S(\vec{r},t) = \int_{\varphi_A}^{\varphi_B}\partial\varphi\int_h^{R(\varphi)}\partial R\,S(t-R/c) \tag{10}$$

where the upper limit of the inner integral (Fig. 5) [6] is

$$R(\varphi) = \sqrt{\rho(\varphi)^2+h^2} = \sqrt{d^2\sec(\varphi)^2+h^2} \tag{11}$$

Eq. (10) is then transformed to (12) shown at the page bottom since the close-form $S(t)$ is on hand.

3.2. Evaluation of Vector Integral Components in Eq. (6)

Eq. (6) is expressed in the local polar coordinates (A11) (Fig. 5) by making the variable changes as follows

$$\vec{I}^V(\vec{r},t) = \int_{\varphi_A}^{\varphi_B}\partial\varphi\cdot(\hat{u}\cos(\varphi)+\hat{v}\sin(\varphi))C(\varphi,t) \tag{13}$$

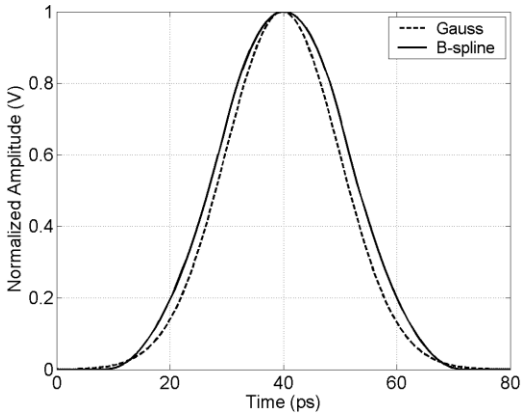
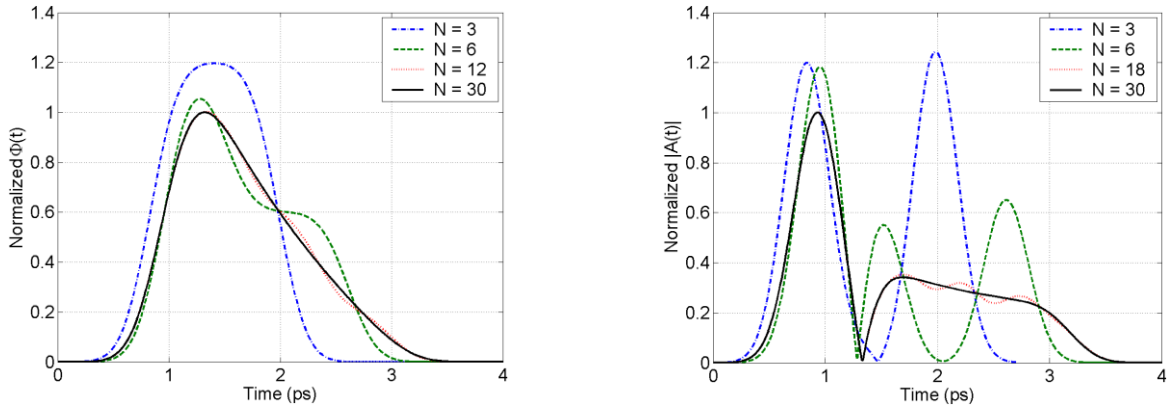


Figure 2: Signal functions including Gauss pulse with σ=10 ps and quadratic B-spline with Δt = 2/3πσ ≈ 21 ps.

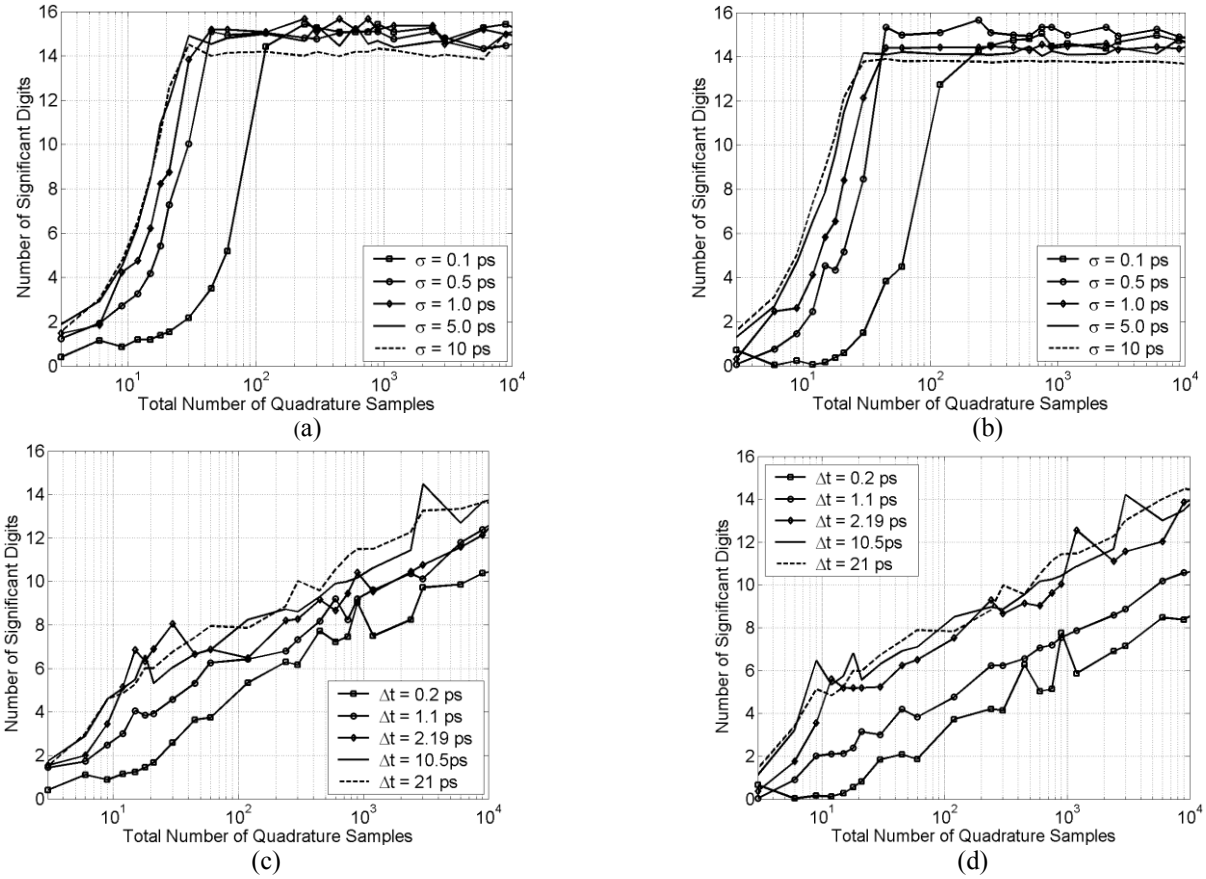
$$I^S(\vec{r},t) = c\left[(\varphi_B-\varphi_A)\bar{S}(t-h/c) - \int_{\varphi_A}^{\varphi_B}\partial\varphi\cdot\bar{S}\left(t-\sqrt{d^2\sec(\varphi)^2+h^2}\,/c\right)\right] \tag{12}$$

$$\dot{C}(\varphi,t) = \int_0^{R(\varphi)}\partial R\cdot RS(t-R/c) = -c\left[\frac{d}{\cos(\varphi)}S\left(t-\frac{d}{c\cdot\cos(\varphi)}\right) + c\left\{\bar{S}\left(t-\frac{d}{c\cdot\cos(\varphi)}\right)-\bar{S}(t)\right\}\right] \tag{15}$$



(a) (b)

Figure 3: Transient potential waveforms for different Gauss quadratures computed for the canonical Gaussian pulse with σ=0.2 ps: (a) scalar and (b) vector magnitude.



(a) (b)

(c) (d)

Figure 4: Number of significant digits versus number of quadrature samples: (a) scalar potential for Gaussian pulse; (b) magnitude of vector potential for Gaussian pulse; (c) scalar potential for quadratic B-spline; (d) magnitude of vector potential for quadratic B-spline.

$$C(\varphi,t)=\int_{h}^{R(\varphi)}\partial R\sqrt{R^2-h^2}\,S(t-R/c) \qquad (14)$$

where the upper integration limit of (14) is defined by (11).

In the most general cases, the integral (14) is not analytically solvable for an arbitrary *S(t)* except two practical cases. In 2D geometry, viz. *h*=0, Fig. 1, integration by parts is possible for arbitrary time bases that leads to the formal result (15) shown at the previous page bottom for the time derivative of (14).

In 3D geometry, viz. *h*>0, Eq. (14) is closed-form integrable for the local polynomial time-domain basis since the retardation

$$(t-R/c)^n=\sum_{k=0}^{n}(-1)^k\binom{n}{k}t^{n-k}(R/c)^k \qquad (16)$$

yields the time-independent analytically integrable factors

$$B_k(\varphi) = \int_h^{R(\varphi)} \partial R \sqrt{R^2 - h^2}\, R^k, k = 0...n \qquad (17)$$

4. Numerical Studies

The same right source triangle from [6] is used with the vertexes $\vec{r}_1 = (0,0,0)$, $\vec{r}_2 = (1,0,0)$, $\vec{r}_3 = (0,1,0)$ with all dimensions noted in mm. Two temporal basis signals are considered (Fig. 2): (1) the Gaussian pulse specified by the parameter σ that defines its approximate duration $2\pi\sigma$; (2) the shifted quadratic B-spline function spanned over $3\Delta t$. The identity $2\pi\sigma=3\Delta t$ is approximately hold to equalize the signal durations. Fig. 3 demonstrates some numerical results similarly to Fig. 5cd [4] derived for the transient potentials at $\vec{r} = (2,2,0)$ and σ = 0.2 ps for several different Gauss quadratures.

The number of significant digits versus the number of quadrature samples is numerically studied in Fig. 4 for both the signals parameterized with respective σ and Δt. This is done in time-domain similarly to the frequency domain studies [8]. Here Matlab is employed to perform all the numerical tests with the accuracy up to 15 significant digits. The numerical convergence is different for the two signals in Fig. 4 unlike their similar visual appearance (Fig. 2) because accuracy of the Gauss quadratures relies on continuity of integrand derivatives. Specifically, the quadratures for the Gauss pulse converge rapidly towards the machine precision because the integrand is infinitely differentiable unlike the B-spline signal with already discontinues second time derivative. The convergence rate for the scalar and vector potential quadratures is fairly comparable. Results of other simulations, which are not shown here, demonstrate the same convergence rate for arbitrary 2D and 3D source-observer geometries

5. Conclusions

The developed numerical quadratures for the transient potentials differ from prior studies [2-4] because the integral limits are not longer dynamically linked to time. As a result, the burden to compute the sphere-triangle intersects is completely avoided being replaced by simple translations in time for the analytical integrands in (12) and (15). Since properties of temporal bases affect greatly the numerical convergence as illustrated in Fig. 4, such time functions must be deliberately selected and optimized in this regard.

While the paper is focused on flat triangle patches with the RWG spatial modes, the algorithm described herein can be also straightforwardly extended to quadrilateral patches with relevant spatial vector bases and volume polyhedral elements (prisms, tetrahedrons and hexahedrons).

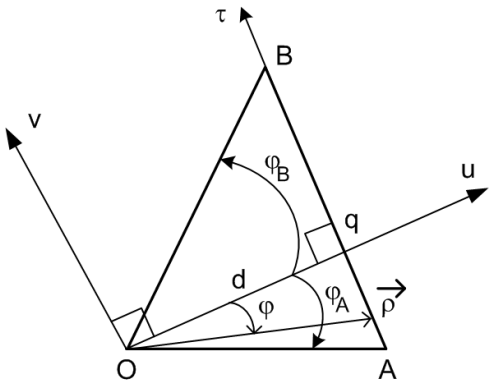


Figure 5: Geometrical relations for integration over a subtriangle represented in local Cartesian $\{u,v\}$ and $\{\rho,\varphi\}$ polar coordinates.

6. Appendix: Major Geometrical Relations for Source Triangles and Subtriangles

Each source triangle, Fig. 1, is characterized by its unit normal vector; area; height of the observation point above the source triangle plane; foot of the observation point projection on the source plane as follows:

$$\vec{n} = \frac{(\vec{r}_2 - \vec{r}_1) \times (\vec{r}_3 - \vec{r}_2)}{|(\vec{r}_2 - \vec{r}_1) \times (\vec{r}_3 - \vec{r}_2)|} \qquad (A1)$$

$$A = \frac{\vec{n} \cdot [(\vec{r}_2 - \vec{r}_1) \times (\vec{r}_3 - \vec{r}_2)]}{2} \qquad (A2)$$

$$h = \vec{n} \cdot (\vec{r} - \vec{r}_1) \qquad (A3)$$

$$\vec{r}_o = \vec{r} - h\vec{n} \qquad (A4)$$

Each source subtriangle (i=1,2,3), Fig. 5, is described by unit edge tangent vector; foot of the perpendicular from the observation point projection to the triangle edge; distance between the projected observation point and the foot:

$$\vec{\tau}_i = \frac{\vec{r}_{i+1} - \vec{r}}{|\vec{r}_{i+1} - \vec{r}|} \qquad (A5)$$

$$\vec{q}_i = \vec{r}_i + t_i \vec{\tau}_i,\ t_i = (\vec{r}_o - \vec{r}) \cdot \vec{\tau}_i \qquad (A6)$$

$$d_i = |\vec{q}_i - \vec{r}_o| \qquad (A7)$$

Additionally, limits of polar integration; factor $s_i = \pm 1$ used in the signed partial integrals (3-4); and unit vectors of the local Cartesian coordinates (Fig. 5) are defines as follows:

$$\varphi_{Ai} = \operatorname{atan}[((\vec{r}_i - \vec{q}_i) \cdot \vec{\tau}_i)/d_i] \qquad (A8)$$

$$\varphi_{Bi} = \operatorname{atan}[((\vec{r}_{i+1} - \vec{q}_i) \cdot \vec{\tau}_i)/d_i] \qquad (A9)$$

$$\vec{s}_i = -\left[\vec{\tau}_i \times \frac{(\vec{r}_i - \vec{r}_o)}{|(\vec{r}_i - \vec{r}_o)|}\right] \cdot \vec{n} \qquad (A10)$$

$$\hat{v}_i = \vec{\tau}_i,\ \hat{u}_i = \frac{\vec{q}_i - \vec{r}_0}{|\vec{q}_i - \vec{r}_0|} \qquad (A11)$$

References

[1] S. M. Rao and D. R. Wilton, “Transient scattering by conducting surfaces of arbitrary shape,” *IEEE Trans*. *Antennas Propag*., vol. 39, pp. 56-61, Jan. 1991.

[2] E. Bleszynski, M. Bleszynski, and T. Jaroszewicz, "Fast time-domain integral equations approach for wide band pulse propagation in dispersive media", *Ultra-Wideband Short-Pulse Electromagnetics 6,* Kluver Academic/Plenum Publishers, pp. 143-158, 2003.

[3] B. Shanker, L. Mingyu, J. Gao, and E. Michielssen, “Time domain integral equation analysis of scattering from composite bodies via exact evaluation of radiation fields,” *IEEE Trans*. *Antennas Propag*., vol. 57, pp. 1506-1520, May 2009.

[4] J. Pingenot, S. Chakraborty and V. Jandhyala, “Polar integration for exact space-time quadrature in time domain integral equations,” *IEEE Trans*. *Antennas Propag*., vol. 54, pp. 3037-3042, Oct. 2006.

[5] H.A. Ulku and A.A. Ergin, “Analytical Evaluation of Transient Magnetic Fields Due to RWG Current Bases”, *IEEE Trans*. *Antennas Propag*., vol. 55, pp. 3565-3575, Dec. 2007

[6] Z. Zhu, J. Huang, B. Song and, J. White, “Improving the robustness of a surface integral formulation for wideband impedance extraction of 3D structures, “ *Proc*. *IEEE/ACM Int*. *Conf*. *Computer-Aided Design*, pp. 592 – 597, 2001.

[7] M. A. Khayat and D. R. Wilton, “Numerical evaluation of singular and near-singular potential integrals,” *IEEE Trans*. *Antennas Propag*., vol. 53, pp. 3180-3190, Oct. 2005.

[8] R.D. Graglia and G. Lombardi, “Machine precision evaluation of singular and nearly singular potential integrals by use of Gauss quadrature formulas for rational functions**,**” *IEEE Trans*. *Antennas Propag*., vol. 56, pp. 981 - 998, April 2008.

A Compact Dual-Band Antenna for 2.4/5.2 GHz WLAN Applications

Peng Zhang and Wen-Xun Zhang

State Key Laboratory of Millimeter Waves, Southeast University, Nanjing, 210096;
Corresponding author, E-mail: wxzhang@ieee.org

Abstract

In this paper, a dual-band printed dipole antenna with a very compact size is presented, which is structured as an antipodal dipole etched on different sides of a coated dielectric substrate, and fed by a 50 Ω microstrip-line with a couple of shunt stubs over a truncated ground plate. It has achieved two separated bandwidths of 6.9 % at 2.4 GHz and 5.7 % at 5.2 GHz frequency bands respectively for WLAN application. The design principle of this proposed antenna prototype, and the comparison of its simulated and measured performances are discussed in detail.

1. Introduction

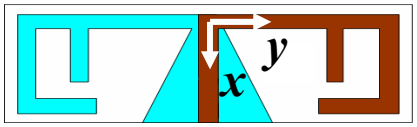
The wireless local area network (WLAN) technology, as a valuable and cost-effective solution of high-speed data communication, expects a physically smaller dual-band antenna with good impedance matching and radiation properties, for integrating more systems into one module. This antenna should be printed on a planar structure with light weight, and easy to be embedded; also its feeding circuit should be simplified for avoiding the transmission loss [1].

A number of kinds of dual-band antennas had been developed as reported in [1]-[6], some possess simple structure but large sizes as in [1]-[3]; and some involve balun structure with design complexity as in [4]-[6].

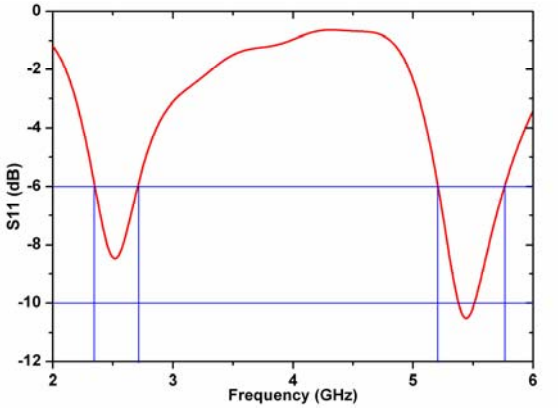
In this paper, a compact dual-band printed dipole antenna is designed and tested. Both the simulated and measured results show that satisfying IEEE 802.11b/g (2.40~2.48 GHz) and IEEE 802.11a (5.15~5.35 GHz indoor band) standards simultaneously.

2. Structural design with parametric study

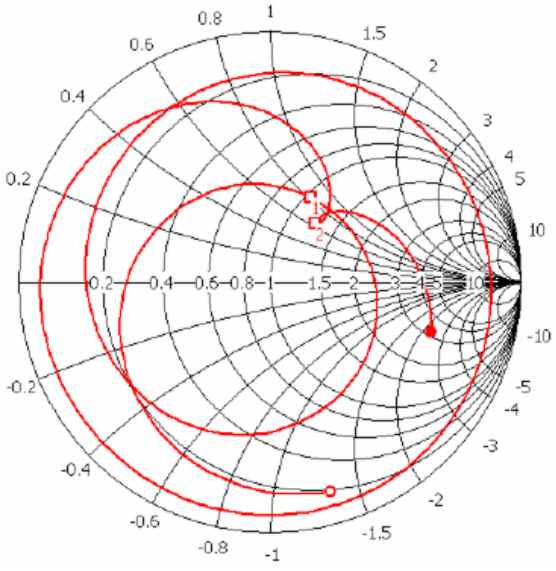
An initial antipodal dipole antenna printed on different sides of a coated dielectric substrate FR-4 with thickness of 0.8 mm and relative permittivity of 4.4 is proposed as shown in Figure 1(a), it is fed by a 50 Ω microstrip-line over a truncated tapered ground plate. The dual-band property of proposed antenna is performed by two separated resonance mechanism in structure, where both arms of antipodal dipole are furcated into a shorter stub for higher-band and a longer but folded branch for lower-band. By means of coordinating the structural parameters using commercial EM-simulation software CST Microwave Studio, a desired feature of S_{11}-frequency response within both dual-band 2.35~2.70 GHz and 5.20~5.76 GHz is obtained as shown in Figure 1(b); however it does not satisfy the specification of return-loss as $20\log|1/S_{11}|\geq 10$ dB. Refer to its input impedance curve on Smith Chart, which displays more inductive as shown in Figure 1(c). In order to compensate the inductivity, a couple of capacitances could be adopted at the input port of feed-line.



(a) Antenna structure



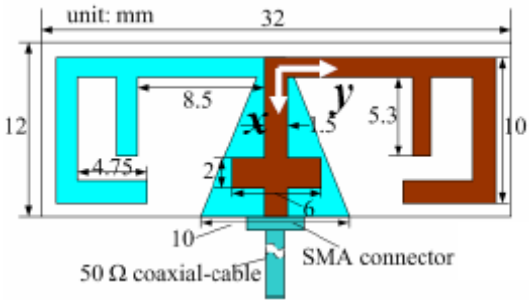
(b) Curve of S_{11}-frequency response



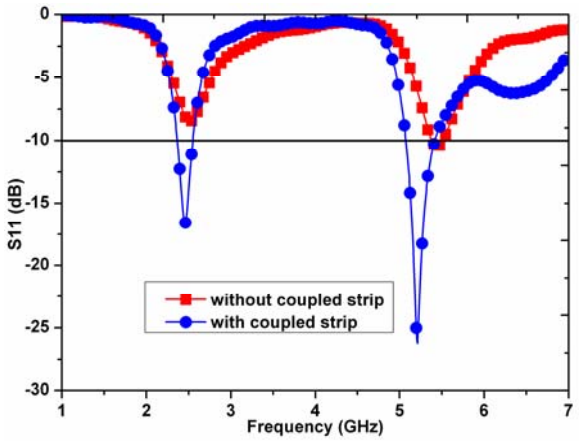
(c) Input impedance curve on Smith chart

Figure 1 Initial design of antipodal dipole antenna.

Thus an improved printed antipodal dipole antenna with a couple of shunt capacitive stubs is designed as shown in Figure 2(a). By running the performance simulation and parameter filtration again, an optimal set of parameters is abstracted as labeled at Figure 2(a), where the length of dipole is about a half wavelength in lower-band. The curves of S_{11}-frequency response of both improved and initial antennas (with/without capacitive stubs) are compared in Figure 2(b), where the improved bandwidths of 2.36~2.55 GHz and 5.07~5.42 GHz for VSWR ≤ 2:1 (i.e. return-loss≥10 dB) is achieved. Furthermore, the radiation patterns and curves of gain-frequency response at both bandwidths are simulated too, which will be compared with the measured results in the same figures as below.



(a) Antenna structure



(b) Curve of S_{11}-frequency response

Figure 2 Improved design of antipodal dipole antenna

3. Simulated and measured performances

A prototype of the antenna under improved design and precise fabrication is shown in Figure 3, it was tested for S_{11} by using a Rohde & Schwarz ZVL vector network analyzer at first, and then for radiation patterns and directive gain in a standard EM-chamber in sequence.

The measured and simulated results of S_{11}-curves are good agreement with each other as shown in Figure 4. The measured bandwidths are about 6.9% corresponding to 2.39~2.56 GHz as the lower-band; and also about 5.7% corresponding to 5.15~5.45 GHz as the higher-band. They are slightly narrower than the simulated bandwidths but enough to cover the 2.4/5.2 GHz operation bands for WLAN applications.

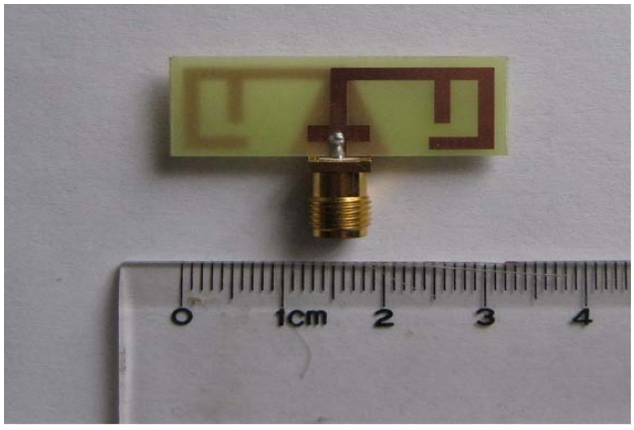


Figure 3 Prototype of antenna under improved design

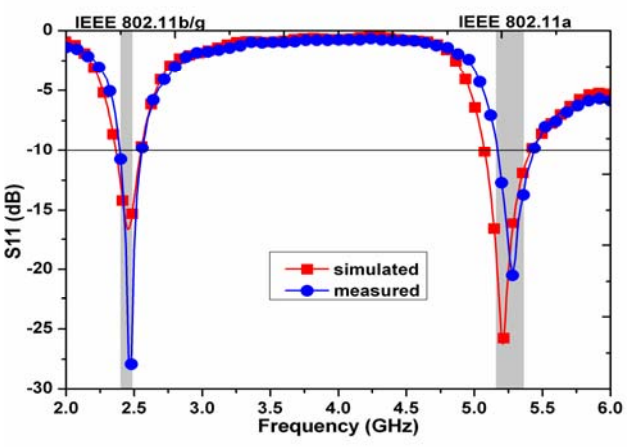


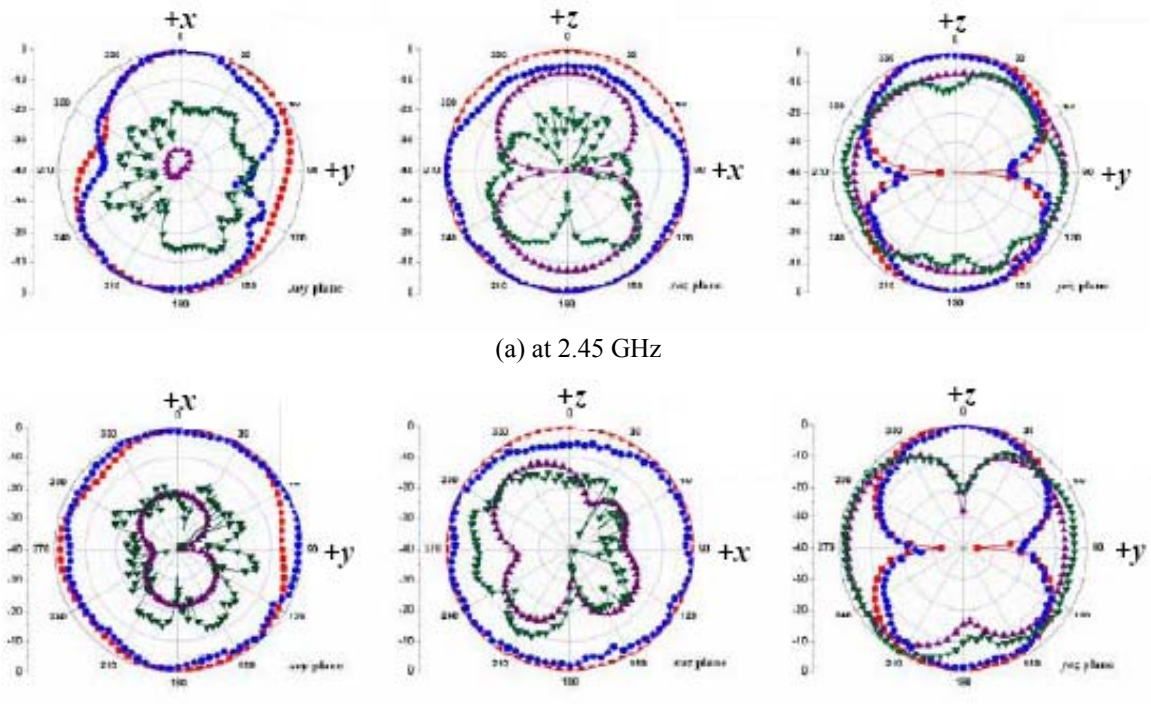
Figure 4 Curve of S_{11}-frequency response

Both the simulated and measured radiation patterns at 2.45 and 5.25 GHz are illustrated in Figure 5. Where the patterns in *xoz* plane are almost omni-directional as well as a simple dipole; but the radiation along *y*-axis is no longer a null since the contribution from the segment parallel to *x*-axis; the radiation of resultant field components in three coordinate planes approach to isotropy as desired.

Both the simulated and measured gains within the lower- and higher-bands are plotted in Figure 6. The measured gain varies as 1.56~2.04 dBi within the lower band, and 0.68~3.18 dBi within the higher band. Though there are some difference (<1 dB) from simulated gains, anyway both have the gain (≥1.5 dB) similar to a simple dipole.

4. Conclusion

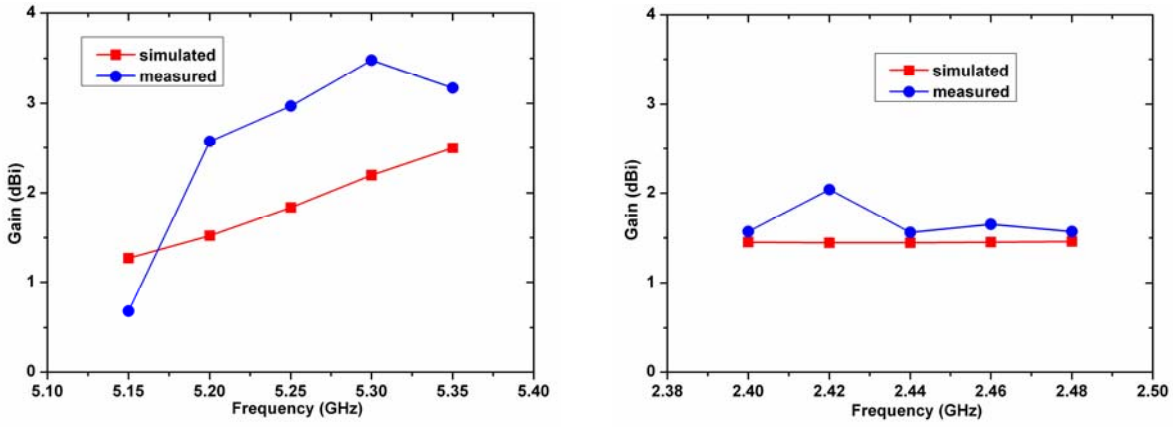
In this paper a very compact printed dipole antenna with a integrated Balun is proposed. Its impedance matching of VSWR<2:1 is achieved within dual-band 2.39~2.56 GHz and 5.15~5.35 GHz with good omni-directional radiation in the H-plane. This antenna with simple structure, good performance, low cost and easy assembly, is a qualified candidate for WLAN communication applications.



(a) at 2.45 GHz

(b) at 5.25 GHz

Figure 5 Simulated and measured radiation patterns



(a) lower-band (b) higher-band

Figure 6 Simulated and measured gain-frequency response

Acknowledgement

This work was supported by the High-tech 863 project (2007AA01Z264). Much appreciation is to CST Corporation for offering free license.

References

[1] H. M. Chen, J. M. Chen, P. S. Cheng, et al. Feed for dual-band printed dipole antenna, Electron Letters, 40 (2004), 1320-1321.

[2] Y. L. Kuo, K. L. Wong. Printed double-T monopole antenna for 2.4/5.2 GHz dual-band WLAN operations, IEEE Transactions on Antennas and Propagation, 57 (2009), 2187-2192.

[3] M. H. Ho, G. L. Chen. Reconfigured slot-ring antenna for 2.4/5.2 GHz dual-band WLAN operations, IET Microwaves, Antennas and Propragation 1 (2007), 712-717.

[4] Q. Q. He, B. Z. Wang, J. He. Wideband and dual-band design of a printed dipole antenna, IEEE Antennas and Wireless Propagation Letters 7 (2008), 1-4.

[5] Q. Y. Zhang, Q. X. Chu, Y. Wang. Compact printed dual-band dipole with wideband integrated balun, Electron Letters 45 (2009), 1209-1210.

[6] X. Li, L. Yang, S. X. Gong, et al. Dual-band and wideband design of a printed dipole antenna integrated with dual-band balun, Progress In Electromagnetics Research Letters 6 (2009), 165-174.

Design of a 60 GHz Metamaterial Antenna for Wireless BAN Applications

Alessio Brizzi[1], Lianhong Zhang[1], Alice Pellegini[1], Yang Hao[1*]

[1]School of Electronic Engineering and Computer Science, Queen Mary University of London, UK
*Professor Yang Hao, yang.hao@eecs.qmul.ac.uk

Abstract

A 60GHz metamaterial antenna is presented for applications in wireless body-area networks (WBANs). The antenna is based on the concept of resonant cavity and it comprises a cylindrical woodpile structure made from low loss alumina through extrusion free-forming techniques. The proposed antenna exhibits an omnidirectional radiation pattern with an enhanced gain on the plane normal to the cylinder axis. Such characteristics are extremely useful for on-body communication, since it improves the signal coverage for wireless sensors located on the body surface while reducing the energy loss in off-body radiation.

1. Introduction

In the past few years, ever increasing request for different on-body applications focused the research activity on the investigation and design of new specific antennas for Body Area Networks (BANs) [1].

The typical frequencies used for BAN applications are in the range from 400 MHz to 10 GHz that overlaps with the already crowded cellular band. Therefore the suitability for on-body applications of higher frequencies in V band, is being investigated. Specifically, in order to allow communication in general applications, commissions of several countries established an unlicensed bandwidth of 7 GHz, as indicated in Table 1 [2], located around the frequency of 60 GHz.

Table 1: Unlicensed frequency bands for several countries

Country	Frequency Band [GHz]
USA	57.05-64
Canada	57-64
Europe	57-64
Japan	59-66
Australia	59.4-62
Korea	57-64

Many advantages can be obtained in different fields by using such a frequency band. In games and entertainment, for instance, the possibility of having a higher data rate allows applications based on the transmission of uncompressed data streaming.

In military field, both the increased free space attenuation and the maximum exhibited by the atmospheric absorption around 60GHz allow to reduce interference from other systems and radar cross section from targets.

For what concerns BAN applications at V band, the tissues of the human body, in particular the skin, exhibits a very high electric conductivity which yields a low penetration depth and introduces additional losses in the system that could completely shadow the transmitted signal. In order to compensate these attenuations, directive antennas are found to be suitable to allow communication in such environment. On the other hand, the received power could be strongly affected by the incorrect alignment between transmitter and receiver. Therefore, antennas which present omnidirectional pattern on the plane parallel to the human body and high directivity on the orthogonal one represent a good solution to address these issues. Furthermore, an antenna with these radiation properties is not significantly affected by the proximity of the human body.

Moreover, a properly designed pattern shape allows to confine the energy in proximity of the human body. This behavior permits communication among sensors network placed on the human body reducing the off-body transmission. Indeed, as recent studies have demonstrated, a pacemaker can be hacked to be reconfigured or to access to private data [3][4]. Therefore, in this sense, the confinement of energy in medical field allows to limit interferences on implantable devices for patient monitoring.

In order to exploit the aforementioned features, the design of a cylindrical resonant cavity antenna, working in V band, is presented in this paper. By starting from the original antenna designed by Y. Lee [5] to work at a frequency of 94 GHz, the new structure, here shown, is based on the concept of the resonator antenna introduced by Trentini [6]. In general, an increase of the directivity can be obtained by adding a Partially-Reflecting Sheet (PRS) in front of the antenna. In the case shown in this paper the PRS has been realized as an EBG woodpile cylindrical cavity made of alumina, whose dimensions have been calculated according to the desired resonant mode.

The feeder has been realized by using the internal conductor of a coaxial cable.

The design of cylindrical cavity, the feeder and the antenna matching, supported by simulation, will be shown in this paper.

2. Design of Cylindrical Resonant Cavity and Antenna

The designed concept of the proposed antenna is depicted in Fig. 1. As mentioned above, the aim of this study was to obtain a radiator exhibiting an omnidirectional radiation pattern on the azimuth plane and high directivity. In order to address these issues, a cylindrical resonator antenna was chosen. For the sake of clarity let us consider the conformal woodpile Electromagnetic Band Gap (EBG) structure shown in Fig. 1. In order to obtain a cost-effective prototype, the free-forming extrusion technique [7] has been chosen to manufacture the antenna, adapting the design procedure used in [5] at W band. As a first step, the unit element of the woodpile structure has been designed in order to exhibit a band gap around 60GHz. The spacing *s* between the elements determines the frequency of the band gap, while the ratio between *s* and the thickness of the filaments *w* affects its width. Since the unit cell for the woodpile structure is a modified version of the one presented in [5], the *w* and *s* parameters had to be set by means of an ad hoc parametric analysis: the planar woodpile structures were illuminated by a plane wave and the transmitted field, measured by a probe, was analysed.

The optimum dimensions were found to be s=1.8mm and w=0.6mm. The presence of the desired band gap around 60GHz can be observed in Fig. 2.

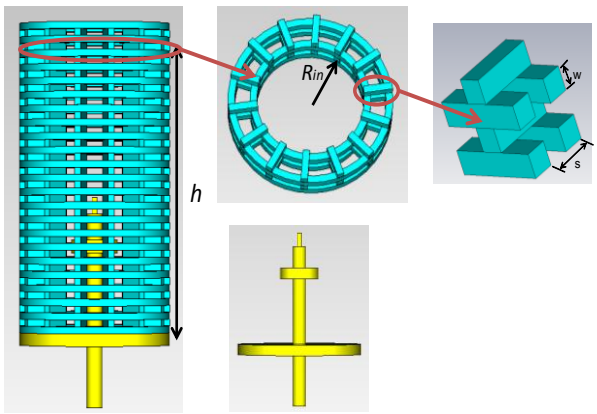


Figure 1: Cylindrical Resonant Cavity Antenna: Woodpile EBG structure and feeder.

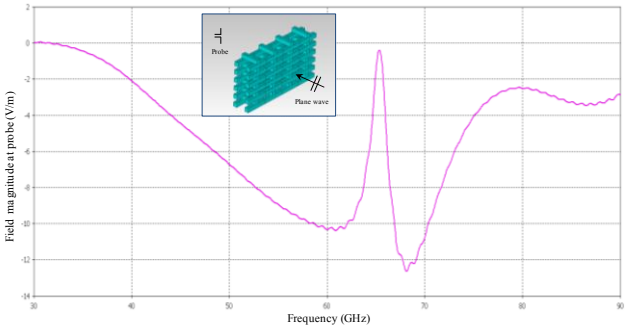


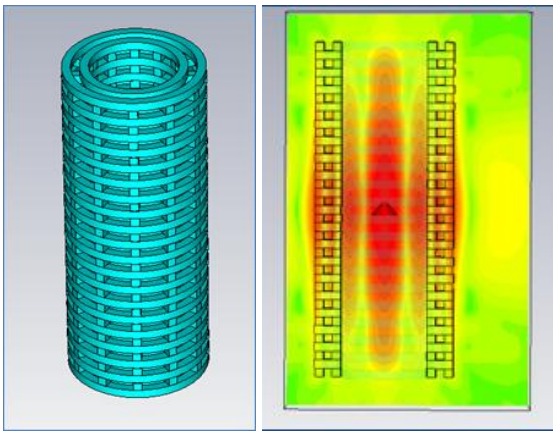
Figure 2: magnitude of the transmitted field at probe.

The designed unit cell was used to create the cylindrical resonator. Since a uniform and vertically polarised electric field was required, the cavity had to be designed in order to sustain a TM_{0n0}-type mode. The general equation giving the resonance frequency of a general TM_{mnp} modes is:

$$f_{mnp} = \frac{1}{2\pi\sqrt{\varepsilon\mu}}\sqrt{\left(\frac{\chi_{mn}}{R}\right)^2 + \left(\frac{p\pi}{H}\right)^2}, \qquad (1)$$

where *m*, *n* and *p* are integer numbers (*m*, *p*=0, 1, 2, 3…, *n*=1, 2, 3…), *R* and *H* are, respectively, the radius and the height of cylinder, χ_{mn} is the *n*-th zero of *m*-th order Bessel Function $J_m(\chi_{mn}) = 0$. It can be noticed how, in the case of TM_{0n0} modes, the resonance frequency depends only on the radius of the cavity [8]. Taking this equation into account, the internal radius R_{in} of the woodpile cylinder was calculated.

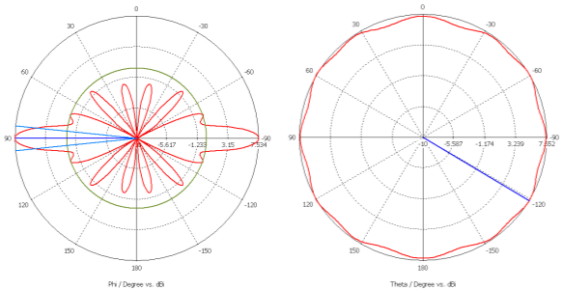
The radius corresponding to the TM_{010} mode could not be considered because of manufacturing constraints, it was not possible to realize a cavity with R_{in} lower than 2mm. Therefore the cavity was designed to support the TM_{020} mode, corresponding to R_{in}=4.4mm. The number of radial elements *N* and the total height *h* of the cylinder affect the directivity of the antenna, as well as its profile. In order to have a trade-off between directivity and dimensions, the parameters were set equal to *N*=14 and *h*=26.5mm. In order to verify the resonant behaviour of the designed structure, the woodpile cylinder was excited by means of a vertical elementary dipole placed in its central point. The electric field over a vertical cut plane including the axis of the cavity was evaluated. The results of this analysis are shown in Fig. 3, where the electric field distribution, obtained at 58 GHz, has depicted. The shift of the expected resonance frequency can be explained by considering that the woodpile EBG acts as a partially reflecting surface and has a finite thickness that is not negligible with respect to the wavelength. As a result of this, some energy penetrates inside the sheet, and the actual reflection does not happen exactly on the internal surface but inside the woodpile structure.



(a) (b)

Figure 3: Cylindrical cavity: woodpile structure (a) and electric field distribution at 58 GHz (b).

Having verified the correct behaviour of the cavity, the radiation pattern at the resonant frequency was evaluated. As mentioned above, the antenna should have an omnidirectional radiation pattern with a high directivity on the azimuthal plane. The result of the simulation carried on at 58 GHz is depicted in Fig. 4, showing that the designed cavity meets the design spedifications: in particular, the maximum directivity is 7.55 dBi, and the half power beam width (HPBW) is 11.7 dBi.



(a) (b)

Figure 4: Radiation pattern of cylindrical cavity at 58GHz: (a) elevation plane and (b) azimuth plane.

2.1. Cavity feeder and antenna matching

In order to obtain the desired properties in the actual antenna, a feeding structure, able to excite the same mode as the ideal short dipole, had to be designed. The feeder had to be able to generate a vertically polarised electric field. As proposed in [5] and in [9] for similar antennas working at different frequencies, the internal conductor of a 1mm coaxial cable has been used as a feeder for the antenna, with a copper disc used to hold the cavity (Fig. 5). Both the penetration of the cable inside the cavity h_1 and the length of the monopole h_2 affect the shape of the radiation pattern as well as the maximum directivity. An analysis by means of parametric simulations was carried out, and the above mentioned dimensions were set to h_1=6.6mm and h_2=2.5mm. The radiation pattern of this structure is reported in Fig. 6: it is possible to notice that it retains the desired omnidirectionality on the azimuth plane, while the maximum directivity is 7.43 dBi.

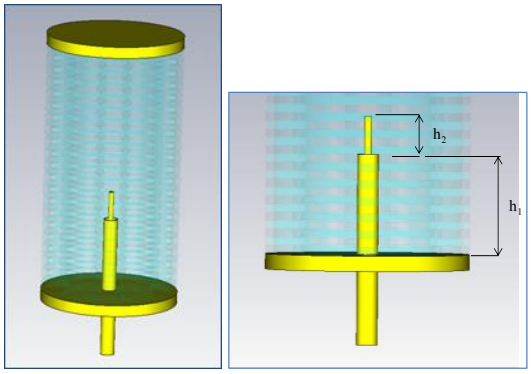
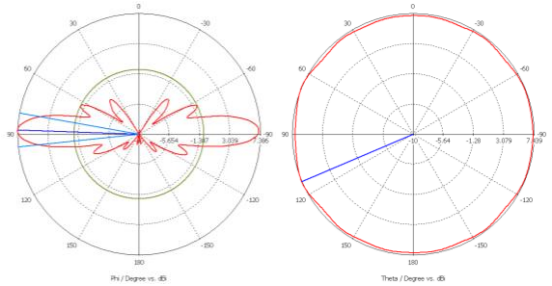


Figure 5: Antenna feeding structure.

Although the radiation characteristics of this configuration antenna are acceptable, the insertion loss is extremely high: the S_{11} at 58GHz is about -2dB. By changing h_2 it is possible to change both real and imaginary part of the input impedance, thus obtaining an acceptable return loss lower than -10dB. But, as already mentioned, this also affects the radiation pattern, resulting in a complete loss of the desired characteristics. Hence a further degree of freedom had to be included in the design. Because of manufacturing limitations due to the limited space inside the cavity, the matching techniques used at lower frequencies could not be used [9][10][11]. For this reason, a novel and practically viable solution had to be found.



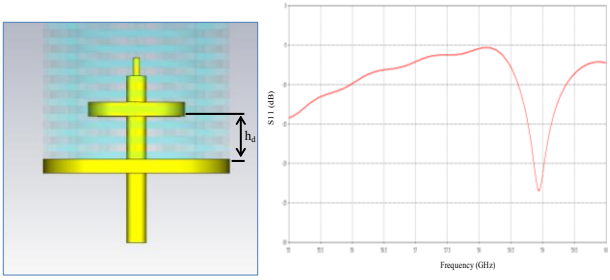
(a) (b)

Figure 6: Radiation pattern of cylindrical cavity with feeder at 58GHz: (a) elevation plane and (b) azimuth plane

To this aim, a copper disc connected to the external conductor of the coaxial cable was used to modify the input impedance, as depicted in Fig. 7 (a). Specifically, the position of the disc h_d was adjusted together with h_1 and h_2, thus obtaining a good matching while retaining the radiation characteristics already achieved. The simulated S_{11} obtained for h_1=9.5mm, h_2=1.3mm and h_d=2.1mm is reported in Fig. 7 (b), while the corresponding radiation pattern is depicted in Fig. 8. As a result of the introduction of the

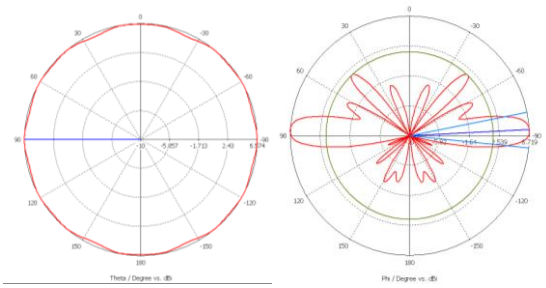
copper disc, the resonance frequency shifted to 58.8 GHz, and the maximum directivity slightly decreased to 6.72 dBi.

The complete antenna exhibits the desired omnidirectional pattern on the plane normal to the axis of the cavity, with directivity equal to 6.72 dBi at 58.8 GHz and a corresponding S_{11} equal to -17.4 dB.



(a) (b)

Figure 7: Matched antenna: (a) modified feeder and (b) simulated S_{11}.



(b) (b)

Figure 8: Radiation pattern of matched antenna: (a) azimuth plane and (b) elevation plane.

3. Conclusions

A cylindrical resonant cavity antenna, working in V band, has been presented in this paper. In particular the design, the analysis and simulation of the investigated antenna have been shown. The trade-off obtained between high directivity and omnidirectionality allows confining the energy in proximity of the human body, and makes this antenna suitable for BAN applications. As future work, a campaign of measurement will be held.

Acknowledgements

The authors would like to thank EPSRC for supporting this research and Dr Yoonjae Lee for his precious advices. The authors thank also Prof. Julian R. G. Evans and Dr Xuesong Lu, with the Department of Chemistry, University College London, for providing alumina prototypes.

References

[1] P. S. Hall, Y. Hao, S. L. Cotton, Progress in Antennas and Propagation for Body Area Networks, *Proceedings of International Symposium on Signals, System and Electronics*, 2010.

[2] R. Fisher, 60 GHz WPAN Standardization within IEEE 802.15.3c, *International Symposium on Signals, Systems and Electronics, 2007. ISSSE '07*, pp. 103-105, August 2007.

[3] S. Gollakota, H. Hassanieh; B. Ransford, D. Katabi; K. Fu, They Can Hear Your Heartbeats: Non-Invasive Security for Implanted Medical Devices, *Special Interest Group on Data Communication SIGCOMM*, Toronto 2011.

[4] D Halperin, T.S. Heydt-Benjamin, B. Ransford, S.S. Clark, B. Defend, W. Morgan, K. Fu, T. Kohno, W.H. Maisel, Pacemakers and Implantable Cardiac Defibrillators: Software Radio Attacks and Zero-Power Defenses, *2008 IEEE Symposium on Security and Privacy*, pp. 129-142

[5] Y. Lee, X. Lu, Y. Hao, S. Yang, C. G. Parini, J. R. G. Evans, Cylindrical EBG Antenna for Short Range Gigabit Wireless Communications at Millimeter-Wave Bands, *Electron. Lett.*, Vol. 45, Issue 3, 2009.

[6] G. V. Trentini, Partially Reflecting Sheet Arrays, *IRE Transactions on Antennas and Propagation*, Vol. 4, n. 4, 666-671, 1956.

[7] X. Lu, Y. Lee, S. Yang, Y. Hao, R. Ubic, J. R. G. Evans, and C. G. Parini, Rapid Prototyping of Millimetrewave Ceramic Metamaterials: Simulations and Experiments, *Microw. Opt. Techn. Let.*, Vol. 92, no. 2, 371-378, 2009.

[8] C. A. Balanis, *Advanced Engineering Electromagnetics*, John Wiley and Sons, New York, 1989.

[9] H. Boutayeb, T. A. Denidni, K. Mahdjoubi, A Tarot, A. Sebak, L. Talbi, Analysis and Design of a Cylindrical EBG-Based Directive Antenna, *Transactions on Antennas and Propagation*, Vol. 54, n. 1, pp 211-219, 2006.

[10] H. Chreim, E. Pointereau, B. Jecko, and P. Dufrane, Omnidirectional Electromagnetic Band Gap Antenna for Base Station Applications, *IEEE Antennas Wireless Propag. Lett.*, Vol. 6, 499-502, 2007.

[11] C. Biancotto, P. Record, Beam Forming Dielectric Cylindrical EBG Antenna, *Loughborough Antennas and Propagation Conference*, 2009.

TRANSVERSE TRANSMISSION LINE METHOD FOR SPHERICAL COORDINATES AND ANTENNA APLICATIONS

H. C. C. Fernandes* and A. S. Silva Neto
Department of Electrical Engineering – Federal University of Rio Grande do Norte, Brazil
*corresponding author: humbeccf@ct.ufrn.br, almirneto_ma@hotmail.com

Abstract

This paper presents a development of a full wave TTL-Transverse Transmission Line method, for the study of antennas resonator in spherical coordinates. This work involves the study of electromagnetic fields of the spherical antenna resonator for use in missile and satellite.

1. Introduction

This LTT-Transverse Transmission Line method, describes the electric and magnetic fields in spherical coordinates in the transverse directions ϕ and θ as a function of the fields in the direction r, cross dielectric interfaces. Figure 1 shows the initial inspiration for the application of this method in spherical coordinate's surface, spherical missile and satellite [1-15].

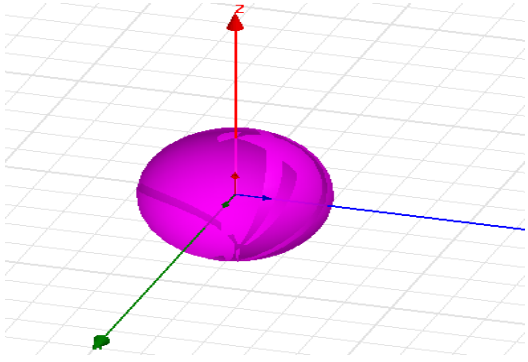


Figura 1. Spherical coordinates.

2. Theory

The LTT method is developed starting from Maxwell's equations for spherical coordinates [8-10]:

$$\nabla \times \vec{E} = -\frac{\partial \vec{B}}{\partial t} \quad (1)$$

$$\nabla \times \vec{H} = J + \frac{\partial \vec{D}}{\partial t} \quad (2)$$

Then performing the curl in spherical coordinates:

$$\nabla \mathrm{X}\, \vec{E} = \frac{1}{r\, sen\theta}\left[\frac{\partial}{\partial\theta}(sen\theta H\phi) - \frac{\partial H\theta}{\partial\phi}\right]\hat{a}r + \frac{1}{r}\left[\frac{1}{sen\theta}\frac{\partial Hr}{\partial\phi} - \frac{\partial}{\partial r}(rH\phi)\right]\hat{a}\theta + \frac{1}{r}\left[\frac{\partial}{\partial r}(rH\theta) - \frac{\partial Hr}{\partial\theta}\right]\hat{a}\phi \quad (3)$$

$$\nabla \mathrm{X}\, \vec{H} = \frac{1}{r\, sen\theta}\left[\frac{\partial}{\partial\theta}(sen\theta E\phi) - \frac{\partial E\theta}{\partial\phi}\right]\hat{a}r + \frac{1}{r}\left[\frac{1}{sen\theta}\frac{\partial Er}{\partial\phi} - \frac{\partial}{\partial r}(rE\phi)\right]\hat{a}\theta + \frac{1}{r}\left[\frac{\partial}{\partial r}(rE\theta) - \frac{\partial Er}{\partial\theta}\right]\hat{a}\phi \quad (4)$$

Relating the electric fields of the same direction, we obtain:

$$\mathrm{j}\omega\varepsilon\, \mathrm{r}E_r = \frac{\partial H_\phi}{\partial\theta} + \frac{1}{sen\theta}H_\phi cos\theta - \frac{1}{sen\theta}\frac{\partial H_\theta}{\partial\phi} \quad (5)$$

$$j\omega\varepsilon r E_\phi = H_\theta + r\frac{\partial H_\theta}{\partial r} - \frac{\partial H_r}{\partial\theta} \quad (6)$$

$$j\omega\varepsilon r E_\theta = \frac{1}{sen\theta}\frac{\partial H_r}{\partial\phi} - H_\phi - r\frac{\partial H_\phi}{\partial r} \quad (7)$$

Relating the magnetic field of the same direction, we obtain:

$$-\mathrm{j}\omega\mu\mathrm{r}H_r = \frac{\partial E_\phi}{\partial\theta} + \frac{1}{sen\theta}E_\phi cos\theta - \frac{1}{sen\theta}\frac{\partial E_\theta}{\partial\phi} \quad (8)$$

$$-j\omega\mu r H_\phi = E_\theta + r\frac{\partial E_\theta}{\partial r} - \frac{\partial E_r}{\partial\theta} \quad (9)$$

$$-j\omega\mu r H_\theta = \frac{1}{sen\theta}\frac{\partial E_r}{\partial\phi} - r\frac{\partial E_\phi}{\partial r} - E_\phi \quad (10)$$

According to the equations of the electric and magnetic fields above, we find: E_ϕ, E_θ, $H_\phi$and H_θ as function of E_r and H_r:

Finding E_ϕ:

Substituting the equation (10) in (6):

$$j\omega\varepsilon r E_\phi = \left(-\frac{1}{j\omega\mu r}\frac{1}{sen\theta}\frac{\partial E_r}{\partial \phi} + \frac{1}{j\omega\mu}\frac{\partial E_\phi}{\partial r} + \frac{1}{j\omega\mu r}E_\phi\right) + r\frac{\partial}{\partial r}\left(-\frac{1}{j\omega\mu r}\frac{1}{sen\theta}\frac{\partial E_r}{\partial \phi} + \frac{1}{j\omega\mu}\frac{\partial E_\phi}{\partial r} + \frac{1}{j\omega\mu r}E_\phi\right) - \frac{\partial H_r}{\partial \theta}$$

Multiplying by (-jωμ):

$$j\omega\varepsilon r E_\phi = -\frac{1}{j\omega\mu r}\frac{1}{sen\theta}\frac{\partial E_r}{\partial \phi} + \frac{1}{j\omega\mu}\frac{\partial E_\phi}{\partial r} + \frac{1}{j\omega\mu r}E_\phi - r\frac{\partial}{\partial r}\left(\frac{1}{j\omega\mu r}\frac{1}{sen\theta}\frac{\partial E_r}{\partial \phi}\right) + r\frac{\partial}{\partial r}\left(\frac{1}{j\omega\mu}\frac{\partial E_\phi}{\partial r}\right) + r\frac{\partial}{\partial r}\left(\frac{1}{j\omega\mu r}E_\phi\right) - \frac{\partial H_r}{\partial \theta}$$

Then:

$$\omega^2\mu\varepsilon r E_\phi = -\frac{\partial E_\phi}{\partial r} - \frac{\partial E_\phi}{\partial r} - r\frac{\partial^2 E_\phi}{\partial r^2} + j\omega\mu\frac{\partial H_r}{\partial \theta} + \frac{1}{sen\theta}\frac{\partial^2 E_r}{\partial r \partial \phi}$$

Finding H_θ:

Substituting the equation (6) in (10):

$$-j\omega\mu r H_\theta = \frac{1}{sen\theta}\frac{\partial E_r}{\partial \phi} - r\frac{\partial}{\partial r}\left(\frac{1}{j\omega\varepsilon r}H_\theta + \frac{1}{j\omega\varepsilon r}r\frac{\partial H_\theta}{\partial r} - \frac{1}{j\omega\varepsilon r}\frac{\partial H_r}{\partial \theta}\right) - \left(\frac{1}{j\omega\varepsilon r}H_\theta + \frac{1}{j\omega\varepsilon r}r\frac{\partial H_\theta}{\partial r} - \frac{1}{j\omega\varepsilon r}\frac{\partial H_r}{\partial \theta}\right)$$

Multiplying by (jωε):

$$+\omega^2\mu\varepsilon r H_\theta = +j\omega\varepsilon\frac{1}{sen\theta}\frac{\partial E_r}{\partial \phi} - r\frac{\partial}{\partial r}\left(\frac{1}{r}H_\theta\right) - r\frac{\partial}{\partial r}\left(\frac{1}{r}r\frac{\partial H_\theta}{\partial r}\right) + r\frac{\partial}{\partial r}\left(\frac{1}{r}\frac{\partial H_r}{\partial \theta}\right) - \frac{1}{r}H_\theta - \frac{1}{r}r\frac{\partial H_\theta}{\partial r} + \frac{1}{r}\frac{\partial H_r}{\partial \theta}$$

Then:

$$\omega^2\mu\varepsilon r H_\theta = -2\frac{\partial H_\theta}{\partial r} - r\frac{\partial^2 H_\theta}{\partial r^2} + j\omega\varepsilon\frac{1}{sen\theta}\frac{\partial E_r}{\partial \phi} + \frac{\partial^2 H_r}{\partial r \partial \theta}$$

Finding E_θ:

Substituting (9) in (7):

$$j\omega\varepsilon r E_\theta = \frac{1}{sen\theta}\frac{\partial H_r}{\partial \phi} - \left(-\frac{1}{j\omega\mu r}E_\theta - \frac{1}{j\omega\mu r}r\frac{\partial E_\theta}{\partial r} + \frac{1}{j\omega\mu r}\frac{\partial E_r}{\partial \theta}\right) - r\frac{\partial}{\partial r}\left(-\frac{1}{j\omega\mu r}E_\theta - \frac{1}{j\omega\mu r}r\frac{\partial E_\theta}{\partial r} + \frac{1}{j\omega\mu r}\frac{\partial E_r}{\partial \theta}\right)$$

Multiplying by (-jωμ):

$$j\omega\varepsilon r E_\theta = \frac{1}{sen\theta}\frac{\partial H_r}{\partial \phi} + \frac{1}{j\omega\mu r}E_\theta + \frac{1}{j\omega\mu r}r\frac{\partial E_\theta}{\partial r} - \frac{1}{j\omega\mu r}\frac{\partial E_r}{\partial \theta} + r\frac{\partial}{\partial r}\left(\frac{1}{j\omega\mu r}E_\theta\right) + r\frac{\partial}{\partial r}\left(\frac{1}{j\omega\mu r}r\frac{\partial E_\theta}{\partial r}\right) - r\frac{\partial}{\partial r}\left(\frac{1}{j\omega\mu r}\frac{\partial E_r}{\partial \theta}\right)$$

Then:

$$\omega^2\mu\varepsilon r E_\theta = -\frac{\partial E_\theta}{\partial r} - \frac{\partial E_\theta}{\partial r} - r\frac{\partial^2 E_\theta}{\partial r^2} + \frac{\partial^2 E_r}{\partial r \partial \theta} - \frac{1}{sen\theta}\frac{\partial H_r}{\partial \phi}j\omega\mu$$

Finding H_ϕ:

Substituting (7) in (9):

$$-j\omega\mu r H_\phi = \left(\frac{1}{j\omega\varepsilon r}\frac{1}{sen\theta}\frac{\partial H_r}{\partial \phi} - \frac{1}{j\omega\varepsilon r}H_\phi - \frac{1}{j\omega\varepsilon r}r\frac{\partial H_\phi}{\partial r}\right) + r\frac{\partial}{\partial r}\left(\frac{1}{j\omega\varepsilon r}\frac{1}{sen\theta}\frac{\partial H_r}{\partial \phi} - \frac{1}{j\omega\varepsilon r}H_\phi - \frac{1}{j\omega\varepsilon r}r\frac{\partial H_\phi}{\partial r}\right) - \frac{\partial E_r}{\partial \theta}$$

Multiplying by (jωε):

$$\omega^2\mu\varepsilon r H_\phi = \left(\frac{1}{r}\frac{1}{sen\theta}\frac{\partial H_r}{\partial \phi} - \frac{1}{r}H_\phi - \frac{1}{r}r\frac{\partial H_\phi}{\partial r}\right) + r\frac{\partial}{\partial r}\left(\frac{1}{r}\frac{1}{sen\theta}\frac{\partial H_r}{\partial \phi} - \frac{1}{r}H_\phi - \frac{1}{r}r\frac{\partial H_\phi}{\partial r}\right) - \frac{\partial E_r}{\partial \theta}\,j\omega\varepsilon$$

Then,

$$\omega^2\mu\varepsilon r H_\phi = -2\frac{\partial H_\phi}{\partial r} - r\frac{\partial^2 H_\phi}{\partial r^2} + \frac{1}{sen\theta}\frac{\partial^2 H_r}{\partial r \partial \phi} - \frac{\partial E_r}{\partial \theta}\,j\omega\varepsilon$$

Considering,

$$k^2 = \omega^2\mu\varepsilon \qquad (11)$$

$$\frac{\partial}{\partial \theta} = -j\alpha_n \qquad (12)$$

$$\frac{\partial^2}{\partial r^2} = {k_r}^2 = \gamma^2 \quad (13)$$

$$\frac{\partial}{\partial \varphi} = -j\beta_k \quad (14)$$

$$\frac{\partial}{\partial r} = -\gamma \quad (15)$$

Where:

γ is the propagations constant in the radial direction, r;

$\propto_n$ is the spectral variable in the θ direction;

β_k is the spectral variable in the φ direction. k is the wave number.

Applying the Fourier transform domain (FTD) in the equations to find E_φ, E_z, H_φ and H_z:

$$\tilde{E}_\phi = \frac{1}{(k^2 r - 2\gamma + r\gamma^2)}\left(-\frac{1}{sen\theta}\frac{\partial \tilde{E}_r}{\partial r} j\beta_k + \alpha_n \tilde{H}_r \omega\mu\right) \quad (16)$$

$$\tilde{H}_\theta = \frac{1}{(k^2 r - 2\gamma + r\gamma^2)}\left(\frac{1}{sen\theta}\omega\varepsilon\beta_k \tilde{E}_r + j\alpha_n \frac{\partial \tilde{H}_r}{\partial r}\right) \quad (17)$$

$$\tilde{E}_\theta = \frac{1}{(k^2 r - 2\gamma + r\gamma^2)}\left[-\frac{1}{sen\theta}\omega\mu\beta_k \tilde{H}_r - j\alpha_n \frac{\partial \tilde{E}_r}{\partial r}\right] \quad (18)$$

$$\tilde{H}_\phi = \frac{1}{(k^2 r - 2\gamma + r\gamma^2)}\left[-\frac{1}{sen\theta}\frac{\partial \tilde{H}_r}{\partial r} j\beta_k + \alpha_n \tilde{E}_r \omega\varepsilon\right] \quad (19)$$

3. Wave Equation Solution in Spherical Coordinates

The Laplacian operator of E_r and H_r are:

$$\nabla^2 E_r = \vec{\nabla}.\vec{\nabla}E_r \quad (28)$$

$$\nabla^2 H_r = \vec{\nabla}.\vec{\nabla}H_r \quad (29)$$

Considering that:

$$\vec{\nabla} = \frac{\partial}{\partial r}\hat{a}_r + \frac{1}{r}\frac{\partial}{\partial \theta}\hat{a}_\theta + \frac{1}{rsen\theta}\frac{\partial}{\partial \varphi}\hat{a}_\varphi \quad (30)$$

$$\vec{\nabla}E_r = \frac{\partial E_r}{\partial r}\hat{a}_r + \frac{1}{r}\frac{\partial E_r}{\partial \theta}\hat{a}_\theta + \frac{1}{rsen\theta}\frac{\partial E_r}{\partial \varphi}\hat{a}_\varphi \quad (31)$$

$$\vec{\nabla}H_r = \frac{\partial H_r}{\partial r}\hat{a}_r + \frac{1}{r}\frac{\partial H_r}{\partial \theta}\hat{a}_\theta + \frac{1}{rsen\theta}\frac{\partial H_r}{\partial \varphi}\hat{a}_\varphi \quad (32)$$

Substituting (28) into (30) and (31) we can write that $\nabla^2 E_r\ is$:

$$\nabla^2 E_r = \frac{\partial}{\partial r}\left(\frac{\partial E_r}{\partial r}\hat{a}_r + \frac{1}{r}\frac{\partial E_r}{\partial \theta}\hat{a}_\theta + \frac{1}{rsen\theta}\frac{\partial E_r}{\partial \varphi}\hat{a}_\varphi\right)\hat{a}_r + \frac{1}{r}\frac{\partial}{\partial \theta}\left(\frac{\partial E_r}{\partial r}\hat{a}_r + \frac{1}{r}\frac{\partial E_r}{\partial \theta}\hat{a}_\theta + \frac{1}{rsen\theta}\frac{\partial E_r}{\partial \varphi}\hat{a}_\varphi\right)\hat{a}_\theta + \frac{1}{rsen\theta}\frac{\partial}{\partial \varphi}\left(\frac{\partial E_r}{\partial r}\hat{a}_r + \frac{1}{r}\frac{\partial E_r}{\partial \theta}\hat{a}_\theta + \frac{1}{rsen\theta}\frac{\partial E_r}{\partial \varphi}\hat{a}_\varphi\right)\hat{a}_\varphi \quad (33)$$

Developing the terms of the equation (33):

$$\nabla^2 E_r = \frac{\partial}{\partial r}\frac{\partial E_r}{\partial r}\hat{a}_r\hat{a}_r + \frac{\partial E_r}{\partial r}\frac{\partial \hat{a}_r}{\partial r}\hat{a}_r + \frac{\partial E_r}{\partial \theta}\frac{\partial}{\partial r}\frac{1}{r}\hat{a}_\theta\hat{a}_r + \frac{1}{r}\frac{\partial}{\partial r}\frac{\partial E_r}{\partial \theta}\hat{a}_\theta\hat{a}_r + \frac{1}{r}\frac{\partial E_r}{\partial \theta}\frac{\partial \hat{a}_\theta}{\partial r}\hat{a}_r + \frac{1}{r}\frac{1}{sen\theta}\frac{\partial}{\partial r}\frac{\partial E_r}{\partial \varphi}\hat{a}_\varphi\hat{a}_r + \frac{1}{sen\theta}\frac{\partial E_r}{\partial \varphi}\frac{\partial}{\partial r}\frac{1}{r}\hat{a}_\varphi\hat{a}_r + \frac{1}{r}\frac{\partial E_r}{\partial \varphi}\frac{\partial}{\partial r}\frac{1}{sen\theta}\hat{a}_\varphi\hat{a}_r + \frac{1}{r}\frac{\partial E_r}{\partial \varphi}\frac{1}{sen\theta}\frac{\partial \hat{a}_\varphi}{\partial r}\hat{a}_r + \frac{1}{r}\frac{\partial}{\partial \theta}\frac{\partial E_r}{\partial r}\hat{a}_r\hat{a}_\theta + \frac{1}{r}\frac{\partial E_r}{\partial r}\frac{\partial \hat{a}_r}{\partial \theta}\hat{a}_\theta + \frac{1}{r}\frac{\partial E_r}{\partial \theta}\frac{\partial}{\partial \theta}\frac{1}{r}\hat{a}_\theta\hat{a}_\theta + \frac{1}{r}\frac{1}{r}\frac{\partial}{\partial \theta}\frac{\partial E_r}{\partial \theta}\hat{a}_\theta\hat{a}_\theta + \frac{1}{r}\frac{1}{r}\frac{\partial E_r}{\partial \theta}\frac{\partial \hat{a}_\theta}{\partial \theta}\hat{a}_\theta + \frac{1}{r}\frac{1}{sen\theta}\frac{\partial E_r}{\partial \varphi}\frac{\partial}{\partial \theta}\frac{1}{r}\hat{a}_\varphi\hat{a}_\theta + \frac{1}{r}\frac{1}{r}\frac{\partial E_r}{\partial \varphi}\frac{\partial}{\partial \theta}\frac{1}{sen\theta}\hat{a}_\varphi\hat{a}_\theta + \frac{1}{r}\frac{1}{r}\frac{1}{sen\theta}\frac{\partial}{\partial \theta}\frac{\partial E_r}{\partial \varphi}\hat{a}_\varphi\hat{a}_\theta + \frac{1}{r}\frac{1}{r}\frac{\partial E_r}{\partial \varphi}\frac{1}{sen\theta}\frac{\partial \hat{a}_\varphi}{\partial \theta}\hat{a}_\theta + \frac{1}{rsen\theta}\frac{\partial}{\partial \varphi}\frac{\partial E_r}{\partial r}\hat{a}_r\hat{a}_\varphi + \frac{1}{rsen\theta}\frac{\partial E_r}{\partial r}\frac{\partial \hat{a}_r}{\partial \varphi}\hat{a}_\varphi + \frac{1}{rsen\theta}\frac{\partial E_r}{\partial \theta}\frac{\partial}{\partial \varphi}\frac{1}{r}\hat{a}_\theta\hat{a}_\varphi + \frac{1}{rsen\theta}\frac{1}{r}\frac{\partial}{\partial \varphi}\frac{\partial E_r}{\partial \theta}\hat{a}_\theta\hat{a}_\varphi + \frac{1}{rsen\theta}\frac{1}{r}\frac{\partial E_r}{\partial \theta}\frac{\partial \hat{a}_\theta}{\partial \varphi}\hat{a}_\varphi + \frac{1}{rsen\theta}\frac{1}{sen\theta}\frac{\partial E_r}{\partial \varphi}\frac{\partial}{\partial \varphi}\frac{1}{r}\hat{a}_\varphi\hat{a}_\varphi + \frac{1}{rsen\theta}\frac{1}{r}\frac{\partial E_r}{\partial \varphi}\frac{\partial}{\partial \varphi}\frac{1}{sen\theta}\hat{a}_\varphi\hat{a}_\varphi + \frac{1}{rsen\theta}\frac{1}{r}\frac{1}{sen\theta}\frac{\partial}{\partial \varphi}\frac{\partial E_r}{\partial \varphi}\hat{a}_\varphi\hat{a}_\varphi + \frac{1}{rsen\theta}\frac{1}{r}\frac{1}{sen\theta}\frac{\partial E_r}{\partial \varphi}\frac{\partial \hat{a}_\varphi}{\partial \varphi}\hat{a}_\varphi \quad (34)$$

Where:

$$\frac{\partial \hat{a}_r}{\partial \theta} = \hat{a}_\theta$$

$$\frac{\partial \hat{a}_\theta}{\partial \theta} = -\hat{a}_r$$

$$\frac{\partial \hat{a}_\varphi}{\partial r} = -\text{sen}\theta\hat{a}_r - \cos\theta\hat{a}_\theta$$

$$\frac{\partial \hat{a}_r}{\partial \varphi} = \text{sen}\theta\ \hat{a}_\varphi$$

$$\frac{\partial \hat{a}_\theta}{\partial \varphi} = \cos\theta\ \hat{a}_\varphi$$

Then, the result of equation (34) is:

$$\nabla^2 E_r = \frac{\partial^2 E_r}{\partial r^2} + \frac{\cos\theta}{r^2 sen\theta}\frac{\partial E_r}{\partial \theta} + \frac{2}{r}\frac{\partial E_r}{\partial r} + \frac{1}{r^2}\frac{\partial^2 E_r}{\partial \theta^2} + \frac{1}{r^2 sen^2\theta}\frac{\partial^2 E_r}{\partial \varphi^2} \quad (43)$$

Finding $\nabla^2 H_r$.

Substituting (29) into (30) and (32) we can write that $\nabla^2 H_r\ is$:

$$\nabla^2 H_r = \frac{\partial}{\partial r}\left(\frac{\partial H_r}{\partial r}\hat{a}_r + \frac{1}{r}\frac{\partial H_r}{\partial \theta}\hat{a}_\theta + \frac{1}{rsen\theta}\frac{\partial H_r}{\partial \varphi}\hat{a}_\varphi\right)\hat{a}_r + \frac{1}{r}\frac{\partial}{\partial \theta}\left(\frac{\partial H_r}{\partial r}\hat{a}_r + \frac{1}{r}\frac{\partial H_r}{\partial \theta}\hat{a}_\theta + \frac{1}{rsen\theta}\frac{\partial H_r}{\partial \varphi}\hat{a}_\varphi\right)\hat{a}_\theta + \frac{1}{rsen\theta}\frac{\partial}{\partial \varphi}\left(\frac{\partial H_r}{\partial r}\hat{a}_r + \frac{1}{r}\frac{\partial H_r}{\partial \theta}\hat{a}_\theta + \frac{1}{rsen\theta}\frac{\partial H_r}{\partial \varphi}\hat{a}_\varphi\right)\hat{a}_\varphi \quad (44)$$

Then, the result of equation (45) is:

$$\nabla^2 H_r = \frac{\partial^2 H_r}{\partial r^2} + \frac{\cos\theta}{r^2 sen\theta}\frac{\partial H_r}{\partial \theta} + \frac{2}{r}\frac{\partial H_r}{\partial r} + \frac{1}{r^2}\frac{\partial^2 H_r}{\partial \theta^2} + \frac{1}{r^2 sen^2\theta}\frac{\partial^2 H_r}{\partial \varphi^2} \quad (46)$$

In agreement with Helmholtz, the equation of wave of E_r and H_r spherical coordinates it is:

$$\nabla^2 E_r + \omega^2 \mu\varepsilon E_r = 0 \quad (47)$$

$$\nabla^2 H_r + \omega^2 \mu\varepsilon H_r = 0 \quad (48)$$

Substituting $\nabla^2 E_r$ e $\nabla^2 H_r$:

$$\nabla^2 E_r = \frac{\partial^2 E_r}{\partial r^2} + \frac{\cos\theta}{r^2 sen\theta}\frac{\partial E_r}{\partial \theta} + \frac{2}{r}\frac{\partial E_r}{\partial r} + \frac{1}{r^2}\frac{\partial^2 E_r}{\partial \theta^2} + \frac{1}{r^2 sen^2\theta}\frac{\partial^2 E_r}{\partial \varphi^2} + \omega^2 \mu\varepsilon E_r = 0 \quad (49)$$

$$\frac{\partial^2 H_r}{\partial r^2} + \frac{\cos\theta}{r^2 sen\theta}\frac{\partial H_r}{\partial \theta} + \frac{2}{r}\frac{\partial H_r}{\partial r} + \frac{1}{r^2}\frac{\partial^2 H_r}{\partial \theta^2} + \frac{1}{r^2 sen^2\theta}\frac{\partial^2 H_r}{\partial \varphi^2} + \omega^2 \mu\varepsilon H_r = 0 \quad (50)$$

Where:

$$k^2 = \omega^2 \mu\varepsilon \quad (51)$$

$$k_c{}^2 = \gamma^2 + k^2 \quad (52)$$

$$\frac{\partial^2}{\partial r^2} = \gamma^2 \quad (53)$$

Then, the result of (49) and (50) equations are:

$$\frac{\partial^2 E_r}{\partial r^2} + \frac{\cos\theta}{r^2 sen\theta}\frac{\partial E_r}{\partial \theta} + \frac{2}{r}\frac{\partial E_r}{\partial r} + \frac{1}{r^2}\frac{\partial^2 E_r}{\partial \theta^2} + \frac{1}{r^2 sen^2\theta}\frac{\partial^2 E_r}{\partial \varphi^2} + k_c{}^2 E_r = 0 \quad (54)$$

$$\frac{\partial^2 H_r}{\partial r^2} + \frac{\cos\theta}{r^2 sen\theta}\frac{\partial H_r}{\partial \theta} + \frac{2}{r}\frac{\partial H_r}{\partial r} + \frac{1}{r^2}\frac{\partial^2 H_r}{\partial \theta^2} + \frac{1}{r^2 sen^2\theta}\frac{\partial^2 H_r}{\partial \varphi^2} + k_c{}^2 H_r = 0 \quad (55)$$

Applying the Boundary Conditions in r=a:

$$\tilde{H}_{\varphi 1} = \tilde{H}_{\varphi 2} = \tilde{H}_{\varphi a} \quad (56)$$

$$\tilde{H}_{\theta 1} = \tilde{H}_{\theta 2} = \tilde{H}_{\theta a} \quad (57)$$

$$\tilde{E}_{\varphi 1} = \tilde{E}_{\varphi 2} = \tilde{E}_{\varphi a} \quad (58)$$

$$\tilde{E}_{\theta 1} = \tilde{E}_{\theta 2} = \tilde{E}_{\theta a} \quad (59)$$

$$\tilde{H}_{\varphi 1} - \tilde{H}_{\varphi 2} = -\tilde{J}_\theta \quad (60)$$

$$\tilde{H}_{\theta 1} - \tilde{H}_{\theta 2} = \tilde{J}_\varphi \quad (61)$$

After applications of the boundary conditions, the Dyadic Green functions are determined, and the complex resonant frequency is obtained numerically. The numerical results are then calculated using computational programs developed in Fortran Power Station and Matlab.

1. Conclusions

A new mathematical full wave TTL-Transverse Transmission Line method, in spherical coordinates, for use in spherical antennas was presented. Numerical results will be presented for the resonant frequency as functions of the diameter and of the dielectric substrate, as PBG -Photonic Band Gap and semiconductor materials.

References

[1] B. Constantine, "Advanced Engineering Electromagnetics", John Wiley&Sons. 1989.

[2] B. Eugene. "Física Matemática", LTC, 1988;

[3] D. Cheng, “Field and wave electromagnetics”, Addison-Wesley, 1989.

[4] D. Marcuse, “Light transmission optics”, Van Nostrand Reinhold, 1972.

[5] D. Pozar, “Microwave engineering”, Addsion-Wesley, 1990.

[6] G. Keiser, “Optical fiber communications”, McGraw-Hill, 1991.

[7]H.Roger, “Time-Harmonic electromagnetic”, IEEE. 2001.

[8] H.C.C.Fernandes and M. C. Silva, “Dynamic TTL Method Applied to the Fin-Line Resonators”, Journal of Microwaves and Optoeletronics, Vol.2, N.o 3, pp.57-66, ISSN 1516-7399, jul. 2001.

[9] H.C.C.Fernandes, “TTL Method Applied to the Fin-line Resonators”, Journal of Eletromagnectic Waves and Applications, MIT-USA, Vol. 15, Nº 7, pp.933-943, July 2001.

[10] H.C.C.Fernandes, R. R. C. Franca and D.B. Brito, “Asymmetric Fin Line and Coupler at Millimeter Waves on PBG Substrate”, Journal of Infrared, Millimeter, and Terahertz Waves”, V. 32,Nº 1, pp. 116-125, Jan. 2011.

[11] J. Jackson, “Classical eletrodynamics”, John Wiley, 1999.

[12] M. Abramowitz, I. Stegun (ed), “Handbook of Mathematical Functions”, Dover, 1965.

[13]M. Sean, “Advanced Mathematical Methods for Scientists and Engineers”, apr. 2001.

[14]S. Mattew, “Numerical techniques in electromagnetics”, 2ª ed. 2001.

[15] M. Abramowitz, I. Stegun , “Handbook of Mathematical Functions”, Dover, 1965.

High-Impedance Surface Absorbers: Theory and Applications

F. Costa[1*], **A. Monorchio**[1]

[1] Department of Information Engineering, University of Pisa, Via G. Caruso, 56122 – Pisa, Italy
[*]corresponding author: filippo.costa@iet.unipi.it

Abstract

A review of the most popular thin absorbing structures based on High-Impedance Surfaces (HIS) is presented. The perfect absorption can be achieved by exploiting either dielectric or ohmic (resistive) losses. The former absorption phenomenon can be achieved by employing a resonant structure, often referred to as Perfect Metamaterial Absorber, comprising for instance a metallic frequency selective surfaces located above a thin grounded dielectric substrate. The metamaterial is able to provide an angularly stable perfect matching in a very limited frequency range as the substrate losses and the dielectric thickness are suitably chosen. Alternatively, if a lossy frequency selective surface is employed in front of a grounded dielectric substrate both narrowband and wideband absorbing structures can be designed by exploiting ohmic losses.

1. Introduction

Recent developments in the synthesis of metamaterials has generated a great interest on thin electromagnetic absorbing materials due to the high number of practical applications [1] - [12]. Thin absorbing structures are beneficial to reduce the radar signature of targets [1], to synthesize power imaging devices [6], [7] or to improve the electromagnetic compatibility of electronic devices [13]. A wide operating bandwidth is one of the main requirements across the microwave range but frequency selective narrowband absorbing structures are desirable in THz range to design novel photodetectors [7], microbolometers [8] and phase modulators [9]. Promising and potentially revolutionary applications of metamaterial absorbers at optical frequencies regard the use of such structures as frequency selective emitters to improve the efficiency of thermophotovoltaic solar cells [10], [11].

A simple structure allowing the synthesis of both narrowband and wideband thin absorbers is a High-Impedance Surface (HIS) [14]. The absorbing panel consists of a lossy or metallic frequency selective surface over a thin grounded dielectric slab. As the suitable amount of loss is introduced in the resonant structure, a perfect absorption can be achieved at a single frequency or across a large band. A ultra-narrowband absorption can be performed by exploiting dielectric losses of the commercial substrates only. This kind of structures are frequently referred to as Perfect Metamaterial Absorbers [12]. On the contrary, if a more wideband performances are needed, resistive losses can be introduced the periodic pattern through lumped resistors or resistive inks.

2. Problem formulation

A 3D sketch of the analyzed absorbing structure is reported in Figure 1. Some of the most common periodic elements are reported in the figure. The analyzed structure is basically a subwavelength resonant cavity characterized by an input impedance approaching to infinite and a reflection phase crossing zero at the resonance [14], [15]. The amount of power absorbed by the resonant cavity at the resonance is determined by the value of the real part of the input impedance since the imaginary part of the input impedance of a lossy structure is close to zero at the resonance . The magnitude of the reflection coefficient of HIS at normal incidence reads:

$$\left|\Gamma\right| \approx \frac{\mathrm{Re}\left\{Z_{HIS}\right\} - \zeta_0}{\mathrm{Re}\left\{Z_{HIS}\right\} + \zeta_0} \qquad (1)$$

where Z_{HIS} represents the input impedance of the absorbing HIS structure and ζ_0 is the characteristic impedance of free space at normal incidence. The input impedance of the HIS structure Z_{HIS} is equal to the parallel connection between the two complex impedances Z_{FSS} and Z_d. The impedances of the grounded substrate and the frequency selective surface in presence of a lossless or even lossy dielectric can be computed analytically on the basis of some well justified approximations [16]. By deriving an explicit expression of the real part of the input impedance of the high-impedance surface, which is directly related to the amount of loss at the resonance, several properties of the HIS absorber having immediate practical implications can be easily extracted.

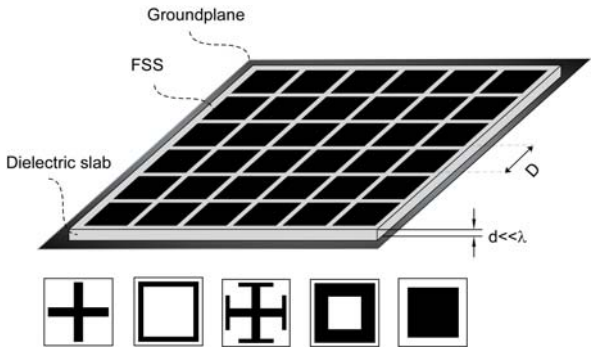


Figure 1- 3D sketch of the HIS absorber with some of the most common unit cell pattern. The periodic pattern can be metallic or resistive.

2.1. Derivation of the real part of the HIS input impedance

In order to derive the expression of the real part of the input impedance Z_H, the expressions of the grounded substrate impedance, Z_d, and the FSS impedance, Z_{FSS}, are separately derived on the basis of simple approximations and then combined. The grounded substrate input impedance is inductive until the substrate thickness is lower than a quarter wavelength whereas the periodic array on top of it is basically an FSS with a capacitive impedance before its proper resonance and with an inductive impedance after it.

Assuming $\varepsilon_r^{'} \gg \varepsilon_r^{''}$, the real and the imaginary part of the input impedance can be expressed as follows [16]:

$$\mathrm{Re}\{Z_d\} \simeq \frac{\zeta_0}{\sqrt{\varepsilon_r^{'}}}\left[\frac{\varepsilon_r^{''}}{2\varepsilon_r^{'}} tg\left(k_0 d\sqrt{\varepsilon_r^{'}}\right) - \left(k_0 d \frac{\varepsilon_r^{''}}{2\sqrt{\varepsilon_r^{'}}}\right)\left(1+tg^2\left(k_0 d\sqrt{\varepsilon_r^{'}}\right)\right)\right] \quad (1)$$

$$\mathrm{Im}\{Z_d\} \simeq \frac{\zeta_0}{\sqrt{\varepsilon_r^{'}}}\left[tg\left(k_0 d\sqrt{\varepsilon_r^{'}}\right)\right]$$

where ζ_0 is the characteristic impedance of free space; k_0 is the free space propagation constant and d is the thickness of the dielectric substrate. The real part of the input impedance depends both on the real and imaginary part of the dielectric permittivity while the imaginary part of Z_d is almost equal to the lossless case.

The impedance of a frequency selective surface can be represented through a series LC circuit and a couple of resistors which take into account both dielectric and ohmic losses [17]:

$$Z_{FSS} = R_0 + R_D + \left(1-\omega^2 LC\right)\Big/\left(j\omega C\right) \quad (2)$$

where C and L represent the capacitance and the inductance of the FSS. The capacitance of an FSS printed on a dielectric substrate is computed by multiplying the unloaded capacitor by the real part of the effective dielectric permittivity due the surrounding dielectrics.

The capacitor formed between the adjacent elements has a loss component since the electric field lines are concentrated in a lossy medium. Such loss component is readily represented by the following series resistor [16]:

$$R_D \simeq \frac{-\varepsilon_r^{''}}{\omega C\left(\varepsilon_r^{'}+1\right)} \quad (3)$$

The FSS series resistor R_D is inversely proportional to the FSS capacitance.

The ohmic resistor connected in series with the aforementioned dielectric resistor can be evaluated by weighting the classical expression of the surface resistance valid for metals or resistive inks with the ratio between metalized area and periodicity of the unit cell [2]:

$$R_o \approx \frac{S}{A}\frac{1}{\sigma\delta} \quad if \quad t < \delta$$
$$R_o \approx \frac{S}{A}\frac{1}{\sigma t} \quad if \quad t > \delta \quad (4)$$

Where t, δ and σ represent the thickness, the skin-depth and the electrical conductivity of the metallic/resistive pattern, respectively. $S=D^2$, D is the cell periodicity and A is the surface area of the lossy element within a single unit cell. The relation (4) implies that the smaller is the scattering area, the smaller is the surface resistance leading to a certain fixed lumped resistance (same amount of loss).

If the FSS is made of copper, ohmic losses obtained according to relation (4) are generally two orders of magnitude lower than the dielectric resistor (3). Conversely, if the metal is replaced with a resistive ink, the resistor assumes values higher than the dielectric resistor. Ohmic losses comes from the currents flowing on an imperfect conductor and they are increasingly important as the working frequency raises. As matter of fact, the ohmic resistor is comparable with the dielectric one in THz range and it dominates across optical regime [18].

The calculation of the unloaded capacitance can be accomplished by retrieving the reflection coefficient of a full-wave simulation [19]. As the substrate thickness is reduced (which is the case of thin metamaterial absorbers) the influence of higher-order (evanescent) Floquet modes reflected by the ground plane must be taken into account by adequately correcting the capacitance and the inductance values [17], [20].

As already remarked, the input impedance of the HIS structure Z_H is equal to the parallel connection between the two complex impedances Z_{FSS} and Z_d. At the resonance of the lossy structure, the imaginary part of the input impedance Z_H crosses the zero. After some simple algebraic operations, the real part of the input impedance Z_H at the resonance is derived [16]:

$$\mathrm{Re}\left\{Z_H^{res}\right\} \simeq \frac{\left(\mathrm{Im}\{Z_d\}\right)^2}{\left(\mathrm{Re}\{Z_d\}+R_O+R_D\right)} \quad (5)$$

By replacing the relations (1), (3), (4) in (5), the real part of the input impedance at the resonance can be explicitly written. The expression in (5) contains all the degrees of freedom of the HIS absorber: it is a function of the FSS capacitance, of the electrical substrate thickness and of the real and imaginary part of the dielectric permittivity. $\mathrm{Re}\{Z_d\}$ is usually much smaller than $\mathrm{Re}\{Z_{FSS}\}$ at the main resonance of the HIS [16].

Depending of the prevalent nature of losses, different type of absorbers can be identified from relation (5):

- $R_D >> R_O$: Ohmic losses negligible with respect to dielectric losses. The loss component is determined by the substrate properties. The substrate thickness and the FSS element needs to be chosen in order to maximize the absorption at the desired frequency. The structure is typically *very narrowband*.

- $R_D \sim R_O$: Both ohmic and dielectric losses contribute to absorption at the resonance. The resistors' values are typically comparable in THz range because ohmic losses start to play a important role also in metallic resonant structures. They can assume comparable values also in the microwave range if low-loss substrates are employed. The structure is typically *very narrowband*.
- $R_O >> R_D$: Ohmic losses are predominant. It is typically the case of lossy frequency selective surfaces manufacture with resistive inks. Ohmic losses due to metallic patterns are predominant also in optical range even if the structure is completely metallic. The structure is typically *moderately narrowband or wideband*.

3. Numerical Examples

a) Narrowband configuration

In this section the difference between HIS absorbers made up of metallic or resistive FSSs are clarified through a numerical example. In Figure 2 the dielectric and the ohmic resistance of the FSS impedance are compared with the real part of the substrate input impedance for a HIS absorber comprising a simple cross shaped FSS. The substrate is a commercial FR4.

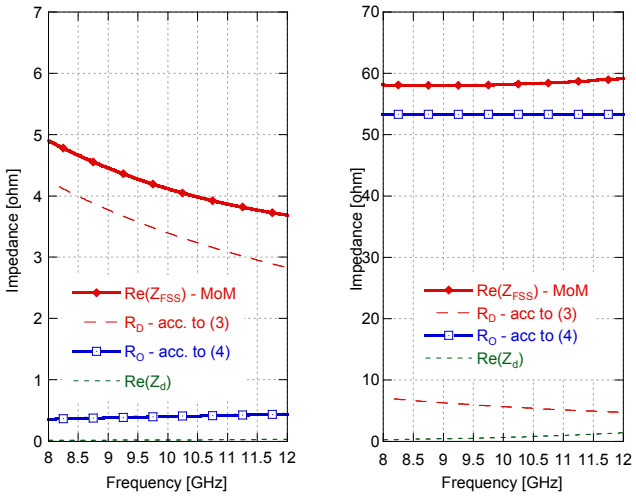


Figure 2 – Dielectric and ohmic components of the real part of the FSS impedance compared with the real part of the grounded substrate input impedance for absorbing structures comprising a metallic or a resistive FSS.

In the former case the dielectric resistor is much higher than the ohmic resistor while in the latter case the losses introduced in the periodic pattern make the ohmic resistor predominant. The use of metallic FSSs forces the choice of the substrate thickness leading, according to relation (5), to value of the real part of the HIS input impedance close to the free space impedance at the resonance. If Figure 3 the reflection coefficient of the thin absorber comprising a metallic and a resistive cross is shown. Due to the very small substrate thickness, the absorption bandwidth of the metallic absorber is very narrow. The use of resistive patterns introduces an additional degree of freedom in the relation (5). For this reason, the substrate thickness leading to a matching of the HIS input impedance with the free space impedance can be arbitrary selected. In order to maintain a perfect absorption at the resonance while the substrate thickness is increased the surface resistance of the FSS needs to be enhanced. The bandwidth of the absorber is directly proportional on the substrate thickness [13]. Anyway, once fixed the substrate thickness, the use of tightly coupled patch arrays allows to maximize the absorption bandwidth [2], [13]. In this case the surface resistance of the metallic pattern is higher with respect to the cross element case. The reflection coefficient of the 1.6 mm thick absorber comprising a resistive patch array is reported in Figure 3 for comparison. The electrical and geometrical parameters of the simulated structures are reported in Table 1.

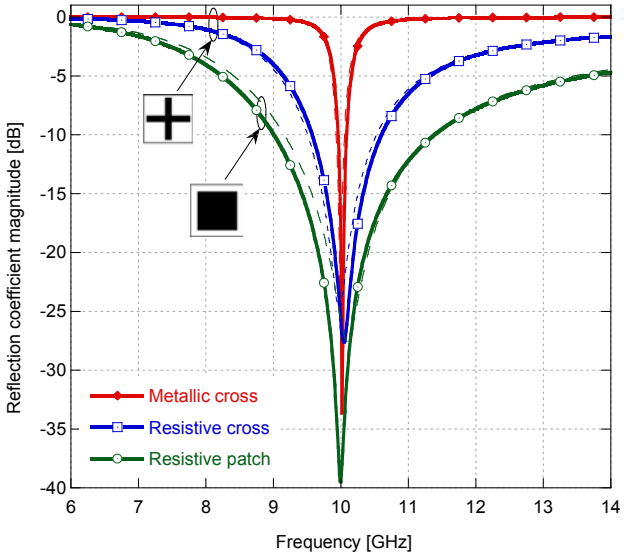


Figure 3 – Reflection coefficient of a High-Impedance Surface comprising both metallic and resistive FSSs. Continuous line: MoM simulation, Dashed line: Transmission line model.

Table 1: Electrical and geometrical parameters of the analyzed absorbing structures.

FSS Element	Z_s [ohm/sq]	d [mm]	D [mm]	ε_r
Metallic Cross	~ 0.03	0.5	8.96	4.5-j0.088
Resistive Cross	5	1.6	8.1	4.5-j0.088
Resistive Patch	40	1.6	3.7	4.5-j0.088

a) Wideband configuration

High-impedance surfaces can be efficiently employed also to design wideband and ultra-wideband absorbers [2], [21]. One layer wideband absorbers are efficiently synthesized through resonant elements as for instance a square loop. In

[21] a capacitive method is adopted to design wideband non-magnetic absorbers employing subwavelength patch type FSSs. The methodology is convenient as the number of resistive layers exceeds two. Indeed, in the latter case, the use of resonant elements would require periodicities exceeding one wavelength and hence the onset of grating lobes. Two layers absorbers comprising resonant FSS, such as for instance a cross frame FSS [19] stacked on a ring FSS, are still more performing than capacitive designs but they require large periodicities. In Figure 4 the reflection coefficient achieved with one-layer, two-layers and three layers resistive HIS absorbers are compared. The most relevant geometrical parameters are reported in Table 2. The table reports also the minimum physical thickness for an ideal absorbing structure characterized by the same absorption properties achieved for each configuration analyzed. The limit is computed according to [22]:

$$d \geq \frac{1}{2\pi^2}\left|\int_0^{\infty} \ln\left|R(\lambda)\right| d\lambda\right| \qquad (6)$$

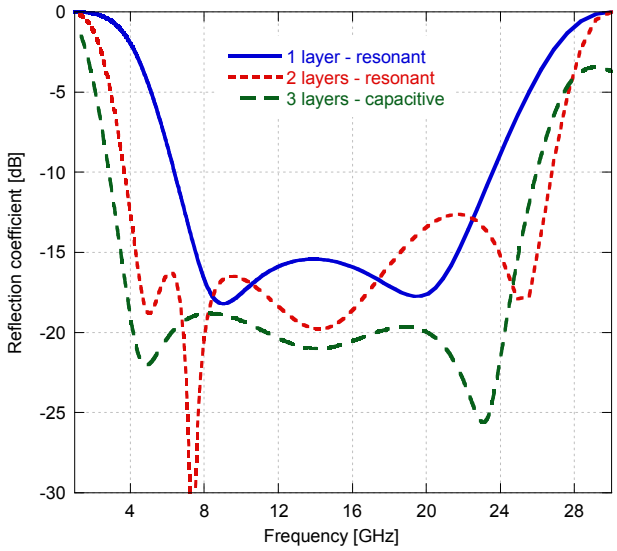


Figure 4 - Reflection coefficient of wideband 1-layer, 2layers and 3-layers HIS absorbers. The 1-layer and 2-layers structures are synthesized by employing resonant FSS elements. The 3-layers structure has been presented in [21].

Table 2: Electrical and geometrical parameters of the analyzed absorbing structures. The physical limit is computed according to [22].

FSS Element	Total thickness [mm]	Physical Limit [mm]	Period. [mm]	FSS element
1-layer	5	4.5	11	ring
2-layers	10	9	20	ring+cross frame
3-layers	15.1	13.3	10	patch

4. Conclusions

The main properties of the electrically this absorber synthesized by employing opportunely designed high-impedance surfaces are discussed by recurring to a simple transmission line model. The differences between an entirely metallic absorber, typically referred to as metamaterial absorber, and HIS absorbers comprising resistive FSSs are highlighted. It is shown that dielectric losses are predominant for metamaterial absorbers while ohmic losses are the most influent in case of resistive losses. The extremely narrow band absorption achievable with metamaterial absorbers is not appealing for application in the microwave range but its employment in THz gap and optical range is promising. Finally the properties of one layer or multi-layers wideband absorbers are presented.

References

[1] Munk, B. A., Frequency Selective Surfaces – Theory and Design, John Wiley & Sons, New York, 2000.

[2] Costa, F., A. Monorchio, G. Manara, "Analysis and Design of Ultra Thin Electromagnetic Absorbers Comprising Resistively Loaded High Impedance Surfaces", IEEE Trans. on Antennas and Propagation, vol. 58, no. 5, pp. 1551-1558, 2010.

[3] Kazemzadeh, A., A. Karlsson, "Multilayered Wideband Absorbers for Oblique Angle of Incidence," IEEE Transactions on Antennas and Propagation, vol.58, no.11, pp.3637-3646, Nov. 2010.

[4] Costa, F., A. Monorchio, "A Frequency Selective Radome with Wideband Absorbing Properties", IEEE Trans. on Antennas and Propagation, in press.

[5] Hong-Kyu J., J. H. Shin, C. G. Kim, "Low RCS patch array antenna with electromagnetic bandgap using a conducting polymer," International Conference on Electromagnetics in Advanced Applications (ICEAA), pp.140-143, 20-24 Sept. 2010.

[6] Yagitani, S., K. Katsuda, M. Nojima, Y. Yoshimura, and H. Sugiura, "Imaging Radio-Frequency Power Distributions by an EBG Absorber," IEICE Trans. Commun., vol. E94-B no.8 pp.2306-2315.

[7] Maier, T. and H. Bruckl, "Wavelength-Tunable Microbolometers with Metamaterial Absorbers," Optics Letters 34 (19), p.3012 (2009).

[8] Kuznetsov, S. A., A. G. Paulish, A. V. Gelfand, P. A. Lazorskiy, V. N. Fedorinin, "Bolometric THz-to-IR converter for terahertz imaging", Appl. Phys. Lett. Vol. 99, 023501, 2011.

[9] Chen, H.-T., W. J. Padilla, M. J. Cich, A. K. Azad, R. D. Averitt, and A. J. Taylor, "A metamaterial solid state terahertz phase modulator," Nature Photonics, vol. 3, 148–151, 2009.

[10] Liu, T. Tyler, T. Starr, A. F. Starr, N. M. Jokerst, and W. J. Padilla, "Taming the blackbody with infrared metamaterials as selective thermal emitters," Phys. Rev. Lett. 107(4), p. 045901, 2011.

[11] Greffet, J. , Controlled Incandescence, Nature 478 (2011) 191.

[12] Landy, N. I., S. Sajuyigbe, J. J. Mock, D. R. Smith, and W. J. Padilla, "Perfect metamaterial absorber," Phys. Rev. Lett., vol. 100, 207402-1-207402-4, 2008.

[13] Del Prete, P., "Reducing Cavity Resonance in Wireless Applications", on RF Globalnet, May 2007.

[14] Sievenpiper, D., L. Zhang, R. F. J. Broas, N. G. Alexopolous, and E. Yablonovitch, "High-impedance electromagnetic surfaces with a forbidden frequency band", IEEE Trans. Microwave Theory Tech., vol. 47, no. 11, pp. 2059–2074, 1999.

[15] Costa, F. , S. Genovesi, A. Monorchio, "On the Bandwidth of High-Impedance Frequency Selective Surfaces," IEEE Antennas Wireless & Propag. Lett., vol. 8, pp. 1341-1344, 2009.

[16] Costa, F., A. Monorchio, "Closed-form Analysis of Reflection Losses in Reflectarray Antennas" IEEE Transaction on Antennas and Propagation, under review.

[17] Costa, F., S. Genovesi, A. Monorchio, G. Manara "Physical mechanisms of a perfect metamaterial absorber studied via an equivalent circuit" submitted to Physical Review B.

[18] Raynolds, E., B. A. Munk, J. B. Pryor and R. J. Marhefka, "Ohmic loss in frequency-selective surfaces", Journal of Applied Physics, vol. 93, no. 9, pp. 5346-5358, 2003.

[19] Costa, F., A. Monorchio, G. Manara "Efficient Analysis of Frequency Selective Surfaces by a Simple Equivalent Circuit Model" IEEE Antennas and Propagation Magazine, in press.

[20] Tretyakov, S. A., C. R. Simovski, "Dynamic model of artificial reactive impedance surfaces," J. of Electromagn. Waves and Appl., vol. 17, no. 1, pp. 131–145, 2003.

[21] Kazemzadeh, A. "Nonmagnetic Ultrawideband Absorber With Optimal Thickness," IEEE Trans. on Antennas and Propagation, , vol.59, no.1, pp.135-140, Jan. 2011.

[22] Rozanov, K. N., "Ultimate Thickness to Bandwidth Ratio of Radar Absorbers," IEEE Trans. on Antennas and Propagation, vol. 48, no. 8, pp. 1230-1234, 2000.

Development of X Band Metamaterial Radar Absorber (*Invited*)

Mahmoud A. Abdalla, Zihrun. Hu

[1]Electronic Engineering Department, MTC University, Cairo, Egypt,
E-mail : maaabdalla@ieee.org
[2] School of Electrical and Electronic Engineering, University of Manchester UK,
E-mail : Z.Hu@manchester.ac.uk

Abstract

A new development of metamaterial applications in radar absorbers for X band is introduced. Two modifications were suggested based on two different approaches which are a new called fan shaped resonator absorber and a modified high impedance metamaterial absorber. Both approaches introduce thin radar absorber (5.3% at centre frequency) with wide bandwidth and high absorption level. The theoretical concepts of each design are explained and validated using full wave simulation. Results illustrate that the new development can achieve wider bandwidth, multiple operating bands; the increase in bandwidth is up to 8 times the conventional one. Moreover, the reported absorbers have capability to operate with different polarizations.

1. Introduction

A great interest has been paid on studying the new characteristics of using artificially constructed structures known as "metamaterials". Metamaterials were introduced for the first time as a theoretical concept in 1967 by the Russian physicist Victor Veselago. He illustrated that if a material can exhibit negative electric permittivity ε and permeability, it has unique electromagnetic properties [1].

The electromagnetic constitutive parameters of a medium, the electric permittivity (ε) and magnetic permeability (μ), are used to describe the material behavior on applying an electromagnetic wave. In 1996, Pendry [2] has realized an artificial 3 D array of thin straight wires that can demonstrate negative permittivity. In 1999, Pendry [3] proposed an artificial magnetic medium consisting of an array of split ring resonators (SRRs) structure which can demonstrate negative permeability. A Composite medium with simultaneous negative permeability and permittivity has been introduced in 2000 [4].

The use of radar absorbing materials (RAM) has been increased in past years in different applications such as communication antennas, anechoic chambers, electromagnetic interference (EMI), electromagnetic compatibility (EMC), and stealth technology. The advance in the use of RAM applications aims to improve their performance in terms of their absorption level, operation bandwidth, enhancement of its physical thickness limitations and their properties for different oblique incident and incident polarizations [5-9].

The design of thin absorbing layers for radar cross section reduction is a challenging task, because the thickness reduction leads to a decrease of the bandwidth. Another problem is the absorber capability for all possible incident polarizations. Metamaterial use in radar absorber has contributed in overcoming the initial problem to introduce very thin metamaterial radar absorber. However, the operating bandwidth and the capability of operation with different polarization is still a challenge.

In this paper, we introduce the novel use of different configurations of metamaterial absorbers for the purpose of enhancement the performance of the RAM. The enhancement includes increasing the absorption level and achieving wide band metamaterial absorber. Comparisons between the performances of the metamaterial absorber based on conventional metamaterial configuration versus our modified ones are introduced. For this purpose, two different RAM were designed at the X band. The full wave electromagnetic wave simulations were employed to calculate the reflection coefficient for a normal incident plane wave.

The commercial software (Ansoft) was employed for co polarized and cross polarized incident wave. Results illustrate that the proposed absorbers can achieve wider bandwidth compared to the conventional one, and capability of operation of different polarizations.

2. Fan Shaped SRR RAM

2.1. Structure and Theory

The design of thin absorbing layers for radar cross section reduction is a challenging task, because the thickness reduction leads to a decrease of the bandwidth. The simplest metamaterial absorber structure based on the use of conventional rectangular shaped SRR, shown in Figure 1 (a) is mainly narrow band and also it works for only for either co polarized and cross polarized wave.

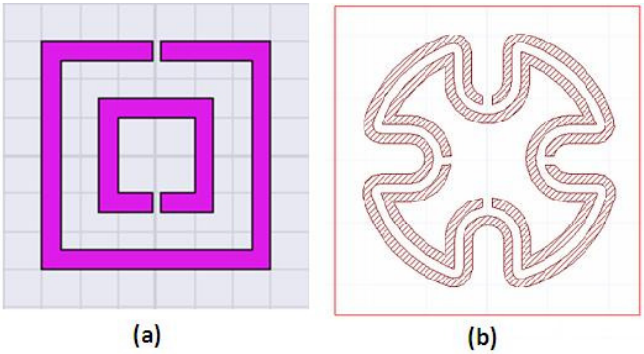


Figure 2: A unit cell geometry of (a) a rectangular SRR (b) a fan shaped SRR

The equivalent circuit of the metamaterial transmission line RAM is shown in Figure 2 (a) and the SRR equivalent circuit is shown in Figure 2 (b). By using a periodic array of SRR over a thin substrate, it can satisfy the absorber equivalent circuit. The principles of achieving wide/multi band absorber may be achieved by proposing new resonator geometry, a fan shaped SRR. The idea of increasing bandwidth of the resonator RAM is based on using SRR geometry that can enhance the parasitic effect so that the whole metamaterial RAM can resonate at different frequencies.

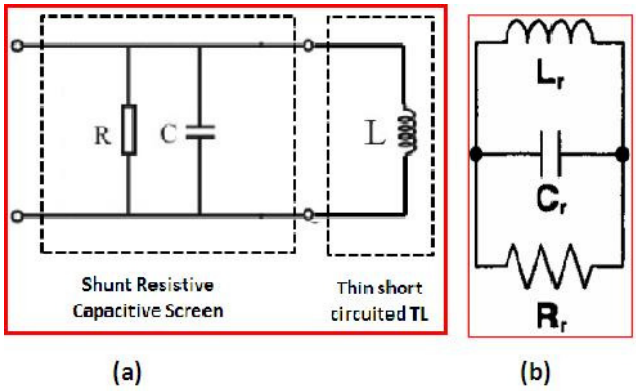


Figure 1: An equivalent circuit of the metamaterial transmission line RAM. (b) A SRR equivalent circuit.

As a suggestion of solving the above drawbacks, in this work, we suggest the use of new fan shaped SRR shown in Figure 1 (b).

For the sake of good comparison, two different RAM layers were designed using conventional SRR and Fan shaped SRR on a lossy FR4 substrate whose relative dielectric constant ε_r= 4.4, a dielectric loss tangent, tan δ = 0.02, and thickness of 1.6 mm. The operating frequency and bandwidth can be designed by the proper selection of the employed unit cell.

2.2. Results

The performance of the fan shaped resonator RAM is presented in this section. The full wave electromagnetic wave simulations were employed to calculate the reflection coefficient for a normal incident plane wave. The commercial software (Ansoft) was employed for co polarized and cross polarized incident wave.

The simulated reflection coefficient for normal incidence of electromagnetic waves upon the metamaterial absorber implemented using rectangular SRR versus the fan shaped SRR are shown in Fig. 3 for the case of co polarized wave.

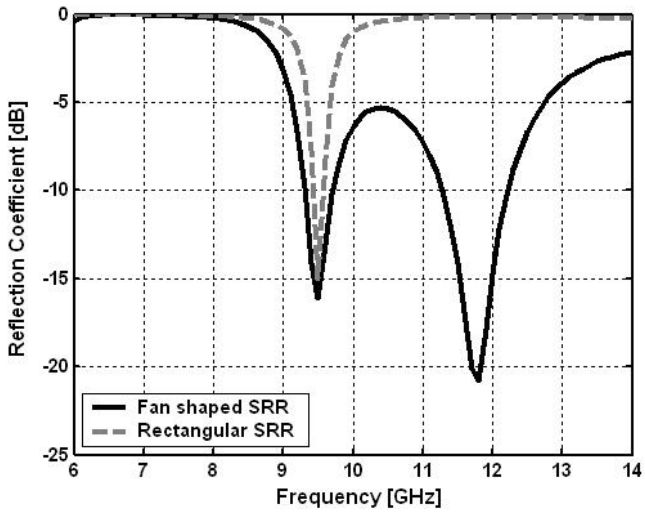


Figure 3: The simulated reflection coefficient of rectangular SRR and fan shaped SRR metamaterial absorber for co-polarized wave.

As illustrated in Figure 3, the conventional rectangular SRR RAM can satisfy electromagnetic wave absorption at approximately 9.5 GHz with close to -15 dB reflection coefficient over a narrow bandwidth (10 dB fractional bandwidth is only 1%). On the other hand, the fan shaped SRR can demonstrate electromagnetic wave absorption centered at the same frequency 9.5 GHz with fractional 10 dB bandwidth of approximately 4.5%. Moreover, the fan shaped SRR absorber can demonstrate a second absorption band at approximately 11.7 GHz which has better than -20 dB reflection coefficient over approximately 10 dB fractional 8 % bandwidth. This means that the fan shaped

SRR metamaterial absorber can increase the bandwidth up to eight times compared to conventional SRR absorber.

Another advantage of the fan shaped is it can satisfy the electromagnetic absorption for either co polarized and cross polarized wave. For confirming of the polarization capability, the simulated reflection coefficients of both aforementioned absorbers assuming a cross polarized incident wave are shown in Figure 4. As shown in the figure, the fan shaped metamaterial absorber can demonstrate almost the same absorption for the two possible cases of co polarized and cross polarized electric field incidence. On contrast to fan shaped case, the conventional rectangular SRR failed to demonstrate any small reflection coefficient over the frequency band of interest as it is nearly 0 dB.

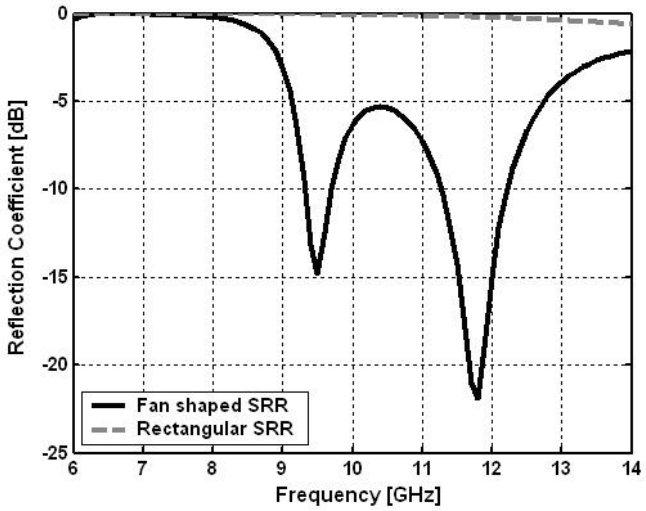


Figure 4: The simulated reflection coefficient of rectangular SRR and fan shaped SRR metamaterial absorber for cross-polarized wave.

3. Slot High Impedance Metamaterial RAM

3.1. Structure and Theory

Another proposal of metamaterial absorber is based on the use of high impedance surface property that can be achieved using metamaterials. This metamaterial absorber is characterized as a thin absorber. Different approaches for the high impedance thin absorber have been proposed by Engheta [9], Kern and Werner [10], and Gao et el using the Sievenpiper high impedance ground plane (HIGP) [11]. However, it is characterized with narrow bandwidth and low absorption level.

In this section we introduce a modified high impedance metamaterial absorber to have wider and higher absorption capability compared to conventional high impedance absorber. Also, the designed RAM is characterized with its capability of operation for both possible cases of polarization.

The layout of the proposed modified high impedance metamaterial absorber is shown in Figure (4). The employed substrate is the same as studied before (FR4 with relative dielectric constant ε_r= 4.4, a dielectric loss tangent, tan δ = 0.02, and thickness of 1.6 mm).

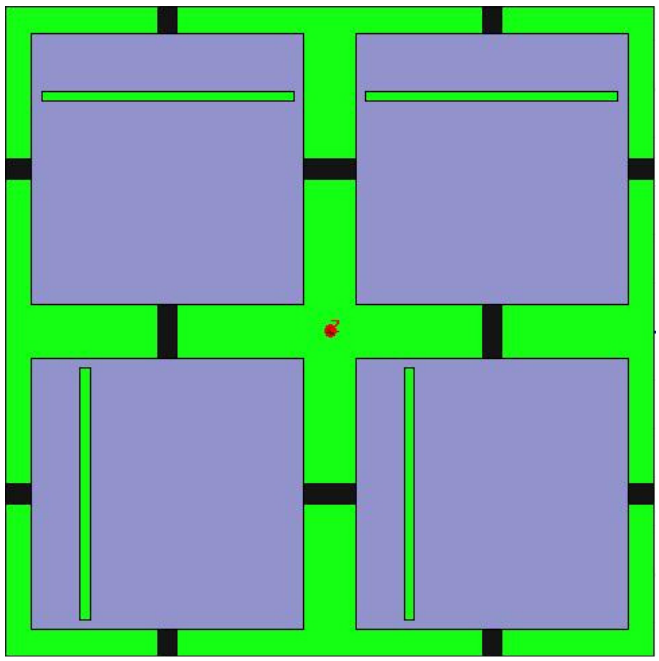


Figure 5 A unit cell geometry of the modified high impedance metamaterial absorber

3.2. Results

The performance of the proposed modified HIGP metamaterial resonator is presented in this section. Similar to previous studied case, the RAM performance was investigated using the electromagnetic full wave electromagnetic wave simulations to calculate the reflection coefficient for a normal incident plane wave. The commercial software (Ansoft) was employed for co polarized and cross polarized incident wave.

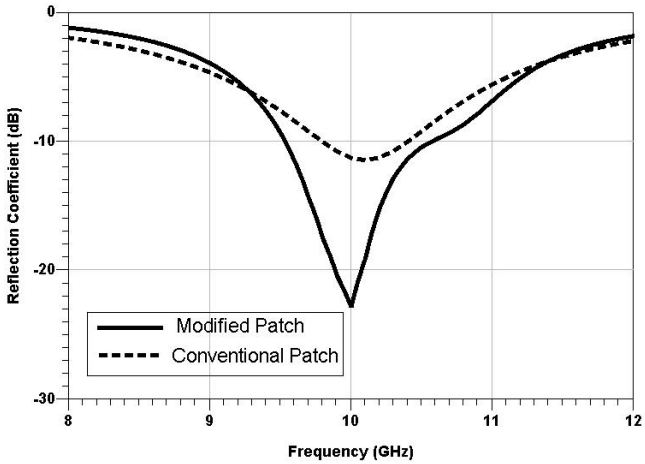


Figure 6: The simulated reflection coefficient of the modified slotted patch RAM

The simulated reflection coefficient of the modified HIGP patch versus conventional one is shown in Figure 6. As shown in the figure, the modification done to the patch has resulted in increasing the return loss at the centre frequency, 10 GHz to better than 20 dB instead of approximately 12 dB. The modified patch RAM has a minimum 10 dB return loss from 9.5 GHz to 10.5 GHz whereas it is only from 9.85 GHz to 10.4 GHz in case of conventional patch RAM. In other words, the fractional bandwidth has increases to 10% instead of 5.5% which is almost double value enhancement.

For the sake of completeness, the modified absorber was re-investigated for the case of cross polarization incident wave. The study is also done as a comparative study versus the conventional HIGP metamaterial patch antenna and the results is illustrated in Figure 7. As shown in the figure, the conventional patch HIGP metamaterial absorber has similar 10 dB narrow bandwidth and its reflection coefficient can not go below -12 dB within this bandwidth; similar to the co polarized incident case illustrated in Figure 5. On the other hand, the modified patch HIGP metamaterial absorber has wider 10 dB which is almost from 9.5 GHz to 10.5 GHz which is approximately the same 10 dB reflection coefficient bandwidth of the modified patch HIGP metamaterial absorber illustrated in Figure 5. However, it is obvious that the modified patch HIGP metamaterial absorber response is different within this bandwidth from the co-polarized incident wave. But, these changes can be accepted since they take places below -15 dB at which only it reveal no more that only 3% of the incident power may reflect back.

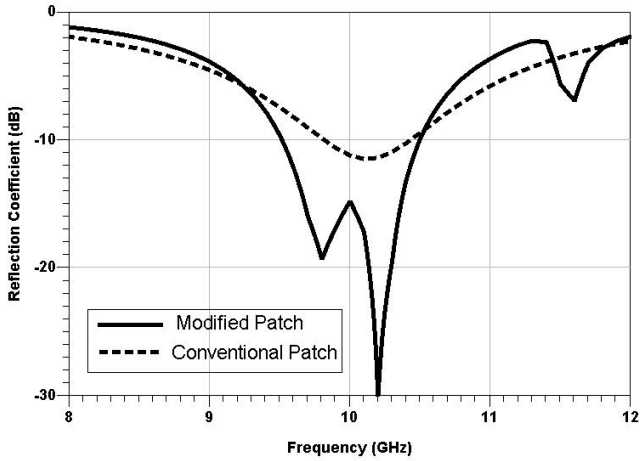


Figure 7: The simulated reflection coefficient of the modified slotted patch RAM

4. Conclusions

A new development for wide/multi band metamaterial radar absorber material using new type of split ring resonator, called fan shaped SRR and modified HIGP metamaterial absorber has been discussed. The performance of the two reported metamaterial absorbers were investigated and compared versus the conventional rectangular SRR absorber/HIGP patch metamaterial absorber. The results confirm that both reported new developed metamaterial absorbers can introduce wider and multiple bands compared to conventional ones. The bandwidth for fan shaped SRR absorber has dual band with approximately 8% bandwidth, up to 8 times increase compared with conventional one. The modified HIGP absorber has almost 10% bandwidth which is almost doubled the conventional one. Also, both absorber absorbers can sustain their performance for both co polarized and cross polarized waves.

References

[1] Veselago V. G. "The electrodynamics of substances with simultaneously negative values of ϵ and &mu," Soviet Physics - Uspekhi, vol. 10, 509-14, 1968.

[2] Pendry J. B., A. J. Holden, D. J. Robbins, and W. J. Stewart, "Low frequency plasmons in thin-wire structures," Journal of Physics: Condensed Matter, vol. 10, 4785-809, 1998.

[3] Pendry J. B., A. J. Holden, D. J. Robbins, and W. J. Stewart, "Magnetism from conductors and enhanced nonlinear phenomena," IEEE Transactions on Microwave Theory and Techniques, vol. 47, 2075-84, 1999.

[4] Smith D. R., W. J. Padilla, D. C. Vier, S. C. Nemat-Nasser, and S. Schultz, "Composite medium with simultaneously negative permeability and permittivity," Physical Review Letters, vol. 84, 4184-7, 2000

[5] Amano M. and Y.Kotsuka, “A novel microwave absorber with surfaceprinted conductive line patterns,” in IEEE MTT-S Digest, Jun. 2002,1193–1196.

[6] Costa F., A. Monorchio, and G. Manara, “Ultra-thin absorber by using high impedance surfaces with frequency selective surfaces,” in Proc. IEEE Int. Symp. on Antennas Propagation., Honolulu, USA, 2007,.861–864.

[7] A. Tennant and B. Chambers, “A single-layer tunable microwave absorber using an active FSS,” IEEE Microw. Wireless Compon. Lett., Vol. 14, No. 1, 46–47, 2004.

[8] Shen Z. and H Wang "On the optimum design of a thin absorbing screen", in Proc, Antennas and Propagation Society International Symposium, Honolulu, USA 2007 6039 – 6042.

[9] Engheta, N.: ‘Thin absorbing screens using metamaterial surfaces’. IEEE Antennas and Propagation Society (AP-S) Int. Symp. and USNC=URSI National Radio Science Meeting, San Antonio, TX, USA, 2002, pp. 16–21

[10] Kern, D.J., and Werner, D.H.: ‘A genetic algorithm approach to the design of ultra-thin electromagnetic bandgap absorbers’, Microw. Opt. Technol. Lett., 2003, 38, (1), pp. 61–64

[11] Q. Gao, Y. Yin, D.-B. Yan and N.-C. Yuan, "Application of metamaterials to ultra-thin radar-absorbing material design", Electronics Lett., 2005, Vol. 41, No. 17, pp 17-18.

An Analytical model for Plasmonic Radar Absorbers

A. Noor[1], and Z. Hu[2]
[1]GIK Institute , Pakistan
[2]University of Manchester, U.K.
[*]corresponding author: adnannoor@giki.edu.pk

Abstract-This paper the frequency response of a plasmonic absorber is investigated using analytical techniques. Effect of thickness, permittivity, permeability and loss tangents of the plasmonic materials is studied using transmission line model for plane wave propagation.

Introduction:

The Metamerials have been widely investigated due to their wide range of applications in electromagnetic/microwaves, as it is possible to realize metamaterials having constitutive parameters not commonly found among natural materials [1].

Plasmonic materials are materials with negative permittivity. Plasmonic materials for microwave range are usually metamaterials, as plasmonic behavior in natural materials is usually found only in visible and ultraviolet range [2,3].

Radar absorbers are traditionally realized through a layer of lossy dielectric or magnetic material [4-7]. The basic idea is to match the impedance of conducting surface covered with the absorber material to that of free space, so that any incoming wave would be completely absorbed[4-7].

Modeling the plane wave propagation as a transmission line[5], a conducting ground plane covered with a material can be considered as a short circuited transmission line. The impedance observed at material/free space interface is then given by[5]

$$Z_i = Z_o \tanh(\gamma l) \quad (1a)$$

$$\gamma = j\omega\sqrt{\varepsilon\mu} \quad (1b)$$

$$Z_o = \sqrt{\frac{\mu}{\varepsilon}} \quad (1c)$$

where Z_o is the characteristic impedance, Z_i the total impedance observed at the material/air interface, l is the thickness of the layer, and gamma the propagation constant of the wave in the material.

By using a lossy material it is possible to construct a radar absorber, by choosing the parameters of layer so that Z_i become equal to free space impedance[5-7]. The same concept can be extended to plasmonic materials and plasmonic absorbers have been reported recently[8,9].

Plasmonic metamaterial would usually consist of artificial resonant structures embedded in free space or a dielectric[2]. Permitivity of a plasmonic material is given be the following equation [2].

$$\varepsilon = \varepsilon_b \left[1 - \frac{f_p^2}{f^2 - i\alpha f_p f} \right] \quad (2)$$

where f_p is the plasma frequency, and alpha is loss coefficient of the plasmonic material(usually about 0.16 for good conductors [3]), and ε_b is the permittivity of the background material in which the plasmonic structures are embedded.. Inserting equation (2) in (1a) would then give

the impedance observed at the absorber layer. Reflection coefficient can then be given by[5].

$$\Gamma = \frac{Z_i - \eta}{Z_i + \eta} \qquad (3)$$

Analytical Results:

Equations (1)-(3) were used to analyze the absorption characteristics of a plasmonic layer over a PEC plane. Plasma frequency of the plasma was assumed to be 10GHz and thickness to be 10mm. The absorber was then analyzed for various values of alpha and permittivity of matrix(background material) . The results are shown in figures 1-3.

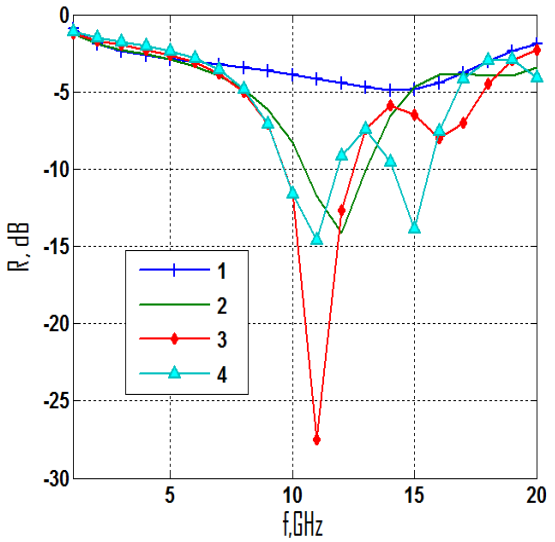


Fig 1: Power reflection coefficient for various values of permittivity, alpha 0.4, permeability 1, thickness 10mm, plasma frequency 10GHz

It can observed from the results that the absorption increases with increasing loss coefficient of the plasma. The optimum value of permittivity in this case is between 2 and 3. This is the result expected form the theory as higher losses would result in higher level of absorption, and the transmission line theory predicts an optimum value for the permittivity of any matching circuit[5-7].

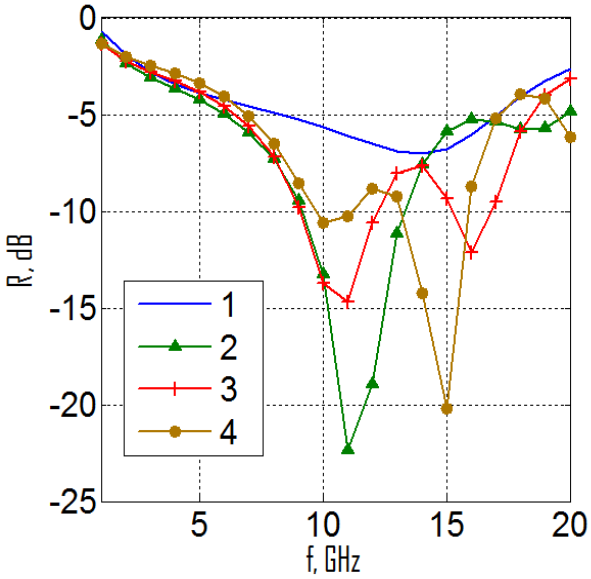


Fig 2: Power reflection coefficient for various values of permittivity, alpha 0.6, permeability 1, thickness 10mm, plasma frequency 10GHz

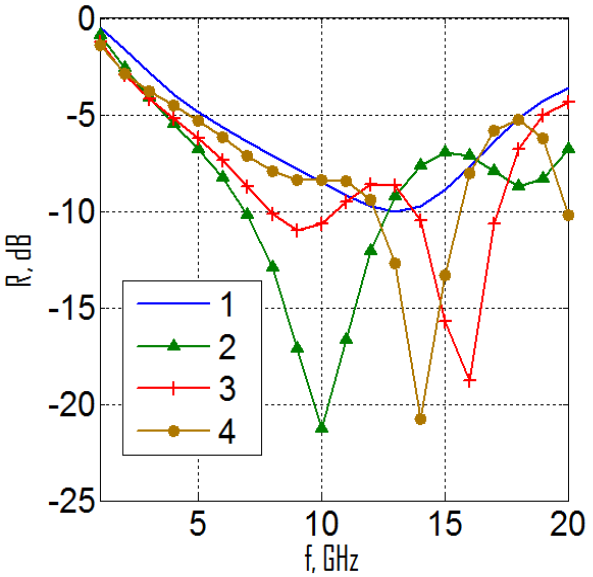


Fig 3: Power reflection coefficient for various values of permittivity, alpha 1, permeability 1, thickness 10mm, plasma frequency 10GHz

Another factor that determines the performance of an absorber is the permeability. In order to study the effect of permeability, the power reflection coefficient was computed for various values of permeability of the matrix material, with alpha 0.6, matrix permittivity 2 and thickness 10mm. The results are shown in Fig. 4

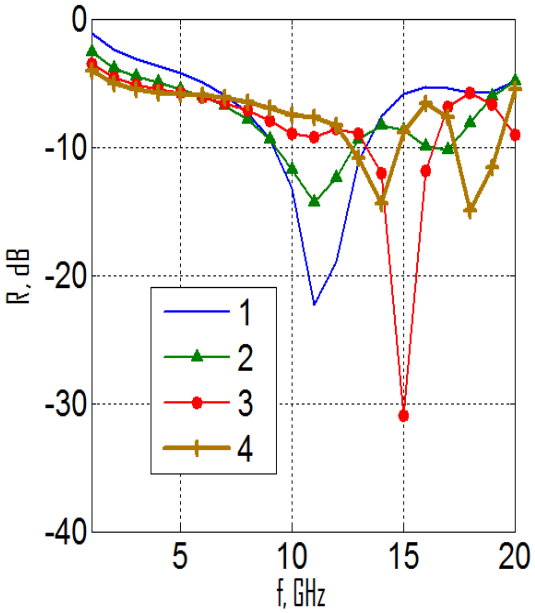


Fig 4: Power reflection coefficient for various values of permeability, permittivity 2, alpha 0.6, thickness 10mm, plasma frequency 10GHz

The result shows the optimum value of permeability to be 1. Another important parameter is the plasma frequency, as it determines the permittivity of a plasmonic material at a given frequency[2]. The power reflection coefficient was then computed for various plasma frequencies. The values for matrix permittivity, permeability, loss factor, and layer thickness were 2, 1, 0.6, and 10mm respectively. The results are shown in Fig.5

From the results it can be observed that the optimum value for the plasma frequency is 10-12GHz.

Furthermore power reflection coefficient was also computed for various values of layer thickness. Results are shown in Fig 6. The absorption bandwidth increases with increasing plasmonic layer thickness, as is expected from the theoretical work done by Rosanov[10].

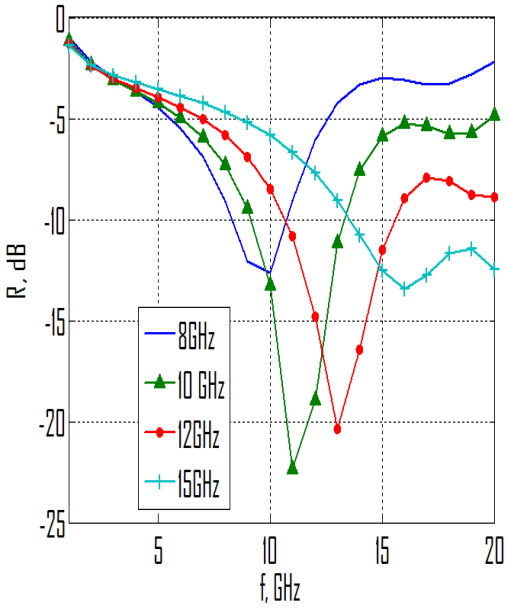


Fig 5: Power reflection coefficient for various values of plasma frequency, permittivity 2, permeability 1, alpha 0.6, thickness 10mm.

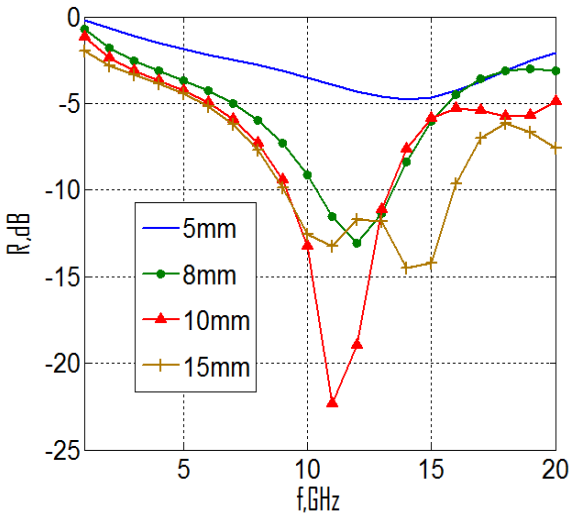


Fig 6: Power reflection coefficient for various values of plasma layer thickness, permittivity 2, alpha 0.6,

permeability 1, plasma frequency 10GHz

Conclusion:

A simple analytical model for analysis was given based on transmission line model of plane wave propagation, and a simple model for plasmonic material permittivity. The model was then used to analyze the plasmonic absorber (i.e. layer of plasma over a conducting plane) for various plasma parameters. This simple model can be used to analyze absorbers based absorbers by first calculating exact or approximate values of the parameters used in equation (1)-(3). This model would be very useful for quick approximate analysis of complex plasmonic structures.

REFERENCES

[1]. Caloz, C, H. Okabe, T. Iwai, and T. Itoh, "Transmission line approach of lefthanded (LH) materials," USNC/URSI National Radio Science Meeting, vol.1, San Antonio, TX, p. 39, June 2002.

[2]. Pendry, J. B. , A. J. Holden, W. J. Stewart, and I. Youngs, "Extremely low frequency plasmons in metallic meso structures," Phys. Rev. Lett., vol. 76, pp.

[3]. Alù, A., and N. Engheta, "Plasmonic materials in transparency and cloaking problems: mechanism, robustness, and physical insights," Optics Express, vol. 15, no. 6, pp. 3318-3332, 19 March 2007.

[4]. W. Dallenbach, and W. Kleinsteuber, "Reflection and Absorption of Decimetre-Waves by Plane Dielectric Layers," Hochfreg Eleklroak, vol. 51, pp. 152-156, 1938.

[5]. Pozar, D.M. "Microwave Engineering," 2nd Ed, John Wiley & Sons, 1999.

[6]. W. W. Salisbury, "Absorbent body for electromagnetic waves," US Patent 2599 944, filed May 11 , 1943, granted June 10, 1952.

[7]. W. H. Emerson, "Electromagnetic wave absorbers and anechoic chambers through the years," IEEE Transactions on Antennas and Propagation, vol. 21,no. 4, pp. 484-490, July 1973.

[8]. Hao, J, J. Wang, X Liu, W. J. Padilla, L. Zhou, and M. Qiu "High performance optical absorber based on a plasmonic metamaterial," Appl. Phys. Lett. 96, 251104 , 2010

[9]. Lv, D., C. Tong, and J. Wang "RCS simulation of plasma-coated targets modeled by NURBS surfaces," in IEEE Asia Pacific Microwave Conference (APMC 2009), pp. 673-676, 7-10 Dec. 2009.

[10]. K.N. Rozanov and S.N. Starostenko , "Numerical study of bandwidth of radar absorbers", Eur. Phys. J. AP 8, pp. 147-151 (1999)

Millimeter-Wave Elastomeric Antennas

Sami Hage-Ali[1], Yovan Orlic[1,*], Nicolas Tiercelin[1], Ronan Sauleau[2], Philippe Pernod[1], Vladimir Preobrazhenski[1,3] and Philippe Coquet[1]

[1]LIA LEMAC: IEMN, UMR CNRS 8520, PRES Université Lille Nord de France, EC Lille Université de Lille 1, 59651, Villeneuve d'Ascq, France
[2]UMR CNRS 6164, Université de Rennes 1, 35042 Rennes cedex, France
[3]LIA LEMAC: Wave Research Center, GPI RAS, 38 Vavilov str., Moscow, 119991, Russia
*corresponding author, E-mail: yovan.orlic@ec-lille.fr

Abstract

This paper describes the realization of mechanically-reconfigurable millimeter wave antennas printed on ultra soft Polydimethylsiloxane (PDMS) elastomeric substrates. The antennas are fabricated using a metal transfer process from silicon wafer to the elastomer. The interest of building antennas on ultra-soft substrate is to achieve mechanical reconfiguration of the antenna parameters. Three mechanically-reconfigurable antennas are presented: two are frequency agile antennas using two different actuation means - the first one is pneumatically actuated, the second one uses electromagnetic actuation and the third antenna presented here is a beam steering antenna. The design and fabrication process are detailed, and computed and measured performances are given for each antenna.

1. Introduction

The worldwide unlicensed 60 GHz-band is very attractive for high speed data links such as multipoint wireless indoor communications, automotive radars, target acquisition systems or wireless sensor networks. Working in this frequency range implies important free space loss but also the possibility to use relatively small and highly directive antennas compared to antennas at lower frequency.

For such applications, specific antenna features are required, and in particular beam steering and frequency agility. In order to attain this versatility, most usual strategies rely on active components such as varactors [1], PIN diodes [2, 3] or MEMS switches [4, 5]. Those solutions tend to add complexity to the system and generally face high cost and important losses as the operating frequency increases. In this context, mechanically tunable antennas represent a promising alternative solution.

We present here several kinds of mechanically-tunable antennas which tuning methods are based on the deformation of the substrate itself. Flexibility of the substrate is therefore a key property. The more flexible the substrate is, the less energy it needs to be deformed. Other mechanical properties also need to be considered, depending on the required integrity and durability of the system, in particular fatigue resistance, given the great number of cycles the system can be submitted to, and shear resistance, because the substrate is generally used in the form of a thin film.

The electromagnetic properties of the substrate are also critical, especially as frequency increases. In our substrate choice, we focused on the essential parameters and targeted a material with low Young modulus (E), low dielectric constant and low loss tangent coefficient.

Many soft substrates have been used to create flexible antennas: Kapton (E = 5.5 GPa) [6], poly-ethyleneterephthalate (PET) (E = 3 GPa) [7], benzocyclobutene (BCB) (E = 2.9 GPa) or Liquid Crystal Polymer (LCP) (E=2.5 GPa) [8]. Tiercelin, Coquet *et al.* have been the first to propose an ultra soft material, Polydimethylsiloxane (PDMS) (E = 1.82 MPa) as a substrate suitable for radiofrequency applications up to millimeter band [9, 10, 11]. Furthermore, PDMS is low cost, biocompatible, chemically inert, transparent and compatible with numerous microfabrication techniques.

Different research groups have then successfully used PDMS in a wide range of RF devices such as integrated conformal antennas [12], stretchable or frequency agile liquid metal based antennas [13, 14, 15] or thin metallization stretchable antennas [16]. All those devices are operating below 10 GHz.

Using methods derived from the work of Tiercelin *et al.*, we have developed a technique to transfer different kinds of conductor (metal or alloy) on thin PDMS film. This method was used to yield mechanically tunable antennas. In the following sections will be presented three tunable radiofrequency devices. The fabrication process is detailed, and the resulting performances are shown.

2. Frequency agile antennas

As introduced before, one solution to take advantage of the wide available spectrum around 60 GHz, consist in using antenna whose resonant frequency can be tuned. We first present the principle of the mechanical tuning of antennas, then two prototypes with different actuation means are shown.

2.1. Principle: Microstrip antenna over an air cavity

Microstrip antennas supported over an air cavity have first been studied by Lee *et al.* in 1984 [17]. They are composed

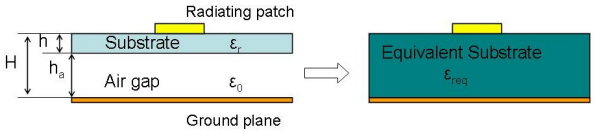


Figure 1: Microstrip antenna suspended over an air cavity

of a radiating element supported by a dielectric over an air gap and a ground plane at the bottom. As seen in Fig. 1, such an antenna can be approximated by the same radiating patch over an uniform substrate having a permittivity:

$$\varepsilon_{req} = \left(\frac{\varepsilon_r(h+h_a)}{h+\varepsilon_r h_a}\right) = \left(\frac{\varepsilon_r H}{h+\varepsilon_r(H-h)}\right) \quad (1)$$

Then, the patch effective permittivity can be calculated for $H < W$, where W is the patch width, by:

$$\varepsilon_{reff} = \frac{\varepsilon_{req}+1}{2} + \frac{\varepsilon_{req}-1}{2}\left(1+12\frac{H}{W}\right)^{-1/2} \quad (2)$$

and the antenna resonant frequency is:

$$F_{res} = \left(\frac{c_0}{2L_e\sqrt{\varepsilon_{eff}}}\right) \text{ with } L_e = L + \Delta L \quad (3)$$

where c_0 is the speed of light in vacuum, L_e is the effective patch length and ΔL is the extension of the physical length of the radiating element due to fringing effect.

ΔL can be approximated using the following equation:

$$\frac{\Delta L}{H} = 0,412\frac{(\varepsilon_{reff}+0,3)(\frac{W}{H}+0,264)}{(\varepsilon_{reff}-0,258)(\frac{W}{H}+0,8)} \quad (4)$$

From those equations, one can see that a variation of the air gap height h_a induces a frequency shift. Two opposite effects are competing. For smaller values of h_a, ε_{req} decreases, thus the resonance frequency F_{res} increases as h_a increases. For higher values of h_a, the predominant effect comes from the increase of ΔL and F_{res} decreases as h_a goes up. Therefore it is possible to shift the antenna resonance frequency by changing the height of the air gap.

The advantages of using such a method to tune an antenna resonance frequency are twofold: the frequency selection can be continuous.

To implement this idea, the next step is to find a suitable actuation mean. A dimensional study can reveal some criteria relevant to the actuator choice:

- The horizontal surface of a 60 GHz patch antenna supported by a membrane is around 1 cm^2. The actuation system should fit in the same dimensions.

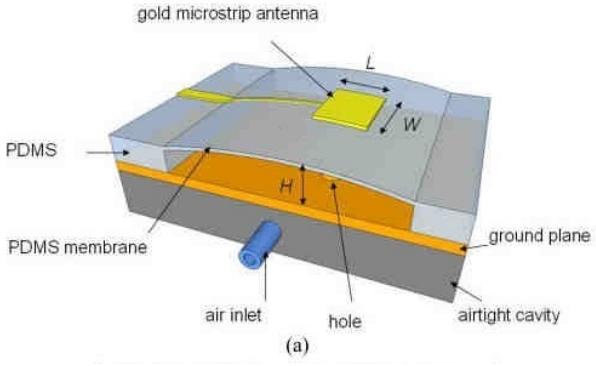


Figure 2: Schematic view of the inflatable antenna

- The available bandwidth ranges from 5 GHz to 10 GHz depending on the region. To get a 8 GHz tunability, the membrane vertical displacement should be around 500 μm.
- To get a 0.1 GHz frequency precision, the spacial precision needs to be around 5 μm.

Two actuation systems potentially matching those criteria have been used and two frequency agile antennas have been designed and characterized.

2.2. Inflatable antenna

The first one is an inflatable antenna, represented Fig. 2, where an airtight cavity is inflated or deflated via an air inlet going through the ground plane. Inflating or deflating the cavity changes the radiating patch height, thus shifting the resonance frequency as explained before.

The radiating patch is fed by a microstrip line. This microstrip line is printed over the bulk part of the PDMS as well as over the membrane part. The effective permittivity shifts at the bulk/membrane transition. In order to keep a matched impedance and limit the losses a special transition had been designed.

2.2.1. Fabrication process

One of the greatest challenges in the fabrication, common to all devices presented here, is the metallization of PDMS. Due to the high thermal expansion of the PDMS, direct metallization is generally hard to realize and give poor results, especially for microwave applications, where high conductivity and thick metallization are required.

Here we use a metallization process based on an upside down approach, using a sacrificial layer. The process (Fig. 3) is the following:

a) First a 100 nm molybdenum sacrificial layer is sputtered on a 3 inches silicon wafer.
b) Then a 40 nm gold seed layer is deposited by evaporation and patterned by lift-off.
c) Using this seed layer a 1.5 μm gold layer is electroplated in a resin mold made by photolitography.

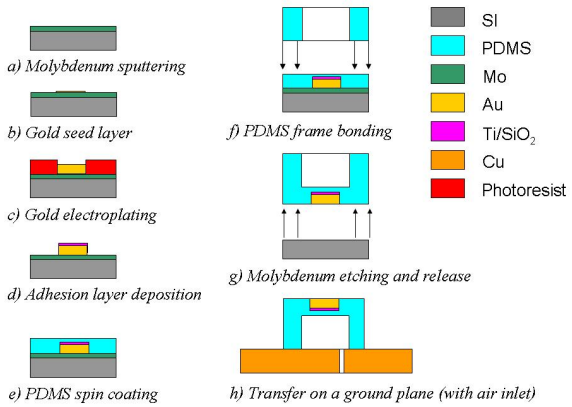


Figure 3: Inflatable antenna fabrication process

d) An adhesion layer is then deposited over the gold layer and patterned again by lift off.
e) This adhesion layer ensures the bonding between the gold conductor and a thin PDMS layer (20 μm) which is spin coated over the structure.
f) On a separate wafer coated with C_4F_8 a thick (180 μm) PDMS layer is spin-coated, cut as a frame and pealed-off the wafer. This layer can then be bonded over the structure: the PDMS has the property to stick to himself by forming covalent bond when activated by a O_2 plasma. The edge of the frame needs to be carefully aligned with the line transition described before.
g) The molybdenum sacrificial layer is etched by hydrogen peroxide releasing the structure.
h) Finally the device is placed on a copper ground plane in which a hole has been drilled allowing the air flow to inflate or deflate the formed cavity.

A final prototype is shown in Fig. 4.

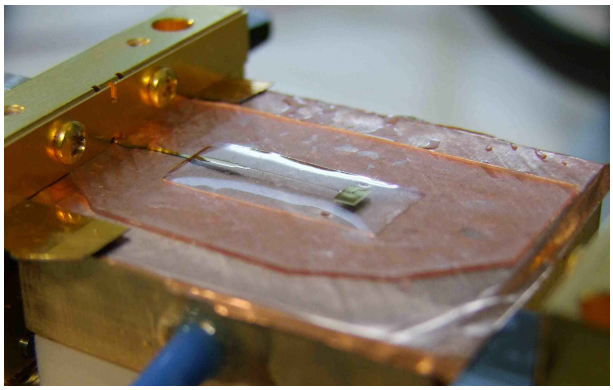


Figure 4: Inflatable antenna under characterisation

2.2.2. *Results*

In the characterization process, the antenna is inflated or deflated using an electronic syringe pump in order to control precisely the quantity of injected fluid. The air volume required to vary from a deflated position (H = 90 μm) to the inflated position (H = 575 μm) is 55 μl. This volume is compatible with the integration of a microfluidic pump [18].

The impedance measurements have been performed using an Anritsu Universal test fixture 3680V coupled to an Agilent E8361A network analyzer with TRL calibration. During this measurement the radiating patch height has been measured using a microscope, first by focusing on the patch, then using a high precision z-translation stage, focusing on the ground plane. This method is 5 micron-scale precise.

The measured reflection coefficients are represented in Fig. 5. Each curve presents two peaks: the first one is the actual resonance frequency, the second one at a higher frequency, is attributed to mechanical mismatches between the test fixture and the feeding line or at the bulk/membrane transition.

There is a 8.2% resonance frequency shift from 55.35 GHz for H = 200 μm to 51.0 GHz for H = 575 μm. The -15 dB bandwidth is larger than 4.8 GHz in all inflated cases.

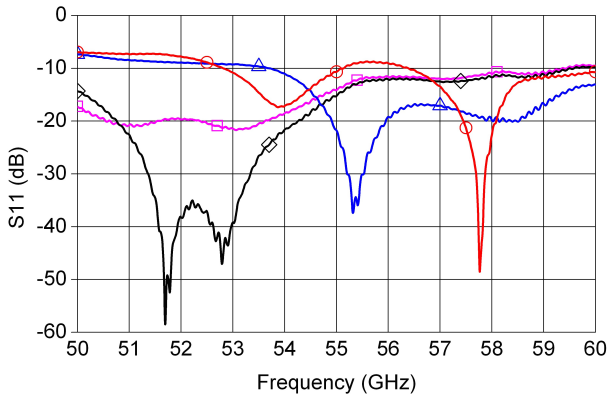


Figure 5: Measured reflection coefficients for the inflatable antenna. Red : H = 90 μm, Blue : H = 200 μm, Black : H = 450 μm, Pink : H = 575 μm

2.3. Iron-Platinum antenna

The second frequency agile antenna is based on the same principle of a radiating patch suspended over an air cavity. The difference is the actuation method. Instead of gold, the radiating patch and feeding line are made of iron-platinum alloy ($Fe_{50}Pt_{50}$, $\sigma = 10.10^6$ S.m^{-1}) which was annealed in a hard magnetic phase and magneto-static actuation is used.

A schematic view of the antenna is represented in Fig. 6:

2.3.1. *Fabrication process*

Another process has been developed to fabricate this antenna. The major difficulty come from the fact that iron-

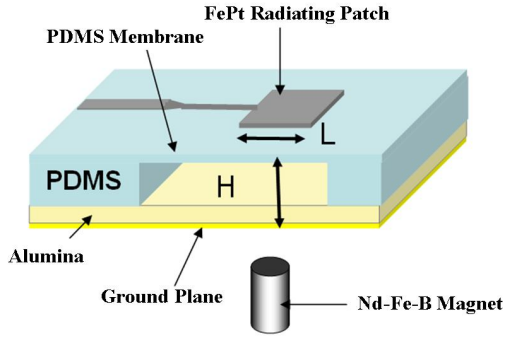


Figure 6: Iron-Platinum antenna principle

platinum needs to be annealed under secondary vacuum at high temperature in order to crystallize in a hard magnetic phase. The manufacturing process is represented in Fig. 7.

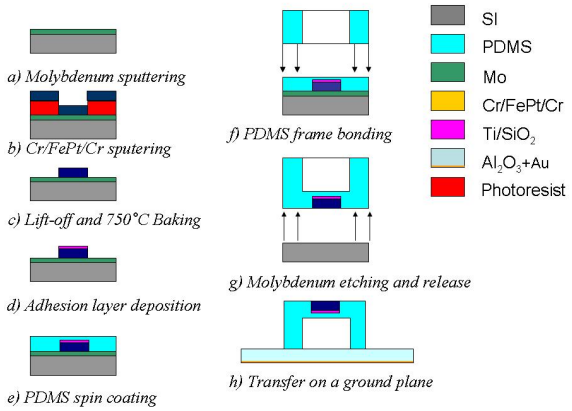


Figure 7: Iron-Platinum antenna fabrication process

a) As in the previous process, a 100 nm molybdenum sacrificial layer is sputtered on a 3 inches silicon wafer
b) Then a 1.2 μm FePt layer is sputtered between two 100 nm chromium layers. The chromium layers are used as protection against diffusion and oxidation that may occur during the annealing process.
c) The deposited metal is patterned by lift-off and annealed at 750 °C under secondary vacuum for 30 min.

The rest of the process is similar to the one used to fabricate inflatable antenna.

d) The same adhesion layer is deposited over the gold layer and patterned by lift off
e) A thin PDMS layer (20 μm) is spin-coated over the structure.
f) A thick PDMS layer cut as a frame is bonded over the thin PDMS layer.
g) The molybdenum layer is etched by hydrogen peroxide releasing the structure.
h) The structure is transferred this time on an alumina strate which has been metallized on one its bottom.

Fig 8 is a picture of the fabricated FePt antenna.

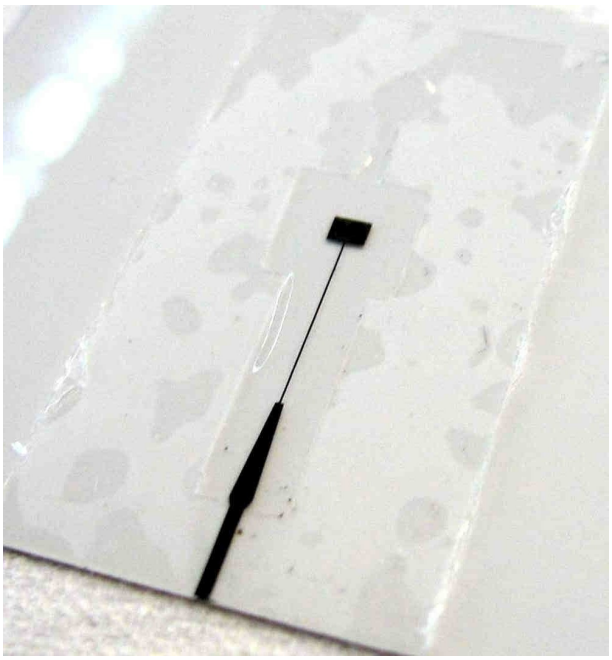


Figure 8: Picture of the iron-platinum antenna

2.3.2. *Results*

First experiments demonstrates the feasibility of this concept even if the process needs to be enhanced, in particular regarding the mechanical resistance of the metallization which tends to break due to stress mismatch between the different layers. Nonetheless some preliminary characterizations have been carried out with early prototypes. The material and method previously exposed are used in the same way. The measured reflection coefficients are represented in Fig 9.

The tunability is limited to 1.9 GHz from 56.6 GHz to 58.5 GHz. This result is quite far from the expected tunability computed with the commercial code HFSS which is 29.8 GHz between 36 GHz for H = 170 μm and 65.8 GHz for H = 500 μm. Due to the brittleness of Iron-Platinum alloy, new devices with a gold layer for a better conductivity and strength are under investigation. Such an improvement in the fabrication process should greatly improve the performance of this antenna.

3. Mechanical beam steering antenna

The third device presented here is a patch array antenna which can rotate thanks to PDMS torsion hinges. It is

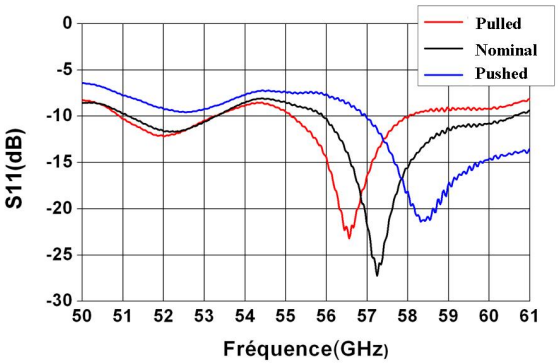


Figure 9: Reflection coefficients for the FePt antenna

shown that, the metallization process and the substrate softness and resistance also allow the fabrication of flexible interconnects such as the one presented in Fig 10. Such a flexible transmission line can be used to feed an antenna and act as a torsion hinge allowing the radiating elements to rotate and be directed toward any direction.

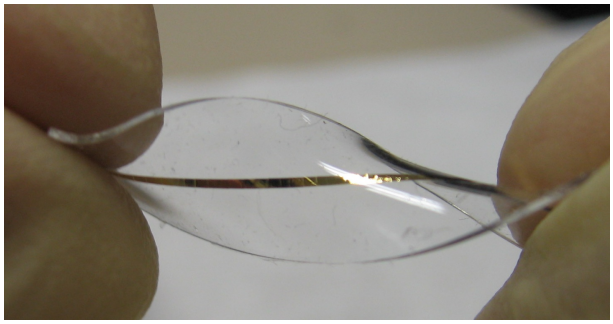


Figure 10: Twisted line on PDMS

3.1. Fabrication process

The fabrication process is similar to previous one. In order to minimize losses and increase gain, the radiating patches are also supported on a membrane . The major difference is that the thick PDMS layer bonded in the sixth step of the process represented in Fig 3 is metallized on its bottom.

Once the PDMS structure is fabricated and released, a metallized silicon pad is bonded on the bottom of the antenna using epoxy glue and silver lacquer to realise the electrical continuity. The structure is then transfered on an epoxy frame used as a support. This assembly process is represented Fig 11.

3.2. Results

An antenna under characterisation is represented in Fig 12.

The most interesting feature of this antenna array is that it exhibits a continuous beam steering. Its gain is constant for steering angles over $\pm 90\,^{\circ}$, far beyond the state of the art

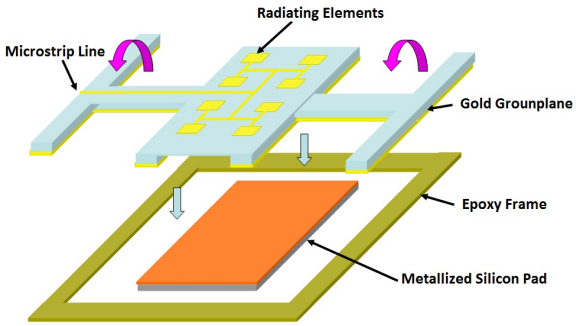


Figure 11: Final assembly of the antenna

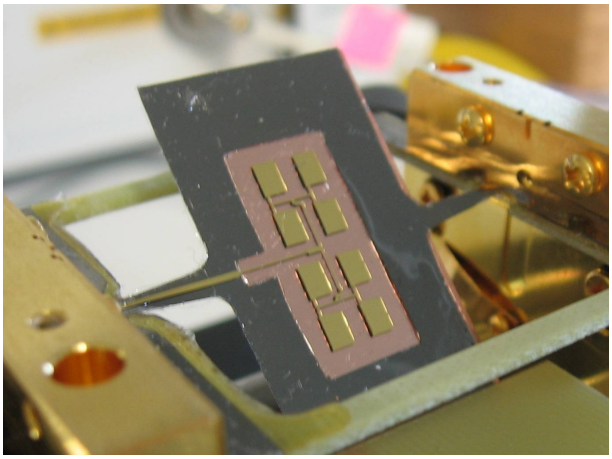


Figure 12: Beam steering antenna under characterization

for conventional beam scanning antennas. The measured reflection coefficients for different angles are represented in Fig 13. These coefficients are practically constant for angle ranging from -90 ° to +100 °.

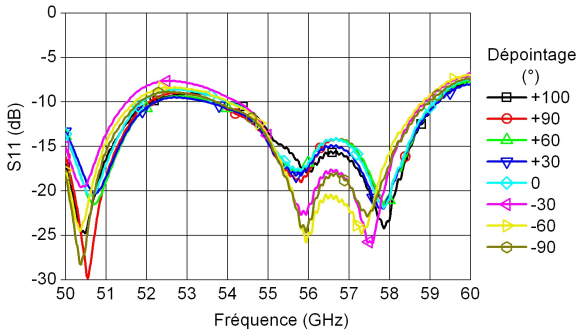


Figure 13: Measured reflection coefficients for the beam steering antenna

4. Conclusions

Several antenna prototypes presented here demonstrate that PDMS is a suitable substrate for millimeter wave devices. The obtained results also demonstrate the interest of mechanical reconfiguration in this field where agility is a key

feature.

As explained above, PDMS easy handling coupled to the metallization process enables the fabrication of a wide range of devices composed of different metals or alloys. This versatility associated with the PDMS extreme softness allow us to envision new millimeter-wave systems with original actuation means.

References

[1] Z. Jin and A. Mortazawi, "An L-band tunable microstrip antenna using multiple varactors," in *Antennas and Propagation Society International Symposium, 2003. IEEE*, vol. 4, june 2003, pp. 524 – 527 vol.4.

[2] H. Jiang, M. Patterson, C. Zhang, and G. Subramanyam, "Frequency agile microstrip patch antenna using ferroelectric thin film varactor technology," in *Antennas and Propagation Society International Symposium, 2009. APSURSI '09. IEEE*, june 2009, pp. 1 –4.

[3] F. Yang and Y. Rahmat-Samii, "Patch antenna with switchable slot (pass): Dual-frequency operation," *Microwave and Optical Technology Letters*, vol. 31, no. 3, pp. 165–168, 2001. [Online]. Available: http://dx.doi.org/10.1002/mop.1388

[4] E. Erdil, K. Topalli, M. Unlu, O. Civi, and T. Akin, "Frequency tunable microstrip patch antenna using RF MEMS technology," *Antennas and Propagation, IEEE Transactions on*, vol. 55, no. 4, pp. 1193 –1196, april 2007.

[5] N. Kingsley, D. Anagnostou, M. Tentzeris, and J. Papapolymerou, "RF MEMS sequentially reconfigurable sierpinski antenna on a flexible organic substrate with novel dc-biasing technique," *Microelectromechanical Systems, Journal of*, vol. 16, no. 5, pp. 1185 –1192, oct. 2007.

[6] H. Khaleel, H. Al-Rizzo, D. Rucker, and Y. Al-Naiemy, "Flexible printed monopole antennas for WLAN applications," in *Antennas and Propagation (APSURSI), 2011 IEEE International Symposium on*, july 2011, pp. 1334 –1337.

[7] H. Kang and J. Song, "Electrically tunable rectangular microstrip antenna," *Electronics Letters*, vol. 46, no. 1, pp. 18–19, 2010. [Online]. Available: http://link.aip.org/link/?ELL/46/18/1

[8] W. Khan, S. Bhattacharya, C. Patterson, G. Ponchak, and J. Papapolymerou, "Low cost 60 GHz RF front end transceiver integrated on organic substrate," in *Microwave Symposium Digest (MTT), 2011 IEEE MTT-S International*, june 2011, pp. 1 –4.

[9] N. Tiercelin, P. Coquet, R. Sauleau, V. Senez, and H. Fujita, "Polydimethylsiloxane membranes for millimeter-wave planar ultra flexible antennas," *Journal of Micromechanics and Microengineering*, vol. 16, no. 11, p. 2389, 2006. [Online]. Available: http://stacks.iop.org/0960-1317/16/i=11/a=020

[10] S. Hage-Ali, N. Tiercelin, P. Coquet, R. Sauleau, H. Fujita, V. Preobrazhensky, and P. Pernod, "A millimeter-wave microstrip antenna array on ultra-flexible micromachined polydimethylsiloxane (pdms) polymer," *Antennas and Wireless Propagation Letters, IEEE*, vol. 8, pp. 1306 –1309, 2009.

[11] S. Hage-Ali, N. Tiercelin, P. Coquet, R. Sauleau, V. Preobrazhensky, and P. Pernod, "A millimeter-wave inflatable frequency-agile elastomeric antenna," *Antennas and Wireless Propagation Letters, IEEE*, vol. 9, pp. 1131 –1134, 2010.

[12] Z. Wang, L. Zhang, Y. Bayram, and J. Volakis, "Multilayer printing of embroidered RF circuits on polymer composites," in *Antennas and Propagation (APSURSI), 2011 IEEE International Symposium on*, july 2011, pp. 278 –281.

[13] M. R. Khan, G. J. Hayes, J.-H. So, G. Lazzi, and M. D. Dickey, "A frequency shifting liquid metal antenna with pressure responsiveness," *Applied Physics Letters*, vol. 99, no. 1, p. 013501, 2011. [Online]. Available: http://link.aip.org/link/?APL/99/013501/1

[14] M. Kubo, X. Li, C. Kim, M. Hashimoto, B. J. Wiley, D. Ham, and G. M. Whitesides, "Stretchable microfluidic radiofrequency antennas," *Advanced Materials*, vol. 22, no. 25, pp. 2749–2752, 2010. [Online]. Available: http://dx.doi.org/10.1002/adma.200904201

[15] S. Cheng, A. Rydberg, K. Hjort, and Z. Wu, "Liquid metal stretchable unbalanced loop antenna," *Applied Physics Letters*, vol. 94, no. 14, p. 144103, 2009. [Online]. Available: http://link.aip.org/link/?APL/94/144103/1

[16] Q. Liu, K. Ford, R. Langley, A. Robinson, and S. Lacour, "Flexible dipole and monopole antennas," in *Antennas and Propagation (EUCAP), Proceedings of the 5th European Conference on*, april 2011, pp. 2052 – 2056.

[17] K.-F. Lee, K. Ho, and J. Dahele, "Circular-disk microstrip antenna with an air gap," *Antennas and Propagation, IEEE Transactions on*, vol. 32, no. 8, pp. 880 – 884, aug 1984.

[18] H. Kim, A. Astle, K. Najafi, L. Bernal, and P. Washabaugh, "A fully integrated high-efficiency peristaltic 18-stage gas micropump with active microvalves," in *Micro Electro Mechanical Systems, 2007. MEMS. IEEE 20th International Conference on*, jan. 2007, pp. 131 –134.